EIGHTH SYMPOSIUM ON

turbulent shear flows

SEPTEMBER 9–11, 1991
TECHNICAL UNIVERSITY OF MUNICH
MUNICH, GERMANY

VOLUME 2

SESSIONS 19–31, POSTER SESSIONS

EIGHTH SYMPOSIUM ON
TURBULENT SHEAR FLOWS
Technical University of Munich
September 9-11, 1991

AN ALGEBRAIC PROPERTY OF THE TURBULENT STRESS AND ITS POSSIBLE USE IN SUBGRID MODELING

M. Germano

Politecnico di Torino - Dip. di Ing. Aeronautica e Spaziale
C.so Duca degli Abruzzi 24,10129 Torino,Italy

ABSTRACT

A new approach to the study of turbulence,based on the general algebraic properties of the *filtered representations* of a turbulent field at different filtering levels,is presented.New quantities, the *generalized central moments* and the *generalized turbulent stresses* are introduced,and an algebraic identity that relates these quantities at different levels is deduced.This new approach extends the statistical approach to a general implicit or explicit filtering operator and it represents in the opinion of the author a simple way to study the *similarity* of the turbulence at different levels. A particular application of this approach to the subgrid scale (SGS) modelling in the large eddy simulation (LES) of turbulent flows,based on the definition and the utilization of the *resolved turbulence*,is discussed.

INTRODUCTION

The idea that stands at the basis of the dynamic SGS models recently tested with success in the LES of the transitional and the turbulent channel flows, Germano *et al.* (1990),and in the LES of compressible flows and transport of a scalar, Moin *et al.* (1991),is very simple. In the LES of turbulent flows the large scale of the turbulent field can be captured,and a large amount of information is collected It is spontaneous to try to utilize this information in order to adapt the SGS model dynamically and in an interactive way to the *real* calculated turbulent field. Loosely speaking,if we interpret the SGS model mainly as a way of introducing an appropriate turbulent viscosity, we could guess on testing procedures that in some way or another check the real amount required by that particular turbulent flow.Such *intelligent* model,that in particular should recognize where the flow is laminar and should account for an eventual backscatter from small scales to larger scales,cannot have,in the opinion of the author,a *universal* form,but in some way or another must actively interact with the resolved scale.In this paper some possible ways to test the resolved scale in order to produce an interactive procedure that dynamically adapt the model to the calculations are presented.They are based on a new algebraic approach to the study of turbulence that in some sense extends to a general filtering or averaging or splitting operator the statistical approach.The need for a new theoretical approach intermediate between the statistical approach and the *coherent structures* approach seems largely requested at the present moment in the study of turbulence. New splitting procedures of the turbulent flow different from the Reynolds decomposition are actually proposed and in use not only in the LES computation of turbulent flows but also in some multi-level techniques and in a lot of experimental procedures where the turbulent field is analyzed in terms of non statistical quantities. The main problem of such decompositions is that the usual algebraic properties of the statistical averages are no longer valid.In particular the mean value of the fluctuations is generally different from zero,so that its fundamental role in the Reynolds decomposition is largely reduced when we consider a general filtering operator. As a consequence the formal analysis of the turbulence in terms of the fluctuations is not so simple as in the case of the statistical average,and a simple extension of the statistical approach can be founded on different quantities defined without recourse to the fluctations.In the following such new quantities,the *generalized central moments*, and in particular the generalized central moments of the second order of the components of the velocity field, the *generalized turbulent stresses*,are defined.They do not involve explicitly the fluctuations,they reduce to the usual statistical expressions in the case of a statistical operator and they give a simple and unified description of the algebraic structure of the filtered turbulent field and the filtered turbulent equations.This new approach is in particular well fitted to examine the *similarity* among the turbulence at different levels.Peculiar to

a decomposition in terms of mean values and fluctuations is the vision of a turbulent field that is the *sum* of different contributions. Peculiar to this new approach is the idea of the *comparison* of different representations,or numerical realizations,at different filtering levels.In particular it will be shown that it is quite spontaneous in a numerical realization to analyze the *resolved turbulence* in order to extract informations useful for an interactive modelling.Fundamental in order to do that is an algebraic identity that relates the generalized turbulent stresses at different levels.In the following all these points are exposed in detail.

FILTERING ALGEBRA.THE GENERALIZED TURBULENT STRESSES. AVERAGING INVARIANCE OF THE FILTERED EQUATIONS.

In the LES of the turbulent flows the large scale of the turbulent field is captured and the residual small scale is modeled The scale of the splitting between small and large scales is dictated by the numerical resolution,and in the physical space it is explicitly given by the grid length.As such the LES theory is intimately associated to the numerical computations,and,as Leonard (1974) pointed out,a LES splitting procedure can be formally represented by a *filter* generally expressed as a convolutional integral applied to the original turbulent field.More generally we will interpret an explicit or implicit filter as a linear operator F that when applied to a turbulent quantity α produces the *filtered representation* $<\alpha>_f$,and it is of some interest to examine the related algebraic properties.Pioneering works on the *filtering algebra* applied to turbulence are the papers of Kampè de Fèriet (1957) and Rota (1960),but their studies were mainly directed to the analysis of the *Reynolds operators*,provided with the well known properties

$$<\alpha<\beta>_f>_f=<\alpha>_f<\beta>_f \qquad (1)$$

$$<<\alpha>_f>_f=<\alpha>_f \qquad (2)$$

The LES operators are not Reynolds operators,and in general the mean value of the mean value is not equal to the mean value.The analysis of the algebraic properties of the *non-Reynolds operators* has been conducted on the same basis of the statistical approach,and in particular the well known procedure of decomposing a turbulent quantity in a mean value and a fluctuation was adopted

$$\alpha=<\alpha>_f+\alpha' \qquad (3)$$

The main problem of turbulence modeling is to express the turbulent stress

$$\tau_f(u_i,u_j)=<u_iu_j>_f-<u_i>_f<u_j>_f \qquad (4)$$

in terms of the resolved filtered quantities.In the case of a statistical Reynolds operator the turbulent stress is simply given in terms of the fluctuations by the well known expression

$$\tau_f(u_i,u_j)=<u_i'u_j'>_f \qquad (5)$$

but when F is a general filtering operator the expression of the turbulent stress $\tau_f(u_i,u_j)$ in terms of the fluctuations is not so simple,Deardorff (1970), Leonard (1974),Schumann (1975).New terms,called the Leonard term and the cross term appear,and the separate modeling of each of them give some problems owing to their intrinsic non-Galileian invariance,Speziale (1985).A different *algebraic* approach to the problem has been followed by the present author,Germano (1986),(1987) and (1990).This approach does not require any decomposition in mean values and fluctuations,but is mainly based on the introduction of new quantities,the *generalized central moments*,Germano (1991),that in some sense extend to the non-Reynolds operators the statistical relations between the *moments* and the *central moments*. Given the turbulent fields $\alpha,\beta,\gamma,.....$,the *moments* are expressed by

$$<\alpha\beta>_f \quad <\alpha\beta\gamma>_f \quad .....$$

and the *generalized central moments*

$$\tau_f(\alpha,\beta) \quad \tau_f(\alpha,\beta,\gamma) \quad .....$$

are defined by the statistical relations

$$\tau_f(\alpha,\beta) = <\alpha\beta>_f-<\alpha>_f<\beta>_f$$

$$\begin{aligned}\tau_f(\alpha,\beta,\gamma) &= <\alpha\beta\gamma>_f-<\alpha>_f\tau_f(\beta,\gamma)\\ &\quad -<\beta>_f\tau_f(\gamma,\alpha)-<\gamma>_f\tau_f(\alpha,\beta)\\ &\quad -<\alpha>_f<\beta>_f<\gamma>_f\\ ..... &= ..... \end{aligned} \qquad (6)$$

The generalized central moments of the second order related to the Cartesian velocity components u_i,u_j

$$\tau_f(u_i,u_j)=<u_iu_j>_f-<u_i>_f<u_j>_f$$

will be in particular called *generalized turbulent stresses*,and we notice that in the case that F is a statistical Reynolds operator they reduce to the well known expressions

$$\tau_f(\alpha,\beta) = <\alpha'\beta'>_f$$

$$\tau_f(\alpha,\beta,\gamma) = <\alpha'\beta'\gamma'>_f \qquad (7)$$

If we now assume that F is commuting with the space and time derivatives.and if we derive from the Navier-Stokes equations the evolutionary equations for the generalized central moments,the result is very simple and surprising at the same time.*In terms of the generalized central moments the filtered equations are exactly the Reynolds equations, so that the algebraic structure of the closure is the same for every linear commuting filter.* This is what we call the *averaging invariance* of the turbulent equations.

THE RESOLVED TURBULENCE AND THE RESOLVED TURBULENT STRESSES

Let us now indicate as usual the average with an overline.The averaged equations for a turbulent incompressible flow are given by the expressions

$$\frac{\partial \bar{u}_j}{\partial x_j} = 0 \tag{8}$$

$$\frac{\partial \bar{u}_i}{\partial t} + \bar{v}\,\frac{\partial \bar{u}_i}{\partial x_j} = \frac{\partial \bar{\pi}_{ij}}{\partial x_j} - \frac{\partial \tau_{ij}}{\partial x_j} \tag{9}$$

$$\bar{\pi}_{ij} = -\bar{p}\delta_{ij} + 2\nu \bar{s}_{ij} \tag{10}$$

where

$$\bar{s}_{ij} = \frac{1}{2}\left(\frac{\partial \bar{u}_i}{\partial x_j} + \frac{\partial \bar{u}_j}{\partial x_i}\right) \tag{11}$$

The generalized turbulent stress τ_{ij} is given by the expression

$$\tau_{ij} = \overline{u_i u_j} - \bar{u}_i\,\bar{u}_j \tag{12}$$

and the evolutionary equations are given by

$$\frac{\partial \tau_{ij}}{\partial t} + \bar{u}_k \frac{\partial \tau_{ij}}{\partial x_k} = \nu \frac{\partial^2 \tau_{ij}}{\partial x_k \partial x_k} + P_{ij} + D_{ij} + \varphi_{ij} - \varepsilon_{ij} \tag{13}$$

where

$$P_{ij} = -\tau_{ik}\frac{\partial \bar{u}_j}{\partial x_k} - \tau_{jk}\frac{\partial \bar{u}_i}{\partial x_k}$$

$$\varphi_{ij} = 2(\overline{p s_{ij}} - \bar{p}\,\bar{s}_{ij})$$

$$\varepsilon_{ij} = 2\nu\left(\overline{\frac{\partial u_i}{\partial x_k}\frac{\partial u_j}{\partial x_k}} - \frac{\partial \bar{u}_i}{\partial x_k}\frac{\partial \bar{u}_j}{\partial x_k}\right)$$

$$D_{ij} = \frac{\partial d_{ijk}}{\partial x_k}$$

$$d_{ijk} = -\{\tau_{ijk} + (\overline{p u_j} - \bar{p}\,\bar{u}_j)\delta_{ik} + (\overline{p u_i} - \bar{p}\,\bar{u}_i)\delta_{jk}\} \tag{14}$$

and τ_{ijk} is the generalized central moment of the third order

$$\tau_{ijk} = \overline{u_i u_j u_k} - \bar{u}_i\tau_{jk} - \bar{u}_j\tau_{ki} - \bar{u}_k\tau_{ij} - \bar{u}_i\bar{u}_j\bar{u}_k \tag{15}$$

We notice that the contracted form of Eq.(13) gives the equation

$$\frac{\partial K}{\partial t} + \bar{u}_k\frac{\partial K}{\partial x_k} = \nu\frac{\partial^2 K}{\partial x_k \partial x_k} + \frac{1}{2}P_{kk} + \frac{1}{2}D_{kk} - \frac{1}{2}\varepsilon_{kk} \tag{16}$$

where K,the generalized turbulent energy,is given by

$$2K = \tau_{kk} \tag{17}$$

and the turbulent energy production $\mathcal{P}$ is given by

$$\mathcal{P} = \frac{1}{2}P_{kk} = -\tau_{kl}\bar{s}_{lk} \tag{18}$$

It is easy to see that in terms of these quantities the algebraic structure of the closure is the same,and the basic ingredients of turbulence modeling can be generally applied to different filters.In particular the Smagorinsky (1963) model, based on a balance between production and dissipation,can be always adopted,provided that we express everything in terms of the particular filtered quantities.This averaging invariance suggests a large *insensitivity* of turbulence modeling to the particular implicit or explicit filter used,and a largely independent algebraic structure of the closure,so that the more important parameter in turbulence modelling remains the *scale*.In the large eddy simulation of turbulent flows the scale can be changed by changing the level of the numerical resolution,so that it could be appealing to recur to *multi-level modelling* in which different scales are introduced. Usually the multi-level procedures are based on spectral *splitting* operators,Tchen (1973), Schiestel (1987),and the term *split spectrum* closures has been also introduced,Launder (1989).Also in this case the approach of the present author is slightly different.If we consider the attitude of a numerical experimenter in turbulence,we notice that he is more interested to the *comparison* between different numerical representations at two different numerical levels than to the decomposition in fluctuations that by definition are unresolved and out of reach.In other words the LES of the turbulent flows is based on the fact that a new *physical* scale introduced in the problem is the grid scale,and from this point of view a possible LES multi-level procedure could be based on two different computations at two different levels with two different length scales and on the comparison of

the results.Obviously to conduct two different LES computations at the same time is not so simple,so that something different could be excogitated.If we are convinced that the generalized turbulent stresses are really the more natural and physical extension of the Reynolds stresses,we could introduce an explicit *test filter* G and extract from the resolved scale new *similar* and homogeneous quantities,the *resolved turbulent stresses* in order to test the *resolved* turbulence. For example we can extract from the resolved scale the resolved turbulent stresses given by the relation

$$\tau_g(< u_i >_f, < u_j >_f) = << u_i >_f < u_j >_f >_g - < u_i >_{fg} < u_j >_{fg} \quad (19)$$

or the resolved turbulent energy,or the resolved production, or the resolved dissipation,or anything that we would like to test.The use that we can do of these quantities is till now undefined,but a simple algebraic identity provides us with some useful information about the physical meaning of the resolved quantities.Let us indicate with FG the new level that we reach by applying to the F-level the test filter G.It is easy to see that,Germano (1990),

$$\tau_{fg}(u_i, u_j) = < \tau_f(u_i, u_j) >_g + \tau_g(< u_i >_f, < u_j >_f) \quad (20)$$

The physical meaning of this algebraic relation is very simple: the turbulent stress at the FG-level

$$\tau_{fg}(u_i, u_j) = < u_i u_j >_{fg} - < u_i >_{fg} < u_j >_{fg} \quad (21)$$

is equal to the G-averaged value of the turbulent stress at the F-level plus the *resolved turbulent stress* $\tau_g(< u_i >_f, < u_j >_f)$ extracted from the resolved level F.We notice that this stress can be explicitly calculated in a Large Eddy Simulation,and in the following the possible use of this algebraic property in subgrid modelling is discussed.

THE INTERACTIVE USE OF THE RESOLVED TURBULENCE IN SGS MODELING

This new approach represents in the opinion of the author a simple way to study the turbulence at different levels and to explore the *similarity* between them.In particular the analysis of the *resolved* turbulence at the resolved scale in a LES computation based on the *resolved turbulent stresses* can be a useful tool for improving and adapting in an interactive way the SGS model to the real turbulent field.We notice that till now it has not been necessary to assume a particular form for the filtering operator F. This point deserves some comments,and first of all we notice that our *algebraic* or *operational* approach formally applies to all linear operators that commute with the space and time derivatives. The statistical operator,the infinite time average

$$< u_i(\vec{x}) >= \lim_{T\to\infty} \frac{1}{2T} \int_{t-T}^{t+T} u_i(\vec{x}, t')\, dt' \quad (22)$$

the finite time average

$$< u_i(\vec{x}, t; T) >= \frac{1}{2T} \int_{t-T}^{t+T} u_i(\vec{x}, t')\, dt' \quad (23)$$

the box average

$$< u_i(\vec{x}, t; l) >= \frac{1}{l^3} \int_x^{x+l} \int_y^{y+l} \int_z^{z+l} u_i(\vec{x}', t)\, d^3\vec{x}' \quad (24)$$

are typical examples.Sharp cut-off filters in the spectral space, volume averages,Gaussian filters

$$< u_i(\vec{x}, t; l) > = \int u_i(\vec{x}', t')\ \mathcal{G}\left(\vec{x} - \vec{x}'; l\right) d^3\vec{x}' dt' \quad (25)$$

where

$$\mathcal{G}\left(\vec{x} - \vec{x}'; l\right) = \left(\frac{6}{\pi l^2}\right)^{\frac{3}{2}} \exp\left(-\frac{6\left(\vec{x} - \vec{x}'\right)^2}{l^2}\right) \quad (26)$$

have been proposed and used in the past and belong to the category of filters considered in this paper, and also a numerical discretization is by itself an *implicit* filter provided with generally unknown properties,Rogallo & Moin (1984). As a consequence the discussion is about prefiltering explicitly or not the equations,in order to remove or not the indeterminacy of the numerical discretization.In our opinion the *algebraic* properties of an homogeneous discretization scheme,an *implicit* filter,are largely the same of an explicit filter.Owing to the *averaging invariance* we think that there is a large insensitivity of the results to the real filter applied,and that the most important point is its *scale* and not its particular explicit or implicit shape.In order to use such strong dependence on scales,a simple multilevel application of the algebraic identity (20) to SGS modeling is exposed in the following. The simplest SGS parameterization of the unresolved turbulent stress $\tau_f(u_i, u_j)$ is given by the Smagorinsky model in which it is assumed that the turbulent dissipation is in equilibrium with the turbulent production.The Smagorinsky model is functionally expressed in terms of the implicitly or explicitly resolved F-scale $< u_i >_f$ and of its characteristic length scale l_f and it contains a *universal constant* c_S

that unfortunately is not so universal and constant as one would like. Evidence exists,Rogallo & Moin (1984),that the Smagorinsky constant decreases in the presence of mean shear, where the large scale mean velocity gradient is probably overestimated and it must be supplemented at the wall by empirical wall functions. In order to extend the range of application of the Smagorinsky model we can improve the consistency of the model with the results that are obtained and to adjust in *real time* the model to them.In doing that we can use the algebraic relation (20).If we indicate symbolically with

$$M(< u_i >_f, < u_j >_f; l_f, c_S) \approx \tau_f(u_i, u_j)$$

the functional expression of the Smagorinsky model at the F-level and with

$$M(< u_i >_{fg}, < u_j >_{fg}; l_{fg}, c_S) \approx \tau_{fg}(u_i, u_j)$$

the corresponding expression at the FG-level,we can *consistently* write on the basis of the algebraic relation (20)

$$\begin{aligned} M(< u_i >_{fg}, < u_j >_{fg}; l_{fg}, c_S) \; &= \\ < M(< u_i >_f, < u_j >_f; l_f, c_S) >_g \; &+ \\ \tau_g(< u_i >_f, < u_j >_f) & \end{aligned} \tag{27}$$

and the more consistent and appropriate Smagorinsky *constant* c_S can be derived. We notice that the *constant* c_S so calculated depends on the position,the time and the indices i, j,so that it is not a *constant* at all As regards the dependence on the indices i, j a scalar procedure should probably only pretend that the turbulent energy production $\mathcal{P}_{fg}$ at the FG-level

$$\mathcal{P}_{fg} = -\tau_{fg}(u_i, u_j) < s_{ij} >_{fg}$$

is consistent with the resolved sample..n this case we can apply the algebraic identity (20) in the contracted form

$$\begin{aligned} \tau_{fg}(u_i, u_j) < s_{ij} >_{fg} \; &= \\ < \tau_f(u_i, u_j) >_g < s_{ij} >_{fg} \; &+ \\ \tau_g(< u_i >_f, < u_j >_f) < s_{ij} >_{fg} & \end{aligned} \tag{28}$$

so that we can write

$$\begin{aligned} M(< u_i >_{fg}, < u_j >_{fg}; l_{fg}, c_S) < s_{ij} >_{fg} \; &= \\ < M(< u_i >_f, < u_j >_f; l_f, c_S) >_g < s_{ij} >_{fg} \; &+ \\ \tau_g(< u_i >_f, < u_j >_f) < s_{ij} >_{fg} & \end{aligned} \tag{29}$$

and a local *isotropic* value of the Smagorinsky constant can be obtained This particular model was proposed by the author,Germano (1990), at the 1990 Summer Program of the Center for Turbulence Research and the interaction theory-computation, Germano *et al.* (1990),has greatly improved this suggested procedure as follows.It was clear from the first numerical results that the dependence on time of the Smagorinsky constant should be eliminated.Such dependence can be eliminated by a time average or a space average if some simmetry plane for the turbulence exists and in the case of homogeneous turbulence a volume average could be the best choice,Moin *et al.* (1991). We notice that the model depends only on the ratio of the filter lengths l_{fg}/l_f,and it goes to zero with the resolved turbulent stress $\tau_g(< u_i >_f, < u_j >_f)$,so that it is able to recognize when the flow is *laminar* at the resolved level. The optimal size of the ratio l_{fg}/l_f is not so critical,Moin *et al.*,and a good choice is 2. This model was implemented by applying explicit spectral cut-offs filters and it was tested *a priori* by using the DNS database of Kim,Moin & Moser (1987) for turbulent channel flow and that of Zang,Gilbert & Kleiser (1990) for transitional flow.In order to determine its accuracy it was also tested *a posteriori* in the LES of transitional and fully developed turbulent channel flow.The results are in satisfactory agreement with the direct simulation data and the model has been recently extended by Moin *et al.* (1991) to the compressible turbulence with excellent results.

CONCLUSIONS

The algebraic identity (20) that relates the generalized turbulent stresses at two different level with the resolved turbulent stress can be interpreted in two different ways.It can be seen as a *consistency* rule that in some way or another can be introduced and used in the turbulence modeling and it can be read as a *similarity* rule between the turbulence extracted by the resolved level and the turbulence at two other different levels Both these interpretations can suggest different uses,and the LES results obtained with the dynamic Smagorinsky model give confidence on useful applications.We notice that these results have been produced in the framework of a new *operatorial* approach to the study of turbulence that extends the Reynolds theory and in some sense is a first step towards a general theory that should go from the direct to the statistical approach.The author is actively involved in such a program since some years,and it is a particular pleasure to acknowledge here the Center for Turbulence

Research of the Stanford University and the NASA Ames.In its confident and lively climate the author has experienced a genuine and stimulating cientific cooperation.
The financial support from the *Ministero Italiano dell'Università e della Ricerca Scientifica e Tecnologica* is greatly appreciated.

References

[1] Deardorff J.W. 1970 *A Numerical Study of Three Dimensional Channel Flow at Large Reynolds Numbers* J. Fluid Mech. Vol.41 pp.453-480

[2] Germano M. 1986 *A Proposal for a Redefinition of the Turbulent Stresses on the Filtered Navier-Stokes Equations* Phys.Fluids 29,2323-2324

[3] Germano M. 1987 *On the Non-Reynolds Averages in Turbulence* AIAA Paper 87-1297

[4] Germano M. 1990 *Averaging invariance of the turbulent equations and similar subgrid scale modeling* CTR Manuscript 116,Center for Turbulence Research,Stanford Univ. and NASA-Ames

[5] Germano M.,Piomelli U.,Moin P.& Cabot W.H. 1990 *A dynamic subgrid-scale eddy viscosity model* In Proc. of the 1990 Summer Program of the Center for Turbulence Research, Stanford Univ. and NASA-Ames,pp. 5-18 Also to appear in the Phys. Fluids A.

[6] Germano M. 1991 *Averaging invariance of the turbulent equations* Submitted to J.Fluid Mech.

[7] Kampè de Fèriet J. 1957 *La notion de moyenne dans la theorie de la turbulence* Rend. Seminario Mat. e Fis. di Milano, Vol. XXVII,pp.167-207

[8] Kim J.,Moin P. & Moser R. 1987 *Turbulence statistics in fully developed channel flow at low Reynolds number* J.Fluid Mech.,Vol 177, pp 133-166

[9] Launder B.E. 1989 *Second moment closure : present ... and future?* Int. J. Heat and Fluid Flow, Vol 10,pp. 282-300

[10] Leonard A. 1974 *Energy Cascade in Large-Eddy Simulations of Turbulent Fluid Flows* Adv. in Geophysics,Vol.18A,pp.237-248

[11] Moin P.,Squires K.,Cabot W. & Lee S. 1991 *A dynamic subgrid-scale model for compressible turbulence and scalar transport* CTR Manuscript 124,Center for Turbulence Research,Stanford Univ. and NASA-Ames

[12] Rogallo R.S. & Moin P. 1984 *Numerical Simulation of Turbulent Flows* Ann.Rev.Fluid Mech.,Vol 16,pp.99-137

[13] Rota G.C. 1960 *Spectral theory of smoothing operators* Proc.Nat.Acad. Sci. USA,vol 46,pp. 863-868

[14] Schiestel R. 1987 *Multiple-time-scale modeling of turbulent flows in one point closures* Phys.Fluids Vol. 30 pp.722-731

[15] Schumann U. 1975 *Subgrid Scale Model for Finite Difference Simulations of Turbulent Flows in Plane Channels and Annuli* J.Comput.Phys. Vol.18,pp.376-404

[16] Smagorinsky J. 1963 *General Circulation Experiments with the Primitive Equations.I The Basic Experiment* Mon.Weather Rev. Vol.91 pp.99-164

[17] Speziale C.G. 1985 *Galilean Invariance of Subgrid-Scale Stress Models in the Large Eddy Simulation of Turbulence* J.Fluid Mech. vol.156 pp.55-62

[18] Tchen C.M. 1973 *Repeated cascade theory of homogeneous turbulence* Phys.Fluids Vol. 16 pp.13-30

[19] Zang T.A.,Gilbert N. & Kleiser N. 1990 *Direct numerical simulation of the transitional zone* In *Instability and transition*,M.Y.Hussaini and R. G.Voigt eds.,Springer-Verlag,New York,283-299

Technical University of Munich
September 9-11, 1991

STOCHASTIC BACKSCATTER IN THE NEAR WALL REGION OF LARGE-EDDY SIMULATIONS

P.J.Mason and D.J.Thomson

U.K. Meteorological Office, London Road, Bracknell,
Berkshire RG12 2SZ, United Kingdom

ABSTRACT

The ability of a large-eddy simulation to represent the large-scale motions in the interior of a turbulent flow is well established but concerns remain for the behaviour close to rigid surfaces. With the exception of low Reynolds number flows, the large-eddy description in the flow interior must be matched to some description of the flow near the surface in which all except the larger scale 'inactive' motions are averaged. This near surface region should be characterised by the usual logarithmic velocity profile, but past simulations have failed to give this profile in the matching region. An obvious failing of the Smagorinsky model is its failure to represent stochastic subgrid stress variations. It is shown here that including these variations leads to a marked improvement in the velocity profile.

INTRODUCTION

In most turbulent flows the transports of heat and momentum are dominated by large-scale motions whose properties depend on some integral characteristics of the flow. As a result, time-average closure techniques which depend on local mean gradients are often inadequate, whilst large-eddy simulations offer the potential for accurate predictions. A large-eddy simulation involves calculating the large-scale turbulent motions explicitly with a three-dimensional numerical model whilst the smaller scale motions are parametrised. Away from boundaries and significant statically stable stratification, this approach seems both rational and is in practice insensitive to the details of the parametrisation of small-scale motions. The rationality arises when the distinction between the large-scale (resolved-scale) and parametrised motions (subgrid-scale) falls within an inertial subrange. In such cases theory and results from applications suggest that a simple eddy viscosity may provide an adequate parametrisation (subgrid-scale model).

The modelling of the near surface region differs considerably from the modelling of the flow interior. In most large-eddy simulations the mesh spacing parallel to surface is constant with distance from the boundary whilst the mesh is usually refined in the vertical near the surface. This refinement does not allow the resolution of the truly three-dimensional motions which occur on a decreasing scale as the surface is approached, but is essential to allow a proper resolution of quasi-two-dimensional motions which occur near the surface and which derive from the 'interior' eddies. The limit to model representation of three-dimensional motions is set by the resolution parallel to the boundary. The subgrid model and/or boundary conditions near the surface thus need to represent the near-surface eddies whose scale varies in proportion to distance from the surface. On the one hand this can be expected to be difficult as, in contrast to the flow interior, it involves the main production scales. On the other hand there are some encouraging factors. At these heights there is a local balance between the ensemble-average turbulence energy production and dissipation. Near the surface, the characteristic scale of the turbulent motions becomes smaller than the scale of the numerical mesh parallel to the surface, and, with this implied volume averaging, there is some hope of the subgrid stresses becoming deterministic functions of the resolved velocity as the surface is approached. The gravest difficulties can be anticipated to be at the 'matching' height where the magnitudes of the resolved and subgrid stresses are comparable. At this height the worst of everything prevails. The subgrid stresses are large and would be expected to have statistical fluctuations.

In this study we examined a typical simulation with a Smagorinsky subgrid model. In common with other such simulations, the simulation fails to maintain the correct logarithmic velocity profile in the matching region, the velocity gradients in this region being too great. A series of simulations with varying resolution and different near-surface mixing-

length descriptions were conducted to try to improve the flow profile in the matching region. No adequate solution to the difficulties was found. Some further simulations were then conducted with a stochastic subgrid model to represent the non-deterministic character of the subgrid stresses. The results obtained show a marked improvement in the near-wall mean velocity and temperature profiles.

MODEL DESCRIPTION

The large eddy simulation technique used in the present study is fairly standard and is based on the Smagorinsky (1963) subgrid model with the subgrid Prandtl number, Pr, taken to be 0.7. In the interior of the flow the subgrid mixing-length l is set equal to a constant l_0 which, according to the theoretical arguments of Lilly (1967), we may relate to a filter scale l_f by $l_f = l_0/C_f$, where C_f is about 0.2. Near the wall l must vary as $\kappa(z + z_0)$, where κ is von Karman's constant and z_0 is the roughness length, in order to provide the correct behaviour near the surface. In the matching region between the near-surface region and the interior we shall consider simple but arbitrary matches such as

$$1/l^n = 1/l_0^n + 1/(\kappa(z + z_0))^n \qquad (1)$$

where n is a constant.

In this study the simulations are confined to two flows in which a logarithmic velocity profile is expected. The first flow considered is a neutral static stability planetary boundary layer with a passive scalar whose source is a constant surface flux. The specific parameters selected are a surface roughness length z_0 of 0.1m and a geostrophic wind U_g of $10ms^{-1}$, with a domain depth of 1200m, a domain length in the x direction of 3200m and a lateral domain width of 1600m. The lateral boundaries are periodic. The number of grid points used is 40 x 40 x 24 in the x,y and z directions. The z direction mesh has a variable spacing with smaller grid intervals close to the surface. The value of l_0 used is 10m and C_s (the ratio of l_0 to the grid spacing) has a value of about 0.2 in the lower third of the domain but decreases to about 0.15 close to the upper boundary.

The second flow considered is very similar but lacks the small complicating influence of the Coriolis force. The flow considered is turbulent flow in a horizontally infinite channel with a stress-free (but rigid) upper surface and constant imposed pressure gradient. The lower rigid non-slip surface is assumed rough with the same value of z_0 as used in the planetary boundary layer case. The channel depth is 1000m. In order to provide high spatial resolution of the eddies critical in determining the lower part of the boundary layer, the length of the domain has been limited to 1000m and the width to 600m. This will clearly cause the loss of significant larger-scale eddies and this must be noted in considering the results. The number of mesh points used are 54 x 54 x 64 so that relative to the planetary boundary layer simulation the resolution has been increased by a factor of about 4 in all three directions. In the interior of the flow Δz is 19m, with most of the mesh refinement occurring below 200m. The various simulations used values of l_0 varying from 2m to 5m, corresponding to values of C_s (based on the grid spacing in the interior) between about 0.13 and 0.32.

SMAGORINSKY MODEL RESULTS

We first consider the neutral static stability planetary boundary layer simulation with the standard Smagorinsky subgrid model and a mixing-length profile given by Eq. (1) with $n = 2$. Fig. 1 shows the vertical profiles of non-dimensional velocity shear S_v and passive scalar gradient S_θ in the lowest third of the boundary layer, where S_v and S_θ are defined by

$$S_v = \left(\left(\frac{\partial \overline{u}}{\partial z} \right)^2 + \left(\frac{\partial \overline{v}}{\partial z} \right)^2 \right)^{1/2} \frac{\kappa(z + z_0)}{u_\tau}$$

and

$$S_\theta = \frac{\partial \overline{\theta}}{\partial z} \frac{\kappa(z + z_0)}{\theta_* Pr}.$$

Here u_τ is the friction velocity and $\theta_* = -H_0/u_\tau$. These quantities should take a value of unity within the strict near-surface logarithmic layer. For further reference the non-dimensional shear obtained from a mixing-length solution of the channel flow problem described above is also shown (the channel and planetary boundary layer flows are of course expected to be very similar near the surface) with the mixing-length given by

$$\frac{1}{l} = \frac{1}{\kappa(z + z_0)} + \frac{1}{l_m} \qquad (2)$$

and $l_m = 80$m. This mixing-length solution is shown to illustrate what might be considered an acceptable variation of non-dimensional shear within the nominally logarithmic region. The simulation results show, for both the velocity and scalar profiles, a severe error. The non-dimensional shear shows a maximum value of about 2 at a height of order the characteristic height of the matching region. Such errors are we believe detectable in all past high Reynolds number simulations of comparable boundary layers.

Noting that the shear stress profile is forced by momentum budget considerations to be realistic we can comment on what features of the simulation may have caused the problem. The most trivial cause would be too small a value of subgrid-scale mixing-length in the matching region. If the resolved motions remain unchanged then a correct velocity profile must be obtainable by use of a suitable value of mixing-length. The other cause might be the resolved motions. Two not entirely separate changes to the resolved motions might resolve the problem. Firstly an increase in the resolved $\overline{uw}$ would cause the subgrid part of $\overline{uw}$ to reduce and hence would reduce the mean velocity gradient. Alternatively an increase in the size of the resolved motion deformation would, for fixed subgrid mixing-length and mean velocity gradient, lead to an increased subgrid shear stress. However, because the shear stress profile is forced to be realistic, the subgrid stress cannot increase and so the mean velocity gradient would decrease. Similar considerations apply to the passive scalar gradients.

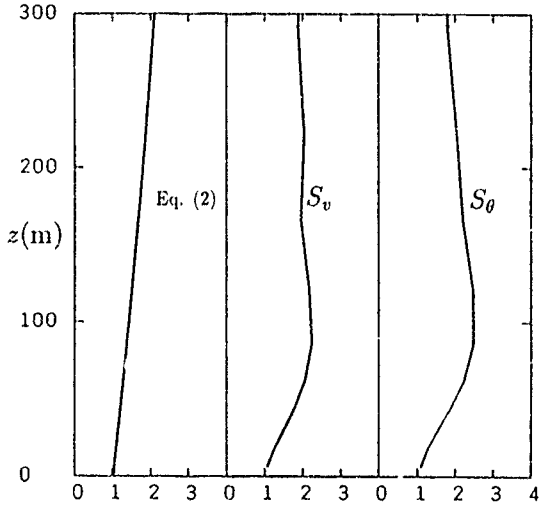

Fig 1: Profiles of the non-dimensional shear and passive scalar gradient in the planetary boundary layer simulation without backscatter. Only the lower part of the domain is shown. Also shown is the non-dimensional shear obtained from a mixing-length solution with the mixing-length given by Eq (2).

In order to investigate this problem a series of simulations of infinite Reynolds number turbulent flow in a free surface channel flow were conducted as described above. The first question to address is whether the error will vanish as the resolution increases. Profile D in Fig. 2 is from a simulation with the same shape for the profile of l as used with the planetary boundary layer simulation but the filter scale and mesh spacings are a factor of about 3 to 4 smaller. The velocity profile shows a qualitatively similar error but the height scale over which it occurs is reduced, and the size of error is also slightly reduced. In consequence of these quantitative changes the solution is more satisfactory but the error remains substantial. Velocity profiles B, C, D, E, F and G show the consequence of varying the mixing-length profile and the filter scale with fixed mesh spacing. These changes alter the height scale of the error but none produce a marked improvement. These tests suggest that perhaps no mixing-length variation with height would be satisfactory.

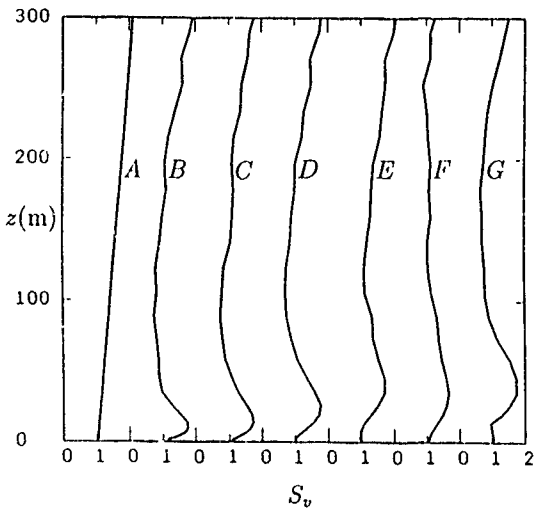

Fig. 2: Profiles of the non-dimensional shear from simulations of flow in a free surface channel (without backscatter). Only the lower part of the domain is shown. Profile B is from a simulation with $l_0 = 2$m and $n = 1$ in Eq. (1). Profile C is from a simulation with $l_0 = 3$m and $n = 1$. Profile D is from a simulation with $l_0 = 3$m and $n = 2$. Profile E is from a simulation with $l_0 = 3$m and with $l = \kappa(z + z_0)/[1 + h^3/(6 + h)]^{1/2}$, where $h = \kappa(z + z_0)/l_0$, replacing Eq. (1). This mixing-length profile was chosen by estimating the profile which would correct profile D, assuming that the resolved stress remained the same. Profile F is from a simulation with $l_0 = 5$m and $n = 2$. Profile G is from a simulation with $l_0 = 5$m and $n = \infty$. Profile A is the non-dimensional shear obtained from a mixing-length solution with the mixing-length given by Eq. (2)

In the matching region the simulation seems to lack resolved stress. A possible cause of this problem is the neglect of statistical fluctuations in subgrid stress. Fluctuations in subgrid stress will scatter energy from the subgrid scales to the resolved scales. This process is further likely to be of maximum importance precisely in the matching region where the subgrid stresses are large but the subgrid length scale is still comparable with the scale of the filter operation.

THE BACKSCATTER MODEL

It has long been recognised that subgrid-scale

stresses should have stochastic fluctuations and that these fluctuations lead to a backscatter of energy from the subgrid scales (e.g. Leslie and Quarini 1979, Kraichnan 1976). We can consider the velocity field as divided into a resolved part $\langle u \rangle$ and a subgrid part $u - \langle u \rangle$ with the subgrid part giving rise to the subgrid stresses. A deterministic subgrid model (such as the Smagorinsky model) relates such subgrid stresses to the gradients of the resolved $\langle u \rangle$, $\langle v \rangle$ and $\langle w \rangle$ fields. If we consider that the subgrid-scale eddies have a characteristic length scale l and characteristic time scale T, then, from consideration of the statistics of forming the average stress over a volume of scale l_f from eddies of scale l, the variance of the stress (for a fixed resolved velocity field) will, for $l \ll l_f$, be proportional to $(l/l_f)^3 u_{*l}^4$, where u_{*l} is a local subgrid turbulent velocity scale. Also, if l is of order l_f we expect the stress variance to be of order u_{*l}^4. In both cases the stress will vary on a time scale T. Based on these ideas we assume a stress variance $\sigma_{stress}^2 \propto (l/l_f)^3 u_{*l}^4$ and a consequent rate of energy backscatter given by

$$\frac{\sigma_{stress}^2}{l_f^2} T \propto \frac{l^3}{l_f^5} u_{*l}^4 T.$$

Noting that $T \propto l/u_{*l}$ and that the dissipation ϵ is proportional to u_{*l}^3/l, we obtain an energy backscatter rate

$$C_B \left(\frac{l}{l_0}\right)^5 \epsilon.$$

Here C_B is a constant which is expected to be of order unity.

Considering the application of the filter operation to a turbulent flow, it is physicaliy clear that if the filter is applied to widely separated flow volumes then the values of subgrid stress fluctuations will be uncorrelated. If however we consider points closer in space than the filter scale, the subgrid stress fluctuations will be correlated. We therefore have a random stress field varying on the filter scale. On scales greater than the filter scale the random stress values imply an energy backscatter with a k^4 spectrum in accord with theoretical expectations (Kraichnan 1976).

In implementing the backscatter, we follow Leith (1990). Instead of introducing random stresses we adopt a random forcing derived from a vector potential. The spatial spectrum of the potential is white on scales greater than the filter scale leading to the desired k^4 spectrum of the energy backscatter. The random stresses are uncorrelated from one time-step to the next and have a magnitude chosen to ensure that the rate of energy backscatter is correct. Backscatter of scalar variance was also included for completeness; however, as a result of the passivity and linearity of the scalar, this has no influence on the mean profiles.

An estimate of C_B can be made using EDQNM theory (Chasnov 1991). Using the backscatter expressions in Chasnov (1991) a value of $C_B = 1.4$ is obtained for an infinite inertial subrange (Chasnov private communication). In this study C_B is found to have profound effects and we are able to see what value of C_B gives the best results. As noted below, a value of about 1.4, when used with $n = 2$ in Eq. (1), is found to be optimal. Owing to the various assumption in the implementation this empirically determined value should not be considered precise. We are however encouraged by the evidence that C_B is of order unity and in agreement with Chasnov's value.

RESULTS OBTAINED WITH BACKSCATTER

The backscatter model described above has been applied in simulations of the neutral static stability planetary boundary layer. Fig. 3 shows the resulting vertical profiles of non-dimensional velocity shear and passive scalar gradient for $n = 2$ and $C_B = 1.4$. They can be compared with the profiles in Fig. 1 obtained without backscatter. The simulation with backscatter has a realistic velocity profile. The scalar profile is also very much improved and we note the possibility that an accurate profile might require the Prandtl number in the subgrid model to vary in the matching region.

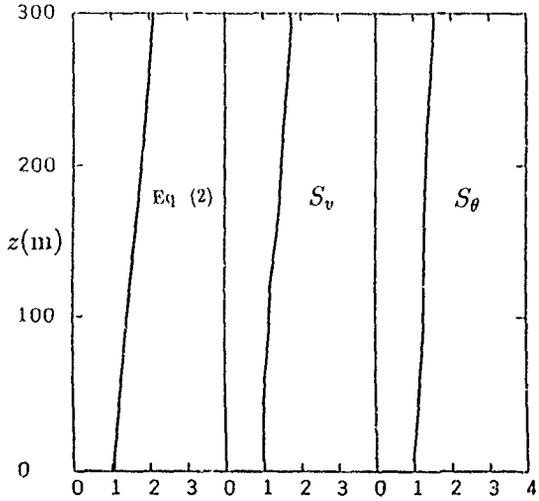

Fig. 3. Profiles of the non-dimensional shear and passive scalar gradient in the planetary boundary layer simulation with backscatter. Only the lower part of the domain is shown. Also shown is the non-dimensional shear obtained from a mixing-length solution with the mixing-length given by Eq. (2).

In the simulation without backscatter the sur-

face stress u_*^2 has a value of 0.141 (Geostrophic drag coefficient $C_G = 1.41 \times 10^{-3}$) whilst with backscatter the surface stress increases to 0.189 ($C_G = 1.89 \times 10^{-3}$). This latter value is in better agreement with observations, with the Rossby number similarity coefficients estimated by Grant (1986) suggesting a value of $C_G = 2.0 \times 10^{-3}$ (Grant 1986) for these conditions. We note the limited resolution used in the present study and do not seek detailed comparison with planetary boundary layer data.

The conclusion here is that the backscatter has had entirely beneficial effects. Other flow statistics either show little modification or are improved. It is perhaps especially significant that the velocity gradient problem did not improve significantly with increased resolution. Without remedy, this problem would seriously impair the value of high Reynolds number simulations. The success of the backscatter model gives hope that the optimism concerning the many future applications of large-eddy simulation is well founded.

Future high resolution studies should allow more careful refinement of the stochastic model. In particular it would seem desirable to quantify the backscatter process by analysis of high resolution velocity fields in either direct or large-eddy simulations.

REFERENCES

Chasnov J.R. 1991 Simulation of the Kolmogorov inertial subrange using an improved subgrid model. *Phys. Fluids*, A**3**, 188-200.

Grant A.L.M. 1986 Observations of boundary layer structure made during the KONTUR experiment. *Q. J. R. Meteorol. Soc.*, **112**, 825-841.

Kraichnan R.H. 1976 Eddy viscosity in two and three-dimensions. *J. Atmos. Sci.*, **33**, 1521-1536.

Leith C.E. 1990 Stochastic backscatter in a subgrid-scale model: Plane shear mixing layer. *Phys. Fluids*, A**2**, 297-299.

Leslie D.C. and Quarini G.L. 1979 The application of turbulence theory to the formulation of subgrid modelling procedures. *J. Fluid Mech.*, **91**, 65-91.

Lilly D.K. 1967 The representation of small-scale turbulence in numerical simulation experiments. *Proc. Tenth IBM Scientific Computing Symp. on Environmental Sciences*, Thomas J. Watson Research Center, Yorktown Heights, 195-210.

Smagorinsky J. 1963 General circulation experiments with the primitive equations: 1. The basic experiment. *Mon. Weather Rev.*, **91**, 99-164.

TURBULENT SHEAR FLOWS
Technical University of Munich
September 9-11, 1991

LARGE EDDY SIMULATION OF FULLY-DEVELOPED TURBULENT PIPE FLOW

F. Unger and R. Friedrich

Lehrstuhl für Fluidmechanik
Technische Universität München, Germany

ABSTRACT

An investigation of the fully-developed, statistically stationary, axisymmetric turbulent flow through straight circular pipes is presented using the large eddy simulation (LES) technique. This flow offers the simplicity of inhomogeneity of the mean quantities in one direction only. The simulation is done in a cylindrical coordinate system. Special attention is paid to the singularity at the pipe center line. To verify the quality of the simulations, statistical results for high Reynolds number are compared with experimental data of Laufer (1954), Lawn (1971) and Perry & Abell (1975) and good agreement is obtained. In addition the instantaneous turbulent flow field is visualized and discussed.

NOMENCLATURE

C_1, C_2	constants of the SGS model
$D_{\alpha\beta}$	deformation tensor
E_{SGS}	subgrid scale energy
p	pressure
R, L	pipe radius and length
Re	global Reynolds number, $Re = u_{cl}2R/\nu$
Re_τ	Reynolds number, $Re_\tau = u_\tau R/\nu$
u_{cl}, u_b, u_τ	center line,bulk flow and friction velocity
$v_\alpha, v_z, v_\varphi, v_r$	velocity components
Δ	length scale
ΔA_α	grid cell surface
ΔV	grid volume
ν, ν_{turb}	kinematic and turbulent viscosity
$\xi_\alpha, z, \varphi, r$	coordinate directions (longitudinal, circumferential, radial)
$\tau_{\alpha\beta}$	shear stress tensor
$\delta_{\alpha\beta}$	Kronecker symbol
$<\phi>$	statistical mean value
$\overline{\phi}$	surface or volume averaged (GS) quantity
ϕ'	deviation from grid scale quantity
ϕ''	(Reynolds) fluctuating quantity

INTRODUCTION

The fully-developed, statistically axisymmetric turbulent flow through straight circular pipes has been the subject of numerous investigations in the past which were mostly of experimental nature. Some of these studies show differences in the reported rms-turbulence level of up to 25% which are due to insufficient flow development length, ill-conditioned hot-wire calibration method, inaccuracy in wall-distance measurement and several other factors. This is important to know when computational results are judged on the basis of such data.

One numerical study, namely that of Leonard & Wray (1982), seems to us remarkable because it treats the singularity on the pipe axis in a rigorous manner and presents a new numerical technique in which spectral expansions of the velocity components in the azimuthal and streamwise directions and global polynomials in the radial direction are used. Tests have been performed for a Reynolds number of 3000 corresponding to a flow regime where interesting transitional phenomena occur. One drawback of this new method is its limitation to periodic flows which means that practical flow simulations like sudden expansions and contractions or vortical flow leading to breakdown cannot be handled. Such complex flow situations may be suitably treated with finite difference techniques like the present provided a proper way is found to take care of the singularity on the axis. The studies of Orszag & Patera (1983) and Priymak, Rozhdestvensky & Simakin (1982) are like Leonard & Wray's work direct simulations at very low Reynolds number.

We do not know of any numerical investigation of the instantaneous high Reynolds number flow field in a straight pipe. To our knowledge the present paper presents the first large eddy simulation of such a flow.

In the following sections we discuss the filtered equations and the subgrid scale model, the integration technique along with boundary and initial conditions. The results for a global Reynolds number of 50000 comprise statistical as well as instantaneous flow quantities.

BASIC EQUATIONS

The equations describing the resolvable (grid scale, GS) flow quantities are derived from the integral conservation equations for mass and momentum applied to a finite grid volume ΔV ('volume balance procedure', Schumann (1975)). The GS quantities are defined as averages over the grid volume ΔV, or their corresponding surfaces ΔA_j.

Using a cylindrical grid and staggering of variables the filtered equations have the following non-dimensional form:

Mass:

$$\sum_\alpha \left(\Delta A_\alpha \overline{v_\alpha}\,|_{(\xi_\alpha+\Delta\xi_\alpha/2)} - \Delta A_\alpha \overline{v}_\alpha\,|_{(\xi_\alpha-\Delta\xi_\alpha/2)}\right) = 0\,,$$

$$\xi_\alpha = (z, \varphi, r)\,, \tag{1}$$

Momentum:

$$\begin{aligned}
&\Delta V \frac{d\overline{v_\alpha}}{dt} + \\
&\sum_\beta \Big(\Delta A_\beta \left(\overline{v_\alpha}\,\overline{v_\beta} + \overline{v'_\alpha v'_\beta} + \overline{p}\delta_{\alpha\beta} - \overline{\tau_{\alpha\beta}}\right)|_{(\xi^*_\beta+\Delta\xi_\beta/2)} \\
&- \Delta A_\beta \left(\overline{v_\alpha}\,\overline{v_\beta} + \overline{v'_\alpha v'_\beta} + \overline{p}\delta_{\alpha\beta} - \overline{\tau_{\alpha\beta}}\right)|_{(\xi^*_\beta-\Delta\xi_\beta/2)}\Big) \\
&- (\mathrm{Term})_\alpha = 0,
\end{aligned} \tag{2}$$

where ξ^*_β describes the staggered position.
$(\mathrm{Term})_\alpha$ contains the additional curvature terms:

$$\begin{aligned}
(\mathrm{Term})_z &= 0\,, \\
(\mathrm{Term})_\varphi &= \frac{\Delta V}{r}\left(-\overline{v_\varphi}\,\overline{v_r} - \overline{v'_\varphi v'_r} + \overline{\tau_{\varphi r}}\right)_{\xi^*_\varphi}\,, \\
(\mathrm{Term})_r &= \frac{\Delta V}{r}\left(\overline{v_\varphi}^2 + \overline{v'_\varphi v'_\varphi} + \overline{p} - \overline{\tau_{\varphi\varphi}}\right)_{\xi^*_\varphi}\,.
\end{aligned} \tag{3}$$

The shear stress is defined as

$$\overline{\tau_{\alpha\beta}} = \frac{1}{Re_\tau}\overline{D_{\alpha\beta}}\,, \quad \text{where} \quad Re_\tau = \frac{u_\tau R}{\nu} \tag{4}$$

The deformation tensor is determined from the filtered velocities, viz.

$$\overline{D_{\alpha\beta}} = \begin{bmatrix} 2\delta_z\overline{v_z} & \frac{1}{r}\delta_\varphi\overline{v_z} + \delta_z\overline{v_\varphi} & \delta_r\overline{v_z} + \delta_z\overline{v_r} \\ \dots & \frac{2}{r}(\delta_\varphi\overline{v_\varphi} + \overline{v_r}) & r\delta_r(\frac{\overline{v_\varphi}}{r}) + \frac{1}{r}\delta_\varphi\overline{v_r} \\ . & . & 2\delta_r\overline{v_r} \end{bmatrix} . \quad (5)$$

δ_α represents a central finite difference operator

The SGS stresses $-\overline{v'_\alpha v'_\beta}$, which are a result of the velocity decomposition into a GS part and a SGS part have to be expressed in terms of GS quantities. This is done by using Smagorinsky's (1963) model:

$$\overline{v'_\alpha v'_\beta} = -\nu_{turb}\overline{D_{\alpha\beta}} \quad (6)$$

$$\nu_{turb} = \min(l_{mix}, C_1\Delta)^2 \frac{1}{2}\overline{D_{\alpha\beta}}^2 \quad (7)$$

$$l_{mix} = 0.14 - 0.08r^2 - 0.06r^4 \quad \text{Nikuradse (1932)} \quad (8)$$
$$C_1 = 0.1 \quad \text{Deardorff (1971)}$$

The length scale Δ is calculated from the mesh size Near the wall the mixing length l_{mix} replaces the value for $C_1\Delta$ in the case of coarse grids. We have tested two different formulas for Δ, which show significant differences near the center line:

$$\Delta = \Delta V^{1/3} = (r\Delta r\Delta\varphi\Delta z)^{1/3} , \quad (9)$$

$$\Delta = \sqrt{\frac{(r\Delta\varphi)^2 + (\Delta r)^2 + (\Delta z)^2}{3}} \quad (10)$$

The first expression, (9) is due to Deardorff (1971) Employing this, the length scale Δ vanishes at the axis. This leads to an eddy viscosity which is also zero in this region. The second expression, (10) is taken from Bardina, Ferziger & Reynolds (1980) and produces a finite value for the length scale at the axis giving a more physically realistic non-zero value for the eddy viscosity Figures 1a,b compare these length scales and show their influence on the time averaged eddy viscosity

NUMERICAL MODEL & BOUNDARY CONDITIONS

The momentum equations are integrated in time on a staggered grid using a second-order leapfrog scheme. The use of Chorin's (1968) projection method leads to a Poisson equation for the pressure which is solved with direct methods Fast Fourier transformation in axial and circumferential directions reduces the 3D problem to a set of 1D Helmholtz problems which are solved in parallel with a tridiagonal-matrix algorithm. The use of Fourier transform implies periodic boundary conditions in the streamwise and the circumferential directions. Resolution restrictions require special formulations for the wall boundary conditions According to Schumann (1975) the wall shear stress components are in phase with the tangential velocity components. In the model for the circumferential stress a modification proposed by Piomelli et al (1989) is adopted which replaces the proportionality factor by that computed for the streamwise direction. At the pipe center line no boundary conditions are needed in the present finite volume formulation. Since the grid surface ΔA_r goes to zero the momentum and mass flux is zero too. The first mesh volume needs some special treatment only due to the staggered grid which is used to integrate the momentum equations. Minor approximations become necessary in the diffusion terms in which variables must be specified at positions where they are not defined.

For the very first simulation initial values for the velocity field have to be specified. This is done by adding random velocity fluctuations to empirical mean flow distributions. The latter are specified by setting $< \overline{v_\varphi} >$ and $< \overline{v_r} >$ to zero, $< \overline{v_z} >$ is calculated according to a power law. The fluctuations are Gaussian random numbers which are normalized to one, weighted with experimental rms-values and made divergence free by applying the Poisson solver once.

GEOMETRY AND FLOW PARAMETERS

The real counterpart of our numerical experiment is a four diameter long section of a smooth pipe in which the turbulent flow is fully developed The characteristic length for nondimensionalization is the pipe radius R. In terms of R the computational domain has the size of $8\times2\pi\times1$ in the (z,φ,r)-cylindrical coordinate system and the Reynolds number based on u_τ is Re_τ=1100. Using a $128\times64\times16$ grid the minimal dimensionless distance to the wall is y^+=34. Grid and geometry are illustrated in figure 2. The chosen Reynolds number is equivalent to a global Reynolds number of Re=50000, which corresponds to Laufer's (1954) experiment. The grid is equidistant in the r,z-directions. Cells which are nearly 'isotropic' can be found at r=0.6. As a result of the flat cells near the center line, stability requirements impose a very small time step Δt=$5\cdot10^{-4}$. The whole simulation takes 90 characteristic times T_0=L/u_b, time averaging starts after $36T_0$ and correlations have built up after $56T_0$. Such a simulation takes about 10 CPU-hours on a CRAY-YMP.

RESULTS

There are many ways to extract information from LES data. First of all we like to look at the behaviour of statistical flow quantities, because they allow for comparisons with experimental results. This is done in the first part of this section. In the second part we investigate and visualize instantaneous flow quantities, the formation of typical flow structures and examine their behaviour at critical positions such as the pipe center line. Results of the first part give us confidence in the quantitative accuracy of the shape and dynamics of large scale structures treated in the second part.

Part 1: Statistical quantities

Since the mean flow is homogeneous in the circumferential and longitudinal directions there is only one nonzero mean velocity component, v_z. Figure 3 shows the radial distribution of v_z non-dimensionalized with the mean centerline velocity in comparison with data of Laufer (1954). The difference between the simulation and the experiment near the pipe wall are due to the small number of grid points in radial direction Recall that the pipe radius is divided into 16 cells only. Finer grids would of course do a better job in resolving the steep near wall gradients, they are, however, more expensive. The logarithmic representation of v_z in terms of u_τ, in figure 4 reflects this lack of resolution, in the first grid point at least. The dashed line marks Coles' (1968) logarithmic law and triangles correspond to experimental data of Perry & Abell (1975) at a global Reynolds number of $78\cdot10^4$. The *rms*-values of the three velocity components are compared with experiments in figure 5. The computed profiles contain a resolved (GS) part and a subgrid scale (SGS) part according to the definition

$$v_{\alpha,RMS} = \sqrt{< v'^2_\alpha > + \frac{2}{3}E_{SGS}} . \quad (11)$$

$$E_{SGS} = \frac{\nu^2_{turb}}{(C_2\Delta)^2} , \quad (12)$$

$$C_2 = 0.094 \quad \text{Deardorff (1971)} .$$

Our result for the longitudinal component lies within the bandwith of experimental error. The low level of Laufer's data is discussed in Perry & Abell's (1975) paper. The obviously too low level of the fluctuations computed near the centerline can most likely be attributed to the flat grid cells there. Otherwise the LES performs well and leads to good agreement with the experiment. The total shear stress in figure 6 consists of a GS-part (solid line), a SGS-part (dashed) and a viscous part (dashed-dotted) and shows the analytically expected linear shape. Figure 7 presents the (v_r,v_z)-correlation coefficient which reflects very good agreement with Laufer's experiment. An often measured and very sensitive quantity is the longitudinal power spectrum of the three fluctuating velocity components. Figures

8a,b compare spectra measured by Lawn (1971) with our LES data at two different radial positions. The agreement is good at low and moderate wave numbers. The steep fall-off of the spectra for higher wave numbers at position r/R=0.35 may be due to the decrease in two cell surfaces for $r \rightarrow 0$. Our aim in the future is to improve on that using different grid systems.

Part 2: Instantaneous flow quantities

In figure 9abc the three velocity components reveal their own typical flow structure. The longitudinal velocity represented in figure 9a is the only component with a nonzero mean velocity implying steep gradients near the pipe wall. It produces very elongated structures without especially remarkable features. The v_φ-component in figure 9b on the other hand is organized in large scale structures having a typical inclination angle with respect to the wall. Figure 9c illustrates the spotty character of the v_r-component. It can be observed from all the three velocity components that the near wall region is dominated by high intensity fluctuations whereas the region near the centerline shows only weak fluctuations. This is confirmed by the fluctuating velocities in a plane perpendicular to the axis in figure 10ab. Instead of v_r'' and v_φ'' the cartesian components v_x'' and v_y'' are plotted. Special attention should be given to the centerline region. The figures do not show any obvious artificial influence of the axis, i.e. large scale structures are free to cross the axis. A snapshot of fluctuating velocity vectors in figure 11 demonstrates the possibility for such crossings. Finally a perspective view of the contour surface of the instantaneous longitudinal velocity is presented in figure 12 for v_z=0.95u_{cl}. The highly rugged surface gives an impression of the ongoing dynamics.

CONCLUSIONS

The presented data of fully-developed pipe flow at high Reynolds numbers demonstrate that cylindrical coordinates can be quite successfully used in large-eddy simulations and provide good agreement with experimental results. Nevertheless improvements should be made in the near future avoiding too elongated mesh cells and thus too strong restrictions in the Courant numbers. Further work is going on in this direction.

ACKNOWLEDGEMENT

The authors wish to thank the German Research Association (DFG) for supporting these studies in its Priority Research Programme 'Strömungssimulation mit Hochleistungsrechnern'

REFERENCES

BARDINA,J., FERZIGER,J.H. & REYNOLDS,W.C. 1980 Improved subgrid scale models for large eddy simulation AIAA paper No. 80-1357.

CHORIN,A.J. 1968 Numerical solution of the Navier-Stokes equations. Mathematics of Computations 22, 745-762.

COLES,D.E. 1968 Proc. AFOSR-IFP-Stanford Conf. on Computation of Turbulent Boundary Layers (ed. D.E.Coles & E.A.Hirst, vol. 2, p. 1)

DEARDORFF,J.W. 1971 On the magnitude of the subgrid scale eddy viscosity. J.Comp.Phys. 7, 120-133

LAUFER,J. 1954 The structure of turbulence in fully-developed pipe flow. NACA Rep. 1174

LAWN,C J. 1971 The determination of the rate of dissipation in turbulent pipe flow. J.Fluid Mech., 48, part 3, 477-505.

LEONARD,A. & WRAY,A. 1982 A new numerical method for the simulation of three-dimensional flow in a pipe. Proc. 8th International conference of numerical methods in fluid dynamics, Aachen.

NIKURADSE,J. 1932 Gesetzmäßigkeiten der turbulenten Strömung in glatten Rohren. VDI-Forschungsheft, 361.

ORSZAG,S.A. & PATERA,A.T. 1983 Secondary instability of wall-bounded shear flows. J. Fluid Mech., 128, 347-385.

PERRY,A.E. & ABELL,C.J. 1975 Scaling laws for pipe-flow turbulence. J.Fluid Mech., 67, part 2, 257-271.

PIOMELLI,U., FERZIGER,J., MOIN,P. & KIM,J. 1989 New approximate boundary conditions for large-eddy simulations of wll-bounded flow. Phys. Fluids A, 1, 1061-1068.

PRIYMAK,V.G., ROZHDESTVENSKY,V.L. & SIMAKIN,I.N. 1982 Turbulent flow instabilities in channels an pipes. Fluid Mechanics-Soviet Research, 16, 6.

SCHUMANN,U. 1975 Subgrid scale model for finite difference simulations of turbulent flows in plane channels and annuli. J.Comp. Phys.18, 376-404.

SMAGORINSKY,J.S. 1963 General circulation experiments with the primitive equations. Mon. Weather Rev. 91, 99-164.

FIGURES

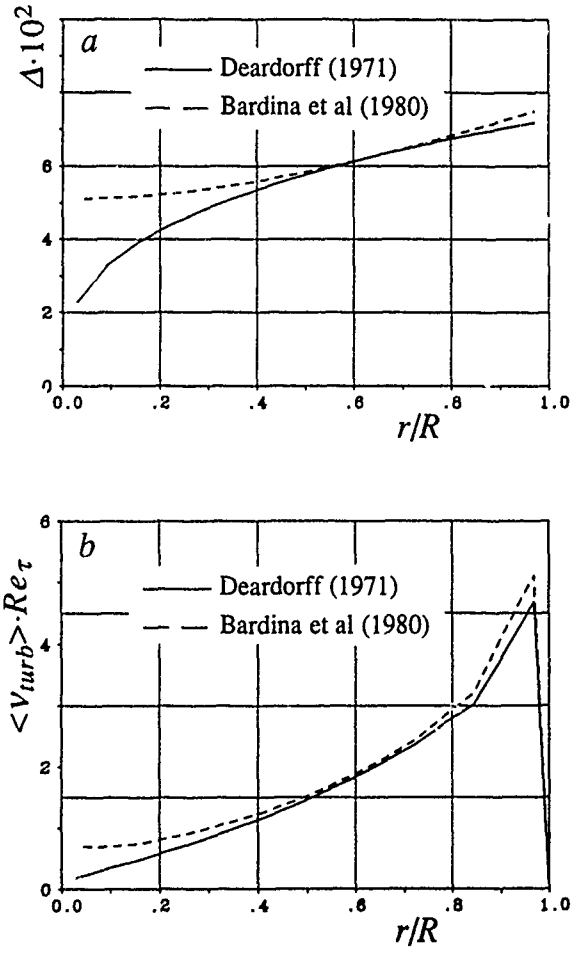

Fig.1 a) Lengthscale Δ, b) Time averaged turb. visc. ν_{turb}

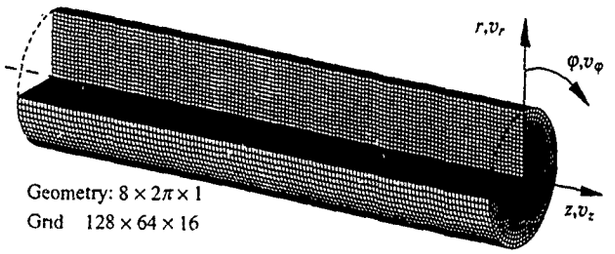

Fig.2 Geometry of the simulated flow

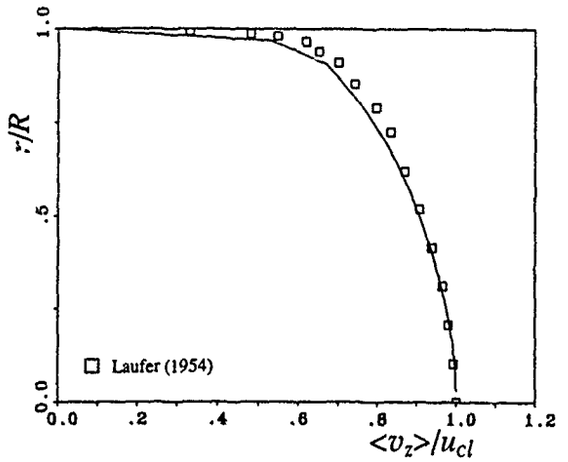

Fig.3 Mean axial velocity scaled with the centerline velocity

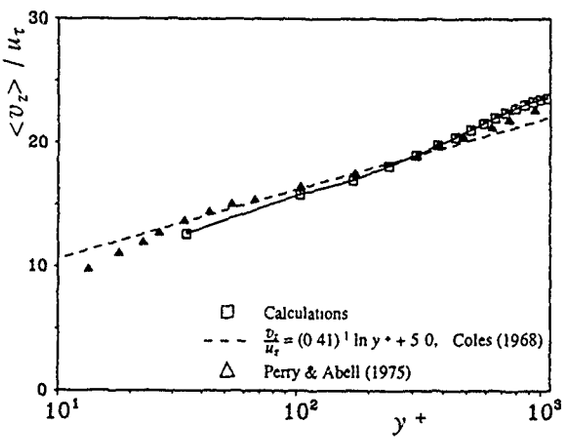

Fig.4 Mean axial velocity in a logarithmic representation

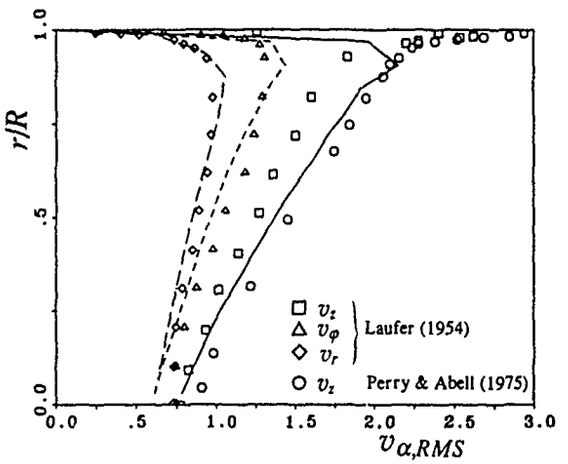

Fig.5 Profiles of the turbulence intensities

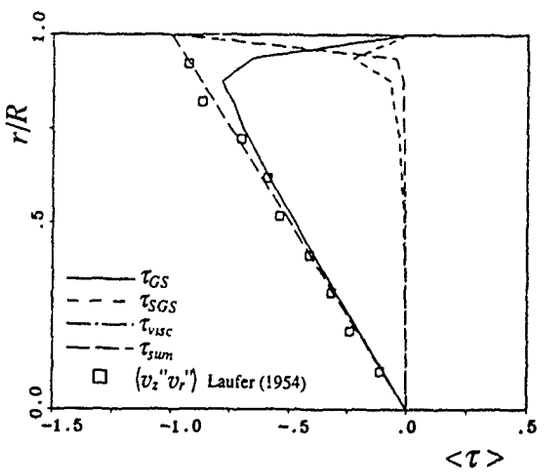

Fig.6 Distribution of the various shear stress components

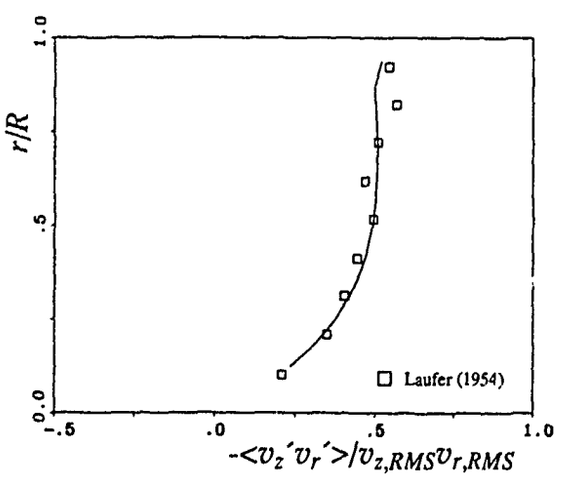

Fig.7 Correlation-coefficient

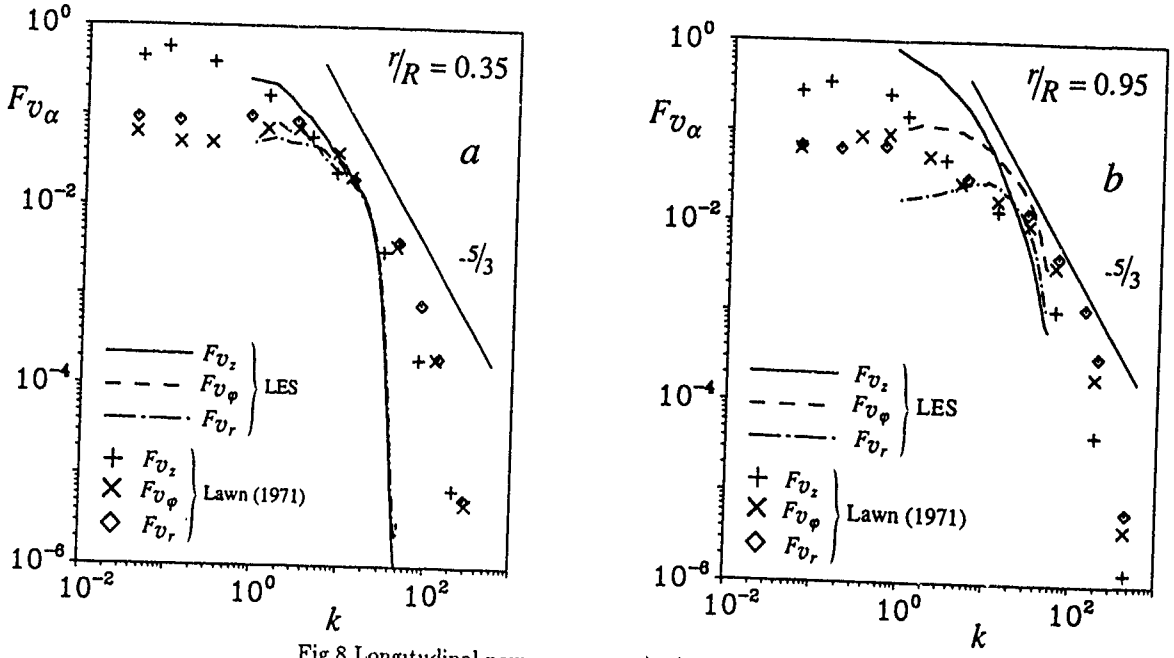

Fig.8 Longitudinal power spectra, a) r/R=0.35, b) r/R=0.95

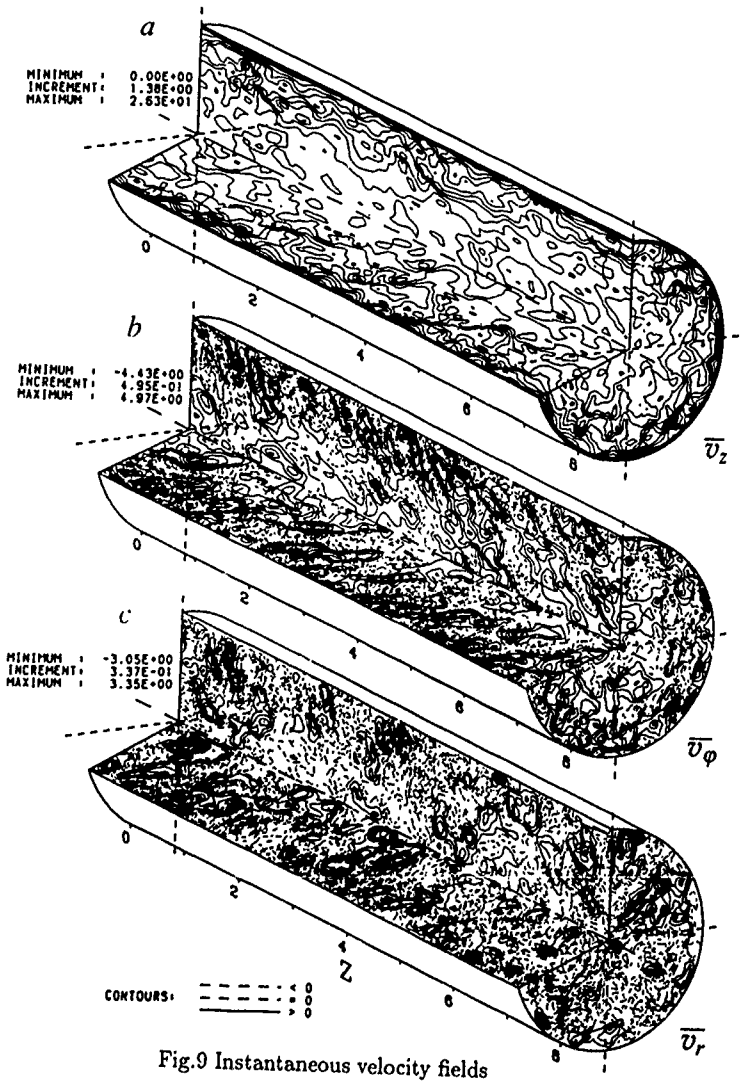

Fig.9 Instantaneous velocity fields

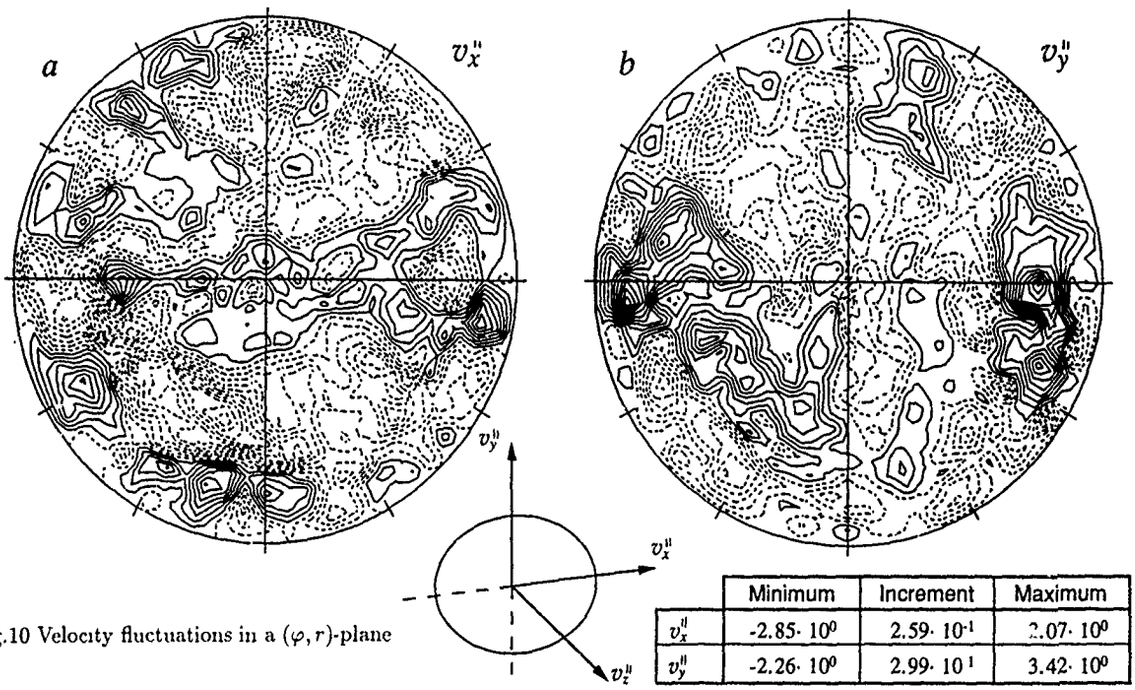

Fig.10 Velocity fluctuations in a (φ, r)-plane

	Minimum	Increment	Maximum
v_x''	-2.85· 10^0	2.59· 10^{-1}	3.07· 10^0
v_y''	-2.26· 10^0	2.99· 10^{-1}	3.42· 10^0

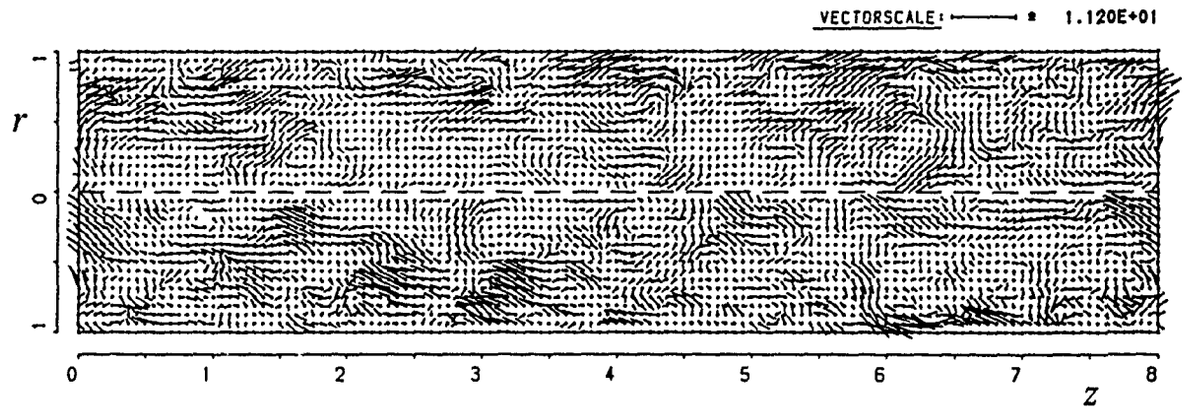

Fig.11 (v_z'', v_r'')-vectors in a (z, r)-plane

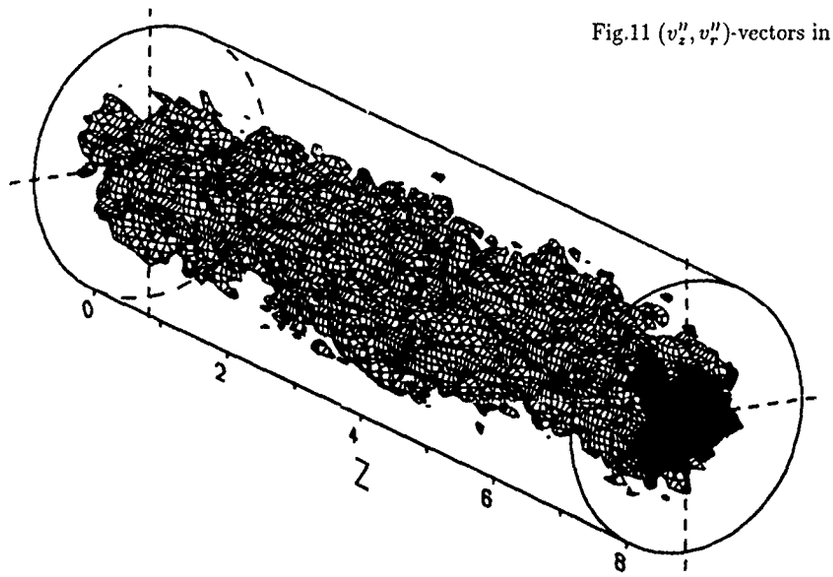

Fig.12 Perspective view of the axial velocity, $v_z = 0.95 u_{cl}$

EIGHTH SYMPOSIUM ON
TURBULENT SHEAR FLOWS
Technical University of Munich
September 9-11, 1991

LARGE-EDDY SIMULATION OF TURBULENT FLOW OVER AND AROUND A CUBE IN A PLATE CHANNEL

H.Werner and H.Wengle +

Institut für Strömungsmechanik und Aerodynamik
Universität der Bundeswehr München, LRT/WE7
8014 Neubiberg, Federal Republic of Germany

ABSTRACT

The concept of large-eddy simulation (LES) has been applied to simulate turbulent flow over and around a single cube mounted on the bottom of a plate channel for a Reynolds number of 50000 (based on the incoming mean bulk velocity and obstacle height). Here we present, as a first part of the evaluation of the data, mainly results for the three-dimensional mean fields (velocity, vorticity, Reynolds stress, enstrophy, helicity) and a few interesting views of the instantaneous fields. Having engineering application in mind, this flow problem represents an ideal case for testing and evaluating solution concepts like LES or solutions of the Reynolds-averaged Navier-Stokes equations.

INTRODUCTION

The purpose of our work is to apply the concept of large-eddy simulation (LES) to turbulent flow over and around flow obstacles with sharp edges and corners. The work is motivated by the need for applications of the LES concept to engineering applications involving (a) high Reynolds number flow, (b) three-dimensionality of the *mean* flow and (c) non-periodic boundary conditions in the main flow direction. In this paper we present results from a numerical simulation of turbulent flow over and around a cube mounted on the bottom of a plate channel. For the example presented here, we selected (a) a Reynolds number of about 50000, based on mean bulk velocity and obstacle height (which is equal to the channel half width), (b) a three-dimensional obstacle, creating a flow field without any homogeneous direction, which makes it necessary to provide the statistics by time-averaging only, and (c) a *single* obstacle, i.e. not allowing the use of periodic boundary conditions in the main flow direction

Earlier related work on LES of turbulent flow over a periodic arrangement of cubes in a simulated atmospheric boundary layer has been published by Murakami, Mochida & Hibi (1987), results for the flow over a periodic arrangement of square ribs in a channel have been presented by Kobayashi, Kano & Ishihara, (1985), and results from our own earlier work on flow over a single square rib on the bottom of a plate channel can be found in Werner & Wengle (1988, 1989).

MATHEMATICAL MODELS, SOLUTION TECHNIQUE AND EVALUATION OF THE STATISTICS

The governing equations describing the resolvable flow quantities (grid scale, GS) are derived from the integral conservation equations for mass and momentum applied to a finite grid volume $\Delta V = \Delta x * \Delta y * \Delta z$ following the 'volume balance method' of Schumann, U. (1975). From this it follows that GS quantities of the three velocity components $U_\alpha(\alpha = 1,2,3)$ are defined as averages over the corresponding surfaces, $\Delta A_\alpha(\alpha = 1,2,3)$ of the grid volumes, ΔV.

The subgrid scale (SGS) stresses arising from the nonlinear convection terms are evaluated by the Smagorinsky-Lilly model (with $c_1 = 0.1$) which relates the subgrid stresses to the GS velocity field via an eddy viscosity model. In grid volumes next to walls, we used for the mixing length the smaller value of $\kappa * x_\alpha$ and $0.1 * (\Delta x * \Delta y * \Delta z)^{1/3}$ respectively (x_α is the distance normal to a wall).

The geometry of the computational domain and of the flow obstacle is evident from figure 1. Measured in units of the reference height H (height of the cube) of the problem, the dimensions of the domain were (X,Y,Z)=(10,7,2), and for the results presented here we used (NX,NY,NZ)=(144,92,58) grid points.

The governing equations are solved numerically on a staggered and non-uniform grid using second order finite-differencing in time and space (explicit leap-frog for time discretization, central differencing for convection terms and time-lagged diffusion terms). The problem of pressure-velocity coupling is solved iteratively (point-by-point relaxation).

The direct results from LES are the time-dependent and three-dimensional data fields for the GS quantities of the three velocity components and the pressure. Figure 2a shows a sample of the instantaneous flow field in a vertical plane through the center of the cube. By time-averaging of the instantaneous flow field, the mean flow field (fig. 2b) is obtained, and as soon as the mean velocity field has reached stable (i.e. time-independent) values, the fluctuating velocity field (fig. 2c) can be evaluated as the difference of the two fields, which leads to the classical Reynolds-decomposition of a turbulent flow field. Finally, from the fluctuating fields, the root-mean-square values, e.g. for velocity, vorticity and pressure fluctuations can be calculated, as well as the Reynolds stresses and other statistics desired.

INFLOW AND WALL BOUNDARY CONDITIONS

At the inflow section, we used at each time step the instantaneous flow field of a LES result of the corresponding (fully developed) channel flow (see figure 1). Boundary conditions at horizontal and vertical walls were specified by assuming that at the grid points (P) closest to the wall, (a) the instantaneous velocity components tangential to the wall (u_P, v_P) are in phase with the instantaneous wall shear stress components (τ_{wb}, τ_{vb}) and (b) the instantaneous velocity distribution is assumed to follow the linear law-of-the-wall $u^+ = z^+$ for $z^+ \leq 11.81$, and for $z^+ = z_m > 11.81$ it is continued by a power-law description of the form $u^+ = A(z^+)^B$ (with A=8.3 and B=1/7). The velocity components tangential to a wall at the grid point next to the wall (u_P, v_P) can be related to the corresponding wall shear stress components by integrating the velocity distribution over the height of the first

+ *to whom correspondence should be sent*

grid element, and the resulting expression can be resolved *analytically* for the wall shear stress component, i.e.

$$|\tau_{ub}| = \frac{2\mu|u_P|}{\Delta z} \qquad \text{for} \qquad |u_P| \le \frac{\mu}{2\rho\Delta z} A^{\frac{2}{1-B}}$$

$$|\tau_{ub}| = \rho\left[\frac{1-B}{2} A^{\frac{1+B}{1-B}} \left(\frac{\mu}{\rho\Delta z}\right)^{1+B} + \frac{1+B}{A}\left(\frac{\mu}{\rho\Delta z}\right)^{B} |u_P|\right]^{\frac{2}{1+B}}$$

$$\text{for} \qquad |u_P| > \frac{\mu}{2\rho\Delta z} A^{\frac{2}{1-B}}$$

(Δz is the vertical width of the grid volume next to the wall, z_m is the upper boundary of validity of the linear-law-of-the-wall). Though theoretically not fully satisfying, from an application point of view this procedure offers the advantage that the averages $< \tau_{ub} >$ and $< u_P >$ are *not* required (in particular in flow situations in which these variables may be slowly varying in time), and numerical problems are avoided in evaluating the commonly used relation $\tau_{ub} = u_P < \tau_{ub} > / < u_P >$ in reattachment regions. In consequence of the experimental results from Ruderich & Fernholz (1986) we have abandoned the use of the logarithmic-law-of-the-wall.

DISCUSSION OF RESULTS AND CONCLUSIONS

The results shown in this paper are made dimensionless using a reference height $L_{ref} = H$ (H=cube height) and a reference velocity $U_{ref} = U_b$ (U_b=mean bulk velocity, see fig. 1). Note, that in our nomenclature, Z is the coordinate normal to the walls of the plate channel.

LES provides insight into the time-dependent large-scale structure of a turbulent flow field. An *instantaneous* view of the velocity vectors projected onto a vertical plane through the center of the cube (fig 2a) exhibits an extremly complicated flow field. The interaction of different processes like the development of a three-dimensional shear layer, the reattachment of flow on the bottom plate behind the flow obstacle, the recirculation of highly turbulent flow and its reentrainment into the free shear layer takes place within a spatial regime which is significantly smaller compared to the case of flow over a square-rib, see Werner & Wengle (1988, 1989): the mean recirculation length is about 2.0 for the flow over a cube, and about 7.0 for the square-rib. Strong horizontal fluctuations in the lateral direction close to the walls can be observed in the small recirculation regimes in front and on top of the cube and in the large recirculation regime behind the flow obstacle (fig. 4) The creation of strong horizontal fluctuations by splashing down of tongues of fluid material can be seen in figure 5.

The *mean* structure of the flow field (e.g. mean velocity, mean vorticity, second order statistics, mean enstrophy, mean helicity) can be provided by time-averaging only. For the results shown here, we started averaging for the first-order statistics after 60 reference times, samples for the first-order statistics have been collected over 160 reference times (taking one sample at every 40th time step), samples for the second-order statistics have been collected over the latest 110 reference times. *One* reference time is equivalent to the time a tracer particle needs to travel with bulk velocity U_b (see fig. 1) over a distance of *one* obstacle height H. Figure 1 shows vertical profiles of the mean U-velocity component; the profiles are quite smooth, indicating that a sufficient number of samples has been taken for the first-order statistics. From distributions of the mean U-velocity component close to the bottom plate (Z=0.01=location of first vertical grid point) and close to the top face of the cube (Z=1.01), the different mean recirculation lenghts can be approximately determined to XF=0.9, XR1=1.75, XR2=0.2 and XT=0.75 (fig. 3a,b). In a vertical cut normal to the main flow direction at a dimensionless position X=0.88 behind the cube (fig. 3d), two pairs of counter-rotating mean vortices can be observed (one pair very close to the side walls of the cube, and the other one at Y=+1.5 and Y=-1.5 from the center of the cube). In that vertical plane, the lateral shape of the mean shear layer also becomes visible (fig 3d).

As an example for the second order statistics, figure 6 shows vertical profiles of the Reynolds stress $- < uw >$ and of the turbulent energy (in a vertical plane through the center of the cube). The smoothness of the profiles is not quite satisfying, indicating that still more samples are desirable for the second-order statistics.

The evaluation of the *mean* vorticity field in figure 7 gives an interesting view of the geometry of the mean shear layer behind the cube. In addition, figure 7a shows on the right hand side the mean vorticity vectors projected onto vertical planes normal to the main flow direction (the length of a vorticity vector is proportional to the strength of the local mean vorticity) On the left hand side, isolines of the mean total enstrophy are shown, indicating the same geometry of the 3D shear layer as exhibited by the arrows of the velocity vectors in fig. 3d An interesting perspective view of the shape of the 3D mean recirculation zone is given in fig. 7b by an isosurface of the mean total enstrophy $< \omega_x^2 + \omega_y^2 + \omega_z^2 >$ (for an arbitrarily chosen value of 20.0).

Finally, we evaluated the so-called helicity $\vec{v} \cdot \vec{\omega}$ of the flow field: e.g. fig. 8a shows a perspective view of a mean helicity iso-surface for a value of 0.25. If the *instantaneous* helicity density is normalized as $cos\theta = \vec{v} \cdot \vec{\omega} / |\vec{v}||\vec{\omega}|$ it can be interpreted as the cosine of the angle between velocity vector and vorticity vector. For example, fig. 8b gives a perspective view of the instantaneous locations of $cos\theta = 0.90 (\theta = 25°)$. Regions of small helicity values are equivalent to regions of large values of $\vec{v} \times \vec{\omega}$ (the non-linear term of the Navier-Stokes equation in rotation form), in regions of small angles between $\vec{v}$ and $\vec{\omega}$ it is reasonable to expect that the local structure will be helical (an ideal case would be $cos\theta = 1.0$, i.e. $\vec{v}$ and $\vec{\omega}$ are aligned).

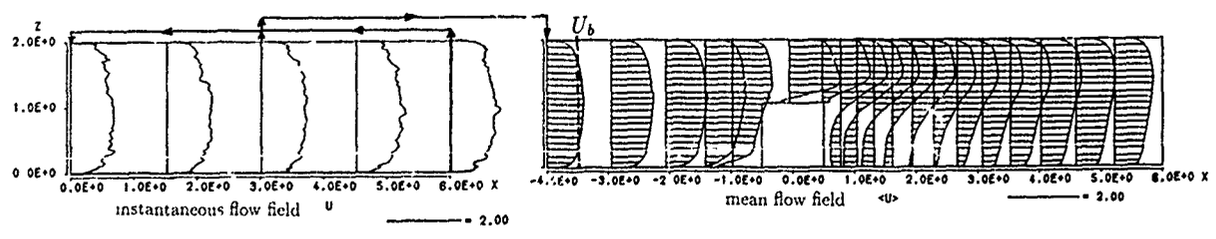

Fig. 1: Geometry of computational domain and inflow boundary conditions

left: channel flow $NX * NY * NZ = 54 * 92 * 58$ grid points
right: flow over cube $NX * NY * NZ = 144 * 92 * 58$ grid points

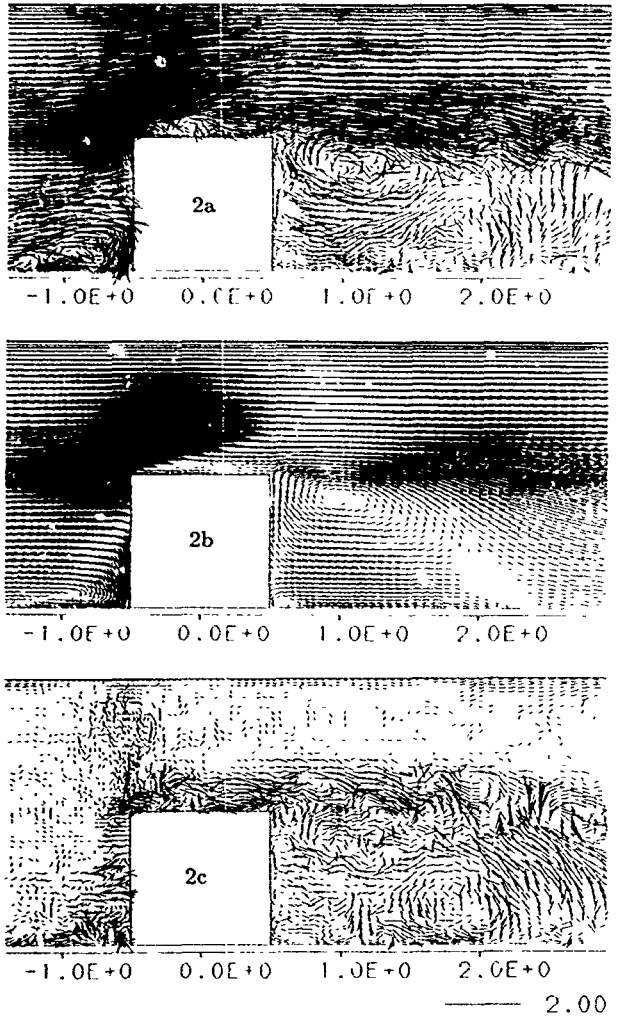

Fig. 2: Reynolds-decomposition of flow field:
instantaneous flow (2a) = mean flow (2b) + fluctuating flow (2c)
in a vertical plane at Y=0 through center of the cube

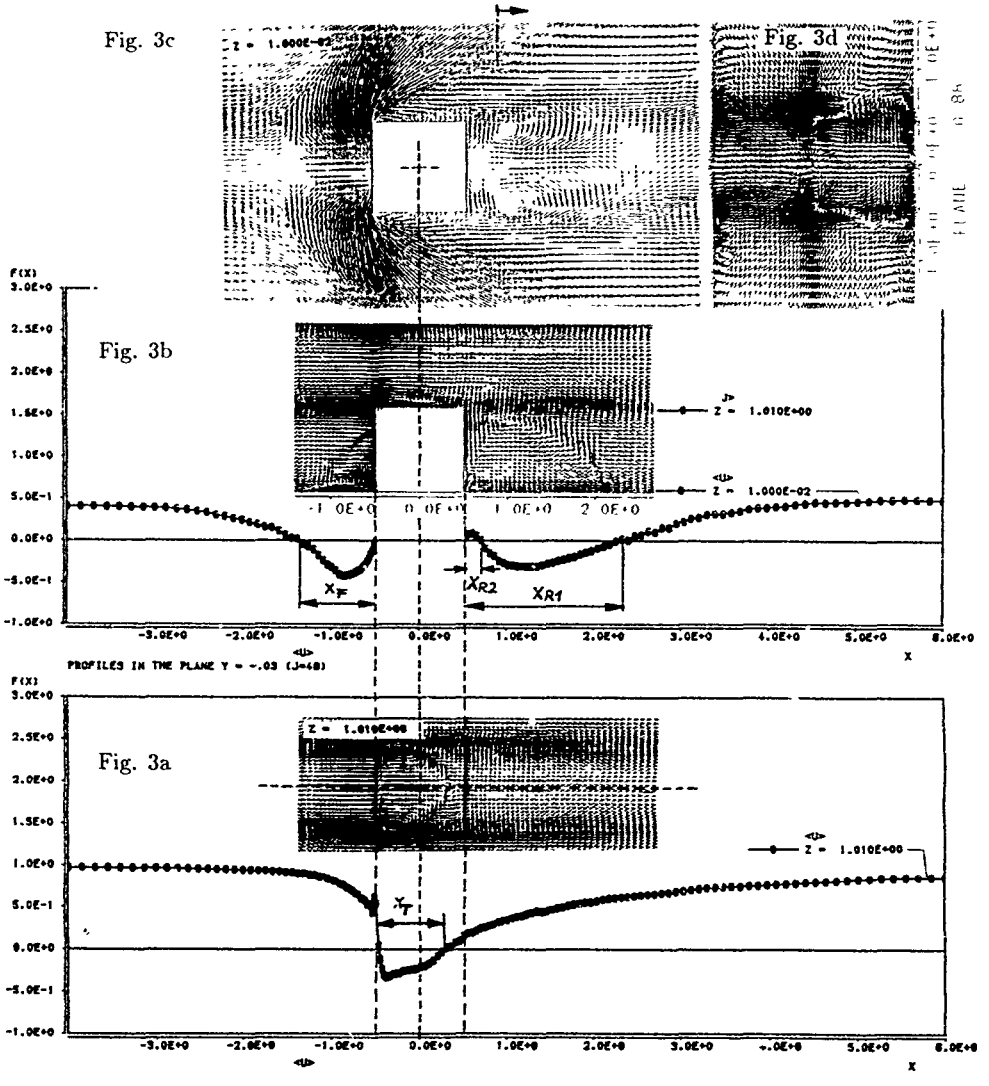

Fig. 3: Determination of mean recirculation lengths

Fig. 3a,b: from profiles of mean velocity at heights Z = 0.01 and Z = 1.01 at Y = 0
Fig. 3c. mean velocity vectors at Z = 0.01
Fig. 3d: mean velocity field (directions of velocity vectors) at X = 0.88

Fig. 4a

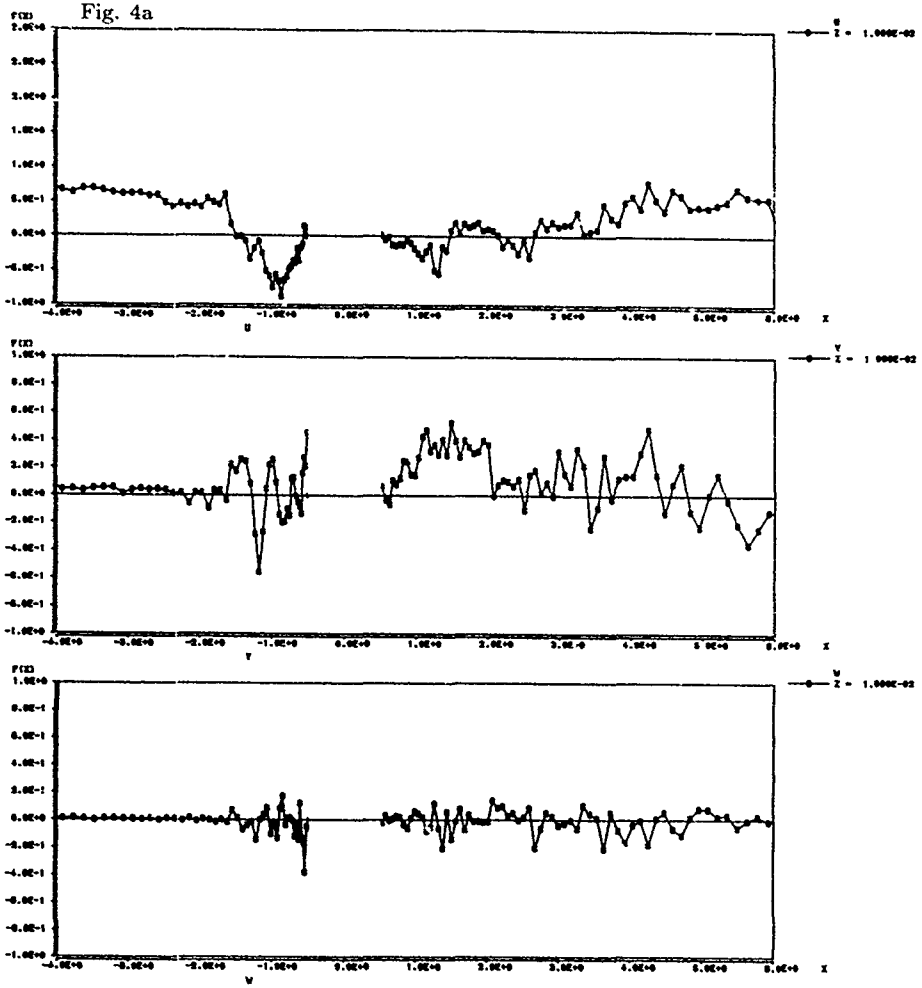

Fig. 4b

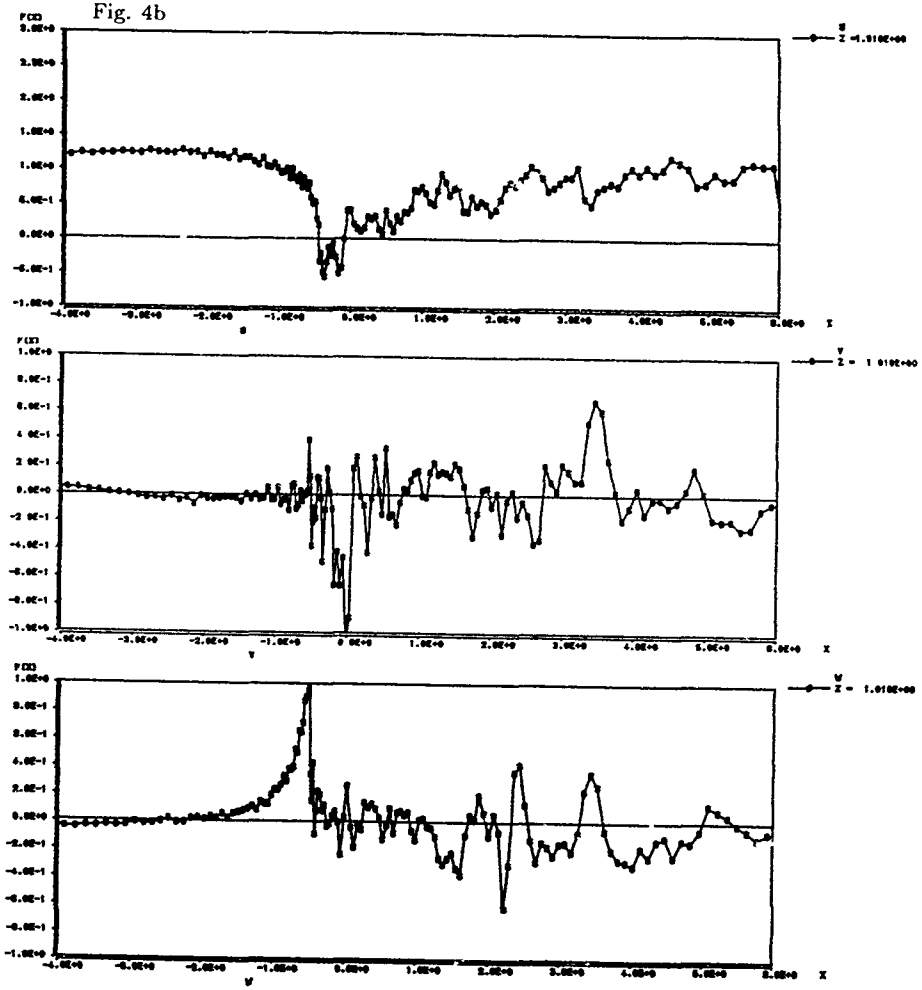

Fig. 4c

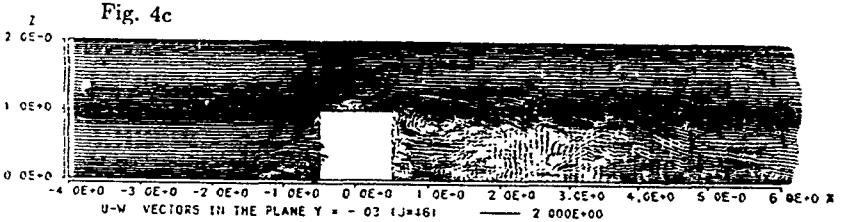

Fig. 4: Instantaneous velocity field

profiles of instantaneous velocities along a line through center of the cube at Y = 0
Fig. 4a: close to the bottom plate at heigth Z = 0.01
Fig. 4b: close to the top face of the cube at Z = 1.01
Fig. 4c: instantaneous velocity vectors in a vertical plane at Y = 0

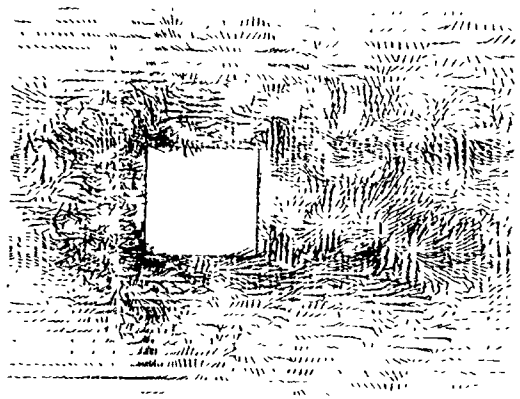

Fig. 5: Fluctuating flow field
in a horizontal plane close to the bottom plate at Z = 0.01

Fig. 6a

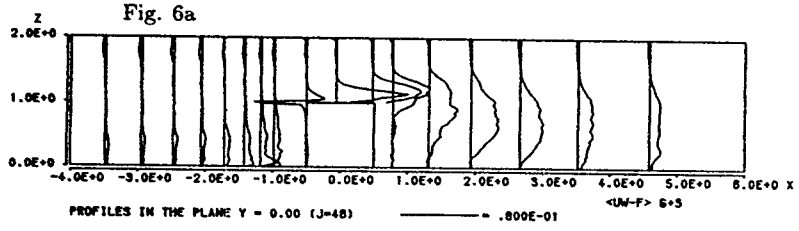

Fig. 6b

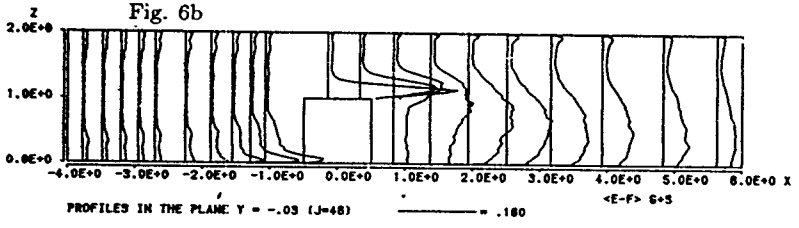

Fig. 6: Second order statistics

Fig. 6a: vertical profiles of Reynolds shear stress $- < uw >$
Fig. 6b: vertical profiles of turbulent energy E-F
in a vertical plane at Y = 0

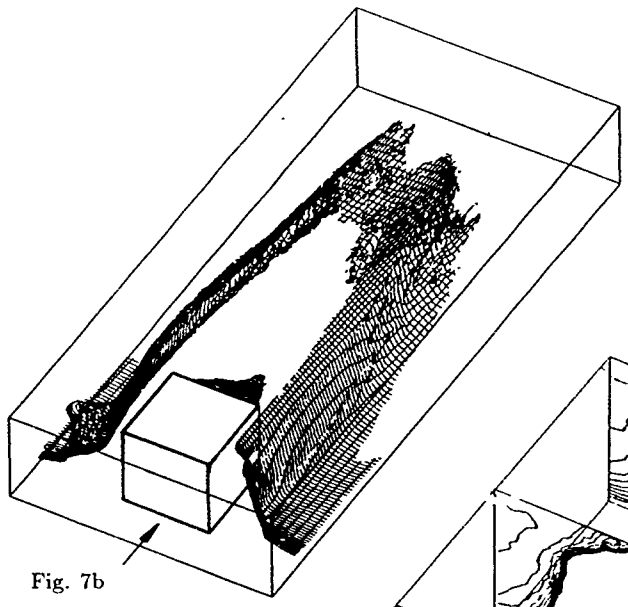

Fig. 7b

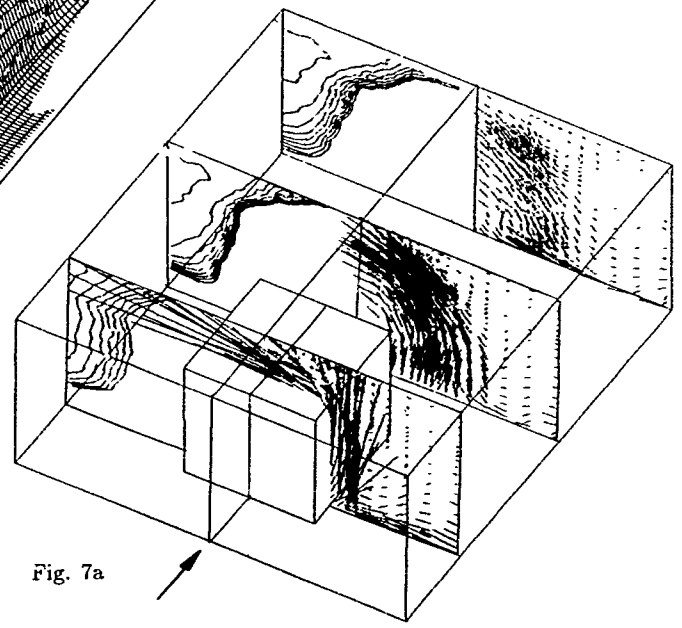

Fig. 7a

Fig. 7: Mean vorticity field
Fig. 7a:
right half: vorticity vectors projected onto vertical planes at X = -0.3, +1.0, +2.5
left half...: isolines of total mean enstrophy $< \omega_x^2 + \omega_y^2 + \omega_z^2 >$
Fig. 7b: isosurface of total mean enstrophy (isosurface cut open at Z = 1 4)

Fig. 8a

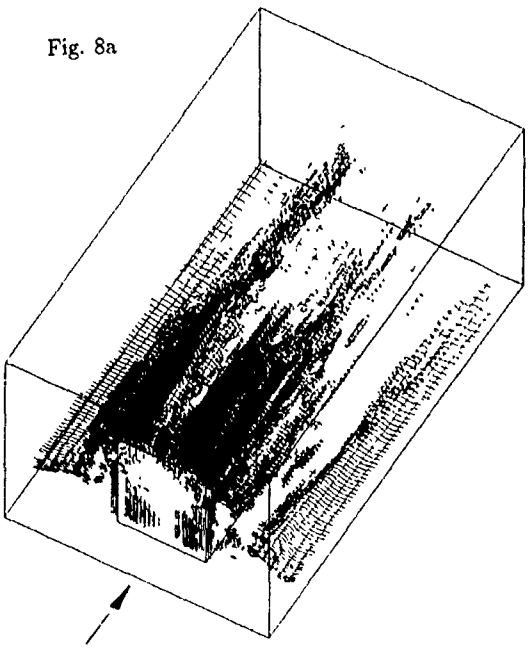

Fig. 8b

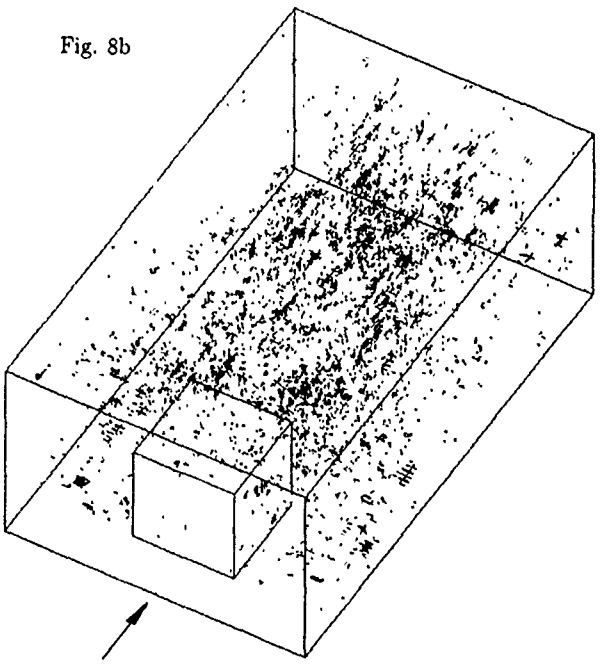

Fig. 8: Isosurfaces of helicity

Fig. 8a: mean helicity $< \vec{v} \cdot \vec{\omega} >$
Fig. 8b: instantaneous helicity density $cos\theta = \vec{v} \cdot \vec{\omega} / |\vec{v}||\vec{\omega}| = \pm 0.9$

From the results presented here it can be concluded that the case of turbulent flow over a cube in a plate channel represents a flow problem which is very well suited for testing and validating numerical simulation techniques and turbulence models. Corresponding experimental data will be available in the near future from Larousse, Martinuzzi & Tropea (1991). For applying the solution concept "large-eddy-simulation" about 300 CPU hours on a CRAY/Y-MP must be spent to provide sufficiently stable second-order statistics For every mean variable to be evaluated a three-dimensional array must be assigned in the computer programm , and the number of grid points used for the results presented here should be considered to be a minimum to reach satisfying agreement with experimental data for the second-order statistics and to provide sufficiently accurate results needed for the validation of statistical turbulence models involved in solving the Reynolds-averaged Navier-Stokes equations.

ACKNOWLEDGEMENT

This work is currently supported by the German Research Society, Priority Research Program, Project No. Ro 497/5 (Römer/Wengle). We also gratefully acknowledge the support by the computing center of the Universität der Bundeswehr München, by the Leibniz Computing Center of the Bavarian Academy of Sciences, and by Convex Computer GmbH, GS Bayern.

REFERENCES

BAETKE, F., WERNER, H. & WENGLE, H., 1987
Computation of turbulent flow around a cube on a vector computer, Proc.6th Symposium on Turbulent Shear Flows, Sept. 7-9, Toulouse, France.

KOBAYASHI,T., KANO,M. & ISHIHARA,T. 1985
Prediction of turbulent flow in two-dimensional channel with turbulence promoters, Bull. JSME,Vol. 28, No. 246, 2948-2953.

LAROUSSE, A., MARTINUZZI, R. & TROPEA, C. 1991
Flow around surface-mounted three-dimensional obstacles, Proc 8th Symposium on Turbulent Shear Flows, Sept. 9-11, Technical University of Munich, Munich.

MURAKAMI, S., MOCHIDA, A. & HIBI, K. 1987
Three-dimensional numerical simulation of air flow around a cubic model by means of large eddy simulation, J.Wind Engng. and Ind Aerodynamics, 25, 291-305.

RUDERICH, R. & FERNHOLZ, H.H. 1986
An experimental investigation of a turbulent shear flow with separation, reverse flow, and reattachment, J.Fluid Mech. 163, 283-322.

SCHUMANN, U., 1975
Subgrid scale model for finite difference simulations of turbulent flows in plane channels and annuli, J.Comp.Phys.18, 376-404.

WERNER, H. & WENGLE, H. 1988, 1989
Large-eddy simulation of turbulent flow over a square rib in a channel,
Proc.2nd European Turbulence Conference, August 30 - September 2, 1988, Berlin,
in: Advances in Turbulence 2, Springer.,
Proc.7th Symposium on Turbulent Shear Flows, August 21-23, 1989, Stanford University, USA.

TURBULENT SHEAR FLOWS
Technical University of Munich
September 9-11, 1991

NUMERICAL SIMULATION OF TURBULENT CONVECTIVE SHEAR FLOWS OVER WAVY TERRAIN

A. Dörnbrack, K. Krettenauer and U. Schumann
DLR, Institut für Physik der Atmosphäre
W-8031 Oberpfaffenhofen, Germany

ABSTRACT

Thermal convection of a Boussinesq fluid in a layer confined between two infinite horizontal walls is investigated by large eddy simulation (LES) for zero and finite horizontal mean motion. The lower surface height varies sinusoidally in one direction in order to investigate the effect of complex terrain on the turbulent motion. Several cases are considered with amplitude δ up to $0.15H$ and wavelength λ between $1H$ and $8H$. In the windless cases, the gross features of the flow statistics such as profiles of turbulence variances and fluxes are found to be not very sensitive to the variations of wavelength, amplitude, domain-size and resolution whereas details of the flow structure are changed considerably. The mean flow causes a systematic change of the temporal development of the flow structure.

INTRODUCTION

Much is known about thermal convection over homogeneous horizontal surfaces. Land surfaces are, however, rarely homogeneous. They are often undulated and form hilly terrain. Even when the amplitude of such hilly terrain stays below the mean height of the atmospheric boundary layer, one might expect that topography has appreciable effect on the flow structure.

From field observations on the structure of the atmospheric convective boundary layer, various authors (see for a review Krettenauer and Schumann, 1991) found that "gently rolling terrain" has generally little effect with respect to the intensity of turbulence but changes the flow structure as measured by the characteristic length-scales of the motions. E.g. Kaimal et al. (1982) found a 30 % increase in the length-scale of the spectrum of vertical velocity and a 60 % reduction of the length-scale of temperature.

Most previous LES considered flows over plane surfaces (Schmidt and Schumann, 1989, Nieuwstadt, 1990). Krettenauer and Schumann (1989) investigated the thermal convection for various finite Rayleigh numbers and zero mean flow over sinusoidal waves by means of direct simulation. In this paper, we extend the previous study to LES for infinite Rayleigh number including the case of nonzero mean wind speed. The effect of topography, turbulent convection and mean wind on the turbulence structure is investigated for a Boussinesq fluid confined in a layer between two infinite horizontal walls.

METHOD AND MODEL PARAMETERS

The lower surface height h varies sinusoidally in the streamwise direction with an amplitude δ up to $0.15\,H$ and a wavelength λ of $1\,0H$ to $4\,0H$ (inclination up to 43°) in different cases, where H is the mean fluid layer height. We implemented a subgrid-scale (SGS) model which is similar to that used by Schmidt and Schumann (1989) into a numerical scheme which uses terrain following coordinates according to $\eta(z,h) = H(z-H)/(H-h)$. The numerical method, which employs a second-order finite-difference scheme, follows proposals of Clark (1977).

Constant heat flux (temperature flux $Q_s = \overline{w'\vartheta'_s}$) is prescribed at the lower surface of the fluid layer. The momentum fluxes at the lower rough surface ($z_0/H = 1 \cdot 10^{-4}$) are computed using the Monin-Obuchow relationships. At the flat top an adiabatic frictionless boundary condition is applied which approximates a strong capping inversion of an atmospheric convective boundary layer. For cases $\bar{u} \neq 0$ we use the BKD boundary condition which reduces the reflection of gravity waves as described by Schmidt and Schumann (1989). In both horizontal directions, the model domain extends over the same length (from 4 to $8H$) with periodic lateral boundary conditions. The horizontal mean velocity in the x-direction, $\bar{u}$, is prescribed and varies between 0 and $4\,w_*$, where $w_* = (\beta g Q_s z_i)^{1/3}$ ($z_i = H$ for the runs with $\bar{u} = 0$) is the convective velocity scale (β = volumetric thermal expansion coefficient of the fluid, g = gravity); $t_* = H/w_*$ is the convective time-scale.

RESULTS

a) Convection for zero mean horizontal flow speed

For flat surfaces the flow statistics have been found to compare very well with measurements taken by Adrian et al. (1986) in a comparable laboratory study. Examples of such comparisons are shown in **Fig. 1**.

For convection over undulating terrain, we have identified some rather surprising effects of the unidirectional terrain-variation on three-dimensional motions. In particular we found that a two-dimensional model would be misleading since the results demonstrate that three-dimensional motions are enforced by terrain. So, we can observe circulations with axis parallel as well as perpendicular to the wave crests, which cannot be predicted with two-dimensional models. On the other hand, undulating terrain has rather small effects on the mean turbulence profiles as long as the wavelength λ is less than $4\,H$ and the wave amplitude δ less than $0.15\,H$.

In **Fig. 2** we see convection patterns which are composed of large-scale components at scales of the order H plus small-scale random turbulent motions. The flow structure is little affected by the sinusoidal waves for $\lambda/H \leq 2$ and $\delta/H \leq 0.15$. But, they persist over longer time intervalls (at least 5 convective time scales t_*) in the presence of surface waves which fix the motion patterns (**Fig. 3**) Our results confirm field observations with respect to changes in the horizontal length scales (Kaimal et al., 1982). A complete documentation was published by Krettenauer (1991)

b) Convection for positive mean horizontal flow speed

As a next step in our investigations towards realistic atmospheric cases, we began to simulate the flow over sinusoidal waves with prescribed mean horizontal flow velocity $\bar{u}$. The aim of this part of our study is to investigate the combined influence of the undulating surface, the convective motion and the mean advection of wind on the turbulence structure. We chose a special configuration which is relevant for applications in atmospheric physics. The domain size is typical for the meso-scale of atmospheric motions. The wavelength is $\lambda/H = 1$ and the prescribed temperature flux at the surface is $Q_s = 0.1\,Km/s$. We compare four cases:

(A) $\delta/H = 0$, $\bar{u} = 0$;
(B) $\delta/H = 0$, $\bar{u} = 5\,m/s$;
(C) $\delta/H = 0.05$, $\bar{u} = 0\,m/s$;
(D) $\delta/H = 0.05$, $\bar{u} = 5\,m/s$.

For all simulations we assumed that the initial temperature field is stably stratified with an uniform gradient $\partial\Theta/\partial z \approx 3\,K/km$. Further, we add random perturbations *ranf* to initiate turbulent motions:

$$\Theta = 300K + \frac{\partial\Theta}{\partial z} \cdot z + T_* \cdot ranf \ .$$

Depending on the height of the inversion z_i the ratio $\bar{u}/w_*$ is about 3 to 4 for runs (B) and (D).

Fig. 4a shows the temporal development of $\Theta(\eta)$ (averaged over planes $\eta = const.$). These profiles look similiar for all runs and mark typical mean profiles of a convective boundary layer (superadiabatic lapse rate in the surface layer, a well mixed layer with $\partial\Theta/\partial z \approx 0$, the entrainment zone, and above it the stable atmosphere). **Fig. 4b** depicts the temporal evolution of the volume averaged kinetic energy of turbulent motion (TKE) which first decreases to a minimum and then achieves an approximately steady state for times greater 100 min. This behaviour is caused by the development of the transfer spectrum in wave number space. The following interval up to $t = 200min$ was chosen to average the vertical profiles of momentum flux $\overline{uw}$ and heat flux $\overline{w\vartheta}$ which are displayed in **Fig. 5**.

With regard to $\overline{u'w'}$, considerably differences between the runs can be seen whereas the heat fluxes differ only little. The differences are caused by the effect of mean advection (compare (A) and (C) with (B) and (D)) as well as the effect of orography (compare (A) with (C) and (B) with (D)). As expected, the absolute values are larger for runs with $\bar{u} \neq 0$ because $\overline{u'w'}$ is proportional to the gradients of mean velocity. For $\delta/H = 0$ (case B) $|\,\overline{u'w'}\,|$ is nearly constant in the surface layer and decreases monotonously in the mixed layer. Above the inversion height z_i the momentum flux has a small negative value which is supposed to originate from the wave transport and can be denoted by wave drag. Consistently, $|\,\overline{u'w'}\,|$ has a larger nearly constant value for run (D) in this layer. Also the absolute value in the mixed layer shows the influence of the little mountain: a vertically more extended domain with a larger value of $|\,\overline{u'w'}\,|$.

The mean flow causes a systematic change of the flow structure (**Fig. 6**). Obviously, as can be

seen from contour plots of Θ, the upward motion causes upwards propagating perturbations in the stable layer. These oscillations are of an irregular nature for $\bar{u} = 0$ whereas for $\bar{u} \neq 0$ internal gravity waves grow in the stably stratified troposphere. In contrast to the horizontally homogeneous case, we observe for $\bar{u} = 0$ in the layer up to $z = z_i$ that the thermals are fixed near the crest of the hill for all times (Krettenauer ,(1991).

The situation in the well mixed layer is totally different for runs with mean wind. Due to the strong shear the updraughts are elongated and inclined. As argued by Mahrt (1991), these updraughts become asymmetric with sharp horizontal convergence and sharp horizontal changes of velocity and temperature at the upstream edge of the thermals. These so called microfront zones are generated by horizontal convergence between faster horizontal motion of descending air and slower horizontal motion of the updraughts Orography included, we observe over the whole integration period upward flow at the upwind side and downward flow at the lee-side of the crest. Therefore, we conclude that the surface undulation triggers these flow patterns. Also the gravity waves above them are caused by the joint action of surface undulations and gradient of mean wind. The flow streamlines, as indicated by the isolines of Θ, oscillate at a comparable amplitude and have a wavelength of about $\lambda/2$.

Fig. 7a shows the contour plots of the vertical velocity field w at $\eta = 50\,m$. The runs A and C show randomly distributed thermal elements. These elements are deformed by the mean wind in the horizontally homogeneous case B. Due to this deformation in the streamwise direction, the convective cells grow together and form rolls with axis in the x-direction. The vertical extension of these rolls is closely connected to the mean shear. When orography is present, these flow patterns are overlayed by rolls with axis parallel to the crest and wave fronts.

Fig. 7b doesn't show any systematic difference in the vertical velocity field between the runs. But, looking at the temporal development of these rolls we observe more or less stationary thermals for $\bar{u} = 0$, which change their position only little. For $\bar{u} \neq 0$ (run B) the rolls walk through the computational domain and in layers with strong mean shear we also have rolls with axis in the streamwise direction. In contrast to run B, these structure are absent for run D and the thermal is fixed near the crest of the hill over whole integration time. The mean statistics of turbulence variances in terms of horizontally averaged vertical profiles also show surprisingly little systematic variation between all cases.

The rather good agreement of results from cases with $\bar{u} = 0$ and $\bar{u} \neq 0$ shows that finite difference errors from mean horizontal advection are small. However, for larger horizontal wind speed, we still have to make sure that the flow structure is only little affected by numerical approximation errors. As a next step, we plan a systematic study for various flow and surface parameters as well as a theoretical investigation of the complicated problem.

CONCLUSIONS

This study presents results from two different numerical experiments by means of large eddy simulation. In the first part, we studied the effect of topography on the turbulence structure for thermal convection of a Boussinesq fluid without mean wind. In order to check the new subgrid-scale model we compared the LES results with laboratory measurements. Both results agree very well. The gross features of the flow statistics such as profiles of turbulence variances and fluxes are found to be not very sensitive to the variations of wavelength, amplitude, domain-size and resolution whereas details of the flow structure are changed considerably. The orography has the largest effect for $\lambda = 4H$. In the second part, first results have been presented of studies of combined action of wavy surface, thermal convection and mean advection. The mean flow causes a systematic change of the flow structure. Due to mean shear, roll pattern with axis along as well as perpendicular to the streamwise direction develop. These were absent in the windless cases.

REFERENCES

Adrian, R. J., Ferreira, R. T. D. S., Boberg, T., 1986: Turbulent thermal convection in wide horizontal fluid layers. Experiments in Fluids 4, 121-141.

Clark, T., 1977: A small-scale dynamical model using a terrain-following coordinate transformation. J. Comput. Phys., 24, 186-215.

Kaimal, J. C., Eversole, R. A., Lenschow, D. H., Stankow, B. B., Kahn, P. H., Businger, J. A., 1' 2: Spectral characteristics of the convective boundary layer over uneven terrain. J. Atmos. Sci. 39, 1098-1114.

Krettenauer, K , 1991: Numerische Simulation turbulenter Konvektion über gewellten Flächen. Dissertation, TU Munich.

Krettenauer, K., Schumann, U., 1989: Direct numerical simulation of thermal convection over a wavy surface. Meteorol. Atmos. Phys. 41, 165-179.

Krettenauer, K., Schumann, U., 1991: Numerical simulation of turbulent convection over a wavy terrain. J. Fluid Mech., to appear.

Mahrt, L., 1991: Eddy asymmetry in the sheared heated boundary layer. J. Atmos. Sci. 48, 472-492.

Nieuwstadt, F. T. M., 1990: Direct and large-eddy simulation of free convection. Proc. 9th Intern. Heat Transfer Conference, Jerusalem, 19-24 August 1990, Vol. I, pp. 37-47.

Schmidt, H., Schumann, U., 1989: Coherent structure of the convective boundary layer deduced from large-eddy simulation. J. Fluid Mech., 200, 511-562.

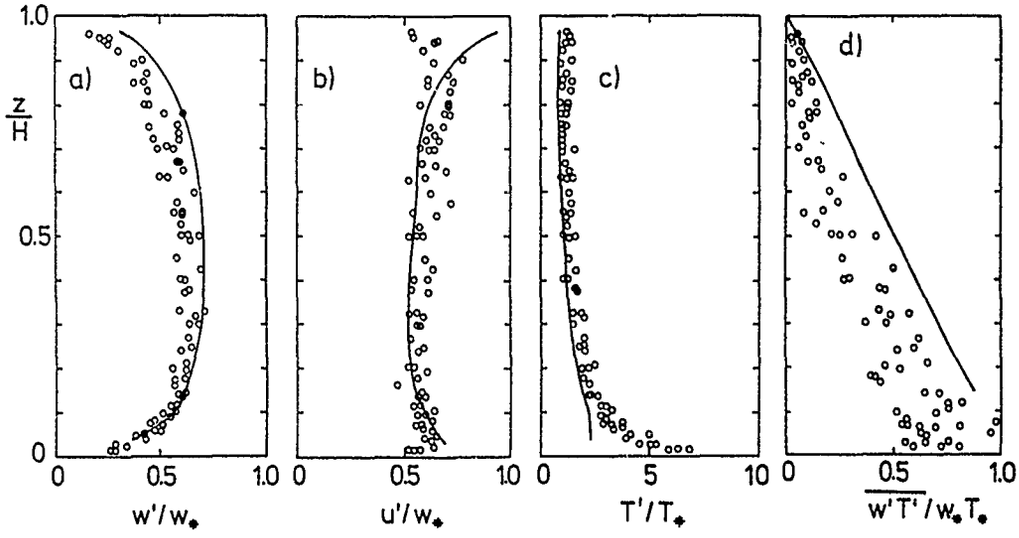

Fig. 1 Root-mean-square fluctuations of a) vertical velocity variance w', b) horizontal velocity variance u', c) temperature variance T', versus height for the LES-case with flat surface. Full curves in a), b) and d) enclose the sum of resolved and SGS contributions, the curve c) depicts the resolved part only. The circles represent the experimental results of Adrian et al. (1986).

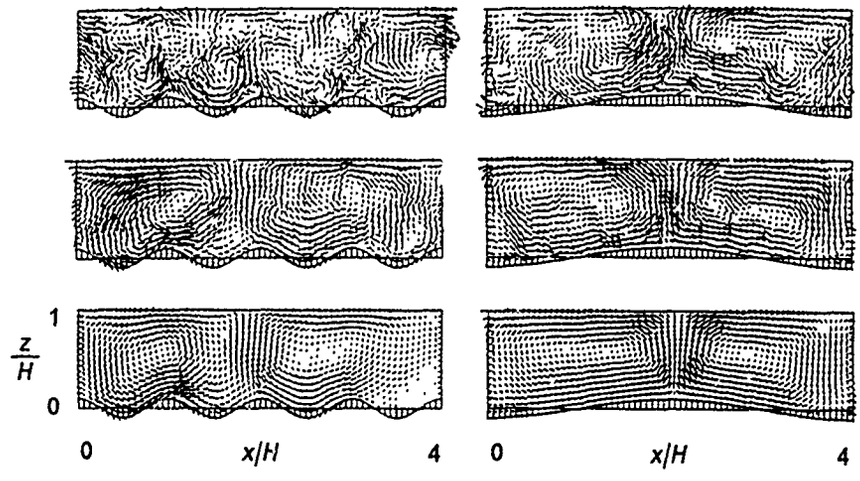

Fig. 2 Influence of wavelength of orography on velocity field in the LES in a vertical plane for various averages and wavelengths. Left: $\lambda = H$. Right: $\lambda = 4H$. Top: Instantaneous result at $t = 35\,t_*$. Middle: Result averaged from $t/t_* = 30$ to 35. Bottom: Result averaged over the same time interval and in addition over the y-coordinate. Maximum normalized velocity vectors, from top to bottom, left: 2.20, 1.50, 1.03; right: 2.59, 1.63, 1.34.

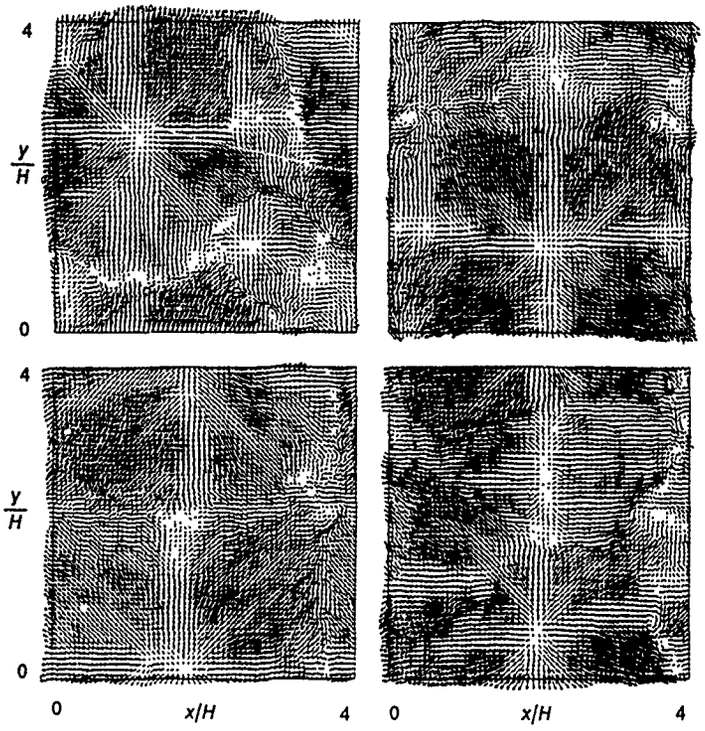

Fig. 3 Velocity field in a horizontal plane for various wavelength (time averaged from $t/t_* = 30$ to 35. Top-left: flat surface; top-right: $\lambda = H$; bottom-left: $\lambda = 2H$.; bottom-right: $\lambda = 4H$.. Maximum normalized velocity vectors: 1.69, 1.79, 1.93, 1.91, respectively.

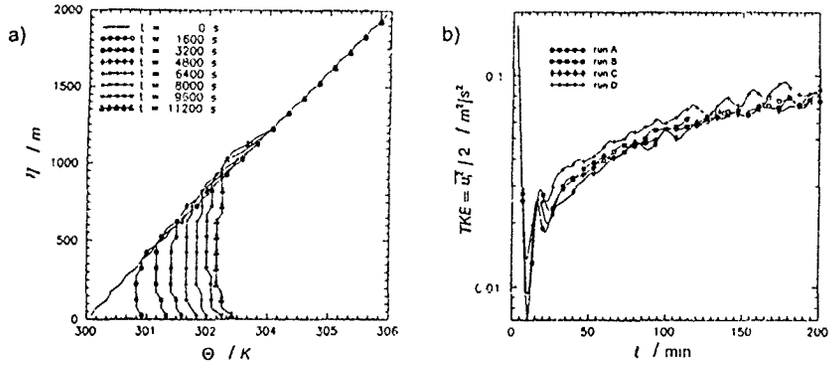

Fig. 4 a) Temporal evolution of the profiles of mean potential temperature (averaged over planes $\eta = const.$) for run (C). b) Spatially averaged kinetic energy of turbulent motion versus integration time t for different runs.

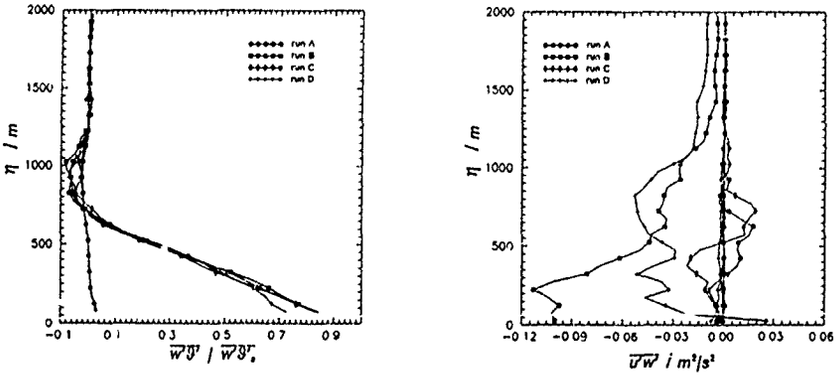

Fig. 5 Turbulent temperature and momentum flux versus height η for runs (A) to (D). All curves are averaged over planes $\eta = const.$ and the time period $100\,min \leq t \leq 200\,min$ and they depict resolved and subgrid parts.

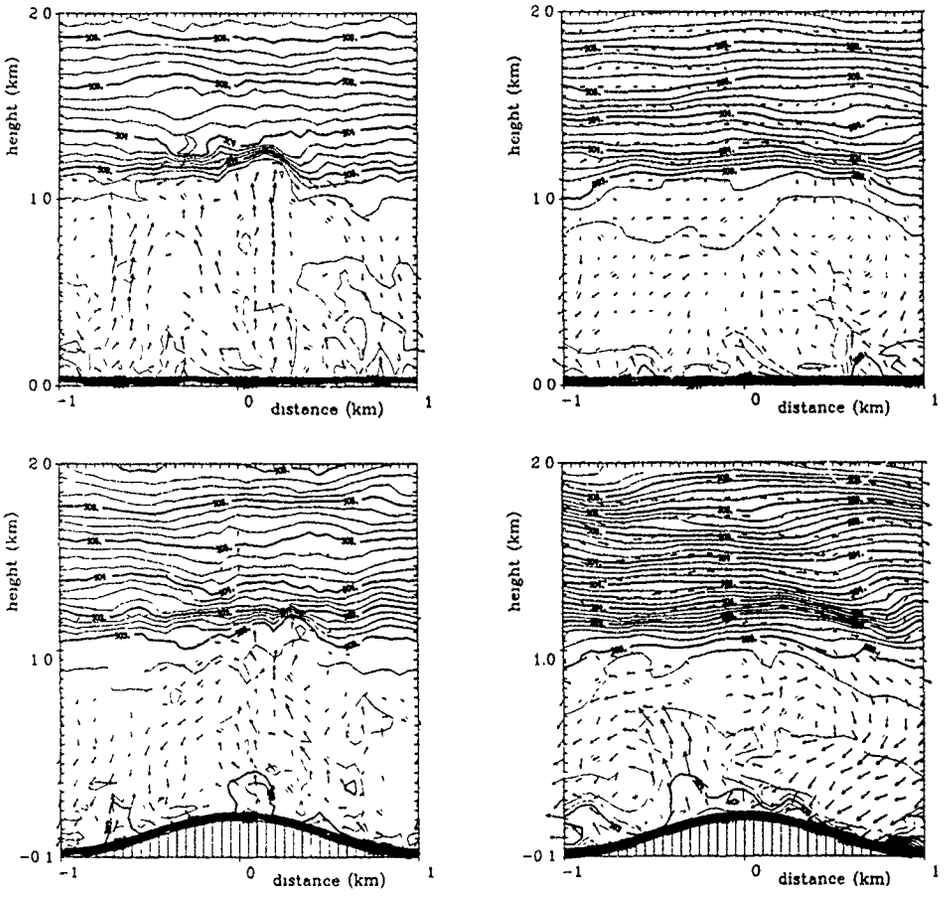

Fig. 6 Influence of $\bar{u}$ and of orography on the temperature and velocity field in a vertical plane $y = 0$. Top left: run A, top right: run B, bottom left: run C, bottom right: run D. Contour plots of Θ ($\Delta\Theta = 0.1\ K$), and $u - w$-vectors. The velocity in x-direction is reduced by $5\ m/s$ for cases with mean wind. The maximum vector is $3.31\ m/s$ for all runs. The figure shows instantaneous results at $t \approx 3h$.

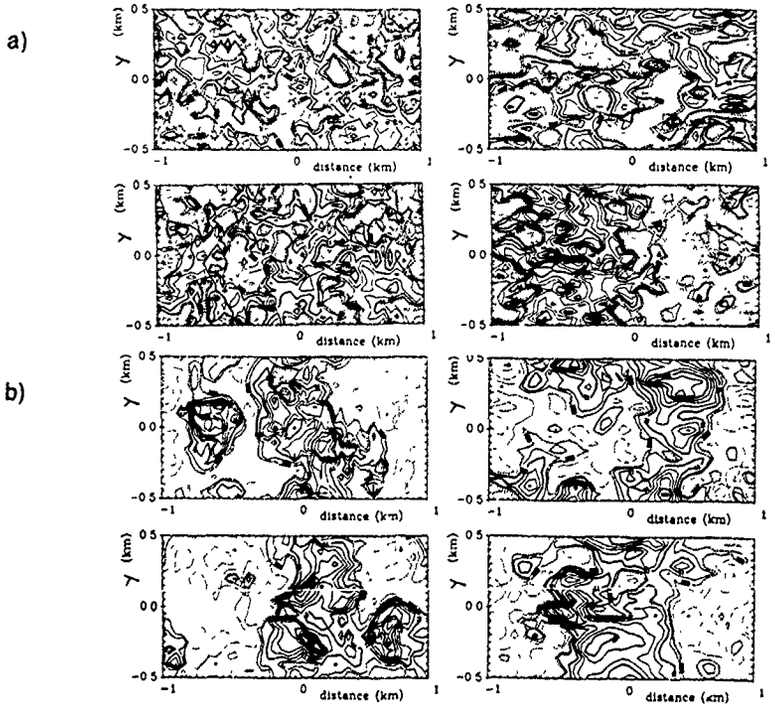

Fig. 7 Influence of horizontal mean flow $\bar{u}$ in x-direction and of orography on the vertical velocity field in two horizontal planes $\eta = 50m$ (a) and $\eta = 600\ m$ (b). The runs are denoted as in Fig.6, the contour increment is $\Delta w = 0.4\ m/s$. Solid lines denote positive, dashed lines negative values.

EIGHTH SYMPOSIUM ON
TURBULENT SHEAR FLOWS
Technical University of Munich
September 9-11, 1991

CALCULATION OF VORTEX SHEDDING PAST A SQUARE CYLINDER WITH VARIOUS TURBULENCE MODELS

R. Franke* and W. Rodi

Sonderforschungsbereich 210, University of Karlsruhe
Kaiserstr. 12, 7500 Karlsruhe, Germany

*) present address: Dornier GmbH, 7990 Friedrichshafen, Germany

ABSTRACT

The vortex-shedding flow past a square cylinder at Re = 22.000 was calculated with various turbulence models. The 2D periodic shedding motion was resolved in an unsteady calculation, and the superimposed stochastic turbulent fluctuations were simulated both with the k-ε eddy-visocity model and with a Reynolds-stress equation model. For both models, the viscosity-affected near-wall region was either bridged by wall functions or was resolved with a simpler one-equation model using a prescribed length-scale distribution. The k-ε model with wall functions does not yield unsteady vortex motion while the other model variants do. The two-layer k-ε model underpredicts severely the periodic fluctuations and also the Stanton number and drag coefficient. The Reynolds-stress-equation models yield considerably better agreement with experiments, but tend to overpredict the periodic fluctuating motion and also miss some other details of the flow behaviour.

1. INTRODUCTION

The flow past slender, bluff structures is frequently associated with periodic vortex shedding causing dynamic loading on the structures. For the design of such structures, the unsteady loading forces must be known and hence methods for predicting the flow and the forces are of great practical importance. For situations with low Reynolds numbers, successful calculations have been obtained for square and circular cylinders by solving numerically the unsteady Navier-Stokes equations, e.g. Lecointe and Piquet (1989), Franke et al. (1990). For situations with high Reynolds numbers, which usually occur in practice, stochastic three-dimensional turbulent fluctuations are superimposed on the periodic vortex-shedding motion. A resolution of these motions in a direct simulation is not feasible at present. Tamura et al. (1990) have reported such calculations without a turbulence model, but for the higher Reynolds numbers considered by them, the small-scale turbulent motion could certainly not be resolved by the numerical grids used. They employed a third-order upwind differencing scheme which introduces numerical damping and basically takes over the role of a subgrid-scale model in a large-eddy simulation. The results obtained by Tamura et al. (1990) are certainly very interesting and surprisingly successful, but the approach of relying on numerical damping instead of a subgrid-scale model requires further examination. The work has shown, however, that large-eddy simulations are possible for vortex-shedding flow at high Reynolds numbers, but such calculations are very costly. Hence, there is still a need for more economic calculation methods based on the use of a turbulence model for simulating the influence of the stochastic fluctuations on the periodic vortex-shedding motion. So far, successsful applications of a turbulence model to vortex-shedding flow have not been reported. It should be mentioned here that steady calculations for the time-mean field using standard turbulence models were not successful (e.g. Majumdar and Rodi, 1985) since the strong momentum exchange by the periodic vortex motion is not accounted for in this approach.

The aim of the research reported here was to test various established turbulence models in calculations of high-Reynolds-number vortex-shedding flows. One candidate was the k-ε turbulence model as this is presently the most widely used model in practice. The preliminary study of Franke et al. (1989) evaluating the detailed experiments of Cantwell and Coles (1983) has shown already that this eddy-viscosity model is unlikely to yield satisfactory results since it does not take proper account of history and transport effects which are of eminent importance in unsteady vortex-shedding flows. A Reynolds-stress-equation model was therefore considered necessary to account for the transport and history effects, and hence the model of this type due to Launder, Reece and Rodi (1975) was also tested. Two approaches were used for the treatment of near-wall regions, namely the wall-function approach and the two-layer approach in which the viscosity-affected near-wall region is resolved with a simpler one-equation model. The test calculations were carried out for two-dimensional vortex-shedding flow past a square cylinder. For this, detailed measurements have recently become available for a Reynolds number of Re = 22.000 (Lyn, 1990).

2. CALCULATION PROCEDURE

2.1 Mean-Flow Equations

In flows with periodic unsteadiness, an instantaneous quantity f can be separated into (see Fig. 1)

$$f = \underbrace{\overline{f} + \tilde{f}}_{<f>} + f' \qquad (1)$$

where $\overline{f}$ is the time-mean value, <f> the ensemble-average value, $\tilde{f}$ the periodic fluctuation and f' the stochastic turbulent fluctuation. In the calculations presented here, equations governing the temporal and spatial variation of the ensemble-averaged velocity components and pressure representing the mean flow are solved. These are the ensemble-averaged continuity and momentum equations, which in tensor notation read as follows:

$$\frac{\partial < u_i >}{\partial x_i} = 0 \qquad (2)$$

$$\frac{\partial < u_i >}{\partial t} + < u_j > \frac{\partial < u_i >}{\partial x_j} = -\frac{1}{\rho}\frac{\partial < p >}{\partial x_i} + \frac{\partial}{\partial x_j}\left[\left(\nu \frac{\partial < u_i >}{\partial x_j} - < u_i' u_j' >\right)\right] \qquad (3)$$

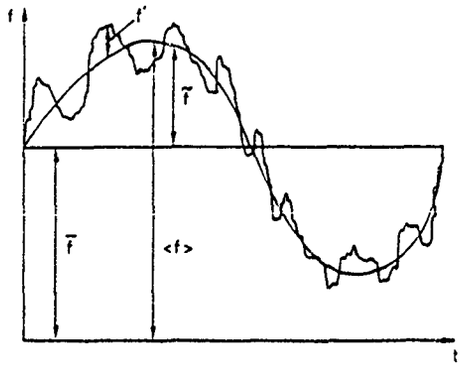

Fig. 1: Definition of mean and fluctuating values in periodic unsteady motion

In the present 2D calculations, only the velocity components <u> and <v> are present and all quantities depend only on x and y (see Fig. 2 for coordinate system). In the momentum equations, the correlation $<u_i' u_j'>$ between the fluctuating velocities appears which represents the Reynold stresses and needs to be simulated by a statistical turbulence model. In laminar vortex-shedding flow at low Reynolds numbers, this term is absent and the only stresses acting are the viscous ones. In the present work, the calculation procedure of Franke et al. (1990) for laminar flows was extended by incorporating various turbulence models into the numerical solution procedure.

2.2 Turbulence Models

Before the turbulence models used are introduced, the problem areas associated with the challenging vortex-shedding flow considered are discussed briefly with respect to turbulence modelling. Three sub-areas of the flow can be identified:

(i) Stagnation Flow

In front of a bluff body, a stagnation flow exists which behaves virtually like potential flow. Except very near the wall, stresses (viscous and turbulent) have very little influence on the mean-flow behaviour. However, any turbulence and associated stresses generated in this region influence the flow behaviour downstream, e.g. the separated shear layer on the upper and lower surface of a square cylinder. If turbulent fluctuations are present, there is no shear-stress production on the stagnation line but only normal-stress production which governs the turbulence level in this region. The normal-stress production depends on the separation between the normal stresses $<u'^2>$ and $<v'^2>$ which is grossly overpredicted by an isotropic eddy-viscosity model and requires for a realistic simulation a Reynolds-stress-equation model (Taulbee and Tran, 1988).

(ii) Attached and Detached Shear Layers on Side Walls

In the vicinity of the side walls of a square cylinder, a complex flow field develops with partly attached and partly detached shear layers, possible reattachment on the side wall, as well as laminar-turbulent transition. Here, inertial forces, viscous and turbulent stresses interplay, and the region is of considerable importance for the development of the vortex-shedding flow as here the origin of the vortex instability is located. The details of the flow mechanisms in this region are not well understood, and the phenomena are difficult to describe by a turbulence model. Because of the influence of viscous forces, wall functions are unlikely to be very suitable.

(iii) Wake Region

In the wake past the cylinder, convection and turbulent stresses dominate and the viscous forces are negligible. The vortices generated in the region discussed under (ii) are convected downstream forming a vortex street. The periodic vortex motion is damped by turbulent stresses. The modelling of turbulence in this region mainly affects the vortex frequency but not so much the amplitude of the forces acting on the body. History and transport effects are particularly important in this region so that an eddy-viscosity model is unlikely to do justice to this region (see Franke et al., 1989).

Two different models for simulating the turbulent stresses in the bulk of the flow away from walls were tested and are briefly introduced in the following. The two approaches used for treating the near-wall region are described thereafter. The actual turbulence-model equations are not given since only models have been used which are fairly standard by now and have been described elsewhere (e.g. Rodi, 1980). For all equations, the ensemble-average form has been employed.

k-ε model. The standard form of the k-ε model was applied to many steady flows and had some success also for calculating separated flows, even though the accuracy of the predictions was not as high as for shear-layer flows. Here, the standard k-ε model is simply adopted for ensemble-averaged quantities. The Reynolds stresses are calculated from the eddy-viscosity relation

$$-<u_i'u_j'> = <\nu_t>\left(\frac{\partial <u_i>}{\partial x_j}+\frac{\partial <u_j>}{\partial x_i}\right)-\frac{2}{3}<k>\delta_{ij} \quad (4)$$

The eddy viscosity $<\nu_t>$ is related to the kinetic energy <k> and its dissipation rate <ε>and the spatial and temporal distribution of these quantities is determined from model transport equations.The standard values were adopted for the empirical constants (see Rodi, 1980).

Reynolds-Stress Equation (RSE) Model. In order to account better for the important transport and history effects in vortex-shedding flows, a second-order closure model was tested which does not employ the eddy-viscosity hypothesis but determines the individual turbulent stresses $<u_iu_j>$ from transport equations. The standard model of Launder, Reece and Rodi (1975) was adopted, with wall corrections to the pressure-strain terms due to Gibson and Launder (1978).The wall corrections effect damping of the normal fluctuations near the wall and enhance the fluctuations parallel to the wall. Again, standard values were taken for the empirical constants (see Franke, 1991).

Near-Wall Treatment. For both turbulence models described above, two approaches were tested for handling the near-wall region. Wall functions are still used in most practical calculations and were therefore tested also here. In this approach, the viscous sublayer is not resolved but the first grid point in a numerical calculation is located outside this layer. Based on the assumption of the logarithmic velocity distribution and of local equilibrium of turbulence (production = dissipation) the flow quantities at this grid point with wall distance y_c are related to the friction velocity $U_\tau = (\tau_{wall}/\rho)^{1/2}$ by

$$u_c = \frac{u_\tau}{\kappa} ln(y^+E) \qquad k_c = \frac{u_\tau^2}{\sqrt{c_\mu}} \qquad \epsilon_c = \frac{u_\tau^3}{\kappa \cdot y_c} \quad (5)$$

Here, $y^+ = U_\tau y/\nu$ is a dimensionless wall distance. In connection with the RSE model, the shear stress at point c is set equal to U_τ^2, and invoking local equilibrium conditions on the stress equations yields the normal stresses at the first grid point.

The assumptions of a logarithmic velocity distribution and of local equilibrium of turbulence are violated in separated flows (see e.g. Rodi, 1991), especially near separation and reattachment regions. One way around this problem would be to use low-Reynolds-number versions of the models employed away from the wall. For the k-ε model, a variety of such versions is available, but they have virtually all been tested only for attached boundary layers. For RSE models, low-Re versions are still under development and not yet ready for application to a complex flow. In both cases, such model versions require very fine numerical resolution near the wall which has an adverse effect on the computational effort required. For these reasons, a two-layer approach was adopted here in which the viscosity-affected near-wall region is resolved by a simpler one-equation model, which does not solve a dissipation-rate equation but uses a prescribed length-scale distribution and hence requires less numerical resolution near the wall. The one-equation model is then matched to the model used away from the wall. In calculations with both the k-ε model and the RSE model away from the wall, the one-equation model due to Norris-Reynolds (1975) was adopted near the wall. The k-ε-based two-layer model was already tested quite extensively for steady flows, including separated flows (see Rodi, 1991). The Norris-Reynolds model employs the eddy-viscosity hypothesis and calculates the eddy viscosity from:

$$<\nu_t^{NR}> = f_\mu c_\mu \sqrt{<k>} L\,, \qquad f_\mu = 1 - e^{(-0.198\sqrt{<k>}y_w/\nu)} \quad (6)$$

where f_μ is a damping function similar to the van Driest function accounting for the reduction of turbulent momentum exchange very near the wall. The kinetic energy <k> is obtained from the same <k>-equation as used in the k-ε model, while the length scale L is assumed to vary linearly with distance from the wall as $L = \kappa y_w/c_\mu^{3/4}$ in the very thin near-wall layer where the model is applied ($\kappa = 0.4187$, $c_\mu = 0.09$). The dissipation rate <ε> appearing as source term in the <k>-equation is not obtained from an equation but calculated from the following algebraic relation:

$$<\epsilon> = \frac{<k>^{3/2}}{L}\left[1+\frac{2\kappa^2\nu}{c_\mu^{1.5}\sqrt{<k>}L}\right] \quad (7)$$

When used in combination with the RSE model, only the shear stress in the viscous sublayer is calculated with the aid of an eddy viscosity relation according to (6). The normal stresses appearing in the momentum equations are determined by assuming $<u_iu_j>/<k>$ = constant across the viscous sublayer. The ratio taken is the one resulting from the RSE model at the matching

point between this model and the one-equation model, while <k> is taken from the k-equation. This approach is certainly very crude and does not account for the damping of the normal fluctuations very near the wall, but in the thin region where the one-equation model is employed the flow has boundary-layer character and the normal stresses are small compared with the shear stress so that they do not need to be determined very accurately.

The matching between the one-equation model and the model used further away from the wall should be effected near the edge of the viscous sublayer where viscosity effects have become small. This is the case when the damping function at f_μ in (6) has a value near unity, and in the calculations presented the matching was done where $f_\mu = 0.95$. For fully turbulent boundary layers this corresponds to $y^+ \approx 83$. For good near-wall resolution, the first grid point should be located at $y^+ \approx 1$. When the viscous sublayer is resolved with the one-equation model, the no-slip conditions are used as boundary conditions, i.e. both velocity components are zero and also the turbulent kinetic energy <k>.

2.3 Numerical Solution Procedure

The differential equations governing the mean-flow and the turbulence field were solved numerically with an extended version of the program TEACH developed by Gosman and Pun (1973). This employs a finite-volume method for solving the equations in primitive variables on a two-dimensional staggered grid. The coupling between continuity and momentum equations was achieved with the SIMPLEC predictor-corrector algorithm of van Doormal and Raithby (1984), which is an improved version of the SIMPLE algorithm incorporated in the original TEACH program. The central/upwind hybrid spatial discretization scheme in the original TEACH program was replaced by the QUICK scheme (Quadratic Upwind Interpolation for Convective Kinematics) proposed by Leonard (1979). This scheme combines the high accuracy of a third-order scheme with the stabilising effect of uwpind weighting. A disadvantage of the scheme is its unboundedness, which may cause over- and undershoots. It should be mentioned that central/upwind hybrid differencing introduced too much damping so that no unsteady vortex shedding resulted. For time discretization, the fully implicit first-order Euler scheme was chosen. It provides high stability but requires small time steps in order to obtain accurate solutions (more than 100 time steps per period were used). The resulting system of linear difference equations was solved by the strongly implicit method of Stone (1968). A more detailed description of the numerical method is given in Franke (1991). The computational domain in which the equations were solved and the outer boundary conditions are shown in Fig. 2. In connection with wall functions, a 70 x 64 grid was used with $\Delta y_c/D = 0.022$. For calculations with the two-layer approach, in which the viscosity-affected sublayers are resolved, a 186 x 156 grid was used with the first point at a distance from the wall of $\Delta y_c/D = 0.00125$. On an IBM 3090, the calculation time to cover one shedding period was typically 1/2 hour for the RSE model with wall functions and 5 hours for the two-layer RSE-model.

3. CALCULATION RESULTS AND COMPARISON WITH EXPERIMENTS

3.1 Experimental Data

The availability of experimental data is crucial for the testing of turbulence models. In the case of unsteady vortex-shedding flows, a proper testing of the models can only be done when results of time-resolved measurements are available which give information on the temporal variation of ensemble-averaged quantities and separate the fluctuations into periodic and turbulent ones. Such detailed data on flows past bluff bodies are rare, but recently Lyn (1990) has completed time-resolved two-channel LDA measurements in the wake past a square cylinder at Re = 22.000. In these experiments, the shedding period was divided into 20 phase angles, for which the velocity-component and Reynolds-stress distributions were reported as ensemble-averaged values in a plane perpendicular to the cylinder. The turbulence level in the oncoming flow was 2%. The only other fairly detailed measurements of the flow past a square cylinder known to the authors are those of Durao et al. (1988) for Re = 14.000. However, these authors obtained only time-averaged

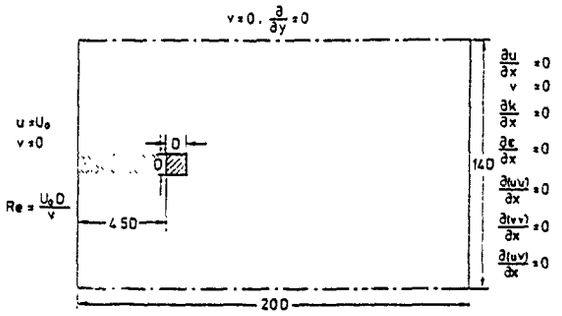

Fig. 2: Calculation domain and boundary conditions

data and did not separate the fluctuations into periodic and turbulent components. The flow situation investigated by Lyn (1990) was therefore taken as test case.

3.2 Integral Parameters and Time-Mean Distributions

The calculations with the k-ε model using wall functions yielded a steady solution and no vortex shedding. Apparently this combination of model and near-wall treatment introduces too strong damping so that a periodic vortex-shedding motion cannot persist. Periodic vortex shedding was obtained with the other three model variants, and a sequence of streamlines covering approximately one period is shown in Fig. 5 below. Values of various integral parameters predicted with the turbulence-model variants tested are compared in Table 1 with experimental values. The parameters considered are the dimensionless shedding frequency (Strouhal number $St = fD/U_0$), the time-averaged drag coefficient $\overline{c_D}$ and the amplitudes of the oscillations in drag coefficient c_D and lift coefficient c_L. The k-ε model yields too low shedding frequency and drag coefficient, the latter however being somewhat higher than that obtained in the stationary solution with wall functions. The drag coefficient does not oscillate, but there is a small oscillation in the lift coefficient. Results obtained with a modified two-layer κ-ε model are also included in Table 1. In this model, the unrealistic normal-stress production of k in the stagnation region due to the use of an isotropic eddy-viscosity model, which leads to excessive k-levels (see Fig. 5 below) is suppressed in front of the body (shaded area in Fig. 2). This measure reduces significantly the k-level in the front part and influences mainly the vortex formation regions near the side walls of the cylinder. The prediction of the integral parameters is improved somewhat by this measure. Further improvement is achieved by use of the RSE models. In combination with wall functions, the predicted Strouhal number and drag coefficient are now in good agreement with the measured ones. When the two-layer variant is used, these quantities are predicted too high; by switching from wall functions to a two-layer approach, the shedding frequency increases while the amplitude of the oscillating forces acting on the body is reduced. This detail of the calculation is not well understood at the present time. Consistent with the increase in $\overline{c_D}$ when moving from the standard k-ε model to the two-layer RSE model is a reduction of the base pressure. The distribution of the time-mean pressure along the cylinder

Table 1: Integral Parameters

	Turbulence models					Experiments
	k-ε with wall f.	two layer k-ε	mod. two-layer k-ε	RSE with wall funct.	two-layer RSE	
St	stationary	.124	.129	.136	.159	Lyn .135 Durao .139
$\overline{c}_D$	1.55	1.79	1.89	2.15	2.43	2.05-2.23
$\tilde{c}_D$	-	0.0	0.0	.383	.079	-
$\tilde{c}_L$	-	.323	.883	2.11	1.84	-

walls is compared in Franke (1991) with various experiments carried out at different Reynolds numbers and free-stream turbulence levels. The experimental results themselves differ by about 15 to 20%. The base pressure predicted by the RSE model with wall functions falls between the measurement results, while the k-ε model predictions yield too high and the predictions with the two-layer RSE model too low base pressures.

Fig. 3 displays the distribution of the time-mean velocity $\bar{u}$ along the centre-line and gives information on the length of the time-averaged separation zone behind the cylinder. Experimental data from Lyn's (1990) and Durao et al.'s (1988) experimental study are included. The data agree fairly well in the near-cylinder region, but the centreline velocity measured by Lyn approaches the free-stream velocity much slower than that measured by Durao et al. The reasons for this difference and for the very slow increase of the centreline velocity in Lyn's experiments are not clear. While, as expected, the velocity distribution in front of the cylinder is influenced very little by the turbulence model used, there are fairly large differences in the wake region, and in particular regarding the length of the separation zone. The k-ε model variants overpredict the length of this zone considerably, indicating that there is not enough momentum exchange introduced by these models. Since in vortex-shedding flows the momentum exchange is mainly due to the periodic vortex-shedding motion (see e.g. Cantwell and Coles 1983, Franke 1991), this also means that the periodic fluctuations are underpredicted significantly, as will be confirmed shortly. The modified k-ε model predicts a somewhat shorter separation zone, pointing to a more realistic simulation of the periodic vortex-shedding motion. Both RSE model variants predict on the other hand too short separation bubbles, and there is little difference between the results obtained with the two versions near the cylinder; there are larger differences further downstream but these should not be taken too seriously since here there may be an influence of the different numerical grids used, which are quite coarse in this downstream region.

The distribution of the total (periodic plus turbulent) fluctuating kinetic energy along the centreline shown in Fig. 4 gives a clue to the results discussed so far and in particular to the differences between the various turbulence models. The two-layer k-ε model can be seen to underpredict severely the fluctuation level behind the cylinder, while the RSE models give approximately the correct level and distribution of the total fluctuations. The differences between the RSE calculations using wall functions and the two-layer approach are of the same order as the differences between the experimental values of Lyn (1990) and Durao et al. (1988), but the two-layer version yields a higher fluctuation level, which is consistent with the higher Strouhal number and drag coefficient predicted. The modified k-ε model, in which the k-production in front of the body is suppressed, yields a somewhat improved fluctuation level which, however, is still far below the measured one. This shows that the problems with the k-ε model originate only to a small extent from the excessive k-production by this model in the stagnation region. The effect of this excessive production can be seen best in Fig. 5, which displays the distribution of the time-mean turbulent kinetic energy $\bar{k}$ along the centreline. Fairly large k-levels are produced right in front of the cylinder which are unrealistic. When the RSE models are used, much lower k-levels result in the stagnation region. Behind the cylinder, all models can be seen to underpredict considerably the level of turbulence energy on the centreline and particularly so in and near the separation region. Since the RSE models predict the correct level of total fluctuation energy, this means that they overpredict the periodic fluctuations. The k-ε models yield higher turbulent fluctuation levels in the wake than the RSE models and this may cause a damping of the periodic fluctuating motion and in turn the observed underprediction of this motion. The use of the two-layer approach in connection with the RSE model increases the turbulent fluctuations in the separation region. This may cause the reduced amplitudes in the drag and lift forces on the cylinder, but apparently on the whole the periodic fluctuations are increased rather than reduced as can be seen from Fig. 4 and can also be inferred from the increased Strouhal number and mean drag coefficient.

3.3 Phase-Dependent Results

Since the Reynolds-stress models gave much more realistic

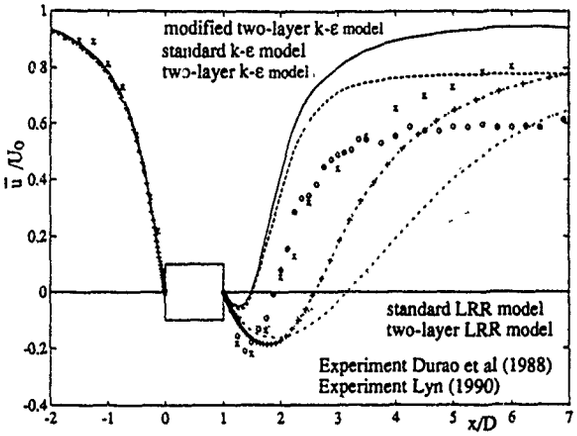

Fig. 3: Time-mean velocity $\bar{u}$ along the centre line

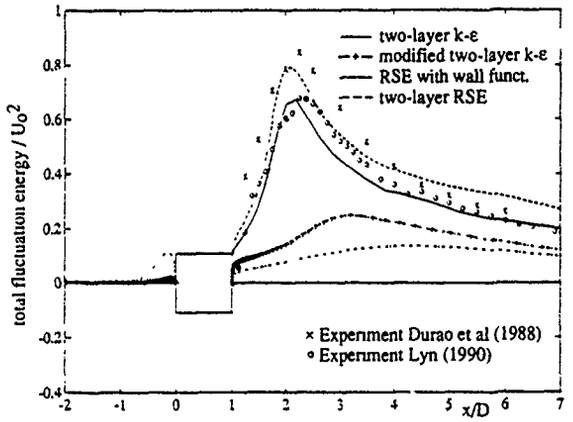

Fig. 4: Total kinetic energy of fluctuations (periodic + turbulent) along centre line

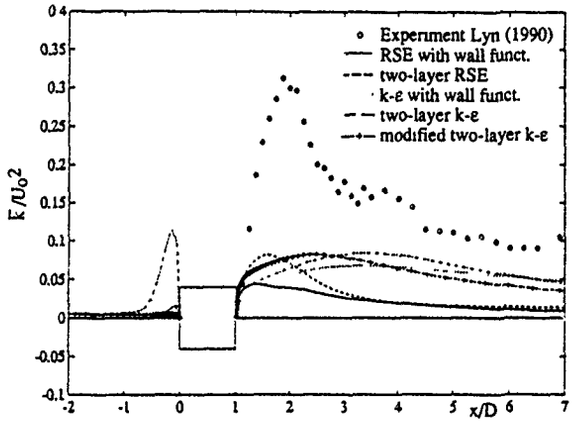

Fig. 5: Time-mean turbulent kinetic energy $\bar{k}$ along centre line

fluctuation levels than the k-ε model, phase-dependent results are only presented for the calculations with the RSE models. Fig. 6 shows the streamlines predicted with the RSE model using wall functions at three phases; at two of the phases experimentally determined streamlines are available and are also given for comparison. The streamlines predicted with the two-layer RSE model are not significantly different. The alternating vortex shedding can be seen clearly, and there is reasonable agreement about the streamline development with the experiments. However, certain differences can be noted. At some phases, the predictions do not show a negative <u>-velocity on the leeward

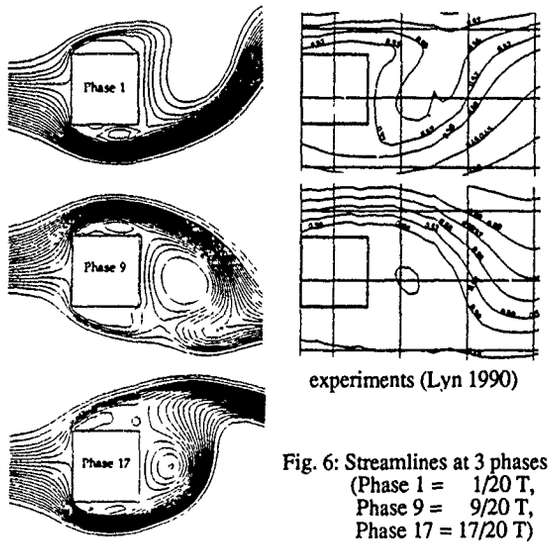

experiments (Lyn 1990)

calculations, RSE wall funct.

Fig. 6: Streamlines at 3 phases
(Phase 1 = 1/20 T,
Phase 9 = 9/20 T,
Phase 17 = 17/20 T)

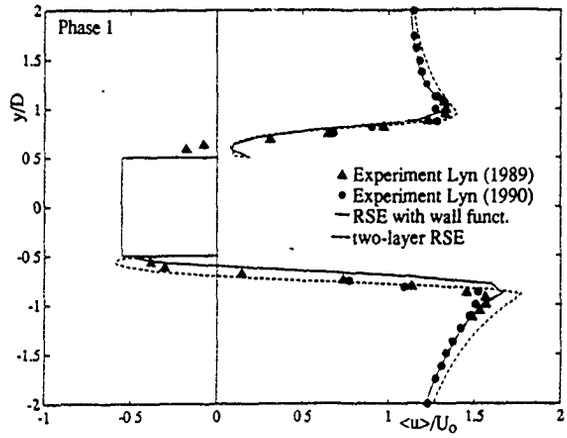

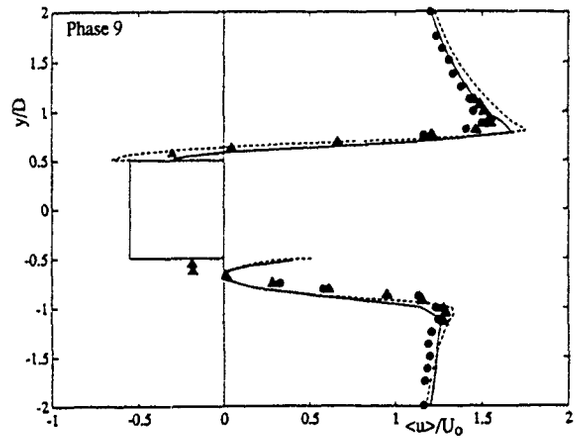

Fig. 7: Profiles of <u> at x-location of rear cylinder wall for 2 phases

side of the cylinder while the experiments indicate that the velocity is negative at all times (for further evidence see Franke, 1991). Also, the model predicts temporary reattachment of the separated flow on the side walls near the rear corner (e.g. phase 1, topside) which was not found in the experiments. This can be seen more clearly in Fig. 7 where the <u>-velocity distribution at the x-position of the rear cylinder wall is compared with measurements. Here, in addition to Lyn's (1990) two-channel measurements also Lyn's (1989) one-channel measurements extending closer to the wall are included. At the two phases considered (1 and 9) the calculations do not show negative velocities on one of the side walls while in the experiments the velocity very near the wall is always negative. Considering the results at all phases (which could not be included here) the two-layer RSE model gives slightly better agreement with the measurements than the model using wall functions. However, the discrepancies point to a weakness of the model in underpredicting the size of the separation zone near the side walls. Fig. 8 presents the variation of the ensemble-averaged lateral velocity <v> along the centreline for two phases. The agreement with the

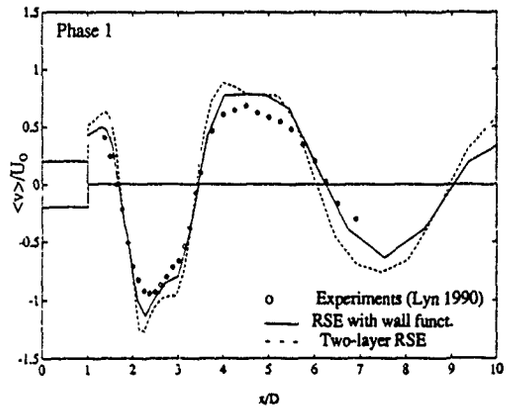

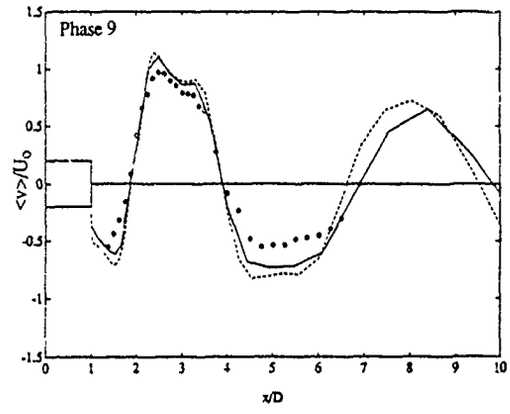

Fig. 8: Lateral velocity <v> along centre line at 2 phases

measurements is fairly good, both with respect to the maximum values and to the zero crossings, the latter being a measure of the size of the shed vortices. There is no significant difference here between the model using wall functions and the two-layer approach. Similar distributions for the velocity component <u> as given in Franke (1991) show inferior agreement with experiments, firstly because in the downstream region the time-mean u-velocity is overpredicted, as can be seen from Fig. 3, but also because near the rear cylinder wall the velocity is not always negative as it was found in the experiments.

Finally, Fig. 9 compares calculated and measured <k>-contours at one phase. The differences between calculations obtained with the two RSE variants are not very significant compared with the differences to the experiments. Of course, the asymmetry in the contour lines is basically the same in the calculations and experiments, as must be expected from the similarity of the streamlines, but the maxima of <k> in the experimental data are located much closer to the centreline than in the calculations. This points to a weakness of the present calculation model which appears to predict the centres of the vortices considerably further from the centreline than the experiments indicate. This is supported by a comparison of the RMS values of the periodic fluctuations $\tilde{u}$ on the centreline, which are virtually zero in the experiment and take on a sizeable value in the predictions (Franke, 1991).

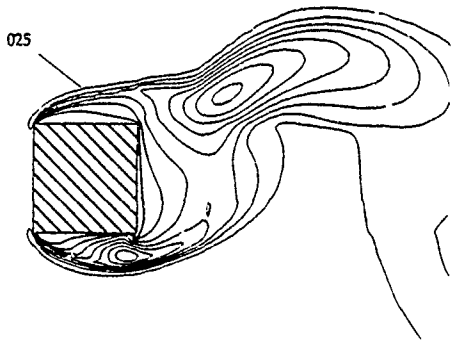

calculations, 2-layer RSE

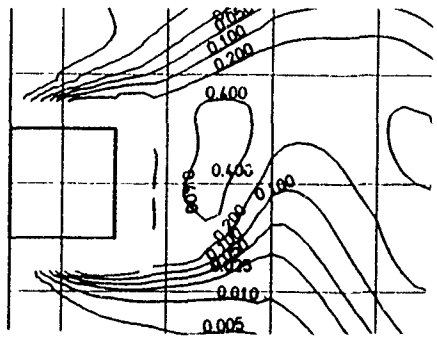

experiments (Lyn 1990)

Fig. 9: <k> contours at phase 1

4. CONCLUSIONS

Time-dependent calculations of vortex-shedding flow past a square cylinder were carried out with various turbulence models and near-wall treatments. The k-ε eddy-viscosity model combined with wall functions introduces too much damping so that no vortex shedding is predicted. With the two-layer approach, the model does predict vortex shedding but the periodic motion is considerably too small so that there is too little momentum transport resulting in a too long time-mean separation zone and too low values of the Strouhal number and drag coefficient. The RSE models predict the correct level of total fluctuations, but overpredict the periodic component while they considerably undepredict the level of turbulence fluctuations in the wake. Concerning the Strouhal number and mean drag coefficient, the RSE model with wall functions yields the best agreement with the experiments while the two-layer RSE model produces too high values. Concerning other flow features there is not too much difference in the calculations obtained with the two model variants. Both versions yield a reattachment on the side walls and positive u-velocity near the rear wall at certain times during one period which was not observed in the experiments. These predicted features are probably due to an overprediction of the periodic fluctuations. Also, the vortex centres are calculated too far from the centre line of the cylinder. A refinement of the RSE model making it more responsive to unsteady effects may improve the calculations. However, the limits of conventional turbulence models are probably reached in this flow with large-scale vortex structure and a better reproduction of the details probably calls for a large-eddy simulation.

5. ACKNOWLEDGEMENTS

The work reported here was sponsored by the Deutsche Forschungsgemeinschaft through the Sonderforschungsbereich 210. The calculations were carried out on the IBM 3090 computer of the University of Karlsruhe. The authors are grateful to Mrs. R. Zschernitz for her expert typing of the manuscript.

6. REFERENCES

Cantwell, B. and Coles, D., 1983, An experimental study of entrainment and transport in the turbulent near-wake of a circular cylinder. J. Fluid Mech., Vol. 136, pp. 321-374.

Franke, R., 1991, Numerische Berechnung der instationären Wirbelablösung hinter zylindrischen Körpern, Ph.D. Thesis, University of Karlsruhe.

Franke, R., Rodi, W. and Schönung, B., 1989, Analysis of experimental vortex-shedding data with respect to turbulence modelling, Proc. 7th Turbulent Shear Flow Symposium, Stanford, USA.

Franke, R., Rodi, W. and Schönung, B., 1990, Numerical calculation of laminar vortex-shedding flow past cylinders, J. Wind Engineering and Industrial Aerodynamics, Vol. 35, pp. 237-257.

Gibson, M.M. and Launder, B.E., 1987, Ground effects on pressure fluctuations in the atmospheric boundary layer, J. Fluid Mech., Vol 86, p- 491.

Gosman, A.D. and Pun, W.M., 1973, Calculation of recirculating flows, Lecture Notes for Course entitled "TEACH", Imperial College, London.

Launder, B.E., Reece, G.J. and Rodi, W., 1975, Progress in the development of a Reynolds-stress turbulence closure, J. Fluid Mech., Vol. 68, pp. 537-566.

Lecointe, Y. and Piquet, J., 1989, Flow structure in the wake of an oscillating cylinder, J. Fluids Engineering, Vol. 111, pp. 139-148.

Leonard, B.P., 1979, A stable and accurate convective modelling procedure based on quadratic upstream interpolation, Comp. Meth. Appl. Mech. and Eng., Vol. 19, pp. 59-98.

Majumdar, S. and Rodi, W., 1985, Numerical calculations of flow past circular cylinders, Proc. 3rd Symp. on Num. and Phys. Aspects of Aerodynamic Flows, Long Beach, California.

Norris, H.L. and Reynolds, W.C., 1975, Turbulent channel flow with moving wavy boundary, Department Mech. Eng. Rept. FM-10, Stanford University.

Rodi, W., 1980, Turbulence Models and their Application in Hydraulics, Int. Association for Hydraulic Research, Delft, The Netherlands.

Rodi, W., 1991, Experience with two-layer turbulence models combining the k-ε model with a one-equation model near the wall, AIAA paper 91-0216.

Stone, H.L., 1968, Iterative solution of implicit approximations of multidimensional partial differential equations, SIAM J. Num. Anal., Vol. 3, No. 3, pp. 530-558.

Tamura, T., Ohta, I. and Kuwahara, K., 1990, On the reliability of two-dimension simulation for unsteady flows around a cylinder-type structure, J. Wind Engineering and Industrial Aerodynamics, Vol. 35, pp. 275-298.

Taulbee, D.E. and Tran, L, 1988, Stagnation streamline turbulence, AIAA J., Vol. 26, pp. 1011-1013.

van Doormal, J.P. and Raithby, R.D., 1984, Enhancement of the SIMPLE method for predicting incompressible fluid flows, Num. Heat Transfer, Vol. 7, pp. 147-163.

TURBULENT SHEAR FLOWS
Technical University of Munich
September 9-11, 1991

COMPUTATIONS OF A SEPARATED TURBULENT BOUNDARY LAYER

K.N. Atkinson and I.P. Castro

Department of Mechanical Engineering,
University of Surrey,
Guildford, Surrey GU2 5XH, U.K.

ABSTRACT

Numerical solutions of a separated turbulent boundary layer, obtained using standard k-ε and differential stress models, are presented. To achieve satisfactory separation the dissipation equation in both models had to be modified in the upstream part of the boundary layer; without this modification both models failed to predict separation. Despite the final solutions showing reasonable agreement with experiment in terms of skin friction and boundary layer growth rates, they are far from adequate in terms of the behaviour of Reynolds stresses and turbulence kinetic energy. This is particularly true around separation for both turbulence models but also, in the case of the differential stress model, in the whole of the separated region.

It is argued that the usual assumptions embodied by such models do not really reflect the nature of the turbulence in strongly adverse pressure gradient and/or separated flow regions.

1. INTRODUCTION

At the 1980/81 Stanford Conference on Complex Turbulent Flows one of the test cases considered was the separated turbulent boundary layer of Simpson et al (1981). The flow was computed using a variety of turbulence models, the most complex of which was a five-equation differential model; the rest were either variants of the k-ε model or one-equation eddy-viscosity models. All were successful in predicting separation, but with hindsight this was probably because realistic length scale behaviour at the wall was imposed.

In more recent computations, using the k-ε model, De Henau et al (1990) found that the boundary layer could not be made to separate with the standard form of the model. However, even in the simpler case of an equilibrium adverse pressure gradient boundary layer, the model's predictions have been found to be poor (Rodi and Scheuerer, 1986), with the shear stress and skin friction values being overpredicted. Rodi and Scheuerer attribute this problem to the model's overprediction of the turbulent length scale in the vicinity of the wall, and argue that the production term in the dissipation equation should be enhanced so as to increase the dissipation and so reduce the length scale and hence the wall shear stress. By using a modification by Hanjalic and Launder (1980) which has this effect, they obtained accurate predictions of equilibrium adverse pressure gradient boundary layers. In the more complex case of a separated turbulent boundary layer the tendency to overpredict the shear stresses keeps the boundary layer attached when measurements indicate that it should separate, as was shown to be the case by De Henau et al.

In this paper the conclusion of De Henau et al is confirmed and, more importantly, it is shown that a similar conclusion holds in the case of the more sophisticated differential Reynolds stress turbulence model. Separation cannot be achieved using either model in its standard form, but satisfactory separation can be achieved by modifying the dissipation equation in the upstream part of the boundary layer, although this still leaves serious inaccuracies in the mean flow and turbulence structure in the separated region, particularly for the differential stress model.

2. TURBULENCE MODELS

The turbulence stresses were modelled by the standard k-ε model and by a differential stress model similar to that of Launder et al (1975), but in both cases the equation for dissipation of turbulence energy was modified in the attached part of the boundary layer upstream of the separation point.

The dissipation rate of turbulence energy is obtained from a transport equation of the form

$$\frac{D\varepsilon}{Dt} = D_\varepsilon + C_{\varepsilon 1}\frac{\varepsilon}{k}P_k - C_{\varepsilon 2}\frac{\varepsilon^2}{k} \qquad (1)$$

where D_ε represents the diffusion of ε and P_k represents the generation of turbulence kinetic energy. In the k-ε model D_ε is given by

$$D_\varepsilon = \frac{\partial}{\partial x_i}\left((\nu + \frac{\nu_T}{\sigma_\varepsilon})\frac{\partial \varepsilon}{\partial x_i}\right) \qquad (2)$$

where ν_T is the turbulent viscosity, and in the differential stress model (DSM) it is given by

$$D_\varepsilon = \frac{\partial}{\partial x_j}\left((\nu\delta_{ij} + C_\varepsilon \overline{u_i u_j}\frac{k}{\varepsilon})\frac{\partial \varepsilon}{\partial x_i}\right) \qquad (3)$$

For two-dimensional thin shear flows, the generation term P_k is given by

$$P_k = -(\overline{u^2} - \overline{v^2})\frac{\partial U}{\partial x} - \overline{uv}\frac{\partial U}{\partial y} \qquad (4)$$

The modification to (1), proposed by Hanjalic and Launder (1980), essentially consists of enhancing the irrotational part of the mean strain in (4), as follows

$$P_k = -\frac{C_{\varepsilon 3}}{C_{\varepsilon 1}}(\overline{u^2} - \overline{v^2})\frac{\partial U}{\partial x} - \overline{uv}\frac{\partial U}{\partial y} \qquad (5)$$

where $C_{\varepsilon 3} > C_{\varepsilon 1}$. $C_{\varepsilon 1}$ has a value of 1.44 and Hanjalic and Launder give $C_{\varepsilon 3}$ a value of 4.44.

The turbulence kinetic energy equation in the k-ε model is retained in its standard form, i.e.

$$\frac{Dk}{Dt} = D_k - (\overline{u^2} - \overline{v^2})\frac{\partial U}{\partial x} - \overline{uv}\frac{\partial U}{\partial y} - \varepsilon \qquad (6)$$

where D_k is the modelled diffusive transport term, but the normal stresses in (5) and (6) are expressed in terms of the turbulence kinetic energy as $(\overline{u^2} - \overline{v^2}) = 0.33k$, which is experimentally observed in many less complex

flows. The preceding modifications were applied in the attached part of the boundary layer up to the computed separation point.

In the differential stress model the Reynolds stresses are obtained from individual modelled transport equations which, for reasons of space, are not repeated here. The closure approximations are those described by Launder et al (1975) ('Model 2' in their paper), with the values for the various constants given in Table 1.

$C_{\varepsilon 1}$	$C_{\varepsilon 2}$	C_ε	C_s'	C_1	γ
1.44	1.92	0.16	0.22	1.8	0.6

Table 1. Values of constants in turbulence models. Nomenclature as Launder et al (1975).

3. COMPUTATIONAL DETAILS

3.1 Solution procedure

The equations described in the previous section, together with equations for mass and momentum conservation, were solved using the Harwell-FLOW3D solution procedure (Burns & Wilkes, 1987). This is a finite-volume procedure based on a non-orthogonal boundary-fitted coordinate system. The mean velocity components, in Cartesian coordinates, and pressure are stored at the centroids of control volumes based on a boundary-fitted coordinate system, and the equations are transformed into curvilinear coordinates and integrated over a simple rectangular grid The pressure is obtained using the SIMPLE algorithm, or more modern variants (SIMPLEC, PISO), and the interpolation method of Rhie & Chow (1983) is used to avoid the problem of chequerboard oscillations in the pressure field.

The convection terms in the equations were approximated by higher-order differencing schemes. In the k-ε solutions the well known QUICK scheme of Leonard (1979) was used on the momentum equations and the bounded higher-order scheme of Gaskell and Lau (1988) was used on the turbulence equations. In the DSM solutions second-order upwind differencing (e.g. Hodge et al, 1979) was used on all equations.

3.2 Geometry and solution domain

The geometry of Simpson et al (1981) and the solution domain are shown in figure 1. The geometry consists of a channel with a curved upper wall connected to a low speed wind tunnel; the curvature of the upper wall creates an adverse pressure gradient which causes the turbulent boundary layer on the lower wall to separate. Separation on the upper wall is prevented by a boundary layer control system which extracts the boundary layer and introduces two-dimensional high-speed wall jets at locations along the upper wall.

Measurements of mean velocity components and Reynolds stresses in the separation region and in the attached boundary layer upstream are presented in Simpson et al (1981) and in more detail in Simpson et al (1980) and Shiloh et al (1980). Accurate measurements of the separation region were obtained by using a directionally sensitive laser anemometry system. However, these extend only to a point part of the way along the separation bubble. Beyond this point the flow was increasingly three-dimensional.

3.3 Boundary conditions

Boundary conditions are required for the axial and vertical mean velocity components U and V, the dissipation rate ε, the individual Reynolds stresses $\overline{u^2}$, $\overline{v^2}$, $\overline{w^2}$, $\overline{uv}$, (in DSM calculations) and the turbulence kinetic energy k (in k-ε calculations).

The inlet to the solution domain was located in the parallel section of the channel at x = 1.63m. At this location the boundary layer has reached a fully-developed state and has a clearly defined logarithmic region. Measured profiles of U, $\overline{u^2}$, $\overline{v^2}$, $\overline{w^2}$ and $\overline{uv}$, at the inlet location were available from Simpson's reports; the freestream velocity at this location was 21.8m/s. The turbulence kinetic energy k was computed from the individual normal stresses and the vertical mean velocity V was assumed to be zero. To obtain the inlet dissipation rate ε in the boundary layer it was assumed that the turbulence length scale L was equal to min(κy, 0.085δ) where y is distance from the wall and δ is the boundary layer thickness. The dissipation rate was then obtained from

$$\varepsilon = C_\mu^{3/4} \frac{k^{3/2}}{L} \qquad (7)$$

The constants κ and C_μ have values of 0.41 and 0.09 respectively.

At the outlet boundary (well beyond reattachment) the axial derivatives of all quantities were assumed to be zero, which is a much more satisfactory procedure than applying boundary conditions within the separated region, as was done in some of the computations for the Stanford Conference.

One option for the outer boundary condition would be to use the wind tunnel upper wall and extract mass through it, as was done in the experiments. In the present work, the outer boundary of the solution domain was defined using a measured inviscid flow streamline, as suggested by the Stanford Conference organisers. This extends only as far as the last measurement station, so it was continued by a smooth curve beyond the channel outlet to x = 9m. Provided this extension is chosen sensibly it has virtually no effect on the details of the solution where the measurements are available. For the bounding streamline, a streamline coordinate system (s,n,b) may be defined where s is the coordinate tangential to the streamline, n is normal to s and lies in the x-y plane and b is normal to s and n. Boundary conditions for the mean velocity components and Reynolds stresses in Cartesian coordinates and for ε were derived by applying the symmetry conditions:

$$U_n = \overline{u_s u_n} = \frac{\partial(U_s, \overline{u_s^2}, \overline{u_n^2}, \overline{u_b^2}, \varepsilon)}{\partial n} = 0 \qquad (8)$$

from which it follows that $\partial k/\partial n = 0$.

At the wall standard logarithmic wall functions as described by, for example, Launder and Spalding (1974) were applied, although it is recognised that within the

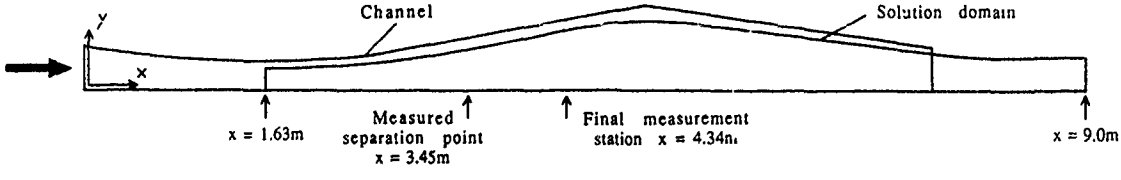

Figure 1. Geometry and solution domain.

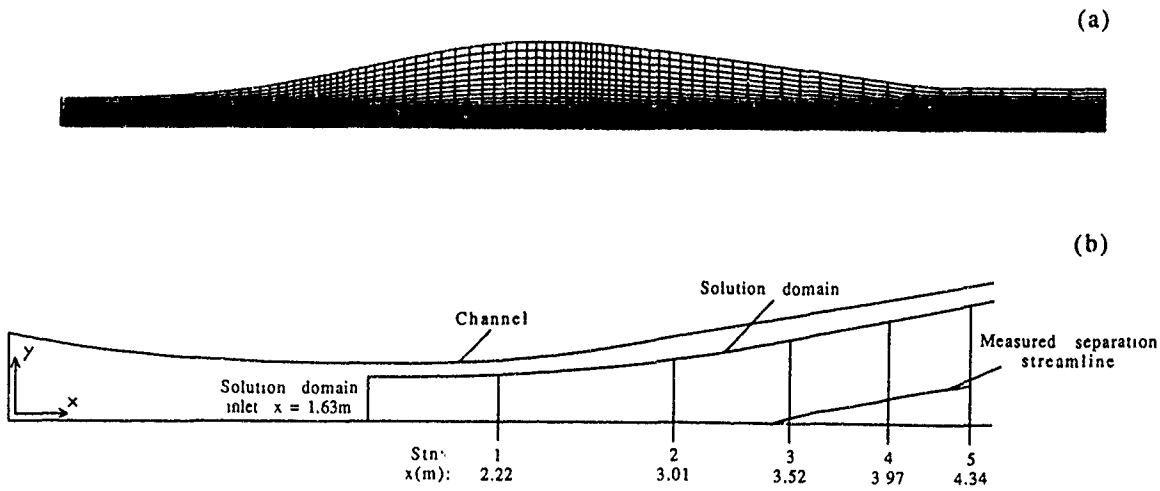

Figure 2. (a) Computational grid - note that only half the number of axial grid lines are shown. (b) Measurement stations.

separated region standard log-law behaviour does not occur.

3.4 Computational grid

The computational grid is shown in figure 2a. The dependent variables were stored at the centroids of control volumes formed by grid lines running vertically from the wall to the inviscid flow streamline and lengthwise from the inlet plane to the outlet plane. The lengthwise grid lines were arranged so that their relative spacing was constant from inlet to outlet.

The vertical grid lines were arranged in four sections, each containing either a uniform expansion or uniform contraction in spacing. First there was a uniform contraction in spacing from the inlet plane to the measured separation point at x = 3.45m. Then there was a uniform expansion to the midpoint of the computed recirculation bubble at x = 4.425m, followed by a uniform contraction to the location of the computed reattachment point at x = 5.4m. Finally there was a uniform expansion to the outlet plane at x = 9.0m. The grid spacing at the separation and reattachment points was 0.04m. It was found that using smaller spacings than this had no effect on the solutions.

The lengthwise grid lines were arranged so that their spacing expanded uniformly away from the wall. At the inlet plane the spacing at the wall was 0.002m. This ensured that the near-wall centroid fell well within the logarithmic region over a large section of the upstream attached boundary layer.

The computations presented in section 4 were obtained on a grid containing 80 x 40 grid lines. The vertical grid lines were arranged so that the mesh expansion ratio in each section of the grid was the same; this gave mesh expansion ratios of about 1.06. The mesh expansion ratio in the vertical direction was 1.04. Solutions were also obtained on a grid containing 120 x 60 grid lines to check for grid-independence and these were found to be virtually identical to those on the 80 x 40 grid.

4. RESULTS OF COMPUTATIONS

In this section the k-ε and DSM solutions are compared with experimental measurements. Computed and measured profiles of mean velocity and turbulence quantities are presented for five axial stations, indicated in figure 2b. Two of these are within the attached boundary layer upstream of the measured separation region and three are within the separation region itself, one close to the separation point - note the measured separation streamline included in the figure.

4.1 k-ε solutions

It was found that the boundary layer could not be made to separate with the standard k-ε model, in agreement with the finding of De Henau et al (1990). Satisfactory separation was achieved when the modification to the dissipation equation (see Section 2) in the attached part of the boundary layer was applied. The location of the separation point was dependent on the value of $C_{\varepsilon 3}$ used. An increase in $C_{\varepsilon 3}$ caused a more rapid reduction in the wall shear stress, so the boundary layer separated earlier. Table 2 presents the computed separation point for $C_{\varepsilon 3}$ values of 2.5, 4.44 and 5.5 - note that the measured separation point was at about x = 3.45m.

$C_{\varepsilon 3}$	2.50	4.44	5.50
x_{sep} (m)	4.03	3.54	3.39

Table 2. Effect of $C_{\varepsilon 3}$ on the computed separation point in the k-ε solutions.

In figure 3 detailed comparisons of computed and measured mean velocity and turbulence energy are presented for the axial stations indicated in figure 2b. In the separation region the level of agreement between the computed and measured mean velocity profiles for $C_{\varepsilon 3}$ = 2.5 is very poor because the separation point is too far downstream. The level of agreement for $C_{\varepsilon 3}$ = 4.44 and 5.5 is much better because the separation point is predicted more accurately, but there are still significant differences in the profiles: the positive velocities in the outer part of the boundary layer and the negative velocities in the back-flow region are too small.

At station 2, in the attached boundary layer, the near-wall velocities for all $C_{\varepsilon 3}$ values are too high, indicating that the wall shear stress is too high at this location. This is confirmed in figure 4 which compares computed skin friction coefficients for each $C_{\varepsilon 3}$ value with measurements. The skin friction values agree with measured values around the separation point (for $C_{\varepsilon 3}$=4.44 and 5.5) and in the initial zero pressure gradient region, but are a little too high in the strong adverse pressure gradient region upstream of the separation point.

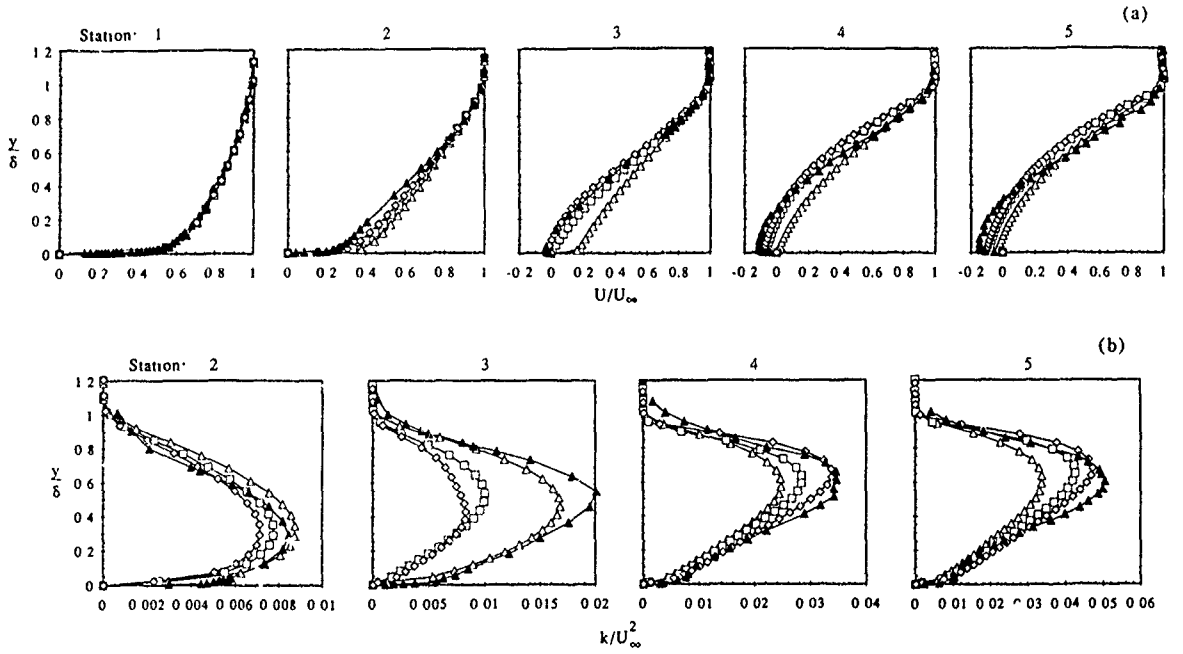

Figure 3. U-velocity and turbulence energy profiles for k-ε model; Δ, $C_{\varepsilon 3}$ = 2.5; □, 4.44; ◇, 5.5; ▲, measured. (a) U-velocity, (b) turbulence energy.

Figure 3b shows that the turbulence energy for $C_{\varepsilon 3}$=4.44 and 5.5 is reasonably well predicted in the attached part of the boundary layer and at stations 4 and 5 in the separation region, but is much too low around the separation point. In fact the turbulence energy falls sharply as the separation point is approached, before rising in the separation region. This can be seen clearly in figure 5 which shows profiles of computed turbulence energy for y/δ = 0.3. Simpson's measurements of normal stresses indicate that this computed sudden fall in turbulence energy is erroneous. Thus although the modification reduces the wall shear stress and causes separation, it produces an unrealistic fall in turbulence energy around the separation point. This does not seem to have been noted in the previous (limited) work using the Hanjalic & Launder modification but is not really surprising since the length scale reduction (leading to the required lower wall shear stress) is obtained via an effectively imposed increase in turbulence dissipation rate. This leads naturally to reductions in either the total turbulence energy or, in the case of the differential stress model, the individual Reynolds stresses.

Finally, figure 6 compares the computed and measured growth in boundary layer thickness. As $C_{\varepsilon 3}$ is increased the thickness of the separation region grows more rapidly, but even for $C_{\varepsilon 3}$ = 5.5 the growth is not quite as rapid as measured.

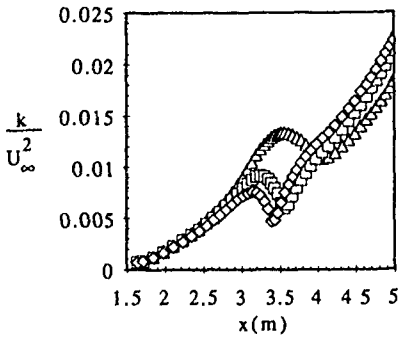

Figure 5. Turbulence energy at y/δ = 0.3 for k-ε model. Legend as in figure 3.

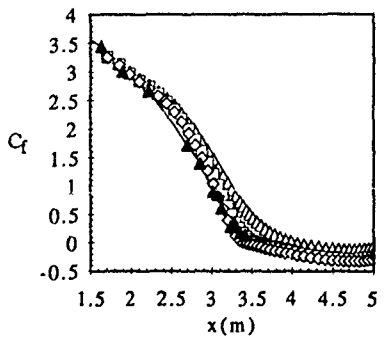

Figure 4. Skin friction coefficient for k-ε model. Legend as in figure 3.

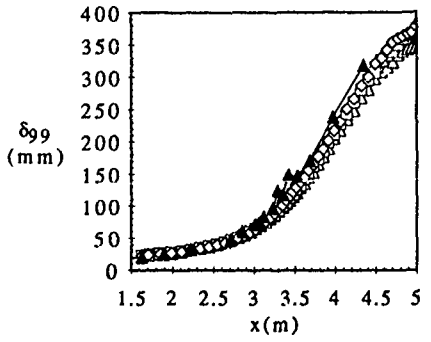

Figure 6. Boundary layer thickness, δ_{99}, for k-ε model. Legend as in figure 3.

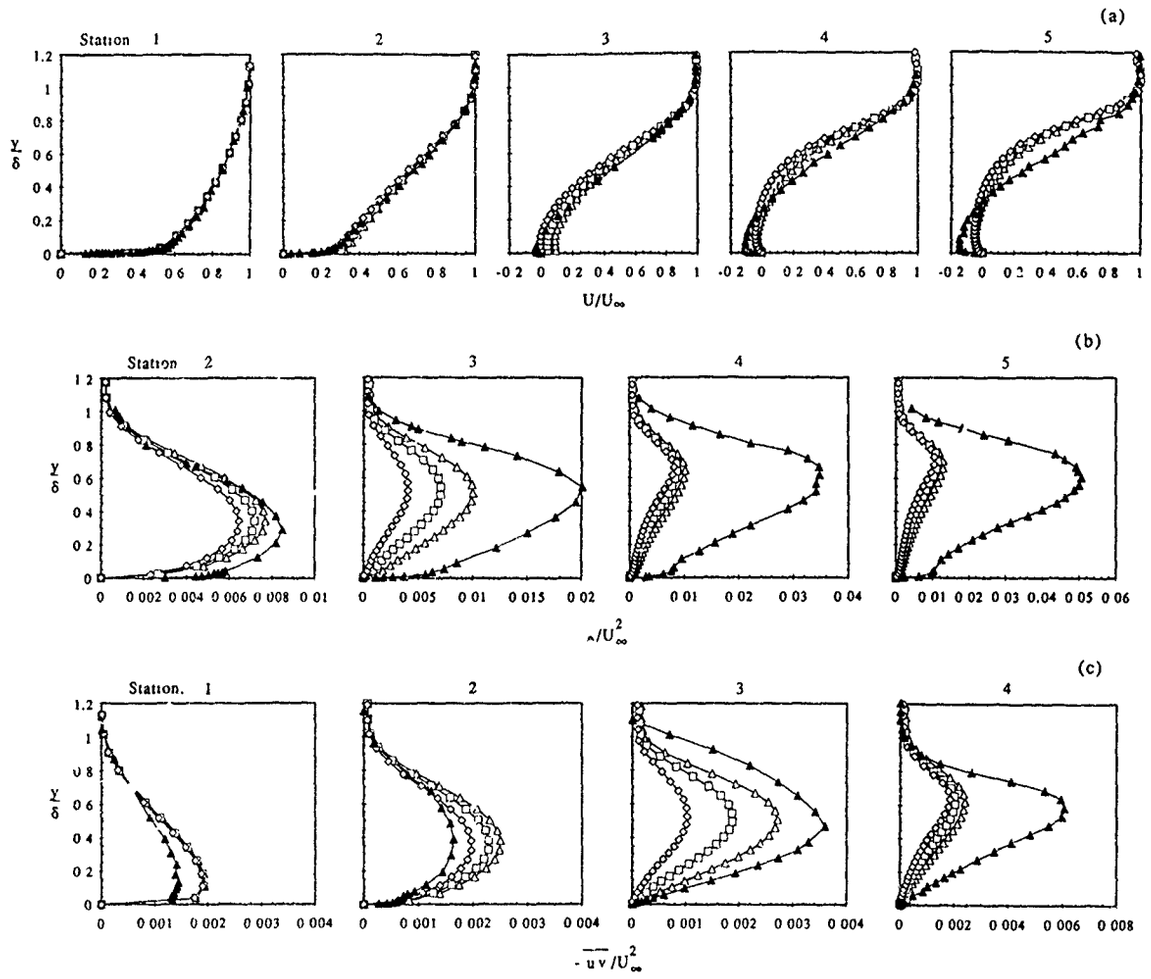

Figure 7. U-velocity, turbulence energy and shear stress profiles for DSM model; Δ, $C_{\varepsilon 3}$ = 4.44; □, 5.5; ◇, 7.0; ▲, measured. (a) U-velocity, (b) turbulence energy, (c) shear stress.

4 2 DSM solutions

The boundary layer could not be made to separate with the standard form of the differential stress model, but, as in the k-ε solutions, satisfactory separation could again be achieved by applying the modification to the dissipation equation in the attached part of the boundary layer. The location of the separation point again depended on the value of $C_{\varepsilon 3}$ used, but a higher value of $C_{\varepsilon 3}$ was required to achieve the same separation point as before. Table 3 presents the location of the separation point for $C_{\varepsilon 3}$ values of 4.44, 5.5 and 7.0. Previously, the separation point for $C_{\varepsilon 3}$ = 5.5 occurred upstream of the measured separation point, but now it occurs downstream.

$C_{\varepsilon 3}$	4.44	5.50	7.00
x_{sep} (m)	3.85	3.68	3.49

Table 3. Effect of $C_{\varepsilon 3}$ on the computed separation point in the DSM solutions.

Figure 7 presents computed and measured mean velocity, turbulence energy and shear stress profiles for the axial stations in figure 2b. At station 2, in the attached part of the boundary layer, the near-wall velocity is accurately calculated for $C_{\varepsilon 3}$ = 7.0. Figure 8 compares the computed and measured skin friction values and shows that the skin friction is accurately calculated for $C_{\varepsilon 3}$ = 7.0 at this station (x = 3.01m), but that the computed values are again too high over most of the adverse pressure gradient region.

At station 3 separation has occurred for $C_{\varepsilon 3}$ = 7.0, in agreement with the measurements, but not for $C_{\varepsilon 3}$ = 4.44 and 5.5. The velocities for $C_{\varepsilon 3}$ = 7.0 are too small in the outer part of the boundary layer and also in the small back-flow region - note that overall continuity is satisfied because the freestream velocity is higher than measured. The profiles for $C_{\varepsilon 3}$ = 4.44 and 5.5 have small

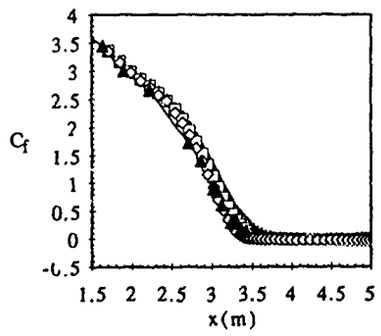

Figure 8. Skin friction coefficient for differential stress model. Legend as in figure 7

but unrealistic peaks at the near-wall centroid, and further downstream negative velocities first appear at a location above the near-wall centroid. Increasing $C_{\varepsilon 3}$ eliminates this behaviour and it does not occur for $C_{\varepsilon 3}$=7.0. The differences between the computed and measured profiles for all $C_{\varepsilon 3}$ values increase with downstream distance and at stations 4 and 5 the positive velocities in the outer part of the boundary layer and the negative velocities in the back-flow region are much too small.

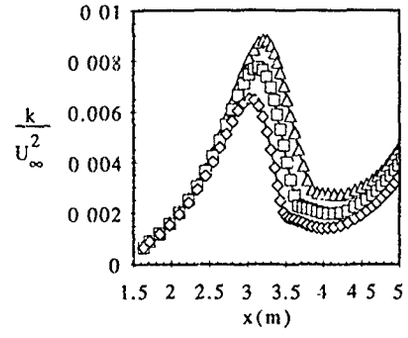

Figure 9. Turbulence energy at y/δ = 0.3 for differential stress model. Legend as in figure 7.

In figure 7 it can be seen that the turbulence energy and shear stress in the separation region are much too small for all $C_{\varepsilon 3}$ values. Figure 9 shows computed values of turbulence energy for y/δ = 0.3, and it can be seen that the turbulence falls sharply as the separation point is approached, as in the k-ε solutions, but does not recover to the measured levels as before

Despite the differences in the computed and measured mean velocity and turbulence quantities in the separation region, the growth of the boundary layer is accurately predicted, as may be seen from figure 10, which compares the computed growth in boundary layer thickness with measurement. This should probably not be taken as evidence of some 'low-order' validity of the turbulence model, since the location of the outer boundary streamline is being imposed. The predictions of the turbulence structure within the separated region do not agree with the implications of either Simpson's measurements or the more recent detailed studies of separated regions undertaken in our own laboratory (e.g. Dianat & Castro, 1991). Even if the turbulence predictions around separation were more accurate, we would not expect current turbulence models to handle the separated flow itself very well (Castro, 1991).

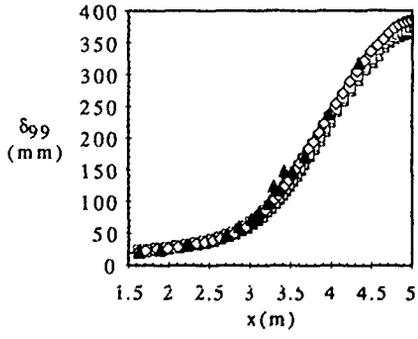

Figure 10. Boundary layer thickness, δ_{99}, for differential stress model. Legend as in figure 7.

5. CONCLUSIONS

The major conclusion is that turbulent boundary layer separation cannot be adequately predicted by the standard k-ε model or the differential stress model. Hanjalic & Launder's (1980) modification to the dissipation equation produced separation but left serious errors in the separation region, particularly when applied to the differential stress model. These were at least partly due to the modification itself, and it seems clear that the separation process cannot be adequately modelled by simple changes to the dissipation equation. However, the poor quality of the DSM solutions suggests that current modelling assumptions do not really reflect the nature of the flow both up to separation *and* in the separation region itself.

6. ACKNOWLEDGEMENTS

The financial support of the Procurement Executive, Ministry of Defence, is gratefully acknowledged, as is the valuable assistance of our colleague, Dr. A. R. Packwood.

7. REFERENCES

Burns, A.D. & Wilkes, N.S. (1987) 'A finite difference method for the computation of fluid flows in complex three dimensional geometries', AERE R 12342.

Castro, I.P. (1991) 'Turbulence in separated regions', *Proc of IUTAM Conf. on Separated Flows and Jets*, ed. Kozlov V.V., Springer-Verlag (to appear).

De Henau, V., Raithby, G.D. & Thompson, B.E. (1990) 'Prediction of flows with strong curvature and pressure gradient using the k-ε turbulence model', *ASME J. Fluids Engng.*, **112**, 40-47.

Dianat, M. & Castro, I.P. (1991) 'Turbulence in a separated boundary layer', *J Fluid Mech.* **226**, 91-123

Gaskell, P.H. & Lau, A.K.C. (1988) 'Curvature-compensated convective transport: SMART, a new boundedness preserving transport algorithm', *Int J. Num. Meth. Fluids* **8**, 617-641.

Hanjalic, K. & Launder, B.E. (1980) 'Sensitizing the dissipation equation to irrotational strains', *ASME J. Fluids Engng.* **102**, 34-40.

Hodge, J.K., Stone, A.L. & Miller, T.E. (1979) 'Numerical solution for airfoils near stall in optimized boundary-fitted curvilinear coordinates', *AIAA J.* **17**, 458-464.

Launder, B.E., Reece, G.J. & Rodi, W. (1975) 'Progress in the development of a Reynolds-stress turbulence closure', *J. Fluid Mech.* **68**, 537-566.

Launder, B.E. & Spalding, D.B. (1974) 'The numerical computation of turbulent flows', *Comp. Meth Appl. Mech. Engng.* **3**, 269-289.

Leonard, B.P. (1979) 'A stable and accurate convective modelling procedure based on quadratic upstream interpolation', *Comp. Meth. Appl. Mech. Engng.* **19**, 59-98.

Rhie, C.M. & Chow, W.L. (1983) 'Numerical study of the turbulent flow past an airfoil with trailing edge separation', *AIAA J.* **21**, 1527-1532.

Rodi, W. & Scheuerer, G. (1986) 'Scrutinizing the k-ε turbulence model under adverse pressure gradient conditions', *ASME J. Fluids Engng.* **108**, 174-179.

Shiloh, K., Shivaprasad, B.G. & Simpson, R.L. (1980) 'Measurements of the transverse velocity of a separating turbulent boundary layer', *Project SQUID Report SMU-5-PU*, Southern Methodist University, Dallas, Texas.

Simpson, R.L., Chew, Y.-T. & Shivaprasad, B.G. (1980) 'Measurements of a separating turbulent boundary layer', *Project SQUID Report SMU-4-PU*, Southern Methodist University, Dallas, Texas.

Simpson, R.L., Chew, Y.-T. & Shivaprasad, B.G. (1981) 'The structure of a separating turbulent boundary layer. Part 1. Mean flow and Reynolds stresses', *J. Fluid Mech.* **113**, 23-51.

TURBULENT SHEAR FLOWS
Technical University of Munich
September 9-11, 1991

NON-ORTHOGONAL CALCULATION PROCEDURES USING SECOND MOMENT CLOSURE

S. Sebag*, V. Maupu*, D. Laurence

E.D.F., D.E.R, LNH
6, quai Watier, BP.49, 78401 CHATOU Cedex, FRANCE

ABSTRACT:

Two different two-dimensional curvilinear finite-volume (FV) codes with both k-ε model and a Reynolds Stress Transport Model (RSTM) [1,2] have been achieved for application to recirculating flows in non rectangular geometries. Such a geometry is encountered in a flow across rod bundles in heat exchangers in which accurate predictions of turbulence characteristics are required prior to tentative modelling of heat transfer at the walls. The paper focuses on the implementation of wall boundary conditions within the Cartesian framework. Numerical predictions of the tube bundle flow are compared with experiment : The level of turbulent kinetic energy, overestimated by the eddy viscosity model, is better predicted by RSTM and improved by slight modifications which aim at overcoming some weaknesses of the standard model in strongly anisotropic flows on one hand, and in impinging regions on the other hand.

NOMENCLATURE

Reynolds Stress Transport Equations :

$$\frac{\partial \overline{u_i u_j}}{\partial t} + \overline{U_k}\frac{\partial \overline{u_i u_j}}{\partial x_k} = P_{ij} + \Phi_{ij} + d_{ij} - \varepsilon_{ij}$$

where :

$$P_{ij} = -\left(\overline{u_i u_k}\frac{\partial \overline{U_j}}{\partial x_k} + \overline{u_k u_j}\frac{\partial \overline{U_i}}{\partial x_k}\right)$$

$$\Phi_{ij} = -\overline{\frac{p}{\rho}\left(\frac{\partial u_i}{\partial x_j} + \frac{\partial u_j}{\partial x_i}\right)}$$

$$d_{ij} = \frac{\partial}{\partial x_k}\left(\overline{u_i u_j u_k} + \delta_{jk}\frac{\overline{u_i p}}{\rho} + \delta_{ik}\frac{\overline{u_j p}}{\rho} - \nu\frac{\partial \overline{u_i u_j}}{\partial x_k}\right)$$

$$\varepsilon_{ij} = 2\nu\overline{\frac{\partial u_i}{\partial x_k}\frac{\partial u_j}{\partial x_k}}$$

Reynolds Stress Transport Model (RSTM)

* The pressure strain correlation Φ_{ij} associated with the deviatoric part of ε_{ij} is the main contribution to the model. Following Launder, Reece and Rodi [1], it is decomposed into three terms :

$$\phi_{ij} = \Phi_{ij} + \left(\varepsilon_{ij} - \frac{2}{3}\varepsilon\delta_{ij}\right) = \phi_{ij,1} + \phi_{ij,2} + \phi_{ij,w}$$

a return to isotropy (slow) term :

$$\phi_{ij,1} = -C_1\frac{\varepsilon}{k}\left(\overline{u_i u_j} - \frac{2}{3}k\delta_{ij}\right)$$

an isotropization of production (rapid) term :

$$\phi_{ij,2} = -C_2\left(P_{ij} - \frac{2}{3}P\delta_{ij}\right)$$

and a wall echo term (Gibson Launder) [2] :

$$\phi_{ij,w} = C_1'\frac{\varepsilon}{k}\left(\overline{u_k u_m}n_k n_m\delta_{ij} - \frac{3}{2}\overline{u_k u_i}n_k n_j - \frac{3}{2}\overline{u_k u_j}n_k n_i\right) f\left(\frac{l}{x_n n_n}\right)$$
$$+C_2'\left(\phi_{km,2}n_k n_m\delta_{ij} - \frac{3}{2}\phi_{ki,2}n_k n_j - \frac{3}{2}\phi_{kj,2}n_k n_i\right) f\left(\frac{l}{x_n n_n}\right)$$

•diffusive transport of Reynolds stresses and dissipation rate : two distinct models have been employed, a tensorial one, following Daly and Harlow [3], hereafter referred to as DH-diffusion :

$$d_{ij} = C_s'\frac{\partial}{\partial x_k}\left(\frac{k}{\varepsilon}\overline{u_k u_m}\frac{\partial}{\partial x_m}\overline{u_i u_j}\right)$$

$$d_\varepsilon = C_\varepsilon\frac{\partial}{\partial x_k}\left(\frac{k}{\varepsilon}\overline{u_k u_m}\frac{\partial \varepsilon}{\partial x_m}\right)$$

and an "eddy viscosity" one, referred to as EV-diffusion :

$$d_{ij} = \frac{\partial}{\partial x_k}\left(\frac{\nu_T}{\sigma_k}\frac{\partial}{\partial x_k}\overline{u_i u_j}\right)$$

$$d_\varepsilon = \frac{\partial}{\partial x_k}\left(\frac{\nu_T}{\sigma_\varepsilon}\frac{\partial}{\partial x_k}\varepsilon\right)$$

•Equation of the dissipation rate ε :

$$\frac{\partial \varepsilon}{\partial t} + \overline{U_k}\frac{\partial \varepsilon}{\partial x_k} = d_\varepsilon + C_{\varepsilon 1}\frac{\varepsilon}{k}P - C_{\varepsilon 2}\frac{\varepsilon^2}{k}$$

notations :

a_{ij}	turbulent stress anisotropy tensor = $\frac{\overline{u_i u_j}}{k} - \frac{2}{3}\delta_{ij}$
A	2D invariance coefficient = $1 - \frac{9}{8}(A_2 - A_3)$
A_2	second anisotropy tensor invariant = $a_{ik}a_{ki}$
A_3	third anisotropy tensor invariant = $a_{ik}a_{ki}a_{ii}$
C_μ	$= \left(\frac{\overline{uv}}{k}\right)^2$ (set to 0.09 in the k-ε model)
d_{ij}	diffusive transport of $\overline{u_i u_j}$
E	logarithmic law constant
k	turbulent kinetic energy = $.5\cdot\overline{u_i u_i}$
l	characteristic turbulence length scale : $\frac{C_\mu^{3/4}k^{3/2}}{\kappa\ \varepsilon}$
n_j	component of the unit vector normal to the wall
P	generation rate of $k = .5\cdot P_{ii}$
P_{ij}	generation rate of $\overline{u_i u_j}$
R_e	Reynolds Number $= U_0 D/\nu$

* Part of the research work of these authors was undertaken during their stay at the University of Manchester Institute of Science and Technology.

U_0 reference velocity

$\overline{U_i}$ mean velocity component

u_i Cartesian fluctuating velocity component

u,v,w surface adapted fluctuating velocity component

u_* friction velocity via $u_* = \sqrt{\sqrt{C_\mu}\, k}$

u_τ friction velocity via $u_\tau = \dfrac{|\overline{U}|\,\kappa}{\ln(E\,y^+)}$

x_i Cartesian direction coordinate

x,y,z wall surface adapted coordinate

y^+ non dimensional distance to the wall = yu_*/ν

ε_{ij} dissipation rate of $\overline{u_i u_j}$

ε dissipation rate of $k = .5 * \varepsilon_{ii}$

Φ_{ij} pressure-strain correlation

ν kinematic viscosity

ν_T eddy viscosity, $\dfrac{C_\mu k^2}{\varepsilon}$

κ Karman Constant = 0.41

τ_w wall shear stress = $-\mu \left.\dfrac{\partial U}{\partial y}\right|_{wall}$

constants :

C_1	C_2	C'_1	C'_2	C'_s	C_ε	$C_{\varepsilon 1}$	$C_{\varepsilon 2}$	σ_k	σ_ε
1.8	0.6	0.5	0.3	0.22	0.18	1.44	1.92	1.	1.3

In anisotropic flows, Launder et al [4] suggest a dependence of the ε equation constants in terms of the anisotropy tensor invariants :

$$C_{\varepsilon 1} = 1 \qquad C_{\varepsilon 2} = \frac{1.92}{1 + 0.6\sqrt{A_2}\,A}$$

INTRODUCTION:

To our knowledge, FV RSTM computations have yet been limited to flows in non rectangular geometries with a low degree of complexity, where only orthogonal grids are required. On the other hand, in these distorted flow domains, where recirculation occurs, second moment closure models markedly prove their superiority upon eddy viscosity models in that they better take into account the interaction between curvature related strain and turbulence anisotropy whereas a k-ε model strictly aligns the principal axes of the two tensors.

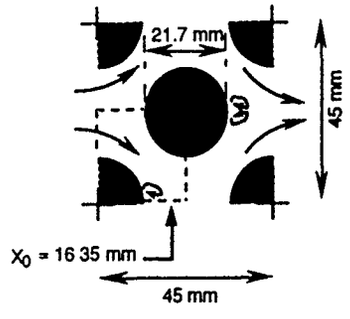

Figure 1 : flow domain within a tube bundle (dashed lines : domain of computation)

A non orthogonal grid (NOG) is required for the geometry of Fig. 1 which by symmetry and periodicity represents the fully developed cross-flow within a tube bundle (experiment of Simonin et al. [5]). This NOG (Fig. 4) enables refinement of the mesh in the leeward corner precisely where maximum difference between k-ε model and RSTM may be found. After presentation of the two solutions procedures which have been implemented, results obtained on this geometry will be discussed.

NUMERICAL SOLUTION PROCEDURES:

The numerical implementation has been carried out in two different solution procedures, both using Cartesian decomposition of vector and tensors.

The first numerical solution procedure (NSP1) is based on a semi-staggered variable arrangement (Fig. 2) which naturally (one order of derivation corresponds to one grid-swapping) couples Reynolds stresses to the mean flow variables.

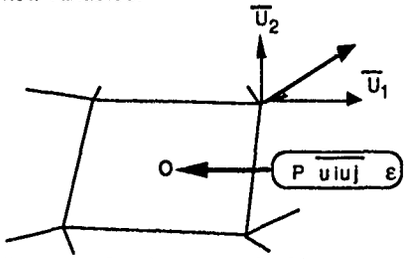

Figure 2 : Semi-staggered grid arrangement.

The second one (NSP2) uses a collocated arrangement (Fig. 3) in which the coupling of various variables is re-established by interpolation practices [6],[7] similar to those employed by Rhie and Chow [8] for pressure and by Obi et al. for the Reynolds stresses on rectangular grids [9].

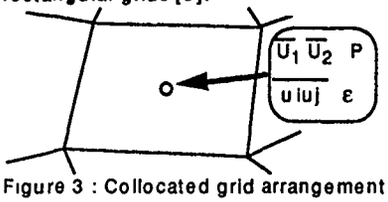

Figure 3 : Collocated grid arrangement.

The two procedures also differ from one another in algorithmic details :

NSP1 is a time marching procedure solving the unsteady equations by fractional steps [10]:

1) advection of variables by a Lagrangian method,
2) a diffusion and source term step solved in the incremental form with a linear system coupling all variables,
3) a pressure correction step ensuring mass conservation,

all linear systems are solved by a three level conjugate residual algorithm with a diagonal preconditioning for step 2.

NSP2 solves the steady equations in an iterative way (under-relaxation). At any iteration, governing equations are solved one by one. The Power Law Differencing Scheme is used for transport terms and source terms are selectively implicited [11]. Mean velocity and pressure fields are coupled by a pressure correction -SIMPLEC- [12] algorithm and tri-diagonal linear systems are solved by a fully vectorized Red-Black algorithm.

The geometry, NOG and use of Cartesian coordinates require generalization of boundary conditions for the RSTM.

BOUNDARY CONDITIONS :

No major difficulties lie in the implementation of boundary conditions (for the flow domain shown in Fig. 1, symmetry and anti-periodicity conditions are applied), except for wall boundary conditions (WBC).

RSTM is rooted in a high Reynolds number assumption, and therefore it is not valid up to the wall. As a WBC in complex geometry, it is thus advisable, for sake of simplicity, to use a wall function approach despite its well known shortcomings :

1) its strict domain of validity is the one dimensional Couette flow

2) Existing wall functions all focus on a wall surface adapted framework while equations need to remain tractable when transferred back into the Cartesian framework.

Relating to this, NSP1 and NSP2 have two separate implementations presented here-below :

Concerning NSP1 [13], WBC on the total stresses are interpreted as limiting values for the turbulent force imposed on the mean flow: Let **R** be the Reynolds stress tensor and (N, T) respectively the normal and tangent to the wall, and dF the resulting force : $dF = \mathbf{R}\,N$

4 assumptions need to be made to define the 4 stresses :

- the turbulent shear stress approaches the wall shear stress towards the wall i.e. $dF.T = \tau_w/\rho$ *(A1)*

- a Neuman condition is applied to k : $\frac{\partial k}{\partial n} = 0$ *(A2)*

- for 2D flows, one can assume : $\frac{\partial \overline{w^2}}{\partial n} = 0$ *(A3)*

- finally as a fourth frame independent condition we write : $\frac{\partial (dF.N)}{\partial n} = 0$ *(A4)*

(where "dF.N" is obviously nothing else but $\overline{v^2}$)

As a matter of fact, these BC are equivalent to:

$$\frac{\partial \overline{u^2}}{\partial n} = 0 \; ; \; \frac{\partial \overline{v^2}}{\partial n} = 0 \; ; \; \frac{\partial \overline{w^2}}{\partial n} = 0 \; ; \; \overline{uv} = \tau_w/\rho$$

Returning to the Cartesian framework leads to a system of four equations:

$$\left(\overline{u_2^2} - \overline{u_1^2}\right) n_1 n_2 + \overline{u_1 u_2}\left(n_1^2 - n_2^2\right) = -\tau_w/\rho$$

$$n_1^2 \frac{\partial \overline{u_1^2}}{\partial n} + n_2^2 \frac{\partial \overline{u_2^2}}{\partial n} + 2 n_1 n_2 \frac{\partial \overline{u_1 u_2}}{\partial n} = 0$$

$$\frac{\partial \overline{u_1^2}}{\partial n} + \frac{\partial \overline{u_2^2}}{\partial n} = 0$$

$$\frac{\partial \overline{u_3^2}}{\partial n} = 0$$

This coupled system is easily implemented in the semi-staggered code since all stress are solved fully coupled and implicitly.

τ_w is evaluated from two approximations of the friction velocity, one, u^*, resulting from the definition of C_μ :

$$u^* = \sqrt{\sqrt{C_\mu}\, k}$$

while the other one is obtained from the logarithmic law :

$$u_\tau = \frac{|\overline{U}|\,\kappa}{\ln(E\,y^+)}$$

This leads to the following variegation :

$$\tau_w/\rho = -\,\mathrm{sign}(\overline{U})\, u^* u_\tau$$

Besides the wall value of ε is chosen as :

$$\varepsilon_{wall} = \frac{u^{*3}}{\kappa\; 0.2\,\Delta y}$$

ε_{wall} is only used in the diffusion term and the fraction of the space discretisation 0.2 Δy allows the gradient of dissipation to be compatible with the local equilibrium at the cell face.

It should be noted here that, by assuming the local equilibrium, one has entirely set the value of C_μ. From the modelled stress equations, using the standard values of the RSTM constants, one finds :

$$C_\mu \approx 0.065$$

This is in agreement with the channel flow experiment of El Tebany and Reynolds [14].and it is recalled at this stage that the usual value of 0.09 had been set from a free shear layer experiment [15].

An alternative used in NSP2 [16] is to solve an Algebraic Stress Model in the near wall cells to retrieve more general Dirichlet conditions on the stresses in the surface adapted frame and then simply recover the values in the Cartesian coordinates. However, in this collocated procedure, the wall function approach demands a modification of the turbulent kinetic energy equation in the near wall cell which satisfies the local equilibrium. It is obtained by forcing the following equality :

$$-\overline{uv}\frac{\partial \overline{U}}{\partial y}_{\text{near wall}} \approx \varepsilon_{\text{near wall}} \approx \frac{u^{*3}}{\kappa\, y}$$

and by assuming a zero gradient diffusive flux at the wall for k.

Following Rodi [15], if the transport of Reynolds stresses is assumed to be proportional to the transport of k with $\overline{u_i u_j}/k$ as ratio of proportionality :

$$\left.\frac{\overline{u_i u_j}}{k}\right|_{\text{near wall}} = \frac{2}{3}\delta_{ij} + \frac{(1 - C_2)(P_{ij} - \frac{2}{3}P\delta_{ij}) + \phi_{ij,w}}{P + (C_1 - 1)\varepsilon}$$

In the surface adapted framework, a local Couette flow approximation reads :

$$\left.\frac{\overline{u^2}}{k}\right|_{\text{near wall}} = \frac{\frac{2}{3}(C_1 + 2 - 2C_2 + C_2 C_2') + C_1'\frac{\overline{v^2}}{k}}{C_1}$$

$$\left.\frac{\overline{v^2}}{k}\right|_{\text{near wall}} = \frac{\frac{2}{3}(C_1 + C_2 - 1 - 2C_2 C_2')}{C_1 + 2C_1'}$$

$$\left.\left(\frac{\overline{uv}}{k}\right)^2\right|_{\text{near wall}} = \frac{\overline{v^2}}{k}\left(\frac{1 - C_2 + 1.5C_2 C_2'}{C_1 + 1.5C_1'}\right) = C_\mu$$

However, as far as the turbulent shear stress is concerned, in order to keep benefit of the variegation used in NSP1, the following expression is employed :

$$\left.\overline{uv}\right|_{\text{near wall}} = \tau_w/\rho = -\,\mathrm{sign}(\overline{U})\, u^* u_\tau$$

RESULTS :

As detailed in Fig. 4, the flow-field can be decomposed into 3 regions where the mean flow is undergoing compression, acceleration and sudden expansion.

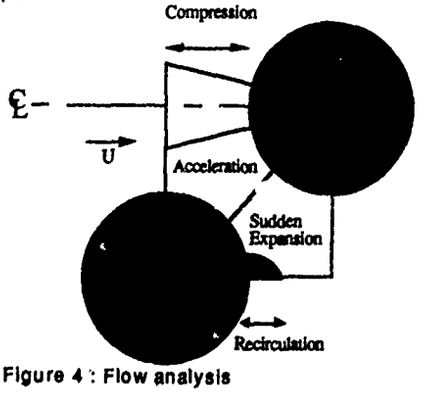

Figure 4 : Flow analysis

For the present report, most of the results are

presented in the expansion zone of the periodic field at location X_0 (Fig. 1) and compared with the experiment of Simonin and Barcouda. The Reynolds number based on the diameter of the tubes is equal to 18 000.

Details of the predictions presented in following figures are summarized in Table 1. Bold cells denote underlying comparisons.

Figure	5	6	7	8
Numerical Procedure	NSP1, NSP2	NSP1	NSP1	NSP1 NSP2(kε)
Turbulence Model	RSTM	RSTM	RSTM	RSTM, k-ε
Turbulent diffusion	EV DH	DH	DH	DH
$(C_{\varepsilon 1}, C_{\varepsilon 2})$	(1., f(A2,A))	(1., f(A2,A))	(1.44,1.92), (1., f(A2,A))	(1., f(A2,A))
$\phi_{ij,w}$	locally cancelled	=0, standard,l ocally cancelled	locally cancelled	locally cancelled

Differences occur between NSP1 and NSP2 with the same eddy viscosity turbulent diffusion model (Fig. 5). Even though treatment of convection terms and pressure-continuity steps differ, they cannot be responsible of such a divergence in the results since k-ε results with both numerical solution procedures are very similar (Fig 8). Stress boundary conditions are enough different to explain such discrepancies.

Besides, one should note the high sensitivity to the turbulent diffusion modelling which affects the level of turbulence (Fig. 5b) as well as the mean momentum (Fig. 5a).

The presence of the wall reflection terms greatly improves the description of the recirculation region (Fig. 6) with a raising of turbulent shear stress and kinetic energy but the upstream flow of the expansion (y>8) shows a non physical behaviour of $\phi_{ij,w}$ modelling. If one considers a one dimensional approach in the vicinity of a stagnation point ($\partial\overline{U}_1/\partial x_1 < 0$), it is noticeable that $\phi_{11,w}+\phi_{22,w}$ acts as a source term in the 2D turbulent kinetic energy equation. This creates an artificial spot of turbulent kinetic energy which is carried down along the tube sides and still visible at location X_0. As a matter of fact the wall echo term modelling is designed to take into account the attenuation of normal Reynolds stress near a surface,only in a local Couette flow approximation. The best compromise is thus obtained by accounting for the only physical effect, i.e. the downstream tube effect, and to cancel locally the effect of the impinged surface upon wall echo redistribution. The extent of the recirculation region is nevertheless affected through the anti-periodicity condition.

Fig. 7 shows that the classical ε equation with constant underpredicts turbulent fields. Velocity profile is also badly captured with a too long recirculation zone. By taking into account the anisotropy through these coefficients, Launder et al's proposal successfully rectifies mean and turbulent profiles.

Fig. 8 compares NSP1 and NSP2 k-ε model predictions with final RSTM results (obtained in NSP1 after modification of ε equation and correction of wall echo "tricky" effects). As noticed previously both procedures predict similar k-ε results but, unlike experimental data, this model reverses the turbulence maximum near the upstream wall. In a 1D approach of the flow upstream a stagnation point (see above discussion), eddy viscosity assumption leads to :

$$P_k = 4\,\nu_T \left(\frac{\partial \overline{U}_1}{\partial x_1}\right)^2$$

which unrealistically forces the positivity of the production term (Fig. 8d). The amount of artificial turbulent energy is then convected from the impingement region along the tube wall.

Whatever the model is, mean velocity profiles are not far from experiment (Fig. 8a). Besides rapid distorsion coefficient σ (ratio of characteristic turbulent and mean strain time scales) :

$$\sigma = k/\varepsilon\sqrt{S_{ij}S_{ij}} \text{ where } S_{ij} = \frac{1}{2}\left(\frac{\partial \overline{U}_i}{dx_j} + \frac{\partial \overline{U}_j}{dx_j}\right)$$

exceeds 3 in the high shear region which tends to prove a predominancy of rapid term upon non linear term.

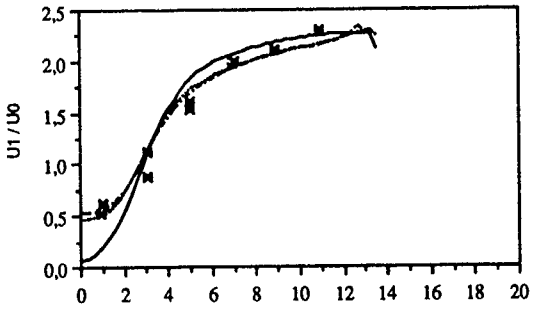

(5.a) : longitudinal mean velocity component

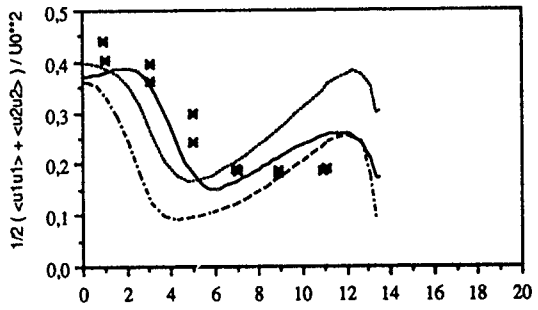

(5.b) · 2D turbulent kinetic energy

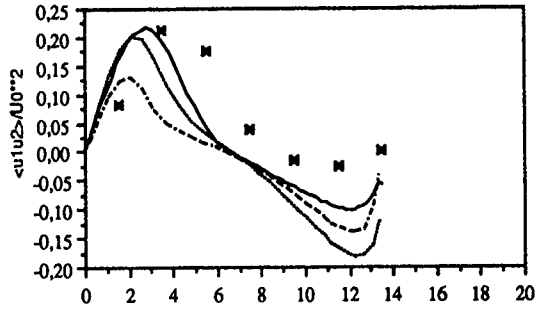

(5.c) : turbulent shear stress

✖ Exp. data from Simonin and Barcouda

NSP1 + EV-diffusion

NSP1 + DH-diffusion

NSP2 + EV-diffusion

Figure 5 : Comparison of the two numerical solution procedures (NSP1 and NSP2) : RSTM predictions at location X_0 ; influence of the turbulent diffusion term modelling

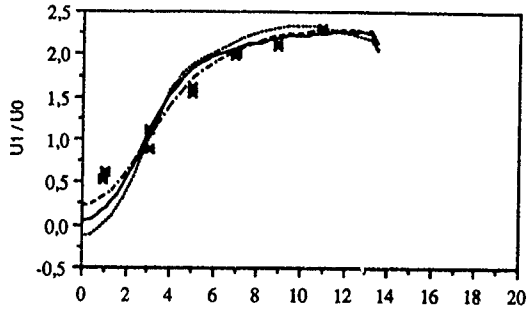

(6.a) : longitudinal mean velocity component

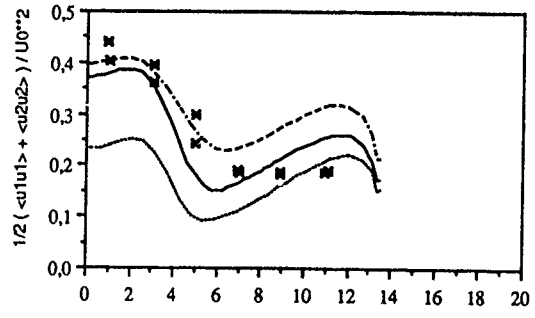

(6.b) : 2D turbulent kinetic energy

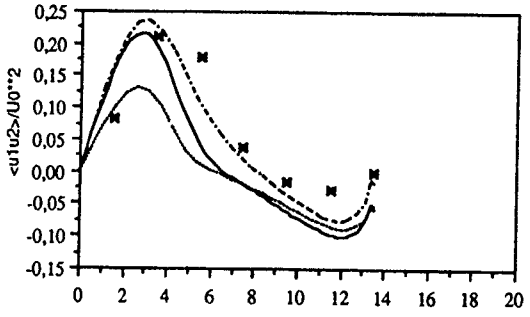

(6.c) : turbulent shear stress

✱ Exp. data from Simonin and Barcouda

——— no wall echo term

—— wall echo term of downstream tube only

-·-·-· wall echo term of both tubes

Figure 6 : RSTM predictions obtained with NSP1 at location X_0 : influence of the wall echo term $\phi_{ij,w}$.

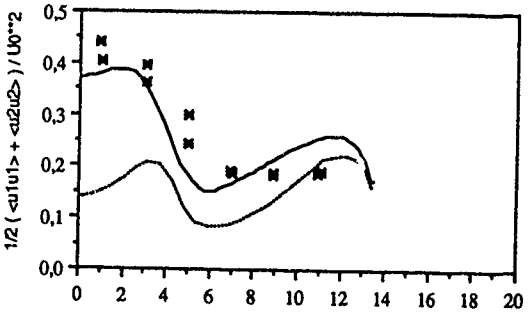

(7.b) : 2D turbulent kinetic energy

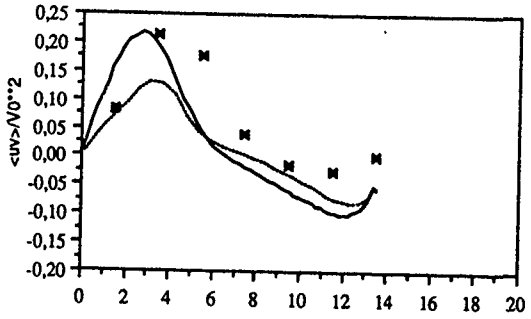

(7.c) : turbulent shear stress

✱ Exp. data from Simonin and Barcouda

——— ε equation with $C_{\varepsilon 1}$ = 1.44, $C_{\varepsilon 2}$ = 1.92

—— ε equation with $C_{\varepsilon 1}$, $C_{\varepsilon 2}$ related to anisotropy invariants

Figure 7 : RSTM predictions obtained with NSP1 at location X_0 : influence of the ε equation modelling

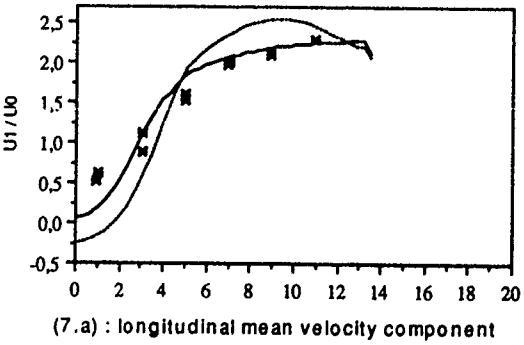

(7.a) : longitudinal mean velocity component

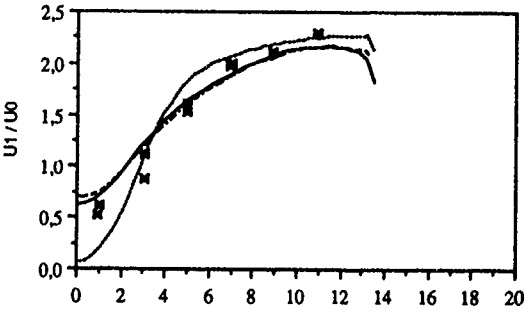

(8.a) : longitudinal mean velocity component

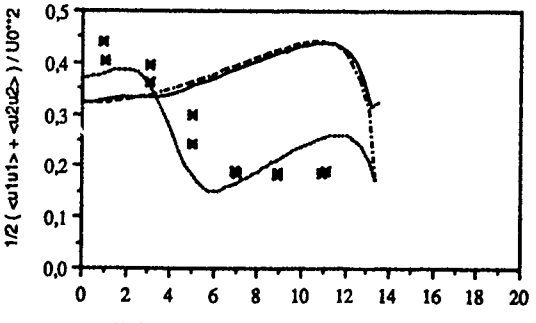

(8.b) : 2D turbulent kinetic energy

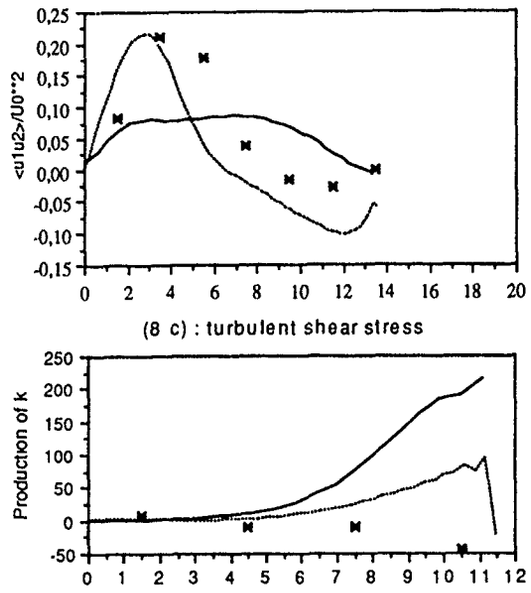

(8 c) : turbulent shear stress

(8.d) . production term P_k along the axis of symmetry upstream the tube

✖ Exp data from Simonin and Barcouda

RSTM with NSP1

k ε model with NSP1

k ε model with NSP2

Figure 8 : comparison of k-ε predictions obtained with NSP1, NSP2 and RSTM predictions obtained with NSP1.

CONCLUSION

Predictions of a fully developed flow across a tube bundle have been obtained with a k-ε model and a Reynolds stress model, both implemented in two different numerical solution procedures. Similar results are obtained with NSP1 and NSP2 when the eddy viscosity model is used whereas divergences in the wall boundary condition treatment make the two RSTM results far from one another. The semi-staggered FV approach (NSP1), avoiding interpolation stabilizing techniques, leads to a robust procedure which is meant to overcome deterioration of numerical stability by strong source terms occurring in curvature, rotation or buoyancy dominated flows [18] On the other hand, the collocated procedure (NSP2) is more versatile in testing various turbulence models and also more suitable for multigrid methods [19].

The flow is believed to be dominated by rapid distortion, and this was confirmed by the fact that both RSTM and k-ε model are giving velocity fields close to the experimental data. On the other hand, turbulence characteristics predicted by the RSTM are significantly better than those of the the k-ε model, due to a better description of the anisotropy. Accounting for the anisotropy.in the ε equation constants improved again the results, together with a local suppression of the wall echo terms which seems unsuitable for an impinging flow.

In a same way, boundary conditions are shown to be of significant importance in the level of turbulence. Local equilibrium badly reflects the anisotropy at the wall and remaining discrepancies noted so far may be coming from this assumption. A low Reynolds number modelling would certainly lead to a better prediction, and because of the rapid distortion again, a refined modelling of rapid part of the pressure-strain terms might improve the prediction [20].

ACKNOWLEDGEMENT

The authors are very grateful to Prof B E. Launder, Prof. M. A. Leschziner, and Pr. D. Jeandel for helpful discussions and constant concern in this research work.

REFERENCES:

1 Launder B.E., Reece G.J. and Rodi W. 1975 Progress in the development of a Reynolds stress turbulence closure. J Fluid Mech. 68.

2 Gibson M M. and Launder B.E. 1978 Ground effects on pressure fluctuations in the atmospheric boundary layer. J. Fluid Mech. 86 (3).

3 Daly B.J. and Harlow F.H. 1970 Transport equations in turbulence. Physics of Fluids 13(11).

4 Launder B.E., Haroutunian V. and Ince N. 1988 A new proposal for the ε transport equation. 3rd Biennial Colloquium on Computational Fluid Dynamics,UMIST.

5 Simonin O. and Barcouda M. 1988 Measurements and prediction of turbulent flow entering a staggered tube bundle", Proc. 4th Int. Symp. on applications of LDA to fluid mech. , Lisbon, Portugal.

6 Maupu V., Lien F.S., and Leschziner M.A. 1990 Stable implementation of a second-moment closure model in a non-staggered, non-orthogonal finite-volume solution procedure. 4th Biennial Colloquium on Computational Fluid Dynamics,UMIST.

7 Maupu V. 1990 Turbulence Models (k-ε and Rij-ε) in a collocated, non-orthogonal, finite-volume solution procedure. EDF report HE-41/90.17.

8 Rhie C.M. and Chow W.L. 1982 A numerical study of the turbulent flow past an isolated airfoil with training edge separation. AIAA paper 82-0998.

9 Obi S., Peric M. and Scheuerer G. 1989 A finite-volume calculation procedure for turbulents flows with second-order closure and collocated variable arrangement. Proc. 7th Symposium on Turbulent Shear Flows, Stanford University 17 - 4.

10 Laurence D. 1989 Code ULYSSE · note de principe. EDF report HE-41/89.32.

11 Leschziner M.A. 1987 Introduction to the modelling of turbulence. VKI Lecture Notes in Series 1987-06, WRF, Brussels.

12 Van Doormal J P. and Raithby G.D. 1984 Enhancements of the SIMPLE method for predicting incompressible fluid flows. Num. Heat Transfer, Vol. 7, PP.147-163.

13 Sebag S. 1991 Modèle aux tensions de Reynolds sur maillages structurés non orthogonaux, application à un écoulement dans un faisceau de tubes en quinconce. Thèse Ecole Centrale de Lyon.

14 El Tebany M.M.M. and Reynolds A.J. 1981 Turbulence in plane channel flows J. Fluid Mech 111, 283-318.

15 Rodi W. 1980 Turbulence models and their application in hydraulics. IAHR Publishing.

16 Sebag S. 1990 A new set of boundary conditions for the Reynolds stress tensor in curvilinear geometries. EDF report HE-41/90.40.

17 Sebag S. and Laurence D. 1990 Reynolds stress transport model simulations of turbulent recirculating flows in complex domains. Proc. Int. Symp. on Engineering Turbulence Modelling and Measurements, Dubrovnic, Yugoslavia, Elsevier Science Publishing.

18 Iacovides H. 1990 Development of a coupled solution procedure for the NS equations. 4th Biennial Colloquium on Computational Fluid Dynamics,UMIST.

19 Lien F.S and Leschziner M.A. 1990 Multigrid convergence acceleration for complex flow including turbulence. Proc. Third European Conference on Multigrid Methods, Bonn.

20 Launder B.E. and Tselepidakis D.P. 1991 Directions in second-moment modelling of near-wall turbulence. AIAA_0219.

EIGHTH SYMPOSIUM ON
TURBULENT SHEAR FLOWS
Technical University of Munich
September 9-11, 1991

TURBULENCE STRUCTURE OF A BACKWARD FACING STEP FLOW USING LES DATA

Y. Morinishi*) and T. Kobayashi**)

*)Department of Mechanical Engineering, Nagoya Institute of Technology,
Gokiso-cho Showa-ku, Nagoya 466, Japan

**)Institute of Industrial Science, The University of Tokyo,
7-22-1 Roppongi Minato-ku, Tokyo 106, Japan

ABSTRACT

Turbulence structure of a backward facing step flow is investigated using the numerical flow field which is computed by large eddy simulation (LES). The Reynolds number based on step height and main flow is 46000. Reliability of this data has been already confirmed by the comparisons between experimental and numerical data. The profiles of mean velocities, Reynolds stresses, triple products and the budget of Reynolds stresses are indicated, and turbulence structure of a separating flow field is numerically discussed.

NOMENCLATURE

X_i	; coordinates in tensor notation
U_i	; mean velocity component in X_i direction
u_i	; fluctuating velocity component in X_i direction
x,y,z	; longitudinal, vertical and spanwise coordinates
U,V	; mean velocity components in x and y directions
u,v,w	; fluctuating velocity components in x, y and z directions
Uo	; main flow at the inlet section
H	; step height
Re	; Reynolds number based on step height and main flow

INTRODUCTION

The turbulent flow over the backward facing step has been investigated by many experimental and numerical methods. Although the geometry of the backward facing step is still simple, this flow contains many features of the complex flow phenomena such as separation, reattachment and reverse flow. It has been recognized that the conventional ensemble mean turbulent models underpredict or overpredict the reattachment length which is the most basic factor in this flow. Large eddy simulation (LES) technique can provide the detailed informations of the time-dependent and three dimensional turbulent flow fields at the high Reynolds number. Reliability of LES has been promoted in some basic flow fields, and it is needed to investigate the capability of LES for the practical problems.

We have already computed the backward facing step flow using the LES [1]. The calculation results of mean velocity, turbulent distribution and reattachment length were compared with corresponding experimental values. Although this computation was done under relatively small spanwise grid number (20) and narrow spanwise computational region (2H), good agreement between computational and experimental data were shown on the mean velocities and turbulences.

In this paper, larger spanwise grid number (80) and wider spanwise computational region (4H) are set up, and turbulence structure of a separating flow is numerically investigated using LES data.

COMPUTATIONAL CONDITIONS

The basic equations of LES are grid scale (GS) continuity and momentum equations. Subgrid scale (SGS) model is the Smagorinsky model with a variable length scale [1,2]. These equations are then solved using an Adams-Bashforth scheme of the 2nd order in time and the 2nd order central finite difference formulae in space. Pressure fields are solved using a simultaneous iteration method for velocity and pressure [3].

The computational flow field is a channel with the backward facing step of step ratio 1.5. At the inlet of the channel, fully developed channel flow fields which are computed in driver section (2Hx2Hx4H) are specified instantaneously. The outlet is located at 30H downstream from the step where the first derivatives of flow properties in x direction are set at zero. A spanwise computational region is 4H, and cyclic boundary condition is used for this direction. The Spalding's law of the wall [1,4] is supposed for the wall boundary. Reynolds number based on step height H and main flow Uo is 46000. The numerical grid number in all directions are 230x50x80. Ensemble mean values are counted out using 5000 time steps and spanwise numerical points. The computational conditions are shown in Table 1.

Table 1. Computational conditions.

Computational region	32H (+2H) x 3H x 4H
Numerical grid number	210 (+20) x 50 x 80
Scheme in time	Adams-Bashforth (Δt=0.01)
Scheme in space	Central (2nd order)
Solution for pressure	HSMAC
Inlet B.C	Fully developed channel flow
Outlet B.C	d/dx=0 (for u, v and w)
Spanwise B.C	Cyclic (for u, v, w and p)
Wall B.C.	Spalding's law of the wall
SGS model	Smagorinsky model with variable length scale
Reynolds number	46000

RESULTS AND DISCUSSIONS

The turbulent structure of the separated region of the flow over backward facing step is discussed using LES data.

The contour plot of the stream lines for mean velocity field is shown in Fig. 1. The computational reattachment length is about 7.0H, which is almost the same as the corresponding experimental result [5,6]. Comparisons between experimental and LES data about the mean velocities and Reynolds stresses have already done in the previous (coarse grid) computation. No basic difference between the previous and present data is observed on the turbulent quantities.

Figure 2 indicates the schematic mechanism of the budget for the turbulent shear stresses in the two dimensional flows. On the spanwise turbulent intensity, redistribution by the pressure-strain term has the predominant effect, since there is no production term for the spanwise intensities in the two dimensional flows.

Mean velocity field behind the step has a separating bubble in which strong reverse flow exists. The mean longitudinal velocity profiles in Fig. 3 show that the minimum value of reverse flow is $-0.25U_o$ at X/H=3. The vertical distances from the wall at which the peak values of reverse flow exist decrease with increasing longitudinal coordinate in the separating region. The velocity gradient of the mixing layer behind the step makes the dominant production for $\overline{uv}$ and $\overline{uu}$ respectively. The separating region at the section just behind the step is not a dead water area, and has the peak

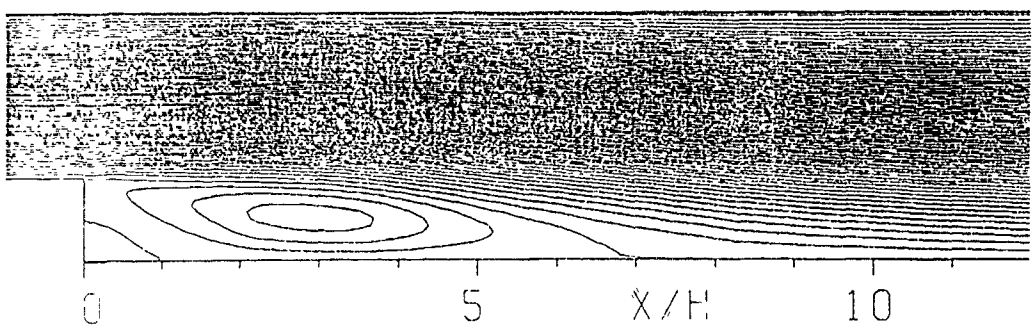

Figure 1. Stream lines of mean velocity field.

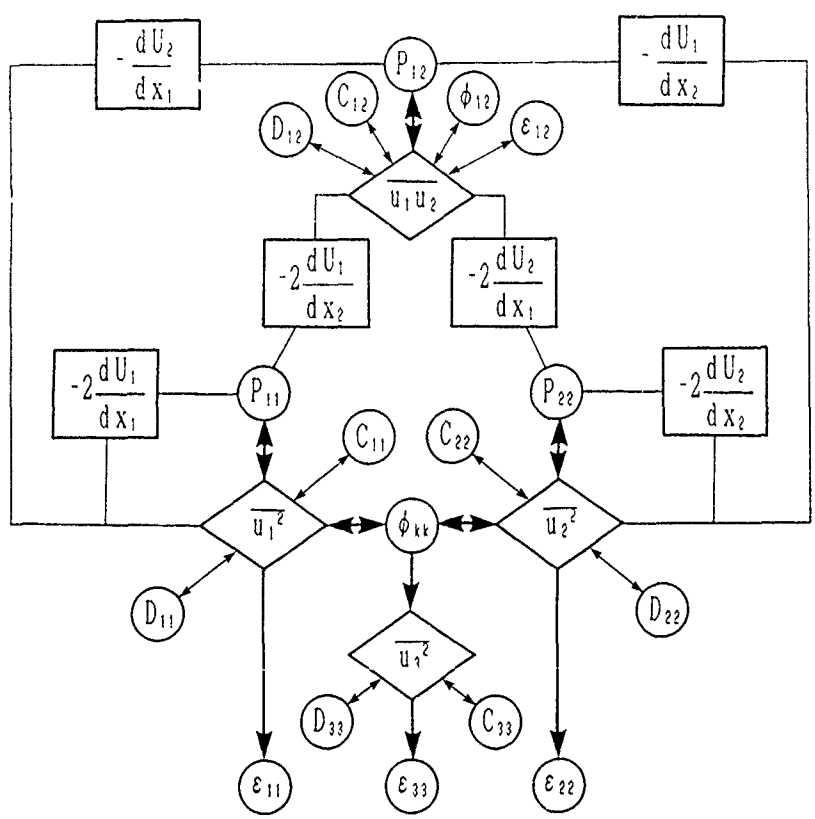

Figure 2. Mechanism of production for turbulent shear stresses in two dimensional turbulence.

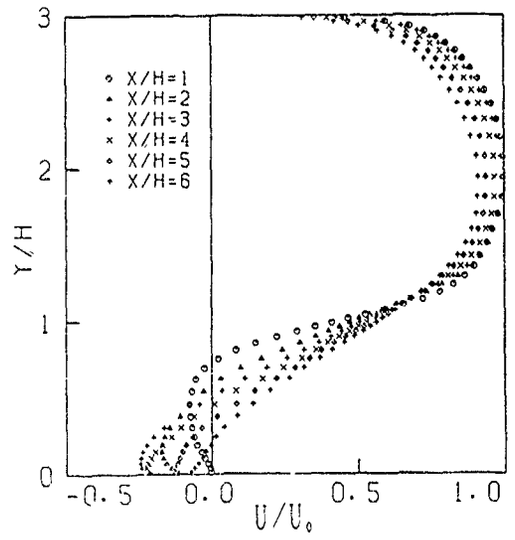

Figure 3. Longitudinal mean velocity profiles.

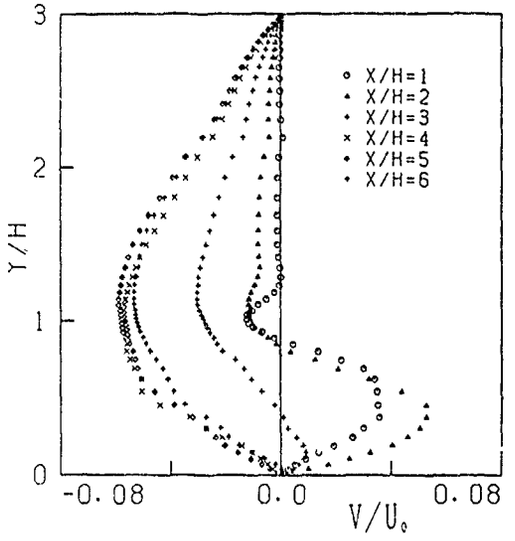

Figure 4. Vertical mean velocity rofiles.

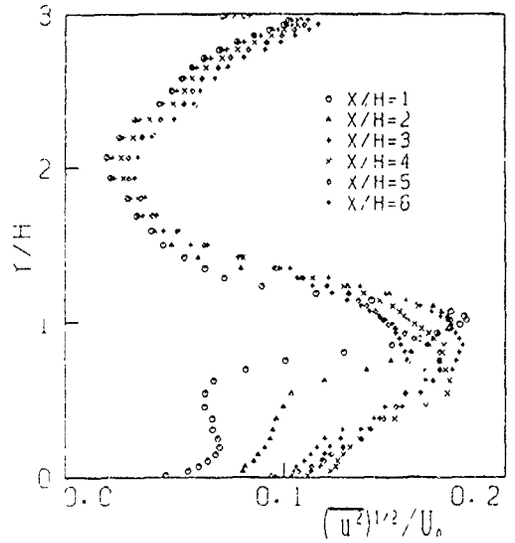

(a) Longitudinal turbulent intensity

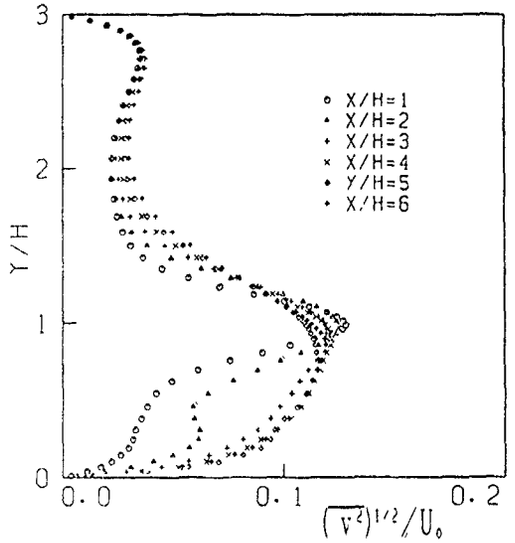

(b) Vertical turbulent intensity.

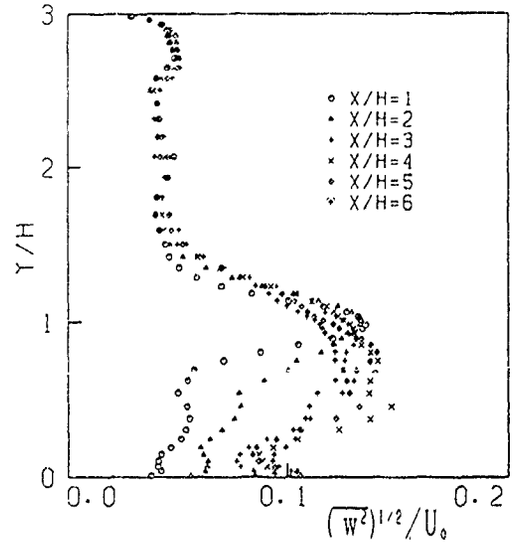

(c) Spanwise turbulent intensity.

Figure 5. Turbulent intensitles profiles.

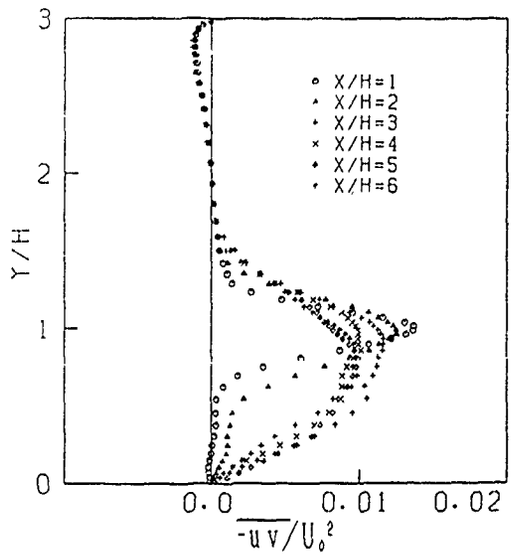

Figure 6. Reynolds shear stress profiles.

value of -0.08Uo for longitudinal velocity component. The longitudinal gradient of U in the separating region slightly affects on the production term of $\overline{uu}$. This effect yields the positive production near the step and near the reattachment point.

Figure 4 shows the vertical mean velocity profiles. The maximum and minimum values of the vertical component are 0.05 at the section of X/H=2 and -0.058 at the section of X/H=5 respectively. The negative velocity gradient in the section just behind the step and in the separating region near the reattachment point produces relatively large production of $\overline{vv}$.

Turbulent intensities and Reynolds shear stress profiles at different downstream sections are plotted in Fig. 5(a), (b), (c) and Fig. 6. Although grid resolution near the wall is not enough to resolve the wall turbulence structure, the turbulent profiles of channel flow are qualitatively maintained near the upper wall. The sharp distributions of turbulences in the section just behind the step are produced by the vertical gradient of U, and spread to downstream. Turbulent intensities and Reynolds stress increase with increasing the longitudinal coordinate from X/H=1 to X/H=3 in the separating region. Longitudinal turbulent intensity profile near the step side wall at the section of X/H=1 has the peak point which is produced by the production corresponding to the longitudinal velocity gradient of U.

Figures 7,8,9 and 10 show the profiles of the triple products related to the diffusion of the budgets of Reynolds stresses. In the mixing layer just behind the step, these terms are roughly asymmetrical about the inflection point. In the separating region near the reattachment point, the triple products have the peak point. It is well known that the main contribution to the triple products come from the large eddies . Therefore it

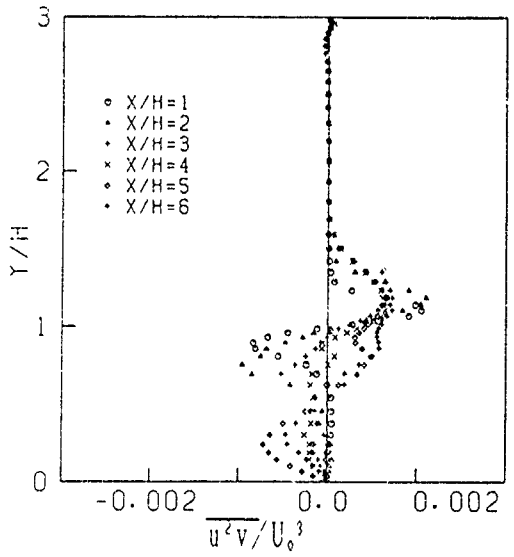

Figure 7. Triple product $\overline{uuv}$.

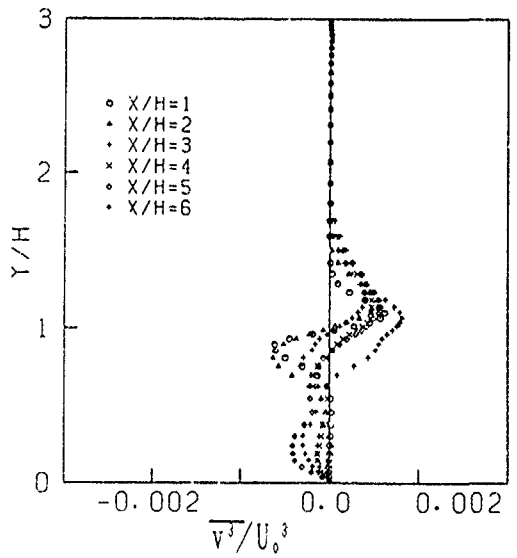

Figure 8. Triple product $\overline{vvv}$.

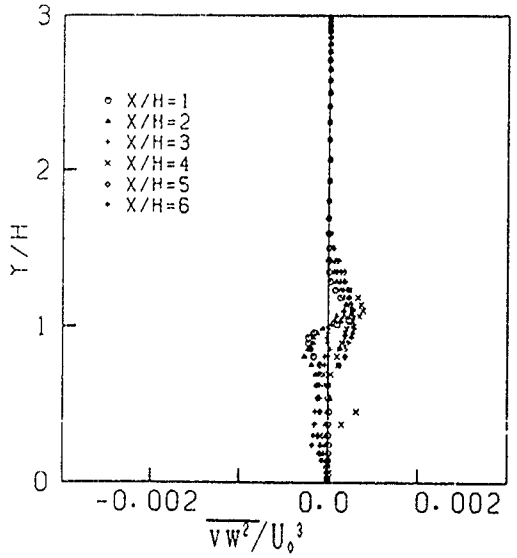

Figure 9. Triple product $\overline{vww}$.

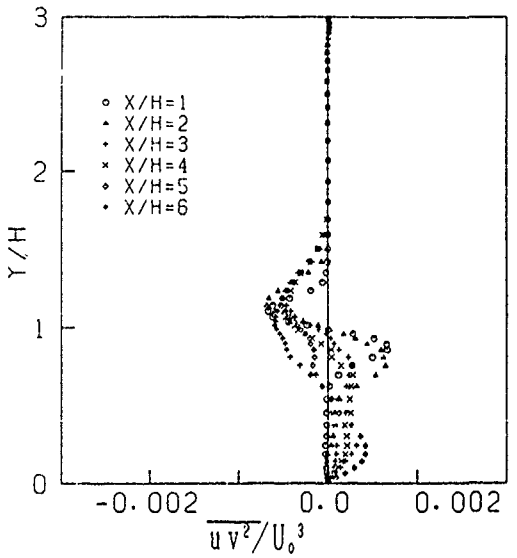

Figure 10. Triple product $\overline{uvv}$.

is probable that the active motions of the large eddies exist in the mixing layer behind the step and in the region near the reattachment point.

Figures 11,12 and 13 show the typical budgets of Reynolds stresses. The budgets of the turbulent normal stresses $\overline{uu}$ and $\overline{vv}$ at the section of X/H=2 are shown in Figs. 11 and 12. At the region of the mixing layer behind the step, the production term of $\overline{uu}$ through the vertical gradient of U is predominant. The production term of $\overline{vv}$ through the vertical gradient of V is shown in this region, too. Behavior of the pressure-strain terms in the region of mixing layer behind the step indicates that the turbulence energy is redistributed from $\overline{uu}$ to $\overline{vv}$ and $\overline{ww}$. The profiles of the diffusion terms correspond to the action of the triple products. At the region near the step side wall of the section just behind the step, the positive production of $\overline{uu}$ and the negative production of $\overline{vv}$ are peculiar. These terms relate to the longitudinal gradient of

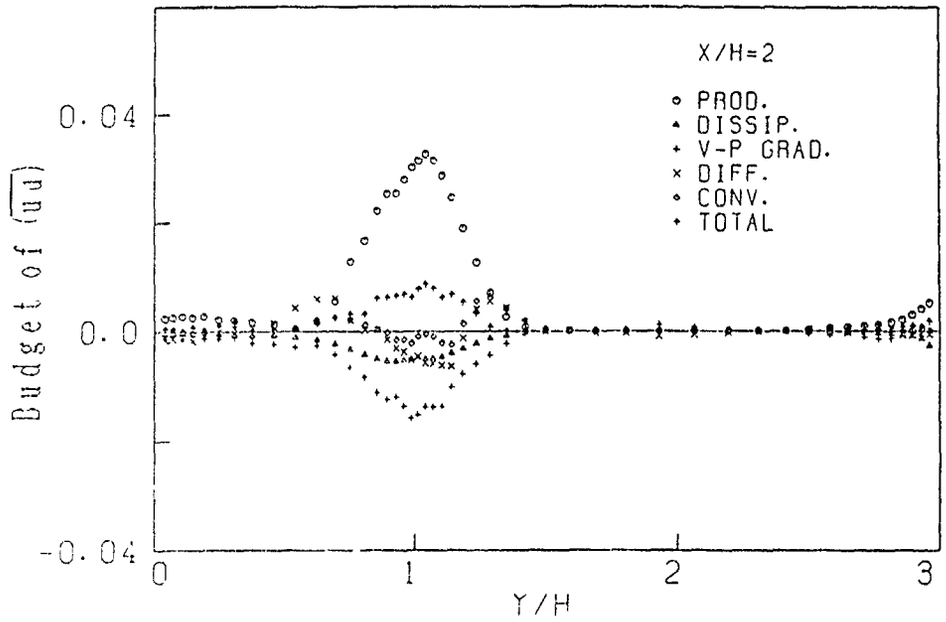

Figure 11. Budget of $\overline{uu}$ at the section of X/H=2.

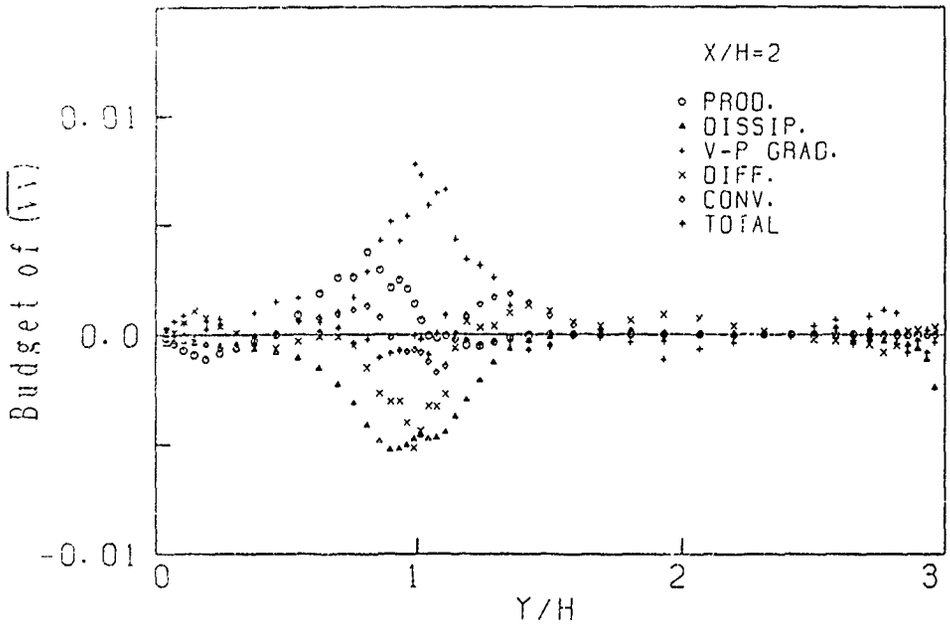

Figure 12. Budget of $\overline{vv}$ at the section of X/H=2.

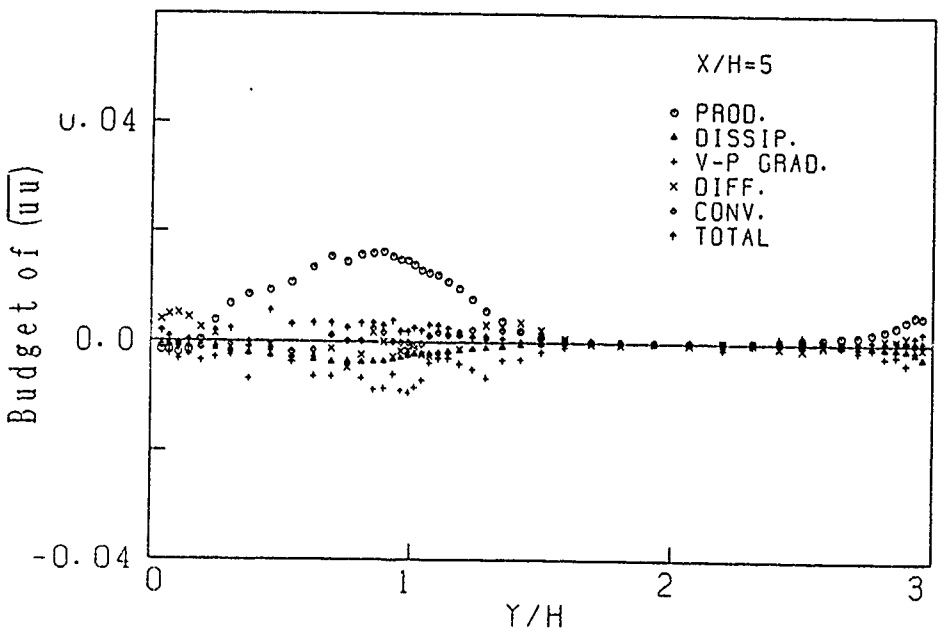

Figure 13. Budget of $\overline{uu}$ at the section of X/H=5.

U or the vertical gradient of V. Figure 13 shows the budget of turbulent normal stress $\overline{uu}$ at the section of X/H=5. In the region near the reattachment point, the diffusion term is predominant. Similar behavior of the diffusion terms is shown in the budgets of the normal stresses and turbulence energy at the section near the reattachment point. The diffusion terms of this region are intensely affected by the action of the triple products.

CONCLUSIONS

Turbulent structure of a separating flow field is numerically discussed on the flow over a backward facing step. Ensemble mean data are estimated by using the data computed by large eddy simulation. According to the discussions on the profiles of mean velocities, Reynolds stresses, triple products and the budget of Reynolds stresses, turbulence structure of separating region in the backward facing step flow can be roughly classified into following regions;

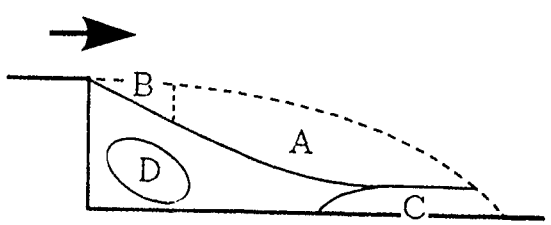

Figure 14. Turbulence structure of separating region

The region on mixing layer behind the step (Region A in Fig. 14).

The region just behind the step, where the production terms correspond to dV/dy are appeared in $\overline{vv}$ (Region B in Fig. 14).

The region near the reattaching point, where the diffusion terms related to the triple products are predominant (Region C in Fig. 14).

The region near the step side wall of the section just behind the step, where the production terms which are due to dU/dx and dV/dy are predominant (Region D in Fig 14).

REFERENCES

[1] MORINISHI,Y. & KOBAYASHI,T., 1990 Large Eddy Simulation of Backward Facing Step Flow, Engineering Turbulence Modelling and Experiments (Rodi and Ganic, Editors), Elsevier, pp279-286.

[2] YOSHIZAWA,A., 1989 Subgrid-scale modeling with a variable length scale, Phys. Fluids A1(7), pp1293-1295.

[3] HIRT,C.W & COOK,J.L., 1972 Calculating Three-Dimensional Flows around Structures and over Rough Terrain. J. Comput. Phys. 10, pp324-340.

[4] SPALDING,D.B., 1961 A Single Formula for the "Law of the Wall", Trans. ASME, J. Appl. Mech. 28, pp455-458.

[5] KIM,J., KLINE,S.J. & JOHNSTON,J.P., 1980 Investigation of a Reattaching Turbulent Shear Layer: Flow Over a Backward-Facing Step. Trans. ASME, J. Fluid Eng., 102, pp302-308.

[6] ITOH,N. & KASAGI,N., 1989 Turbulence Measurement in a Separated and Reattaching Flow over a Backward-Facing Step with the Three-Dimensional Particle Tracking Velocimeter, J. of the flow visualization society of Japan, 34, pp245-248.

EIGHTH SYMPOSIUM ON
TURBULENT SHEAR FLOWS
Technical University of Munich
September 9-11, 1991

SECOND-MOMENT MODELLING OF RECIRCULATING FLOW WITH A NON-ORTHOGONAL COLLOCATED FINITE-VOLUME ALGORITHM

F S. Lien and M.A. Leschziner

Department of Mechanical Engineering,
University of Manchester Institute of Science and Technology,
Manchester, M60 1QD, UK

ABSTRACT

The incorporation of Reynolds-stress closure into a non-orthogonal, collocated finite-volume framework in which the discretisation of convection is non-diffusive presents a number of algorithmic problems not encountered in more traditional schemes employing staggered, rectilinear volume arrangements. Three issues requiring special consideration are the tensorially correct incorporation of the wall-related pressure-strain terms which are important fragments in the stress closure, boundary conditions at curved walls, and iterative stability. The first issue, in particular, arises because the wall-related terms are tied to the orientation of the wall relative to the directions of the Reynolds stresses. The paper report practices which address all three problem areas. Three complex applications are reported, among them the flow through a sinusoidal pipe constriction and shock-induced separation over a channel bump.

INTRODUCTION

Over the past few years, CFD for general turbulent flow has advanced along two major fronts without significant cross-links. Numerically, there has been a dramatic shift away from simple rectilinear geometries towards complex domains requiring the use of body-fitted meshes. A number of strategies have been pursued, but the one which seems to emerge as offering the best compromise between flexibility and algorithmic simplicity adopts a Cartesian or cylindrical-polar velocity decomposition within a non-orthogonal finite-volume framework. Such schemes have been developed, for example, by Peric (1985), Shyy & Braaten (1986) and Majumdar et al (1989). Moreover, a number of commercial packages - for example, FLOW3D and FLUENT/BFC - are based on this approach. Physically, there has been a similarly strong shift away from eddy-viscosity models towards second-moment closure. This shift has been motivated, principally, by the realisation that only the latter type of models is able to capture, in any fundamentally sound sense, the interaction between curvature-related strain and turbulence transport.

The importance of curvature in all recirculating and swirling flows naturally favours the combination of second-moment models with elliptic-flow solvers. While this turns out to be a non-trivial task, such models have been successfully incorporated into a number of recirculating-flow algorithms [e.g. McGuirk et al (1985), Gaskell & Lau (1987), Jones & Manners (1988) and Lin & Leschziner (1989)]. However, with very few exceptions, such schemes are applicable to Cartesian or cylindrical-polar meshes only, and most adopt a staggered finite-volume arrangement. One procedure based on the collocated approach is that of Obi et al (1989), but this applies to regular grids only, while a scheme by Sebag & Laurence (1990) adopts a non-orthogonal, semi-staggered formulation.

Combining second-moment closure with a non-orthogonal, collocated scheme is a particularly challenging task. Apart from 'ordinary' complexities associated with non-orthogonality, the main difficulties arise from boundary conditions, the awkward tensorial nature of the highly influential wall-reflection terms in the pressure-strain components of the Reynolds-stress equations, and from the fact that storage of all stresses at the same spatial location is a strong source of numerical instability or physically unrealistic oscillatory behaviour.

This paper present practices directed towards all three problem areas, realised within a recently developed non-orthogonal-grid methodology combining second-moment closure, non-diffusive discretisation and multigrid convergence acceleration. That same methodology has also been extended to compressible flow, including transonic domains, and one of the applications presented below relates to shock-induced separation from a channel bump.

BASIC NUMERICAL FRAMEWORK

The discretisation process is preceded by a transformation of the Cartesian forms of the flow-governing equations to forms involving spatial derivatives along the non-orthogonal co-ordinates, involving the use of the Jacobian transformation matrix. Because the velocity components are chosen to remain Cartesian (or, more generally, cylindrical polar, toroidal or adapting to an arbitrary, user-defined datum line), they can be treated as scalars, thus circumventing the complexities associated with fully covariant differentiation of vectors and tensors.

With ξ and η representing the non-orthogonal directions and r being the radial co-ordinate, the transport equation for any scalar property Φ can be written in the following form:

$$\frac{\partial}{\partial\xi}\left\{ \rho r U\Phi - \frac{r^2}{(rJ)}\, q_1^{\Phi}\, \rho_\xi \right\} + \frac{\partial}{\partial\eta}\left\{ \rho r V\Phi - \frac{r^2}{(rJ)}\, q_2^{\Phi}\, \Phi_\eta \right\} = rJ\, S^{\Phi} \quad ...(1)$$

where U and V are contravariant velocity components,

$$U = uy_\eta - vx_\eta$$
$$V = vx_\xi - uy_\xi$$

J is the Jacobian of the transformation, rJ is the ratio of corresponding volumes (areas) in physical and transformed (ξ,η) space, and S^{Φ} contains diffusive terms involving mixed derivatives, sources and sinks, including pressure terms in the case of momentum. For isotropic diffusivity Γ_Φ, the q^{Φ}-terms are:

$$q_1^{\Phi} = \Gamma_\Phi\,(y_\eta^2 + x_\eta^2)$$

$$q_2^{\Phi} = \Gamma_\Phi\,(y_\xi^2 + x_\xi^2)$$

The above terms will be redefined later in the context of anisotropic turbulence transport.

Next, the equation is integrated over the volume shown in Fig. 1 to yield, after application of the Gauß Divergence Theorem, a balance of face fluxes and volume-integrated net sources:

$$(\rho rU)_e\,\Phi_e - (\rho rU)_w\,\Phi_w + (\rho rV)_n\,\Phi_n - (\rho rV)_s\,\Phi_s = rJS_\Phi$$
$$+ \left[(rq_1^{\Phi}/J)_e + (rq_1^{\Phi}/J)_w + (rq_2^{\Phi}/J)_n + (rq_2^{\Phi}/J)_s\right]\Phi_P$$
$$- \left[(rq_1^{\Phi}/J)_e\,\Phi_E + (rq_1^{\Phi}/J)_w\,\Phi_W + (rq_2^{\Phi}/J)_n\,\Phi_N + (rq_2^{\Phi}/J)_s\,\Phi_S\right] \quad ...(2)$$

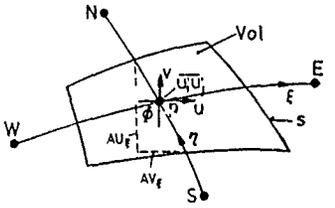

Fig. 1: Finite volume and storage arrangement

The convection fluxes are approximated either by the 'Hybrid' (upwind/central-) differencing scheme of Patankar (1980) or by the quadratic scheme QUICK of Leonard (1979) or by van Leer's TVD scheme MUSCL (1979). The last scheme is also used for all turbulence-model equations.

As seen from Fig. 1, the velocity components and pressure are stored together at cell-centred nodes. This would normally lead to 'chequerboard oscillations' when pressure gradients are approximated by central differencing, reflecting a computational decoupling between velocity and pressure gradient The difficulty may be overcome, however, by using the method of Rhie and Chow (1983) which, essentially, introduces a measure of artificial fourth-order pressure smoothing. For the east and north faces of the cell shown in Fig. 1, the Rhie and Chow interpolation may, for plane flow, be written:

$$U_e = [\overline{(u - DU_\xi\ \delta_\xi p)}_e + \overline{DU_{\xi,e}}\ (p_P - p_E)]y_\eta - [\overline{(v - DV_\xi\ \delta_\xi p)}_e + \overline{DV_{\xi,e}}\ (p_P - p_E)]x_\eta \quad ..(3)$$

$$V_n = [\overline{(v - DV_\eta\ \delta_\eta p)}_n + \overline{DV_{\eta,e}}\ (p_P - p_N)]x_\xi - [\overline{(u - DU_\eta\ \delta_\eta p)}_n + \overline{DU_{\eta,n}}\ (p_P - p_N)]y_\xi \quad . \quad (4)$$

where $\delta_\xi p_P \equiv (p_w - p_e)$, $\delta_\eta p_P \equiv (p_s - p_n)$;

overbars denote averages, evaluated at faces 'e' and 'n', respectively, from values pertaining to volumes which abut at the face in question, DU_ξ, DV_ξ - say at point P - are the projected areas, AU_ξ and AV_ξ, identified in Fig 1, divided by the coefficient multiplying the velocity U_P in the final form of finite-volume momentum equation (2) (i.e for $\Phi=U_P$).

The pressure itself is determined by using the SIMPLE pressure-correction algorithm of Patankar (1980) This is modified to include a *density-retardation* methodology permitting an accurate capturing of shocks [Lien & Leschziner (1992)] One example presented later has been computed with this methodology.

IMPLEMENTATION OF SECOND-MOMENT CLOSURE

Present closure form

The closure adopted herein is the high-Re Reynolds-stress variant of Gibson and Launder (1987) In terms of Cartesian tensor notation, for plane flows, this closure may be written as follows.

$$\frac{\partial \rho u_k\ \overline{u_i'u_j'}}{\partial x_k} = D_{ij} + P_{ij} - \frac{2}{3}\rho\delta_{ij}\epsilon + \Phi_{ij} \quad . \quad (5)$$

in which

$$D_{ij} = \frac{\partial}{\partial x_k}\left[C_k\ \rho\ \overline{u_k'u_\ell'}\ \frac{k}{\epsilon}\ \frac{\partial\ \overline{u_i'u_j'}}{\partial x_\ell}\right],$$

$$P_{ij} = -\rho\ \overline{u_i'u_k'}\ \frac{\partial u_j}{\partial x_k} - \rho\ \overline{u_j'u_k'}\ \frac{\partial u_i}{\partial x_k},$$

$$\Phi_{ij} = \Phi_{ij1} + \Phi_{ij2} + \Phi_{ijw1} + \Phi_{ijw2}$$

$$\Phi_{ij1} = -c_1\ \rho\ \frac{\epsilon}{k}\left[\overline{u_i'u_j'} - \frac{\delta_{ij}}{3}\ \overline{u_k'u_k'}\right]$$

$$\Phi_{ij2} = -c_2\ \rho\left[P_{ij} - \frac{\delta_{ij}}{3}\ P_{kk}\right]$$

$$\Phi_{ijw1} = c_1'\ \rho\ \frac{\epsilon}{k}\left[\overline{u_k'u_m'}\ n_k n_m\ \delta_{ij} - \frac{3}{2}\ \overline{u_k'u_i'}\ n_k n_j - \frac{3}{2}\ \overline{u_k'u_j'}\ n_k n_i\right] f$$

$$\Phi_{ijw2} = c_2'\ \rho\left[\Phi_{km2}\ n_k n_m\ \delta_{ij} - \frac{3}{2}\ \Phi_{ik2}\ n_k n_j - \frac{3}{2}\ \Phi_{jk2}\ n_k n_i\right] f$$

In the last two contributions, n_i is the wall-normal unit vector in the direction i and $f = C_\mu^{0.75}\ k^{1.5}/\epsilon\kappa\Delta n$ with Δn being the wall-normal distance

In principle, the equations of set (5) are discretised in precisely the same manner as any other for any property Φ, i.e. the equations are transformed, as expressed by form (2), and then integrated over the finite volume in Fig. 1. However, in the course of the discretisation and solution process, three issues require special consideration, namely stability, boundary conditions and the tensorially correct incorporation of the wall-reflection terms Φ_{ijw}. The last issue arises because the wall-reflection approximations are clearly tied to the orientation of the wall, via f. Each issue is considered separately below.

Boundary conditions

In the context of using high-Re transport models of turbulence within finite-volume schemes, it is standard practice to adopt log-law-based relations to bridge the semi-viscous near-wall region. One feature of this treatment is the solution of the turbulence energy or stress equations over the near-wall cells with cell-integrated productions and dissipation terms evaluated from the log law.

The treatment adopted here is different and involves a prescription of all stresses at the near-wall nodes. Values for the stresses in the log-law region may be derived by focusing on the stress equations applicable to local energy equilibrium, $0.5P_{kk}=\epsilon$, and setting the wall-distance function f=1. Adopting the wall-oriented Cartesian frame of reference shown in Fig. 2, this route can be shown to lead to:

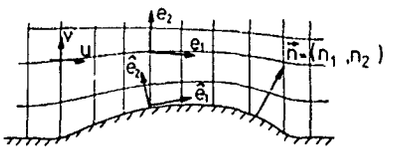

Fig. 2. Wall- and mesh-oriented co-ordinate systems

$$\left.\begin{aligned}
\hat{\overline{u'^2}} &= \frac{k(4c_1+2c_1^2-4c_1c_2+2c_1c_2^*+6c_1'+6c_1c_1'-6c_1'c_2)}{3c_1(c_1+2c_1')} = 1.098k\\
\hat{\overline{v'^2}} &= \frac{2(-1+c_1+c_2-2c_2^*)k}{3(c_1+2c_1')} = 0.247k\\
\hat{\overline{w'^2}} &= 2k - \overline{u'^2} - \overline{v'^2} = 0.653k\\
-\hat{\overline{u'v'}} &= \sqrt{\left[\frac{1-c_2+1.5c_2^*}{c_1+1.5c_1'}\right]\left[\frac{2(-1+c_1+c_2-2c_2^*)}{3(c_1+2c_1')}\right]}\ k = 0.255k
\end{aligned}\right\} \quad (6)$$

with the last obtained with the aid of

$$\epsilon \cong \frac{u_\tau^3}{\kappa\Delta n} \quad ...(7)$$

Next, the above stresses in wall-oriented co-ordinates must be transformed to the primary Cartesian system in which the velocity-vector is decomposed within the numerical scheme. This can be achieved by:

$$\left[\sigma_{ij}\right] = A^T\left[\hat{\sigma}_{ij}\right] A \quad .. (8)$$

where $\hat{\sigma}$ is the wall-oriented stress system and σ is the primary Cartesian one With the wall-oriented unit vectors denoted by $\hat{e}_i$ and decomposed into components associated with the primary

Cartesian system,

$$\left.\begin{aligned}\hat{e}_1 &= (t_1,\ t_2,\ 0)\\ \hat{e}_2 &= (n_1,\ n_2,\ 0)\\ \hat{e}_3 &= (\ 0,\ 0,\ 1)\end{aligned}\right\} \quad \ldots(9)$$

as shown in Fig. 2, A arises as:

$$A = \begin{bmatrix} t_1 & t_2 & 0 \\ n_1 & n_2 & 0 \\ 0 & 0 & 1 \end{bmatrix} \quad \ldots(10)$$

and A^T is the transpose of A. Hence, the Cartesian stresses may be evaluated as.

$$\left.\begin{aligned}\overline{u'^2} &= \overline{\hat{u}'^2}\ t_1^2 + \overline{\hat{v}'^2}\ n_2^2 + 2\overline{\hat{u}'\hat{v}'}\ t_1 n_1\\ \overline{v'^2} &= \overline{\hat{u}'^2}\ t_2^2 + \overline{\hat{v}'^2}\ n_2^2 + 2\overline{\hat{u}'\hat{v}'}\ t_2 n_2\\ \overline{u'v'} &= \overline{\hat{u}'^2}\ t_1 t_2 + \overline{\hat{v}'^2}\ n_1 n_2 + \overline{\hat{u}'\hat{v}'}\ (t_1 n_2 + t_2 n_1)\end{aligned}\right\} \quad (11)$$

The above stresses are used as boundary conditions for the inner field

Wall-reflection terms

The task at hand may be illustrated by focusing on any single curved wall, as shown in Fig. 2, with the wall-normal vector being (n_1,n_2). The wall-distance function f may then be related to Cartesian, velocity-oriented components by

$$f_x = n_1^2\ f;\quad f_y = n_2^2\ f,\quad f_{xy} = n_1\ n_2\ f \qquad .(12)$$

With the above transformed wall-distance-function components, it can be shown that the stress equations (for 2D plane cases) may be written:

$$C_{ij} - D_{ij} = \alpha_1\ P_{11} + \alpha_2\ P_{22} + \alpha_3\ P_{12} + 0.5\ \alpha_4\ P_{kk} + \rho\frac{\epsilon}{k}\left[\alpha_5\ \overline{u'^2} + \alpha_6\ \overline{v'^2} + \alpha_7\ \overline{u'v'}\right] + \alpha_8 \rho\epsilon \quad . \quad (13)$$

with the α-coefficients tabulated below for $\overline{u'^2}$, $\overline{v'^2}$ and $\overline{u'v'}$.

$\overline{u_i u_j} = \overline{u'^2}$	$\overline{u_i u_j} = \overline{v'^2}$	$\overline{u_i u_j} = \overline{u'v'}$
$\alpha_1 = 1-c_2 + 2c_2^* f_x$	$\alpha_1 = -\ c_2^* f_x$	$\alpha_1 = 1.5\ c_2^* f_{xy}$
$\alpha_2 = -c_2^* f_y$	$\alpha_2 = 1 - c_2 + 2c_2^* f_y$	$\alpha_2 = 1.5\ c_2^* f_{xy}$
$\alpha_3 = c_2^* f_{xy}$	$\alpha_3 = c_2^* f_{xy}$	$\alpha_3 = 1 - c_2 + 1.5 c_2^* (f_x+f_y)$
$\alpha_4 = \frac{2}{3}(c_2 - 2c_2^* f_x + c_2^* f_y)$	$\alpha_4 = \frac{2}{3}(c_2 - 2c_2^* f_y + c_2^* f_x)$	$\alpha_4 = -\ 2c_2^* f_{xy}$
$\alpha_5 = -(c_1 + 2c_1' f_x)$	$\alpha_5 = c_1' f_x$	$\alpha_5 = -\ 1.5\ c_1' f_{xy}$
$\alpha_6 = c_1' f_y$	$\alpha_6 = -(c_1 + 2c_1' f_y)$	$\alpha_6 = -\ 1.5\ c_1' f_{xy}$
$\alpha_7 = -\ c_1' f_{xy}$	$\alpha_7 = -\ c_1' f_{xy}$	$\alpha_7 = -(c_1 + 1.5\ c_1' [f_x+f_y])$
$\alpha_8 = \frac{2}{3}(c_1 - 1)$	$\alpha_8 = \frac{2}{3}(c_1 - 1)$	$\alpha_8 = 0$

Table 1 α-coefficients in equation (13)

The above relations have been derived via two entirely different routes, one involving the direct insertion of the wall-distance transformations into the wall-reflection terms of equation (5) and the other proceeding through a rigorous transformation of all terms in Φ_{ijw}. Both routes are found to lead to identical results (details may be found in Lien (1991))

Stability

Low iterative stability is a serious difficulty in elliptic solvers, particularly those based on a collocated arrangement and using non-diffusive discretisation. In essence, the difficulty arises from the absence of eddy-viscosity terms and a numerical decoupling of stresses from related strains. The problem has been addressed here by extracting apparent viscosities from the (ξ,η)-*transformed* partial differential equations governing the stresses. It can be shown that terms appearing naturally in the stress equations allow the interpretation:

$$\nu_{ij} = \frac{1-c_2 + 1.5\ c_2^*(f_i+f_j)}{c_1 + 1.5\ c_1'(f_i+f_j)}\ \frac{k\overline{u'_i}^2}{\epsilon} \quad (i\neq j) \quad . \quad (14)$$

$\longrightarrow$ which is associated with the strain $\left[\frac{\partial u_i}{\partial \xi_j}\right]$

while for i=j (no summation),

$$\nu_{ii} = \frac{2 - \frac{4}{3}\ c_2 + \frac{2}{3}\ c_2^*(4f_i+f_j)}{c_1 + 2c_1' f_i}\ \frac{k\overline{u'_i}^2}{\epsilon} \quad \ldots(15)$$

$\longrightarrow$ which is associated with the strain $\left[\frac{\partial u_i}{\partial \xi_i}\right]$

where $c_2^* = c_2 c_2'$, and f_i and f_j are either f_x or f_y, as defined by equation (12) Insertion of the above viscosities into the u-momentum equation, for example, leads to:

$$\left.\begin{aligned} q_1^u &= \mu_1\ y_\eta^2 + \mu_{12}\ x_\eta^2\\ q_2^u &= \mu_{11}\ y_\xi^2 + \mu_{12}\ x_\xi^2\end{aligned}\right\} \quad .. \ (16)$$

$$S_\Phi = -\left\{(ry_\eta)\frac{\partial}{\partial\xi}\ p_x^{ux} + (-ry_\xi)\frac{\partial}{\partial\eta}\ p_y^{uy}\right\} - \frac{\partial}{\partial\xi}(-rx_\eta)\ \rho\tilde{\overline{uv}}_x - \frac{\partial}{\partial_\eta}(rx_\xi)\ \rho\tilde{\overline{uv}}_y \quad . \quad (17)$$

with

$$\left.\begin{aligned} p^{ux} &= p + \rho\tilde{\tilde{u}}_x^2\\ p^{uy} &= p + \rho\tilde{\tilde{u}}_y^2\end{aligned}\right\} \quad .. \ (18)$$

$$\left.\begin{aligned} \rho\tilde{\tilde{u}}_x^2 &= \rho\overline{u'^2} + \frac{\mu_{11}}{(rJ)}(ry_\eta)\ u_\xi\\ \rho\tilde{\tilde{u}}_y^2 &= \rho\overline{u'^2} + \frac{\mu_{11}}{(rJ)}(-ry_\xi)\ u_\eta\\ \rho\tilde{\overline{uv}}_x &= \rho\overline{u'v'} + \frac{\mu_{12}}{(rJ)}(-rx_\eta)\ u_\xi\\ \rho\tilde{\overline{uv}}_y &= \rho\overline{u\ v} + \frac{\mu_{12}}{(rJ)}(rx_\xi)\ u_\eta\end{aligned}\right\} \quad .. \ (19)$$

The addition of normal stresses to the pressure, as done in relations (18) which are inserted into equations (17), is of considerable significance to stability, in the context of the Rhie & Chow interpolations (3) and (4). It should be evident that the interpretation of normal stresses as pressure fragments means that any cell-face velocity is not merely sensitised to the pressure differences centred on that face but only to the normal-stress difference. In effect, this practice introduced (artificial) fourth-order normal-stress diffusion in addition to fourth-order pressure diffusion.

RESULTS

The capabilities and performance of the above methodology are exemplified by three examples: a flow behind a backward-facing step [Durst & Schmidt (1985)] computed with a deliberately distorted mesh, a flow through a sinusoidal pipe constriction [Deshpande & Giddens (1980)] and a transonic flow over a channel bump ['Case B' of Delery (1983)] in which the shock induces boundary-layer separation. All cases are two-dimensional, although the code (in conjunction with eddy-viscosity modelling) applies to and has been used for three-dimensional flows, including multigrid acceleration [Lien & Leschziner (1990)].

Fig. 3 and 4 compare k-ϵ and Reynolds-stress-model calculations performed with a 200x50 grid, with the aid of a 3-level multigrid convergence-acceleration scheme, for Durst &

Schmidt's step. QUICK was used to approximate the convection of momentum, while convection of turbulence quantities was discretised by means of the MUSCL/TVD scheme. Only streamfunction plots and a few velocity profiles have been included here, although extensive comparisons with experimental data have been performed. The experimental reattachment length is about 8, and the stress model is seen to predict this value well. However, there is some evidence that grid skewness generally increases sensitivity to grid density, and hence further grid refinement is needed to justify confidence in the predicted solutions. Indeed, closer inspection of the streamlines reveals 'kinks' whose positions coincide with those at which the grid disposition changes abruptly. Whilst there are no dramatic differences between the solutions returned by the k-ϵ model and the stress closure, the latter evidently predicts a longer recirculation zone, a secondary corner eddy and steeper shear strains in the curved, separated shear layer. All may be attributed to curvature-induced attenuation of turbulence and have been observed in previous calculations of similar flows Contrary to observations by Obi et al (1989), Lasher & Taulbee (1990) and Sebag & Laurence (1990), no abnormal reversal in the direction of the separation streamline is predicted as the point of reattachment is approached. This defect has been attributed to an inappropriate amplification, rather than attenuation, of the wall-normal turbulence intensity by the wall-related contribution to the pressure-strain model, Φ_{ijw2} One might suspect that the severe grid skewness at the lower wall could have suppressed the manifestation of this genuine model defect However, test calculations by the authors with a Cartesian mesh, somewhat coarser than the 200x50 non-orthogonal one, yielded a solution very similar to that shown in Fig 3. Interestingly, a replacement of the rounded (experimental) inlet profile by a uniform one was found to provoke a directional reversal of the separation streamline On the other hand, the present authors have observed that variations in the treatment of wall-boundary conditions can have a considerable influence on the manner in which the separation streamline approaches the reattachment point Hence, the authors are not entirely convinced that the the anomaly is linked solely to Φ_{ijw2}

Figs 5 to 8 show solutions obtained with the high-Re k-ϵ model, a low-Re k-ϵ variant of Lien (1991)+ and with the stress-model for the flow through Deshpande & Giddens' sinusoidal pipe constriction As in the previous case, a combination of QUICK and MUSCL was used for approximating convection, here over grids varying between 120x24 and 120x40. The comparison of streamfunction plots in Fig 5 reveals some trents which are consistent with those observed in the previous case For example, the stress closure predicts, here too, steeper velocity gradients in the shear layer bordering the separation zone. However, there are also marked differences Thus, here, the tendency of the separation streamline to double up at the point of reattachment is evident, a feature which may have been enhanced by the nearly uniform velocity profile ahead of separation. None of the models returns the correct behaviour of the centreline velocity and the wall pressure, but the stress model clearly responds more sensitively to the adverse pressure gradient beyond the throat, inducing earlier separation and diminishing the consistent tendency towards an excessive recovery of pressure Interestingly, the comparison conveys the message that relaminarisation of the boundary layer during the acceleration phase ahead of the throat does not seem to play an essential role in the separation process Implicit in this statement is, however, the assumption that the low-Re k-ϵ model gives a realistic representation of the history of relaminarisation in the flow beyond the throat, just ahead of separation.

Firally, Figs. 9 to 11, give results obtained with the high-Re k-ϵ model and the stress closure for the transonic bump flow of Delery. For the latter model, solutions are reported for two grids, one containing 95x35 and the other 130x50 lines Fig. 9 gives an overall view of the flow field in terms of Mach-number contours, and the plots reveal the characteristic λ-shock structure arising from the interaction of the normal shock with the wall boundary layer. Fig. 10 compares the predicted pressure variations along the bump wall and the duct-centre plane with Delery's experimental data. The centreline variation has been included to convey the shock-capturing capability of the procedure; this is not well brought out in Fig. 9, the appearance of which is marred by minor oscillations around the shock. The characteristic pressure plateau in Fig. 10 is a reflection of the separation zone, and the comparison gives a clear indication that the Reynolds-stress model is considerably more sensitive to the shock, yielding earlier separation and a more extensive recirculation zone. This behaviour is broadly consonant with that observed earlier, particularly in the previous pipe constriction. The higher sensitivity of the boundary layer to the shock predicted by the stress model is confirmed by the velocity profiles given in Fig. 11. Evidently, separation occurs earlier (the first location, x/H=1.9, is within the λ-shock), and the displacement of the boundary is larger; indeed, displacement is too large, which then inhibits recovery downstream of the reattachment point. Further results for velocity and turbulence quantities may be found in Lien (1991). It is finally interesting to note that earlier calculations by Dimitriadis and Leschziner (1990) for a similar transonic flow (Delery's 'Case C') with a cell-vertex scheme and an *algebraic* variant of the present Reynolds-stress model show differences between k-ϵ and stress-model solutions which are quite similar to those reported here.

+ This model has been specifically constructed to yield a near-wall length scale in accord with that used in Wolfshtein's one-equation model (1969).

CONCLUSIONS

The paper reported the successful inclusion of full second-moment closure into a general, non-orthogonal, collocated finite-volume scheme in which convection is approximated by essentially non-diffusive convection schemes. Particular emphasis was put on numerical practices pertaining to stability, wall-boundary conditions and the wall-related fragments of the pressure-strain model. The application examples reported, whilst necessarily giving a rather superficial and incomplete view, serve to reinforce earlier observations that, for separated flow, second-moment closure offers benefits relative to the eddy-viscosity framework. They also confirm previously reported weaknesses, however. Thus, there is evidence of an insufficient rate of recovery following reattachment, and of an erroneous representation of the reattachment process itself. The latter may be alleviated, but not eliminated, by modifications to the wall-function-based near-wall treatment, and this points to the need for new proposals for modelling the influence of wall-induced pressure reflections on the pressure-strain process

REFERENCES

DELERY, J , (1983), J. AIAA, Vol. 21, p. 180

DESHPANDE, M.D. & GIDDENS, D.P., (1980), JFM 97(1), p. 65.

DIMITRIADIS, K.P. & LESCHZINER, M.A., (1990), "Modelling shock/boundary layer interaction with a cell-vertex scheme and second-moment closure"., Proc. 12th Int. Conf. on Numerical Methods on Fluid Dynamics, Oxford, Lecture Notes in Physics, p. 371 (K.W Morton, ed.), Springer Verlag.

DURST, F. & SCHMITT, F., (1985), "Experimental studies of high Reynolds number backward-facing step flows", Proc. 5th Symp. Turbulent Shear Flows, Cornell University, p. 5.19.

GASKELL, P.H. & LAU, A.K.C., (1987), "An assessment of direct stress modelling for elliptic turbulent flows with the aid of a non-diffusive, boundedness-preserving, discretization scheme", Proc. 5th Int. Conf. on Numerical Methods in Laminar and Turbulent Flows, Montreal, Pineridge Press, Swansea, p. 351.

GIBSON, M.M. & LAUNDER, B.E., (1987), JFM, 85, p. 491.

HAFEZ, M., SOUTH, J. & MURMAN, E., (1979), J. AIAA, Vol. 17, p. 838.

JONES, W.P. & MANNERS, A., (1988), "The calculation of the flow through a two-dimensional faired diffuser", Proc. 6th Symp. on Turbulent Shear Flows, Toulouse, p. 17.7.1.

LASHER, W.C. & TAULBEE, D.B., (1990), *Engineering Turbulence Modelling and Experiments*, Elsevier, (eds. Rodi and Ganić, p. 195.

VAN LEER, B., (1979), JCP, Vol. 32, p. 101.

LEONARD, B.P , (1979), Comp. Meths. Appl Mech. Engng., 19, p. 59.

LIEN, F.S., (1991), "Computational modelling of 3D flow in complex ducts and passages", Ph.D. Thesis in preparation, University of Manchester

LIEN, F S. and LESCHZINER, M.A., (1990), "Multigrid convergence acceleration for complex flow including turbulence", Third European Conf. on Multigrid Methods", Bonn, To be published in ISNM by Birkhauser Verlag, Basel (1991)

LIEN, F.S. & LESCHZINER, M.A., (1992), "Modelling shock/turbulent- boundary-layer interaction with second-moment closure within a pressure-velocity strategy", submitted to AIAA 30th Aerospace Science Meeting, Reno.

LIN, C A. & LESCHZINER, M A., (1989), "Computation of three-dimensional injection into swirling flow with second-moment closure", Proc. 6th Int. Conf on Numerical Methods in Laminar and Turbulent Flows, Swansea, Pineridge Press, Swansea, p. 1711.

MAJUMDAR, S., RODI, W. and SCHONUNG, B , (1989), Finite Approximations in Fluid Mechanics II, Notes on Numerical Fluid Mechanics, Vieweg Verlag.

MCGUIRK, J J , PAPADIMITRIOU, C. & TAYLOR, A.M.K.P., (1985), "Reynolds-stress model calculations of two-dimensional plane and axisymmetric recirculating flows", Paper presented at 5th Symp. on Turbulent Shear Flows, Cornell University.

OBI, S., PERIC, M. & SCHEUERER, G., (1989), "A finite-volume calculation procedure for turbulent flows with second-order closure and collocated variable arrangement", Proc. 7th Symp. Turbulent Shear Flows, Stanford Univ., p 17 4

PATANKAR, S V , (1980), *Numerical Heat Transfer and Fluid Flow*, McGraw-Hill, New York.

PERIC, M. (1985), "A finite volume method for the prediction cf three dimensional fluid flow in complex ducts", Ph.D Thesis, Univ of London.

RHIE, C M & CHOW, W L , (1983), J AIAA, 21 p. 1525.

SEBAG, S & LAURENCE, D , (1990), *Engineering Turbulence Modelling and Experiments*, Elsevier, (eds. Rodi and Ganić), p. 175.

SHYY, W & BRAATEN, M.E., (1986), "Int. J. Numerical Methods Fluids, 6, p 861.

WOLFSHTEIN, M.W., (1969), Int J. Heat Mass and Transfer, 12, p 301

Acknowledgement: The authors are grateful to the UK Science and Engineering Research Council which supported the present work via grants GR/E26808 and GR/F86816

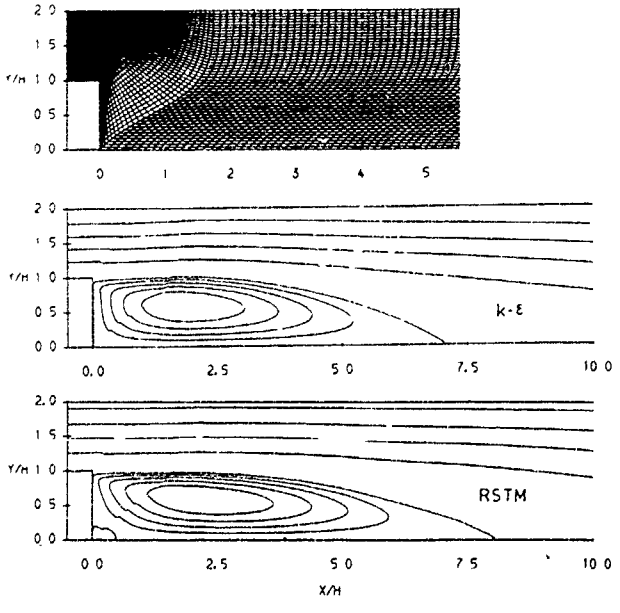

Fig. 3: Backward-facing step: grid and streamfunction contours

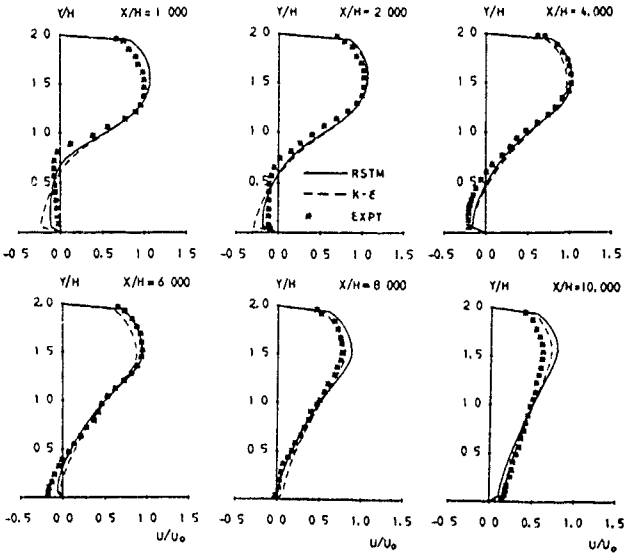

Fig. 4: Backward-facing step: velocity profiles

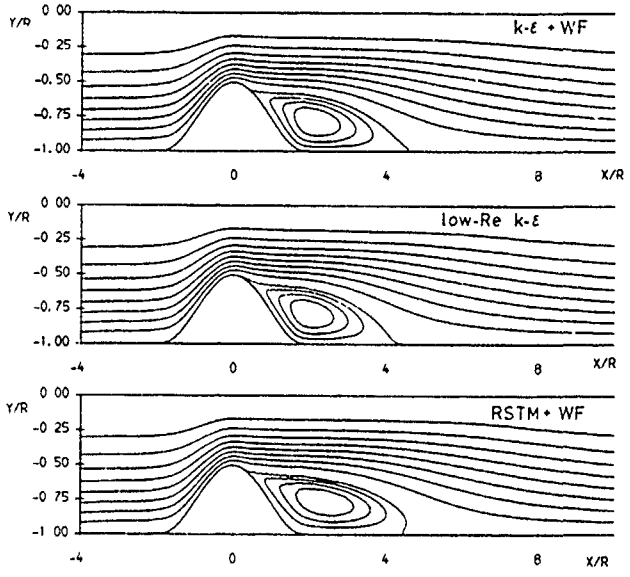

Fig 5: Pipe constriction: streamfunction contours

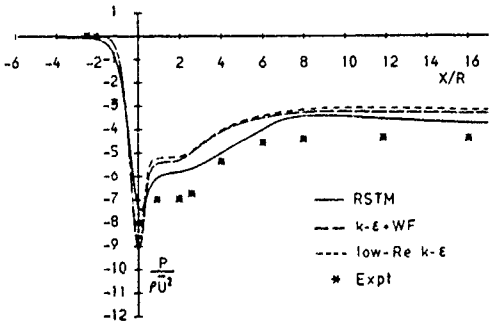

Fig. 6: Pipe constriction: wall static pressure

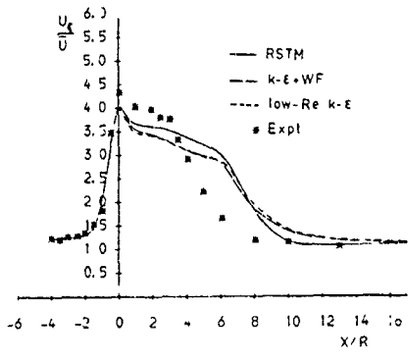

Fig 7: Pipe constriction centreline velocity

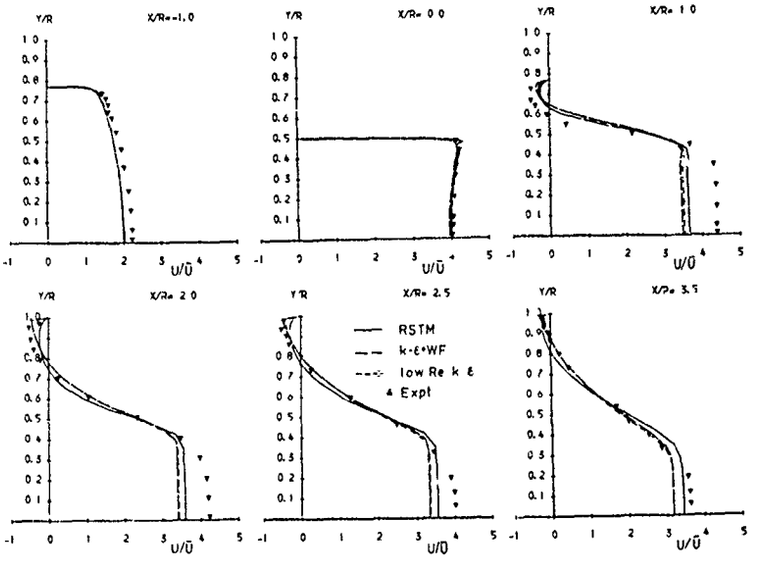

Fig. 8 Pipe constriction: velocity profiles

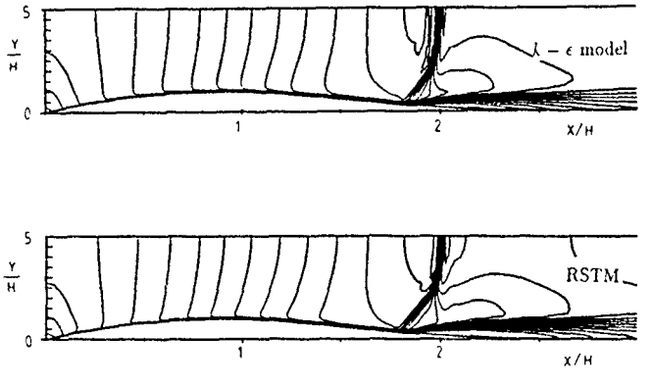

Fig 9. Transonic bump. Mach contours

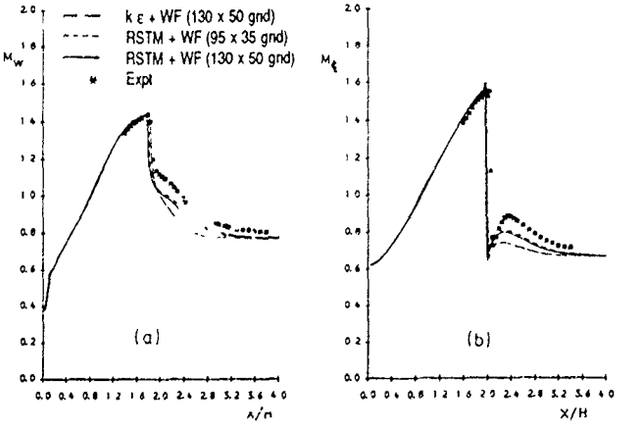

Fig 10· Transonic bump: (a) pressure along bump wall; (b) pressure along centre plane

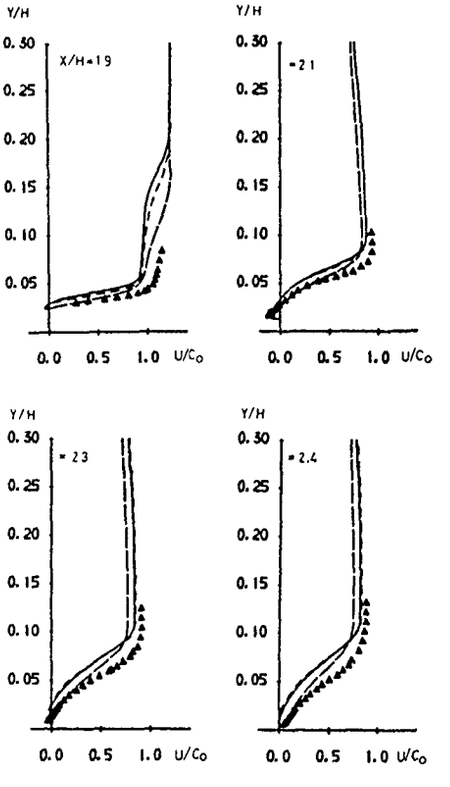

Fig. 11: Transonic bump: velocity profiles (Key as in Fig 10)

EIGHTH SYMPOSIUM ON
TURBULENT SHEAR FLOWS
Technical University of Munich
September 9-11, 1991

Direct Simulation of a Supersonic Reacting Mixing-Layer

O.H.Planche and W.C.Reynolds
Department of Mechanical Engineering
Stanford University

Abstract

An important aspect of supersonic combustion is the proper mixing of fuel and oxidizer. In the present work, temporal direct numerical simulations of the reacting compressible shear layer are presented. Although the Reynolds number is low, we believe that the general flow structures found are characteristic of what would be found for the large scale structures of high Reynolds number turbulent reacting compressible mixing layers. Results indicate that with heat release and at large Mach numbers, the mixing of fuel and oxidizer by large-scale engulfment of fluid from both sides is not likely to occur. Instead, fluid from each of the free streams is first mixed with product and then diffuses to the reaction zone.

1. Introduction

For the plane reacting compressible shear layer, the existence of two maxima of the mean density-vorticity profile ($\overline{\rho\omega}$) leads to the existence of two distinct instability modes, the 'outer modes' [1]. Each of these outer modes is associated with one of the free streams. Its greatest disturbance amplitudes occur in this stream and its phase velocity is comparable with the mean velocity at the $\overline{\rho\omega}$ peak in this stream.

The development of two-dimensional and three-dimensional reacting mixing layers has been simulated to study several aspects of the evolution of the layer, including (1) non linear effects associated with the growth of a single mode, (2) the interaction between the fast and the slow outer modes and its consequences on the mixing process, (3) the absence of pairing for compressible reacting mixing layers and its consequences on the mechanism for the mixing layer growth, and (4) the obliquity of the large-scale structures.

Two-dimensional simulations are performed using an extension of the Poinsot-Lele code [2] for diffusion flames. A Pade scheme with accuracy of sixth order in space and third order Runge-Kutta in time is used [3,4]. All the calculations are performed on a regular mesh, with equal mesh sizes in the x (streamwise) and the y (cross-stream) directions. The boundary conditions are periodic in x and non-reflecting in y.

The mean flow consists of a reacting plane free shear layer between a low-speed air flow and a high-speed mixture of fuel and inert gas. The mean velocity and temperature profiles are initialized using the compressible boundary layer equations. A self-similar solution is obtained, by assuming an infinite reaction rate, Prandtl and Lewis numbers equal to unity, constant specific heats, and viscosity μ proportional to temperature T. Perturbations are added to the mean profile in the form of eigenfunctions of unstable modes from temporal linear stability analysis, in which viscous and molecular diffusion effects were ignored. Unless otherwise specified, the amplitudes (defined as the ratio of the largest velocity fluctuation to the fast-stream velocity) are 0.002 for the fundamentals and 0.0004 for their subharmonics.

The fluid dynamics equations solved are:

$$\frac{\partial \rho}{\partial t} + \frac{\partial \rho u_i}{\partial x_i} = 0,$$

$$\frac{\partial \rho u_i}{\partial t} + \frac{\partial \rho u_i u_j}{\partial x_i} + \frac{\partial p}{\partial x_i} = \frac{\partial \tau_{ij}}{\partial x_j},$$

$$\frac{\partial \rho e_t}{\partial t} + \frac{\partial \rho u_i (e_t + p/\rho)}{\partial x_i} = \frac{\partial u_i \tau_{ij}}{\partial x_j} - \frac{\partial q_i}{\partial x_i} + \beta \dot{w},$$

$$\frac{\partial \rho Y_f}{\partial t} + \frac{\partial \rho u_i Y_f}{\partial x_i} = \frac{\partial}{\partial x_i}(\rho D \frac{\partial Y_f}{\partial x_i}) - \dot{w},$$

$$\frac{\partial \rho Y_o}{\partial t} + \frac{\partial \rho u_i Y_o}{\partial x_i} = \frac{\partial}{\partial x_i}(\rho D \frac{\partial Y_o}{\partial x_i}) - r\dot{w}$$

The chemical scheme is single step and irreversible and the reaction rate is

$$w = A\rho^2 Y_f Y_o e^{-Ze/T}$$

Ze is the nondimensional activation temperature, chosen equal to 2. The heat flux is q_j, τ_{ij} is the viscous stress tensor, $e_t = e_i + u_j^2/2$ is the total energy density, and Y_f and Y_o are the mass fractions of fuel and oxidizer. The heat release parameter, defined as $\beta \equiv \Delta H_f/(C_p T_1)$ is chosen equal to 2. The vorticity thickness δ_ω is used as the characteristic length, and the reference temperature and viscosity are those of the fast stream. The velocities are nondimensionalized by the sound velocity of the fast free stream. In the present application, $Sc = Pr = Le = 1$, $\mu = \mu_{ref}(T/T_{ref})^{0.76}$, the Mach number of the fast stream is $M_1 = 3.2$ and the Mach number of the slow stream $M_2 = 1.6$ yielding a convective Mach number $M_c = 0.8$ and flame convective Mach numbers $M_{f1} = M_{f2} = 0.3$. The flame convective Mach numbers are defined by:

$$M_{f1} = \frac{\overline{U_1} - \overline{U_f}}{\overline{U_1} - \overline{U_2}} \left(\frac{\overline{c_1} + \overline{c_2}}{\overline{c_1} + \overline{c_f}} \right) M_c$$

$$M_{f2} = \frac{\overline{U_f} - \overline{U_2}}{\overline{U_1} - \overline{U_2}} \left(\frac{\overline{c_1} + \overline{c_2}}{\overline{c_f} + \overline{c_2}} \right) M_c$$

where $\overline{c_1}$, $\overline{c_2}$ and $\overline{c_f}$ are the sound velocities in the fast stream, in the slow stream and in the flame region, and $\overline{U_1}$, $\overline{U_2}$ and $\overline{U_f}$ the fluid velocities in those regions. As noted by [1], the flame convective Mach numbers are likely to be the preferred parameters for correlating compressibility effects. Here, for flame convective Mach numbers equal to 0.3, the large scale structures should be two-dimensional.

The mass fraction of fuel and oxidizer are both equal to 0.2. The molar mass and the ratio of specific heats are constant. The Reynolds number and Damkohler are defined as

$$Re = \Delta U \delta_\omega / \nu_{ref}$$

$$Da = A\rho_f Y_{f\infty} e^{-Ze/T_f} \delta_\omega / \Delta U$$

For a reacting shear layer, the large variations of transport properties due to temperature variations requires the use of large Reynolds numbers. In our simulations we have used a Reynolds number equal to 4000, and approximately 150000 grid points in 2D.

Three-dimensional simulations are performed using an extension of the Sandham-Reynolds code [5] to diffusion flames. The main purpose of this 3-D run is to study the effects of heat release on the obliquity of the large scale structures of the compressible reacting mixing layer. A Pade scheme with accuracy of sixth order in y, Fourier modes in x

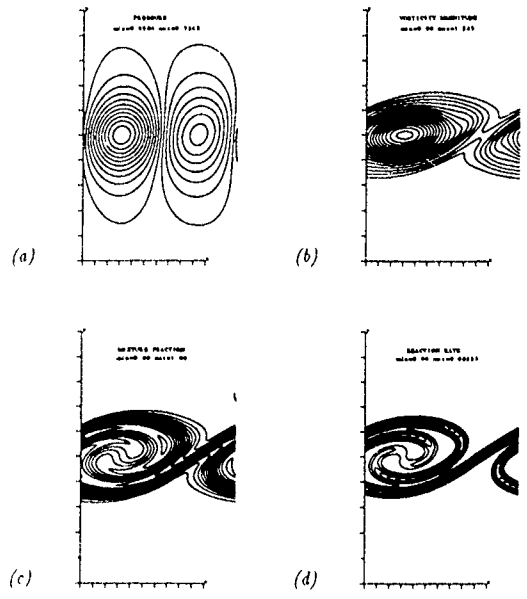

FIGURE 1 Contour of (a) pressure, (b) vorticity, (c) mixture fraction and (d) reaction rate of a typical large scale structure of a low Mach number ($M_c = 0.05$) no heat release reacting mixing layer

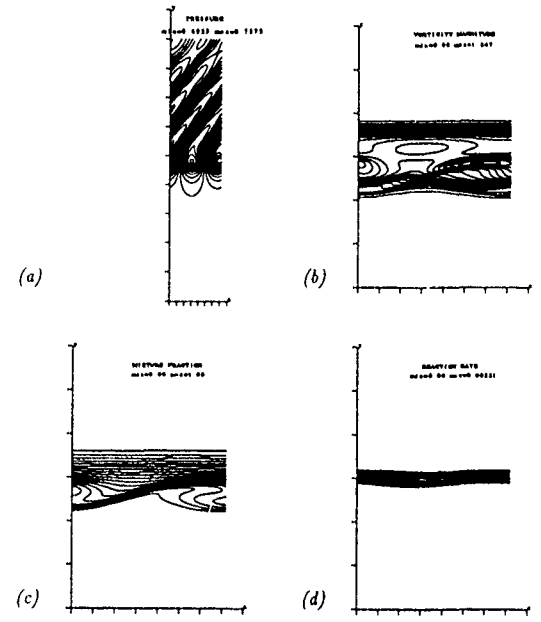

FIGURE 2 Contour of (a) pressure, (b) vorticity, (c) mixture fraction and (d) reaction rate of a typical slow outer mode of a compressible reacting shear layer ($M_c = 0.8$) with heat release ($T_f = 3$)

and z and third order Runge-Kutta in time are used A hyperbolic tangent mapping is used to keep the majority of the grid points in the vortical region of the layer The boundary conditions are periodic in x (streamwise direction) and z (spanwise direction) and non-reflecting in the y direction

The initialization and the notation are the same as in the two-dimensional simulations One 3-D simulation has been performed using 64x300x64 points 8 instability modes were included in the simulation one fast and one slow outer mode, their subharmonics, one fast and one slow 45 degree mode and their 45 degree subharmonics The amplitudes of the fundamentals are 0.002 and the amplitudes of their subharmonics 0.001

2. 2-D simulations results

The 2-D simulations confirm the existence of the outer modes for compressible and incompressible shear layers For compressible reacting shear layers, it is shown (1) that the fast and the slow outer mode develop without interacting and (2) that no pairing occurs between one outer mode and its subharmonic For incompressible shear layers, simulations initialized with the fast and slow outer modes and their 'central subharmonic' leads to the coupling of the outer modes, suggesting that (3) the outer modes are not the significant instability modes of the reacting incompressible shear layer

2.1 Overview of one compressible outer mode

2-D simulations initialized with only the slow outer mode show that this mode develops on its respective side of the reaction zone with out spreading across the whole layer Similar results are obtained for the fast outer mode

For later comparison, figure 1 shows the fluctuations of (a) pressure, (b) vorticity, (c) mixture fraction, and (d) reaction rate for a low Mach number reacting mixing layer without heat release Note the large-scale entrainment of fluid from both sides by the instability mode and the increase in flame surface displayed by the reaction rate

Figure 2 shows the corresponding results for a typical developed slow outer mode of a reacting compressible shear layer. Only the vortical region of the computational domain is shown The Damkohler number is equal to 6 but similar results are obtained for lower Damköhler numbers Here, fuel is almost undisturbed and diffuse to the reaction zone, while oxidizer and hot product are mixed by the large-scale structure The chemical reaction occurs at the interface of the fuel and the hot mixture of product and oxidizer, and no additional flame surface is created The slow outer mode generates radiating pressure waves in the fast stream The angle of those waves ($sin\theta \approx 1/(M_1 - M_2)$) and the absence of such pressure waves in the slow stream, indicates that the slow outer mode approximately travels at the slow stream velocity

Figure 3 shows the time variation of the kinetic energy of the slow outer mode The energy grows, saturates and then sharply decays. This decay is related to the existence of the radiating pressure waves, carrying energy away from the layer This behavior is different from what is observed for non-reacting incompressible mixing layers, where after saturation of the instability mode, the vorticity thickness and the kinetic energy in that mode exhibits a damped oscillation in time [5]

2.2 Interaction of the fast and slow outer modes

2-D simulations of reacting shear layers initialized with only the fast and the slow outer mode indicate that the two outer modes simultaneously develop on their respective side of the mixing layer without interacting Figure 4 shows the results in this case at the same time as in Fig 2 The amplification rates of the two outer modes being different, the slow mode is almost at its saturation point whereas the fast outer mode is still growing. Opposite results can be found depending on the position of the flame, on its temperature and on the free stream temperature ratio [1] Each outer mode generates radiating pressure waves in the opposite stream, modulated at the frequency $f = L_x/(\overline{U_1} - \overline{U_2})$ where L_x is the wavelength of the instability modes The time variation of the maximum reaction rate (Fig 5), vorticity thickness, and maximum vorticity also exhibits this oscillatory behavior, due to the constantly varying phase difference between the two outer modes.

Note by comparing with Fig. 2 that the slow outer mode is not disturbed by the presence of the fast outer mode The vorticity and mixture fraction contour overlap in the slow side of the mixing layer. The fast outer mode remains associated with the fast free stream and only mixes fuel and product, whereas the slow outer mode remains associated with the slow free stream and only entrains oxidizer and product This suggests a two-step mixing process where fluid from each of the free streams is first mixed with product and then diffuses to the reaction zone as described in Fig. 6.

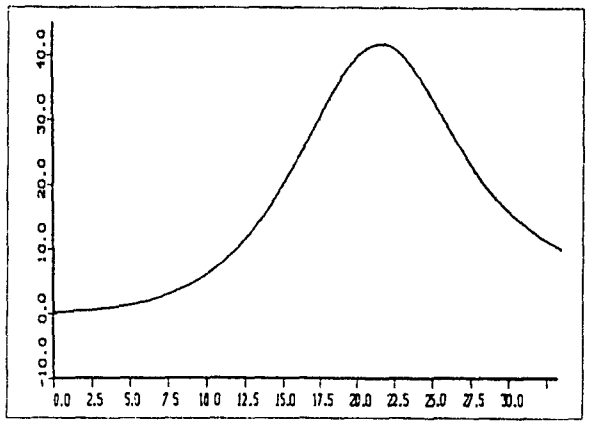

FIGURE 3 Time variation of the kinetic energy of the slow outer mode of figure 2

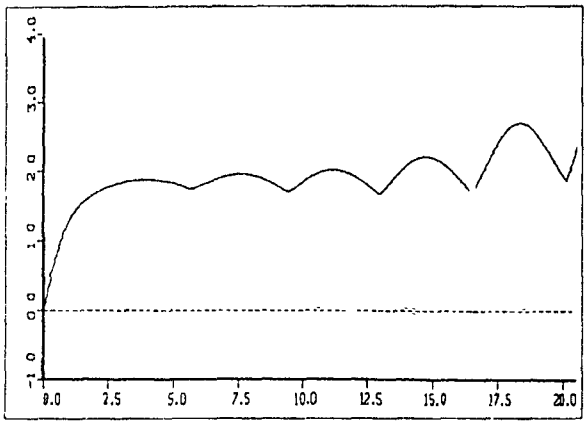

FIGURE 5 Time variation of the maximum reaction rate for the reacting compressible shear layer of figure 4

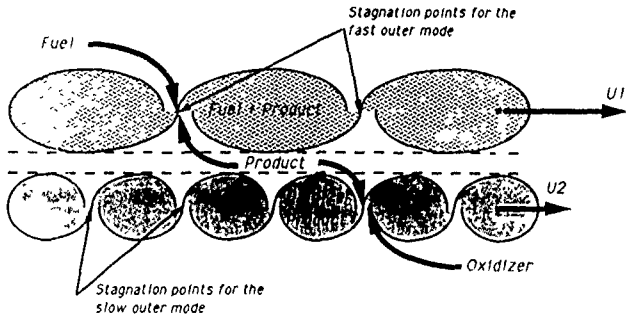

FIGURE 6 Schematic of the reacting mixing layer

The existence of two bumps on the pdf of the mixture fraction Z (Fig 7a) confirms this two-step mixing process One bump is located at $Z = 0.75$, corresponding to equally mixed fuel ($Z = 1$) and product ($Z = 0.5$) and the other one at $Z = 0.25$ corresponding to equally mixed oxidizer and product Note the absence of product here, which markedly differs from the typical low Mach number non-reacting shear layers results. The mixture fraction exhibits two ramps (Fig 7b), reminiscent of the ramps experimentally observed by Clemens in the non reacting case at Mc=0.62 [6]. Those ramps are the direct consequence of the existence of the outer modes, with the Clemens results suggesting that outer modes might be present at moderate convective Mach numbers even in the non reacting case.

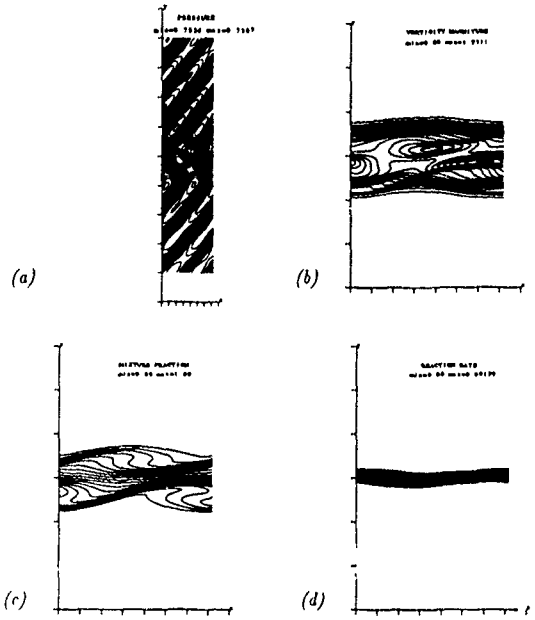

FIGURE 4 Contour of (a) pressure, (b) vorticity, (c) mixture fraction and (d) reaction rate for simulation started with the fast and the slow outer mode of a compressible reacting shear layer ($M_c = 0.8$) with heat release ($T_f = 3$)

These results are significant in terms of the effects of the outer modes on the reaction rate For incompressible reacting mixing layers, large-scale structures increase the flame surface area, which increases the total reaction rate For compressible reacting shear-layers, the mechanism is different The reaction zone remains plane and no additional flame surface is created, but the large scale structures *feed* the flame region with a hot mixture of fuel and product on one side and a hot mixture of oxidizer and product on the other side The local reaction rate gets larger, thus increasing the total reaction rate

2.3 Interaction of the outer mode with its subharmonic

In the third section of our work we examine the interaction of one outer mode with its subharmonic for reacting shear layers. For non reacting mixing layers, the usual mechanism of interaction is pairing, where energy is transfered from the fundamental to the subharmonics in one eddy turnover time Figure 8 sketches the phase velocities of the instability modes of a reacting mixing layer versus wavelength at two different Mach numbers [1] Note the absence of central instability modes at high Mach numbers.

For reacting incompressible shear layers, simulations [7] indicate that the energy transfer does not occur in one step as in the non-reacting case. The phase difference between the fundamental and its subharmonic (which is a central mode and thus has a different phase speed from the outer modes) is constantly changing in time and energy is transfered from the fundamental to the subharmonic through a succession of pairings and tearings Simulations initialized with the fast and slow outer modes and their central subharmonics show that the outer modes interact and couple, resulting in large-scale structures similar to what is observed for non reacting shear layers. This result suggests that outer modes are not significant instability modes for incompressible reacting shear layers.

In the reacting compressible case, no central subharmonics exists. The fast outer mode has fast outer subharmonics and the slow outer mode slow outer subharmonics Our simulation shows that pairings do not occur between outer modes and their subharmonics. The time variation of the kinetic energies of one fast outer mode and of its subharmonics, shows that those two modes grow, saturate and then decay independently from one another, similar to what we observed in Section

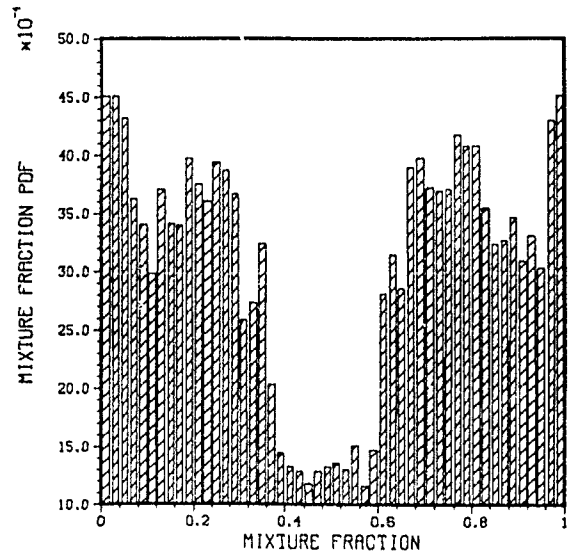

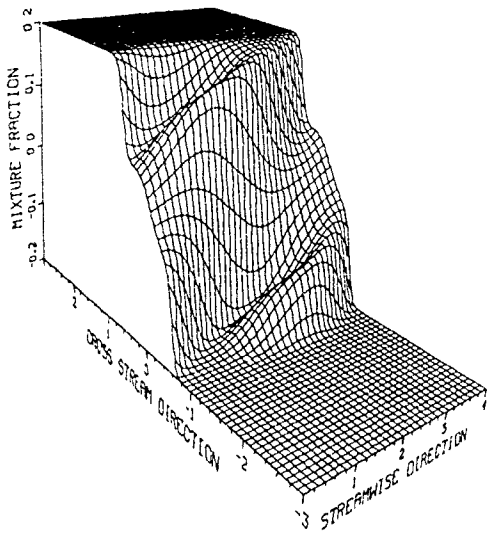

FIGURE 7 (a) Pdf and (b) carpet plot of the mixture fraction of the reacting mixing layer of figure 1 at a slightly later time

2 1 This suggests that (1) unlike what was observed for the incompressible non-reacting shear layers, in the reacting compressible case, a large distribution of instability modes will be present at a given time in the shear layer, all having different growth rates, with some growing, some saturating and some decaying Fast outer modes will remain in the fast sublayer and slow outer modes in the slow sublayer (2) The growth mechanism will not be through pairing but will result from the various growth rates of all the instability modes present in the layer at a given instant of time

3. Early 3-D simulations results

Three dimensional direct numerical simulations were used to investigate the following question Does heat release cause the large structures of the reacting shear layer (slow outer modes in the slow sublayer and fast outer modes in the fast sublayer) to remain two-dimensional at high Mach numbers as predicted by linear stability analysis This result is important in terms of its effects on the entrainment and the subsequent mixing process At this writing, the simulation has been run for 80 hours on the Cray-YMP The flow time non-dimensionalized by the fast stream velocity and the initial vorticity thickness is approximately t=22 which is still in the linear range Guided by 2-D simulations, we estimate non-linear effects to become significant around t=40 Figure 9 shows the variation of the kinetic energy of the various modes Note that the 2-D modes grows significantly faster than the 3-D ones, thus confirming linear stability results The growth rate agrees well with values obtained using the linear stability analysis

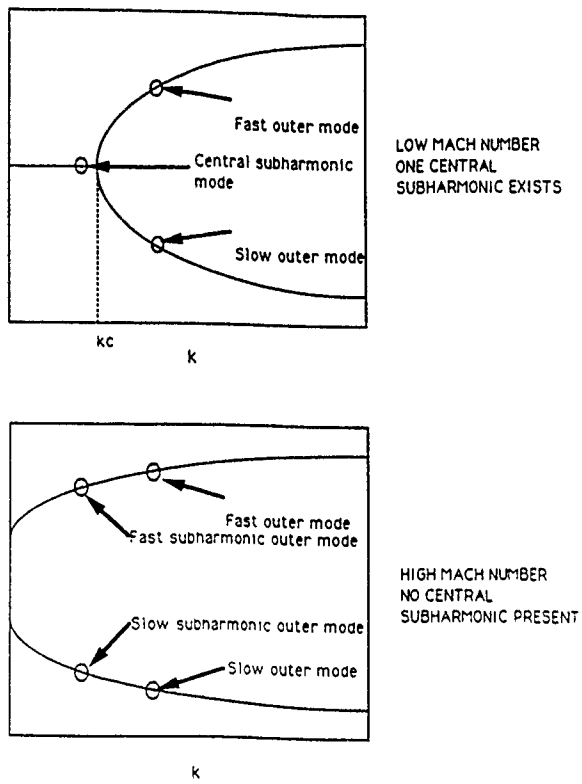

FIGURE 8 Schematic of the phase velocity of the instability modes of the reacting mixing layer (a) Low Mach number (b) High Mach number

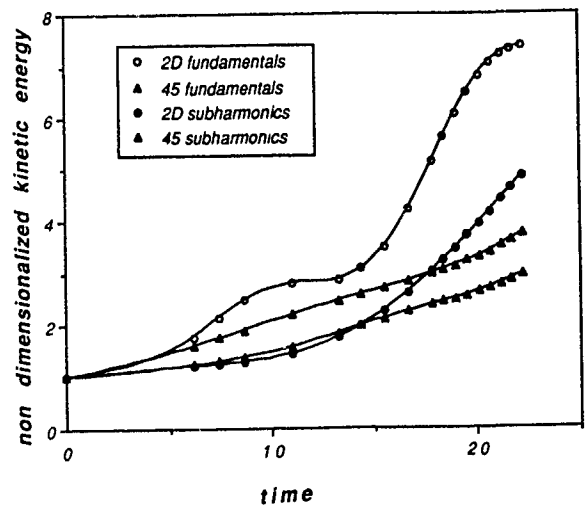

FIGURE 9 Time variation of the total kinetic energy of the 2-D and 45 degree instability modes

At this point of the simulation no interaction is observed between the fast and the slow outer modes The perspective view of the high vorticity region (vorticity magnitude equal to 90% of the maximum vorticity) show the existence of the two sublayers inside the shear layer (Fig. 10) The hot flame region separates the two sublayers and is unaffected by the presence of the instability modes. no additional flame surface is created

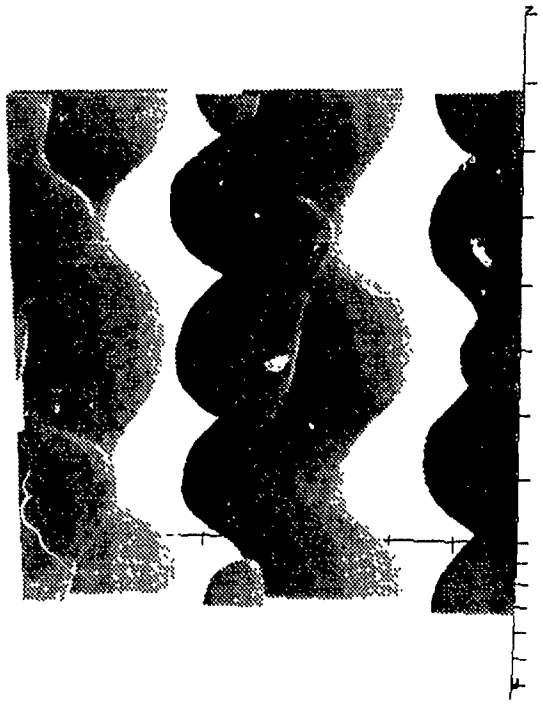

FIGURE 10 Surface of constant vorticity (90 % of the maximum vorticity at time t=20)

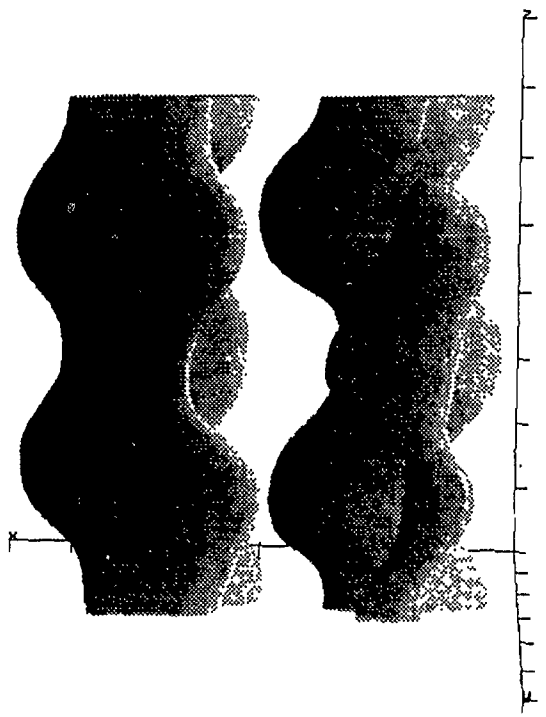

FIGURE 11 Surface of constant vorticity (90 % maximum vorticity at time 22)

Figure 11 shows the same information as in Fig 10 at a slightly different time Note that although the time lag between the two figures is small, the appearance of the mixing layer has markedly changed The two layers are travelling at two different speeds and "snapshots' taken from the top or the side of the mixing layer are constantly varying with time This suggests that clearly organized structure will be harder to distinguish in the reacting compressible case than in the non-reacting incompressible case Experimentally, looking at their indirect manifestations, such as pressure waves will be a way to establish their existence

Simulation is continuing on both the Cray YMP and the hypercube, to study the interaction between fundamentals and subharmonics as well as interaction between fast and slow outer modes From our 2-D simulation results the expected results are an absence of pairing (energy being transfered continuously from the fundamental to the subharmonic, instead of in one time as in pairing) and an absence of interaction between the fast and the slow modes

4. Conclusions

Temporal 2-D and 3-D direct numerical simulations have been used to study the large-scale structures of compressible reacting mixing layers Our results indicate that reacting compressible shear layers can be seen as the reunion of two non-interacting fast and slow sublayers Instability modes developing in the fast or the slow sublayer were shown to be two-dimensional and no pairing was observed in our simulations It was shown that mixing of fuel and oxidizer by large-scale entrainment of fluid from both side was not likely to occur for reacting compressible shear layers, and a two-step mixing mechanism was proposed where fluid from each of the free streams is first mixed with product and then diffuses to the reaction zone

REFERENCES

1 Planche, O H and Reynolds, W C AIAA Paper No 91-0739 (1991)
2 Poinsot, T J and Lele, S K Boundary conditions for direct simulations of compressible viscous reacting flows CTR manuscript 102 Stanford University
3 Lele S K AIAA Paper No 89-0374
4 Wray, A A Very low storage time advancement schemes Internal report, NASA Ames Research Center
5 Sandham, N D and Reynolds, W C Numerical investigation of the compressible mixing layer Report No TF 45 Stanford University
6 Clemens, N T An experimental investigation of scalar mixing in the supersonic shear layer Ph D Thesis, Stanford University, 1991
7 Planche O H Ph D thesis in preparation A numerical investigation of the compressible reacting mixing layer Stanford University

ACKNOWLEDGEMENT This work is supported by the AFOSR program in supersonic combustion Computational support is provided through the NASA/Stanford Center for Turbulence Research

EIGHTH SYMPOSIUM ON
TURBULENT SHEAR FLOWS
Technical University of Munich
September 9-11, 1991

COMPRESSIBLE HOMOGENEOUS SHEAR: SIMULATION AND MODELING

S Sarkar, G Erlebacher, and M Y Hussaini

Institute for Computer Applications in Science and Engineering
NASA Langley Research Center
Hampton, VA 23665

ABSTRACT

The present study investigates compressibility effects on turbulence by direct numerical simulation of homogeneous shear flow A primary observation is that the growth of the turbulent kinetic energy decreases with increasing Mach number The compressible dissipation and the pressure-dilatation are shown to contribute to the reduced growth of kinetic energy Models are proposed for these dilatational terms and verified by direct comparison with the simulations. The differences between the incompressible and compressible fields are brought out by the examination of spectra, statistical moments, and structure of the rate of strain tensor

1. INTRODUCTION

We consider the case of spatially homogeneous turbulence sustained by a parallel mean velocity field $\overline{u} = (Sx_2, 0, 0)$ with a constant shear rate S (see Fig 1) Such a flow is perhaps the simplest idealization of turbulent shear flow where there are no boundary effects, and where the given mean flow is unaffected by the Reynolds stresses Nevertheless, the crucial mechanisms of sustenance of turbulent fluctuations by a mean velocity gradient, and the energy cascade down to the small scales of motion are both present in this flow.

The homogeneous shear flow problem has been studied experimentally by Tavoularis and Corrsin (1981) among others Rogallo (1981) and Rogers and Moin (1987) have investigated the incompressible homogeneous shear problem at great depth through direct numerical simulations These simulations, albeit at low turbulence Reynolds numbers, have provided turbulence statistics which are in good agreement with experiments performed at relatively higher Reynolds numbers Furthermore, since the simulations provide global instantaneous fields, the turbulence can be studied in much greater detail than in physical experiments

Recently there has been a spurt of activity in the direct numerical simulation (DNS) of three-dimensional compressible turbulence Decaying isotropic turbulence has been studied by Passot (1987), Erlebacher et al (1990), Sarkar et al (1989), and Lee, Lele and Moin (1990) The simulations of Erlebacher et al (1990) identified different transient regimes including a regime with weak shocks, and also showed that a velocity field which is initially solenoidal can develop a significant dilatational component at later times Sarkar et al (1989) investigated the statistical moments associated with the compressible mode in their simulations, and determined a quasi-equilibrium in these statistics for moderate turbulent Mach numbers which was then used to model various dilatational correlations Lee, Lele and Moin (1990) studied eddy shocklets which developed in their simulations when the initial turbulent Mach number was sufficiently high ($M_t > 0.6$) Kida and Orszag (1990) primarily studied power spectra, and energy transfer mechanisms between the solenoidal and dilatational components of the velocity in their simulations of forced isotropic turbulence

Physical experiments have not been and perhaps cannot be performed for homogeneous shear flows at flow speeds which are sufficiently high to introduce compressible effects on the turbulence However, direct numerical simulation of this problem could provide meaningful data, especially since DNS for the incompressible problem has been successful in giving realistic flow fields The compressible problem was considered by Feiereisen et al (1982) who performed relatively low resolution 64^3 simulations and concluded that compressibility effects are small. Recently Blaisdell et al. (1990) have also considered compressible shear flow. We have performed both 96^3 and 128^3 simulations which have allowed us to obtain some interesting new results regarding the influence of compressibility on the turbulence. In contrast to the results of Feiereisen et al., our simulations which start with incompressible initial data develop significant rms levels of dilatational velocity and density We find that the growth rate of the kinetic energy decreases with increasing Mach number as well as increasing rms density fluctuations and show that the compressible dissipation and pressure-dilatation contribute to this effect Since these dilatational terms are important consequences of compressibility, we propose models for the pressure-dilatation and compressible dissipation to be used in computations of engineering turbulent flows

Further details on second-order moments, thermodynamic statistics, probability density functions and higher-order moments can be found in Sarkar, Erlebacher and Hussaini (1991) and will not be discussed here In this paper, we will present new results comparing the compressible and incompressible components by examination of spectra and structural statistics of the rate of strain tensor

2. GOVERNING EQUATIONS

The compressible Navier-Stokes equations are written in a frame of reference moving with the mean flow $\overline{u}_1$ This transformation, which was introduced by Rogallo (1981) for incompressible homogeneous shear, removes the explicit dependence on $\overline{u}_1(x_2)$ in the exact equations for the fluctuating velocity, thus allowing the imposition of periodic boundary conditions in the x_2 direction The relation between x_i^* and the lab frame x_i is

$$x_1^* = x_1 - Stx_2 \quad , \quad x_2^* = x_2 \quad , \quad x_3^* = x_3$$

Here S denotes the constant shear rate $\overline{u}_{1,2}$ In the transformed frame x_i^*, the compressible Navier-Stokes equations take the form

$$\partial_t \rho + (\rho u_i')_{,i} - St(\rho u_2')_{,1} = 0 \tag{1}$$

$$\begin{aligned} \partial_t(\rho u_i') + (\rho u_j' u_i')_{,j} &= -p_{,i} + \tau'_{ij,j} - S\rho u_2'\delta_{i1} \\ &+ St(\rho u_2' u_i')_{,1} + Stp_{,1}\delta_{i2} - St\tau'_{i2,1} \end{aligned} \tag{2}$$

$$\begin{aligned} \partial_t p + u_j' p_{,j} + \gamma p u'_{j,j} &= Stu_2' p_{,1} + \gamma Stp\tau'_{2,1} + \Phi \\ &+ (\gamma - 1)\kappa[T_{,jj} - 2StT_{,12} + S^2t^2T_{,11}] \end{aligned} \tag{3}$$

$$p = \rho RT \tag{4}$$

where $\Phi = \tau_{ij} u_{i,j}$ is the dissipation function, u_i' the fluctuating velocity, ρ the instantaneous density, p the pressure, T the temperature, R the gas constant, and κ the thermal conductivity The viscous stress is

$$\tau_{ij} = \mu(u_{i,j} + u_{j,i}) - \frac{2}{3}\mu(u_{k,k})\delta_{ij}$$

where μ is the molecular viscosity which is taken to be constant All the derivatives in the above system are evaluated with respect to the transformed coordinates x_i^*.

A Fourier collocation method is used for the spatial discretization of the governing equations A third order, low storage Runge-Kutta scheme is used for advancing the solution in time.

3. RESULTS

We have performed simulations for a variety of initial conditions and obtained turbulent fields with Taylor microscale Reynolds numbers Re_λ up to 35 and turbulent Mach numbers M_t up to 0.6. Note that $Re_\lambda = q\lambda/\nu$ where $q = \sqrt{\overline{u_i' u_i'}}$ and $\lambda = q/\sqrt{\overline{\omega_i' \omega_i'}}$, while $M_t = q/\bar{c}$ where $\bar{c}$ is the mean speed of sound. The computational domain is a cube with side 2π. The results discussed here were obtained with a uniform 96^3 mesh overlaying the computational domain.

3.1. COMPRESSIBILITY EFFECT ON KINETIC ENERGY

Figs 2-5 show results from simulations which start with incompressible data, that is, density is constant and the divergence $\nabla \cdot \mathbf{u} = 0$, but have different initial Mach numbers $M_{t,0}$. The initial pressure is calculated from the Poisson equation, and the temperature is obtained from the ideal gas equation of state. The DNS results of Fig. 2 show that the level of the kinetic energy K at a given time decreases with increasing $M_{t,0}$. Thus an increase in compressibility level, *decreases* the growth of turbulent kinetic energy in the case of homogeneous shear flow. See Table 1 for the initial parameters of the DNS cases.

In order to explain the phenomenon of reduced growth rate of kinetic energy, we consider the equation governing the kinetic energy of turbulence in homogeneous shear which is

$$\frac{d}{dt}(\bar{\rho}K) = \bar{\rho}\mathcal{P} - \bar{\rho}\epsilon_s - \bar{\rho}\epsilon_c + \overline{p'd'} \tag{5}$$

where $\mathcal{P} = -S\widetilde{u_1''u_2''}$ is the production, $\epsilon_s = \overline{\nu\omega_i'\omega_i'}$ the solenoidal dissipation rate, $\epsilon_c = (4/3)\overline{\nu d'^2}$ the compressible dissipation rate and $\overline{p'd'}$ the pressure-dilatation. The last two terms represent the explicit influence of the non-solenoidal nature of the fluctuating velocity field in the kinetic energy budget. The overbar over a variable denotes a conventional Reynolds average, while the overtilde denotes a Favre average. A single superscript $'$ represents fluctuations with respect to the Reynolds average, while a double superscript $''$ signifies fluctuations with respect to the Favre average.

The quantitative contribution of the pressure-dilatation and compressible dissipation to the kinetic energy budget is shown in Fig. 3. It can be seen from Fig. 3 that these terms act as a drain on the kinetic energy, and can modify the the kinetic energy budget by as much as 25%. The pressure-dilatation $\overline{p'd'}$ (solid curve in Fig. 8) is highly oscillatory. Though $\overline{p'd'}$ can be both positive or negative it tends to be predominantly negative.

The predominantly negative values of $\overline{p'd'}$ in homogeneous shear is in contrast to the predominantly positive values reported in Sarkar et al. (1989) for the case of decaying isotropic turbulence. To understand this contrasting behavior of $\overline{p'd'}$ we write the exact equation for the pressure variance which is applicable to both these flows

$$\frac{d}{dt}\overline{p'^2} = -2\gamma\bar{p}\,\overline{p'd'} - (2\gamma - 1)\overline{p'p'd'} - 2\epsilon_p + \phi_p \tag{6}$$

where ϕ_p is a term depending on mean viscosity and mean conductivity which is negligible compared to ϵ_p. Here $\epsilon_p = (\gamma - 1)R\kappa\,\overline{p'T_{,j}'T_{,j}'}$ and can be called the pressure dissipation term by virtue of being a sink on the rhs of Eq. (6). Comparing Eq. (5) and Eq. (6) it is clear that $\overline{p'd'}$ acts to transfer energy between the kinetic energy of turbulence $\bar{\rho}K$ and the potential energy of the turbulence $\overline{p'^2}/(2\gamma\bar{p})$. In the case of homogeneous shear the rms values of the velocity and pressure increase with time. Now, the third term on the rhs of Eq. (6) is always negative and therefore a sink for the pressure variance. For small $p'/\bar{p}$ we can neglect the second term on the rhs of Eq. (6) with respect to the first term. Therefore for $\overline{p'^2}$ to *increase* with time, a source term is necessary which implies that $\overline{p'd'}$ be *negative* in accord with the DNS results. We note that a similar analysis of the equations for $\overline{\rho'^2}$ and $\overline{T'^2}$ indicates that $\overline{\rho'd'}$ and $\overline{T'd'}$ also have to be predominantly negative in this flow.

In decaying isotropic turbulence $\overline{p'^2}$ must decay with time, however, because ϵ_p is sufficient to ensure decay of $\overline{p'^2}$ the sign of $\overline{p'd'}$ cannot be determined from Eq. (6). Alternatively, we consider the exact density variance equation which for homogeneous shear flow is

$$\frac{d}{dt}\overline{\rho'^2} = -2\bar{\rho}\overline{\rho'd'} - \overline{\rho'\rho'd'} \tag{7}$$

For small $\rho'/\bar{\rho}$, the first term on the rhs of Eq. (6) dominates the second term. Therefore for $\overline{\rho'^2}$ to decrease with time it is necessary that $\overline{\rho'd'}$ be predominantly positive. If we assume that the thermodynamic fluctuations are approximately isentropic in this case (DNS supports this assumption), it immediately follows that $\overline{p'd'}$ is also predominantly positive in decaying isotropic turbulence. Thus, the role of $\overline{p'd'}$ as a mechanism for energy transfer between the kinetic energy and potential energy dictates its differing signs in homogeneous shear and unforced isotropic turbulence.

The earlier work of Sarkar et al. (1989) had shown that, in isotropic turbulence, the ratio F of kinetic energy and potential energy of the compressible component $\simeq 1$, which implies a tendency toward equipartition between the kinetic and potential energies of the fluctuating compressible mode. DNS of homogeneous shear shows that the partition factor F approaches and oscillates around an equilibrium value of approximately 0.95 indicating that approximate equipartition in the energies associated with the compressible mode holds in the case of homogeneous shear too.

3.2. COMPRESSIBLE AND SOLENOIDAL SPECTRA

The Fourier component of the velocity is decomposed into components perpendicular and parallel to the wave number vector from which the solenoidal spectrum $E_s(k)$ and compressible spectrum $E_c(k)$ are calculated. Fig. 4 compares the solenoidal and compressible spectra at St=7 (when $M_t = 0.43$) for Case 3. The slopes of the compressible and incompressible spectra are similar for the intermediate wave numbers $10 < k < 48$. The solenoidal spectrum at $St = 7$ is compared in Fig. 5 between Case 1 which is an incompressible run and a compressible run (Case 3). Case 3 has initial $M_t = 0.3$ and the initial velocity and pressure fields are the same as in Case 1. From Fig. 5 it appears that the shape of the solenoidal spectrum in Case 3 is not altered in the intermediate wave number range from the incompressible case, even though the compressible fluctuations are non-negligible - $\rho_{rms}/\bar{\rho} = 0.12$ and $\chi_k = K_c/K = 0.05$. However, the pressure spectrum in Fig. 6 shows significant differences between Cases 1 and 3. In the compressible case, the pressure spectrum seems to be relatively flatter than in the incompressible case.

4. MODELING THE DILATATIONAL TERMS

We showed in Fig. 3 that the compressible dissipation ϵ_c and the pressure-dilatation $\overline{p'd'}$ contribute significantly to the kinetic energy budget and therefore require modeling. In Sarkar et al. (1991) we proposed a model for the compressible dissipation $\epsilon_c = \alpha_1\epsilon_s M_t^2$ based on an asymptotic analysis and DNS of isotropic turbulence. Fig. 7 shows that, after starting from a variety of initial conditions, $\epsilon_c \simeq 0.5\epsilon_s M_t^2$, suggesting that $\alpha_1 = 0.5$.

Our direct numerical simulations of isotropic turbulence and homogeneous shear flow provided a data base for the pressure-dilatation and suggested a theoretical approach towards modeling it. The evolution of the pressure dilatation $\overline{p'd'}$ for case 3 is depicted by the solid curve in Fig. 8. From numerical experiments, it was found that the nominal time period of the oscillations in $\overline{p'd'}$ decreased approximately linearly with the speed of sound. This suggested that one could isolate the oscillatory part of $\overline{p'd'}$ by decomposing the fluctuating pressure p' into the sum of an incompressible part $p^{I'}$ and a compressible part $p^{C'}$. The component $p^{I'}$ is associated with the incompressible velocity field $\mathbf{u}^I$ which is divergence-free ($\nabla \cdot \mathbf{u}^I = 0$) and satisfies the usual Poisson equation

$$\nabla^2 p^{I'} = -2\bar{\rho}\widetilde{u}^I_{m,n}u^{I'}_{n,m} - \bar{\rho}u^{I'}_{m,n}u^{I'}_{n,m} \tag{8}$$

and the remainder $p' - p^{I'}$ is the compressible pressure $p^{C'}$. Since

$$p' = p^{I'} + p^{C'}$$

we have

$$\overline{p'd'} = \overline{p^{I'}d'} + \overline{p^{C'}d'}$$

Fig. 8 shows the evolution of $\overline{p^{C'}d'}$ and $\overline{p^{I'}d'}$ for Case 3. The oscillations are substantial only for $\overline{p^{C'}d'}$, and furthermore, the peaks and valleys in the evolution of $\overline{p^{C'}d'}$ in Fig. 8 seem to be much more symmetric around the origin than those in $\overline{p'd'}$. In order to gauge the relative importance of the two components $\overline{p^{C'}d'}$ and $\overline{p^{I'}d'}$ of the pressure-dilatation in the evolution of the turbulent kinetic energy, we calculate the time integrals of these components. The integrated contribution of $\overline{p^{I'}d'}$ is about an order of magnitude larger than that of $\overline{p^{C'}d'}$ in Case 3. Examination of other DNS cases indicates that, in general, $\overline{p^{C'}d'}$ has a negligible contribution to the turbulent kinetic energy evolution relative to $\overline{p^{I'}d'}$. Therefore, it seems that only the component $\overline{p^{I'}d'}$ of the pressure-dilatation requires modeling in shear flows.

In order to model $\overline{p^{I'}d'}$, we consider the Poisson equation Eq. (8) for the incompressible pressure. After splitting the pressure into a rapid part $p^{R'}$ and a slow part $p^{S'}$, we obtain the following exact expressions for the rapid pressure-dilatation and slow presure-dilatation:

$$\overline{p^{R'}d'} = 2\bar{\rho}\widetilde{u}^I_{m,n}\int \frac{k_m k_j}{k^2}E^{IC}_{nj}\,d\mathbf{k} \tag{9}$$

$$\overline{p^{S'}d'} = \bar{\rho}\int \frac{k_m k_l k_j}{k^2}(\widehat{u_l u_j}^I\hat{u}^{C*}_m - \widehat{u_l u_j}^{I*}\hat{u}^C_m)\,d\mathbf{k} \tag{10}$$

Here $\hat{\phi}^*$ denotes the complex conjugate of the Fourier transform $\hat{\phi}$ and E^{IC}_{nj} represents the spectrum of the mixed Reynolds stress tensor $\overline{u_n^{I'}u_j^{C'}}$. Using scaling arguments (see Sarkar (1991) for details) to

simplify Eqs (5)-(10) we find that $\overline{p^{Rl}d^l}$ depends on the production $\mathcal{P}$ while $\overline{p^{Sl}d^l}$ depends on the dissipation ϵ. Finally, we propose the following model for the pressure-dilatation:

$$\overline{p^l d^l} = -\alpha_2 \bar{\rho} \mathcal{P} M_t^2 + \alpha_3 \bar{\rho} \epsilon_s M_t^2 \qquad (11)$$

where $\mathcal{P} = -\tilde{u}_{i,j}\widetilde{u_i'' u_j''}$ is the production of kinetic energy, $M_t = \sqrt{2K/\gamma R\tilde{T}}$ the turbulent Mach number and ϵ_s the solenoidal dissipation. Because the production $\mathcal{P} = 0$ in decaying isotropic turbulence, the variation of the incompressible pressure-dilatation with ϵ_s can be verified using DNS of isotropic turbulence. The ratio $\overline{p^l d^l}/(\bar{\rho}\epsilon_s M_t^2)$ is shown as a function of non dimensional time in Fig 9. This ratio reaches an equilibrium value by a time of 0.25, substantiating the validity of the second term in Eq. (11). Based on the DNS value of the equilibrium ratio, the model coefficient α_3 in Eq. (11) is taken to be 0.2. The remaining part of the model for the pressure-dilatation is calibrated against simulations of homogeneous shear flow. Fig 10 shows that, in accord with our model, the rapid part of the pressure-dilatation scales as $\bar{\rho}\mathcal{P}M_t^2$. The ratio $(\overline{p^l d^l} - 0.2\epsilon_s M_t^2)/(\bar{\rho}\mathcal{P}M_t^2)$ reaches an approximate equilibrium value of -0.4, suggesting that the model coefficient $\alpha_2 = 0.4$.

5. STRUCTURE OF THE RATE OF STRAIN TENSOR

In this section, we study the structure of the rate of strain tensor S_{ij} in compressible homogeneous flow. Because the flow is anisotropic, it is important to consider characteristics of the flow with respect to all three coordinate directions. The most fundamental quantity for such a study is the tensor $u_{i,j}$, which is the sum of the symmetric rate of strain tensor $S_{ij} = 0.5(u_{i,j} + u_{j,i})$ and the antisymmetric rotation tensor $\Omega_{ij} = 0.5(u_{i,j} - u_{j,i})$. The latter tensor describes the instantaneous rotation of individual fluid elements, while the former tensor describes the straining of these elements. This study is motivated by observed differences in the streak patterns of the irrotational and the solenoidal components of the velocity vector (u_i^C and u_i^I). These differences were brought out by plotting the magnitude of u_i^C and u_i^I in the $x-y$, $x-z$ and $y-z$ planes, and noting some strong qualitative differences between the solenoidal and irrotational parts. These differences can be characterized by considering separately the rate of strain tensors S_{ij}^C and S_{ij}^I, respectively based on u_i^C and u_i^I. The properties of these tensors are best put forth by considering the statistics of the eigenvalues and eigenvectors.

Let $\lambda_1 \le \lambda_2 \le \lambda_3$ be the three eigenvalues of the rate of strain tensor. (A superscript I or C on any quantity refers to quantities based on either the solenoidal or the irrotational component of the velocity vector.) Associated with these eigenvalues, let $\mathbf{f}_i$ the eigenvector of S_{ij} associated with λ_i. Some immediate properties of the eigenvalues are

$$\sum_{i=1}^{3} \lambda_i^I = 0$$

$$\sum_{i=1}^{3} \overline{(\lambda_i^I)^2} = \frac{1}{2}\overline{\omega^{I2}}$$

$$\sum_{i=1}^{3} \overline{(\lambda_i^C)^2} = \overline{d^{I2}}$$

After the eigenvectors are normalized to unity, we compute the angle θ_{ij} between eigenvector $\mathbf{f}_i$ and the unit vector in coordinate direction j. Pdf's of $|\cos\theta_{ij}|$ over a subset of the flow field then provide information on structural differences in the flow as they relate to deformation of material lines and surfaces for both the solenoidal and dilatational components of the flow. The cosine of θ is chosen instead of θ so that the probability density functions (pdfs) of a Gaussian field are flat. The sampling is done on a grid resolution of $48 \times 48 \times 12$ although the simulation was performed on a 96^3 mesh. Jaggedness in the histogram plots are directly related to an insufficient number of sample points. We performed spot checks of our pdfs at a higher sampling of $96 \times 96 \times 24$ and observed only the expected smoothing of the curves, but no qualitative change.

We consider results from one simulation with initial parameters $S = 10$, $Re = 125$, $M_t = 0.4$, constant density, divergence free velocity, and pressure calculated from the usual Poisson equation for incompressible flow. The data was analyzed at $St = 1, 3, 5, 7, 9, 11$, and plotted using a variety of data reduction techniques. Only the most relevant plots are shown here. A more extensive discussion of this analysis is available in Erlebacher, Sarkar and Hussaini (1991).

The peak of the pdf of a stochastic variable occurs at a value of the variable which we call the most probable variable. Time histories of the most probable λ_i^I and λ_i^C, $i = 1, 2, 3$ are shown in Figs 11 and 12 respectively. As expected, the most probable values λ_i are significantly larger for the solenoidal component, consistent with $\overline{\omega^2} >> \overline{d^2}$. The most probable solenoidal eigenvalues remain approximately constant in time, whereas the maximum irrotational eigenvalue increases in time. This indicates that, on average, the lengthening of fluid elements due to the irrotational strain field increases with time. Although the most probable λ_1^C is approximately constant in time, its minimum (taken over the 3-D field) decreases (Fig 13). Consequently, the effect of regions with large compression intensifies with time. This effect will be studied further with the use of conditional probability density functions. In Fig. 14, we plot the pdf of $\cos\theta_{23}^I$ at $St = 1, 3, 5, 7, 9$ and 11. The structure of the curve remains almost invariant in time. We find that this is true for all θ_{ij}^I, *except* for θ_{i3}^I. By comparison with similar plots obtained from DNS of incompressible homogeneous shear flow, we find that compressibility has only very subtle effects on the spatial structure of the solenoidal rate of strain tensor. Only the most probable inclinations of the eigenvectors with the spanwise direction seem affected by compressibility. Further conclusions await a more detailed analysis. Finally, the last two figures illustrate some of the structural differences found in the solenoidal and irrotational components of S_{ij}. Fig 15 shows the pdf's of $\cos\theta_{3i}^I$, while $\cos\theta_{3i}^C$ is plotted in Fig 16. These correspond to $St = 11$. One sees from Fig 15 that, for the solenoidal field, the eigenvector $\mathbf{f}_3$ has no preferred orientation with respect to the spanwise direction. However, this vector has approximately a 45 degree orientation with respect to the x and y directions. We note that this eigenvalue (λ_3) is positive and corresponds to an expansion of fluid elements in the corresponding principal axis direction. Figure 16 on the other hand show a completely different character of S_{ij}^C. Its interpretation is not yet clear. However, the characteristics of Fig. 16 are found in many of our shear flow simulations.

REFERENCES

Blaisdell, G A , Reynolds, W C , Mansour, N N , Zeman, O , and Aupoix, B (1990) *43rd Annual Meeting of the APS/Division of Fluid Dynamics*, Cornell University, N Y (November 1990)

Erlebacher, G , Hussaini, M Y , Kreiss, H O , and Sarkar, S (1990) *Theoret Comput Fluid Dynamics*, 2, 73

Erlebacher, G , Sarkar, S and Hussaini, M Y , Analysis of structures in compressible homogeneous turbulence, *ICASE Report*, in preparation (1991)

Feiereisen, W J , Shirani, E , Ferziger, J H , and Reynolds, W C (1982) In *Turbulent Shear Flows 3*, pp 309-319 Springer-Verlag, Berlin

Kida, S and Oszag, S A (1990) Energy and Spectral Dynamics in Forced Compressible Turbulence Submitted to *J Fluid Mech*

Lee, S , Lele, S K , and Moin, P (1990) Eddy-shocklets in Decaying Compressible Turbulence *CTR Manuscript 117*

Passot, T (1987) Simulations numeriques d'ecoulements compressibles homogenes en regime turbulent · application aux nuages moleculaires *Ph D Thesis, University of Paris*

Rogallo, R S (1981) Numerical Experiments in Homogeneous Turbulence *NASA TM 81315.*

Rogers, M M , and Moin, P (1987) The Structure of the Vorticity Field in Homogeneous Turbulent Flows *J Fluid Mech.*, 176, 33

Sarkar, S., Erlebacher, G , Hussaini, M Y , and Kreiss, H O (1989) The Analysis and Modeling of Dilatational Terms in Compressible Turbulence. *ICASE Report No 89-79, J. Fluid Mech* (in press)

Sarkar, S., Erlebacher, G , Hussaini, M Y , and Kreiss, H O (1991) Direct Simulation of Compressible Turbulence in a Shear Flow. *ICASE Report No 91-29.* to appear in

Sarkar, S. (1991) Modeling the Pressure-dilatation Correlation. *ICASE Report*, in preparation.

Tavoularis, S., and Corrsin, S (1981) Experiments in Nearly Homogeneous Turbulent Shear Flow with a Uniform Mean Temperature Gradient. *J. Fluid Mech.*, 104, 311.

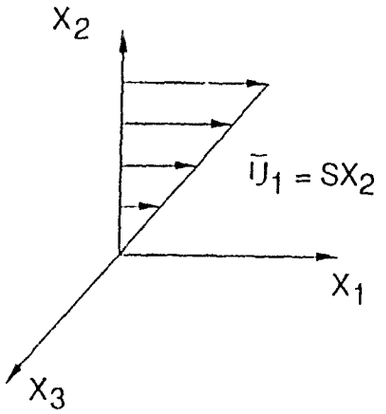

Figure 1 Schematic of homogeneous shear flow

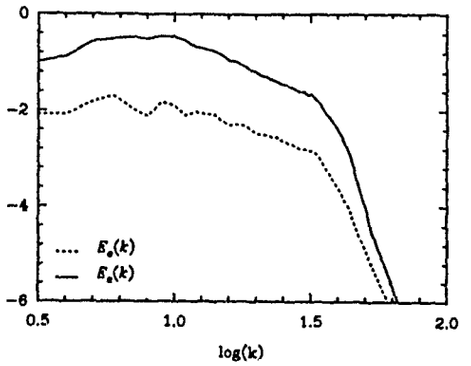

Fig. 4. Solenoidal and irrotational velocity spectra for Case 3.

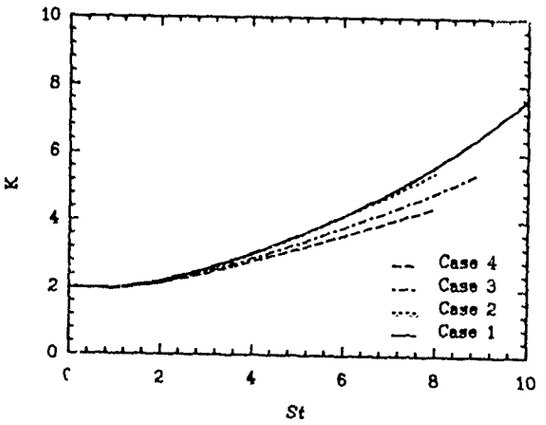

Fig. 2. Time evolution of turbulent kinetic energy.

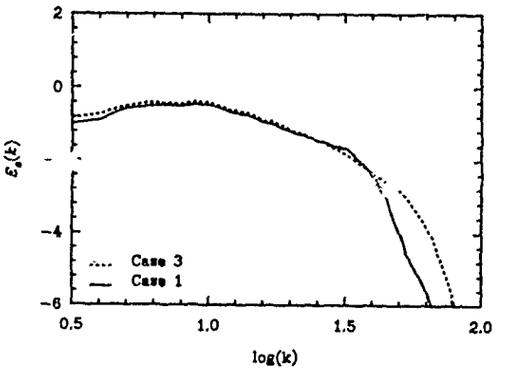

Fig. 5. Solenoidal velocity spectra for compressible and incompressible runs.

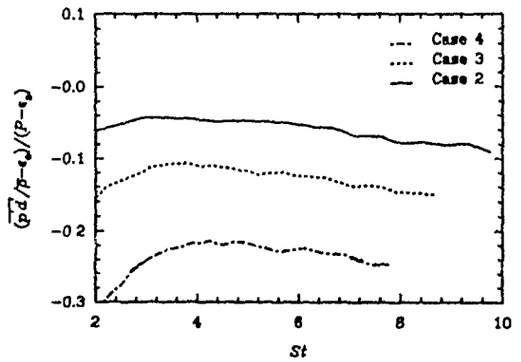

Fig. 3. Contribution of explicit compressibility terms to the kinetic energy budget.

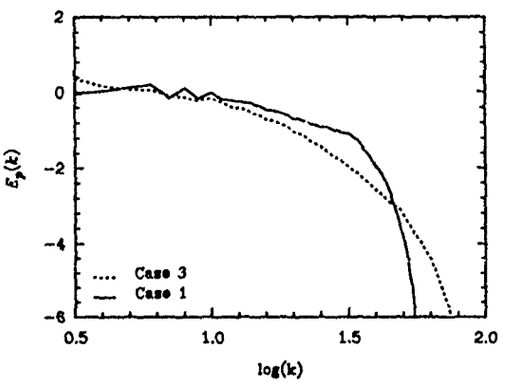

Fig. 6. Pressure spectra for compressible and incompressible runs.

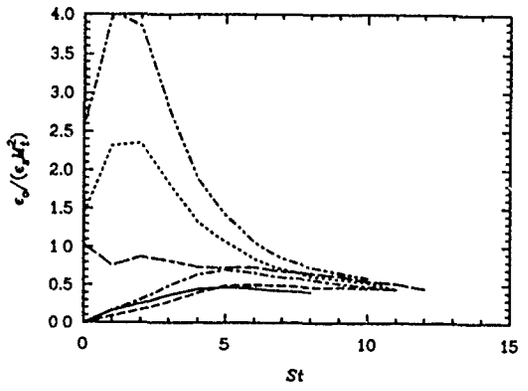

Fig. 7. Compressible dissipation in homogeneous shear flow.

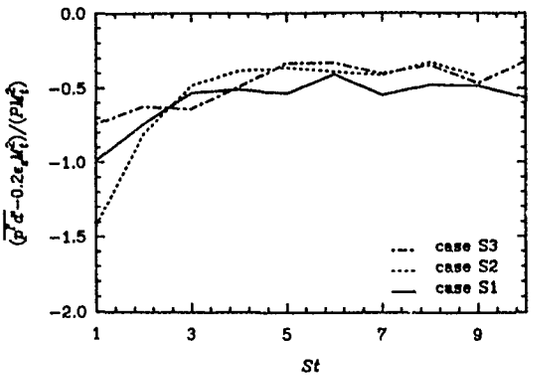

Fig 10. Incompressible pressure–dilatation in homogeneous shear turbulence.

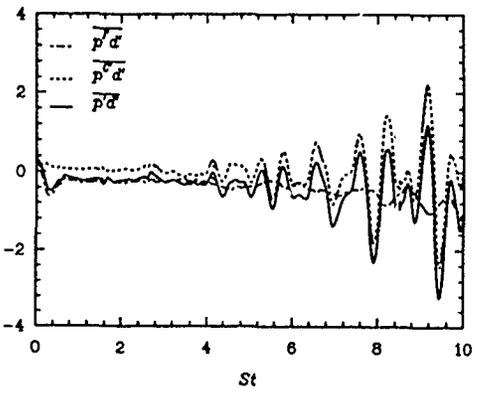

Fig. 8. Evolution of pressure–dilatation in homogeneous shear flow.

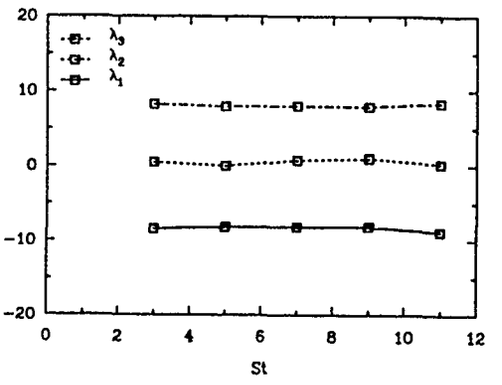

Fig. 11. Time history of most probable λ_i^I, i=1,2,3.

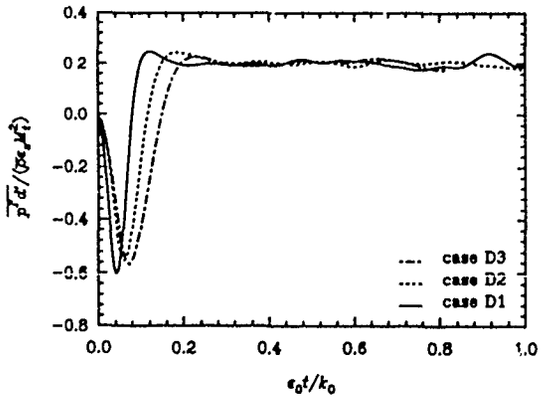

Fig. 9. Incompressible pressure–dilatation in decaying isotropic turbulence.

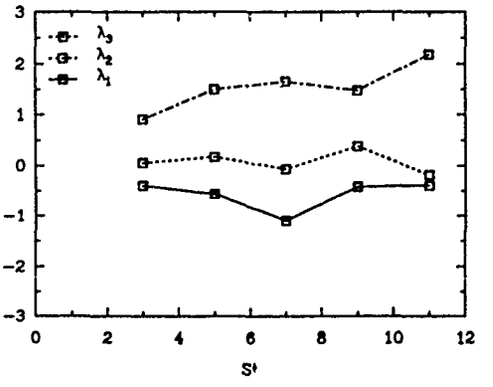

Fig. 12. Time history of most probable λ_i^C, i=1,2,3.

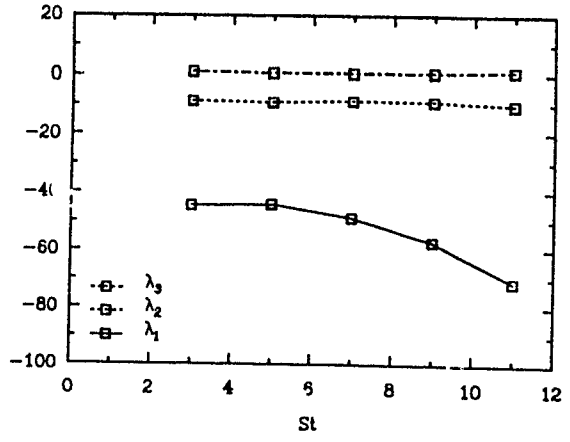

Fig. 13. Time history of mininum of λ_i^C, i=1,2,3.

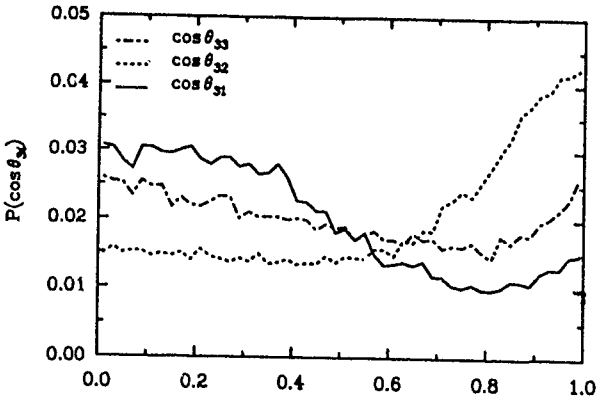

Fig 16. Pdf of $\cos\theta_{3i}^C$, i=1,2,3.

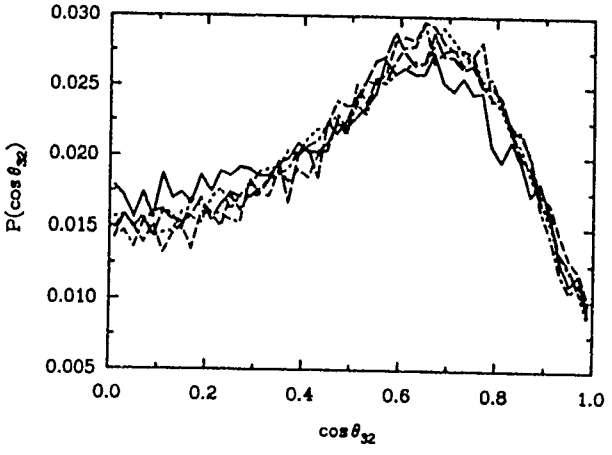

Fig. 14. Pdf of $\cos\theta_{32}$ at st=1,3,7,9.

Table 1 Parameters for the DNS cases of homogeneous shear flow

Case	S	ν	$M_{t,0}$	$R_{\lambda,0}$	ρ'	d'
1	10	1/150	0 0	24	0	0
2	10	1/150	0 2	24	0	0
3	10	1/150	0 3	24	0	0
4	10	1/150	0 4	24	0	0

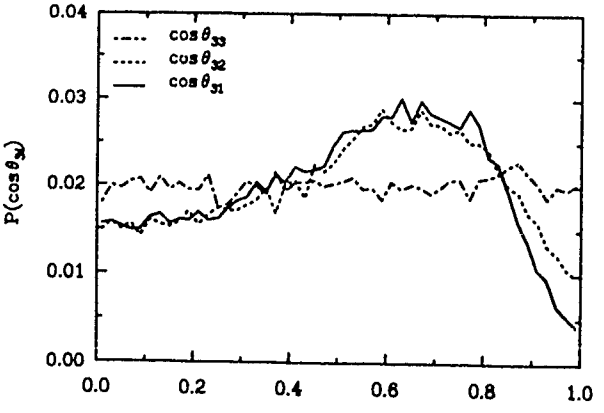

Fig 15. Pdf of $\cos\theta_{3i}^I$, i=1,2,3.

EIGHTH SYMPOSIUM ON
TURBULENT SHEAR FLOWS
Technical University of Munich
September 9-11, 1991

Simulation and Modeling of Homogeneous Compressible Turbulence Under Isotropic Mean Compression

By G. N. Coleman and N. N. Mansour

NASA Ames Research Center, Moffett Field, CA 94035 U. S A.

ABSTRACT

Compressible homogeneous turbulence subjected to isotropic mean compression is simulated numerically for high and low turbulent Mach numbers, at various compression rates. We find that at low Mach numbers, the effects of viscosity variations on the development of the turbulent kinetic energy can be significant. A model consistent with the invariance of the Navier-Stokes equations to spherical compression, that takes into account variable viscosity effects is proposed. At high Mach numbers, the distribution of energy between the acoustic and solenoid fields is found to depend upon initial conditions. The simulation results are also used to evaluate two-equation compressible turbulence models

INTRODUCTION

One of the most pressing needs in the field of turbulence modeling today is that of correctly incorporating the effects of compressibility into one-point closures. Because of uncertainties in compressible turbulence models, the ability to adequately predict flows such as those associated with internal combustion engines, hypersonic flight, supersonic combustion and astrophysics is currently rather limited The goal of this study is to increase our understanding of compressible turbulence by considering the simple limiting case of homogeneous compressible turbulence subjected to isotropic ("spherical") mean compression. Our main objective is to generate direct numerical simulations (DNS) of the spherically-compressed case, for various turbulent Mach numbers and compression rates, and use the results to modify turbulence models so that they correctly predict this flow. By "tuning" the models in this manner, it is felt that they will provide better predictions for all flows.

FLOW DESCRIPTION

The fluid is assumed to be a viscous, compressible ideal gas with constant specific heats. The mean straining is given by the isotropic compression

$$\widetilde{u}_{i,j}(t) = S(t)\delta_{ij}, \qquad [1]$$

where the mean dilatation, $\widetilde{u}_{i,i} = 3S(t)$, is negative, and $\widetilde{u}_i$ is the Favre averaged mean velocity. In what follows, Favre averaged quantities are denoted by a tilde, and ensemble averaged variables by angle brackets Single and double primes represent respectively, deviations from the Favre and ensemble average: eg. $u_i = \widetilde{u}_i + u_i'' = \langle u_i \rangle + u_i'$. The list of parameters which govern the flow includes: (1) the initial compression rate, defined here by $S(Sq^2/\epsilon)_0$ (a zero subscript is used throughout to denote an initial value), where q^2 is $\langle \rho u_i'' u_i'' \rangle / \langle \rho \rangle$, twice the turbulent kinetic energy per unit mass, and $\epsilon = \epsilon_s + \epsilon_d$ is the total rate of turbulent kinetic energy dissipation due to both solenoidal and dilatational velocity fluctuations: $\epsilon_s = \widetilde{\nu}\langle \omega_i' \omega_i' \rangle$ and $\epsilon_d = \frac{4}{3}\widetilde{\nu}\langle u_{i,i}'' u_{j,j}'' \rangle$ ($\widetilde{\nu} = \widetilde{\mu}/\langle \rho \rangle$, ω_i' is the fluctuation vorticity and μ and ν are the dynamic and kinematic viscosity, respectively); (2) the compression history, $S(t)$; (3) the initial turbulent Reynolds number, $(Re_T)_0 = (q^4/\epsilon\widetilde{\nu})_0$; (4) the initial turbulent Mach number $(M_T)_0 = (q/\widetilde{c})_0$, where $\widetilde{c}$ is the sound speed based on the mean temperature, $\widetilde{T}$; (5) the molecular Prandtl number, Pr; (6) the ratio of specific heats, γ; (7) the temperature dependence of the dynamic viscosity, $\mu(T)$; (8) the initial magnitude and spectra shapes of the density and temperature fields; and (9) the initial partitioning of turbulent kinetic energy between the solenoidal and dilatational fields, and the respective initial spectra shapes.

The DNS code of Blaisdell, Mansour & Reynolds (1991) (henceforth BMR) is used to produce the results. The program computes numerical solutions of the compressible Navier Stokes equations, for various types of mean deformation. All the relevant scales of motion are resolved (so that no turbulence model is required), by utilizing a Fourier spatial discretization and Runge-Kutta time advance algorithm

We assume

$$\mu(T) = \mu(\widetilde{T}_0)\left(\frac{T}{\widetilde{T}_0}\right)^n, \qquad [2]$$

and $\widetilde{\mu} = \mu(\widetilde{T})$. The viscosity exponent, n, is taken to be either 0.67, 0.75 or (for reasons discussed below) $1/(\gamma - 1)$. To maintain the homogeneity of the turbulence, the compression history must follow (BMR)

$$S(t) = S_0/(1 + S_0 t). \qquad [3]$$

The other parameters used for each run are given in the appendix, as are details regarding generation of the initial conditions.

Two-equation model

For isotropic turbulence under spherical compression, the off-diagonal Reynolds stresses are negligible. We therefore choose to focus our attention upon two-equation models. A form appropriate for compressible flow is (BMR, Speziale & Sarkar 1991, Reynolds 1980)

$$\frac{1}{2}q_{,t}^2 + \widetilde{u}_j \frac{1}{2}q_{,j}^2 = \mathcal{P} + \mathcal{D}_{q^2} - \langle u_i'' \rangle \langle p \rangle_{,i} + \Pi_d - \epsilon_s - \epsilon_d, \qquad [4]$$

$$\epsilon_{s,t} + \widetilde{u}_j \epsilon_{s,j} = \frac{\epsilon_s}{q^2}(2C_1\mathcal{P} - 2C_2\epsilon_s) + 3(1 - C_3)\epsilon_s S + \mathcal{D}_{\epsilon_s} \qquad [5]$$

where $\mathcal{P} = -\widetilde{u_i'' u_j''}\widetilde{u}_{i,j}$ is the production of $q^2/2$, $\mathcal{D}_{q^2}$ and $\mathcal{D}_{\epsilon_s}$ prepresent turbulent and viscous diffusion and $\Pi_d = \langle p' u_{i,i}'' \rangle / \langle \rho \rangle$ is the pressure-dilatation term. The q^2 transport equation is exact (except for the fact that terms involving correlations of fluctuating viscosity – which have

been found to be negligible by BMR – have been omitted), while the transport equation for ϵ_s is a model. C_1, C_2 and C_3 are modeling constants; popular values are $C_1 = 1.44$, $C_2 = 1.83$ and $C_3 = (7 - 2C_1)/3$ (Speziale & Sarkar 1991). $\mathcal{P}$ is modeled using an eddy viscosity approach, so that $\mathcal{P} = 0.5C_\mu(q^4/\epsilon_s)(\widetilde{S}_{ij}\widetilde{S}_{ij} - 3S^2) - q^2S$ with $\widetilde{S}_{ij} = \frac{1}{2}(\widetilde{u}_{i,j} + \widetilde{u}_{j,i})$ and $C_\mu = 0.09$ (Patel *et al.* 1985) Given parameterizations for the two compressibility terms, Π_d and ϵ_d, the equation set is closed.

Applied to the special case of isotropic compression, Eqs. [4] and [5] reduce to

$$\frac{dq^2/2}{dt} = \mathcal{P} - \epsilon_s - \epsilon_d + \Pi_d, \qquad [6]$$

$$\frac{d\epsilon_s}{dt} = C_1\mathcal{P}\frac{\epsilon_s}{q^2/2} + 3(1 - C_3)\epsilon_s - C_2\frac{\epsilon_s^2}{q^2/2} \qquad [7]$$

with $\mathcal{P} = -q^2S$. Our objective is to use DNS results to test some proposed closures for Π_d and ϵ_d, and to evaluate the constants in (and form of) the ϵ_s equation We begin with the later task, by considering the flow in which the velocity fluctuations are small compared to the local sound speed.

LOW MACH NUMBER CASES

When the turbulent Mach number, M_T, is very small, the fluctuation velocity field is effectively solenoidal, implying that ϵ_d and Π_d are both negligible The low Mach number DNS results presented in this section are thus primarily useful as a means for evaluating the ϵ_s equation. We first turn our attention to compressions at very rapid rates, since this allows us to compare Eq [7] and DNS results with rapid distortion theory (RDT) (see also Coleman & Mansour 1991)

Rapid Spherical Compression

Dissipation histories from two low Mach number rapid compression runs, with $(Sq^2/\epsilon)_0 = -47$, are given in Fig 1 The time span shown represents half of the total available, since at $|S_0|t = 1$ the volume collapses to zero (see Eq [3]) The first of the DNS data (shown by the symbols), is Wu *et al* 's(1985) Case SQF, which assumed the fluctuating velocity was divergence free, so that M_T was exactly zero. Very good agreement is found between Wu's data and the present simulation results (run c3dh, dotted curve), which uses $(M_T)_0 = 0.04$ (the other run parameters are given in the appendix). Also shown in Fig 1, as the dashed curve, is the model Eq [7] prediction, using $C_2 = 1\,92$ and $C_3 = (7 - 2C_1)/3$, the standard value quoted above. The large difference between the model and the DNS histories is at first glance puzzling, since this value of C_3 was advocated by Reynolds (1980) and Morel & Mansour (1982) as a means of exactly matching rapid isotropic compression. However, in setting the value for C_3, Reynolds and Morel & Mansour were matching RDT for constant kinematic viscosity. Coleman & Mansour (1991) have shown that the effect of variable viscosity is important, and

$$C_3 = \left(7 - \frac{3}{\widetilde{u}_{i,i}\widetilde{\nu}}\frac{d\widetilde{\nu}}{dt} - 2C_1\right)\Big/3 \qquad [8]$$

will reproduce the RDT and DNS results. In Fig. 1, predictions using Eq.[8] are shown as the chain-dot and solid curves, for C_2 equal to 1.92 and 0, respectively; very good agreement with the simulation data is observed.

Intermediate and Slow Spherical Compressions

While the correct treatment of terms dominant during a rapid compression is apt to improve the overall behavior

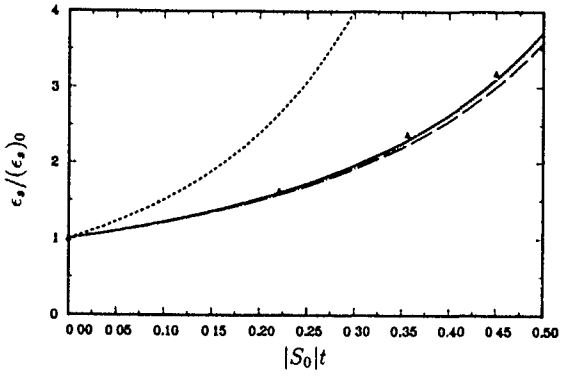

FIGURE 1. Evolution of the solenoidal part of ϵ during a rapid spherical compression, $(Sq^2/\epsilon)_0 = -47$ and $M_T \simeq 0$; Δ, Wu *et al.*'s1985 DNS Case SQF, $M_T = 0$; ·····, present DNS run c3dh, $(M_T)_0 = 0\ 04$; ----, Eq. [7] prediction using $C_3 = (7-2C_1)/3$, $C_2 = 1.92$; —·—, Eq. [7] prediction using Eq. [8] for C_3, with $C_2 = 1.92$; ——, Eq. [7] prediction using Eq. [8] for C_3, with $C_2 = 0$.

of the ϵ_s equation, it provides no guarantee of an accurate prediction for flows experiencing compression at low or intermediate rates. The mean production term is faithfully represented in the ϵ_s equation when Eq. [8] is used for C_3, but the manner in which Eq [7] models the terms which are important away from the rapid compression regime, namely the vortex-stretching and destruction terms, are crucial in more general situations This is the subject of the present section.

The key to modeling arbitrary isotropic compressions is found in a conclusion attributed to Spiegel & Frisch in a recent paper by Cambon, Mao & Jeandel (1991): that the form of the Navier-Stokes equations is unchanged by the transformation which maps a decaying isotropic flow to one experiencing spherical compression, provided $M_T = 0$ and the variations of kinematic viscosity are the same for the decaying and compressing flows. This result is demonstrated by the DNS data shown in Fig. 2. The solid and dashed curves trace q^2 histories of an intermediate compression, $(Sq^2/\epsilon)_0 = -2.5$, for cases with constant (run c3dq) and variable viscosity (c3dl), respectively. The later uses in Eq. [2] the exponent $n = 3/4$, and the former $n = 1/(\gamma - 1)$. Setting $n = 1/(\gamma - 1)$ leads to (since for the mean flow the isentropic relations are a very good approximation), $d\widetilde{\nu}/dt = 0$. The dotted curve in Fig. 2 is the result of mapping the isotropic decay evolution (run ixxb), which began from the same state as the compression runs, according to the Spiegel-Frisch transformation:

$$u_{*i}(\mathbf{x}_*, t_*) = \left(\frac{\langle\rho(t)\rangle}{\langle\rho(0)\rangle}\right)^{-1/3} u_i(\mathbf{x}, t)$$
$$t_* = \int_0^t \left(\frac{\langle\rho(\tau)\rangle}{\langle\rho(0)\rangle}\right)^{2/3} d\tau, \qquad [9]$$

where the "starred" quantities represent the unmapped isotropic decay variables, and the "unstarred" those of the mapped spherically-compressed flow. The fact that the solid and dotted curves correspond shows the density fluctuations are negligible for these runs, while the divergence of the dashed and dotted curves points to the importance of the viscosities exhibiting the same behavior, for the transformation to be exact.

The Spiegel-Frisch result implies that to accurately model an isotropic compression of any rate, one need only obtain

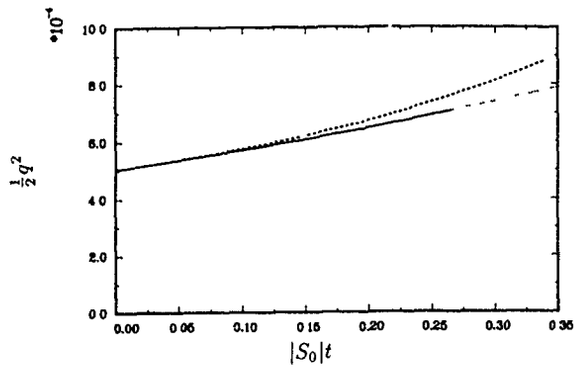

FIGURE 2. Evolution of turbulent kinetic energy for intermediate rate spherical compression, $(Sq^2/\epsilon)_0 = -2.5$ and $(M_T)_0 = 0.03$; ----, run c3dl, $n = 3/4$; ——, c3dq, $n = 1/(\gamma-1)$ (i.e. $d\tilde{\nu}/dt = 0$); · · , ixxb, mapped isotropic decay

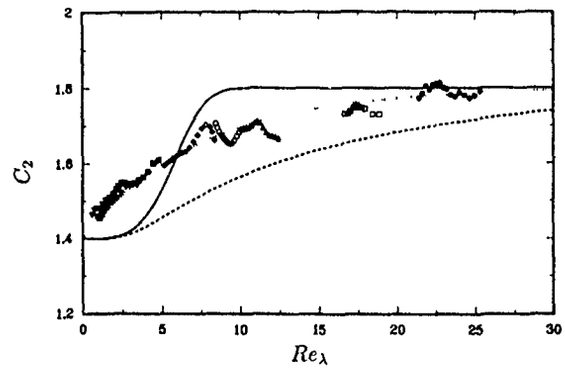

FIGURE 3. Variation of C_2 with Re_λ; Open symbols, 128^3 DNS; Solid symbols, 256^3 DNS (Wray & Mansour 1991); ——, Hanjalić & Launder (1976); ----, Lumley (1978); · ····· , Eq. [11].

an accurate model of isotropic decay with time-varying viscosity. We first consider the $\tilde{\nu}$ = constant case, so that $d\epsilon_s/dt = \tilde{\nu} d\omega^2/dt$ (where $\omega = \sqrt{\langle \omega_i' \omega_i' \rangle}$). Eq [7] predicts

$$\frac{d\epsilon_s}{dt} = -2C_2 \frac{\epsilon_s^2}{q^2}. \qquad [10]$$

To determine C_2, we appeal to the recent direct simulations of incompressible isotropic decay of Wray & Mansour (1991). Fig. 3 shows the development of C_2 with $Re_\lambda = (5Re_T/3)^{1/2}$ predicted by the simulations, and the models of Hanjalić & Launder (1976) and Lumley (1978) The Lumley model consistently underpredicts the DNS data for the range of Re_λ shown, while the Hanjalić & Launder curve reaches the high Re_λ limit too quickly. Although the models and data all appear to agree on the very small Re_λ limit of $C_2 \simeq 1.4$, the behavior as $Re_\lambda \to 0$ is very different; no evidence of the $dC_2/dRe_\lambda = 0$ variation assumed by both models is found in the low Re_λ simulation results. Modeling C_2 by a curve fit of the DNS data, we have

$$C_2 = -0.4 \exp(-0\ 13 Re_\lambda) + 1.8, \qquad [11]$$

which produces the dotted curve shown in Fig. 3

Using Eq. [9], the Spiegel-Frisch transformation, Eq. [10] maps to the $\tilde{\nu}$ = constant isotropic compression model,

$$\frac{d\epsilon_s}{dt} = -4S\epsilon_s - 2C_2 \frac{\epsilon_s^2}{q^2}. \qquad [12]$$

This result was first found by Cambon *et al.* (1991), who only consider the constant viscosity case. It is identical to the result one obtains by applying Eq. [7] directly to spherical compressions when using Eq. [8] with $d\tilde{\nu}/dt = 0$, and is therefore consistent with Reynolds' and Morel & Mansour's $\tilde{\nu}$ = constant RDT work.

As we have seen, via Fig. 2, even at intermediate compression rates the variation of $\tilde{\nu}$ is important during the compression. Therefore, in order to account for the usual situation in which $d\tilde{\nu}/dt \neq 0$, and fully take advantage of the Spiegel-Frisch transformation, a realistic model of variable viscosity isotropic decay must be developed. In an attempt to do so, we consider the transport equation for the enstrophy, ω^2, and assume that the imbalance between the vortex stretching and viscous destruction terms induced by variations of $\tilde{\nu}$ is governed by the parameter $(1/q^2)d\tilde{\nu}/dt$.

Since in general, $d\epsilon_s/dt = \tilde{\nu} d\omega^2/dt + \omega^2 d\tilde{\nu}/dt$, this leads to the following model for variable-$\tilde{\nu}$ isotropic decay:

$$\frac{d\epsilon_s}{dt} = \omega^2 \frac{d\tilde{\nu}}{dt} - 2C_2 \frac{\epsilon_s^2}{q^2} - C_{2_\nu} \frac{1}{q^2} \frac{d\tilde{\nu}}{dt} \epsilon_s \omega \qquad [13]$$

Provided Eq [13] is valid, the Eq. [9] mapping implies that a low Mach number spherical compression of any rate would then be described by

$$\begin{aligned} \frac{d\epsilon_s}{dt} = & -4S\epsilon_s + \omega^2 \frac{d\tilde{\nu}}{dt} \\ & - 2C_2 \frac{\epsilon_s^2}{q^2} - C_{2_\nu} \left(\frac{\langle \rho(t) \rangle}{\langle \rho(0) \rangle} \right)^{2/3} \epsilon_s \frac{\omega}{q^2} \frac{d\tilde{\nu}}{dt} \end{aligned} \qquad [14]$$

The first two terms on the RHS of Eq. [14] follow from the variable viscosity RDT findings of the previous section; C_2 is modeled by Eq. [11]. We are now in the process of evaluating the $C_{2\nu}$ term by DNS of variable viscosity isotropic decay.

HIGH MACH NUMBER CASES

Up to this point, our discussions have dealt with "compressing" flows, those in which compressibility affects only the mean density. There are many situations, however, where density fluctuations are important. In this section, we address the issues related to these flows, in which M_T is not small.

"Synthetic" Initial Conditions

The first issue we consider is the effect of isotropic compression on the acoustic variables. During their study of compressible homogeneous shear flow, BMR found that the mean shear drives the acoustic (dilatational) field to a unique state, regardless of the magnitude of initial conditions – even when no development time was allowed for the turbulence to mature before the shear was imposed Two parallel runs, c3dr and c3ds, with identical initial Mach numbers ($M_T = 0\ 3$) and compression rates ($(Sq^2/\epsilon)_0 = -2.5$), but different acoustic initial conditions, were performed to see if spherically-compressed turbulence is similar in this regard. One run, c3dr, began with no initial dilatational velocity or fluctuation density, temperature or pressure; the other, c3ds, began with one-fourth of the turbulent kinetic energy in the dilatational component, and fluctuation density and absolute temperature fields both equal to 15 percent of their volume averaged means (with the pressure given by the ideal gas law). All non-zero fields for both runs assumed

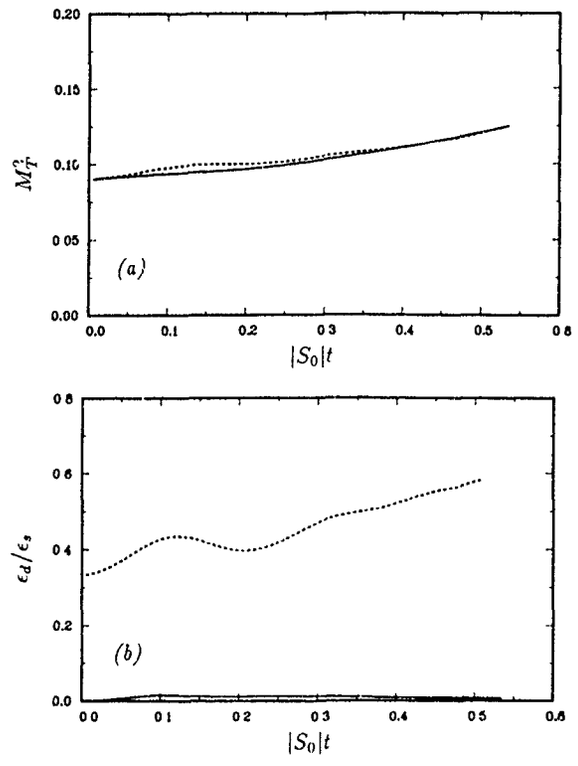

FIGURE 4. Histories of *(a)* turbulent Mach number and *(b)* ratio of dilatational to solenoidal dissipation; $(Sq^2/\epsilon)_0 = -2.5$ and $(M_T)_0 = 0.3$, ——. c3dr, acoustic fields initially zero; ----, c3ds, $(q^2_{dil}/q^2_{total})_0 = 1/4$, $(\rho_{rms}/\langle\rho\rangle)_0 = (T_{rms}/\langle T\rangle)_0 = 0.15$.

"top-hat" initial spectra (BMR), and the compression began immediately upon the "synthetic" undeveloped fields (see appendix for other run parameters)

The Mach number histories for the parallel runs are given in Fig 4a, and are very similar to each other However, the variations of the dilatational dissipation (Fig. 4b) and pressure-dilatation correlation (not shown) are quite distinct. Since the histories have progressed, without converging, to over half of the total possible compression time, $0 \le |S_0|t < 1$ (see Eq [3]), it appears that unlike shear, spherical compression does not drive the acoustic field to a unique state This behavior is a result of the fact that the only coupling between the solenoidal and acoustic fields is due to nonlinear interactions, which are slow compared to the turbulence time scale at this Reynolds number It implies that ϵ_d and Π_d models must account for initial conditions if they are to work correctly during isotropic compression. The degree to which one Π_d model succeeds is taken up in the next section, as part of a discussion of high M_T data which are generated using for initial conditions – rather than the synthetic fields of this section – developed isotropic decaying turbulence.

"Natural" Initial Conditions

As with the spherically-compressed flow, acoustic variables in decaying isotropic turbulence do not converge to unique values which are independent of their initial conditions (cf. BMR). Because of this, a certain amount of arbitrariness exists in specifying "natural" initial conditions for the high Mach number simulations. For the present computations, the initial acoustic field is the result of beginning with a purely solenoidal field, allowing it to decay and develop dilatational fluctuations, before the compression is imposed, at the point where $M_T = 0.44$, $\rho_{rms} = 0.03\langle\rho\rangle$, $T_{rms} = 0.02\langle T\rangle$ and 9 percent of the turbulent kinetic energy is in the dilatational field. Three separate compression speeds were chosen, defining three cases, runs c3db ($(Sq^2/\epsilon)_0 = -4.7$), c3dc (-12.5) and c3dd (-1.25).

The initial field was not in exact acoustic equilibrium, since the dilatational energy was not evenly split into the kinetic and potential energy partitions The ratio of the two is defined by the parameter, $\mathcal{F} = \gamma\langle\rho\rangle\langle p\rangle q^2_{dil}/\langle p'_c p'_c\rangle$, where p_c is the so-called "compressible pressure" (Sarkar *et al* 1989). Both high and low M_T isotropic decay simulations have shown that after an initial transient, well developed compressible turbulence reaches acoustic equilibrium, characterized by $\mathcal{F} \simeq 1$ (Sarkar *et al* 1989, Lee *et al.* 1991, BMR). Instead of being about one, the initial condition used here saw $\mathcal{F} \simeq 0.6$. (During the determination of $\mathcal{F}$, we found that for this flow, the compressible pressure fluctuations $\langle p'_c p'_c\rangle$ accounted for approximately 80 percent of the total fluctuations, $\langle p'p'\rangle$) We intend to repeat these high M_T cases using $\mathcal{F} \simeq 1$ initial conditions, so that the effect of spherical compression upon the partitioning of the acoustic energy may be determined.

From the present runs we are able to observe that the compression rate strongly affects the evolution of the Mach number, the dilatational dissipation and the pressure-dilatation correlation (Fig. 5). In particular, we note in Fig 5b that for the initial condition used, the level of ϵ_d is very small, never more than 4 percent of the total dissipation. One of the predictions of RDT is that ϵ_d/ϵ_s will remain constant during a rapid spherical compression (Coleman *et al.* 1991); the DNS results support this finding, since the rate of change of ϵ_d/ϵ_s decreases as the compression rate increases.

From a modeling standpoint, the most significant result is the behavior of pressure-dilatation term shown in Fig. 5c. The magnitude of Π_d is seen to be a significant fraction of the total dissipation, and demonstrates a great dependence on compression rate Beginning from the initial condition level, where the pressure-dilatation in the unstrained field acts as a source of turbulent kinetic energy (supplied by the potential energy of the pressure field), the compression in all cases causes a reduction of Π_d. At the slow rate, it approaches zero and remains slightly positive, when $|S|$ is large however, the pressure-dilatation is driven to very large negative values, with magnitude many times that of the total dissipation rate (see Fig. 6a), representing an important kinetic to potential energy conversion. In Fig. 6, we test the ability of Aupoix *et al* 's(1990) Π_d model to duplicate the DNS histories for the largest and smallest compression rates (note the expanded vertical and horizontal scales in Fig. 6a). The model assumes

$$\frac{d\langle\rho\rangle\Pi_d}{dt} = -C_{A1}\langle\rho\rangle\frac{M_T^2}{2\tau_A}\frac{dq^2}{dt} - C_{A2}\frac{\langle\rho\rangle}{\tau_A}\Pi_d, \qquad [15]$$

where $\tau_A = (1/2)^{3/2}(q^2/\epsilon)M_T$, $C_{A1} = 0.25$ and $C_{A2} = 0.20$. While the trend for the $(Sq^2/\epsilon)_0 = -1.25$ case is roughly correct (Fig 6b), that for the rapid compression (Fig. 6a) is not. Given that the slow compression performance is about as good as that found for isotropic decay (see Figure 5 of Aupoix *et al.* 1990), and the poor response for large $|S|$ found here, it seems as if the major deficiency of the model is the strain rate sensitivity – although part of the poor showing could be due to the fact that it has been tested against a flow in acoustic nonequilibrium. This issue will be clarified in the future. Aupoix *et al.* have acknowledged

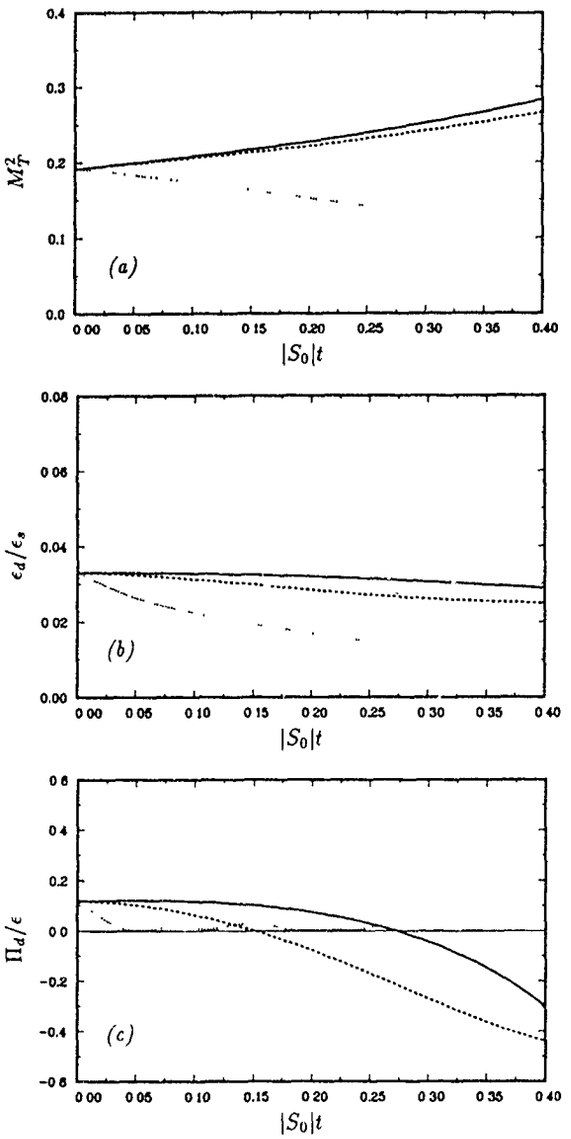

FIGURE 5. Evolution of *(a)* turbulent Mach number, *(b)* ratio of dilatational to solenoidal dissipation, and *(c)* pressure-dilatation, $(M_T)_0 = 0.44$, ——, c3db, $(Sq^2/\epsilon)_0 = -47$; ----, c3dc, $(Sq^2/\epsilon)_0 = -12.5$; · · , c3dd, $(Sq^2/\epsilon)_0 = -1.25$

the model's weakness for flows with strong initial condition dependence and have tentatively proposed model transport equations for both Π_d and ϵ_d, which might alleviate some of the shortcomings observed here.

Zeman (1991) has recently proposed an algebraic model for Π_d, which he uses to predict some of our DNS results (as discussed in these proceedings). While we cannot expect an algebraic model to do well in an initial condition dependent flow when compared directly to the pressure-dilatation histories, Zeman has found some success when it is one component of a set of modeling equations. It is also possible that when the Aupoix proposal is combined with other model equations, the overall performance might be better than implied by the above test.

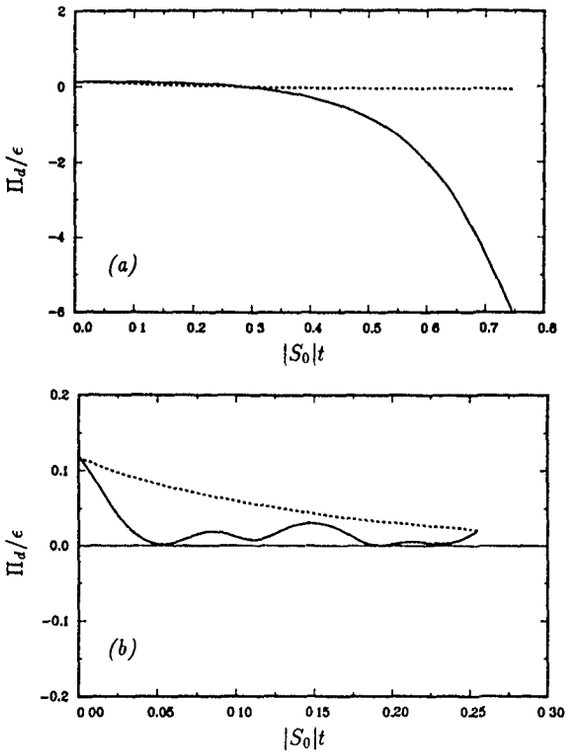

FIGURE 6. Pressure-dilatation histories, $(M_T)_0 = 0.44$; *(a)* Run c3db, $(Sq^2/\epsilon)_0 = -47$; *(b)* Run c3db, $(Sq^2/\epsilon)_0 = -1.25$. ——, DNS, ----, Aupoix *et al* (1990) Eq. [15].

CONCLUSIONS

The DNS data imply that for compressible turbulence models to correctly predict isotropic compression, the variation of kinematic viscosity induced by the compression must be accounted for For a rapid spherical compression, this may be done by using Eq. [8] for C_3, which implies that this model "constant" is a function of the bulk compression At non-rapid compression rates, Eq. [14] is proposed, but further testing is needed. For constant-$\tilde{\nu}$ isotropic decay, a new model for C_2, Eq. [11], has been constructed. The high M_T flows have been found to exhibit a strong dependence on acoustic initial conditions, which implies that models for ϵ_d and Π_d which are sensitive to initial conditions are apt to be the most successful.

ACKNOWLEDGEMENTS

Thanks are due Greg Blaisdell for his contributions to this work. GNC has been supported during this project by the National Research Council, and computer resources have been supplied by the Advanced Computational Facility and the National Aerodynamic Simulator at NASA Ames Research Center.

APPENDIX

All the DNS runs reported herein use 96^3 grid points, and choose $Pr = 0.7$ and $\gamma = 1.4$ as fixed parameters; variable parameters are listed in Tables 1 and 2. Table 2 gives the acoustic initial conditions: the ratio of dilatational to total turbulent kinetic energy, and the (rms to volume average) density fluctuation and (absolute) temperature fluctuation ratios. The compression rate, turbulent Reynolds and Mach numbers, viscosity exponent (Eq. [2]) and type of initial condition are given in Table 1. Two methods of generating initial conditions are employed, one termed "synthetic," the other "natural." The runs which use the "natural" approach (those with 'N' entered in the IC column of Table 1), begin with random, isotropic velocity, density and temperature fields with prescribed analytic spectra (either "top-hat" or "exponential" (Blaisdell *et al.* 1991)), and allow the turbulence to decay without imposed strain to a mature state (such that the velocity derivative skewness $\simeq 0.4$), before the compression is imposed upon the mature field characterized by the Table 1 and 2 values In the two runs which use "synthetic" initial conditions (denoted in Table 1 by an 'S'), no development time is allowed before the compression begins upon a field defined by the analytic spectra The last three runs listed, c3dk, c1da, and c1db, are not used in this paper, but along with c3db, are discussed by Zeman (1991) later in these proceedings For c1da and c1db, the mean compression is one-dimensional, i e. $\widetilde{u}_{i,j}(t) = S(t)\delta_{i1}\delta_{1j}$.

Table 1 Non-acoustic Run Parameters

Run	$-(Sq^2/\epsilon)_0$	$(q^4/\epsilon\widetilde{\nu})_0$	$(M_T)_0$	n	IC
c3dh	47 0	21	0.04	0 75	N
c3dl	2 5	52	0 03	0.75	N
c3dq	2 5	52	0.03	$1/(\gamma-1)$	N
ixxb	0	52	0.03	0.75	N
c3dr	2 5	200	0.30	0.67	S
c3ds	2.5	200	0.30	0.67	S
c3db	47.0	500	0 44	0 67	N
c3dc	12 5	500	0.44	0 67	N
c3dd	1.25	500	0.44	0.67	N
c3dk	47.0	21	0 02	0.67	N
c1da	47.0	500	0.44	0.67	N
c1db	47.0	21	0.02	0 67	N

Table 2. Acoustic Run Parameters

Run	$(q^2_{\rm dil}/q^2_{\rm total})_0$	$(\rho_{\rm rms}/\langle\rho\rangle)_0$	$(T_{\rm rms}/\langle T\rangle)_0$
c3dh	0.00	0.00	0 00
c3dl	0 00	0 00	0.00
c3dq	0.00	0.00	0.00
ixxb	0.00	0.00	0.00
c3dr	0	0	0
c3ds	0.25	0.15	0.15
c3db	0.09	0.03	0.02
c3dc	0.09	0.03	0.02
c3dd	0.09	0.03	0.02
c3dk	0.00	0.00	0.00
c1da	0.09	0.03	0.02
c1db	0.00	0.00	0.00

REFERENCES

AUPOIX, B., BLAISDELL, G.A., REYNOLDS, W.C. & ZEMAN, O. 1990 Modeling the turbulent kinetic energy equation for compressible, homogeneous turbulence, Proceedings of the Summer Program, NASA/Stanford Center for Turbulence Research.

BLAISDELL, G.A., MANSOUR, N.N. & REYNOLDS, W.C. 1991 Numerical simulation of compressible homogeneous turbulence, Department of Mechanical Engineering, Stanford Univ., Thermosciences Div. Report TF-50.

CAMBON, C., MAO, Y. & JEANDEL, D. 1991 On the application of time dependent scaling to the modeling of turbulence undergoing compression, submitted to *European J. Mech.*

COLEMAN, G.N. & MANSOUR, N.N. 1991 Modeling the rapid spherical compression of isotropic turbulence, to appear in *Phys. Fluids A* (tentatively 3(9)).

COLEMAN, G.N., BLAISDELL, G A. & MANSOUR, N.N. 1991 Direct simulation and modeling of irrotationally-strained compressible homogeneous turbulence, in preparation.

HANJALIĆ,K. & LAUNDER, B.E. 1976 Contribution towards a Reynolds-stress closure for low-Reynolds-number turbulence, *J. Fluid Mech.* 74(4) 593

LEE, S , LELE, S.K. & MOIN, P. 1991 Eddy shocklets in decaying compressible turbulence, *Phys. Fluids A* 3(4) 657.

LUMLEY, J.L. 1978 Computational modeling of turbulent flows, *Advances in Applied Mechanics,* 18 123.

MOREL, T. & MANSOUR, N.N 1982 Modeling of turbulence in internal combustion engines, SAE Paper No. 820040, Warrendale, PA.

PATEL, V.C., RODI, W. & SCHEUERER, G. 1985 Turbulence models for near-wall and low Reynolds number flows· A review, *AIAA J* 23(9) 1308

REYNOLDS, W.C. 1980 Modeling of fluid motions in engines: An introductory overview, in *Combustion Modeling in Reciprocating Engines* (ed. J N. Mattavi & C.A. Amann) Plenum Press.

SARKAR, S., ERLEBACHER, G , HUSSAINI, M.Y. & KREISS, H O. 1989 The analysis and modeling of dilatational terms in compressible turbulence, ICASE Report No. 89-79.

SPEZIALE, C.G. & SARKAR, S. 1991 Second-order closure models for supersonic turbulent flows, AIAA Paper No. 91-0217.

WRAY, A.A. & MANSOUR, N.N. 1991 Private communication.

WU, C.-T., FERZIGER, J.H. & CHAPMAN, D.R. 1985 Simulation and modeling of homogeneous, compressed turbulence, Department of Mechanical Engineering, Stanford Univ., Thermosciences Div. Report TF-21.

ZEMAN, O. 1991 Compressible turbulence subjected to shear and rapid compression, in these proceedings.

EIGHTH SYMPOSIUM ON
TURBULENT SHEAR FLOWS
Technical University of Munich
September 9-11, 1991

COMPRESSIBLE TURBULENCE SUBJECTED TO SHEAR AND RAPID COMPRESSION

Otto Zeman
Center for Turbulence Research
Stanford University
Stanford, CA 94305-3030

ABSTRACT

First, this paper reviews the physics and modeling of compressibility effects in homogeneous decaying, and shear-driven turbulence. Second, the principal subject is investigation of the effects of pressure and dilatational fields in turbulence subjected to rapid spherical (3D), and one-directional (1D) compression. On the basis of the direct numerical simulation results of Coleman (1991), it is shown that in 1D rapid compression the pressure-dilatation correlation ($\overline{pu_{j,j}}$) is responsible for unusually high energy transfer from the kinetic to pressure modes. This transfer mechanism leads to considerable turbulent kinetic energy losses even when turbulence is virtually incompressible. A parametric model for $\overline{pu_{j,j}}$ is developed to capture this anisotropic rapid effect, and the model results are compared with the Coleman data. The model is then tested against the direct simulations of turbulence/normal shock interactions (Lee, 1991). It is shown that apart from the energy transfer due to $\overline{pu_{j,j}}$, another important mechanism within the shock is associated with the acceleration term (containing the mean pressure gradient).

INTRODUCTION

The measure of the compressibility effects on turbulence is the so-called r.m.s. Mach number M_t, based on an r.m.s. fluctuating speed and the sonic speed corresponding to the background (mean) temperature. The sonic speed can be considered as a new intrinsic velocity scale which limits the propagation of perturbations through the fluid and sets a limit, in a statistical sense, on the velocity fluctuations as well. As the r.m.s. Mach number increases, the velocity fluctuations are accompanied by growing levels of density and pressure fluctuations and a growing degree of coupling between the vortical and dilatational (acoustic) fields. Utilizing Helmholtz' decomposition and Favre averaging, one can identify two explicit terms in the turbulence energy equations which depend on the dilatational field and provide the vortical/acoustic mode coupling. These are: 1) the dilatation dissipation defined as $\epsilon_d = 4/3\overline{\mu(u_{j,j})^2}/\overline{\rho}$, and 2) the pressure-dilatation correlation term $\Pi_d = \overline{pu_{j,j}}/\overline{\rho}$

Zeman (1990) suggested that turbulence, at a sufficiently large M_t, may generate shock-like structures or shocklets, which entail high levels of the dilatation dissipation ϵ_d. The existence of turbulent shocklets has been recently confirmed in direct numerical simulations (DNS) of decaying turbulence (Lee, Lele, and Moin 1990) and in the DNS of shear-driven turbulence as well (Blaisdell, 1990). In laboratory flows, the most prominent effect of compressibility on turbulence is the inhibition of shear layer growth rate with the (convective) Mach number M_c as observed in experiments of Papamoschou and Roshko (1988), Sammy and Elliott (1989), and others. Zeman(1990) argued that the growth rate inhibition is due to the (anomalous) dilatation dissipation caused by turbulent shocklets and, on the basis of a stochastic shocklet model, inferred a parametric expression to quantify ϵ_d. Inclusion of this anomalous dissipation in a second-order closure model provided the growth rate reduction in agreement with the experimental data.

The importance of the pressure-dilatation Π_d for turbulence energetics has, so far, not been fully appreciated. As illustrated in Zeman & Blaisdell (1990) and Zeman (1991), Π_d mediates the exchange between the kinetic and potential energies. The potential energy is meant to be the energy associated with the compression work; it is proportional to the pressure fluctuation variance $\overline{p^2}$. In equilibrium flows such as self-preserving shear layers and flat plate boundary layers, Π_d appears to be negligible. However, in unsteady turbulent flows controlled by initial conditions and in flows with rapid (mean) compression, the contribution of Π_d in the turbulence energy budget can be significant, and its knowledge is indispensable for computation of the variances of pressure and density fluctuations (see also Zeman, 1991a).

In the following a brief review is presented of the current understanding of compressibility effects in two generic (DNS) flows, decaying and shear-driven turbulence. The effects of mean rapid compression on turbulence (with non-zero values of M_t) are the main subjects of this paper. The problems to be addressed are: 1) homogeneous three- and one-dimensional rapid compression (hereafter abbreviations 3D, or 1D are used) and 2) response of shear-free turbulence to a passage through normal shock.

COMPRESSIBLE DECAYING, AND SHEAR-DRIVEN TURBULENCE

The fundamental energy-governing equations in the Favre average setting are

$$1/2\frac{\partial q^2}{\partial t} = P_s - (\epsilon_s + \epsilon_d - \Pi_d),$$

$$\frac{\partial \tilde{T}}{\partial t} = (\epsilon_s + \epsilon_d - \Pi_d)c_v^{-1}, \qquad (1)$$

accompanied by the equation of state $\overline{p} = \overline{\rho}R\tilde{T}$, where tilde and bar denote, respectively, Favre and Reynolds averages. Defined previously, Π_d is the pressure-dilatation term, P_s represents the shear production of turbulence due to the (constant) mean shear S, and $q^2 = \widetilde{u_j u_j}$ is twice the Favre-averaged kinetic energy. The separation of the total dissipation in the solenoidal (ϵ_s), and dilatational (ϵ_d) parts is feasible due to the Helmholtz' decomposition of the velocity field (Zeman, 1990) and is strictly valid only in flows which are homogeneous in the mean. The definition of the r.m.s. Mach number is $M_t = q/a$ where the sonic speed a is based on the mean temperature $\tilde{T}$. In the absence of compressibility effects ($M_t << 1$), the Reynolds stress tensor components $\widetilde{u_i u_j}$ can be computed by means of a standard turbulence closure model (for details see Zeman, 1991a). Here we discuss merely the physics and modeling associated with the compressible terms.

Dilatation dissipation: In high Reynolds number turbulence the only significant source of dilatational dissipation ϵ_d is due to eddy shocklets. On the basis of a stochastic shocklet model, Zeman (1990) inferred a parametric expression

$$\epsilon_d \propto \epsilon_s F(M_t, K). \qquad (2)$$

The shocklet dissipation function $F(M_t, K)$ is an integral functional of a pdf $p(m, K)$ of fluctuating Mach number m. The parameter K characterizes a departure from Gaussianity of m and has been defined as the kurtosis i.e $K = \overline{m^4}/(\overline{m^2})^2$. From the direct simulations of homogeneous turbulence, K was estimated as $K \approx 4$ (Zeman & Blaisdell 1990) and $F(M_t, 4)$ approximated as

$$F(M_t) = 1 - exp\{-((M_t - 0.25)/0.80)^2\}$$
$$F(M_t) = 0, \; if \; M_t < 0.25 \qquad (3)$$

We note that ϵ_d is negligible (w.r.t. ϵ_s) when $M_t < 0.3$. Physically, it means that shocklets cannot occur below a certain threshold value of M_t. In the simulations of Lee et al (1991), the shocklets were found only when M_t exceeded values of about 0.3. In most of the computational examples presented in this paper, ϵ_d is unimportant, the solenoidal dissipation ϵ_s is determined from a standard modeling equation (independent of M_t).

Pressure-dilatation correlation: Zeman (1991) proposed that in shocklet free decaying or shear-driven turbulence, the principal balance in the pressure variance equations is

$$\frac{1}{2}\frac{D\overline{p^2}}{Dt} \approx -\overline{p}^2 a^2 \Pi_d \qquad (4)$$

and proposed a closure for Π_d based on an heuristic argument that in the absence of forcing, the pressure fluctuations will tend to relax to an equilibrium value $p_e(M_t)$ at a rate dictated by an acoustic time scale $\tau_a \propto L/a$. This has led to the closure equation

$$-2\Pi_d \overline{p}^2 a^2 = \frac{D\overline{p^2}}{Dt} = -\frac{\overline{p^2} - p_e^2}{\tau_a} \qquad (5)$$

The equilibrium variance p_e^2 was inferred from theory and DNS data as

$$\frac{p_e^2}{\overline{p}^2 q^2 a^2} = P_e(M_t) = \frac{M_t^2 + M_t^4}{1 + M_t^2 + M_t^4}, \qquad (6)$$

with the acoustic time scale $\tau_a = 0.2 M_t \tau$. It is noted that in these flows, the turbulence time scale is related to vortical turbulence, i.e., $\tau = q^2/\epsilon_s$.

The DNS data of Blaisdell (1990) confirmed that (4) is a valid assumption for a range of r.m.s. Mach numbers $0.05 < M_t < 0.7$. The model (5) accounts for the initial condition influence on the (transient) behavior of turbulence. when the initial pressure (or density) fluctuation level is much higher (or lower) then the equilibrium value p_e, potential energy $\overline{p^2}$ is transferred to (or extracted from) the kinetic mode. This energy exchange takes place on the acoustic time scale τ_a.

In the equilibrium regime of homogeneous shear turbulence ($St \geq 2$), the model represented by Eqs (4)-(6) can be tested for prediction of two quantities Π_d and of the (normalized) pressure variance $\overline{p^2}/\overline{p}^2$. The pressure variance as a function of M_t is shown in Fig 1, where the cross-hatched area represents the spread of DNS data reproduced from Blaisdell (1990) (plotted only for $t > 3S^{-1}$). The values of $\overline{p^2}$ are very close to, but always smaller than, the equilibrium pressure variance $p_e^2(q^2, M_t)$ (not shown), the subtle difference between $\overline{p^2}$ and p_e^2 is according to (5), responsible for the sign and magnitude of Π_d. Comparison of the relative quantity Π_d/ϵ_s is shown in Fig. 2. Both figures support the model mechanism of relaxation to equilibrium. We note that another viable model for Π_d in shear turbulence has been proposed by Aupoix et al (1990). This model, however, is not capable of dealing with the initial condition effects.

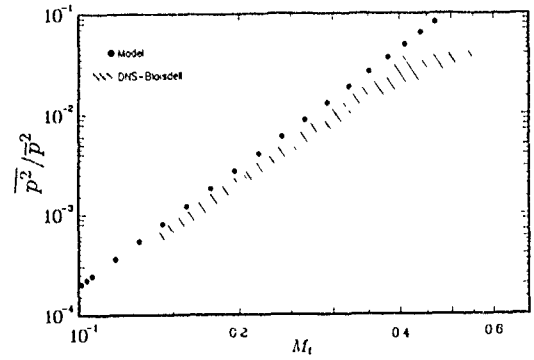

Fig. 1 Pressure variance dependence on r.m.s. Mach number in homogeneous shear turbulence: DNS-model comparison.

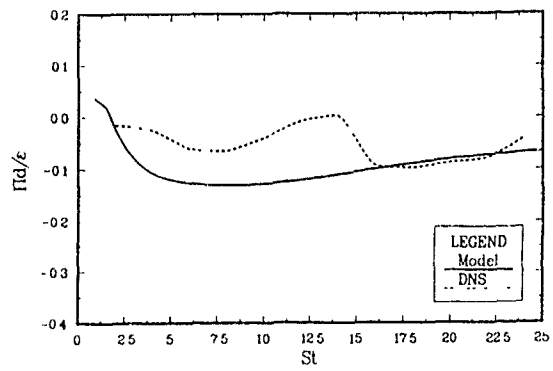

Fig. 2. Evolution of the pressure dilatation normalized by total dissipation; otherwise same as in Fig. 1.

RAPID HOMOGENEOUS COMPRESSION: 3D VS 1D

Recently, Coleman (1990) performed direct simulations of compressible turbulence subjected to rapid spherical (3D) and 1D compression for different initial values of the r.m.s. Mach number $M_{to} = 0.02$ and 0.44. These DNS experiments have relevance to the flows of practical interest: the internal combustion engine flow and turbulence/shock interactions taking place e.g. in a compression corner flow. The purpose of this section is to elucidate the physics of rapidly compressed turbulence and describe the recent modeling effort in this area. Perhaps the most important finding is that due to strong interactions between fluctuating pressure, dilatation ($u_{j,j}$), and vorticity in the 1D rapid compression, the pressure dilatation term Π_d cannot be discarded even for $M_t << 1$. This is contrary to the current wisdom that turbulence under such conditions can be considered incompressible.

The important parameters of the flows in question are the initial Mach number M_{to}, initial timescale $\tau_o = (q^2/\epsilon_s)_o$, and the initial rate of compression $A(t = 0) = A_o$. Denoting the mean velocity field by U_i we define the spherical compression by
$U_{1,1} = U_{2,2} = U_{3,3} = \nabla \cdot \mathbf{U}/3 = -A(t)$, and 1D compression by $U_{1,1} = \nabla \cdot \mathbf{U} = -A(t)$. The condition of spatial homogeneity demands that

$$A(t) = \frac{A_o}{1 - A_o t}, \qquad (7)$$

and the compression is considered rapid if $A_o \tau_o >> 1$.

In the Coleman simulations discussed here, $A_o \tau_o \approx 47$ and therefore, in principle, a rapid theory could be utilized to determine the evolution of q^2 and, if need be, $\overline{p^2}$. The 3D rapid compression of incompressible isotropic turbulence (with $M_{to} << 1$) is a trivial problem of no interest to us except as a reference flow. If, however, M_{to} is sufficiently high to produce initial dilatation and pressure fluctuations, the rapid theory is more involved. Here, we use the results of the modified rapid theory of Sabel'nikov (1975) to determine a free constant in the rapid part of the model for Π_d. The relevant set of equations to describe rapid spherical compression of isotropic turbulence are

$$1/2\frac{\partial q^2}{\partial t} = -\frac{1}{3}q^2 \nabla \cdot \mathbf{U} - (\epsilon_s + \epsilon_d - \Pi_d),$$

$$\frac{\partial \widetilde{T}}{\partial t} = -(\gamma - 1)\nabla\cdot\mathrm{U}\,\widetilde{T} + (\epsilon_s + \epsilon_d - \Pi_d)c_v^{-1},$$

$$\frac{1}{2}\frac{\partial \overline{p^2}}{\partial t} = -\gamma\nabla\ \mathrm{U}\overline{p^2} - \gamma\overline{p}\,\overline{p}\Pi_d. \qquad (8)$$

and the usual equation of state. Equations in (8) require a closure for Π_d, and for the total dissipation $\epsilon_t = \epsilon_s + \epsilon_d$. There is virtually no dilatation dissipation in this flow and therefore ϵ_d is neglected. The equation for the solenoidal dissipation ϵ_s requires a special treatment because the molecular viscosity varies during compression. We used the ϵ_s equation proposed by Coleman & Mansour (1991) (in these proceedings) which yields a perfect agreement with the DNS data

Rapid distortion theory suggests that the pressure dilatation term Π_d have a rapid contribution, linear in $\overline{p^2}\nabla$ U. Hence, a new expression

$$\overline{p}\Pi_d\gamma\overline{p} = \frac{\overline{p^2} - p_e^2}{2\tau_a} + c_d\overline{p^2}\nabla\ \mathrm{U} \qquad (9)$$

has been proposed to account for the rapid compression contribution The free constant c_d has been determined from the rapid theory as $c_d = (5-3\gamma)/12$ (note that $c_d = 0$ for monatomic gases, and 0 066 in air). The details of the calculations leading to the determination of c_d are described in Sabel'nikov (1975) and Zeman & Coleman (1991). We note that in analogy with pressure-strain terms, we have in (9) the slow (relaxation) term and the rapid (compression) term. Here, however, the rapid condition requirement is $|\nabla\cdot\mathrm{U}|\tau M_t >> 1$, or in terms of the initial parameters

$$A_o\tau_o M_{to} >> 1 \qquad (10)$$

This new rapid condition is pertinent to the dilatational field and is stronger than the condition $A_o\tau_o >> 1$ for the solenoidal field

Finally, we note that during the rapid compression, the turbulence lengthscale (L) and timescale (τ) no longer depend on ϵ_s and therefore a relation such as $L \propto q^3/\epsilon_s$ may not be appropriate We can construct a lengthscale equation which yields the rapid limit satisfying $L^n\overline{p} = const.$ and the equilibrium limit $L \to q^3/\epsilon_s$ (when $\nabla\cdot\mathrm{U} \to 0$)·

$$\frac{DL}{Dt} = L\{\frac{0\,9}{\tau} + \frac{1}{n}\nabla\ \mathrm{U}\}, \qquad (11)$$

where n is an integer denoting the dimension of compression (or expansion) Eq. (11) is exactly valid only for rapid spherical compression; in 1D compression (n=1), it approximates the lengthscale variation in the direction of compression Now, in principle, τ in the modeling equations should be proportional to L/q We found, however that L/q decreased too rapidly and had undesirable effects on the model results We therefore used in the following calculations a timescale based on the geometric average: $\tau = \sqrt{qL/\epsilon_s}$.

DNS computations of rapidly compressed turbulence (in 1D and 3D) of Coleman (1991) for two initial Mach numbers M_{to} = 0 02 (Case A) and 0.44 (Case B) are presented in Figs 3, 4, 5, and 6 The initial field was a freely decaying turbulence with equilibrium pressure (density) fluctuations dependent only on M_{to}. The initial, rapid parameter $A_o\tau_o = 47$ was the same for both cases A and B. The 3D compression case is fairly straightforward: the kinetic energy growth (Fig. 3) is virtually identical for both cases A and B, and the pressure variance growths (in Fig. 4) are nearly the same. The DNS data agree well (within 4% error) with the rapid compression limit whereby the pressure dilatation Π_d is neglected (also $\epsilon_t = 0$). According to (7) and (8) this limit yields simple expressions:

$$\frac{q^2}{q_o^2} = (\frac{\overline{\rho}}{\rho_o})^{2/3} = (\frac{3}{1 - A_o t})^{2/3}, \quad \frac{\overline{p^2}}{p_o^2} = (\frac{3}{1 - A_o t})^{2\gamma}$$

which are independent of $M_t \approx M_{to}$. The evolution Π_d/ϵ_t for 3D compression only is shown in Fig. 5, the model-predicted values of Π_d. Here, the best match with the DNS data was achieved with the rapid part of the model in (9) discarded. It turned out that the rapid part of (9) (with $c_d = 0.066$) yielded undesirable (negative) contributions to Π_d immediately at the onset of the compression which is in disagreement with the DNS data.

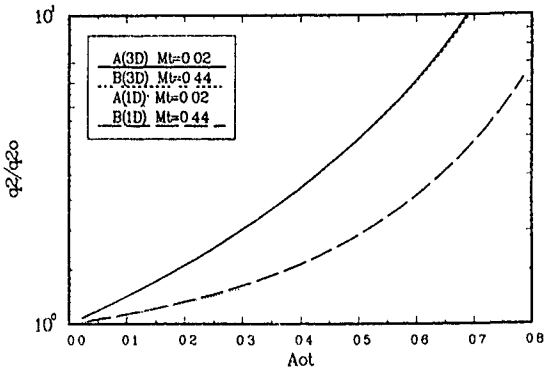

Fig. 3 Evolution of kinetic energy during rapid compression in 1D and 3D. Case A is for M_{to} = 0.02; Case B is for M_{to} = 0.44 DNS data of Coleman (1991)

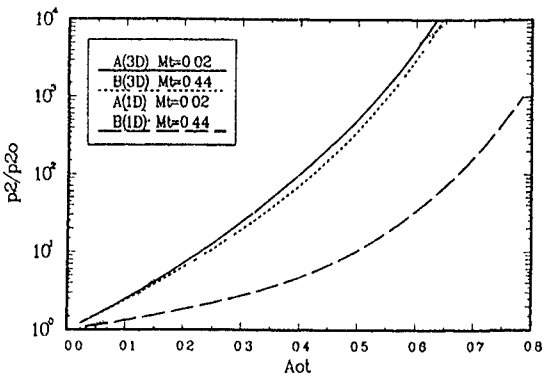

Fig. 4. Evolution of pressure variance; otherwise the same as Fig. 3.

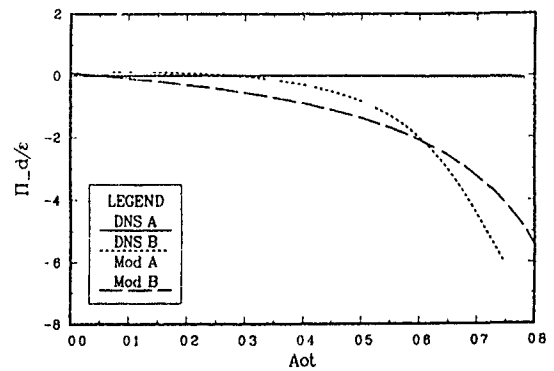

Fig 5 Evolution of the normalized pressure dilatation for 3D rapid compression: DNS data and model results.

Our conclusion is that overall, the 3D rapid compression of isotropic turbulence is a relatively simple modeling problem, however, this is not so in the case of 1D compression. Inspection of the Coleman DNS data in Figs 3 and 4 reveals some striking differences between 3D and 1D compression for the low Mach number case A. This is most clearly evident in the DNS data of $\overline{p^2}$. While the growth of pressure fluctuations agrees again with the rapid theory for Case B, it is seen that in the low M_t

case A, the relative growth of $\overline{p^2}$ is much more rapid. By the time $A_o t = 0.5$, the amplification of $\overline{p^2}$ in Case A is by the order $O(100)$ larger then in Case B. This unexpected behavior can be traced to the pressure-dilatation term shown for 1D compression in Fig. 6 Contrary to expectation, Π_d/ϵ_t grows much faster in Case A (with $M_{to} = 0.02 << 1$) than in Case B. This results in an unusually high energy transfer from the kinetic to pressure-fluctuation mode and thus to a significant loss of kinetic energy to $\overline{p^2}$, despite turbulence being nearly incompressible. This also explains the difference in the kinetic energy evolutions in 1D compression as indicated by the DNS data in Fig. 3.

Attempting to model this phenomenon, we have found that the isotropic compression model for Π_d in Eq. (9) is entirely inadequate since it does not distinguish between isotropic and anisotropic (directional) compression. Inspecting the conservation equation for $\overline{pu_{j,j}}$, we identified a new important term which appears to be responsible for strong dilatation/vorticity interactions in anisotropic compression From this term's form, the following contribution to Π_d was inferred (see Zeman & Coleman (1991) for details)

$$\Pi_d^A = -c_A \frac{p'}{\overline{\rho} M_t^2} q^2 \tau (S_{ij}^*)^2 \qquad (12)$$

where S_{ij}^* is the trace-free deformation tensor defined as $S_{ij}^* = \frac{1}{2}(U_{i,j} + U_{j,i} - \frac{2}{3}\nabla \cdot U \delta_{ij})$, c_A is an adjustable constant, and $p' = (\overline{p^2})^{1/2}$ Note that the contribution (12) is nonzero only if the compression is anisotropic (for 1D compression $(S_{ij}^*)^2 = \frac{2}{3}(\nabla \cdot U)^2$) A preliminary value of the free constant is $c_A = 0.0001$. It is of interest to note that an analogous term of the form $-M_t^{-1} \tau q^2 \overline{\rho'^2}/\overline{p}^2 (\nabla \cdot U)^2$ has also been suggested by Taulbee & VanOsdol (1991). However, in their final expression, Taulbee and VanOsdol retained only the linear term in $\nabla \cdot U$, which is similar to the rapid term in Eq (9) Similarly, Horstman (1987) proposed a closure for Π_d of the form $-\overline{M}^2 q^2 \nabla \cdot U$ where $\overline{M}$ is the mean local Mach number (in a boundary layer)

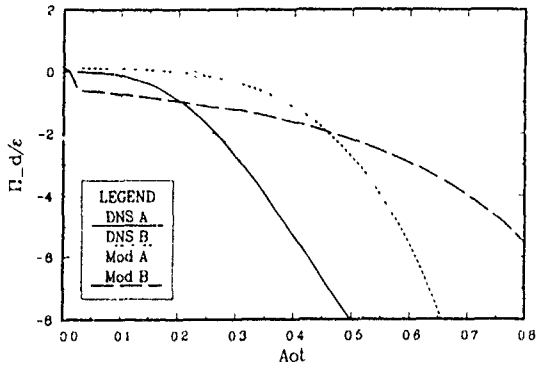

Fig. 6. Evolution of the normalized pressure dilatation for 1D rapid compression: DNS data and model results.

The DNS-model comparisons of the pressure dilatation and pressure variance in 1D rapid compression are in Figs. 6 and 7. It is seen that the model is capable of replicating the important feature of 1D compression: the difference in the kinetic-to pressure energy transfer and the resulting amplification rate of $\overline{p^2}$ between the low and high Mach number cases. It can be shown that without the anisotropic rapid term (12), the predictions for the low M_t case A would be virtually identical with Case B, hence in gross error. The unique effect of anisotropic rapid compression of nearly incompressible turbulence is also evident in shock-produced compression of turbulence as shown in the following section. In conclusion, in 1D rapid compression, the quadratic contribution (in $\nabla \cdot U$) in the pressure dilatation Π_d is more important than the linear one, and it is expected to be so, for example, in supersonic compression corner flows.

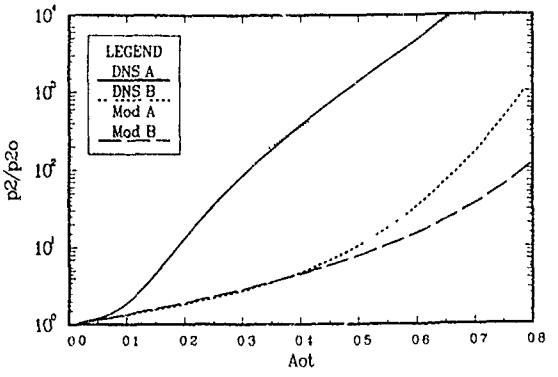

Fig. 7. DNS-model comparison of the pressure-variance evolution for 1D compression with the anisotropic pressure dilatation model

RESPONSE OF TURBULENCE TO A PASSAGE THROUGH SHOCKS

Here, we present the results of model simulation and comparison with the DNS data of Lee (1991) of the response of initially isotropic turbulence to a normal shock. To simplify the model computations, the mean shock flow is prescribed by the Rankine-Hugeniot relations. This is justified as long as the r.m.s velocities ($u' = \sqrt{q^2/3}$) are small compared to the jump across the shock ΔU, typically for the present computations $u'/\Delta U \leq 0.1$ The flow is inhomogeneous in and axisymmetric about the direction $x \equiv x_1$ normal to the shock, the mean quantities $U_1(x_1)$, $\overline{\rho}(x_1)$, and $\overline{p}(x_1)$ are known. The turbulence equations to be solved are

$$\frac{D\widetilde{u_1^2}}{Dt} = -2\widetilde{u_1^2} U_{1,1} - \frac{2}{\overline{\rho}} \overline{p}_{,1} \overline{u}_1 - \Pi_{11}^o - \frac{2}{3}(\epsilon_s - \Pi_d) - \frac{1}{\overline{\rho}}(T_{111} + 2\overline{pu_1})_{,1}$$

$$\frac{1}{2}\frac{Dq^2}{Dt} = -\widetilde{u_1^2} U_{1,1} - \frac{1}{\overline{\rho}} \overline{p}_{,1} \overline{u}_1 - (\epsilon_s - \Pi_d) - \frac{1}{2\overline{\rho}}(T_{j,j1} + 2\overline{pu_1})_{,1} \qquad (13)$$

Here, the operator $D/Dt \equiv U_1 \frac{\partial}{\partial x_1}$, $T_{j,1} = \overline{\rho u_i u_j u_1}$ are the nonzero third moments or fluxes in the x_1 direction. Π_{ij}^o are trace-free pressure-strain terms of the same form as in incompressible turbulence, these contains the customary slow and rapid terms, where the trace-free mean strain tensor S_{ij}^* must be used. Both $T_{j,1}$ and Π_{ij}^o are given in Zeman (1990); discussion of the pressure flux $\overline{pu_1}$ is deferred to the following paragraph. A version of the ϵ_s equation (in 1D) required to solve (13) is described in Zeman & Coleman (1991), and the L equation is as in (11) with $n = 1$. A new, inhomogeneous term in Eq (13) is the so-called acceleration term: the product of the mean pressure gradient $\overline{p}_{,1}$ and the fluctuation velocity average $\overline{u}_1 = -\overline{\rho' u_1}/\overline{\rho}$. A customary approach to modeling $\overline{u}_1$ has been utilization of the so-called Strong Reynolds Analogy (SRA) which yields $\overline{u}_1 \propto -\overline{u_1^2}/U_1$ According to the DNS data, this estimate is of wrong sign and results in gross errors (gain instead of loss of kinetic energy); we strongly suggest that the application of SRA be avoided in modeling turbulent boundary layers in the presence of shocks A more appropriate approach is to use a model rate equation for the mass flux $\overline{\rho' u_i}$:

$$\frac{D\overline{\rho' u_i}}{Dt} \approx -\frac{\overline{\rho' u_i}}{\tau_a} - \overline{u_i u_j}\,\overline{\rho}_{,j} - \overline{\rho' u_j} U_{i,j}. \qquad (14)$$

The first term on the RHS of (14) is a relaxation term, which drives the mass flux to zero (after the shock) on the fast acoustic timescale τ_a in accordance with the DNS data. Eq.(14) yields, within the shock, $\overline{\rho' u_1} < 0$, i.e the acceleration term in (13) dampens turbulence as expected by the Rayleigh-Taylor analogy. Application of the SRA yields an opposite (destabilizing) effect, which is unphysical.

Modeling the pressure flux $\overline{pu_i}$ is not straightforward. It would appear that in the incompressible limit $M_t \to 0$, $\overline{pu_i}$ should be negligible; however, in the vicinity of the shock, this is not so. It may be more appropriate to utilize the observed fact that the fluctuations of density and temperature are positively correlated (as opposed to SRA) so that

$$\overline{pu_i} = c_p \overline{\rho' u_i} a^2, \qquad (15)$$

where the mass flux $\overline{\rho' u_i}$ can be determined from (15). For the strictly adiabatic relation $T'/\tilde{T} = (\gamma - 1)\rho'/\overline{\rho}$, the constant $c_p = 1.0$. Note that according to (15), the divergence $(\overline{pu_i})_{,i}$ needed in (13) contains terms that would reduce the magnitude of the acceleration term.

The principal purpose of the preliminary computations presented next is to test the effect of the pressure dilatation and acceleration terms on the overall (modeled) response of turbulence to the shock and comparison with the DNS results. For simplicity we neglected the total energy flux divergence in (13). This is not entirely justified since the flux divergence is expected to yield energy gain, this gain is, however, of order $O(M_t)$ smaller than the remaining terms in (13).

The simulated flow is decaying isotropic turbulence subjected to compression through a normal shock with the upstream Mach number $M_1 = 1.18$ with the density (and velocity) ratio $\overline{\rho}_2/\overline{\rho}_1 = 1.31$. The r.m.s. Mach number immediately before the shock is $M_{to} = 0.13$, hence the initial compressibility-induced effects are relatively small. The results, using the modeling equations (13), (14), and (15), are presented in Figs. 8, 9, and 10. We remark that since the shock profiles of mean quantities are prescribed, the model is unable to reproduce the extremely high fluctuations levels associated with the shock motion. These fluctuations are passive and affect little the turbulence response to the shock.

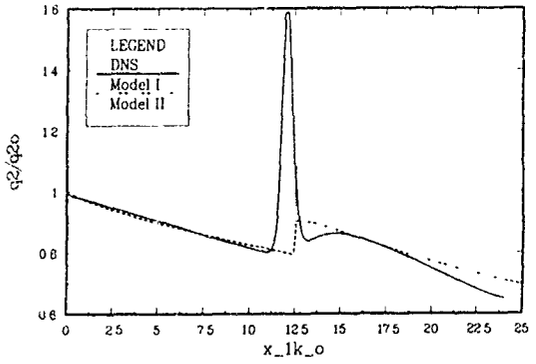

Fig. 8 Response of turbulence kinetic energy to the passage through normal shock: comparison of model prediction with DNS data of Lee (1991). Model I: with $c_A = 0.0004$ in Eq. (12); Model II. $c_A = 0.0$

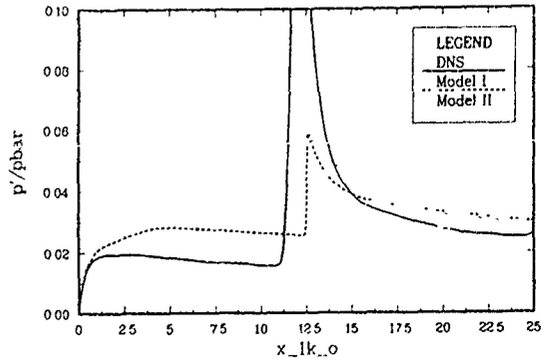

Fig. 9 Response of pressure variance, otherwise the same as Fig. 8.

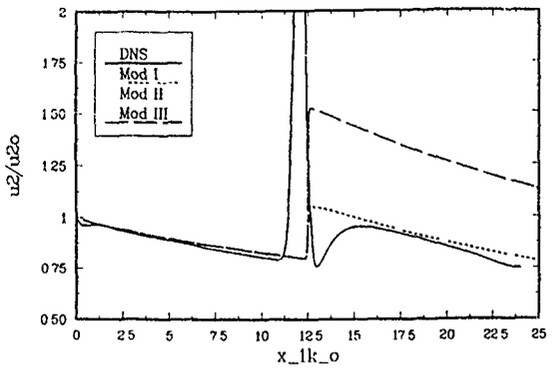

Fig. 10 Response of the streamwise component of kinetic energy ($\widetilde{u_1^2}$), otherwise the same as Fig. 8, except Model III (see text)

Here, Model I represents a base model with the acceleration term included and modeled with the aid of Eq. (14). The pressure dilatation model consists of Eq. (9) and the anisotropic contribution Π_d^A in (12). Model II results show the effect of neglecting Π_d^A, and Model III (only in Fig. 10) is the base model where the mass flux $\overline{u}_1 = -\overline{\rho' u_i}/\overline{\rho}$ in the acceleration term in (13) is evaluated according to SRA, i.e., $\overline{u}_1 = \widetilde{T' u_1}/\tilde{T}$. Since the heat flux $\widetilde{T' u_1}$ (computed from an equation analogous to (14)) is negative, the acceleration term provides, in this case, a large gain in the $\widetilde{u_1^2}$ budget. According to Fig. 10, Model III overpredicts the $\widetilde{u_1^2}$ amplification through the shock by about 200%. We emphasize that the model results presented here are only tentative and serve to point out the relative importance of various mechanisms in the shock/turbulence interactions. The detailed work on this problem is in progress.

SUMMARY

The subject of the presented work has been investigation of the pressure-dilatation interactions in shear-driven and rapidly compressed turbulence. The principal finding is that turbulence subjected to rapid directional (anisotropic) compression produces high negative values of the pressure-dilatation correlation, which in turn leads to a considerable transfer (loss) of turbulent kinetic energy to pressure fluctuations. This transfer mechanism has been found to be important even in nearly incompressible turbulence and is expected to be of importance in flows of practical interest such as internal combustion engine and turbulence/shock interactions.

A new model for the pressure-dilatation term has been proposed to account for this rapid compression effects. Preliminary modeling results indicate that a significant kinetic energy losses to pressure fluctuations may occur in the shock/turbulence interactions.

REFERENCES

AUPOIX, B., BLAISDELL, G. A., REYNOLDS, W. C. & ZEMAN, O. 1990 Modeling the turbulent kinetic energy equation for compressible, homogeneous turbulence, in Proceedings of the 1990 Summer Program, CTR, Stanford University.

BLAISDELL, G. A., 1990, *Numerical simulations of compressible homogeneous turbulence*, Ph. D. Thesis, Mechanical Engineering Dept., Stanford University.

COLEMAN, G. N. & MANSOUR, N. N. 1991 Direct simulations of homogeneous compressible turbulence under isotropic mean compression, in these proceedings.

HORSTMAN, C. C. 1987 Prediction of hypersonic shock-wave/turbulent-boundary-layer interaction, AIAA Paper 87-1367.

LEE, S 1991, personal communication.

LEE, S , LELE, S. & MOIN P 1991 Eddy shocklets in decaying compressible turbulence, Phys. Fluids **A 3**, 657.

PAPAMOSCHOU, D & ROSHKO, A. 1988 The compressible turbulent shear layer an experimental study, J. Fluid Mech. **197**, 453

SAMIMY, M & ELLIOTT, G S 1990 The effects of compressibility on the characteristics of free shear layers, AIAA J , **28**, 129.

TAULBEE, D. & VANOSDOL, J 1991 Modeling turbulent compressible flows the mass fluctuating velocity and square density, AIAA paper 91-0521.

ZEMAN, O 1990 Dilatation dissipation The concept and application in modeling compressible mixing layers, Phys Fluids A 2, 178.

ZEMAN, O 1991 On the decay of compressible isotropic turbulence, Phys. Fluids **A 3**

ZEMAN, O 1991a Toward a constitutive relation in compressible turbulence, in Proceedings of John Lumley's 60th Birthday Symposium, 1990.

ZEMAN, O & BLAISDELL, G A 1990 New physics and models for compressible turbulence, in Advances in Turbulence 3, eds A V. Johansson & H P Alfredsson, Springer-Verlag, 1991

ZEMAN, O & COLEMAN, G N 1991 Rapidly compressed turbulence in one and three dimensions. simulations, physics, and modeling, in preparation

EIGHTH SYMPOSIUM ON
TURBULENT SHEAR FLOWS
Technical University of Munich
September 9-11, 1991

Effect of Mach number on Communication between Regions of a Shear Layer

Dimitri Papamoschou

Department of Mechanical and Aerospace Engineering
University of California, Irvine, CA 92717, USA

ABSTRACT

A physical interpretation of the stabilizing effect of Mach number on free shear flows is offered. The effect of Mach number on communication between regions of a shear layer addressed and quantified in the limit of geometric acoustics. The sound emitted by a high-frequency acoustic source, located inside a shear layer, is studied. The generalized Snell's law is used to construct acoustic rays which are shown to be highly distorted because of the Mach-number gradient. Sound-intensity calculations reveal that the influence of the source on the surrounding medium becomes confined to a smaller and smaller area as the Mach number increases. It is proposed that the inhibited communication among regions of the flow field is a fundamental reason for the inherent stability of compressible shear flows.

INTRODUCTION

Perhaps the most characteristic effect of Mach number on free shear flows is that it suppresses their growth and instability. Landau (1944) first showed that the vortex sheet becomes stable when the relative Mach number exceeds a critical value ($\sqrt{2}$ for the equal-density case). Early linear analyses (Lin 1953, Gropengiesser 1970) and single-stream experiments (Sirieix & Solignac 1966) found that the growth rates of compressible, finite-thickness shear layers, decrease sharply with increasing Mach number. Recent linear analyses (Ragab & Wu 1988, Zhuang *et.al* 1988), computations (Sandham & Reynolds 1989) and two-stream experiments (Chinzei *et al* 1986, Papamoschou & Roshko 1988) covering a larger range of conditions, confirmed the above trends. The experiments, in particular, showed that at high Mach numbers the turbulent shear-layer growth rate decreases to as little as one fifth of the incompressible value. Despite recent significant gains in the compressible turbulence field, a physical explanation of the basic mechanism by which compressibility reduces the growth rate is not yet well established.

While compressible shear flows generally contain density gradients, density effects alone are not responsible for the large reduction in growth rates. Brown and Roshko (1974) showed that the growth rate of the subsonic, variable-density shear layer changed only by about 50% when the density ratio was varied by a factor of 50. There is, therefore, a large effect associated with the Mach number itself. Morkovin (1987) stresses that upstream and cross-flow communication is essential for instabilities at supersonic and hypersonic speeds. This point is primarily based on Mack's (1984) linear stability analysis, where it is shown that the most unstable waves are those whose phase speed is subsonic relative to the free-stream velocity.

In abstract terms, we may attribute the flow stability to the hindrance of communication among parts of the shear flow caused by the Mach number. Morkovin suggests the existence of zones of influence, defined by Mach cones, outside which a disturbance is not felt. Breidenthal's (1990) compressible-turbulence model is based on the assumption that turbulent eddies whose rotational Mach number is greater than unity do not participate in fluid entrainment, while those with rotational Mach number of unity or less engulf fluid like incompressible eddies. The mixing-length model of Kim (1990) for a supersonic shear layer assumes that disturbances do not penetrate outside a region bounded by relative sonic velocities.

The above models are useful because they capture the *essential nature* of supersonic flow. However, they are incomplete in the following sense. first, there is strong experimental and theoretical evidence (see references above) that stabilization starts at low values of the Mach number where relative sonic velocities cannot be defined, second, the fact that the relative velocity is greater than sonic does not prove that information will not propagate outside the region bounded by that velocity. We must be reminded that, in a shear layer, we are dealing with a smoothly-varying velocity profile. Traditional examples that illustrate lack of communication in supersonic flow, such as a supersonic airplane approaching an observer on the ground, can be used here only in a heuristic sense.

The present study attempts to address the effect of Mach number on propagation of information in a shear layer with smoothly varying velocity profile in a more quantitative, albeit *still idealized*, manner. It should be stated at the outset that sound propagation in the presence of Mach-number gradients has been the topic of numerous studies, some referenced later. The intent of this paper is not to add to the existing theory, but rather to use that theory to understand and quantify the hindrance of communication caused by the Mach number in a shear layer, in a manner that may help further refinement of compressible-turbulence models. Geometric acoustics theory is used because of its relative simplicity and capability to produce a "picture" of the sound field by ray tracing.

GEOMETRIC ACOUSTICS THEORY

At high Mach numbers, the acoustic wave length of the dominant instability is similar to or smaller than the characteristic thickness of the shear layer. Further elaboration on this topic can be found in the discussion section. It is thus possible that geometric acoustics, and the related ray theory, could be a reasonable approximation for studying sound propagation in a compressible shear layer, at least for obtaining qualitative trends. The approximation improves

as the acoustic wavelength becomes much smaller than the characteristic thickness of the refractive-index gradient (a generalized definition of sound refrac ive index in a moving medium is presented later).

The study of geometric acoustics in a moving medium has been extensive, so here we mention only a few selected works. The subject was first addressed by Lord Rayleigh (1945) who presented the basic principles behind sound propagation in wind shear and used simple arguments to expanded Snell's law to include velocity gradients The fundamental wave and energy equations were formally established by Blockhintzev (1946) whose "energy invariance" law allows calculation of acoustic intensity once the ray paths are known Hayes (1968) developed concise equations for ray geometry and acoustic energy in a three-dimensional environment and showed that these equations hold even when the moving medium is unsteady, in the linearized sense

Ray construction has been a popular method for obtaining an overall view of the acoustic field and for calculating acoustic intensity Some of the early ray constructions were performed by Kornhauser (1953), who considered the problem of a source in a linear velocity gradient More recently, ray construction has been used for calculating the acoustic field in ducts containing shear flows (Grimm & Hurst 1979), as well as sound propagation and caustic formation in a boundary layer (Kriegsmann & Reiss 1983)

Here we will examine the sound field generated by a source in a shear layer as monitored by an observer moving with the fluid, with emphasis on the effect of Mach number on ray distortion and the resulting acoustic intensity distribution We consider a parallel shear layer with velocity dependent only on the transverse coordinate y, and examine how an acoustic source inside the shear layer is felt in the surrounding flow field To facilitate the analysis, we place ourselves in the frame of reference moving with the local flow velocity This transformation is depicted in Fig. 1.

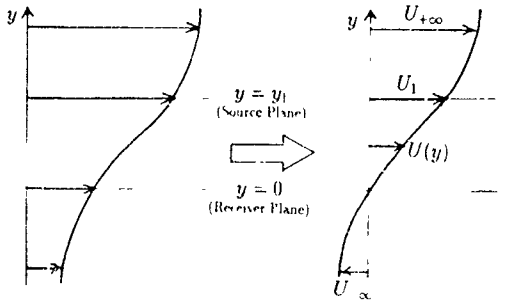

Fig 1 Transformation to receiver frame of reference

The frame on which we are stationary is located on the plane $y = 0$ which, for the purposes of this paper, will act as the "receiver" plane From this plane, we see a velocity distribution $U(y)$ The acoustic source is taken to be fixed relative to the receiver and is located at $(0, y_1)$ On the "source" plane $y = y_1$, the velocity is U_1 The edges of the shear layer are defined by the velocities $U_{+\infty}$ and $U_{-\infty}$. We will restrict ourselves to a two-dimensional problem where all interactions occur on the $x - y$ plane We are interested in the geometry of the ray that connects point $(0, y_1)$ on the source plane with point $(x_0, 0)$ on the receiver plane (Fig 2) The group velocity, V, consists of the geometric sum of the local velocity vector and the local speed-of-sound vector. The speed-of-sound vector is inclined at the wave-normal angle θ with respect to the vertical.

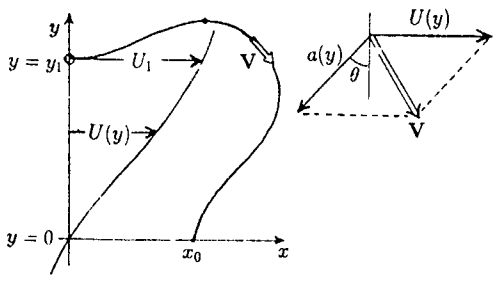

Fig 2 Ray path and group velocity

Lord Rayleigh (1945) postulated that the velocity of the trace of an acoustic wave front on an interface between gases of slightly-different velocities is constant and arrived at at the following relation between U, a, and θ:

$$\sin\theta = \frac{a}{U + C} \tag{1}$$

where C is a constant. This relation has been verified by more rigorous treatments of ray theory, such as the work of Hayes (1968)

Relating the constant C in Eq.(1) to the conditions U_1, a_1 and θ_1 at the ray origin $(0,y_1)$, we obtain the following form of Eq (1):

$$\sin\theta = \sin\theta_1 \left[\frac{a}{a_1 + (U - U_1)\sin\theta_1} \right] \tag{2}$$

which can be seen as Snell's law of refraction generalized to a moving medium

RAY CONSTRUCTION

Given the conditions at the ray origin (U_1, a_1, θ_1) and the velocity and speed-of-sound distributions, construction of the rays is now possible since θ is known from Eq.(2). The differential equations for the rays $dx/xt = U - a\sin\theta$ and $dy/dt = -a\cos\theta$ were integrated using a 4^{th}-order Runge-Kutta method with variable time step. Computations were performed an a personal AT-386 computer. The ray constructions shown here correspond to a=constant and $U(y)$ described by a hyperbolic-tangent profile of the form

$$\begin{aligned} U(y) &= A + B\tanh(\alpha y + \beta) \\ A &= \frac{U_{+\infty} - U_{-\infty}}{2} \\ B &= \frac{U_{+\infty} + U_{-\infty}}{2} \\ \beta &= \tanh^{-1}\left(\frac{A}{B}\right) \\ \alpha &= \tanh^{-1}\left(\frac{U_1 - A}{B}\right) - \beta \end{aligned} \tag{3}$$

The velocity profile is such that y_1=1 (i.e., the distance between source and receiver plane stays constant) for all prescribed values of U_1, $U_{+\infty}$ and $U_{-\infty}$

All rays originate at $(0, y_1)$, and the receiver (zero-velocity) plane is at $y = 0$ The Mach number at the ray origin is $M_1 = U_1/a$. The free-stream velocity above the ray origin is $U_{+\infty}$ and that below the receiver plane is $U_{-\infty}$, defined positive. If the ray origin and receiver are chosen to be at the edges of the shear layer, then $U_{+\infty} = U_1$ and $U_{-\infty} = 0$. In the present constructions, $U_{+\infty} = 1.5U_1$ and $U_{-\infty} = 0.5U_1$.

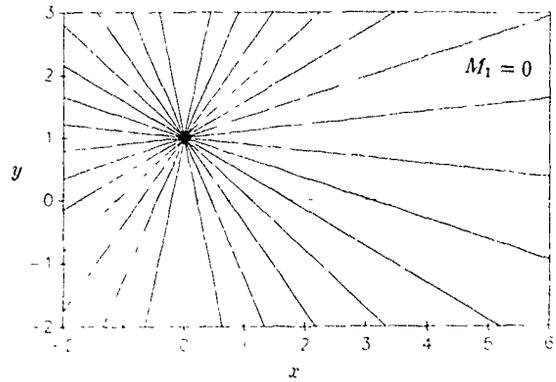

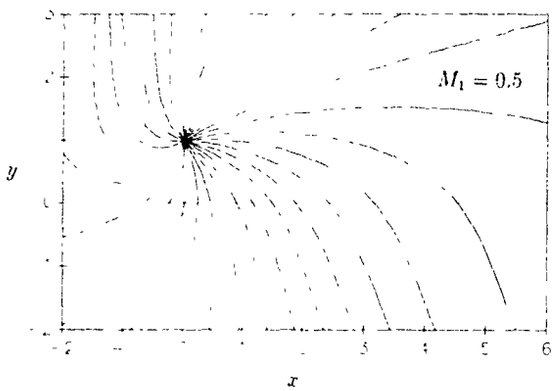

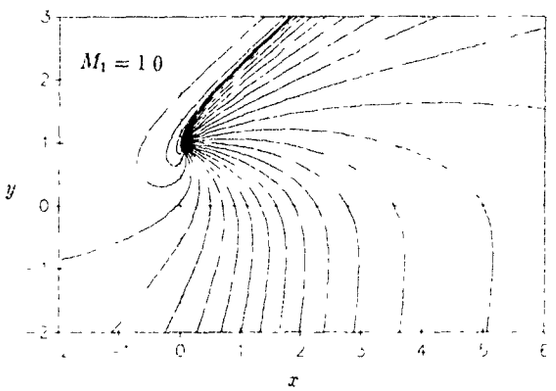

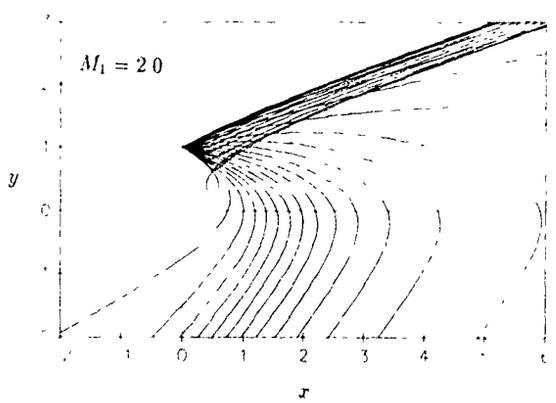

Fig. 3 Ray construction for different M_1's. Speed of sound is constant.

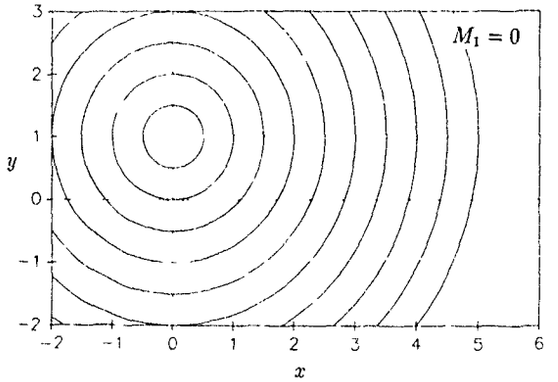

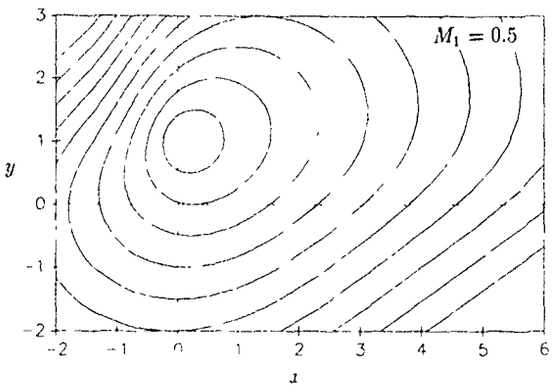

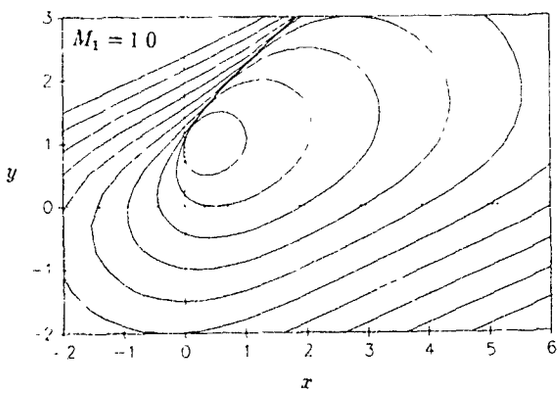

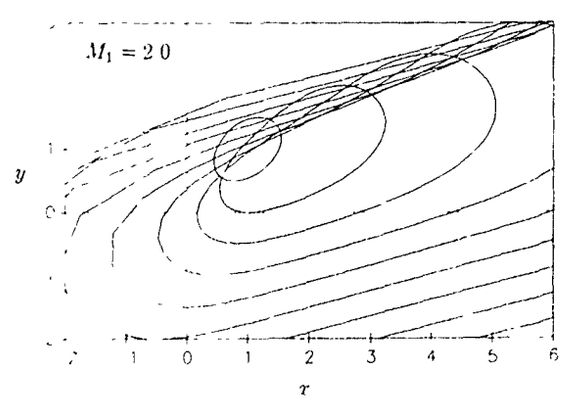

Fig. 4 Wave fronts corresponding to the rays of Fig. 3 Time interval between waves is 0.5, with $a = 1$

Fig. 3 shows the ray paths for M_1=0, 0.5, 1 0, and 2.0 The rays correspond to θ_1 ranging from 0 to 300° in 12° increments For M_1=0, the rays are straight, since no gradients are present. As M_1 increases, the rays get progressively more distorted In the cases with $M_1 > 1$, certain rays that are originally directed away from the receiver plane get reflected from the upper flow region and eventually cross the receiver plane. Although not included on the figure, some rays that cross the receiver plane get reflected from the lower flow region and cross the receiver plane once more.

Knowing the geometry of the ray paths we can also construct the wave fronts, shown in Fig. 4. The time interval between wave fronts is 0.5, with $a = 1$ and $y_1 = 1$. As expected, the wave fronts also become distorted as the Mach number increases The wave-front geometries for the M_1=2 case are particularly interesting as they illustrate that, even though the velocity at the source is supersonic, the signal eventually propagates upstream of the source This is due to the ray reflections from the lower flow region, as illustrated in Fig 7.

ACOUSTIC INTENSITY DISTRIBUTION

Of interest now is to find the sound intensity received by point $(x,0)$ from an acoustic source at $(0,y_1)$. The sound intensity is commonly defined as $I = \overline{p'^2}/(\rho a)$ where p' is the acoustic pressure fluctuation and ρ the density of the medium A fundamental energy-conservation law in incompressible geometric acoustics is that the product of intensity and ray-tube area remains constant. For the compressible case, the conservation law for I, derived by Blochintzev (1946) and by Hayes (1968), is of the form

$$\frac{I\, a\, A_n}{\Omega^2} = \text{constant} \qquad (4)$$

where A_n is the ray-tube area, defined by the intersection of adjacent rays with wave fronts, and $\Omega = \omega/(1 - M\sin\theta)$ the sound frequency heard by an observer moving with the medium, with ω the frequency of the acoustic source Note that the expression in Eq (4) cannot be evaluated at the source Rather, an assumption must be made as to the value of the acoustic energy flux IaA_n/Ω^2 conserved within each ray tube

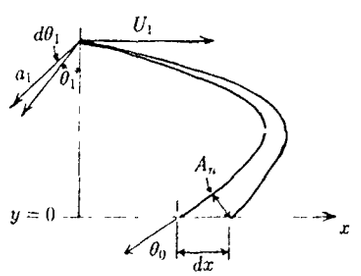

Fig 5 Ray-tube geometry

To define a ray tube, we consider two adjacent rays originating from the source with wave-normal angles θ_1 and $\theta_1 + d\theta_1$, as shown in Fig. 5. We now make the assumption that the source is omnidirectional, that is, the energy flux is uniformly distributed with θ_1 Consequently, each ray tube contains an energy flux $\mathcal{E}d\theta_1$, where $\mathcal{E}$ is a constant. The energy invariance of Eq.(4) becomes

$$\frac{I\, a\, A_n}{\Omega^2} = \mathcal{E}d\theta_1$$

On the receiver plane, where $M = 0$, the wave fronts are perpendicular to the rays This gives $A_n(x,0) = dx\cos\theta_0$, where dx is the "footprint" of the ray tube on the x-axis and θ_0 the angle at which it crosses the x-axis (Fig 5). Also, we note that $\Omega(x,0) = \omega$=constant, since $M(x,0)$=0 For $a = a_1$=constant, the intensity on the x-axis is

$$I(x) = \frac{\omega^2\mathcal{E}}{a_1}\frac{d\theta_1}{dx\cos\theta_0}$$

In this paper, we will be comparing intensity distributions created by a source with constant $\mathcal{E}$ and ω, hence the first fraction on the right-hand side will remain constant. For the sake of simplicity, and without losing any information on the Mach-number effect, we set $\omega^2\mathcal{E}/a_1 = 1$ and obtain

$$I(x) = \left(\cos\theta_0\,\frac{dx}{d\theta_1}\right)^{-1} \qquad (5)$$

The derivative $dx/d\theta_1$ was computed by numerical integration (4^{th}-order Runge Kutta) of the relation $dx = (U - a\cos\theta)dt$, in connection with Eq (2)

Computations of $I(x)$ were carried out for the conditions corresponding to the ray constructions in Fig 3. The intensity distributions are shown in Fig 6, where it is observed that they become narrower as M_1 increases At high M_1, the intensity reaches very low values not far from the source It is instructive to connect these distributions to the ray constructions of Fig 3 The low intensities are generally associated with rays that cross the $y = 0$ plane after reflecting from the upper or lower flow regions, with resulting large ray-tube areas

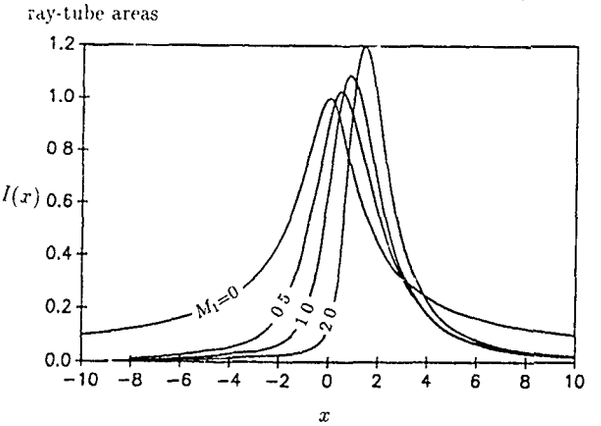

Fig 6 Acoustic intensity distributions

INTEGRATED INTENSITY

The intensity distributions of Fig. 6 indicate that, as the Mach number at the source location increases, communication between the source and the receiver plane is confined to a smaller region. To make quantitative comparisons among the different distributions, we examine the integrated intensity along x

$$E = \int_{-\infty}^{+\infty} I(x)dx \qquad (6)$$

where E can be seen as a measure of the total acoustic energy flux received on the $y = 0$ plane. From Eq (5), we

have

$$E = \int_{-\infty}^{+\infty} \frac{d\theta_1}{\cos\theta_0 \, dx} dx = \int_{\theta_1 - lim} \frac{d\theta_1}{\cos\theta_0} \qquad (7)$$

Note that the integral in x is converted to an integral in θ. The relation between θ_0 and θ_1 is known through Eq.(2)

$$\sin\theta_0 = \frac{a_0 \sin\theta_1}{a_1 - U_1 \sin\theta_1} \qquad (8)$$

thus evaluation of the integral in Eq.(7) is straight-forward once the limits for θ_1 are determined. To find these limits, we must establish the range of θ_1 for which rays actually cross the $y = 0$ plane. Obviously, the rays that do not cross the receiver plane do not contribute to the energy flux received Also, attention must be paid to which rays cross the receiver plane twice.

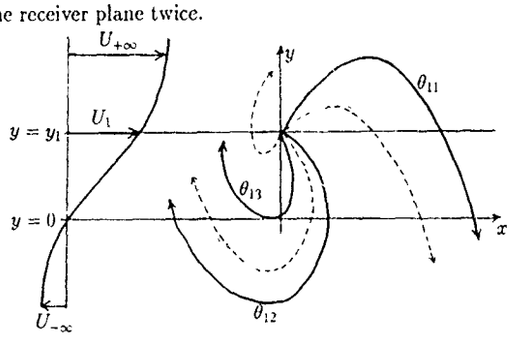

Fig 7 Ray reflections from shear-layer boundaries.

The sketch of Fig 7 helps us visualize the discussion that follows First, we note that no reflections can occur in the uniform free stream outside the layer Therefore, all reflections will occur within the edges of the shear layer, defined by the velocities $U_{+\infty}$ and $U_{-\infty}$. We now examine the ray paths as θ_1 increases from $-\pi$ Let θ_{11} be the value of θ_1 corresponding to the first reflection on the upper boundary ($U = U_{+\infty}$, $a = a_{+\infty}$, $\sin\theta = -1$), which produces the rightmost ray that crosses the $y = 0$ plane As θ_1 increases beyond θ_{11}, the rays cross the receiver plane and exit to the lower free stream until the first reflection on the lower boundary ($U = -U_{-\infty}$, $a = a_{-\infty}$, $\sin\theta = +1$) occurs at the value $\theta_1 = \theta_{12}$ For $\theta_1 > \theta_{12}$, all rays that are initially directed downwards get reflected upwards. Consequently, they cross the receiver plane twice, until the reflection occurs above $y = 0$. The last ray crossing the receiver plane ($U = 0$, $a = a_0$, $\sin\theta_0 = +1$) corresponds to $\theta_1 = \theta_{13}$. For $\theta_1 > \theta_{13}$, no more rays cross the receiver plane.

Since the conditions under which rays reflect from the boundaries are known, the values of the corresponding θ_1's are readily obtained from Eq.(2). We have.

$$\theta_{11} = -\pi + Sin^{-1}\left(\frac{a_1}{a_{+\infty} + U_{+\infty} - U_1}\right)$$

$$\theta_{12} = Sin^{-1}\left(\frac{a_1}{a_{-\infty} + U_{-\infty} + U_1}\right) \qquad (9)$$

$$\theta_{13} = Sin^{-1}\left(\frac{a_1}{a_0 + U_1}\right)$$

and Eq (8) becomes·

$$E = \int_{\theta_{11}}^{\theta_{12}} \frac{d\theta_1}{\cos\theta_0} + 2\int_{\theta_{12}}^{\theta_{13}} \frac{d\theta_1}{\cos\theta_0} \qquad (10)$$

The last integral is multiplied by two because, for $\theta_{12} < \theta_1 < \theta_{13}$, the rays cross the receiver plane twice, hence deliver their energy flux twice If the receiver is chosen to be located at the lower edge of the shear layer, then $\theta_{12} = \theta_{13}$ and the last integral vanishes. It is interesting to note that the result given by Eq.(10) does not depend on the specific functions that describe $U(y)$ and $a(y)$ but only on the free-stream, source, and receiver conditions

Calculations of E were performed for constant speed of sound and for the following free-stream conditions:
(a) $U_{+\infty} = U_1$, $U_{-\infty} = 0$ (no reflections);
(b) $U_{+\infty} = 1.5U_1$, $U_{-\infty} = 0.5U_1$ (moderate reflections);
(c) $U_{+\infty} = 3U_1$, $U_{-\infty} = 2U_1$(strong reflections).
The integrated intensity E is plotted versus M_1 in Fig. 8 First, we note that for M_1=0, $E = \infty$. This is not surprising as we realize that the straight rays of the incompressible, uniform-density case, create a footprint of infinite extent on the x-axis. However, as M_1 becomes finite, E also becomes finite and decreases with increasing M_1, reaching an asymptotic value at high M_1. The magnitude of E is higher when ray reflections occur, as is expected from Eq (10)

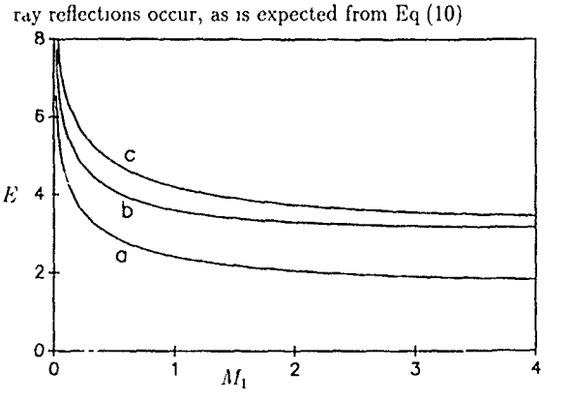

Fig 8 Integrated intensity versus M_1 for
(a) no ray reflections;
(b) moderate reflections;
(c) strong reflections

DISCUSSION

The intensity curves of Fig. 6 warrant some discussion. Let us start by noting that sound propagation gets altered significantly even at low values of the Mach number This is further demonstrated by the integrated intensity plots of Fig 7 Hence the velocity difference need not be sonic or supersonic for the Mach number effect on communication to become dominant

If we were located at the same streamwise position as the source ($x = 0$), we would feel a gradual loss of sound intensity as the Mach number at the source location increases, but we would not be completely cut off from the source even at high Mach numbers At $M_1 = 1$, for example, the intensity loss would be about 40%. The $M_1 = 1$ case represents communication between the edges and the center of a region bounded by relative sonic velocities. It is only when $M_1 > 2$ that communication at $x = 0$ becomes significantly restricted, but is still non-zero

As M_1 increases, communication is inhibited both upstream and downstream of the source, with the upstream communication being attenuated faster with distance than the downstream communication. This may provide some physical insight into the cause of stability at high Mach numbers. Since communication between fluid particles is vital for the onset and development of turbulent interac-

tions (perhaps best illustrated in shear-flow computations using vortex methods), lack or hindrance of communication will lead to slower responses to a given perturbation, hence increased stability

The present study has been restricted to constant speed of sound, primarily to highlight the effects of Mach number uncoupled from effects of density variation The equations presented here, however, are general enough that they can be applied to cases with speed-of-sound variation, provided $a = a(y)$ only

The central question is, of course, how applicable are the present results to a turbulent compressible shear layer. In reality, the flow is unsteady and the disturbance wavelengths may not be short enough for geometric acoustics to be valid. However, there is reason to believe that the underlying assumptions of this study, *i.e.* steady flow and small wavelength, may not be as unrealistic as one might initially think The linear stability analysis of Mack (1984) has shown that, at high Mach numbers, the most unstable, higher-mode waves occur at frequencies about three times those of the first-mode waves Experiments on shear layers by Papamoschou (1989) have indicated that the large-scale turbulent structure is very inactive at high Mach numbers: there is imperceptible structure rotation and no evidence of pairing In recent schlieren visualizations of supersonic shear layers at very high Reynolds numbers by Hall *et.al* (1991), large-scale structures are not discernible but small-scale turbulence is prevalent. Thus, there is increasing, albeit preliminary, evidence that small scale turbulence may be the dominant source of instability at high Mach numbers, which would be in line with the small-wavelength assumption of this study Furthermore, since supersonic shear layers grow so slowly, with fluctuation levels substantially lower than in the incompressible case (Sammy & Elliot 1990), they are much less unstable than their subsonic counterparts Note that Hayes (1968) has shown that ray theory is still valid in flow with small unsteadiness.

It is hoped that the above findings and discussion will aid in the construction of more refined compressible turbulence models that take into account the intricate ways in which sound can propagate in a shear flow at high Mach numbers The analysis presented here represents a first step towards that goal, and in the future needs to be expanded beyond the restrictions of geometric acoustics

CONCLUSION

Geometric acoustics theory has been applied to study the effect of Mach number on the sound field created by a source inside a two-dimensional shear layer It is found that the Mach number severely distorts the acoustic rays, creating regions where little signal is heard Sound-intensity distributions on a streamwise plane become narrower with increasing Mach number, indicating a diminishing influence of the source on the surrounding medium The study suggests that the Mach number inhibits acoustic interactions in the shear layer, which is offered here as a fundamental explanation for the stability observed at high Mach numbers

REFERENCES

BLOCKHINTZEV, D. 1946 The propagation of sound in an inhomogeneous and moving medium I. *J Acous Soc Am.* **18(2)**, 322-330

BROWN, G L & ROSHKO, A 1974 On density effects and large-scale structures in turbulent mixing layers. *J Fluid Mech.*, **64(4)**, 775-781.

CHINZEI, N , MASUYA, G., KOMURO, G., MURAKAMI, T. & KUDOU, K 1986 spreading of two-stream supersonic mixing layers *Phys. Fluids* **29**, 1345-1347.

GRIMM, D W. & HURST, C.J. 1979 A geometric acoustics approach to the study of sound propagation in ducts containing shear flows *J. Acous. Soc. Am.* **66(6)**, 1867-1875.

GROPENGIESSER, H 1970 Study of the stability of boundary layers in compressible fluids *NASA TT-F-12*, 786.

HALL, J.L., DIMOTAKIS, P E., & ROSEMANN, H. 1991 Experiments in non-reacting compressible shear layers. *AIAA-91-0629*

HAYES, W.D 1968 Energy invariant for geometric acoustics in a moving medium. *Phys Fluids* **11(8)**, pp. 1654-1656.

KIM, S C. 1990 New mixing length model for supersonic shear layers *AIAA J* **28(11)**, 1999-2000

KORNHAUSER, E T. 1953 Ray theory in moving fluids. *J Acous Soc. Am* **25(5)**, 945-949.

KRIEGSMANN, G.A. & REISS, E L 1983 Acoustic propagation in wall shear flows and the formation of caustics *J Acous Soc. Am.* **74(6)** pp. 1869-1879.

LANDAU, L. 1944 Stability of tangential discontinuities in compressible fluid. *Dokl. Akad Nauk. SSSR* **44(4)**, 1944, pp 139-141

LIN, C.C. 1953 On the stability of the laminar region between two parallel streams in a gas. *NACA Report TN 2887.*

MACK, L M 1984 Boundary-layer linear stability theory. *AGARD Report R-709.*

MORKOVIN, M V 1987 Transition at hypersonic speeds. *NASA-CR-178315, ICASE Interim Report 1*

PAPAMOSCHOU, D. 1989 Structure of the compressible turbulent shear layer *AIAA-89-0126.*

PAPAMOSCHOU, D. & ROSHKO, A 1988 The turbulent compressible shear layer. an experimental study. *J. Fluid Mech.* **197**, 453-477

RAGAB, S A and WU, J.L 1988 Instabilities in turbulent free shear layers formed by two supersonic streams. *AIAA-88-0038*

LORD RAYLEIGH 1945 Theory of Sound, Vol 2, p.132 Dover, New York, 1945.

SAMIMY M & ELLIOTT, G.S 1990 Effects of compressibility on the characteristics of free shear layers *AIAA J* **28(3)**, 438-445

SANDHAM, N & REYNOLDS, W 1989 The compressible mixing layer: linear theory and direct simulation. *AIAA-89-0371*

SIRIEIX, M & SOLIGNAC, J.L 1966 Contribution a l'etude experimentale de la couche de melange turbulent isobare d'un ecoulement supersonique. *Symposium on Separated Flow, AGARD Conf Proc.* **4(1)**, 241-270

ZHUANG, M KUBOTA, T & DIMOTAKIS P.E. 1988 On the instability of inviscid, compressible shear layers *AIAA-88-3558-CP*

EIGHTH SYMPOSIUM ON
TURBULENT SHEAR FLOWS
Technical University of Munich
September 9-11, 1991

Analysis of turbulent mixing models.

J.-Y. Chen*), W. Kollmann**)

*) Combustion Research Facility, Sandia National Laboratories, Livermore, CA 94551-0969, Research supported by the United States Department of Energy, Office of Basic Energy Sciences, Division of Chemical Sciences.
**) MAME Department, University of California at Davis, CA 95616

Abstract.

The mixing model based on pairwise interaction of notional particles in scalar space is analyzed. The equations for the higher normalized moments show that the model based on uniform probability for the outcome of the mixing interaction does not approach a Gaussian pdf in the limit of decaying or maintained turbulence. Further analysis of the mixing model generalized to conditional pdfs shows that mixing can be regarded as jump process, where selected notional particles undergo mixing and particles not selected remain unaffected. The jump rate pdf is shown to depend on the pdf itself reflecting the availability of mixing partners. Finally, it is shown that a modification of the pdf describing the amount of mixing during pairwise interaction leads to a mixing model which is governed by a Fokker-Planck type equation.

1.0 Introduction.

The calculation of turbulent flows with chemical reactions based on pdf methods requires a closure model for mixing. Two approaches have been developed to deal with this aspect of pdf methods. First, simplified mechanisms for mixing in a turbulent environment were proposed and their statistical properties lead to closure models (Dopazo 1975,1979, Janicka et al 1979, Pope 1982,1985) and second, mappings were proposed to express the pdf in terms of a Gaussian and the Jacobian of the nonlinear mapping (Chen,Chen and Kraichnan 1989). Following the first approach a class of closure models based on the notion of pairwise interaction will be analyzed. It will be shown that either a jump process or the approximation of a smooth process satisfying a Fokker-Planck type equation results depending on the shape of a pdf describing the degree of mixing.

The pdf transport equation for the set of l thermo- chemical variables can be given for high Reynolds numbers in the form (see Kollmann, 1987)

$$\langle\rho\rangle\{\frac{\partial\tilde{f}_1}{\partial t}+\tilde{v}_\beta\frac{\partial\tilde{f}_1}{\partial x_\beta}+\sum_{j=1}^{l}\frac{\partial}{\partial\varphi_j}(Q_j(\varphi_1,\cdots,\varphi_l)\tilde{f}_1)\}=$$

$$-\frac{\partial}{\partial x_\alpha}(\langle\rho\rangle\langle v''_\alpha|\Psi_j=\varphi_j\rangle\tilde{f}_1)$$

$$-\langle\rho\rangle\sum_{j=1}^{l}\sum_{k=1}^{l}\frac{\partial^2}{\partial\varphi_j\partial\varphi_k}(\langle\epsilon_{jk}|\Psi_j=\varphi_j\rangle\tilde{f}_1) \qquad (1)$$

where the density-weighted pdf $\tilde{f}_1$ is defined by

$$\tilde{f}_1\equiv\frac{\rho(\varphi_1,\cdots,\varphi_l)}{\langle\rho\rangle}f_1(\varphi_1,\cdots,\varphi_l;\underline{x},t) \qquad (2)$$

and the scalar dissipation rates ϵ_{ij} in the conditional expectations are defined by

$$\epsilon_{ij}\equiv\Gamma\frac{\partial\Psi_i}{\partial x_\alpha}\frac{\partial\Psi_j}{\partial x_\alpha} \qquad (3)$$

with $\Gamma_i=\Gamma_j=\Gamma$. For homogeneous flows without chemical reaction the pdf equation describes turbulent mixing at a single point

$$\frac{\partial\tilde{f}_1}{\partial t}=-\sum_{j=1}^{l}\sum_{k=1}^{l}\frac{\partial^2}{\partial\varphi_j\partial\varphi_k}(\langle\epsilon_{jk}|\Psi_j=\varphi_j\rangle\tilde{f}_1) \qquad (4)$$

Any closure model for the mixing process described by (4) should share as many properties as possible with the exact term. It should preserve normalisation and mean values and decrease variances and covariances. The pdf should remain nonnegative and should not spread outside the domain of allowable states. The presently available models for the mixing process in the pdf equation have several shortcomings (Pope, 1985 and Chen and Kollmann, 1989). The development of improved mixing models requires careful analysis of the physics of mixing and the mathematical properties of the corresponding terms in the equation for the pdf. The case of a single scalar variable will be considered for this purpose.

2.0 Moment analysis of the pair interaction model.

The class of mixing models to be considered in detail is given by

$$\left(\frac{\partial\tilde{f}_1}{\partial t}\right)_{mix}=\frac{1}{\tau}\{\int_0^1 d\varphi'\int_0^1 d\varphi''\tilde{f}_1(\varphi')\tilde{f}_1(\varphi'')T(\varphi',\varphi'',\varphi)$$

$$-\tilde{f}_1(\varphi)\} \qquad (8)$$

The properties of this class of models can be assessed in terms of the normalized higher moments

$$\mu_n\equiv\frac{\langle\Psi'^n\rangle}{\langle\Psi'^2\rangle^{\frac{n}{2}}} \qquad (9)$$

In particular skewness μ_3 and flatness μ_4 will be considered. The central part of the mixing model is the kernel T. It is the probability that the interaction of a material point $\Psi=\varphi'$ with a point $\Psi=\varphi''$ produces the values $\Psi=\varphi$

and $\Psi = \varphi' + \varphi'' - \varphi$ and is called the transition probability $T(\varphi', \varphi'', \varphi)$. T must satisfy the requirements

$$T(\varphi', \varphi'', \varphi) = T(\varphi', \varphi'', \varphi' + \varphi'' - \varphi) \tag{10}$$

$$T(\varphi', \varphi'', \varphi) = 0 \; for \; \varphi \notin [\varphi', \varphi''] \tag{11}$$

and T is pdf with respect to φ

$$\int_0^1 d\varphi T(\varphi', \varphi'', \varphi) = 1 \tag{12}$$

Conditions (10)-(12) lead to a class of transition pdfs constructed as follows

$$T(\varphi', \varphi'', \varphi) = G(\zeta) H(\varphi', \varphi'', \varphi) \tag{13}$$

where

$$\zeta(\varphi', \varphi'', \varphi) \equiv \frac{2}{|\varphi' - \varphi''|}[\varphi - \frac{1}{2}(\varphi' + \varphi'')] \tag{14}$$

and

$$H(\varphi', \varphi'', \varphi) = \begin{cases} \frac{1}{|\varphi'' - \varphi'|} & \text{for } \varphi \in [\varphi', \varphi''] \\ 0 & \text{otherwise.} \end{cases} \tag{15}$$

and G is a nonnegative symmetric function defined on $[-1, 1]$ such that

$$\int_{-1}^1 d\zeta G(\zeta) = 2 \tag{16}$$

holds If $G = 1$ is chosen the mixing model of Dopazo (1979) and Janicka et al. (1979) is recovered and for $G(\zeta) = 2\delta(\zeta)$ Curl's (1963) droplet interaction model is obtained The function $G(\zeta)$ describes the extent of mixing and is analogous to the pdf $A(\alpha)$ introduced by Pope (1982) for the same purpose The moment equations follow from (8) by integration

$$\frac{\partial}{\partial t}\langle \Psi^n \rangle = \frac{c_f}{\tau}\{J_n - \langle \Psi^n \rangle\} \tag{17}$$

where

$$J_n \equiv \int_0^1 d\varphi \varphi^n \int_0^1 d\varphi' \int_0^1 d\varphi'' f(\varphi') f(\varphi'') G(\zeta(\varphi', \varphi'', \varphi))$$

$$H(\varphi', \varphi'', \varphi) \tag{18}$$

The triple integral can be expressed in terms of the moments of the pdf f and after lengthy manipulations the following result is obtained

$$J_n = \frac{1}{2^{n+1}} \sum_{k=0(2)}^{n} \binom{n}{k} M_k^n m_k \tag{19}$$

where the summation is carried out with increment two (even terms only). M_k^n is defined by

$$M_k^n \equiv \sum_{p=0}^{k} \sum_{q=0}^{n-k} (-1)^p \binom{k}{p} \binom{n-k}{q} \langle \Psi^{p+q} \rangle \langle \Psi^{n-p-q} \rangle \tag{20}$$

and G possesses finite moments of even order, because

$$m_k \equiv \int_{-1}^1 d\zeta \zeta^k G(\zeta) \leq \int_{-1}^1 G(\zeta) = 2 \tag{21}$$

holds. The moment equations are then given by

$$\frac{\partial}{\partial t}\langle \Psi^n \rangle = \frac{c_f}{\tau}\{\frac{1}{2^{n+1}} \sum_{k=0(2)}^{n} \binom{n}{k} m_k \sum_{p=0}^{k} \sum_{q=0}^{n-k} (-1)^p$$

$$\binom{k}{p} \binom{n-k}{q} \langle \Psi^{p+q} \rangle \langle \Psi^{n-p-q} \rangle - \langle \Psi^n \rangle\} \tag{22}$$

Inspection of the right hand side shows that no moments of order higher than n appear. An easy calculation shows that the right hand side of (22) for $n \leq 1$ is indeed zero, hence are normalisation and mean value preserved in time. The equation for the second moment

$$\frac{\partial}{\partial t}\langle \Psi^2 \rangle = -\frac{c_f}{4\tau}(2 - m_2)(\langle \Psi^2 \rangle - \langle \Psi \rangle^2) \tag{23}$$

can be solved analytically for given $G(\zeta)$ and time scale τ independent of Ψ The solution can be inserted into the equation for the third moment, which can then be solved This process can be continued up to the nth level and it becomes clear that the mixing model (8) corresponds to moment equations that are linear with time dependent coefficients The segregation parameter for a binary mixture follows from (2) and (22)

$$\frac{\partial}{\partial t}\alpha_{AB} = -\frac{c_f}{4\tau}(2 - m_2)\alpha_{AB}$$

and shows that α_{AB} decays with a rate determined by the time scale and the second moment of the transition pdf

The earlier analysis of Pope (1982), Kosaly (1986) and Kosaly and Givi (1987) showed that the normalized higher moments of even order diverge and that the skewness ($n = 3$) remains constant if the time scale τ is constant Equation (22) reproduces these results. It follows from (22) and (23) that

$$\frac{\partial \mu_3}{\partial t} = 0 \tag{24}$$

and

$$\frac{\partial \mu_4}{\partial t} = \frac{c_f}{16\tau}(2 - 2m_2 + m_4)(\mu_4 + 3). \tag{25}$$

hold It follows from $m_2 \leq 1$ and $m_4 \geq 0$ that μ_4 grows exponentially for constant time scale τ. The time scale τ is, however, not constant in homogeneous turbulence unless it is maintained by an external force field. If $\tau = \tau_0 t^m$ with an exponent larger than unity, then the normalized moments cease to grow with time and the limiting form of the pdf depends essentially on the transition pdf The measurements of Comte-Bellot and Corrsin (1971) show that the time scale formed with the kinetic energy and the integral length scale has an exponent $m = 1.025$ in their grid generated turbulence. The normalized moments would not grow over all bounds in this flow.

3.0 Analysis of the mixing model: Jump process.

The integral form of the mixing model indicates that it may be regarded as jump process. This is in fact the approximation used in the numerical simulation, where only a randomly selected subset of notional particles takes part in the mixing operation and the rest remains unaffected. The analysis will be carried out in two steps: First the pdf equation corresponding to a stochastic differential equation containing the increment of a jump process will be derived. This is a

fairly standard procedure and can be found for instance in Gardiner (1983, ch.3.4). Let the sde be given by

$$dY = -Adt + B^{\frac{1}{2}}dW + dJ \tag{26}$$

where dW denotes the increment of a standard Wiener process

$$\langle dW(t)\rangle = 0$$

and

$$\langle dW(t)dW(t+dt)\rangle = dt$$

and dJ is the increment of the jump process The pdf equation is now sought for the conditional pdf $f(y,t|y_0,t_0)$ defined by

$$f(y,t|y_0,t_0)dy = Prob\{y \le Y(t) \le y+dy, Y(t_0) = y_0\} \tag{27}$$

where $t_0 \le t$ must hold Several conditions are now imposed on this pdf to insure that the equation governing its temporal evolution exists. Let $\epsilon > 0$, then the following conditions must hold uniformly in y,z,t:

$$\lim_{\Delta t\to 0}\frac{1}{\Delta t}f(y,t+\Delta t|z,t) = W(y|z,t) \; for \; |y-z| \ge \epsilon \quad (C\,1)$$

$$\lim_{\Delta t\to 0}\frac{1}{\Delta t}\int_{|y-z|<\epsilon} dy(y-z)f(y,t+\Delta t|z,t) = A(z,t)+O(\epsilon) \tag{C 2}$$

$$\lim_{\Delta t\to 0}\frac{1}{\Delta t}\int_{|y-z|<\epsilon} dy(y-z)^2 f(y,t+\Delta t|z,t) = B(z,t)+O(\epsilon) \tag{C 3}$$

Conditions (C 2) and (C 3) must also hold uniformly with respect to ϵ. The function $W(y|z,t)$ may be singular but must be at least integrable The definition (C 1) implies that $W(y|z,t)$ describes the expected rate of jumps of size $|y-z|$ per unit time. Integrating W over all possible values y leads to the expected rate of jumps (or mean time scale for the jumps)

$$\int_{-\infty}^{\infty} dyW(y|z,t) = R(z,t) \tag{28}$$

originating at the value $Y(t) = z$. The conditions (C.2) and (C.3) imply furthermore that W is related to the drift velocity A and the diffusivity B by

$$\int_{|y-z|<\epsilon} (y-z)W(y|z,t) = A(z,t)+O(\epsilon) \tag{29}$$

and

$$\int_{|y-z|<\epsilon} (y-z)^2 W(y|z,t) = B(z,t)+O(\epsilon) \tag{30}$$

Finally, it should be noted that the Lindeberg condition (see Gardiner (1983), ch.3.4), which states that the sample paths of the stochastic process $Y(t)$ are continuous if for $\epsilon > 0$ $W(y|z,t) = 0$ holds with probability one, allows proper interpretation of W. It follows that $W \neq 0$ implies indeed sample paths with jumps. The transport equation for $f(y,t|z,t')$ can be obtained by multiplying the pdf f with an arbitrary, twice continuously differentiable function $Q(y)$ that vanishes together with its normal derivative at the boundary of the range of values of Y and integrating over this range. Exploiting the conditions imposed on f and the smoothness of $Q(y)$ leads to the equation for the pdf f (see Gardiner 1983). It emerges in the form

$$\frac{\partial f}{\partial t} + \frac{\partial}{\partial y}(Af) = \frac{1}{2}\frac{\partial^2}{\partial y^2}(Bf) + \int dx[W(y|x,t)f(x,t|z,t') - W(x|y,t)f(y,t|z,t')] \tag{31}$$

The solution is determined by the initial condition

$$f(y,t|z,t) = \delta(y-z) \tag{32}$$

The equation for the single point pdf $f(y,t)$ can be obtained without difficulty by multiplication of (31) and (32) with $f(z,t')$ and integration over z. The resulting pdf equation is identical with (31) and the initial condition becomes

$$f(y,t') = f_0(y)$$

where f_0 denotes the given initial pdf. Equation (31) is the tool for the analysis of the mixing model (8). We note that the integral model (8) can be recast as

$$\left(\frac{\partial f(y,t|z,t')}{\partial t}\right)_{mix} = \int_0^1 dx f(x,t|z,t')\frac{1}{\tau}\int_0^1 dy'' f(y'',t|z,t')T(x,y'',y) - \frac{1}{\tau}f(y,t|z,t') \tag{33}$$

because the derivation of the mixing model can be carried out for the conditional pdf $f(y,t|z,t')$ without any modifications. Comparison of (33) with (31) indicates that the definition

$$W^*(y|x,t) \equiv \frac{1}{\tau}\int_0^1 dy'' f(y'',t|z,t')T(x,y'',y) \tag{34}$$

puts the mixing model into the form of a jump process. The property to check is the existence and the value of the integral

$$\int_0^1 dx W^*(x|y,t) = \frac{1}{\tau}\int_0^1 dx\int_0^1 dy'' f(y'',t|z,t')T(y,y'',x)$$

It follows at once from (12) that

$$\int_0^1 dx W^*(x|y,t) = \frac{1}{\tau} \tag{35}$$

holds and the mixing model emerges in the form

$$\left(\frac{\partial f(y,t|z,t')}{\partial t}\right)_{mix} = \int_0^1 dx[f(x,t|z,t')W^*(y|x,t) - f(y,t|z,t')W^*(x|y,t)] \tag{36}$$

equivalent to the pdf equation for jump processes ($A = B = 0$ in (31)). The probability W^* for jumps from x to y per unit time for the mixing model depends according to (34) on the probability $f(y'',t|z,t')$ of finding an element with $Y = y''$ such that y is the interval $[x,y'']$ and the probability $T(x,y'',y)$ for the interaction of x with y'' to produce an element with $Y = y$

4.0 Analysis of the mixing model: Relation to the Fokker -Planck equation.

The pdf equation for pure mixing was shown to have the form of a master equation for a jump process (36). It is instructive to consider the limit of this equation for the jump size approaching zero. It is known that jump processes can approximate diffusion processes in this limit (Gardiner 1983). The investigation of the mixing model for the limit of vanishing step size is based on the following consideration In each time step all the notional particles representing an approximation of the pdf participate in the mixing step and the time step controls the amount of mixing. It follows that a new parameter ϵ measuring the amount of mixing must be introduced into the mixing model. The pdf for the jump rate is modified to include ϵ

$$W(y|x,t,\epsilon) \equiv \frac{1}{\tau}\int_0^1 dy'' f(y'',t|z,t')T(x,y'',y,\epsilon) \qquad (37)$$

via the transition pdf T

$$T(x,y'',y,\epsilon) = G(\zeta,\epsilon)H(x,y'',y) \qquad (38)$$

where

$$\zeta(x,y'',y) \equiv \frac{2}{|x-y''|}[y - \frac{1}{2}(x+y'')] \qquad (39)$$

denotes the centered variable defined in $[-1,1]$ and H is defined by (15) The shape function G controls the amount of mixing if it is modified to allow mixing only in the ϵ-neighbourhood of the states before mixing: $G(\zeta,\epsilon) > 0$ for $(y \in [x, x+\epsilon] \cup [y''-\epsilon, y'']$ for $x < y)$ or $(y \in [x-\epsilon, x] \cup [y'', y''+\epsilon]$ for $x > y)$ and $G(\zeta,\epsilon) = 0$ otherwise Clearly, if ϵ approaches zero no mixing takes place and if $\epsilon = 1/2(x+y'')$ the original model is recovered The analysis is now carried out with the shape function defined by

$$G(\zeta,\epsilon) = A\{\delta(\zeta+1-\epsilon) + \delta(\zeta-1-\epsilon)\} \qquad (40)$$

where A denotes a quantity depending on ϵ only Note that this definition of the shape function gives the maximal amount of mixing for the restricted range and is symmetric as required for the pair exchange model The jump rate pdf emerges now in the form

$$W(y|x) = \frac{A}{\tau}\{h(x-y)\int_0^y dy' \frac{f(y')}{x-y'}\delta(\zeta+1-\epsilon)$$

$$+h(y-x)\int_y^1 dy' \frac{f(y')}{y'-x}\delta(\zeta-1-\epsilon)\} \qquad (41)$$

where h denotes the unit step function The integrals can be evaluated and

$$W(y|x,\epsilon) = \frac{A}{\tau}\frac{1}{2+\epsilon}\{h(x-y)f(\frac{y-1/2\epsilon x}{1-1/2\epsilon})$$

$$+h(y-x)f(\frac{y+1/2\epsilon x}{1+1/2\epsilon})\} \qquad (42)$$

is obtained. The two integrals constituting the mixing model (36) can now be evaluated if the pdf f is analytic. Taylor series expansion for $\epsilon \ll 1$ (using $(1-1/2\epsilon)^{-1} = 1+1/2\epsilon - 1/4\epsilon^2 + O(\epsilon^3)$) leads to

$$f(\frac{y-1/2\epsilon x}{1-1/2\epsilon}) = f(y - 1/2\epsilon(x-y) + O(\epsilon^2))$$

which is expanded to third order leads to

$$f(\frac{y-1/2\epsilon x}{1-1/2\epsilon}) = f(y) - \frac{1}{2}\epsilon(x-y)\frac{\partial f}{\partial y} + \frac{1}{8}\epsilon^2(x-y)^2\frac{\partial^2 f}{\partial y^2} + O(\epsilon^3)$$

A similar expansion for

$$f(\frac{y+1/2\epsilon x}{1+1/2\epsilon}) = f(y) + \frac{1}{2}\epsilon(x-y)\frac{\partial f}{\partial y} + \frac{1}{8}\epsilon^2(x-y)^2\frac{\partial^2 f}{\partial y^2} + O(\epsilon^3)$$

leads to the expansion for the jump rate pdf

$$W(y|x,\epsilon) =$$

$$\frac{A}{2\tau}\{f(y) + \frac{1}{2}\epsilon[(x-y)\frac{\partial f}{\partial y}(h(y-x) - h(x-y)) - f(y)]$$

$$+\frac{1}{8}\epsilon^2[(x-y)^2\frac{\partial^2 f}{\partial y^2} - 2(x-y)\frac{\partial f}{\partial y}(h(y-x) - h(x-y))] + O(\epsilon^3)\} \qquad (43)$$

The integrals in (36) are evaluated over the interval $[0^-, 1^+]$ to preserve the normalization, which implies that

$$f(0) = f(1) = \frac{\partial f}{\partial y}(0) = \frac{\partial f}{\partial y}(1) = 0$$

holds. The mixing model appears now in the form of a power series with respect to ϵ

$$\left(\frac{\partial f(y,t|z,t')}{\partial t}\right)_{mix} =$$

$$\frac{\epsilon A}{2\tau}\{\frac{1}{2}\frac{\partial f}{\partial y}[\int_0^y dx f(x)(x-y) - \int_y^1 dx f(x)(x-y)]$$

$$-\frac{1}{2}f(y)[\int_y^1 dx f(x) - \int_0^y dx f(x)] + \frac{1}{8}\epsilon[\frac{\partial^2 f}{\partial y^2}\int_0^1 dx f(x)(x-y)^2$$

$$-2\frac{\partial f}{\partial y}(\int_0^y dx f(x)(x-y)$$

$$-\int_y^1 dx f(x)(x-y)) - 4f(y)\int_0^y dx f(x)] + O(\epsilon^2)\} \qquad (44)$$

This relation shows clearly that for time scales of the order ϵ a Fokker-Planck-type equation results for the mixing model with the shape function modified according to (40). It follows that the drift term reduces the variance and the interaction of a notional particle with a randomly selected mixing partner appears as random stirring in scalar space Numerical verification of this result is presently carried out

5.0 Conclusions.

The mixing model based on pairwise interaction of notional particles in scalar space was analyzed The dynamics of higher normalized moments shows that the model based on uniform probability for the outcome of the mixing interaction does not approach a Gaussian pdf in the limit of decaying turbulence The normalized moments approach finite limit values if the mixing time scale varies according to the experimental evidence but Gaussianity is not recovered. The analysis of the mixing model can be generalized to conditional pdfs and it follows that mixing can be regarded as jump process, where selected notional particles undergo mixing and particles not selected remain unaffected. The jump

rate pdf was shown to depend on the pdf itself reflecting the availability of mixing partners. Finally, it was shown that a modification of the pdf describing the amount of mixing during pairwise interaction leads to a mixing model which is governed by a Fokker-Planck type equation. The mixing interaction has to be carried out with a time scale proportional to a new scale ϵ. If ϵ is sufficiently small the mixing model appears as drift and diffusion in scalar space.

References

Chen, H., Chen, S. and Kraichnan, R. H (1989), "Probability Distribution of a Stochastically Advected Scalar Field", Phys Rev Lett. 63, 2657.

Chen, J.-Y and Kollmann, W (1989), "Mixing models for turbulent flows with exothermic reactions", Proc. Seventh Conf. Turbulent Shear Flows, Stanford Univ.

Comte-Bellot, G and Corrsin, S. (1971), "Space-time correlation measurements in isotropic turbulence", JFM 48, 273

Curl, R. L (1963), "Dispersed Phase Mixing. I Theory and Effects in Simple Reactors", A I Ch E. J 9, 175.

Dopazo, C (1975), "Probability Function Approach for a Turbulent Axisymmetric Heated Jet. Centerline Evolution" Physics Fluids 18, 397

Dopazo, C (1979), "Relaxation of initial Probability Density Functions in the Turbulent Convection of Scalar Fields", Physics Fluids 22, 20.

Gardiner, C. W. (1983). Handbook of stochastic methods, Springer Series in Synergetics vol 13, Springer Verlag.

Janicka, J., Kolbe, W. and Kollmann, W. (1979), "Closure of the Transport Equation for the Probability Density Function of Scalar Fields", J Non-equil. Thermodyn 4, 27

Kollmann, W (1987), "Pdf-transport Equations for Chemically Reacting Flows", Proc. US-France Workshop on Turb React Flows, Rouen,vol 2, 20-1

Kosaly, G. (1986), "Theoretical Remarks on a Phenomenological Model of Turbulent Mixing", Comb. Sci. Techn 49, 227

Kosaly, G and Givi, P (1987), "Modeling of Turbulent Molecular Mixing", Comb. Flame 70, 101.

Pope, S. B. (1982), "An Improved Turbulent Mixing Model", Comb Sci. Technol 28, 131

Pope, S B (1985), "Pdf Methods for Turbulent Reacting Flows", Progr Energy Comb Sci. 11, 119.

EIGHTH SYMPOSIUM ON
TURBULENT SHEAR FLOWS
Technical University of Munich
September 9-11, 1991

MATHEMATICAL MODELLING OF JET DIFFUSION FROM FLAMES IN THE ATMOSPHERE USING A SECOND MOMENT TURBULENCE MODEL

Hermilo RAMIREZ-LEON, Claude REY and Jean-François SINI

LABORATOIRE DE MECANIQUE
DES TRANSFERTS TURBULENTS ET DIPHASIQUES.
E.N.S.M. 1 Rue de la Noë, 44072 NANTES Cédex 03
FRANCE.

ABSTRACT

The paper describes a second order closure model for calculating strongly heated turbulent flows such as plumes, and turbulent jet diffusion from flames in the atmosphere. In such flows, the temperature dependent density variations are not negligible, and the usual Boussinesq approximation is not justified. Therefore, it is necessary to use mathematical models derived from the variable density flow equations without such restrictive simplifications. The model presented in this paper is based on a formulation arising from a first order series expansion on the relative pressure fluctuations (Eq. 1), a linearization of the thermal variation of the physical properties (μ et κ) (Eq. 2) and a new analysis of the dissipation mechanisms for compressible fluids .

NOMENCLATURE

B^*_{ab} Expansion effects for any $\overline{ab}$ correlation.

D_{ab} Diffusion for any $\overline{ab}$ correlation.

$\frac{D}{Dt} = \frac{\partial}{\partial t} + \bar{U}_j \frac{\partial}{\partial x_j}$ Mean material derivative.

E Dissipation rate of κ with constant dynamic viscosity.

E_θ Dissipation rate of $\overline{\theta^2}/2$ with constant conductivity coefficient.

$\mathcal{K}$ Thermal diffusivity.

P_{ab} Production for any $\overline{ab}$ correlation.

$\bar{P}$, p Mean and fluctuating pressure.

R $\mathcal{R}/m$.
$\mathcal{R}$ constant of ideal gas.
m molar mass of the gas.

$\bar{T}$, θ Mean and fluctuating temperature.

$\bar{U}_i$, u_i Mean and fluctuating components of velocity.

$\overline{u_i u_j}$ Reynolds stresses.

$\overline{u_i \theta}$ Scalar fluxes.

x_i Cartesian space coordinates.

ϵ Dissipation rate of κ.

ϵ_θ Dissipation rate of $\overline{\theta^2}/2$.

Φ_{ij}, $\Phi_{i\theta}$ Pressure-interaction terms.

κ Turbulent kinetic energy.

μ Dynamic viscosity.

$\overline{\theta^2}$ Temperature variance.

ρ Density.

INTRODUCTION

For the development of the turbulence statistical equations for flows with density variations, two ways of decomposition have been proposed:

- Favre (1965) and Chassaing (1985) proposed a statistical decomposition named mean weighted averaging: the instantaneous physical variables are split as:

Macroscopic quantities	non-zero mean random variable
$\tilde{\Psi} = \frac{\overline{\rho\Psi}}{\rho}$	$\psi = \Psi - \tilde{\Psi}$

- Rey (1985, 1990, 1991) investigated another decomposition of the density variation turbulence mechanisms, using the classical random variable with zero mean (Reynolds decomposition). The turbulent processes are splitted as:

isovolumetric turbulence mechanisms	turbulence mechanisms change by volume variations

The main advantage in this last proposition, consists in the ability to identify in this formulation the mechanisms that are in

incompressible fluid flows. Particularly, the classical second order closures (Launder *et al*, 1985; Lumley, 1983)) are still valid for the isovolumetric turbulence mechanisms. Furthermore the statistical terms interacting with volume variations are all known or negligible.

This formulation arises from a first order series expansion on the relative pressure fluctuation:

$$\frac{1}{\rho} = \frac{RT}{\bar{P}}\left(1 - \frac{p}{\bar{P}}\right) \qquad (1)$$

Then the statistical process applied in the equations is the usual Reynolds averaging approach. The model presented in this paper is based on olumetric variations given by Eq (1) and the analysis of the thermal variations of the physical properties (viscosity and thermal diffusivity) linearized as follow:

$$\mu(T) = \mu_0 + A(T - T_0) \quad ; \quad \mathcal{K}(T) = \mathcal{K}_0 + B(T - T_0) \qquad (2)$$

where the subscript o refers to reference values.

THE CONTINUITY EQUATION.

The main difficulty of this formulation concerns the closure of the set of equations because the velocity divergence is not zero. In this model the continuity equation is written as

$$\text{div } \bar{U}_i - \mathcal{F} = 0 \qquad (3)$$

As a first attempt we write

$$\text{div } \vec{U} = -\vec{U}\left(\frac{1}{\bar{P}}\frac{\partial P}{\partial x_i} - \frac{1}{\bar{T}}\frac{\partial T}{\partial x_i}\right)$$

then $\mathcal{F}$ is expressed using Reynolds averaging on the right-hand side. Keeping only the dominant terms, $\mathcal{F}$ can be written as:

$$\mathcal{F}=\bar{U}_i\left(\frac{1}{\bar{T}}\frac{\partial \bar{T}}{\partial x_i} - \frac{1}{2\bar{T}^2}\frac{\partial \overline{\theta^2}}{\partial x_i}\right) + \frac{1}{\bar{T}}\frac{\partial \overline{u_i\theta}}{\partial x_i} - \frac{\overline{u_i\theta}}{\bar{T}^2}\frac{\partial \bar{T}}{\partial x_i} - \frac{1}{2\bar{T}^2}\frac{\partial \overline{u_i\theta^2}}{\partial x_i} \qquad (4)$$

The divergence condition in Eq. 3 must be solved together with the transport equations. It will be directly satisfied by an extended version of the artificial compressibility implicit method (Ramirez-Leon *et al*, 1991).

SET OF EQUATIONS.

From these considerations a set of equations can be written in the following general form as:

$$\left.\begin{array}{l} \text{Classical description as for incompressible flows (Iv)} \\ \quad + \dfrac{RT}{\bar{P}} \end{array}\right\} \boxed{\begin{array}{l}\text{turbulence isovolumetric mechanisms of transport}\end{array}}$$

$$\left.\begin{array}{l} \\ \quad + \end{array}\right\} \boxed{\begin{array}{l}\text{turbulence isovolumetric mechanisms of molecular diffusivity}\end{array}}$$

$$\left.\begin{array}{l} \text{deviation} \\ \text{(Vv)} \end{array}\right\} + \boxed{\begin{array}{l}\text{turbulence mechanisms change by volume variations}\end{array}} = 0 \qquad (5)$$

This formulation is valid for mean quantities $\bar{U}_i$ or $\bar{T}$ and for all turbulent correlations $\left(\overline{u_iu_j}, \kappa, \epsilon, \overline{u_i\theta}, \overline{\theta^2}, \epsilon_\theta, \overline{u_iu_ju_k}, \overline{u_iu_j\theta}, \ldots\right)$.

TURBULENCE MODELLING.

The statistical second moment transport equations are derived using the volumetric variation equation Eq. (1). As an example, the heat fluxes $\overline{u_i\theta}$ equation is given hereafter:

$$\frac{D\overline{u_i\theta}}{Dt} = -P_{i\theta} - D_{i\theta} + \Phi_{i\theta} - \epsilon_{i\theta} + B^*_{i\theta} \qquad (6)$$

----------(Iv)---------- -(Vv)-

where

$$\frac{D\overline{u_i\theta}}{Dt} = \frac{\partial \overline{u_i\theta}}{\partial t} + \bar{U}_k\frac{\partial \overline{u_i\theta}}{\partial x_k} \qquad (6.1)$$

$$P_{i\theta} = \overline{u_k\theta}\frac{\partial \bar{U}_i}{\partial x_k} + \overline{u_iu_k}\frac{\partial \bar{T}}{\partial x_k} + \frac{1}{C_p}\frac{R\bar{T}}{\bar{P}}\overline{u_iu_k}\frac{\partial \bar{P}}{\partial x_k} \qquad (6.2)$$

$$D_{i\theta}= \frac{\partial \overline{u_iu_k\theta}}{\partial x_k} - \frac{R\bar{T}}{\bar{P}}\mu_0\frac{\partial}{\partial x_k}\left(\mathcal{P}\frac{\partial \overline{u_i}}{\partial x_k} + \frac{\overline{u_i}}{Fr}\frac{\partial \overline{\theta}}{\partial x_k}\right) + \frac{\overline{R(\bar{T}+\theta)}}{\bar{P}}\frac{\partial \overline{p\theta}}{\partial x_i} - \frac{1}{C_p}\frac{R\bar{T}}{\bar{P}}\bar{U}_k\frac{\partial \overline{pu_i}}{\partial x_k} \qquad (6.3)$$

$$\Phi_{i\theta} = \frac{\overline{R(\bar{T}+\theta)}}{\bar{P}}\,p\,\frac{\partial \theta}{\partial x_i} \qquad (6.4)$$

$$\epsilon_{i\theta}= \frac{R\bar{T}}{\bar{P}}\left(\mu_o + \frac{\mathcal{K}_o}{C_p}\right)\overline{\frac{\partial u_i}{\partial x_k}\frac{\partial \theta}{\partial x_k}} \qquad (6.5)$$

$$B^*_{u\theta}= \frac{\overline{\theta^2}}{\bar{T}}\left(\frac{R}{\bar{P}}\theta\frac{\partial p}{\partial x_i} + \frac{D\bar{U}_i}{Dt} + \frac{\partial \overline{u_iu_k}}{\partial x_k} + g_i\right) + \frac{\overline{u_i\theta}}{\bar{T}}\left(\frac{D\bar{T}}{Dt} + \frac{\partial \overline{u_k\theta}}{\partial x_k}\right) \qquad (6.6)$$

Similarly to (6), the full set of equations is derived for all dependent variables and can be written as follow:

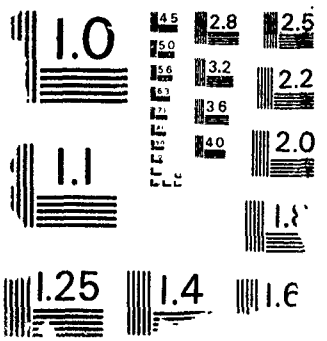
1.0
1.1
1.25
1.4
1.6
2.8
2.5
3.2
2.2
3.6
2.0
4.0

$$\frac{D\overline{u_i u_j}}{Dt} = - P_{ij} - D_{ij} + \Phi_{ij} - \epsilon_{ij} + B^*_{ij} \qquad (7)$$

$$\frac{D\kappa}{Dt} = - P_{\kappa} - D_{\kappa} + \Phi_{\kappa} - \epsilon_{\kappa} + B^*_{\kappa} \qquad (8)$$

$$\frac{D\overline{\theta^2}}{Dt} = - P_{\theta^2} - D_{\theta^2} + \Phi_{\theta^2} - \epsilon_{\theta^2} + B^*_{\theta^2} \qquad (9)$$

$$\frac{DE}{Dt} = - P_{E} - D_{E} - \epsilon_{E} + B^*_{E} \qquad (10)$$

$$\frac{DE_{\theta}}{Dt} = - P_{E\theta} - D_{E\theta} - \epsilon_{E\theta} + B^*_{E\theta} \qquad (11)$$

----------(Iv)---------- -(Vv)-

With regard to Eq (2), the right-hand side of equations (5-10) clearly separates the "isovolumetric" effects (Iv), which are similar to the corresponding terms in the equations for an incompressible fluid, from the expansion effects (Vv).

The exact definition of dissipation terms includes a temperature dependent diffusivity coefficient. So, new cumbersome correlations appear in the system. This difficulty can be avoided if using a simplified form. Assuming high Reynolds number and local isotropy hypothesis, the dissipation terms are expressed as:

$$\epsilon = \frac{R\bar{T}}{\bar{P}} \frac{\bar{\mu}}{\mu_0} E \quad ; \quad E = \mu_0 \overline{\frac{\partial u_i}{\partial x_j} \frac{\partial u_i}{\partial x_j}} \qquad (12)$$

$$\epsilon_{\theta} = \frac{\bar{\kappa}}{\kappa_0 C_p} \frac{R\bar{T}}{\bar{P}} E_{\theta} \quad ; \quad E_{\theta} = \kappa_0 \overline{\frac{\partial \theta}{\partial x_j} \frac{\partial \theta}{\partial x_j}} \qquad (13)$$

where the diffusivity coefficients thermal dependance involving temperature fluctuations have been neglected.

So, this set of equations is open and the selection of the proper models for closure must now be considered.

SELECTION OF CLOSURE MODELS.

The second term of (6.3) can be neglected assuming a high Reynolds number and $\epsilon_{i\theta}$ is set equal to zero based on the local isotropy assumption.

If we were to keep the incompressible flow closure methods, difficulties would arise from both the pressure correlations and third moment terms. Therefore, the closure model has been determined in the following way:

Pressure correlations terms.

A model for the so-called pressure-rate-of-strain correlation is first presented. This term may be written by means of a Poisson equation, as

$$\boxed{\overline{\frac{R(\bar{T}+\theta)}{\bar{P}} p \frac{\partial \varphi}{\partial x_j}}} = \boxed{\text{part generated from a mutual interaction between turbulence components}} + \boxed{\text{interaction between the mean strain and turbulence}}$$

-----slow part------- -rapid part-

(14)

where φ stands for u_i, θ, $u_i u_k$, $u_i\theta$, etc.

In the incompressible fluid case, for $\varphi = u_i$, the rapid part is commonly modeled using the return-to-isotropy concept and the slow part using the isotropization-of-production concept. For the compressible fluid case, Ramirez-Leon *et al* (1990) showed that this formulation is still valid. Similarly, for $\varphi = \theta$, we can write

$$\Phi_{i\theta} = -C_{\Phi\theta,1} \frac{\overline{u_i\theta}}{\tau_m} + C_{\Phi\theta,2} \frac{\overline{u_i u_j}}{\kappa} \frac{\overline{u_i\theta}}{\tau_m} + C_{\Phi\theta,3} \overline{u_k\theta} \left(\frac{\partial \bar{U}_i}{\partial x_k} + \frac{\partial \bar{U}_k}{\partial x_i} \right)$$

------slow part------ --rapid part--

(15)

where τ_m is a mixed time scale, $C_{\Phi\theta,1} = 3.31$, and $C_{\Phi\theta,2} = 3.46$. The value of $C_{\Phi\theta,3} = 0.45$ has been modified from the incompressible value (Launder *et al*, 1975), in such a way to include the expansion effects.

Vandromme *et al* (1983), have found that a similar formulation is appropriate for compressible fluid flows.

Pressure-diffusion terms.

The pressure-diffusion terms are supposed to have a weak influence in the development of a two-dimensional turbulent flow. These terms have been neglected.

Third order correlations.

The exact equations for the triple products have been thoroughly derived. In these equations, the convection, the main strain production, and the diffusive transport by pressure and molecular action have been omitted. Furthermore we used the gaussian approximation for the fourth moments. The final form of triple correlations is:

$$\boxed{\text{triple correlations}} = - C_c \left\{ \boxed{\text{The simple gradient-diffusion form}} - \boxed{\text{volumetric expansion part}} \right\}$$

-------(Iv)-------- ---(Vv)

As an example, we give the modeled equation for $\overline{u_i u_k \theta}$ correlations:

$$\overline{u_i u_k \theta} = -C_{uu\theta} \tau_m \left[\overline{u_l u_k} \frac{\partial \overline{u_i\theta}}{\partial x_l} \right.$$

---(Iv)---

$$\left. - \frac{\overline{u_i\theta^2}}{\bar{T}} \left(\bar{U}_l \frac{\partial \bar{U}_k}{\partial x_l} + \frac{\partial \overline{u_k u_l}}{\partial x_l} + g_k \right) - \frac{\overline{u_i u_k \theta}}{\bar{T}} \left(\bar{U}_l \frac{\partial \bar{T}}{\partial x_l} + \frac{\partial \overline{u_k\theta}}{\partial x_k} \right) \right]$$

----------(Vv)----------

(16)

where an "isovolumetric" part (Iv) and a volumetric expansion part (Vv) appear.

Finally, the modeled equation for the turbulent heat fluxes can be written as:

$$\frac{D\overline{u_i\theta}}{Dt} = -P_{i\theta}$$

$$-\frac{\partial}{\partial x_k}\left[C_{\phi\theta,1}\frac{\overline{u_i\theta}}{\tau_m} - C_{\phi\theta,2}\frac{\overline{u_iu_j}}{\kappa}\frac{\overline{u_i\theta}}{\tau_m} - C_{\phi\theta,3}\overline{u_k\theta}\left(\frac{\partial\overline{U_i}}{\partial x_k}+\frac{\partial\overline{U_k}}{\partial x_i}\right)\right]$$

$$+C_{uu\theta}\tau_m\left[\overline{u_lu_k}\frac{\partial\overline{u_i\theta}}{\partial x_l} - \frac{\overline{u_i\theta^2}}{\overline{T}}\left(\overline{U_l}\frac{\partial\overline{U_k}}{\partial x_l}+\frac{\partial\overline{u_ku_l}}{\partial x_l}+g_k\right)\right]$$

$$-C_{uu\theta}\tau_m\frac{\overline{u_iu_k\theta}}{\overline{T}}\left(\overline{U_l}\frac{\partial\overline{T}}{\partial x_l}+\frac{\partial\overline{u_k\theta}}{\partial x_k}\right)$$

$$-\frac{\overline{\theta^2}}{\overline{T}^2}\left[-C_{\phi\theta,1}\frac{\overline{u_i\theta}}{\tau_m}+C_{\phi\theta,2}\frac{\overline{u_iu_j}}{\kappa}\frac{\overline{u_i\theta}}{\tau_m}+C_{\phi\theta,3}\overline{u_k\theta}\left(\frac{\partial\overline{U_i}}{\partial x_k}+\frac{\partial\overline{U_k}}{\partial x_i}\right)\right]$$

$$+\frac{\overline{\theta^2}}{\overline{T}}\left(\frac{D\overline{U_i}}{Dt}+\frac{\partial\overline{u_iu_k}}{\partial x_k}+g_i\right)+\frac{\overline{u_i\theta}}{\overline{T}}\left(\frac{D\overline{T}}{Dt}+\frac{\partial\overline{u_k\theta}}{\partial x_k}\right) \qquad (17)$$

The complete set of equations is derived using similar considerations.

A detailed description of the present model will appear elsewhere (Ramirez-Leon *et al*, 1992)

NUMERICAL PROCEDURE.

The previous section has outlined a closed system of elliptic partial differential equations (6-11).

A finite difference approximation has been used involving the M.A.C. method with centered-differences for diffusion termes and an upwind-weighted scheme for the advection terms. At each time step, the divergence condition (3) is directly satisfied by means of an implicit iterative method. This method is derived from the artificial compressibility method (Chorin, 1967) extended to non-zero divergence flow (see Eqs (3) and (4)).

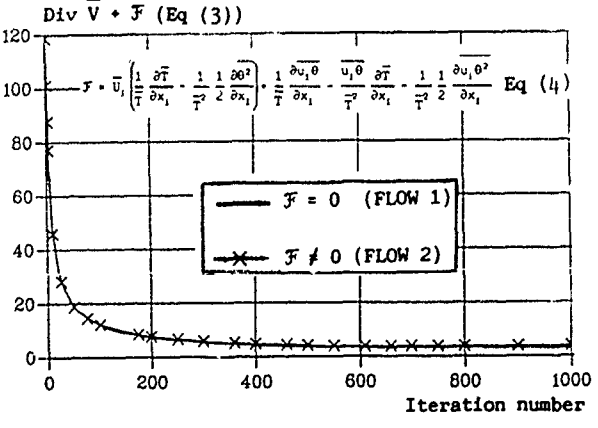

Fig 1. Convergence of the continuity equation. (Eq (3)).

As can be seen on Fig. 1, the convergence curves for an incompressible flow calculation (Chorin's method) and for a non-Boussinesq flow calculation (present method) are not significantly different.

SIMULATIONS OF A STRONGLY HEATED JET.

Preliminary numerical calculations were carried out with a simplified version of the model. The aim was only to test the sensivity of the non-Boussinesq extra terms originated from the volume variations.

This initial tests were run neglecting the compressibility condition in the continuity equation (3) (i.e. $\mathcal{F} = 0$). Therefore, only the volumetric effects appearing in the transport equations (denoted Vv in Eq 5) are accounted for.

This paper is restricted to these calculations, the full model results are presented on slides in this Symposium and will be soon published by Ramirez-Leon *et al* (1992).

Two heated plane jets with the same exit Froude number, are considered. The exit velocity and temperature conditions are presented in Table 1.

Table 1. Exit conditions

flow	temperature (K)	width (m)	velocity (m/s)	Froude Number
1	22	80	5	0.4
2	470	3.7	5	0.4

A vertical weakly-heated jet (ΔT = 22 K, denoted Flow 1) and a vertical strongly-heated jet (ΔT = 470 °K, denoted Flow 2) were calculated in such a way to compare the transversal turbulent profiles.

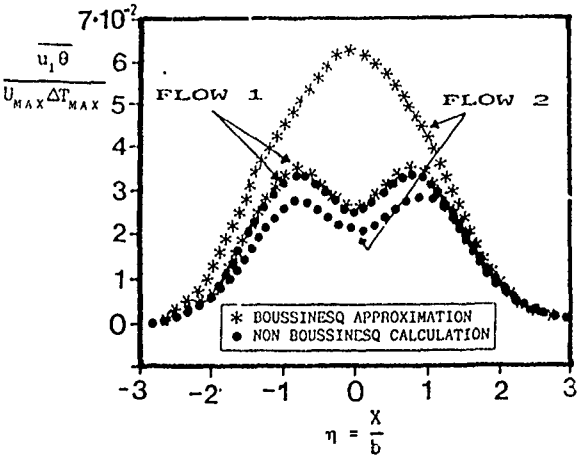

Fig 2. Transversal profile of the vertical turbulent heat flux in heated jets.
- • With volumetric expansion effects.
- * Without volumetric expansion effects.

The longitudinal and the transversal heat fluxes and the temperature variance profiles, normalized with the axial velocity and the centre-line temperature excess, are plotted (star symbols) on the figures 2, 3, 4 respectively.

Here η denotes the horizontal space coordinate normalized with the half width b of the mean velocity. The same calculations were also carried out avoiding volumetric expansion contributions (terms Vv) on turbulence mechanisms (circle full symbols).

As it is readily apparent, the extra terms affect the turbulent thermal fields of the strongly heated jet. They induce a strong decrease on the longitudinal turbulent heat flux level. This influence is negligible in the weakly heated jet.

As it can be seen in Fig. 4, the horizontal heat flux is only slightly affected. This illustrates the non-isotropic influence of the "extra terms" contributions. Nevertheless, the variation is still significant.

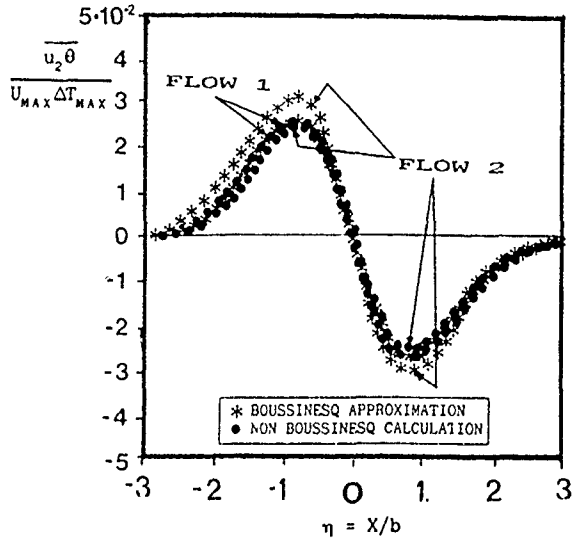

Fig 3. Transversal profile of the horizontal turbulent heat flux. (Symbols as Fig 1)

CONCLUSION.

An extended non-Boussinesq model is presented in the framework of turbulence modelling for variable density flows. Interesting results are found in the preliminary calculations for symmetrical plane heated jets; e.g., non-Boussinesq terms induce a strong decrease (over 60%) of the longitudinal turbulent heat flux $\overline{u_1\theta}$. A synthetic presentation of the extended model is given. It has been applied to vertical plumes and flame jets spreading in a uniform stagnant atmosphere. The most interesting results are presented in the Symposium.

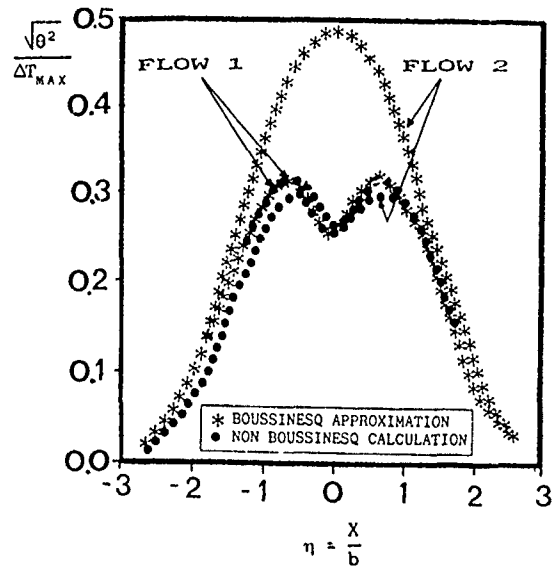

Fig 4. Transversal profile of the temperature variance. (Symbols as Fig 1)

6. BIBLIOGRAPHY.

* Chassaing P., (1985). Mélange turbulent des gaz inertes dans un jet de tube libre. J. Méc. Théo. et App., vol 4, no 3, pp 375-389.

* Chorin A. J., (1967). A numerical method for solving incompressible viscous flows problems. J. comput. Phys. 2,12-26

* Favre A.J., (1965). Equations des gaz turbulents compressibles. J. de Mécanique 4, 361-421 .

* Launder B.E., Reece G.J. and Rodi W., (1975). Progress in the development of a Reynolds stress turbulence closure. J. Fluid. Mech. 68, pp 537-566.

* Levi-Alvares, S., Rey, C. and Sini, J. F., (1989). On the modelling of non Boussinesq flows. Euromech 249, Madrid, Spain.

* Lumley J. L., (1975). Pressure strain correlation. Phys. of fluids 18, no 6, p 750.

* Ramirez-Leon H. (1990). Mise en évidence des modèles de presso-corrélation pour les écoulements compressibles. ENSM-LMTTD. Report No H 90-2, France.

* Ramirez-Leon H., Sini J. F. and Rey C. (1991). Un schéma de compressibilité artificielle pour les écoulements à masse volumique variable. ENSM-LMTTD. Report No HS1-2, France.

* Ramirez-Leon H., Rey C. and Sini, J. F. (1992). A new second closure model for turbulent strongly heated flows. To appear.

* Rey C., (1985). Mise en évidence des effets de la variation de la masse volumique dans les équations aux corrélations des champs turbulents de vitesse et de température. Journées d'étude (IMST), Marseille, France.

* Rey C., Rosant J. M., (1990). Influence of density variations on small turbulent structures of temperature in strongly heated flows. 9th IHTC, Jerusalem. In "Heat transfer 1990", G. Hestoni Ed., Hemisphere Pub. Co., vol 2, pp. 405-409.

* Rey C., Blaquart B., Boudjemaa A., (1991). Experiments on free convection turbulence. 2nd World Conf. on Experimental Heat Trans., Fluid Mech. and Thermo., Dubrovnik, june 1991.

* Vandromme D., Ha minh H., Viegas J. R., Rubesin M. W. and Kollmann W., (1983). Second order closure for the calculation of compressible wall bounded flows with an implicit Navier stokes solver. IVth Symp. on Turb. Shear Flows. Karlsruhe, Germany.

EIGHTH SYMPOSIUM ON
TURBULENT SHEAR FLOWS
Technical University of Munich
September 9-11, 1991

DIRECT NUMERICAL SIMULATION TO TEST SOME MODELS OF PREMIXED REACTING TURBULENT HOMOGENEOUS AND ISOTROPIC FLOWS

H.J.Moon, A.Picart and R.Borghi

Laboratoire de Thermodynamique
Université de Haute Normandie, U A. C.N.R.S. 230
B.P. 118
76134 Mont-Saint-Aignan Cedex, France

ABSTRACT

Here, we present new results on the comparaison between two models of turbulent combustion and the results of the Direct Numerical Simulation of premixed reacting turbulent homogeneous and isotropic flows. The first model to be compared is a combination between a presumed P.D.F. model and the I.E.M. model (Interaction by Exchange with the Mean). The second model is the Curl's model (1963) where a P.D.F. transport equation is solved by a method of Monte Carlo. The numerical experiment under study is a turbulent premixed medium with pockets of burned gases This allows the study of the problem of the autoignition.

INTRODUCTION

All the models that have been so far for the predictions of turbulent reacting flows rest on closure assumptions, similarly to the mathematical turbulence models that have been proposed for non reactive turbulent flows. Some of these assumptions have been tested against experiments, but only to a small extend. There is a great need of detailed verifications of the proposed assumptions, and experimental verifications in reacting flows are far more delicate. An other advantage of the Direct Numerical Simulation is that we can easily separate the several different phenomena which interact in turbulent reactive flows, with which several different closure assumptions are associated, and it is quite impossible, in a physical experiment, to test separately these different assumptions.

To our knowledge, the most recent work which deals with the same aims is described by P.A.McMurtry and P.Givi (1989). Contrarly to P.A.McMurtry and P.Givi who are interested with the non premixed case, we present here results only in the premixed case.

I DIRECT NUMERICAL SIMULATION

We consider here a $3D$ homogeneous incompressible turbulent flow field. So, the governing equations for the flow field are the following Navier-Stokes equations:

$$\frac{\partial u_\alpha}{\partial x_\alpha} = 0 \qquad (1)$$

$$\frac{\partial u_\alpha}{\partial t} + u_\beta \frac{\partial u_\alpha}{\partial x_\beta} = \frac{-1}{\rho}\frac{\partial p}{\partial x_\alpha} + \nu \frac{\partial^2 u_\alpha}{\partial x_\beta{}^2} \qquad (2)$$

where ν is the molecular viscosity, p the pressure, ρ the density. Initially, a given energy spectrum is imposed by the relation

$$E(k) = k^4 exp(-2k^2/16) \qquad (3)$$

where k is the wavenumber. Then the turbulence is free-evolving. Due to the given spectrum, the initial Reynolds number based on the integral scale is about 50. The numerical method to solve the set of equations is a pseudo-spectral method (with 32^3 or 64^3 grid meshes). This method has been used by several authors (e.g. E.S.Oran and J.P.Boris (1987), S.A.Orszag (1972), P.A.McMurtry and P.Givi (1989)) due to its high spatial accuracy to solve homogeneous isotropic turbulent flows.

The equation governing the evolution of the perfectly premixed turbulent scalar field is:

$$\frac{\partial C}{\partial t} + u_\alpha \frac{\partial C}{\partial x_\alpha} = \frac{\nu}{Sc}\frac{\partial^2 C}{\partial x_\alpha{}^2} + \dot{W} \qquad (4)$$

where Sc is the Schmidt number, C the scalar field and $\dot{W}$ the reaction rate. The Schmidt number was chosen equal to 0.36 in order to avoid an increase of the energy at the spectrum cut-off. The Lewis number (the ratio of the heat diffusion over the mass diffusion) is equal to 1 and the flow is isenthalpic. In this case, one can demonstrate easily that the temperature is linearly related to C. That's the reason why we have chosen a reaction rate depending only on C (and not on the temperature) given by the relation:

$$W(C) = -42\frac{C(1-C)^5}{\tau_r} \qquad (5)$$

where τ_r is a characteristic chemical time ($1/\tau_r = \int_0^1 \dot{W}(C)dC$). The quantity $(1-C)$ holds for the temperature, and the usual Arhenius law for the kinetics is replaced by a power law. $C = 0$ corresponds to burned mixture and $C = 1$ to unburned mixture. At $t = 0$. we have large pockets of unburned mixture with small pockets of partially burned mixture in order to initiate the reaction. As time increases, an autoignition phenomena takes place in a turbulent medium. This phnomena is similar to the study of C.Dopazo and E.E.O'Brien (1974). On the Fig.1, we can see that the hypothesis $Le = 1$ and $h = cste$

is not at all restrictive since with $le = 0\,5$ or $Le = 1.5$ with a reaction rate given by $\dot{W} = -42C(1-T)^5/\tau_r$ the results are similar althought C and T are no more linked. The spectrum of the scalar fluctuations is the same that the velocity spectrum.

The Damkhöler number ($= \tau_T/\tau_r$ where τ_T is the characteristic turbulent time) is near unity in all the results presented but it has been slightly varied to see its influence.

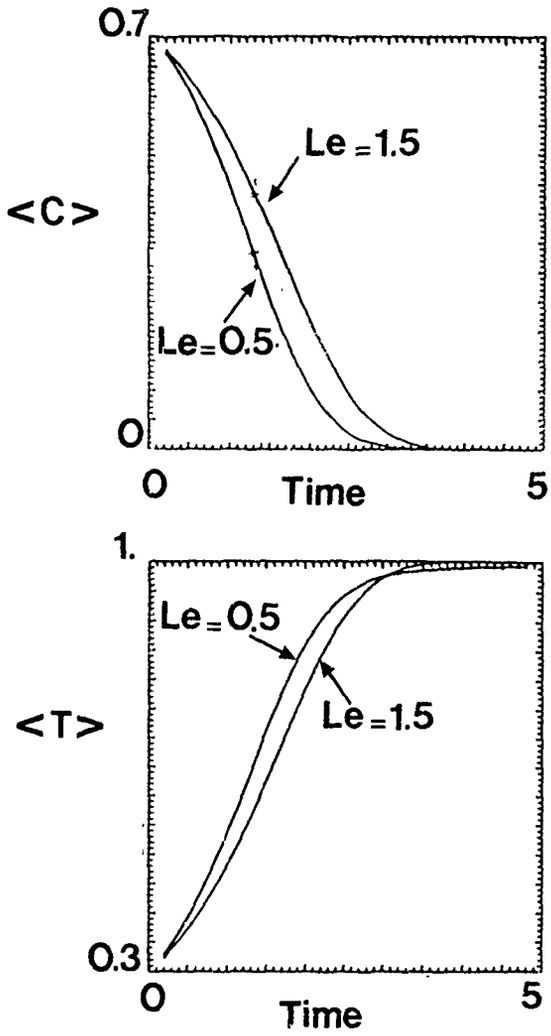

Fig.1. Evolution with time of the mean concentration (upper Fig.) and of the mean temperature (lower Fig.) computed by the D.N.S. for two values of the Lewis number

II MODELISATION

Two models for turbulent combustion have been used. The one which combines the presumed p.d.f. model to the lagrangian equations, where the combustion is supposed to be sudden, and the other based on the transport equations for p.d.f. with a curl's closure for the mixing term.

1. NEW PRESUMED P.D.F. MODEL: "AUTO-IGNITION"

1.1)

We used here lagrangian equations derived from I.E.M. model for a homogeneous isotropic turbulence field as :

$$\frac{dC}{dt} = \frac{\overline{C} - C}{\tau_{ex}} + W(C) \tag{6}$$

$$\frac{d\phi}{dt} = \frac{\overline{\phi} - \phi}{\tau_{ex}} \tag{7}$$

Assuming that the reaction is sudden, the trajectory is formed by the line AI, IS and SB in the phase space (Fig.2). I is a point on AM that we determine by

$$C_I - \overline{C} = \tau_{ex}|W(C_I)| \tag{8}$$

τ_{ex} being the turbulent exchange time in the medium. This is an implicit relation that permit us to determine C_I, function of τ_{ex}, of the chemistry and of $\overline{C}$. We could see it's solution by the line 1 in Fig 3.

The point S is supposed to be near zero: $\dot{W}(C_s)=(\overline{C}-C_s)/\tau_{ex}$ (see the line 2 in Fig.3).

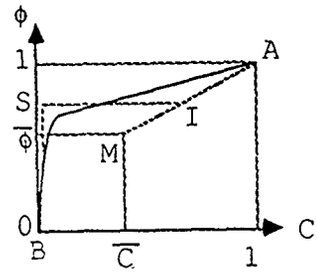

Fig.2. Phase diagram of the I.E.M. model

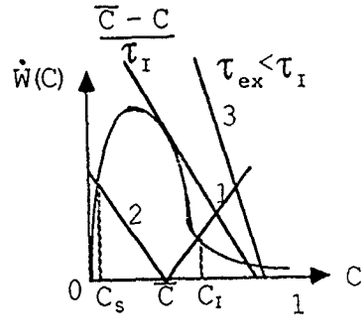

Fig.3. Plot of the different solutions for the Eq. (8) depending on the value of the exchange time τ_{ex}

If τ_{ex} is small enough, $\frac{1}{\tau_{ex}}$ is too high and the slope does not permit us to find a C_s near zero, only C_s near $\overline{C}$ exist (see the line 3 in Fig.3). That implies that there exist a certain value of τ_{ex} function of $\overline{C}$ and of the chemistry for which there is no inflammation. For this case, we represented the form of the p.d.f. by the ones of Fig.4 (see

H.J.Moon et al (1989)). and $\overline{W}$ is calculated with $\int_0^1 \dot{W}(C)P(C)dC$.

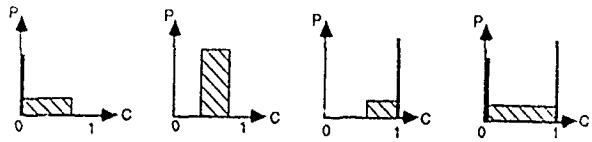

Fig.4. The 4 presumed shape of the P.D.F. in the initial model

In the case where $\tau_{ex} > \tau_I$, we have proposed new presumed p.d.f. that resembles to the p.d.f. of $\tau_{ex} < \tau_I$ but with a slight difference. τ_I represents the case when the line $(\overline{C}\text{-}C)/\tau_I$ is adjacent to the curve $\dot{W}(C)$. For $0 < C < C_I$ we assumed that there is no presence of the probability for C since after the ignition, C is consumed infinitely fast. Three parameters depending on $\overline{C}$, $\overline{C'^2}$ are needed to define the form of p.d.f. d1,b,d0 for the shape (1) and d1,b, and C_M for the shape (2) (see Fig.5).

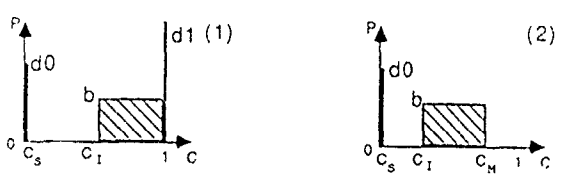

Fig.5. The 2 new shapes of the P.D.F. used when $\tau_{ex} > \tau_I$

The governing equations for homogenous, isotropic, incompressible turbulent reactive flows are.

$$\frac{d\overline{C}}{dt} = \overline{W} \tag{9}$$

$$\frac{d\overline{C'^2}}{dt} = -2\epsilon_c + 2\overline{C'W} \tag{10}$$

where, $\epsilon_c = D\overline{\frac{\partial C'}{\partial x_i}\frac{\partial C'}{\partial x_i}}$. For the modelling of the dissipation rate of $\overline{C'^2}$, ϵ_c, we have assumed a direct proportionality between the dissipation time scale for the turbulence kinetic energy and the variance of fluctuations of a reacting specie ($\tau_{ex} \alpha\ \tau_T$), which yields, $\epsilon_c = \frac{\overline{C'^2}}{\tau_{ex}} = C_D\frac{\overline{C'^2}}{\tau_T}$.

1.2.) CALCULATION OF $\overline{W}$ AND $\overline{C'W}$

the calculation of $\overline{W}$ with $\int_0^1 \dot{W}(C)P(C)dC$ is not so simple as it appears since if we suppose C_s and P(C) ≈0 for $0 < C < C_I$ we will have an indetermination. In fact, for $C = C_s$,we have $\dot{W}(C_s)=\frac{\overline{C}-C_s}{\tau_{ex}}$, and as $C_s \approx 0$, we have $\dot{W}(C)\approx\overline{C}/\tau_{ex}$ that resolve the indetermination in C=0.

For the reaction rate, we have

$$-\dot{W}(C) = \frac{dC}{dt} - \frac{\overline{C}-C}{\tau_{ex}} = \frac{1}{\tau_{ex}}\frac{dC}{d\phi}(\overline{\phi}-\phi) - \frac{\overline{C}-C}{\tau_{ex}} \tag{11}$$

since I is on AM

$$P(\phi_I) = P(C_I)\frac{dC}{\partial\phi_I} = \frac{1-\overline{C}}{1-\overline{\phi}}P(C_I) \tag{12}$$

and as on AI there is no reaction (or very little), and by integrating the previous equation with the assumption that the trajectory is very flat between I and S, finally, we obtain :

$$\overline{W} = -\frac{\overline{C}}{\tau_{ex}}d0 - \frac{\phi_I-\overline{\phi}}{\tau_{ex}}\frac{1-\overline{C}}{1-\overline{\phi}}P(C_I)C_I \tag{13}$$

Where d0 and $P(C_I)(=b)$ is given by the form of P(C). To calculate $\overline{C'W}$ we use the same principle and we have

$$\overline{C'W} = \frac{\overline{C}^2}{\tau_{ex}}d0 - \frac{C_I-\overline{C}}{\tau_{ex}}P(C_I)C_I(\frac{C_I}{2}-\overline{C}) \tag{14}$$

2. CURL'S CLOSURE

The Curl's model is expressed by a transport equation for the p.d.f. In the homogeneous reacting flow considered here, the evolution of the probability is given by

$$\frac{\partial P(C)}{\partial t} = \frac{\partial}{\partial C}(P(C)\dot{W}(C)) + 2\omega\int_0^1 P(C+C')P(C-C')dC' - \omega P(C) \tag{15}$$

(See R.L.Curl (1963), S.Pope (1982), P.A.McMurtry and P.Givi (1989)) where ω is the appropriate turbulence frequency. This equation is valid only in a homogeneous medium, with mean velocity zero. In the Eq.(15), the 1st r.h.s. term is the reactive term which represents a convection term in the probability space while the 2nd r.h.s. term is a molecular diffusion term which destroys the fluctuations also in the probability space. The resolution of this equation is done by the method of Monte-Carlo and we have used the method employed by C.Dopazo [1979]. $C_c/\tau_T dtN$ particles are randomly selected out of the N particles representing the scalar p.d.f. at time t and they are mixed by curl's procedure; C_c being a closure constant. Each of the particles present on the flow will evolve independantly by the p.d.f. transport equation That is the main difference between this model and the presumed p.d.f. which is based on transport equations for mean variables.

III RESULTS

1)

We have used the same initial conditions of Direct Numerical simulation and compared the results The initial conditions of D.N.S and the presumed p.d.f. model:

$\overline{C}$=0.78, $\overline{C'^2}$=0.030, τ_{T_0}=2.0 .

The initial conditions of D.N.S and the curl's model:

$\overline{C}$=0.78, $\overline{C'^2}$=0.017, τ_{T_0}=2.0

where τ_{T_0} is the initial turbulence characteristic time.

The curve marked A represent the Direct Numerical Simulation and B the models. The comparison with the presumed p.d.f. model is shown at the left side and the curves at the right side correspond to curl's model (see Fig 6). Except the evolution of the $\overline{C'^2}$ with time for the presumed p.d.f. model, $\overline{C}(t)$ and $\overline{\dot{W}}(C)$ seem to fit quite well the evolution of Direct simulation.

The agreement of coalescence/dispersion model with the Direct Simulation is very good. In this case, the better concordance is obtained for a value of C_c=2.5.

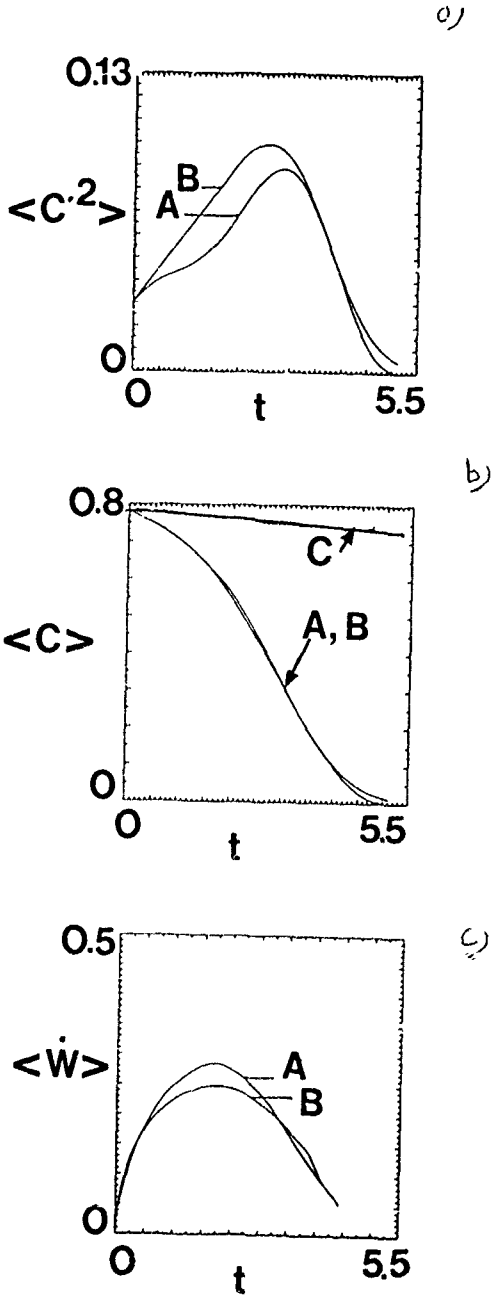

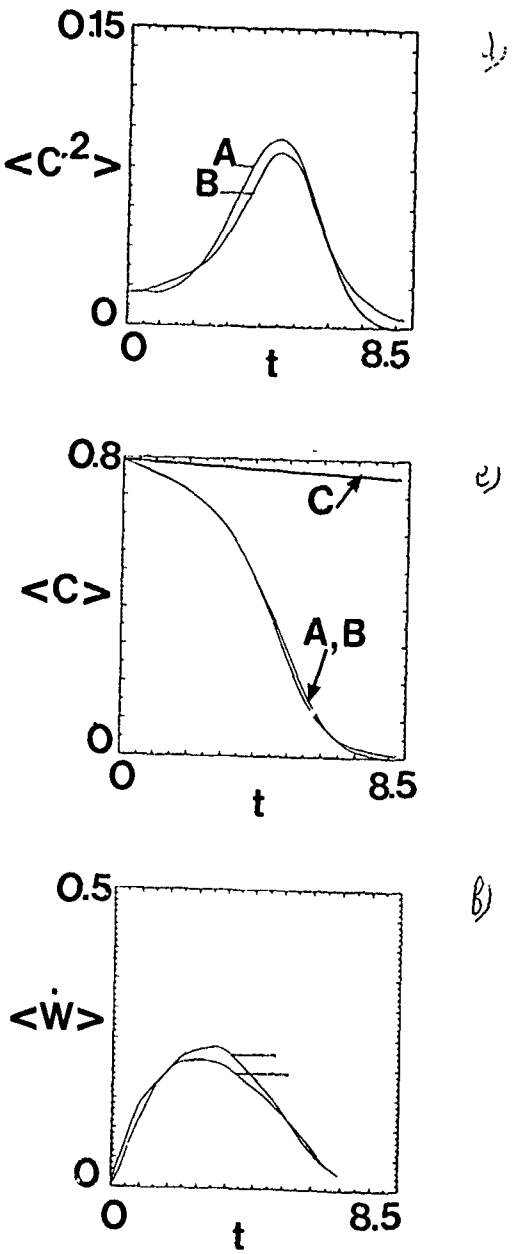

Fig.6. Evolution versus time of the scalar variance (curve a,d), the mean scalar (curve b,e), of the reaction rate (curve c,f). A holds for numerical simulation, B holds for model in this set of curves. For the curves c and d, C means a reactive scalar which evolves without any turbulence. The set of curves (a,c,e) is for the evolution computed by the P.D.F. ignition while the set (b,d,f) is the results of the Curl's model.

2)

If we compare qualitatively (Fig.7) the shape of the P.D.F. computed by the direct numerical simulation and the shape of the presumed P.D.F., we can note that the presumed P.D.F. shape approximate fairly well the one's of the numerical simulation. The time evolution of the shape of the P.D.F. computed by the direct numerical simulation shows clearly that a hollow appears in a range

of values of C; this justifies the correct prediction of $< C >$, $< C'^2 >$ and $< \dot{W} >$. This new presumed P.D.F. depends more on the chemistry (with the introduction of C_l in the shape)than the precedent P.D.F. This new P.D.F. allow to better represent the effect of the chemical reaction.

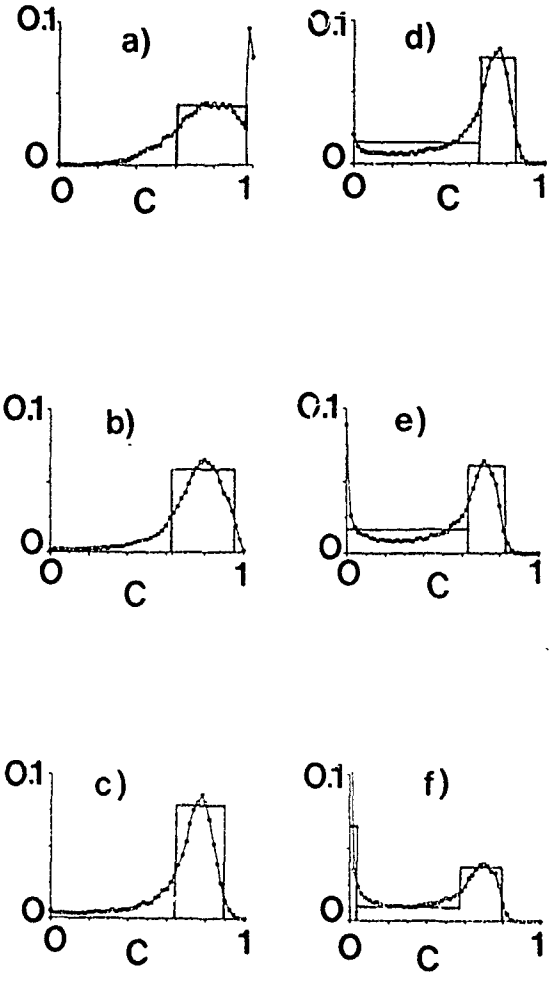

Fig.7. P.D.F. of the reactive scalar for different times computed by the D.N.S. compared with the P.D.F. constructed with rectangle and Dirac.

On the Fig.8, we have plotted the position of the particles which are used to solve the equation of transport of the joint P.D.F. $P(C,\phi)$ by the method of Monte Carlo. We can see the width of the P.D.F. by the spreading of the dots and its value by the density of the dots. As time goes on, the mean value of the inert scalar is conserved while the mean value of the reactive scalar decreases toward zero The joint P.D.F. computed by the direct numerical simulation are very similar to the one's computed by the Curl's model.

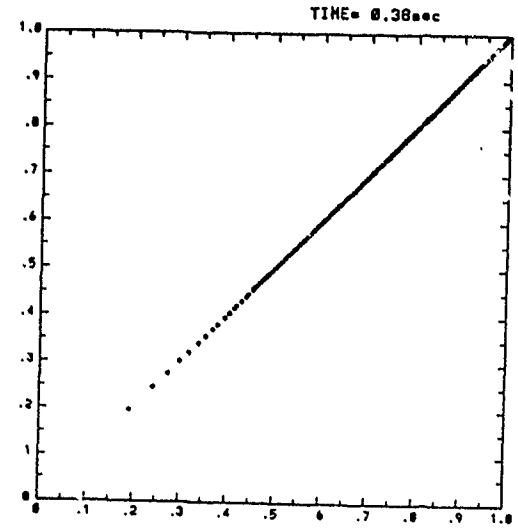

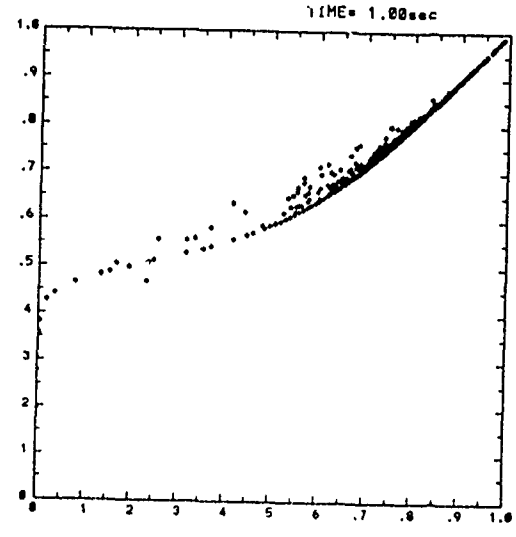

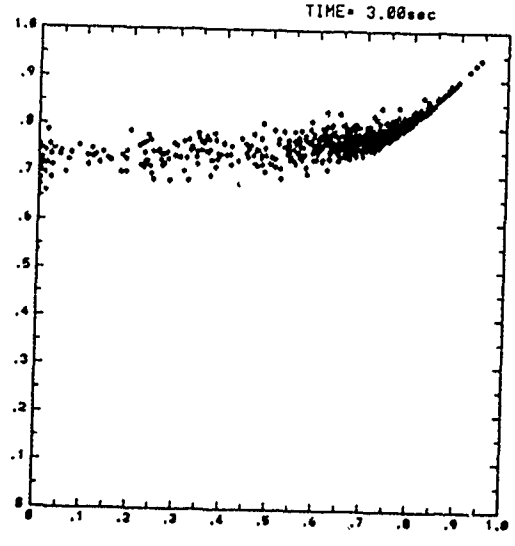

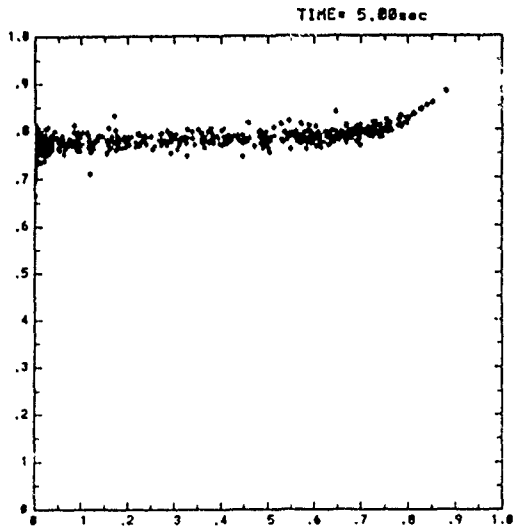

Fig.8. Joint P.D.F. of the inert scalar ϕ and the reactive scalar C computed by the Curl's models for different times.

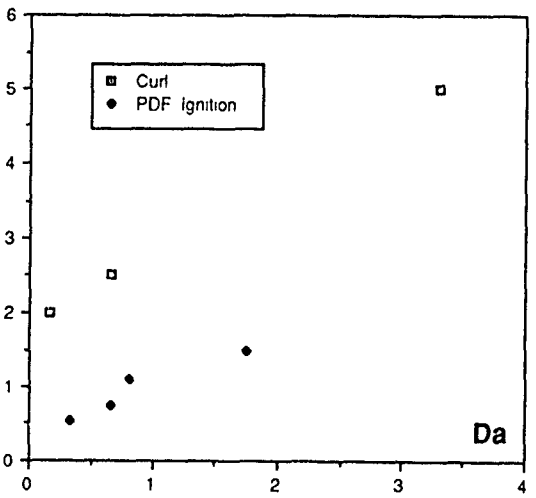

Fig.9. Evolution versus the Damköhler number of the constant of the 2 models.

3)

The Fig.9 shows the evolution of the constant Cd used in the model of the P.D.F. ignition and the constant C_C used in the Curl's model for different Damköler number.The definition of the Damköhler number is $Da = \tau_{t_0}/\tau_r$ where τ_{t_0} is the initial characteristic turbulence time . This characteristic time is the same in all the case in order to have the same evolution for the turbulence. During the comparaison between the models and the direct numerical simulation, the value of the constant (Cd or C_c) is kept really constant. But, to obtain fairly good comparaisons between the models and the simulation, these constants must be modified when the Damköler number varies. In a turbulent reacting medium, the ratio τ_t/τ_c where τ_c is a characteristic turbulent time of the reactive scalar field, has not always the same evolution with time. This fact explains why the constant is dependant of the Damköler number.

IV CONCLUSION

The work described here give us interesting information on the agreement of models with regard to the D.N.S. The evolution of the mean scalar values $\overline{C}$,$\overline{C'^2}$, $\overline{W}$ agree well in both the two models.

In the two models, appear a characteristic exchange time. The investigation we have made in order to study the influence of the Damkhöler number demonstrates that the characteristic exchange time is dependent of this number since we have to change the constant when this number changes.

In the comparisons presented here, the constants are not time dependent. With the D.N.S. we found that they are not really constant with time. Rather than using the characteristic turbulent velocity time, it would be better to use a characteristic time evaluated by the characteristic turbulent scalar field since the ratio between the two times vary with time for a reactive flow. For that, it is necessary to solve a scalar dissipation transport equation in the models.

Acknowledgements: Computing time (on a CRAY 2) for the Direct Numerical Simulation was allocated by the scientific commitee of the "Centre de Calcul Vectoriel pour la Recherche".

REFERENCES

Curl,R.L.1963, AIChE J. 9,175

Dopazo, C. 1979, Phys. Fluids, 22, 20

Dopazo,C.,O'Brien,E.E. 1974, A probabilistic approach to the autoignition of reaction turbulent mixtures, Acta Astronaut. 1, 1239-1255

McMurtry, P. A., Givi, P. 1989, Combust. flame, 77,171

Oran, E.S., and Boris, J.P. 1987, Numerical Simulation of Reactive Flow, Elsevier, New York

Moon, H.J., Picart, A., Borghi, R. 1989, Joint Meeting of the British and French Section of the Combustion Institute, Rouen. April 17-21, 205

Orszag, S. A. 1972, in Statistical Models and Turbulence, Lecture Notes in Physics, 12, Springer-Verlag

Pope, S.B. 1982, Combustion Science Technology, 28,131

EIGHTH SYMPOSIUM ON
TURBULENT SHEAR FLOWS
Technical University of Munich
September 9-11, 1991

A CONTINUOUS MIXING MODEL FOR PDF SIMULATIONS AND ITS APPLICATIONS TO COMBUSTING SHEAR FLOWS

A.T. Hsu*) and J.-Y. Chen**)

*) Sverdrup Technology, Inc.
NASA Lewis Research Center, Cleveland, OH 44135, USA

**) Combustion Research Facility
Sandia National Laboratories, Livermore, CA 94551, USA

ABSTRACT

The problem of time discontinuity (or jump condition) in the coalescence/dispersion (C/D) mixing model is addressed in this work. A C/D mixing model continuous in time is introduced. With the continuous mixing model, the process of chemical reaction can be fully coupled with mixing. In the case of homogeneous turbulence decay, the new model predicts a pdf very close to a Gaussian distribution, with finite higher moments also close to that of a Gaussian distribution. Results from the continuous mixing model are compared with both experimental data and numerical results from conventional C/D models.

1. INTRODUCTION

Accurate prediction of turbulent reacting flows requires the solution of an evolution equation for the probability density function (pdf) of the thermo-chemical variables using Monte Carlo simulation. Since the pdf equation, like most equations describing turbulent motion, is not closed, closure models have to be devised. For the pdf of scalars, the terms in the pdf equation that need modeling are molecular mixing and turbulent convection. The present work deals with the modeling of molecular mixing.

Most of the mixing models are based on the coalescence/dispersion (C/D) model by Curl (1963). This model is known to have deficiencies, and efforts had been made to correct these deficiencies, for example, Janicka, et al. 1979 and Pope 1982. The most recent efforts have been devoted to the problem of coupling between mixing and chemical reaction. Chen and Kollmann (1991) proposed a reaction conditioned model that allows correct prediction of combustion in the flame-sheet regime. Norris and Pope (1991) proposed a new model based on ordered pairing that aimed at the same end.

All the existing models suffer in one respect, namely, they are discontinuous in time: once a pair of particles are chosen to participate in mixing, their properties will jump abruptly regardless of the step size of the time integration. This phenomenon, clearly non-physical, could cause difficulty in coupling the processes of mixing and chemical reaction. In the present work, a new model that is continuous in time is proposed. With this new model, the processes of molecular mixing and chemical reaction can be fully coupled.

In the case of homogeneous turbulence decay of a scalar, one expects a Gaussian distribution for the pdf, and finite values for the higher moments. Pope (1982) pointed out the modified Curl model could not produce the correct pdf for this problem, and the higher even moments from that model tend to infinity; he suggested an age biased sampling process to overcome these shortcomings. The present continuous model, as we will show, predicts a pdf distribution very close to Gaussian for homogeneous turbulence decay, and gives finite higher moments with values close to that of a Gaussian distribution.

The continuous mixing model is applied to the study of both non-reacting and reacting flows, and the results are compared with earlier calculations by Hsu (1991) as well as with experimental data.

2. MOLECULAR MIXING MODELS

The evolution equation of a single point probability density function of scalar random variables $\psi_1, ..., \psi_n$ — representing the species mass fraction and temperature — can be written as

$$\begin{aligned} & \bar{\rho}\partial_t \tilde{P} + \bar{\rho}\tilde{v}_\alpha \partial_\alpha \tilde{P} + \bar{\rho}\sum_{i=1}^{N} \partial_{\psi_i}\{w_i(\psi_1, ..., \psi_N)\tilde{P}\} \\ = & - \partial_\alpha(\bar{\rho} < v''_\alpha | \phi_k(x) = \psi_k > \tilde{P}) \\ & - \bar{\rho}\sum_{i=1}^{N}\sum_{j=1}^{N} \partial^2_{\psi_i\psi_j}(< \epsilon_{ij} | \phi_k(x) = \psi_k > \tilde{P}) \end{aligned} \quad (1)$$

where the terms represent the rate of time change, mean convection, chemical reaction, turbulent convection, and molecular mixing, respectively; $\tilde{P}$ is the density-weighted joint pdf:

$$\tilde{P} = \rho P/\bar{\rho}, \quad (2)$$

ϵ is the scalar dissipation:

$$\epsilon_{ij} = D\partial_\alpha \phi_i \partial_\alpha \phi_j, \quad (3)$$

(where D is the diffusion coefficient), and $< x|y >$ denotes the mathematical expectation of a random function x conditioned upon y.

The left hand side of the above equation can be evaluated exactly and requires no modeling; the right hand side terms contain the conditional expectation of the velocity fluctuation and the conditional expectation of the scalar dissipation, which are new unknowns and require modeling. In the present work we concentrate on the modeling of the second term, namely, the conditional expectation of the scalar dissipation, referred to as molecular mixing in the following.

2.1 The Modified Curl Model

The simplest and most used mixing model is the modified Curl model, which assumes binary interaction between sample fluid particles. As described by Pope (1985), in a Monte Carlo simulation, the continuous pdf is replaced by delta functions

$$P^*(\psi; t) = \frac{1}{N}\sum_{n=1}^{N} \delta(\psi - \phi_n(t)), \quad (4)$$

where each delta function represents one sample fluid particle of an ensemble of N particles. The evolution of P^* entails the movement of the particles in the ψ−space, or the evolution of the individual values of ϕ_n's.

With the modified Curl model, the change of ϕ_n due to molecular mixing is achieved by the following binary interaction process: divide the flow domain into small cells, each containing N sample particles. Given a small time interval δt and a turbulent time scale τ, select randomly N_{mx} pairs of particles,

$$N_{mx} = 0.5\frac{\delta t}{C\tau}N, \tag{5}$$

($C = 6.0$) and let a pair, say, m and n, mix as follows

$$\phi_n(t+\delta t) = A\phi_m(t) + (1-A)\phi_n(t) \tag{6}$$
$$\phi_m(t+\delta t) = A\phi_n(t) + (1-A)\phi_m(t) \tag{7}$$

where $A = 0.5\xi$, with ξ a random variable uniformly distributed on the interval [0,1]. The remaining $N - 2N_{mx}$ particles remain unchanged:

$$\phi_n(t+\delta t) = \phi_n(t) \tag{8}$$

This model does not represent the true physical process since the properties of the sample particles change discontinuously regardless the size of the time interval δt. This deficiency can be best illustrated by rearranging eq. 6 and dividing it by δt

$$\frac{(\phi_n(t+\delta t) - \phi_n(t))}{\delta t} = \frac{A}{\delta t}(\phi_m(t) - \phi_n(t)) \tag{9}$$

The derivative $\frac{d\phi_n}{dt}$ does not exist because as δt goes to zero the right hand side of the equation becomes infinite since both A and the difference between $\phi_m(t)$ and $\phi_n(t)$ are finite. This means that there is a sudden jump in the value of the scalar quantities, which is typical of a Poisson process, but is non-physical in the present case since the flow properties of turbulence are continuous.

2.2 Continuous Mixing Model

One can see from the previous section that the modified Curl model relies on the parameter N_{mx} to control the extent of mixing. On the individual particle level, it assumes complete mixing once the particle is selected as one of the mixing pair, without considering the size of δt.

In order to achieve continuous mixing, we propose the following model: during a time interval δt, we assume that all the particles within a cell participate in mixing. The extent of the mixing is controlled at the individual particle level. That is to say, the N particles within a given cell are randomly grouped into $N/2$ pairs; the properties of all the particles change according to eqs. 6 and 7. The extent of mixing now has to be controlled at the individual particle level through the parameter A, which is redefined as

$$A = C'\xi\frac{\delta t}{\tau} \tag{10}$$

where $C' = 2.0$. With this new definition, eq. 9 can be written, in the limit $\delta t \to 0$,

$$\frac{d\phi_n}{dt} = C'\frac{\xi}{\tau}(\phi_m(t) - \phi_n(t)). \tag{11}$$

The above equation states that the change of ϕ_n due to mixing is proportional to the difference between ϕ_m and ϕ_n, and inversely proportional to the turbulence time scale τ.

2.3 The Coupling of Mixing and Reaction

The processes of mixing and chemical reaction are essentially decoupled when one uses the discontinuous C/D models. In contrast, with the above continuous model, coupling become natural since, for a given particle, mixing and chemical reaction can be described with a single equation:

$$\frac{d\phi_n}{dt} = C'\frac{\xi}{\tau}(\phi_m(t) - \phi_n(t)) + w_n, \tag{12}$$

where w_n is the chemical source term.

Since the continuous mixing model allows full coupling of the reaction and mixing processes, the C/D model with reaction zone conditioning by Chen and Kollmann (1991) can be easily implemented in the present model to simulate the fast reaction in the flame sheet regime. Here a modified finite difference version of eq. 12 has to be used since w_n is infinity in case of fast reaction.

3. RESULTS AND DISCUSSIONS

The continuous mixing model described in the previous section has been validated using both non-reacting and reacting flow test cases. The results and their comparisons with earlier calculations (Hsu, 1991) using the modified Curl model as well as with experimental data are presented in this section.

3.1 Homogeneous Turbulence Decay of a Scalar

The case of decaying fluctuation of a passive scalar in homogeneous turbulence is used to test the continuous mixing model. The initial condition is

$$P^*(\psi;t) = \frac{1}{N}\left[\sum_{n=1}^{N/2}\delta(\psi-1) + \sum_{n=N/2+1}^{N}\delta(\psi+1)\right], \tag{13}$$

that is, in the Monte Carlo simulation, half of the particles are ascribed the value 1, and the other half -1.

The pdf distribution of the normalized variable $(\psi - < \phi >)/\sigma$, where $< \phi >$ is the mean and σ is the standard deviation, in the homogeneous turbulence decay problem converges to a single curve after certain time, and the correct distribution should be Gaussian. Fig. 1 and 2 are the pdf distributions from the modified Curl model and the present model, both compared to a normal distribution. One can see that the pdf from the modified Curl model deviates considerable from Gaussian, while the result from the present model is fairly close to a Gaussian distribution.

The evolution history of the rms and fourth and sixth moments of the scalar fluctuation are calculated using both the modified Curl model and the present continuous model. Fig. 3 shows the results from the modified Curl model. One can see that although the rms from that model behaves well, the fourth and sixth moments grow quickly out of bound, oscillating at a level several order of magnitudes higher than the value of Gaussian distribution. These results are similar to what Pope (1982) had observed. Fig. 4 shows the results for the same set of quantities from the present model. The rms behaves similar to that from the modified Curl model. The fourth and sixth moments, on the other hand, are quite different from those of the previous model; they

rise smoothly to the value predicted by Gaussian distribution. Although the values do not seem to converge, they remain finite, and are of the same order of magnitude as that of the Gaussian distribution.

The above shown results clearly showed the advantage of the present model over that of the modified Curl model. Pope (1982) had devised an age biased scheme that achieved the same end, which required an additional variable, namely the age of the particles, and two extra adjustable parameters. In contrast, the present model needs no extra work or parameters.

3.2 Heated Turbulent Jet

Extensive experimental results for a heated turbulent plane jet have been reported by many authors (Bashir, et al. 1975, Browne et al., 1984, Uberoi and Singh, 1975, Jenkins, 1976, Antonia, et al., 1983). The turbulent jet has a slightly higher temperature than the ambient. Measurements of both the the mean temperature and the rms of the temperature fluctuations were given. We compared the solutions for the heated turbulent jet from the new model with experimental data as well as with previous solutions (Hsu, 1991) obtained using the modified Curl model.

In the present study, a combined CFD—Monte Carlo algorithm is used. The mean flow field is obtained by solving the Navier-Stokes equation and a two-equation turbulence model using a finite difference scheme. The temperature is treated as a conserved scalar and simulated by the pdf equation.

Fig. 5 shows the comparisons of the the mean temperature distribution from the pdf Monte Carlo simulations and experimental data from various authors. The figure shows that both mixing models predicts the mean temperature distribution accurately.

The results for standard variation, or rms, of the temperature distribution are given in Fig. 6. Although the two solutions do not show significant difference, the new model seems to agree slightly better with the experimental data. The skewness and the flatness, i.e., the third and fourth moments of the temperature fluctuation, are given in Figs. 7 and 8; the comparisons show that in the present case of a turbulent jet the statistical behavior of the new model is similar to that of the modified Curl model.

3.3 Hydrogen-Fluorine Diffusion Flame

The continuous model has been applied to the H_2—F_2 diffusion flame studied earlier by Hsu (1991). The flow conditions are set according to an experiment performed by Hermanson and Dimotakis (1989). The flame consists two streams. The upper stream contains 96% of N_2 and 4% of F_2, the flow velocity is $U_1 = 22\,m/s$; the lower stream contains 96% of N_2 and 4% of H_2, with velocity $U_2 = 8.8\,m/s$. The estimated Damköhler number is ranged from 25 to 130 (Hermanson and Dimotakis, 1989), and a fast chemistry model is deemed appropriate in the calculation. Again a modified version of eq. 12 is used to accommodate the fast chemistry.

Fig. 9 shows the temperature rise due to combustion. In the figure, δ_T is the shear layer thickness determined by 1% of the temperature rise, ΔT is the actual temperature rise due to combustion, (the two streams have the same temperatures initially,) and ΔT_{adj} is the adiabatic flame temperature assuming complete reaction. Details on the flow conditions can be found in Hermanson and Dimotakis (1989). The agreement between numerical predictions and experimental data is fairly good, and a comparison of the results from the continuous model and that from the modified Curl model shows that both performed well for this case.

3.4 Combination with Reaction Zone Conditioning

Chen and Kollmann (1991) developed a mixing model based on reaction zone conditioning, aimed at the coupling of reaction and mixing. We have shown in Section 2.3 that with the present model, the processes of reaction and mixing can be fully coupled; therefore it is only natural to apply the reaction zone conditioning suggested by Chen and Kollmann here.

The H_2—F_2 diffusion flame problem is reformulated such that the chemical reaction is confined to a very narrow zone near stoichiometry. By applying reaction zone conditioning to the continuous mixing model, we were able to produce a scatter plot of the temperature vs. mixture fraction in which all the points reached the equilibrium temperature. This result is shown in Fig. 10. The mixture fraction here is defined as the molar concentration of fuel divided by the total molar concentration, and stoichiometry is located at $f = 0.5$.

4. CONCLUSIONS

A turbulence mixing model that is continuous in time has been introduced. The deficiency of non-physical jump condition in the mixing process is removed in the new model. It has been shown that the new model is superior to the existing modified Curl model (Janicka, et al., 1979) in that it can predict a Gaussian distribution and finite higher moments in the case of homogeneous turbulence decay; it has accomplished what the age biased sampling scheme (Pope, 1982) is designed for, without the extra parameters required by that scheme. The numerical results from the present model compare well with experimental data

ACKNOWLEDGEMENT

The work of the first author is supported by the NASA Lewis Research Center under Contract NAS3-25266 with L. Povinelli as monitor. The second author is supported by the Unite States Department of Energy, Office of Basic Energy Sciences, Division of Chemical Sciences.

REFERENCES

Antonia, R.A., Browne, L.W.B., Chambers, A.J., and Rajagopalan, S., 1983, Budget of the Temperature Variance in a Turbulent Plane Jet. Int. J. Heat Mass Transfer, 26-1, 41-48.

Ashir, J. and Uberoi, M.S., 1975, Experiments on Turbulent Structure and Heat Transfer in a Two Dimensional Jet. Physics of FLuids, 18-4, 405-410.

Browne, L.W.B., Antonia, R.A., and Chembers, A.J., 1984, The Interaction Region of a Turbulent Plane Jet. J. Fluid Mech., 149, 355-373.

Chen, J.-Y. and Kollmann, W., 1991, Mixing Models for Turbulent Flows with Exothermic Reactions. Turbulent Shear Flows, Springer-Verlag, 7, 277.

Curl, R.L., 1963, Dispersed Phase Mixing, I, Theory and Effects of Simple Reactors. A.I.Ch.E.J. 9, 175.

Hermanson, J.C. and Dimotakis, P.E., 1989, Effects of Heat Release in a Turbulent, Reacting Shear Layer. J. Fluid Mech. 199, 333-375.

Hsu, A.T., 1991, The Study of Hydrogen Diffusion Flames Using PDF Turbulence Models. AIAA Paper 91-1780.

Janicka, J., Kolbe, W., and Kollmann, W., 1979, Closure of the Transport Equation for the Probability Density Function Scalar Field. J Non-Equilib. Thermodyn. 4, 47.

Jenkins, P.E. and Goldschmidt, V.W., 1973, Mean Temperature and Velocity in a Plane Turbulent Jet, ASME J. Fluids Eng., 95, 581-584.

Norris, A.T. and Pope, S.B., 1991, Turbulent Mixing Model Based on Ordered Pairing. Combust. and Flame, 83, 27-42.

Pope, S.B., 1982, An Improved Turbulence Mixing Model. Combust. Sci. Tech., 28, 131,

Pope, S.B., 1985, PDF Methods for Turbulent Reactive Flows. Prg. Energy Combust. Sci., 11, 119-192.

Uberoi, M.S. and Singh, P.I., 1975, Turbulent Mixing in a Two-Dimensional jet, Physics of Fluids, 18-7, 764-769.

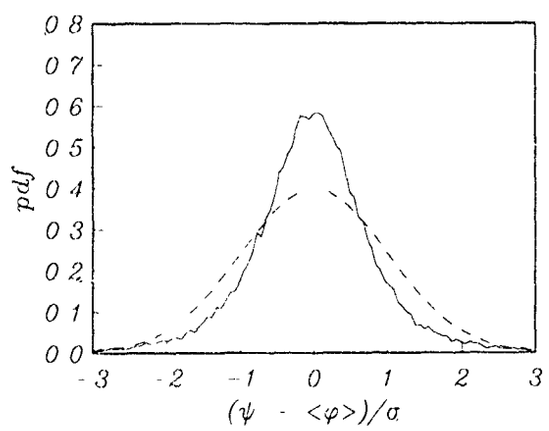

Figure 1. Asymptotic pdf distribution for a scalar in homogeneous turbulence. — modified Curl model; - - - Gaussian.

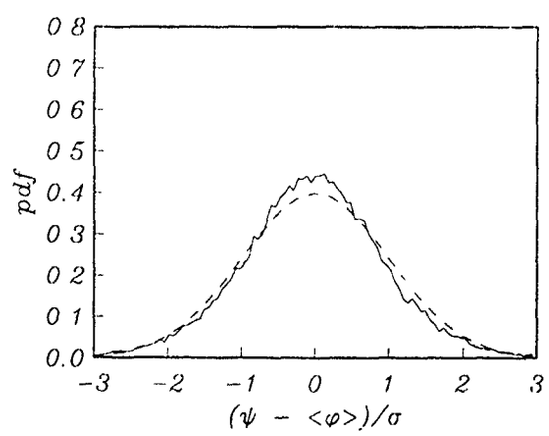

Figure 2. Asymptotic pdf distribution for a scalar in homogeneous turbulence. — present model; - - - Gaussian.

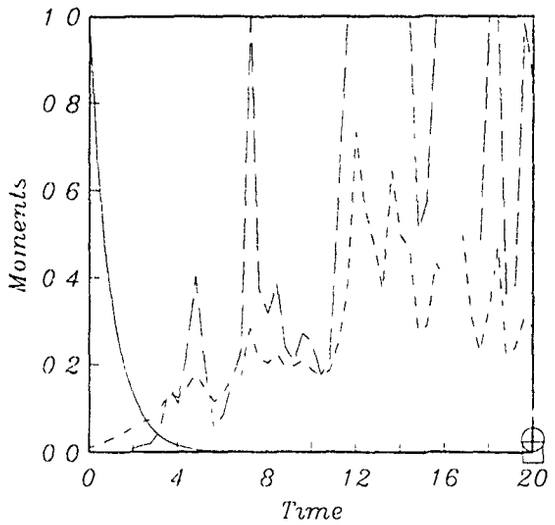

Figure 3. Evolution of moments from the modified Curl model. — standard deviation, - - - 0.01 × fourth central moment, - - 0.0001 × sixth central moment, o 0 01 × fourth moment for Gaussian distribution, □ 0.0001 × sixth moment for Gaussian distribution.

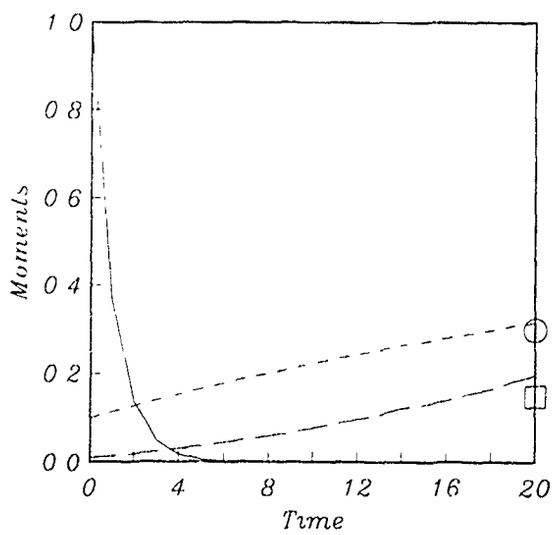

Figure 4. Evolution of moments from the present model. — standard deviation, - - - 0.1 × fourth central moment, - - 0.01 × sixth central moment, o 0.1 × fourth moment for Gaussian distribution, □ 0.01 × sixth moment for Gaussian distribution.

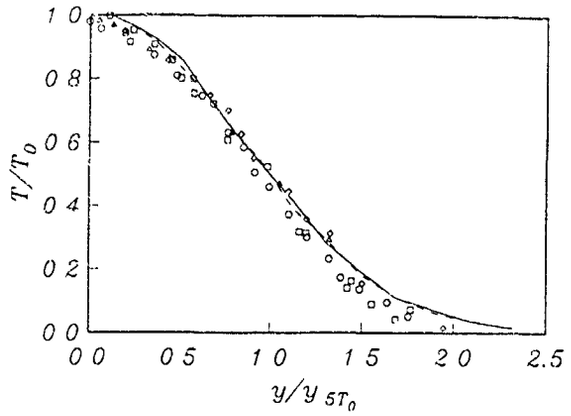

Figure 5. Mean temperature in heated plane jet. — continuous mixing model, - - - modified Curl model, Δ Browne et al. (1984), □ Bashir and Uberoi (1975), ◇ Uberoi and Singh (1975), ○ Jenkins and Goldschmidt (1973).

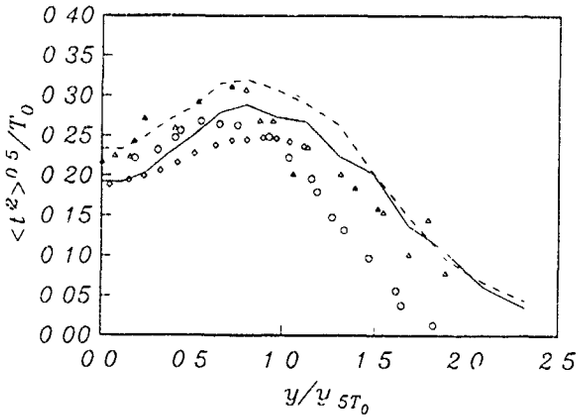

Figure 6. RMS of temperature variance in heated plane jet. — continuous mixing model, - - - modified Curl model, ◇ Antonia et al. (1983), ○ Bashir and Uberoi (1975), Δ Uberoi and Singh (1975).

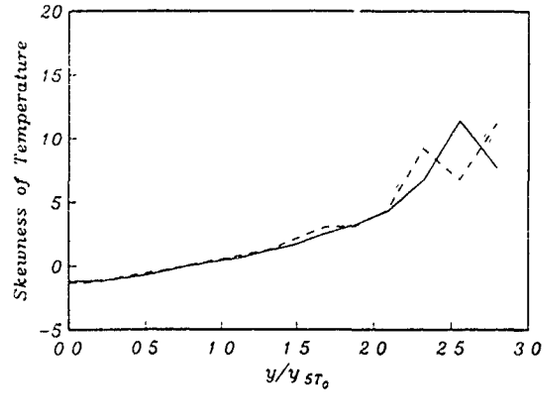

Figure 7. Skewness of temperature variance in heated plane jet. — continuous mixing model, - - - modified Curl model.

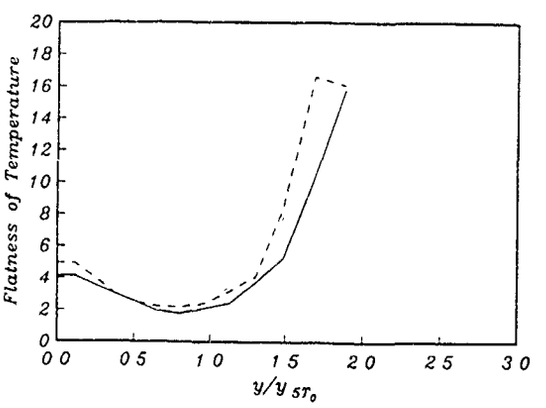

Figure 8. Flatness of temperature variance in heated plane jet. — continuous mixing model, - - - modified Curl model.

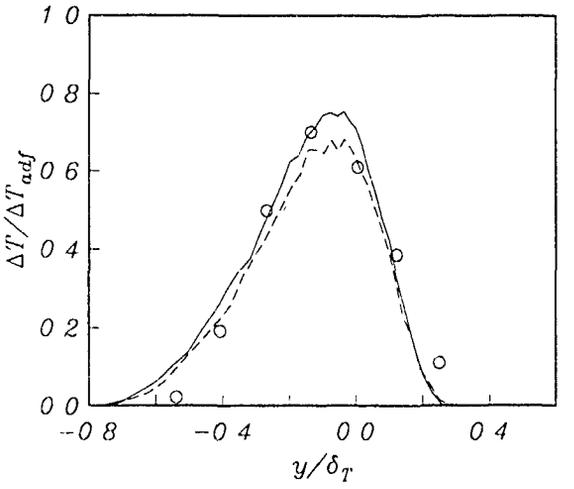

Figure 9. Temperature rise in an H_2–F_2 diffusion flame. — continuous mixing model, - - - modified Curl model, ○ Hermanson and Dimotakis (1989).

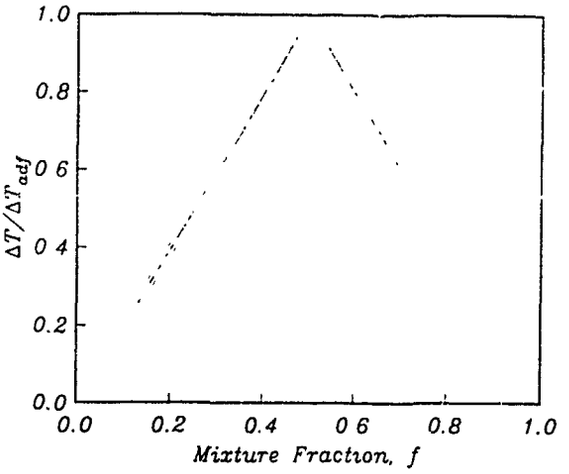

Figure 10. Joint pdf between temperature and mixture fraction on the centerline of the H_2–F_2 diffusion flame; reaction is restricted to a narrow zone at stoichiometry; results are obtained by applying reaction zone conditioning (Chen and Kollmann, 1990) to the continuous mixing model.

EIGHTH SYMPOSIUM ON
TURBULENT SHEAR FLOWS
Technical University of Munich
September 9-11, 1991

Modelling of Transient Compressible Turbulent Reacting Flows

R.P. Lindstedt and V. Sakthitharan

Mechanical Engineering Department, Imperial College,
Exhibition Road, London SW7 2BX

Abstract

The present paper addresses a number of issues of relevance to the modelling of turbulent gaseous explosions These include the removal of cold front boundary problems which may lead to a numerically induced transition to detonation and the formulation of sufficient temporal and spatial resolution criteria to eliminate or substantially reduce numerical inaccuracies This is accomplished by comparing the results of transient computations with the results from the solution of the corresponding steady problem using an eigenvalue technique. A reaction model giving good agreement with measurements of turbulent burning velocities is derived on the assumption that as first approximation flames exhibit a fractal behaviour at high turbulence Reynolds numbers It is shown that with an inner cutoff based on the Kolmogorov scale and a fractal dimension of 7/3 the turbulent burning velocity is dependent upon the ratio of the laminar burning velocity and Kolmogorov velocity

Introduction

Turbulent gas explosions exhibit complex behaviours and are very sensitive to interactions with obstacle induced shear layers and re-circulation zones The types of flames under consideration can readily be produced under laboratory conditions in fuel-air mixtures in the presence of obstacles e.g Lindstedt & Michels (1989) A particularly interesting feature of these flames is that they propagate for long times at around sonic velocity prior to transition to detonation. This kind of behaviour has also been observed in field scale trials To model turbulent flames under these conditions is very demanding Firstly, turbulence Reynolds numbers are frequently very high and estimates of Karlowitz numbers based on the Kolmogorov scale indicate that these are exceeding unity by order(s) of magnitude. Furthermore, if the transition to detonation (DDT) is to be considered then direct kinetic effects must be included. In the present study auto-ignition effects are not treated and only processes leading up to DDT are considered

Despite these difficulties the area of modelling of turbulent gaseous explosions has received a fair amount of attention due to the obvious practical implications e.g. Hjertager (1982) However, until recently surprisingly little effort has been directed towards investigating the numerical behaviour of the most frequently utilised reaction models - versions of the Eddy Break Up model - under conditions typical of confined premixed flame and gaseous explosions Furthermore, while many modifications to these models have been suggested, the implications of such modifications on the resulting turbulent burning velocity and their numerical behaviour has received little attention Catlin & Lindstedt (1991) have shown how a general eigenvalue technique can be applied to investigate the behaviour of turbulent reaction models and have defined the requirements in terms of flame resolution and Courant numbers for transient numerical computations necessary to ensure well behaved solutions for the standard BML form, e.g Cant & Bray (1989), of the Eddy Break Up (EBU) model. In addition it was noted that common modifications to this reaction model frequently introduced to ensure uniqueness of the numerical solution, such as switching off the reaction rate below some (small) value of the reaction progress variable, will have large effects on the predicted turbulent burning velocity. For example a cutoff set at a value of the reaction progress variable of 0.01 will result in a reduction in the predicted turbulent burning velocity by around 40% with the use of standard modelling constants The case treated in the analysis by Kolmogorov et al (1937) which is applicable in the case where the flame front merges with the cold front, e g in the absence of a diffusion zone ahead of the flame, was found not to be attainable in transient numerical computations due to cold front boundary problems However, with carefully controlled computations transient solutions in good agreement with the eigenvalue analysis can be obtained even with cold front quenching criteria reduced to within an order of magnitude of the truncation error limit The complete removal of cold front quenching criteria and/or inappropriate temporal or spatial resolution of the flame was shown to lead to a limiting case of a numerically induced Chapman-Jouget detonation in a constant turbulence field.

In the present paper past work is extended in two ways, (i) the eigenvalue technique by Catlin & Lindstedt (1991) is applied to the formulation of a turbulent reaction model based on the presumption of a fractal behaviour of turbulent flames at large turbulence Reynolds numbers and (ii) transient flames are studied in a decaying turbulence field

Governing Equations

The current paper considers the customary Navier-Stokes equations in Cartesian geometry along with a fuel mass fraction equation and an energy equation written in terms of the total internal energy, e g incorporating chemical bond energies The mass conservation and momentum equations may be written as,

$$\frac{\partial \bar{\rho}}{\partial t} + \frac{\partial}{\partial x_i}\left\{ \bar{\rho}\, \tilde{U}_i \right\} = 0 \qquad (1)$$

$$\frac{\partial \bar{\rho}\, \tilde{U}_j}{\partial t} + \frac{\partial}{\partial x_i}\left\{ \bar{\rho}\, \tilde{U}_i \tilde{U}_j \right\} = - \frac{\partial \bar{P}}{\partial x_j} - \frac{\partial}{\partial x_i}\left\{ \bar{\rho}\, \widetilde{U_i'' U_j''} \right\} \qquad (2)$$

The turbulence model is the standard k - ε model e g Jones & Whitelaw (1982) with a modification to the ε-equation introduced to account approximately for rapid distortion as suggested by Morel & Mansour (1982).

$$\bar{\rho}\frac{\partial \tilde{k}}{\partial t} + \bar{\rho}\, \tilde{U}_j \frac{\partial \tilde{k}}{\partial x_j} = \frac{\partial}{\partial x_j}\left\{ \frac{\mu}{\sigma_k}\frac{\partial \tilde{k}}{\partial x_j} \right\} - \bar{\rho}\, \widetilde{U_i'' U_j''} \frac{\partial \tilde{U}_i}{\partial x_j} - \frac{\mu_T}{\bar{\rho}^2}\frac{\partial \bar{\rho}}{\partial x_i}\frac{\partial \bar{P}}{\partial x_i} - \bar{\rho}\, \tilde{\varepsilon}$$

$$\bar{\rho}\frac{\partial \tilde{\varepsilon}}{\partial t} + \bar{\rho}\,\tilde{U}_j\frac{\partial \tilde{\varepsilon}}{\partial x_j} = \frac{\partial}{\partial x_j}\left\{\frac{\mu}{\sigma_\varepsilon}\frac{\partial \tilde{\varepsilon}}{\partial x_j}\right\} - C_2\,\bar{\rho}\,\frac{\tilde{\varepsilon}^2}{\tilde{k}} - C_3\,(\bar{\rho}\,\tilde{\varepsilon})\,\frac{\partial \tilde{U}_i}{\partial x_i}$$

$$- C_1\frac{\tilde{\varepsilon}}{\tilde{k}}\left\{\bar{\rho}\,\widetilde{U_i''U_j''}\frac{\partial \tilde{U}_i}{\partial x_j} + \frac{\mu_T}{\bar{\rho}^2}\frac{\partial \bar{\rho}}{\partial x_i}\frac{\partial \bar{P}}{\partial x_i}\right\} \qquad (4)$$

$$\bar{\rho}\,\widetilde{U_i''U_j''} = \frac{2}{3}\delta_{ij}\left\{\bar{\rho}\,\tilde{k} + \mu_T\frac{\partial \tilde{U}_i}{\partial x_i}\right\} - \mu_T\left\{\frac{\partial \tilde{U}_i}{\partial x_j} + \frac{\partial \tilde{U}_j}{\partial x_i}\right\} \qquad (5)$$

where $\mu_T = C_\mu\,\bar{\rho}\,\tilde{k}^2/\tilde{\varepsilon}$ and $\tilde{k} = \frac{1}{2}\widetilde{U_i''U_j''}$ (6)

The modeling constants in the above equations have their standard values as defined by Jones & Whitelaw (1982) and Morel & Mansour (1982) e.g. $C_1 = 1.44$, $C_2 = 1.92$, $C_3 = 0.33$, $C_\mu = 0.09$, $\sigma_k = 1.00$ and $\sigma_\varepsilon = 1.22$. The scalar equations may be written in the general form as,

$$\frac{\partial \bar{\rho}\,\tilde{\phi}}{\partial t} + \frac{\partial}{\partial x_i}\left\{\bar{\rho}\,\tilde{U}_i\,\tilde{\phi}\right\} = -\frac{\partial}{\partial x_i}\left\{\bar{\rho}\,\widetilde{U_i''\phi''}\right\} + \overline{\rho\,S(\phi)} \qquad (7)$$

If the assumption of a uniform mixture with no change in mean molecular weight is introduced along with the assumption of gradient transport the source term and the flux terms in the energy equation may be written as,

$$\overline{\rho\,S(e)} = -\,\bar{P}\,\frac{\partial \tilde{U}_i}{\partial x_i} \qquad (8)$$

$$\bar{\rho}\,\widetilde{U_i''e''} = -\left\{\frac{\mu_T}{\sigma_{Pr}/\gamma}\frac{\partial \tilde{e}}{\partial x_i} + \left(\frac{\mu_T}{\sigma_{Sc}} - \frac{\mu_T}{\sigma_{Pr}/\gamma}\right)\sum_{k=1}^{nsp} h_k\frac{\partial \tilde{Y}_k}{\partial x_i}\right\}$$

The turbulent Prandtl and Schmidt numbers have been assigned values of 0.75. The ratio of specific heats (γ) is assumed constant at 1.3. Gradient transport is also assumed for the fuel mass fraction flux,

$$\bar{\rho}\,\widetilde{U_i''Y_{Fu}''} = -\frac{\mu_T}{\sigma_{Sc}}\frac{\partial \tilde{Y}_{Fu}}{\partial x_i} \qquad (10)$$

For ease of discussion the reaction progress variable is introduced and is in the present work defined as,

$$\tilde{c} = 1 - \tilde{Y}_{Fu}/Y^o_{Fu} \qquad (11)$$

It should here be noted that in the general case the reaction progress variable is a function of the local mixture fraction (f) as well as the local fuel mass fraction. However, in the present case of a homogeneous mixture the mixture fraction equation need not be solved. The source term in the fuel mass fraction equation is discussed in detail in the section below. It has further been assumed that the fuel (methane) undergoes a one step reaction as,

$$CH_4 + O_2 \text{ -------> } CO_2 + 2H_2O \qquad (12)$$

Thermodynamic data have been evaluated using JANAF polynomials. The final temperature in the products is 2340 K giving an expansion ratio ($\tau = T_f/T_o - 1$) across the flame of 6.85.

The above equation set is solved as appropriate using a version of the PISO algorithm with a variable number of implicit correctors and with full splitting error control e.g. Catlin & Lindstedt (1991).

Reaction Model

To formulate a suitable reaction model for a strongly turbulent deflagration is a demanding task. As discussed above it has been shown that numerical problems can readily be removed from the BML form of the EBU reaction model and that the $u_T \propto u'$ link can be maintained in transient computation in a constant turbulence field with values of u' in excess of 25 m/s - a necessary requirement for explosion modelling. However, even with the removal of numerically induced difficulties it is clear that the turbulent burning velocities predicted by this model are in substantial error in regions of high turbulence. As a result modifications have been suggested to the EBU model which account for quenching effects at high turbulence levels. For an excellent and recent review see Bray (1990). One of the most interesting frameworks for deriving modifications to the EBU model was suggested by Gouldin and co-workers (1989) who introduced an expression based on the assumption of a fractal behaviour of flames at high turbulence levels. The suggested rate expression may readily be re-written in Favre averaged quantities as,

$$\overline{\rho R_C} = C_{EBU}\,\bar{\rho}\,u_L\left[\frac{l_l\,f}{l_k}\right]^{D-2}\frac{(1+\tau)}{(1+\tau\tilde{c})}\frac{\tilde{c}(1-\tilde{c})}{\delta_f} \qquad (13)$$

In the above expression l_l and l_k are the integral and Kolmogorov length scales respectively, u_L the unstrained (or strained) laminar burning velocity and δ_T a measure of the thickness of the turbulent flame brush. The term f is an empirical function which will not be used in the present work and is thus not discussed further.

It is not the intention to here provide a detailed discussion of the applicability of fractal based models for turbulent flames. It is simply noted that at high turbulence levels there appears to be general agreement between measurements (Mantzaras et al (1989), North & Santavicca (1990)) and derivations based on treating the flame as a passive surface (Gouldin et al (1989)) or as a dynamic interface (Kerstein (1988)), that flames in high turbulence are to a first approximation fractal with a fractal dimension (D) of around 2.33. However, it should be noted that at low turbulence levels D may be as low as 2.11. As in the present work only high turbulence Reynolds numbers are considered the fractal dimension will be assumed to be 7/3.

The turbulent flame thickness appearing in equation (13) above can readily be removed if it is noted that it is essentially proportional to the integral length scale in the cold flow. The factor or proportionality is largely dependent upon the definition of the thickness of the turbulent flame brush but is almost without exception in the range 1 to 10. Catlin & Lindstedt (1991) have shown that this indeed holds for mixing controlled reaction models after the removal of cold front boundary problems. The transported *pdf* computations by Anand & Pope (1987) also give a turbulent flame thickness proportional to the integral length scale in the cold flow with the addition of a linear dependence upon the expansion ratio (τ) across the flame. Consequently, assuming $\delta_T = l_l$ appears to be an acceptable approximation and the revised reaction model may at this stage be written as,

$$\overline{\rho R_C} = C_{EBU}\,\bar{\rho}\,u_L\left[\frac{l_l}{l_k}\right]^{\frac{1}{3}}\frac{(1+\tau)}{(1+\tau\tilde{c})}\frac{\tilde{c}(1-\tilde{c})}{l_l} \qquad (14)$$

One further issue which has been debated at some length is the appropriate inner cutoff of the fractal expression. In eq. (14) it has been assumed that the inner cutoff corresponds to the Kolmogorov scale. Peters (1986) have suggested that the inner cutoff could instead be proportional to the Gibson scale which will result in the following rate expression,

$$\overline{\rho R_C} = C_{EBU}\,\bar{\rho}\,u_L\left[\frac{l_l}{l_G}\right]^{\frac{1}{3}}\frac{(1+\tau)}{(1+\tau\tilde{c})}\frac{\tilde{c}(1-\tilde{c})}{l_l} \qquad (15)$$

As the Gibson and integral scales are defined as $l_G = u_L^3 / \tilde{\varepsilon}$ and $l_I = 3/2\ u'^3/\tilde{\varepsilon}$ respectively, it can readily be shown that under the present assumptions the reaction rate source term reduces to the standard BML form of the EBU reaction model,

$$\overline{\rho R_C} = C_{EBU}\,\tilde{\rho}\left(\frac{3}{2}\right)^{\frac{1}{3}}\frac{(1+\tau)}{(1+\tau\tilde{c})}\frac{\tilde{c}(1-\tilde{c})}{t_I} \qquad (16)$$

While the Gibson scale cutoff is attractive from a theoretical viewpoint the above result appears at present not to be in good agreement with experimental data even for moderate turbulence Reynolds numbers Consequently, the present work adopts an inner cutoff based on the Kolmogorov scale. Some experimental support also exists e g North & Santavicca (1990) that the inner cutoff most probably is smaller than the Gibson scale Under the simplifying assumptions above the reaction rate based on the Kolmogorov scale cutoff may be written as,

$$\overline{\rho R_C} = C_{EBU}\,\tilde{\rho}\left(\frac{u_L}{v_k}\right)\left(\frac{\tilde{\varepsilon}}{\tilde{k}}\right)\left(\frac{(1+\tau)}{(1+\tau\tilde{c})}\right)\tilde{c}(1-\tilde{c})$$

$$\text{where } v_k = (\nu_L\,\varepsilon)^{\frac{1}{4}} \qquad (17)$$

This is an interesting result as it in essence is the standard EBU model modified by the ratio of the laminar burning velocity to the turnover velocity of eddies on Kolmogorov scale. The implications of this reaction rate expression are explored in the section below

One final point remains to be addressed. It is now well known that the c(1-c) expression does produce cold front boundary problems There are several ways of eliminating this numerical artefact In the present work it has been assumed that reaction rate is zero below a Favre averaged progress variable of 0 01 In the present work the eigenvalue analysis by Catlin & Lindstedt (1991) is used in the section below to analyse the behaviour of the above reaction rate expression for variations in turbulence properties, laminar burning characteristics and expansion ratios across the flame

Eigenvalue Analysis

An important distinction between the analysis by Kolmogorov et al (1937) and the present eigenvalue analysis is that the restriction that the first derivative of the reaction rate source term should be non-zero as c --> 0 is removed. This is particularly useful in the current case as it enables more general turbulent reaction models to be investigated As a starting point the above conservation equations are simplified for a steadily propagating 1D planar flame in an incompressible fluid and a constant turbulence field to give,

$$(\rho u)_o\frac{d\tilde{c}}{dx} = \frac{d}{dx}\left(\frac{\mu}{\sigma_{Sc}}\frac{d\tilde{c}}{dx}\right) + \overline{\rho R_C} \qquad (18)$$

A simple coordinate transformation is now introduced as,

$$\frac{d}{d\xi} = \frac{\mu}{\sigma_{Sc}}\frac{1}{(\rho u)_o}\frac{d}{dx} \qquad (19)$$

and the resulting equation may be written as

$$\frac{d\tilde{c}}{d\xi} = \frac{d}{d\xi}\left(\frac{d\tilde{c}}{d\xi}\right) + \overline{W(c)}\,\Lambda \qquad (20)$$

If the effect of temperature on the laminar viscosity is taken into account the resulting source is,

$$\overline{W(c)} = \tilde{c}^{\,n}(1-\tilde{c})\frac{(1+\tau)}{(1+\tau\tilde{c})^{41/12}},\ \Lambda = \frac{C_\mu C_t}{\sigma_{Sc}}\frac{u_I}{v_k}\frac{k}{u_o^2} \qquad (21)$$

where the parameter 'n' has been introduced for reasons outlined below. It should be noted that in equation (21) only the density ratio across the flame appears The last term may be rewritten as (with the turbulent burning velocity denoted $u_T = u_0$)

$$u_T = \sqrt{\frac{C_\mu C_t}{\sigma_{Sc}}\frac{u_I}{v_k}\frac{k}{\Lambda}} \qquad (22)$$

Equation (20) above may readily be integrated using a Runge-Kutta-Nystrom method and a binary search procedure applied to determine the resulting eigenvalue The appropriate boundary condition at the cold front is,

$\frac{dc}{d\xi} = c_o$ at the cold front ($c_o = 10^{-2}$ in the present work)

Eigenvalues can readily be determined for a wide range of parameters and be related to the resulting turbulent burning velocity via equation (22). The dependence of the latter upon the expansion ratio across the flame is the first parameter to be considered. The results obtained by the solution of equations (20,21) for different values of 'n' are shown in Fig 1 where the results have been normalised by the turbulent burning velocity obtained with an expansion ratio (τ) of 7 A comparison with the result from the transported *pdf* computations by Anand & Pope (1987) have also been included As can be seen it appears that n=2 gives better agreement with the transported *pdf* computation than the more commonly used n=1 This is quite different from the earlier version of the BML form of the EBU model used in the studies by Cant & Bray (1989) and Lindstedt & Catlin (1990) for which n=1 25 gives the best agreement

The final issue is that of the modelling constant C_{EBU} For the exponent n=1 the data by Bradley and co-workers (1984), see below, is fitted very successfully with this constant being equal to 1 while 0 67 improves the agreement further For the case n=2 which gives optimal agreement with the transported *pdf* computations the computed eigenvalue increases from 0 104 to 3 12 As a consequence the modelling constant is increased in proportion to a value of 20.

The agreement between the eigenvalue analysis and transient 1D computations was first tested as a function of flame resolution The approach to a steady limiting value for two flames propagating in an open ended flame tube 6m in length can be found in Fig 2. The flame tube was resolved by 1202 computational nodes and an integral length scale of 0 25 m was specified along with u' = 5 m/s and u'=25 m/s respectively The turbulent burning velocities were obtained from the transient computations by evaluating the reaction integral across the flame and as an additional measure the results where checked by dividing the particle velocity ahead of the flame by the expansion ratio (τ). Ignition was obtained by specifying a hot gas pocket at ambient pressure. The turbulent burning velocities in Fig. 2 have been normalised by those determined from the eigenvalue analysis of 5.75 m/s and 15.7 m/s respectively. The agreement at the end of the computation is very satisfactory with errors less than 5% The effect of a reduction in the resolution of the integral length scale was also tested for the case of u'=5 m/s Resolution of the latter by 50, 25 and 12 computational nodes respectively, resulted in turbulent burning velocities of 1.65, 1 10 and 1.04 times the value obtained by the eigenvalue analysis. The required resolution of the flame is consequently roughly twice that necessary for the BML form of the EBU model. Temporal resolution was ensured in the present study by limiting the forward step to a maximum Courant number of 0.25 based on the particle velocity.

Comparison with Measurements

One problem in evaluating any model for premixed turbulent combustion is the absence of suitable experimental data The most comprehensive set of data for one particular geometry is that compiled by Bradley and co-workers (1984) As the present study is concerned only with methane - air flames comparisons are made with 3 flames of stoichiometries 0 75, 0 89 and 1 00 The laminar burning velocities required for the above combustion model were obtained from the global reaction scheme by Jones and Lindstedt (1988) which gives laminar flame speeds of 0 25, 0 345 and 0 385 m/s for the above stoichiometries The laminar viscosities also required in the evaluation of the Kolmogorov velocity where evaluated using a standard formulation,

$$\mu = \mu_{298}\left(\frac{T}{298}\right)^{\frac{2}{3}}$$

In Fig 3 the measured turbulent burning velocities for the leanest flame (Φ=0 75) are compared with the current model and the standard EBU model resulting from the assumption of an inner cutoff corresponding to the Gibson scale As can be seen the agreement between the current model and measurements is very satisfactory until values of u'/u_l exceeds 20 For higher turbulence levels the agreement is not surprisingly deteriorating In Fig 4 the agreement between the present model based on normal unstrained laminar flame properties is compared with measurements Again the agreement between the experiments and the current model is surprisingly good However, at values of u'/u_l in excess of 30 there is deteriorating agreement with the measured data The simplicity of the present turbulent reaction model formulation allows readily for the introduction of strained laminar burning velocities into equation (17) To this end the strained laminar burning velocities computed by Dixon-Lewis and co-workers (1990) for stoichiometric methane-air flames are used directly with the assumption that to a first approximation the strain rate is proportional to the inverse of the Kolmogorov time scale The result of this approximation is also shown in Fig 4 where the line corresponding to the prediction based on the strained laminar flame speed has been terminated at the extinction points of the strained planar laminar flame (a_q 2500 , s) It should be noted that the extinction point of tubular strained flames is lower still As can be seen the agreement with experimental data does not improve and the indications are that the laminar flames extinguish much too soon This must cast some doubt on the validity of the inclusion of strained laminar flame data in a simple manner into turbulent flame computations, or alternatively that the strainrate is the appropriate parameter to consider Regarding extinction characteristics it is well known that flames burning against burnt products do display very different extinction characteristics Thus the agreement at least with respect to this feature is likely to be much improved with the use of such data

Important issues do arise in the context of the applicability of the type of model suggested here for highly turbulent flames Evaluation of Karlowitz numbers based on the Kolmogorov scale and the characteristic reaction times of the fuel breakdown layer of laminar flames yield values significantly above unity even at very moderate turbulence levels As a consequence it appears questionable to treat the flame as a passive surface under these conditions Interestingly the form of the correction factor to the EBU model derived above indicates a dynamic balance between the laminar burning velocity and the Kolmogorov scales The behaviour of the ratio of the latter is shown in Fig 5 where as an example the case of a stoichiometric methane-air flame propagating into a turbulence field with an integral length scale of 0.25m is considered At low turbulence levels e g u'/u_l=1 the ratio of u_l/v_k is around 8 and hence strong flame acceleration is predicted by the interaction with eddies on the Kolmogorov scale However, at high turbulence levels the ratio goes significantly below unity causing the observed decrease in the rate of burning discussed above It must here be emphasised that the behaviour at low turbulence levels is likely to be exaggerated due to the assumptions made of an appropriate fractal dimension of 7/3 However, agreement between predictions and measurements appear plausible even in this region

Transient Flames in Decaying Turbulence

In the present section the above reaction model is applied to two cases, (i) where an established flame is propagated into a decaying turbulence field and (ii) where a confined flame is ignited in a decaying turbulence field The conditions chosen for the first two cases correspond to a moderately strong flame resulting from values of u' of 5 m/s and an initial turbulence length scale 0 25 In the first case a flame is propagated in a constant turbulence field for a sufficiently long time to establish a nearly steady flame ($t\,u'/l_l$ = 0 8) after which the turbulence field is allowed to decay. The flame initially slows down but then appears to approach an almost steady propagation velocity at around 90% of that obtained in the case of a constant turbulence field as shown in Fig 6. This result is surprising and it appears that an increase in the ratio of the laminar burning velocity to the turnover time of eddies on the Kolmogorov scale partly compensates for the decay in u' To attempt to elucidate this behaviour further a computation in which a flame was ignited directly in a decaying turbulence field in a closed vessel was performed The result from this computation can also be found in Fig 6 The interesting point is that even for this case a constant turbulent burning velocity appears to be approached at a value of around 80% of that obtained in a constant turbulence field Further investigations are required to clarify the reasons for this behaviour It can be noted that direct simulations by El-Tahry et al (1991) also obtain results which show that a flame ignited in a decaying turbulence field approaches a burning velocity similar to that of the flame in the corresponding steady turbulence field This indicates that the results obtained in the present study may not be unreasonable

Conclusions

The reformulation of the transient flame propagation problem to a form applicable to steady flame propagation in a constant turbulence field has been used as a basis for an eigenvalue analysis It has been shown that provided sufficient numerical resolution of the turbulent flame is ensured excellent agreement between transient computations and the eigenvalue procedure is obtained A turbulent reaction model was derived based on the assumption of fractal behaviour of flames at high turbulence levels and comparisons with experimentally obtained turbulent burning velocities give very encouraging results The effect of strain on the laminar burning velocity has also been incorporated and it was shown that some doubts exist over the appropriateness of the inclusion of strained laminar flame data in a simple manner into turbulent flame computations The computation of moderately strong flames in decaying turbulence fields show that the final turbulent burning velocity appears to approach a similar value to that obtained for the flame in the corresponding steady turbulence field

Acknowledgement

The authors would like to gratefully acknowledge the financial support of British Gas plc under the Research Scholarship award scheme for part of the present work

REFERENCES

ANAND, M S. and POPE, S B 1987 Comb. and Flame 67, p. 142

ABDEL-GAYED, R G , AL-KHISHALI, K.J. & BRADLEY, D. 1984 Proc. Roy Soc Lond. A391 , pp. 393-414

BRAY, K N C. 1990 Proc. Roy Soc. Lond A 431, pp 315-335

CANT, R S. & BRAY, K N C , 1989 Comb and Flame 76, p 243

CATLIN, C.A & LINDSTEDT, R P 1991 Comb and Flame (To Appear)

DIXON - LEWIS, G. Invited Lecture 23rd Symp.(Int) on Comb July 1990

EL-TAHRY, S.H , RUTLAND, C. & FERZIGER, J 1991 Comb and Flame 83, pp 155-173

GOULDIN, F C , BRAY, K.N.C & CHEN, J Y 1989 Comb and Flame 77, pp 241-260

HJERTAGER, B H 1982 Comb Sci and Tech 27, pp 159-170

JONES, W P & LINDSTEDT, R P. 1988 Comb and Flame 73, pp 233-249

JONES, W.P. & WHITELAW, J.H. 1982 Comb and Flame 48, p 1

KERSTEIN, A R 1988 Comb Sci and Tech 60, p 411

KOLMOGOROV, A , PETROVSKY, I & PISCOUNOFF, N. 1937 Bull Math Mech Sci Moscow State University 1(A)

LINDSTEDT, R P & MICHELS, H J 1989 Comb. and Flame 76 pp 169-181

MANTZARAS, J., FELTON, P G & BRACCO, F V 1989 Comb. and Flame 77, pp. 295-310

MOREL, T & MANSOUR, M N 1982 SAE Paper 820040

NORTH, G L & SANTAVICCA, D A 1990 Comb Sci and Tech 72, pp 215-232

PETERS, N 1986 21st Symp (Int) on Combustion, The Comb Inst , p 1231

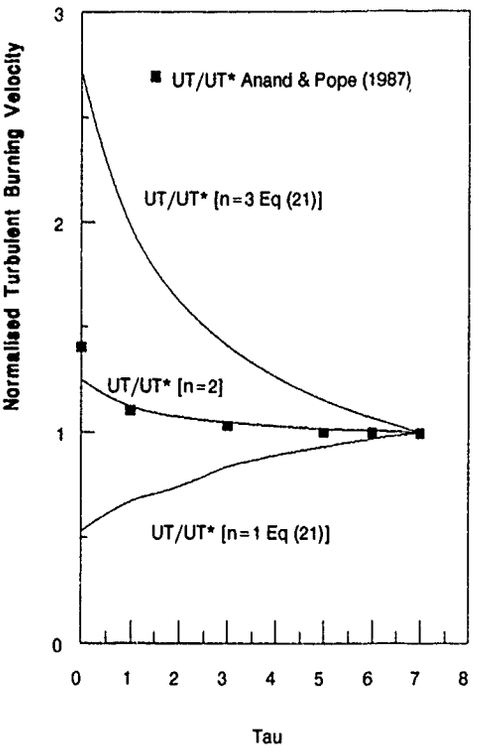

Figure 1
Dependence of Turbulent Burning Velocity on the Expansion Ratio Across the Flame

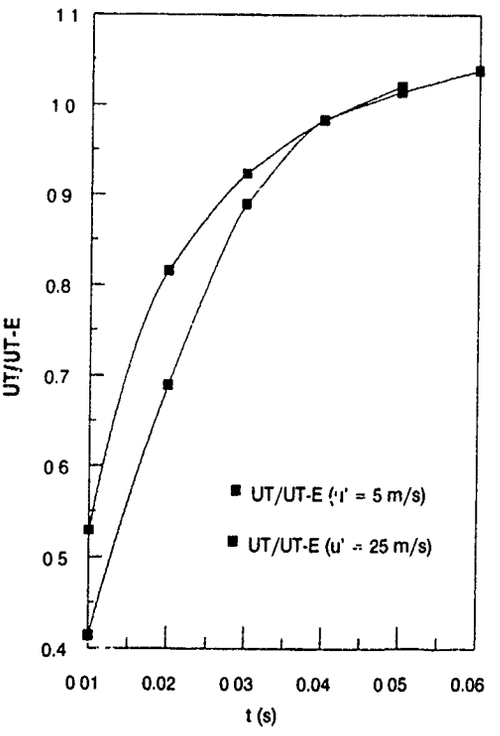

Figure 2
Turbulent Burning Velocity Normalised by the Result from the Eigenvalue Analysis

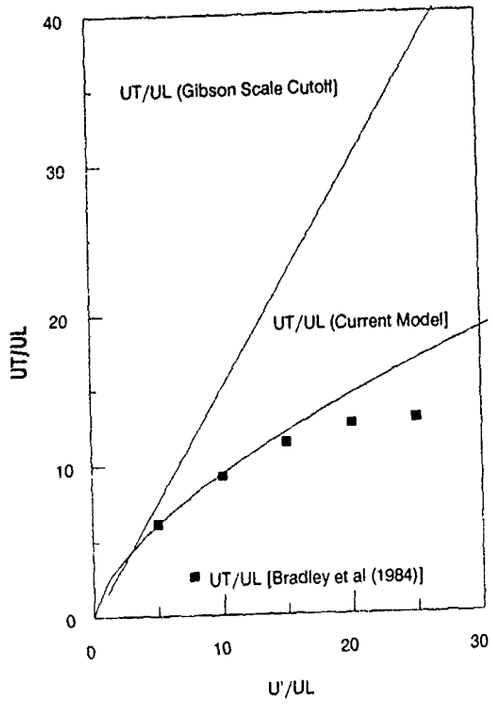

Figure 3
Comparison of Measured Turbulent Burning Velocities with Predictions using Different Inner Cutoffs

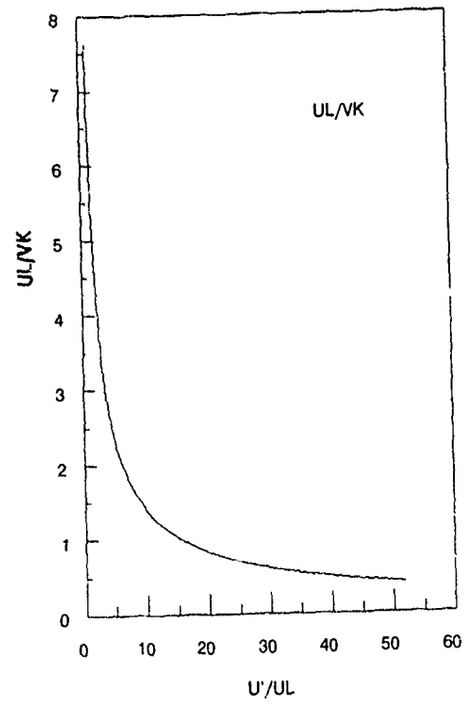

Figure 5
The Ratio of Laminar Burning Velocity to the Turnover Velocity of Kolmogorov Scale Eddies

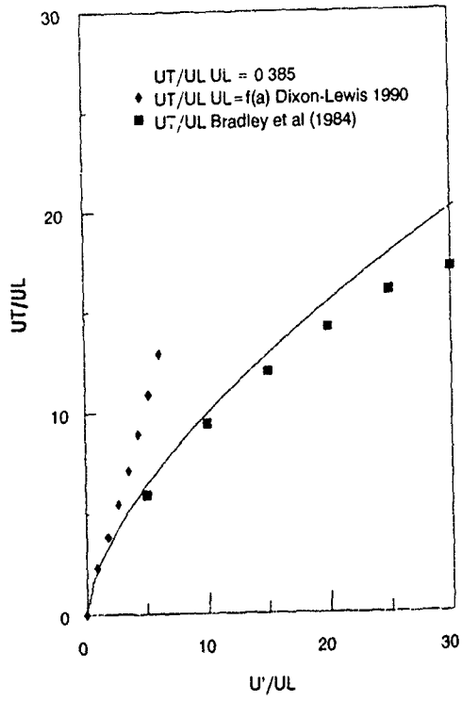

Figure 4
Comparison of Measured and Computed Turbulent Burning Velocities with Predictions Based on Strained and Unstrained Laminar Flames

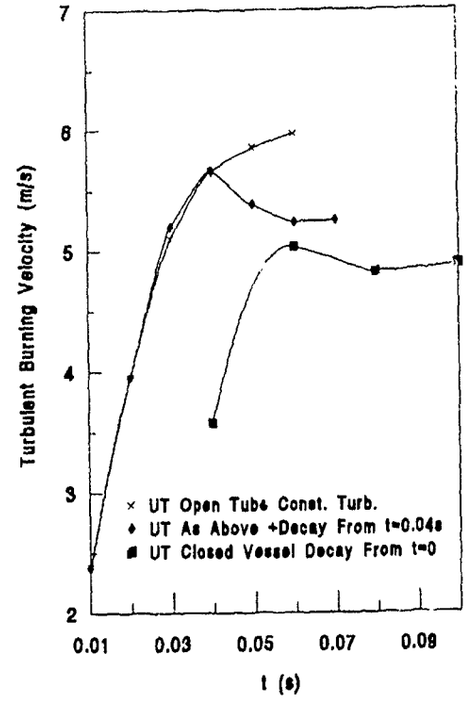

Figure 6
Comparison of Turbulent Flames Propagating in Open and Closed Tubes in Decaying Turbulence

EIGHTH SYMPOSIUM ON
TURBULENT SHEAR FLOWS
Technical University of Munich
September 9-11, 1991

COMPRESSIBILITY EFFECTS IN TURBULENT FAR WAKES.

J.P Bonnet*), J. Delville*), S. Sapin*), P. Sullivan**) and R. Yeru*)

*) Centre d'Etudes Aérodynamiques et Thermiques, LEA CNRS 191
43 rue de l' aérodrome, F-86036 Poitiers Cedex, France
**) Mechanical Engineering, Clarkson University, Postdam NY 13676, USA

Abstract

An experimental investigation of the Mach number effects in two-dimensional far wakes is presented. Three regimes are studied: subsonic (Mach 0.1), Mach 2.0 and Mach 4.2, in the developped part of the initially turbulent wakes. Hot wire anemometry is used to give one point statistics and conventional space-time correlations (STC). It is shown that, like in boundary layers, the intermittent part of the wakes are of less transversal extend in the supersonic cases. The spectra are strongly modified in the vicinity of the axis. The scales and the shapes of the STC are also quite sensitive to the Mach number. The supersonic wakes seems to be more strongly structurated than the equivalent subsonic one, with slight differences between Mach 2 and 4.

1. Introduction

The experimental knowledge of the compressibility effects on turbulent flows takes an increasing importance; associated to the recent developments of numerical prediction and to the revival of industrial interest in high speed propulsion. More precisely, compressibility arising from the supersonic regime should be adressed. Up to now, the influences of the Mach number have been and are still examined experimentally in details mainly in the case of Boundary Layers and Jets or Mixing Layers. For these kinds of flows, the compressible character of the velocity fluctuation field can be invoked, increasing considerably the difficulty of any numerical prediction. The large scale behaviour of these flows is now assumed to be play a crucial role. The structures of the flows and thier evolution with the Mach number are important as well as for the physical interpretation of the mechanisms as for the validation of advanced numerical codes.

The present work deals with the study of turbulent far wakes, in subsonic and supersonic external flows. For the small deficit wakes, at the difference of the two other configurations (mixing and boundary layers), the velocity gradients and the turbulence level remain very small. This last characteristic induces that *a-priori* the velocity fluctuations can be condidered as quite incompressible, at least up to moderate values of the external Mach numbers. These considerations have to be kept in mind when analysing the differences between sub and supersonic wakes.

The study of supersonic wakes is indeed more delicate than in the subsonic case. In particular when large scales are to be investigated, the sophisticated analysis performed by several authors (for example [19], [12], [2]) must be restricted to more simple ones. The main approaches are visaulizations [6], [1] and STC [11]. The results presented here are complementary measurements in the subsonic flat plate wake previuosly studied [8] and in the M=2 wake [9] previously studied. In addition, new results are presented in a M = 4 wake, allowing to judge the supersonic effects for higher Mach numbers. The essential features of one and two points statistics, based on high order moments, spectra and STC are presented.

2. Experimental apparatus

2.1 Wind tunnels

The supersonic measurements are performed in an open blowdown wind tunnel of 150mm × 150mm test section, operating at 6 and 14.10^5 Pa generating pressures (for M=2 and 4 respectively). The blowdown tunnel has a maximum running time of 1 minute. The temperature decrease is measured and less than 0.3 degree per second. The model is a full span flat plate, placed without incidence in the axis of the wind tunnel as described in Fig.1. The leading edge is located upstream of the 2D interchangeable sonic throats to avoid parisitic shockwaves. The local Mach number at this location is less than 0.85. The thickness of the plate is 3mm and the trailing edge is a symmetric wedge of 3° total angle. The length of the plate in the supersonic part is 0.8m. At the trailing edge, the Reynolds numbers are of the order of 6.10^7; the boundary layers are fully turbulent.

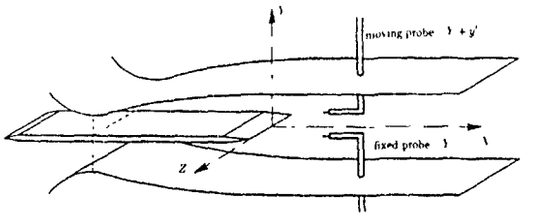

Fig.1 - Experimental arrangement (supersonic) and coordinates.

Subsonic experiments are performed in an open wind tunnel of 30 × 30 cm^2 section, driven at a mean speed of 36 m/sec; the length of the test section is 1.2 m; the model is also a 3 mm thick flat plate with the leading edge located in the convergent region. Sandpaper is glued on the two faces of the plate 1 m upstream of the trailing edge. The Reynolds number based on the total length of the plate is of order of 3.10^6. As for the supersonic cases, the boundary layers are fully turbulent at the trailing edge, with a thickness of about 9 mm. The trailing edge is bevelled from 50 mm upstream with 3% slope.

2.2 Hot-Wire anemometry

Supersonic hot-wire anemometry. The measurements are performed in the supersonic flows with Constant Temperature Anemometers specially adapted from DANTEC 55M01 /M12 symmetrical bridge [5] with 2.5μm wires (0.5mm long). The bandwidth at the high overheat ratio used ($\simeq$ 0.8) is greater than 300kHz. As usual in supersonic flows, a small slack is

given to the wires in order to avoid strain-gage parasitic effects. Prior any use, each wire is checked and each anemometer is adjusted in a small calibration wind tunnel reproducing Mach, wire-Reynolds numbers and temperature characteristics of the measurements.

Due to compressibility effects, it is well known that the supersonic turbulent flows are characterized not only by fluctuations of velocity but also of density and temperature. The hot-wire anemometer is sensitive to mass-flux fluctuations: $(\rho u)'$ and total temperature fluctuations: T_t'. If the wire is operated at high overheat ratio, it can be assumed that the anemometer output is mainly sensitive to mass-flux [13]. The constant-temperature operation allows, in addition, to accept linearity of the output in term of $(\rho u)'$. The mode diagram technique, allowing theoretically to separate the ρ and u contributions [11] has not been performed here, due to the rapid increase in resulting experimental complexity.

Two probes are simultaneously used: one is kept stationary, and the traversing mechanism holds the moving probe. The displacements are driven by stepping motor with 1mm steps. The positions during the runs are optically checked. A time dilatation of 16.1 is obtained by recording high-pass filtered anemometers outputs on an analog tape recorder (Bell & Howell M14G) with 2 (0-500 kHz bandwidth) channels and two different velocities: recording at 120 ips and reproducing at 7.5 ips. Further digital sampling is performed at an equivalent physical frequency of 800 kHz after a low-pass filtering at 320 kHz, and a sample size of about 1 second.

Subsonic hot-wire anemometry The measurements are performed by use of a home made rake of 23 subminiatures hot-wires (dia. 2.5 μm, 0.5 mm long) and TSI 1750 anemometers [10] The velocity signals are simultaneously sampled at a rate of 50 kHz and for each channel 800 records of 1024 conversions are considered. For each wire i, the instantaneous velocity is related to the the anemometer voltage by a a calibration rule which can take into account the temperature drift of the mean flow: $(T_\infty - T_{w_i}).e_i^2 = a_i + b_i.u_i^{n_i}$.

2 3 Numerical procedure

As well spectra as correlations are estimated by use of FFT techniques The spectrum is then defined as $E_u(Y;f) = \langle \hat{u}(Y;t)^* \, \hat{u}(Y;t) \rangle$ where $\widehat{\ }$ denotes the Fourier transform and $\langle\ \rangle$ time average; indeed, u stands for ρu in the supersonic case. The space time correlation $r_{uu}(Y, Y+y', \tau) = \langle u(Y,t).u(Y+y';t+\tau) \rangle$ is calculated from the inverse Fourier transform of $E_{uu}(Y, Y+y', f) = H_{Y,Y+y'}(f) \langle \hat{u}(Y,t)^* . \hat{u}(Y+y';t) \rangle$ where $H_{Y,Y+y'}(f)$ is the transfer function between the two channels corresponding to the probes position Y and $Y+y'$. This correction is needed only in the supersonic case where the experimental procedure involves analog storage of the signals for relatively high frequencies and is then very sensitive to phase drifts (due to possible head misalignements, etc...); $H_{Y,Y+y'}(f)$ is measured by using calibrated signals. In this paper, only the correlation coefficients $R_{uu}(Y, Y+y'; \tau) = r_{uu}(Y, Y+y'; \tau) / r_{uu}^{1/2}(Y;0) / r_{uu}^{1/2}(Y+y';0)$ are considered.

3. Results

3.1. Previous evidences of compressibility effects in supersonic far wakes.

Systematic measurements of mean values in supersonic flows have been previously performed [4]. These results essentially concern the mean velocity evolutions downstream of the flat plate for Mach numbers of 1.6, 2., 3.3 and 4.2 The results, when compared with the subsonic cases [15] [16], lead to the following main conclusions [4]:

• The main defect velocity and wake thicknesses evolutions are not strongly affected by the supersonic character of the flow. However, the generation of the wake is predominant:

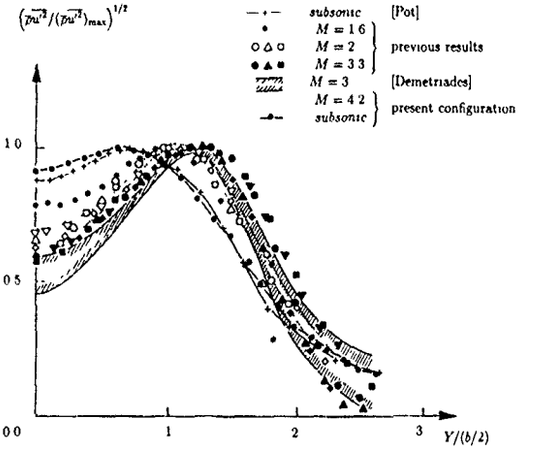

Fig.2 - Transverse repartition of the longitudinal mass-flux fluctuations.

as also quoted by Wygnanski, [19], the memory of the origin of the wake persits far downstream.

• The initially turbulent thin flat plate wakes follow a downstream evolution that can be divided in three successive parts : the near wake, the intermediate wake and finally the developped wake [16]. For the present experiments [4], [8], full similarity is observed at Mach 2 and 4 and for the subsonic wake, for dowstream distances greater than 300 momentum thickness θ.

• Important compressibility effects have been evidenceded on the transverse (y) distribution of the energy of the longitudinal velocity fluctuations.

The Fig. 2 shows the results obtained in the above-mentioned subsonic and supersonic wakes. For comparisons, subsonic results of Pot [15] are presented, altogether with the supersonic measurements of Demetriades [11] (This author has, since 1967, emphasized, this difference between subsonic and supersonic wakes). More precisely, two main characteristics can be pointed out:

i) The minimum/maximum ratio of the longitudinal velocity fluctuations is smaller for supersonic wakes. (Fig.3a); these results translates a more important transverse evolution of the turbulent activity in supersonic wakes than in subsonic ones.

ii) The location (Y_m) of the maximum of turbulent kinetic energy is nearer the wake axis in the subsonic case (Fig.3b). Then, from the conventional one-point statistical properties, the supersonic character appears to be influent on the distribution of the energy fluctuations. Some other results [4] show that the structure parameter of the Reynolds tensor is also affected by the Mach number.

This situation is different from the case of the boundary layers, where the influence of the Mach number on the statisti-

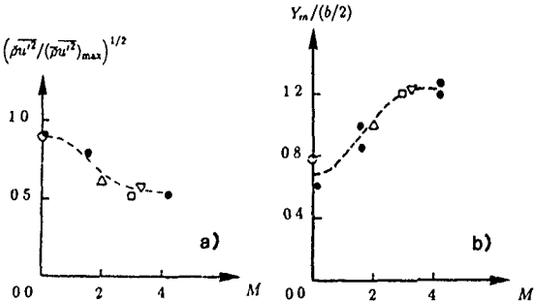

Fig.3 - Mach number effect on the turbulence min/max ratio and on the transverse location of the maximum

cal properties seems very small. However, it has been shown that the Mach number influences the shape of the other edge (observable on higher moments, skewness, flatness and intermittency) and the shapes and characteristic lengthes of the correlations [18]. On an other hand, the Mach number has a tremendous well known effect directly on the speading rate (see for example [3]) *and* energy distribution [7] of supersonic mixing layers.

Then, it appears that, from conventional statistics, the supersonic wakes behaves in a quite different way when compared with others engineering basic flows.

3.2. Mean flows characteristics

The main characteristics of the 3 wakes under study are presented in Table 1. U_0 is the minimun (axis) mean velocity value when U_∞ is the external velocity; the wake thickness is defined as b, the distance between the two locations where the velocity is $(U_\infty + U_0)/2$. Y_m is the transverse position of the maximum of longitudinal velocity fluctuations, θ is the momentum thickness ($\theta = \int \rho\overline{U}/U_\infty(1-\overline{U}/U_\infty)\,dy$). X is the distance from the trailing edge where the detailed measurements are taken, Y is the transverse location of the stationary probe and y' is the transverse separation between probes All the experiments presented here correspond to the far wake region, the dowstream distance being of order of the 500 to 600 momentum thicknesses.

	M=0.1	M= 2.0	M=4.2
U_∞ m/s	39.5	474.	625
U_0 m/s	36.8	436.	591
b mm	23.2	18.0	21.0
Y_m mm	7.2	10.0	14.0
θ mm	1.6	1.3	1.3
X/θ	613.	492.	638.
Re_θ	$4.2\ 10^3$	$1.2\ 10^5$	$0.98\ 10^5$
α deg	-	62	58

Table 1

3.3. One-point statistics

The spectra of the longitudinal velocity component (M=0.1) or of the mass-flux fluctuations (M=2. and 4.) are plotted on Fig 4 for 3 locations within the wake: on the wake axis, at the maximum of turbulence (Y_m) and at an intermediate position ($Y_m/2$). These spectra are plotted as $fE(f)$ vs $\log f$ (f is the frequency and E the power spectrum), the area under each curve being proportional to the energy. No attempt to normalize the energy is made, although the frequency is normalized with b and the convection velocity U_c, the conventional characteristic scaling of far wakes [19], [2], [9]; U_c is taken equal to the external velocity U_∞.

It can be observed that, in the internal part of the wakes, the spectra do not seem to be strongly affected by the Mach number. Whatever the Mach number is, sharp peaks lying around $fb/U_\infty \sim 0.4$-0.5 are clearly observable, showing that structures of mean size of twice the conventional wake width, b, may be present in the flows (assuming , as generally admitted, a convection velocity close to the external one).

Contrarily, on the wake axis, important differences between M=0.1 and supersonic wakes can be observed. Despite broadband spectra, supersonic wakes are relatively more energetic at higher frequencies. Practically they loose the lower typical characteristic frequency behaviour observable in the external part. In the center wake region of supersonic flows, typical energetic frequencies lie roughly around $fb/U_\infty = 1$, i-e. twice the typical frequency observed in the external part. Then, the supersonic wakes seem to have larger spectral evolutions in Y direction than the subsonic one does.

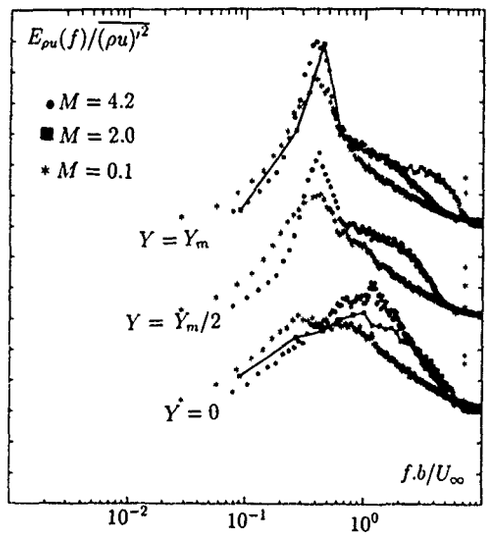

Fig.4 - Energetic lin-log plot of the spectra for subsonic, Mach 2 and 4 wakes on the wake axis, at $Y = Y_m/2$ and $Y = Y_m$. Arbitrary vertical scale, frequency values normalized with U_∞/b

This first remark is confirmed by the observation of the higher moments. Fig. 5a and b present the skewness $(\overline{(\rho u)^{'3}}/\overline{(\rho u)^{'2}}^{3/2})$ and the flatness $(\overline{(\rho u)^{'4}}/\overline{(\rho u)^{'2}}^{2})$ factors for the two extreme Mach numbers and several Y locations. It can be observed that the supersonic wake behaves in a quite different way that the subsonic one. On the wake axis, the signals are positively skewed in the supersonic wake (Fig. 5.a), this behaviour can be the trace of locally higher velocities occurenc that are not observed in the subsonic wake.

On other hand, the skewness values are everywhere higher in the supersonic flow, comparable values being observed only

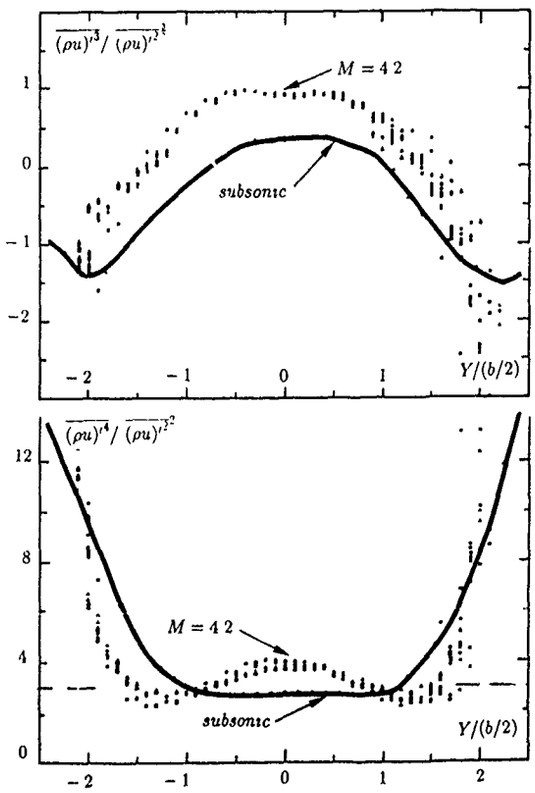

Fig.5 - Comparison of skewness and flatness factors of longitudinal velocity and mass-flux fluctuations in subsonic and M=4.2 wakes

for $Y/b \sim 1$ The comparison on the Fig. 5.b shows here also that the differences between supersonic and subsonic wakes are real both on the axis (higher flatness for the supersonic) and in the external part.

The part of the wake where the signals are more or less gaussian is very small, even not present, in the M=4 wake, contrarily of the subsonic one, where quasi-gaussian signals are observed on nearly a half wake width.

As far as the intermittency can be estimated to be proportional to the inverse of the flatness factor, it is evident that the intermittency profile of the supersonic wake is largely fuller than for the subsonic equivalent flow. A comparable Mach number effect is well known for boundary layers [14]; the measurements of Smits et al [18] show very close conclusion in the comparisons of third and fourth order moments in incompressible and supersonic (M=3) boundary layers.

3 4 Two-point correlation data

More detailed informations can be deduced from two-point correlation; in the present experiments, only correlations with transverse (y') separations are available Some results concerning streamwise separations in the Mach 2 wakes can be found in [9].

The principal results are obtained when the stationary probe is located at Y=0, $Y_m/2$ and Y_m· the iso-countours on the wake axis are plotted on Fig.6; the mid-position of the reference point is considered on Fig.7 and the maximum of fluctuation is used for the results of Fig.8. Let us recall that these two last positions don't correspond to the same values of Y/b for the different wakes, due to the strong influence of the Mach number on the ratio Y_m/b (see Fig.2). This effect explains the increasing relative distance between the wake axis and the location of the stationary probe observed between a, b and c on Fig.8 and 9

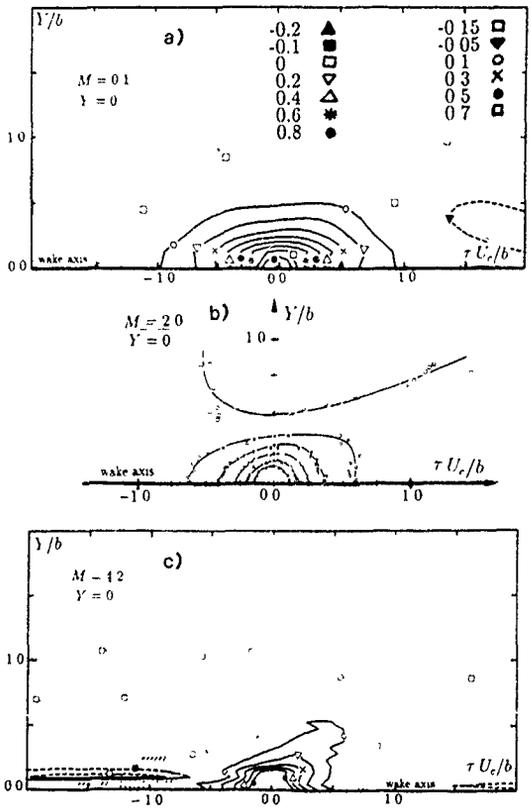

Fig.6 - Iso-contours of the correlation coefficient R_{11} on the wake axis of the wakes. All scales normalized with b and U_∞
a) $M_\infty = 0.1$; b) $M_\infty = 2.$; c) $M_\infty = 4.$
———— : positive correlations.. . . . . : zero correlation.
- - - - - - - - - : negative correlations

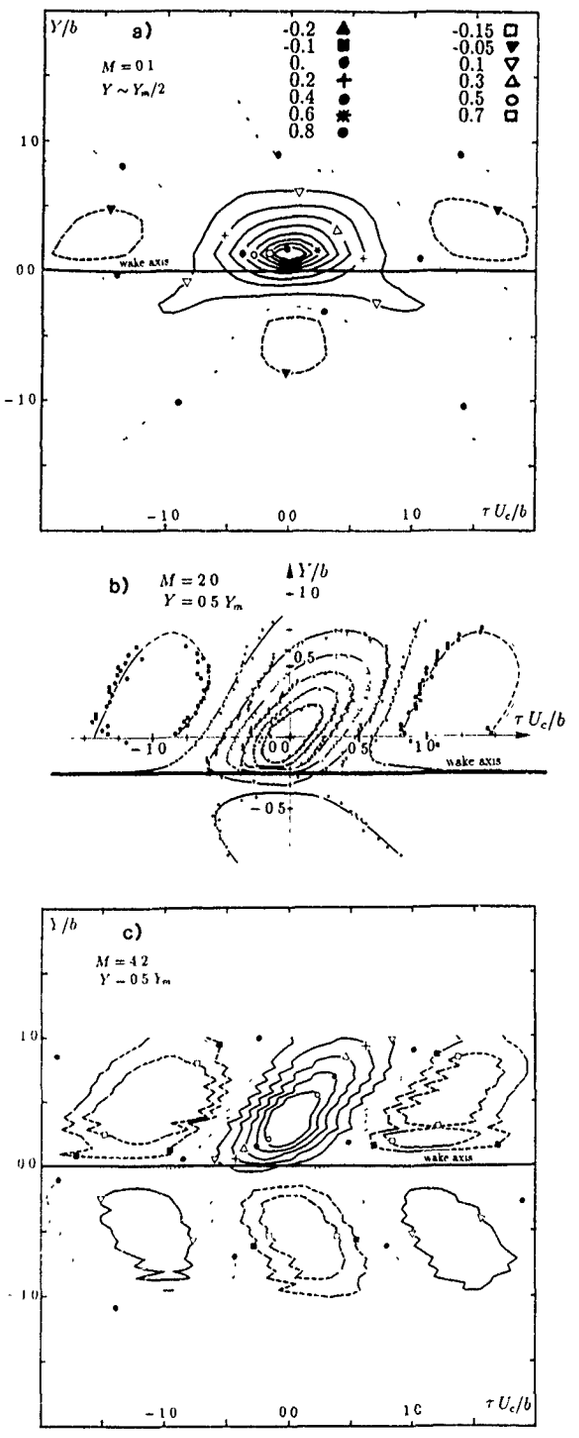

Fig.7 - Iso-contours of the correlation coefficient R_{11} at $Y = Y_m/2$
a) $M_\infty = 0.1$; b) $M_\infty = 2.$; c) $M_\infty = 4.2$

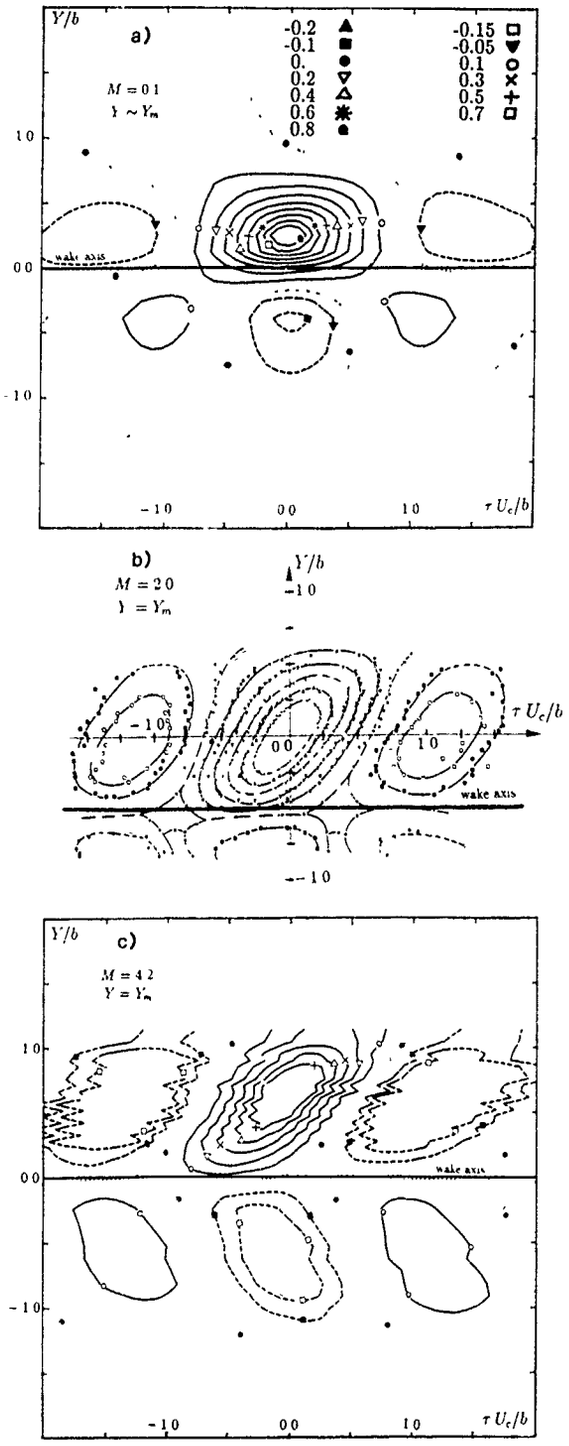

Fig.8 - Iso-contours of the correlation coefficient R_{11} at $Y = Y_m$
a) $M_\infty = 0.1$; b) $M_\infty = 2$; c) $M_\infty = 4.2$

These iso-contours plots show global equivalent characteristics in shape on the axis despite important effects on the relative sizes between the three configurations. Contrarily, as the reference point is placed at $Y_m/2$ or Y_m, the differences between the regimes appear more pronounced. The more streaking feature is the striking structuration of the supersonic cases: marked negative correlation zones are observed both for positive and negative time delays. On other hand, a marked tilt of the iso-contours can be observed in the two supersonic cases. These characteristics are also associated to a decrease of the overall characteristic size when the Mach number increases, however with a less influence than observed on the axis. An other feature appearing from the comparison of the three Mach numbers of Fig.7 and 8 is the role played by the wake axis: when the stationary probe is off the axis, the null correlation with zero-time delay is obtained when the moving probe is crossing the axis for the supersonic wakes. This is not at all the case for the subsonic wake, as it can be more precisely observed on Fig 9.

In a complementary way, the plots of the time-correlations are given in Fig.10. The abovementionned evolutions of the typical time length scales with the Mach numbers are evidenced. Plotted in non-dimensionned scale, inside the wakes, the supersonic flows corresponds to a more rapid decrease

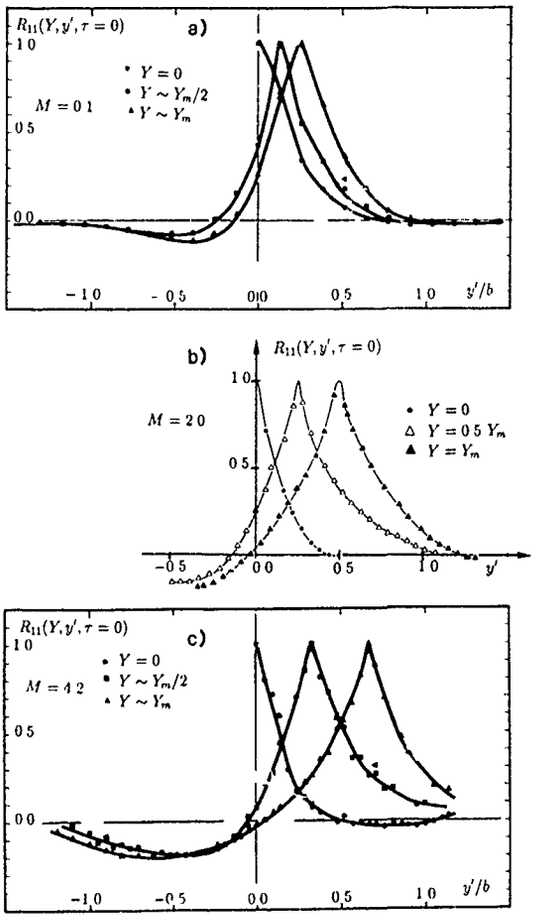

Fig.9 - Typical plots of the space-correlation coefficient: $R_{11}(Y, y'; \tau = 0)$ for $Y = 0$; $Y_m/2$, and b (excepted for $M = 2$) (non-dimensionalization with b)
a) $M_\infty = 0.1$; b) $M_\infty = 2.$; c) $M_\infty = 4.2$

of the correlations. This behaviour is associated with large negative values. It is clear from these figures that the calculations of the integral scales are not obvious, due to the evolution of the correlation shapes; following the definition chosen (the integral of the absolute value, the zero-crossing distance or other concepts), the conclusions are difficult to draw. Nevertheless, the overall qualitative evolutions of the sizes are confirmed. In addition to these size considerations, the inclination of the iso-structures can be evaluated. In the subsonic case, the iso-correlations do not exhibit any preferred orientation, the shapes nearly correspond to ellipses which longer axis is nearly aligned with the wake axis. For the supersonic case, the quasi-elliptic contours are inclined with angles of order of 60 degrees for M=2 and 4 (see Table 1). This preferred tilt seems to be a specific characteristic of the supersonic regime.

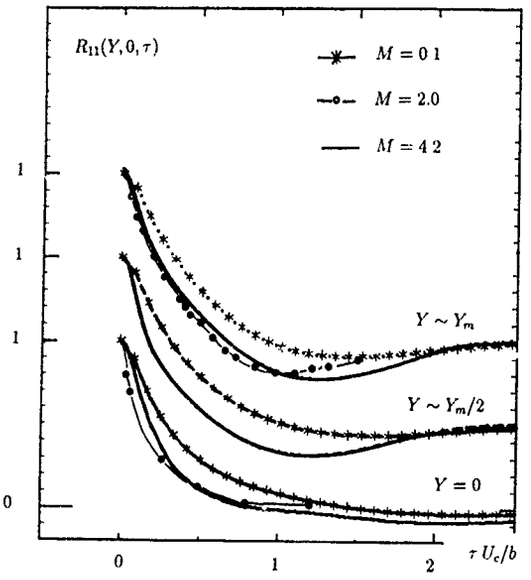

Fig.10 - Typical plots of the time-correlation coefficient: $R_{11}(Y', y' = 0, \tau)$ **for** $Y = 0$; $Y_m/2$ (excepted $Y = Y_m/2$ for $M = 2$)

4. Conclusion

The present measurements show marked influence of the supersonic regime in the structuration of far wakes The main effect is a more pronounced structuration of the supersonic cases. This appears on the distribution of the energy and is clearly linked with a relative larger transverse extent of the turbulent activity for supersonic wakes. The intermittency evolution between turbulent and free stream conditions is much more localized and placed far from the axis for the Mach numbers of 2 and 4. The spectra show that, near the axis of the supersonic wakes, the charcateristic shedding frequencies are less energetic and, instead of sizes of roughly the wakes thichness, typical sizes of half this thickness are more energetic. The external and internal regions of wakes seems more statistically different when the regime becomes supersonic. This description is at this time not associated with turbulence model. The approach of Smits [17], based on hairpins description in the case of boundary layers, can be extended to the wake configurations. However, such an extension is not obvious due to the large differences between the large scales structures of these two configurations. Lastly, the marked influence of the Mach number on the intermittency distribution is quite comparable with the observations done for boundary layers. Providing these observations are performed in both cases in low velocity gradients and low turbulence activity regions, the mechanisms invoked by the model of Smits can be still valid for the wake configuration. On other hand, the use of this analysis remains limited, because it requires the knowledge of longitudinal STC not measured here.

As far as the transverse space-time correlations are concerned, it appears that the supersonic wakes are much more spatially structurated than subsonic one. In particular in supersonic cases, high levels of negative correlations can be observed, and the wake axis plays an important role, separating the regions of positive and negative correlations. Lastly, a preferred inclination of the structures (of about 60° relative to the streamwise direction) issued from the iso-correlations is observed only in the supersonic wakes. Such an influence of the compressiblity due to the supersonic character seems to be a particular characteristic of the wake configuration.

Lastly, it should be noticed that the principal effects of the supersonic character of the wakes are quite similar for Mach numbers 2 and 4.2.

Aknowledgement. This study was partially supported by a CNRS/NSF Cooperation programme.

References

[1] Althaus W. *"Experimental investigation of vortex formation in the wake of a flat plate for subsonic and supersonic free stream Mach numbers"*, Exp. in Fluids 9, 267-272 (1990)

[2] Antonia R. A. *"Average wavelength of organised structures in the turbulent far wake of a cylinder"*, Exp. in Fluids, Vol. 5, pp. 298-304, (1987)

[3] Birch S. F. & Eggers J. M. *"A critical review of the experimental data for developed free shear layers"*, NASA SP 321, (1972)

[4] Bonnet J P. *"Etude des effets de compressibilité sur la turbulence dans les sillages supersoniques"*, Contrat DRET 87/034, (1989)

[5] Bonnet J.-P. & Alziary De Roquefort T. *"Determination an optimisation of frequency response of constant temperature hot-wire anemometers in supersonic flows"*, Rev. Sci. Instrum. 51, 234-239, (1980)

[6] Bonnet J. P. & Chaput E. *"Large scale structures visualizations in a high Reynolds number, turbulent flat plate wake at supersonic speed"*, Experiments in Fluids 4, 350-356, (1986)

[7] Bonnet J. P., Chaput E. & Knani M. A. *"Apercu des influences de la compressibilité sur les écoulements cisaillés libres en régime supersonique. Ecoulements à masse volumique variable"*, L Fulachier ed., No. 7 IMST 86-10, pp. 201-212, (1985)

[8] Bonnet J -P., Delville J. & Garem J H. *"Space and space-time longitudinal velocity correlations in the turbulent wake of a flat plate in incompressible flow"*, Exp in Fluids 4, 189-196 (1986)

[9] Bonnet J -P., Jayaraman V. & Alziary de Roquefort T. *"Structure of a high Reynolds number turbulent wake in supersonic flow"*, J. Fluid Mech. vol. 143, 99. 277-304. (1984)

[10] Delville J., Bellin S., Garem J.H. & Bonnet J P. *"Analysis of structures in a turbulent plane mixing layer by use of pseudo visualization based on hot wire anamometry"* Advances in Turbulence II, Fernolz & Fiedler Ed., 251-256, (1989)

[11] Demetriades A. *"Turbulence correlations in compressible wake"*, J.F.M. 74, 251-267, (1976)

[12] Hussain A. K. M. F. & Hayakawa M. *"Eduction of large-scale structures in a turbulent plane wake"*, J.F M., Vol. 180, pp. 193-229, (1987)

[13] Mokovin M. K. *"Fluctuations and hot-wire anemometry in compressible flows"* AGARDograph 24, (1956)

[14] Owen F K., Horstman C.C. & Kussoy M.I. *"Mean and fluctuating flow measurements of a fully developped, non-adiabatic, hypersonic boundary layer"* J.F.M. 70, 393-413, (1975)

[15] Pot P. J. *"Measurements in a 2-D wake merging into a boundary layer"*, Data Rep. NRL TR 79063 L, (1979)

[16] Ramaprian B. R. & Petel V. C. *"The symmetric turbulent wake of a flat plate"*, AIAA J. 20, 1228-1235, (1982)

[17] Smits A. J. *"New developments in understanding supersonic turbulent boundary layers"* 12th Symposium on Turbulence, Missouri-Rolla, IL4.1-19, (1990)

[18] Smits A. J., Spina E.F., Alwing A.E, Fernando E.M. Donovan J.F. *"A comparison of the turbulence structure of subsonic and supersonic boundary layers"*, Phys. Fluids, A1 (11), 1865-1875, (1989)

[19] Wygnanski I. & Champagne F. & Marasli B *"On the large-scale structures in two-dimensional, small-deficit, turbulent wakes"*, J.F.M., Vol. 168, pp. 31-71, (1986)

EIGHTH SYMPOSIUM ON
TURBULENT SHEAR FLOWS
Technical University of Munich
September 9-11, 1991

The Effect of Compressibility on Conserved Scalar Entrainment in a Plane Free Shear Layer*

Jacqueline H. Chen
Combustion Research Facility
Sandia National Laboratories
Livermore, California 94551-0969

Abstract

This paper describes a numerical investigation of entrainment by organized motions in a compressible plane free shear layer. Insights obtained from the results of recent three-dimensional direct numerical simulations of a temporal compressible mixing layer, at low and moderate convective Mach numbers, are used to explain the effect of the large-scale structure dynamics on the transport of a conserved scalar. At moderate convective Mach number entrainment is found to occur in several intermediate steps producing a marching instantaneous concentration profile. Conserved scalar statistics and fast chemical reaction results at low and moderate convective Mach numbers are compared. Finally, the instantaneous streamline pattern at moderate convective Mach number is presented in a convective frame, and the three-dimensional critical points of the velocity gradient tensor are classified.

1. Introduction and Background

The plane compressible free shear layer has been a topic of renewed interest in recent years due to mixing and combustion issues related to supersonic flight. The persistence of turbulent large-scale structures at high Mach number led Papamoschou and Roshko [1988] to characterize the compressibility of the flow in a convective frame in which the large-scale structures are stationary. In this frame, the intrinsic Mach number of the flow is the convective Mach number (M_c), defined as $M_c=(U_1-U_2)/(c_1+c_2)$ where c_1 and c_2 are the respective freestream sound speeds and U_1 and U_2 are the respective freestream velocities. Using the convective Mach number, Papamoschou and Roshko were able to collapse the growth rate data onto a single curve for a wide range of freestream conditions, and further showed that the growth rate decreases as the convective Mach number increases.

More recent results from experiments (Clemens and Mungal [1990], Fourgette *et al.* [1990]) and direct numerical simulations (Sandham and Reynolds [1991]) of nonreacting plane free shear layers and reacting round jets show that the underlying structure in a free shear layer changes as the convective Mach number increases. Experimental evidence suggests that as the convective Mach number increases the large-scale motions become significantly more three-dimensional. Flow visualization images taken at $M_c = 0.62$ by Clemens and Mungal [1990] show that the structures are highly three-dimensional, and that the spanwise rollers, which are the dominant structures at M_c=0.29 due to the Kelvin-Helmholtz instability, are no longer present with any degree of regularity. Linear stability predictions by Sandham and Reynolds [1991] show that as the convective Mach number increases above 0.6, the shear layer is more unstable to oblique disturbances than it is to the Kelvin-Helmholtz instability. Therefore, it is not surprising that the structures resulting from the primary instability at moderate convective Mach number are three-dimensional. Based on direct numerical simulation results obtained for a temporal shear layer, Sandham and Reynolds [1991] modeled the large-scale structure resulting from the primary instability at moderate convective Mach number as a pair of lambda vortices, with the downstream vortex inverted. The plan view passive scalar images of Clemens and Mungal [1990] exhibit streamwise streakiness which may represent the legs of the lambda vortices.

For low convective Mach number free shear layers, phenomenological models for mixing and chemical reaction have been developed based on experiments by Konrad [1976] among others that demonstrate the significance of organized large-scale motions in entrainment and mixing processes. In the Broadwell-Breidenthal model (Broadwell and Breidenthal [1982]), free stream fluid is engulfed into the layer by the churning motion of the spanwise rollers over a dimension on the order of the layer thickness. The entrained fluid is subsequently mixed down to the Kolmogorov scale and ultimately exists either in thin laminar diffusion layers or in homogenized cores of the spanwise rollers.

The entrainment mechanism at moderate convective Mach number is poorly understood due to the difficulty in obtaining measurements under extreme flow conditions. Current measurements have focused primarily on passive scalars which have integrated history effects built in. For a complicated three-dimensional flow it is very difficult to deduce from passive scalar images the kinematics responsible for the scalar transport. Direct numerical simulations complement the experiments because they reproduce the low wave number motions very accurately; and, more importantly, because they provide passive scalar as well as pressure, velocity, and vorticity information simultaneously. While the high wave number motions at large Reynolds numbers are not currently accessible in simulations, the low wave number motions, which are responsible for the entrainment of fluid into the layer, are.

In the present work, simulations were performed of moderate $(M_c=0.8)$ and low $(M_c=0.4)$ convective Mach number free shear layers at similar Reynolds numbers. To compare the different entrainment mechanisms, the following results will be presented: (1) instantaneous structure of the large-scale motions, (2) conserved scalar statistics and fast chemistry results, and (3) three-dimensional topology of the velocity field moving at the convective velocity.

2. Numerical Method

The numerical method used in this work was developed by Sandham and Reynolds [1991]; therefore, only a brief summary is provided here. The full compressible Navier-Stokes equations are solved for the temporally-evolving mixing layer using a spectral collocation method. The spatial derivatives are obtained using spectral and higher-order finite difference techniques and the solution is advanced in time explicitly using a compact third-order accurate Runge-Kutta method. Periodic boundary conditions are imposed in the streamwise (x) and spanwise (z) directions where the spatial derivatives are obtained spectrally. Characteristic nonreflecting boundary conditions are imposed in the major gradient direction (y) to prevent acoustic waves from affecting the solution. The grid points are uniform in the spectral directions and are stretched algebraicly in y, with approximately half of the points inside the shear layer. To minimize aliasing problems, the solution is overresolved and the energy spectra is monitored during the course of a run. Additional Fourier modes

* Research supported by the United States Department of Energy, Office of Basic Energy Sciences, Division of Chemical Sciences.

are included as the resolution becomes marginal.

In the present study, all of the initial fields were perturbed with random noise at 2.5% of the freestream velocity. This choice of initial disturbances was selected to mimic an unforced mixing layer. The mean velocity was modeled by an error function, and the mean temperature was derived from the Crocco-Busemann relationship. Random noise was applied to the temperature, density, and all components of the velocity field In addition to the hydrodynamic fields, a conserved scalar with an initial hyperbolic tangent profile was carried along, having values of unity in the high-speed stream and zero in the low-speed stream. The dimensions of the computational box in the streamwise and spanwise directions, $2L_x$ and L_z, were chosen to support the growth of both a fundamental and its subharmonic in the streamwise direction, and only a fundamental in the spanwise direction.

The simulations described in the following sections were performed at an initial Reynolds number *(Re)* of 800 based on the initial vorticity thickness (δ_o) and the velocity difference (U_1-U_2), at convective Mach numbers (M_c) of 0.4 and 0.8, and at Schmidt and Prandtl numbers of unity. The lower Mach number simulation was performed to provide a baseline against which the higher Mach number results could be compared.

3. Instantaneous Structure

The developed structure at $M_c=0.4$ and $M_c=0.8$ is shown in perspective plots of the conserved scalar and pressure in Figure 1. At $M_c=0.8$, large values of the vorticity magnitude correspond to the mean vorticity which remains largely in vortex sheets. The rotational regions tend to have lower values of vorticity magnitude, consequently, rotational regions are better delineated by the pressure minima than by the vorticity magnitude. From the pressure and scalar isocontours it is evident that the structure at the higher Mach number is much more three-dimensional. The spanwise rollers which dominate the $M_c=0.4$ simulation are completely absent at $M_c=0.8$. Instead, they are replaced by oblique vortices which comprise the legs of two lambda vortices, similar to the structure reported in Sandham and Reynolds [1991]. Note that the vortices are tilted with respect to the shear layer centerline, $y=0$. The head of the upstream lambda is tilted toward the high-speed stream while the head of the downstream lambda is tilted toward the low-speed stream.

Figure 2 shows several side *(x-y)*, plan *(x-z)*, and end *(z-y)* view slices through the $M_c=0.8$ conserved scalar data. The plan view slice through the midplane, $y=0$, (Figure 2a) best reveals the three-dimensionality of the large-scale motions; there is no evidence of any spanwise structure in this plane. Instead, there exist several pockets of partially mixed fluid with the mixture fraction favoring either the low- or the high-speed side. These

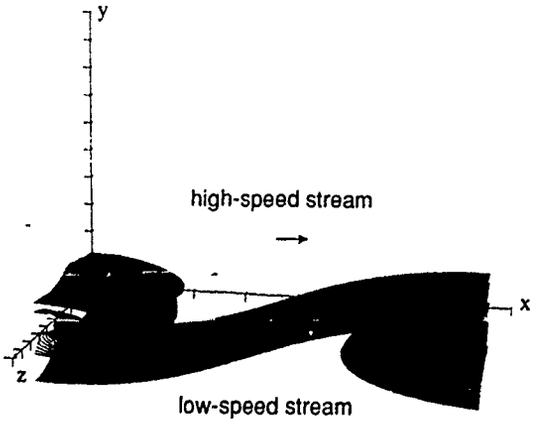

(a)

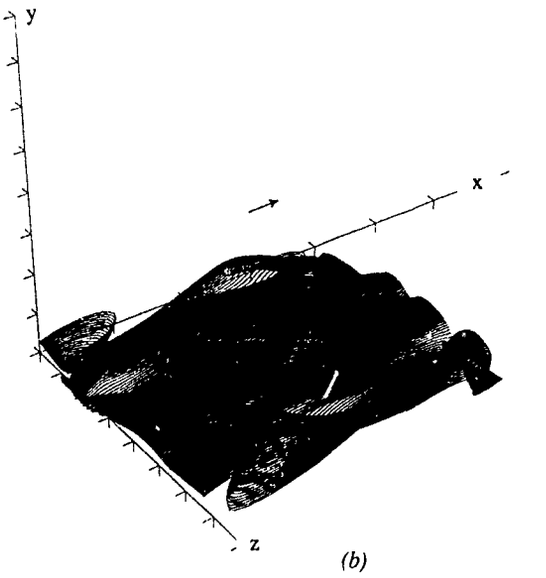

(b)

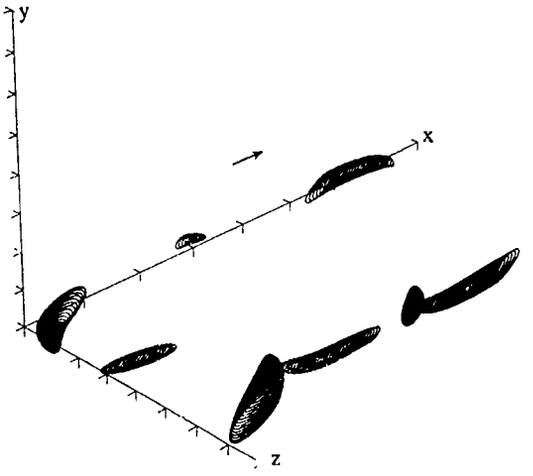

(c)

Figure 1. Perspective plots at $Re=1600$ of the conserved scalar at $\xi=0.5$ for *a)* $M_c=0.4$, *b)* $M_c=0.8$, and pressure minima at *10%* p_{max} for *c)* $M_c=0.8$.

pockets of partially mixed fluid exhibit a streamwise preference, and are adjacent to smaller rotational regions, corresponding to projections of the legs of the lambda vortices in this plane. The end view slices (Figure 2b) taken at several streamwise locations show the manner in which freestream fluid is entrained into the layer. Depending upon the particular streamwise location, irrotational fluid is entrained into the layer in one of three ways: (1) pure low- and high-speed fluid is drawn into the layer in one continuous motion, (2) pure high- speed fluid is entrained and mixed with partially mixed fluid inside the layer, or (3) pure low-speed fluid is entrained and mixed with partially mixed fluid inside the layer. Near the streamwise locations where the tips of adjacent lambda vortices are on top of one another, entrainment occurs mainly by methods (2) and (3) above. In regions in between, entrainment occurs mainly by method (1).

4. Conserved Scalar Statistics and Fast Chemistry Results

Statistics of the conserved scalar field at $M_c=0.4$ and $M_c=0.8$ are used to simulate fast chemical reactions in the manner detailed in Mungal and Dimotakis [1984]. The primary objective of this calculation is to obtain a qualitative comparison of the histogram of the conserved scalar and the chemical product profiles at low and moderate convective Mach numbers. In Mungal and Dimotakis [1984], the temperature rise due to a

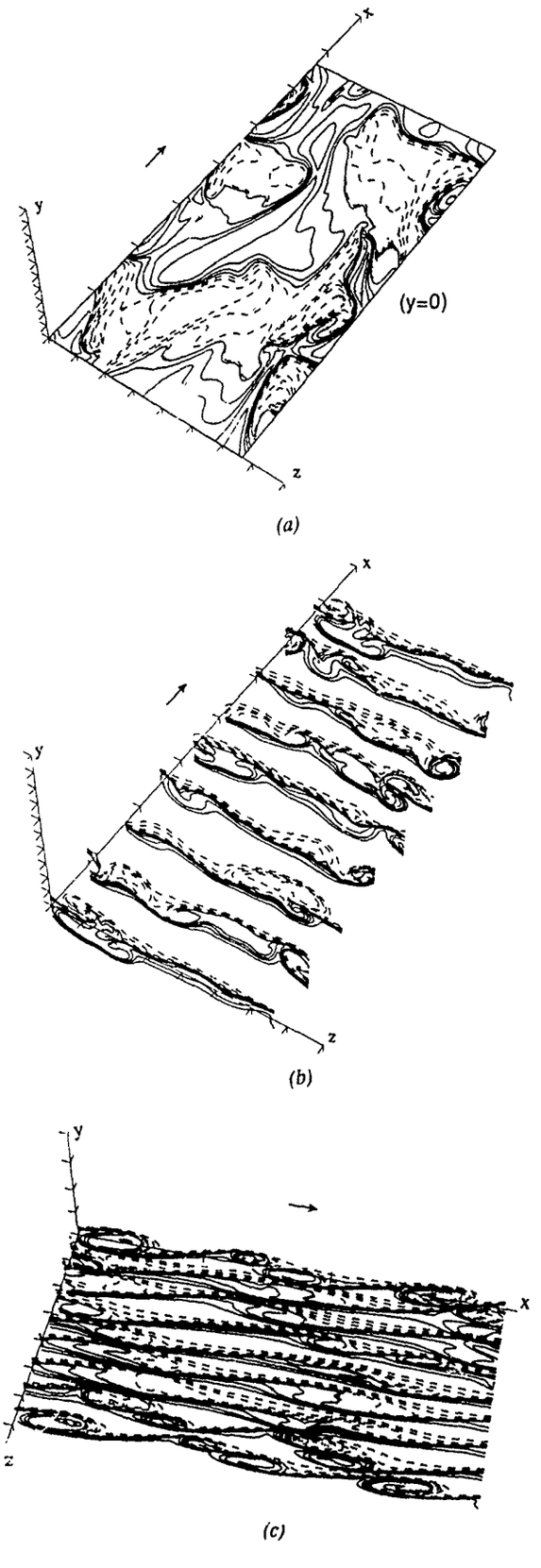

Figure 2. Contour plots of the conserved scalar at $Re=1600$, $M_c=0.8$ for *a)* plan, *b)* end, and *c)* side view slices. Solid lines correspond to $0<\xi<0.5$ and broken lines correspond to $0.5<\xi<1.0$.

fast reaction is obtained by integrating the product of a weight function and the probability density function (p.d.f.) of the conserved scalar. The weight function is adjusted to achieve the desired reactant equivalence ratio. It has its peak at the equivalence ratio and decreases linearly to zero in the two freestreams. The equivalence ratio, ϕ, is defined as the ratio of the reactant concentrations in the freestreams, $\phi=(c_{02}/c_{01})$. Here, a simple one-step reaction, $A+B \rightarrow AB$, is assumed. The product concentration is maximum at the stoichiometric mixture fraction (ξ_s), which for the above reaction, occurs at $\xi_s=\phi/(1+\phi)$. Given the p.d.f. of the conserved scalar, the product profile and thickness can be readily computed. In the present study, the p.d.f. is replaced by a histogram, obtained by averaging the mixture fraction in the homogeneous directions, x and z, from a single realization.

Histograms of the conserved scalar at $Re=1600$ are presented in Figure 3. Note that there are fundamental differences in the shape of the histograms for the two cases. At $M_c=0.4$, the histogram exhibits three humps, corresponding to unmixed fluid in the high- and low-speed streams and fluid mixed at the entrainment ratio. The central peak at the entrainment ratio extends across the lateral extent of the layer, in agreement with the p.d.f. obtained in shear layer experiments by Konrad [1976]. In contrast, at $M_c=0.8$, the histogram marches across the lateral extent of the layer; there is *no* central peak at the entrainment ratio. Moreover, at a given y location there appear to be *two* preferred mixture fractions. The two peaks may originate from 'upwash' and 'downwash' regions in the flow produced by the churning motion of the two counter-rotating legs of the lambda vortex. Low-speed fluid is being pumped up or high-speed fluid is being pushed down. The induced motion by

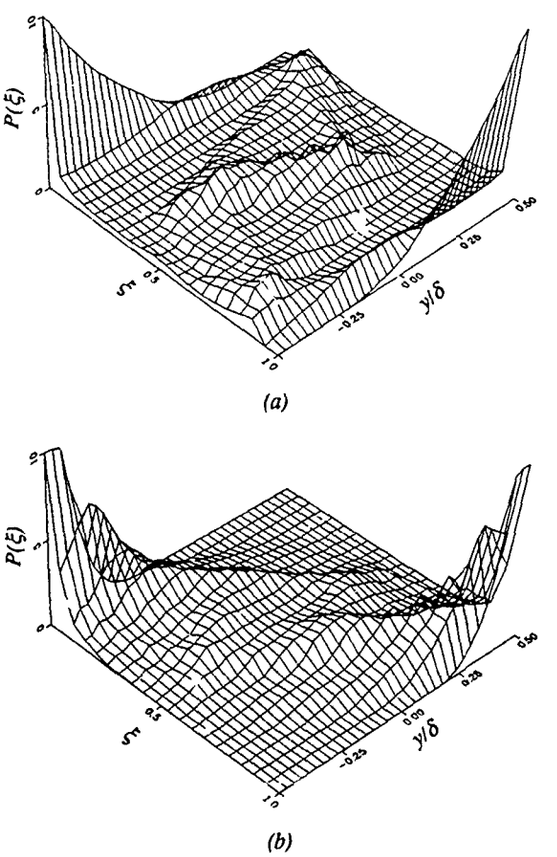

Figure 3. Histogram of the conserved scalar at $Re=1600$, *a)* $M_c=0.4$ and *b)* $M_c=0.8$.

the lambda vortices is illustrated in Figure 4.

The marching character of the histogram may be attributed to the inclined orientation of the lambda vortices in the lateral direction. The tips of the vortices are located close to one of the freestreams, and therefore, tend to preferentially entrain fluid from that side of the layer. A raised tip close to the high-speed side tends to entrain high-speed fluid which subsequently mixes with partially mixed fluid inside the layer; conversely, a depressed tip close to the low-speed side tends to entrain pure low speed fluid which then mixes with partially mixed fluid inside the layer. Therefore, rather than having one region of fluid mixed at the entrainment ratio, at moderate Mach numbers there exist two or more regions of fluid at a mixture fraction favoring the high- and low-speed sides. In a recent 'sonic eddy' compressible turbulence model by Breidenthal [1990], it is hypothesized that for very large convective Mach numbers, the instantaneous concentration profile would consist of many small steps, approaching a smooth mean profile. In this limit, the concept of gradient diffusion would become applicable. In the present work, entrainment occurs over one step at $M_c=0.4$, and over two steps at $M_c=0.8$. It is uncertain, whether, at higher convective Mach numbers, the number of steps would continue to increase, or whether it would remain at two.

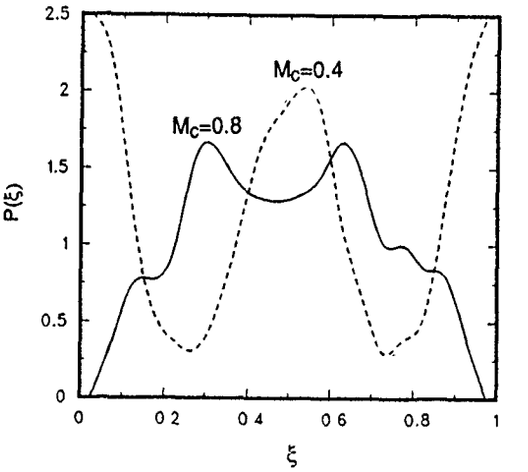

Figure 5. Midplane *(y=0)* through the histogram of the conserved scalar at *Re=1600*.

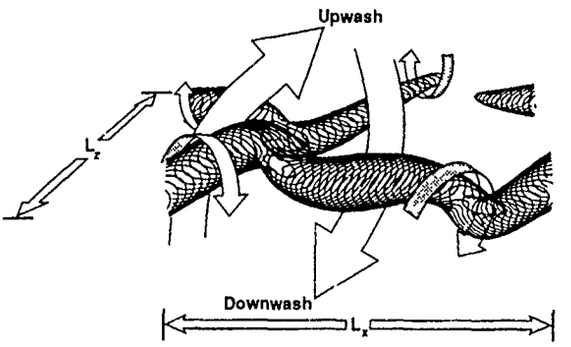

Figure 4. Conceptual drawing illustrating the generation of 'upwash' and 'downwash' regions by the lambda vortices.

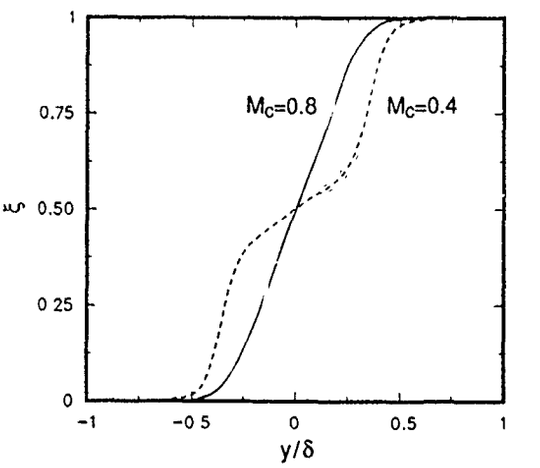

Figure 6. Mean concentration profile.

Figure 5 shows a slice of the histograms for the two cases corresponding to the midplane, *y=0*. There are several differences in the shape of histogram worth pointing out. First, at $M_c=0.4$, there are intrusions of pure high- and low- speed fluid deep in the layer as evidenced by the two humps centered at a mixture fraction *(ξ)* of zero and unity. These intrusions are the tongues of freestream fluid that are engulfed into the layer as the spanwise rollers turn over. On the other hand, at $M_c=0.8$, there are no tongues of pure fluid present near the center of the layer; therefore, the range of mixture fractions that are populated is narrower. Recent compressible shear layer experiments by Clemens *et al.* [1991] also show a narrower range of mixed fluid at $M_c=0.62$ compared to $M_c=0.28$. Second, at $M_c=0.8$, there are two peaks in the mixture fraction, at $\xi=0.3$ and $\xi=0.65$, instead of one at the entrainment ratio. As previously discussed, the origin of the two peaks may come from the induced motion of the legs of the vortices.

The conserved scalar mean profiles are shown in Figure 6 for the two cases. A triple inflection point exists in the mean for $M_c=0.4$ indicating the presence of homogeneous structure cores separated by tongues of pure freestream fluid. On the other hand, at $M_c=0.8$ the mean varies almost linearly from the low- to the high-speed stream with no evidence of pure fluid penetrating into the layer.

In Figure 7, the histograms of the conserved scalar were used to derive the temperature rise due to a fast reaction at $M_c=0.4$ and $M_c=0.8$ for different inverse equivalence ratios corresponding to the so-called 'flip' experiments by Mungal and Dimotakis [1984]. At $M_c=0.4$ (Figure 7a), the peaks in the normalized product profile all lie close to the entrainment ratio. This is expected since the histogram is non-marching. Note that there are secondary shoulders present near the edges of the layer indicating that the tongues of nearly pure freestream fluid have penetrated deep into the layer. Similar results were obtained in two-dimensional spatially-evolving mixing layer simulations by Lowery and Reynolds [1986]. However, subsequent three-dimensional simulations showed that streamwise vortices inhibit the lateral extent of the tongues [Lowery and Reynolds [1986], Buell and Mansour [1989]). In the present simulations, the streamwise vortices are relatively weak due to the random initial forcing. In Figure 7b, the normalized product profiles are shown for $M_c=0.8$. Here there is a larger shift away from the rich reactants as a result of the marching character of the histogram. Second, unlike the lower Mach number case, the maximum product is not attained at an equivalence ratio of unity; instead, the maximum product is formed for the flip experiments, with more product formed on the top and bottom sides of the layer.

The product thickness normalized by the 1% visual thickness is plotted against the stoichiometric mixture fraction in Figure 8 for the two cases. While the specific values of the product thickness are overpredicted due to diffusion effects at the Reynolds number of the present simulations, the overall shape of the product thickness as a function of the stoichiometry is correct. Note, that at $M_c=0.4$, the familiar 'gull wing' shape is reproduced, with the maximum product formed at the

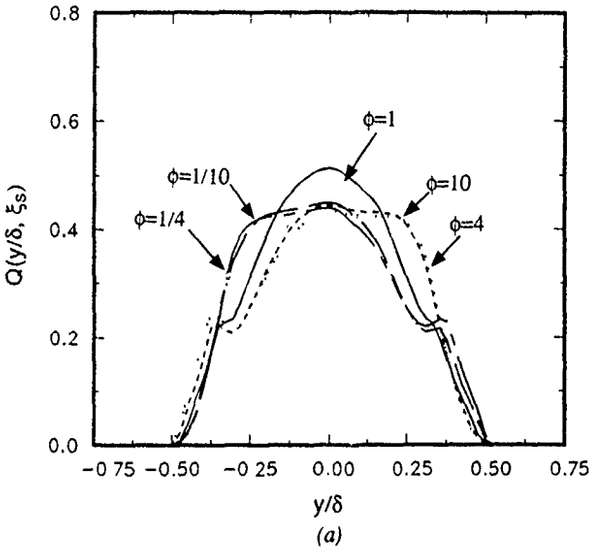

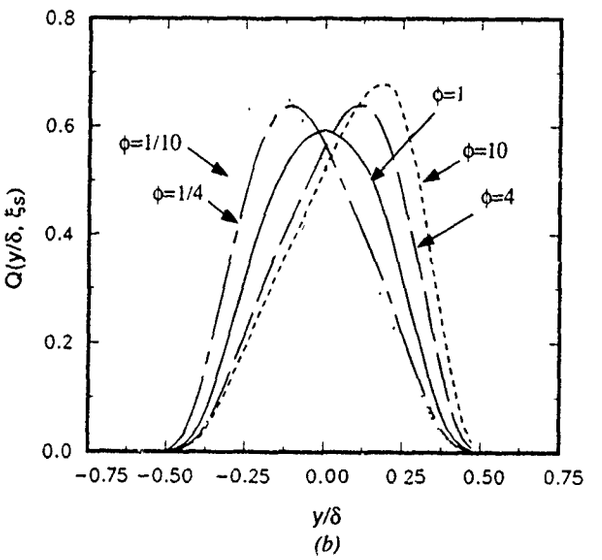

Figure 7. Normalized chemical product at $Re=1600$ for *a)* $M_c=0.4$ and *b)* $M_c=0.8$.

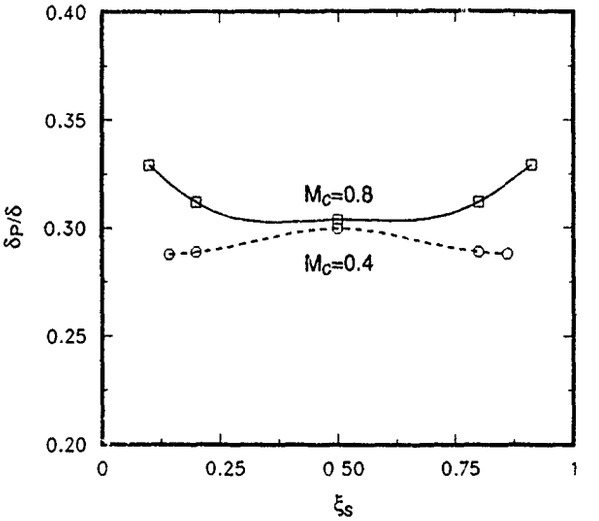

Figure 8. Normalized product thickness vs. stoichiometric mixture fraction.

entrainment ratio of unity for a temporal layer. At $M_c=0.8$, the shape is reversed, with more product being attained at a stoichiometric mixture fraction of 0.2 and 0.8, than of 0.5. Finally, for the same Reynolds number, slightly more product is formed at higher convective Mach number over a wide range of stoichiometric mixture fractions. This result is somewhat inconclusive, however, since the Reynolds number dependency of the product thickness has not been determined due to the limited range available in the present simulations.

5. Topology of the Velocity Field

In this section, the topology of the velocity field at $M_c=0.8$ is determined from instantaneous streamline patterns, obtained by integrating the instantaneous velocity in a frame of reference moving at the convective velocity. In this reference frame, the flow pattern is plotted in Figure 9 as projected streamlines in the three orthogonal planes. The streamlines were initialized near the critical points, where the velocity magnitude is nearly zero. The location of the critical points relative to the flow structure is determined by comparing Figure 4 with Figure 9. Figure 9a shows the projected streamline pattern in the x-z plane at $y=0$, while Figures 9b and 9c are y-z and x-y planes near the tips of two adjacent lambda vortices (near A in Figure 9a). The flow pattern clearly identifies two pairs of counter-rotating vortices that are focal in nature separated by three-dimensional saddle points. In between the two lambda vortices, near A in Figure 9a, there is a three-dimensional critical point corresponding to a stable-node/saddle/saddle topology according to the classification methodology of Chong, Perry, and Cantwell [1990]. A saddle point exists in the y-z and x-y planes, and a stable-node exists in the x-z plane. The saddle point in the x-y plane is clearly shown in Figure 9b where the streamline patterns for several adjacent z planes are plotted. Note that the saddle topology changes to two saddle points separated by an unstable node over a very small distance. The other saddle point at A is shown in Figure 9c. In this figure, the saddle point is between four focal regions corresponding to the legs of the vortices. The local topology is consistent with the idea of entrainment occurring in two steps across the layer, at least in the vicinity of this critical point. A second critical point exists at B of the unstable-node/saddle/saddle type. This critical point is a saddle in the x-z and y-z planes and an unstable-node in the x-y plane. The unstable node is shown in Figure 9b. A third critical point exists at C which is also an unstable-node/saddle/saddle. However, this critical point is a saddle in the x-z and x-y planes and an unstable-node in the y-z plane. The unstable node is shown in Figure 9c. A fourth critical point exists at D of the same type as B. Based on the present flow pattern, it is clear that at $M_c=0.8$, pure fluid is being entrained from the top and bottom sides in at least two steps. Further work remains to classify all of the critical points in the flow, to determine their relationship to one another, and to follow their temporal evolution.

6. Conclusions

Comparisons of direct numerical simulations at convective Mach numbers of 0.4 and 0.8 suggest that entrainment and mixing occur more locally at the higher convective Mach number. Fluid is entrained into the layer in one of two ways: (1) pure fluid from the low- and high-speed streams is engulfed in one continuous motion in regions between the tips of the lambda vortices; or (2) pure fluid is engulfed in several intermediate steps, with pure high- or pure low-speed fluid mixing with partially mixed fluid inside the layer in regions near the tips of the lambda vortices. The apparent source of the partially mixed fluid is the local upwash/downwash regions created by the induced motion of the legs of the vortices. The conserved scalar statistics suggest that, at $M_c=0.4$, the concentration profile is non-marching due to the presence of the global spanwise rollers. On the other hand, at $M_c=0.8$ and a comparable Reynolds

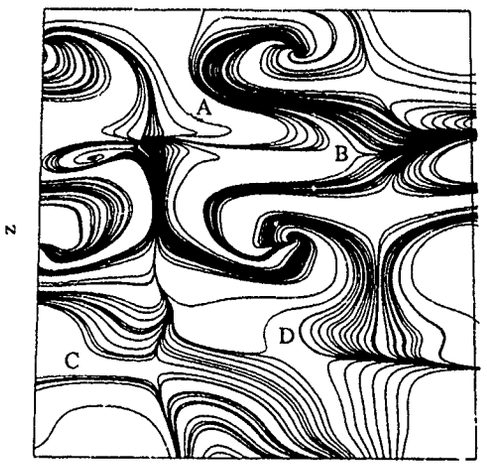

(a)

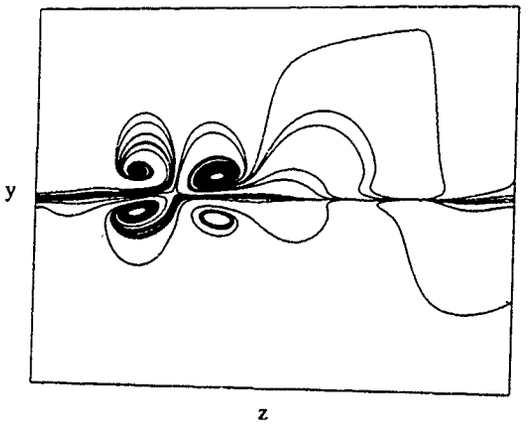

(b)

(c)

Figure 9. Projected sureamline patterns at $Re=1600$, $M_c=0.8$ *a) x-z* plane at *y=0*, *b) y-z* plane at A, and *c) x-y* plane at A. The symbols A, B, C, and D denote the location of critical points.

number, the instantaneous concentration profile is marching with the existence of *two* preferred mixture fractions at a given *y* location. The mean concentration and product profiles for the two cases reflect the non-marching and marching character of the instantaneous concentration profiles. Finally, the instantaneous streamline pattern at $M_c=0.8$ is consistent with the concept of entrainment occurring in multiple steps.

Acknowledgements

The author is grateful to Dr. N. D. Sandham for the use of his compressible flow code, and to Drs. M. G. Mungal, B. J. Cantwell, N. N. Mansour, N. T. Clemens, and P. H. Paul for many enlightening discussions. Support for this work was provided by the Department of Energy's Office of Basic Energy Sciences, Division of Chemical Sciences.

References

BREIDENTHAL, R. E. 1990 The sonic eddy - a model for compressible turbulence. *AIAA Paper* 90-0495.

BROADWELL, J. E. & BREIDENTHAL, R. E. 1982 A simple model of mixing and chemical reaction in a turbulent shear layer. *J. Fluid Mech.* **125**, 397-410.

BUELL, J. & MANSOUR, N. 1989 Asymmetric effects in three-dimensional spatially-developing mixing layers. *Turbulent Shear Flows* **7**.

CHONG, M., PERRY, A. E. & CANTWELL, B. J. 1990 A general classification of three-dimensional flow fields. *Physics of Fluids A* **2(5)**, 765-777.

CLEMENS, N. T. & MUNGAL, M. G. 1990 Two- and three-dimensional effects in the supersonic mixing layer. *AIAA Paper* 90-1978.

CLEMENS, N. T., PAUL, P. H., MUNGAL, M. G., & HANSON, R. K. 1991, *AIAA Paper* 91-1720 (to appear).

FOURGETTE, D. C., MUNGAL, M. G. & DIBBLE, R. W. 1990 Time evolution of the shear layer of a supersonic axisymmetric jet at matched conditions. *AIAA Paper* 90-0508.

KONRAD, J. H. 1976 An experimental investigation of mixing in two-dimensional turbulent shear flows with applications to diffusion-limited chemical reactions. *Ph. D. Dissertation, Cal. Tech.*

LOWERY, P. & REYNOLDS, W. C. 1986 Numerical simulation of a spatially-developing forced, plane mixing layer. Mechanical Engineering Report TF-26.

MUNGAL, M. G. & DIMOTAKIS, P. E. 1984 Mixing and combustion with low heat release in a turbulent shear layer. *J. Fluid Mech.* **148**, 349-382.

PAPAMOSCHOU, D. & ROSHKO, A. 1988 The compressible turbulent shear layer: an experimental study. *J. Fluid Mech.* **197**, 453-477.

SANDHAM, N. D. & REYNOLDS, W. C. 1991 Three dimensional simulations of large eddies in the compressible mixing layer. *J. Fluid Mech.* **224**, 133-159.

EIGHTH SYMPOSIUM ON
TURBULENT SHEAR FLOWS
Technical University of Munich
September 9-11, 1991

COMPRESSIBILITY EFFECTS ON LARGE STRUCTURES IN FREE SHEAR FLOWS

M. Samimy, G.S. Elliott, and M.F. Reeder
Department of Mechanical Engineering
Ohio State University
Columbus, Ohio 43210, U.S.A.

ABSTRACT

Space-time correlations and filtered Rayleigh scattering based flow visualizations were used to study compressibility effects on large structures in mixing layers. Two high Reynolds number mixing layers with M_c = 0.51 (case 1) and 0.86 (case 2) were studies. Previous LDV results had indicated no compressibility effects on the growth rate but some on the turbulence characteristics of case 1; however, there were major compressibility effects on both the growth rate and the turbulence characteristics of case 2. The streamwise correlations showed 4-5 times faster decay rate for case 2 than case 1. While the spanwise correlation for case 1 showed trends similar to incompressible mixing layers, the behavior of case 2 was totally different. The pressure fluctuations in the fully developed region of case 2 developed significant rms variation in spanwise direction with a well defined pattern. Based on pressure measurements and flow visualizations one could conclude that the structures in case 1 are similar to those in subsonic case however less organized. In case 2 the structures seem to be nearly spatially stationary across the span of mixing layer and highly three dimensional. The structures in this case seem to be composed of vortices spanning the mixing layer and inclined in both the streamwise and the spanwise directions. It is postulated that perhaps each large structure is consists of two or more of these structures with oblique angles of different sign connected at the edges of the mixing layer.

INTRODUCTION

The observation of large scale spanwise structures in incompressible planar free shear flows by Brown & Roshko (1974) drastically altered researchers's perceptions of mixing and entrainment processes in these flows. These structures were initially thought to be a manifestation of low Reynolds number flows thus reminiscence of transition to turbulence. However, similar large scale structures were later observed in higher Reynolds number mixing layers. Later study by Bernal & Roshko (1986) has shown that streamwise streaks or structures are embedded within the spanwise large structures.

Large scale structures have also been observed in high Reynolds number compressible mixing layers (e.g. Chinzei et al, 1986, Papamoschou & Roshko, 1988, Elliott & Samimy, 1990, Clemens et al, 1990, Shau & Dolling, and Messersmith et al, 1991). Even though Morkovin hypothesized compressibility effect in mixing layers in 1964 (also, Bradshaw, 1977), it was only recently that a compressibility parameter was identified (Bogdanoff, 1983 and Papamoschou & Roshko, 1988) which correlates the reduction in the growth rate and also in Reynolds stresses (Elliott & Samimy, 1990). This parameter was called convective Mach number, M_c, by Papamoschou & Roshko. Ragab & Wu (1989) and Sandham & Reynolds (1989) have shown that the oblique instability waves achieve a larger growth rate than 2-D instability waves at higher convective Mach numbers.

Previously, we used LDV to measure detailed mean flow and turbulence characteristics of cases 1 and 2 (Samimy & Elliott, 1990 and Elliott & Samimy, 1990). While case 1 depicts the beginning of the compressibility effect on the growth rate of mixing layers, case 2 shows over 50% drop in the growth rate. Between cases 1 and 2 there is over a factor of 2 drop in Reynolds shear stress and over 20% drop in the lateral turbulence fluctuations. The stability results of Ragab & Wu (1988) and Sandham & Reynolds (1989) have shown that at case 1 only two-dimensional instability waves are amplified, however, at case 2 two-dimensional and oblique waves are amplified almost equally. The objective of this research was to use these two flowfields to explore the effects of compressibility on the structures in mixing layers by using pressure correlation measurements and flow visualizations.

EXPERIMENTAL FACILITY AND INSTRUMENTATION

The experiments were conducted at the Ohio State University Aeronautical and Astronautical Research Laboratory (AARL). The high Reynolds number wind tunnel has a 152.4 x 152.4 mm test section. The tunnel is set up in a dual-stream configuration in which two independent streams merge downstream of a splitter plate to form a constant pressure mixing layer as shown in Fig. 1. The tunnel was operated in two different configurations. The Mach numbers, convective Mach numbers, velocity and density ratios, and stagnation temperatures of two streams are shown below.

	M_1	M_2	M_c	U_2/U_1	ρ_2/ρ_1	T_T(K)
case 1	1.8	0.51	0.51	0.36	0.64	290
case 2	3.0	0.42	0.86	0.24	0.36	290

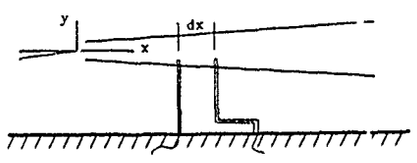

Fig. 1 Schematic of the test section with pressure probes in it.

The incoming high speed boundary layer was fully turbulent with Reynolds number based on the momentum thickness, $Re_{\theta\theta}$, of 27700 and 24700 for the Cases 1 and 2, respectively. At AARL, the cold and dry air generated at 16.4 MPa (2400 psi) by two four-stage compressors is stored in two storage tanks with 42.5 m^3 (1500 ft^3) capacity. The air is fed into the tunnel by two separate control valves. Therefore, flow to both streams can independently be controlled. The tunnel can be operated from a few minutes to several minutes depending on the nozzles used.

Fast response pressure transducers were used for space-time correlation measurements. Figure 1 gives a schematic of the pressure probes arrangement in the shear layer. The two probes were fitted with Endevco fast response differential pressure transducers, model 8514-20, with a sensitivity from 0 to 20 psi. The pressure sensitive diaphragm of these transducers is approximately 0.7 mm in diameter and an estimated frequency response of better than 50 kHz which is higher than what is required in these experiments. The pressure transducers were mounted perpendicular to the incoming streams, extending about 10 mm out of the probe tip to approximately measure the static pressure fluctuations. An Ectron model 563F signal conditioner was used with each transducer to provide the excitation voltage and to amplify the output signal. A 5520 MASSCOMP computer was used to acquire and process 100 blocks of data per measurement location with 1024 samples per block and 250 kHz sampling rate.

Filtered Rayleigh scattering (FRS) was use for flow visualizations. A Quanta Ray model GCR-4 Nd:YAG laser was used as a light source. Pulse width and energy per pulse of the laser were 8 ns and 500 mJ at a wave length of 532 nm (2nd harmonic). An injection seeder was used to narrow the linewidth and also to add some tuning capability. The 9 mm diameter beam from the laser is passed through a spherical lens to narrow the sheet made by expanding the beam through a cylindrical lens. The scattered light in the test section is collected through a molecular filter into an intensified CCD camera and recorded on a super VHS tape for post processing of the images. The main component that makes FRS flow visualization system different from standard Rayleigh scattering technique is the molecular filter placed in front of the camera. The molecular filter is basically an optical cell with a small amount of iodine crystal in it. When this cell is evacuated the low partial pressure of the iodine causes it to form vapor. Since iodine has absorption bands around the incident laser light of 532 nm, the laser can be tuned across the absorption bands. The cell used here is 25.4 cm long and similar to that used by Miles et al (1991), which is operated in the optically thick regime where the filter has a relatively sharp cutoff characteristic. Figure 2 shows the basic concept of using this filter in optically thick regime for flow visualizations. Because the Rayleigh signal is so weak and it takes a high amount of laser energy to form an image, there is usually a problem with background scattering and reflections from the windows and walls of the wind tunnel. Since this noise is unshifted having the same wave length as the incident light and scattering from molecules/particles within the flow have a Doppler shift, the laser can be tuned to an absorption band of the iodine and the background light can be filtered out. Miles et al

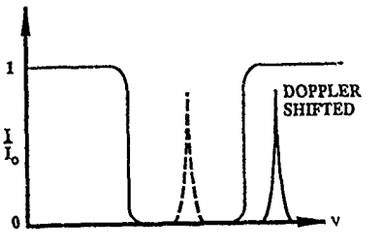

Fig. 2 The concept of FRS with a sharp cutoff molecular filter.

(1991) have discussed the technique in more detail. Although only flow visualization results are presented here, a multiple camera system is currently being developed to obtain instantaneous velocity and density measurements. For this case a sloping instead of a sharp cutoff filter needs to be used. This is similar, to some degree, to a system developed by Komine et al (1991).

EXPERIMENTAL RESULTS AND DISCUSSIONS

1. Pressure Results

Streamwise and Lateral Variations. Figure 3 shows streamwise evolution of power spectrum for case 1 at about the center of the shear layer ($y^* \approx 0$). The lateral nondimensional coordinate is defined as $y^* = (y-y_{ref})/\delta_w$ where y is the lateral location measured from the top surface of the splitter plate, y_{ref} is the lateral distance from the splitter plate where the measured convective velocity using spatial correlation matches the theoretical value, and δ_w is the local vorticity thickness. The downward shift in the broadband peak in the power spectrum, which is well defined in downstream locations, is due to the interaction among large scale structures and similar to incompressible results (Hussain & Zaman, 1985). Based on our previous results, the flow for this case is fully developed for x>150 mm (Samimy & Elliott, 1990). The case 2 shows a similar downshift in the frequency, however, the broadband peak frequency is not as well defined.

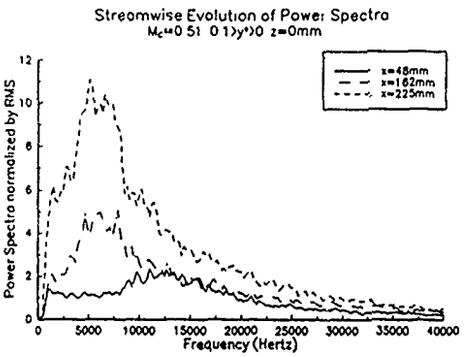

Fig. 3 Power spectra for various streamwise locations for the case 1.

Figure 4 shows the streamwise coherence for both cases in only one lateral location in the fully developed region. When $dx/\delta_w \approx 0.5$, the coherence levels are comparable for two cases. The coherence level drops by about 50% with increasing probe-separation to $dx/\delta_w = 1$ and 4.7, respectively, for cases 1 and 2. This indicates tremendous compressibility effect on the organization of large structures. Note that the local Reynolds numbers

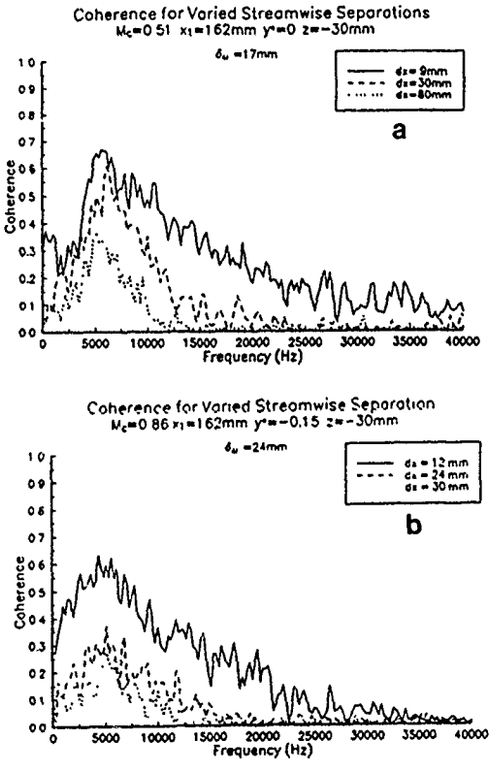

Fig. 4 Streamwise coherence for various separation distance in the fully developed region (a) case 1 and (b) case 2.

are comparable for the two cases. The streamwise correlations show a similar compressibility effect (Fig. 5). The results obtained in other lateral locations and also in the developing region show similar compressibility effect (Reeder, 1991).

The convective Mach number concept was introduced by Bogdanoff (1983) and Papamoschou and Roshko (1988) and has been used since then by many to correlate compressibility effect. The concept is based on the existence of a saddle point between two Brown and Roshko (1974) type spanwise two-dimensional rollers at which the two streams of the mixing layer stagnate in the coordinate system travelling with the rollers. The concept breaks down at supersonic convective Mach numbers (Papamoschou, 1991, McIntyre & Settles, 1991). The streamwise spatial correlations shown in Fig. 5 can be used directly to calculate the average convective velocity thus the convective Mach number. Instead we have calculated the convective velocity of individual structures (Reeder, 1991). Figure 6 shows histograms of convective velocity for case 2 at two lateral locations. The following observations can be made: 1) even at $y^* \approx 0$ where the average U_c is equal to the theoretical U_c, structures have a wide range of convective velocities and 2) both the average and the distribution change with y^*. The results for case 1 show similar characteristics but less lateral variations. The lateral variation of average U_c has been reported before in both incompressible and compressible mixing layers (Jones et al, 1973 and Ikawa & Kubota, 1975). In light of these results and flow visualization results to follow which show highly three dimensional

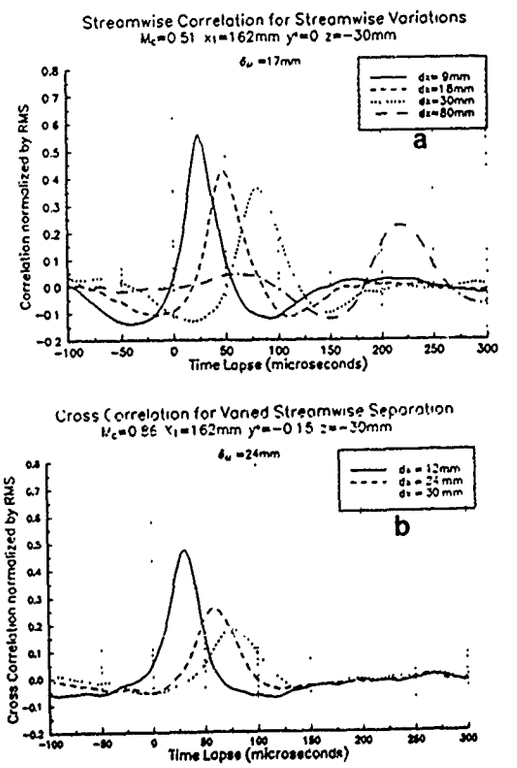

Fig. 5 Streamwise space-time correlations for various separation distance in the fully developed region (a) case 1 and (b) case 2.

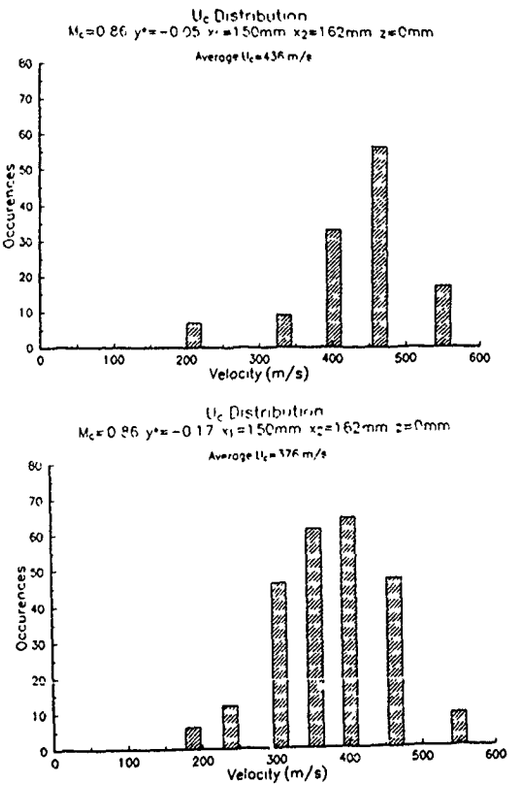

Fig. 6 Histograms of U_c at various lateral positions in the fully developed region for case 2.

nature of large structures in case 2, two things need to be kept in mind: 1) that while M_c is a good indicator of compressibility level, one should not overemphasize it, 2) any U_c measurements depend a great deal on the lateral position where they are taken, and 3) any U_c, and thus M_c measurements based on a limited number of structures could potentially produce highly erroneous results.

Spanwise Variations. The rms pressure fluctuations in the developing region, at about $100\theta_0$ from the splitter plate where θ_0 is the momentum thickness of incoming high speed flow, did not show any observable variations in the spanwise direction in either case (Reeder, 1991). Some spanwise variations with no apparent pattern were developed downstream in case 1 (Reeder, 1991). However, variations up to 3 fold with a relatively distinct pattern can be seen in the fully developed region of case 2 (Fig. 7). The tunnel span is from 0 to ±76 mm, but the measurements are taken only in the midsection of the tunnel far from the side walls. The results in Fig. 7 indicate that some sort of structures have been developed in case 2 where these structures seem to be nearly spatially stationary. The maximum rms pressure producing region of these structures seems to start from the low speed side and to branch out in spanwise direction as the legs extend in the lateral direction.

As was discussed earlier, stability analysis of Ragab and Wu (1989) and Sandham and Reynolds (1989) show that oblique instability waves are more amplified than two-dimensional ones at high compressibility levels. In fact, direct numerical simulations of Sandham and Reynolds with two initial oblique instability waves of opposite signs produced a pressure field which appears similar to the experimental results described in the above paragraph. However, their results showed two horseshoe type vortices; one with the head at high speed side and the other similar to the one described above.

Spanwise correlations normalized with rms at $y^* = -0.21$ for case 1 dropped from 0.27 to 0.08 when dz/δ_w was changed from 0.25 to 1.2 in the fully developed region of the mixing layer. The maximum correlations occurred at zero time delay signifying two-dimensional nature of the structures. These behaviors are similar to incompressible mixing layer results (Browand & Troutt, 1980). Figure 8 shows the spanwise correlation for case 2 in the fully developed region at two y^* locations. The general trend of these correlations indicate the complex nature of the structures. When one probe is at z = 0, $y^* = -0.6$, and $dz/\delta_w = 0.17$, the peak correlation level is relatively high and positive with a small time shift. However, the correlation

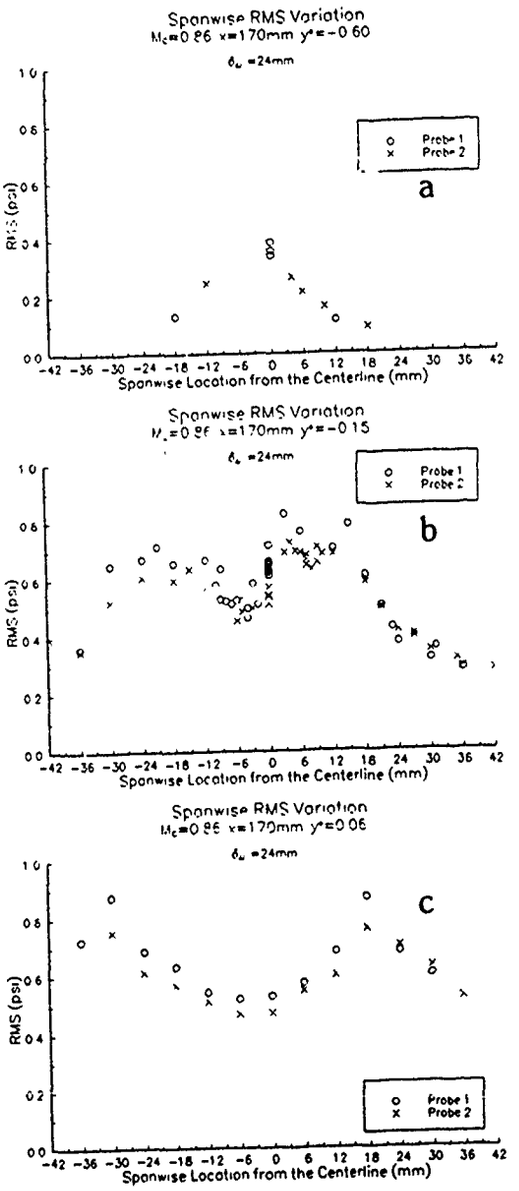

Fig. 7 RMS pressure fluctuations across the span of case 2 in the fully developed region at y^* = (a) -0.6, (b) -0.15 and (c) 0.06.

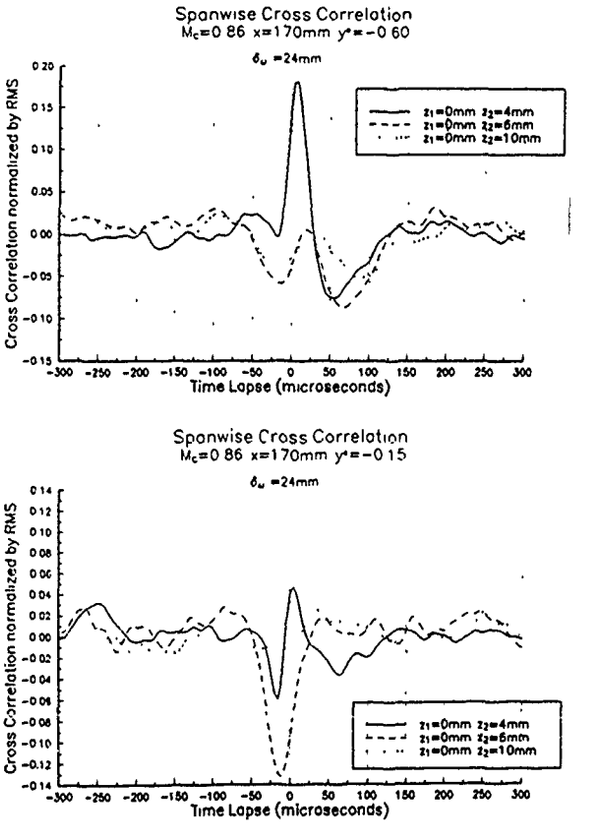

Fig. 8 Spanwise space-time correlations for varied spanwise separations and for varied spanwise and lateral locations for case 2.

peak changes sign and the level drops significantly with relatively large time shift for $dz/\delta_w \geq 0.25$. At $y^* = -0.15$ location, at small dz/δ_w both positive and negative correlations are present, but when dz/δ_w is increased the correlations is negative and the level of correlations first increases and then drops. Table 1 shows the correlation level, the time shift and the angle of structures from spanwise axis for $y^* = -0.15$ and $dz/\delta_w = 0.25$. The angle is calculated using $\beta = \tan^{-1}(U_c*\tau/dz)$, where U_c is the theoretical convective velocity. More detailed results are reported by Reeder (1991).

Table 1
Cross Correlation Data
x=170mm y*=-0.15 dz=0.258

		Primary Peak	Secondary Peak
z_1(mm)	z_2(mm)	Level /τ(μsec)/ β	Level /τ(μsec)/ β
-42	-36	-0.055 / -12 / 38°	
-36	-30	—no correlation—	
-30	-24	-0.12 / -2 / 7°	
-24	-18	-0.08 / -10 / 33°	
-21	-15	-0.10 / -4 / 15°	
-18	-12	-0.07 / 4 /-15°	
-12	-6	-0.07 / 12 /-38°	
-9	-3	-0.05 / -4 / 15°	
-6	0	-0.07 / -16 / 46°	
-3	3	-0.13 / -10 / 33°	
0	6	-0.12 / -12 / 38°	
3	9	-0.13 / -8 / 27°	
6	12	-0.10 / 0 / 0°	
12	18	-0.12 / -4 / 15°	
15	21	-0.10 / -4 / 15°	
18	24	-0.047 / 40 /-69°	-0.045 / 0 / 0°
21	27	-0.053 / 48 /-72°	-0.045 / 0 / 0°
24	30	-0.06 / 32 /-64°	
30	36	-0.06 / 52 /-74°	+0.04 / -44 / 71°
36	42	+0.04 / -40 / 69°	

The picture of the structures arising from the results presented so far is a complex one. All the indications are that the most dominant structures are highly three-dimensional inclined both in the mean flow direction (x) and in the spanwise direction (z) and they are nearly spatially stationary. An element of structure may be a horseshoe type vortex with the head in the low speed side and the legs, inclined both in the streamwise and the spanwise directions extending toward the high speed side. The element of structure could also be a single vortex tube type spanning the mixing layer and inclined in both the streamwise and the spanwise directions. Most probably, a large structure is composed of a few of these elements with oblique angles of different signs connected at either edge of mixing layer.

2. Flow Visualizations

As was discussed earlier, filtered Rayleigh scattering technique was used for flow visualizations. The background noise was removed by the molecular filter. As with the standard Rayleigh scattering technique, the signal is proportional to density and to the radius of molecules/particles to the sixth power. In a typical supersonic flow facility, the oil and water particles are removed by oil separators, dryers, and filters. Yet no matter how efficient these processes are, some water moisture will remain in the flow system. Depending upon the flow conditions such as pressure and temperature, the moisture may condense and form water particles in the test section (Wegener & Mack, 1958). In our case, the condensation occurs only in the high speed stream of case 2. These particles are so small that we cannot detect them with our LDV system in which case we use atomized oil particles on the order of 0.5 to 1 μm. Our estimate is that these condensed particles are in the order of 0.01 μm. These particles which are about an order of magnitude larger than molecules in the air provided scattering media for the flow visualizations. Therefore, in the visualization photographs, the bright regions mark the fluid from high speed side, and the dark regions the fluid mark the low speed side. To get a better contrast in the photographs we have limited the grey scale to two.

Figure 9 shows side view (x-y plane) of the flowfield for case 2 from about 40 to $350\theta_0$ in (a) and from about 300 to $540\theta_0$ in (b) where θ_0 is the incoming boundary layer momentum thickness of high speed stream. One identifies very large structures with nearly equal spacing in streamwise direction and many smaller structures on the edges of each large structure can be seen. These two photographs were taken at two different times. The exposure time for all the photographs is 8 ns. Figure 10 shows the spanwise view (y-z plane) of structures at an axial location of

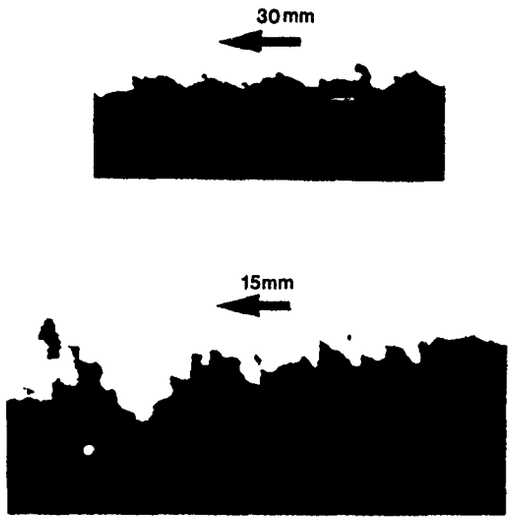

Fig. 9 FRS visualization of x-y plane for case 2.

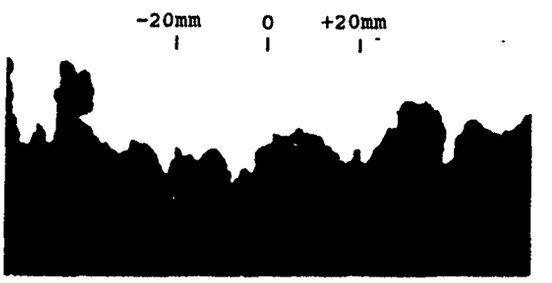

Fig. 10 FRS visualization of y-z plane for case 2.

about $490\theta_0$. The photograph shows various structures in the spanwise direction confirming very low spanwise correlation levels shown in Fig. 8. Figure 11 shows the plan view (x-z plane) cutting through the shear layer just slightly above the splitter plate in the axial location extending from about 280 to $430\theta_0$. In these photographs, one easily observes oblique structures.

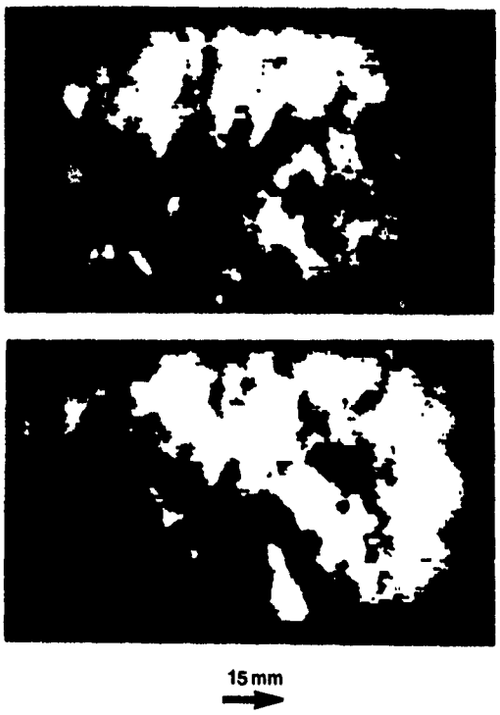

Fig. 11 FRS visualization of x-z plane for case 2.

The technique utilized here is based on a pulsed YAG laser with 8 ns pulse duration and 10 pulse/second repetition rate. In taking these photographs, the flow is frozen for about 8 ns while a photograph is taken, but there is no time relation between two successive photographs or frames. However, we have taken hundreds of frames and observed them individually. The results of these observations are be summarized here. There are large scale structures seen in both streamwise and spanwise views. These structures grow both in the streamwise and spanwise directions. Sometimes they seem to have very well organized patterns in both directions. The plan view photographs show both spanwise and oblique structures. In some photographs, either there are no structures or the structures do not seem to have any pattern. A possible explanation for spanwise photographs may be that in each frame the sheet of light cuts through different parts of the structures, e.g. the core or the braid section of structures. But the only explanation for the streamwise and the plan views is that the structures are very poorly organized in time and are highly three-dimensional. This is what one would also conclude from coherence and correlation results discussed earlier.

CONCLUSIONS

The behavior of case 1 is similar to incompressible mixing layers in many ways. However, case 2 shows totally different behavior. It seems that the higher compressibility case can support oblique structures; therefore, the structures are highly three dimensional and complex for case 2. All indications are that these structures are nearly spatially stationary in spanwise direction spanning the mixing layer and inclined in both the streamwise and the spanwise direction. They have both positive and negative angles, and if they travel together they may connect at either edge of the mixing layers.

Acknowledgements

The research is supported by ONR (with Dr. S. J. Lekoudis) and NASA Lewis (with Dr. K.B.M.Q. Zaman). The authors would like to thank colleagues Diana D. Glawe and Stephen A. Arnette and AARL staff for their help.

REFERENCES

Bernal, L.P. and Roshko, A., 1986, "Streamwise vortex structure in plane mixing layers," J. Fluid Mech, 170, 499-525.

Bogdanoff, D.W., 1983, "Compressibility effects in turbulent shear layers," AIAA J., 21, 926-927.

Bradshaw, P., 1977, "Compressible turbulent shear layers," Ann Rev Fluid Mech, 63, 449-464.

Browand, F.K., and Troutt, T.R., 1980, "A note on spanwise structure in the two-dimensional mixing layer," J. Fluid Mech., 917, 771-781.

Brown, G.L. and Roshko, A., 1974, "On density effects and large scale structure in turbulent mixing layers," J. Fluid Mech, 64, 775-816.

Chinzei, N., Masuya, G., Komuro, T., Murakami, A., and Kodou, K., 1986, "Spreading of two stream supersonic turbulent mixing layer," Phys Fluids, 29, 1345-1347.

Clemens, N.T. and Mungal M.G., 1990, "Two- and three-dimensional effects in the supersonic mixing layer," AIAA-90-1978.

Elliott, G.S. and Samimy, M., 1990, "Compressibility effects in free shear layers," Phys Fluids, 2, 1231-1240.

Hussain, A.K.M.F. and Zaman, K.B.M.Q., 1985, "An experimental study of organized motions in the turbulent plane mixing layer," J. Fluid Mech, 159, 85-104.

Ikawa, H. and Kubota, T., 1975, "Investigation of supersonic turbulent mixing layer with zero pressure gradient," AIAA J., 13, 566-572.

Jones, G., Planchon, H.P., and Hammersly, R.J., 1973, "Turbulent correlation measurements in a two-stream mixing layer," AIAA J., 11, 1146-1150.

Komine, H., Brosnan, S.J., Litton, A.B., and Stappa erts, "Real-time Doppler global velocimetry," AIAA-91-0337.

Messersmith, N.L., Dutton, J.C., and Krier, H., 1991, "Experimental investigation of large scale structures in compressible mixing layers," AIAA Paper 91-0244.

Miles, R.B., Lempert, W.R., and Forkey, J., "Instantaneous velocity fields and background suppression by filtered Rayleigh scattering," AIAA-91-0357.

Morkovin, M.V., 1961, "Effects of compressibility on turbulent flows," Mechanique de la Turbulence, Marseille, France.

Papamoschou, D. and Roshko, A., 1988, "The compressible turbulent mixing layer: an experimental study," J. Fluid Mech, 197, 453-477.

Papamoschou, D., 1991, "Structure of the compressible turbulent shear layer," AIAA J., 29, 680-681.

Ragab, S.A. and Wu, J.L., 1989, "Linear instabilities in two-dimensional compressible mixing layers, Phys Fluids, 1, 957-966.

Reeder, M.F., 1991, "A study of the effects of compressibility in mixing layers using two-probe pressure correlations," MS Thesis, Ohio State University.

Samimy, M. and Elliott, G.S., 1990, "Effects of compressibility on the characteristics of free shear layers," AIAA J., 28, 957-966.

Sandham, N.D. and Reynolds, W.C., 1989, "A numerical investigation of the compressible mixing layer," Report No. TF-45, Stanford University.

Shau, Y.R. and Dolling, D.S., 1990, "The detection of large scale structure in undisturbed and disturbed compressible turbulent free shear layers," AIAA Paper 90-0711.

Wegener, P.P. and Mack, L.M., 1958, "Condensation in supersonic and hypersonic wind tunnels," in Advances in Applied Mechanics, Academic Press.

EIGHTH SYMPOSIUM ON
TURBULENT SHEAR FLOWS
Technical University of Munich
September 9-11, 1991

THE EFFECTS OF VISCOSITY AND DIFFUSION ON A SUPERSONIC MIXING LAYER

P. Vuillermoz* and E.S. Oran**
* Société Européenne de Propulsion
27207 Vernon, France
** Laboratory for Computational Physics and Fluid Dynamics
Naval Research Laboratory, Washington, DC 20375

ABSTRACT

Time-dependent two-dimensional numerical simulations of high-speed, compressible, confined, temporally evolving supersonic mixing layers between hydrogen and oxygen gas streams are used to examine the differences between Euler and Navier-Stokes solutions and the effects of convective Mach number. The computations show that the Euler solutions are reasonably accurate in the convective-mixing stage of the flow, when large-scale structures dominate. As the convective Mach number increases, the mixing and turbulent levels are reduced.

INTRODUCTION

The successful design of propulsive engines for hypersonic vehicles requires accurate prediction of the mixing and combustion efficiency in high-speed flows. In order to achieve this predictive capability, we need an improved understanding of the dominant processes. In this paper, we have begun to address several of these complex issues. In particular, we focus on the numerical solution of the mixing of a hydrogen and oxygen stream so that we are studying the features of a high-speed shear layer between two gases of very different densities

Since the Brown and Rosko [1974] observations, many experimental studies have confirmed the existence of large-scale coherent structures in turbulent mixing layers for both high and low Reynolds numbers. Papamoschou et al. [1986] and Clemens et al. [1990] showed the effects of compressibility on the growth of the shear layer, and recently, Dimotakis [1989] summarized experiments on the entrainment and mixing processes. There have been a number of theoretical stability analyses and concommitant numerical simulations of both spatially and temporally evolving shear layers. Ragab and Wu [1990] and Jackson and Grosch [1989] have shown that for high M_c, there are several unstable modes and three-dimensional modes become important. Sandham and Reynolds [1989] and Lele [1989] have considered two-dimensional and three-dimensional direct numerical simulations. Using vortex-dynamics methods, Soteriou et al. [1991] have studied the effects of density gradients.

In the work presented below, we solve the equations describing a *temporally evolving shear layer*, where one stream is molecular oxygen and the other is molecular hydrogen. This approach allows us to focus on the structure of the flow and the details of the turbulent structures and determine what is required to adequately resolve the flowfield in the different mixing regimes. In particular, we compare solutions of the Euler equations for this flow to solutions of the complete set of Navier-Stokes equations that also contain descriptions of molecular diffusion and thermal conduction (referred to as the NS+ equations).

PHYSICAL AND NUMERICAL MODEL

General Formulation

We solve the time-dependent, two-dimensional, compressible, Navier-Stokes equations for a multispecies gas, including the effects of molecular diffusion and thermal conduction. The balance equations for the densities, momentum, and energy are

$$\frac{\partial \rho}{\partial t} = -\nabla \cdot (\rho \mathbf{v}) , \tag{1}$$

$$\frac{\partial n_i}{\partial t} = -\nabla \cdot (n_i \mathbf{v}) - \nabla \cdot (n_i \mathbf{v}_{di}) \qquad i = 1,...,N_s , \tag{2}$$

$$\frac{\partial \rho \mathbf{v}}{\partial t} = -\nabla \cdot (\rho \mathbf{v}\mathbf{v}) - \nabla \cdot \mathbf{P} , \tag{3}$$

$$\frac{\partial E}{\partial t} = -\nabla \cdot (E\mathbf{v}) - \nabla \cdot (\mathbf{v} \cdot \mathbf{P}) - \nabla \cdot (\mathbf{q}) , \tag{4}$$

The mass fraction of species i is Y_i, defined by

$$n_i = \frac{\rho Y_i}{W_i} , \tag{5}$$

where n_i is the number density and W_i the molecular weight of the species i. The auxiliary equation for pressure $\mathbf{P}$ and heat conductive flux $\mathbf{q}$ are

$$\mathbf{P} \equiv P(\rho,T)\mathbf{I} + \frac{2}{3}\mu_m(\nabla \cdot \mathbf{v})\mathbf{I} - \mu_m[(\nabla \mathbf{v}) + (\nabla \mathbf{v})^T] \tag{6}$$

and

$$\mathbf{q} = -\lambda_m \nabla T + \rho \sum_i h_i Y_i \mathbf{v}_{di} . \tag{7}$$

We assume an ideal-gas equation of state: $P = \rho RT$. The specific enthalpy h_i can be written as

$$h_i = \int_0^T C_{p_i} dT + h_{i_0} , \tag{8}$$

where C_{p_i} and h_{i_0} are the specific heat at constant pressure and heat of formation of species i, respectively. We neglect the radiative fluxes and the Soret and Dufour effects (thermal diffusion).

Diffusion Model

The diffusion velocities $\mathbf{v}_{d_i}$ are solutions of the following system of equations (see, for example, Oran and Boris [1987]),

$$\nabla X_i = \sum_j \frac{X_i X_j}{D_{ij}}(\mathbf{v}_{dj} - \mathbf{v}_{di}) + (Y_i - X_i)\left(\frac{\nabla P}{P}\right), \quad (9)$$

where, for each species i, X_i is the mole fraction, $\mathbf{v}_{d_i}$ the diffusion velocity, and D_{ij} the diffusivity of the species i into the species j.

These diffusion velocities must obey to the condition of mass conservation such that

$$\sum_i Y_i \mathbf{v}_{di} = 0 . \quad (10)$$

We approximate the solution of the system of equations (9) and (10) by a gradient law, as proposed by Coffee and Heimerl [1981],

$$\hat{\mathbf{v}}_{di} = -\frac{1}{X_i} D_i^m \nabla X_i \qquad D_i^m = \frac{1 - Y_i}{\sum_{j \neq i} X_j / D_{ij}} . \quad (11)$$

Then we correct these velocities in order to insure the mass conservation, equation (10),

$$\mathbf{v}_c = -\sum_j Y_j \hat{\mathbf{v}}_{dj} \quad \text{and} \quad \mathbf{v}_{di} = \hat{\mathbf{v}}_{di} + \mathbf{v}_c . \quad (12)$$

This approximation becomes rigorously correct in the binary case if we neglect the pressure effect on diffusion.

Numerical Integration

The different physical processes are solved separately and their effects are then coupled together by timestep-splitting methods (Oran and Boris [1987]). The convection is solved using a standard Flux-Corrected Transport (FCT) algorithm This is a nonlinear, monotone algorithm that is fourth-order accurate in phase. The integration is carried out by a two-step predictor-corrector procedure with, successively, a diffusive and antidiffusive step. The first step modifies the linear properties of a high-order algorithm by adding diffusion during convective transport to prevent dispersive ripples from arising. The added diffusion is removed in an antidiffusion step. The result is that the calculations maintain the high order of accuracy without requiring artificial viscosity to stabilize them. The physical diffusion terms are solved in conservative finite-volume form by second-order centered algorithms. An overall global timestep is chosen by evaluating the individual stability criteria of each type of process in the computations and then selecting the minimum of these.

THE MODEL PROBLEM

In the one-dimensional problem, we compute the evolution of a mixing layer between two gases starting from a step profile for each variable in the y direction. We do this by solving the full set of equations (1) - (4), but assuming that there are no variations along the x direction. That is, $\partial\varphi/\partial x = 0$, where φ represents ρ, $\rho\mathbf{v}$, $\{n_i\}$, and E. The boundaries at the bottom and the top of the domain are open. The solution of this problem provides initial conditions for the two-dimensional shear layer.

The two-dimensional computational domain, shown in Figure 1, consists of a rectangle of length L and height $H = L/2$. The left and right boundaries are periodic, which means that $\varphi(0, y) = \varphi(L, y)$, and the bottom and top boundaries are slip wall conditions, $\rho v_y = 0$ and $\partial\varphi/\partial y = 0$ where $\varphi = \{\rho, \rho v_x, \{n_i\}, E\}$ at $y = 0$ and $y = H$. The computational cell size is always kept uniform in the x and y directions and are in the range $\Delta x = \Delta y = (2.5 - 10) \times 10^{-5}$ m, so that the timesteps are in the range $(2-8)\times 10^{-3}$ μs. A typical computation described below requires about 10,000 timesteps.

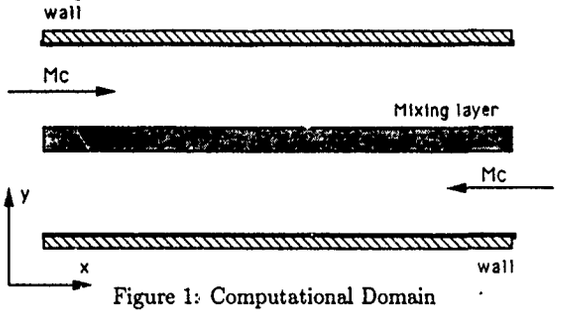

Figure 1: Computational Domain

Computational Diagnostics

A number of different global and instantaneous parameters are used to characterize the flows:

1) The convective Mach number M_c and the convective velocity of the coherent structures U_c can be approximated from known properties of the flow assuming a stagnation point in the center of each coherent structure. This analysis, suggested by Papamoshou and Roshko [1986], leads to

$$U_c = \frac{(a_1 U_2 + a_2 U_1)}{(a_1 + a_2)} \quad \text{and} \quad M_c = \frac{(U_2 - U_1)}{(a_1 + a_2)}, \quad (13)$$

where a_1 and a_2 are the speeds of sound for the streams 1 and 2, respectively.

2) The energy transfer for two-dimensional turbulence can be described by the field of enstrophy, ω^2. Enstrophy for two-dimensional turbulence has properties similar to vorticity for three-dimensional turbulence (Batchelor [1969]), that is, there is a cascade process, independent of the viscosity, to higher wavenumbers where the enstrophy is dissipated. The global intensity of the turbulent flow may be characterized by $M_\omega = \sqrt{< \omega^2 >^{-1}}$, where the $< >$ indicates an average taken over the computational domain. For an incompressible, homogeneous turbulent flow, M_ω is a linear function of time (Batchelor [1969]).

3) Mixing efficiency between different gases can be described in terms of mole fraction, X_i, or mass fraction, Y_i. For the binary mixture, we define two global parameters, $M_X = 4 < X_1\ X_2 >$ and $M_Y = 4 < Y_1\ Y_2 >$, that vary between 0 and 1. For the limit of fully mixed material, $M_X^\infty = 1$ and $M_Y^\infty = 4W_1W_2/(W_1 + W_2)^2$. For the hydrogen and oxygen mixture we are considering, $M_Y^\infty = 0.22$. The parameter $M_{\nabla Y} =< \nabla Y_{H_2}\ \nabla Y_{H_2} >$ is related to the dissipation of scalar energy in the computational domain

and describes the density of mixing interfaces developing in the domain.

THE ONE-DIMENSIONAL PROBLEM

One-Dimensional Mixing Layer

In the one-dimensional problem, one stream is molecular hydrogen and the other is molecular oxygen. Initially the computation shows a transient characterized by two acoustic waves moving away from the interface to the top and the bottom of the domain. After that, the static pressure returns to its initial uniform value and a negative transverse velocity v_y is generated within the developing mixing layer. Figure 2, profiles of density and temperature for $M_c = 0.6$, shows that the motion is directed from the heavy fluid towards the light fluid. This explains the evolution of ρ which itself is not directly affected by the molecular diffusion process. The temperature reaches a maximum in the middle of the layer showing the transformation of kinetic energy into internal energy by viscous dissipation. In addition, graphs of these profiles as a function of $\eta = y/\sqrt{\nu t}$ show that the solution is self-similar (Vuillermoz and Oran [1991]). This is a characteristic of flows such as mixing layers that do not have any particular length scale, a feature previously noted by Sandham and Reynolds [1989].

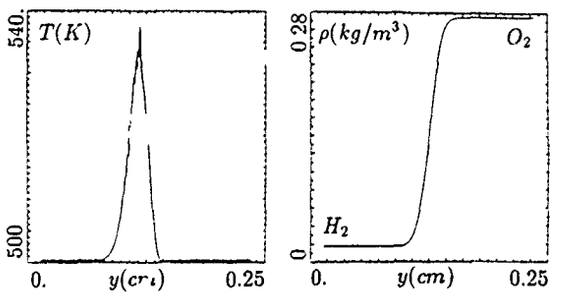

Figure 2: One-dimensional Results

Two-Dimensional Initialization

The two-dimensional configuration is Kelvin-Helmholtz unstable. We use the one dimensional computation to provide initial conditions, and then trigger the instability by superimposing a set of harmonic ($\Omega = 2\pi/\Lambda$) and subharmonic ($\Omega/2$) pressure disturbances. In the calculations presented below, we have chosen the wavelength of the instability, Λ, such that $\Lambda/L = 2$, 4, and 8 and $\alpha = 0.05$.

THE TWO-DIMENSIONAL PROBLEM

Analysis of the Turbulent Scales

The main feature of a turbulent flow is the wide range of its energy spectrum. The largest scales may be characterized by a length l and a velocity U, and the smallest dissipative scales may be characterized by a length η and velocity u. If we assume that there is an equilibrium between the convection and the dissipation of turbulent energy, we can compare the large and small scales. This assumption means that the characteristic time t_c of the transport of turbulent energy by the large eddies is equal to the times t_v and t_d of its dissipation by viscosity or diffusion, $t_c = t_v = t_d$, where

$$t_c = \frac{l}{U} \ , \ t_v = \frac{U^2}{\epsilon_t} \text{ and } t_d = \frac{1}{\epsilon_Y} . \qquad (14)$$

Here ϵ_t is the dissipation of turbulent kinetic energy, $k = \frac{1}{2} < U'^2 >$, and ϵ_Y is the dissipation of turbulent scalar energy, $\frac{1}{2} < Y'^2 >$, which may be written as

$$\epsilon_t = \frac{\mu}{\rho} < \mathbf{S}'\mathbf{S}' > = \frac{\mu}{\rho \tau^2} \qquad (15)$$

and

$$\epsilon_Y = D < \nabla Y' \nabla Y' > = \frac{D}{\eta_Y^2} , \qquad (16)$$

where η_Y is the mixing scale, S is the tensor of deformation and $\tau = \eta/u$. Note that the prime indicates fluctuation of the variable.

If we define the Kolmogorov scale η_k as that scale where the molecular viscosity transforms the kinetic energy into heat (that is, the scale at which the Reynolds number is of order unity, $Re_k = \rho \eta_k u/\mu \sim 1$), we obtain

$$\frac{\eta_k}{l} = Re^{-\frac{1}{4}} , \qquad (17)$$

where $Re = \rho l U/\mu$ is the Reynolds number of the large scale

In the same way, the equilibrium condition allows us to evaluate η_Y,

$$\frac{\eta_Y}{l} = P_e^{-\frac{1}{2}} , \qquad (18)$$

where P_e is the Peclet number such that $P_e = lU/D = S_c Re$ and $S_c = \mu/\rho D$ is the Schmidt number. When $S_c = 1$, η_Y is the Taylor scale.

In our case, the large scales are bounded by the width of the computational domain and their velocity scales with the difference of velocities across the shear layer. Then, we can assume that,

$$l \sim H \text{ and } U \sim (U_2 - U_1) = M_c(a_1 + a_2) \qquad (19)$$

This assumption allows us to asses the small scales. Several values computed for the hydrogen-oxygen mixing layer are reported in Table 1

Table 1. Estimations of Kolmogorov and mixing scales

$l(mm)$	M_c	Re	$\eta_k(m)$	$\eta_Y(m)$
5.0	0.6	1.85×10^4	3.1×10^{-6}	3.7×10^{-5}
5.0	1.2	3.70×10^4	1.9×10^{-6}	2.6×10^{-5}

Discussion and Analysis of Mixing Regimes

In order to isolate and examine the effects of molecular diffusion, we performed three NS+ calculations that were the same except for the values of the diffusion coefficients. These computations were performed for a system with $L =$ 1.0 cm, 200 × 100 computational cells, and $\Delta x = \Delta y =$

5.0×10^{-5} m. In one case, the molecular diffusion is turned off completely. In another, the actual values of physical diffusion were used, as in the previous computations. In the final case, we multiplied the physical values by two. The results of the comparison are presented in Figure 3 that shows various diagnostics defined above as a function of a dimensionless time t/t_0, where $t_0 = H/\Delta U$.

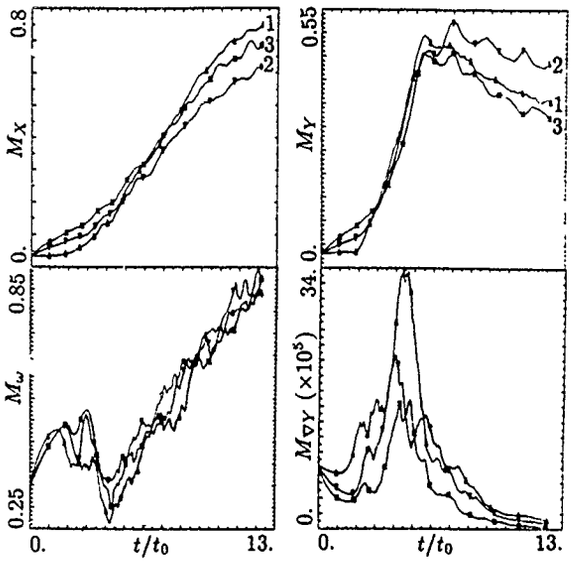

Figure 3: Effect of Diffusion
(1: no diffusion, 2: 1 x diffusion, 3: 2 x diffusion)

The M_Y and $M_{\nabla Y}$ show that there are three stages in the mixing procedure. In the initial growth stage, a laminar growth stage extending to about $t/t_0 \sim 2$, the large structures grow as a consequence of the initial perturbation on the flowfield. The large vortices roll up and grow almost independently of each other. In the first mixing stage extending to about $t/t_0 \sim 5$, which we call the convective-mixing stage, the vortices begin to interact with each other and convective mixing dominates. Mixing occurs as these structures merge and grow and the interfaces between the oxygen and hydrogen stretch and deform. The generation of stretched interfaces corresponds to a sharp growth in the intensity of the scalar dissipation $M_{\nabla Y}$. Finally, there is the stage that occurs when the widths of the interfaces reach the order of magnitude of η_Y and they are destroyed by molecular diffusion. The $M_{\nabla Y}$ drops very quickly, M_Y relaxes to its asymptotic value, 0.22 in this case, and M_ω linearly increases, as predicted for homogeneous turbulence. The two last stages shown in the computation, the turbulent stages, have been described in the theoretical analysis of Broadwell and Breidenthal [1982].

We can interprete these results by considering two parameters, the mean length of an interface in the domain, l_i, and mean width of a structure in the domain, δ_i, which we can estimate from

$$M_X = \frac{\delta_i l_i}{S_{tot}} \text{ and } M_{\nabla Y} = \frac{l_i}{\delta_i} \qquad (20)$$

which assumes that $\nabla Y_{H_2} \sim 1/\delta_i$. Figure 4 compares these quantities as computed from the results of the Figure 3. The quantity δ_i does not change much during the convective-mixing stage whereas l_i increases quickly and independently of the diffusion. When the diffusive-mixing stage begins, the turbulent structures broaden in proportion to the diffusion coefficient and the destruction of the turbulent scales is controlled by the amount of molecular diffusion.

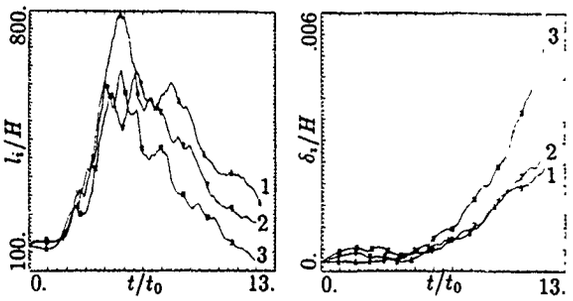

Figure 4: Width and Length of Turbulent Structures
(1: no diffusion, 2: 1 x diffusion, 3: 2 x diffusion)

Figure 5 shows instantaneous contours of mass fraction of hydrogen during the three regimes described above. We note the apparent change from a very regular structure to the extremely mixed structure at the end of the computation. As time evolves, we see the shear layer expanding towards the lighter fluid on the bottom, an effect noted by Soteriou et al. [1991].

Comparison between Euler and NS+ computations

A previous study (Vuillermoz and Oran [1991]) showed that the transition between the two mixing stages does not depend on whether or not we include the viscosity or the diffusion. Moreover, this transition occurs at the same dimensionless time, proving that it is only a function of the large-scale convection. This observation is so in agreement with the Broadwell and Breidenthal theory. They provided an estimate of the time t_k needed for a large eddy to break up and dissipate at the Kolmogorov scale. If the Reynolds number is high enough, the first-order approximation of this characteristic time does not depend on the viscosity,

$$t_k = \frac{l}{U} \times [1 + \mathcal{O}(Re^{-1/2})] \, . \qquad (21)$$

Figure 5 compares the results of an Euler and NS+ computations for the case presented before. It shows typical instantaneous profiles of hydrogen mass fraction Y_{H_2} in the initial growth stage, the convective-mixing stage, and the diffusive-mixing stage. In the first stage $t/t_0 \sim 1$, the Euler and NS+ calculations are very similar. Differences begin to appear in the next two mixing stages. During the convective-mixing regime, smaller turbulent scales are generated in the Euler solution, whereas the NS+ solution looks smoother. In the diffusive-mixing stage, the spectrum of turbulent scales appears significantly broader for the Euler calculation. Figure 6a shows M_Y for this case and indicates that viscosity and diffusion do not have a strong influence on the average mixing during the convective regime. However, we see that the NS+ calculation reaches its final value much faster than the inviscid calculation.

Figure 6b shows M_Y for a calculation with the same number of cells, 200 x 100, but for Δx half the size. The NS+ calculation shows no clear transition from the laminar

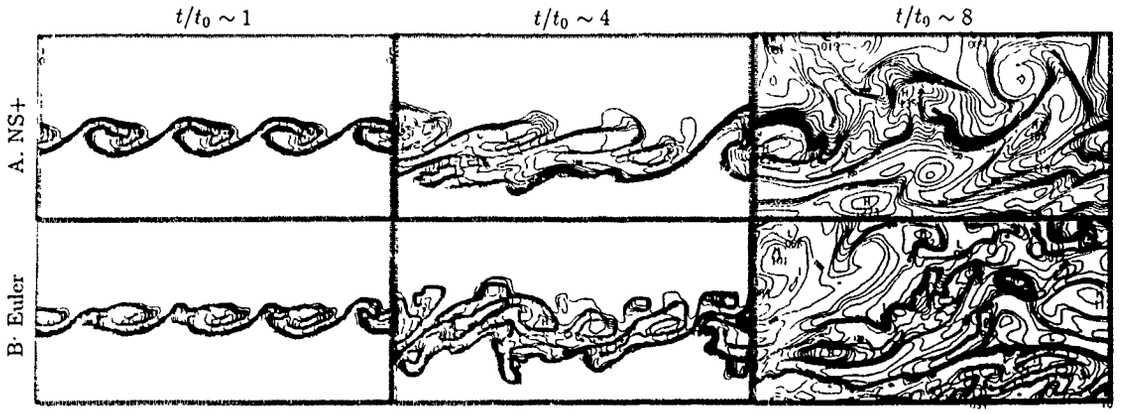

Figure 5: Instantaneous contours of Y_{H_2}

to the turbulent scale at $t/t_0 \sim 2$, nor does it show the overshoot in values that we have been seeing at $t/t_0 \sim 5$ at the transition from convective to diffusive mixing. This can be explained on the basis of the difference in the Reynolds numbers of these NS+ computations. For the larger system with $L = 1$ cm, we can estimate $Re = 1.8 \times 10^4$ (Table 1), and for $L = 0.5$ cm, $Re = 0.9 \times 10^4$. This difference in the mixing process can be interpreted as a Reynolds number transition, as explained by Koochesfahani and Dimotakis [1986].

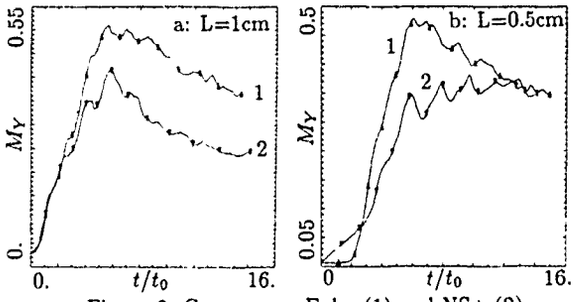

Figure 6: Comparison Euler (1) and NS+ (2)

Figure 7 shows the instantaneous scalar energy dissipation $\nabla Y_{H_2} \nabla Y_{H_2}$ during the diffusive-mixing stage. There is a notable difference here in the number and width of interfaces in the domain, indicating the inadequacy of the Euler solution. This kind of diagnostic has been computed from scalar measurements in incompressible jets by Dahm et al. [1989], whose results for liquid mixing show qualitative agreement with the computations for the general shape of the structures.

Effect of Convective Mach Number

We have considered four convective Mach numbers for which summaries of the evolution of the global parameters as a function of dimensionless time, t/t_o, are shown in Figure 8. Here $t_0 = H/\Delta U = H/M_c(a_1 + a_2)$, so that the dimensionless time is a function of M_c. For the two lowest values of M_c, 0.3 and 0.6, the mixing efficiencies are very close. As M_c increases, there is a delay in the onset of the convective-mixing regime, as shown in M_Y and $M_{\nabla Y}$. This can be understood by noting that an increase in M_c changes the amplification rates of the first excited modes. A further increase in M_c results in a decrease in the efficiency of mixing, as shown for 0.9 and especially notable for 1.2. This trend is a well known effect of compressibility. These results are consistent with those obtained by Lele [1989] and Sandham and Reynolds [1989] who observed the trend for mixing between the gases, whereas here we are seeing it for gases with different molecular weights. Figure 9 shows the

Figure 7: Instantaneous Scalar Dissipation
(A: Euler, B: NS+)

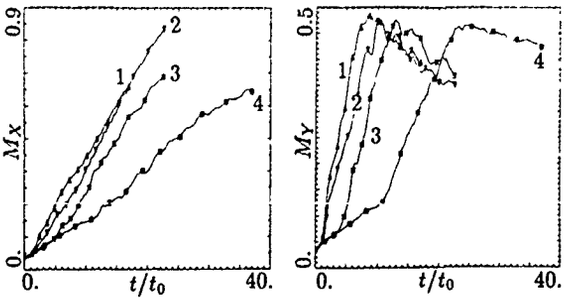

Figure 8: Effect of Convective Mach Number
(M_c = 0.3 (1), 0.6 (2), 0.9 (3), 1.2 (4))

instantaneous pressure and $Y_{H_2}(1 - Y_{H_2})$ for the computation with $M_c = 1.2$. The vortex layer is thin and shocks are evident. At high values of M_c, the structure not only shows the main mode, but also the growth of high-frequency secondary modes, as seen previously by Ragab and Wu [1990].

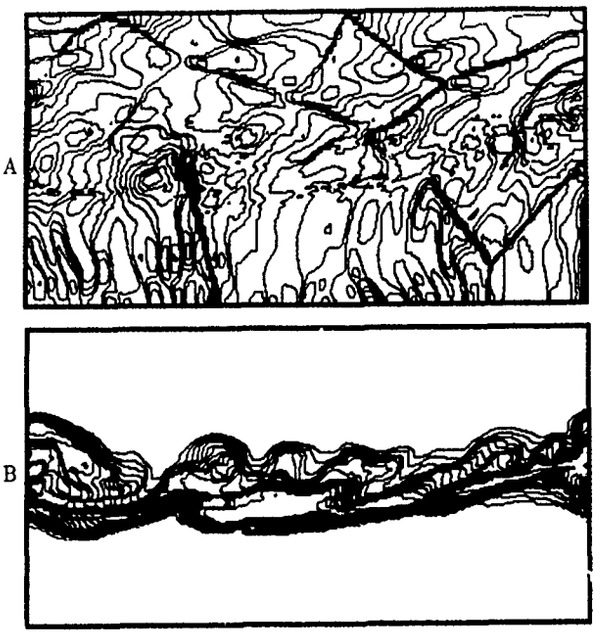

Figure 9: Instantaneous Field for $M_c = 1.2$
(A: Pressure , B: $Y_{H_2}(1 - Y_{H_2})$)

DISCUSSION AND CONCLUSION

In this paper, we examined the evolution to turbulence of a two-dimensional shear layer with molecular hydrogen gas on one side and molecular oxygen gas on the other. These results show that there are three mixing regimes:

1. The initially unstable laminar stage in which the structures grow as a consequence of the initial perturbation,
2. The convective-mixing regime, in which the vortices begin to interact with each other and mixing occurs as these structures merge and grow,
3. The diffusive-mixing regime in which the large structures break down and molecular diffusion dominates.

These regimes correspond to those described by Broadwell and Breidenthal [1982]. Our results show that the initial laminar stage is strongly affected by the diffusion, but the transition to the convective regime appears independent of the viscosity and the diffusion. We note that the Euler simulations are accurate enough to describe the dynamics of the turbulent flow during the convective-mixing regime and to predict the turbulent entrainment. However, the dissipation of the mixing scales during the diffusive-mixing regime requires including the molecular diffusive processes.

Finally, we have performed a series of computations in which the convective Mach number is varied in the range 0.3 to 1.2. These computations show that the onset of the convective-mixing regime is delayed as M_c is increased. It confirms that the mixing as well as the turbulence is reduced when the level compressibility increases.

There are several important as yet unstudied aspects of the types of flows that are described above. One is the effects of chemical reactions and heat release on the flow field. In particular, we plan to study how the relative sizes of the chemical time and the mixing times can affect combustion efficiency. Another important aspect of the flows described is the effect of three dimensionality. We are currently investigating both of these problems.

ACKNOWLEDGMENTS

This work is funded by ONR through the Naval Research Laboratory and SEP (Vernon, France).

REFERENCES

BATCHELOR, G.K., 1969, *Phys. Fluids*, 233.

BROADWELL, J.E., and R.E. BREIDENTHAL, 1982, *J. Fluid Mech.*, 125, 397–410.

BROWN, G.L., and A. ROSHKO 1974, *J. Fluid Mech.*, 64, 775–816.

CLEMENS, N.T., M.G. MUNGAL, T. BERGER, U. VANDSBURGER, 1990, AIAA Paper 90-0500.

COFFEE, T.P., J.M. HEIMERL, 1981, *Combust. Flame*, 43, 273–289.

DAHM, W.J.A., and K.A. BUCH, 1989, *Turbulent Shear Flows*, vol. 7, Springer (New York).

DIMOTAKIS, P.E., 1989, AIAA Paper 89-0262.

JACKSON, T.L., and C.E. GROSCH, 1989, ICASE Report 89-38, NASA LRC, VA.

KOOCHESFAHANI, M.M , and P.E. DIMOTAKIS, 1986, *J. Fluid Mech.*, 170, 83–112.

LELE, S.K., 1989, AIAA Paper 89-0374.

ORAN, E.S., and J.P. BORIS, 1987, *Numerical Simulation of Reactive Flow*, Chapter 13, Elsevier.

PAPAMOSCHOU, D., and A. ROSHKO, 1986, AI per 86-0162.

PATNAIK, G., K.J. LASKEY, K. KAILASANATH, E.S. ORAN, T.A. BRUN, 1989, NRL Memo. 6555, NRL, Washington, DC.

RAGAB, S.A., and J.L. WU, 1990, AIAA Paper 90-0712.

SANDHAM, N.D., and W.C. REYNOLDS, 1989, Stanford University Report TF-45, Stanford, CA.

SOTERIOU, M.C., O.M. KNIO, A.F. GHONIEM, 1991, AIAA Paper 91-0081.

VUILLERMOZ, P., E.S. ORAN, 1991 submitted to *Phys. Fluids A*.

EIGHTH SYMPOSIUM ON
TURBULENT SHEAR FLOWS
Technical University of Munich
September 9-11, 1991

REACTIVE MIXING LAYER BETWEEN PRESSURE REFLECTING BOUNDARIES

J.P. Chollet *) and R.J. Gathmann *) **)

*)Institut de Mécanique de Grenoble
(U.M.R 101: C.N.R.S., Université J.Fourier, Inst. Nat. Polytech. de Grenoble)
B.P. 53 X, 38041 Grenoble Cédex, France
**)SNECMA Villaroche

ABSTRACT

Supersonic mixing layers develop instabilities when they are confined between rigid pressure reflecting boundaries. A direct numerical simulation is performed for two as well as three- dimensional spatial calculations of non stationary reactive gas flows. Cellular detonation is used as a test case and simulations are calculated for flows between rigid flat plates. Chemical reactions are also considered in order to possibly deal with turbulent combustion in high speed aircraft scramjet engines.

INTRODUCTION

Efficiency of future high speed aircraft engines will strongly depend on mixing properties of supersonic reacting flows. The mixing layer is used as a relevant prototype of turbulent flow featuring basic mixing between fuel and oxydant, for instance in scramjet combustion chambers (figure 1). From the mean shear, large coherent eddy structures develop. The most unstable modes tend to create quasi bi dimensional Kelvin-Helmoltz eddies (in (x, y) plane of figure 1). Due to vorticity stretching, turbulence evolves towards full three dimensionality through more or less intricate spatial patterns as it apppears from numerous and extensive experimental and numerical studies of incompressible mixing, see for instance Comte, Lesieur & Lamballais (1991), Comte, Lesieur, Laroche & Normand (1989). Because of eddy merging the layer thickens with dramatic effects on scalar transport and diffusion.

When the two streams which feed the shear layer are made of different species O and F which react one with the other according to $\nu_O O + \nu_F F \rightarrow \nu_P P$, chemistry closely interacts with flow dynamics; ν_i are stochoiometric coefficients. Some of the basic mechanisms can be conveniently studied by assuming a constant ρ density and simple isothermal reaction rates, Chollet (1990), Chollet, Gathmann & Vallcorba (1990). Three dimensionalisation is observed to strongly change global reaction efficiency : high reaction rates concentrate in rather narrow regions along isosurfaces $\Phi = \hat{0}$ as the reaction gets faster (with larger values of Damkhöler number Da), Φ is a conserved scalar. Such constant-ρ approximations are also valuable for practical cases related to comparisons with experiments, atmospheric pollution and reactions in liquid flows, Chollet & Vallcorba (1991).

In order to model turbulent combustion, compressibility needs to be fully taken into account because of close interactions between dynamics, thermodynamics and chemistry. Owing to compressibility, new features can develop : *(i)* density ρ variations induced by heat which is realeased by chemical reactions; because of space scattering and time fluctuations of these heat sources, characteristic length scales associated to these ρ variations extend on a wide range. *(ii)* waves which can propagate at finite values c_i with shocks developing at the edge from supercritical to subcritical regimes.

The regime, either supersonic (supercritical) or subsonic (subcritical) depends on Mach numbers, $M_1 = \frac{u_1}{c_1}$ and $M_2 = \frac{u_2}{c_2}$. Both velocity $u_i(\vec{x}, t)$ in the stream i and sound speed c_i evolve with time and space ; heat realeased from chemical reactions can induce significant variations of $c_i(\vec{x}, t)$. When the layer develops in a boundless medium (figure 1 a) no reference spatial coordinate systems is prescribed and the M_i are not relevant for layer stability analysis. A more significant criterion is based on the relative velocity $u_1 - u_2$, the convective Mach number $M_c = \frac{u_1 - u_2}{c_1 + c_2}$. From instability theories and numerical simulations the Kelvin Hemoltz instability is observed to be damped for $M_c > 0.6$, inhibiting layer thickening, Greenough, Riley, Soestrino, & Eberhardt, (1989), Soestrino, Greenough, Eberhardt & Riley, (1989), Tam & Hu (1989). Flows under current interest are transonic as far as M_c is concerned even with supersonic streams $M_i > 1$. Nevertheless, computation depends on M_i values, at least when calculating spatial evolutions, through boundary conditions: subsonic flow depends on both upstream and downstream conditions, which can make the simulation more difficult to handle.

In most of real problems, from models of scramjets to laboratory experiments, flow regions are bounded by rigid boundaries which induce *(i)* reflexion of waves in a process which is not local in space, since waves can travel along significantly long distances , *(ii)* zero velocity along the plate and therefore the development of a boundary layer, in the close neighbourhood of the boundary. The evolution of the relative thickness δ_b/h of the boundary layer with x is a dominant feature. $\delta_b(x)$ growth is not necessarily monotonous because of the pressure field $p(\vec{x}, t)$ which evolves with time and space, partly because of waves pattern. Therefore layer detachements can occur; if δ_b evolutions are smooth enough, local decrease of δ_b yields inversions of layer curvature.

Full simulation of turbulent flows between rigid plates would need a very fine space grid in the neighbourhood of the boundaries in order to describe sharp gradients for both velocity and thermal fields. Moreover 2D approximations can-

not trace hairpin structures or bursting events which could be dominant features for heat exchange and scalar transport, at least in large Reynolds number flows. Because such full simulationss including the boundary layer are beyond computer capabilities, several levels of modelling are considered here: *(i)* 2D simulations with detailed calculations of the boundary layer, that is with no-slip condition on $\vec{u}$ field, *(ii)* 2D and 3D simulations of flows with free-slip (for $\vec{u}$) pressure reflecting boundaries. The latter case seems to be a rather drastic assumption, since it fails to model strong gradients regions. Nevertheless, by reflecting pressure the effect of walls can be made sensitive even in flow region far from boundaries.

Waves interact with mixing regions which are known to evolve with time through various turbulence interactions including merging of eddy structures. Also calculations must be simulations resolving explicitely the non stationarity of phenomena.

In turbulent combustion, dynamics interact with thermodynamics and chemistry; nevertheless characteristic scales of phenomena differ. Chemistry operates at very small scales $\mathcal{L}_c$, the order of molecule size, which is much smaller than any scale explicitely taken into consideration by fluid dynamicists. Thermodynamics of gas has characteristic length scales $\mathcal{L}_T$ the order of mean free path of molecules. $\mathcal{L}_c$, $\mathcal{L}_T$ are much smaller than Kolmogorov scales η; then for fluid dynamicists, chemistry and thermodynamics can be viewed as local in space and then modeled by algebric equations.

. for thermodynamics, the ideal gas equation :

$$\frac{p(\vec{x},t)}{\rho(\vec{x},t)} = \frac{RT(\vec{x},t)}{M(\vec{x},t)} \tag{1}$$

where p and T are pressure and temperature respectively; ρ and M are the density and the molar weight of the gazeous mixture. R is the universal gas constant.

. the chemical reaction rate is computed according to Arrhenius law :

$$\dot{w} = BT^{\alpha}\exp(-\frac{E_A}{RT})\frac{\rho^{(\nu_O+\nu_F)}}{M_O^{\nu_O}M_F^{\nu_F}}Y_O^{\nu_O}Y_F^{\nu_F} \tag{2}$$

B, α and the activation energy E_A are specific to the chemistry under consideration. Fluid composition is handled through mass fractions Y_i of species i. Characteristic properties of the gazeous mixture evolve in time and space; any f, for instance c_v, c_p, ..., is calculated as :

$$f(\vec{x},t) = \sum_{i=1}^{n} f_i Y_i(\vec{x},t) \tag{3}$$

SIMULATION OF REACTING GAS FLOWS

Equations

Together with equations (1) and (2), usual gas dynamics equations are written for continuity, momentum and enery, under a conservative form. The vector $\mathbf{U}$ of unknown functions :

$$\mathbf{U}(\vec{x},t) = (\rho,\ \rho u_x,\ \rho u_y,\ \rho u_z,\ \rho E,\ \rho Y_i,\ \rho Y_{i+1}, ...) \tag{4}$$

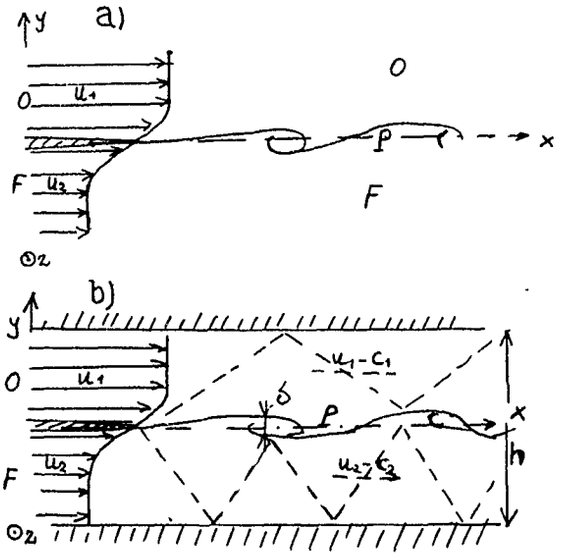

Figure 1: High speed mixing layer with reactive species: a) in an infinite medium, versus b) between rigid reflecting boundaries

with total energy : $E = \frac{1}{2}(u^2+v^2+w^2)+\frac{\varepsilon_p}{M}$ evolves according to :

$$\frac{\partial \mathbf{U}}{\partial t} + \frac{\partial \mathbf{F(U)}}{\partial x} + \frac{\partial \mathbf{G(U)}}{\partial y} + \frac{\partial \mathbf{H(U)}}{\partial z} = \mathbf{D} + \mathbf{S} \tag{5}$$

with

$$\mathbf{F(U)} = (\rho u_x,\ \rho u_x^2 + p,\ \rho u_x u_y,\ \rho u_x u_z,\ (\rho E + p)u_x,\ \rho Y_i u_x,\ \rho Y_{i+1} u_x,\ ...) \tag{6}$$

and similar expressions for $\mathbf{G}$ and $\mathbf{H}$; as soon as chemical reactions which can build up strong ∇T or ∇Y_i are considered, $\mathbf{D}$ diffusive terms need to be accurately taken into consideration. $\mathbf{S}$ are computed from (2). Formulation is detailed by Gathmann (1991).

Computation domain, initial and boundary conditions

Flows under consideration here must be simulated with spatial evolutions along streamwise x direction because : *(i)* the inaccuracies induced by temporal approximations are enhanced by chemistry, *(ii)* the evolution of the relative thickness $\delta(x)/h$ needs to be computed accurately, *(iii)* realistic upstream- downstream boundaries can be specified.

Periodic streamwise boundary conditions which are used in the so called temporal approximation can be partly misleading even if they allow to use unstability theories to predict layer growth, Soestrino *et al* (1989). In such conditions, layer thickening is misrepresented, leading to a poor prediction of entrainment rates, which induces errors in scalar Y_i

transport estimations and then in the calculation of global reaction rates. This effect seems to be emphasized by reactions which develop in braid regions generating high rates $\dot{w}$ values at the border of the layer, contrary to the low values of vorticity or product concentration Y_P. Because of boundaries in y direction, accurate prediction of spatial evolution of $\delta(x)/h$ is needed. For free slip conditions wave evolving patterns strongly depend on $\delta(x)/h$. With no-slip conditions, the evolution is even more space dependent with the evolutions of $\delta(x)/h$ and $\delta_b(x)/h$. Spatial calculations can be run with various boundary conditions and then get closer to industrial configurations. Of course, such spatial calculations require many computational nodes and consume large computer memory and CPU time.

Numerical schemes

The numerical method was developed in order to be accurate for : *(i)* advection and wave propagating terms, *(ii)* diffusion terms *(iii)* strong gradients handling. Moreover, the numerical diffusion must be weak enough in order to let instabilities and then turbulence develop. The numerical scheme is splitted into basic operators so that solutions at time $n+2$ are computed from solutions at time n through :

$$\mathbf{U}^{(n+2)} = \Psi^{\frac{1}{2}} \mathcal{L} \Psi \mathcal{L}^{-1} \Psi^{\frac{1}{2}} \mathbf{U}^{(n)} \qquad (5)$$

$\mathcal{L}$ stands for the hyperbolic operator which is, itself, splitted into $\mathcal{L} = L_x L_y L_z$ ($\mathcal{L}^{-1} = L_z L_y L_x$) with basic operators L_i for each spatial direction i. L_i is built with a Riemann solver, a PPM (parabolic piecewise method) interpolation Collela & Woodward (1984), a ρ discontinuity detection and treatment. Ψ deals with both diffusive terms (molecular viscosity ν and species diffusivities D_i) and chemical sources and is discretized through a finite volume formulation, time stepping is either explicit or semi-implicit depending on the values of characteristic chemical times. In order to save computing effort, the time step $\Delta t(t)$ is varied during the flow evolution and chosen as the highest value allowed by characteristic times built on advection, wave propagation, chemistry. These times evolve with $(\vec{x}, t)$, for instance both wave speed $c(\vec{x}, t)$ and chemistry depend on temperature $T(\vec{x}, t)$ evolutions. Details about the simulation code are given by Gathmann (1991)

DIRECT NUMERICAL SIMULATIONS

Detonation as a test case for the numerical simulation

The numerical code has been used for various flow configurations with or without chemical reactions, in subsonic or supersonic regimes. The 2D simulation of a cellular detonation, as in Schöffel & Ebert (1989) in a premixed flow is a test case of special interest because of *(i)* a two step reaction, *(ii)* strong thermal effect, *(iii)* strong pressure gradient, *(iv)* pressure reflexion on lateral boundaries.

Lateral boundary conditions are still free slip and reflective for pressure. Upstream fluid is made of premixed species (fresh gas) with a uniform velocity profile. Downstream fluid is made of burnt gas escaping freely from the computation domain. Recurring translations along x direction are carried out in order to keep the front inside the computation domain. The detonation is initiated by a strong pressure gradient, just like in the classical shock tube problem. In order to get realistic phenomena, chemistry is splitted into: *step 1* initiation with high activation temperature T_A, *step 2* strong heat release. On figure 2, a wave pattern is observed to reflect on the walls, generating cellular instabilities with strong pressure spikes emerging from an ever moving front. From a turbulent view-point, this case is of particular interest, since behind the detonation, ρ discontinuity develops along slipstreams Williams (1988), creating shear and then producing eddy structures at distinctive scales as observed on figure 3. Typical distribution of density is shown in figure 4 with discontinuities along the detonation front and slipstreams. As compared to similar studies Schöffel & Ebert (1989), our treatment of the L_i operator brings greater accuracy and the capability of studying turbulence in the shear regions behind the detonation front. Of course, such *snapshots* hardly suggest the strong unsteady characters of both detonation front and velocity shear, which are correctly represented by the simulation

Mixing layer between rigid boundaries

2D simulations have been performed for supersonic mixing layers with varying boundary conditions and sound speed c_i at flow inlet. The inflow velocity profile is based upon a mean *tanhy* profile with a white noise added in the shear region. The downstream condition is designed to act as free outflow.

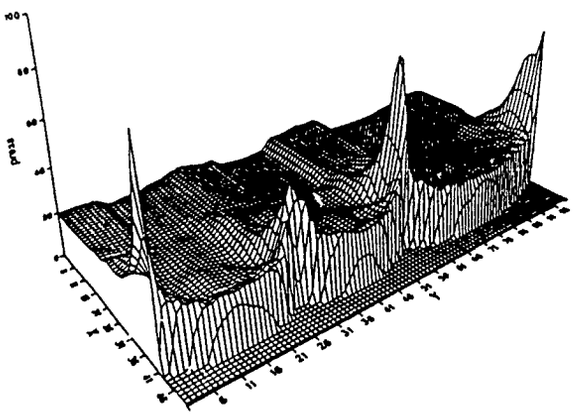

Figure 2: Pressure peaks evolving in a detonation which occurs between two rigid plane boundaries, from a two dimensional numerical simulation with a two step chemical reaction.

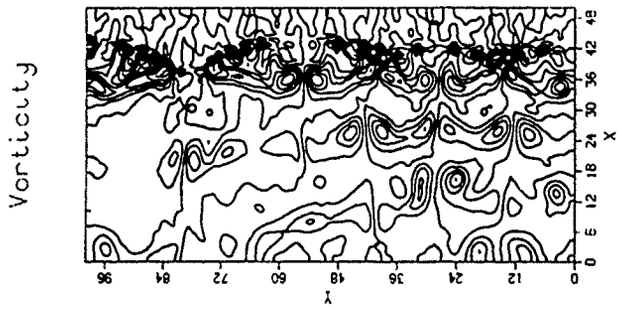

Figure 3: Vorticity $\omega(\vec{x}, t_1)$ field behind the detonation front from a two dimensional simulation.

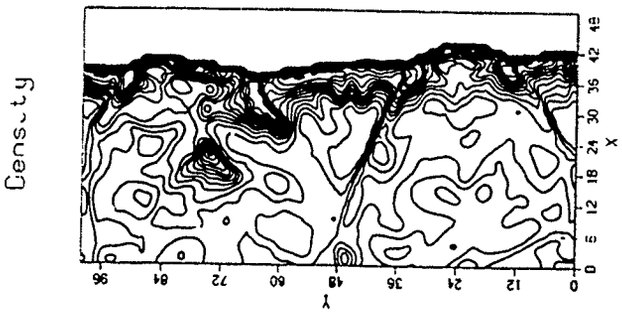

Figure 4: Density $\rho(\vec{x}, t_1)$ field behind the detonation front from a two dimensional simulation.

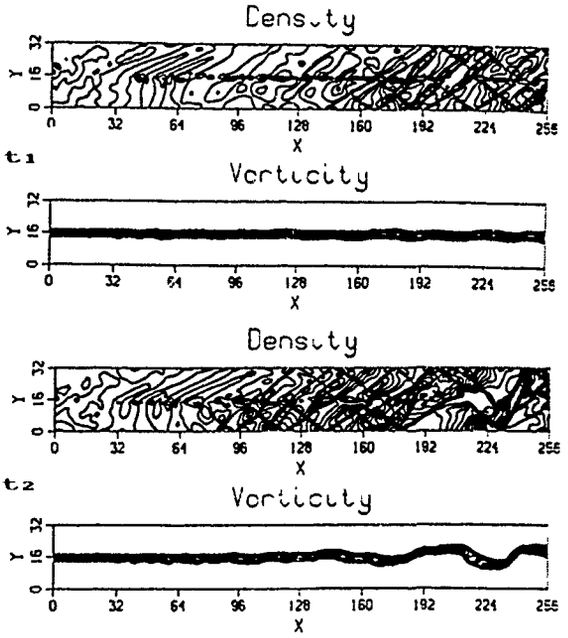

Figure 5: Supersonic mixing layer between rigid plane boundaries $c_1 = 1/6$, $c_2 = 1/6$ and convective Mach number $M_c = 3$; two dimensional direct simulation. Density ρ and vorticity ω at times t_1 and t_2.

Results of computations with convective Mach number much greater than the critical value considered in free mixing layer (≈ 0.6) are given in figures 5 and 6 for a free slip, pressure reflecting wall boundary. In figure 5, sound speed c_i has the same value on both sides which explains the global symmetry of fields These fields evolve continuously with time and these pictures correspond to times $t_1 = 600\frac{\delta_\omega}{u_1}$ and $t_2 = 800\frac{\delta_\omega}{u_1}$. Waves with reflexions on the upper and lower plates develop relatively regular patterns on the density field, rather symmetrically when $c_1 = c_2$ (figure 5). For $c_1 \neq c_2$ (figure 6), wave patterns are observed to develop almost exclusively in the higher c_i stream. Vorticity fields exhibit evidence of developing instabilities, especially in figure 6, enhancing all mixing processes. An extensive comparison with Papamoschou (1989) experiments and simulations with no slip conditions along the walls is given in Gathmann(1991) and Gathamnn & Chollet (1991). Convective speed of eddy structures is observed to be close to the higher speed in any configuration, including both supersonic streams (as in figure 6). The assymetryc development of the mixing layer appears to be enhanced by the boundary layer growth which is more significant in the high speed side than in the low speed side.

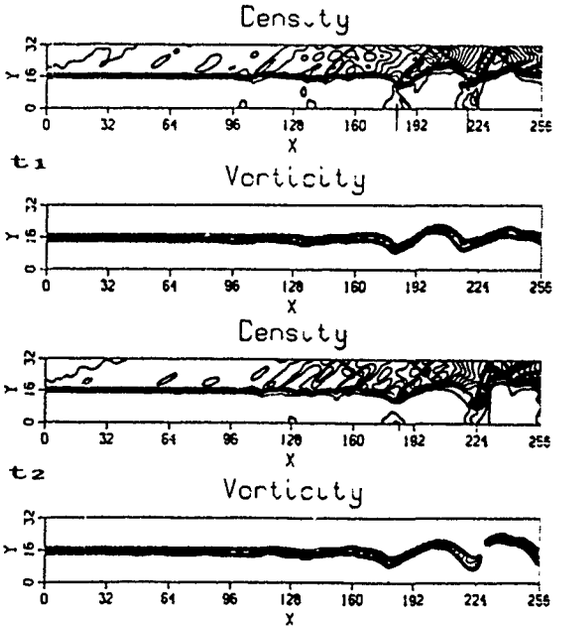

Figure 6: Supersonic mixing layer between rigid plane boundaries $c_1 = 1/3$, $c_2 = 1/6$ and convective Mach number $M_c = 2$; two dimensional direct simulation. Density ρ and vorticity ω at times t_1 and t_2.

Three dimensional simulations of mixing layers

2D assumptions are restrictive as : *(i)* impairing vorticity stretching (source term for $\vec{\omega}$ is zero), *(ii)* limiting wave propagation to $x - y$ plane then forbidding oblique modes which are likely to develop in the mixing layer configuration. The numerical code in 2D configurations can be used,

unchanged, in full three dimensional calculations. Preliminary results are given in figure 7 with a space resolution $128 \times 32 \times 32$. Same upstream conditions are given as in the 2D calculations, a *tanh* mean velocity profile with white noise superimposed, free outflow is specified at the downstream boundary. Periodicity is assumed in the spanwise direction, the walls prescribe free-slip but presure reflective conditions. Differences between the two cross sections of figure 7 suggest three dimensional effects. Just like in previous results, wave patterns seem to develop, thanks to the walls; oblique modes could possibly develop

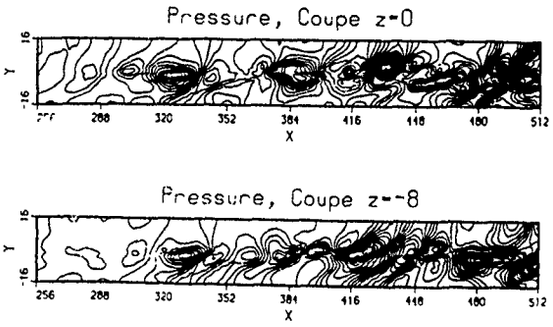

Figure 7: Three dimensional simulation of mixing layer between rigid planes, two cross sections of pressure field $p(\vec{x}, t_i)$

CONCLUSIONS

Distinctive features of the present work are : *(i)* the computation of spatial evolutions, closer to real shear flows than temporal approximations which fail to predict accurate layer thickening rates, *(ii)* an explicit account of viscous and diffusive terms whose importance can be enhanced by reactive processes, *(iii)* a scheme which is at least second order accurate even in steep gradients regions, *(iv)* a natural build up of unstable modes with inlet flow only triggered by a random noise *(v)* three dimensional as well as two dimensional simulations

The demonstrative case of the two dimensional detonation has been used to check the behaviour of the code, especially : *(i)* the accuracy of the treatment of density discontinuities and shocks as well as smoother evolutions, *(ii)* the possible generation of flow structure from the combination of a two step chemical reactions and compressibility effects, *(iii)* the generation of strong (turbulent) vorticity regions behind schoks and along slipstream surfaces *(iv)* the effect of pressure reflecting boundaries

When confined between rigid plates the evolution of high speed mixing layers strongly depends on wave reflexion on boundaries even when the wall layer is not explicitely taken into account. When sound speeds c_i depart one from the other, unsymmetric pattern favours mixing processes. Three dimensional simulations are currently in progress since the growth of oblique modes could significantly change typical flow patterns. Other shear flow configurations have been simulated with the same numerical code, especially under expanded jets, Gathmann & Chollet (1991). These jets must be computed with three dimensional codes, axisymmetric ones could not reproduce the development of azimutal instabilities. The under expanded jet is characterized by very strong pressure gradients, like on both sides of the detonation fronts or of the schock waves in the mixing layer which develops between walls. A 5 step chemical reaction with the explicit computation of mass fractions of 7 species is currently under implementation into this jet simulation in order to study NO_x evolutions behind aircraft engines outlets. Similar reduced chemical schemes for fuel-air combustion will be introduced in the mixing layer calculation in ordre to contribute to scramjet engine design.

Acknowledgements

Part of this work was supported by C.N.R.S. through G.D.R. Mécanique des Fluides Numériques and G.D.R. Hypersonique.

REFERENCES

CHOLLET, 1990, Direct numerical simulations of reactive shear flows and particles, *2nd Summer School ERCOFTAC*, Oxford.

CHOLLET, J.P., GATHMANN, R.J., VALLCORBA, M.R., 1990, Reactive mixing layers and turbulent combustion, Advances in Turbulence 3, European Turbulence Conference, Stockholm, july 3-6, 1990, Springer Verlag.

CHOLLET, J.P., VALLCORBA, M.R., 1991, Direct numerical simulations of 2-D and 3-D turbulent reactive mixing layers, Int., ERCOFTAC Work. on chem.reactions and Phys.properties in Turb.liquids, Lausanne

CHOLLET, J.P., VALLCORBA, M.R., GATHMANN, R., 1990, Direct numerical simulations of turbulent combustion in mixing layers, *Turbulence and Coherent Structures*, ed. M. Lesieur and O. Métais, Kluwer Acad.pub.

COLELLA, P., WOODWARD, P.R., 1984, The piecewise parabolic method (PPM) for gas-dynamical simulations, *J. Comp. Phys.*, **54**, 174-201.

COMTE, P., LESIEUR, M., LAMBALLAIS, E., 1991, Direct numerical simulations of natural and controlled transition of three-dimensional mixing layers, workshop Large scale structures in non linear physics, Villefranche, to be published in lect. notes in Phys., Springer- Verlag.

COMTE, P., LESIEUR, M., LAROCHE, H., NORMAND, X. , 1989, Numerical simulations of turbulent plane shear layers, *Turbulence Shear Flows 6*, Springer-Verlag, 360-380.

GATHMANN, R.J., 1991, Analysis of the effect of sidewalls and concomitant boundary layers on supersonic 2-D shear-layer instability, 1st European Symposium on Aerothermodynamics for Space Vehicles, ESTEC /ESA, Noordwijk, the Netherlands, 28-30 mai,

GATHMANN, R.J., CHOLLET, J.P., 1991, Instabilities in supersonic shear flow applied to aerodynamics and propulsion systems : numerical simulations, 4th symposium on comp. fluid dynamics, Davis, California, 8-12 sept

GATHMANN, R.J., HEBEKER, F.K., 1989, Modelling a one-dimensional convection-diffusion problem with an Arrhenius source term, *IBM TR* 89.11.019, IBM Germany, Heidelberg Scientific Center,

GREENOUGH, J., RILEY, J.J., SOESTRINO, M., EBERHARDT, D., 1989, The effects of walls on a compressible mixing layer, *AIAA 89-0372 27th aerospace sc. meeting*, Reno.

NORMAND, X., LESIEUR, M, 1991, Numerical experiments on transition in the compressible boundary layer over an insulated flat plate, Theor. and Comput. Fluid Dyn., under press.

PAPAMOSCHOU, D., 1989, Structure of the compressible turbulent shear layer, 27th Aerospace Sc. Meeting, Reno, AIAA-89-0126.

PICART, A., BORGHI, R., CHOLLET, J.P., 1988, Numerical simulation of turbulent reactif flows : new results and discussion, 6th Symposium on Turbulent Shear Flows, Toulouse, sept 7-9.

SCHÖFFEL, S.U., EBERT,F., 1989, Numerical analyses concerning the spatial dynamics of an initial gazeous ZDN detonation, *Dynamics of Explosions*, ed. by Kuhl, Bowen, Leyer, **114**, Progresss in astronautics and aeronautics AIAA.

SOESTRINO, M., GREENOUGH, JA., EBERHARDT, D.S., RILEY, J.J, 1989, Confined compressible mixing layers: part 1. three dimensional instabilities, *AIAA-89-1810*, AIAA 20 th Fluid Dyn., Plasma Dyn. and Lasers Conf., New York.

TAM,C.K.W., HU, F.Q., 1989, The instability and acoustic wave modes of supersonic mixing layers inside a rectangular channel, *J.Fluid Mech*, **203**, 51-76

WILLIAMS, F.A., 1988, Combustion theory, *Addison-Wesley Pub. Company*

EIGHTH SYMPOSIUM ON
TURBULENT SHEAR FLOWS
Technical University of Munich
September 9-11, 1991

MOMENTUM, HEAT, AND MASS TRANSFER IN TURBULENT PIPE FLOW DESCRIBED BY THE ERSR MODEL

Edward E. Musschenga, Peter J. Hamersma, and Jan M.H. Fortuin,
University of Amsterdam, Department of Chemical Engineering,
Nieuwe Achtergracht 166, 1018 WV Amsterdam,
The Netherlands.

ABSTRACT

A model is presented for a *quantitative* prediction of the transfer processes in a turbulent pipe flow. In this so-called Extended Random Surface Renewal (ERSR) model the tube wall is assumed to be covered by a mosaic of fluid elements of *random age* and *laminar flow* with unsteady profiles of velocity, temperature, or concentration. The distribution and the mean value of the ages of the fluid elements at the tube wall, calculated from f and Re with the ERSR model agree quantitatively with the experimental results obtained from velocity signals measured with a LDA in turbulent pipe flow at $5{\cdot}10^3 < Re < 43{\cdot}10^3$.

The equations derived for the time-averaged axial *velocity* profile in the wall region, and those for calculating *heat* and *mass* transfer coefficients, agree with correlations presented in literature. The analogy between the transfer processes is elucidated by introducing a momentum-transfer coefficient.

NOMENCLATURE

a	thermal diffusivity ($a = \lambda/\rho c_p$), m^2 s^{-1}
a	averaging time in Eq.(54), s
C	Constant defined in Eq.(29), 1
d	tube diameter, m
D	diffusivity, m^2 s^{-1}
f	Fanning friction factor, 1
$J(t)$	instantaneous local flux at the tube wall
$\bar{J}(\theta)$	local flux averaged over a time θ
$\bar{J}$	time-averaged local flux
k	mass-transfer coefficient, m s^{-1}
k_m	momentum-transfer coefficient, m s^{-1}
k_0	fixed value of k in Eq.(54), 1
n_0	characteristic burst frequency, Hz
N	number of time intervals measured beween $(\theta - \frac{1}{2}\Delta\theta)$ and $(\theta + \frac{1}{2}\Delta\theta)$, 1
N_0	total number of time intervals measured, 1
$q_w(t)$	inst. local heat flux at the tube wall, W m^{-2}
$\bar{q}_w$	time-averaged local heat flux, W m^{-2}
t	time, s
t_0	characteristic or mean age, s
T	temperature, K
u	instantaneous local axial velocity, m s^{-1}
$\bar{u}$	time-averaged local axial velocity, m s^{-1}
u_b	fluid velocity in the bulk, m s^{-1}
$\langle u \rangle$	place and time-averaged fluid velocity, m s^{-1}
u^*	friction velocity ($u^* = \sqrt{(\bar{\tau}_w/\rho)}$), m s^{-1}
y	distance from the tube wall, m
y^+	dimensionless distance from the wall ($y^+ = yu^*/\nu$), 1
z	dimensionless variable ($z = y/(2\sqrt{(\nu t)})$), 1

Greek Symbols

α	heat transfer coefficient, W m^{-2} K^{-1}
Γ	gamma function ($\Gamma(4/3) \approx 0.893$), 1
Δc	concentration difference, e.g. mol m^{-3}
ΔT	temperature difference, K
$\Delta(\rho u)$	momentum difference per unit of volume, kg m^{-2} s^{-1}
$\Delta\theta$	small part of the time interval θ, s
θ	age or time interval between successive bursts, s
$\bar{\theta}$	mean age or mean value of θ, s
$\bar{\theta}_{exp}$	measured value of $\bar{\theta}$, s
θ^+	dimensionless mean age ($\theta^+ = u^*/(\bar{\theta}_{exp}/\nu)$), 1
λ	thermal conductivity, W m^{-1} K^{-1}
ν	kinematic viscosity ($\nu = \eta/\rho$), m^2 s^{-1}
$\tau_w(t)$	instantaneous shear stress locally exerted on the wall by a laminar flowing fluid element, Pa
$\bar{\tau}_w$	time-averaged local wall-shear stress, Pa
$\varphi(\theta)$	age distribution, s^{-1}

Dimensionless numbers

Fa	Fanning number	($Fa = k_m d/\nu$), 1
Fo	Fourier number	($Fo = \nu t_0/d^2$), 1
Nu	Nusselt number	($Nu = \alpha d/\lambda$), 1
Pr	Prandtl number	($Pr = \nu/a$), 1
Re	Reynolds number	($Re = \rho\langle u\rangle d/\eta$), 1
Sc	Schmidt number	($Sc = \nu/D$), 1
Sh	Sherwood number	($Sh = kd/D$), 1

1. INTRODUCTION

Accurate prediction of the exchange of momentum, heat, and mass between a turbulent fluid flow and an interface is often required for equipment design in industry.

In turbulent bounded shear flows the major part of the resistance to the exchange of heat or mass between the bulk of the fluid and the interface is often confined to the so-called 'viscous sublayer'. The classical theories consider the sublayer motion as a steady mean flow upon which small turbulent fluctuations are imposed. However, hydrodynamic studies of many investigators such as Kline *et al.* (1967), and Corino and Brodkey (1969) indicate the existence of motions of well-ordered *fluid elements*, suggesting that the wall region in a turbulent fluid flow consists of a mosaic of *laminar flowing* fluid elements which are *renewed randomly*.

In 1935 Higbie pointed out that industrial contactors often operate with repeated brief contacts between phases in which the contact times are to short for the steady state to be achieved. Higbie advanced a theory that in e.g. a *packed tower* used for gas absorbtion, the liquid flows across each packing piece in laminar flow and is remixed at the positions of discontinuity between the packing elements. At such a position a fresh liquid surface is formed which, as it moves along the packing element, absorbs gas at a decreasing rate until it is mixed at the next discontinuity. If the flow of the liquid near the *gas-liquid* interface is assumed to be plug flow, the mass transfer can be calculated as a semi-infinite diffusion of mass into a stagnant liquid during its residence time on a packing element. In this case Higbie assumed that all liquid elements have equal contact times or *equal ages*.

In *turbulent* flowing liquids Danckwerts (1951) introduced the *random* surface-renewal concept to describe the mechanism of *gas absorption*, where mass transfer occurs from the gas-liquid interface to the bulk of the liquid. The basis of this random surface-renewal concept is that liquid elements at the *gas-liquid* interface are exchanged randomly in time with elements from the bulk of the turbulent liquid. For the relatively short ages of these liquid elements at the gas-liquid interface, the elements are assumed to be *stagnant* or *plug flowing*, and the transfer of mass is calculated using the penetration theory.

The surface-renewal concept has been applied to *turbulent shear flows* by other authors, such as Hanratty (1956), Einstein and Li (1956), Pinczewski and Sideman (1974), Thomas (1980), and Loughlin *et al.* (1985). A survey of surface renewal models was published by Sideman and Pinczewski (1975).

In *turbulent pipe flow* each fluid element at the tube wall is shear bounded, which results in a *laminar* flow in the fluid elements with a time-dependent velocity gradient at the interface. If this velocity gradient is not taken into account and the fluid elements are assumed to be stagnant, or plug flowing, the surface-renewal theory applied to turbulent pipe flow, predicts that Sh or Nu is proportional to the square root of Sc or Pr.

However, it is found experimentally that Sh or Nu is proportional to the 1/3 power of Sc or Pr for values of $Sc > 1$ or $Pr > 1$. Therefore, a suitable model for the description of the transfer processes in turbulent pipe flow for values of $Sc > 1$ or $Pr > 1$, can only be obtained if at least both a *random age* and a *laminar flow with a time-dependent velocity gradient* are ascribed to the fluid elements at the tube wall.

Fortuin and Klijn (1982) were the first who developed a RSR model for turbulent pipe flow to describe *momentum* transfer from fluid elements of *random age* and *laminar flow with a time-dependent velocity gradient* to the tube wall. This approach resulted in a relationship between the mean age t_0 of the fluid elements at the tube wall, the friction factor f, and the Reynolds number Re. The random distribution of the ages of the fluid elements at the tube wall has already been derived from velocity signals measured with a laser-Doppler anemometer (LDA) by Van Maanen and Fortuin (1982, 1983). A quantitative agreement between measured and calculated values of t_0 has been obtained by Musschenga *et al.* (1990).

In the present study the RSR model of Fortuin and Klijn is extended to describe heat and mass transfer in turbulent pipe flow. The resulting 'Extended Random Surface Renewal' (ERSR) model is described in the present paper, and will be used:

- to derive the relationship between f, Re, and t_0; this relationship is verified experimentally using a LDA;
- to calculate the mean axial velocity profile in the wall region;
- to derive equations for a quantitative prediction of heat and mass transfer coefficients;
- to elucidate the analogy between momentum, heat, and mass transfer in turbulent pipe flow.

2 THE ERSR MODEL

Modelling of transfer phenomena in turbulent pipe flow should preferably be based on the *observed behaviour* of the fluid in the wall region. Hydrodynamic studies have shown that a fluid in turbulent motion may be considered as a mass of fluid elements of indefinite shape and size, which continually change their conformation and position. The fluid elements intermittently move from the bulk of the turbulent fluid towards the interface where they replace other fluid elements. The phenomenon of the inrush and ejection of a fluid element is called a 'burst'. The fluid elements are assumed to maintain their identity during their residence time at the tube wall while momentum and heat or mass are exchanged simultaneously between the fluid elements and the interface. The time interval between two successive bursts, which is much greater than the short time required for the renewal process, is considered as the age of a fluid element at the tube wall.

For the mathematical formulation of the transfer mechanisms it is unimportant whether the renewal of the fluid elements at the interface is caused by the inrushing high-momentum fluid elements or, as suggested by Einstein and Li (1956), by the spontaneous breakdown of the viscous sublayer due to instabilities.

In the ERSR model it is assumed that during turbulent pipe flow the exchange of momentum, heat, and mass between the tube wall and the bulk of the fluid is governed by the velocity profiles in the fluid elements, and the age (distribution) of the fluid elements at the interface.

2.1 *Velocity profiles in fluid elements*

In the fluid elements at the tube wall plug flow may be assumed in e.g. the description of heat transfer, if the penetration depth of heat is larger than the penetration depth of momentum ($Pr < 1$). However, if the penetration depth of heat is small compared with the penetration depth of momentum ($Pr > 1$), laminar flow has to be assumed with a velocity gradient at the interface.

2.2 *Renewal of fluid elements*

If it is assumed that the chance of renewal of each fluid element at a fixed position at the tube wall is the same, irrespective of its age or position at the tube wall, it can be shown (Danckwerts, 1951; Fortuin and Klijn, 1982) that the chance $\varphi(\theta)d\theta$ to find a fluid element with an age between θ and $\theta + d\theta$ can be obtained from:

$$\varphi(\theta)d\theta = (1/t_0)e^{-\theta/t_0}\,d\theta \qquad (1)$$

In Eq. (1) t_0 represents a characteristic value of the age of the fluid elements at the tube wall; this value is dependent on the flow conditions. The mean age of the fluid elements at the interface follows from:

$$\bar{\theta} = \int_0^\infty \theta\, e^{-\theta/t_0}\, d(\theta/t_0) = t_0 \qquad (2)$$

The reciprocal value of the mean age t_0 is defined as the characteristic burst frequency n_c.

2.3 *Mean flux at random surface renewal*

If $J(t)$ represents an instantaneous local momentum, heat, or mass flux in a fluid element at the interface of a turbulent flowing fluid, the value averaged during its residence time at the interface follows from:

$$\bar{J}(\theta) = (1/\theta)\int_0^\theta J(t)dt \qquad (3)$$

If the fluid elements at that position at the tube wall are renewed randomly in time, the local flux, averaged over all possible ages of the fluid elements ($0 < \theta < \infty$), follows from:

$$\bar{J} = \frac{\int_0^\infty \theta \left\{ (1/\theta)\int_0^\theta J(t)dt \right\} e^{-\theta/t_0}\, d(\theta/t_0)}{\int_0^\infty \theta\, e^{-\theta/t_0}\, d(\theta/t_0)} \qquad (4)$$

Rearrangement of Eq. (4) results in:

$$\bar{J} = (1/t_0)\int_{\theta=\infty}^{\theta=0} \left\{ \int_0^\theta J(t)dt \right\} d(e^{-\theta/t_0}) \qquad (5)$$

Partial integration of Eq. (5) leads to:

$$\bar{J} = (1/t_0)\int_0^\infty e^{-\theta/t_0}\, J(\theta)d\theta \qquad (6)$$

The result of this integral is not changed if θ is replaced by t, so that:

$$\bar{J} = (1/t_0)\int_0^\infty J(t)\, e^{-t/t_0}\, dt \qquad (7)$$

3. MOMENTUM TRANSFER

It may be assumed that at a constant Reynolds number in a fully developed turbulent fluid flow through a straight, smooth tube, the time-averaged local shear stress $\bar{\tau}_w$ at an arbitrary fixed position at the tube wall is equal to that at each other position at the wall. In the ERSR model the momentum transfer to the tube wall is approximated by that in a turbulent fluid flow along a flat wall. This approximation is only valid if the curvature of the tube wall is negligible, which approximately holds for turbulent pipe flow if $Re > 10^4$ (Fortuin and Klijn, 1982).

Upon its arrival at the wall, an inrushing fluid element gradually looses momentum as a result of viscous interaction with the wall. In this fluid element, which originally travelled with a uniform bulk velocity, a velocity profile starts to develop. The development of this velocity profile, and the unsteady transfer rate of momentum to the wall, can be described by the following reduced equation of motion:

$$\partial u/\partial t = \nu\, \partial^2 u/\partial y^2 \qquad (8)$$

This equation, for a fluid with constant density and viscosity, can be solved using the following initial and boundary conditions:

$$\begin{array}{llll} \text{I.C.} & t = 0; & y > 0; & u = u_b, \\ \text{B.C.} & t > 0; & y = 0; & u = 0, \\ \text{B.C.} & t > 0; & y = \infty; & u = u_b. \end{array} \qquad (9)$$

The solution to Eq. (8) under the conditions of Eq. (9) is:

$$u/u_b = \text{erf}(z), \quad \text{where} \quad z = \frac{y}{2\sqrt{(\nu t)}} \qquad (10)$$

Using Eq. (10) the instantaneous shear stress $\tau_w(t)$ locally exerted on the wall by a fluid element is obtained from:

$$\tau_w(t) = \eta\left[\frac{\partial u}{\partial y}\right]_{y=0} = \nu\rho u_b(\pi\nu t)^{-1/2} \qquad (11)$$

The time-averaged local wall-shear stress $\bar{\tau}_w$ for randomly renewed fluid elements at the tube wall can be derived from Eqs (7) and (11) by substituting $\tau_w(t)$ for $J(t)$:

$$\bar{\tau}_w = \nu\rho u_b(\nu t_0)^{-1/2} \qquad (12)$$

It may be assumed that $u_b \approx \langle u \rangle$ if $Re > 10^4$. Combining Eq. (12) with the definition of the Fanning friction factor:

$$f = \bar{\tau}_w/(\tfrac{1}{2}\rho\langle u\rangle^2) \qquad (13)$$

results in the following equation:

$$f = 2\left[\frac{d}{\sqrt{(\nu t_0)}}\right]\left[\frac{\nu}{\langle u\rangle d}\right] = 2Fo^{-1/2}\,Re^{-1} \qquad (14)$$

Equation (14), first introduced by Fortuin and Klijn (1982), gives the relationship between f, Re, and t_0. Rewriting Eq. (14), and using $t_0 = 1/n_0$ result in:

$$t_0 = (1/n_0) = (\tfrac{1}{2}f\cdot Re)^{-2}\, d^2/\nu \qquad (15)$$

In the present paper Eq. (15) will be verified by results obtained from velocity signals measured with a LDA

4. THE VELOCITY PROFILE IN THE WALL REGION

The time-averaged local axial velocity is obtained in a similar way as it has been done for the time-averaged wall-shear stress. As a consequence the following equation holds:

$$\bar{u} = (1/t_0)\int_0^\infty e^{-t/t_0}\, u(t)dt \qquad (16)$$

Substitution of Eq. (10) and $z_0 = y(4\nu t_0)^{-1/2}$ into Eq. (16), and taking into account that $\bar{u}$ is a function of y only, it can be obtained that.

$$\bar{u}(y)/u_b = 1 - \frac{2}{\sqrt{\pi}}\int_0^\infty e^{-(z^2 + z_0^2/z^2)}\, dz \qquad (17)$$

After substitution of the solution to the definite integral in Eq. (17) and using Eq. (14), the following velocity profile for the wall region in turbulent pipe flow is obtained:

$$\bar{u}(y)/u_b = 1 - e^{-y/\sqrt{(\nu t_0)}} = 1 - \exp\left[-\frac{y}{d}\,\frac{f}{2}\,Re\right] \qquad (18)$$

This equation can be rewriten in the commonly used u^+ versus y^+ notation, resulting in:

$$u^+ = \left[1 - e^{-y^+\sqrt{(f/2)}}\right] / \sqrt{(f/2)} \qquad (19)$$

From Eq. (19) it can be obtained that according to the ERSR model the velocity profile in the wall region is slightly dependent on the Reynolds number. Close to the wall, however, the calculated profiles quantitatively agree with correlations for the semi-empirical 'universal velocity profile'. It may be noted that for the calculation of velocity profiles with Eq. (19) only the value of the friction factor is needed. A correlation giving sufficiently accurate values for f for Newtonian fluid flow through straight, smooth tubes is (Eck, 1973):

$$f = 0.07725\left[\log(Re/7)\right]^{-2} \qquad (2100 < Re < 10^8) \qquad (20)$$

5. HEAT TRANSFER

It may be assumed that at a constant Reynolds number in a fully developed turbulent fluid flow through a straight, smooth tube, the time-averaged local heat flux $\bar{q}_w$ at an arbitrary fixed position at the tube wall is equal to that at each other position at the wall if the temperature difference between the tube wall and the fluid in the turbulent core has the same value.

In the following it will be assumed that the tube wall has locally a constant temperature T_w, and that the bulk of the fluid has locally a constant temperature T_b, where $T_w > T_b$. When a fluid element with a uniform velocity u_b and a temperature T_b comes from the turbulent core and arrives at the wall, both momentum and heat are exchanged by diffusion between the interface and the fluid element. After a certain residence time θ the fluid element is replaced suddenly by a new fluid element from the turbulent core, and again momentum and heat are exchanged by diffusion between the new fluid element and the interface. The heat accumulated in a single fluid element is thus conveyed to the turbulent core during this surface renewal process.

5.1 *Heat transfer into fluid elements with laminar flow (Pr>1)*

The heat flux from the tube wall into a laminar flowing fluid element encounters an approximately linear velocity profile if the penetration depth of heat is small with regard to that of momentum ($Pr > 1$). Upon its arrival at the wall, the fluid element gradually decelerates and the velocity of the laminar flow near the interface becomes smaller. The velocity profile in this fluid element can be obtained from Eq. (10). For small values of z the relative velocity may be approximated by:

$$u/u_b \approx \left[\frac{2z}{\sqrt{\pi}}\right] - \left[\frac{y}{\sqrt{(\pi\nu t)}}\right] \qquad (21)$$

After its arrival at the wall the velocity profile in the fluid element is assumed to be *independent* of the longitudinal coordinate x. As a consequence the *velocity* in the fluid element is only a function of the distance y to the wall and the time t. In this case the heat transfer can be described as a semi-infinite diffusion of heat from the interface into a laminar flowing fluid element with a *velocity gradient* $(\partial u/\partial y)_{y=0}$ which is only time dependent and does not change in the direction of x. However, the *temperature gradient* $(\partial T/\partial y)_{y=0}$ changes in the flow direction. Assuming a quasi-steady state, this heat transfer problem is approximately governed by the following differential equation:

$$u\,\partial T/\partial x = a\,\partial^2 T/\partial y^2 \qquad (22)$$

provided that heat conduction of the fluid in the flow direction is small compared with the forced convective transport in this direction, so that liquid metals are excluded. Further it is assumed that:

$$\partial T/\partial x = (\partial T/\partial t)/(\partial x/\partial t) \approx (1/u_b)\,\partial T/\partial t \qquad (23)$$

Combination of Eqs (22) and (23) results in:

$$(u/u_b)\,\partial T/\partial t = a\,\partial^2 T/\partial y^2 \qquad (24)$$

The initial and boundary conditions are:

$$\begin{array}{lllll} \text{I.C.} & t = 0; & y > 0; & T = T_b, \\ \text{B.C.} & t > 0; & y = 0; & T = T_w, \\ \text{B.C.} & t > 0; & y = \infty; & T = T_b. \end{array} \qquad (25)$$

After substitution of Eq. (21) and $\nu/a = Pr$ into Eq. (24), it can be shown that the solution to Eq. (24) under the conditions of Eq. (25) is:

$$(T_w - T)/(T_w - T_b) = \frac{1}{\Gamma(4/3)}\int_0^\xi e^{-\xi^3}\, d\xi \qquad (26)$$

where:

$$\xi = \left[\frac{4Pr}{3\sqrt{\pi}}\right]^{1/3}\cdot\left[\frac{y}{2\sqrt{(\nu t)}}\right] \qquad (27)$$

The instantaneous local heat flux $q_w(t)$ from the interface into a laminar flowing fluid element is:

$$q_w(t) = -\lambda\left[\frac{\partial T}{\partial y}\right]_{y=0} = C\lambda(T_w - T_b)(\pi\nu t)^{-1/2}\, Pr^{1/3} \qquad (28)$$

where:

$$C = \frac{(\pi/6)^{1/3}}{\Gamma(4/3)} = 0.9026 \qquad (29)$$

The time-averaged local heat flux $\bar{q}_w$, averaged over all possible ages of the fluid elements at the tube wall ($0 < \theta < \infty$), can be obtained from Eqs (7) and (28):

$$\bar{q}_w = C\lambda(T_w - T_b)(\nu t_0)^{-1/2}\, Pr^{1/3} \qquad (30)$$

Defining $\bar{q}_w = \alpha(T_w - T_b)$ and the dimensionless heat-transfer coefficient or Nusselt number, $Nu = \alpha d/\lambda$, Eq. (30) can be rearranged to:

$$Nu = Cd(\nu t_0)^{-1/2}\, Pr^{1/3} \qquad (31)$$

Combining Eqs (14) and (31) results in the following equation for the *Nusselt number*:

$$Nu = C(f/2)Re\, Pr^{1/3} \qquad (Pr > 1) \qquad (32)$$

Using the following correlation given by McAdams (1954) for turbulent pipe flow:

$$f = 0.046\, Re^{-0.2} \qquad (10^4 \leqslant Re \leqslant 2\cdot 10^5) \qquad (33)$$

we obtain from Eqs (29), (32), and (33):

$$Nu = 0.021\, Re^{0.80}\, Pr^{1/3} \qquad (Pr > 1) \qquad (34)$$

Eq. (34) is approximately equal to the following well-known correlation presented by Colburn (1933):

$$Nu = 0.023\, Re^{0.80}\, Pr^{1/3} \qquad (Pr > 1) \qquad (35)$$

5.2 Heat transfer into fluid elements with plug flow ($Pr < 1$)
The heat flux from the tube wall into a fluid element encounters approximately a fluid flowing with the bulk velocity if the penetration depth of heat is large compared with the penetration depth of momentum ($Pr < 1$). The heat transfer may then be approximated by an unsteady diffusion of heat into a plug flow. This heat transfer problem is approximately governed by Eq. (24) in which $u = u_b$, resulting in:

$$\partial T/\partial t = a\, \partial^2 T/\partial y^2 \qquad (36)$$

The solution to Eq (36) under the conditions of Eq. (25) is:

$$(T_w - T)/(T_w - T_b) = \mathrm{erf}\left[\frac{y}{2\sqrt{(at)}}\right] \qquad (37)$$

Combination of Eqs (28) and (37) results in:

$$q_w(t) = \lambda(T_w - T_b)(\pi at)^{-1/2} \qquad (38)$$

The value of $\bar{q}_w$ can be obtained using Eqs (7) and (38):

$$\bar{q}_w = \lambda(T_w - T_b)(at_0)^{-1/2} \qquad (39)$$

Combining Eqs (14) and (39) it may be stated that:

$$Nu = (f/2)Re\, Pr^{1/2} \qquad (Pr < 1) \qquad (40)$$

This result is in agreement with the fact that if $Pr < 1$ measured values of Nu fit better with an equation in which Nu is proportional to $Pr^{1/2}$.

6. MASS TRANSFER

The ERSR model can in a similar way be applied to derive equations for calculating mass-transfer coefficients in turbulent pipe flow. After introducing the dimensionless mass-transfer coefficient or Sherwood number ($Sh = kd/D$) and the Schmidt number ($Sc = \nu/D$) it can be obtained that:

$$Sh = C(f/2)Re\, Sc^{1/3} \qquad (Sc > 1) \qquad (41)$$

$$Sh = (f/2)Re\, Sc^{1/2} \qquad (Sc < 1) \qquad (42)$$

where C is given in Eq. (29).

7. ANALOGY BETWEEN THE TRANSFER PROCESSES

7.1 Introduction
In the foregoing sections it has been shown that the transfer of momentum, heat, and mass in turbulent pipe flow can be described in an analogous way with the ERSR model.
It is well known that the momentum flux to the interface, i.e. the shear stress exerted on the interface, is described by using a relationship between the friction factor and the Reynolds number. The heat and mass fluxes to or from the interface however, are described by using transfer coefficients. This difference in approach is traditional in engineering practice, and probably due to the fact that originally transport phenomena in turbulent flows were studied by engineers of different disciplines.
Colburn (1933), and Chilton and Colburn (1934) introduced correlations based on the analogy between momentum, heat, and mass transfer in turbulent pipe flow. They proposed an *empirical* analogy for $Re > 10^4$ in long smooth pipes, which can be represented by:

$$j_h = Nu/(Re\cdot Pr^{1/3}) = f/2 \qquad (43)$$

where j_h is the '*j-factor*' for heat transfer, and

$$j_d = Sh/(Re\, Sc^{1/3}) = f/2 \qquad (44)$$

where j_d is the '*j-factor*' for mass transfer. In the next section the values of j_h and j_d calculated with the ERSR model will be given. Further, it will be shown that the analogy between the transfer processes in turbulent pipe flow can be elucidated by introducing a *momentum-transfer coefficient* k_m.

7.2 The analogy according to the ERSR model
A momentum-transfer coefficient for turbulent pipe flow can be defined by:

$$\bar{\tau}_w = k_m(\rho u_b - \rho u_w) \qquad (45)$$

where $(\rho u_b - \rho u_w)$ is the axial momentum difference per unit of volume between the bulk of the fluid and the fluid at the pipe wall. As u_w is zero it may be stated that.

$$\bar{\tau}_w = k_m(\rho u_b) \qquad (46)$$

Combining Eqs (12) and (46) gives:

$$k_m = \nu/J(\nu t_0) \qquad (47)$$

Introducing a dimensionless momentum-transfer number, called the Fanning number $Fa = k_m d/\nu$, Eq. (47) results in:

$$Fa = k_m d/\nu = d/J(\nu t_0) \qquad (48)$$

The three dimensionless numbers governing the transfer processes in turbulent pipe flow can also be defined by:

$$Fa = \frac{k_m \Delta(\rho u)}{\nu\Delta(\rho u)/d}, \quad Nu = \frac{\alpha\Delta T}{\lambda\Delta T/d}, \text{ and } Sh = \frac{k\Delta c}{D\Delta c/d} \qquad (49)$$

Eq. (49) shows that each of these dimensionless numbers is equal to the ratio between the total flux of momentum, heat, or mass due to both *molecular diffusion and forced convection* and the flux of momentum, heat, or mass due to *molecular diffusion* only. From Eqs (14), (32), (41), and (48) it is obtained that according to the ERSR model the *transfer equations for turbulent pipe flow* for values of $Pr > 1$ or $Sc > 1$ can be written as:

$$Fa = (f/2)Re \qquad (50)$$

$$Nu = C(f/2)Re\, Pr^{1/3} \qquad (Pr > 1) \qquad (51)$$

$$Sh = C(f/2)Re\, Sc^{1/3} \qquad (Sc > 1) \qquad (52)$$

The *key* to make this set of equations operational for the calculation of transfer coefficients is a correlation between f and Re, see e.g. Eqs (20) or (33).
It is interesting to note that according to the ERSR model the factors j_h and j_d of Chilton and Colburn can be calculated too. From Eqs (43), (44), (51), and (52), it is obtained that for heat and mass transfer in turbulent pipe flow for $Pr > 1$ or $Sc > 1$ the following equations hold (where C is given in Eq. (29)):

$$j_h = C(f/2) \quad \text{and} \quad j_d = C(f/2) \qquad (53)$$

8. SURFACE-RENEWAL MEASUREMENTS USING A LDA

According to the ERSR model, the exchange of momentum, heat, and mass between the tube wall and the core in turbulent pipe flow is governed by the distribution and the mean value of the ages of the fluid elements at the tube wall. The distribution and

the mean value of these ages can be derived from velocity signals measured with a laser-Doppler anemometer during turbulent pipe flow, followed by a discrimination procedure to detect the bursts. The time interval between two successive bursts is considered as the age of a fluid element at the tube wall. The mean value of the *measured* time intervals is indicated as $\bar{\theta}_{exp}$.

8.1 *Experimental set-up*

The set-up consists of a 51 mm inner diameter, smooth copper pipe with a horizontal, straight section of 8.5 m. There is sufficient entry and exit length for the turbulent fluid flow to be fully developed in the test section. The test section, situated 5.5 m beyond the entrance of the straight pipe, consists of a 1.4 m long glass tube with an inner diameter of 51 mm in which the velocity of light-scattering particles in the intersection volume of two coherent laser beams of a laser-Doppler anemometer is used to measure the instantaneous local axial fluid velocity Tap water is applied as measuring liquid.

A laser-Doppler anemometer, operating in the reference beam mode, was used. The laser-Doppler anemometer consists of a Spectra Physics 15 mW He-Ne laser (wavelength 632.8 nm) and quality optics, assembled by the Institute of Applied Physics TNO-TU Delft, The Netherlands. In the optical arrangement used, the angle between the two laser beams was 20.96°, which resulted in a measuring volume with a length of 210 μm and a diameter of 39 μm in air.

8.2 *The burst detection criterion*

The burst-detection criterion of Blackwelder and Kaplan (1976), also called the 'VITA technique' was applied to the velocity signals measured with the LDA. This criterion reacts on the fluctuating component of the axial velocity signal crossing the time-averaged local axial velocity $\bar{u}$ in a relatively short time. This corresponds to sharp accelerations or sharp decelerations. According to this criterion a burst occurs if:

$$\frac{\overline{(u')^2}^{a} - \left[\overline{u'}^{a}\right]^2}{\overline{(u')^2}^{ent}} > k, \quad \text{where} \quad u' = u - \bar{u} \qquad (54)$$

In Eq (54) $\overline{}^{a}$ denotes averaging over a (short) time of a seconds and $\overline{}^{ent}$ means averaging over the *entire* signal; k is a dimensionless constant In the present study an additional condition of positive slope has been added, so that only *accelerations* will be counted as bursts. Application of this criterion requires the specification of two parameters, i.e , the *averaging time a* and the dimensionless *threshold level k*. A detailed description of the specification of these parameters has been described elsewhere (Musschenga *et al.*, 1990).

9. RESULTS AND DISCUSSION

Experimental results in the range $5.0 \cdot 10^3 \leq Re < 60 \cdot 10^3$ were obtained at temperatures ranging from 280 K to 295 K (the temperature was constant during each particular experiment). The distribution and the value of $\bar{\theta}_{exp}$ were determined from velocity signals measured at $y^+ = 36$, applying the detection criterion represented as Eq. (54) and an additional condition of positive slope, using $a = (34.8 \cdot 10^{-3}) \cdot t_0$ and $k = k_0 = 1.13$.

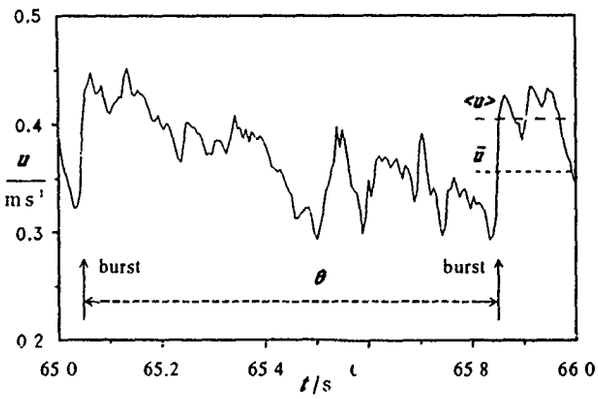

Fig 1. Instantaneous local axial velocities plotted against time, measured at $Re = 15.0 \cdot 10^3$ and $y^+ = 36$, showing two successive bursts ($\nu = 1.38 \cdot 10^{-6}$ m² s⁻¹).

9.1 *Measured and calculated age distributions*

In Fig. 1 an example is given of the signals representing the instantaneous local axial velocities measured at $Re = 15.0 \cdot 10^3$, showing two successive bursts. The time interval between the bursts is considered as the age θ of a fluid element at the tube wall. In Fig. 2 an age distribution obtained from the LDA measurements at $Re = 31.3 \cdot 10^3$ is represented as a histogram. In this figure the values of $N/\Delta\theta$ have been plotted against the residence time θ. The solid curve in Fig. 2 represents the age distribution calculated from f and Re with the ERSR model. This distribution is calculated with (Musschenga *et al.*,1990):

$$N/\Delta\theta = (N_0/t_0)e^{-\theta/t_0} \qquad (55)$$

Fig. 2 shows a quantitative agreement between the histogram representing the measured age distribution, and the solid curve representing the distribution calculated from f and Re with the ERSR model. The results measured and calculated in the range $5.0\,10^3 \leq Re \leq 43.4\,10^3$ show a similar good agreement.

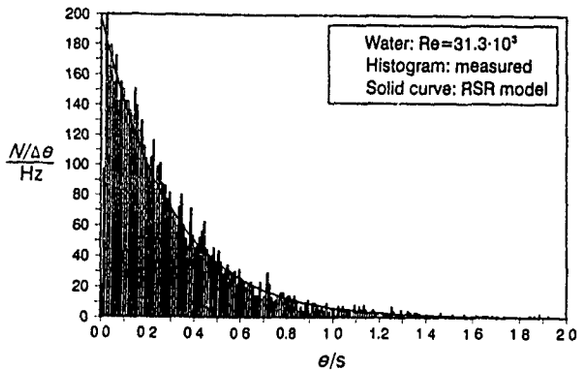

Fig. 2. Age distribution determined in a turbulent pipe flow at $Re = 31.3 \cdot 10^3$. The histogram represents the age distribution measured with a LDA; the solid curve represents the age distribution calculated from f and Re with Eq. (55) of the ERSR model ($\nu = 1.04 \cdot 10^{-6}$ m² s⁻¹; $t_0 = 0.291$ s; $a = (34.8 \cdot 10^{-3}) \cdot t_0$; $k_0 = 1.13$; $N_0 = 5759$; $\Delta\theta = 0.01$ s).

9.2 *Comparison between t_0 and $\bar{\theta}_{exp}$*

In Fig. 3 the ratio $t_0/\bar{\theta}_{exp}$ is plotted versus Re. This figure shows that for $5.0 \cdot 10^3 \leq Re \leq 43.4 \cdot 10^3$ the values of t_0 *calculated* from f and Re with the ERSR model agree quantitatively with those *measured* with the LDA in turbulent pipe flow. The measured values $\bar{\theta}_{exp}$ at $Re > 43.4 \cdot 10^3$ are larger than the calculated values t_0 This is probably due to the measured values because at increasing Reynolds numbers the ratio between the length of the LDA measuring volume and the boundary-layer thickness increases. As a consequence the velocity signals obtained at these larger Reynolds numbers refer to instantaneous velocities averaged over a considerable part of the boundary layer.

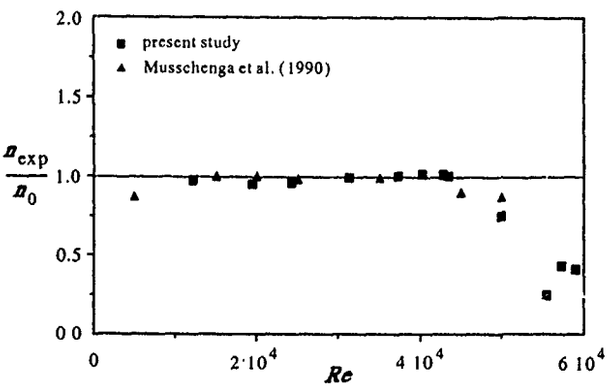

Fig. 3. The ratio $t_0/\bar{\theta}_{exp}$ measured in a turbulent pipe flow at $y^+ = 36$, is plotted against Re, where $a = (34.8 \cdot 10^{-3}) \cdot t_0$ and $k_0 = 1.13$. The deviation of $t_0/\bar{\theta}_{exp}$ from one at $Re > 43.4 \cdot 10^3$ is discussed in Section 9.2.

From the results represented in Section 9 it may be concluded

that both the *distribution* and the *mean value* of the ages of the fluid elements at the tube wall, measured with a LDA, closely agree with those calculated from f and Re with the ERSR model. The measured *random* age distributions confirm the investigations of Van Maanen and Fortuin (1982, 1983), and verify Danckwerts' (1951) assumptions concerning the random-age distribution of fluid elements at the interface in a turbulent fluid flow.

10. COMPARISON WITH LITERATURE DATA

10.1 *Mean age of the fluid elements at the tube wall*

In Fig. 4 a compilation of experimental data concerning the mean ages measured in turbulent pipe flow has been plotted against Re. The crosses (+) refer to data presented by Meek (1972).

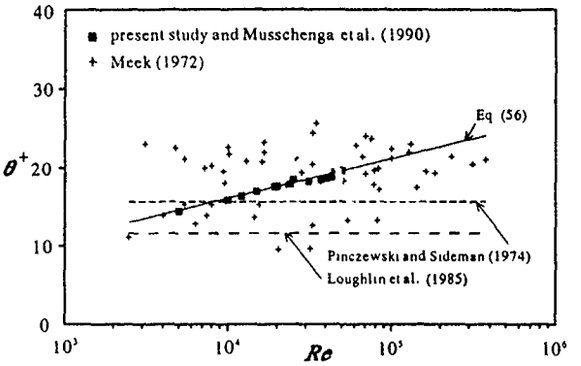

Fig 4. Comparison between our measured values of θ^+ (solid squares) and the θ^+ values (crosses) presented by Meek (1972) The solid line represents Eq (56) calculated with the ERSR model. The dashed lines represent the dimensionless mean ages proposed by Pinczewski and Sideman (1974), and Loughlin et al (1985). (Parameters in Eq. 54: $a = (34.8 \cdot 10^{-3}) \cdot t_0$; $k_0 = 1.13$).

To compare our results with these data, $\theta^+ = u^* / (\bar{\theta}_{exp}/\nu)$ is plotted against Re in Fig 4 According to the ERSR model the quantity $u^* / (\bar{\theta}_{exp}/\nu)$ can be represented by $u^* / (t_0/\nu)$. Combining Eqs (13), (15), and (20) results in:

$$\theta^+ = u^* / (t_0/\nu) = 5.0882 \log(Re) - 4.300 \qquad (56)$$

From Eq. (56) it is obtained that according to the ERSR model a linear relationship is expected between the variables plotted in Fig. 4. This linear relationship closely agrees with our experimental results in the range $5.0 \cdot 10^3 \leq Re \leq 43.4 \cdot 10^3$. Further, the theoretical solid line 'agrees' with the 'cloud' of experimental data presented in literature. The dashed lines in Fig. 4 refer to values of θ^+ proposed by Pinczewski and Sideman (1974), and Loughlin *et al.* (1985), who assumed that the value of $u^* / (\bar{\theta}_{exp}/\nu)$ is independent of the Reynolds number.

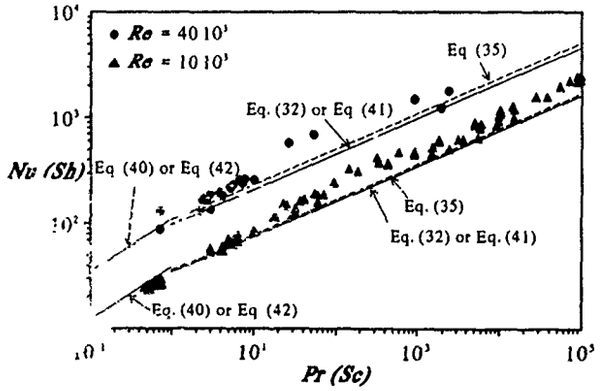

Fig. 5. Comparison between values of Nu or Sh calculated with the ERSR model (solid lines), and experimental values of Nu and Sh (symbols) presented in literature by Friend and Metzner (1958), Harriott and Hamilton (1965), and Mizushina et al. (1971). The dashed lines represent values of Nu calculated with Eq. (35) of Colburn (1933).

10.2 *Heat and mass transfer coefficients*

In Fig. 5 values of Nu or Sh calculated with the ERSR model are compared with experimental values presented in literature. In this figure values of Nu or Sh are plotted versus Pr or Sc for two different values of Re. The solid lines represent values of Nu or Sh calculated with Eqs (32) or (41) for $Pr > 1$ or $Sc > 1$, and calculated with Eqs (40) or (42) for $Pr < 1$ or $Sc < 1$. In these two cases Eqs (20) and (29) were applied. The dashed lines represent values of Nu calculated with Eq. (35). From Fig. 5 it can be seen that the values of Nu and Sh calculated from f and Re with the ERSR model closely agree with both the experimental data and the correlation of Colburn (1933).

11. CONCLUSIONS

- The time intervals between successive bursts in a turbulent pipe flow are distributed randomly.
- The mean age t_0 of the fluid elements at the tube wall can be calculated from f and Re with the ERSR model.
- The calculated time-averaged axial velocity profile in the wall region of a turbulent pipe flow closely agrees with correlations presented in literature.
- Heat and mass transfer equations for turbulent pipe flow, derived from the ERSR model closely agree with correlations from literature, based on experimental data.
- The introduction of a Fanning number for momentum transfer ($Fa = k_m d/\nu$) elucidates the analogy between momentum, heat, and mass transfer in turbulent pipe flow. The Fanning number is comparable with the Nusselt number for heat transfer and the Sherwood number for mass transfer.
- The Chilton and Colburn factors j_h for heat transfer, and j_d for mass transfer follow from the ERSR model.
- The relationship between the friction factor and the Reynolds number is the *one and only* correlation needed in the ERSR model for a quantitative prediction of the momentum, heat, and mass transfer coefficients.

Acknowledgements - The authors wish to thank: the Netherlands Foundation for Chemical Research (SON) for the financial aid from the Netherlands Organisation for Scientific Research (NWO), and Messrs. E. Grolman, E P.S. Schouten, and W. Visser for their contribution to the experimental part of this study.

REFERENCES

Blackwelder, R.F and Kaplan, R.E., 1976, *J Fluid Mech* 76, 89-112.
Chilton, T.H and Colburn, A.P., 1934, *Ind. Eng. Chem.* 26, 1183-1187
Colburn, A.P., 1933, *Trans. AIChE J.* 29, 174-209.
Corino, E R. and Brodkey, R.S., 1969, *J. Fluid Mech.* 37, 1-30.
Danckwerts, P V., 1951, *Ind. Engng Chem* 43 (6), 1460-1467.
Eck, B., 1973, *Tech. Strömungslehre*, Springer-Verlag, New York.
Einstein, H.A and Li, H., 1956, *Trans. Am. Soc. Civil. Engrs* 82, 293-320
Fortuin, J.M.H. and Klijn, P.-J., 1982, *Chem. Engng Sci.* 37, 611-623.
Friend, W.L. and Metzner, A.B., 1958, *AIChE J.* 4 (4), 393-402.
Hanratty, T.J., 1956, *AIChE J* 2 (3), 359-362.
Harriott, P and Hamilton, R.M., 1965, *Chem. Engng Sci.* 20, 1073-1078.
Higbie, R., 1935, *Trans. Am. Chem. Engr.* 31, 365-389.
Kline, S.J., Reynolds, W.C , Schraub, F.A., and Runstadler, P.W., 1967, *J. Fluid Mech.* 30, 741-773
Loughlin, K.F., Abul-Hamayel, M.A., and Thomas, L.C., 1985, *AIChE J.* 31 (10), 1614-1620.
Maanen, H.R.E. van, and Fortuin, J.M.H., 1982, *Proc. of the 1st Int. Symp. on Appl. of Laser Tech. to Fluid Mechanics*, Lisbon, 1982.
Maanen, H.R.E. van, and Fortuin, J.M.H., 1983, *Chem. Engng Sci.* 38, 399-423.
McAdams, W.H., 1954, *Heat Transmission*, 3rd Edition. McGraw-Hill, New York.
Meek, R.L., 1972, *AIChE J.* 18, 854-855.
Mizushina, T., Ogino, F., Oka, Y., and Fukuda, H., 1971, *Int. J. Heat Mass Transfer* 14, 1705-1716.
Musschenga, E.E., Hamersma, P.J. and Fortuin, J.M.H., 1990, *Proc. of the 5th Int. Symp. on Appl. of Laser Tech. to Fluid Mechanics*, Lisbon, 1990, paper 16.6.
Pinczewski, W.V. and Sideman, S., 1974, *Chem. Engng Sci.* 29, 1969-1976.
Sideman, S. and Pinczewski, W.V., 1975, *Topics in Transport Phenomena*. Hemisphere Publishing Corporation, Washington.
Thomas, L.C., 1980, *Int. J. Heat Mass Transfer* 23, 1099-1104.

EIGHTH SYMPOSIUM ON
TURBULENT SHEAR FLOWS
Technical University of Munich
September 9-11, 1991

SCALING OF THE TURBULENT NATURAL-CONVECTION BOUNDARY LAYER ALONG A HOT VERTICAL PLATE

R.A.W.M. Henkes

Delft University of Technology, Department of Applied Physics,
P.O. Box 5046, 2600 GA Delft, The Netherlands.

ABSTRACT

By numerically solving the turbulent boundary-layer equations along a hot vertical plate for air and water up to a Rayleigh number of 10^{25}, the proper scalings and wall functions are derived. Turbulence is modelled by different low-Reynolds-number $k-\varepsilon$ models. In the outer layer the length, velocity and temperature are scaling with the height y, the velocity maximum v_{max} and the temperature difference $v_{max}^2/(g\beta y)$ respectively. In the inner layer proper scalings do not seem to exist. In particular the wall-heat transfer does not scale with the commonly used $Ra_y^{1/3}$-law.

INTRODUCTION

The proper scalings, giving the so-called wall functions, for turbulent forced-convection boundary layers are well-known and have the typical logarithmic profiles. On the contrary, the proper scalings and wall functions for the turbulent natural-convection boundary layer along a hot vertical plate are not well defined yet.

Making some physical assumptions in their analytical approach, George & Capp (1979) gave a first proposal for the wall functions for the turbulent natural-convection boundary layer. Different scalings were formulated for the inner layer (*i.e.* from the wall up to the position of the velocity maximum) and for the outer layer (*i.e.* from the position of the velocity maximum up to the outer edge). Henkes & Hoogendoorn (1990) studied the scalings by numerically solving the boundary-layer equations in the Boussinesq approximation, using low-Reynolds-number $k-\varepsilon$ models for the turbulence. A shortcoming of this study was that the calculations were only performed up to $Ra_y=10^{12}$ (Ra_y is the local Rayleigh number, in which y is the coordinate along the plate). At this maximum Rayleigh number transition effects were still visible in the numerical results. Therefore the present paper extends the calculations up to $Ra_y=10^{25}$. Furthermore Prandtl number effects are studied here by considering both air and water. The outer-layer scalings as derived from the calculations up to $Ra_y=10^{12}$ indeed persist in the new calculations up to $Ra_y=10^{25}$: wall functions in the outer layer do exist. On the contrary, the calculations up to $Ra_y=10^{25}$ suggest that proper scalings and wall functions for the inner layer do not exist.

MATHEMATICAL TREATMENT

The turbulent boundary-layer equations under the Boussinesq approximation read:

$$\frac{\partial u}{\partial x} + \frac{\partial v}{\partial y} = 0$$

$$u\frac{\partial v}{\partial x} + v\frac{\partial v}{\partial y} = g\beta(T-T_\infty) + \nu\frac{\partial^2 v}{\partial x^2} - \frac{\partial}{\partial x}\overline{u'v'} \qquad (1)$$

$$u\frac{\partial T}{\partial x} + v\frac{\partial T}{\partial y} = \frac{\nu}{Pr}\frac{\partial^2 T}{\partial x^2} - \frac{\partial}{\partial x}\overline{u'T'}.$$

Here x is the coordinate perpendicular to the plate, and y is the coordinate along the plate; (u,v) is the velocity vector in the direction (x,y); T is the temperature and T_∞ is the isothermal environment temperature; g is the gravitational acceleration; β is the coefficient of thermal expansion; ν is the kinematic viscosity and Pr is the Prandtl number. The dimensionless solution only depends on x/y, Pr and the Rayleigh number Ra_y ($= g\beta\Delta T y^3 Pr/\nu^2$, with $\Delta T = T_w - T_\infty$).

As a result of the Reynolds averaging, the Reynolds stress $-\overline{u'v'}$ and the turbulent heat flux $-\overline{u'T'}$ appear in the equations. These quantities are represented by the eddy-viscosity concept:

$$-\overline{u'v'} = \nu_t\frac{\partial v}{\partial x}\ ; \quad -\overline{u'T'} = \frac{\nu_t}{\sigma_T}\frac{\partial T}{\partial x}. \qquad (2)$$

Here σ_T is the turbulent Prandtl number for the temperature (we take $\sigma_T=0.9$). The turbulent viscosity ν_t is modelled by a $k-\varepsilon$ model (k is the turbulent kinetic energy ($k=\overline{u_i'u_i'}$), and ε is the turbulent energy dissipation rate):

$$u\frac{\partial k}{\partial x} + v\frac{\partial k}{\partial y} = \frac{\partial}{\partial x}\left[\nu + \frac{\nu_t}{\sigma_k}\right]\frac{\partial k}{\partial x} + P_k - \varepsilon + D \qquad (3)$$

$$u\frac{\partial \varepsilon}{\partial x} + v\frac{\partial \varepsilon}{\partial y} = \frac{\partial}{\partial x}\left[\nu + \frac{\nu_t}{\sigma_\varepsilon}\right]\frac{\partial \varepsilon}{\partial x} +$$

$$+ (c_{\varepsilon 1} f_1 P_k - c_{\varepsilon 2} f_2 \varepsilon)\frac{\varepsilon}{k} + E$$

$$\text{with } P_k = \nu_t\left(\frac{\partial v}{\partial x}\right)^2, \quad \nu_t = c_\mu f_\mu \frac{k^2}{\varepsilon}.$$

The equations (3) contain both high-Reynolds-number terms (c_μ, $c_{\varepsilon 1}$, $c_{\varepsilon 2}$, σ_k, σ_ε) and low-Reynolds-number functions (f_μ, f_1, f_2, D, E). The standard $k-\varepsilon$ model (taking $f_\mu=f_1=f_2=1$ and $D=E=0$) formally only holds if the local turbulence-based Reynolds number ($Re_t=k^2/\nu\varepsilon$) is large. If Re_t is small, for example close to a fixed wall, a proper choice of the low-Reynolds-number functions is required to achieve the correct damping of turbulence. Many different low-Reynolds-number $k-\varepsilon$ models have been formulated in the literature.

The equations are discretized with the finite-volume method. Because of the parabolic character of the equations, an y-marching numerical method can be used to solve the system.

The following boundary conditions are prescribed:

$y = y_{start}$: laminar v- and T-profiles

$y = y_{trans}$: perturbation in k and ε,

$$e.g.\ k=0.5\ v_0^2\ ,\ \varepsilon=c_\mu^{1/2}\ k\left|\frac{\partial v}{\partial x}\right|$$

$x = 0$: $u=v=0$, $T=T_w$ (4)

k, ε specified by model

($k=0$ $\varepsilon=\infty$ for standard $k-\varepsilon$)

$x = x_\infty$: $v=k=\varepsilon=0$, $T=T_\infty$

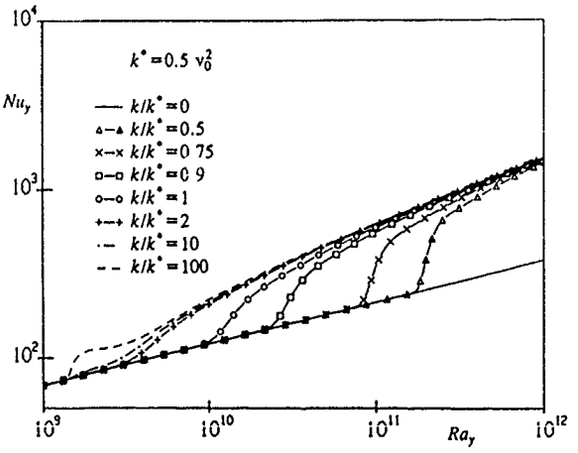

FIGURE 1. Transition for air with different amounts of introduced energy (Chien model, 100×100 grid).

Here $v_0=(g\beta\Delta T\nu)^{1/3}$. The calculations are started at a height corresponding to $Ra_y=10^9$. At y_{start} the laminar similarity solution for the hot vertical plate is prescribed. Turbulence is introduced at the height y_{trans} (corresponding to $Ra_y=1.5\times10^9$ for air and 1.5×10^{10} for water) by switching on the turbulence model and by prescribing an amount of turbulent kinetic energy. The precise laminar-turbulent transition turns out to largely depend on (i) the turbulence model, (ii) the numerical grid and (iii) how much and where energy is introduced. Figure 1 shows the dimensionless wall-heat transfer (Nusselt number, $Nu_y=-(y/\Delta T)(\partial T/\partial x)_w$) as a function of Ra_y for decreasing introduced energy: decreasing the energy delays the transition. If no energy is introduced, the solution remains on the laminar branch. Fortunately, once the turbulent branch is reached, the solution for increasing Ra_y does not depend on the transition process. Figure 2 shows ν_t for different $k-\varepsilon$ models (denoted by the names of the authors who formulated the specific low-Reynolds-number $k-\varepsilon$ model) at $Ra_y=10^{15}$. At this Rayleigh number the transition is complete, because low-Reynolds-number effects in the outer layer are now absent: differences in the profiles (scaled with v_{max} and y) are totally due to different choices for the high-Reynolds-number constants.

ACCURACY

The numerical accuracy of the calculations was verified by refining the grid from 25×25 up to 400×400 points. Table 1 shows the results for air at $Ra_y=10^{11}$ with the standard $k-\varepsilon$ model. The results indeed become grid-independent for increasing number of grid points. For the results to be presented in the sequel a 100×100 grid was used up to $Ra_y=10^{13}$ and a 200×200 grid for larger Rayleigh numbers.

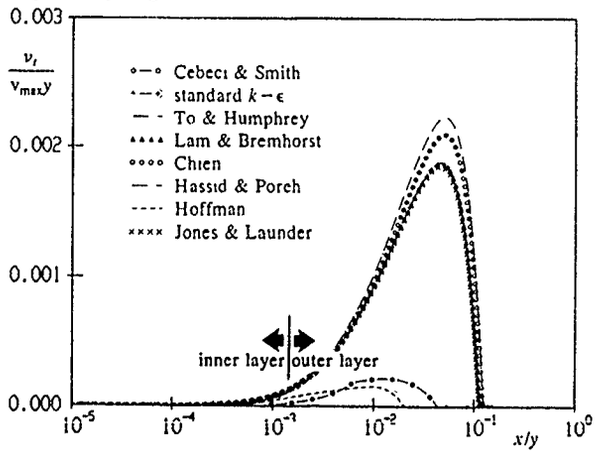

FIGURE 2. Turbulent viscosity for air at $Ra_y=10^{15}$.

Table 2 compares the turbulent results with different models for air at $Ra_y = 10^{11}$ and for water at $Ra_y = 10^{13}$. Details of the (low-Reynolds-number) $k-\varepsilon$ models were given by Henkes & Hoogendoorn (1989) and by Henkes (1990). The calculated maximum of the velocity and the turbulent viscosity is compared with the experiments of Tsuji & Nagano (1989). The wall-heat transfer is compared with a value fitted to different existing experiments. Differences between the models are larger for the wall-heat transfer than for the velocity maximum. This is not surprising as the effect of the low-Reynolds-number functions is strongest in the inner layer. The low-Reynolds-number models of Lam & Bremhorst, Chien and Jones & Launder perform best. These models were also found to perform best for the forced-convection boundary layer in the study of Patel *et al.* (1981). The standard $k-\varepsilon$ model largely overpredicts for the wall-heat transfer. None of the models predict the maximum of the turbulent viscosity in agreement with the experiment; $\nu_{t,\max}$ for almost all $k-\varepsilon$ models is roughly twice too large.

TABLE 1. Numerical accuracy for air at $Ra_y = 10^{11}$ with standard $k-\varepsilon$ model

grid	$\frac{Nu_y}{Ra_y^{1/3}}$	$\frac{v_{\max}}{\sqrt{g\beta\Delta T y}}$	$\frac{\nu_{t,\max}}{\nu}$
25×25	0.1750	0.3622	257.3
50×50	0.1789	0.3570	241.1
100×100	0.1806	0.3549	233.4
200×200	0.1814	0.3540	229.7
400×400	0.1817	0.3537	226.9

TABLE 2. Comparison of models for air at $Ra_y = 10^{11}$ and for water at $Ra_y = 10^{13}$.

model	(a) air $\frac{Nu_y}{Ra_y^{1/3}}$	(a) air $\frac{v_{\max}}{\sqrt{g\beta\Delta T y}}$	(a) air $\frac{\nu_{t,\max}}{\nu}$	(b) water $\frac{Nu_y}{Ra_y^{1/3}}$	(b) water $\frac{v_{\max}}{\sqrt{g\beta\Delta T y}}$	(b) water $\frac{\nu_{t,\max}}{\nu}$
experiment	0.119	0.344	120	0.119	--	--
standard $k-\varepsilon$	0.181	0.355	233	0.381	0.243	544
To & Humphrey	0.164	0.346	210	0.218	0.208	459
Lam & Bremhorst (Dirichlet)	0.132	0.320	241	0.088	0.166	436
Lam & Bremhorst (Neumann)	0.132	0.320	240	0.088	0.166	435
Chien	0.138	0.329	261	0.137	0.184	509
Hassid & Poreh	0.161	0.323	231	0.161	0.184	461
Hoffman	0.083	0.422	26	0.082	0.218	60
Jones & Launder	0.114	0.335	175	0.085	0.175	373

SCALINGS

To find the proper scalings, the calculations with the standard $k-\varepsilon$ model and the low-Reynolds-number models of Chien and Jones & Launder are performed up to $Ra_y = 10^{25}$. The Ra_y dependence of a quantity ϕ is written as $\alpha\, Ra_y^{\gamma}$, with $\gamma = (Ra_y/\phi)[\partial\phi/\partial Ra_y]$. The infinite-Rayleigh-number limit of γ, in the case it exists, defines the proper scaling for a quantity.

All the quantities in the outer layer give a constant γ for increasing Rayleigh number. For example, figure 3 follows the scaled maximum turbulent kinetic energy, *i.e.* $(2k_{\max}/3)^{1/2}/v_{\max}$, and the scaled stream function at infinity, *i.e.*

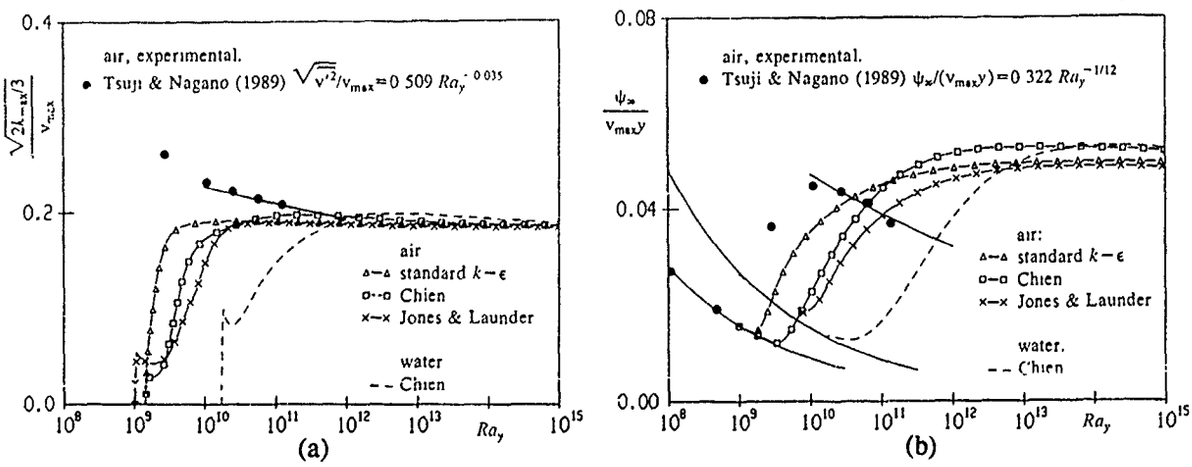

FIGURE 3. Scaling of different quantities in outer layer; (a) maximum of turbulent kinetic energy, (b) stream function at outer edge.

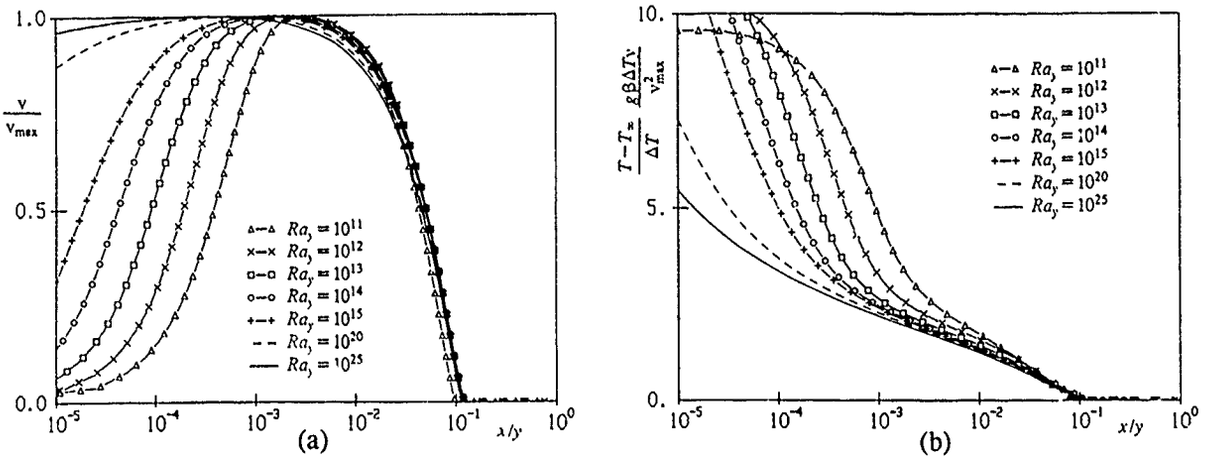

FIGURE 4. Wall functions in outer layer (Chien model); (a) velocity, (b) temperature.

$\psi_\infty/(v_{max}\,y)$ (the stream function is defined by $\partial\psi/\partial x = v$, $\partial\psi/\partial y = -u$, $\psi = 0$ at $x = 0$). It is clear that indeed the proper scalings are used in this figure, because the lines become horizontal for increasing Rayleigh number: y and v_{max} are the proper length and velocity scale in the outer layer (the figure only gives the results up to $Ra_y = 10^{15}$, but the lines remain horizontal up to at least $Ra_y = 10^{25}$). Table 3 summarizes the outer-layer scalings for different quantities. Values of γ are independent of the $k-\varepsilon$ model used. Differences in the values for the proportionality constant α are small and only due to differences in the high-Reynolds-number constants. There is no difference in the results for air and water (*i.e.* there is no Prandtl number effect).

Because we calculate that y and v_{max} are the proper length and velocity scale in the outer layer, the buoyant term in the boundary-layer equations (1) is of the same order of magnitude as the other terms if the characteristic temperature difference is taken as $v_{max}^2/(g\beta y)$. The calculated outer-layer scalings lead to the following wall functions in the outer layer:

$$\frac{v}{v_{max}} = f_v^o\left[\frac{x}{y}\right]$$
$$\left[\frac{T-T_\infty}{\Delta T}\right]\frac{g\beta\Delta T\,y}{v_{max}^2} = f_t^o\left[\frac{x}{y}\right]. \qquad (5)$$

The existence of these wall functions for increasing Rayleigh number is checked in figure 4 for air with the Chien model. These wall functions hold irrespective of the Prandtl number.

In contrast to the outer-layer scalings, none of the inner-layer quantities give fully Ra_y-independent γ-values for increasing Rayleigh number. Also differences between the models in the inner layer, mainly differences in α, do not disappear. The dependence of α on the turbulence model is not surprising, because the low-Reynolds-number functions become active in the inner layer. Figure 5 shows the wall-heat transfer (Nu_y) for air. γ increases from 3/8 at $Ra_y = 10^{12}$ to 0.435 at $Ra_y = 10^{25}$, showing that the difference with $\gamma = 1/3$, as measured up to about $Ra_y = 5\times10^{11}$, becomes larger for increasing

TABLE 3. Outer-layer scalings (Chien model).

quantity	laminar		turbulent
	air	water	air and water
$\frac{u_{max}}{v_{max}}$	$-2.11\ Ra_y^{-1/4}$	$-3.61\ Ra_y^{-1/4}$	-0.0702
$\frac{\psi_\infty}{y v_{max}}$	$2.82\ Ra_y^{-1/4}$	$4.91\ Ra_y^{-1/4}$	0.0497
$\frac{(2k_{max}/3)^{1/2}}{v_{max}}$	0.	0.	0.183
$\frac{x_{kmax}}{y}$	--	--	0.0354
$\frac{v_{t,max}}{y v_{max}}$	0.	0.	0.00202
$\frac{x_{vt,max}}{y}$	--	--	0.0487

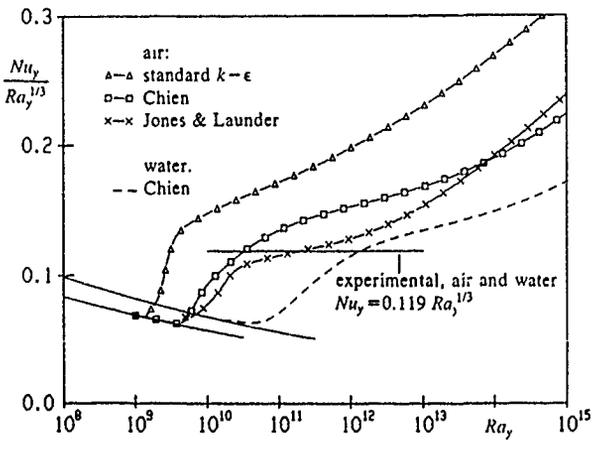

FIGURE 5. Ra_y-dependence of wall-heat transfer.

TABLE 4. Ra_y-dependence in inner layer (Chien model).

(a) air

quantity	laminar	turbulent		
		$Ra_y = 10^{15}$	$Ra_y = 10^{20}$	$Ra_y = 10^{25}$
Nu_y	$0.387\ Ra_y^{1/4}$	$0.0195\ Ra_y^{0.404}$	$0.00819\ Ra_y^{0.426}$	$0.00511\ Ra_y^{0.435}$
c_{fy}	$1.76\ Ra_y^{-1/4}$	$0.0948\ Ra_y^{-0.154}$	$0.0129\ Ra_y^{-0.103}$	$0.00562\ Ra_y^{-0.0871}$
$\frac{v_{max}}{\sqrt{g\beta\Delta Ty}}$	0.555	$0.734\ Ra_y^{-0.0311}$	$0.499\ Ra_y^{-0.0218}$	$0.435\ Ra_y^{-0.0195}$
x_{vmax}/y	$1.25\ Ra_y^{-1/4}$	$0.0237\ Ra_y^{-0.0854}$	$0.00680\ Ra_y^{-0.0535}$	$0.00503\ Ra_y^{-0.0482}$

(b) water

quantity	laminar	turbulent		
		$Ra_y = 10^{15}$	$Ra_y = 10^{20}$	$Ra_y = 10^{25}$
Nu_y	$0.459\ Ra_y^{1/4}$	$0.0211\ Ra_y^{0.394}$	$0.00310\ Ra_y^{0.446}$	$0.00266\ Ra_y^{0.449}$
c_{fy}	$2.08\ Ra_y^{-1/4}$	$0.599\ Ra_y^{-0.222}$	$0.00547\ Ra_y^{-0.0985}$	$0.00251\ Ra_y^{-0.0826}$
$\frac{v_{max}}{\sqrt{g\beta\Delta Ty}}$	0.263	$0.351\ Ra_y^{-0.0239}$	$0.251\ Ra_y^{-0.0160}$	$0.247\ Ra_y^{-0.0157}$
x_{vmax}/y	$1.68\ Ra_y^{-1/4}$	$0.0696\ Ra_y^{-0.109}$	$0.00966\ Ra_y^{-0.0580}$	$0.00774\ Ra_y^{-0.0535}$

Rayleigh number. Therefore the calculations suggest that the application of the commonly known wall-heat transfer law $Nu_y \div Ra_y^{1/3}$ is doubtful for $Ra_y > 10^{12}$, where no experiments are known yet. Of course experiments in that regime are needed to give a final answer. The scaling with the laminar velocity scale $(g\beta\Delta Ty)^{1/2}$ for the velocity maximum in the experiments of Tsuji & Nagano (1989) is confirmed by the calculations in figure 6. According to table 4, which summarizes the Rayleigh-number dependence for different inner-layer quantities, only a very small Ra_y dependence in γ persists. In this table the wall-shear stress coefficient c_{fy} is defined by $2\nu(\partial v/\partial x)_w/g\beta\Delta Ty$. Because γ-values in the calculations remain Ra_y-dependent even up to

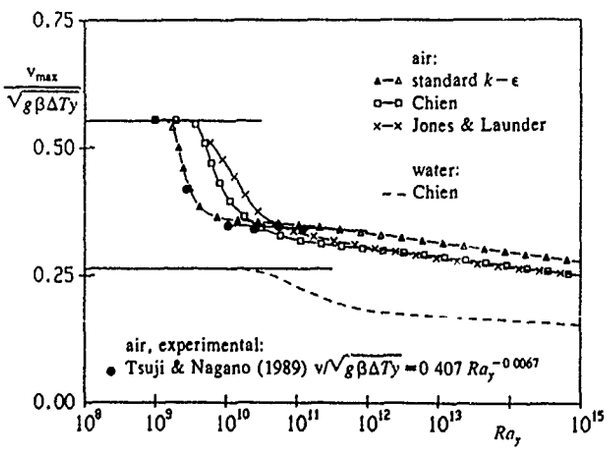

FIGURE 6. Ra_y-dependence of velocity maximum.

$Ra_y = 10^{25}$, perfect scalings and wall functions in the inner layer do not seem to exist. A *best fit* for the results up to about $Ra_y = 10^{15}$ (figure 7) is given by the velocity profile v/v_{max} *vs* $(x/v_{max})(\partial v/\partial x)_w$ and the temperature profile $(T - T_\infty)/\Delta T$ *vs* ζ $(= xNu_y/y)$. This velocity profile does not agree with George & Capp's (1979) analytical wall function for the velocity in the inner layer, giving $v/(g\beta\Delta T\nu)^{1/3}$ *vs* ζ. The temperature profile does agree with George & Capp's wall function.

George & Capp proposed the following wall functions for the outer layer, irrespective of the Prandtl number.

$$\frac{v_{max} - v}{(g\beta\Delta T\delta Q_T)^{1/3}} = f_v^o\left(\frac{x}{\delta}\right)$$

$$\left(\frac{T - T_\infty}{\Delta T}\right)\frac{(g\beta\Delta T\delta Q_T)^{1/3}}{Q_T} = f_T^o\left(\frac{x}{\delta}\right). \qquad (6)$$

Here δ is the boundary-layer thickness and Q_T is the velocity scale $-\nu(\partial T/\partial x)_w/Pr\Delta T$. The boundary-layer thickness is usually defined as $\delta = \psi'_\infty/v_{max}$; this indeed is proportional to y according to table 3. The proportionality for the velocities holds if

$$Nu_y = C^*\ Pr^{1/2}\ Ra_y^{1/2}\left[\frac{v_{max}}{\sqrt{g\beta\Delta Ty}}\right]^3 \qquad (7)$$

in which C^* is a constant (also independent of Pr). Comparison of the calculations for Nu_y and

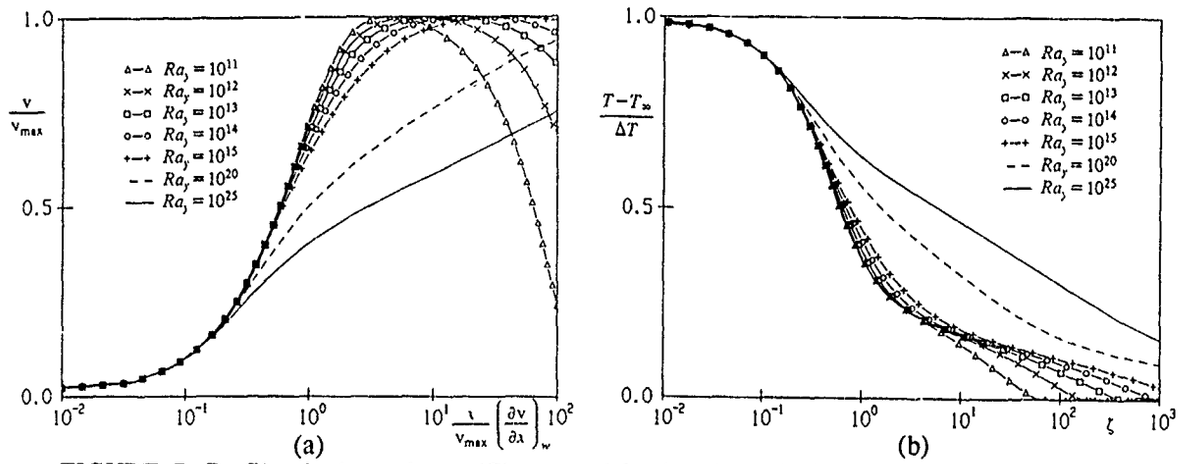

FIGURE 7. Profiles in inner layer (Chien model, air); (a) velocity, (b) temperature.

v_{max} in table 4 shows that this relation indeed holds for increasing Rayleigh number; the large-Rayleigh-number calculations ($Ra_y = 10^{25}$) with the Chien model give a Ra_y independent, and also practically Pr independent, value for C^*, namely 0.0506 for air and 0.0529 for water. Therefore George & Capp's outer-layer length scale, δ, and velocity scale, $(g\beta\Delta T\delta Q_T)^{1/3}$, are similar to the calculated length scale, y, and velocity scale, v_{max}: this gives a full consistency between George & Capp's wall functions in the outer layer and the calculated wall functions.

CONCLUSION

Accurate solutions of the turbulent boundary-layer equations along the hot vertical plate in an isothermal environment were obtained for air and water up to $Ra_y = 10^{25}$. Low-Reynolds-number modifications of the standard $k-\varepsilon$ model are needed to predict quantities in the inner layer (like the wall-heat transfer) reasonably close to the experiments. The standard $k-\varepsilon$ model largely overpredicts the wall-heat transfer. The low-Reynolds-number models of Lam & Bremhorst, Chien and Jones & Launder give the best prediction for the wall-heat transfer. The $k-\varepsilon$ models strongly overpredict the maximum of the turbulent viscosity by about 100%.

The proper scalings and wall functions can be derived from the $k-\varepsilon$ solutions by examining the Ra_y dependence of quantities ϕ in $\phi = \alpha Ra_y^{\gamma}$. Model differences mainly influence the α values in the inner layer, whereas γ is almost independent of the model used. γ for quantities in the inner layer does not become fully Ra_y-independent. For example γ for the wall-heat transfer (Nu_y) for air increases from 3/8 at $Ra_y = 10^{12}$ to 0.435 at $Ra_y = 10^{25}$, showing that the difference with $\gamma = 1/3$, as measured up to about $Ra_y = 5\times10^{11}$, becomes larger for increasing Rayleigh number. Because γ remains Ra_y-dependent, wall functions in the inner layer do not seem to exist. A best fit for the results up to about $Ra_y = 10^{15}$ is given by the velocity profile v/v_{max} vs $(x/v_{max})(\partial v/\partial x)_w$ and the temperature profile $(T-T_\infty)/\Delta T$ vs ζ ($= xNu_y/y$). This velocity profile does not agree with George & Capp's (1979) analytical wall function, but the temperature profile does agree. The γ values in the outer layer become independent of Ra_y for $Ra_y \to \infty$, implying that wall functions in the outer layer exist. The proper length scale is y and the proper velocity scale is v_{max}. The proper temperature scale is $v_{max}^2/(g\beta y)$. These outer-layer scalings are consistent with George & Capp's proposal. v_{max} itself approximately scales with the laminar velocity scale $(g\beta\Delta T y)^{1/2}$.

REFERENCES

George, W.K. & Capp, S.P. 1979 A theory for natural convection turbulent boundary layers next to heated vertical surfaces. Int. J. Heat Mass Transfer 22, 813-826.

Henkes, R.A.W.M. & Hoogendoorn, C.J. 1989 Comparison of turbulence models for the natural convection boundary layer along a heated vertical plate. Int. J. Heat Mass Transfer 32, 157-169.

Henkes, R.A.W.M. 1990 Natural-convection boundary layers. Ph.D. thesis. Delft University of Technology, The Netherlands.

Henkes, R.A.W.M. & Hoogendoorn, C.J. 1990 Numerical determination of wall functions for the turbulent natural convection boundary layer. Int. J. Heat Mass Transfer 33, 1087-1097.

Patel, V.C., Rodi, W. & Scheuerer, G. 1981 Evaluation of turbulence models for near-wall and low-Reynolds number flows. Proc. 3rd Symp. on Turbulent Shear Flows, California, pp. 1-8.

Tsuji, T. & Nagano, Y. 1989 Velocity and temperature measurements in a natural convection boundary layer along a vertical flat plate. Experimental Thermal Fluid Sci. 2, 208-215.

EIGHTH SYMPOSIUM ON
TURBULENT SHEAR FLOWS
Technical University of Munich
September 9-11, 1991

THERMALLY DRIVEN TURBULENT BOUNDARY LAYER

T.Tsuji, Y. Nagano and M. Tagawa

Department of Mechanical Engineering
Nagoya Institute of Technology
Gokiso-cho, Showa-ku, Nagoya 466, Japan

ABSTRACT

The budgets of turbulent energy, Reynolds shear stress, mean square scalar variance and turbulent heat fluxes have been evaluated in a thermally driven boundary layer in air along a vertical flat plate. In the near-wall region, the velocity-gradient correlation plays an important role in turbulent energy production and thermal energy is directly converted into kinetic energy through this correlation. Consequently, Reynolds shear stress and streamwise turbulent heat flux near the wall, which are normally considered to have close relations with the energy production process, behave differently from those in the ordinary turbulent boundary layers. On the other hand, the energy transfer in the outer region of the boundary layer becomes a process similar to that observed in the usual boundary layer.

NOMENCLATURE

c_p specific heat at constant pressure
E dissipation rate of mean flow energy
Gr_x Grashof number, $g\beta(T_w - T_\infty)x^3/\nu^2$
g acceleration of gravity
k turbulent energy, $(\overline{u^2} + \overline{v^2} + \overline{w^2})/2$
p pressure fluctuation
q_w wall heat flux
T mean fluid temperature
t temperature fluctuation
t_τ friction temperature, $q_w/\rho c_p u_\tau$
U, V mean velocities in x and y directions
u, v, w velocity fluctuations in x, y and z directions
u_τ friction velocity, $\sqrt{\tau_w/\rho}$
x, y, z streamwise, normal and spanwise coordinates
y^+ dimensionless distance from wall, $u_\tau y/\nu$
α thermal diffusivity
β volumetric expansion coefficient, $1/T_\infty$
ε dissipation rate of k, $\varepsilon_u + \varepsilon_v + \varepsilon_w$
$\varepsilon_u, \varepsilon_v, \varepsilon_w, \varepsilon_t$ dissipation rates of $\overline{u^2}/2$, $\overline{v^2}/2$, $\overline{w^2}/2$ and $\overline{t^2}/2$
$\varepsilon_{uv}, \varepsilon_{ut}, \varepsilon_{vt}$ dissipation rates of $\overline{uv}$, $\overline{ut}$ and $\overline{vt}$
ν kinetic viscosity
ρ density
τ_u time scale of velocity field, k/ε
τ_t time scale of thermal field, $(\overline{t^2}/2)/\varepsilon_t$
τ_w wall shear stress
$\overline{(\ )}$ time mean value

Subscripts
w wall condition
∞ ambient condition

Superscript
$+$ dimensionless quantities normalized by wall variables

INTRODUCTION

Turbulent natural convection boundary layer in air along a vertical plate is typical turbulence of thermally driven flow. The turbulence structure in this boundary layer has been generally considered not to differ significantly from that in forced convection, though the buoyancy effect is being added. However, when investigating the boundary layer, some marked characteristics different from those in ordinary turbulent boundary layers have been found with respect to the viscous sublayer structure and Reynolds shear-stress near the wall (Tsuji & Nagano 1988a, b). Also, no coherent structures such as intermittent bursts and low-speed streaks observed in the near wall region of ordinary wall shear flows were found to exist in this boundary layer (Tsuji, Nagano & Tagawa 1990).

The present study aims to trace the origin of the structure peculiar to turbulence driven by buoyancy force. We have investigated the budgets of turbulent energy, Reynolds shear stress, mean square scalar variance and turbulent heat fluxes on the basis of velocity and temperature measurements in the turbulent natural convection boundary layer, and have examined the essential factors associated with the formation of turbulent structure. The information obtained in the present study is very important to construct a turbulence model for turbulent buoyant flows.

EXPERIMENTAL APPARATUS AND INSTRUMENTATION

The apparatus used for the present study is the same as that described by Tsuji and Nagano (1988a). The flat surface generating flow was a copper plate 4 m high and 1 m wide. Uniform surface temperature $T_w = 60$ ℃ was obtained by electrical heating. Ambient fluid temperature T_∞ was about 16 ℃. For the measurements of fluid velocity and temperature, two types of probe were used. One comprised a normal hot-wire and a cold-wire of 3.1 μm diameter tungsten, and was mainly used to measure streamwise velocity and temperature. The lengths of the wires were 1.5 mm ($\simeq 6\nu/u_\tau$) and 3.5 mm ($\simeq 14\nu/u_\tau$), respectively, and the cold-wire was located 2.5 mm ($\simeq 10\nu/u_\tau$) upstream of the hot-wire. The other consisted of a cold-wire and V-shaped hot-wires (Tsuji & Nagano 1989) combined in an X-array, which were constructed by symmetrically bending 3.1 μm diameter and 1.5 mm long tungsten wires at the center. This probe was used to measure streamwise and normal (or spanwise) velocities and temperature.

BASIC TURBULENT QUANTITIES IN VELOCITY AND THERMAL FIELDS

The profiles of mean velocities, mean tempera-

ture and intensities of velocity and temperature fluctuations in the turbulent boundary layer, which are obtained simultaneously with V-shaped hot-wire/cold-wire arrangement, are shown in Fig. 1. In evaluating u_τ and t_τ, the wall shear stress τ_w and the wall heat flux q_w were obtained from the near-wall profiles of velocity and temperature (Tsuji & Nagano 1988a). The results measured with a normal hot-wire and a cold-wire are also presented for comparison. Excellent agreement between measurements obtained in different manner for each profile verifies the high reliability of the present results. Mean velocity U^+ becomes maximum at $y^+ \simeq 40$. The distinctive feature of this profile is that the relation $U^+ = y^+$ does not hold even at $y^+ \simeq 1$ and the logarithmic velocity profile cannot be seen at all (Tsuji & Nagano 1988a). In the T^+ profile, however, the relation $T^+ = Pr y^+$ holds for $y^+ \leqq 5$, and the logarithmic profile appears in the region $y^+ > 30$ as in the usual boundary layer. The maximum intensity of streamwise velocity fluctuation $\sqrt{\overline{u^2}}$ occurs at $y^+ \simeq 250$ in the outer layer (beyond the maximum velocity location). The intensities $\sqrt{\overline{v^2}}$ and $\sqrt{\overline{w^2}}$ are smaller than $\sqrt{\overline{u^2}}$ in the entire flow zone and become maximum at almost the same location as the $\sqrt{\overline{u^2}}$ maximum. The intensity of temperature fluctuation $\sqrt{\overline{t^2}}$ becomes maximum at $y^+ \simeq 15$ in the inner layer (from the wall to the maximum velocity location).

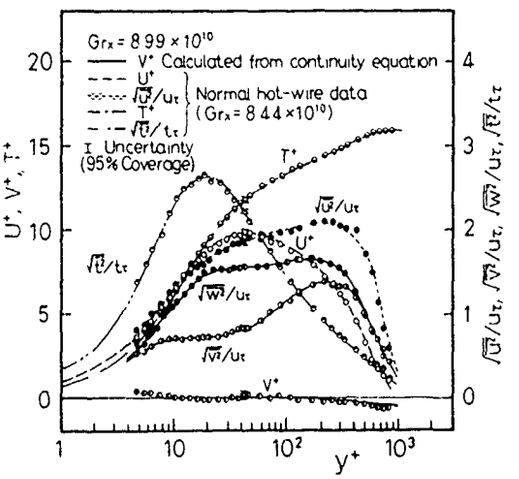

Fig. 1 Profiles of mean velocities, mean temperature and intensities of velocity and temperature fluctuations

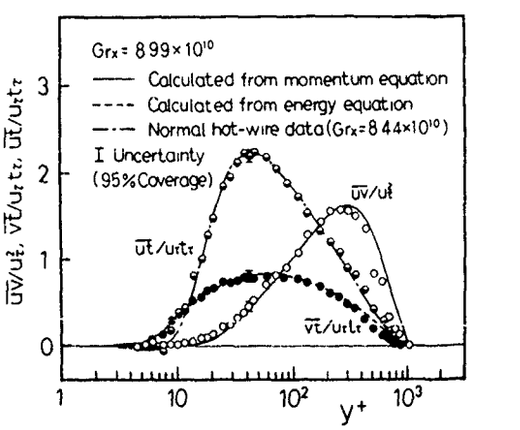

Fig. 2 Reynolds shear stress and turbulent heat fluxes

The distributions of Reynolds shear stress $\overline{uv}$, streamwise turbulent heat flux $\overline{ut}$ and normal turbulent heat flux $\overline{vt}$ obtained with the V-shaped hot-wire probe are shown in Fig. 2. In the figure, the solid and broken lines indicate the calculated values of $\overline{uv}$ and $\overline{vt}$, respectively, which are estimated from mean momentum and energy equations with the measurements of the streamwise variations in mean velocity and mean temperature profiles. Both measured $\overline{uv}$ and $\overline{vt}$ agree very well with the calculated values. Also, the streamwise turbulent heat flux $\overline{ut}$ measured simultaneously agrees very well with the measured result obtained by using the normal hot-wire probe.

From these comparisons, the present measurements for Reynolds shear stress and turbulent heat fluxes are judged to be sufficiently reliable. The $\overline{uv}$ value near the wall is almost zero and increases in the positive direction as the maximum velocity location is approached. Consequently, in the inner layer of the natural convection boundary layer, Reynolds shear stress has no relation with the mean velocity gradient. The normal turbulent heat flux $\overline{vt}$ becomes smaller than the streamwise turbulent heat flux $\overline{ut}$ in most of the boundary layer. The $\overline{vt}$ distribution corresponds rather well to the measured result for the usual boundary layer (Hishida, Nagano & Tagawa 1986). The streamwise turbulent heat flux $\overline{ut}$, which takes about zero near the wall, increases rapidly in the positive direction near the maximum $\sqrt{\overline{t^2}}$ location and reaches maximum at the location almost equivalent to the maximum velocity location. Thus, the $\overline{ut}$ distribution is also fairly different from that in the usual boundary layer in which $\overline{ut}$ takes a negative value near the wall in the case of heated flow.

BUDGETS OF TURBULENT ENERGY, REYNOLDS SHEAR STRESS, TEMPERATURE VARIANCE AND TURBULENT HEAT FLUXES

As demonstrated above, the natural convection boundary layer has unique characteristics in the turbulent structure, which are rarely seen in other turbulent boundary layers. Next, we examine the energy transfer processes which link the velocity and thermal boundary layers.

By using the boundary-layer approximation for the governing equations of the velocity and thermal fields in thermally driven flows (Monin & Yaglom 1971), the transport equations for mean flow and turbulent energy components, Reynolds shear stress, temperature variance and turbulent heat fluxes may be written as follows:

Mean flow energy

$$\underbrace{\frac{U}{2}\frac{\partial U^2}{\partial x} + \frac{V}{2}\frac{\partial U^2}{\partial y}}_{(a)} - \underbrace{\overline{uv}\frac{\partial U}{\partial y}}_{(b)} + \underbrace{\frac{\partial U\overline{uv}}{\partial y}}_{(c)} - \underbrace{\frac{\nu}{2}\frac{\partial^2 U^2}{\partial y^2}}_{(e)} - \underbrace{g\beta U(T - T_\infty)}_{(f)} + \underbrace{E}_{(g)} = 0 \qquad (1)$$

Turbulent energy components

$$\underbrace{\frac{U}{2}\frac{\partial \overline{u^2}}{\partial x} + \frac{V}{2}\frac{\partial \overline{u^2}}{\partial y}}_{(a)} + \underbrace{\overline{uv}\frac{\partial U}{\partial y}}_{(b)} + \underbrace{\frac{1}{2}\frac{\partial \overline{u^2 v}}{\partial y}}_{(c)} + \underbrace{\frac{1}{\rho}\overline{u\frac{\partial p}{\partial x}}}_{(d)} - \underbrace{\frac{\nu}{2}\frac{\partial^2 \overline{u^2}}{\partial y^2}}_{(e)} - \underbrace{g\beta\,\overline{ut}}_{(f)} + \underbrace{\varepsilon_u}_{(g)} = 0 \qquad (2)$$

$$\underbrace{\frac{U}{2}\frac{\partial \overline{v^2}}{\partial x}+\frac{V}{2}\frac{\partial \overline{v^2}}{\partial y}}_{(a)}+\underbrace{\frac{1}{2}\frac{\partial \overline{v^3}}{\partial y}}_{(c)}+\underbrace{\frac{1}{\rho}\overline{v\frac{\partial p}{\partial y}}}_{(d)}-\underbrace{\frac{\nu}{2}\frac{\partial^2 \overline{v^2}}{\partial y^2}}_{(e)}+\underbrace{\varepsilon_v}_{(g)}=0 \quad (3)$$

$$\underbrace{\frac{U}{2}\frac{\partial \overline{w^2}}{\partial x}+\frac{V}{2}\frac{\partial \overline{w^2}}{\partial y}}_{(a)}+\underbrace{\frac{1}{2}\frac{\partial \overline{vw^2}}{\partial y}}_{(c)}+\underbrace{\frac{1}{\rho}\overline{w\frac{\partial p}{\partial z}}}_{(d)}-\underbrace{\frac{\nu}{2}\frac{\partial^2 \overline{w^2}}{\partial y^2}}_{(e)}+\underbrace{\varepsilon_w}_{(g)}=0 \quad (4)$$

Reynolds shear stress

$$\underbrace{U\frac{\partial \overline{uv}}{\partial x}+V\frac{\partial \overline{uv}}{\partial y}}_{(a)}+\underbrace{\overline{v^2}\frac{\partial U}{\partial y}}_{(b)}+\underbrace{\frac{\partial \overline{uv^2}}{\partial y}}_{(c)}+\underbrace{\frac{1}{\rho}\left(v\overline{\frac{\partial p}{\partial x}}+u\overline{\frac{\partial p}{\partial y}}\right)}_{(d)}-\underbrace{\nu\frac{\partial^2 \overline{uv}}{\partial y^2}}_{(e)}-\underbrace{g\beta\overline{vt}}_{(f)}+\underbrace{\varepsilon_{uv}}_{(g)}=0 \quad (5)$$

Temperature variance

$$\underbrace{\frac{U}{2}\frac{\partial \overline{t^2}}{\partial x}+\frac{V}{2}\frac{\partial \overline{t^2}}{\partial y}}_{(a)}+\underbrace{\overline{vt}\frac{\partial T}{\partial y}}_{(b)}+\underbrace{\frac{1}{2}\frac{\partial \overline{vt^2}}{\partial y}}_{(c)}-\underbrace{\frac{\alpha}{2}\frac{\partial^2 \overline{t^2}}{\partial y^2}}_{(e)}+\underbrace{\varepsilon_t}_{(g)}=0 \quad (6)$$

Turbulent heat fluxes

$$\underbrace{U\frac{\partial \overline{ut}}{\partial x}+V\frac{\partial \overline{ut}}{\partial y}}_{(a)}+\underbrace{\overline{vt}\frac{\partial U}{\partial y}+\overline{uv}\frac{\partial T}{\partial y}}_{(b)}+\underbrace{\frac{\partial \overline{uvt}}{\partial y}}_{(c)}+\underbrace{\frac{1}{\rho}t\overline{\frac{\partial p}{\partial x}}}_{(d)}-\underbrace{\frac{\partial}{\partial y}\left(\nu\overline{t\frac{\partial u}{\partial y}}+\alpha\overline{u\frac{\partial t}{\partial y}}\right)}_{(e)}-\underbrace{g\beta\overline{t^2}}_{(f)}+\underbrace{\varepsilon_{ut}}_{(g)}=0 \quad (7)$$

$$\underbrace{U\frac{\partial \overline{vt}}{\partial x}+V\frac{\partial \overline{vt}}{\partial y}}_{(a)}-\underbrace{\overline{vt}\frac{\partial U}{\partial x}+\overline{v^2}\frac{\partial T}{\partial y}}_{(b)}+\underbrace{\frac{\partial \overline{v^2t}}{\partial y}}_{(c)}+\underbrace{\frac{1}{\rho}t\overline{\frac{\partial p}{\partial y}}}_{(d)}-\underbrace{\frac{\partial}{\partial y}\left(\nu\overline{t\frac{\partial v}{\partial y}}+\alpha\overline{v\frac{\partial t}{\partial y}}\right)}_{(e)}+\underbrace{\varepsilon_{vt}}_{(g)}=0 \quad (8)$$

where,

$$\left.\begin{aligned} E &= \nu\left(\frac{\partial U}{\partial y}\right)^2 \\ \varepsilon_u &= \nu\left[\overline{\left(\frac{\partial u}{\partial x}\right)^2}+\overline{\left(\frac{\partial u}{\partial y}\right)^2}+\overline{\left(\frac{\partial u}{\partial z}\right)^2}\right] \\ \varepsilon_v &= \nu\left[\overline{\left(\frac{\partial v}{\partial x}\right)^2}+\overline{\left(\frac{\partial v}{\partial y}\right)^2}+\overline{\left(\frac{\partial v}{\partial z}\right)^2}\right] \\ \varepsilon_w &= \nu\left[\overline{\left(\frac{\partial w}{\partial x}\right)^2}+\overline{\left(\frac{\partial w}{\partial y}\right)^2}+\overline{\left(\frac{\partial w}{\partial z}\right)^2}\right] \end{aligned}\right\} \quad (9)$$

$$\left.\begin{aligned} \varepsilon_{uv} &= 2\nu\left(\overline{\frac{\partial u}{\partial x}\frac{\partial v}{\partial x}}+\overline{\frac{\partial u}{\partial y}\frac{\partial v}{\partial y}}+\overline{\frac{\partial u}{\partial z}\frac{\partial v}{\partial z}}\right) \\ \varepsilon_t &= \alpha\left[\overline{\left(\frac{\partial t}{\partial x}\right)^2}+\overline{\left(\frac{\partial t}{\partial y}\right)^2}+\overline{\left(\frac{\partial t}{\partial z}\right)^2}\right] \\ \varepsilon_{ut} &= (\nu+\alpha)\left(\overline{\frac{\partial u}{\partial x}\frac{\partial t}{\partial x}}+\overline{\frac{\partial u}{\partial y}\frac{\partial t}{\partial y}}+\overline{\frac{\partial u}{\partial z}\frac{\partial t}{\partial z}}\right) \\ \varepsilon_{vt} &= (\nu+\alpha)\left(\overline{\frac{\partial v}{\partial x}\frac{\partial t}{\partial x}}+\overline{\frac{\partial v}{\partial y}\frac{\partial t}{\partial y}}+\overline{\frac{\partial v}{\partial z}\frac{\partial t}{\partial z}}\right) \end{aligned}\right\}$$

In the above set, the terms (a) – (g) represent advection, production, turbulent diffusion, velocity(or temperature)-pressure gradient correlation, molecular diffusion, buoyancy production and dissipation, respectively. The values of each term in these equations are estimated by using measured values and their balances are shown in Figs. 3 – 5 and 8 – 11. The budget of $\overline{w^2}/2$ is omitted, because of the difficulty in measuring the turbulent diffusion term $\partial\,\overline{vw^2}/\partial y$. As commonly done, we assume isotropy of dissipated motion, we estimate dissipation terms as $\varepsilon_u = \varepsilon_v = \varepsilon_w = \varepsilon/3$ and $\varepsilon_{uv} = \varepsilon_{ut} = \varepsilon_{vt} = 0$. The ε value is obtained by integrating the u fluctuation spectra multiplied by square wave number. The velocity-pressure gradient correlation, temperature-pressure gradient correlation and dissipation rate ε_t were evaluated as the closing terms in the budgets from the measured values of all the other terms in relevant equations. To prevent confusion, less contributive terms are not shown in Figs. 3 - 5 and 8 – 11.

Figure 3 presents the balance of mean flow energy normalized by u_τ^4/ν. The energy produced by buoyancy, which becomes maximum at $y^+ \simeq 10-15$, is transported to the near-wall region by molecular diffusion and to the outer layer by turbulent diffusion. Also, part of the energy is convected downstream. In the outer layer, the mean flow energy is consumed for the production of turbulent energy through deformation of the mean motion by Reynolds shear stress, $-\overline{uv}(\partial U/\partial y)$, in a way similar to the case in the usual boundary layer. However, in the inner layer, the turbulent energy is countertransferred to the mean flow through Reynolds shear stress, which never occurs in the ordinary turbulent boundary layer.

The balances of the turbulent energy $\overline{u^2}/2$ and $\overline{v^2}/2$ normalized by u_τ^4/ν are shown in Figs. 4 and 5, respectively. The buoyancy production $g\beta\,\overline{ut}$ appears in the $\overline{u^2}/2$ balance. In the outer layer, the sum of production terms due to buoyancy and deformation of the mean motion is balanced with the sum of turbulent diffusion, velocity-pressure

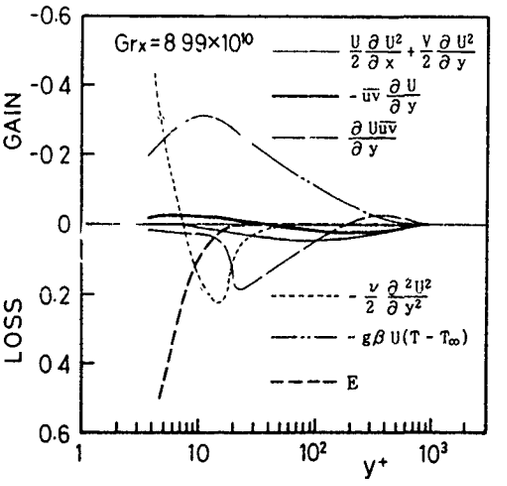

Fig. 3 Balance of mean flow energy $U^2/2$

gradient correlation and dissipation terms. It is apparent that the energy is transferred to the other fluctuating velocity components through the velocity-pressure gradient, while being transported to the inner layer and outermost region by the turbulent diffusion. In the near-wall region, however, the marked energy production by the velocity-pressure gradient correlation $\overline{u(\partial p/\partial x)}$ is observed, and is balanced with the production due to deformation of the mean motion, molecular diffusion and dissipation. Consequently, turbulent energy is countertransferred to mean flow through Reynolds shear stress. Such an energy transfer process hardly appears in the ordinary turbulent boundary layer, because the velocity-pressure gradient term is generally considered to play a dominant role of energy redistribution provided that the pressure diffusion is small.

On the other hand, there is no buoyancy production in the $\overline{v^2}/2$ balance. In the outer layer, the energy $\overline{v^2}/2$, transferred from $\overline{u^2}/2$ through the velocity-pressure gradient correlation, is consumed by dissipation and turbulent diffusion as in the usual boundary layer. However, a large energy production through the velocity-pressure gradient correlation $\overline{v(\partial p/\partial y)}$ is also seen in the near-wall region. As mentioned above, because the velocity-pressure gradient correlation $\overline{u(\partial p/\partial x)}$ plays a role of not a loss but a gain of $\overline{u^2}/2$, the production through $\overline{v(\partial p/\partial y)}$ is never the redistribution from that. This produced energy is consumed by turbulent diffusion toward the outer layer, molecular diffusion toward the wa and dissipation.

The energy transfer process in the thermally driven boundary layer, which differs remarkably from that in the ordinary turbulent boundary layer, is explained as follows. In the thermally driven flow, the energy of fluid flow has its source in the thermal energy supplied from a heated plate. The balance of the thermal energy (including the potential energy) may be expressed by the following equation with the boundary-layer approximation (Monin & Yaglom 1971):

$$U\frac{\partial T}{\partial x} + V\frac{\partial T}{\partial y} + \frac{\partial \overline{vt}}{\partial y} - \alpha\frac{\partial^2 T}{\partial y^2} + \frac{1}{c_p}\left[g\beta U(T - T_\infty) - \frac{1}{\rho}\left(\overline{u\frac{\partial p}{\partial x}} + \overline{v\frac{\partial p}{\partial y}} + \overline{w\frac{\partial p}{\partial z}}\right) + g\beta\,\overline{ut} - E - \varepsilon\right] = 0 \qquad (10)$$

In the above equation, the terms enclosed in the bracket are generally of very low order and usually neglected for the thermal energy budget. However, they are very important for investigating the production and dissipation of mean flow and turbulent energies. Thus, the terms are, in fact, the buoyancy production, velocity-pressure gradient correlation and dissipation terms in Eqs. (1)– (4). Thermal energy is converted into kinetic energy through these terms. Therefore, it is evident that the velocity-pressure gradient correlation plays a role of turbulent energy production in the near-wall region where the thermal energy is very high. Moreover, it can be easily understood that the production rates near the wall for the balances of $\overline{u^2}/2$ and $\overline{v^2}/2$ become nearly equal, since destruction or conversion of the thermal energy has no directional preference.

An energy transfer process near the wall based on the above discussion is depicted in Fig. 6. This figure indicates that it is never unnatural for the distributions of turbulent quantities to contrast markedly with those in the ordinary turbulent boundary layer appearing near the wall as shown in Figs. 1 and 2. Figure 7 illustrates the possible energy transfer process in the outer layer. In this region, the energy transfer can be considered to be a similar process as seen in the usual boundary layer.

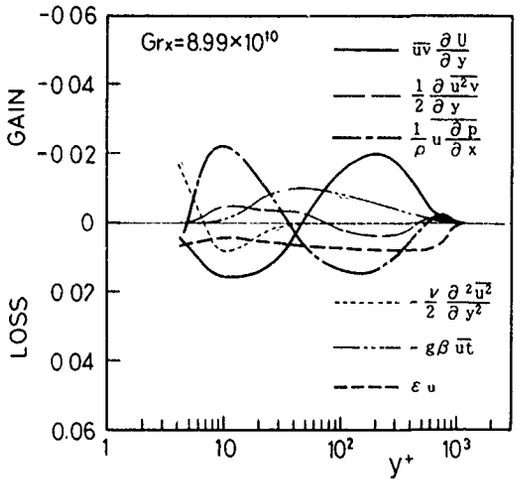

Fig. 4 Balance of turbulent energy $\overline{u^2}/2$

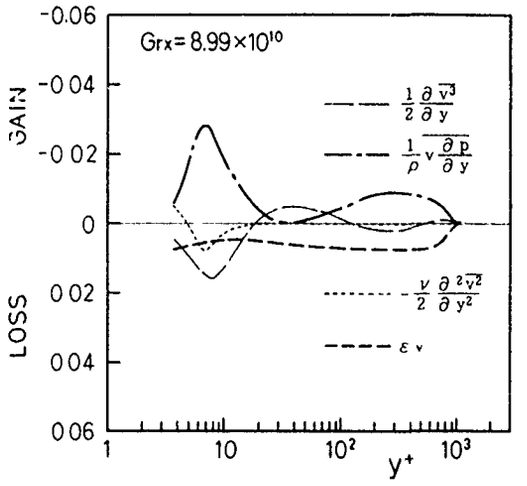

Fig. 5 Balance of turbulent energy $\overline{v^2}/2$

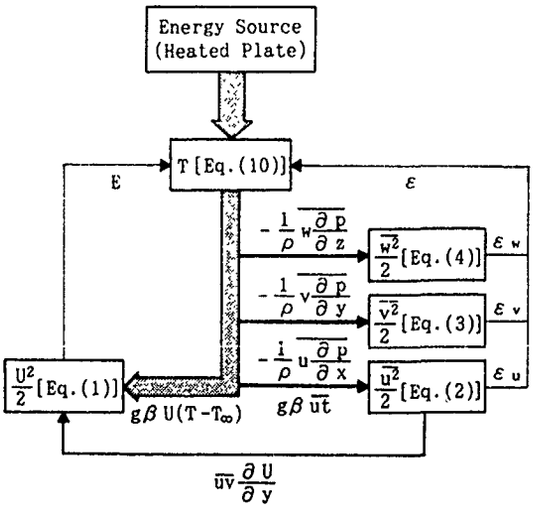

Fig. 6 Energy transfer process in near-wall region

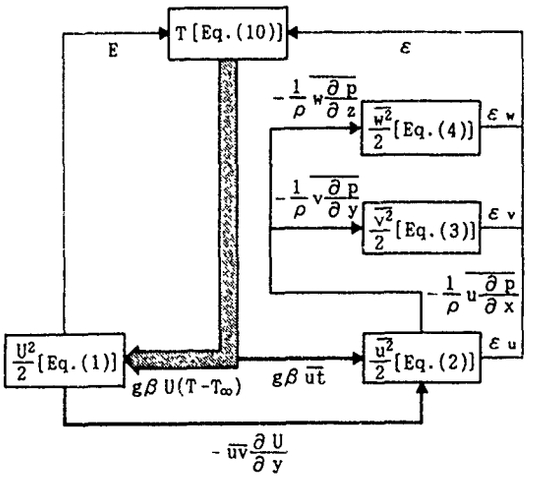

Fig. 7 Energy transfer process in outer region

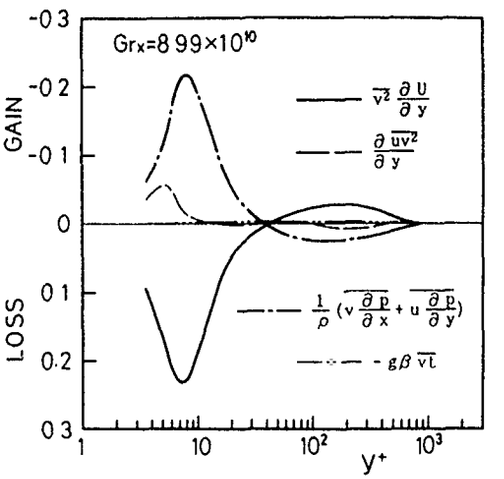

Fig. 8 Balance of Reynolds shear stress $\overline{uv}$

There have been some theoretical studies using turbulence models for the natural convection boundary layer (To & Humphrey 1986; Heiss, Straub & Catton 1988; Nagano, Yin & Tsuji 1989; Henkes & Hoogendoorn 1989, 1990). Among these studies, Nagano, Yin & Tsuji (1989) proposed a model based on an assumption that a velocity fluctuation is composed of a forced-convection component and a buoyancy-influenced component. This model reflects to some extent the above-mentioned turbulent characteristics of the thermally driven boundary layer, since some production terms other than the buoyancy production $g\beta\,\overline{ut}$ are consequently added in the turbulent energy equation. For this reason, the profiles of turbulent quantities shown in Figs. 1 and 2 have been well predicted with this model.

The balance of the Reynolds shear stress normalized by u_τ^4/ν is shown in Fig. 8. The production and velocity-pressure gradient correlation are clearly the dominant terms through the whole boundary layer region. In the near-wall region, the turbulent diffusion also contributes to the balance. The molecular diffusion does not appear at all, although it contributes to the balance near the wall in the usual boundary layer (Nagano & Hishida 1985). The disappearance of the molecular diffusion results from the fact that Reynolds shear stress becomes almost zero in the near-wall region as shown in Fig. 2.

Figure 9 shows the balance of half the temperature variance $\overline{t^2}/2$ normalized by $u_\tau^2 t_\tau^2/\nu$. The maximum production of temperature fluctuations occurs at $y^+ \simeq 15$, and the intensity of temperature fluctuation becomes maximum there as seen in Fig. 1. In the inner layer, the produced temperature fluctuations are transported toward the wall by turbulent and molecular diffusions. This balance shows little difference from that obtained in the usual boundary layer (Nagano & Hishida 1985; Krishnamoorthy & Antonia 1987).

The balances of streamwise and normal heat fluxes, $\overline{ut}$ and $\overline{vt}$, normalized by $u_\tau^3 t_\tau/\nu$, are shown in Figs. 10 and 11, respectively. The $\overline{ut}$ balance presents great complexity, reflecting the peculiar $\overline{ut}$ distribution as shown in Fig. 2. In the near-wall region, the production term of $\overline{ut}$ contributes as a large loss and is balanced with the other terms contributing as gains. On the other hand, the $\overline{vt}$ balance is mainly dominated by the production and temperature-pressure gradient correlation. The normal heat flux is transported toward the wall by the molecular diffusion and toward the outer layer by the turbulent diffusion.

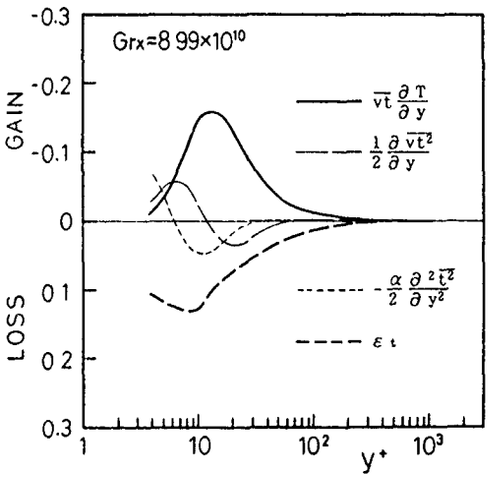

Fig. 9 Balance of temperature variance $\overline{t^2}/2$

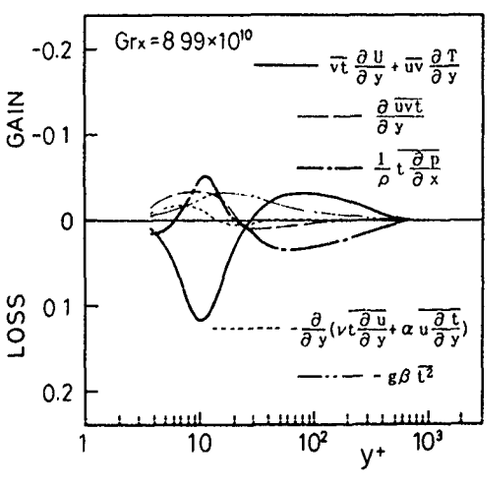

Fig. 10 Balance of streamwise heat flux $\overline{ut}$

This balance has a resemblance to that in the ordinary turbulent boundary layer (Nagano & Hishida 1985).

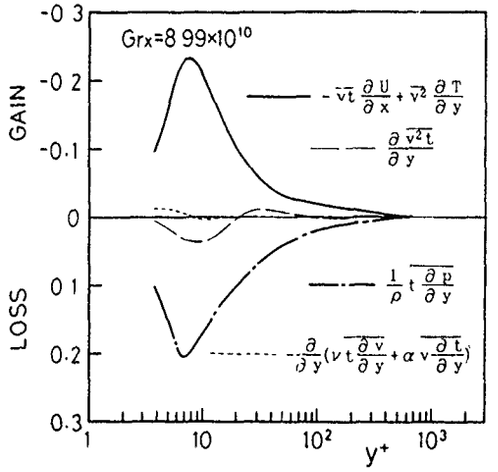

Fig. 11 Balance of normal heat flux $\overline{vt}$

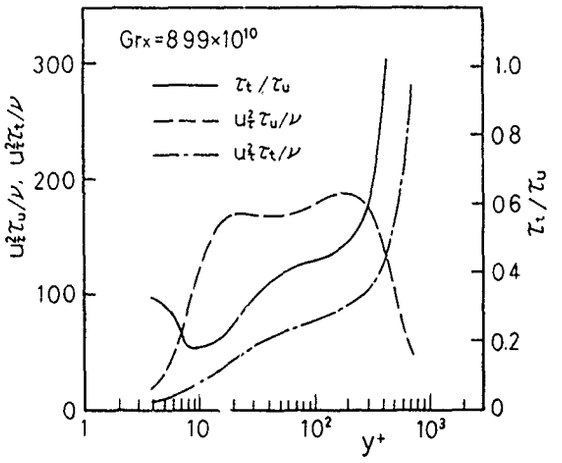

Fig. 12 Time scales of velocity and temperature fluctuations

TIME SCALES OF VELOCITY AND TEMPERATURE FLUCTUATIONS

Time scales of velocity and temperature fluctuations, τ_u ($= k/\varepsilon$) and τ_t ($= \overline{t^2}/2)/\varepsilon_t$), needed to construct a better turbulence model for thermally driven flows, are presented in Fig. 12. The time scale τ_u takes a profile corresponding with those of the intensities $\sqrt{\overline{u^2}}$ and $\sqrt{\overline{w^2}}$, since the dissipation rate of turbulent energy is estimated to become nearly constant in most of the boundary layer as shown in Figs. 4 and 5. On the other hand, the time scale τ_t increases monotonously from the near-wall to the outer region. Thus, the ratio τ_t/τ_u varies with the location in the boundary layer, whereas this ratio appears to be fairly uniform in forced convection, i.e., $\tau_t/\tau_u \simeq 0.5$ (Nagano & Hishida 1985). This result indicates that the turbulence models mainly based on the time scale of velocity fluctuation would fail to make a correct prediction of the thermal field (Nagano, Yin & Tsuji 1989).

CONCLUDING REMARKS

It has been clarified in the present study why the energy transfer process near the wall in the the thermally driven turbulent boundary layer differs remarkably from that observed in forced convection. In the near-wall region, the velocity-pressure gradient correlation plays an important role of turbulent energy production and converts a part of thermal energy directly into the turbulent energy. Consequently, the unique distributions of Reynolds shear stress and streamwise turbulent heat flux appear near the wall, which are rarely seen in the ordinary boundary layer.

The present evaluation of each term in the transport equations for turbulent energy, Reynolds shear stress, temperature variance and turbulent heat fluxes is believed to be suitable for the development of new models concerning thermally driven turbulent flows.

REFERENCES

Heiss, A., Straub, J. & Catton, I. 1988 Application of turbulence models to natural convection from a vertical isothermal plate. In *Proc. 25th National Heat Transfer Conf.*, Vol. 2, pp. 181-190. Houston.

Henkes, R. A. W. M. & Hoogendoorn, C. J. 1989 Comparison of turbulence models for the natural convection boundary layer along a heated vertical plate. *Intl J. Heat Mass Transfer* 32, 157-169.

Henkes, R. A. W. M. & Hoogendoorn, C. J. 1990 Numerical determination of wall functions for the turbulent natural convection boundary layer. *Intl J. Heat Mass Transfer* 33, 1087-1097.

Hishida, M., Nagano, Y. & Tagawa, M. 1986 Transport processes of heat and momentum in the wall region of turbulent pipe flow. In *Proc. 8th Intl Heat Transfer Conf.*, Vol. 3, pp. 925-930. San Francisco.

Krishnamoorthy, L. V. & Antonia, R. A. 1987 Temperature-dissipation measurements in a turbulent boundary layer. *J. Fluid Mech.* 176, 265-281.

Monin, A. S. & Yaglom, A. M. 1971 *Statistical fluid mechanics.* Vol. 1, pp. 52-59. MIT Press, Cambridge.

Nagano, Y. & Hishida, M. 1985 Production and dissipation of turbulent velocity and temperature fluctuations in fully developed pipe flow. In *Proc. 5th Symposium on Turbulent Shear Flows*, pp. 14.19-14.24. Cornell Univ., New York.

Nagano, Y., Yin, Y. & Tsuji, T. 1989 Numerical prediction of turbulent buoyant flows. In *Proc. 7th Symposium on Turbulent Shear Flows*, pp. 12.1.1-12.1.6. Stanford Univ., Stanford.

To, W. M. & Humphrey, J. A. C. 1986 Numerical simulation of buoyant, turbulent flow - 1. Free convection along a heated, vertical, flat plate. *Intl J. Heat Mass Transfer* 29, 573-592.

Tsuji, T. & Nagano, Y. 1988a Characteristics of a turbulent natural convection boundary layer along a vertical flat plate. *Intl J. Heat Mass Transfer* 31, 1723-1734.

Tsuji, T. & Nagano, Y. 1988b Turbulence measurements in a natural convection boundary layer along a vertical flat plate. *Intl J. Heat Mass Transfer* 31, 2101-2111.

Tsuji, T. & Nagano, Y. 1989 An anemometry technique for turbulence measurements at low velocities. *Exp. Fluids* 7, 547-559.

Tsuji, T., Nagano, Y. & Tagawa, M. 1990 Experiment on spatial and temporal turbulent structures of a natural convection boundary layer. In *Heat Transfer in Turbulent Flow*, HTD-Vol. 138 (ed. R. S. Amano et al.), pp. 19-26. ASME, New York.

EIGHTH SYMPOSIUM ON
TURBULENT SHEAR FLOWS
Technical University of Munich
September 9-11, 1991

THE PREDICTION OF CONVECTIVE HEAT TRANSFER IN ROTATING SQUARE DUCTS

T. Bo, H. Iacovides and B.E. Launder

Department of Mechanical Engineering, UMIST,
PO Box 88, Manchester. M60 1QD. U.K.

ABSTRACT

This paper presents a numerical study of developing flow through a heated duct of square cross-section rotating in an orthogonal mode. Two different turbulence models have been employed. An effective viscosity model (EVM) and an algebraic stress model (ASM). In both cases simplified near-wall models were employed in which the solution of the ϵ transport equation was not carried out. At moderate rotational speeds the EVM heat transfer predictions are found to be in close agreement with existing measurements. At high rotational rates rotational buoyancy effects are shown to become important. EVM predicted heat transfer behaviour while still reasonable, begins to deviate from the experimental one. The ASM model with a simplified near-wall extension has been found to be even less appropriate when rotational buoyancy is significant

1. INTRODUCTION

How is the heat-transfer coefficient on the inside of a tube affected by the tube's rotation about an axis perpendicular to its own? The question is an important one to address in designing the internal cooling passages of gas turbine blades. In the application in question the rotation introduces two body forces: that due purely to rotation (the Coriolis force) and that associated with the varying centrifugal force over the duct's cross section due to the significant variations in coolant density. Moreover, these forces act both in the mean momentum equations and directly on the turbulent velocity fluctuations. The net outcome of these several influences is hard to foresee, still less to quantify The secondary mean motion induced by Coriolis forces may be expected to increase mixing while the Coriolis forces acting on the Reynolds stresses will tend to suppress turbulent transport on the suction face and augment it on the pressure surface. Reference to data of vertical flow in strongly heated (stationary) tubes indicates that for upflow (i.e. motion in opposition to the acceleration vector), near-wall turbulent transport is inhibited, while in downflow it is augmented - the effect on Nusselt number being the reverse of that found in laminar flow [1]. Just what the contribution of buoyancy might be in the presence of the strong Coriolis-induced secondary motions found in rotating tubes is open to question.

The problem of predicting turbulent flow in rotating ducts has been a live one for several years since (at least in the case of fully developed flow) the numerical task is not too severe. There has, however, been a dearth of experimental data for the uniform-density case just the admirable but limited Ito-Nanbu [2] friction-factor correlation. In the case of heat transfer, none of the available data seemed to have overcome the problem of heat conduction effects in the pipe wall. This situation has been greatly improved by the recent data of Wagner et al. [3] who for the first time provide, for the case of a square-sectioned duct, a sufficiently comprehensive set of data to allow one to discern the distinct contributions of buoyant and Coriolis forces to the level of Nusselt number. The present paper has focused on two test cases from this last study with the purpose of determining how successful different levels or engineering turbulence model are at capturing the measured thermal behaviour. The models in question are presented in §2 together with a summary of the more important features of the solver. Comparisons of the predicted and measured Nusselt number variations along the tube are reported in §3.

2. THE MATHEMATICAL MODEL

2.1 The Mean Field Equations

The Reynolds and continuity equations describing the motion of turbulent flow in an arbitrarily rotating coordinate system may be written

$$\frac{\partial}{\partial x_j}(\rho U_j U_i) = -\frac{\partial P}{\partial x_i} + \frac{\partial}{\partial x_j}\left\{\mu\left[\frac{\partial U_i}{\partial x_j}+\frac{\partial U_j}{\partial x_i}\right] - \rho\overline{u_i u_j}\right\} - 2\rho\epsilon_{ij}\rho_j\,\Omega_p\,U_j - \rho\{\Omega_j\times_j\Omega_i - \Omega_j\times_i\Omega_j\} \quad (1)$$

$$\frac{\partial}{\partial x_i}(\rho U_i) = 0 \quad (2)$$

The local density ρ is related to the mean temperature θ through

$$\rho = \rho_0\theta_0/\theta \quad (3)$$

and the temperature is obtained from the energy equation

$$\frac{\partial}{\partial x_j}(\rho U_j\theta) = \frac{\partial}{\partial x_j}\left\{\lambda\frac{\partial\theta}{\partial x_j} - \rho\overline{u_j\theta}\right\} \quad (4)$$

3. THE TURBULENCE MODEL

The turbulence stresses have been modelled in two different ways; through an eddy viscosity model (EVM) and through an algebraic second-moment (ASM) closure. This modelling approach allows us to investigate the influence exerted by non-isotropic turbulence on mean flow and heat transfer through rotating ducts. Earlier work carried out by the authors in both rotating and stationary duct flows [4,5] has shown that the flow equations need to be solved for the entire flow domain including the viscosity affected near-wall regions. In the fully turbulent region of the flow both the EVM and the ASM models entailed the solution of transport equations for the turbulence energy (k) and its viscous dissipation rate (ϵ). In this first set of developing flow computations only the k transport equation was solved across the wall sublayer regions. The near-wall ϵ distribution was obtained from a prescribed near-wall length scale.

k and ϵ transport equations

$$\frac{\partial}{\partial x_j}\{\rho U_j k\} = d_k + \rho P_k - \rho\epsilon \quad (5)$$

$$\frac{\partial}{\partial x_j}\{\rho U_j\epsilon\} = d_\epsilon + c_{\epsilon 1}\frac{\epsilon}{k}\rho P_k - c_{\epsilon 2}\,\rho\,\frac{\epsilon^2}{k} \quad (6)$$

where P_k, the generation of turbulence energy, contains mean shear and buoyant terms:

$$P_k = -\overline{u_i u_j}\frac{\partial U_i}{\partial x_j} - \overline{\frac{\rho' u_i}{\rho}}\{\Omega_j x_j \Omega_l - \Omega_j \Omega_j x_i\} \quad (7)$$

$$\text{and } \overline{\frac{\rho' u_i}{\rho}} = -\overline{\frac{u_i \theta}{\theta}} \quad (8)$$

When the EVM closure is adopted, the diffusion rate of the various dependent variables is obtained from simple gradient diffusion approximations

$$d_\varphi = \frac{\partial}{\partial x_j}\left\{\left[\mu + \frac{\mu_t}{\sigma_\varphi}\right]\frac{\partial \varphi}{\partial x_j}\right\} \quad \varphi = k, \epsilon \quad (9)$$

$$\overline{u_i u_j} = \frac{2}{3} k \delta_{ij} - \nu_t\left\{\frac{\partial U_i}{\partial x_j} + \frac{\partial U_j}{\partial x_i}\right\} \quad (10)$$

$$\overline{u_i \theta} = -\frac{\nu_t}{\sigma_\theta}\frac{\partial \theta}{\partial x_i} \quad (11)$$

where the turbulent viscosity ν_t is obtained from

$$\nu_t = c_\mu k^2/\epsilon \quad (12)$$

In the case of the ASM closure

$$d_\varphi = \frac{\partial}{\partial x_j}\left\{\left[\nu \delta_{ij} + c_\varphi \frac{k}{\epsilon}\overline{u_l u_j}\right]\frac{\partial \varphi}{\partial x_l}\right\} \quad \varphi = k, \epsilon \quad (13)$$

$$\frac{\overline{u_i u_j} - \frac{2}{3}\delta_{ij}k}{k} = \frac{(1-c_2)(P_{ij} - \frac{2}{3}P_k \delta_{ij})}{\epsilon(c_1 - 1 + f_s + P_k/\epsilon)} + \frac{f_w \varphi^w_{ij}}{\epsilon(c_1 - 1 + f_s + P_k/\epsilon)} - \frac{(H_{ij} - \frac{1}{3}H_k \delta_{ij})}{\epsilon(c_1 - 1 + f_s + P_k/\epsilon)} + \frac{0.06k\left[\frac{\partial U_i}{\partial x_j} + \frac{\partial U_j}{\partial x_i}\right]\exp(-y^*/2.67)}{\epsilon(c_1 - 1 + f_s + P_k/\epsilon)} \quad (14)$$

$$\overline{u_i \theta} = -c_\theta \frac{k}{\epsilon}\overline{u_i u_j}\frac{\partial \theta}{\partial x_j} \quad (15)$$

$$\text{where } P_{ij} = -\overline{u_i u_k}\frac{\partial U_i}{\partial x_k} - \overline{u_j u_k}\frac{\partial U_j}{\partial x_k} - 2\Omega_p\left\{\epsilon_{ipq}\overline{u_q u_j} + \epsilon_{jpq}\overline{u_q u_i}\right\} - \overline{\frac{u_i \rho'}{\rho}}\left\{\Omega_k x_k \Omega_j - \Omega_k \Omega_k x_j\right\} - \overline{\frac{u_j \rho'}{\rho}}\left\{\Omega_k x_k \Omega_i - \Omega_k \Omega_k x_i\right\} \quad (16)$$

φ^w_{ij} is the wall echo part of the pressure-strain correlation approximated via the proposal of Gibson and Launder [6].

The remaining terms in equation (14) have been recently devised from within the authors' group [7,8] in order to produce a simple near-wall extension of the ASM model. These low-Re terms are empirical in nature and have been tuned to give reasonable accord with experiment for fully developed flow in a non-rotating straight pipe. They also led to marked improvement of the flow field in flow through an S-bend [7]. The resulting near-wall stress model, though crude in nature, nevertheless allows us to investigate the influence of turbulence anisotropy within the viscosity-affected sublayer on three-dimensional boundary layers. Here:

$$f_s = \exp(-y^*/4) \quad (17)$$

$$f_w = [1 - \exp(-0.12y^*)][1 + \exp(-0.03y^*)] \quad (18)$$

$$H_{ij} = f_H\left\{\overline{u_i u_\ell}\frac{\partial \sqrt{k}}{\partial x_\ell}\frac{\partial \sqrt{k}}{\partial x_j} + \overline{u_j u_\ell}\frac{\partial \sqrt{k}}{\partial x_\ell}\frac{\partial \sqrt{k}}{\partial x_i}\right\} \quad (19)$$

$$f_H = \{13 + 6y^*\}\exp(-0.07y^*) \quad (20)$$

$$\text{where } y^* = \frac{y\sqrt{k}}{\nu} \quad (21)$$

with y being the distance from the wall to the point in question.

Within the near-wall region the dissipation rate and turbulent viscosity for the EVM are obtained from:

$$\epsilon = k^{3/2}/\ell_\epsilon \quad (22)$$

$$\nu_t = C_\mu \sqrt{k}\,\ell_\mu \quad (23)$$

where

$$\left.\begin{aligned}\ell_\epsilon &= 2.5y(1 - \exp(-0.263y^*)\\ \ell_\mu &= 2.5y(1 - \exp(-0.016y^*)\end{aligned}\right\} \quad (24)$$

The near-wall dissipation rate with the ASM is also obtained from equation (23) but with ℓ_ϵ defined as

$$\ell_\epsilon = 2.5y(1 - \exp(-0.235y^*) \quad (25)$$

For fully developed flow in a straight pipe the above model generates a broadly correct shear stress variation across the sublayer. No attempt has been made however to satisfy the limit of two-component turbulence.

The flow equations are solved for a Cartesian coordinate system rotating in orthogonal mode, Figure 1. The solution domain covers a rectangular half-section of the square duct on one side of the duct symmetry plane. A three-dimensional parabolic solution procedure is employed. The solver, which has been described in a number of earlier publications [4,9], is of finite-volume type with staggered locations for the velocity and turbulent stress components, relative to the pressure. For the discretization of the cross-stream mean flow convection, the non-diffusive QUICK scheme is employed.

The cross-stream mesh consisted of 35 x 67 nodes, 10 of which are located within the near-wall 1-equation region. Earlier work on rotating and also stationary ducts [5,11] shows that such a cross-stream mesh is sufficiently fine to reduce numerical errors to insignificant levels. A total of 200 planes were employed in the streamwise direction covering a duct length of 20 hydraulic diameters. The y^+ value at the interface between the high and the low-Reynolds number regions was between 50 and 80.

4. PRESENTATION AND DISCUSSION OF COMPUTATIONS

Two cases of developing flow through a rotating duct of square cross-section have been computed, corresponding to inverse Rossby number values of 0.12 and 0.24. In both cases the flow Reynolds number was 25000 and the flow direction is away from the axis of rotation (outward flow). In solving for the thermal field a uniform wall temperature was prescribed. The rotational Rayleigh numbers, based on the difference between the wall and fluid temperatures at inlet are 2.5×10^7 and 10^8 for the lower and higher rotational speeds respectively. The experimental study of Wagner et al. [3] provides measurements of the side averaged Nusselt number values for these two cases.

The hydrodynamic entry conditions that more closely resemble those of the experimental study are those corresponding to fully developed flow in a stationary duct. As far as the thermal field is concerned, the fluid enters the duct with uniform temperature. In the subsequent Nusselt number comparisons, in order to minimize the effects of any inconsistencies between the numerical and the experimental entry conditions, the levels of the side averaged Nusselt number values were normalized with those corresponding to stationary duct flow at the same stage of thermal development.

To distinguish clearly between the effects of Coriolis and buoyancy forces, computations have also been carried out with ρ held strictly constant thus suppressing buoyant influences.

Figure 2 shows the k-ϵ predictions of the mean flow development over the first 12 hydraulic diameters for the lower rotational speed case. They show that the Coriolis induced secondary flow gradually transports the high momentum fluid from the centre of the duct towards the pressure side, leaving slow moving fluid on the suction side of the duct The corresponding constant density flow predictions show no significant differences indicating that at this combination of flow parameters, rotational buoyancy effects are of minor importance.

Figure 3 presents the corresponding mean flow plots for the higher rotational speed case. Because of the stronger secondary velocity, the rate of flow development is now faster than it was in the case of Ro = 0.12. The stronger Coriolis force also leads to the development of thinner boundary layers on the pressure side and thicker ones at the suction side than in the previous case. Another important observation is that there are now significant differences between the constant density and the buoyant flow predictions. Clearly at this higher rotational speed case rotational buoyancy effects play a major role in determining the flow development and for outward flow they enhance the Coriolis effects.

Nusselt number comparisons between the experimental data and the EVM predictions are presented in Figure 4. At the lower rotational speed (Figure 4a) the effects of rotation on mean heat transfer are well captured by the EVM model. Exclusion of the rotational buoyancy terms from the flow equations does lead to some deterioration in the EVM Nusselt number predictions. Nevertheless the relatively small differences between the constant density and buoyant flow predictions confirm that rotational buoyancy effects are of minor importance for this case

The higher rotational speed comparisons shown in Figure 4b reveal a different picture. There are now considerable differences between the buoyant and non-buoyant flow predictions over the developing flow region but as the flow approaches full development these differences with buoyancy effects included are substantially reduced. Nusselt number predictions are reasonably close to the experimental data. Nevertheless the experimental behaviour at Ro = .24 is not reproduced by the EVM model with the same degree of fidelity as that observed at Ro = 0.12 Along the suction side of the duct in particular, the observed strong reduction in the side-averaged Nusselt number levels is not fully captured.

The predicted development of the local Nusselt number over the first 12 diameters is presented in Figure 5. The local distribution of Nu appears to be consistent with the mean flow behaviour The deviation from symmetry increases with downstream distance and for a given position it increases with rotational speed Another noticeable feature of the local distribution of Nusselt number is the strong variation that develops along the top side at the higher rotational speed.

Figure 6 presents comparisons between the ASM Nusselt number predictions and the experimental measurements. The ASM comparisons are confined to the case of the higher rotational speed. The use of the ASM for the case of the lower rotational speed had similar, though weaker, effects on the resulting predictions. The non-buoyant flow prediction of the Nusselt number development is similar to the corresponding k-ϵ prediction. The only noticeable difference is that the ASM scheme returns lower heat transfer levels along the suction side. When the buoyancy effects are included the ASM model predicts substantially higher heat transfer levels along the pressure side and also along the suction side. This response of the ASM model to buoyancy effects therefore leads to the prediction of the correct heat transfer levels along the pressure side of the rotating duct but also to unrealistically high wall heat fluxes along the suction side. It thus appears that the use of the present ASM model results in unrealistically high turbulence levels in the vicinity of the suction surface. The question arises whether the excessive levels of Nu result from too low levels of ϵ (i.e. to too large near-wall length scales) or from the basic ASM constitutive equation. Since virtually the same practice for obtaining ϵ is adopted in both the ASM and EVM schemes, the latter seems to be indicated. Accordingly, a further ASM computation was carried out in which the rotational buoyancy terms were included only in the mean flow equations. The resulting computation, shown in Figure 6, indicates that the high heat transfer levels along the duct suction side are caused by the additional generation of turbulence due to rotational buoyancy. The fact that the corresponding EVM terms do not have a similarly strong effect suggests that the generalized gradient-diffusion hypothesis, eq (11), which, in the ASM case is employed to model the turbulent heat fluxes, is responsible for the greater influence of the buoyant generation terms. The over-estimate of the suction-side turbulence levels is probably due to the current simplified version of the near-wall ASM model producing an unrealistically rapid rise in the near-wall shear stresses which in turn leads to excessively high buoyant generation rates of turbulence.

The ASM predictions of the development of the mean flow field are shown in Figure 7. The secondary flow field is stronger and more complex than that resulting from the EVM computations. In the buoyant flow computations the ASM predicts considerably thicker boundary layers along the pressure and top sides than the EVM. Along the suction side, the ASM model application results in thinner boundary layers. The behaviour on the suction side appears to be consistent with the predicted Nusselt number development.

5. CONCLUSIONS

An ASM and an EVM closure have been employed to predict the development of heated flow in a straight duct rotating in orthogonal mode. In both closures only the k transport equation was solved within the near-wall sublayer. Computations have been obtained for values of rotational flow parameters encountered in blade-cooling applications. The EVM model predictions of the Nusselt number are in reasonable agreement with the experimental measurements. These numerical computations also indicate that at high rotational speeds the rotational buoyancy has a substantial effect on the flow development. When rotational buoyancy becomes important the EVM model fails to predict the full extent of the attenuation in heat transfer observed along the duct suction side.

The replacement of the EVM by the more 'advanced' ASM model has however led to the computation of considerably higher (and thus even more unrealistic), heat transfer levels along the suction side. The anomalous behaviour has been traced to the effective buoyant generation terms in the stress budget. One possibility seems to be that, as direct buoyant effects on the *heat-flux* field are not accounted for, eq (11), excessive levels of the buoyant source terms in the $\overline{u_i u_j}$ equations result Further efforts at unravelling the problem will probably also require a more comprehensive treatment of the Reynolds stresses themselves in the viscous region.

6. ACKNOWLEDGEMENTS

The research has been jointly supported by Rolls-Royce plc and RAE Pyestock under Research Brochure B1D2-125D. The camera-ready mats have been produced with appreciated care by Mrs J. Buckley.

Authors' names are listed alphabetically.

7. REFERENCES

1 Cotton, M A and Jackson, J.D., Paper 9-6, 6th Symp. Turb. Shear Flows, Toulouse, France, 1987.

2. Ito, H. and Nanbu, K., J. Basic Engineering, 93, 383, 1971.

3. Wagner, J.H., Johnson, B.V. and Hajek, T.J., ASME Paper 89-GT-272, Int. Gas Turbine Congress, Toronto,

Canada, 1989.

4. Iacovides, H. and Launder, B.E., Paper 1-5, 6th Symp. Turb. Shear Flows, Toulouse, France, 1987.

5. Choi, Y-D., Iacovides, H. and Launder, B.E., ASME J. Fluids Engineering, 111, 59, 1989.

6. Gibson, M.M. and Launder, B.E., J. Fluid Mech., 86, 491, 1978.

7. Abou-Haidar, N.I., Iacovides, H. and Launder, B.E., 77th AGARD Symp., CFD Techniques for Propulsion Applications, San Antonio, Texas, USA, 1991.

8. Li, H., Personal communication, 1990.

9. Iacovides, H. and Launder, B.E., Proc. 4th Int. Conf. on Num. Meth. in Laminar and Turb. Flow, 1023-1045, Swansea, UK, 1985.

10. Iacovides, H. and Launder, B.E., Numerical Heat Transfer, 12, 475, 1987.

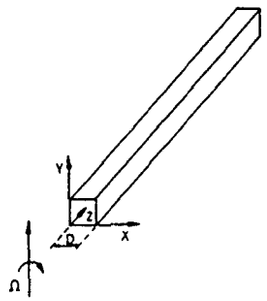

Fig 1 Flow Geometry

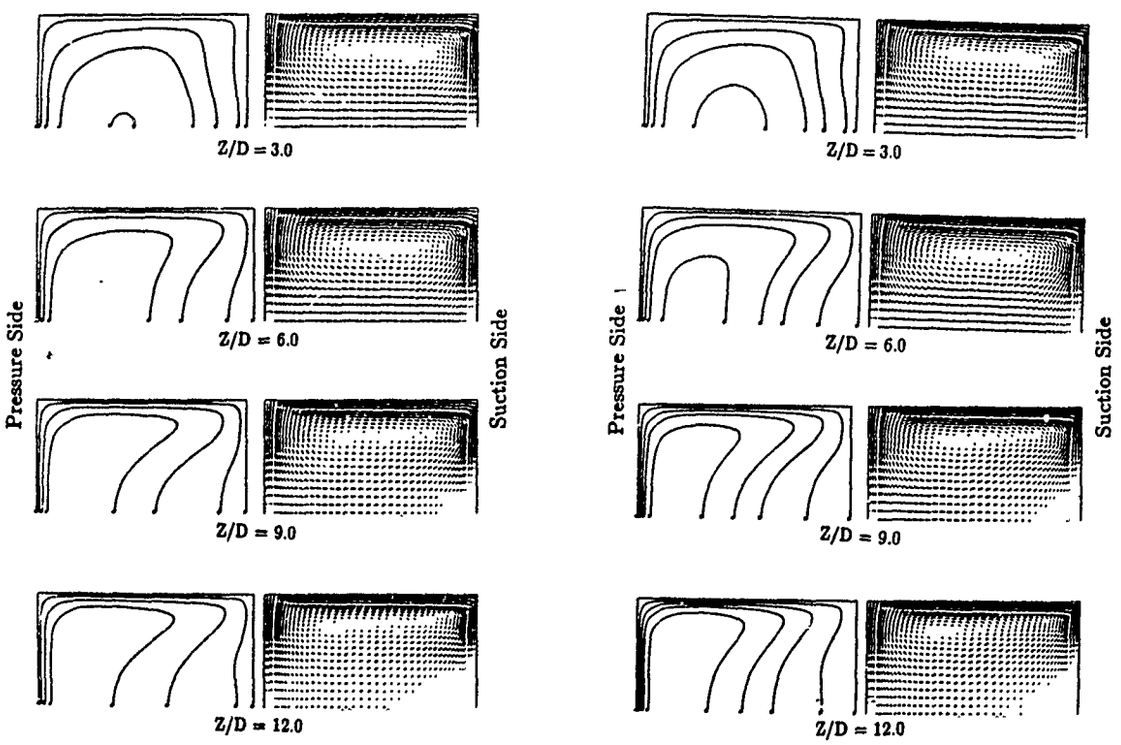

(a) Constant density flow

(b) Buoyant flow

Fig 2 EVM predicted mean flow field development for Ro = 0.12

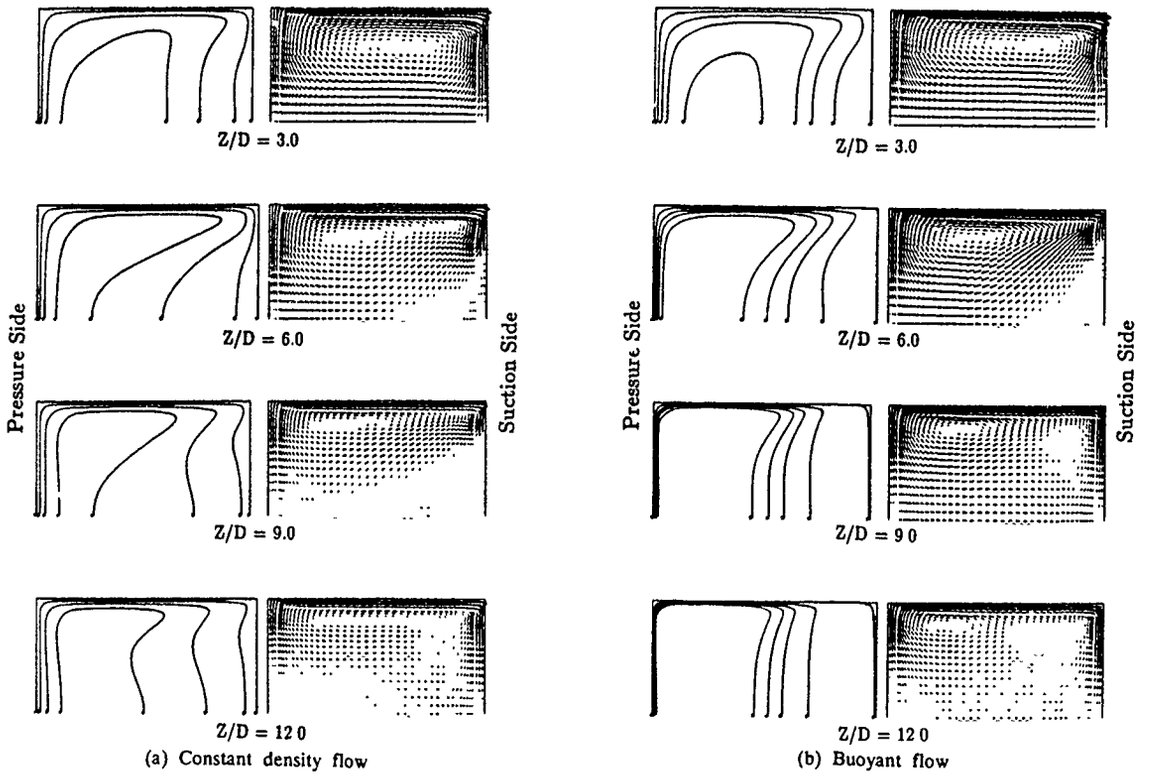

(a) Constant density flow (b) Buoyant flow

Fig 3 EVM predicted mean flow field development for Ro = 0.24

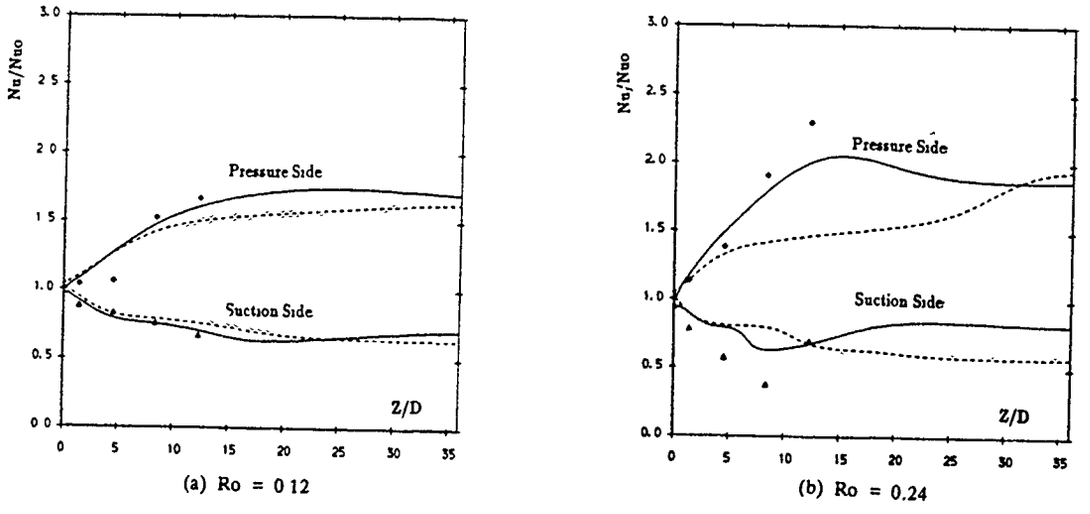

Fig 4 EVM comparisons of side-averaged Nusselt number development

—— EVM buoyant flow
---- EVM constant density flow
Δ Expt. data [3]

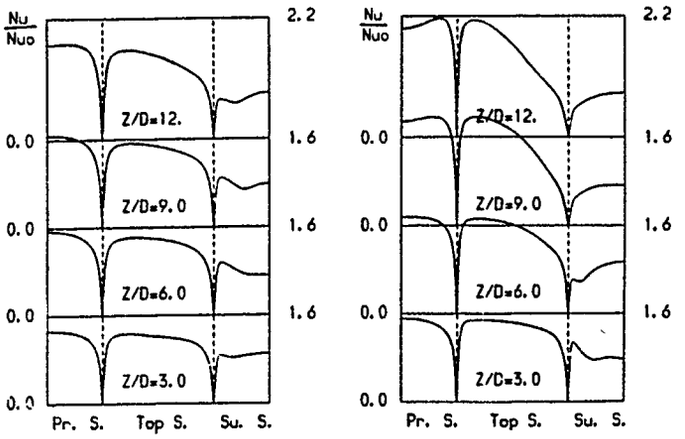

(a) Ro = 0.12 (b) Ro = 0.24

Fig 5 EVM predicted local Nusselt number development

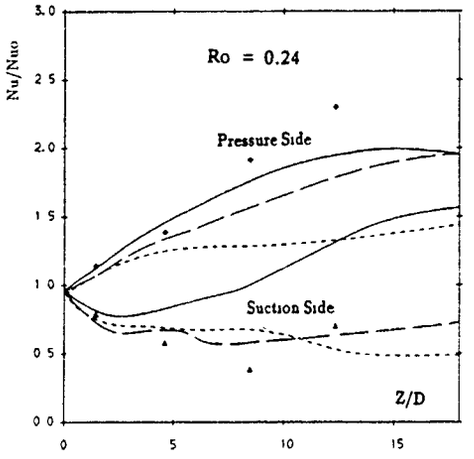

Fig 6 ASM comparisons of side-averaged Nusselt number development

——— ASM buoyant flow
- - - - - - ASM constant density flow
— - — ASM buoyancy effects on mean flow
Δ Expt data [3]

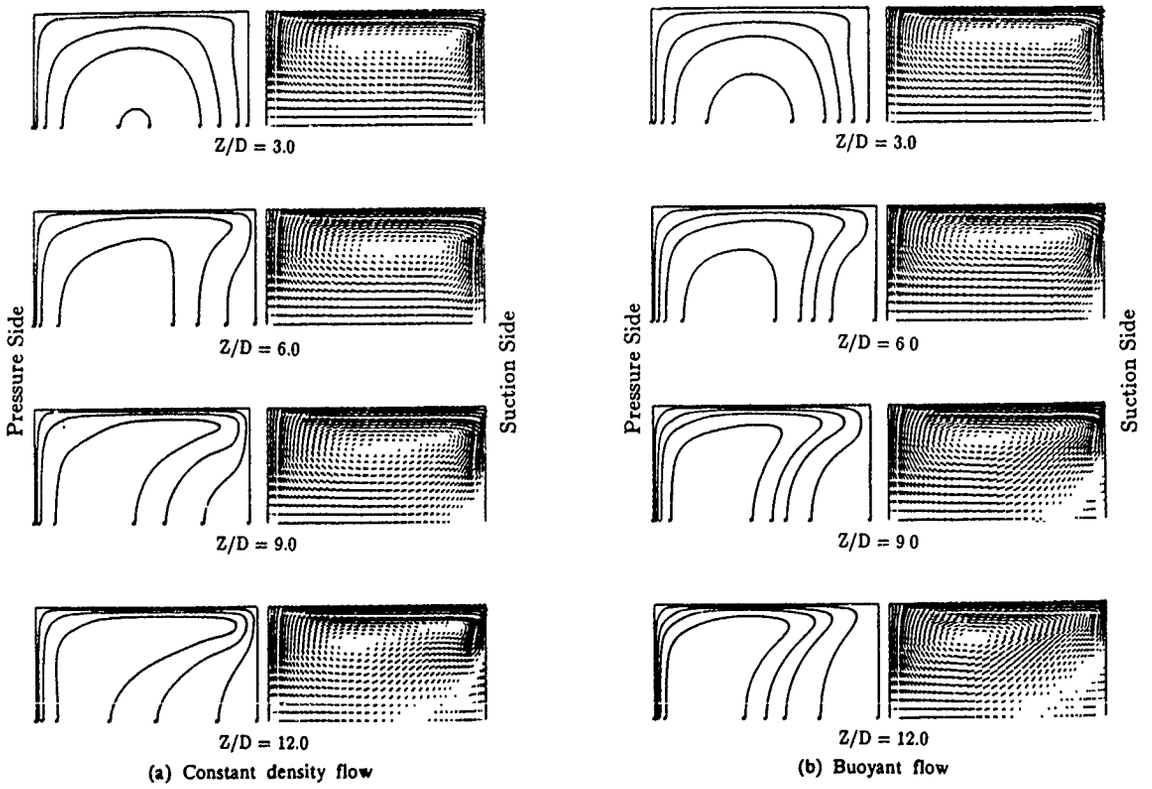

(a) Constant density flow (b) Buoyant flow

Fig 7 ASM predicted mean flow field development for Ro = 0.24

EIGHTH SYMPOSIUM ON
TURBULENT SHEAR FLOWS
Technical University of Munich
September 9-11, 1991

HEAT TRANSFER IN A TURBULENT BOUNDARY LAYER WITH AN INSERTION OF A LEBU PLATE

K. Suzuki, H. Suzuki, K. Inaoka and H. Kigawa

Department of Mechanical Engineering
Kyoto University, Kyoto 606, Japan

ABSTRACT

An experimental study was performed for a turbulent boundary layer disturbed by an insertion of the LEBU (Large Eddy Break-up) plate. Skin-friction coefficient, heat transfer coefficient, and averaged and fluctuating components of streamwise and cross-stream velocities were measured. Quadrant analysis was applied to the measured fluctuating velocity signals. Although the dissimilarity between the momentum transfer and heat transfer was conspicuous in a turbulent boundary layer disturbed by a cylinder, it is not so strong in the present type of disturbed boundary layer. The difference between the two cases is discussed in terms of the results of the applied quadrant analysis.

NOMENCLATURE

C_f : Skin Friction Coefficient ($= 2\tau_w/\rho U_e^2$)
C_p : Specific Heat at Constant Pressure of Fluid [J/kgK]
H : Cross-stream Position of a LEBU Plate [m]
H' : Hole Size Parameter
I_1 : Indicator for Quadrant Analysis
h : Heat Transfer Coefficient [W/m^{2}K]
L : Streamwise Width of a LEBU Plate [m]
St : Stanton Number ($= h/\rho C_p U_e$)
T : Mean Temperature [K]
t : Time [s]
U : Streamwise Mean Velocity [m/s]
u : Streamwise Fluctuating Velocity [m/s]
$-\overline{uv}$: Turbulent Shear Stress [m^2/s^2]
$\langle uv \rangle_1$: Fractional Contribution to $-\overline{uv}$ from the 1th Quadrant of u-v Plane [m^2/s^2]
v : Cross-stream Fluctuating Velocity [m/s]
x : Streamwise Coordinate Measured from the Leading Edge of a LEBU Plate [m]
y : Cross-stream Coordinate Measured from the Flat Plate Surface [m]
δ : Boundary Layer Thickness [m]
ρ : Fluid Density [kg/m^3]
τ : Shear Stress [Pa]

Suffix
e : Free Stream
w : Wall
0 : Undisturbed boundary layer
' : Intensity

INTRODUCTION

An insertion of cylinder into a flat plate turbulent boundary layer is known to generate an interesting feature of turbulent transport processes, i.e. the dissimilarity between the momentum and heat transfer processes in the boundary layer (Kawaguchi, Matsumori and Suzuki (1984), Suzuki, Suzuki and Sato (1988), Suzuki, Suzuki, Kikkawa, Kigawa and Kawaguchi (1991)). By the insertion of cylinder, wall heat transfer is enhanced in the downstream of cylinder but skin friction acting on the same part of flat plate is reduced. This dissimilarity is not a feature of giving any convenience in the analysis of turbulent heat transfer but it is interesting from physical view point. It is also important from a practical view point becuase it suggests a possibility of improving the heat transfer performance of heat ex-changers while suppressing the increase of pressure loss inside the heat exchangers. However, an increase of total momentum loss is not effectively suppressed in the case when a cylinder is inserted. This is because the form drag of an inserted body being an additional source of momentum loss is not small for a cylinder. In order to keep the increase of total momentum loss at low level, another body having smaller form drag must be introduced.

A Large Eddy Break-Up (LEBU) plate is known to be effective in reducing the wall skin friction (Savill and Mumford (1988), Nguyen, Savill and Westphal (1987)) and has small form drag. Therefore, its introduction into a turbulent boundary layer should be interesting from a view point that it can suppress a large increase of total momentum loss. However, unfortunately, there has been no heat transfer study for the case when a LEBU plate is inserted into a turbulent boundary layer. Thus, it is worth to explore if any dissimilarity can be generated by the insertion of a LEBU plate as in the case with the insertion of cylinder or more simply to see what are the effects on heat transfer to be

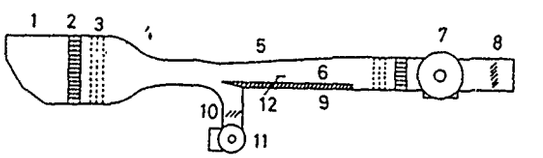

1 Entrance
2 Honeycomb
3 Screen
4 Contraction chamber
5 Upper wall
6 Test section
7 Main blower
8,10 Flow controller
9 Flat plate
11 Suction blower
12 *LEBU plate*

Figure 1 Schematic View of The Used Wind Tunnel

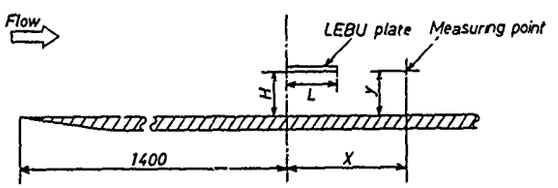

Figure 2 Geometry of The Studied Flow System, Coordinate System and Geometric Parameters

caused by the insertion of a LEBU plate into a turbulent boundary layer. Thus, this article discusses the heat transfer data and some related turbulence data obtained for a flat plate turbulent boundary layer with an insertion of a LEBU plate.

EXPERIMENTAL APPARATUS AND PROCEDURES

Experiments were performed in the wind tunnel used by Suzuki, Suzuki, Kikkawa, Kigawa and Kawaguchi (1991) and its outline is as follows. Figure 1 shows the schematic view of the wind tunnel used in the study. In order to establish the cross-sectional uniformity of the flow at the leading edge of the flat plate, boundary layer developed on the floor of the wind tunnel was sucked into the beneath of the flat plate by an auxiliary blower 11. Its flow rate was adjusted with a controller 10. Main stream velocity was kept at 14m/s within an accuracy of one percent. Main stream turbulence level was below one percent, too. Streamwise non-uniformity of main stream static pressure was minimized by adjusting the slope of the ceiling of the wind tunnel except for an inevitable steep change in the static pressure around the inserted LEBU plate. The magnitude of the pressure non-uniformity attained was within one percent of main stream dynamic pressure.

Figure 2 shows the schematic geometry of the studied flow system together with some geometric parameters and coordinates to be used in the following discussion. A LEBU plate made of bakelite was mounted in a position normal to the flow direction and parallel to the flat plate at a streamwise station of 1400mm downstream from the leading edge of the flat plate, where the thickness of approaching velocity boundary layer was about 28mm when no LEBU plate was inserted. The thickness of temperature boundary layer almost coincided the velocity boundary layer thickness at that position. The thickness of the LEBU plate was 1mm but its streamwise width was changed in three steps. The space between the LEBU plate and the flat plate was also changed in various steps. All the cases for which skin friction and heat transfer measurements were made are tabulated in Table 1.

The surface of the flat plate made of bakelite was covered by thin stainless-steel strips of 50 micronmeter thickness, leaving the first part (from 10mm to 200mm downstream from the leading edge) uncovered. The first part was covered by a sand paper to promote the laminar-to-turbulent transition of the boundary layer. The stainless-steel strips glued on the flat plate surface were heated at almost uniform heat flux (about $1kW/m^2$) by passing an alternating electric current through them. In order to measure the streamwise distribution of surface temperature, ninety alumel-chromel thermocouples of 100 micronmeter diameter were attached to the back surface of the strip glued along the center line of the flat plate. Non-uniformity of the local wall heat flux due to radiative and conductive heat losses was taken into account in the evaluation of local Nusselt number. Conductive heat loss towards the back surface of the flat plate was evaluated by making use of one-dimensional heat conduction equation. The heat-transfer-surface temperature measured with the thermocouples mentioned above and the back surface temperature of the flat plate measured with other set of thermocouples were substituted into the heat conduction equation. For the evaluation of radiative heat loss, 0.2 was used for the emissivity of the stainless-steal surface. Streamwise distribution of local Nusselt number obtained with this method for a normal flat plate boundary layer was confirmed to agree well with the empirical equation given by Johnson and Rubesin (1949) over a whole streamwise positions of - 500mm < x < 840mm, if a virtual origin of boundary layer development is assumed to be a position of 163mm downstream from the leading edge of the flat plate.

Table 1 Streamwise Widths and Cross-stream Positions of LEBU Plate

L/δ	H/δ									
	0.07	0.14	0.25	0.36	0.43	0.50	0.57	0.75	0.86	1.0
0.5	X	X	X	X	X	X	-	X	-	X
1.0	X	X	X	X	-	X	-	X	-	X
1.5	X	X	X	X	X	X	X	X	X	X

For the measurement of skin friction, a Preston tube of 1.2mm outer diameter was used. Conversion from the pressure-difference reading of Preston tube into the skin friction was made by making use of the relationship proposed by Patel (1965).

Measurement of mean fluid temperature was additionally made by traversing a thin thermocouple of 100 micronmeter diameter along y direction at several streamwise stations.

For velocity measurement, a hot-wire anemometry was applied. Streamwise and normal velocity components, u and v, were measured simultaneously with an X-wire probe. Hot-wire was a tungsten wire with copper-plated ends of five micronmeter in diameter and of 1 mm in length. The output signals from the anemometers were digitized on line at the sampling rate of 10kHz for each signal and recorded over about twenty seconds in a magnetic tape recorder. Data processing of the recorded signals were performed later by replaying the tape with a computer at the Kyoto University Data Processing Center. Through the data processing, the intensities of two fluctuating velocity components, u' and v', were calculated. Additionally, quadrant analysis (Lu and Willmarth (1973), Senda, Horiguchi, Suzuki and Sato (1981)) was applied to the recorded fluctuating velocity signals.

Quadrant analysis was devised in order to see which of the four types of elementary fluid motions contribute majorly to the momentum transfer (Lu and Willmarth (1973)). Figure 3 shows the four types of elementary fluid motions corresponding to each of the four quadrants of u-v plane. At every sampling time of velocity signals, the set of u and v signals is digitized and the signs and magnitude of the signals are examined. Depending on the sings and the magnitudes of the two signals, the digitized set of the data is stored into one of the four quadrants or is discarded into the hole shown in the figure. The hole size can be controlled by making use of a Hole-size parameter H'. The hole boundary in the u-v plane is given by the following relationship:

$$|uv| = H'u'v' \qquad (1)$$

If the product between the instantaneous values of u and v at a certain instant does not exceed this threshold, that particular set of u and v data is

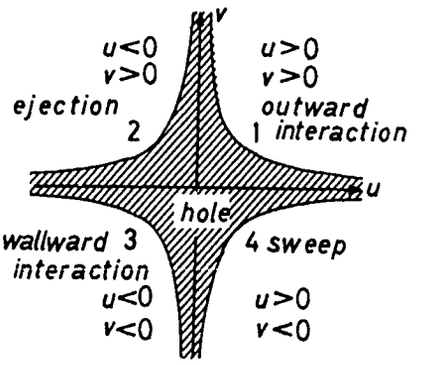

Figure 3 Four Types of Elemetary Fluid Motions in u - v Plane

discarded into the hole. Otherwise, it is stored in one of the four quadrants depending on the signs of u and v. Contribution from each quadrant or of each elementary fluid motion to Reynolds shear stress is calculated by the following conditional sampling:

$$\langle uv \rangle_i = \int u(t)v(t)I_i(t,H')dt \qquad (2)$$

where

$$I_i(t,H') = \begin{cases} 1: & \text{when Eq.(1) is satisfied} \\ 0: & \text{otherwise} \end{cases} \qquad (3)$$

and

i = 1: when u > 0 and v > 0
i = 2: when u < 0 and v > 0
i = 3: when u < 0 and v < 0
i = 4: when u > 0 and v < 0

RESULTS AND DISCUSSIONS

The effect of an insertion of LEBU plate on skin friction is first discussed. Figure 4 shows some examples of the measured streamwise distribution of skin friction coefficient, C_f, for several cases of different values of normal position, H, and of streamwise length, L, of LEBU plate. C_{f0} used in the normalization of C_f is the value of skin friction coefficient measured at the same position for a normal flat plate boundary layer without an insertion of the LEBU plate. As already reported by others (Nguyen, Savill and Westphal (1987), Savill and Mumford (1988)), the value of C_f is reduced by the insertion of LEBU plate. The shape of the distribution of C_f varies clearly with the value of H/δ but not so much with the value of L/δ except for the case of $H/\delta = 0.07$, where δ is the thickness of the approaching boundary layer at x = 0, the insertion position of cylinder. Increase of H/δ is effective to widen the region where skin friction is

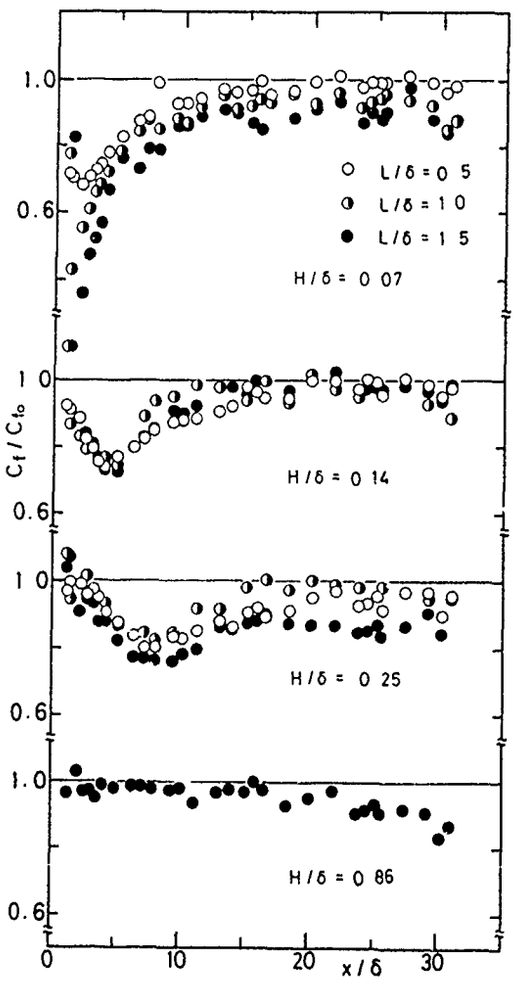

Figure 4 Streamwise Distribution of Skin Friction Coefficient

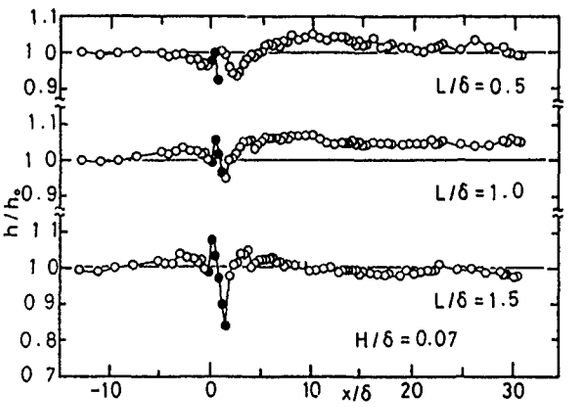

(a) $H/\delta = 0.07$

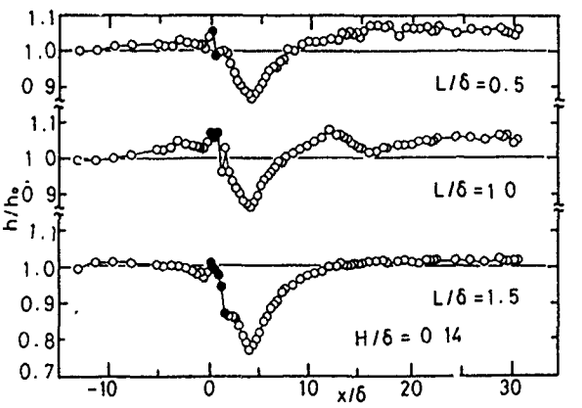

(b) $H/\delta = 0.14$

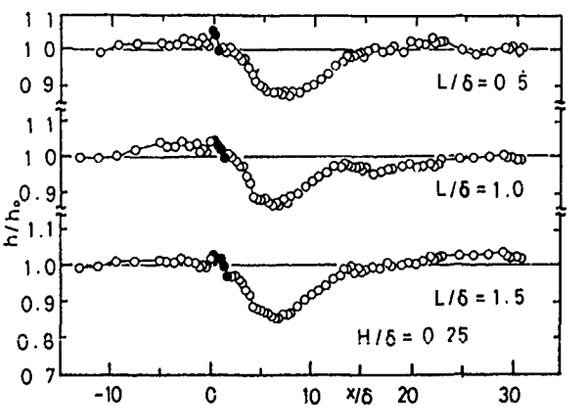

(c) $H/\delta = 0.25$

Figure 5 Streamwise Distribution of Heat Transfer Coefficient

reduced but it leads to shallower depth of the dent of C_f distribution. Therefore, the introduction of LEBU plate is not effective to reduce the wall skin friction at such value of H/δ as of 0.86 or larger than that. When H/δ = 0.07, the minimum value of C_f becomes smaller with an increase of L/δ.

Heat transfer data will next be discussed. Figure 5 shows the measured streamwise distributions of heat transfer coefficient, h, obtained in the three of the four cases for which the distribution of C_f was demonstrated in Figure 4. In the case of H/δ = 0.86, heat transfer data are ommitted because the introduction of LEBU plate is not effective to reduce the wall skin friction in this case. The value of h is plotted in a form normalized with its counterpart measured at the same position for a normal flat plate boundary layer, h_0. Solid circles were used for the values of h measured at the positions underneath the inserted LEBU plate. First, it is clear from this figure that heat transfer is not enhanced by the introduction of LEBU plate into the boundary layer. Since the shapes of the distributions of h and C_f are a little different from each other, a certain level of dissimilarity exists in these cases. However, it is much less conspicuous than the one for a turbulent boundary layer with the insertion of a cylinder previously studied by Suzuki, Kikkawa, Kigawa and Suzuki (1989).

In order to see the degree of the dissimilarity generated in the present flow, the ratio between the Stanton number and the skin friction coefficient is plotted in Figure 6 for all the cases for which the distribution of C_f was presented in Figure 4. This similarity parameter takes a value of about 1.2 in the normal flat plate turbulent boundary layer as measured by Chi and Spalding (1966) if the working fluid is air. When H/δ =0.07 or when the LEBU plate is mounted very close to the flat plate, some noticeable level of dissimilarity is attained when L/δ = 1.0 and 1.5. However, the level of dissimilarity is low in all other cases.

Now, some other data will be presented and discussion will be given to the physical background of the difference found in the above between the present case and the previous case when the cylinder was inserted. Figure 7 shows the cross-stream distributions of averaged velocity and temperature measured at x/δ = 2 for two cases of H/δ = 0.07 and L/δ = 1.5 and H/δ = 0.14 and L/δ = 0.5. It is observed that the velocity field is disturbed by the insertion of LEBU plate but the temperature field is not seriously disturbed. This difference between the two fields may not have been generated if the LEBU plate was heated and its temperature was kept the same as the flat plate surface temperature. The effect of heating of the inserted obstacle was not pronounced in the case when the obstacle was a cylinder (Suzuki, Suzuki and Sato (1988)). However, in the present case, the overall level of dissimilarity is rather low. Therefore, the effect of heating of the immersed body is relatively stronger and it probably cannot be ignored. The difference between the degrees of the distortion appearing in the velocity and temperature profiles due to the

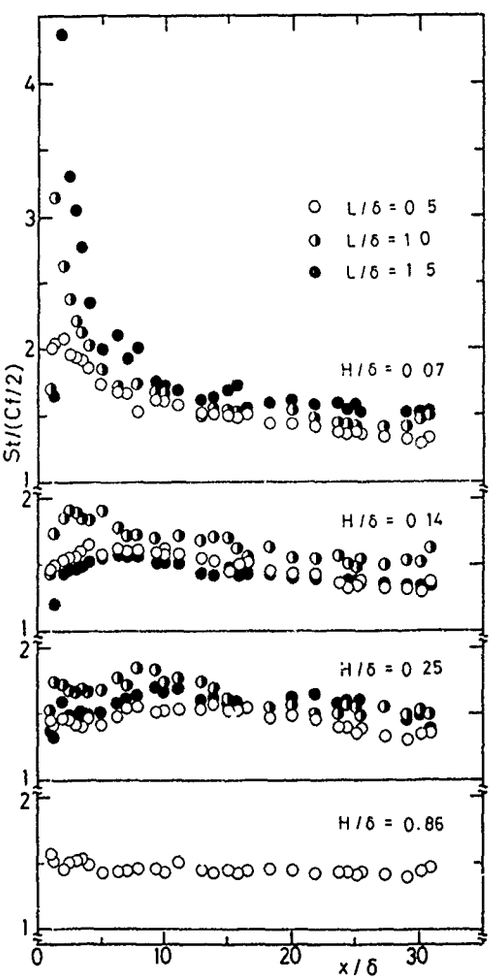

Figure 6 Streamwise Change of Similarity Parameter (Stanton number/Skin Friction Coefficient)

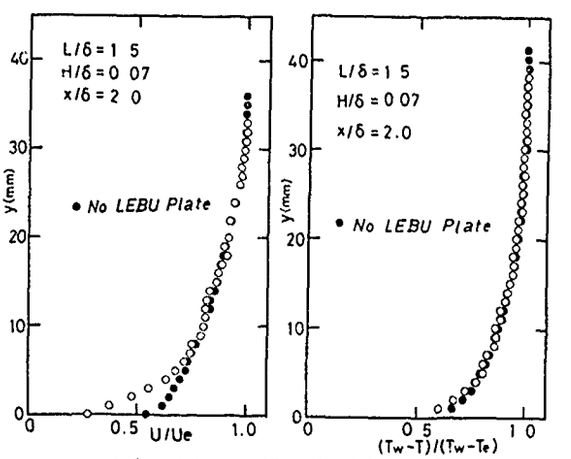

(a) H/δ = 0.07 and L/δ = 1.5

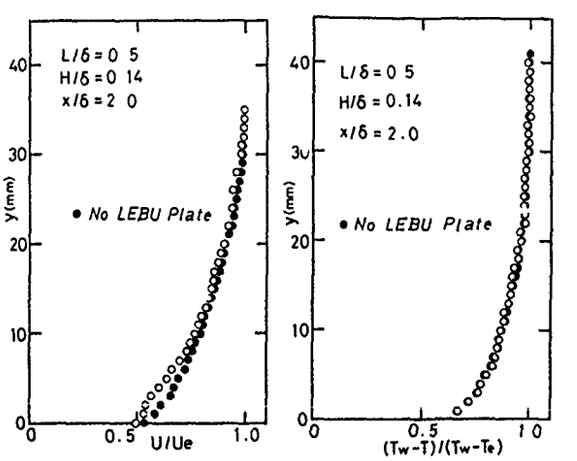

(b) H/δ = 0.14 and L/δ = 0.5

Figure 7 Cross-stream Distributions of Averaged Velocity and Temperature

insertion of LEBU plate is more clearly observed for the case when the LEBU plate is mounted closer to the flat plate. This may be related to the fact that the similarity parameter takes larger value when $H/\delta = 0.07$ than when $H/\delta = 0.14$.

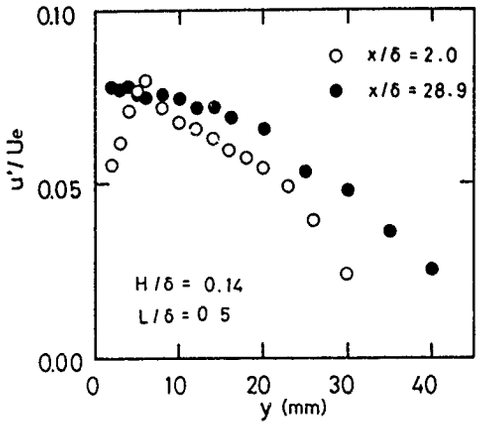

(a) Distribution of u'

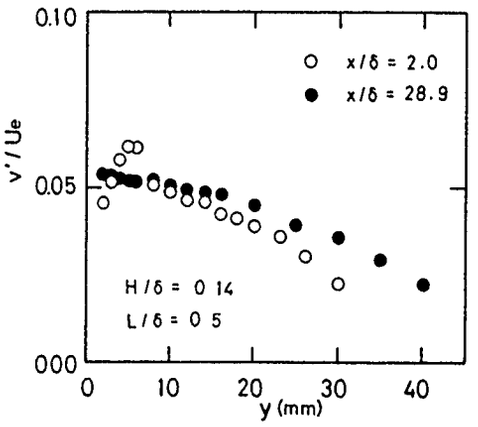

(b) Distribution of v'

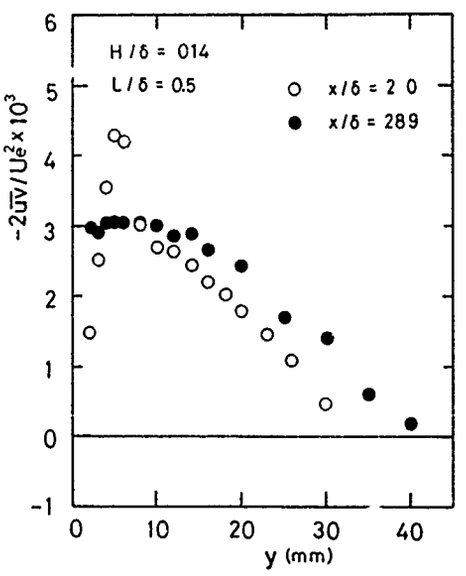

(c) Distribution of $-\overline{uv}$

Figure 8 Cross-stream distributions of u', v' and $-\overline{uv}$

Figures 8 (a) through (c) show the cross-stream distributions of turbulence quantities obtained at the two streamwise locations of $x/\delta = 2$ and 28.9 for a case of $H/\delta = 0.14$ and $L/\delta = 0.5$. Figure 8 (a) shows the distribution of u', the intensity of streamwise velocity fluctuation, Figure 8 (b) the distribution of v', the intensity of cross-stream velocity fluctuation, and Figure 8 (c) presents the distribution of $-\overline{uv}$, the Reynolds shear stress. At $x/\delta = 28.9$, it is judged from Figures 4 and 5 that the boundary layer has almost recovered from the disturbance given by the LEBU plate. Thus, the measured turbulence data at this position may be taken to represent the ones for undisturbed boundary layer. At $x/\delta = 2$, a certain noticeable level of the reductions both of skin friction and heat transfer coefficients are observed. However, at this position, dissimilarity between the momentum transfer and heat transfer is weak for the case of $H/\delta = 0.14$ and $L/\delta = 0.5$, as noticed in Figure 6.

It is observed in Figure 8 (a) that the level of u' at $x/\delta = 2$ does not differ from the one at $x/\delta = 28.9$ even in the middle of the wake and that the disturbance generated by the inserted LEBU plate is weak. Similar feature is observed for the distributions of v' and $-\overline{uv}$ shown in Figures 8 (b) and (c). Particularly, at $x/\delta = 2$, turbulence level near the wall, responsible for wall heat transfer performance (Marumo, Suzuki and Sato (1985)), is reduced by the insertion of the LEBU plate. Thus, this reduction of near-wall turbulence level should have resulted in the reduction of heat transfer coefficient.

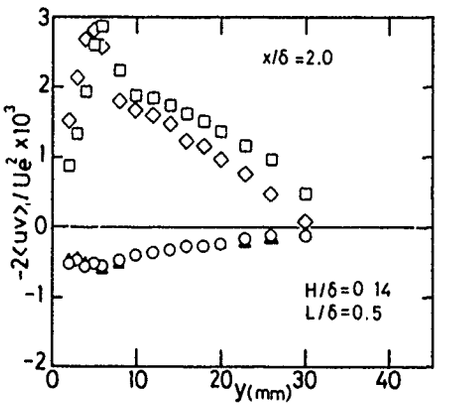

(a) The Results Obtained at $x/\delta = 2$

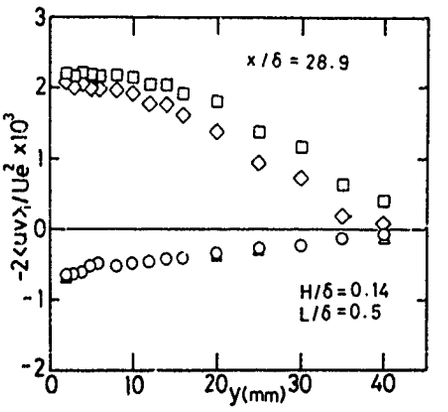

(b) The Results Obtained at $x/\delta = 28.9$

Figure 9 Cross-stream Distribution of Fractional Contribution From Each Quadrant to $-\overline{uv}$
- ○ : i = 1 (Outward Interaction)
- □ : i = 2 (Ejection)
- △ : i = 3 (Wallward Interaction)
- ◇ : i = 4 (Sweep)

Figure 9 shows the results of the quadrant analysis applied to the fluctuating velocity components measured in the present flow. The magnitude of the contribution from each quadrant to the Reynolds shear stress obtained at various normal positions in two streamwise cross-sections of x/δ = 2, close to the LEBU plate, and at x/δ = 28.9, where the turbulent field has almost completely recovered. The hole size parameter H' was set equal to zero in this study. In the case of the boundary layer disturbed by a cylinder located near the wall, it was found by Kawaguchi, Matsumori and Suzuki (1984) and by Suzuki, Suzuki and Sato (1988) that the interactive fluid motions play an important role in generating the dissimilarity between the momentum transfer and heat transfer. However, it is observed in this figure that the insertion of LEBU plate does not alter the intensity of interactive fluid motions significantly. Since the magnitudes of contributions from ejection and sweep events are reduced near the wall as seen in Figure 9, the relative magnitudes of the fractional contributions from two types of interactive fluid motions are raised. These should give the physical background from a view point of turbulence structure for the weak dissimilarity found in the present case.

Now, weaker dissimilarity observed in the present case will be discussed in comparison with the stronger dissimilarity found in the previous case when the boundary layer disturbed by a cylinder. In the case when a cylinder was inserted, cold wallward interaction was intensified most conspicuously (Suzuki, Suzuki and Sato (1988)). This type of fluid motion has the negative streamwise velocity fluctuation and negative cross-stream velocity fluctuation. The intensification of this type of fluid motion must have been produced by the lateral motion of the fluid lump or vortices origined in the central part of the wake of the cylinder, where the velocity defect is large in average. For such vortices effectively to reach the near-wall region, cross-stream component of velocity fluctuation must be large there. To have large velocity defect and intensive v-component fluctuation in the wake, the wake must be thick to some extent. It means that the form drag of the body to be immersed cannot be small. Therefore, to reduce significantly the increase of momentum loss while keeping the reasonable level of enhancement of heat transfer looks to be very difficult. To achieve this, therefore, would require a new challenging idea.

CONCLUDING REMARKS

Heat transfer data were obtained for the flat plate turbulent boundary layer disturbed by a LEBU plate. It was found that the heat transfer coefficient was reduced by the insertion of LEBU plate as well as the skin friction coefficient. Therefore, no significant dissimilarity between the momentum transfer and heat transfer processes was generated. This is quite different from the case when the flat plate turbulent boundary layer was disturbed by an insertion of cylinder. The reduction of heat transfer coefficient was related to the lowered level of near-wall turbulence, which was further related to the break-up of large scale coherent structure of turbulence in the boundary layer. The results of the applied quadrant analysis of the fluctuating velocity signals were also discussed. In the case when the cylinder was inserted, conspicuous intensification of interactive fluid motions, especially of wallward interaction, was observed and it was suggested to be the reason for the noticeable level of dissimilarity between the momentum and heat transfer processes. However, this is not the case of the presently studied flow. No significant intensification of the interactive fluid motions was observed. Reduction of the contribution from the ejection and sweep events to the Reynolds shear stress leads to the relative increase of the fractional contribution from the interactive fluid motions. This results in the weak dissimilarity. Although no distortion appears in the temperature profile in the downstream of LEBU plate, the velocity profile is noticeably distorted. Fluid lumps or vortices origined from the wake region should have lower streamwise momentum. When the wake is wider and deeper, such vortices are produced more frequently. If such vortices are drove into the near wall region, the intensification of the wallward interactive fluid motion can be achieved. However, to bring such vortices near to the wall, realization of intensive turbulence field or, more specifically, intense cross-stream velocity fluctuation, would be necessary. It means that the wake of the immersed body must be wide to some extent or that the form drag of the immersed body should not be small. This indicates that a certain level of dissimilarity can only be attained at the expense of using a body having larger form drag.

REFERENCES

CHI,S.W. and SPALDING,D.B. 1966 Influence of temperature ratio on heat transfer to a flat plate through a turbulent boundary layer in air. Proc. 3rd Int. Heat Transfer Conf., 2, 41-49.

JOHNSON,H.A. and RUBESIN,M.W. 1949 Aerodynamic heating and convection heat transfer - Summary of literature survey. Trans. ASME, 71, 447-456.

KAWAGUCHI,Y., MATSUMORI,Y. and SUZUKI,K. 1984 Structural study of momentum and heat transfer in the near wall region of a disturbed turbulent boundary layer. Proc. 9th Biennial Symp. on Turbulence. 28.1-28.10.

LU,S.S. and WILLMARTH,W.W. 1973 Measurements of the structure of the Reynolds stress in a turbulent boundary layer. J. Fluid Mechanics, 60-3, 481-511.

MARUMO,E., SUZUKI,K. and SATO,T. 1985 Turbulent heat transfer in a flat plate boundary layer disturbed by a cylinder. Int. J. Heat and Fluid Flow, 6-4, 241-248.

NGUYEN,V.D., SAVILL,A.M. and WESTPHAL,R.V., 1987 Skin friction measurements following manipulation of a turbulent boundary layer. AIAA Journal, 25, 498-500.

PATEL,V.C. 1965 1965 Calibration of the preston tube and limitations on its use in pressure gradients. J.Fluid Mechanics, 23, 185-???.

SAVILL,A.M. and MUMFORD,J.C. 1988 Manipulation of turbulent boundary layers by outer-layer devices: skin friction and flow-visualization results. J. Fluid Mechanics, 191, 389-418.

SENDA,M., HORIGUCHI,S., SUZUKI,K. and SATO,T. 1981 A structural study on a turbulent boundary layer with transpiration. Proc. 3rd Symp. on Turbulent Shear Flows, 10.7-10.12.

SUZUKI,H., SUZUKI,K. and SATO,T. 1988 Dissimilarity between heat and momentum transfer in a turbulent boundary layer disturbed by a cylinder, Int. J. Heat Mass Transfer. 31-2, 259-265.

SUZUKI,K., SUZUKI,H., KIKKAWA,Y., KIGAWA,H and KAWAGUCHI, Y. 1991 Study on a turbulent boundary layer disturbed by a cylinder - Effect of cylinder size and position, in Turbulent Shear Flows 7, Springer-Verlag.

EIGHTH SYMPOSIUM ON
TURBULENT SHEAR FLOWS
Technical University of Munich
September 9-11, 1991

STRUCTURAL FEATURES OF A HEATED ROUND TURBULENT JET IN A CROSS-FLOW

Z. Huang, M.S. Low, J.G. Kawall, and J.F. Keffer

Department of Mechanical Engineering

University of Toronto

Toronto, Ontario, Canada M5S 1A4

ABSTRACT

The evolution of a heated round air jet injected into a cross-flow from an elevated source in the form of a circular tube has been investigated experimentally. It is found that a counter-rotating pair of vortices is generated at a downstream location corresponding to approximately one initial jet diameter from the source and that quasi-periodic Kármán-like coherent structures occur in the wake of the jet. Moreover, the results suggest that the vorticity associated with the wake structures originates in the boundary layer vorticity within the tube.

NOMENCLATURE

D – initial jet diameter, mm.

f – frequency, Hz.

R – ratio of the initial jet velocity to the cross-flow velocity, dimensionless.

S_θ – autospectrum of the fluctuating temperature component, $°C^2s$.

t – time, s.

T – instantaneous temperature, $°C$.

$\overline{T}$ – mean temperature, $°C$.

T_0 – ambient temperature, $°C$.

θ – fluctuating temperature component, $°C$.

θ' – root-mean-square temperature, $°C$.

ρ_θ – autocorrelation of the fluctuating temperature component, dimensionless.

τ – time lag, ms.

INTRODUCTION

The behaviour of a turbulent jet in a cross-flow is of considerable importance with respect to technological applications involving mixing, the operation of V/STOL (vertical or short takeoff and landing) aircraft, and the dispersion of effluent discharged into the atmosphere or rivers. Such a flow is also intrinsically interesting, inasmuch as it represents a complex turbulent shear flow whose detailed structure is not fully understood.

There have been numerous studies on a round jet injected perpendicularly from a *ground level source* into a uniform, steady cross-flow (e.g., Keffer and Baines, 1963; Kamotani and Greber, 1972; Andreopoulos and Rodi,1984; Broadwell and Breidenthal, 1984; Sherif and Pletcher, 1988; Fric and Roshko, 1989.) In contrast, there have been very few investigations dealing with the case of a round jet injected from *an elevated source* (such as a chimney stack) into a uniform cross-flow (e.g., Moussa, Trischka and Eskinazi, 1977).

With respect to the ground level source, previous results (e.g., see Fric and Roshko, 1989) have established that, when the ratio of the initial jet velocity to the cross-flow velocity exceeds about 1.5, the near field of the flow involves distorted shear-layer ring vortices at the periphery of the bending jet and wake vortices aligned approximately with the initial jet direction. Moreover, Fric and Roshko (1989) have shown that, upstream from the jet, a horseshoe vortex system is generated at the ground-level surface containing the opening from which the jet is discharged. As the jet bends and moves downstream, the action of the pressure forces and lateral shear produced by the cross-flow causes the initial circular shape of the jet to change to a characteristic kidney-shape, with attendant development of the pair of counter-rotating vortices that are the dominant large-scale feature in the far field of the flow. (These vortices, which are attached to jet, are readily observed in smokestack-plumes and have been described in detail by Turner, 1960.)

In the case of the elevated source, the detailed structure of the flow is more complicated than it is in the case of the ground-level source, in that the former case involves the wake of the elevated source as well as that of the jet.

The present work concerns an experimental investigation of the turbulent jet-flow that results when a *heated* circular jet is injected perpendicularly from an elevated source into a uniform, steady cross-flow. This investigation was undertaken in an effort to gain further insight into the structure of this flow. Here, mean and root-mean-square (RMS) streamwise velocities and temperatures, and autocorrelations and autospectra of temperature signals are presented. (It may be remarked that, by virtue of the heat-mass transfer analogy, the temperature of a heated turbulent jet in a cross-flow is analogous to the concentration of effluent within a polluted jet emitted into a cross-wind, with high/low temperatures corresponding to high/low concentrations; accordingly, the findings of the present work are of relevance to problem of air pollution caused by the continuous release of waste gases from smokestacks.)

EXPERIMENTAL DETAILS

The experiments for this investigation were performed in the variable-speed low-turbulence recirculating wind tunnel situated in the UTME (University of Toronto, Mechanical Engineering) Turbulence Research Laboratory. This tunnel has a test section 3 m in length and 0.91 m by 1.52 m in cross-section and a speed range of about 1 m/s to about 15 m/s. The jet was produced by means of a smooth tube

approximately 0.3 m in length and 50 mm in diameter (D), through which isothermal or heated air could be discharged at two different (average) velocities.

Preliminary experiments were performed with the jet unheated.

The tube, which will, henceforth, be referred to as the stack, was located at the upstream end and along the centre-line of the tunnel and orientated perpendicular to the streamwise direction (i.e., the direction of the wind-tunnel flow). In the case of the heated-jet experiments, the temperature at the stack-exit was approximately 40 °C above the ambient temperature (T_0) and the velocity approximately 13.7 m / s, so that the Reynolds number of the jet at the stack exit was about 34,000.

A Cartesian coordinate system was employed, with x in the streamwise direction, y in the lateral or vertical direction and z in the spanwise direction (perpendicular to the stack-axis). The origin of the coordinate system was taken to be at the tip and in the centre of the stack.

Mean and RMS velocity measurements were obtained with a DANTEC 55P11 normal hot-wire probe, in conjunction with a DANTEC 55M constant-temperature-anemometer system. Mean temperature measurements were obtained with a rake of ten (10) type J thermocouples and a Thermo Electric ELPH 4 thermocouple-indicator. Temperature signals were obtained with a DANTEC 55P31 resistance thermometer (or cold-wire probe), in conjunction with a DANTEC 55M constant-current-anemometer system. These signals were low-pass filtered at 2 kHz and digitized by means of a 12-bit A/D converter attached to a PDP-11 computer. The digitization rate was chosen to be 5000 points per second (to prevent aliasing), and the digital signals were processed on a DEC MICRO-VAX workstation. The length of each signal processed was approximately 36 seconds (equivalent to 180,000 points). Measurements were taken at various y/D locations, ranging from about - 2.0 to 10.0, and various x/D locations, ranging from about 1.0 to about 35.0, for values of the ratio of initial-jet-velocity to cross-wind-velocity (R) ranging from about 1.0 to about 4.0.

RESULTS AND DISCUSSION

Centreline Jet Trajectories

In Fig. 1, centreline trajectories (i.e., y/D versus x/D plots) based on the present mean and RMS velocity-measurements for R = 2 and the centre-line jet trajectory based on mean velocity-measurements for R = 2 reported by Keffer and Baines (1963) are presented. It can be seen that there is general agreement among the results. The detailed behaviour of the present trajectories and that of the Keffer-Baines trajectory are different, however. This difference can be attributed to the influence on the present results of the wake behind the stack.

Vertical Centre-Plane Mean and RMS Velocity Iso-Contours

Mean and RMS velocity iso-contour plots pertaining to the vertical centre-plane of the flow (z/D = 0.0) serve to depict the spread of the jet and its interaction with the cross-flow and the wakes behind the jet and the stack. Figures 2 and 3 show the mean and RMS *velocity* isocontours for R = 3.0. As can be seen, the jet undergoes a significant initial rise within a downstream distance corresponding to a few stack diameters before the cross-flow has enough influence on it to cause it to bend over. Its vertical momentum, however, enables it to continue to rise, relatively slowly, as it moves downstream. Moreover, it can be inferred from Fig. 3 (the RMS results) that, in the near field of the flow, the interaction region below the centreline of the jet, involving the 'jet-wake' and the 'stack-wake', is wide (in the y-direction) and diffuse in comparison with the interaction region above the jet centreiine, which is relatively narrow and sharp.

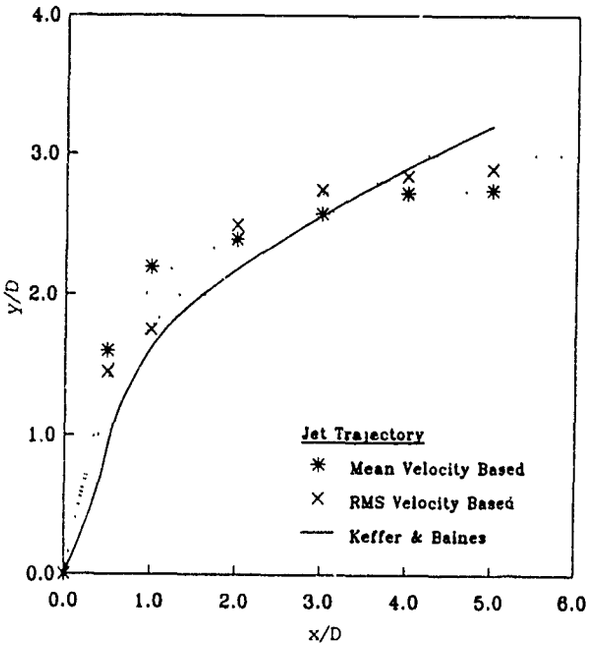

Fig. 1. Centreline jet trajectories for R=2.0.

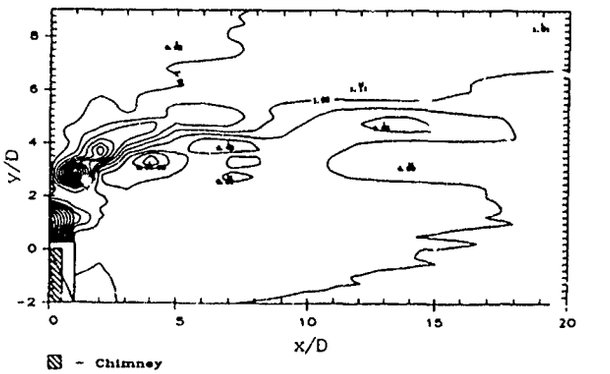

Fig. 2. Vertical centre-plane mean velocity iso-contours for R=3.0.

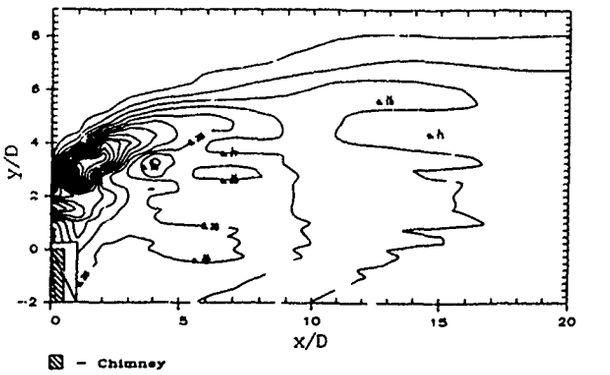

Fig. 3. Vertical centre-plane RMS velocity iso-contours for R=3.0.

Figures 4 and 5 show the mean and RMS *temperature* iso-contours for R = 2.3. These results are entirely consistent with the velocity results (Figs. 2 and 3) as regards the jet rise and the upper and lower interaction regions (above and below the jet centreline). In addition, since temperature acts as a tracer, enabling the 'hot' jet fluid to be distinguished from the 'cold' fluid in the 'jet-wake' and in the 'stack-wake' below the jet, as well as the 'cold' fluid in the free-stream above the jet, the results in Figs. 3 and 4 serve to establish that, on the average, the heated jet fluid does not penetrate the wake of the stack (the upper end of which is located at y/D =0.0); and they serve to define not only the average centreline of the jet but also its average upper and lower boundaries. The configuration of these boundaries indicates that the jet spreads relatively slowly with increasing x/D.

Cross-Stream Mean Temperature Iso-Contours

While the previous vertical centre-plane plots (Figs. 2 - 5) allow the overall spread characteristics of a jet in a cross-wind to be obtained, they do not provide a picture of the average cross-sectional shape of the jet. On the other hand, mean temperature iso-contour plots for a *heated* jet in a cross-wind provide such a picture. Typical examples of such plots are presented in Figs. 6 and 7, which pertain to x/D = 1.0 and x/D = 10.0 respectively and R = 2.0. These plots display the expected features. To be specific, the contour lines are more closely-spaced in the upper part than in the lower part of the flow, especially for the near field (Fig. 6), indicating that as one moves towards the central region of the heated jet from the isothermal free-stream region, a rapid temperature increase occurs; whereas, as one moves towards this region from the 'jet-wake' and 'stack-wake' regions, a gradual temperature increase occurs. Moreover, the kidney-shape of the cross-section of the jet, as described by Keffer and Baines (1963) and others, is clearly evident (Fig. 6). A comparison of the isothermal-contour plots obtained at various downstream locations (e.g., Figs. 6 and 7) establishes that the cross-sectional shape of the jet evolves from the kidney-shape in the 'near field' to a roughly round shape in the 'far field'. We note that the occurrence of the kidney-shape at x/D = 1.0 is consistent with the findings of Fric and Roshko and indicates that the counter-rotating pair of vortices referred to previously begins to form quite early in the evolution of the flow.

Mean and RMS Temperature Profiles

Mean and RMS temperature profiles pertaining to the vertical centre-plane of the flow (z/D = 0) and R = 2.3 are presented in Figs. 8 and 9. As expected, the shapes of these profiles are highly asymmetrical initially (for x/D < ~ 15) but tend to become symmetrical as x/D increases, with the mean profiles attaining symmetry by x/D ≈ 15, much before the RMS profile do so. The profile shapes in question are in conformity with the fact that the lower interaction region is wider and more diffuse than is the upper interaction region. Moreover, it is evident that the jet is fully turbulent by x/d = 3, there being no 'flat regions' in the profiles obtained at this location, and it appears that the mean temperature field is self-similar at and beyond x/D ≈ 15.

Intermittent Temperature Signals

Figures 10 and 11 show typical segments of temperature signals measured in upper and lower intermittent regions above (Fig. 10) and below (Fig. 11) the centreline of the jet at x/D = 3 for R = 2.3 . It is evident from these signal segments that, as expected, the temperature levels in the upper region of the flow are higher than those in the lower region, and the upper interface separating the heated jet fluid and the isothermal free-stream fluid is much sharper than the lower interface separating the jet fluid and the wake fluid.

Autocorrelation Functions and Auto-Spectra of Temperature Signals

Autocorrelation functions and auto-spectra of the temperature signals obtained at x/D =3 for R = 2.3 (segments of which are shown in Figs. 10 and 11), are presented in Figs. 12 - 15. The results pertaining to the lower intermittent region of the flow (Figs. 13 and 15) reveal that it is characterized by a distinct frequency-centred activity, i.e., the quasi-periodic passage of *hot jet fluid,* there being a marked peak in the autospectrum at a frequency of about 50 Hz and a noticeable periodic oscillation in the autocorrelation function with a period of 20 ms. In contrast, the results pertaining to upper region of the flow (Figs. 12 and 14) establish that no such frequency centred activity exists there.

The frequency-centred activity in the lower region can be ascribed to the presence of Kármán-like vortices in the

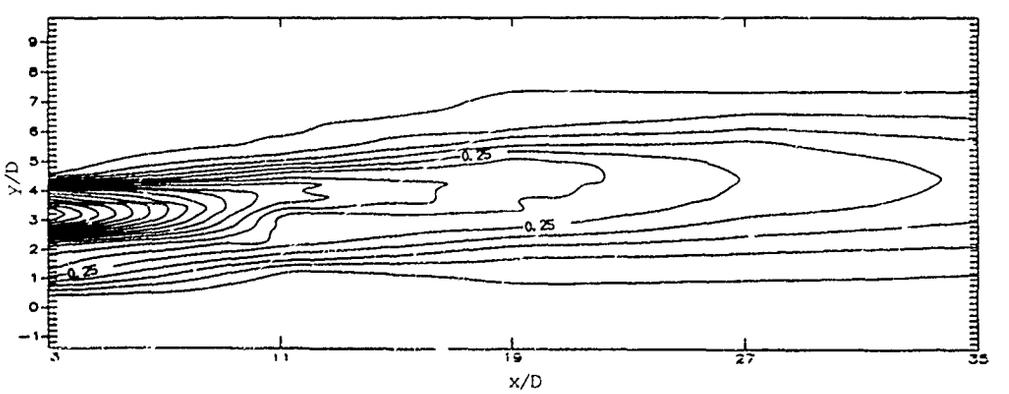

Fig. 4. Vertical centre-plane mean temperature iso-contours for R=2.3.

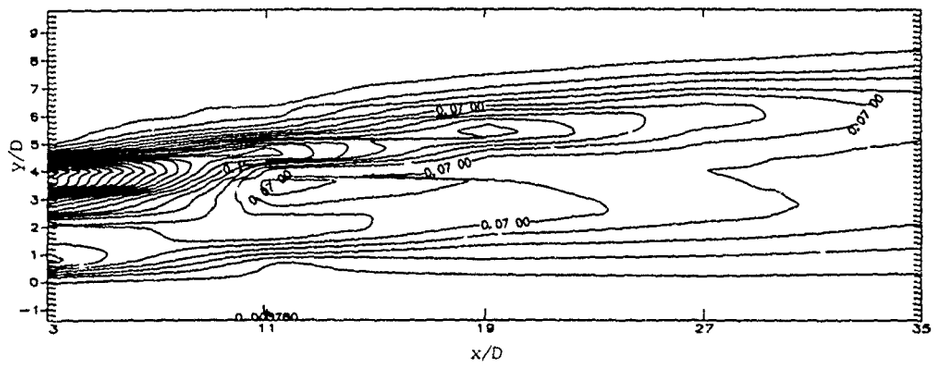

Fig. 5. Vertical centre-plane RMS temperature iso-contours for R=2.3.

wake of the jet. (It should be mentioned that the frequency at which the autospectral peak in question occurs is twice the Strouhal frequency, $0.21U_0/D$, based on the stack diameter, D = 50 mm, and the cross-flow velocity, U_0 = 6 m/s.)

It is interesting to note that, on the basis of their examination of a jet injected from a ground-level source into a cross-flow, Fric and Roshko (1989) reached the conclusion that the vorticity in the wake of the jet originates in the cross-flow boundary layer upstream from the jet. Clearly, this conclusion is *not* supported by the present results, which imply that the vorticity in the wake of the jet examined here originates in the boundary layer vorticity within the stack, i.e , this jet 'does *shed* some of its vorticity'. We note that the boundary layer vorticity within the stack is also the source of the vorticity for the distorted shear-layer ring vortices that are formed, in the near field, at the periphery of the jet.

An inspection of autocorrelation and autospectra obtained at various y/D locations between -2.0 and 10.0 and various x/D locations between 3 and 35 reveals that the frequency-centred activity (centred at 50 Hz) in the lower region of the flow becomes increasingly randomized as x/D increases and, as indicated by Figs. 16 and 17, ceases to exist at and beyond x/D ≈ 15. This inspection reveals as well that frequency-centred activity with a characteristic frequency equal to the Strouhal frequency of 25 Hz begins to develop at x/D ≈ 15 in the upper intermittent region of the flow. This activity, although not as intense as that in the near field of the lower region (see Figs. 13 and 15) is well-established by x/D = 25, as is clearly evident from Figs. 18 and 19, and appears to persist (with much the same intensity) beyond x/D = 35.

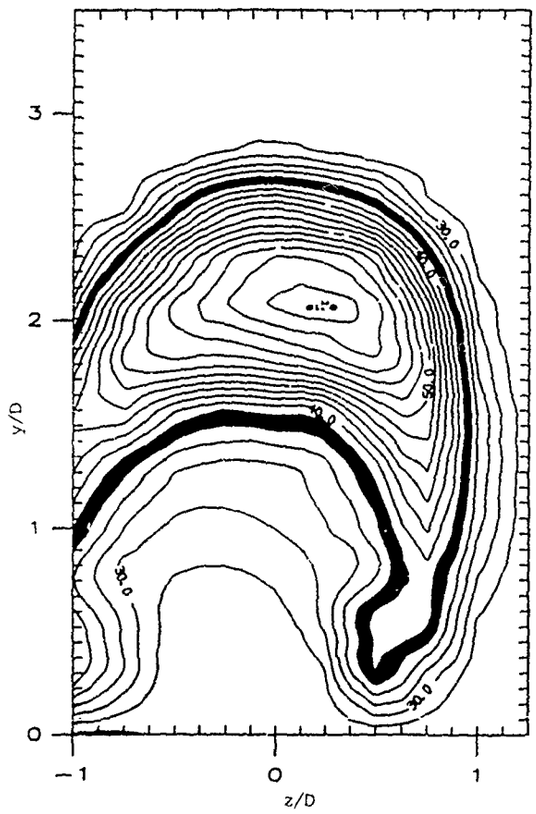

Fig. 6. Cross-stream mean temperature iso-contours at x/D=1.0 for R=2.0.

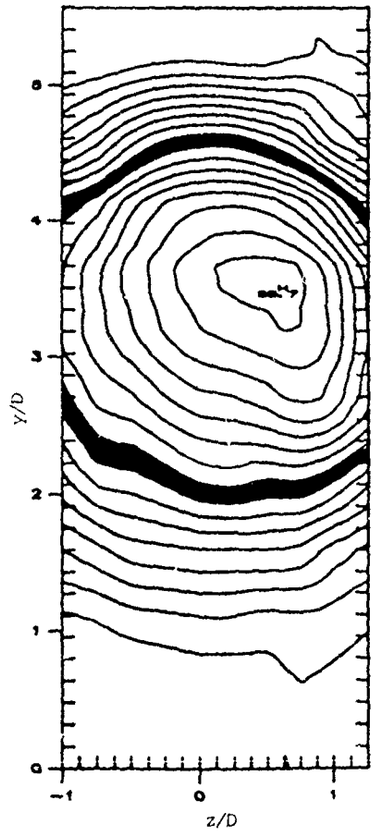

Fig. 7. Cross-stream mean temperature iso-contours at x/D=10.0 for R=2.0.

It is speculated that the far-field frequency-centred activity in the upper region of the present flow is a manifestation of coherent structures resulting from quasi-periodic coalescing of the heated distorted shear-layer ring vortices at the periphery of the bending jet, which are formed with a characteristic frequency much greater than the Strouhal frequency. Both the far-field ring-vortex coalescing (in the upper region) and the near-field vortex shedding from the hot jet (in the lower region) are believed to be governed by the relatively intense Kármán vortex street generated by the stack, via some type of 'lock-in' mechanism. (It should be emphasized that this Kármán vortex street is not detectable by means of temperature signals because the fluid involved is cold; however, it is detectable by means of velocity signals.) Accordingly, the frequency characterizing the far-field frequency-centred activity in the upper region of the flow is the same as the Strouhal frequency associated with the Kármán vortex street; and the frequency characterizing the near field frequency centred activity in the lower region is twice this Strouhal frequency.

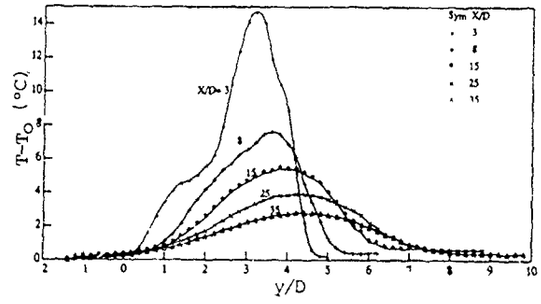

Fig. 8. Mean temperature profiles for R=2.3.

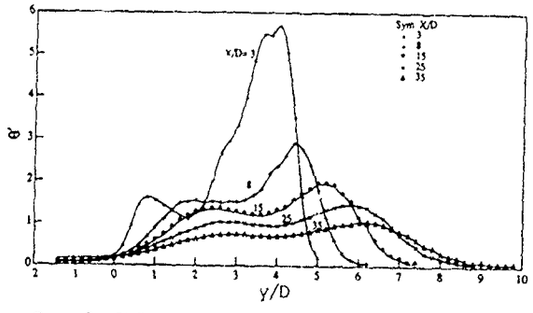

Fig. 9. RMS temperature profiles for R=2.3.

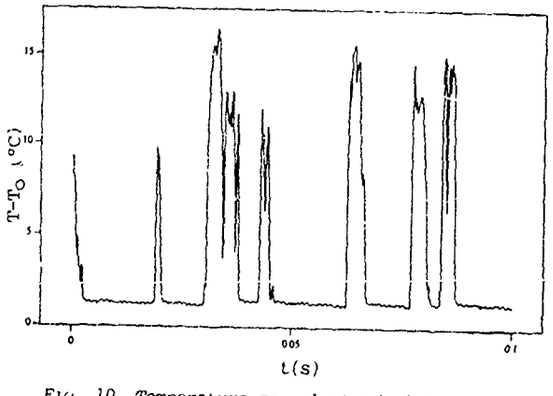

Fig. 10. Temperature signal at x/D=3.0 and y/D=3.9 for R=2.3.

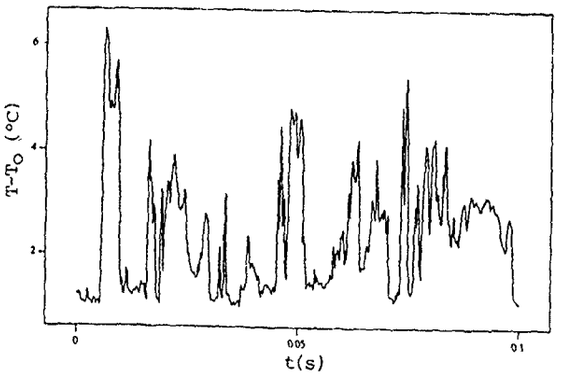

Fig. 11. Temperature signal at x/D=3.0 and y/D=0.5.

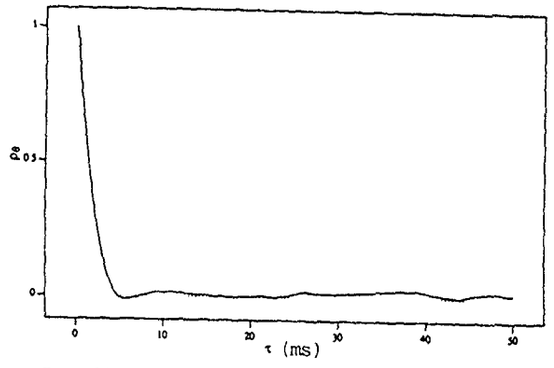

Fig. 12. Temperature autocorrelation function at x/D=3.0 and y/D=3.9 for R=2.3.

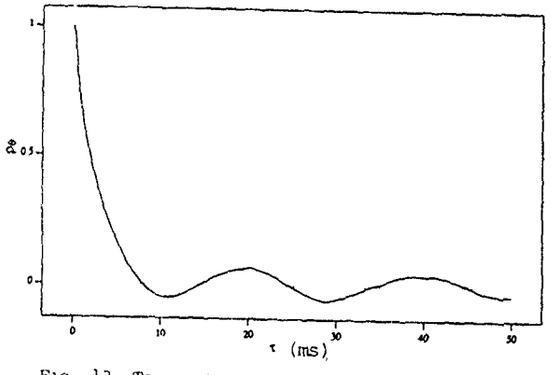

Fig 13. Temperature autocorrelation function at x/D=3.0 and y/D=0.5 for R=2.3.

ACKNOWLEDGEMENT

This research was supported by the Natural Sciences and Engineering Research Council of Canada through Grant A-2746.

REFERENCES

ANDREOPOULOS, J. and RODI, W. 1984 Experimental investigation of jets in a crossflow. *J. Fluid Mech.* 138, 93-127.

BROADWELL, J.E. and BREIDENTHAL, R.E. 1984 Structure and mixing of a transverse jet in incompressible flow, *J Fluid Mech.* 148, 405 - 412.

FRIC, J.F. and ROSHKO, A. 1988 Structure in the near field of the transverse jet, *Proc. 7th Symp. Turbulent Shear Flows,* Stanford, 6.4.1 - 6.4.6.

KAMOTANI, Y. and GREBER, I. 1972 Experiments on a turbulent jet in a cross-flow. *AIAA J.* 10, 1425 - 1429.

KEFFER, J.F. and BAINES, W.D. 1963 The round turbulent jet in a cross-wind, *J. Fluid Mech.* 15, 481 196.

McMAHON, H.M., HESTER, D.D. and PALFREY, J.G. 1971 Vortex shedding from a turbulent jet in a cross-wind. *J. Fluid Mech.* 48, 73 - 80.

MOUSSA, Z.M., TRISCHKA, J.W. and ESKINAZI, S. 1977 The near field in the mixing of a round jet with a cross-stream. *J. Fluid Mech.* 80, 49 - 90.

SHERIF, S.A. and PLETCHER, R.H., 1988 Jet-wake thermal characteristics of heated turbulent jets in cross-flow, *AIAA / ASME / SIAM / APS 1st National Fluid Dynamics Congress 1784 - 1791.*

TURNER, J.S. 1960 A comparison between buoyant vortex rings and vortex pairs. *J. Fluid Mech.* 7, 419 - 432.

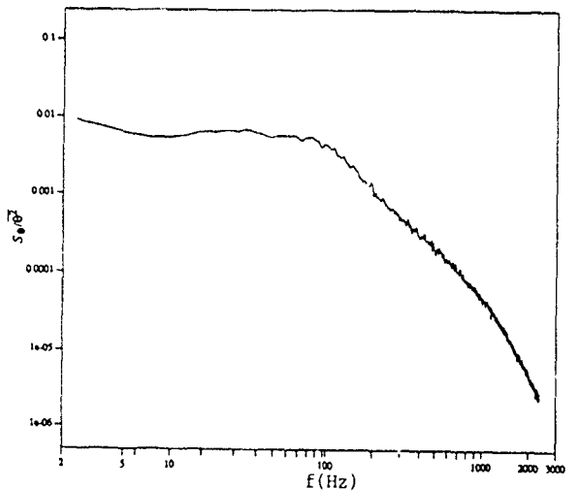

Fig. 14. Temperature autospectrum at x/D=3.0 and y/D=3.9 for R=2.3.

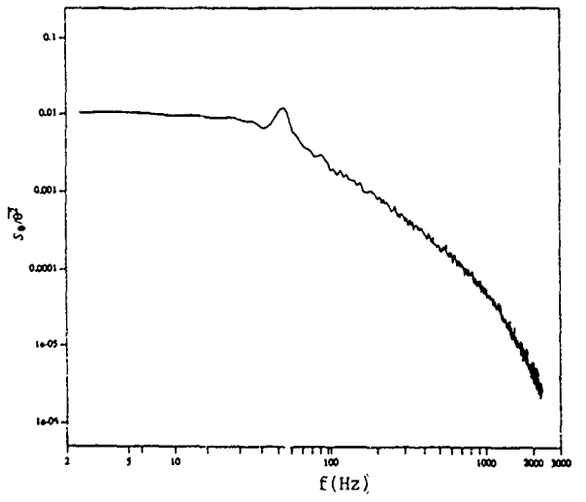

Fig. 15. Temperature autospectrum at x/D=3.0 and y/D=0.5 for R=2.3.

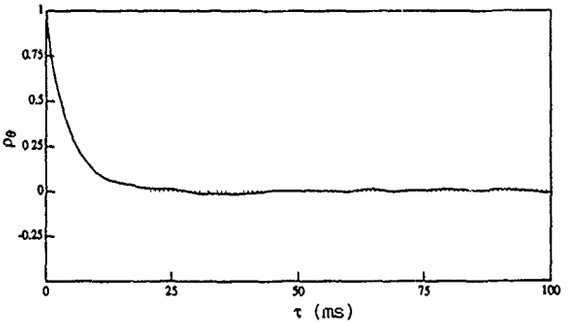

Fig. 16. Temperature autocorrelation function at x/D=15.0 and y/D=0.8 for R=2.3.

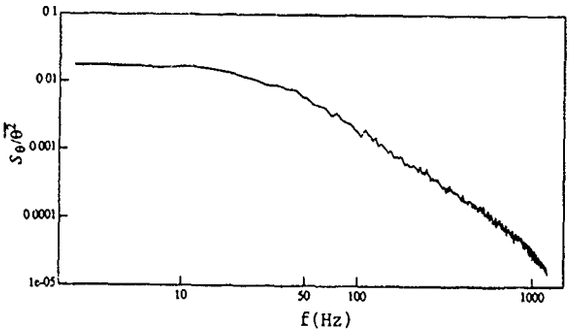

Fig. 17. Temperature autospectrum at x/D=15.0 and y/D=0.8 for R=2.3.

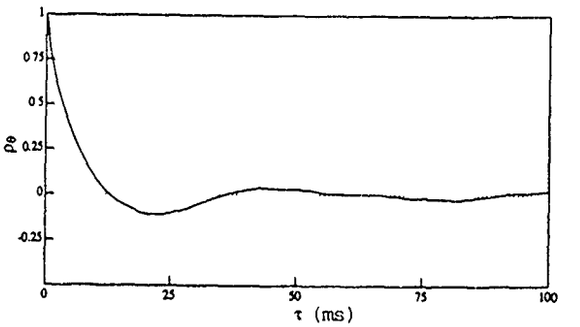

Fig. 18. Temperature autocorrelation function at x/D=25.0 and y/D=5.4 for R=2.3.

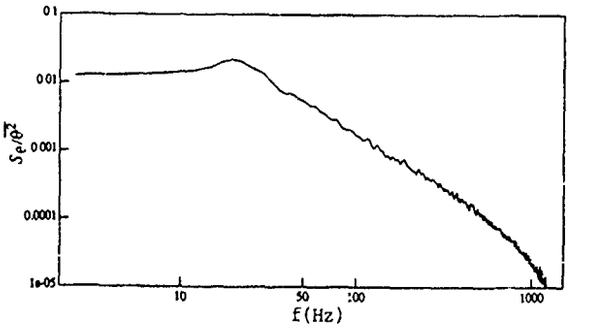

Fig. 19. Temperature autospectrum at x/D=25.0 and y/D=5.4 for R=2.3.

EIGHTH SYMPOSIUM ON
TURBULENT SHEAR FLOWS
Technical University of Munich
September 9-11, 1991

A One-Dimensional Proper Orthogonal Decomposition of the Downstream Flowfield of a Lobed Mixer

Lawrence Ukeiley, Mark Glauser and David Wick
Department of Mechanical and Aeronautical Engineering
Clarkson University
Potsdam, N.Y. 13699

Abstract

A one-dimensional scalar adaptation of the Proper Orthogonal Decomposition was applied to data taken in a lobed mixer flow field. The streamwise velocity data was obtained using a rake of 15 single component hot-wires. Through the application of the Proper Orthogonal Decomposition the amount of streamwise turbulent kinetic energy contained in the various proper orthogonal modes was examined for two different downstream locations. The large eddy or dominant mode was shown to have a significant decrease in this energy between 100 and 150 mm downstream from the lobe. It can be argued that this decrease in energy represents the break down of the large scale streamwise vortical structure. A pseudo flow visualization technique was also employed to help visualize this process.

Introduction

The existence of large scale structures in a lobed mixer flow field was examined through the application of a one-dimensional scalar Proper Orthogonal Decomposition (POD). A lobed mixer is a device that induces rapid mixing through the enhancement of the streamwise vorticity. A cartoon representation of this is shown in figure 1 where the lobed mixer is depicted as a convoluted flat plate mixer. The existence of large scale structure in the free shear layer behind a flat plate was first reported by Brown and Roshko[3]. Conrad[14] was among the first to report evidence of streamwise aligned vortex tubes embedded in the large scale structures found by the flow visualizations of Brown and Roshko. Liu[17] and references therein have attributed the formation of the three-dimensional vortex structure found in free shear layers to hydrodynamic-instability mechanisms. In a more recent study by Lasheras and Meiburg[15] a periodicly perturbed plate was used to generate the shear layer. This was done in an attempt to study the mechanisms that form the three-dimensional structure. They found that the streamwise vorticity could be manipulated by applying different perturbations to the upstream flow conditions. It was also found, for the case of the periodicly perturbed flat plate, that the counter-rotating streamwise vortical structures were embedded in the braids of connecting consecutive Karman vortices.

In the same time period more applied studies were being conducted on flow fields downstream of lobed mixers. Paterson[23] collected the first detailed flow measurements in this flow field. The study showed strong secondary flows along with streamwise vorticity with a spatial extent approximately equivalent to the lobe height. A later study (v. Werle et al[29]) showed the flow field downstream of the lobed mixer could be broken up into three distinct flow development regions. In the first region the streamwise vortex tubes began to develop, became fully developed in the second and dissipated in the third. Eckerle et al[7] conducted a study, in the same facility used in this work, using a Laser Doppler Anemometer. They documented that the three regions reported by Werle et al[29] could be shifted by changing the velocity ratio across the lobes. It was also deduced from their results that the seeds of the large scale vortices originate from the boundary layer of the lobed mixer.

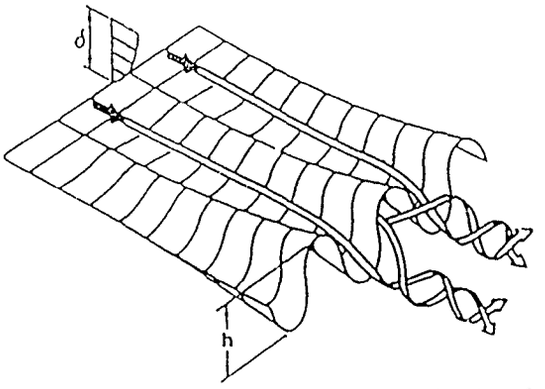

Figure 1 Lobed Mixer Enhancing Streamwise Vorticity from Werle et al[29]

Lumley[19] suggested using the POD technique to objectively identify coherent structures or "*large eddies*" in a turbulent flow. The method was first applied to the wake behind a cylinder by Payne[24]. The results of this study showed that the energy content in the dominant eddy was not significantly larger than that in subsequent eddies. Bakewell and Lumley[2] applied the technique on measurements taken in the near wall region of turbulent pipe flow. These results were more conclusive than the previous experiment, showing the dominant eddy to contain 90% of the total streamwise turbulent energy. Moin[21] applied the POD to data generated by a large eddy simulation of a turbulent channel flow. His results showed that the dominant eddy contained up to 64% of the turbulent kinetic energy. Moin and Moser[22] applied the POD to turbulent channel flow data generated by a direct numerical simulation. In their decomposition the dominant eddy was found to contain as much as 76% of the turbulent kinetic energy. Herzog[13] utilized the POD technique on hot-film measurements taken in the near wall region of a turbulent boundary layer. The results obtained showed that the dominant eigenmode contained approximately 60% of the total kinetic energy, consistent with the results obtained by Moin. Leib et al[16], Glauser et al[9] and Glauser et al[10] applied the POD to the near field region of a turbulent axisymmetric jet. Their results showed that the first eigenmode contained approximately 10% of the total turbulent kinetic energy and that an accurate representation of the flow field can be obtained by using only the first three eigenmodes. Sirovich et

al[25] applied the decomposition technique to turbulent convection flow simulations, for the case of stress-free boundary conditions. For their flow conditions, the first eigenmode contained 43% of the kinetic energy with 60% of the energy being represented by the summation of the first five modes. Chambers et al[4] utilized the POD to examine Monte Carlo simulations of a randomly forced Burgers' equation with zero velocity boundary conditions. They showed that the number of proper orthogonal modes needed to reproduce 90% of the total energy increased with Reynolds number. Delville et al[6] applied the POD to the turbulent wake downstream of a flat plate, using a rake of 21 single component hot-wires, placed perpendicular to the plate. They found that 70% of the mean-square streamwise velocity was recovered within the first three modes. Glezer et al[12] developed an extension to the POD capable of dealing with flows in which long term correlations measurements are not possible. This extended POD was applied to a time periodically forced plane mixing layer. They found that as much as 78% of the information, collected from a rake of 10 wires placed in a cross-stream orientation, was recovered with a 3 mode reconstruction.

In the study discussed here multi-point hot-wire measurements were used to obtain the one-dimensional cross-correlation tensor needed to apply a one-dimensional version of the POD. Measurements were taken using a 2:1 velocity ratio across the lobes. The evolution of the large scale structures were evaluated between 100 and 150 mm downstream of the lobed mixer. The evaluation was done by reconstructing the original velocity field so that techniques such as pseudo flow visualizations could be applied (v. Delville et al[5] and Ukeiley et al[28]). The streamwise turbulent kinetic energy content of the large scale structure along with other turbulence properties were compared at 100 and 150 mm downstream from the lobe as well.

Proper Orthogonal Decomposition

In 1967 Lumley[19] proposed the POD as an unbiased procedure for identifying large scale structures in turbulent flows. It is based on decomposing the strongly inhomogeneous directions in the flow into orthogonal modes using the Karhunen-Loeve expansion[18]. If the candidate structure, ϕ, is projected onto the velocity vector field, $\vec{u}(\vec{r},t)$, as shown below, the result is the structure with the largest mean-square projection on this velocity field;

$$\overline{|\vec{u}\ \ \vec{\phi}|^2} = \overline{|\alpha|^2}. \tag{1}$$

Equation 1 is assumed to be normalized by the modulus of $\vec{\phi}$ since it is the degree of the projection that is of interest and not the amplitude. Through the use of calculus of variations, this maximization process leads to the following integral eigenvalue problem,

$$\int\int\int\int R_{ij}(\vec{x},\vec{x}',t,t')\phi_j^{(n)}(\vec{x}',t')d\vec{x}'dt' = \lambda^{(n)}\phi_i^{(n)}(\vec{x},t) \tag{2}$$

The kernel of equation 2 is the velocity cross-correlation tensor, $R_{ij}(\vec{x},\vec{x}',t,t') = \overline{u_i(\vec{x},t)u_j(\vec{x}',t')}$. Since this tensor exhibits symmetrical features the solutions to this problem are governed by the Hilbert-Schmidt theory (v. Lumley[20]).

The POD reduces to the Harmonic Decomposition in directions which are either homogeneous, stationary or periodic implying that Fourier analysis should be used in these directions.

In the lobed mixer flow, the downstream direction (z) (see figure 2) is assumed to be locally homogeneous for a first order approximation and time is stationary. By applying Fourier analysis to the cross-correlation tensor, the cross-spectral tensor is obtained as follows,

$$\int_{-\infty}^{\infty} R_{ij}(x,x',y,y',\zeta,\tau)e^{-i2\pi(\zeta k_1+\tau f)}d\tau d\zeta = \Phi_{ij}(x,x',y,y',f,k_1), \tag{3}$$

where $\zeta = z - z'$ and $\tau = t - t'$.

Using this cross-spectral tensor as the kernel, equation 2 reduces to;

$$\int \Phi_{ij}(x,x',y,y',f,k_1)\psi_j^{(n)}(x',y',f,k_1)dx'dy' = \lambda^{(n)}(f,k_1)\psi_i^{(n)}(x,y,f,k_1), \tag{4}$$

where the ψ's are the frequency and wavenumber dependent eigenfunctions and x and y denote the remaining inhomogeneous directions (see figure 2). It should be noted that this flow has two directions of strong statistical inhomogeneity.

As a first step in analyzing this flow only a one-dimensional version of the POD was applied. This involves obtaining the one-dimensional cross-spectral tensor in the cross lobe direction (x) and then solving the following integral eigenvalue problem;

$$\int \Phi_{11}(x,x',f)\psi_1^{(n)}(x',f)dx' = \lambda^{(n)}(f)\psi_1^{(n)}(x,f). \tag{5}$$

The process of solving this eigenvalue problem was carried out at both downstream locations separately. The eigenmodes obtained from equation 5 are ortho-normal and can be used to reconstruct the original velocity field (which was decomposed through Fourier analysis) in the following manner;

$$\hat{u}_1(x,f) = \sum_{n=1}^{\infty} a_n(f)\psi_1^{(n)}(x,f), \tag{6}$$

where the random coefficients $a_n(f)$ are calculated by,

$$a_n(f) = \int \hat{u}_1(x,f)\psi_1^{(n)*}(x,f)dx. \tag{7}$$

In the previous equations $\hat{u}_1$ is the Fourier transform of the streamwise velocity component. The energy spectrum can also be obtained from,

$$S(x,f) = \sum_{n=1}^{\infty} \lambda^{(n)}(f)\psi_1^{(n)}(x,f)\psi_1^{(n)*}(x,f), \tag{8}$$

where $\lambda^{(n)}(f)$ are the eigenspectra.

The numerical approximation, detailed by Glauser et al[9], simply consists of replacing the integral in equation 5 by an appropriate quadrature rule (in this study a trapezoidal rule). $\Phi_{11}(x,x',f)$ is then obtained from experimental measurements and utilized in equation 5 to obtain the eigenvalues and eigenfunctions. These eigenfunctions and eigenvalues are then utilized to reconstruct the original random velocity field as well as velocity spectra.

Experiment

The facility used in this experiment was split down the center, by a steel plate, with separately controlled blowers on either side. A front view of the test section with the contours of the lobed mixer superimposed on it is shown in figure 2. The flow conditions at the inlet were documented by Eckerle et al[7]. They found that the boundary layers on the plate were turbulent with an approximate 1% turbulence intensity in the core flow. A rake of hot-wires was placed at y=28.5 mm (see figure 3) for both 100 and 150 mm downstream from the lobe. Figure 3 is an expanded view of the box marked *testing area* in figure 2. The hot-wire rake (v. Ukeiley et al[27]) consisted of 15 probes evenly spaced across a full lobe width.

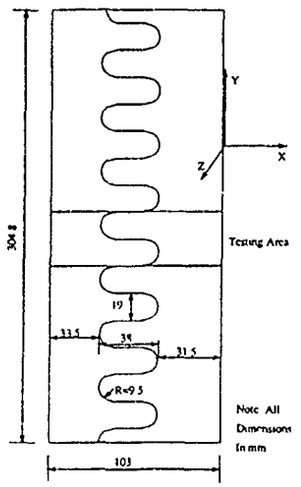

Figure 2 Front View of Lobed Mixer

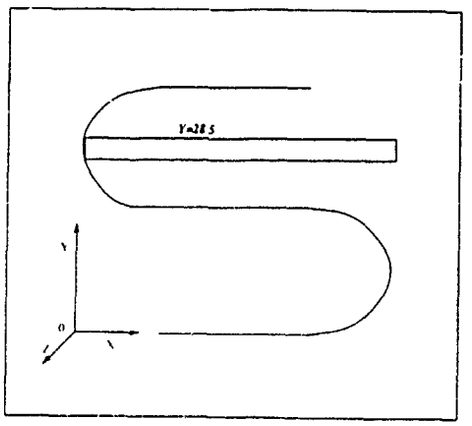

Figure 3 Expanded View of Test Section

A personal computer based data acquisition system was employed to collect the data It consisted of a Zenith 248 computer, a MetraByte DAS-20, 16 channel, 12 bit A/D converter and four MetraByte SSH-4 simultaneous sample and hold boards All data was sampled at a rate of 3 kHz with low-pass anti-aliasing filters set at 1.4 kHz for each channel To ensure an adequate statistical sample, 100 blocks of 256 samples were taken The hot-wires were calibrated using a polynomial scheme as detailed by George et al[8].

Results

Figures 4 and 5 show the mean velocity plotted as a function of the distance across the lobe (x) at z=100 and 150 mm respectively. At z=100 mm, the velocity peaks around the center of the lobe By z=150 mm, the average velocity begins to level out, although the profile is not smooth. These results, although physically difficult to conceptualize, are consistent with LDA data taken in this tunnel Note that at z=150 mm, the profile is much broader than at z=100 mm, where a much steeper mean gradient is observed This would imply that by z=150 mm, the mean shear has been mixed out and the turbulence gains energy at its expense, consistent with the results of Eckerle et al [7] They showed that for a velocity ratio of 2 1 the turbulent kinetic energy, averaged over x and y, increased as a function of downstream (z) distance.

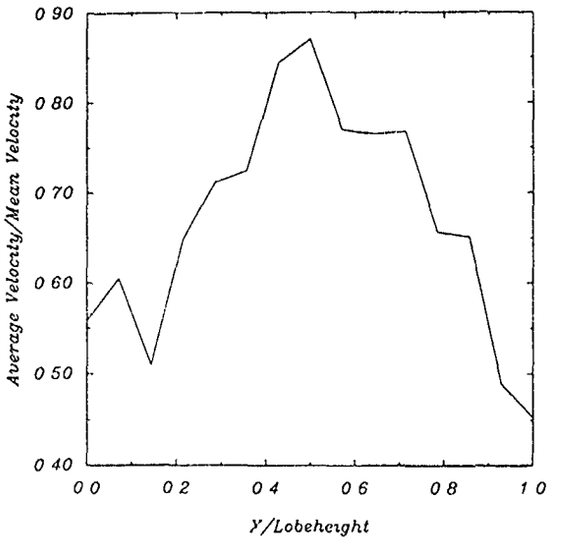

Figure 4. Mean Streamwise Velocity Across Lobe y=28 5, z=100 mm

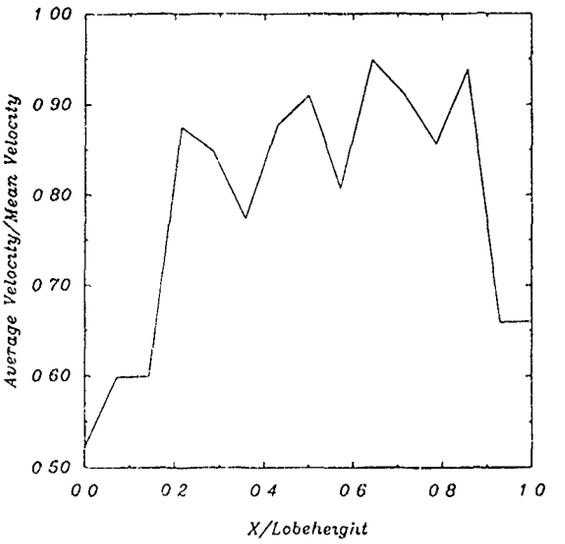

Figure 5 Mean Streamwise Velocity Across Lobe y=28.5, z=150 mm

Figures 6 and 7 show the RMS streamwise fluctuating velocity, plotted versus x position, for the two downstream positions. Values calculated from the reconstruction of the first proper orthogonal mode first three and first five have been superimposed on these figures. By comparing figures 6 and 7 (i.e., z=100 mm to z=150 mm) it is seen that the streamwise turbulent kinetic energy in the flow field is more evenly distributed across the x direction at 150 mm downstream. This implies that as the flow progresses downstream the two streams mix and this energy becomes fairly well distributed across the whole region The peaks in the RMS plots at z=100 mm are slightly shifted to the low speed side implying that the streamwise vortex tubes have been shifted. When examining the reconstructed values shown in figures 6 and 7 the first mode reconstruction shows that the most energetic spatial locations are reproduced first, i e., the spatial location corresponding to wire 10, x=.027. It can also be inferred from these figures that subsequent modes fill in the other spatial locations until the profile has been reproduced Note that for both downstream locations the first proper orthogonal mode contributes significantly to the RMS profiles

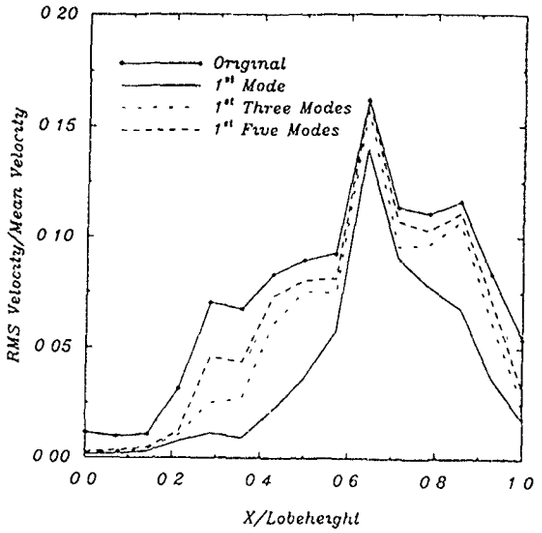

Figure 6. Streamwise RMS Velocity (Original, 1st Mode, 1st Three Modes and 1st Five Modes) y=28 5 mm, z=100 mm

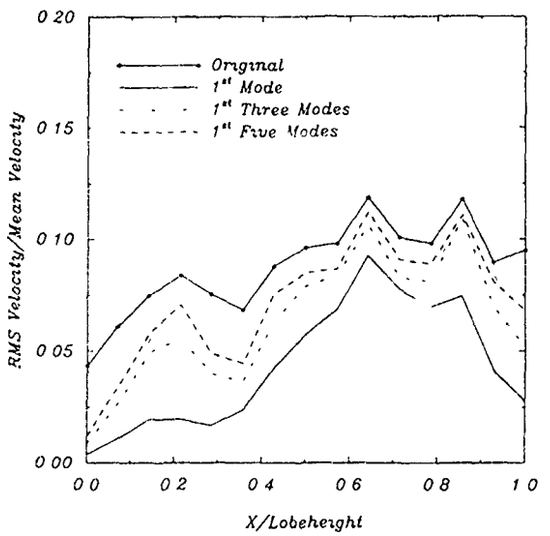

Figure 7 Streamwise RMS Velocity (Original, 1st Mode, 1st Three Modes and 1st Five Modes) y=28 5 mm, z=150 mm

Eigenspectra

Figures 8 and 9 show the eigenspectra for the first, second and third modes for both z=100 and 150 mm. The eigenvalues shown here represent the contribution to the energy from the streamwise velocity component for each mode, integrated across the lobes The dominance of the first mode is apparent in all of the plots. The total streamwise energy contained in each proper orthogonal mode can be obtained by summing over all frequencies. Figure 10 shows the total streamwise energy in each proper orthogonal eigenmode plotted versus mode number. The curve representing 100 mm downstream shows that the contribution from the eigenmodes decreases and levels out after about 7 modes. From this curve it can also be inferred that the larger scales, represented by the first few modes, contain the majority of the energy at this spatial location. In contrast to this, the curve representing 150 mm downstream, shows a less steep gradient implying that the energy is distributed more evenly over the scales. Table 1 shows the percentage of energy contained in the eigenspectral modes. The percentage of energy contained in the dominant

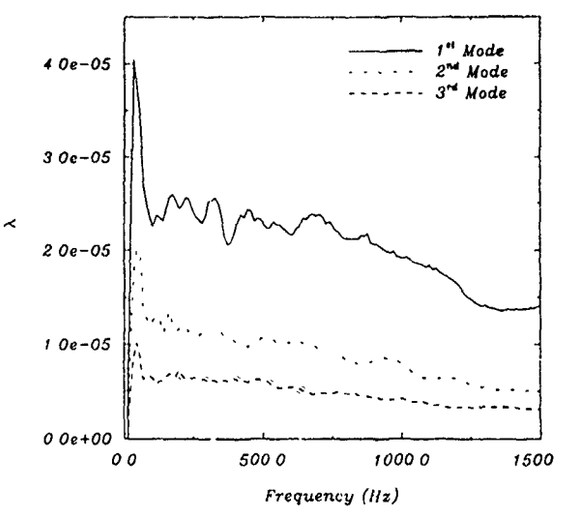

Figure 8 Eigenspectra y=28.5 mm, z=100 mm

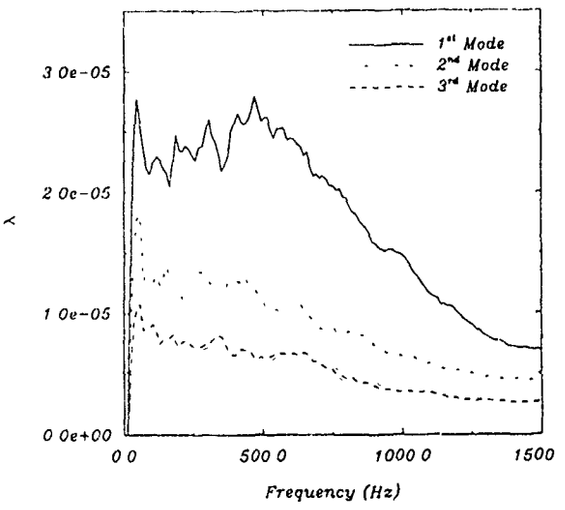

Figure 9: Eigenspectra y=28.5 mm, z=150 mm

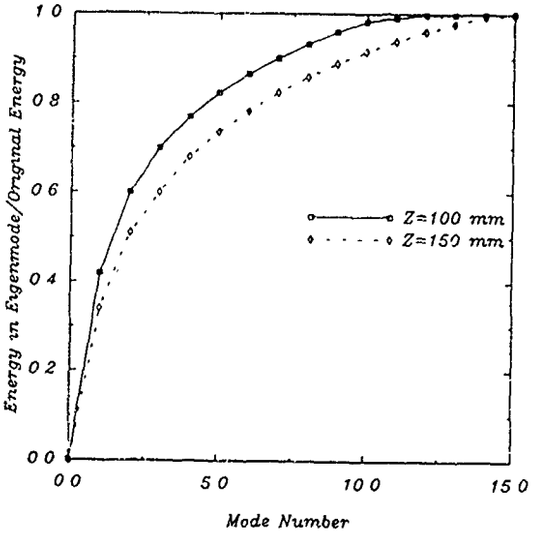

Figure 10: Convergence of Eigenspectra Modes y=28.5 mm

Position y,z(mm)	1st mode	1st 2 modes	1st 3 modes	1st 4 modes	1st 5 modes
28.5, 100	42	60	70	77	82
28.5, 150	34	51	60	68	74

Table 1: Percent Energy In Eigenspectral Modes

mode is noticeably larger at 100 mm downstream than at 150 mm downstream. This is consistent with the earlier suggestion that the energy is distributed over a wider range of scales by 150 mm downstream of the lobed mixer. These results would indicate that the large scale features(coherent structures) have dissipated significantly by 150 mm downstream, which is consistent with the results found by Eckerle et al[7].

Eigenfunctions

The eigenfunctions shown in figure 11 are plotted to examine how their shapes change with downstream position. These eigenfunctions are plotted as a function of x, at a frequency of 700 Hz. This frequency was chosen because it corresponds to a natural shedding phenomenon of this particular lobed mixer as discussed by Ukeiley et al[28]. Figure 11 shows the real part of the eigenfunctions for the first proper eigenmode at both downstream positions. The eigenfunctions in this figure exhibit the same basic shape with only slight magnitude differences at the two downstream positions. This indicates that it might be possible to develop a scaling function which could determine the eigenfunctions at different downstream locations while actually knowing them at only one. This type of scaling function could be helpful in evaluating the severity of the assumption that the streamwise direction is locally homogeneous.

Instantaneous Velocity

Using equation 6 and an inverse Fourier transform routine, the instantaneous velocity-time traces can be reproduced for any of the hot-wire locations. The pseudo flow visualization technique used here is a similar technique to the one developed by Tabatabai et al[26] and Delville et al[5], and is described in more detail by Ukeiley et al[28]. It is a visualization technique that utilizes instantaneous hot-wire anemometer data to create a graphical representation of velocity interactions in a flow field. Since the velocities are sampled simultaneously, each of the hot-wire measurements are at the same instant in time. To develop the pseudo flow visualization plots the samples corresponding to the same time are then plotted as perturbations about a mean vertical line. These plots have

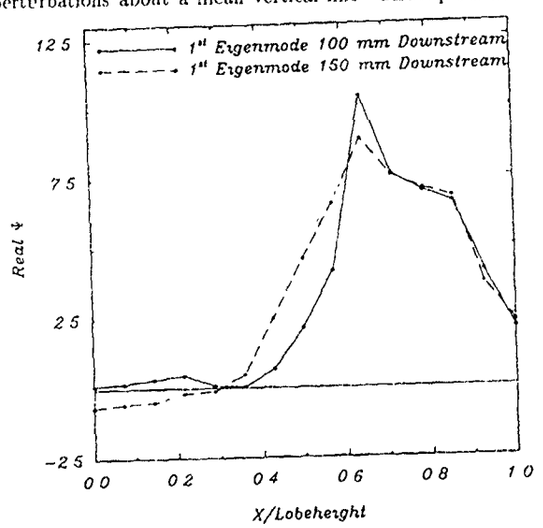

Figure 11: Real Part of First Mode Eigenfunctions for z=100 mm and 150 mm at y=28.5 mm

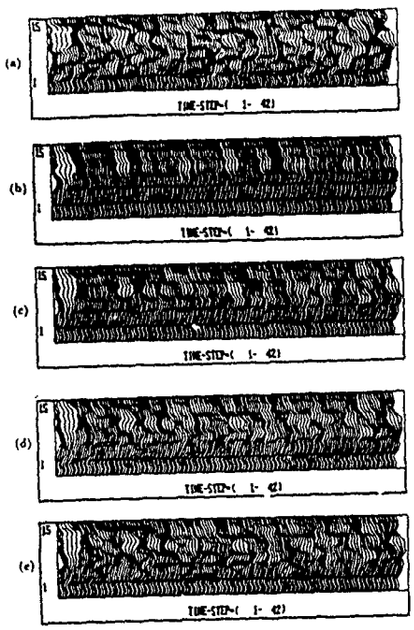

Figure 12: Pseudo Flow Visualization Plots z=100 mm, a) Original Signal b) First Proper Orthogonal Mode c) First Three d) First Five E) First Seven

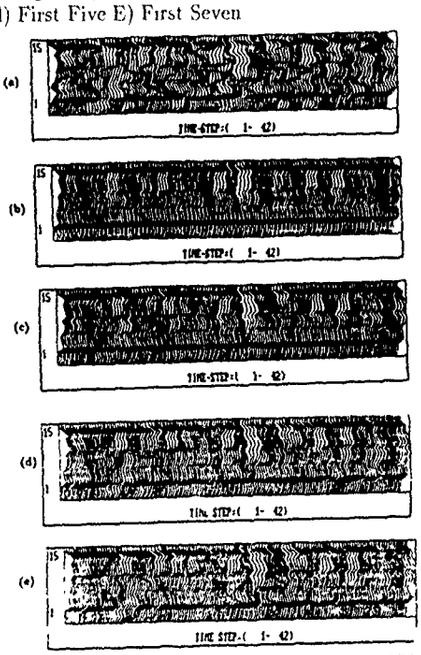

Figure 13: Pseudo Flow Visualization Plots z=150 mm, a) Original Siganl b) First Proper Orthogonal Mode c) First Three d) First Five e) First Seven

wire number as the abscissa and sample number as the ordinate. Using the mean convection velocity, the sampling rate and the distance between probes, the pictures are scaled to an approximate representation of that location in the flow field.

Figures 12 and 13 show pseudo flow visualization plots for positions at z=100 and 150 mm respectively. These plots compare the original signal with a reconstruction using the first proper orthogonal mode, first three, first five and first seven. This idea of viewing different proper orthogonal modes through a pseudo flow visualization technique was first developed by Delville et al[5]. From figure 12 (z=100 mm) it is evident that the first mode representation has the large scale features of the streamwise velocity field. It is also apparent

that as more modes are used in the reconstruction process more small scale features are represented. The pseudo flow visualization plot using the summation of the first seven modes is almost identical to the original signal. Figure 13 shows a similar plot to figure 12 at z=150 mm. In the plot showing the first mode reconstruction the large scale structures are not as evident as those at z=100 mm, which is consistent with table 1 and the RMS velocity analysis. The plot using the first seven modes shows the general trends of the plot using the original signals but is not as good of a representation as it was in figure 12, again consistent with table 1 These results suggest that the first proper orthogonal mode is representative of the large scale feature in the flow field. It also would indicate, as has been speculated, that the low dimensional models for turbulence based on the POD are capturing the overall picture yet losing the fine detail(v. A. bry et al[1] and Glauser et al[11]).

Conclusions

An initial investigation studying the evolution of large scale structures in the downstream region of the lobed mixer was conducted. Through the use of a one-dimensional scalar version of the POD this study has shown the existence and breakdown of these large scale coherent structures. The mean and RMS velocities were examined and determined to be consistent with the results of Eckerle et al[7].

The solution to the eigenvalue problem has shown a rapid convergence of the eigenmodes to the original signal. The large eddy, defined by Lumley to be the dominant eigenmode, contained as much as 42% of the total streamwise kinetic energy It has also been shown that by the fifth mode 82% of this energy has been represented. It was observed that at z=100 mm the dominant eigenmode contained significantly more energy than the same eigenmode at z=150 mm

The RMS streamwise fluctuating velocity and eigenfunction analysis showed the evolution of the flow between 100 and 150 mm downstream The RMS velocity profiles showed the energy becoming more evenly distributed at 150 mm as compared to 100 mm. This implies that larger more dominant scales break down and their energy becomes redistributed over the flow field (shifting to more homogeneous turbulence). This result seems consistent with the results of Eckerle et al[7] who showed the large scale vorticity breaking down between 100 and 150 mm The comparison of the eigenfunctions for the two downstream positions showed that the general shape did not vary much This implies that it may be fruitful to develop scaling functions that can relate eigenfunctions to different downstream positions, thus reducing the data collection procedure

Through the pseudo flow visualization analysis it was shown that the original time trace signals were adequately reproduced using a seven mode reconstruction The large scale features were reproduced using the first mode, yet it took as many as seven modes to reproduce the smaller scale features. The large scale structures obtained using only the first mode are clearly discernible at 100 mm downstream while at 150 mm they are not as apparent.

The results showing the rapid convergence of the eigenspectra and the dominant first mode suggests that it may be beneficial to use the POD in conjunction with the Navier Stokes equations to develop a low dimensional dynamical systems model for this flow (v Aubry et al[1] and Glauser et al[11]).

References

[1] Aubry, N., Holmes, P., Lumley, J.L and Stone, E. (1988) "The Dynamics of Coherent Structures in the Wall Region of a Turbulent Boundary Layer". *J. Fluids Mech* 192

[2] Bakewell, P. and Lumley, J.L (1967) "Viscous Sublayer and Adjacent Wall Region in Turbulent Pipe Flow" *Phys. Fluids* 10(3), No. 9: 1880-89.

[3] Brown, G.L. and Roshko, A. (1974)"On Density Effects and Large Structure in Turbulent Mixing Layers".*J. Fluid Mech.* 64

[4] Chambers, D.H., Adrian, R.J., Moin, P., Stewart, D.S. and Sung, H.J. (1988) "Karhunen-Loeve Expansion of Burgers' Model of Turbulence". *Phys. Fluids* 31(9).

[5] Delville, J., Bellin, S., Garem, J.H. and Bonnet, J.P. (1988)"Analysis of Structures in a Turbulent Plane Mixing Layer by Use of a Pseudo Flow Visualization Method Based Hot-Wire Anemometry". *Advances in Turbulence II.*

[6] Delville, J., Bellin, S. and Bonnet, J.P. (1989) "Use of the Proper Orthogonal Decomposition a Plane Turbulent Mixing Layer". in *Turbulence and Coherent Structures.* Kluwer.

[7] Eckerle, W.A., Sheibani, H. and Awad, J., (1990)"Experimental Measurements of the Vortex Development Downstream of a Lobed Forced Mixer". ASME 90-GT-27.

[8] George, W.K., Beuther, P.D. and Shabbir, A. (1987) "Polynomial Calibrations for Hot Wires in Thermally-Varying Flow". ASME FED-Vol. 53. pp. 3-6.

[9] Glauser, M.N., Leib, S.J. and George, W.K. (1987) "Coherent Structures in the Axisymmetric Jet Mixing Layer". *Turbulent Shear Flows 5*, Springer Verlag.

[10] Glauser, M.N. and George, W.K. (1987) "An Orthogonal Decomposition of the Axisymmetric Jet Mixing Layer Utilizing Cross-Wire Measurements". *Turbulent Shear Flows 6.*

[11] Glauser, M.N., Zheng, X. and Doering C.R. (1989) "The Dynamics of Organized Structures in the Axisymmetric Jet Mixing Layer. in *Turbulence and Coherent Structures.* Kluwer

[12] Glezer, A., Kadioglu, Z. and Pearlstein, J. (1989) "Development of an Extended Proper Orthogonal Decomposition and its Application to a Time Periodically Forced Mixing Layer" *Phys Fluids A* Vol 1, 8, pp. 1363-1373.

[13] Herzog, S. (1986) "The Large Scale Structure in the Near-Wall of Turbulent Pipe Flow". PhD Dissertation, Cornell University.

[14] Konrad, J.H (1976) "An Experimental Investigation of Mixing in Two-Dimensional Turbulent Shear Flows With Applications to Diffusion Limited Chemical Reactions". *Tech. Rep.* CIT-9-PU

[15] Lasheras, J.C. and Meiburg, E. (1990) "Three-Dimensional Vorticity Modes in the Wake of a Flat Plate". *Phys Fluids A*, Vol 2, No 3, pp 371-380.

[16] Leib, S.J., Glauser, M.N. and George, W.K. (1984) "An Application of Lumley's Orthogonal Decomposition to the Axisymmetric Jet Mixing Layer". Proc. 9th Rolla Symp.

[17] Liu, J T C (1989) "Coherent Structures in Transitional and Turbulent Free Shear Flows" *Ann Rev. F Mech.*, 21

[18] Loeve, M. (1963) *Probability Theory II* Springer Verlag.

[19] Lumley, J L (1967) "The Structure of Inhomogeneous Turbulent Flows". *Atm. Turb. and Radio Wave Prop.*. Yaglom and Tatarskv eds Nauka. Moscow, pp 166-178.

[20] Lumley, J.L (1970) *Stochastic Tools in Turbulence* Academic Press, New York

[21] Moin. P. (1984) "Probing Turbulence via Large Eddy Simulation" AIAA-84-0171.

[22] Moin, P. and Moser, R D (1989) "Characteristic-Eddy Decomposition of Turbulence in a Channel" *J Fluid Mech* 200

[23] Paterson, R W , (1982) "Turbofan Mixer Nozzle Flowfield -A Benchmark Experimental Study" *ASME Journal of Engineering for Gas Turbines and Power* , Vol. 106, pp 692-698.

[24] Payne, F R. (1966) "Large Eddy Structure of a Turbulent Wake". PhD Dissertation, Pennsylvania State University

[25] Sirovich, L., Maxey, M and Tarman, H (1987) " Analysis of Turbulent Thermal Convection" *Turbulent Shear Flows 6.*

[26] Tabatabai, M Kawall, J.G. and Keffer, J.F. (1987)"Flow Visualization Using Hot-Wire Anemometry" *Dantec Information* Vol.04.

[27] Ukeiley, L., Wick, D. and Glauser, M. (1990) "A Novel Hot-Wire Rake Design" ASME FED-Vol 97 pp 87-92.

[28] Ukeiley, L., Wick, D. and Glauser, M. (1991) "Coherent Structure Identification in a Lobed Mixer". ASME 91-GT-307.

[29] Werle, M.J., Presz, W. and Paterson R.W. (1987) "Flow Structure in a Periodic Axial Vortex Array". AIAA-87-0160.

EIGHTH SYMPOSIUM ON
TURBULENT SHEAR FLOWS
Technical University of Munich
September 9-11, 1991

25-3

A CIRCULAR JET INJECTED INTO THE WAKE OF A CIRCULAR CYLINDER SET IN A UNIFORM FLOW

Hiroya YAMADA*), Ikuo NAKAMURA**), Shintaro YAMASHITA***)
and Haruhisa YANO*)

*) Department of Mechanical Engineering, Daido Institute of Technology, 2-21, Daido-cho, Minami-ku, Nagoya 457, Japan
**) Department of Mechanical Engineering, Nagoya University, Nagoya 464-01, Japan
***) Department of Mechanical Engineering, Gifu University, Gifu 501-11, Japan

ABSTRACT

An experimental study has been performed on the three-dimensional mixing process in the turbulent jet which was injected into a quiescent fluid as well as into the wake of the cylinder from a circular hole made on the circular cylinder. Even in the case of an injection into quiescent fluid, the flow field exhibits asymmetrical spread, and secondary flow. In the case of the injection into the wake, the asymmetrical spread becomes rather remarkable, and the secondary flow becomes even stronger than with injection into quiescent fluid. Although the decay of the relative maximum velocity in relation to the wake differs according to the injection velocity ratio, it decays in proportion to about $x^{-2/3}$. The turbulence intensity of the wake becomes lower by injection of the jet.

NOMENCLATURE

d	Diameter of the injection hole
D	Diameter of the circular cylinder
L_y, L_z	Half-value width of y- and z-direction in the jet injected into a quiescent fluid, respectively
L''_y, L''_z	Half-value widen of y- and z-direction obtained from the relative velocity profiles in relation to the wake, respectively
R_e	Reynolds number = $U_j d/\nu$
U, u	Mean and fluctuating velocity in the x-direction
$\sqrt{\overline{u^2}}$	RMS value of the fluctuating velocity
U_j	Mean velocity at the exit of the injection hole
U_m	Maximum velocity in the jet
U_0	Reference main-flow velocity at x = -95 mm
U'	Mean velocity in the x-direction of the wake
U'_c	Mean velocity in the central plane of the wake (y = 0)
U_∞	Mean velocity of the uniform flow
U''	Mean velocity relative to the wake = $U - U'$
U''_m	Maximum value of U''
x, y, z	Coordinate system with its origin at the center of the injection hole
η	Dimensionless coordinate obtained by the half-value width
ρ, ν	Density and kinematic viscosity of fluid, respectively
N	Number of revolutions of the small windmill

INTRODUCTION

This report concerns the flow field composed of the circular air jet and the wake of the circular cylinder set perpendicular to the uniform flow from which the jet is injected. Like this flow, configurations appear in cases of the wake of a self-propelled body [1] and a flame holder [2]. Very recently, Higuchi and Kubota examined jet and axisymmetric wake interaction including zero-momentum case [3]. Another important example is the injection from a trailing edge of the film cooling of a gas turbine blade as shown in Fig. 1 [4], since it exerts a large effect on the efficiency of the gas turbine. Many studies on circular jets [5] and circular compound jets injected into the uniform flow [6] have been reported. However, a three-dimensional mixing in a circular jet injected into the wake of a two-dimensional circular cylinder as the present flow field, one of complex turbulent jets, has not been examined.

In this study, the jet was injected from a circular hole made on the circular cylinder as shown in Fig. 2, and the jet was also injected into a quiescent fluid as well as into the wake of the cylinder. It will be clarified experimentally that the three-dimensional mixing process in this turbulent jet, the mean flow properties, the features of the secondary flow and the turbulence properties will be discussed.

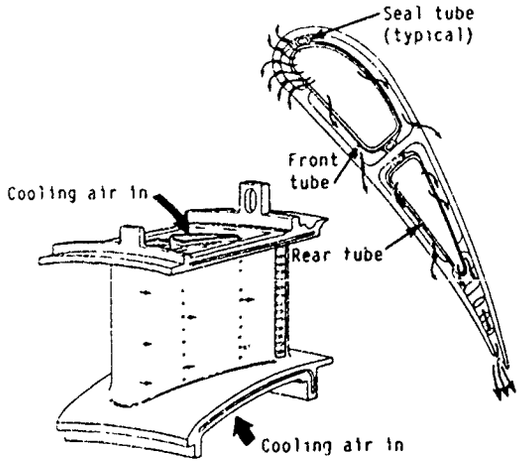

Fig. 1 Injection from a trailing edge of the cooling of the turbine blade

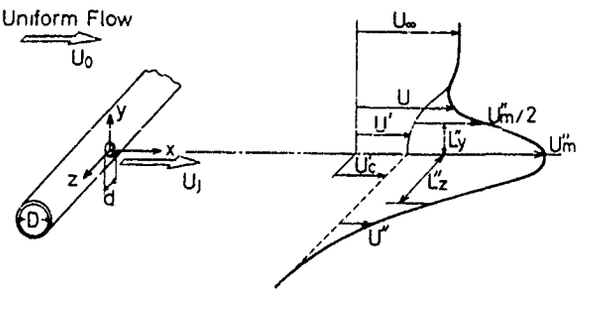

D=5 mm , d=2.5 mm , $U_0 \fallingdotseq$ 20 m/s

Fig. 2 Flow field and coordinate system

EXPERIMENTAL APPARATUS AND METHOD

The measuring cross-section of the wind tunnel used in the present experiment is a square with a side-length of 300 mm, and the turbulence intensity of the main flow is about 0.5 %. The jet is injected from the injection hole of diameter 2.5 mm which is drilled at the center of the span-width of the circular cylinder of the outside diameter 5 mm. The injection flow rate is measured by a laminar flow meter. The ratio of the injection mean velocity to the reference velocity, that is U_j/U_0, is varied in the range of 1, 2 and 3. The corresponding Reynolds number R_e is 3300, 6700, 10000, respectively. The reference velocity U_0 is about 20 m/s. The experiment of injection into the quiescent fluid is carried out for reference with the same Reynolds number as that of wake with $U_j/U_0 = 3$. The measurements were performed at ten cross sections with x/d = 31.8 to 621. The velocity measurement was made using a hot-wire anemometer.

EXPERIMENTAL RESULTS AND DISCUSSION

Mean flow and secondary flow

In the jet field injected from a circular hole drilled on the circular cylinder, since even the case of the injection into the quiescent fluid the secondary flow occurred as shown in Fig. 9(a) as will be explained later, there was a slight asymmetry in the mean velocity profile.

Figures 3 (a) and (b) show the mean velocity profiles in the plane containing the jet-axis in case of the injection into the wake. The chain line in this figure indicates the velocity profile of the wake alone. Figure 3(a) indicates the velocity profiles in the y-direction. In the region at $x/d \leq 141$, the wakes are deformed by the jet, and the velocity profiles have a shape as the jet juts out into the wake. The profile becomes similar downstream of this section, but even far downstream, the velocity profile of the jet is not coincident with that of the

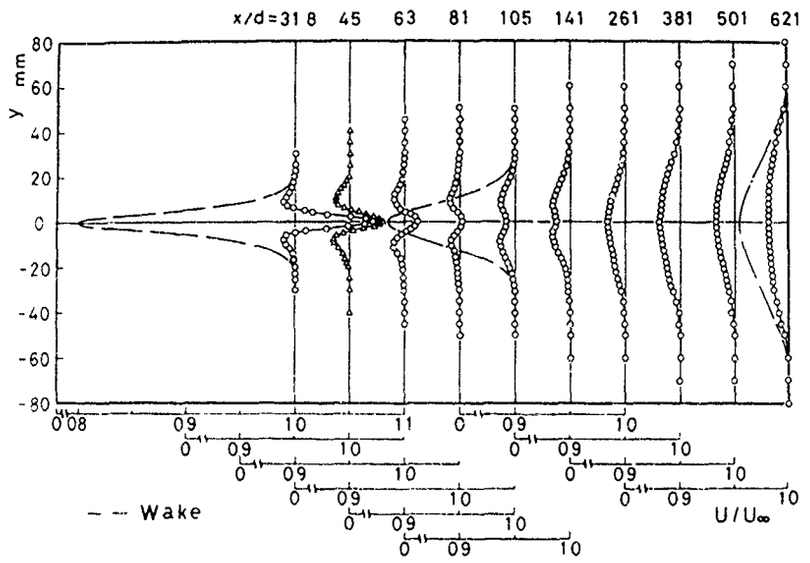

(a) Profiles in the y-direction

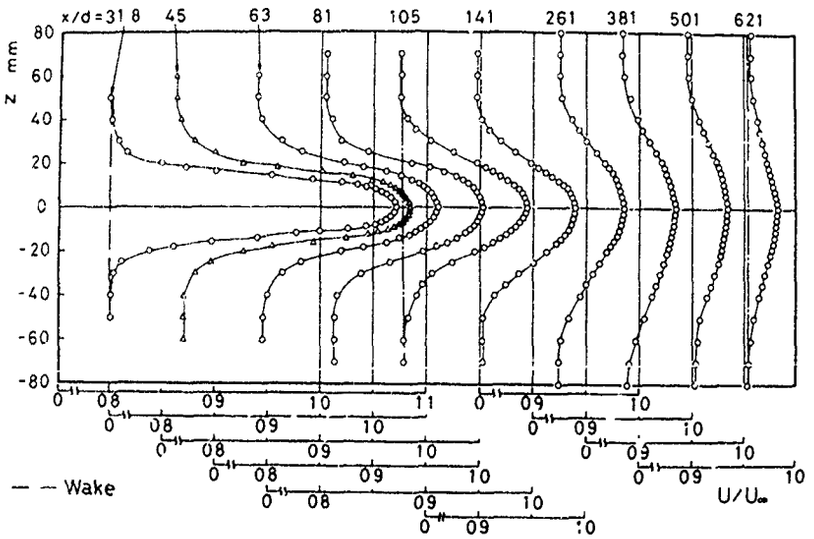

(b) Profiles in the z-direction

Fig. 3 Mean velocity profiles in the central cross-section of the jet ($U_j/U_0 = 3$)

wake. Figure 3(b) shows the velocity profiles in the z-direction.

Figure 4 gives the variations in the x-direction of the center-line mean velocity of the jet and the wake. The center-line velocity in $U_j/U_0 = 3$ decreases rapidly until about $x/d = 100$, but that in $U_j/U_0 = 2$ is nearly constant within this measuring range; also, that in $U_j/U_0 = 1$ increases downstream like the wake. A difference due to velocity ratio is almost unappreciable downstream of $x/d \gtrsim 400$, and the velocity of the wake does not coincide with that of the uniform flow furthermost downstream.

Figure 5 shows the non-dimensional profiles of a relative velocity to the wake in the y- and z-direction, respectively. The two-dimensional [7] and the circular [8][9] compound jet indicate that the relative velocity profile in relation to the uniform flow has similarity at the free-developed-flow region. Though the present profiles are similar at the cross sections of $x/d \gtrsim 31.8$, the difference between the profiles in y- and z-direction is clearly observed. The similar profiles are compared with a Gaussian profile [10] for the jet injected into quiescent fluid. A solid line or ④ in this figure indicates the Gaussian profile. The present profiles in the y-direction well coincide with Gaussian profile except in the outer region, but the profiles in the z-direction differ from the Gaussian profile in the central part of the jet. The comparison between the Gaussian profile and the relative similar profile in the compound jets ① ~ ③ are shown in the upper left-side of the figure. The profile ① represents an experimental equation in the two-dimensional compound jet by Bradbury [7]. The profile ③ indicates an experimental result in the circular compound jet by Tani and Kobashi [8], and the profile ② indicates its theoretical equation by Squire and Trouncer [9].

Figure 6 shows the decay of the relative maximum velocity to the wake. The decay of the relative maximum velocity in the present jet cannot be expressed with $U_m \propto x^{-1}$ as the injection into the quiescent fluid. Therefore, we inferred it to be expressed as $U''_m \propto x^{-n}$, and this figure illustrated by both-logarithms for the purpose of examining decay index n. According to Rajaratnam [11], the circular compound jet has been classified as a strong jet with $U''_m/U_\infty \gg 1$ and a weak jet with $U''_m/U_\infty \ll 1$. In the range of the present experiments, since the U''_m/U_∞ values are 0.27 to 0.02, according to Rajaratnam, the present jet can be considered as the weak jet. Rajaratnam has reported that it can be expressed as $U''_m \propto x^{-2/3}$ in the weak jet. The decay index of the present result differs due to the velocity ratio, and its value nearly equals Rajaratnam's index when $U_j/U_0 = 2$.

Figure 7(a) shows the variations of the half value width which was determined from the relative velocity distribution to the wake. The variations of the half-value width in the present jet cannot be expressed with $L \propto x$ as the injection into the quiescent fluid. Therefore, we inferred that it is expressed with $L'' \propto x^n$, and this figure is illustrated by both-logarithms for the purpose of examine the index n. In the upstream regions near the injection hole, L''_z is remarkably larger than L''_y, but these values tend to become equal in the downstream direc-

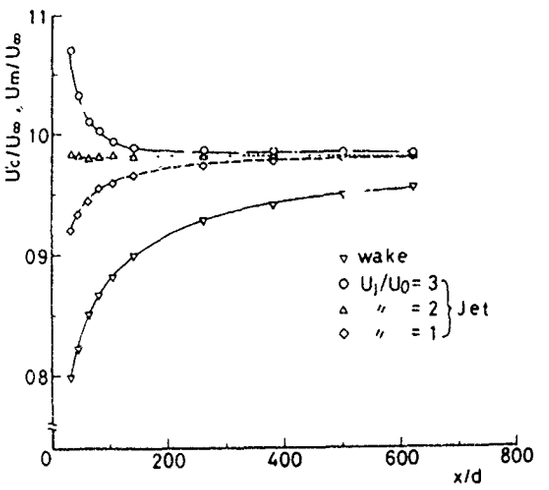

Fig. 4 Variation of the center-line mean velocity of the jet and the wake

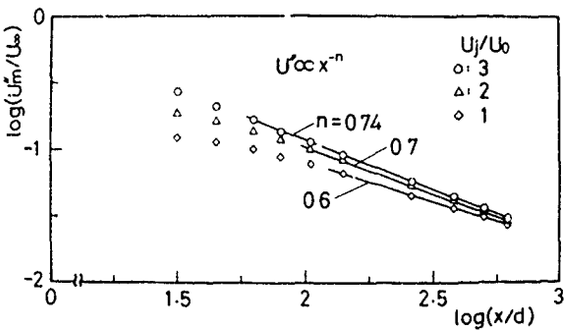

Fig. 6 Variation of the maximum velocity

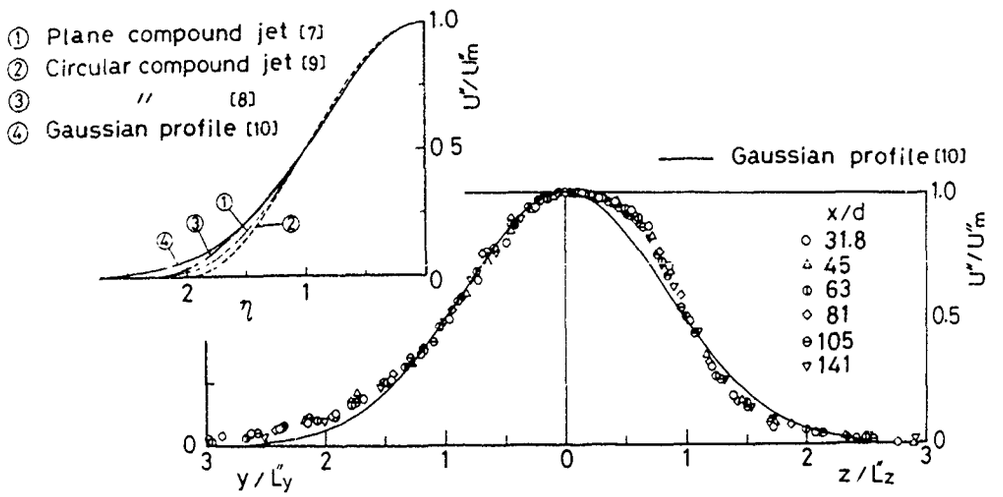

Fig. 5 Dimensionless velocity profiles of the jet ($U_j/U_0 = 3$)

tion. Rajaratnam has been reported that it can be expressed as $L'' \propto x^{1/3}$ in the weak jet. Although the index n of the present results in L''_z differ slightly due to the velocity ratio, its values nearly equal Rajaratnam's index value. But the difference due to the velocity ratio does not appear in L''_y, and its value is about twice that of L''_z.

Figure 7(b) shows the comparison between the half-value width in the injection into the wake and that in the injection into the quiescent fluid. In the upstream region with injection into the quiescent fluid, L_z is slightly larger than L_y, but their values tend to become equal downstream. With injection into the wake, there is a similar variation, but the trend becomes more remarkable than with injection into the quiescent fluid. This is because, in the secondary flow which occurred upstream in the present jet, the injection into the wake became even stronger than the injection into the quiescent fluid.

In order to elucidate further the three-dimensional mixing process in the present jet, the three-dimensional profiles of the mean velocity are shown in Figs. 8 (a) and (b). The jet is jutting out from the uniform flow at x/d = 31.8, and the jet has an asymmetrical shape.

Since the secondary flow can be inferred from the mean velocity profiles mentioned above, to confirm this, a small windmill is used to measure the revolution number and its direction of revolution. The results at typical sections x/d = 31.8 are shown in Figs. 9(a) and (b).

Figure 9(a) shows the result for the injection into the quiescent fluid. Broken lines indicate the isopleths of the mean velocity, and the solid lines with an arrow illustrate the pattern of secondary flow, estimated by the rotation of the windmill. Obviously the secondary flow extends the cross-section of the jet in the z-direction as shown in this figure. Figure 9(b) shows the result of the injection into the wake, and the chain lines indicate the isopleths of the mean velocity. A secondary flow effect as with injection into the quiescent fluid is also recognized in this case, but the revolutions of the small windmill become considerably stronger than those in the injection into the quiescent fluid.

As for the origin of the secondary flow in the injection into the quiescent fluid, we considered that the asymmetry of the induced velocity is produced by the obstruction of the circular cylinder to the entrainment of the surrounding quiescent fluid into the jet, thereby leading to unequal turbulence and the formation of the secondary flow of second class of Prandtl. The maximum revolutions of the small windmill in the injection into the wake becomes about 60 times that observed in the injection into the quiescent fluid. Such a generation of the large revolution component is considered as due to the another reason different from that in the injection into the quiescent fluid. The main difference in both flows is the Kármán vortex which is generated from the circular cylinder. Since a pair of streamwise vortices are formed due to an interaction between the Kármán vortex and a vortex ring which is generated from the jet exit, it is inferred that revolutions of the small windmill shown in Fig. 9(b) can be produced.

Turbulent field

Figures 10(a) and (b) show the turbulence intensity profiles on several planes on the jet-axis in the injection into the wake. The chain lines indi-

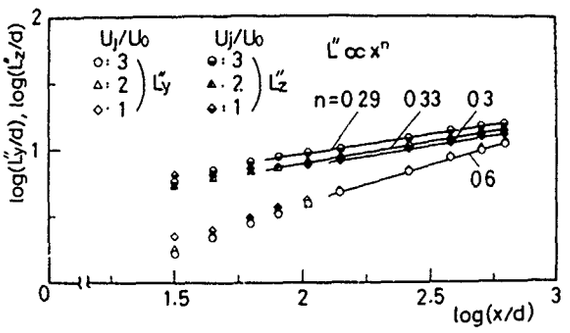

(a) Injection into the wake

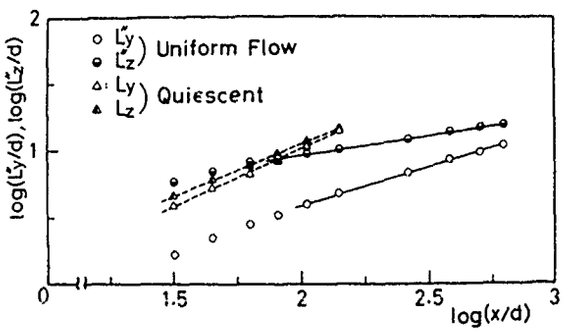

(b) Comparison between the injection into the wake and the quiescent fluid

Fig. 7 Variations of the half-value width

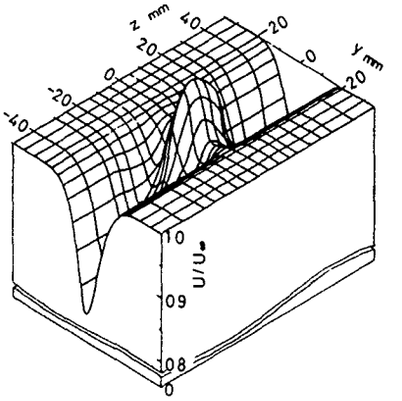

(a) x/d = 31.8

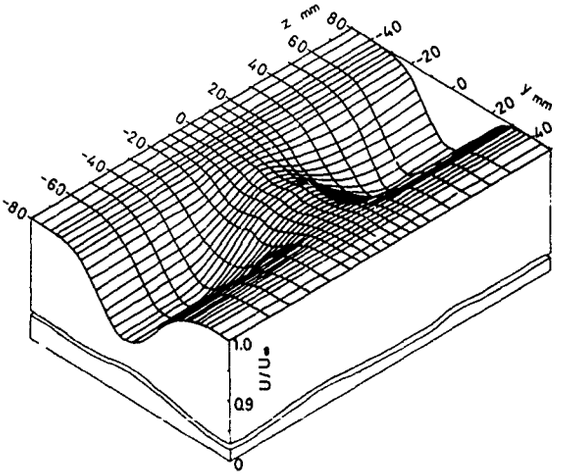

(b) x/d = 141

Fig. 8 Three-dimensional profiles of the mean velocity (U_j/U_0 = 3)

cate intensity profiles of the wake. Figure 10(a) shows the turbulence profiles in the y-direction. Remarkably, the turbulence intensities become low by injection of the je Because the mean velocity profiles vary as shown in Fig. 3(a) by injecting the jet, it is considered that $\partial U/\partial y$ in a turbulent-energy production term; $-\overline{uv}\,\partial U/\partial y$, which makes an important contribution to the turbulent production in the turbulent shear flow field, becomes small due to the injection. A similar phenomenon has been also reported in the experimental result of the circular compound jet by Durão and Whitelaw [6]. Even far downstream in the present experiment, the turbulence intensity profile of the jet is not coincident with that of the wake.

Figure 10(b) shows the turbulence intensity profile in the z-direction. In the downstream region at $x/d \geq 81$, the intensity profiles of the wake are transformed to the hollow-shape due to the jet. But in the upstream region where $x/d \leq 45$, special profiles appear which show the distribution similar to the one of the jet as if it is injected into the quiescent fluid and the effect of the wake is weak. Thus, it is considered that the intensity profiles in the present jet are determined by whether the intensity profile is dominant in the wake or in the jet. Hence, the turbulence intensity of the jet dominates that of the wake in the upstream region at $x/d \leq 45$, whereas the intensity of the wake dominates that of the jet in the downstream region at $x/d \geq 81$, so intensity profiles like those mentioned above will be formed.

Figure 11 shows the variations of turbulence intensity in the jet and the wake along the jet centerline. The variation of the turbulence intensity of the jet in the upstream region at $x/d \leq 150$ differs according to the velocity ratio; thus, there is a similar variation with the wake when $U_j/U_0 = 1$. There is a rather steep decrease when $U_j/U_0 = 3$, and a mild decrease and the lowest intensity when $U_j/U_0 = 2$. It is therefore considered that these phenomena depend upon the relationship between the turbulence intensity of the wake and the jet. Thus, the turbulence intensity of the wake governs that of the jet in all regions of the x-direction when $U_j/U_0 = 1$, whereas the turbulence intensity of the jet is governing that of the wake in the upstream regions when $U_j/U_0 = 3$. Furthermore, there is intermediate relationship when $U_j/U_0 = 2$, because in this case it is considered that the intensity becomes most low. However, the difference due to the velocity ratio in the turbulence intensity does not exist in the downstream region.

Figures 12(a) and (b) show the three-dimensional profiles of the turbulence intensity. The three-dimensional region with the low turbulence intensity of the jet is found in the two-dimensional turbulence intensity profile of the wake.

In order to examine the interference process between the Kármán vortex of the circular cylinder and the jet, the power spectra for the fluctuating velocity is measured in the region from z/D = 10 to -10 at the positions of x/D = 3.6 and y/D = 0.4. The results are shown in Fig. 13. The spectral peak with 825Hz is found at the locations of $z/D \geq \pm 1.6$, and the Strouhal number by using this frequency is 0.21. Thus, the usual Kármán vortex of the two-dimensional circular cylinder exists at these same locations.

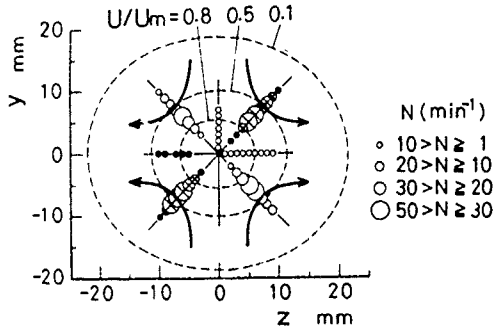

(a) Injection into the quiescent fluid

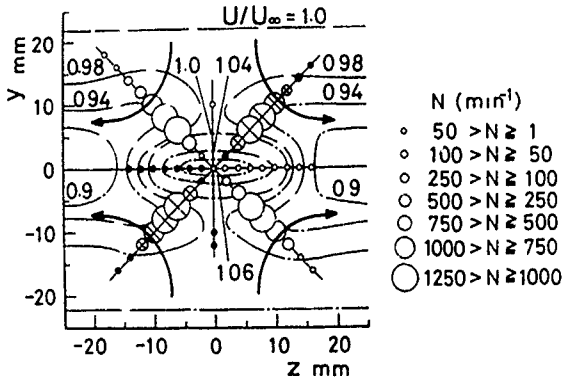

(b) Injection into the wake

○ Clockwise ⊕ Counter-clockwise

Fig. 9 Revolution of the windmill and the secondary flow (x/d = 31.8)

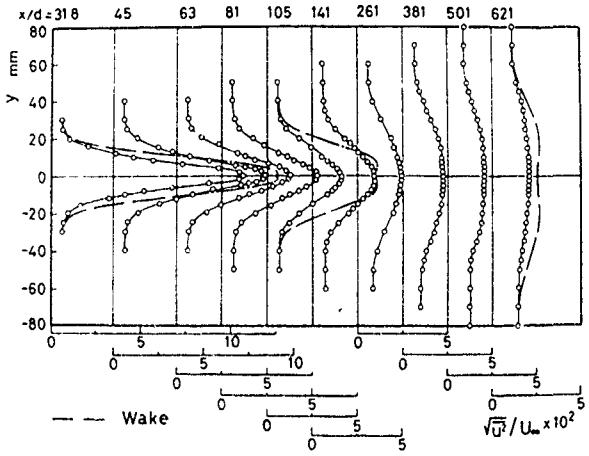

(a) Profiles in the y-direction

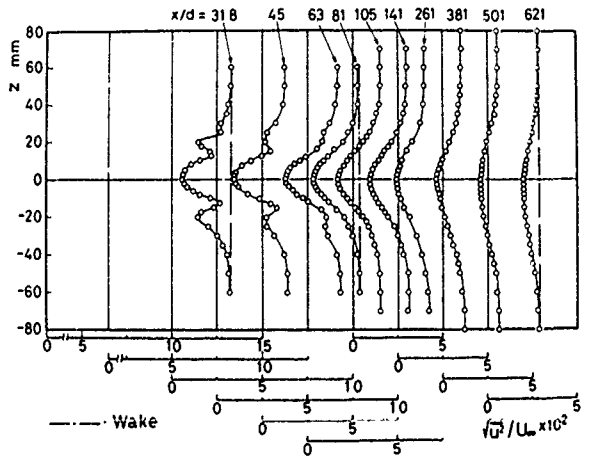

(b) Profiles in the z-direction

Fig. 10 Turbulence intensity profiles in the central cross-section of the jet ($U_j/U_0 = 3$)

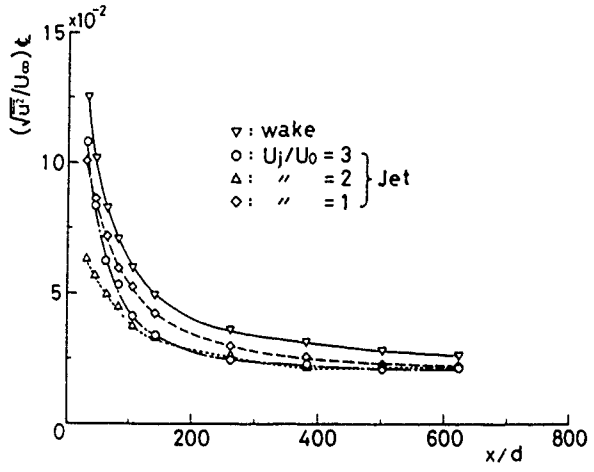

Fig. 11 Variation of the center-line turbulence intensity of the jet and the wake

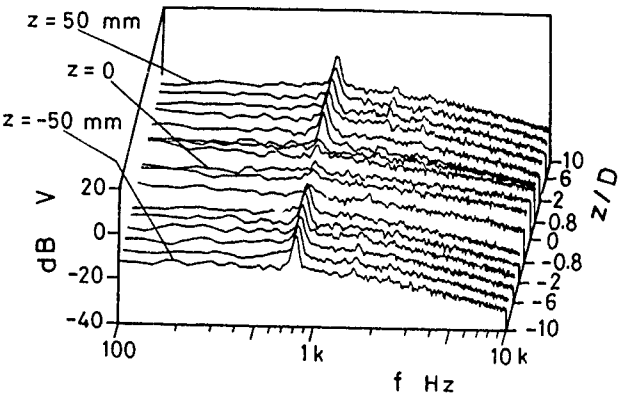

Fig. 13 Spectral distribution behind the circular cylinder (U_j/U_0 = 3)

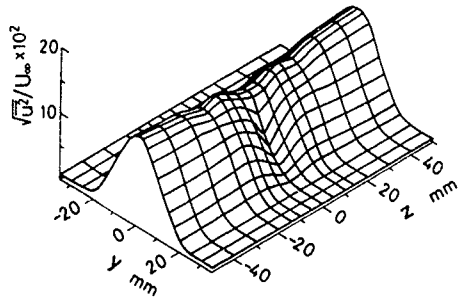

(a) x/d = 31.8

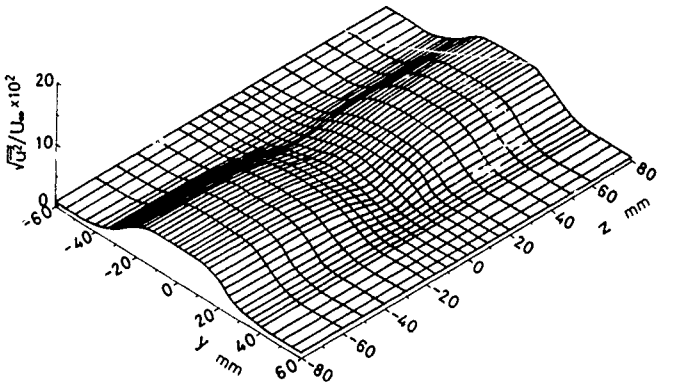

(b) x/d = 141

Fig. 12 Three-dimensional profiles of the turbulence intensity (U_j/U_0 = 3)

However, the peak value is not found in the central part of the z-direction z/D ≲ ±0.8, thereby, it can be said that the Kármán vortex vanish due to the interference with jet.

CONCLUSIONS

A jet which is injected from a circular hole drilled in the rear of a circular cylinder, even in the case of an injection into quiescent fluid, exhibits an asymmetrical spread, and a secondary flow exists. In the case of the injection into the wake, the asymmetrical spread becomes rather remarkable, and the secondary flow becomes even stronger than with injection into quiescent fluid. Although the decay of the relative maximum velocity in relation to the wake differs according to the injection velocity ratio, it decays in proportion to about $x^{-2/3}$.

The turbulence intensity of the wake becomes low by injecting the jet. In the present flow field, the turbulence intensity profile depends upon the relationship between the turbulence intensity of the jet and that of the wake. It was clarified from the power spectra that the Kármán vortex vanishes due to the interference by the jet.

REFERENCE

[1] Cimbala, J. M., and Park, W. J.. J. Fluid Mech., Vol. 213, 1990, P. 479

[2] For example, Tuji, H., and Okano, T., Rep. Inst. Aeronautics., Tokyo Univ., Vol. 3, No. 1, 1962, P. 78

[3] Higuchi, H., and Kubota, T., Phys. Fluids A, Vol. 2, No. 9, 1990, P. 1615

[4] Nirmalan, N. V., and Hylton, L. D., Trans. ASME, J. Turbomachinery, Vol. 112, 1990, P. 447

[5] Wygnanski, I., and Fiedler, H., J. Fluid Mech., Vol. 38, No. 3, 1969, P. 577

[6] Durão, D., and Whitelaw, J. H., Trans. ASME, J. Fluid Eng., Vol. 95, No. 3, 1973, P. 467

[7] Bradbury, L. J. S., J. Fluid Mech., Vol. 23, No. 1, 1965, P. 31

[8] Tani, I., and Kobashi, U., 1st. Japan Natl. Congr. Appl. Mech., 1951, P. 465

[9] Squire, H. B., and Troucer, J., Aeronautical Research Council, R and M, 1944, P. 9

[10] Isigaki, H., Trans. Jpn. Soc. Mech. Eng., Vol. 48, No. 433, B, 1982, P. 1692, in Japanese

[11] Rajaratnam, N., Turbulent Jets, 1976, P. 63, Elsevier

EIGHTH SYMPOSIUM ON
TURBULENT SHEAR FLOW
Technical University of Munich
September 9-11, 1991

TURBULENT MIXING OF MULTIPLE PLANE AND AXISYMMETRICAL JETS

R. Karvinen, P. Saarenrinne and H. Ahlstedt

Tampere University of Technology
P.O.Box 527, SF-33101 Tampere, Finland

ABSTRACT

The mixing of plane and axisymmetrical round jets with a fully developed turbulent velocity profile is studied theoretically and experimentally. It was observed that in the k-ε model the ε-equation must be modified if flow separation exists to the extent that mean velocity is retarded. The mixing of axisymmetrical jets with a hexagonal array can also be handled by approximating them with a two-dimensional axisymmetrical jet. The importance of correct boundary conditions, i.e. the profiles of velocity and turbulence energy at jet outlets, for mixing was found.

OMENCLATURE

b	channel width
$c_{\varepsilon 1}, c_{\varepsilon 2}, c_{\varepsilon 3}$	turbulence-model constants
d_o, d_e	outside and equivalent tube diameter
h	channel wall thickness
k	turbulence kinetic energy
k_1, k_2	experimental constants in self-preserving solutions
r	radial coordinate
r_e	equivalent tube radius $= d_e/2$
T_u	turbulence intensity $\sqrt{\frac{2}{3}k}/U_\infty$
u	streamwise velocity
u_i, u_j	mean velocity components, tensor notation
u_i', u_j'	turbulent velocity components, tensor notation
u_1	velocity defect $U_\infty - u$
u_c	maximum velocity defect
U_∞	bulk mean velocity
x, y	cartesian coordinates
ε	dissipation rate of turbulence energy
ν_t, ν_{eff}	eddy and effective viscosities
$\sigma_k, \sigma_\varepsilon$	turbulence-model constants

INTRODUCTION

The mixing of parallel jets is utilized often in engineering applications. The origin of this work lays also in actual practice, namely in the mixing problem of a fibre-water suspension in the hydraulic headbox of a papermachine, where geometries of Fig. 1 are used to generate the desired flow and turbulence characteristics. The main facts affecting the paper quality are the decay of velocity differences and such turbulence that fibre flocs are broken. Turbulence and velocity profiles can be affected either by a wall friction or a flow separation from an abrupt expansion in a flow geometry. In addition, the spectral

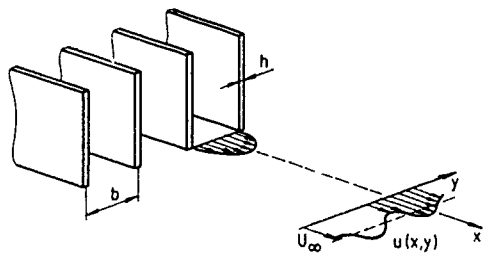

(a) Plane Jets.

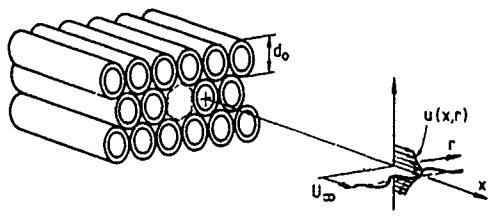

(b) Axisymmetrical jets with a hexagonal array.

Fig. 1. Jet configurations and arrangements.

distribution of turbulence should be such that the movement of fibres with the length of 1...4 mm and the thickness equal to 20...40 μm is affected by turbulence.

There does not exist very much information concerning the mixing of parallel jets in the literature, although single jets have been extensively analyzed, so that the information of published papers can be found even in the books (Rajaratnam 1976; Schetz 1980). When considering the situation in Fig. 1 the flow behaviour is affected by turbulence and velocity at the channel exits. There are some papers where the effect of turbulence in free-boundary flows, i.e. mixing of a single jet or the recovery of a wake has been studied (Patel & Chen 1987; Mohammadian, Saiy & Peerles 1976) but in the case where many jets are coupled together the information is thin. The effects of free-stream turbulence on velocity boundary layer and heat transfer have also been studied considerably in cases where the fluid flow is past an obstacle or a wall (Simonich & Bradshaw 1978). In general, it has been noticed that free-stream turbulence does not appreciable affect the boundary layer near a fixed surface, but if we have a free boundary layer the initial turbulence level of a jet or a free-stream can have a significant effect on the flow behaviour.

In this paper an analysis of the mixing of multiple plane or axisymmetrical jets is given as mentioned above. The mixing process of jets in Fig. 1 is affected by turbulence and velocity profiles of exhausted jets, and also by recirculation. Flow re-

circulation exists in the case of plane jets when wall thickness separating jets is not negligible and for axisymmetrical jets with a hexagonal array recirculation is always present. The research procedure includes analytical, numerical and experimental approaches. The effect of various factors, i.e. velocity and turbulence profiles of exhausted jets and recirculation on the flow behaviour is shown.

FORMULATION OF THE PROBLEM AND SOLUTION PROCEDURES

The flow configurations studied experimentally and theoretically are those in Fig. 1. In the case of mixing of plane jets, the channel height is large compared with the width b. Thus, we have a two-dimensional problem which is governed by elliptic equations near the channel outlet, and at a certain distance from the channels the flow field is parabolic. In Fig. 1(b) a large number of axisymmetric jets are exhausted from parallel tubes with a hexagonal array. In this case the flow field is everywhere three-dimensional, even if the tubes have hexagonal cross sections as shown by a dotted line.

In the case of circular tubes there is always a flow separation and recirculation near the tube outlet even for very thin-walled tubes. In order to simplify the problem it is assumed that the flow field can be handled as a two-dimensional axisymmetrical jet, the cross sectional area of which is the same as a hexagonal tube drawn with a dotted line has in Fig. 1(b). Thus, an equivalent tube diameter d_e is equal to 1.05 times the outside diameter d_o of a tube (see Fig. 2).

The mixing problem described above has been tried to solve theoretically by adopting an analytical and a numerical approach and the validity of the results has been verified experimentally.

Analytical approach

Let us consider the mixing of parallel circular jets in Fig. 1(b). According to two-dimensional assumptions made earlier, the form of the velocity profile of a mixing jet is that shown in Fig. 2. At a certain distance from the jet inlet the velocity defect $v_1(x,r) = U_\infty - u(x,r)$ is small in comparison with the uniform mean velocity U_∞. In that case the momentum equation takes the same form as usually used in analysing wakes

$$-U_\infty \frac{\partial u_1}{\partial x} = \frac{1}{r}\frac{\partial}{\partial r}(r\nu_t \frac{\partial u}{\partial r}) \tag{1}$$

Now, if it is assumed that the eddy viscosity is proportional to the maximum velocity difference $\nu_t = k u_c(x)$ (k is an unspecified constant) a self-preserved turbulent mean velocity profile of mixing axisymmetrical jets with a hexagonal array can be derived using the method of ref. (Cebeci & Bradshaw 1977). The final result not known in the literature is (Karvinen 1991)

$$u(x,r) = U_\infty\{1 + \frac{r_e^2}{k_1}\frac{1}{x}J_0(3.832\frac{r}{r_e})\} \tag{2}$$

where k_1 must be determined experimentally and J_0 is the Bessel function.

The mixing of plane jets far enough downstream from the channel outlet in Fig. 1(a) can also be solved as above except

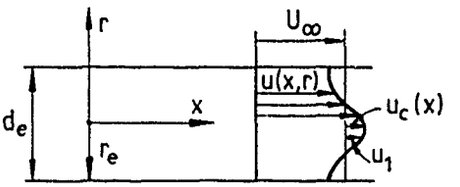

Fig. 2. Definition sketch of approximated circular parallel jets.

that now $r = 1$ in Eq. (1). The resulting self-preserved velocity profile takes the form

$$u(x,r) = U_\infty[1 - \frac{b^4}{k_2}\frac{1}{x}cos(2\pi\frac{y}{b})] \tag{3}$$

where k_2 is again an empirical constant. The result (3) has also been derived earlier using another kind of treatment in analysing the mixing of wakes (Schlichting 1979). The same kind of result as (3) can also be obtained if the eddy viscosity is proportional to x^{-1} (Elsner & Zielinski 1986).

Equations of numerical modelling

The numerical calculations of this study have been performed employing the eddy viscosity concept and the k-ε model. However, it was observed that the standard k-ε model was unable to predict flow behaviour correctly when flow separation exists after channel outlets resulting in recirculating flow and in the retarding the mean velocity. For that reason the turbulence model was modified according to the suggestions of Hanjalić and Launder (1980), so that the transport equations of turbulence kinetic energy and its dissipation rate are in cartesian coordinates

$$\rho(u\frac{\partial k}{\partial x} + v\frac{\partial k}{\partial y}) = \frac{\partial}{\partial x}(\frac{\mu_t}{\sigma_k}\frac{\partial k}{\partial x}) + \frac{\partial}{\partial y}(\frac{\mu_t}{\sigma_k}\frac{\partial k}{\partial y}) + \mu_t(\frac{\partial u}{\partial y})^2 - \rho\varepsilon - \underline{\rho\frac{k}{3}\frac{\partial u}{\partial x}} \tag{4}$$

$$\rho(u\frac{\partial \varepsilon}{\partial x} + v\frac{\partial \varepsilon}{\partial y}) = \frac{\partial}{\partial x}(\frac{\mu_t}{\sigma_\varepsilon}\frac{\partial \varepsilon}{\partial x}) + \frac{\partial}{\partial y}(\frac{\mu_t}{\sigma_\varepsilon}\frac{\partial \varepsilon}{\partial y}) + c_{\varepsilon 1}\frac{\varepsilon}{k}\mu_t(\frac{\partial u}{\partial y})^2 - c_{\varepsilon 2}\rho\frac{\varepsilon^2}{k} - \underline{c_{\varepsilon 3}\rho\frac{\varepsilon}{3}\frac{\partial u}{\partial x}} \tag{5}$$

The empirical constant $c_{\varepsilon 3}$ takes the value 4.44. In the standard k-ε model the terms underlined in Eq. (4) and (5) are missing. These kinds of modified equations have also been used in the calculation of external boundary layers with adverse pressure gradients (Rodi & Scheuerer 1986). Boundary conditions for the governing equations are that gradients of u, v, p, k and ε must be zero both at the centerline of a jet and also at the separating line between two jets. No wall functions were needed. The set of governing equations was solved using the PHOENICS code (Spalding 1981), into which the modifications of the turbulence model were implemented. The PHOENICS code is based on the finite difference method in which an upwind difference scheme is adopted and the iteration is made using the SIMPLEST algorithm.

When use is made of the finite-difference method, it also restricts the shape of control volumes. For this reason also in the numerical modelling of the mixing of circular jets an axisymmetrical assumption such as in the analytical treatment above was adopted.

Experimental research

Experiments were made using air as a flowing fluid. In order to get some generality of results the length of an experimental set-up in Fig. 1 was about 3 m in order to reach fully developed turbulent velocity profiles at jet outlets for both geometries. The width of a channel in the case of parallel plane jets was 14 mm and walls with a different thickness h was used to study the effect of recirculation, caused by flow separation, on the mixing process. The test installation of axisymmetrical jets consisted of the package of round tubes with the outside diameter d_o equal to 28.3 mm and wall thickness 1.7 mm.

Measurements of mean velocity and turbulent fluctuation velocities were determined with a standard constant temperature hotwire anemometer (Dantec). For measuring the streamwise mean velocity and its turbulence a straigth single wire probe was used. In order to get an idea about the isotropy of turbulence also other components of turbulence, in addition to the stream-wise one, were measured by using an X-wire probe. Velocities used in expariments were such that the bulk mean velocity U_∞ after jet mixing varied from 15 m/s to 20 m/s.

RESULTS AND DISCUSSION

The mixing problem could be very easily solved if the analytical solutions shown above can be used. However, it was observed after comparing analytical solutions with the measurements that the constants needed in equations were dependent on the initial condition at jet outlets. Also, the distance were self-preserving solutions are valid is large and the detection of velocity differences is difficult. Thus, it can be concluded that analytical solutions are valuable in the respect that they show the decay of the velocity difference to be proportional to x^{-1} from the outlets for a certain geometry.

In Fig. 3 the decay of the profiles of mean velocity and turbulence kinetic energy is shown for plane jets when the thickness of a channel wall is very small, such that there is no flow recirculation. It can be seen that the effect of a turbulence model modification is very small and the standard k-ε model predicts mean flow behaviour correctly. The required profiles of velocity, turbulence kinetic energy and its dissipation rate at channel outlets were also obtained numerically by calculating fully developed turbulent profiles in a channel. The Reynolds number was equal to 35800. These were in reasonable agreement with measured data in the literature (Hussain & Reynolds 1975). By measuring different components of turbulence it was observed that streamwise, lateral and transverse components have the same kind of shape and that when the distance from a channel outlet increased an isotropic condition was approached. Fig. 4 shows the measured profiles of different turbulence components. In order to evaluate the possibility of two-equation turbulence models to predict flow behaviour, it is enough to measure only the streamwise component of turbulence, of which the kinetic energy of turbulence can be obtained.

The results showing the effect of flow separation on the mixing of plane jets are shown in Fig. 5. The geometry of a channel is the same as in Fig. 3, except that now the wall thickness between channels is 4 mm. The position of a wall is shown also in the figure. The ratio of a wall thickness h and a channel width b is equal to 0.286. Calculations have been made using three kinds of turbulence models: the standard k-ε model, a modified model according to Eq. (4) and (5), and a third one, in which only the ε-equation is modified. Velocity fields of Fig. 3 and 5 were computed on a 51 (streamwise) x 18 (cross-streamwise) grid.

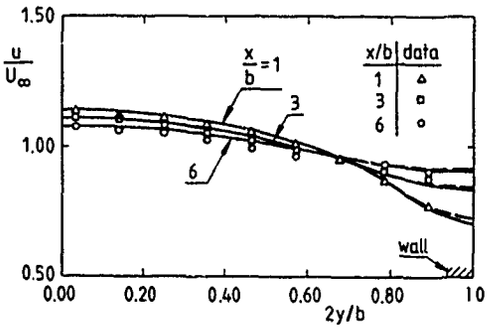

(a) Velocity.

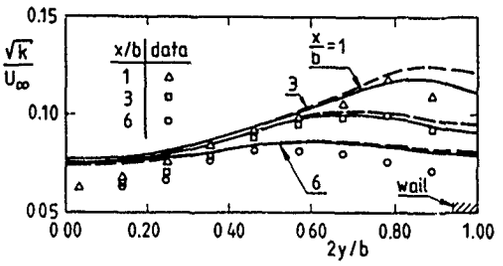

(b) Turbulence kinetic energy.

Fig. 3. Mixing of fully developed turbulent plane jets with negligible wall thickness. —— standard k-ε model, -- - - modified model.

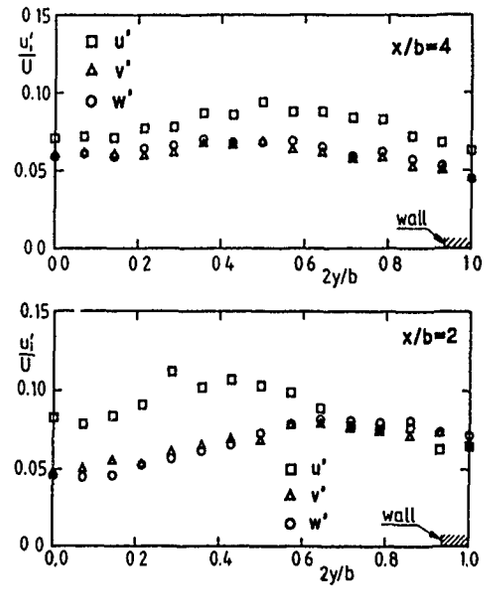

Fig. 4. Profiles of turbulent components for plane jets at different distance from jet outlet.

It can be seen that the model in which only the ε-equation is modified agrees best with measurements. This kind of result was also obtained by Rodi and Scheuerer (1986) when calculating boundary layer flows with an adverse pressure gradient. Although the flow of our paper is quite different from that of Rodi, it seems that the same kind of modelling as in the case of wall flows is also valid for free shear flows. An interesting observation is made if velocity profiles of Fig. 3 and 5 are compared. It is seen that at the distance of $x/b = 6$ from jet outlets the nonuniformity of velocity is almost the same, although at the

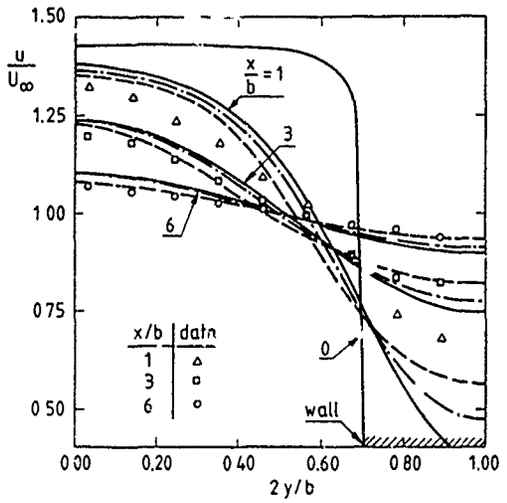

(a) Velocity decay.

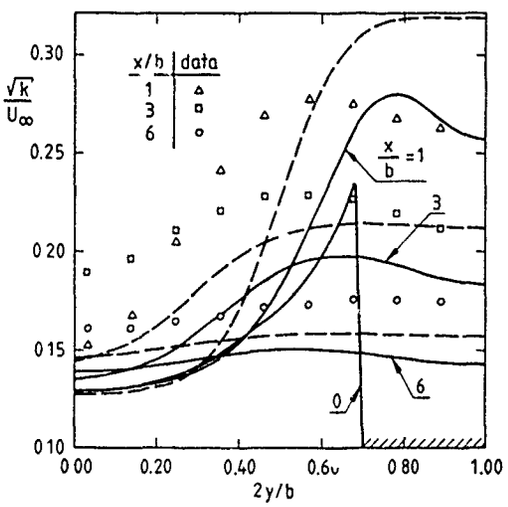

(b) Turbulence kinetic energy.

Fig. 5. Mixing of fully developed turbulent plane jets with flow separation. —— k-ε model, –·– the k- and ε-equation modified, – – – only the ε-equation modified.

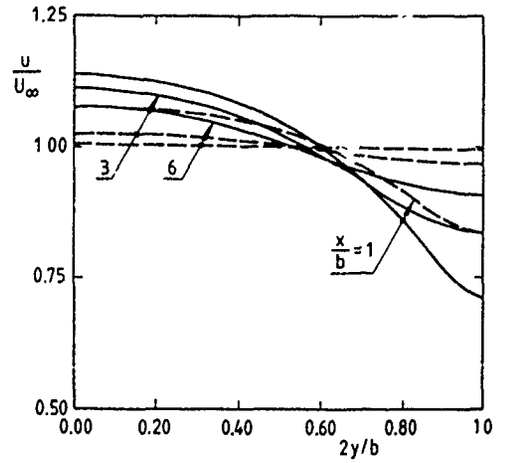

Fig. 6. Effect of kinetic energy distribution at a jet outlet on mixing. —— energy of a fully developed channel flow, – – – uniform energy equal to the maximum value of a fully developed flow.

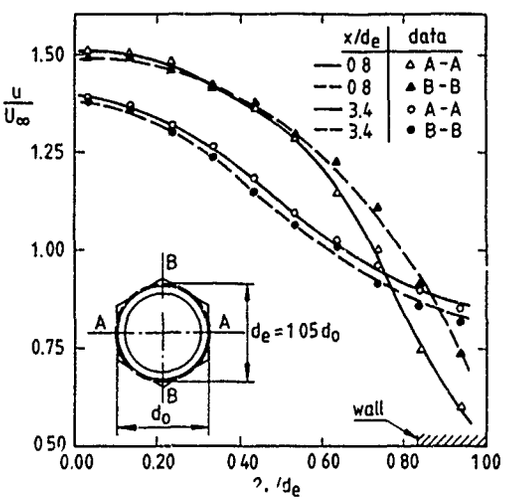

(a) Velocity profiles of mixing round jets.

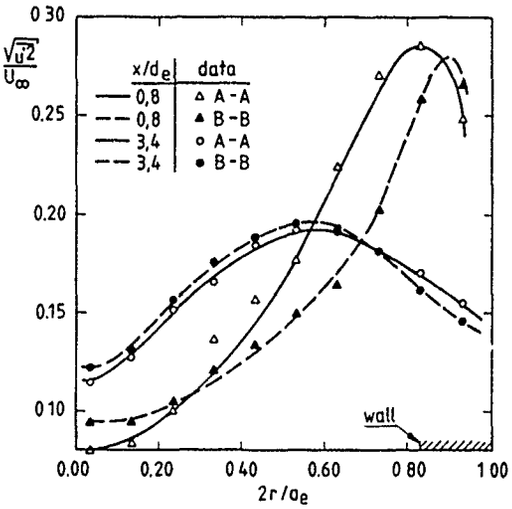

(b) Streamwise component of turbulence.

Fig. 7. Comparison of measured velocities and turbulence energy between different cross-sections in the mixing of round jets.

jet outlets in Fig. 5, maximum velocity is much higher than that in Fig. 3. Thus, the flow separation creates a turbulence which very effectively mixes the flow field and gradually eliminates the nonuniformities of a velocity filed.

The last figure dealing with the mixing of plane jets shows the effect of turbulence kinetic energy of jet outlets on the mixing. In Fig. 6 there are results for two different cases. Solid lines show the decay of velocity profile when at a channel outlet the profiles of velocity, kinetic energy and its dissipation rate are those of a fully developed turbulence channel flow. Dotted lines show similar results, but now it is assumed that the turbulence kinetic energy is uniform everywhere and equal to the maximum value near the wall. The dissipation and velocity profiles are those of a fully developed channel flow. It can be seen that the turbulence kinetic energy has a great effect on mixing, and that the latter is also promoted by an increase in turbulence. In actual practice the turbulence kinetic energy and its dissipation rate cannot be changed freely; on the contrary, they are coupled together.

In numerical modelling the mixing three-dimensional jets has been approximated with a two-dimensional axisymmetrical jet, the cross-section of which is the same as that of an actual three-dimensional flow. In order to verify the validity of this assumption some measurements were made. Fig. 7 shows the behaviour of the profiles of mean velocity and turbulence kinetic energy at the distances of x/d_e equal to 0.8 and 3.4 from jet outlets. In this figure profiles are chosen so as to show the maximum differences across the flow field. It can be seen that there are no essential differences in velocity and turbulence kinetic energy between the cross-sections A-A and B-B. Lines in Fig. 7 are not computed ones but they are fitted to the measurements in order to assist the comparison between measured data in different cross-sections. Thus, it can be concluded that results are not much in error if the mixing of axisymmetrical jets with a hexagonal array is made using a two-dimensional approximation. This simplifies the numerical treatment and it is believed that the errors caused by turbulence models in three dimensions are of the same order as those caused by the approximation.

Finally, a comparison between measurements and numerical calculation using a two-dimensional approximation is made in Fig. 8. It can be seen that if the standard k-ε model is modified, such that there is a velocity gradient term in the ε-equation, results are in reasonable agreement with measured data. The computation was made on a 51 (streamwise) x 18 (radial) grid and the Reynolds number was 26300. In Fig. 8 measured data are taken from cross-section A-A of Fig. 7. We also used the modification of the ε- and k-equations, but the result was not as good as when only the ε-equation was modified. This is a result similar to that noticed in the case of plane jets. Thus it seems that the mixing of decelerating plane and axisymmetrical jets for engineering purposes can be modelled by modifying the ε-equation.

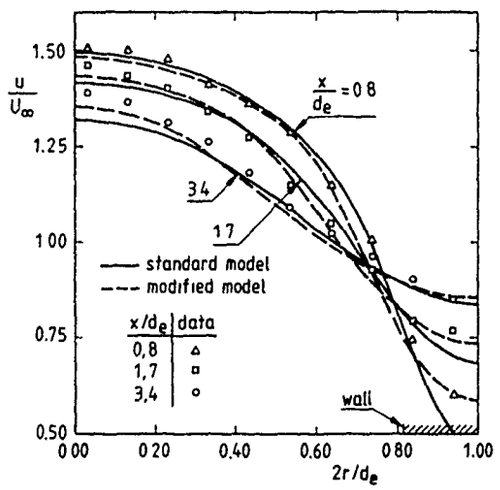

Fig. 8. Comparison of measured and calculated velocities for the mixing of axisymmetrical jets. —— the standard k-ε model, – – – the ε-equation modified.

CONCLUSIONS

On the basis of theoretical and experimental studies of the mixing of parallel plane jets and axisymmetrical jets with a hexagonal array the following conclusions and observations can be made.

1. The standard k-ε model is not capable of predicting flow behaviour if there exists flow separation resulting in recirculating flow after jet outlets. This kind of free shear layer can be modelled correctly if the ε-equation of the standard model is modified to take into account the deceleration of flow.

2. Axisymmetrical jets with a hexagonal array can be treated sufficiently adequately in engineering applications by approximating a three-dimensional flow with an axisymmetrical jet, the cross-section of which is the same as that in an actual flow field.

3. The values and profiles of the velocity and turbulence kinetic energy of jet outlets greatly affect the mixing of jets. In numerical modelling it is very important that these values should be correctly known and given.

REFERENCES

CEBECI, T. & BRADSHAW, P. 1977 *Momentum Transfer in Boundary Layers.* Hemisphere Publishing Corporation.

ELSNER, J. W. & ZIELINSKI, J. 1986 Semi-preservation of momentum and heat transfer in cascade-wake-flows. *Intl J. Heat Mass Transfer* **29**, 293-300.

HANJALIĆ, K. & LAUNDER, B. E. 1980 Sensitizing the dissipation equation to irrotational strains. *J. Fluids Engng* **102**, 34–40.

HUSSAIN, A. K. M. F. & REYNOLDS, W. C. 1975 Measurements in fully developed turbulent channel flow. *J. Fluids Engng* **97**, 568–580.

KARVINEN, R. 1991 *Some Self-Preserved Solutions of Turbulent Free Shear Flows.* Tampere University of Technology, Thermal Engineering, Report.

MOHAMMADIAN, S., SAIY, M. & PEERLES, S. J. 1976 Fluid mixing with unequal free-stream turbulence intensities. *J. Fluids Engng* **98**, 229–235.

PATEL, V. C. & CHEN, H. C. 1987 Turbulent Wake of a Flat Plate. *AIAA J.* **25**, 1078–1085.

RAJARATNAM, N. 1976 *Turbulent Jets.* Elsevier Scientific Publishing Company.

RODI, W. & SCHEUERER, G. 1986 Scrutinizing the k-ε turbulence model under adverse pressure gradient conditions. *J. Fluids Engng* **108**, 174–179.

SCHETZ, J. M. 1980 *Injection and Mixing in Turbulent Flow.* American Institute of Aeronautics and Astronautics.

SCHLICHTING, H. 1979 *Boundary Layer Theory.* McGraw-Hill.

SIMONICH, J. C. & BRADSHAW, P. 1978 Effect of free-stream turbulence on heat transfer through a turbulent boundary layer. *J. Heat Transfer* **100**, 671–677.

SPALDING, D. B. 1981 A general purpose computer program for multi-dimensional one- and two-phase flow. *Maths. Comput. Simul.* **13**, 267–276.

EIGHTH SYMPOSIUM ON
TURBULENT SHEAR FLOWS
Technical University of Munich
September 9-11, 1991

EFFECT OF TABS ON THE EVOLUTION OF AN AXISYMMETRIC JET

K.B.M.Q. Zaman
NASA Lewis Research Center
Cleveland, Ohio 44135, U.S.A.

and

M. Samimy and M. F. Reeder
Department of Mechanical Engineering,
Ohio State University
Columbus, Ohio 43212, U.S.A.

ABSTRACT

The effect of vortex generators, in the form of small tabs at the nozzle exit, on the evolution of an axisymmetric jet was investigated experimentally, over a jet Mach number range of 0.34 to 1.81. The effects of one, two and four tabs were studied in comparison with the corresponding case without a tab. Each tab introduced an "indentation" in the shear layer, apparently through the action of streamwise vortices which appeared to be of the "trailing vortex" type originating from the tips of the tab rather than of the "necklace vortex" type originating from the base of the tab. The resultant effect of two tabs, placed at diametrically opposite locations, was to essentially bifurcate the jet. The influence of the tabs was essentially the same at subsonic and supersonic conditions indicating that compressibility has little to do with the effect.

INTRODUCTION

Tabs, or small protrusions in the flow at the exit plane of a nozzle, have long been known to reduce screech noise from supersonic jets (Tanna, 1977). Bradbury & Khadem (1975), to our knowledge, were the first to make flow field measurements for a subsonic jet under the influence of tabs The tabs were found to increase the jet spread rate significantly. Ahuja & Brown (1989) recently conducted a series of experiments on the effect of tabs on supersonic jets, and reached a similar conclusion in regards to the effect on the flow field. With support from NASA Lewis, the latter investigators continued to study the effect on rectangular jets as well as on the noise radiated from the jet (Ahuja et al., 1990). In terms of the plume reduction i.e., a faster spreading of the axisymmetric jet, the effect of the tabs was so dramatic that the technique has been at times referred to as the "supermixer" (E.J. Rice, private communication) However, the flow mechanisms, even the basic changes in the flow field caused by the tabs, essentially remained unknown.

The obvious technological significance of the ability to increase mixing and reduce noise, even in supersonic jets, provided a strong motivation to pursue the topic further. This led to the present investigation. A detailed flow visualization experiment was conducted together with quantitative measurements of the flow field. Even though questions have remained unresolved, the results provided a clearer insight into the flow field changes caused by the tabs. This is what we would like to describe in this paper. Preliminary results of the experiment were reported by Samimy, Zaman & Reeder (1991). Only key results are discussed here due to space limitation, a more detailed paper is being prepared for Journal submission

EXPERIMENTAL FACILITY

The experiments were carried out in a small supersonic jet facility at NASA Lewis Research Center. The facility is schematically shown in Fig. 1. A converging-diverging nozzle with throat diameter of 0.635 cm and design Mach number of 1.36 was used The Mach number range covered was 0.34 to 1.81, representing subsonic and over- and underexpanded supersonic conditions. The flow visualization pictures were obtained by laser sheet illumination and Schlieren photography. A 4 W argon-ion laser was used for both techniques. The laser sheet illumination was performed in the supersonic jets without any seeding. The cold supersonic jet core caused natural moisture condensation in the mixing layer from the entrained ambient air. Thus, with this technique, the mixing layer region was illuminated.

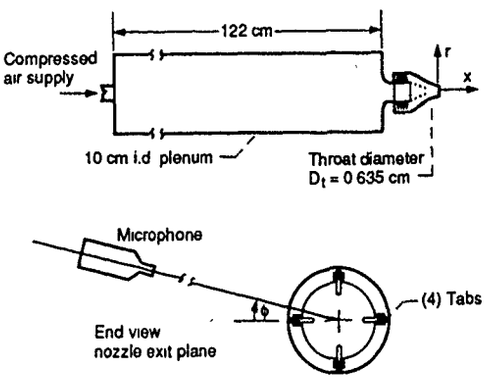

Figure 1 —Schematic of flow facility

A gated double-intensified CCD camera was used to record successive images on a video tape. Standard hot-wire measurements were performed for the subsonic jets. At a jet Mach number of 0.34, hot-wire surveys indicated a flat mean velocity profile with a "nominally laminar" boundary layer at the nozzle exit. The boundary layer state for the supersonic regime remains unknown, but is also likely to be "nominally laminar." For the supersonic jets, a 0.8 mm (od) pitot tube was used to measure total pressure. A special 1 mm (od) static pressure probe, designed after Seiner & Norum (1979), was used to measure the static pressure only on the jet centerline. Probe traverses and data acquisition were done remotely under computer control.

RESULTS AND DISCUSSION

The notations p_t and p_a are used to denote the stagnation pressure and the ambient pressure, respectively; p_{to} denotes stagnation pressure in the plenum chamber. The design Mach number, 1 36 corresponded to a pressure ratio, $p_a/p_{to} = 0.3323$. For any given plenum pressure p_{to}, the notation M_j is used to denote the Mach number had the flow expanded to ambient pressure. In the supersonic regime, pressure ratios $0.3323 < p_a/p_{to} < 0.661$ produced overexpanded jets and $p_a/p_{to} < 0.3323$ produced underexpanded jets. Thus, overexpanded condition existed for $0.79 < M_j < 1.36$, and the flow was underexpanded for $M_j > 1.36$. In the range $0.7 < M_j < 0.79$ ($0.661 < p_a/p_{to} < 0.72$), a normal shock would be expected to occur in the diverging section of the nozzle. The static pressure is denoted by P, P_e representing that at the nozzle exit

Flow Field Data

Figure 2 shows the measured stagnation pressure for eight M_j as indicated. In this and later figures, pairs of curves have been shifted by one major ordinate division, in order to present the data in a concise manner. Each pair in Fig. 2 contains data for the 2-tab case and the corresponding no-tab case. The data have been normalized by the respective plenum pressure, p_{to}.

In the supersonic regions of the flow, the measured stagnation pressure, p_{t2}, corresponds to the stagnation pressure behind the standing bow shock in front of the pitot probe. The oscillations

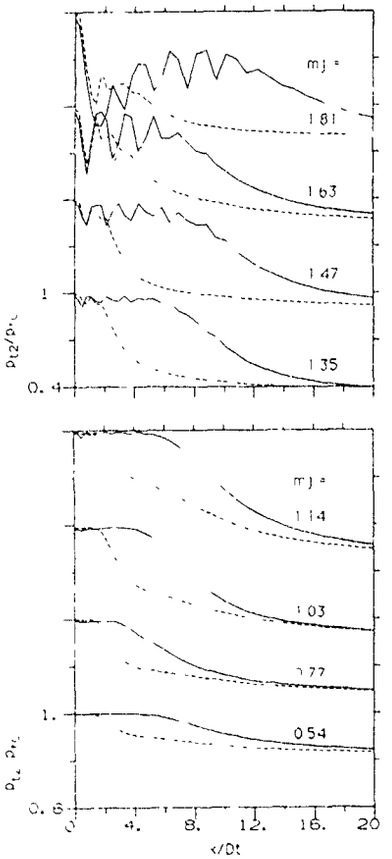

Figure 2 —Centerline variation of stagnation pressure for the eight M_j ———, no tab, ·····, 2-tab Successive pairs of curves are staggered by one major ordinate division

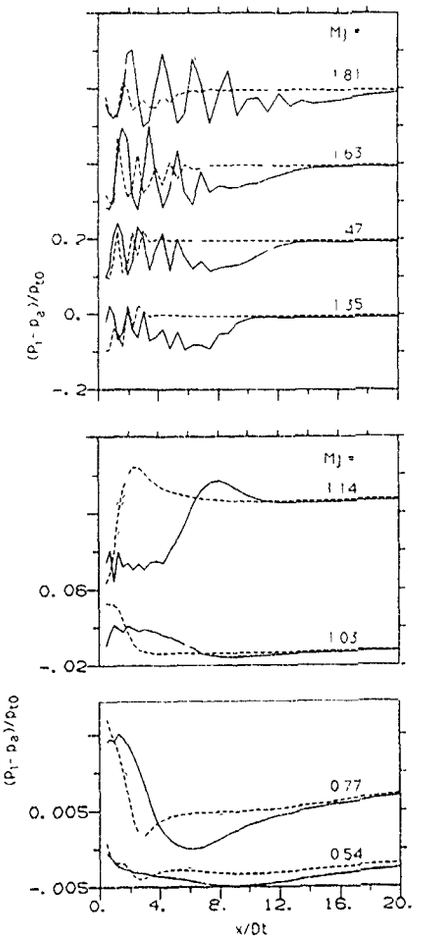

Figure 3 —Centerline variation of static pressure for the eight M_j shown similarly as in figure 2.

in the data near the jet exit are due to the standing shock structure Let us emphasize that due to probe interference there is measurement error and the data in the supersonic regions should be considered only qualitative. However, the data are accurate enough to capture the global features; for example, the number of shocks and their spacings are captured quite well as indicated by comparison with Schlieren photographs discussed later.

It is evident from Fig. 2 that the effect of the tabs is similar over the entire M_j range. Note that in the supersonic regime, the shock structure is affected drastically by the tabs This is accompanied by elimination of screech noise for which data have been presented by Samimy, Zaman & Reeder (1991).

In order to calculate the local Mach number, one needs to measure, besides p_{t2}, either the static pressure before, P_1, or the static pressure after the shock, P_2 In an over- or underexpanded supersonic jet, there is a complex shock/expansion system in the flow itself and it is not an easy task to measure either P_1 or P_2. The double-cone static pressure probe, designed after Seiner & Norum (1979), was fabricated and used only to measure P_1 on the jet centerline. Figure 3 shows the P_1 distributions corresponding to the eight M_j values of Fig. 2. For these data, essentially similar comments can be made as done for the p_{t2} data of Fig. 2 including on the measurement accuracy. Note that even for the subsonic jet at the lowest M_j, the static pressure is negative over a long distance along the centerline, a similar result was reported by Hussain & Clark (1977).

The P_1 and p_{t2} data were combined to calculate the local Mach number variation along the jet axis. Data for $M_j = 1.63$ are shown in Fig. 4 comparing the 1-, 2- and 4-tab cases with the no-tab case. Again, it is clear that the shock/expansion pattern is drastically affected by the tabs. One also finds that while just one tab affects the flow field drastically, effects of two and four tabs are more pronounced.

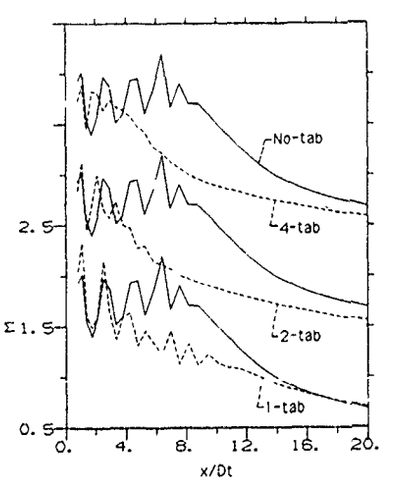

Figure 4.—Centerline variation of Mach number for $M_j = 1.63$ with and without tabs.

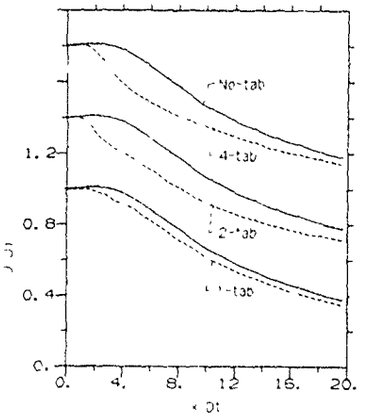

Figure 5 —Centerline variation of mean velocity for M_j = 0.34 with and without tabs

Data for the centerline variation of the mean velocity, measured with a hot-wire at M_j = 0.34, are presented in Fig. 5. Clearly, the potential core of the jet is reduced drastically and a similar inference is made, as with Fig. 4, in regards to the effect of the number of tabs.

While the data of Figs. 4 and 5 show the mean velocity distribution only along the jet centerline, detailed data on radial profiles and far-field noise were also obtained but are not included here. These data showed that four tabs resulted in the most reduction of the far-field noise. However, although four tabs resulted in more initial mixing, as evident from mass flux computed from the radial profiles, the effect of two tabs persisted the farthest downstream. This also becomes evident from the flow visualization results.

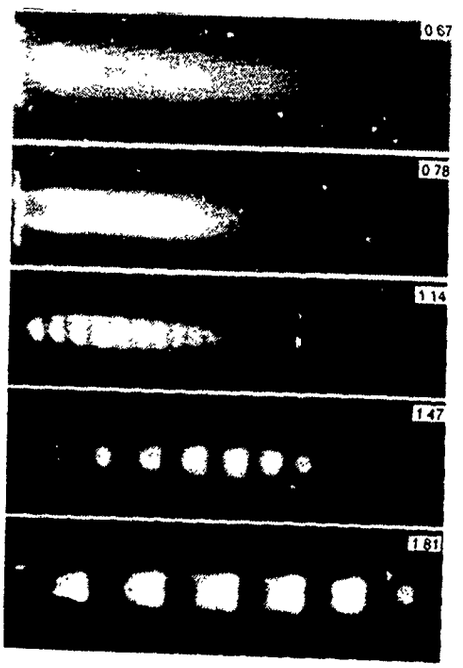

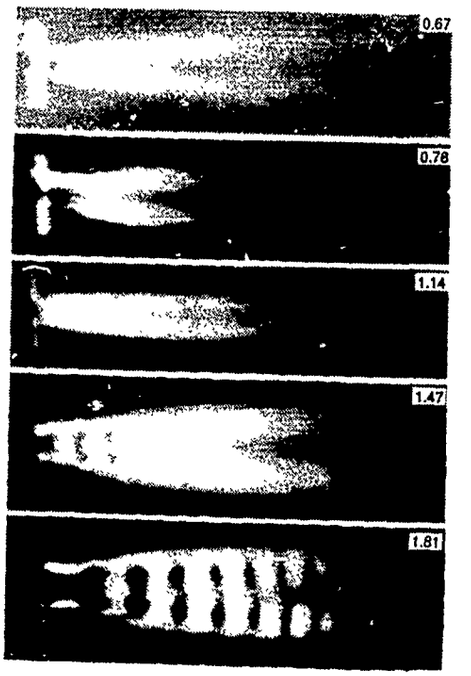

Flow Visualization

Figure 6 shows long exposure Schlieren photographs of the flow field for five M_j *as indicated. The flow is from left to right and the pictures were obtained using a vertical knife-edge, visualizing the density gradients in the streamwise direction. The flow fields approximately cover* x/D_j *range of 0 to 13. The knife-edge position was changed for fine adjustments from case to case; thus, the visual jet width should not be considered as a measure of jet spread.* In Fig. 6(a), flow fields without any tab are shown. The shock spacing increases with increasing M_j in the supersonic regime. Note that the shock spacings, for example at M_j = 1.81, are found to be the same as observed in the p_{t2} and P_t measurements (Figs. 2 and 3). About six shock cells are observed consistently within a x/D_j range of 0 to 12.

Figure 6(b) shows corresponding photographs of the flow *field with two tabs, when viewed parallel to the plane containing the two tabs. It is clear that the jet bifurcates in the plane perpendicular to the tabs, at all* M_j. *In the supersonic regime, the shock spacings have also been significantly reduced (compare with* Fig. 6(a)). When viewed perpendicular to the plane *containing the* two tabs, only one part of the bifurcated jet is seen and thus the jet spread appears less, and these data are not shown. Note that the effect for the overexpanded case at M_j = 1.14 (Fig. 6(b)) appears less than that at other M_j; this point is addressed in the following section.

The bifurcation of the jet observed in Fig 6(b) is commensurate with the radial velocity profiles obtained presently (Samimy, Zaman & Reeder, 1991) as well as by Ahuja & Brown (1989) and Bradbury & Khadem (1975). Ahuja et al. (1990) presented a set of Schlieren data for an underexpanded case that appeared the same as those for the underexpanded cases of Fig. 6(b). The bifurcation effect resembles the effect achieved by dual mode helical acoustic excitation (Parekh, Reynolds & Mungal, 1987), or by simple lateral vibration of the nozzle issuing the jet (Andrade, 1941).

Laser sheet visualization of the mixing region was performed for the supersonic jets. Figure 7(a) shows the jet cross section at four different axial locations for the natural jet at M_j = 1.63. The bright and initially narrow ring shows the mixing layer, which is growing with the streamwise distance eventually covering the entire

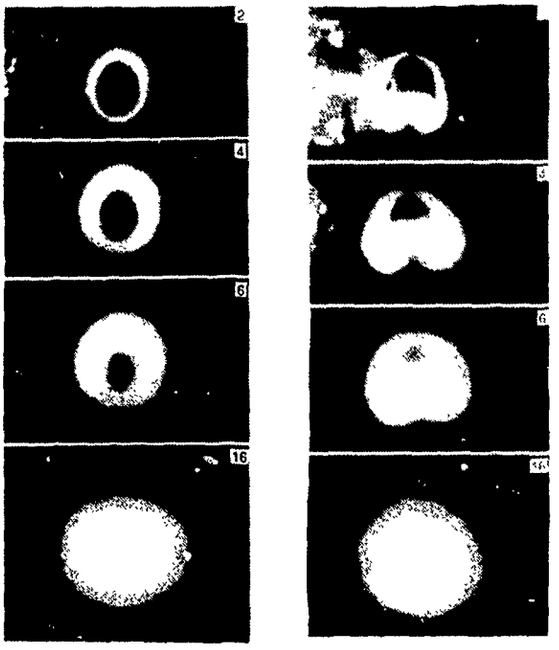

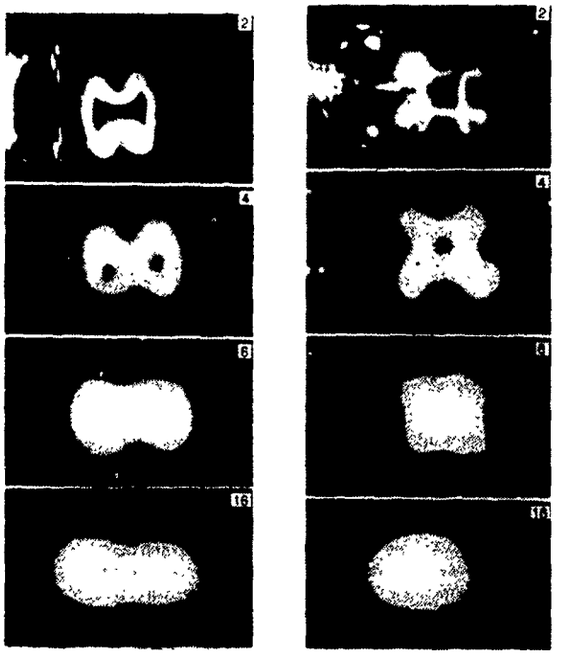

cross section of the jet. The departure from axisymmetry in these pictures is mainly due to the camera angle. Corresponding pictures for the flow field with 1, 2 and 4 tabs are shown in Figs 7(b) to (d), respectively. Again, the camera needed to be adjusted from picture to picture and thus the visual cross sections do not represent the jet spread.

The presence of a tab significantly distorts the mixing layer. The effect is to leave an "indentation" or a bulge into the high speed side which grows and persists far downstream. In a recent experiment using laser sheet illumination, Clemens & Mungal (1991) studied distortions in a plane, compressible mixing layer, produced by shocks originating from the wind tunnel side wall. The distortions reported had curious similarities with the present case, although it appeared that the "bulging" occurred on the lower speed side of their mixing layer. Possible vorticity dynamics producing the distortions in the present case are discussed in the next section.

In Fig. 7, while the jet has regained the axisymmetric shape for the 1- and 4-tab cases by $16D_t$, it has remained quite elongated in the plane perpendicular to the tabs for the 2-tab case. In fact visualization at $30D_t$ for the 2-tab case still shows a very elongated cross section; this is shown in Fig. 8 for $M_j = 1.81$.

The initial evolution of the mixing layer under the action of two tabs is further shown in Fig 9(a) It is clear that each tab produces a large distortion in the mixing layer which grows with downstream distance and results in a bifurcation of the jet by about $3D_t$. Figure 9(b) further documents the effect of two tabs at $x/D_t = 1.5$ for three M_j. Within the range covered, the effect apparently becomes more pronounced with increasing M_j. With increasing M_j the jet core temperature becomes lower, thus, with the technique used for the visualization, the mixing layer may be expected to appear sharper. However, there is also a diminishing effect of the tabs with decreasing M_j as the overexpanded condition is approached. A possible reason for this behavior is addressed in the following section.

DISCUSSION AND CONCLUDING REMARKS

An inference that can be made from this investigation is that compressibility may have little to do with the effect of the tabs The data show essentially the same effect all the way from incompressible to highly underexpanded supersonic conditions. The tabs, however, do weaken the shock structure drastically in the supersonic cases, which is accompanied by elimination of the screech noise. But the basic effect must originate from changes in the vorticity distribution caused by the tabs.

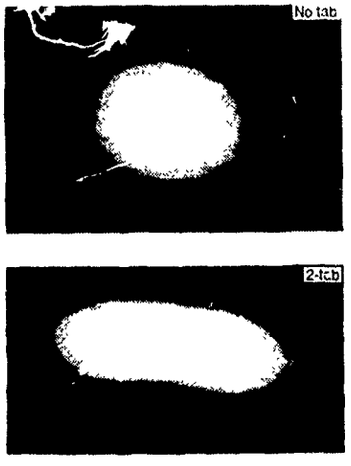

Perhaps, the most illuminating results are the laser sheet visualization pictures of Figs. 7 to 9. The "indentation" in the mixing layer may not be a "passive" wake of the tab. Similar flow visualization pictures (not shown here) in certain overexpanded cases, where the tabs were essentially ineffective, showed that the wake from the tab almost vanished by about two jet diameters. The jet mixing layer in these cases appeared essentially oblivious to the presence of the tabs. In contrast, the flow field is about 50 tab widths downstream, at $4D_t$ in Fig. 7(c), yet the distortion appears to be growing and influencing the entire jet cross section. The distortions introduced by the tabs are also not an artifact of the visualization technique. Radial profiles of Mach number confirmed

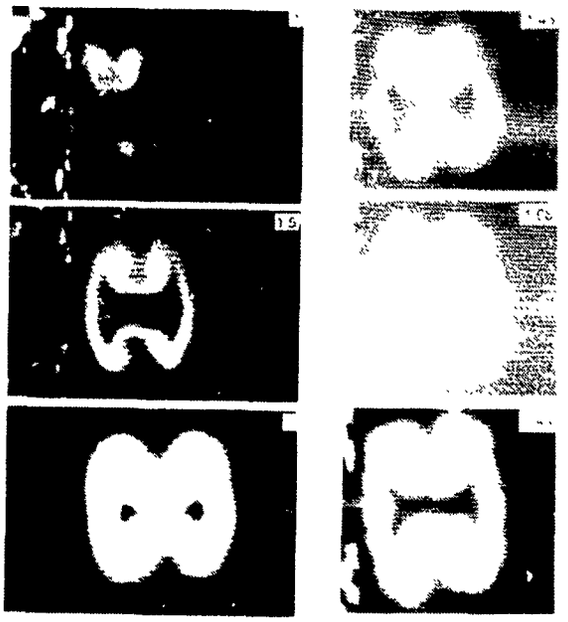

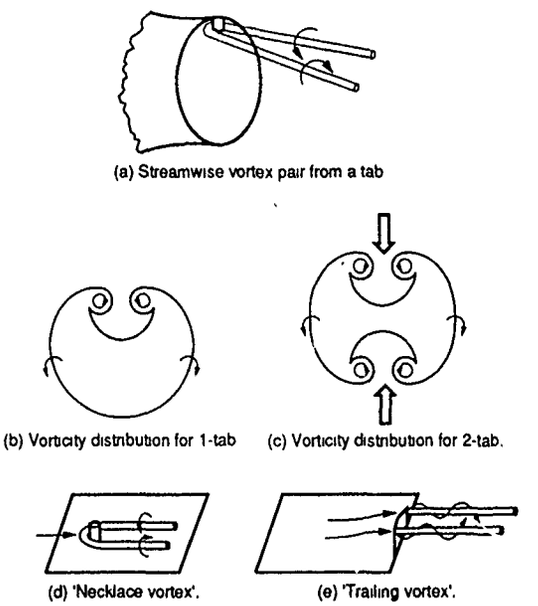

Figure 10 —Likely vorticity dynamics

the distortions This leads us to believe that there must be a significant interaction between the flow field over a tab and the sheet of azimuthal vorticity that emanates from the nozzle The following is a conjecture in regards to the vorticity dynamics

It is likely that a pair of counter-rotating streamwise vortices are shed from each tab as sketched in Fig 10(a). This should be a "stationary" vortex and not like "hairpin" vortices which are shed periodically (Acarlar & Smith, 1987) This is because the photographs in Figs. 7 to 9 are images with a long time exposure where any periodic structure would be averaged out The streamwise vortices interact and evolve with the azimuthal sheet of vorticity issuing from the nozzle. The resultant vorticity distribution on a cross-sectional plane may be expected to be as in Figs. 10(b) and (c) for one and two tabs, respectively.

The strength of the streamwise vortices should eventually decrease to leave only the "indentations" on the mixing layer as observed at $x/D_t \approx 3$ in Fig 9(a). Farther downstream, the bifurcation of the jet may take place in a similar manner as suggested by Hussain and Husain (1989) through what they called a "cut-and-connect" process In fact, these investigators observed a very similar sequence of deformations leading to a bifurcation of a jet originating from an elliptic nozzle

The question then arises as to the origin of the counter-rotating vortex pair sketched in Fig. 10(a) Such "stationary" vortex pairs, formed over protuberances in boundary layer flows, have been variously called a "horseshoe" vortex or "necklace" vortex (Acarlar & Smith, 1987; Bandyopadhyay & Watson, 1988). However, a little scrutiny should indicate that the vortex sketched in Fig. 10(a) is not the same. A necklace vortex is sketched in Fig. 10(d), following Bandyopadhyay & Watson (1988). The sense of rotation in this case is contrary to what is sketched in Fig. 10(a). Lin, Selby & Howard (1991) recently investigated the flow over various vortex generating devices while studying their effect on boundary layer separation. It is interesting that they reported pairs of streamwise vortices from several of these devices to be of the same sign as found here for the tabs.

It is possible that the tab acts as a "winglet" and produces a pair of "trailing vortices." This is sketched in Fig. 10(e), which is similar to the trailing vortices originating from the tips of a wing (e.g , Van Dyke, 1982, p. 51). It should be recognized that in order for the tip vortices to form, the wing should be at an angle of attack producing a resultant lift The tabs, however, are projected normally into the flow. It is plausible that the boundary layer upstream of the tab is lifted up so that the approaching streamlines are at an angle of attack with respect to the tab producing a resultant force acting radially and away from the jet axis. In such a case, the pair of counter-rotating vortices as sketched in Fig 10(e) would be quite realistic.

One may further conjecture that the mechanism of streamwise vortex generation from the "ramps" of Bradbury & Khadem (1975) and from the "wishbones" or "doublets" of Lin, Selby & Howard (1991) are essentially the same as described for the tab. It seems that a triangular shaped tab with the base on the nozzle wall may act similarly (Rogers & Parekh, 1990) However, if this is placed like a "delta wing," with the apex leaning upstream, it seems that vortices of sign opposite to what is sketched in Fig 10(e) will be produced If it is possible to produce such a vortex pair, the "indentation" would be outward into the low speed side of the mixing layer. It is not completely clear if this would really be the case and what the resulting effect would be on the jet evolution

The suggested streamwise vorticity generation is therefore a pressure driven and inviscid phenomenon and not due to wrapping of the viscous boundary layer around the tab. In order for the tab to work, a favorable pressure differential must exist across the tab. It was observed that in the overexpanded cases the effect of the tab was either less or absent. In the overexpanded case, there is an adverse pressure gradient within the diverging section of the nozzle prior to the exit. In severe cases of overexpansion this could even result in a boundary layer separation. It is, therefore, not surprising that the tab does not work in the overexpanded case because the pressure differential across the tab is either diminished or adverse.

Questions have remained in regard to the optimum geometry of the tab. Further investigation is required to determine the optimum height of the tab relative to the boundary layer thickness If the vorticity dynamics are correct, as conjectured above, then the width of the tab would also be a critical dimension as that determines the spacing of the two counter-rotating vortices; this needs to be studied further. It also remains to be demonstrated if the tabs will work in jets with a fully turbulent exit boundary layer and a highly disturbed core flow condition, as expected in a practical jet. These issues need to be sorted out before the method could be understood clearly and applied successfully in practice.

ACKNOWLEDGEMENT

MFR wishes to thank the Ohio Aerospace Institute for a graduate student fellowship. Helpful discussions with Mr T D Norum, Dr. P.R. Bandyopadhyay and Dr. J.M. Seiner of NASA Langley, Prof. C.R. Smith of Lehigh University and Dr. James E. Bridges of NASA Lewis are acknowledged.

REFERENCES

Acarlar, M.S., and Smith, C.R., 1987, A Study of Hairpin Vortices in a Laminar Boundary Layer. Part 1. Hairpin Vortices Generated by a Hemisphere Protuberance. J. Fluid Mech , vol 175, pp. 1-41.

Ahuja, K.K., and Brown, W.H., 1989, Shear Flow Control by Mechanical Tabs. AIAA Paper 89-0994.

Ahuja, K.K., Manes, J P., Massey, K.C. and Calloway, A B , 1990, An Evaluation of Various Concepts of Reducing Supersonic Jet Noise AIAA Paper 90-3982.

Andrade, E.N. Da C., 1941, The Sensitive Flame. Proc Phys. Soc , vol. 53, pp 329-355

Bandyopadhyay, P.R , and Watson, R.D., 1988, Structure of Rough-Wall Turbulent Boundary Layers. Phys. Fluids, vol. 31, pp. 1877-1883.

Bradbury, L.J.S., and Khadem, A.H., 1975, The Distortion of a Jet by Tabs. J. Fluid Mech., vol. 70, no. 4, pp 801-813.

Clemens, N T , and Mungal, M.G , 1991, Effects of Side-Wall Disturbances on the Supersonic Mixing Layer To appear in J Propulsion and Power

Hussain, A.K M.F., and Clark, A.R., 1977, Upstream Influence on the Near Field of a Plane Turbulent Jet. Phys. Fluids, vol. 20, no. 9, pp. 1416-1426.

Hussain, F., and Husain, H.S., 1989, Elliptic Jets. Part 1. Characteristics of Unexcited and Excited Jets. J. Fluid Mech., vol. 208, pp. 257-320.

Lin, J.C., Selby, G.V., and Howard, F.G., 1991, Exploratory Study of Vortex-Generating Devices for Turbulent Flow Separation Control. AIAA Paper 91-0042.

Parekh, D.E., Reynolds, W.C., and Mungal, M.G., 1987, Bifurcation of Round Air Jets by Dual-Mode Acoustic Excitation. AIAA Paper 87-0164.

Rogers, C.B., and Parekh, D.E., 1991, Noise Reduction and Mixing Enhancement by Using Streamwise Vortices in a Compressible Air Jet. Bull., 43rd Annual Meeting, American Physical Soc., (DFD)

Samimy, M., Zaman, K.B.M.Q., and Reeder, M.F., 1991, Supersonic Jet Mixing Enhancement by Vortex Generators. AIAA Paper 91-2263.

Seiner, J.M., and Norum, T.D., 1979, Experiments of Shock Associated Noise on Supersonic Jets. AIAA Paper 79-1526.

Tanna, H.K., 1977, An Experimental Study of Jet Noise, Part II: Shock Associated Noise. J. Sound Vibr , vol. 50, no 3, pp. 429-444.

Van Dyke, M., 1982, An Album of Fluid Motion The Parabolic Press, 1982.

EIGHTH SYMPOSIUM ON
TURBULENT SHEAR FLOWS
Technical University of Munich
September 9-11, 1991

TURBULENCE MODEL TESTING WITH THE AID OF DIRECT NUMERICAL SIMULATION RESULTS

N. Gilbert *) and L. Kleiser

DLR, Institute for Theoretical Fluid Mechanics
D-3400 Göttingen, Germany

ABSTRACT

A database obtained by direct numerical simulation of turbulent channel flow is used for testing and improving turbulence models and modelling assumptions With respect to low-Re k-ε models, wall damping functions are checked. The gradient models for the turbulent diffusion of kinetic energy and dissipation are analysed Modelling of the dissipation-rate terms in the Reynolds-stress equations is discussed. Attention is given to the possibility of calculating certain turbulence model constants directly from the simulation data

INTRODUCTION

To predict turbulent flows for complex geometries turbulence models of different categories (one-, two- and Reynolds-stress-equation models) are used The subject of turbulence modelling has been reviewed quite often, e g. by Rodi (1980), Patel et al (1985), Speziale (1991) and, with particular emphasis on aerodynamic flows, by Rubesin (1989) and Bushnell (1991) Improvements of current models and recent developments in turbulence modelling are discussed e.g by Hanjalic (1990), Launder (1990), Rodi (1988) and Rodi & Mansour (1990). The status of an international project on collaborative testing of turbulence models is reported by Bradshaw et al. (1991).

Until recently turbulence model development has been based mainly on indirect methods, i.e. testing the closure models by comparing the computed results for different applications with experimental or theoretical data for the specific problem. This is because until now there has been no way to measure pressure and velocity fluctuations simultaneously with sufficient spatial accuracy. With the advent of sufficiently powerful supercomputers and highly accurate numerical (mostly spectral) methods, direct numerical simulations (DNS) of inhomogeneous turbulent flows in simple geometries and at moderate Reynolds numbers have now become possible (cf Reynolds 1990). These data bases can be used to test closure models by direct comparisons of the closure formulae with the terms being modelled. The data bases will also provide guidelines for model developers

Considerable work on this subject has been done at the NASA Ames / Stanford Center for Turbulence Research where some of the first direct numerical simulation databases of turbulent flows were generated. These databases are being evaluated continually by turbulence researchers during workshops such as reported by Hunt (1988) and Moin et al. (1990). Mansour et al. (1988) published one of the first papers on direct testing of turbulence closure models for wall-bounded flows

In the present work a database of fully developed turbulent channel flow (generated by the first author in 1988) has been used for testing various turbulence models and/or model assumptions. Only a few results are presented here; a detailed report is given by Gilbert (1991). Similar results based on an earlier simulation are published in Gilbert & Kleiser (1989) and have partly been reported in a paper by Rodi (1988) In the present paper, some DNS data are presented and compared with existing numerical and experimental data. The near-wall behaviour of the $c_\mu \cdot f_\mu$-coefficient in the eddy-viscosity expression used in k-ε models is investigated. A critical evaluation concerning the modelling of diffusion of turbulent kinetic energy and turbulent dissipation by gradient assumptions is given. Finally modelling of the dissipation-rate terms in the Reynolds-stress equations (Launder et al. 1975) is discussed

DIRECT NUMERICAL SIMULATION OF TURBULENT CHANNEL FLOW

As in our earlier simulation (Gilbert 1988, Gilbert & Kleiser 1990), the turbulent channel flow data has been obtained by starting a simulation with slightly disturbed laminar flow and continuing all the way through the transition process up to developed turbulence. The mass flux is kept fixed at all times by imposing an appropriate instantaneous pressure gradient. The numerical resolution in the late transitional and turbulent stages is $N_1 \times N_2 \times N_3 = 160^2 \times 128$ gridpoints in the streamwise (x_1), spanwise (x_2) and normal (x_3) directions. Again we employ a spanwise symmetry condition, which arises naturally for the transition problem and cuts the computing time and memory by a factor of two. This does not appear to adversely effect the obtained turbulence statistics. The turbulent mean wall Reynolds number (based on channel half width h, wall shear velocity v_τ and kinematic viscosity ν) is $Re_\tau \cong 210$. The centre-line Reynolds number is $Re_{CL} \cong 3830$. The fully turbulent flow is calculated over a time interval of $\Delta T^+ \equiv \Delta T\, v_\tau^2/\nu \approx 1000$ wall units. The box lengths in the streamwise and spanwise directions are $L_1^+ \cong 2360$ and $L_2^+ \cong 1180$ and are twice as large as in Gilbert (1988). The sampling time interval of our running time average, which includes horizontal averaging, is $\Delta t^+_{sample} \approx 1$. Averages over horizontal planes, both channel halves and time are denoted by $\langle \cdot \rangle$.

All correlations up to third order moments appearing in the exact k, ε and Reynolds-stress equations were calculated. The overall agreement of the computed turbulence statistics with existing numerical and experimental data at comparable Reynolds numbers is good. Some discrepancies occur in the near-wall region which have also been observed in the turbulent channel flow simulation of Kim et al. (1987) at the somewhat lower Reynolds number $Re_\tau = 180$. Our present results are quite close to the Kim et al. data (Gilbert 1991).

*) Now with BASF AG, Technical Development, ZET/EA, D-6700 Ludwigshafen

In Fig 1 the mean velocity profile is given, which shows a well-developed viscous sublayer and buffer region. Unlike in our earlier simulation, the logarithmic part of the profile is now clearly visible The differences between our data and those of Kim et al. are small Both simulations give a log-law with an additive constant slightly above that given by Dean (1978) In Fig. 2 the computed root-mean-square values of the three velocity fluctuations normalised by the local mean velocity $\langle v_1 \rangle$ are shown. Whereas the two sets of DNS data nearly collapse, the experimental data show considerable scatter. The results of Alfredsson et al. (1988) for $u_1'/\langle v_1 \rangle$ fit our simulation data very well, whereas the recent results of Niederschulte et al (1990) clearly differ

BUDGETS OF TURBULENT KINETIC ENERGY AND DISSIPATION

Fig 3a shows the balance of the kinetic energy k, using the usual notation (see Mansour et al 1988) except for the viscous dissipation rate $\tilde{\varepsilon} = \varepsilon + \partial^2\langle u_3^2 \rangle/\partial x_3^2$ (Here and in the later figures data are given in wall units.) Away from the wall there is an approximate balance between the production P_k and the dissipation ε Closer to the wall turbulent and viscous diffusion transport energy from the region of main production towards the wall and towards the core region of the channel In the ε-balance, shown in Fig 3b, the turbulent production P_ε^4 and dissipation Γ_ε are the dominant terms in the core region of the channel. Near the wall the rate of production by the mean flow $P_\varepsilon^1 + P_\varepsilon^2$ increases and peaks at $y^+ \approx 5$ At this position Γ_ε reaches its minimum value Gradient production P_ε^3 and turbulent diffusion T_ε are relatively small compared with the other terms Nevertheless, as will be seen later, these terms are important in turbulence modelling since they balance the net effect of all other source and sink terms (i e. the sum of $P_\varepsilon^1 + P_\varepsilon^2 + P_\varepsilon^4 - \Gamma_\varepsilon$)

THE EDDY VISCOSITY RELATION IN LOW-RE k-ε MODELS

To account for the direct effect of molecular viscosity on the shear stress, low Reynolds number turbulence models use damping functions f_μ in the Kolmogorov-Prandtl expression for the eddy viscosity, $\nu_t = c_\mu f_\mu k^2/\varepsilon$ The problem of evaluating $c_\mu f_\mu$ from various DNS data has been considered recently by Rodi & Mansour (1990) They found that c_μ depends both on the type of flow (channel or boundary layer) and on the Reynolds number Fig 4 presents our DNS data and a comparison with several models and experimental data In the region of approximate balance between production and dissipation (marked in Fig 4a by vertical bars) c_μ attains a value of ≈ 0.11, which is higher than the standard value of 0.09 but is consistent with $P_k/\varepsilon \approx 0\,8$ being less than one (Rodi & Mansour 1990) The agreement of the f_μ distribution obtained from our simulation, with c_μ chosen as 0 11, with the averaged distribution deduced by Patel et al (1985) from different experiments is very good (Fig. 4b). Two f_μ functions from the k-ε models of Reynolds and of Lam & Bremhorst (see Patel et al. 1985) are also included. Very close to the wall the f_μ obtained from our simulation increases proportional to $1/y$ to ensure the y^3-behaviour of the Reynolds stress. None of the k-ε model functions exhibits this behaviour, and even away from the wall their overall agreement with the simulation data is not very good. A surprisingly good agreement over the whole range (except for the immediate vicinity of the wall) is found with the relationship $f_\mu = 2.92\langle u_3^2 \rangle/k$ derived from a (high Reynolds number) second-moment closure of Gibson & Launder (1978). This result confirms the suggestion of Launder & Tselepidakis (1990) that the rapid reduction of the Reynolds stress $-\langle u_1 u_3 \rangle$ as the wall is approached is due to the damping of $\langle u_3^2 \rangle$ rather than to direct viscous effects.

GRADIENT DIFFUSION HYPOTHESES

A usual assumption in the k-equation is the gradient model for the turbulent diffusion term

$$(1) \qquad -\frac{\partial}{\partial x_k}\langle u_k\,(u_l u_l/2 + p)\rangle = \frac{\partial}{\partial x_k}\left(\frac{\nu_t}{\sigma_k}\frac{\partial k}{\partial x_k}\right)$$

To test this assumption, we calculate both the exact term (l h.s.) and the model term (r.h s.) Since diffusion is very small away from the wall a more critical way of testing the model is to compare the integrated terms, which are shown in Fig. 5a. Over the whole channel the two quantities are nearly proportional so that σ_k is approximately constant The value calculated from our DNS data varies from $\sigma_k = 0\,9$ at $y^+ = 30$ to $\sigma_k = 0.6$ near the channel centre with an average value of $\sigma_k \approx 0.8$, which is lower than the standard value of 1.0 Using a constant value of σ_k the turbulent diffusion in the immediate vicinity of the wall is underpredicted However, this is of minor importance because turbulent diffusion is small there compared to the dissipation and viscous diffusion terms.

Like the diffusion term in the k-equation, turbulent diffusion of dissipation is modelled with a gradient assumption

$$(2) \qquad \begin{aligned} &-\frac{\partial}{\partial x_k}\left\{\nu\langle u_k\left(\frac{\partial u_l}{\partial x_l}\right)^2\rangle + 2\nu\left\langle\frac{\partial p}{\partial x_l}\frac{\partial u_k}{\partial x_l}\right\rangle\right\} \\ &= \frac{\partial}{\partial x_k}\left(\frac{\nu_t}{\sigma_\varepsilon}\frac{\partial \varepsilon}{\partial x_k}\right). \end{aligned}$$

To test this model we again compare the integrated terms which are shown in Fig 5b Away from the wall ($y^+ \gtrsim 30$) the proportionality is acceptable, with σ_ε varying between 1 4 at $y^+ = 50$ and 1.0 near the channel centre, thus bracketing the usual value of $\sigma_\varepsilon = 1\,3$ Near the wall, however, the model of Eq. (2) is completely wrong Computing σ_ε from the DNS data leads to negative values for σ_ε there Again it might be argued that the diffusion term is small in the near-wall region compared with the other terms in the ε-balance so that the deficiency of the gradient model would not be detrimental. But this is not true for the modelled ε-equation Since the net effect of generation and destruction is small compared with the individual terms it is important to have a good model for the "small" diffusion term

DISSIPATION RATE TERMS

Near walls, modifications are also necessary to the high-Re versions of Reynolds-stress equation models. Viscosity enters the Reynolds-stress balance primarily through the dissipation rate terms ε_{ij} The modelling of these terms is based on blending the nonisotropic behaviour near the wall, approximated (Rotta 1951) by

$$(3) \qquad -2\nu\left\langle\frac{\partial u_i}{\partial x_k}\frac{\partial u_j}{\partial x_k}\right\rangle = \varepsilon_{ij}^* \equiv -\frac{\varepsilon}{k}\langle u_i u_j\rangle,$$

with the expression for sufficiently high Reynolds numbers, where the concept of local isotropy holds

$$(4) \qquad -2\nu\left\langle\frac{\partial u_i}{\partial x_k}\frac{\partial u_j}{\partial x_k}\right\rangle = -\frac{2}{3}\delta_{ij}\cdot\varepsilon.$$

The blended form of the ε_{ij} model (cf Hanjalic & Launder 1976) reads

$$(5) \qquad \varepsilon_{ij} = f_\varepsilon \cdot \varepsilon_{ij}^* + (1 - f_\varepsilon) \cdot \frac{2}{3} \delta_{ij} \varepsilon \, .$$

Hanjalic & Launder inferred that the blending function f_ε is a function of the turbulence Reynolds number $Re_T = k^2/(\nu\varepsilon)$ and determined it by computer optimization to be

$$(6) \qquad f_\varepsilon = (1 + \frac{Re_T}{10})^{-1} \, .$$

In a more recent proposal by Fu et al. (1987) f_ε itselfs depends on the anisotropy tensor, using the anisotropy factor A

$$(7) \qquad f_\varepsilon = 1 - \sqrt{A} \, .$$

The anisotropy factor is defined by $A = 1 - 9(A_2 - A_3)/8$ where $A_2 = a_{ij} \cdot a_{ij}$ and $A_3 = a_{ij} \cdot a_{jk} \cdot a_{ki}$ are the second and third invariants of the Reynolds-stress anisotropy tensor $a_{ij} = \langle u_i u_j \rangle / k - 2\delta_{ij}/3$ The value of f_ε in Eq. (6) changes from unity to zero as the Reynolds number Re_T varies from zero to infinity This behaviour is also attained with Eq. (7) because A is zero in 2D turbulence (near walls) and $A = 1$ in isotropic turbulence

Fig 6 shows the two f_ε functions Eqs. (6), (7) computed from the simulation data The difference between the two functions is quite big The function Eq (6) quickly decays within the viscous sublayer ($y^+ < 10$) to its minimal value (which is non-zero because Re_T is finite), whereas Eq. (7) decays more gradually, and roughly linearly, with the wall distance and reaches its minimal value at $y^+ \approx 60 - 80$. The third curve shows an attempt by Launder & Tselepidakis (1990) to use an exponential function depending on Re_T instead of Eq (6). This curve also decays very rapidly The reason is that Re_T rises quickly (within $y^+ \lesssim 20$) to a value of $Re_T \approx 180$, which is maintained over most of the channel (see Fig. 7) A more gradual behaviour of f_ε – which is needed as we shall conclude – would be achieved by using $Re_y = y\sqrt{k}/\nu$ as the independent variable.

A comparison of model predictions with the DNS data, shown in Fig 8, reveals the striking observation (made already by Mansour et al. 1988) that using the wall model Eq. (3) of Rotta throughout leads to better agreement than the blended model Eqs. (5), (6) The blending function of Hanjalic & Launder restricts the influence of the "wall"-terms to the viscous sublayer whereas the blending function Eq (7) of Fu et al (1987) extends it up to the log-law region. We therefore propose to use the Hanjalic & Launder model but with their f_ε function replaced by that of Fu et al (Fu et al. used their f_ε in conjunction with a new wall model which captures the proper near-wall behaviour of ε_{ij} but gives poor results away from the wall). The results of the "new" model are also included in Fig 8. They are clearly superior to those of the original model for ε_{11}, ε_{12} and ε_{33} and still acceptable for ε_{13}.

CONCLUSIONS

Turbulence data from direct numerical simulations has been used to compute the terms in the budgets of the turbulent kinetic energy, the Reynolds stresses and the dissipation rate. Testing of turbulence closure models has been done by direct comparison of the exact terms with the model expressions. Special attention has been given to the possibility of calculating turbulence model constants directly from the simulation data (Gilbert 1991).

The coefficient c_μ in the eddy viscosity expression is calculated from the DNS data as 0.11 instead of the usually applied value of 0.09. A possible explanation is the dependence of c_μ on the ratio P_k/ε which is below 1 (about 0.8) in the log-law region where c_μ is found to be constant. None of the tested damping functions f_μ used in low-Re k-ε models shows acceptable agreement with the simulation data over the whole near-wall region. Some functions rise too fast whereas others approach unity too slowly. The turbulent diffusion of turbulent kinetic energy and dissipation is usually modelled via a gradient-type model. The agreement between such a model and the DNS data in case of the turbulent kinetic energy is good over the whole the channel depth. The model works well also in the case of turbulent dissipation except in the immediate vicinity of the wall.

In Reynolds-stress models the dissipation rate terms ε_{ij} have to be approximated. Modelling of these terms is based on blending the non- isotropic behaviour near the wall (Rotta's model $\varepsilon_{ij} = \langle u_i u_j \rangle \varepsilon/k$) with the expression for local isotropy at high Reynolds numbers, $\varepsilon_{ij} = 2\delta_{ij}\varepsilon/3$. Most models do not work well since the blending functions restrict the influence of the wall term to the viscous sublayer. From the simulation data it follows that a blending function decaying more gradually with the wall distance leads to acceptable agreement with the DNS data for all components. The blending function of Fu et al (1987), $f_\varepsilon = 1 - \sqrt{A}$ where A is the anisotropy factor, does show such gradual behaviour

ACKNOWLEDGEMENT

We would like to thank R Kessler and N Sandham for reviewing a draft version of this paper.

REFERENCES

ALFREDSSON, P.H , JOHANSSON, A.V., HARITONIDIS, J H & ECKELMANN, H. 1988 The fluctuating wall shear stress and the velocity field in the viscous sublayer Phys Fluids 31, 1026-1033.

BRADSHAW, P., LAUNDER, B E. & LUMLEY, J.L. 1991 Collaborative testing of turbulence models. AIAA Paper No. 91-0215

BUSHNELL, D.M 1991 Turbulence modeling in aerodynamic shear flows - status and problems AIAA Paper No. 91-0214.

DEAN, R.B. 1978 Reynolds number dependence of skin friction and other bulk flow variables in two-dimensional rectangular duct flow. J. Fluids Eng. 100, 215-223

ECKELMANN, H. 1970 Experimentelle Untersuchungen in einer turbulenten Kanalströmung mit starken viskosen Wandschichten. Mitt. MPI f. Strömungsforschung und AVA Göttingen Nr. 48.

FU, S , LAUNDER, B.E & TSELEPIDAKIS, D.P. 1987 Accomodating the effects of high strain rates in modelling the pressure-strain correlation. UMIST Mech. Eng. Dept. Report TFD/87/5.

GIBSON, M.M. & LAUNDER, B.E. 1978 Ground effects on pressure fluctuations in the atmospheric boundary layer. J. Fluid Mech. 86, 491-511

GILBERT, N. 1988 Numerische Simulation der Transition von der laminaren in die turbulente Kanalströmung. Dissertation, University of Karlsruhe, Report DFVLR-FB 88-55.

GILBERT, N. 1991 DLR Report in preparation.

GILBERT, N. & KLEISER, L. 1989 Turbulence model data derived from direct numerical simulations. In: Advances in Turbulence 2 (eds. H.-H. Fernholz & H.E. Fiedler), Springer, Berlin, pp. 329-333.

GILBERT, N. & KLEISER, L. 1990 Near-wall phenomena in transition to turbulence. In: Near-Wall Turbulence (eds. S.J. Kline & N.H. Afgan), Hemisphere, New York, pp. 7-27.

HANJALIC, K. 1990 Practical predictions by two-equation- and other fast methods In: Near-Wall Turbulence (eds. S.J. Kline & N.H. Afgan), Hemisphere, New York, pp. 762-781.

HANJALIC, K. & LAUNDER, B.E 1976 Contribution towards a Reynolds-stress closure for low-Reynolds-number turbulence J. Fluid Mech. 74, 593-610

HUNT, J.C.R. 1988 Studying turbulence using direct numerical simulation 1987 Center for Turbulence Research NASA Ames / Stanford Summer Programme J Fluid Mech. 190, 375-392

KIM, J., MOIN, P & MOSER, R D. 1987 Turbulence statistics in fully-developed channel flow at low Reynolds number J Fluid Mech 177, 133-166

KREPLIN, H.-P & ECKELMANN, H. 1979 Behavior of the three fluctuating velocity components in the wall region of a turbulent channel flow Phys. Fluids 22, 1233-1239

LAUNDER, B E. 1990 Phenomenological modelling present and future? In: Whither Turbulence? Turbulence at the Crossroads (ed. J L. Lumley), Springer Lect Notes in Physics 357, pp 439-485.

LAUNDER, B E , REECE, G.J & RODI, W. 1975 Progress in the development of a Reynolds-stress turbulence closure J. Fluid Mech. 68, 537-566

LAUNDER, B E & TSELEPIDAKIS, D P 1990 Contribution to the second-moment modelling of sublayer turbulent transport. In Near-Wall Turbulence (eds S J Kline & N H Afgan), Hemisphere, New York, pp. 818-833

MANSOUR, N N , KIM, J. & MOIN, P. 1988 Reynolds-stress and dissipation-rate budgets in a turbulent channel flow. J. Fluid Mech. 194, 15-44.

MOIN, P , REYNOLDS, W.C. & KIM, J. 1990 (eds.) Studying Turbulence Using Numerical Simulation Databases - III, Proceedings of the 1990 Summer Program. Center for Turbulence Research, NASA Ames / Stanford University.

NIEDERSCHULTE, M.A., ADRIAN, R.J. & HANRATTY, T.J. 1990 Measurements of turbulent flow in a channel at low Reynolds numbers. Experiments in Fluids 9, 222-230.

PATEL, V.C., RODI, W. & SCHEUERER, G. 1985 Turbulence models for near-wall and low Reynolds number flows: a review. AIAA J. 23, 1308-1319

REYNOLDS, W C. 1990 The potential and limitations of Direct and Large Eddy Simulations. In: Whither Turbulence? Turbulence at the Crossroads (ed. J.L. Lumley), Springer Lect Notes in Physics 357, pp. 313-343.

RODI, W. 1980 Turbulence Models and Their Application in Hydraulics. International Association for Hydraulic Research, Delft.

RODI, W. 1988 Recent developments in turbulence modelling. Proc. 3rd Int Symp. on Refined Flow Modelling and Turbulence Measurements, Tokyo, July 26-28, 1988.

RODI, W. & MANSOUR, N.N. 1990 Low Reynolds number k-ε modeling with the aid of direct simulation data. Proceedings of the 1990 Summer Program. Center for Turbulence Research, NASA Ames / Stanford University, pp. 85-106.

ROTTA, J. 1951 Statistische Theorie nichthomogener Turbulenz. Zeitschrift für Physik 129, 547-572.

RUBESIN, M W. 1989 Turbulence modeling for aerodynamic flows AIAA Paper No. 89-0606

SPEZIALE, C G. 1991 Analytical methods for the development of Reynolds-stress closures in turbulence. Ann Rev Fluid Mech. 23, 107-157.

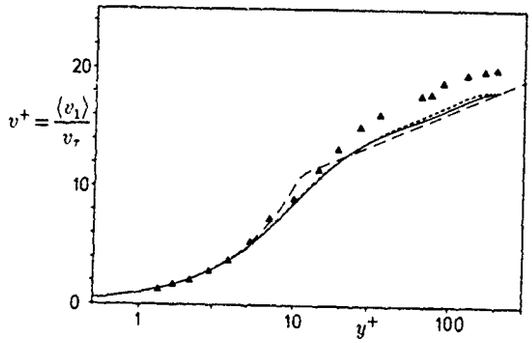

Fig. 1. Mean velocity profile in wall units
—— present DNS,
- - - DNS Kim et al. (1987),
Δ Experiment Eckelmann (1970),
– – $v^+ = 2.44 \cdot \ln y^+ + 5.17$

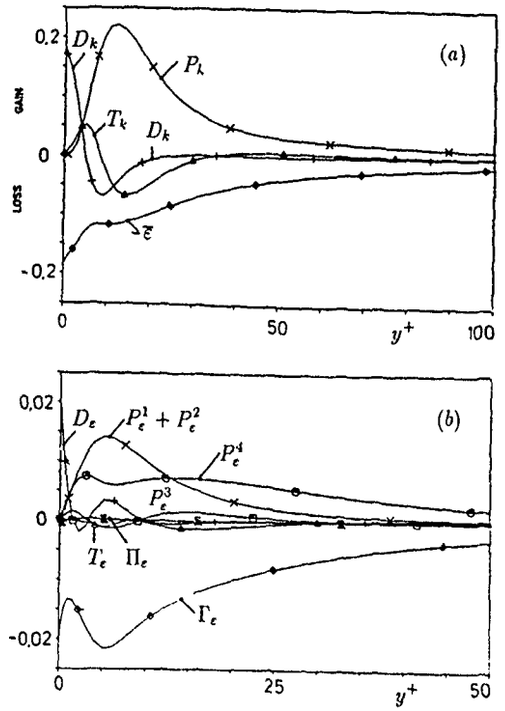

Fig. 3. Terms in the budget of (a) the tu bulent kinetic energy k and (b) the dissipation rate ε

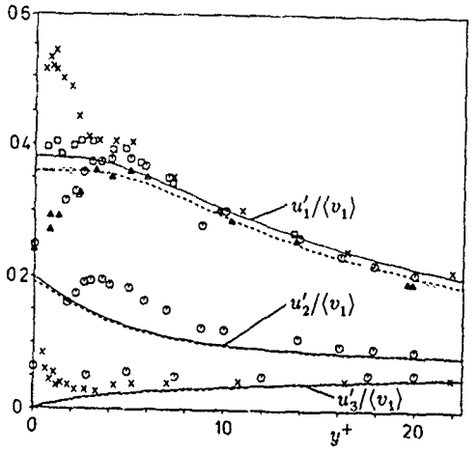

Fig. 2. RMS velocity fluctuations in the near-wall region normalised by the local mean velocity $\langle v_1 \rangle$.
Comparison of DNS results (—— present work, - - - Kim et al. 1987) with experimental data: Δ Eckelmann (1970), ○ Kreplin & Eckelmann (1979), □ Alfredsson et al. (1988), × Niederschulte et al. (1990).

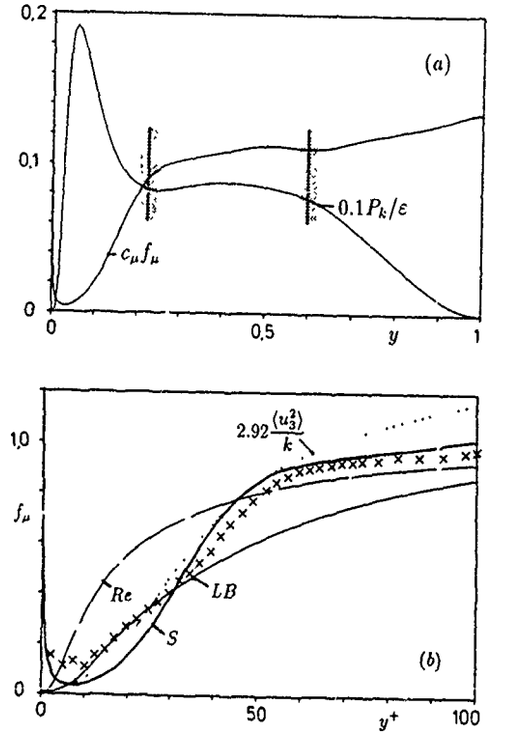

Fig. 4. Eddy-viscosity relation in low-Re k-ε models:
(a) DNS data for $c_\mu f_\mu$ and P_k/ε,
(b) various damping functions f_μ,
×: experimental data (curve fit by Patel et al. 1985),
S: DNS data with $c_\mu = 0.11$, *Re*: model of Reynolds,
LB: model of Lam & Bremhorst, $2.92\,\langle u_3^2 \rangle / k$: model of Gibson & Launder.

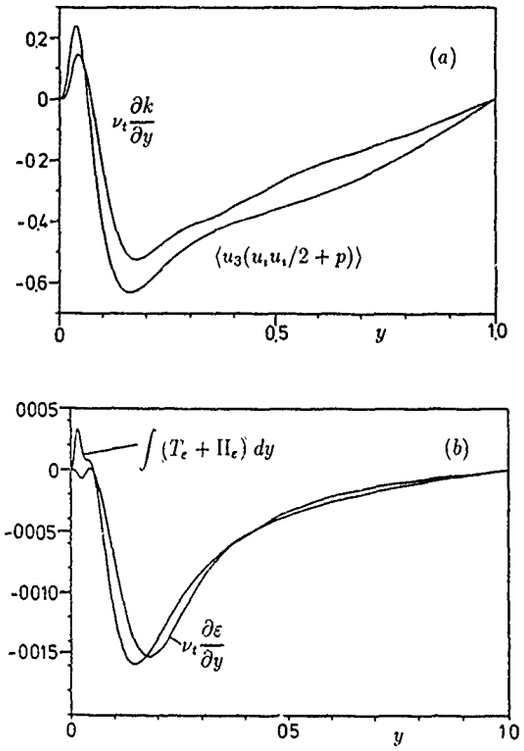

Fig. 5. Exact and modelled turbulent diffusion terms for the turbulent kinetic energy (a) and the dissipation (b).

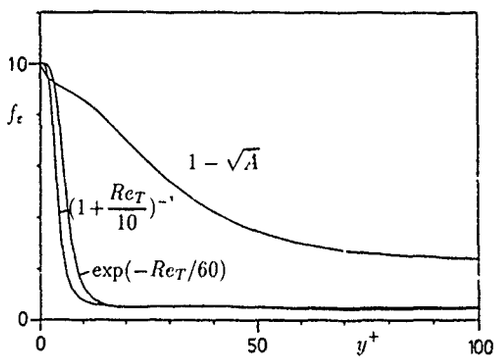

Fig. 6. Blending functions f_ε for the dissipation rate formula

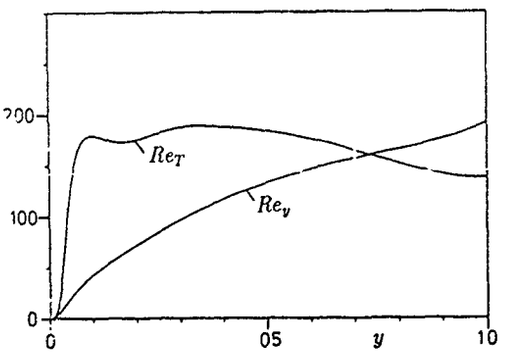

Fig. 7. Variation of turbulence Reynolds numbers Re_T and Re_y across the channel.

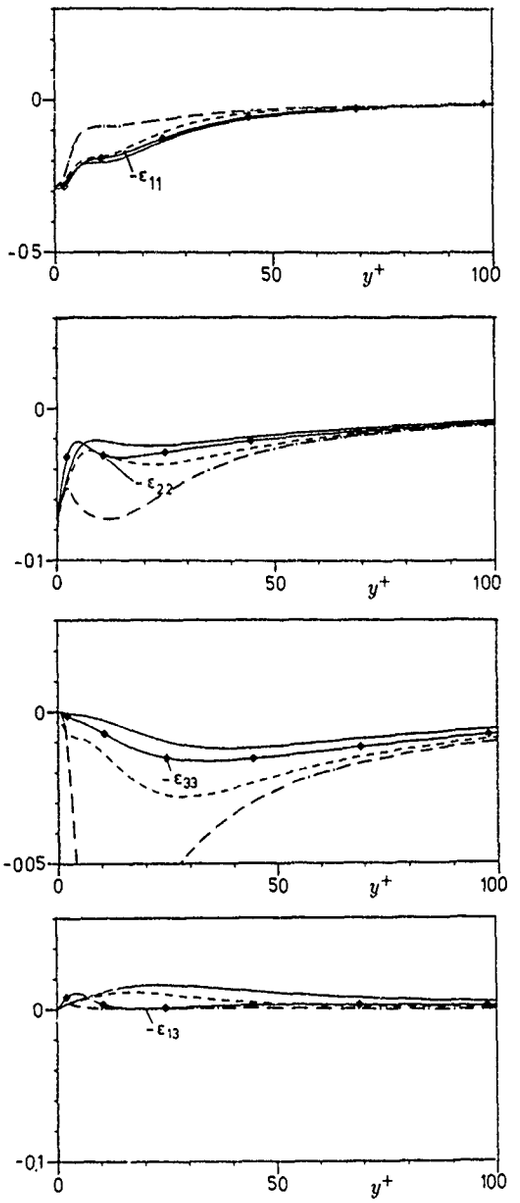

Fig. 8. Distribution of the dissipation rate terms ε_{ij} across the channel.
—◇— DNS data, —— Rotta's (1951) model, Eq. (3),
- · - model of Hanjalic & Launder (1976), Eqs. (5), (6),
- - - present model, Eqs. (5), (7).

EIGHTH SYMPOSIUM ON
TURBULENT SHEAR FLOWS
Technical University of Munich
September 9-11, 1991

K - ε Turbulence Model for Low Reynolds Number Wall-Bounded Shear Flow

G.B. Deng , J. Piquet
CFD Group, LHN-URA 1217 CNRS
ENSM
1, Rue de la Nöe, 44072 NANTES Cedex
FRANCE

Abstract : Direct simulation data for a channel flow and a flat plate boundary layer are used to develop a new k-ε model which predicts the dissipation, the turbulence kinetic energy level and budget correctly, in contract with classical k-ε model and presently available Reynolds stress models.

INTRODUCTION

The overall success of turbulence models is determined in a large measure by the treatment of the vicinity of solid walls. The underlying assumption of the so-called wall function approach, namely the universality of the law of the wall and the related concept of turbulence in equilibrium, severely restricts the range of validity of turbulence models and excludes a possible use in cases with separation or high skewing of velocity profiles. For such complex flow situations, the turbulence model must be solved including the viscous sublayer. This in turn introduces, apart from computational difficulties due to large grid aspect ratios, a modelling problem usually associated with the so-called low Reynolds number corrections : weighting functions are introduced in standard models and are empirically determined, at best, on a correct asymptotic basis, and in such a way that mean velocity and friction velocity predictions agree with experiments, at least for simple flows.

The recent availability of direct simulation channel flow [1][2] and flat plate boundary layer data [3] makes it possible to assess the most representative models [4][5][6][7] which share two main common deficiencies. (i) Although the mean velocity and the Reynolds shear stress are correctly predicted, there is a systematic underprediction of the turbulence kinetic energy. (ii) Close to the wall, the prediction of dissipation fails completely.

Direct numerical data are used in the following to suggest a new two-zone K-ε model, on the basis of the mixing length hypothesis. The most important modifications are the following :

(i) Instead of introducing a universal weighting function, a two-zone mixing length model is used with an algebraic expression, independent on K and ε, close to the wall.

(ii) A new closure for turbulent transport of K is introduced.

(iii) Turbulence dissipation, in the inner zone, consists in two parts. One part, independent on kinetic energy destruction, is modelled by an algebraic term. The other, $\tilde{\varepsilon}$, results from K and a Taylor scale. In the outer zone, ε is given by a new transport equation model.

1. THE MEAN FLOW EQUATIONS

The Reynolds-averaged Navier-Stokes equations for an incompressible flow are :

$$\bar{U}_{i,i} = 0 \quad ; \quad \frac{D\bar{U}_i}{Dt} + [\overline{u'_i u'_j}]_{,j} = -\rho^{-1} \bar{P}_{,i} + \nu \bar{U}_{i,jj} \qquad (1)$$

The turbulence kinetic energy is also solved :

$$\frac{DK}{Dt} = P_{(K)} - T_{(K)} + D_{(K)} + \Pi_{(K)} - \varepsilon \qquad (2)$$

with

$P_{(K)} = -\overline{u'_i u'_j}\,\bar{U}_{i,j}$: production term

$T_{(K)} = \frac{1}{2}[\overline{u'_i u'_i u'_j}]_{,j}$: turbulent transport term

$D_{(K)} = \nu K_{,jj}$: viscous transport term

$\Pi_{(K)} = -\overline{u'_i p'_{,i}}$: pressure-velocity correlation term

$\varepsilon = \nu \overline{u'_{i,j} u'_{i,j}}$: "dissipation"

The equation for ε is as follows :

$$\frac{D\varepsilon}{Dt} = P^1_{(\varepsilon)} + P^2_{(\varepsilon)} + \Gamma_{(\varepsilon)} + P^4_{(\varepsilon)} - T_{(\varepsilon)} + D_{(\varepsilon)} + \Pi_{(\varepsilon)} - Y_\varepsilon \qquad (3)$$

with :

$P^1_{(\varepsilon)} \equiv -2\nu \overline{u'_{i,j} u'_{k,j}}\, S_{ik}$: mixed production term

$P^2_{(\varepsilon)} \equiv -2\nu \overline{u'_{i,k} u'_{i,m}} S_{km}$: generation by the mean velocity gradient

$P^3_{(\varepsilon)} \equiv -2\nu \overline{u'_k u'_{i,m}}\, \bar{U}_{i,km}$: gradient generation of dissipation

$P^4_{(\varepsilon)} \equiv -2\nu \overline{u'_{i,k} u'_{i,m} u'_{k,m}}$: turbulent generation of dissipation

$T_{(\varepsilon)} \equiv \nu [\overline{u'_{i,k} u'_{i,k} u'_j}]_{,j}$: turbulent transport of dissipation

$D_{(\varepsilon)} \equiv \nu \varepsilon_{,jj}$: viscous diffusion of dissipation

$\Pi_{(\varepsilon)} \equiv 2\nu [\overline{u'_{j,k} p'_{,k}}]_{,j}$: pressure transport of dissipation

$Y_\varepsilon \equiv 2\nu^2 \overline{u'_{i,km} u'_{i,km}}$: destruction of dissipation

The closure assumption for Reynolds stresses is the eddy viscosity assumption (4) :

$$\tau_{ij} \equiv -\overline{u'_i u'_j} = -\frac{2}{3} K \delta_{ij} + \nu_T [\bar{U}_{i,j} + \bar{U}_{j,i}] \; ; \; \nu_T = C_\mu f_\mu \frac{K^2}{\varepsilon} \qquad (4)$$

Far from wall boundaries, this closure appears correct with $C_\mu = .09$; $f_\mu = 1$. However, close to the wall, the eddy viscosity level tends to be strongly overpredicted ; the aim of f_μ is to correct this effect. Possible choices for f_μ have been discussed in [5] and the most recent contributions [6][7][8][9] try to follow the asymptotic behavior : $\overline{u'v'} \sim y^3$ when y, the normal distance to the wall, vanishes. However, it appears hopeless to use direct simulation data to improve further the f_μ shape. Fig.1 plots :

$$f_\mu = -\frac{\varepsilon^{+2}\, \overline{u'v'}^{+}}{C_\mu K^{+2} \frac{\partial U^+}{\partial y^+}} \text{ (with } C_\mu = .09) \text{ with respect to } y^+$$

for Spalart's data at R_θ = 300, 670, 1410 and Kim et Al data at R_H = 3250, 7890 and demonstrates the lack of universality of f_μ.

2. THE MIXING LENGTH MODEL

The mixing length model considers a fluid particle A with velocity $\bar{U}_A$ which moves transversally to point B (AB = l) where

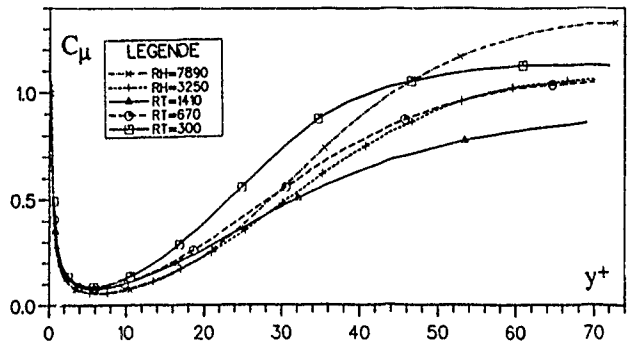

Fig.1. Lack of universality of C_μ for several values of R_H, the channel Reynolds number and R_θ, the flat plate Reynolds number.

the velocity is U_B. Then :

$$- \overline{u'v'} \sim (U_B - U_A)\upsilon \qquad (5)$$

where υ is the characteristic velocity fluctuation in the direction normal to the wall : $[\overline{v'^2}]^{1/2}$. A Taylor series gives :

$$U_B - U_A \sim l \frac{\partial U}{\partial y} + l^2 \frac{\partial^2 U}{\partial y^2} + \quad + \; l \frac{\partial u'}{\partial y} + l^2 \frac{\partial^2 u'}{\partial y^2} \qquad (6)$$

The first series of terms accounts for the influence of the mean velocity, the second series accounts for the influence of the fluctuation. Substituting (6) into (5) and truncating gives :

$$- \overline{u'v'} \sim \upsilon \, l \frac{\partial U}{\partial y} \text{ where } \upsilon = [\overline{v'^2}]^{1/2} \qquad (7)$$

Direct simulation data (fig.2) indicate that :

$$\sqrt{\frac{\overline{v'^2}}{K}} = .63 \, f_V \qquad \text{where } f_V = 1 - \exp(-\frac{y^+}{A^+}) \qquad (8)$$

f_V is nothing else than the so-called Van Driest damping function, with $A^+ = 26.5$. The correct closure assumption needs therefore to specify the length scale l through :

$$l = \frac{- \overline{u'v'}}{\sqrt{v'^2} \; \frac{\partial U}{\partial y}} \qquad (9)$$

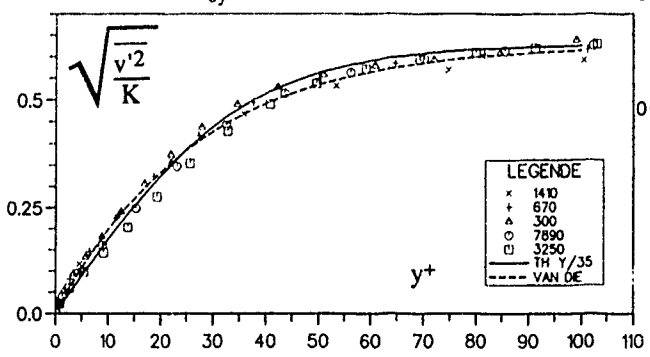

Fig.2. Utility of Van Driest dam g function (- - - -) for the representation of $[\overline{v'^2}/K]^{1/2}$ vs. y^+. ——, $\tanh(y^+/35)$.

It has been demonstrated that the model $C_\mu K^{3/2}/\varepsilon$ fits direct simulation data in the outer region, while the damping function approach $l = C_\mu f_\mu K^{3/2}/\varepsilon$ is not adequate in the inner region where a rather universal behavior of the length scale is found (fig.1). For this reason, an algebraic model is preferred. We have used :

$$l_1 = \kappa y \, f_V + C_1 [1 - \exp(-\frac{y^+}{A_1^+})] \; ; \; C_1 = 1 \; ; \; A_1^+ = 9 \; ; \; \kappa = .41 \qquad (10)$$

While A^+, in f_V, depends both on the pressure gradient and on the blowing rate (see e.g. [10]), the term involving the factor C_1 is needed to correct the slight underestimation of direct simulation data and to account for the asymptotic behavior $l \approx y$ due to $\upsilon \approx y^2$ when $y \to 0$. Fig.3 demonstrates the improvement with respect to the case $C_1 = 0$ in the zone $y^+ \leq 25$. Equation (10) implies : (i) that the mixing length hypothesis is valid close to the wall. (ii) also l does not scale with $K^{3/2}/\varepsilon$ and involves the Van Driest factor f_V. In order to explain this result, we may consider :

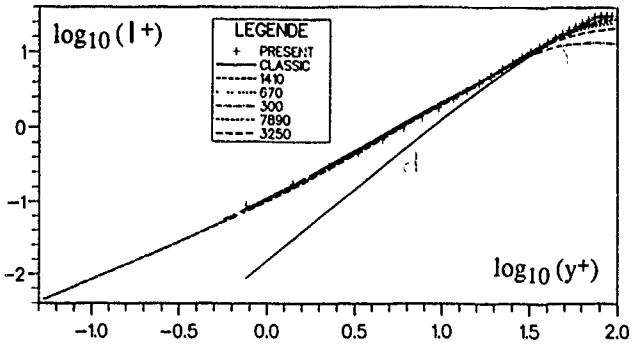

Fig.3. Inner length scale (10). —— cl, case $C_1 = 0$. +, present model. Other curves are direct simulation data with R_T or R_θ indicated.

$$l_u = C_u \frac{[\overline{u'^2}]^{3/2}}{\varepsilon_{11}} \; ; \; l_v = C_v \frac{[\overline{v'^2}]^{3/2}}{\varepsilon_{22}} \; ; \; l_w = C_w \frac{[\overline{w'^2}]^{3/2}}{\varepsilon_{33}} \qquad (11)$$

with $C_u = .065$; $C_v = .19$; $C_w = .11$ which are compared with l. Close to the wall, the best agreement with direct simulation data is provided by l_v without algebraic correction (fig .4), confirming that $\sqrt{K}$ is not the correct characteristic velocity. This is because several types of eddies exist, each of them having their own characteristic velocity and length scales in given directions. We thus introduce the characteristic velocity and length vectors :

$$\mathbf{u} = \sum_{i=1}^{3} u_i \, e_i \; ; \; \mathbf{l} = \sum_{i=1}^{3} l_i \, e_i \qquad (12)$$

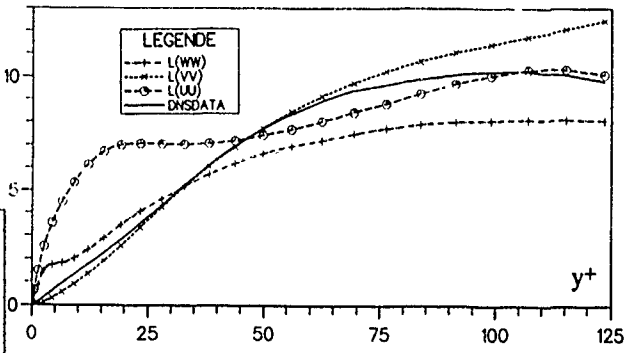

Fig.4. Comparison of length scales l_u, l_v, l_w with direct simulation data at $R_\theta = 3250$.

The eddy-viscosity model becomes :

$$- \overline{u_i'u_j'} = u_l \, l_k \, U_{j,k} + u_j \, l_k \, U_{i,k} \qquad (13)$$

Close to the wall, the characteristic velocity is $[\overline{v'^2}]^{1/2} e_2$, and the characteristic length scale is $\frac{[\overline{v'^2}]^{3/2}}{\varepsilon_{22}} e_2$. Using the following estimations : $[\overline{v'^2}]^{1/2} \sim f_V \sqrt{K}$; $\overline{v'^2}/K \sim K/\varepsilon$, we find :

$$- \overline{u'v'} = C_\mu f_V^2 \frac{K^2}{\varepsilon} \frac{\partial U}{\partial y} \qquad (14)$$

which is similar to [8] which differs from (14) by a sublayer correction factor $[1+4.1\nu\varepsilon^{3/4}/K^{3/2}]$. The classical isotropic model is a particular case of (13) where no eddy dominates :

$$u_l = \sqrt{K} \, e_l \; ; \; l_l = C_\mu \frac{K^2}{\varepsilon} e_l \qquad (15)$$

Therefore :

$$- \overline{u'v'} = (u_1)_1 (l_1)_k \frac{\partial V}{\partial x_k} + (u_2)_2 (l_2)_k \frac{\partial U}{\partial x_k} = C_\mu \frac{K^2}{\varepsilon} [\frac{\partial V}{\partial x} + \frac{\partial U}{\partial y}] \qquad (16)$$

3. MODELLING THE TURBULENT KINETIC ENERGY

When a two equation model is used only two terms need closure assumptions in the K equation, namely the turbulent transport $T_{(K)}$ and the pressure velocity correlation $\Pi_{(K)}$. A first gradient hypothesis forces the turbulent transport to vanish where the kinetic energy peaks, in contrast with direct simulation data. For first type flows, we have used the following closure assumption :

$$T_{(K)} = \frac{\partial}{\partial y}\{\frac{\nu_T}{\sigma_K}[\frac{\partial K}{\partial y} + C_{K1}\sqrt{K}\,l\,\frac{\partial^2\sqrt{K}}{\partial y^2}]\} \qquad (17)$$

Fig.5 demonstrates the improved results obtained with the model (17).

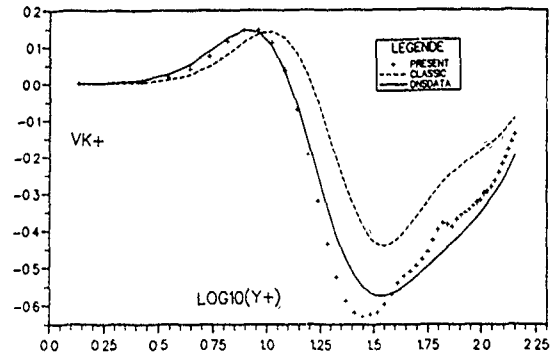

Figure 5. Turbulence transport model. _____ direct simulation data (channel flow; R_H= 3250); ++++ present model (17) with σ_K= .56; C_{K1} = 2.8; ----- classical model .

4. MODELLING THE DISSIPATION

The standard model equation is :

$$\frac{D\tilde{\varepsilon}}{Dt} = f_1 C_{\varepsilon 1}\frac{\tilde{\varepsilon}}{K}P_{(K)} - f_2 C_{\varepsilon 2}\frac{\tilde{\varepsilon}^2}{K} + \frac{\partial}{\partial x_i}[(\nu + \frac{\nu_T}{\sigma_\varepsilon})\frac{\partial\tilde{\varepsilon}}{\partial x_i}] \qquad (18)$$

It has already been shown [4] that f_1 and f_2 account improperly for wall effects. ε behaves in a different way in the viscous sublayer, in the buffer layer and in the outer layer. Therefore, a description of both regions with a single equation appears difficult. Direct simulation data [2] indicate that ε decreases away from the wall to a constant value at a location where K peaks. Further away, ε decreases in a way that is correctly described by classical models. However such models fail to predict the decay of ε away from the wall, even with recent proposals [6][7].

Other authors have demonstrated the interest of working with $\tilde{\varepsilon}$, a regularized ε which behaves like y^2 when $y \to 0$. For instance [11],

$$\tilde{\varepsilon} = \varepsilon - 2\nu[\frac{\partial\sqrt{K}}{\partial y}]^2$$

An asymptotic analysis when $y \to 0$ indicates that $P_{(K)} \sim y^3$; $T_{(K)} \sim y^3$; $\Pi_{(K)} \sim y$; $\tilde{\varepsilon} \sim y^2$ while $\nu K_{,ii} - 2\nu[\frac{\partial\sqrt{K}}{\partial y}]^2 \sim y$. Therefore, it is considered [12] that the pressure velocity correlation, which balances the sum of the two viscous contributions, needs to be modelled. However, the model [12] does not seem satisfactory for the following reasons. (i) Direct simulation data for $\Pi_{(K)}$ lead to dispersed results for all possible choices for the characteristic velocity - U_τ; $U_\tau^* = [\nu\frac{\partial\sqrt{K}}{\partial y}]^{1/2}$ -. (ii) $\nu K_{,ii}$ and $2\nu[\frac{\partial\sqrt{K}}{\partial y}]^2$ are both of order 1 and the accuracy of the discretization must be truly second order accurate in order to do not hide the behavior $\Pi_{(K)} \sim y$. This may be computationally difficult in complex cases. We therefore prefer to model simultaneously :

$$\varepsilon_{(w)} \equiv 2\nu[\frac{\partial\sqrt{K}}{\partial y}]^2 - \Pi_{(K)} \qquad (19)$$

The retained closure is :

$$\varepsilon_{(w)} = \frac{2\nu K}{y^2}f_\varepsilon\,;\; f_\varepsilon = \exp[-\frac{y^{*+}}{6} - \frac{y^{*+2}}{20}]\,;\; y^{*+} = \frac{yU_\tau^*}{\nu} \qquad (20)$$

The term $\varepsilon_{(w)}$ is significant only close to the wall and it decreases very quickly outside the viscous sublayer because of the correction f_ε which may depend on the pressure gradient, on ν and on the characteristic frequencies of the velocity fluctuations. The values of the constants are optimised with direct simulation data (fig.6).

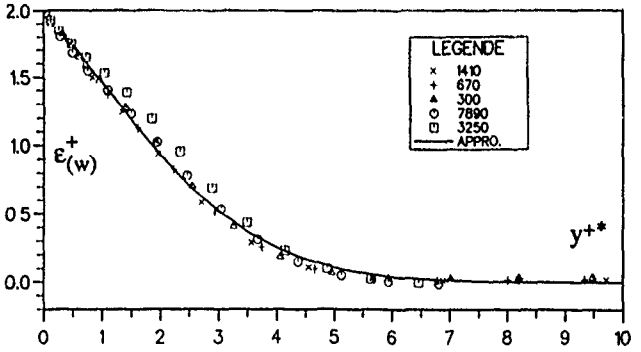

Fig.6. Closure (19)(20) for the dissipation $\varepsilon^*_{(w)}$ in the inner region ($\varepsilon_{(w)}$ is non dimensionalized with the length and velocity scales ν/U_τ^* and U_τ^*). ×, +, Δ, O, □, direct simulation data.

We now examine the model for $\tilde{\varepsilon}$. We consider the following Taylor scales (21):

$$\lambda = \sqrt{\frac{\nu K}{\tilde{\varepsilon}}}\,;\; \lambda_u = \sqrt{\frac{\nu\overline{u'^2}}{\varepsilon_{11}}}\,;\; \lambda_v = \sqrt{\frac{\nu\overline{v'^2}}{\varepsilon_{22}}}\,;\; \lambda_w = \sqrt{\frac{\nu\overline{w'^2}}{\varepsilon_{33}}}$$

λ depends on the Reynolds number (fig.7a) and is roughly constant in the viscous sublayer. λ_v has a very particular behavior while λ_u and λ_w share the same variation for $y^+ > 1$ (fig.7b).

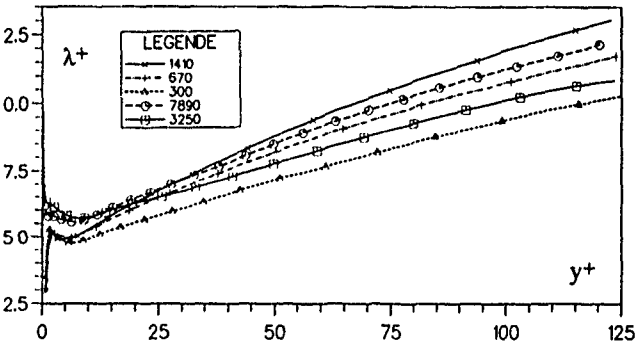

Fig.7a. Taylor Scale λ^+ with $\lambda = [\nu K/\varepsilon]^{1/2}$ non dimensionalized by ν/U_τ and U_τ, as a function of y^+, for several direct simulation data.

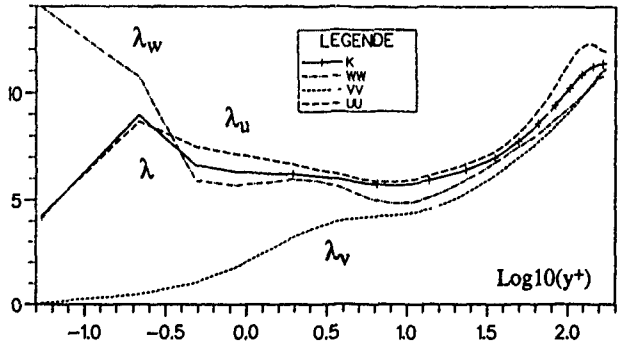

Fig.7b. Taylor scales λ, λ_u, λ_v, λ_w , non dimensionalized by ν/U_τ and U_τ, as a function of y^+.——, λ. – . – . – , λ_w. ....., λ_v. – – – –, λ_u.

The dissipation generation term $P^2_{(\varepsilon)} \equiv -2\nu\, \overline{u'_{i,k}u'_{i,m}}\, S_{km}$ is, like the mixed production $P^1_{(\varepsilon)} \equiv -2\nu\, \overline{u'_{i,j}u'_{k,j}}\, S_{ik}$, of the order $c\eta\,[\frac{u}{\lambda}]^2\frac{u}{l}$, where c and η are the Kolmogoroff velocity and length scales, λ is the Taylor length scale, u and l are the energetic velocity and length scales. For this reason, they are classically modelled together.

$$P^1_{(\varepsilon)} + P^2_{(\varepsilon)} = C_{\varepsilon 1}\frac{\tilde{\varepsilon}}{K}P_{(K)} \qquad (22)$$

This assumption is correct for $P^2_{(\varepsilon)}$, as indicated by fig.8 where direct simulation data have been digitalized from fig.15 of [2].

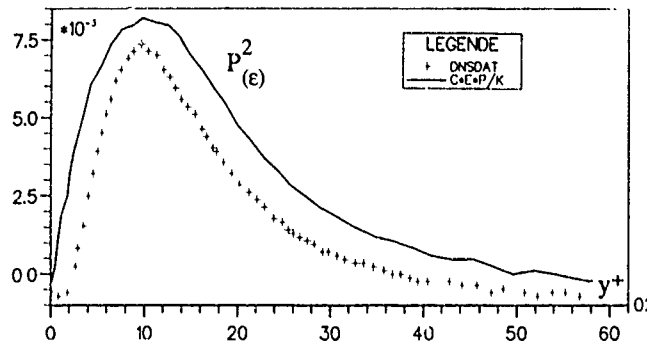

Fig.8. ——, $P^2_{(\varepsilon)}$ model (24). ++++, direct simulation data.

While $P^3_{(\varepsilon)}$ is usually neglected, $P^4_{(\varepsilon)} \equiv -2\nu\, \overline{u'_{i,k}u'_{i,m}u'_{k,m}}$ is usually predominant since it outweighs the destruction of dissipation $Y_{(\varepsilon)}$ [2][13]. Such terms are usually modelled together as $-C_{\varepsilon 4}\frac{\varepsilon^2}{K}$. However, direct simulation data indicate that, although ε^2/K is the correct scale for destruction of dissipation, the decay of ε^2/K with y does not fit with that of $P^4_{(\varepsilon)}$, nor with that of $P^4_{(\varepsilon)} - Y_\varepsilon$. This is because : $\frac{\varepsilon^2}{K} \approx [c\eta\frac{u^2}{\lambda^2}]^2\frac{1}{u^2} \approx \frac{c^2\eta^2u^2}{\lambda^4}$;

$$Y_\varepsilon \approx [c\eta]^2\,[\frac{u^2}{\lambda^2}]^2 \approx \frac{c^2\eta^2u^2}{\lambda^4}\ ;\ P^4_{(\varepsilon)} \approx c\eta\,[\frac{u}{\lambda}]^3 \qquad (23a, b, c)$$

$P^4_{(\varepsilon)}$ and Y_ε should therefore be modelled separately. While

$$Y_\varepsilon = C_{\varepsilon 2}\frac{\varepsilon^2}{K} \qquad (24)$$

the estimation of $P^4_{(\varepsilon)}$ by :

$$P^4_{(\varepsilon)} = C_{\varepsilon 4}\frac{\varepsilon^{3/2}}{\sqrt{\nu}} \approx \frac{1}{\sqrt{c\eta}}[c\eta\frac{u^2}{\lambda^2}]^{3/2} \equiv \frac{c\eta u^3}{\lambda^3} \qquad (25)$$

is in agreement (fig.9) with the order of magnitude (23c).

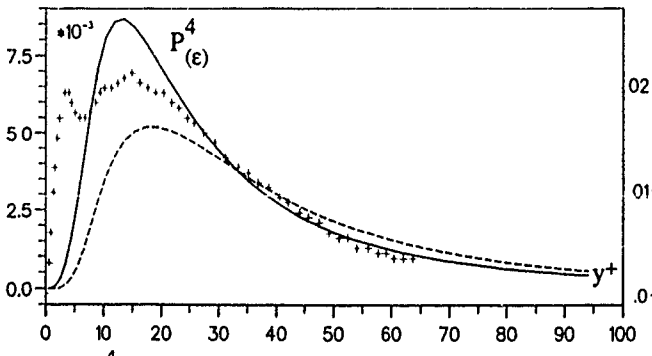

Fig.9. $P^4_{(\varepsilon)}$ model ++++, direct simulation data. ——, .24 $\varepsilon^{3/2}/\sqrt{\nu}$. - - - - -, $\varepsilon^{3/2}\overline{u'v'}$/ K.

Since turbulent and viscous transport are lower, they can be treated in the usual way by a first gradient hypothesis. The final model is :

$$\frac{D\varepsilon}{Dt} = C_{\varepsilon 1}\frac{\varepsilon}{K}P_{(K)} + C_{\varepsilon 4}\frac{\varepsilon^{3/2}}{\sqrt{\nu}} - C_{\varepsilon 2}\frac{\varepsilon^2}{K} + \frac{\partial}{\partial y}[(\nu+\frac{\nu_T}{\sigma_\varepsilon})\frac{\partial \varepsilon}{\partial y}] \qquad (26)$$

In (26) the first term models $P^1_{(\varepsilon)}+P^2_{(\varepsilon)}$. For $y^+ > 20$, in the log law zone, transport and convection may be neglected [2], thus

$$C_{\varepsilon 1}\frac{\varepsilon}{K}P_{(K)} + C_{\varepsilon 4}\frac{\varepsilon^{3/2}}{\sqrt{\nu}} - C_{\varepsilon 2}\frac{\varepsilon^2}{K} = 0 \qquad (27)$$

Coefficients are optimized so as to minimize the l.h.s. of (27). While $C_{\varepsilon 1} = 1$ and $C_{\varepsilon 4} = .24$, $C_{\varepsilon 2}$ depends slightly on the Reynolds number, as indicated in the following table :

	Channel R_H=3,250	Channel R_H=7,890	Flat plate R_θ=300	Flat plate R_θ=670	Flat plate R_θ=1410
$C_{\varepsilon 1}$	1.0	1.0	1.0	1.0	1.0
$C_{\varepsilon 2}$	.24	.24	.24	.24	.24
$C_{\varepsilon 4}$	3.9	4.5	3.9	4.5	4.8

Figs.10 show the correct balance between generation and destruction terms.

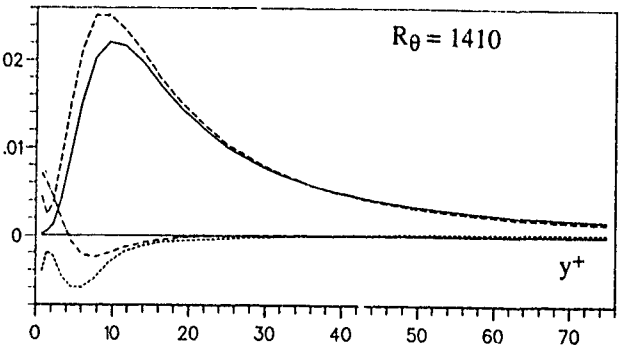

Fig.10. Balance between destruction and generation terms. – . – . , D(ε). - - - - - , P - $Y_{(\varepsilon)}$.— — —,$Y_{(\varepsilon)}$. ——, $P^1_{(\varepsilon)}+P^2_{(\varepsilon)}+P^4_{(\varepsilon)}$

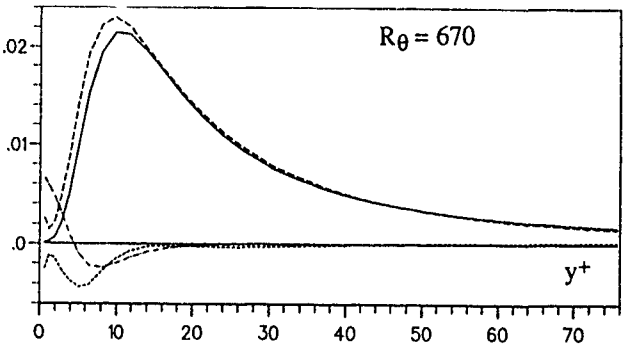

Fig.10. Balance between destruction and generation terms. – . – . , D(ε). - - - - - , P - $Y_{(\varepsilon)}$.— — —,$Y_{(\varepsilon)}$. ——, $P^1_{(\varepsilon)}+P^2_{(\varepsilon)}+P^4_{(\varepsilon)}$

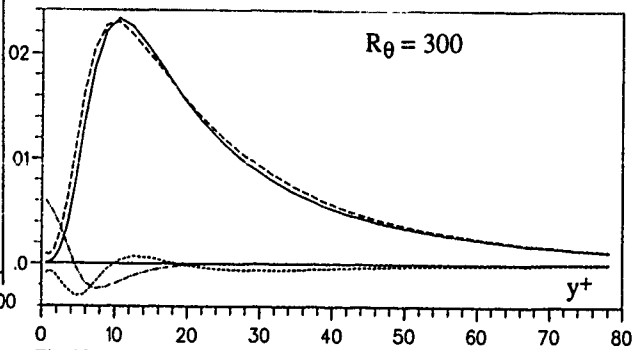

Fig.10. Balance between destruction and generation terms. – . – . , D(ε). - - - - - , P - $Y_{(\varepsilon)}$.— — —,$Y_{(\varepsilon)}$. ——, $P^1_{(\varepsilon)}+P^2_{(\varepsilon)}+P^4_{(\varepsilon)}$

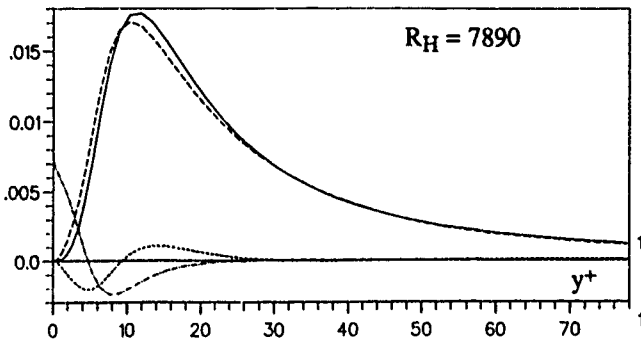

Fig.10. Balance between destruction and generation terms. – . – . , $D(\varepsilon)$. - - - - - , $P - Y_{(\varepsilon)}$.— — —, $Y_{(\varepsilon)}$. ———, $P^1_{(\varepsilon)}+P^2_{(\varepsilon)}+P^4_{(\varepsilon)}$

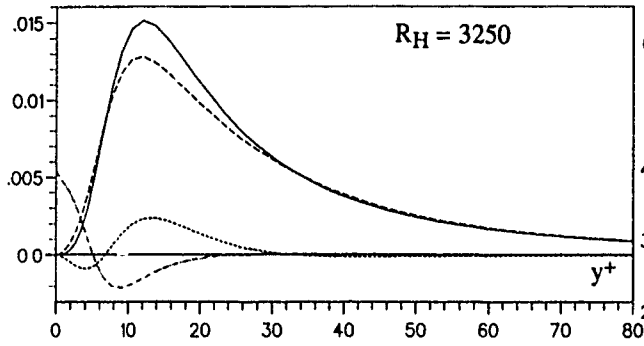

Fig.10. Balance between destruction and generation terms. – . – . , $D(\varepsilon)$. - - - - - , $P - Y_{(\varepsilon)}$.— — —, $Y_{(\varepsilon)}$. ———, $P^1_{(\varepsilon)}+P^2_{(\varepsilon)}+P^4_{(\varepsilon)}$

4. SYNTHESIS

To summarize the equations to be solved in the case of a first type flow, the model is the following :

$$\frac{D\bar{U}}{Dt} = -\frac{\partial P}{\partial x} + \frac{\partial}{\partial y}[(\nu+\nu_T)\frac{\partial \bar{U}}{\partial y}]$$

$$\frac{DK}{Dt} = P_{(K)} + \frac{\partial}{\partial y}[(\nu+\frac{\nu_T}{\sigma_K})\frac{\partial K}{\partial y}] + \frac{\partial}{\partial y}[\frac{\nu_T}{\sigma_K} C_{K1} \sqrt{K}\, l \frac{\partial^2 \sqrt{K}}{\partial y^2}] - \frac{2\nu K}{y^2} f_\varepsilon - \tilde{\varepsilon}$$

$$\frac{D\tilde{\varepsilon}}{Dt} = C_{\varepsilon 1}\frac{\tilde{\varepsilon}}{K} P_{(K)} + C_{\varepsilon 4}\frac{\tilde{\varepsilon}^{3/2}}{\sqrt{\nu}} - C_{\varepsilon 2}\frac{\tilde{\varepsilon}^2}{K} + \frac{\partial}{\partial y}[(\nu+\frac{\nu_T}{\sigma_\varepsilon})\frac{\partial \tilde{\varepsilon}}{\partial y}]$$

where $\nu_T = f_V \sqrt{K}\, l$; $f_V = 1 - \exp(-\frac{y^+}{A^+})$; $A^+ = 26.5$ for $\frac{dP}{dx} \approx 0$

$l = \min(l_i, l_o)$ where $l_i = C_V \{\kappa y f_V + C_l [1 - \exp(-\frac{y^+}{A^+_l})]\}$;

$l_o = C_\mu \frac{K^{3/2}}{\varepsilon}$; $\kappa = .41$; $C_l = 1$; $A^+_l = 9$; $C_\mu = .09$; $C_V = .63$;

$P_{(K)} = \nu_T \left(\frac{\partial U}{\partial y}\right)^2$; $\sigma_K = .56$; $C_{K1} = 2.8$; $f_\varepsilon = \exp(-\frac{y^{*+}}{6} - \frac{y^{*+2}}{20})$;

$y^{*+} = \frac{y U^*_\tau}{\nu}$; $C_{\varepsilon 1} = 1.$; $C_{\varepsilon 4} = .24$; $C_{\varepsilon 2} = 4.5$.

Instead of solving the $\tilde{\varepsilon}$ equation down to the wall with the boundary condition $\tilde{\varepsilon} = 0$, the following boundary condition is used about $y^+ = 20$:

$$\lambda\,|_{y^+=20} = \sqrt{\frac{\nu K}{\varepsilon}} = 5.5$$

MODEL VALIDATION

Results obtained with the present model are presented in figs.11 where a comparison is performed with the Myong & Kasagi model. In the model [6], it appears that the weighting functions are determined in such a way that the mean velocity is correct. K and ε are however not well predicted. In contrast the present model predicts correctly the mean velocity as well as the shear stress and the turbulent kinetic energy.

It is now necessary to apply the model to more complex conditions, and especially to cases where there is a pressure gradient. This work is presently underway.

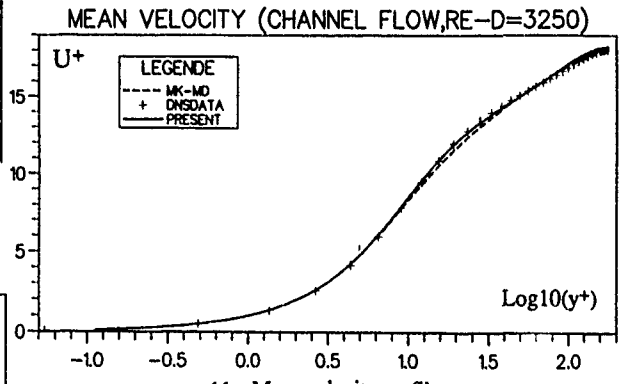

11a. Mean velocity profile

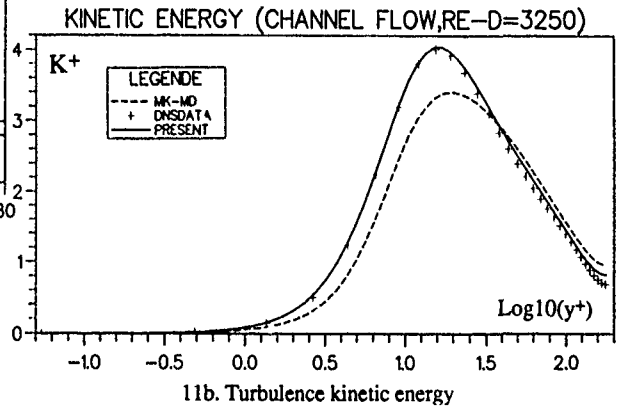

11b. Turbulence kinetic energy

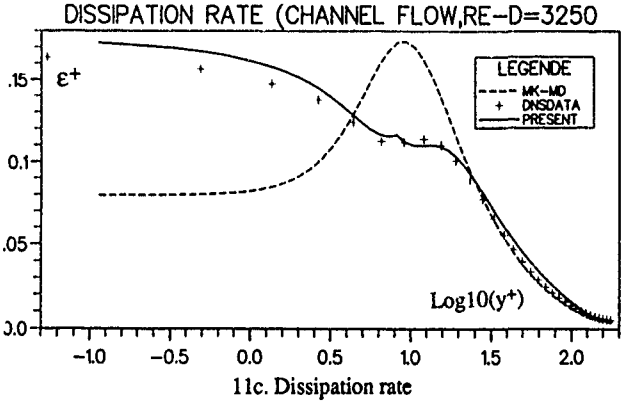

11c. Dissipation rate

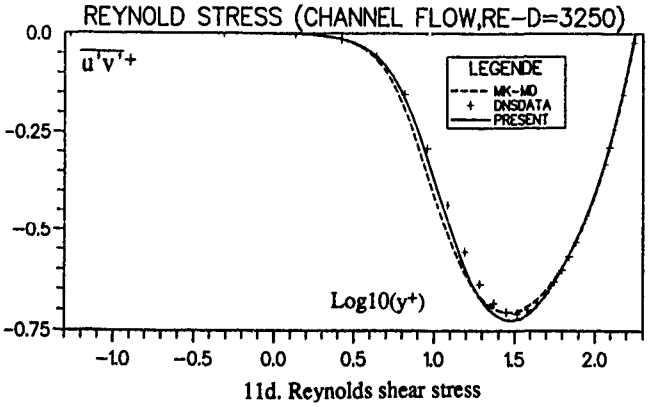

11d. Reynolds shear stress

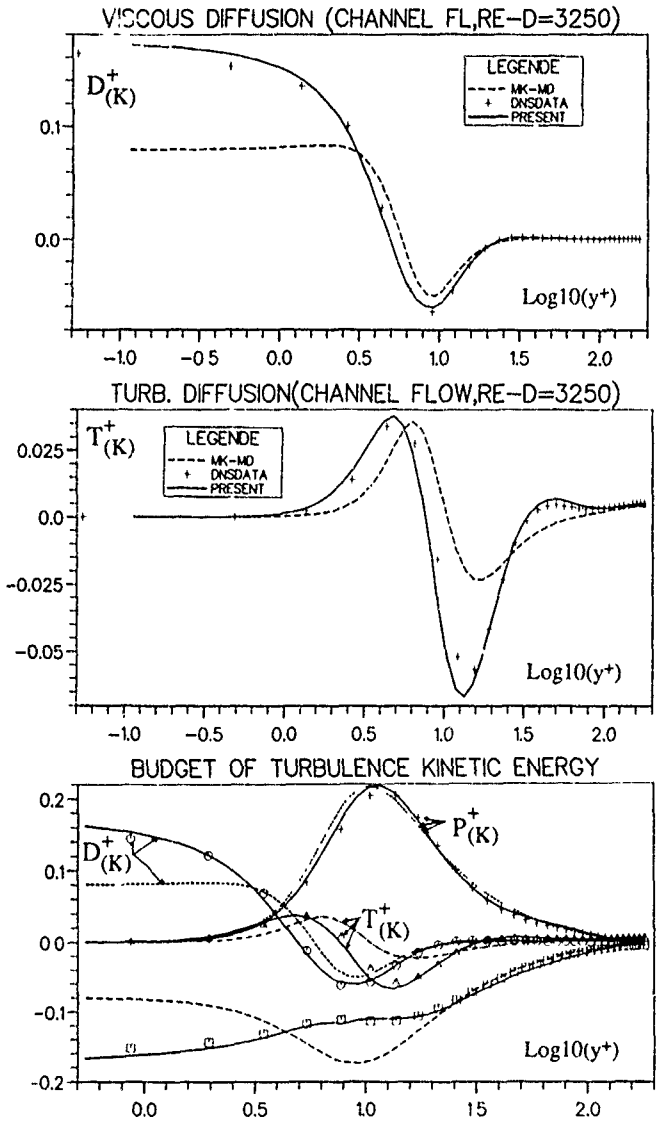

11 . Budget of turbulence kinetic energy.

Fig.11. Channel Flow simulation.+, Direct simulation R_D = 3250. ——, present model. - - - - , model [6].

CONCLUSION

The adequacy of two equation models for the description of complex flow fields has been subject to a lot of controversies in the past. A recent trend of turbulence modelling is to move towards Reynolds stress models which need a higher computational effort. Direct simulation data confirm the weakness of the classical K-ε model in the wall region. However, these data demonstrate also the validity of the mixing length hypothesis on which the K-ε model is based. The classical K-ε model is defective because of the low Reynolds number corrections and also because of the non isotropic character of the flow close to the wall. There, the knowledge of K and of ε does not suffice anymore to estimate the characteristic velocity and the mixing length.

The turbulent viscosity cannot be considered anymore as a simple scalar field. Using the Prandtl mixing length hypothesis, it has been suggested to model Reynolds stresses as the product of a characteristic velocity vector $\mathbf{v}$ and a mixing length vector $\mathbf{l}$ having the same direction which is determined by the flow structure. The modulii of $\mathbf{v}$ and $\mathbf{l}$ can be expressed either by means of K and ε with empirical functions or with algebraic functions. It is believed that a generalisation of such a model may enlarge the field of application of two equation models.

The second important aspect of the work lies in the modelling of generation and destruction of dissipation, namely by the introduction of a term $C_{\varepsilon 4}\frac{\varepsilon^{3/2}}{\sqrt{\nu}}$ in the model. This has been established through an order of magnitude analysis and with the help of direct simulation data.

The last aspect to be considered is the fact that each layer is described by means of its own characteristics rather than introducing weighting functions which do not retain any physical justification. In the outer zone, the flow field is modelled by a standard type K-ε model. In the inner zone, the influence of the wall is important.

Modifications of the standard model are as follows :
(i) an non isotropic model for Reynolds stresses.
(ii) Characteristic velocities are computed using a Van Driest factor which is a normalisation of $\sqrt{\frac{\overline{v'^2}}{K}}$.
(iii) The algebraic mixing length is used.
(iv) The turbulent transport closure is modified by means of a second gradient.
(v) Due to the fact that the dissipation budget is not available, it is not possible to control the complete set of contributions to the vorticity budget. In the viscous sublayer, the key point is the modelling of ε which controls the growth of K. ε has been split into two parts, one is connected to the destruction of dissipation, the other represents the answer of the viscous sublayer to outer stirring. While the former is taken proportional to K, the latter is more important and is described by a decay term. Although the turbulence viscosity modelling is not critical in the viscous sublayer, a correcting term is added in the mixing length expression to enforce the asymptotic property.

Some more work is obviously needed to adapt the wall model to cases where a pressure gradient is present. The wall model might be also usefully applied to a Reynolds stress model. Also, more complex cases are to be considered in a near future.

REFERENCES

1. KIM, J , MOIN, P. & MOSER, R. "Turbulence statistics in fully developed Channel flows at low Reynolds number", *Journ. Fluid Mech.*, **177**, 133-166 (1987)
2. MANSOUR, N.N., KIM, J. & MOIN, P. "Reynolds stress and Dissipation rate budgets in a turbulent channel flow", *Journ. Fluid Mech* , 194, 15-44 (1988)
3. SPALART, P.R. (1988) "Direct Simulation of Turbulent Boundary Layer up to R_θ = 1410", *Journ. Fluid Mech.*, **187**, 61-98 (1988)
4. PATEL, V.C., RODI, W. & SCHEURER, G. "Turbulence Models for Near wall and Low Reynolds Number Flows : A review", *AIAA Journ.*, **23**, 1308-1319 (1985)
5. CHEN, H.C. & PATEL, V.C. "Practical Near wall turbulence models for complex flows including separation", *AIAA Paper 87-1300.*
6. MYONG, H K. & KASAGI, N., "A new Approach to the Improvement of k-ε Turbulence model for Wall bounded Shear Flows", *JSME Int. Journ.* **33**, 63-72 (1990)
7; SPEZIALE, C.G., ABID, R. & ANDERSON, E.C. "A critical Evaluation of Two-Equation Models for Near Wall Turbulence" *AIAA Paper 90-1481*
8. NAGANO, Y. & TAGAWA, M. "An improved K-ε model for Boundary Layer Flows", *Journ Fluids Eng.* **112**, 33-39 (1990)
9. SHIH, T.H. "An improved K-ε Model for Near Wall Turbulence and comparison with Direct Numerical Simulation", *NASA TM 103221, ICOMP-90-16* (1990)
10 REYNOLDS, W.C. "Computation of Turbulent Flows", *Ann. Rev. Fluid Mech.* **8**, 183-209 (1976). Academic Press.
11. HANJALIC, K. & LAUNDER, B.E. "Contribution towards a Reynolds-stress closure for Low Reynolds number Turbulence", *Journ. Fluid Mech.*, **74**, 593-610 (1976)
12. SHIH, T.H. & MANSOUR, N.N. "Modelling of Near wall Turbulence" *NASA TM-103222, ICOMP-90-0017* (1990)
13. TENNEKES, H. & LUMLEY, J.L. "A First Course in Turbulence", Cambridge, Mass. MIT Press (1972).

EIGHTH SYMPOSIUM ON
TURBULENT SHEAR FLOWS
Technical University of Munich
September 9-11, 1991

AN IMPROVED FORM OF THE NEAR-WALL k-ε MODEL BASED ON NEW EXPERIMENTAL DATA

R. I Karlsson*,**), H. Tinoco*) and U. Svenson***)

*) Vattenfall Utveckling AB
S-810 70 ÄLVKARLEBY, Sweden

**) Department of Hydromechanics,
The Royal Institute of Technology,
S-100 44 STOCKHOLM, Sweden

***) Department of Water Resources Engineering
Luleå University of Technology
S-951 87 LULEÅ, Sweden

ABSTRACT

Experimental data from LDV measurements by Karlsson & Johansson (1988) have been used to determine the eddy-viscosity damping function f_μ. This damping function behaves physically correct and approaches one near $y^+ = 60$. By using the same data, the function f_1 is shown to be superfluous. The function f_2 multiplying the production term in the ϵ-equation is obtained by also using the data, together with a series analysis of the ϵ-equation.

The functions f_μ and f_2 have been implemented in the PROBE and PHOENICS computer codes, and the results obtained are in very good agreement with the new experimental data and direct numerical simulation results.

INTRODUCTION

Two-equation, "low Reynolds number" turbulence models generally use three damping functions (see Patel et al., 1985, Mansour et al., 1989) to represent the near-wall effects, namely f_μ for the eddy viscosity ν_t, and f_1 and f_2 for two different terms in the equation for the rate of dissipation of the kinetic energy of turbulence, ϵ. Also, extra terms may be added both to modify ϵ near the wall and to satisfy the corresponding dissipation equation. All these functions are determined in a more or less arbitrary manner, with only general asymptotic behaviour in common.

Mansour et al. (1989) have used data from turbulent channel simulation to compute the budgets for the turbulent kinetic energy, k, and its dissipation rate. Through these budgets, they have shown that different damping functions are needed in order to take into account the effect of the vicinity of the wall, and they have made estimates of the behaviour of these functions.

In the present work, experimental data from LDV measurements in the near-wall region of a turbulent boundary layer by Karlsson & Johansson (1988) and Johansson & Karlsson (1989) are used to determine the different damping functions in a manner similar to that indicated by Mansour et al. (1989). In this way, it is possible to show that the damping function f_1 is superfluous and therefore $f_1 = 1$ here. This study is then completed by a series analysis of the behaviour of ϵ^+ and f_2 as functions of y^+, for $y^+ < 10$, by means of the system for symbolic mathematical computation MAPLE (Char et al., 1988), (the superscript + indicates that the variables have been nondimensionalized with the wall variables $u_* = \sqrt{\tau_w/\rho}$, the friction velocity, and ν, the kinematic viscosity). The results of the implementation of the model in two different codes show a very good agreement with the experimental data (Karlsson & Johansson, 1988; Johansson & Karlsson, 1989) and the results obtained by direct numerical simulations, and are presented in the next to last section of this work. A discussion of the model and some conclusions are given in the last section.

THE DAMPING FUNCTIONS

The function f_μ multiplying the eddy viscosity relation is intended to model both the viscous and pressure strain effects on the shear stress (see Patel et al., 1985), and is defined by

$$f_\mu = \frac{-\overline{uv}^+ \epsilon^+}{C_\mu (k^+)^2 (dU^+/dy^+)}, \qquad (1)$$

where $-\overline{uv}^+$ is the Reynolds stress, C_μ (= 0.09) an empirically determined constant of the two-equation models and dU^+/dy^+ is the mean velocity gradient perpendicular to the wall.

The proper behaviour of this eddy-viscosity damping function near a solid wall has been studied by means of Taylor series expansions, and since $-\overline{uv}^+ \sim (y^+)^3$, $k^+ \sim (y^+)^2$ and $\epsilon^+ \to \epsilon_w^+$ (= $[\partial^2 k^+/\partial y^{+2}]_w$, and ≈ 0.2 according the to the data of Karlsson and Johansson, 1988) as $y^+ \to 0$, it follows that $f_\mu \to 1/y^+$ near the wall, as indicated by Chapman & Kuhn (1986).

Using the data of Karlsson & Johansson (1988) and Johansson & Karlsson (1989), the function f_μ has been computed for the data points by means of expression (1). Based on the aforementioned Taylor analysis, the following analytical expression to fit the experimental data has been obtained

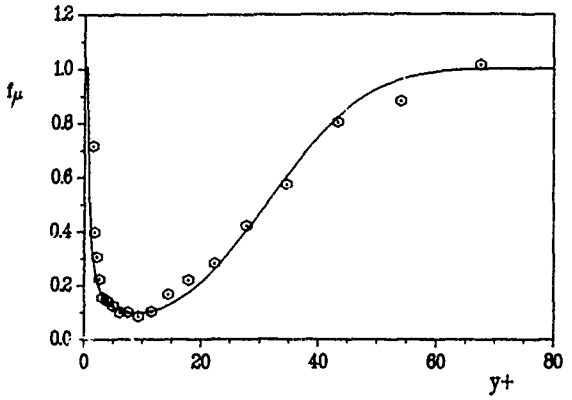

Figure 1. Damping function f_μ.
ooo Experiments, Karlsson & Johansson (1988).
——— Curve fit to present data.

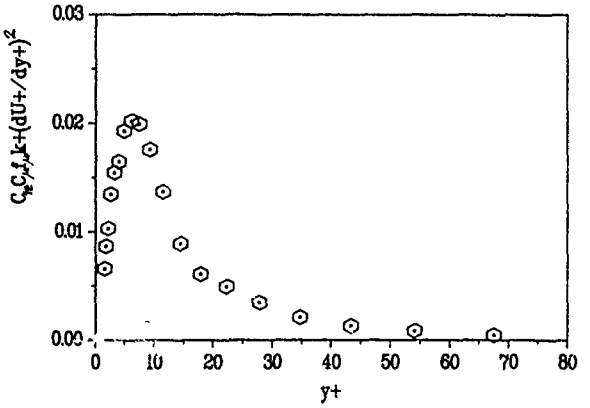

Figure 2. Dissipation production as a function of wall distance.

$$f_\mu = 1 + \frac{0.39}{y^+}\left[1 - 2.468y^+\right] e^{-m(y^+)^n}, \quad (2)$$

where $m = 3.0*10^{-5}$ and $n = 2.9$. The experimental data and the resulting curve fit, equation (2), are shown in Figure 1. As expected, the new damping function behaves physically correct and approaches unity at about $y^+ = 60$ (Patel et al 1985). In this way, one of these empirical damping functions of the model can be determined directly from experimental data

The mixed production term, P_ϵ^1, and the production by mean velocity gradient, P_ϵ^2, in the ϵ-equation (see Mansour et al., 1989) are collectively modelled by a term of the same form as that of the production of ϵ, and a damping function, f_1, is usually introduced in this term to account for near-wall effects, i e.,

$$P_\epsilon^1 + P_\epsilon^2 = f_1\left[\frac{c_{1_\epsilon}\epsilon^+\nu_t^+(dU^+/dy^+)^2}{(k^+)^2}\right]$$

$$= f_1[c_{1_\epsilon}C_\mu f_\mu k^+(dU^+/dy^+)^2], \quad (3)$$

where c_{1_ϵ} is an empirically determined constant of the model. The term multiplying f_1 in equation (3), has been computed using the experimental data of Karlsson & Johansson (1988) and Johansson & Karlsson (1989), and is shown in Figure 2. These results follow, in general, the same form as those of Mansour et al (1989) for $P_\epsilon^1 + P_\epsilon^2$, but with a higher maximum (≈ 0.02) at approximate the same value of y^+ (≈ 7), a difference which may be ascribed the higher Reynolds number of the experiment. This result strongly indicates that the damping function f_1 is not needed and therefore $f_1 = 1$ in this work.

The term for the turbulent production in the ϵ-equation, P_ϵ^4, (see Mansour et al., 1989) is usually modelled by a term proportional to $(\epsilon^+)^2/k^+$ which tends to infinity near the wall. To take into account near-wall effects, this term is modified by an additional damping function, f_2.

Besides, near the wall, this term has to balance the viscous diffusion term (see, e. g., Patel et al., 1985), and a Taylor series analysis shows that $f_2 \sim (y^+)^2$ for $y^+ \to 0$. Assuming that the near-wall effects for this term are limited to the viscous sublayer (Patel et al., 1985), f_2 may be expressed by a function of the form

$$f_2 = 1 - e^{-a(y^+)^2}, \quad (4)$$

where the constant a may be estimated by a Taylor series analysis together with the measurements of Karlsson & Johansson (1988) and Johansson & Karlsson (1989) as shown in the next section.

BEHAVIOUR OF ϵ^+ AND f_2 NEAR THE WALL

Assuming that k^+ modelled by the k-ϵ model follows the experimental data of Karlsson & Johansson (1988) and Johansson & Karlsson (1989), and using a least squares fitting of the data for $y^+ < 10$, it is possible, through the k^+-equation for a boundary layer, to obtain the behaviour of ϵ^+ as function of y^+, i. e.

$$\epsilon^+ = \frac{d}{dy^+}\left[(1 + \nu_t^+/\sigma_k)\frac{dk^+}{dy^+}\right] + \nu_t^+\left[\frac{dU^+}{dy^+}\right]^2, \quad (5)$$

where ν_t^+ is given by

$$\nu_t^+ = \frac{-\overline{uv}^+}{(dU^+/dy^+)}, \quad (6)$$

with $-\overline{uv}^+$ and (dU^+/dy^+) expressed by a least squares fitting of the data of Karlsson & Johansson (1988) and Johansson & Karlsson (1989). Using the system for symbolic mathematical computation MAPLE (Char et al., 1988), the equation (5) is solved, and the result is shown in Figure 3 together with the experimental data for ϵ^+ of Karlsson & Johansson (1988) and Johansson &

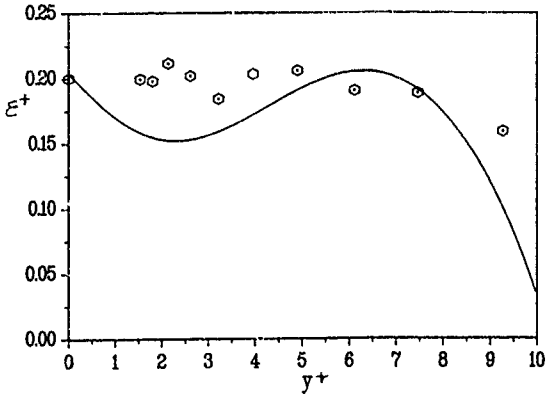

Figure 3. Dissipation rate ϵ^+.
⊙⊙⊙ Exp. Karlsson & Johansson (1988), boundary layer.
——— Series solution.

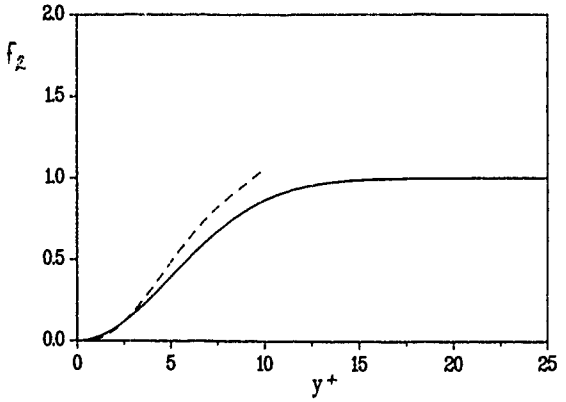

Figure 4. Damping function f_2.
– – – – – Series solution.
——— Proposed function f_2.

Karlsson (1989) According to these results, ϵ^+ has a local maximum for $y^+ \approx 7$ and a local minimum at $y^+ \approx 3$, giving a dependence of ϵ^+ as a function of y^+ with a form which is similar to that for ϵ obtained by direct numerical simulation of channel flow (see Mansour et al., 1989). As compared with the direct numerical simulation results, the present results show, in general, a higher level for ϵ^+ as well as larger difference between the local maximum and minimun which are located somewhat closer to the wall. A difference such as the higher ϵ^+ level, which agrees well with the new experimental data, may be explained by the low Reynolds number at which the direct numerical simulation results have been obtained On the other hand, the experimental data do not clearly show the local minimum and maximum of the series analysis, and this may be due to the relatively large experimental uncertainty in ϵ since it has been obtained by difference, with the pressure-velocity term taken from the direct numerical simulations by Spalart (1988).

In a similar manner, and using the ϵ^+-equation for a boundary layer, it is possible to investigate the behaviour of the damping function f_2 given by

$$f_2 = \frac{k^+}{c_{\epsilon 2}(\epsilon^+)^2} \frac{d}{dy^+}\left[(1 + \nu_t^+/\sigma_\epsilon) \frac{d\epsilon^+}{dy^+} \right] + \frac{c_{\epsilon 1}}{c_{\epsilon 2}} \frac{\nu_t^+}{\epsilon^+} \left[\frac{dU^+}{dy^+} \right]^2, \qquad (7)$$

where ϵ^+ corresponds to the expression obtained in the preceeding analysis through equation (5). The result obtained by MAPLE is shown in Figure 4 together with expression (4) for f_2, with a = 0.020, which is the value giving best agreement with experiments for k^+, ϵ^+ and U^+. It is possible to observe that the results of the series analysis show a steeper increse for y^+ greater that approximately 3, and that it increases beyond 1 for $y^+ > 9$. This later behaviour is probably due to the poor accuracy of the series ananlysis near the higher end of its interval of validity. The steeper increase for $y^+ > 3$ shown by the series analysis, on the other hand, indicates that additional terms higher than quadratic in y^+ are needed for the exponential function in equation (4). But the accuracy of the series analysis is not enough to completely decide this issue, and, therefore, the simpler form given by equation (4) has been kept in the present work

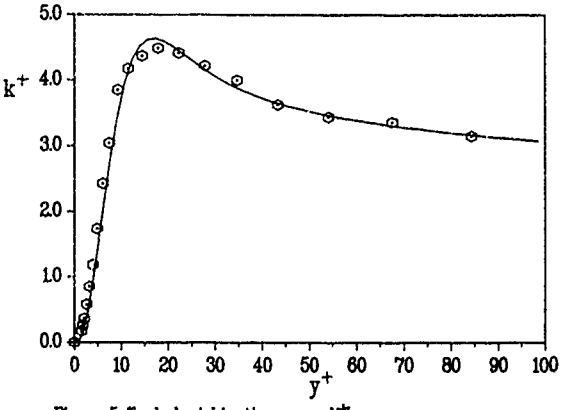

Figure 5. Turbulent kinetic energy k^+.
⊙⊙⊙ Experiment, Karlsson & Johansson (1988).
——— Computed curve.

NUMERICAL RESULTS

The new damping functions, f_μ and f_2, given by equations (2) and (4) respectively, have been implemented both in the PROBE (Svensson 1986) and PHOENICS (Ludwig et al., 1989) computer codes, and results for turbulent channel flow have been obtained. For simulating the channel flow with Re = 23 200 investigated by Hussain & Reynolds (1975), a total of 300 computational cells have been used in the transversal direction (channel half-wide) The results obtained with both programs are similar, but the PHOENICS code has higher accuracy and, therefore, only the results obtained with this program will be shown here.

The predicted values of turbulent kinetic energy, dissipation and velocity profile shown in Figures 5, 6 and 7, respectively, are in good agreement with the new experimental data, the experiments of Hussain & Reynolds (1975) and the results obtained by direct numerical simulations. The difference between the measured velocity profile and the corresponding predicted by this

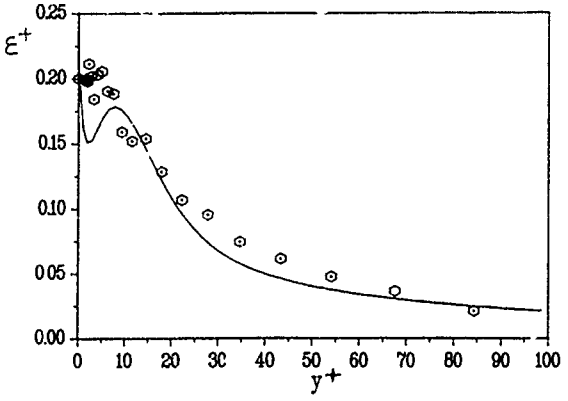

Figure 6. Dissipation rate.
⊙⊙⊙ Exp. Karlsson & Johansson (1988), (boundary layer).
——— Computed curve.

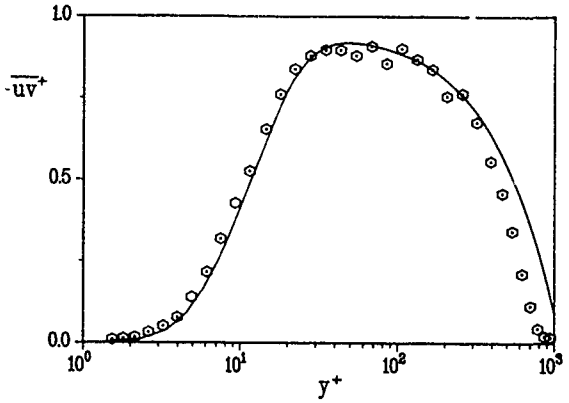

Figure 8. Turbulent shear stress $-\overline{uv}^+$.
⊙⊙⊙ Experiments, Karlsson & Johansson (1988).
——— Computed curve ($=\frac{1}{2}\cdot dU^+/dy^+$)

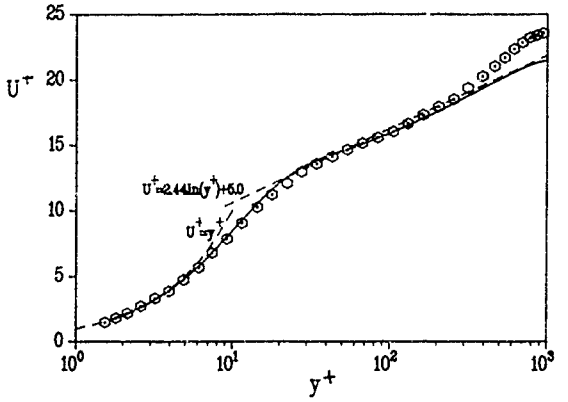

Figure 7. Mean velocity profile.
⊙⊙⊙ Exp. Karlsson & Johansson (1988),(boundary layer).
——— Computed curve.

model near the center of the channel is due to a known weekness of the standard high Reynolds number k-ε model (see e. g. Nagano & Tagawa, 1990) As was pointed out before, the differences between the measured data and the predictions of the model for ε are mainly due to experimental uncertainty and estimation of terms in the energy budget which cannot be directly measured The friction velocity computed from the model is slightly higher than the measured value of Hussain & Reynolds (1975) Figure 8 shows the predicted value of the turbulent shear stress together with the experimental data of Karlsson and Johansson (1988)

DISCUSSION AND CONCLUSIONS

The method described in the preceeding sections utilizes new experimental data together with a series analysis for studying the damping functions and the equations and variables involved and, therefore, eliminates the arbitrariness in determining f_μ and f_2 as well as the need for modifying ε near the wall. It also indicates that only one damping function is needed for the ε-equation.

A series analysis of the equation for k^+ gives the form of the functional dependence between ϵ^+ and y^+, if k^+ corresponds to a least squares fit of the experimental data of Karlsson & Johansson (1988) and Johansson & Karlsson (1989). By means of this result, the form of the damping function f_2 may be determined, confirming that the near-wall effects for the term involved in the ε-equation are limited to the viscous sublayer. In the context of k-ε modelling, the ε profile obtained in this study corresponds to that giving the correct k and U profiles in the boundary layer, as the series analysis shows

It is perhaps of some interest to point out that some functions other than that given by expression (4) have been tested to fit f_2. Some of the functions are as steep as the series solution for $y^+ > 3$ and go beyond 1 before they decrease to unity at $y^+ \approx 20$. The results obtained for k^+, ϵ^+ and U^+ are no better than those obtained with f_2 approximated by expression (4).

The standard high Reynolds number k-ε model predicts a balance between turbulent diffusion of k and dissipation ε in the region near the center of the channel. As a consequence, values of k larger than the experimental values are predicted and the velocity profile is lower than the experimental one Nagano & Tagawa (1990) have solved this problem by increasing the value of the model constant σ_k from 1.0 to 1.4, and, with that, by decreasing the turbulent diffusion of k towards the center of the channel. Several flows indicate, nevertheless, that other transport mechanisms for k, opposed to that of turbulent diffusion, may be present, these mechanisms being not diffusive in their character Therefore, it may be incorrect to model their effects only as a decrease in the turbulent diffusion of k In the present work, no modification of the standard model constants has been done.

REFERENCES

CHAPMAN, D. R. & KUHN, G. D. 1986 The limiting behaviour of turbulence near a wall. J. Fluid Mech. 170, 265-292.

CHAR, B. W., GEDDES, K. O., GONNET, G. H., MONOGAN, M. B. & WATT, S. M. 1988 MAPLE Reference Manual, University of Waterloo, Ontario.

HUSSAIN, A. K. M. F. & REYNOLDS, W. C. 1975 Measurements in fully developed turbulent channel flow. J.Fluids Eng. 568-580.

JOHANSSON, T. G. & KARLSSON, R I. 1989. The energy budget in the near-wall region of a turbulent boundary layer. In **Applications of Laser Anemometry to Fluid Mechanics**, Eds. R.J. Adrian, T. Asanuma, D.F.G. Durao, F. Durst, J H. Whitelaw. Springer-Verlag, Berlin Heidelberg, 3-22.

KARLSSON, R. I. & JOHANSSON, T. G. 1988 LDV Measurements of higher order moments of velocity fluctuations in a turbulent boundary layer In **Laser Anemometry in Fluid Mechanics III**, Eds. R J. Adrian et al. Ladoan - Instituto Superior Tecnico, 1096 Lisbon Codex, Portugal, 273-289.

LUDWIG, J. C , QIN, H Q. & SPALDING, D. B. 1989 rHOENICS-85 Reference Manual, CHAM TR/200, London

MANSOUR, N N., KIM, J. & MOIN, P. 1989 Near-wall k-ε turbulence modeling AIAA Journal 27, 1068-1073.

NAGANO, Y & TAGAWA, M 1990 An improved k-ε model for boundary layer flow J. Fluids Eng. 112, 33-39

PATEL, V. C., RODI, W. & SCHEUERER, G. 1985 Turbulence models for near-wall and low Reynolds number flows. a review. AIAA Journal 23, 1308-1319

SPALART, P. R 1988 Direct simulation of a turbulent boundary layer up to R_θ = 1410 J Fluid Mech 187, 61-98

S 'ENSSON, U. 1986 PROBE - An instruction manual, Rep Oceanography No 10, SMHI, Norrkoping, Sweden.

EIGHTH SYMPOSIUM ON
TURBULENT SHEAR FLOWS
Technical University of Munich
September 9-11, 1991

A $k-\varepsilon-\overline{v^2}$ MODEL WITH SPECIAL RELEVANCE TO THE NEAR WALL TURBULENCE

H. Kawamura

Science University of Tokyo

2641 Yamazaki, Noda-shi, Chiba-ken, 278 JAPAN

ABSTRACT

The near-wall balance of turbulence energy equation has been reexamined and a new $k-\varepsilon-\overline{v^2}$ three equation model is proposed. A model of the pressure diffusion term is introduced; thus exact wall-asymptotic forms are retained in all the terms included. The model is applied to the fully developed channel flow and the results are compared with the existing DNS data. It turns out that the proposed model is able to reproduce the profiles of turbulent energy and the dissipation. Especially, the negative gradient of the dissipation indicated by the DNS is found to be well reproduced by inclusion of the pressure diffusion close to the wall.

NOMENCLATURE

A	"Flattness factor", $A=[1-(9/8)(A_2-A_3)]$
A_2, A_3	Invariants of a_{ij}; $A_2=a_{ij}a_{ji}$; $A_3=a_{ij}a_{jk}a_{ki}$
a_{ij}	Anisotropic tensor $=(\overline{u_iu_j}/k-(2/3)\delta_{ij})$
D	Diffusion term
k	Turbulent energy
P	Production term
Re^*	Reynolds number $=u^*\delta/\nu$
Rt	Turbulent Reynolds number $=k^2/(\nu\varepsilon)$
U_i	Averaged velocity in x_i
U	Averaged velocity in x direction
u_i	Fluctuation velocity in x_i
u,v,w	Fluctuation velocity in x,y,z, respectively.
u^*	Friction velocity
x_i	Coordinate in direction i; if spedified, i=1 is along the mean flow, i=2 normal to a wall
x,y,z	Coordinate in direction of x_1, x_2, x_3, respectivly x is along the mean flow; y normal to a wall
δ	Channel half width
ε	Dissipation
$\hat{\varepsilon}$	Near-wall dissipation Eq (14)
$\tilde{\varepsilon}$	$=\varepsilon-\hat{\varepsilon}$
ν	Kinematic viscosity of fluid
π	Velocity pressure-gradient term (VPG)
π_k	Pressure diffusion term in k-equation
Ψ	Pressure diffusion term
Φ, ϕ	Pressure-strain term
$^+$	Near-wall quantity

INTRODUCTION

The development of the direct numerical simulations (DNS) has revealed many interesting features relevant to the turbulence modeling. One is the appearance of a peak value of the dissipation ε at the wall (see Kim, Moin & Moser (1987), hereafter KMM). The gradient of ε was shown to be "negative" in the immediate vicinity of the wall. According to common experimental results, on the other hand, the peak of ε appeared away from the wall. Almost all of the existing turbulence models also predicted the same trend. At present, however, the negative gradient of ε is widely accepted. The aim of the present work is to propose a "low Reynolds number" version of turbulence model capable of reproducing the negative gradient of the near wall dissipation profile.

An additional attempt in this work is to couple a low Reynolds number type of the two-equation model with an equation of $\overline{v^2}$, the turbulent energy component normal to a wall. Although a two-equation model applicable up to a wall is often referred as "the low Reynolds number model", this terminology is somewhat customary. It has already been recognized that the attenuation function f_μ incorporated in such type of two-equation models are not only due to the low Reynolds number effect but also due to the damping of $\overline{v^2}$ close to the wall; indeed the latter effect is even the dominant one [Launder (1986), hereafter L86 and Kawamura(1986)].

The Taylor series expansion shows that the streamwise and spanwise turbulence components $\overline{u^2}$ and $\overline{w^2}$ vary as y^2 and thus k also as y^2, while the normal one $\overline{v^2}$ increases proportional to y^4. [L86 or Mansour, Kim & Moin (1988), hereafter MKM]. This is the main reason why a very large empirical attenuation is necessitated in the accommodation function f_μ of the $k-\varepsilon$ model. So, the normal component $\overline{v^2}$ must be determined separately from k, for the empirical function f_μ to be eliminated.

To calculate $\overline{v^2}$ up to the wall, a Reynolds stress model applicable to the wall itself is required. This kind of new Reynolds stress equation is currently being developed by Launder and Tselepidakis (1990) (hereafter referred as LT). The rationale there is to retain an exact wall limiting form of each modeled terms as possible. In the present study, their equation for $\overline{v^2}$ is adopted and coupled with the $k-\varepsilon$ model with some necessary modifications.

After completion of the major part of this work, the present author became aware of some related works published recently; i. e., works by Durbin(1990), by Shih & Mansour (1990) and by Lai & So (1990). In Durbin's work the negative gradient of the near wall dissipation was reproduced and in the latter two a new term was introduced into the turbulence energy equation; but all were made in different ways from the present work. So, some discussions are given on those works in the Appendix A.

GOVERNING EQUATIONS

A fully developed turbulent flow between two parallel plates are assumed.

Turbulent energy equation

With an assumption of the fully developed flow, the turbulent energy equation is usually written as

$$D_k + P_k - \varepsilon = 0 \tag{1}$$

These can be modeled as [see e.g. L86]:

$$D_k = \frac{\partial}{\partial y}\left[\left(\nu + C_s \overline{v^2}\frac{k}{\varepsilon}\right)\frac{\partial k}{\partial y}\right] \tag{2}$$

$$P_k = -\overline{uv}\,(\partial U/\partial y) \tag{3}$$

If the near-wall k is expressed in terms of y as

$$k = b_k y^2 + c_k y^3 + \tag{4}$$

then the diffusion term becomes

$$D_k = 2\nu b_k + 6\nu c_k y + \cdots \tag{5}$$

The production term P_k is an order of y^3 and thus negligible The dissipation ε is expanded from its definition as [L86, MKM]

$$\varepsilon = 2\nu b_k + 4\nu c_k y + d_\varepsilon y^2 + \cdots \tag{6}$$

Hence, D_k and ε are balanced in their leading terms $2\nu b_k$, but there remains an imbalance of $2\nu c_k y$ in the order of y. This imbalance is compensated by the velocity pressure-gradient term, which will be abbreviated as VPG hereafter.The definition of the VPG for the i,j component of the Reynolds stress is

$$\pi_{ij} = -\left(\overline{u_i \frac{\partial p}{\partial x_j}} + \overline{u_j \frac{\partial p}{\partial x_i}}\right) \tag{7}$$

In the Reynolds stress equation, this term is usually decomposed into the pressure diffusion Ψ_{ij} and the pressure-strain correlation Φ_{ij}

$$\pi_{ij} = -\left(\frac{\partial}{\partial x_j}\overline{p u_i} + \frac{\partial}{\partial x_i}\overline{p u_j}\right) \qquad \Psi_{ij}$$

$$+ \overline{p\left(\frac{\partial u_i}{\partial x_j} + \frac{\partial u_j}{\partial x_i}\right)} \qquad \Phi_{ij} \tag{8}$$

In the turbulence energy equation, the VPG term appears in the form of

$$\pi_k = \frac{1}{2}\pi_{ii} = -\overline{u_i \frac{\partial p}{\partial x_i}} = -\frac{\partial}{\partial x_i}\overline{p u_i} \tag{9}$$

The last equality holds because the last term in Eq.(8) tends to zero in the turbulent energy equation (i=j) Thus, π_k in the turbulent energy equation can be interpreted purely as the pressure diffusion term As the wall is approached, π_k tends to [MKM]

$$\pi_k \to -2\nu c_k y \qquad (y \to 0) \tag{10}$$

This is the term which compensates the aforementioned imbalance between D_k and ε.

The pressure diffusion is usually neglected or regarded to be contained in the turbulent diffusion term. As long as the near-wall gradient of ε is concerned, however, not only the leading term but also the second order one have to be balanced, since the gradient of ε is proportional to $c_k y$. The approach here is to model only the near-wall pressure diffusion separately and to still regard the far-wall pressure diffusion as contained in the turbulent diffusion term.

Several possibilities exist to represent the form of Eq. (10). After many attempts, an expression, a modification of the model proposed by Yoshizawa (1982), is adopted. This is because it can be reduced from a contraction of each normal components and also because it is diffusive in nature.

Yoshizawa's original proposal for the model of the pressure diffusion of k is

$$\pi_k \sim C_{P'}\frac{\partial}{\partial y}\left(\frac{k^2}{\varepsilon}\frac{\partial k}{\partial y}\right) - C_{P''}\frac{\partial}{\partial y}\left(\frac{k^3}{\varepsilon^2}\frac{\partial \varepsilon}{\partial y}\right) \tag{11}$$

The first term is regarded to be included in the turbulent diffusion; only the last one is retained. It is extended to include the molecular diffusivity as

$$\pi_k \sim -C_{P'''}\frac{\partial}{\partial y}\left[\left(\nu + C_{P'''}\frac{k^2}{\varepsilon}\right)\frac{k}{\varepsilon}\frac{\partial \varepsilon}{\partial y}\right] \tag{12}$$

Finally, a model proposed here for the near-wall pressure diffusion term is

$$\pi_k^* = -0.5\,\nu\frac{\partial}{\partial y}\left(\frac{k}{\varepsilon}\frac{\partial \hat{\varepsilon}}{\partial y}\right) \tag{13}$$

where only the molecular diffusion is retained and ε is replaced by $\hat{\varepsilon}$:

$$\hat{\varepsilon} = 2\nu\,(\partial\sqrt{k}/\partial y)^2 \tag{14}$$

which approximates ε in the vicinity of a wall up to the order of y

In spite of the original proposal to use ε, it turned out that with use of ε the gradient $\partial\varepsilon/\partial y$ tended to zero and thus c_k to 0, which also equates the k-equation up to the order of y Thus, ε has to be replaced by $\hat{\varepsilon}$ in Eq.(13). The numerical coefficient of 0.5 in Eq (13) is a direct consequence of the Taylor series expansion for $y \to 0$. The asterisk * denotes that the term is relevant only to the wall vicinity A tensorial expression for each i,j components is given in Appendix B

With use of the modeled form of Eq (13), the new turbulence energy equation becomes

$$D_k + P_k - \varepsilon + \pi_k^* = 0 \tag{15}$$

which can be balanced up to the order of y. Since c_k is expected to be negative, the contribution of π_k^* is positive in the vicinity of the wall (see Eq.(10)).

Dissipation equation

The dissipation equation is written as

$$D\varepsilon + C_{\varepsilon 1}(\varepsilon/k)P_k - C_{\varepsilon 2}\varepsilon\,\tilde{\varepsilon}/k + E + \pi_\varepsilon^* = 0 \tag{16}$$

where $D\varepsilon$ is the diffusion

$$D\varepsilon = \frac{\partial}{\partial y}\left[\left(\nu + C_\varepsilon \overline{v^2}\frac{k}{\varepsilon}\right)\frac{\partial \varepsilon}{\partial y}\right] \tag{17}$$

with C_ε =0 22 The penultimate term E is a common ingredient of the low-Reynolds-number ε-equation and effective only in the sublayer.

$$E = 2C_{\varepsilon 3}\nu\overline{v^2}(k/\varepsilon)\,(\partial^2 U/\partial y^2)^2 \tag{18}$$

where $C_{\varepsilon 3}$=0 15. The $\tilde{\varepsilon}$ in Eq. (16) is a kind of dissipation defined as $\tilde{\varepsilon} = \varepsilon - \hat{\varepsilon}$, which coincides with ε away from the wall while it varies as y^2 in the vicinity of the wall. Thus the ratio $\tilde{\varepsilon}/k$ stays constant as the wall is approached.

As a counterpart of π_k^*, a new term π_ε^* is introduced into the ε equation. A corresponding form to Eq.(13) would be

$$\pi_\varepsilon^* = -C_{\varepsilon 4}\,\nu\frac{\partial}{\partial y}\left(\frac{\tilde{\varepsilon}}{k}\frac{\partial k}{\partial y}\right) \tag{19}$$

This form is the same as the one already proposed by Launder (1986) by estimating each term appearing in the exact transport equation of ε.

Using the constancy of $\tilde{\varepsilon}/k$ and $\nu \partial^2 k / \partial y^2 = \hat{\varepsilon}$ near the wall, the above expression can be approximated by

$$\pi_\varepsilon^* = - C_{\varepsilon 4} \tilde{\varepsilon} \hat{\varepsilon} / k \qquad (20)$$

The necessity of this term can be verified by the following discussion, too. If $\tilde{\varepsilon}$ is expanded for small y, it becomes

$$\tilde{\varepsilon} = d\varepsilon' y^2 + \cdots\cdots \qquad (21)$$

As the wall is approached, the second and the forth terms of Eq.(16) tend to zero, while the first and the second terms become

$$D\varepsilon \rightarrow 2\nu\, d\varepsilon \text{ and } C_{\varepsilon 2} \tilde{\varepsilon} \varepsilon / k \rightarrow 2\nu C_{\varepsilon 2}\, d\varepsilon' \qquad (22)$$

respectively. Since the value of $C_{\varepsilon 2}$ is specified usually to be 1.92 from the decay of isotropic turbulence, the above two terms never happens to cancel each other; thus a new term like Eqs.(19) or (20) must be introduced into the near-wall dissipation equation. When a form of Eq. (20) is adopted, the relation

$$C_{\varepsilon 4} = [D\varepsilon / (\tilde{\varepsilon}/k) - C_{\varepsilon 2}\, \varepsilon] / \hat{\varepsilon} \qquad (23)$$

holds. If all the variables are nondimensionalized with ν and u_τ, examination of the DNS data [KMM] indicates that $D\varepsilon \sim 0.02$, $\tilde{\varepsilon}/k \sim 0.025$, and $\varepsilon = \hat{\varepsilon} \sim 0.16$ at the wall; thus $C_{\varepsilon 4}$ is about 3 at y=0. However, it decreases rapidly with increase of y. The expression assumed here for $C_{\varepsilon 4}$ is thus $C_{\varepsilon 4} = 3\exp(-10\sqrt{A})$.

The coefficient $C_{\varepsilon 2}$ used recently by Launder and his coworkers [LT] is

$$C_{\varepsilon 2} = 1.92 / [1 + 0.9 (A_2 A)^{1/2}] \qquad (24)$$

The another coefficient $C_{\varepsilon 1}$ is usually assumed to be constant. Kebede and Launder (1985) indicated that $C_{\varepsilon 1}$ has a limiting value of 2 as the wall is approached. Thus $C_{\varepsilon 1}$ is assumed here as

$$C_{\varepsilon 1} = 0.8 [1 + 1.5 \exp(-4.5 A^{1/2})] \qquad (25)$$

The rather small value of 0.8 is assigned above because otherwise the calculated local maximum of ε near the wall is too large compared with the DNS data.

$\overline{v^2}$ Equation

The $\overline{v^2}$ equation adopted here is a slight modification of the Reynolds stress equation by LT. It can be expressed for $\overline{v^2}$ as

$$D_{22} + P_{22} + \Phi_{22} - \varepsilon_{22} + \pi_{22}^* = 0 \qquad (26)$$

As for the diffusion term D_{22}, a common gradient type diffusion is assumed

$$D_{22} = \frac{\partial}{\partial y} \left[\left(\nu + C_s \overline{v^2} \frac{k}{\varepsilon} \right) \frac{\partial \overline{v^2}}{\partial y} \right] \qquad (27)$$

with Cs=0.22. The product on P_{22} is zero for the fully developed channel flow.

The pressure-strain correlation Φ_{22} is decomposed into two parts as usual.

$$\Phi_{22} = \phi_{22,1} + \phi_{22,2} \qquad (28)$$

The return term $\phi_{22,1}$ is expressed [see LT] using the anisotropy tensor and a wall dumping function f_ℓ :

$$\phi_{22,1} = -C_1 a_{22} \varepsilon (1 - f_\ell) \qquad (29)$$

with $C_1 = 5.0 A (A_2)^{1/2}$.

The rapid term $\phi_{22,2}$ is a modification of the common I.P. model.

$$\phi_{22,2} = -C_2 [P_{22} - (2/3) P_k] [1 - 2Cw\, f_w(y)] \qquad (30)$$

The empirical coefficient C_2 is here assumed to be a function of the invariant A; i.e., $C_2 = 0.6 [1 - \exp(-2.5A)]$, so that C_2 tends to zero as the wall is approached. According to LT, the empirical attenuation functions are assumed as $f_\ell(Rt) = \max(1 - Rt/180, 0)$ and $f_w(y) = k (\overline{v^2})^{1/2} / (0.8 \varepsilon y)$ with $Cw = 0.25$.

The dissipation ε_{22} is the bridged form between the isotropic dissipation $(2/3)\varepsilon$ and the near-wall limit of ε_{22}^*.

$$\varepsilon_{22} = (1 - f_\varepsilon)(2/3)\varepsilon + f_\varepsilon\, \varepsilon_{22}^* \qquad (31)$$

According to LT, the near-wall dissipation ε_{22}^* can be expressed as

$$\varepsilon_{22}^* = 4(\overline{v^2}/k)\varepsilon / [1 + 1.5(\overline{v^2}/k)] \qquad (32)$$

The bridging function f_ε is assumed to be $\exp(-20A^2)$.

Since $\overline{v^2} \propto y^4$ for $y \rightarrow 0$, the diffusion term D_{22} approaches to $12\nu y^2$. The dissipation Eq.(32), however, becomes only $8\nu y^2$ and thus does not totally compensates the diffusion. The deference is contributed again by the VPG. Thus the near wall VPG term π_{22}^* is introduced in the $\overline{v^2}$ equation, and modeled as.

$$\pi_{22}^* = -2(\overline{v^2}/k)\hat{\varepsilon} \qquad (33)$$

which tends to $4\nu y^2$ for $y \rightarrow 0$ as expected. Without this contribution, the limiting behaviour of $\overline{v^2} \propto y^4$ cannot be reproduced.

Although the VPG in the turbulence energy equation is purely the pressure diffusion, the one in the $\overline{v^2}$ equation consists of both the pressure diffusion Ψ_{22} and the pressure strain Φ_{22}. It is known that the contribution of the pressure-strain term of $\overline{v^2}$ in the vicinity of the wall is "splatting" the energy to the other stress components. The energy to be "splatted" is fed by the pressure diffusion effect Φ_{22}. This is the the energy which contributes the pressure diffusion π_k^* in k equation. The situation is depicted schematically in Fig. 1.

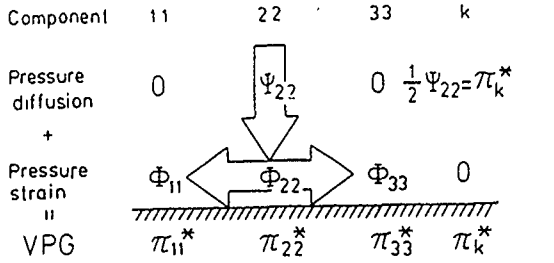

Fig. 1 Velocity pressure-gradient correlation (VPG) in the vicinity of a wall.

Since Ψ_{22} and Φ_{22} are nearly balanced, it is no need to model these two terms separately. The equation (33) represents the combined contribution of these two processes. Hence, the pressure-strain correlation expressed by Eqs. (28)-(30) should be effective exclusive of the immediate vicinity of the wall, where their contribution is already included in Eq. (33). Indeed, Eqs. (29) and (30) increase more gradually than Eq. (33) with increase of y. On the other hand, the pressure diffusion away from the wall is still assumed to be included in the turbulent diffusion term.

Reynolds stress representation

As for the Reynolds stress equation, an algebraic approach is attempted. In a local equilibrium region, a gradient type formulation by Gibson-Launder (1978) is known to represent the Reynolds stress.

$$\overline{uv} = -C_R \frac{k}{\varepsilon} \overline{v^2} \frac{\partial U}{\partial y} \tag{34}$$

Later, Launder (1986) indicated that this formula can be extended up to the viscous sublayer if the attenuation of the normal stress $\overline{v^2}$ is well represented.
In the immediate vicinity of the wall, however, Eq (34) tends to $\overline{uv} \propto y^6$, while the expected variation is $\overline{uv} \propto y^3$. In the derivation of Eq. (34), the production term is assumed to be balanced with the rest of the terms. At the wall vicinity, however, the production is negligible, while the contribution of the molecular diffusion is dominant there.

The balance of $\overline{uv}$ close to the wall is thus

$$\nu \frac{\partial^2}{\partial y^2} \overline{uv} - \varepsilon_{12}^* + \pi_{12}^* = 0 \tag{35}$$

where the VPG π_{12}^* is again required to ensure the correct variation of $\overline{uv} \propto y^3$. The Taylor series expansion indicates [MKM]

$$\varepsilon_{12}^* = 2\overline{uv}(\varepsilon/k) \quad \text{and} \quad \pi_{12}^* = -(1/2)\varepsilon_{12}^* \tag{36}$$

To obtain an algebraic expression, the diffusion term have to be modeled somehow. By considering that the diffusion term tends to $6\nu \overline{uv}/y^2$ and by introducing a correlation coefficient of $C_{Rw} = -\overline{uv}/\sqrt{k}\sqrt{\overline{v^2}}$, the near wall Reynolds stress can be modeled as

$$\overline{uv} = -2C_{Rw}\nu \frac{\sqrt{k}\sqrt{\overline{v^2}}}{y^2} \frac{k}{\varepsilon} \tag{37}$$

This expression varies as y^3 for a small y and diminishes with increase of y. Thus it can be simply added to Eq. (34) resulting

$$\overline{uv} = -C_R \frac{k}{\varepsilon} \overline{v^2} \frac{\partial U}{\partial y} - 2C_{Rw}\nu \frac{(k)^{\frac{1}{2}}(\overline{v^2})^{\frac{1}{2}}}{y^2} \frac{k}{\varepsilon} \tag{38}$$

$$= -\left[C_R + \frac{2C_{Rw}}{y^2}\left(\frac{k}{\overline{v^2}}\right)^{\frac{1}{2}}\right] \overline{v^2} \frac{k}{\varepsilon} \frac{\partial U}{\partial y} \tag{39}$$

where a further approximation of $(\partial U/\partial y) = U^2/\nu$ is introduced The adopted values of the constants are C_R=0 22 and C_{Rw}=0.35

Anisotropic tensor

In the context of the present three equation model, one obtains k and $\overline{v^2}$, but not $\overline{U^2}$ and $\overline{w^2}$ separately. To obtain the anisotropic tensor components and invariants, the following approximation is made.

$$\overline{w^2} = (\overline{U^2} + \overline{v^2})/2 \tag{40}$$

This approximation is widely known to hold in the log-low region of the boundary layer. This assumption yields $a_{33} = 0$ and hence $a_{11} = -a_{22}$ In the viscous sublayer, the assumption of Eq. (40) is rather crude; however, the same relation is retained also in the viscous sublayer for the simplicity.

NUMERICAL CALCULATION

Above equations are discretized and solved numerically for the fully developed channel flow. The following boundary conditions are imposed. At the channel center, all the quantities are symmetric; and at the wall, all but ε is zero. The boundary condition for the dissipation is $\varepsilon = \tilde{\varepsilon}$ (y=0)

Introduction of the pressure diffusion term π_k^* causes some numerical instability. So, it has been found necessary to calculate the equations without π_k^* and π_ε^* firstly and then to introduce them gradually.

In the present dissipation equation, the constancy of $\tilde{\varepsilon}/k$ is utilized in the near wall region. However, because $\tilde{\varepsilon}$ is the difference of ε and $\hat{\varepsilon}$ and they are equal up to their second order close to the wall, it is difficult to ensure numerically the constancy of $\tilde{\varepsilon}/k$ near the wall. To overcome the difficulty, the term $-\tilde{\varepsilon}\tilde{\varepsilon}/k$ is decomposed to $-\tilde{\varepsilon}\varepsilon/k + \tilde{\varepsilon}\hat{\varepsilon}/k$; then the positive term is regarded a source term and the negative term is included in the diagonal element of the discretized Laplacian. As the wall is approached, k tends to zero and the decomposed two terms becomes dominant; thus $\varepsilon = \hat{\varepsilon}$ is ensured.

The mesh size adjacent to the wall is $\Delta y^+ \sim 0.1$ and the mesh size is increased with increase of the distance from the wall, but the maximum size was limited to 2 percent of the channel half width. The total mesh number is about 60-70 depending on the Reynolds number. The calculation can be made easily on a small personal computer.

RESULTS

The calculated budget of the turbulent energy is compared with the DNS data by KMM Figures 2 and 3

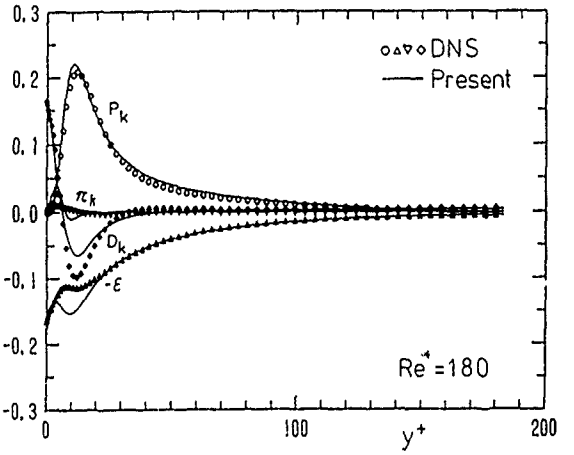

Fig. 2 Budget of turbulence energy: Comparison with DNS data by KMM.

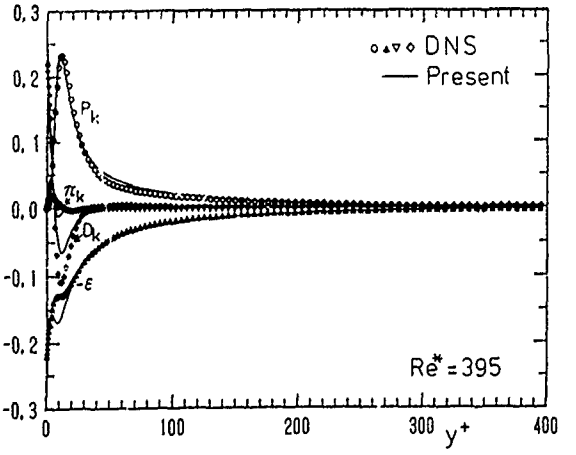

Fig. 3 Budget of turbulence energy: Comparison with DNS data by KMM.

present the budget of turbulence energy for $Re^* = 180$ and 395, respectively. Symbols are the results from DNS and the lines represents those from the present calculations. The near-wall negative gradient of ε is well reproduced by the present results. The DNS data indicate the wall value of ε increases with increase of the Reynolds number; this tendency is well represented also by the present model.

The calculated dissipation shows a local minimum and a maximum away form the wall. The DNS data have a similar tendency but it is much less prominent. This discrepancy is able to be removed by adjusting some coefficients; for example, decreasing $C_{\varepsilon 3}$ and/or $C_{\varepsilon 1}$ are effective. Such adjustment, however, deteriorates other features such as the profiles of the velocity or turbulence energy, so the present set of the coefficients is adopted. The production rate P_k is a little higher than the DNS data for $y^+ > 30$.

The calculated turbulent energy k and the normal stress $\overline{v^2}$ are shown in Fig. 4. A good agreement with the DNS data is obtained. Especially the peak value of k agrees well with the DNS data; such the high value is very hard to be obtained with the common $k-\varepsilon$ models. However, The agreement in the profile of k beyond the peak is not satisfactory.

The velocity profile is compared with the DNS data for $Re^* = 395$ in Fig. 5. The calculated velocity gradient is somewhat larger in the log-law region. These discrepancies in P_k, k profile and the velocity gradient seem to be coupled with each other.

Although there still exist several points to be improved, the present model reproduces the near-wall

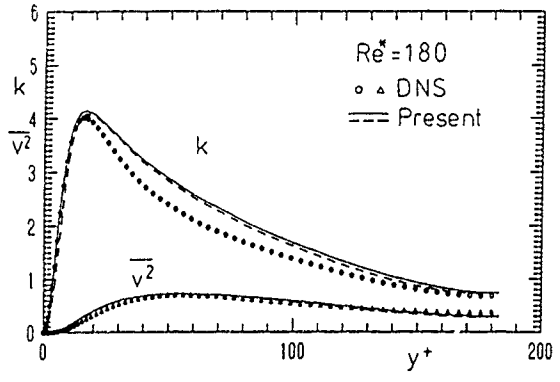

Fig. 4 Turbulence energy and $\overline{v^2}$: Comparison with DNS data by KMM.

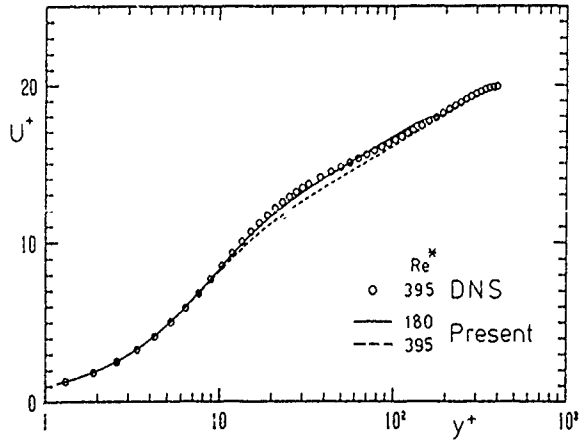

Fig. 5 Velocity profile: Comparison with DNS data.

behaviour of the variables including the negative gradient of ε. The energy budget in the wall vicinity is examined below in some more detail.

An enlarged plot of Fig. 2 is given in Fig. 6, where the sign of ε is reversed. One can notice that the difference between the diffusion and the dissipation is compensated by the pressure diffusion as expected. To examine the effect of π_{ε}^*, a calculation is made with $\pi_{\varepsilon}^* = 0$ while other models being unchanged. The wall value of ε is decreased but the difference is not prominent.

In Fig. 7, both π_k^* and π_{ε}^* are set to be zero. Then the negative gradient of ε is no longer reproduced. One can thus conclude that the introduction of the pressure diffusion term is essential for the reproduction of the negative slope of the dissipation. Physically one may interpret that the near-wall ε is increased to dissipate an additional turbulence energy fed by the pressure diffusion.

The broken line in Fig. 3 is the k and $\overline{v^2}$ profiles with $\pi_k^* = \pi_{\varepsilon}^* = 0$. The difference from the solid lines, i.e., the results with both terms, is small. Thus the inclusion of these two terms does not seem to have so large effect on the turbulence distribution away from the wall.

CONCLUDING REMARKS

Although there exist several points to be improved, it turns out that the proposed model is able to

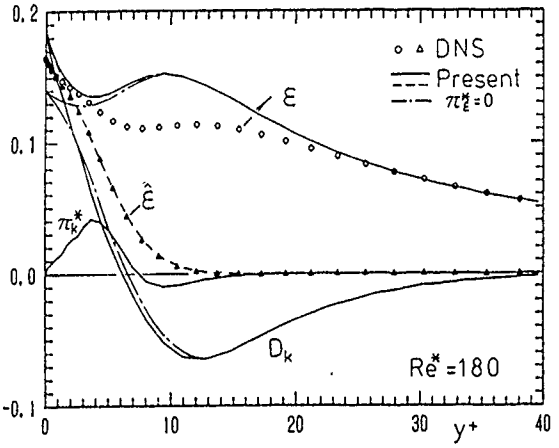

Fig. 6 Budget of turbulence energy close to the wall. —— with π_k^* and π_{ε}^* ; —•— $\pi_{\varepsilon}^* = 0$.

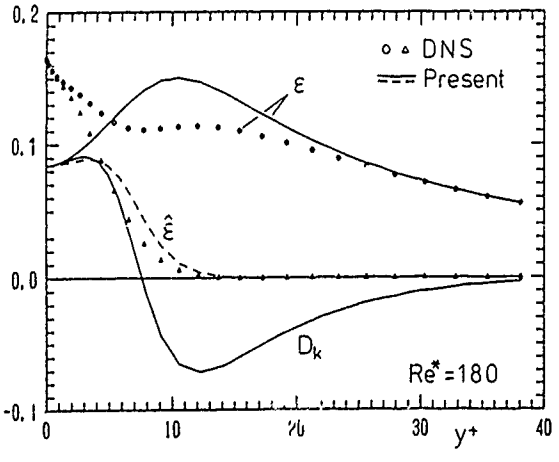

Fig. 7 Budget of turbulence energy close to the wall with $\pi_k^* = \pi_{\varepsilon}^* = 0$.

reproduce the profiles of turbulent energy and the dissipation in the fully developed channel flow without introducing the attenuation function f_μ of the $k-\varepsilon$ model. Especially, the negative gradient of the dissipation indicated by the DNS is well reproduced by inclusion of the pressure diffusion close to the wall.

ACKNOWLEDGEMENTS

The major part of this work has been done during the author's sabbatical leave at University of Manchester Institute of Science and Technology in the summer of 1990. The author appreciates the invaluable discussions and suggestions by Prof. B.E. Launder and Mr. D.P. Tselepidakis. He would thank to the British Council for the financial support and also to Mr. S.Satake for his help in the preparation of the manuscript.

REFERENCES

Durbin, P.A. 1990 Near wall turbulence closure modelling without damping functions. CTR Manuscript 112.

Gibson, M.M. & Launder, B.E. 1978 Ground effects on pressure fluctuations in the atmospheric boundary layer. J. Fluid Mech., Vol. 86, 491-511.

Kawamura, H. (1986) A review on the low Reynold number two-equation model of turbulence. Proc. of NST Symp., 63-65 (in Japanese).

Kebede, W. & Launder, B.E., 1985 Large-amplitude periodic pipe flow: A second-moment closure study. Proc. of 5th Turbulent Shear Flow Symp., 16.23-16.29.

Kim, J., P. Moin & R. Moser, 1987 Turbulence statistics in fully developed channel flow at low Reynolds number. J. Fluid Mech. 177, 133-166. Data compiled in the disket of "Collaborative testing of terbulence models" by P. Bradshow, Stanford University (1990).

Lai, Y.G. & So, R.M.C. 1990 On near-wall turbulent flow modelling. J. Fluid Mech. 221, 641-673.

Launder, B.E. 1986 Low-Reynolds-number turbulence near walls. TFD/86/4.

Launder, B.E. & D.P. Tselepidakis 1990 Contribution to the second-moment modeling of sublayer turbulent transport. Near-Wall Turbulence, 818-833, Hemisphere. Also Tselepidakis, D.P. & B.E. Launder, 1990 Second moment closure for the viscous sublayer. 4th Biennial Colloquium on Computational Fluid Dynamics. UMIST.

Mansour, N.N., J. Kim & P. Moin, 1988 Reynolds-stress and dissipation-rate budgets in a turbulent channel flow. J. Fluid Mech. 194, 15-44.

Shih, T.H. & N.N. Mansour, 1990 Modeling of near-wall turbulence. Engineering Turbulence Modelling and Experiments (ed. W. Rodi & E.N. Ganic), 13-22, Elsevier.

Yoshizawa, A. 1982 Statistical evaluation of the triple velocity correlation and the pressure-velocity correlation in shear turbulence. J. Phys. Soc. of Japan 51, 2326-2337.

Appendix A Review of recent related works

The dissipation equation can be expressed with the present notation as follows:

$$D\varepsilon + (C_{\varepsilon 1}f - C_{\varepsilon 2})\varepsilon/\tau_\varepsilon = 0 \qquad (A1)$$

where τ_ε is interrupted as the time scale of the dissipation evolution. Away from the wall, τ_ε is usually assumed to be k/ε, which however tends to zero as the wall is approached. In the vicinity of the wall, Durbin (1990) discussed that the time scale cannot be less than the Kolmogoroff time scale; thus he limited τ_ε to $C_T(\nu/\varepsilon)^{1/2}$.

With use of the Kolmogoroff time scale, Durbin (1990) showed that Eq. (A1) has a solution of $\varepsilon \sim \varepsilon_o/(1+0.09\,y^{+})^4$ in the vicinity of the wall. The solution indicates a negative gradient at the wall, although its gradient is fairly larger than the DNS data.

Shih and Mansour (1990) pointed out the importance of the pressure diffusion term in the k-equation close to a wall. They proposed a model for the pressure diffusion of k to be propotional to the turbulent diffusion, i.e., to b_k of Eq. (4).

The proposed model is proportional to y in the wall vicinity, but its coefficient does not seem to mathematically coincide with the one obtained from Taylor series expansion i.e., Eq. (10). Their results indicated a slightly negative gradient of the near wall dissipation, although it is not so prominent as that of the DNS.

Lai and So (1990) also reexamined the near wall balance of the Reynolds stress components. Their turbulent energy equation contains a new term of $-\overline{v^2}(\varepsilon/k)$, which is negative in sign and is proportional to y^2. Thus the pressure diffusion term seems not to be incorporated in their treatment.

Appendix B A tensile representation of VPG

If the velocity fluctuations are expanded in Taylor series, one obtains

$$u_1 = b_1 y + c_1 y^2 + \cdots\cdots \qquad (B1)$$

$$u_2 = c_2 y^2 + \cdots\cdots \qquad (B2)$$

$$u_3 = b_3 y + c_3 y^2 + \cdots\cdots \qquad (B3)$$

where i=2 and y denote the direction normal to the wall. With use of these coefficients, VPG and the dissipation in the vicinity of the wall can be represented as [MKM]

$$\pi^{*}_{11} = -4\nu\overline{b_1 c_1}\,y \qquad \pi^{*}_{22} = -4\nu\overline{c_2 c_2}\,y^2 \qquad (B4)$$

$$\pi^{*}_{33} = -4\nu\overline{b_3 c_3}\,y \qquad \pi^{*}_{12} = -2\nu\overline{b_1 c_2}\,y \qquad (B5)$$

and

$$\varepsilon^{*}_{11} = 2\nu\overline{b_1 b_1} + 8\nu\overline{b_1 c_1}\,y \qquad \varepsilon^{*}_{22} = 8\nu\overline{c_2 c_2}\,y^2 \qquad (B6)$$

$$\varepsilon^{*}_{33} = 2\nu\overline{b_3 b_3} + 8\nu\overline{b_3 c_3}\,y \qquad \varepsilon^{*}_{12} = 4\nu\overline{b_1 c_2}\,y \qquad (B7)$$

Noting that $k/\varepsilon \sim y^2/2\nu$ for $y \to 0$, the VPG's can be represented as follows

$$\pi^{*}_{11} = -\frac{\nu}{2}\frac{\partial}{\partial y}\left(\frac{k}{\varepsilon}\frac{\partial \varepsilon^{*}_{11}}{\partial y}\right) \qquad (B8)$$

$$\pi^{*}_{22} = -\frac{\nu}{6}\frac{\partial}{\partial y}\left(\frac{k}{\varepsilon}\frac{\partial \varepsilon^{*}_{22}}{\partial y}\right) \qquad (B9)$$

$$\pi^{*}_{33} = -\frac{\nu}{2}\frac{\partial}{\partial y}\left(\frac{k}{\varepsilon}\frac{\partial \varepsilon^{*}_{33}}{\partial y}\right) \qquad (B10)$$

$$\pi^{*}_{12} = -\frac{\nu}{2}\frac{\partial}{\partial y}\left(\frac{k}{\varepsilon}\frac{\partial \varepsilon^{*}_{12}}{\partial y}\right) \qquad (B11)$$

A general form which satisfys the above asymptotic expresseions is

$$\pi^{*}_{ij} = -\frac{\nu}{2}\left[\frac{\partial}{\partial x_m}\left(\frac{k}{\varepsilon}\frac{\partial \varepsilon^{*}_{ij}}{\partial x_m}\right) - \frac{2}{3}\frac{\partial}{\partial x_m}\left(\frac{k}{\varepsilon}\frac{\partial \varepsilon^{*}_{kl}}{\partial x_m}\right) n_k n_l n_i n_j\right] \qquad (B12)$$

where n_k denotes a unit vector normal to the wall. As described in the text, the near wall dissipation ε^{*}_{ij} has to be replaced by $\varepsilon^{*}_{ij} \simeq \hat{\varepsilon}(\varepsilon_{ij}/\varepsilon)$. An application of the above expressions to the full Reynolds stress equation has not yet been explored.

EIGHTH SYMPOSIUM ON
TURBULENT SHEAR FLOWS
Technical University of Munich
September 9-11, 1991

Experimental Balances for the Second Moments for a Buoyant Plume and Their Implication on Turbulence Modeling

Aamir Shabbir
Center for Modeling of Turbulence and Transition
ICOMP, NASA Lewis Research Center
Cleveland, OH 44135

ABSTRACT

The heat flux and Reynolds stress budgets are presented for a buoyant plume. The terms involving pressure correlations are obtained as the closing terms in these budgets. Despite certain measurement errors, these budgets provide useful information about how various phenomena contribute to the transport of second moments. These experimental results are used to assess the local equilibrium assumption and to investigate why the mechanical to thermal time scale ratio for a buoyant plume is different than the commonly recommended value. Analysis show that this departure is a consequence of the local equilibrium assumption being not satisfied in the present experiment.

NOMENCLATURE

g gravitational acceleration
p fluctuating pressure
r, z radial and vertical coordinates
T, U_i mean temperature and mean velocity component
u, v, w radial, azimuthal and vertical fluctuating velocity components
$\overline{t^2}$ mean squared temperature fluctuations
β coefficient of thermal expansion
β_i buoyancy vector, $= (0, 0, -g\beta)$
ϵ, ϵ_t dissipation rates of k and $\overline{t^2}/2$
ν kinematic viscosity
Γ thermal conductivity

INTRODUCTION

Past two decades have seen a tremendous amount of activity toward the second order closure modeling of turbulence. Many (e.g. Launder et. al. 1975, Lumley 1978) share the view that these models will become the standard tools for the calculation of engineering turbulent flows. Despite their believed importance and large quantity of work published about these models, very little experimental information is available about the budgets of the second moment equations. Part of the problem stems from our inability to measure the pressure correlations. However, if everything else appearing in these equations is known from the experiment, pressure correlations can be obtained as the closing terms. This is the closest we can come to in obtaining these terms from experiment, and despite the measurement errors which might be present in such balances, the resulting information will be extremely useful for the turbulence modelers. The purpose of the present paper is to provide such balances of the Reynolds stress and heat flux equations for the buoyant plume. The details of the experiment are given in Shabbir (1987) and Shabbir and George (1987, 1990). The accuracy of the experiment was checked by carrying out mean momentum and energy equation balances. The kinetic energy and temperature variance balances were also carried out in which the mechanical and thermal dissipation rates were obtained as the closing terms.

In this paper we will use the data reported in Shabbir (1987) to carry out the balances for the heat flux and Reynolds stress equations. We will also look at the implications of these balances on some of the ideas used in turbulence modeling, such as the assumption of local equilibrium and the ratio of the mechanical to thermal time scale.

RESULTS

Heat Flux Budgets

The transport equation for the vertical (streamwise) heat flux can be written as

$$\begin{aligned} U\frac{\partial \overline{wt}}{\partial r} + W\frac{\partial \overline{wt}}{\partial z} = &-\frac{1}{r}\frac{\partial}{\partial r}(r\overline{uwt}) - \frac{\partial}{\partial z}(\overline{wwt}) \\ &- \overline{uw}\frac{\partial T}{\partial r} - \overline{w^2}\frac{\partial T}{\partial z} - \overline{ut}\frac{\partial W}{\partial r} \\ &- \overline{wt}\frac{\partial W}{\partial z} + g\beta\overline{t^2} \\ &- \frac{1}{\rho}\overline{t\frac{\partial p}{\partial z}} - (\nu + \Gamma)\overline{t_{,j}w_{,j}} \end{aligned} \quad (1)$$

Note that the molecular term is written in local cartesian coordinates. The balance of this equation is shown in figure 1. Advection term is the smallest in this balance and, therefore, contributes least to the transport of the heat flux $\overline{wt}$. It is clear that in the central core of the flow ($r/z < 0.04$), the production of this heat flux is maintained by the

mean buoyancy gradients and the turbulent buoyancy force i.e. the source of energy is the gravitational field. The shear production is relatively small in this region. Then there is an intermediate region where the production from mean velocity and gravitational field are of the same order. However, for $r/z > 0.1$ (which approximately corresponds to the plume half width), most of the production is maintained by the mean velocity and buoyancy gradients and the turbulent buoyancy production is only a small fraction of these two. The closing term in the heat flux balances is labeled as Π, and represents the sum of the pressure correlation and the molecular destruction terms i.e.

$$\Pi_i = \frac{1}{\rho} t \overline{\frac{\partial p}{\partial x_i}} - (\nu + \Gamma) \overline{\frac{\partial u_i}{\partial x_j} \frac{\partial t}{\partial x_j}} \qquad (2)$$

The molecular term in (2) is thought to get weaker with increasing Reynolds and Peclet numbers, eventually approaching a value of zero in the limit of local (small scale) isotropy. This term was not measured and, therefore, its magnitude relative to others can not be established.* However, in turbulence modeling, it is customary to combine this term with the pressure correlation term (Lumley 1978) and, therefore, from that point of view not knowing each term separately does not reduce the usefulness of these budgets. Notice that the shape of this term is very similar to the shape of the heat flux $\overline{wt}$ and its magnitude remains large throughout the flow field.

The equation for the radial heat flux is

$$\begin{aligned} U\frac{\partial \overline{ut}}{\partial r} + W\frac{\partial \overline{ut}}{\partial z} = &-\frac{1}{r}\frac{\partial}{\partial r}(\overline{ruut}) - \frac{\partial}{\partial z}(\overline{wut}) - \overline{u^2}\frac{\partial T}{\partial r} \\ &- \overline{uw}\frac{\partial T}{\partial z} - \overline{ut}\frac{\partial U}{\partial r} - \overline{wt}\frac{\partial U}{\partial z} \\ &- \frac{1}{\rho} t \overline{\frac{\partial p}{\partial r}} - (\nu + \Gamma)\overline{t_{,j} u_{,j}} \end{aligned} \qquad (3)$$

The balance of this equation is shown in figure 2. Again, we note that the advection term is quite small as compared to the other dominant terms in the equation. Unlike the $\overline{wt}$ heat flux balance, the shear production is extremely small here. This is because the gradients of mean radial velocity are much smaller than the gradients in the mean vertical (streamwise) velocity. There is no turbulent buoyancy production in this equation and all the production is due to the mean buoyancy gradients. We note that the term representing sum of the pressure correlation and the molecular destruction makes up a substantial part of the budget and its shape is similar to the radial heat flux. We also note that this budget can not be divided into any subregions, where some phenomenon are more dominant than others, because the relative magnitude of each of the terms in equation (3) remains the same across the flow field.

Reynolds Stress Budgets

The transport equation for the Reynolds stress, within Bussinesq approximation, is

$$\begin{aligned} U_k\,(\overline{u_i u_j})_{,k} = &-[\overline{u_i u_j u_k}]_{,k} - (\overline{u_i u_k}\,U_{j,k} + \overline{u_j u_k}\,U_{i,k}) \\ &+ \beta_i \overline{u_j t} + \beta_j \overline{u_i t} + \frac{1}{\rho}(\overline{u_i p_{,j} + u_j p_{,i}}) \\ &- 2\nu \overline{u_{i,k} u_{j,k}} \end{aligned} \qquad (4)$$

where the viscous diffusion term has been neglected since it will be small as compared to the turbulent diffusion.

For reasons of convenience, turbulence modelers do not model the pressure correlation term in the form as it appears in the above equation but rewrite it in a different form by separating it into a deviatoric and a non-deviatoric part. Two ways of doing this have been suggested in the literature and we will look at both of these before deciding which one to use in the present study. The traditional way (see e.g. Launder et. al. 1975) of writing this term is

$$\begin{aligned} -\frac{1}{\rho}(\overline{u_i p_{,j} + u_j p_{,i}}) = &\frac{1}{\rho}\overline{p(u_{i,j} + u_{j,i})} - \frac{1}{\rho}(\overline{pu_i}\delta_{jk} \\ &+ \overline{pu_j}\delta_{ik})_{,k} \end{aligned} \qquad (5)$$

where the first term on the right hand side is the deviatoric part. The second term is the so called pressure diffusion term. Lumley (1975) has instead suggested the following separation

$$\begin{aligned} -(\overline{u_i p_{,j} + u_j p_{,i}}) = -\Big[&\frac{1}{\rho}(\overline{u_i p_{,j} + u_j p_{,i}}) - (\frac{2}{3\rho}) \\ &(\overline{pu_k})_{,k}\delta_{ij}\Big] - (\frac{2}{3\rho})(\overline{pu_k})_{,k}\delta_{ij} \end{aligned} \qquad (6)$$

where the term in the square brackets is the deviatoric part and the last term on the right hand side is the pressure diffusion term. Regardless of which separation is employed a correction or model has to be used for the correlation $\overline{pu_k}$. The model used here is due to Lumley (1978) and is given by $\overline{pu_k} = -\overline{q^2 u_k}/5$. This study indicates that the use of this model with (5) produces so much pressure diffusion that it negates the velocity diffusion (i.e. due to $\overline{u_i u_j u_k}$). On this basis it was concluded to use the separation given by (6) in the present study. Further details about this issue are given in the appendix.

* Temperature and velocity derivatives were not measured to check if the local isotropy existed. The spectral measurements did show a $-5/3$ range but it is not clear that whether this range was long enough to insure local isotropy.

Therefore, using (6) the equation for the Reynolds stress can be re-written as

$$U_k\ (\overline{u_i u_j})_{,k} = -\left[\overline{u_i u_j u_k} + \frac{2}{3\rho}(\overline{pu_k})\delta_{ij}\right]_{,k} - (\overline{u_i u_k}\ U_{j,k} + \overline{u_j u_k}\ U_{i,k}) - \beta_i \overline{u_j t} - \beta_j \overline{u_i t} \left\{-\left[\frac{1}{\rho}(\overline{u_i p_{,j}} + \overline{u_j p_{,i}}) - \frac{2}{3\rho}(\overline{pu_k})_{,k}\delta_{ij}\right] - 2\nu \overline{u_{i,k} u_{j,k}} + \frac{2}{3}\epsilon\delta_{ij}\right\} - \frac{2}{3}\epsilon\delta_{ij} \qquad (7)$$

where $\epsilon = \epsilon_{ii}$. Note that, following Lumley (1978), the anisotropic part of the dissipation part has been combined with the pressure correlation term. The term in the curly parenthesis has a zero trace and will be denoted by Φ_{ij} in the rest of the paper. It is this term whose models have been proposed. Note that the above equation is exact since no approximations have been used so far. Now we introduce the model for the pressure diffusion term, as given above, and with this approximation the above equation becomes

$$U_k\ (\overline{u_i u_j})_{,k} \approx -\left[\overline{u_i u_j u_k} + \frac{2}{15}(\overline{q^2 u_k})\delta_{ij}\right]_{,k} - (\overline{u_i u_k}\ U_{j,k} + \overline{u_j u_k}\ U_{i,k}) + \beta_i \overline{u_j t} + \beta_j \overline{u_i t} + \Phi_{ij} - \frac{2}{3}\epsilon\delta_{ij} \qquad (8)$$

Note that due to the model for the pressure diffusion term this is no longer an exact equation and $\approx$ has been used to emphasize this fact. It is this equation which will be balanced out with the experimental data and the term Φ_{ij} will be obtained as the closing term. It should be reminded that in addition to the measurement errors, any uncertainty in the approximation of the pressure diffusion will also be lumped into Φ_{ij}.

The equation for the streamwise Reynolds stress $\overline{w^2}$ is given by

$$U\frac{\partial \overline{w^2}}{\partial r} + W\frac{\partial \overline{w^2}}{\partial z} \approx -\frac{1}{r}\frac{\partial}{\partial r}(r\overline{uw^2}) - \frac{\partial}{\partial z}(\overline{ww^2}) + \frac{2}{15}\left[\frac{1}{r}\frac{\partial}{\partial r}(r\overline{uq^2}) + \frac{\partial}{\partial z}(\overline{wq^2})\right] - 2\overline{uw}\frac{\partial W}{\partial r} - 2\overline{w^2}\frac{\partial W}{\partial z} + 2g\beta\overline{wt} - \Phi_{zz} - \frac{2}{3}\epsilon \qquad (9)$$

The balance of this equation is shown in figure 3. Advection is the smallest of all the terms. Diffusion term is a gain near the center of the plume and a loss in the rest of the flow. Also, its magnitude near the center is comparable to the other dominant terms in the balance. We note that the buoyancy production is comparable to the production due to mean velocity gradients near the plume center but over the rest of the flow field the shear production is much larger than the buoyancy production. It is also interesting to note that the buoyancy production and dissipation rate approximately balance each other. The closing term in this balance is Φ_{zz} and represents the sum of the pressure correlation term and the anisotropic part of the dissipation. This term is a loss for the $\overline{w^2}$ budget and we note that beyond $r/z = 0.08$ this term and shear production approximately balance each other.

The equation for the radial component $\overline{u^2}$ is given by

$$U\frac{\partial \overline{u^2}}{\partial r} + W\frac{\partial \overline{u^2}}{\partial z} \approx -\frac{1}{r}\frac{\partial}{\partial r}(r\overline{uu^2}) - \frac{\partial}{\partial z}(\overline{wu^2}) + \frac{2}{15}\left[\frac{1}{r}\frac{\partial}{\partial r}(r\overline{uq^2}) + \frac{\partial}{\partial z}(\overline{wq^2})\right] - 2\overline{u^2}\frac{\partial U}{\partial r} - 2\overline{uw}\frac{\partial U}{\partial z} - \Phi_{rr} - \frac{2}{3}\epsilon \qquad (10)$$

and its balance is shown in figure 4. Obviously the advection of $\overline{u^2}$ has the same form as the advection of $\overline{w^2}$. The production due to velocity gradients is a loss near the plume center and is a gain after about $r/z = 0.04$. This is because the radial gradient of the radial mean velocity is positive near the plume center. The mechanical production term is not large. The diffusion term is a loss over most of the flow field and becomes a gain toward the outer edge of the flow field. The sum of the pressure correlation term and the anisotropic part of the dissipation rate is obtained as the closing term in the budget and represents a gain for $\overline{u^2}$. We further note that beyond $r/z = 0.08$ it approximately balances the dissipation rate.

Finally we look at the budget for the shear stress $\overline{uw}$ as shown in figure 5. Its equation is given by

$$U\frac{\partial \overline{uw}}{\partial r} + W\frac{\partial \overline{uw}}{\partial z} \approx -\frac{1}{r}\frac{\partial}{\partial r}(r\overline{uuw}) - \frac{\partial}{\partial z}(\overline{wuw}) - \overline{uw}\frac{\partial U}{\partial r} - \overline{uw}\frac{\partial U}{\partial z} - \overline{u^2}\frac{\partial W}{\partial r} - \overline{uw}\frac{\partial W}{\partial z} + g\beta\overline{ut} - \Phi_{rz} \qquad (11)$$

Both advection and the turbulent buoyancy production are of very small magnitude and over most of the flow field these approximately balance each other. Neglecting these two terms would not cause any significant change in the shear stress balance. We note that the diffusion term is not negligible in this budget. The term Φ_{rz} is essentially balanced by the difference between the shear production and diffusion processes. The shape of Φ_{rz} is obviously similar to that of the shear stress and its peak approximately corresponds to the peak in the shear production.

IMPLICATIONS ON MODELING

Local Equilibrium Assumption

The assumption of local equilibrium implies that the evolution of the turbulence is slow enough to ignore the effects of advection and diffusion (or that these two phenomenon balance each other). For the turbulence kinetic energy it means that the production and dissipation rates balance each other whereas for the heat fluxes and individual Reynolds stresses it implies that the sum of the production and pressure correlation terms balances the respective molecular destruction terms. This idea forms the basis of the algebraic stress models (see e.g. Hossain and Rodi 1982) and we will use the present balances to assess the validity of this assumption.

From the budgets of vertical heat flux (figure 1) it is obvious that the advection and diffusion terms are small and ignoring these will have no significant effect on the heat flux. In the radial heat flux budget the advection and diffusion terms are about 9% of the production term. This may not be a small amount to ignore but one can argue that the neglect of these two terms will introduce an error which is within the other approximations used in the algebraic stress models. Therefore, it seems that for the heat fluxes the algebraic stress model can provide a reasonably good approximation if not an excellent one. However, success of these models will depend on the accuracy of the closure expressions for the pressure temperature-gradient correlation.

The situation in regard to the Reynolds stresses is not as encouraging. From their balances it is clear that the sum of the advection and diffusion terms in the radial and shear stress components is not small as compared to the other terms and neglecting these will introduce a much bigger error. This is specially true near the plume center. So we conclude that the assumption of local equilibrium is not a good approximation for the Reynolds stresses. This will become more evident when we look at the ratio of mechanical to thermal time scale next.

Ratio of Mechanical to Thermal Time Scales

The time scales $\overline{q^2}/\epsilon$ and $\overline{t^2}/\epsilon_t$ represent the eddy turn over times for the mechanical and thermal fields respectively and their ratio is widely used in turbulence models. A universal value of this would un-necessitate a transport equation for the thermal dissipation rate although it is now realized that this ratio can widely vary from one flow to another and that a better approach would be to use a transport equation (see e.g. Newman et al 1981). Full line in figure 6 shows that for the present experiment this ratio is around 3.3 over most of the flow field. This value starts to sharply increase as the outer edge of the plume is approached. The measurement errors are quite large at this location and it is not clear whether this rise is due to the measurement errors alone or also because the mechanical dissipation rate approaches zero faster than the thermal dissipation rate. This value is substantially different than the commonly used value of 2.0 which was recommended by Beguier et. al. (1978) after analyzing several experiments on wall bounded (turbulent flat plate boundary layer, fully developed pipe flow) and boundary free shear flows (heated wake and mixing layer). The dissipation rates were not available for some of these experiments and were obtained by invoking the local equilibrium assumption. The authors further noted that the turbulence was found to be in local equilibrium for near wall flows and that although this was not true for the free shear flows, the production and dissipation rates were still the dominant processes for these flows. The implication was that this was the reason the different experiments and the different methods used in calculating the time scale ratio gave more or less the same result. In the present experiment the production and dissipation processes are certainly the dominant ones but advection and transport are large enough to account for the differences with the study of Beguier et al. Therefore, it is concluded that the reason the current experiment is not in accord with the above mentioned study is that its kinetic energy and temperature variance balances do not satisfy the local equilibrium assumption. This can be further illustrated by calculating the time scale ratio by using the local equilibrium assumption. With this assumption the expressions for the dissipation rates for the buoyant plume reduce to $\epsilon = -\overline{u_i u_j} U_{i,j} - \beta_i \overline{u_i t}$ and $\epsilon_t = -\overline{u_i t} T_{,i}$ The resulting time scale ratio is shown in figure 6 as a broken line and interestingly enough its value is about 2.0 over most of the flow field.

It might be of interest to compare the present results with the homogeneous shear flow experiment of Tavoularis and Corrsin (1981). The time scale ratio for their experiment is about 3.0 which is very close to what is found here for the buoyant plume. Again, if local equilibrium assumption is used, the time scale ratio for their experiment reduces to 2.0. It should be noted that the buoyancy effects are absent in their experiment and that the temperature behaves as a passive scalar. The similarities between the time scale ratios for the two experiments could be due to the fact that the relative magnitudes of the production and dissipation rates are similar in these experiments. It should be emphasized that the purpose of this comparison is not to advocate a new universal value of the time scale ratio.

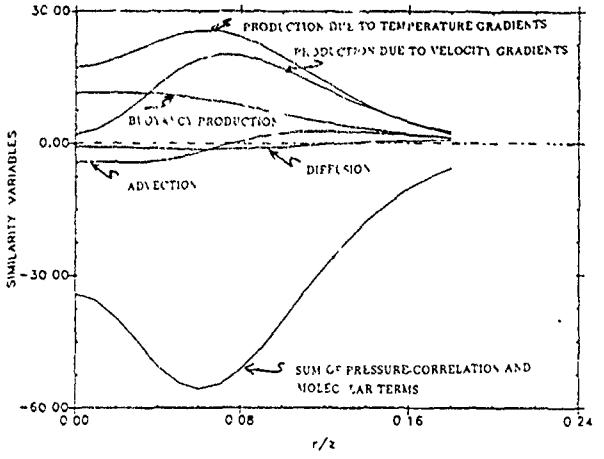

Figure 1. Budget for $\overline{wt}$ equation.

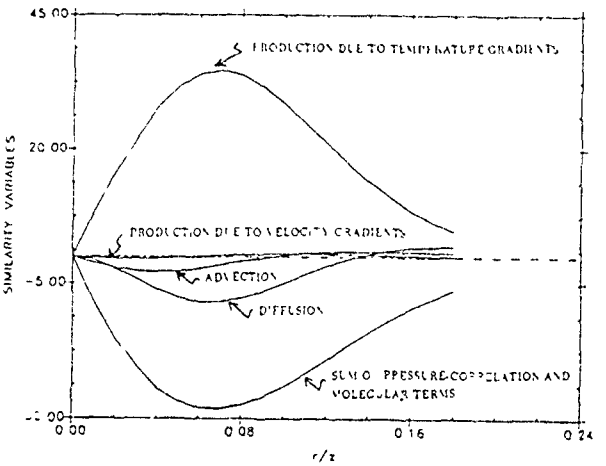

Figure 2. Budget for $\overline{ut}$ equation.

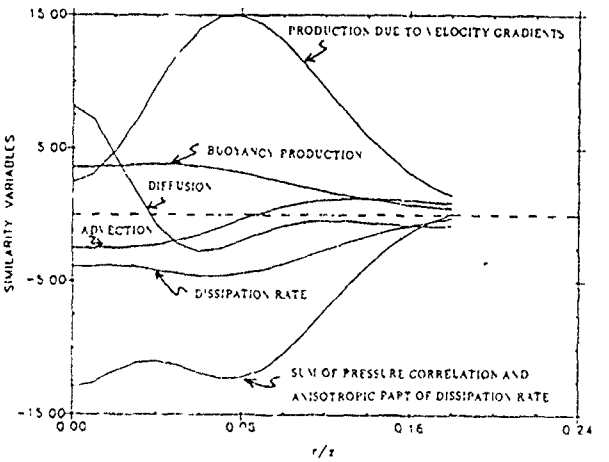

Figure 3. Budget for $\overline{w^2}$ equation.

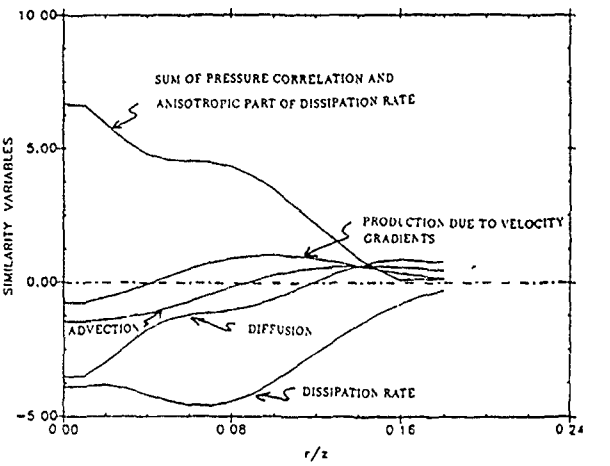

Figure 4. Budget for $\overline{uw}$ equation.

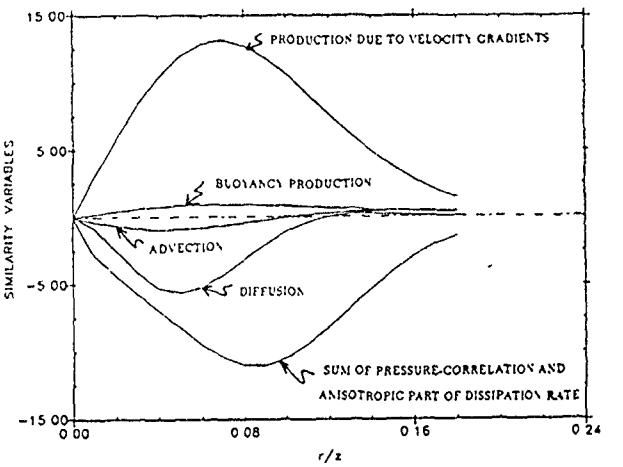

Figure 5. Budget for $\overline{uw}$ equation.

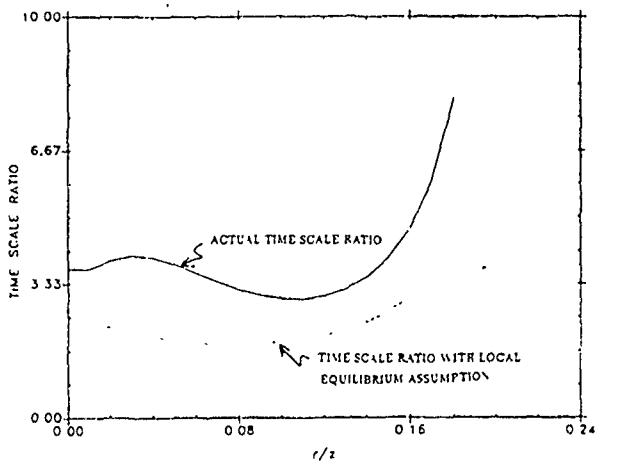

Figure 6. Ratio of mechanical to thermal time scales.

REFERENCES

Beguier, C., I. Dekeyser and B. E. Launder (1978). Phys. Fluids, 21, 307-310.

Hossain and Rodi (1982) Turbulent Buoyant Jets and Plumes. W. Rodi, ed., Pergamon, NY, 121-178.

Launder, B.E., G.J. Reece and W. Rodi (1975). J. Fluid Mech., 68, 537-566.

Lumley, J. L. (1978) Advances in Applied Mechanics, 18, 123-176.

Lumley, J.L. (1975) Phys. Fluids, 18, 750.

Newman, G.R., B.E. Launder and J.L. Lumley (1981) J. Fluid Mech., 111, 217-232.

Shabbir, A. (1987). Ph. D. Dissertation, State University of New York at Buffalo, Buffalo, NY.

Shabbir, A. and W.K. George (1987) Proceedings of the 6th Symposium on Turbulent Shear Flows.

Shabbir, A. and W.K. George (1990) Submitted to J. Fluid Mech.

Tavoularis, S. and S. Corrsin (1981) J. Fluid Mech., 104, 311-348.

Zeman, O. (1981)Anl. Rev. Fluid Mech., 13, 253-272.

ACKNOWLEDGEMENTS Part of the work reported here was supported by the National Research Council, Washington D.C. and the Lewis Research Academy of NASA Lewis Research Center. Support of these agencies is gratefully acknowledged

APPENDIX

Pressure Diffusion Term

Earlier in the paper the issue of two different separations of pressure correlation into a diffusion and a deviatoric term was briefly discussed. It was pointed out that the pressure diffusion is overestimated when the traditional separation of pressure correlation is used with the pressure diffusion model of Lumley (1978).

To illustrate this problem we will compare the velocity diffusion (i.e. due to $\overline{u_i u_j u_k}$) with the pressure diffusion arising due to two different separations. (The model for the correlation $\overline{pu_k}$ is the same in each case and is given by $\overline{pu_k} = -q^2 u_k/5$). Figures 7-9 show such a comparison. For the vertical component, $\overline{w^2}$, the two separations alter the total diffusion only by a small amount and the differences between the two are not very significant. However, for the radial component $\overline{u^2}$, and the shear stress $\overline{uw}$ the results are quite different. We note that if separation given by (6) is used, the pressure diffusion is only a small fraction of the velocity diffusion for the $\overline{u^2}$ and is zero for the shear stress. On the other hand if the traditional separation given by (5) is used , then the pressure diffusion almost negates the velocity diffusion resulting in zero net diffusion. It was on this basis that it was concluded that if Lumley's model for the pressure diffusion is to be used then it should be used in combination with separation given by (6). Similar comments were made by Zeman (1981) in his review. Note that this analysis does not validate or invalidate the closure expression for pressure diffusion. It only shows with which separation it should be used. It should also be pointed out that many researchers ignore the pressure diffusion altogether. In such a case the question of which separation is appropriate is academic. It also seems that in a flow like buoyant plume neglect of pressure diffusion term may be a reasonable approximation.

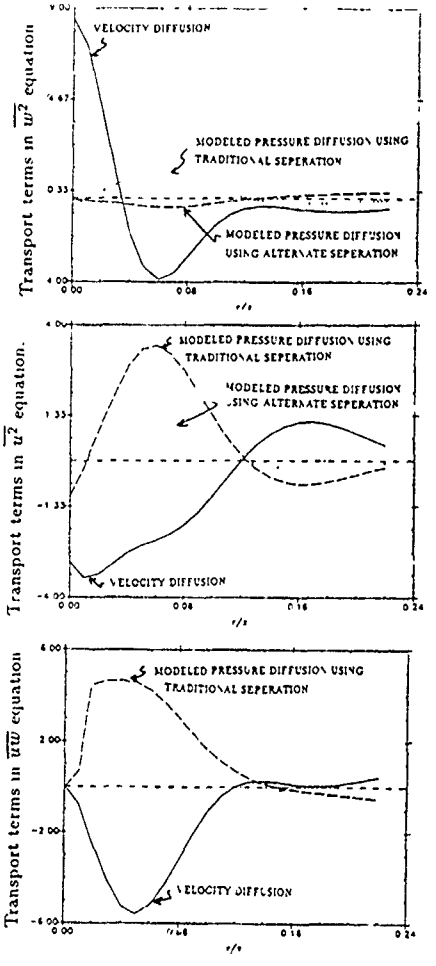

Figure 7. Comparison of modeled pressure diffusion resulting from two different seperations of pressure-correlation.

EIGHTH SYMPOSIUM ON
TURBULENT SHEAR FLOWS
Technical University of Munich
September 9-11, 1991

MODELING PRANDTL NUMBER INFLUENCE ON TURBULENT SCALAR FLUX

N. Shikazono N. Kasagi

Department of Mechanical Engineering
The University of Tokyo

ABSTRACT

In the present study, low Peclet number effects are studied in modeling the pressure-scalar gradient correlation and dissipation terms in the transport equation of the turbulent scalar flux. With the aid of direct numerical simulation (DNS) data bases, it is demonstrated that both terms have dominant roles in the transport equation and should be modeled separately, especially in low Peclet number flows. The anisotropy of these terms are well aligned with that of scalar flux. These relations are then used in deriving a new model. It is shown that the present model gives fairly accurate predictions for the scalar flux in isotropic turbulence and 2-D turbulent channel flows of different Prandtl number fluids

NOMENCLATURE

$a_{i\theta}$; dimensionless scalar flux vector $= \overline{u_i\theta}/2\sqrt{kk_\theta}$
b_{ij} ; anisotropy measure of Reynolds stress tensor $= \overline{u_iu_j}/2k - (1/3)\delta_{ij}$
$e_{i\theta}$; dimensionless dissipation rate of scalar flux $= \epsilon_{i\theta}/\left(\frac{1+Pr}{\sqrt{Pr}}\sqrt{\epsilon\epsilon_\theta}\right)$
k , turbulent kinetic energy $= \frac{1}{2}\overline{u_ku_k}$
k_θ ; half the scalar variance $= \frac{1}{2}\overline{\theta^2}$
p , fluctuating pressure
Pr ; molecular Prandtl number $= \nu/\alpha$
r , ratio of energy-dissipating range timescale to energy-containing range timescale
R , ratio of scalar timescale to mechanical timescale $= (k_\theta/\epsilon_\theta)/(k/\epsilon)$
Re_t ; turbulent Reynolds number $= k^2/\nu\epsilon$
u_i ; fluctuating velocity
U_i ; mean velocity
$\overline{u_iu_j}$; Reynolds stress tensor
$\overline{u_i\theta}$, turbulent scalar flux vector
x_i ; Cartesian coordinates
α ; scalar diffusivity
δ ; channel half width
ϵ ; dissipation rate of k
ϵ_θ ; dissipation rate of k_θ
$\epsilon_{i\theta}$; dissipation rate of scalar flux vector
λ ; Taylor microscale of velocity fluctuation
λ_θ ; Taylor microscale of scalar fluctuation
θ ; fluctuating value of scalar
Θ ; mean value of scalar
ν ; kinematic viscosity
ρ ; density
$\phi_{i\theta}$; pressure-scalar gradient correlation term
$\Phi_{i\theta}$; dimensionless pressure-scalar gradient correlation term
$\psi_{i\theta}$; scalar-pressure gradient correlation term
II ; second invariant of b_{ij}
III ; third invariant of b_{ij}

1. INTRODUCTION

A mathematical model of turbulent scalar transport is needed for solving the Reynolds-averaged scalar equation and hence it is of great importance in many engineering applications. So far, the most common approach in modeling the turbulent scalar flux has relied on the isotropic turbulent scalar diffusivity concept. In this approach, the turbulent scalar flux is related to the mean scalar gradient. In most cases, the unknown turbulent scalar diffusivity is given from the known eddy viscosity by assuming a turbulent Prandtl or Schmidt number. More elaborate models, which express the turbulent scalar diffusivity in terms of the turbulent kinetic energy k, the dissipation rate of turbulence energy ϵ, half the scalar variance k_θ and its dissipation rate ϵ_θ, have been proposed by several researchers (*e.g.*, Nagano & Kim, 1988; Yoshizawa, 1988). In these models, dependence of the turbulent scalar diffusivity upon the time scale ratio ($R = (k_\theta/\epsilon_\theta)/(k/\epsilon)$) is assumed. However, the scalar flux is not generally aligned with the mean scalar gradient, and this means that the turbulent scalar diffusivity expression lacks in universality. An alternative approach is to solve directly the transport equations of scalar fluxes. However, the dependence of the terms on the time scale ratio and the molecular Prandtl number is still an open question at any closure level (see Launder, 1984). This problem should become particularly important when the Prandtl number is far apart from unity.

Recently, many low Reynolds number turbulence models have been proposed as an extention of the high Reynolds num-

ber version (*e.g* , Myong & Kasagi, 1990). This is because there are many practical applications where we have to handle moderate Reynolds number flows; the high Reynolds number hypothesis becomes inadequate. This problem would be emphasized in scalar flux modeling. When a scalar flux model is to be applied to a wide Peclet number range, the model's dependence on the three major parameters, *i.e.*, Pr, R and Re_t, must be carefully examined.

In this study, we pay our attention to the dissipation rate term and the pressure-scalar gradient term in the transport equation of the scalar flux In the widely accepted turbulence modeling, the dissipation rate is set to be zero with an assumption of local isotropy. However, the DNS data bases of Ohtsubo et al (1991) and of Iida & Kasagi (1991) indicate that this is not the case for low Peclet number flows, *i.e.*, the dissipation term becomes the most dominant sink term in the transport equation. Consequently, a proper model for the dissipation rate term should be introduced. As for the pressure-scalar gradient correlation term, an extention to the low Peclet number model should also be necessary for both rapid and slow terms Thus, our aim in this study is to construct models for the dissipation term and the pressure-scalar gradient term which are applicable to low Peclet number flows. The models are then tested by means of the DNS data bases of isotropic turbulence (Iida & Kasagi, 1991) and of fully developed 2-D channel flows of different Prandtl number fluids (Ohtsubo et al., 1991; Kasagi et al., 1991).

2. A MODEL FOR THE DISSIPATION RATE TERM

When the buoyancy effect can be neglected, the transport equation for the scalar flux in a fluid of constant physical properties is given as.

$$\frac{D\overline{u_i\theta}}{Dt} = -\overline{u_iu_k}\frac{\partial\Theta}{\partial x_k} - \overline{u_k\theta}\frac{\partial U_i}{\partial x_k} + \underbrace{\frac{1}{\rho}\overline{p\frac{\partial\theta}{\partial x_i}}}_{\phi_{i\theta}} - \frac{\partial}{\partial x_k}\left(\overline{u_iu_k\theta} + \frac{1}{\rho}\overline{p\theta}\delta_{ik} - \alpha\overline{u_i\frac{\partial\theta}{\partial x_k}} - \nu\theta\frac{\partial u_i}{\partial x_k}\right) \underbrace{- (\alpha+\nu)\overline{\frac{\partial\theta}{\partial x_k}\frac{\partial u_i}{\partial x_k}}}_{\epsilon_{i\theta}} . \quad (1)$$

Since the finest eddies contribute most to the correlation of the dissipation rate, this process is considered to be almost isotropic in a high Peclet number flow. This assumption leads to a model as follows:

$$\epsilon_{i\theta} = 0 \quad (2)$$

Lumley (1978) claimed that the departure from isotropy should be absorbed into the pressure-scalar gradient correlation term $\phi_{i\theta}$ However, as the dependence of $\epsilon_{i\theta}$ and $\phi_{i\theta}$ on the Peclet (Reynolds) number is generally different, each term should be modeled separately.

We define the anisotropy measures of the scalar flux vector and its dissipation vector, respectively, as follows:

$$a_{i\theta} = \frac{\overline{u_i\theta}}{2\sqrt{kk_\theta}} , \quad (3)$$

$$e_{i\theta} = \overline{\frac{\partial u_i}{\partial x_k}\frac{\partial\theta}{\partial x_k}} \Big/ \sqrt{\frac{\epsilon}{\nu}}\sqrt{\frac{\epsilon_\theta}{\alpha}} . \quad (4)$$

In order to constitute an algebraic model for $e_{i\theta}$, we express $e_{i\theta}$ as a function of dimensionless parameters, *i e.*,

$$e_{i\theta} = f(a_{i\theta}, Re_t, Pr, R, b_{ij}, II, III, \cdots), \quad (5)$$

where b_{ij} is an isotropy measure of Reynolds stress tensor, and II and III are its second and third inavariants, respectively. As the Peclet number approaches zero, the range of energy containing eddies overlaps with that of energy dissipating eddies. Thus, the simplest approximation for $e_{i\theta}$ may be written as:

$$e_{i\theta} = a_{i\theta}. \quad (6)$$

Presently, an order estimate analysis is performed first, and the complicated relation between $e_{i\theta}$ and $a_{i\theta}$ is not discussed for simplicity.

The above asymptotic model must be connected with eq. (2) as:

$$e_{i\theta} = a_{i\theta}\, f_{\epsilon 1} , \quad (7)$$

where $f_{\epsilon 1}$ is thought to be a function of the ratio of the timescales of energy dissipating range and of energy containing range (defined as r). According to Tennekes & Lumley (1972), the fine scale motions deviate from the isotropic state due to the effect of mean field distortion. This effect should be proportional to the timescale ratio r, which requires $f_{\epsilon 1} \propto r$ at high Peclet number flows. It is considered that the timescale ratio r consists of four independent timescales, *i.e* , mechanical and scalar timescales for both large scale motions and dissipative motions. Thus, r must generally depend on Pr, R and Re_t; a relevant timescale for the large scale motions may be written as $\frac{k}{\epsilon}\times f(R)$, while a form $\sqrt{\frac{\nu}{\epsilon}}\times f(Pr,R)$ can be adopted as the dissipative motion timescale A somewhat intuitive proposal for the ratio r is given as:

$$r = \frac{\max\left[\sqrt{\frac{\nu}{\epsilon}}, \sqrt{\frac{\alpha k_\theta}{k\epsilon_\theta}}\right]}{1/\left(\frac{\epsilon}{k} + c_1\frac{\epsilon_\theta}{k_\theta}\right)} = \frac{1}{\sqrt{Re_t}}\left(1+\frac{c_1}{R}\right)\max\left[1, \sqrt{\frac{R}{Pr}}\right] . \quad (8)$$

Here, the smaller of the two timescales for the large scale motions, and the larger of the two for the dissipative motions are chosen to construct the ratio r. As this ratio r varies from infinity to zero, the value of $f_{\epsilon 1}$ must change from unity to zero in proportion to r.

An additional function is needed which explains the effect of the gap between the spectra of temperature-gradient fluctuations and of strain-rate fluctuations. In this process, the domnant parameter would be the ratio between the Taylor microscales of velocity fluctuation and of scalar fluctuation (Tennekes & Lumley, 1972), *e.g.*, in isotropic turbulence,

$$\frac{\lambda_\theta}{\lambda} = \sqrt{\frac{12\alpha k_\theta}{\epsilon_\theta}} \Big/ \sqrt{\frac{10\nu k}{\epsilon}} = c_2\sqrt{\frac{R}{Pr}} . \quad (9)$$

This effect is taken into account by introducing a function of $f_{\epsilon 2}$. Finally, the model will take the form:

$$e_{i\theta} = a_{i\theta}\, f_{\epsilon 1}(r)\, f_{\epsilon 2}\left(\sqrt{\frac{R}{Pr}}\right) , \quad (10)$$

which leads to·

$$\epsilon_{i\theta} = \frac{1+Pr}{2\sqrt{PrR}} \frac{\epsilon}{k} \overline{u_i\theta}\, f_{\epsilon 1}(r)\, f_{\epsilon 2}\left(\sqrt{\frac{R}{Pr}}\right). \qquad (11)$$

3. A MODEL FOR THE PRESSURE-SCALAR GRADIENT CORRELATION TERM

The pressure-scalar gradient correlation term $\phi_{i\theta}$ is usually divided into two parts and modeled independently. The rapid term $\phi_{i\theta 2}$, which includes the effect of mean velocity garadient, is conventionally represented as:

$$\phi_{i\theta 2} = B^k_{li} \frac{\partial U_l}{\partial x_k}. \qquad (12)$$

Kinematic constraints such as symmetry condition and trace free condition, are imposed to determine the functional form of B^k_{li}. In addition to these conditions, a realizability condition (Schwarz's inequality) is also imposed in the current modeling procedure (*e g.*, Shih et al., 1990). However, this procedure yields a very complicated expression including high-order products of the Reynolds stresses. The simplest and most widely used model is called IP(Isotropization of Production) model, and given as:

$$\phi_{i\theta 2} = c_{2\theta} \overline{u_k\theta} \frac{\partial U_i}{\partial x_k}. \qquad (13)$$

The recommended value for the coefficient $c_{2\theta}$ is about 0.5 to 0 55.

As for the slow term, a commonly proposed form is:

$$\phi_{i\theta 1} = -c_{1\theta} \frac{\epsilon}{k} \left(\overline{u_i\theta} + c'_{1\theta} b_{ik} \overline{u_k\theta}\right). \qquad (14)$$

A proposal, which includes a term proportional to $b_{ik}\partial\Theta/\partial x_k$, is made by Jones & Musonge (1988). Also, some models contain terms quadratic in b_{ij} (*e.g.*, Craft & Launder, 1989). However, these approaches are not adopted in the present work for simplicity. The value of $c'_{1\theta}$ is frequently assumed to be zero as the first-order approximation. In that case, the value of $c_{1\theta}$ is about 3.0 to 4.0.

The dependence of the coefficients on the timescale ratio R has been widely discussed. One of the modeling requirement is the scalar transformation prorperty. The original form of the scalar equation is linear in θ, and this means that the modeled form must represent this property and that R will not appear in the model equation. However, to achieve a good agreement between the prediction and experimental data, Shih & Lumley (1986) reported that effect of R cannot be ignored. In this section, both rapid and slow terms are modeled in the same procedure as in section 2.

Here, a dimensionless form of the pressure-scalar gradient correlation term $\phi_{i\theta}$ is defined as:

$$\Phi_{i\theta} = \frac{1}{\rho} \overline{p \frac{\partial\theta}{\partial x_i}} \Big/ k\sqrt{\frac{\epsilon_\theta}{\alpha}}. \qquad (15)$$

Generally, $\Phi_{i\theta}$ can be written in terms of dimensionless parameters as:

$$\Phi_{i\theta} = f\left(a_{i\theta}, \frac{k}{\epsilon}\frac{\partial U_i}{\partial x_j}, Re_t, Pr, R, b_{ij}, II, III, \cdots\right). \qquad (16)$$

In the low Peclet number limit, anisotropy of $\Phi_{i\theta}$ is considered to be related directly to $a_{i\theta}$ and $\frac{k}{\epsilon}a_{k\theta}\frac{\partial U_i}{\partial x_k}$. Then, the first-order approximations for both slow part $\Phi_{i\theta 1}$ and rapid part $\Phi_{i\theta 2}$ are written as:

$$\Phi_{i\theta 1} = -c_{1\phi} a_{i\theta}, \qquad (17)$$

$$\Phi_{i\theta 2} = -c_{2\phi} \frac{k}{\epsilon} a_{k\theta} \frac{\partial U_i}{\partial x_k}. \qquad (18)$$

These relations further leads to the dimensional forms as:

$$\phi_{i\theta 1} = -\frac{c_{1\phi}}{2} \frac{\sqrt{Re_t Pr}}{\sqrt{R}} \frac{\epsilon}{k} \overline{u_i\theta}, \qquad (19)$$

$$\phi_{i\theta 2} = -\frac{c_{2\phi}}{2} \frac{\sqrt{Re_t Pr}}{\sqrt{R}} \overline{u_k\theta} \frac{\partial U_i}{\partial x_k}. \qquad (20)$$

These models must be linked with the high Peclet number versions, eqs.(14) and (13), respectively.

First, the effect of the timescale ratio r must be considered. If the fine scale motion has no response to the mean velocity and scalar distortions, the correlation coefficient between them must decrease proportionally to the timescale ratio r. Then, a function $f_{\phi 1}(r)$, which describes this process, is introduced;

$$\phi_{i\theta 1} = -\frac{c_{1\phi}}{2} \frac{\sqrt{Re_t Pr}}{\sqrt{R}} f_{\phi 1}(r) \frac{\epsilon}{k} \overline{u_i\theta}, \qquad (21)$$

$$\phi_{i\theta 2} = -\frac{c_{2\phi}}{2} \frac{\sqrt{Re_t Pr}}{\sqrt{R}} f_{\phi 1}(r) \overline{u_k\theta} \frac{\partial U_i}{\partial x_k}. \qquad (22)$$

The function $f_{\phi 1}(r)$ also changes its value from zero to unity as r varies from zero to infinity.

Secondly, if the spectra of the fluctuations are shifted apart from each other, the two fluctuating variables can correlate only weakly. This process will be expressed by the parameter given by eq.(9), *i.e.*, $\sqrt{R/Pr}$, and hence,

$$\phi_{i\theta 1} = -\frac{c_{1\phi}}{2} \frac{\sqrt{Re_t Pr}}{\sqrt{R}} f_{\phi 1}(r) f_{\phi 2}\left(\sqrt{\frac{R}{Pr}}\right) \frac{\epsilon}{k} \overline{u_i\theta}, \qquad (23)$$

$$\phi_{i\theta 2} = -\frac{c_{2\phi}}{2} \frac{\sqrt{Re_t Pr}}{\sqrt{R}} f_{\phi 1}(r) f_{\phi 2}\left(\sqrt{\frac{R}{Pr}}\right) \overline{u_k\theta} \frac{\partial U_i}{\partial x_k}. \qquad (24)$$

$f_{\phi 1}$ and $f_{\phi 2}$ are chosen so as to transform eqs.(23) and (24) into eqs.(14) and (13) at the high Peclet number limit. The functional form of $f_{\phi 2}$ is discussed in the following.

The pressure-scalar gradient correlation term $\phi_{i\theta}$ can be written as a sum of the scalar-pressure gradient correlation term $\psi_{i\theta}$ and the pressure diffusion term, *i.e.*,

$$\underbrace{\frac{1}{\rho}\overline{p\frac{\partial\theta}{\partial x_i}}}_{\phi_{i\theta}} = \underbrace{-\frac{1}{\rho}\overline{\theta\frac{\partial p}{\partial x_i}}}_{\psi_{i\theta}} + \underbrace{\frac{1}{\rho}\frac{\partial}{\partial x_i}(\overline{p\theta})}_{\text{pressure diffusion}}. \qquad (25)$$

In most practical flows, the pressure diffusion term is small compared to other two terms and, therefore, this term is usually ignored or considered to be absorbed into the turbulent transport term. In that case, models for both $\phi_{i\theta}$ and $\psi_{i\theta}$ should satisfy the condition, *i.e.*,

$$\phi_{i\theta} \approx \psi_{i\theta}. \qquad (26)$$

Using the same modeling procedure as $\phi_{i\theta}$, a model for $\psi_{i\theta}$ can also be obtained, in which $f_{\psi 2}$ appears as $f_{\phi 2}$ appeared in

the model of $\phi_{i\theta}$. Comparing the models of $\phi_{i\theta}$ and $\psi_{i\theta}$, and imposing the condition (26), we obtain:

$$\sqrt{\frac{Pr}{R}} f_{\phi 2} = f_{\psi 2}. \tag{27}$$

In addition, the dependence of $f_{\phi 2}$ on $\sqrt{\frac{R}{Pr}}$ must be the same as that of $f_{\psi 2}$ on $1/\sqrt{\frac{R}{Pr}}$, *i.e.*,

$$f_{\phi 2}\left(\sqrt{\frac{R}{Pr}}\right) = f_{\psi 2}\left(\sqrt{\frac{Pr}{R}}\right). \tag{28}$$

From eqs.(27) and (28), the following function is devised for $f_{\phi 2}$:

$$f_{\phi 2}\left(\sqrt{\frac{R}{Pr}}\right) = \max\left[1, \sqrt{\frac{Pr}{R}}\right], \tag{29}$$

4. APPLICATION TO ISOTROPIC TURBULENCE

In this section, the present models for $\epsilon_{i\theta}$ and $\phi_{i\theta}$ are applied to isotropic turbulence, which is considered to be the most fundumental test case for the models of $\epsilon_{i\theta}$ and of the slow part of $\phi_{i\theta}$. Direct numerical simulations of isotropic tubulence carried out by Iida & Kasagi (1991) are used for the test. In these simulations, scalar fluctuation is also generated with a mean scalar gradient imposed in one direction (x_2), so that there exists a non-zero component of the scalar flux vector, $\overline{u_2\theta}$. The initial turbulent Reynolds number Re_t is set to be about 145, which decreases monotonously with time. Three different Prandtl number fluids are assumed, *i.e.*, Pr=0 025, 0.2 and 0.71.

The transport equation of $\overline{u_2\theta}$ in this flow is written as follows:

$$\begin{aligned} 0 \;=\; & -\frac{\partial \overline{u_2\theta}}{\partial t} - \overline{u_2^2}\frac{\partial \Theta}{\partial x_2} \\ & + \frac{1}{\rho}\overline{p\frac{\partial \theta}{\partial x_2}} - (\alpha+\nu)\overline{\frac{\partial \theta}{\partial x_k}\frac{\partial u_2}{\partial x_k}}. \end{aligned} \tag{30}$$

The DNS budget data for this equation are shown in Fig.1. It is seen that for any Prandtl number case the production term is almost in balance with the sum of pressure-scalar correlation and dissipation terms. However, as the Prandtl number decreases, the dissipation term dominates the pressure-scalar gradient correlation term which corresponds to the slow term in the modeled $\phi_{i\theta}$. This notable trend must be taken into account in order to make the model applicable to a wide Prandtl number range.

In the widely used model, $\phi_{i\theta 1}$ and $\epsilon_{i\theta}$ are to be modeled together as (see Launder, 1984):

$$\phi_{i\theta 1} - \epsilon_{i\theta} = -c_{1\theta}\frac{\epsilon}{k}\overline{u_i\theta}. \tag{31}$$

First, this model is tested by substituting the DNS data into both sides of eq.(31). The results are shown in Fig.2; it is evident that eq.(31) cannot predict all the test cases. Hence, the coefficient $c_{1\theta}$ must be a function of Pr, R ,Re_t and so on.

Model equations (11) and (23) with (29) described in sections 2 and 3 are tested below. Since the Peclet number is considerably low in the present cases, the correlation coefficient must be high enough to consider the functions $f_{\epsilon 1}$, $f_{\epsilon 2}$ and $f_{\phi 1}$ to be a constant near unity. Thus,

$$f_{\epsilon 1} \times f_{\epsilon 2} = 0.7, \tag{32}$$

$$\frac{c_{1\phi}}{2} \times f_{\phi 1} = 0.125, \tag{33}$$

are chosen for the values of the functions. Then, eqs.(11) and (23) are rewritten as:

$$\epsilon_{i\theta} = -0.35\frac{1+Pr}{\sqrt{PrR}}\frac{\epsilon}{k}\overline{u_i\theta}, \tag{34}$$

$$\phi_{i\theta 1} = -0.125\frac{\sqrt{Re_t Pr}}{\sqrt{R}}\frac{\epsilon}{k}\overline{u_i\theta}. \tag{35}$$

With the DNS data substituted into eqs (34) and (35), Fig.3 is obtained. The present models for $\epsilon_{i\theta}$ and $\phi_{i\theta 1}$ give good agreement with the DNS data.

Since the present model test is carried out at very low Peclet number flows, it is hard to deduce the functional expressions for $f_{\epsilon 1}$, $f_{\epsilon 2}$ and $f_{\phi 1}$. More precise data bases, which cover high Peclet number flows (including the budget data of scalar fluxes), are necessary in order to determine the model functions.

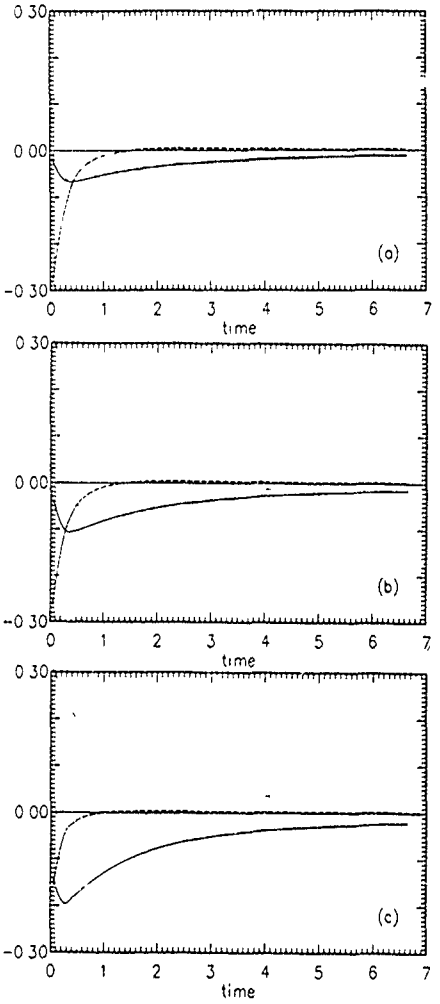

Figure 1 Time development of $\overline{u_2\theta}$ budget in DNS of isotropic turbulence with scalar transport (Iida & Kasagi, 1991):
(a) Pr=0.71, (b) Pr=0.2 and (c) Pr=0.025.
---- $-\overline{u_2^2}\Theta_{,2}$, —— $-(\nu+\alpha)\overline{u_{2,k}\theta_{,k}}$,
$(1/\rho)\overline{p\theta}_{,2}$, — — $-\partial\overline{u_2\theta}/\partial t$.

5. APPLICATION TO 2-D TURBULENT CHANNEL FLOW

The present model is now tested against the DNS data of a fully developed 2-D channel flow of two different Prandtl number fluids performed by Kasagi et al.(1991) and Ohtsubo et al.(1991). The Prandtl number is set to be 0.71 and 0.025, while the Reynolds number based on the channel half width δ and the wall friction velocity is 150. The coordinates x_1, x_2 and x_3 are defined as the streamwise, wall-normal and spanwise directions, respectively.

In this flow, the rapid term $\phi_{i\theta 2}$ due to the mean velocity gradient appears in the transport equation. However, as far as the simplest model eq.(24) is adopted, it will only appear in the $\overline{u_1\theta}$ equation. When the Peclet number is considerably small, $f_{\phi 2}$ can also be considered to be a constant. In this study,

$$\phi_{i\theta 2} = -0.02\frac{\sqrt{Re_t Pr}}{\sqrt{R}}\overline{u_k\theta}\frac{\partial U_i}{\partial x_k} \tag{36}$$

is adopted as a model for the rapid term. Then, this model and also eqs.(34) and (35) are tested by means of the DNS data. The results for $i = 1$ and 2 are shown in Figs.4 and 5, respectively. Here, the modeled $\phi_{i\theta}$ is compared with the scalar-pressure gradient correlation term $\psi_{i\theta}$ in DNS. This is because the modeled $\phi_{i\theta}$ is expected to mimic the whole pressure scrammbling effect when the pressure diffusion term is not modeled. As the effect of wall reflelection is not taken into account, the modeled $\phi_{i\theta}$ overpredicts $\psi_{1\theta}$ and underpredicts $\psi_{2\theta}$ when $Pr = 0.71$. Note that this test case is considered to be rather severe for this simple model which directly relates the anisotropy of $\epsilon_{i\theta}$ and $\phi_{i\theta}$ to $\overline{u_i\theta}$ and $\overline{u_k\theta}\frac{\partial U_i}{\partial x_k}$ without introducing b_{ij}. However, the tendency of each term is predicted in qualitatively good agreement with the DNS data, *i.e.*, $\epsilon_{i\theta}$ dominates $\psi_{i\theta}$ as the Prandtl number decreases.

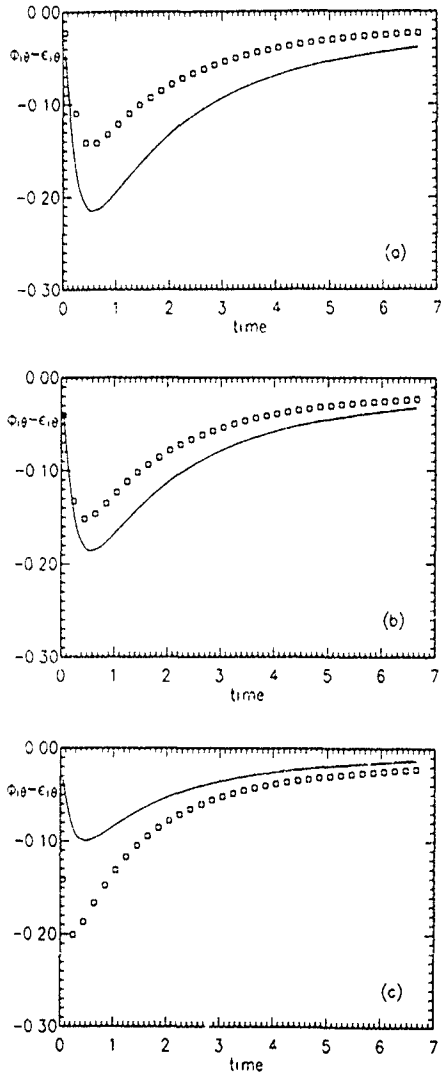

Figure 2 Temporal change of $(\phi_{2\theta 1} - \epsilon_{2\theta})$ in isotropic turbulence with scalar transport:
(a) Pr=0.71, (b) Pr=0.2 and (c) Pr=0.025.
—— model (31), □ DNS.

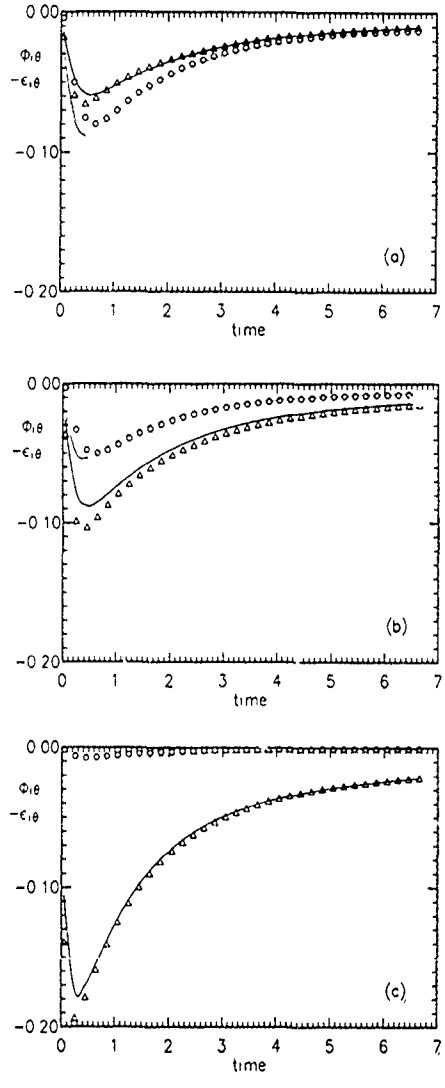

Figure 3 Temporal changes of $\phi_{2\theta}$ and $\epsilon_{2\theta}$ in isotropic turbulence with scalar transport:
(a) Pr=0.71, (b) Pr=0.2 and (c) Pr=0.025.
—— model (34), ... model (35),
○ DNS data for $\phi_{2\theta}$, △ DNS data for $\epsilon_{2\theta}$.

6. CONCLUSIONS

Dependence of the models for $\epsilon_{i\theta}$ and $\phi_{i\theta}$ on Pr, R and Re_t is studied in order to construct a universal scalar flux model which is applicable to wide Prandtl number fluids. Order of magnitude analysis is performed to derive the functional forms of $\epsilon_{i\theta}$ and $\phi_{i\theta}$; the models at the low Peclet number limit are first discussed and then bridged to the high Peclet number expressions In the present study, relatively simple forms which relate anisotropy of $\epsilon_{,\theta}$ and $\phi_{i\theta}$ to $\overline{u_i\theta}$ and $\overline{u_k\theta}\frac{\partial U_i}{\partial x_k}$ are adopted. However, it is easy to extend the present models to more elaborate forms which include higher-order products of Reynolds stresses and their invariants.

The present model is applied to isotropic turbulence of three different Prandtl number fluids with a mean scalar gradient imposed in one direction. The models, in which the bridging functions are assumed constant, give promising results. Another test is performed in a 2-D channel flow, and qualitative agreement is achieved.

Further precise data bases of the budget of the scalar fluxes are needed to determine the functions which appear in the model.

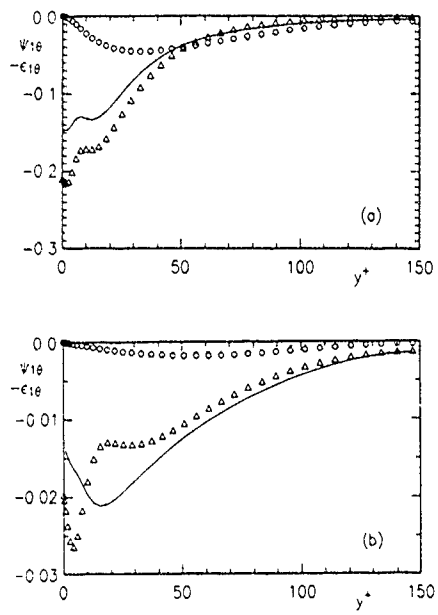

Figure 4 Wall-normal distributions of $\phi_{1\theta}$ and $\epsilon_{1\theta}$ in a 2-D channel flow: (a) Pr=0.71, (b) Pr=0.025.
—— model (34), - - - - model (35) + (36),
○ DNS data for $\psi_{1\theta}$, △ DNS data for $\epsilon_{1\theta}$.

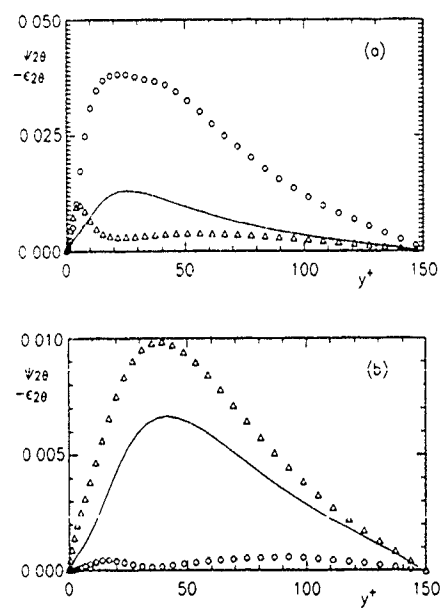

Figure 5 Wall-normal distributions of $\phi_{2\theta}$ and $\epsilon_{2\theta}$ in a 2-D channel flow: (a) Pr=0.71, (b) Pr=0.025.
—— model (34), - - - - model (35) + (36),
○ DNS data for $\psi_{2\theta}$, △ DNS data for $\epsilon_{2\theta}$.

ACKNOWLEDGEMENTS

The authors acknowledge the financial support through the Grant-in-Aid for General Scientific Research (No.01460116) by the Ministry of Education, Sience and Culture.

REFERENCES

CRAFT, T. J. & LAUNDER, B. E. 1989 "A New Model for the Pressure/Scalar-Gradient Correlation and its Application to Homogeneous and Inhomogeneous Free Shear Flows", Proc. 7th Symp. Turbulent Shear Flows, 17.1.1-17.1.6, Stanford University.

IIDA, O & KASAGI, N 1991, Private Communication.

JONES, W. P. & MUSONGE, P. 1988 "Closure of the Reynolds Stress and Scalar Flux Equations", Phys. Fluids, Vol. 31, pp. 3589-3604.

KASAGI, N., TOMITA, Y. & KURODA, A. 1991 "Direct Numerical Simulation of the Passive Scalar Field in a Two-dimensional Turbulent Channel Flow", ASME/JSME Thermal Engineering Proc. 3, pp. 175-182.

LAUNDER, B.E. 1984 "Second-Moment Closure : Methodology and Practice", Turbulence Models and Their Applications, Vol. 2, Eyrolles, Paris

LUMLEY, J L. 1978 "Computational Modelling of Turbulent Flows", Advances in Appl. Mech., 18, pp. 123-176.

MYONG, H. K. & KASAGI, N. 1990 "Prediction of Anisotropy of the Near-Wall Turbulence With an Anisotropic Low-Reynolds number $k-\epsilon$ Turbulence model", ASME J. Fluids Engineering, Vol. 112, pp. 521-523.

NAGANO, Y. & KIM, C. 1988 "A Two-Equation Model for Heat Transport in Wall Turbulent Shear Flows", ASME J. Heat Transfer, Vol. 110, pp 583-589

OHTSUBO, Y , KASAGI, N. & TOMITA, Y. 1991 "Direct Numerical Simulation of Turbulent Heat Transfer of a Low Prandtl Number Fluid", (in Japanese) Proc. 28th National Heat Transfer Symposium of Japan, Vol.I, pp. 16-18.

SHIH, T.-H. & LUMLEY, J. L. 1986 "Influence of Timescale Ratio on Scalar Flux Reluxation: Modelling Sirivat & Warhaft's Homogeneous Passive Scalar Fluctuations.", J. Fluid Mech., Vol. 162, pp. 211-222.

SHIH, T.-H., LUMLEY, J. L. & CHEN, J.-Y. 1990 "Second- Order Modeling of a Passive Scalar in a Turbulent Shear Flow", AIAA Journal, Vol. 28, pp. 610-617.

TENNEKES, H. & LUMLEY, J. L. 1972, A First Cource in Turbulence, MIT Press, Cambridge, Massachusetts.

YOSHIZAWA, A. 1988 "Statistical Modelling of Passive- Scalar Diffusion in Turbulent Channel Flow", J. Fluid Mech., Vol. 195, pp. 541-555.

EIGHTH SYMPOSIUM ON
TURBULENT SHEAR FLOWS
Technical University of Munich
September 9-11, 1991

JOINT STATISTICS BETWEEN A PASSIVE SCALAR AND ITS DISSIPATION IN A TURBULENT BOUNDARY LAYER

F. ANSELMET, H. DJERIDI, L. FULACHIER

Institut de Mécanique Statistique de la Turbulence
Unité Mixte N° 380033 Université d'Aix-Marseille II/CNRS
12, avenue Général Leclerc, 13003 Marseille, France.

ABSTRACT

A weakly heated turbulent boundary layer on a flat plate is considered. The linkage between temperature fluctuations θ and the contribution $(\varepsilon_\theta)_x$ to its dissipation rate from the streamwise gradient is investigated through spectral analysis as well as probability density functions. The assumption of statistical independence is examined.

INTRODUCTION

As it is underlined by Bilger (1989) in a recent review paper, new results "improving our understanding of turbulent transport and mixing of scalars, including the structure of scalar-dissipation fields" are eagerly awaited. Indeed, the mean value $\overline{\varepsilon_\theta}$ of the scalar dissipation is an important quantity which is featuring in second order modelling of turbulent flows -either through the scalar to mechanical time-scale ratio $R(=\tau_\theta/\tau)$ or through solving the $\overline{\varepsilon_\theta}$ transport equation. Studying the instantaneous scalar dissipation ε_θ and its link with the scalar fluctuation θ gives informations about the interdependence of small and large scales, and experiments are all the more necessary since even direct numerical simulations cannot presently resolve with sufficient occurracy the dissipative scales except for low Reynolds number flows. An other interest in investigating a passive scalar θ and its dissipation rate ε_θ is related to turbulent reacting flow models involving a conservative contaminant : in both premixed (Bray, 1980) and diffusion (Bilger, 1980) flames, the average rate of creation or destruction of chemical species can be related to the joint probability density function (jpdf) of θ and ε_θ . Furthermore, in probability density function models of inhomogeneous turbulent flows (Pope and Chen, 1990), a length or time scale is provided using the jpdf of velocity and its dissipation rate. Borghi and Gonzalez (1986), in their applications of Lagrangian models to turbulent combustion, are also relating important quantities such as characteristic time scales to the jpdf of an inert scalar and its dissipation.

Generally speaking, even for a passive scalar, little information is available on the mean dissipation $\overline{\varepsilon_\theta}$, very little about the jpdf $P(\theta, \varepsilon_\theta)$, and especially as far as reacting flows are concerned. Nevertheless, thorough measurements of mean scalar dissipation rates were performed with the cold wire technique by Krishnamoorthy and Antonia (1987) in a slightly heated turbulent boundary layer -showing that $\overline{\varepsilon_\theta}$ is strongly nonisotropic close to the wall- and by Antonia and Browne (1986) in a slightly heated turbulent wake -pointing out that the dissipation is larger than the isotropic value near the wake centreline and especially near the region of maximum production. Dissipation statistics were obtained by Namazian et al. (1988) in the developing region of an isothermal methane jet issuing into still air using Raman scattering : the dissipation is isotropic on the centreline but nonisotropic in the shear layer near the jet exit where the scalar and dissipation are found to be highly correlated. Such a strong correlation is in opposition to Bilger's (1976) conjecture that θ and ε_θ might be statistically independent so that their jpdf can be replaced by the product of the marginal pdfs. This result seems also different from that obtained by Anselmet and Antonia (1985) in a weakly heated turbulent plane jet : iso-jpdf contours between temperature and an approximation to ε_θ evaluated from the temperature temporal derivative are roughly similar to the contours of the product of the marginal pdfs. Nevertheless, when these results are thoroughly examined (Fig.5, p.1052, Anselmet and Antonia, 1985), it is obvious that this hypothesis is strictly verified only for $y/L_u = 1$ (y, lateral distance from the axis, L_u, velocity half-width) where the skewness S_θ of temperature fluctuations is practically zero and the intermittency factor γ is about 1 (Browne et al., 1984) ; on the axis, where $S_\theta = -0.8$ and $\gamma = 1$, the assumption of independence is more approximative. Thus, one may wonder whether the statistical independence between θ and ε_θ is related to the symmetry of temperature fluctuations. A similar trend is observed in direct numerical simulations of the turbulent mixing of a passive scalar (Eswaran and Pope, 1988) where it is found that the conditional scalar dissipation $\langle \varepsilon_\theta / \theta = \theta_0 \rangle$ (for a given value θ_0 of θ) is strongly dependent on θ_0 for small times corresponding to a bimodal pdf of θ, and becomes independent of θ_0 at long times when the θ distribution tends to a gaussian.

In addition to the scalar field dissymetry, a relevant feature may be the intermittent character of some regions of the flow, so that another question arises : what is happening when intermittency is strong, i.e. $\gamma << 1$? In order to analyze a turbulent flow which has both regions where the skewness of scalar fluctuations is strongly positive or negative and regions where the intermittency factor strongly departs from unity, a weakly heated boundary layer has been studied. It is worth recalling that ε_θ is made from three terms

$$\varepsilon_\theta = \alpha \left[\left(\partial\theta/\partial x \right)^2 + \left(\partial\theta/\partial y \right)^2 + \left(\partial\theta/\partial z \right)^2 \right]$$

where α is the thermal diffusivity, x the streamwise distance, y the normal to the wall one and z is along the spanwise direction. As previously mentioned, it is well established that the contribution to the mean dissipation related to the longitudinal gradient can be much smaller than the two other ones, but only a first step relative to the linkage between θ and

$(\varepsilon_\theta)_x$ $(=\alpha(\partial\theta/\partial x)^2)$ is considered in this paper owing to the difficulty of such measurements. This provides useful information to be completed by other more critical measurements, such as those of ε_θ, which are in progress and will be presented in other papers.

EXPERIMENTAL ARRANGEMENT AND MEASURING METHODS

Experiments are carried out in the turbulent boundary layer developed on the working section floor of a low-speed wind tunnel (0.56x0.56 m^2). The wall is heated to a constant temperature T_w relative to the ambiant temperature T_e of 10K from the beginning of the layer. At the measuring station, the free stream velocity is U_e = 12m/s, the boundary layer thickness is δ = 62mm, the momentum thickness Reynolds number is 4900, and the friction velocity and temperature are u^* = 0.46m/s and θ^* = 0.47K, respectively. Temperature is acting as a passive scalar : a typical value of the ratio Gr/Re^2 (where Gr is the Grashof number $g\delta^3(T_w-T_e)/\nu^2T_e$ and Re is the Reynolds number $U_e\delta/\nu$) is 1.4×10^{-4} for the present conditions. The pressure gradient is slightly negative, the Clauser parameter $\Pi = (\delta_1/\delta u^{*2})dp_e/dx$ being equal to -0.019 (the displacement thickness δ_1 is 8.1 mm).

Temperature fluctuation measurements are performed with cold wires (Pt-10% Rh) of diameter d equal to 0.63 µm. These cold wires are operated with in house constant-current circuits. The heating current is equal to 0.2 mA such that the velocity sensitivity of the wire is practically negligible and the signal to noise ratio is large enough to allow correct dissipation measurements. The wire time constant M is very small since 0.63 µm diameter wires are used : M ≈ 30 µs for y^+ = 2.4 (where $y^+ = yu^*/\nu$, with y, distance from the wall), corresponding to the measurement point closest to the wall, resulting in a cut-off frequency of 5 KHz to be compared with the Kolmogorov frequency f_K $(=U/2\Pi\eta$, with η, Kolmogorov length scale) which is about 2.5 KHz. At $y^+ \approx 180$, in the region where f_K is maximum, these frequencies are equal to 8 KHz and 12 KHz respectively. For results presented herein no correction is made to take into account the influence of M : such a study is in progress, but it seems that the main problem is related to the spatial integration resulting from the wire length ($l \approx 0.35$ mm), which is about 4 η close to the wall (y^+ = 2.4) and about 3 η at y^+ = 180. Such wire lengths are consistent with those used by Krishnamoorthy and Antonia (1987), i.e. l/η=4.5 at y^+ = 180, and those recommended by Wyngaard (1971) whose analysis shows a 10 % attenuation of $\overline{\varepsilon_\theta}$ with l/η = 3. This wire length ($l^+ \approx 10$) is also in agreement with that used by Klewicki and Falco (1990), $l^+ \approx 7$, for measurements of the velocity time derivative skewness, with a momentum Reynolds number equal to the present one.

A special study has been performed concerning end-conduction effects which are resulting in an attenuation of temperature variance measurements (Parenthoen et al., 1982). Figure 1 shows the temperature r.m.s. θ'/θ^* profiles measured with the Wollaston wire used herein ($l \approx 0.35$ mm $\approx$ 600 d) and with a fully etched wire of equal length, together with the reference curve obtained with a Wollaston wire ($l \approx 1600$ d) by Anselmet et al. (1990). A fully etched wire has been considered since only such wires can be tractable for ε_θ measurements with a four sensor probe: about 70 % weakening is obtained over the boundary layer and as much as 100 % in the wall vicinity ($y^+ \leq 10$). In fact, temperature spectra F_θ determined with these two kinds of wires are practically identical when normalized to unity : this is due to the dumping of the wire transfer function from very low frequencies less than one hertz.

The longitudinal temperature derivative has been estimated using Taylor's hypothesis which has been validated both experimentally (Krishnamoorthy, 1987) and numerically (Piomelli et al., 1989). Figure 2 compares profiles of the mean values $\overline{(\varepsilon_\theta)_x}$ determined with a Wollaston wire in the present study and by Krishnamoorthy and Antonia (1987). With a fully etched wire, an attenuation similar to that already discussed for the temperature variance θ'^2 is obtained. When those values are corrected to take into account the

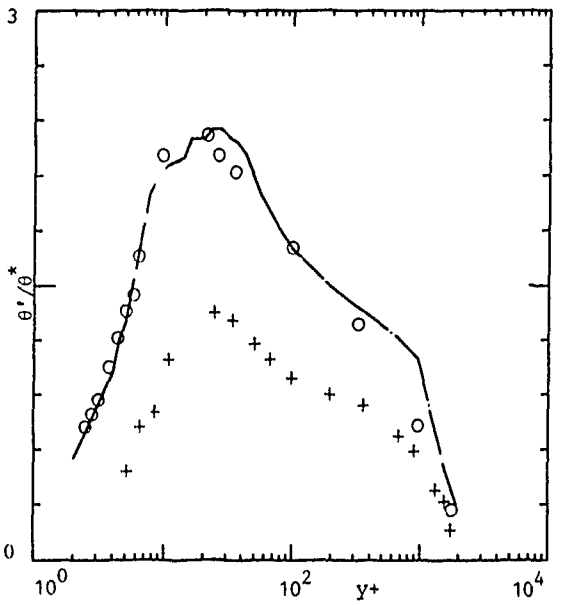

Fig.1. Temperature r.m.s. — · — Anselmet et al. (1990) (Wollaston wire l/d = 1600) ; present measurements : o Wollaston wire, l/d= 600 ; + fully etched wire, l/d= 600.

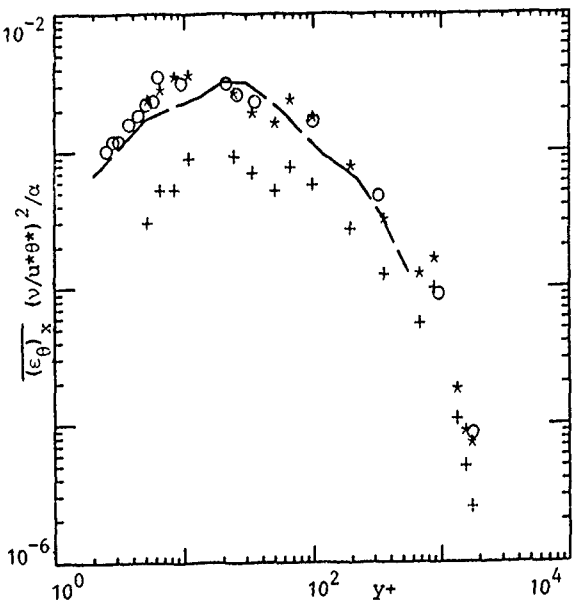

Fig.2. Mean dissipation rate. — — Krishnamoorthy and Antonia (1987) ; present measurements : o Wollaston wire ; + fully etched wire ; * fully etched wire corrected for temperature r.m.s. attenuation.

weakening of θ'^2 indicated on figure 1, $\overline{(\varepsilon_\theta)_x}$ profiles are practically identical : this feature is in agreement with the invariance of temperature spectra F_θ since the quantity $\overline{(\varepsilon_\theta)_x}/\theta'^2$ is proportional to $\int f^2 F_\theta df$, where f is frequency. Consequently, scalar dissipation timescales $\tau_\theta = \theta'^2/\overline{(\varepsilon_\theta)_x}$ measured with the two kinds of wires are almost the same (Fig. 3).

The temperature derivative has been obtained with an analogue circuit providing a linear gain variation up to frequencies larger than 50 KHz. The signals from the cold wire and from the differentiator have been low-pass filtered at f_c = 10KHz before on-line digitalizing (37.5 KHz/channel). Thus, the Kolmogorov frequency is in the range 0.25 f_c (at y^+ = 2.4) to 1.2 f_c (at $y^+ \approx 180$ where f_K is maximum). The high resolution (15 bits) A/D converter is connected to a microcomputer where data (1 M-points corresponding to about 14s duration) are stored. Since this study requires the determination of instantaneous dissipation $(\varepsilon_\theta)_x$, it is important to check that the squared temperature derivative signal is not noise contamined in the high frequency range. Fig. 4 gives - in log-log scales - the spectra of θ, $\partial\theta/\partial t$ and $(\partial\theta/\partial t)^2$ close to the wall where measurements are most critical (the distance y^+ = 3 will be systematically presented instead of y^+ = 2.4 hereafter because, at the latter position, high frequency interferencies occur, but these frequencies do not contribute to the linkage between θ and $(\varepsilon_\theta)_x$) : the high frequency behaviour shows noise does not significantly disturb signals. It is worth mentioning the $\partial\theta/\partial t$ spectrum is identical with that calculated from F_θ.

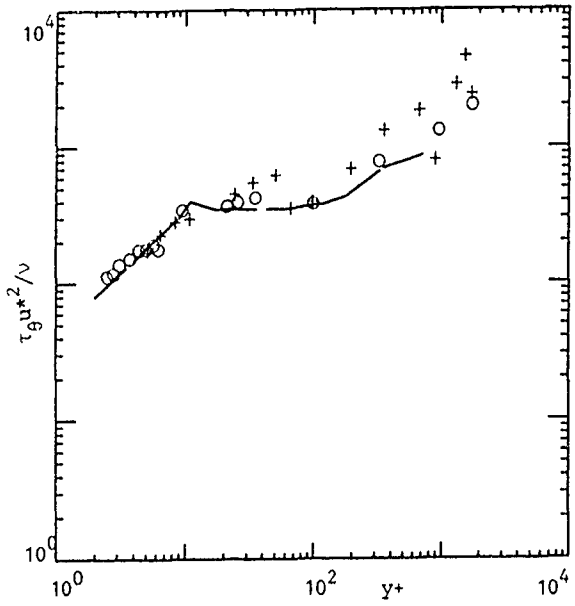

Fig.3. Temperature dissipation timescale.
— — Krishnamoorthy and Antonia (1987) ; o Wollaston wire ; + fully etched wire.

RESULTS AND DISCUSSION

In order to study the linkage between θ and $(\varepsilon_\theta)_x$, their correlation coefficient ρ has been firstly determined (Table 1) for various distances from the wall ranging from the sublayer to the intermittent region. Close to the wall, ρ is rather strongly negative whereas it is reaching positive values of the same order of magnitude in the outer part of the boundary layer

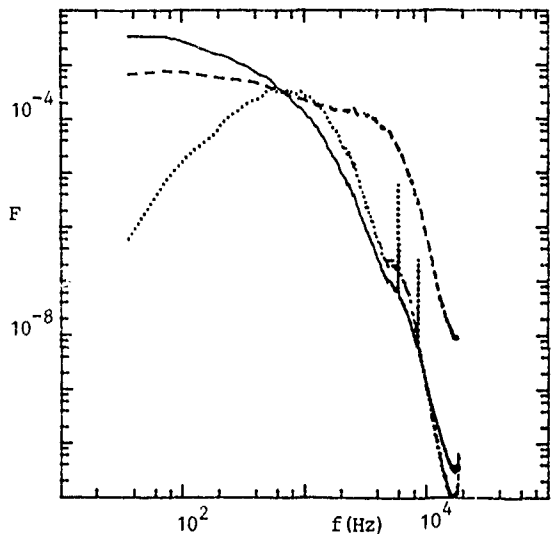

Fig.4. Typical spectra in the wall vicinity (y^+ = 3).
—— θ ; ····· $\partial\theta/\partial t$; - - $(\partial\theta/\partial t)^2$.

y^+	2.4	2.7	3	4.7	5.5	6	9
ρ	-0.29	-0.27	-0.28	-0.24	-0.24	-0.16	-0.14
γ	1	1	1	1	1	1	1
S_θ	-1.1	-1.1	-1.1	-0.88	-0.82	-0.65	-0.35

y^+	20	25	35	95				
y/δ				0.049	0.16	0.47	0.76	0.88
ρ	-0.06	-0.04	-0.02	0.01	0.06	0.09	0.21	0.30
γ	1	1	1	1	1	0.98	0.61	0.28
S_θ	-0.07	0.00	0.02	0.06	0.26	0.41	1.2	3.1

Table 1. Distribution of correlation coefficient ρ and intermittency factor γ in the boundary layer.

where the intermittency factor γ is about 0.3. In these two regions, ρ retains the same sign as the temperature skewness factor which also differs significantly from zero. In order to underline the contribution of individual frequencies f to ρ, co-spectra E (such that $\int Edf = \rho$) between θ and $(\varepsilon_\theta)_x$ are shown on figure 5 in the form fE vs f on a logarithmic scale, for typical distances from the wall. For y^+ = 3 and y/δ = 0.88, the contribution to ρ is due to rather low frequencies of about the same magnitude as the macroscale characteristic frequency (which is close to the frequency corresponding to the most energetic temperature fluctuations). At positions where ρ is almost zero (such as y^+ = 95), the co-spectrum is small whatever the frequency : this is mainly related to the symmetry of the temperature signal.

Another way to investigate the interdependence between θ and $(\varepsilon_\theta)_x$ is to analyse their jpdf. Figure 6 shows iso-jpdf contours at y^+ = 95 are practically identical with iso-contours of the product of the two marginal pdfs ($\alpha = \theta/\theta'$ and $\beta = ((\varepsilon_\theta)_x - \overline{(\varepsilon_\theta)_x})/(((\varepsilon_\theta)_x - \overline{(\varepsilon_\theta)_x})^2)^{1/2}$. In fact, the observed independence is resulting from the balance between positive and negative temperature fluctuations which is contributing to an almost zero overall correlation coefficient : iso-contours (not presented here) of the quantity $\alpha\beta P(\alpha,\beta)$, such that $\int \alpha\beta P(\alpha,\beta)d\alpha d\beta = \rho$, show that, for each contribution ($\alpha>0$ or $\alpha<0$), the linkage significantly differs from zero. In regions where temperature fluctuations are strongly dissymmetric (y^+ = 3, Fig.7, and y/δ = 0.88, Fig.8), the assumption of independence does not hold

at all - ~ one was expecting from table 1.

From the jpdf analysis one can also compute the conditional scalar dissipation such that $<(\varepsilon_\theta)_x/\theta=\theta_o> = \int \beta P(\alpha_o,\beta)d\beta$. In the region where temperature fluctuations are almost symmetrical (Fig.9,y^+=95),

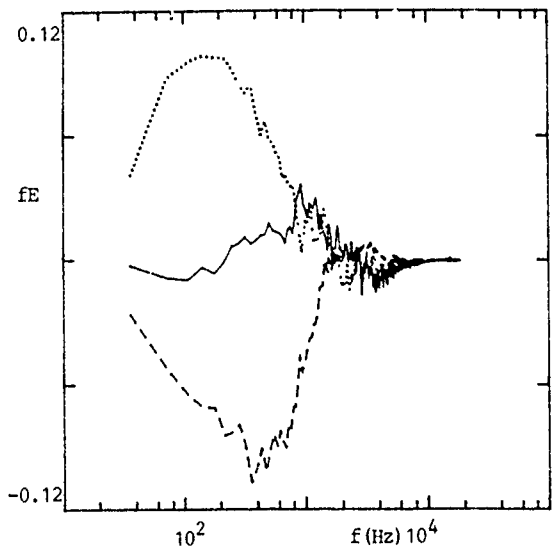

Fig.5. Cospectra between θ and $(\varepsilon_\theta)_x$; - - $y^+ = 3$; — $y^+ = 95$; ..... $y/\delta = 0.88$.

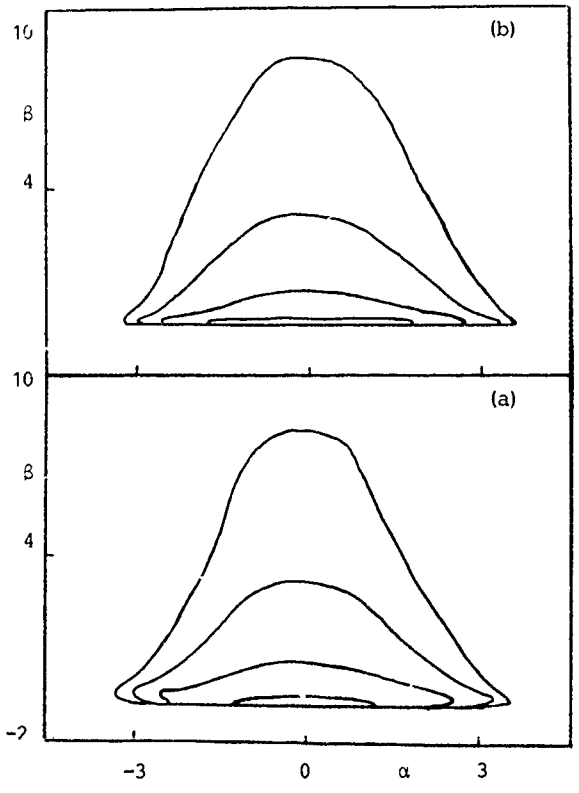

Fig.6. Independence test for the jpdf between θ and $(\varepsilon_\theta)_x$ at $y^+ = 95$ ($\rho = 0.01$)
a. θ and $(\varepsilon_\theta)_x$ jpdf
b. product of the marginal θ and $(\varepsilon_\theta)_x$ pdfs.
Outer to inner contours correspond to 0.001, 0.01, 0.1 and 1 respectively.

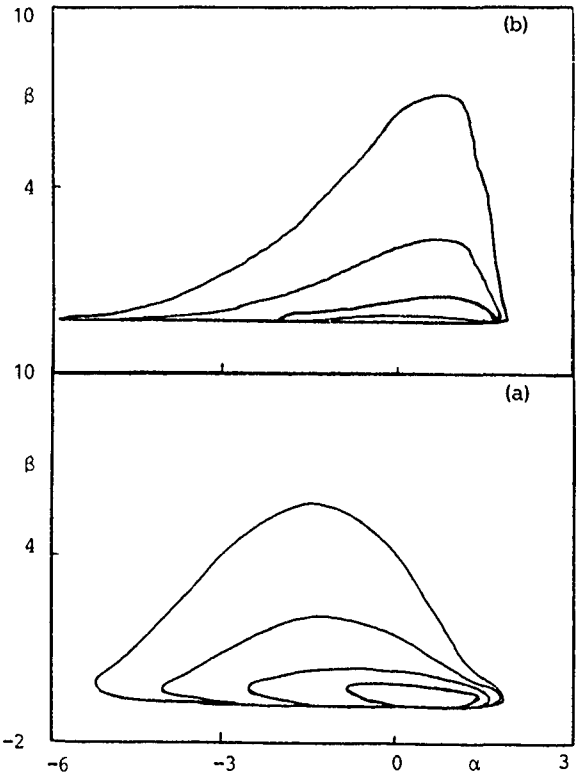

Fig.7.Interdependence test for the jpdf between θ and $(\varepsilon_\theta)_x$ at $y^+ = 3$ ($\rho = -0.28$)
a. θ and $(\varepsilon_\theta)_x$ jpdf
b.Product of the marginal θ and $(\varepsilon_\theta)_x$ pdfs.
Contours same as fig. 6.

the θ pdf is practically gaussian and the conditional dissipation is almost equal to zero for all α_o ($= \theta_o/\theta'$) values, resulting from the statistical independence already mentioned at this distance (Cf. Fig. 6). It is worth mentioning that $\int <(\varepsilon_\theta)_x/\alpha = \alpha_o> d\alpha_o$ should be equal to zero but this integral is somewhat different from zero due to troncature errors. Close to the wall (Fig. 10, $y^+ = 3$), the θ pdf is dissymmetrical - owing to the limit resulting from the wall temperature - and $<(\varepsilon_\theta)_x/\theta = \theta_o>$ strongly depends on θ_o, retaining relatively large negative values for positive temperature fluctuations and positive ones for θ_o negative. These behaviours for both $y^+ = 95$ and $y^+ = 3$ corroborate results obtained by Eswaran and Pope (1988) from direct numerical simulations of the turbulent mixing of a passive scalar. A similar trend is observed in the intermittent region (Fig 11, $y/\delta = 0.88$), but the dissymetric features are opposite with respect to those obtained close to the wall and the dissymmetries are more clearly marked ; that is in agreement with the θ skewness factors S_θ (see table 1). However, for these two latter positions, the absolute values of correlation coefficients between θ and $(\varepsilon_\theta)_x$ are practically equal. On the other hand, one can imagine that the strong intermittent nature of the flow far away from the wall ($y/\delta = 0.88$, $\gamma = 0.28$) also plays an important role for the linkage between the large and small structures : the probabilistic analysis previously presented has been applied again considering only the turbulent portions of the signals. The correlation coefficient ρ is then 0,21 instead of 0.30: intermittency makes the linkage more pronounced but is not at all the main cause for that.

and the jpdf contours (Fig. 12) are not very different from those relative to the initial signals (Fig. 8).

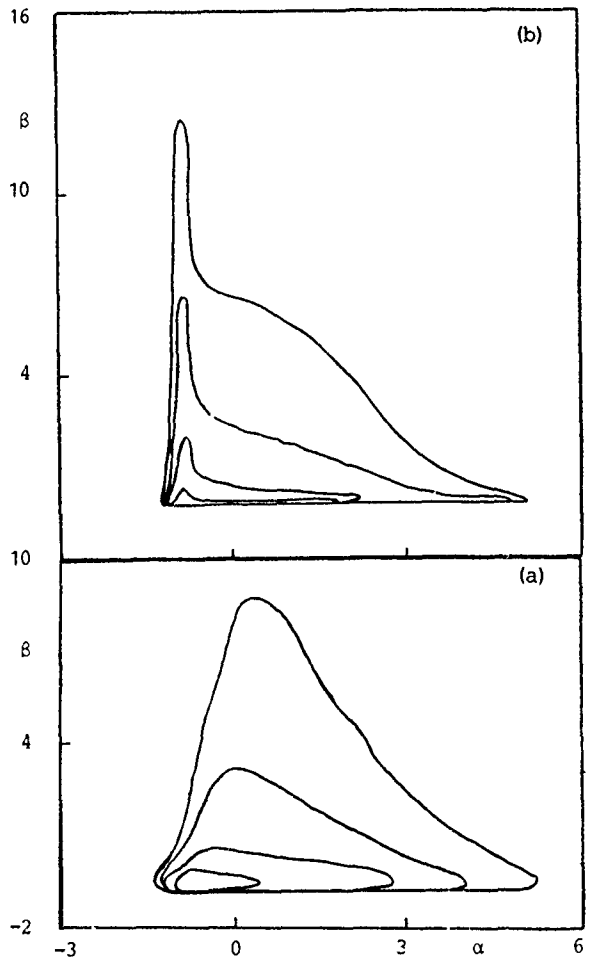

Fig.8 Interdependence test for the jpdf between θ and $(\varepsilon_\theta)_x$ at $y/\delta = 0.88$ (ρ=0.30)
a. θ and $(\varepsilon_\theta)_x$ jpdf
b. product of the marginal θ and $(\varepsilon_\theta)_x$ pdfs.
Contours same as Fig.6.

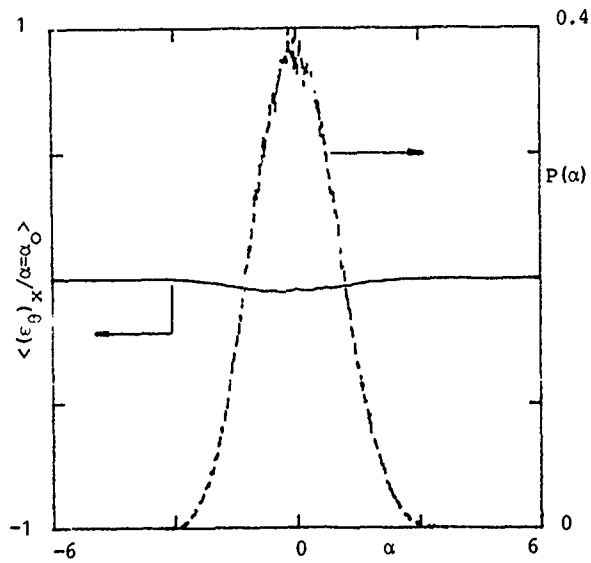

Fig.9.Conditional dissipation and temperature pdf at $y^+ = 95$. ___ $<(\varepsilon_\theta)_x/\alpha=\alpha_o>$; - - P(α).

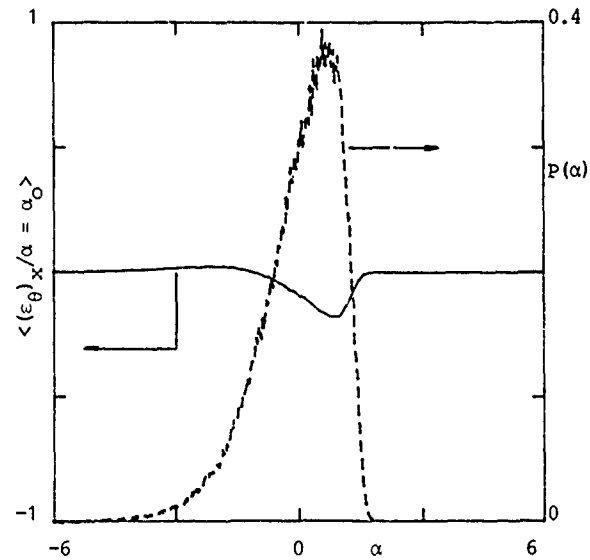

Fig.10.Conditional dissipation and temperature pdf at $y^+ = 3$ (same as Fig. 9).

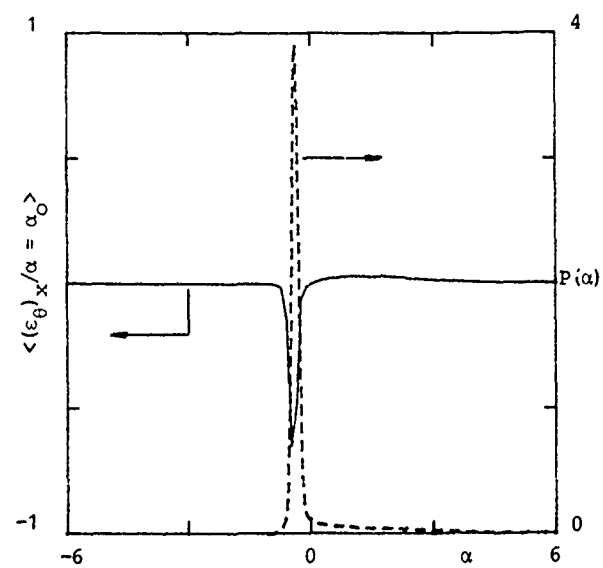

Fig.11. Conditional dissipation and temperature pdf at $y/\delta = 0.88$ (same as Fig.9).

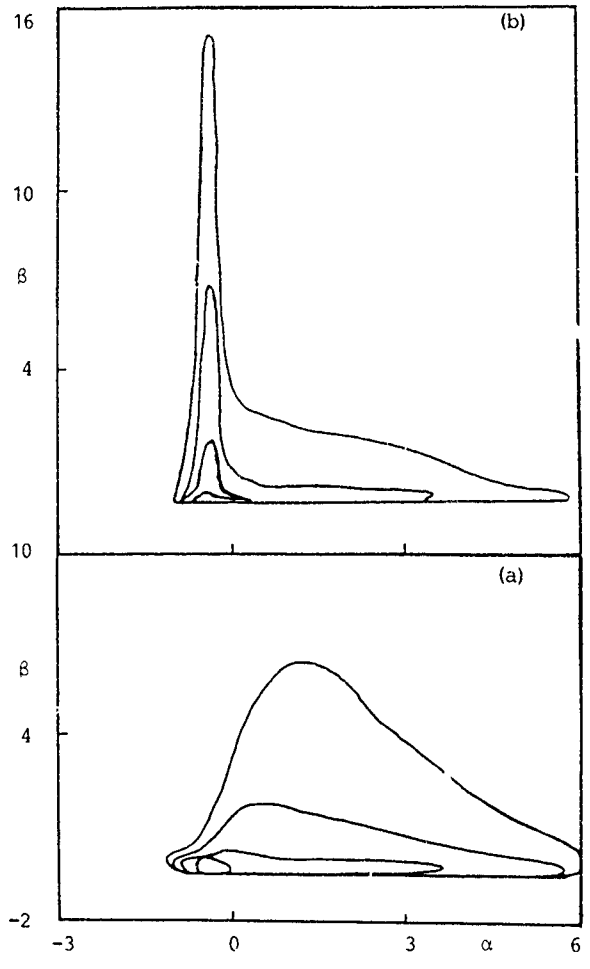

Fig 12 Interdependence test for the jpdf between θ and $(\varepsilon_\theta)_x$ at $y/\delta = 0.88$ when intermittency is accounted for ($\rho = 0.21$)
a. θ and $(\varepsilon_\theta)_x$ jpdf
b. product of the marginal θ and $(\varepsilon_\theta)_x$ pdfs.
Contours same as Fig. 6.

CONCLUSION

The assumption of statistical independence between θ and $(\varepsilon_\theta)_x$ is sound only in regions where θ fluctuations are almost symmetrical. Close to the wall ($y^+ < 15$) and in the outer part ($y/\delta > 0.4$) the interdependence is quite strong. It is appearing from measurements in progress of θ, $(\varepsilon_\theta)_y$, $(\varepsilon_\theta)_z$ and the total dissipation ε_θ that this result would not be invalided.

ACKNOWLEDGEMENTS

This work is supported under grants with Electricité de France, Gaz de France and Société Nationale d'Etude et de Construction de Moteurs d'Avions. We are grateful to M. Astier for his technical assistance.

REFERENCES

ANSELMET, F. & ANTONIA, R.A. 1985 Joint statistics between temperature and its dissipation in a turbulent jet Phys. Fluids 28, 1048-1054.

ANSELMET, F., ANTONIA, R.A., BENABID, T. & FULACHIER, L. 1990 Effect of wall suction on the transport of a scalar by coherent structures in a turbulent boundary layer. In Struct. Turb. and Drag Red., ed. Gyr, A., Springer-Verlag, 349-356.

ANTONIA, R.A. & BROWNE, L.W.B. 1986 Anisotropy of the temperature dissipation in a turbulent wake. J. Fluid Mech. 163, 393-403.

BILGER, R.W. 1976 Turbulent jet diffusion flames. Prog. Energy Combust. Sci. 1, 87-109.

BILGER, R.W. 1980 Turbulent flows with nonpremixed reactants. In Topics in Applied Phys., eds. Libby, P.A. & Williams, F.A., Springer-Verlag, 44, 65-113.

BILGER, R.W. 1989 Turbulent diffusion flames. Annual Rev. Fluid Mech. 21, 101-135.

BORGHI, R. & GONZALEZ, M. 1986 Application of Lagranglan models to turbulent combustion. Combustion and Flame 63, 239-250.

BRAY, K.M.C. 1980 Turbulent flows with premixed reactants. In Topics in Applied Phys., eds. Libby, P.A. & Williams, F.A., Springer-Verlag, 44, 115-183.

BROWNE, L.W.B., ANTONIA, R.A. & CHAMBERS, A.J. 1984 The interaction region of a turbulent plane jet. J. Fluid Mech. 149, 355-373.

ESWARAN, V. & POPE, S.B. 1988 Direct numerical simulations of the turbulent mixing of a passive scalar. Phys. Fluids 31, 506-520.

KLEWICKI, J.C. & FALCO, R.E. 1990 On accurately measuring statistics associated with small-scale structure in turbulent boundary layers using hot-wire probes. J. Fluid Mech. 219, 119-142.

KRISHNAMOORTHY, L.V. 1987 Measurements in the near-wall region of a turbulent boundary layer. Ph. D. Thesis, Univ. of Newcastle (Australia).

KRISNAMOORTHY, L.V. & ANTONIA, R.A. 1987 Temperature-dissipation measurements in a turbulent boundary layer. J. Fluid Mech. 176, 265-281.

NAMAZIAN, M., SCHEFFER, R.W. & KELLY, J. 1988 Scalar dissipation measurements in the developing region of a jet. Combustion and Flame 74, 147-160.

PARANTHOEN, P., PETIT, C. & LECORDIER, J.C. 1982 The effect of the thermal prong-wire interaction on the response of a cold wire in gaseous flows. J. Fluid Mech. 124, 457-473.

PIOMELLI, U., BALINT, J.L. & WALLACE, J.M. 1989 On the validity of Taylor's hypothesis for wall-bounded flows. Phys. Fluids A1, 609-611.

POPE, S.B. & CHEN, Y.L. 1990 The velocity-dissipation probability density function model for turbulent flows. Phys. Fluids A2, 1437-1449.

WYNGAARD, J.C. 1971 Spatial resolution of a resistance wire temperature sensor. Phys. Fluids 14, 2052-2054.

EIGHTH SYMPOSIUM ON
TURBULENT SHEAR FLOWS
Technical University of Munich
September 9-11, 1991

THE INFLUENCE OF DENSITY ON THERMAL MOTION

M.J.V. Neves* and P.D. Almeida**
* Faculdade de Engenharia, Universidade do Porto
Rua dos Bragas, 4099 Porto Codex, Portugal
** Universidade do Minho, Largo do Paço, 4700 Braga, Portugal

ABSTRACT

This paper deals with "thermals", in the sense of convective flows originated by the quick release of a fluid inside another one of different density, the two fluids being miscible. Firstly, a theoretical model to describe the motion is presented. The particular feature of the model is that two zones with different characteristics are considered: (i) the zone of flow establishment and (ii) the zone of established flow. Experiments with fluids with large density differences were carried out to test the model and evaluate parameters such as the spreading rate, the inertial coefficient, the length of the zone of flow establishment and the location of the virtual origin.

1. INTRODUCTION

A thermal is defined here as an instantaneous release of buoyancy. This is different from a plume, for instance, whose generation is due to a continuous source of buoyancy. If the density of the fluid is greater than that of the ambient we have the so called "dense thermal". The study of this flow is of interest, for example, for a better understanding of the mechanisms involved in the process of dumping sludge into the sea. On the other hand, "light thermals" have an upward motion and have been of interest in various studies, such as cumulous clouds, explosions and atmospheric pollution. Besides these practical cases, thermals have been helpful for the study of turbulence fundaments.

However, it seems that experiments on thermals are relatively scarce and some fundamental questions have not received appropriate answers yet. That is the case of the spreading rate, for example. There are doubts if we can talk about an universal spreading rate, or if it varies and, in this case, which are the conditioning parameters. Other pertinent questions are the geometry of the thermal and the evaluation of the virtual mass. Also the effect of large density differences on thermal motion is still not clear, as pointed out by Turner (1986) in a review of the entrainment concept, where he recognizes that "though for most geophysical purposes the Boussinesq approximation gives adequate accuracy, the problem os mixing between fluids with large density differences is a fundamental one, which merits further attention".

In this paper a theoretical model for the analysis of this kind of problems is presented first, and then compared with experimental results.

2. THEORY

Escudier and Maxworthy (1973) developed an interesting theory for the thermal motion but they did not compare it with experimental results. Our experiments confirm their theory in regions far from the source, but the agreement is poor in intermediate and near zones. A possible explanation is that they did not consider a zone of flow establishment.

As a matter of fact, we think that two distinct zones in the thermal motion should be considered. Within a certain distance from the source the thermal exhibits an appendix - see top of Fig. 1 - which becomes smaller and smaller until it completely disappears. The first zone will be called the "zone of flow establishment" (ZFE) and the second one the "zone of established flow" (ZEF).

The shape of the cloud is not easy to qualify precisely. It is similar to a cauliflower but, as it will be seen, it is not necessary to assume a particular shape for the development of the theory. So, let the volume and the surface area be generically expressed by

$$volume = K_v b^3 \tag{1}$$

$$area = K_a b^2 \tag{2}$$

where b represents the horizontal radius of the cloud and K_v and K_a are coefficients which is not necessary to quantify.

It seems plausible that a virtual mass should be considered, at least close to the origin, and the inherent added mass will be represented by:

$$Added\ \ mass = K_M(K_v b^3 \rho_a) \tag{3}$$

where ρ_a is the ambient density and K_M the inertial coefficient.

Assuming that inside the thermal the density (ρ) and the velocity (u) are uniformly distributed, the momentum equation can be written as

$$\frac{d}{dt}[(K_v \rho b^3 + K_M K_v \rho_a b^3)u] = F \tag{4}$$

where F represents the buoyancy force defined by

$$F = K_v(\rho - \rho_a)g b^3 \tag{5}$$

If the ambient density is uniform the buoyancy is conserved, hence

$$F = F_o = K_v(\rho_o - \rho_a)g b_o^3 \tag{6}$$

where the index "o" applies to $t = 0$, the instant when the thermal is released.

By integrating (4) and taking into account (5), we have

$$u = \frac{\rho - \rho_a}{\rho + K_M \rho_a} g t \tag{7}$$

Passing to the mass conservation equation, by using the entrainment concept introduced by Morton et al. (1956), it can be written as

$$\frac{d}{dt} K_v \rho b^3 = K_a b^2 \rho_a \alpha' u \tag{8}$$

where α' is the entrainment coefficient.

By substituting ρ from (5) and considering that

$$u = \frac{dz}{dt} \tag{9}$$

we have

$$\frac{db}{dz} = \frac{\alpha' K_a}{3K_v} = \alpha \tag{10}$$

There are reasons to suppose that the spreading rate α might be different from ZFE to ZEF, therefore we will write down, denoting by z_e the length of ZFE:

(i) For $z \leq z_e$(ZFE), $\quad \frac{db}{dz} = \alpha_e$ (11)

(ii) For $z > z_e$(ZEF), $\quad \frac{db}{dz} = \alpha$ (12)

By integrating we have:

(i) $z \leq z_e$, $\quad b = b_o + \alpha_e z$ (13)

(ii) $z > z_e$, $\quad b = (b_o + \alpha_e z_e) + \alpha(z - z_e)$ (14)

Now, the two zones will be analised separately.

Zone of flow establishment

Equations (9) and (7) in conjunction with the substitution of ρ from (5) lead to

$$\left[\left(\frac{b}{b_o}\right)^3 + \beta_e\right]\frac{dz}{dt} = \beta_e g t^2 \tag{15}$$

where

$$\beta_e = \frac{\Delta_o}{1 + K_{Me}} \tag{16}$$

$$\Delta_o = \frac{\rho_o - \rho_a}{\rho_a} \qquad (17)$$

K_{Me} represents the value of K_M - Eq. (3) - in the zone of flow establishment.

Substituting $\left(\frac{b}{b_e}\right)$ from (13) and integrating (15) we obtain

$$(\alpha_e z_*)^4 + 4(\alpha_e z_*)^3 + 6(\alpha_e z_*)^2 + 4(1+\beta_e)(\alpha_e z_*) = \frac{2\alpha_e}{1+K_{Me}} t_*^2 \qquad (18)$$

This equation was made dimensionless by introducing the scales

$$l_s = b_o \qquad (19)$$

$$t_s = \left(\frac{b_o}{\Delta_o g}\right)^{1/2} \qquad (20)$$

$$u_s = \frac{l_s}{t_s} = (\Delta_o g b_o)^{1/2} \qquad (21)$$

and considering the relative values

$$z_* = \frac{z}{l_s} \quad , \quad t_* = \frac{t}{t_s} \quad , \quad u_* = \frac{u}{u_s} \qquad (22)$$

Taking into account equations (13), (6) and (7), respectively, the "radius" of the thermal, the dilution and the velocity at a certain level can be expressed as

$$b_* = \frac{b}{b_o} = 1 + \alpha_e z_* \qquad (23)$$

$$S_* = \frac{\rho_o - \rho_a}{\rho - \rho_a} = b_*^3 \qquad (24)$$

$$u_* = \frac{t_*}{(1+K_{Me})b_*^3 + \Delta_o} \qquad (25)$$

The asymptotic behaviour of the thermal when $z \to 0$ can be expressed as follows:

$$t_* = [2(1+K_{M_e}+\Delta_o)]^{1/2} z_*^{1/2} \quad ; \quad b_* = 1 \quad ;$$

$$S_* = 1 \quad ; \quad u_* = \left(\frac{2z_*}{1+K_{M_e}+\Delta_o}\right)^{1/2} \qquad (26)$$

Zone of established flow

In ZEF the relationship between z and t can also be obtained by integrating (15), but now $\left(\frac{b}{b_e}\right)$ is defined by (14). Under the condition $t = t_e$ for $z = z_e$, that integration leads to

$$[\alpha(z_* - z_{e*})]^4 + 4A[\alpha(z_* - z_{e*})]^3 + 6A^2[\alpha(z_* - z_{e*})]^2 + 4(A^3+\beta)[\alpha(z_* - z_{e*})] = \frac{2\alpha}{1+K_M}(t_*^2 - t_{e*}^2) \qquad (27)$$

where

$$A = 1 + \alpha_e z_{e*} \qquad \text{and} \qquad \beta = \frac{\Delta_o}{1+K_M} \qquad (28)$$

The "radius", dilution and velocity of the thermal are now defined by

$$b_* = A + \alpha(z_* - z_{e*}) \qquad (29)$$

$$S_* = \frac{\rho_o - \rho_a}{\rho - \rho_a} = b_*^3 \qquad (30)$$

$$u_* = \frac{t_*}{(1+K_M)b_*^3 + \Delta_o} \qquad (31)$$

The asymptotic behaviour when $z \to \infty$ is expressed as follows:

$$t_* = \left[\frac{\alpha^3(1+K_M)}{2}\right]^{1/2} z_*^2 \quad ; \quad b_* = \alpha z_* \quad ;$$

$$S_* = (\alpha z_*)^3 \quad ; \quad u_* = [2\alpha^3(1+K_M)]^{-1/2} z_*^{-1} \qquad (32)$$

It should be noted that the parameter Δ_o is present in (26) but not in (32). This means that density differences give rise to different behaviours near the origin but, in non-dimensional coordinates, all the thermals should exhibit the same behaviour far from the origin. This is very clear from the experiments.

3. EXPERIMENTS

3.1. Description

One of the aims of the experimental work was to investigate the influence of density on the flow characteristics, namely in the case of very high densities, that could question the Boussinesq approximation. For that purpose, a tank with a cross

section of 0.45x0.45m^2 filled with drinking water up to the height of 0.50m was used, and small volumes of denser solutions were released at the surface, - see Table 1 - previously combined with potassium permanganate for visualization.

Table 1 - Conditions of each experiment

Run	Solution	Density (Kg/m^3)	Volume (ml)
1	Sodium chloride	1063	0.5
2	" "	"	1.0
3	" "	"	2.0
4	" "	"	4.0
5	" "	1182	5.0
6	" "	"	3.0
7	" "	"	1.0
8	" "	"	0.3
9	Calcium chloride	1458	0.3
10	" "	"	1.0
11	" "	"	4.0

Another point we wanted to examine was the influence of the initial size of the cloud. Therefore, different volumes from 0.3ml to 5ml were used, and it can be anticipated that no different behaviours were observed. The volume was measured with a syringe, used to fill hemispherical spoons of different sizes, adequate to the samples, whose discharge was made very carefully, in order to avoid initial velocity.

On the wall of the tank there was a metric scale, and the horizontal diameter of the cloud, as well as the time elapsed after being released, were measured every 5 cm. Each experiment was repeated six to twelve times, in order to obtain representative average values.

3.2. Experimental results

The results of the experiments are shown in Figures 2 and 3. The first one suggests that in the zone where the radius was really measured ($z_* > 10$), a linear development can be accepted, with a spreading rate $\alpha = 0.25$, independent of the density. The speed of the motion in its initial phase did not permit direct measurements in regions close to the origin, that is, direct evaluation of α_*.

Anyway, considering the shortness of the zone, this could give rise to appreciable relative errors, hence an indirect method based on the kinematic of the flow was used instead, as will be indicated further.

The kinematic aspects are shown in Fig. 3 and, as a first observation, we would say that the asymptotic trend expected from Eq. (32) is confirmed. That asymptote offers, possibly, the most practical way of evaluating K_M. Making $\alpha = 0.25$, it seems that $K_M \cong 0$. As a matter of fact, these were the values used to compare Eq. (27) - the general solution for ZEF - with the experimental results. On the other hand, for distances relatively short Eq. (27) is quite sensitive to the parameters α_*, z_{v*} and K_{M_*}, related to ZFE, therefore the adjustment of this equation to the experimental data was the criterion adopted for the selection of those parameters - Table 2 -.

Table 2 - Selected parameters

ρ_*	Virtual origin	Zone of flow establishment			Zone of established flow	
(Kg/m^3)	z_{v*}	K_{M*}	α_*	z_{v*}	K_M	α
1063	4.0	0.5	0.26	2	0	0.25
1182	6.9	0.5	0.43	4	0	0.25
1458	8.4	0.5	0.47	5	0	0.25

The observation that the largest values of α_* are associated with the largest values of z_{v*} is a subject which deserves some reflection. It is a situation only understandable if there is a "décalage" between the straight lines that represent the linear growth of the cloud, that is, if the virtual sources are different, as shown in Fig. 4, from where we deduce

$$z_{v*} = \frac{z_{*}(\alpha_* - \alpha) + 1}{\alpha} \qquad (33)$$

Fig. 3 allows the acceptance of this explanation, though for values of ρ_o so different as 1063 Kg/m^3 and 1458 Kg/m^3 the "décalage" is so small that can be ignored for practical purposes.

4. CONCLUSIONS

This paper reports a theoretical and experimental study on the motion of the thermals. The consideration

of a zone of flow establishment as a transition to the zone of established flow is the main novelty of the theoretical model. It was compared with experimental data, with the particularity that very heavy fluids have been used. Principal conclusions:

(i) In the zone of established flow, and independently of the density, a constant spreading rate $\alpha = 0.25$ was found, as well as $K_M \cong 0$, which means that the added mass is irrelevant in this zone. However, the virtual origin seems to depend on density, the greater the density, the farther from the real origin;

(ii) The length of the zone of flow establishment is relatively small, though increasing with density, and a maximum value of $5b_o$ was deduced from the experiments. In this zone it seems plausible $K_{M_1} \cong 0.5$, which is the representative value for a sphere. The spreading rate α_1 was found to increase with density. As the spreading rate is related to the entrainment coefficient α' by Eq. (10), it seems possible to deduce α' by analising the geometry of the cloud. We hope to do that in the future, as an effort for better understanding the relationship between entrainment and densimetric effects.

5. ACKOWLEDGEMENTS

The experimental work was done at the Arizona State University (USA) and the facilities provided by Professor Fernando are gratefully acknowledged.

We also would like to thank NATO Scientific Affairs Division, Instituto Nacional de Investigação Científica and Instituto de Hidráulica e Recursos Hídricos / Universidade do Porto.

6. REFERENCES

ESCUDIER, M.P. & MAXWORTHY, T. 1973 On the motion of turbulent thermals. J. Fluid Mech., 61, 541-552.

KOH, R.C.Y. 1983 Ocean disposal of municipal wastewater: impacts on the coastal environment. National Oceanic and Atmospheric Administration, vol. 1, 129-175.

MORTON, B.R., TAYLOR, G.I. & TURNER, J. S. 1956 Turbulent gravitational convection from maintained and instantaneous sources. Proc. Roy. Soc. A 234, 1.

NEVES, M.J.V. 1985 Estudo de jactos turbulentos. PhD thesis, Universidade do Porto, Portugal.

SCORER, R.S. 1957 Experiments on convection of isolated masses of buoyant fluid. J. Fluid Mech., 2, 583.

TURNER, J.S. 1986 Turbulent entrainment: the development of the entrainment assumption, and its application to geophysical flows. J. Fluid Mech., 173, 431-471.

WANG, C.P. 1971 Motion of an isolated buoyant thermal. The Physics of Fluids, vol. 14, 1643-1647.

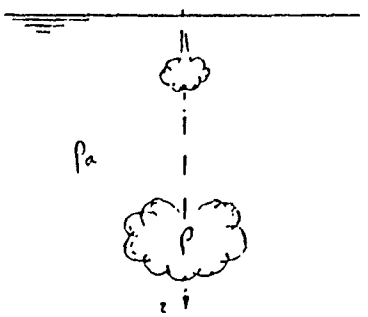

Fig. 1. Development of a thermal

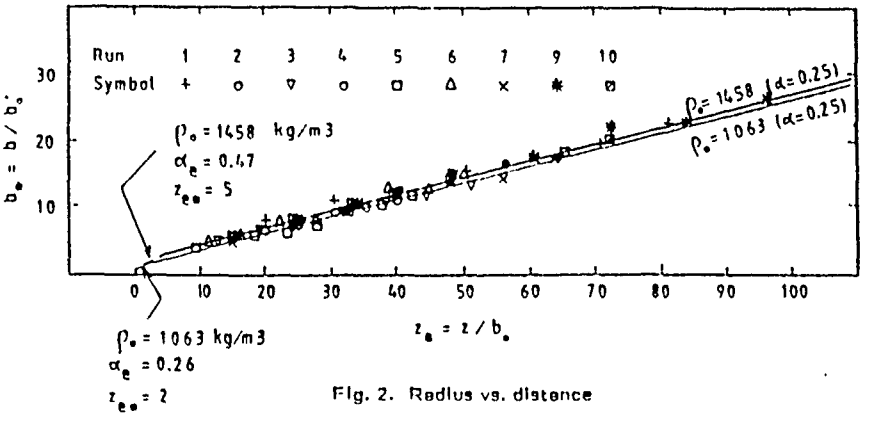

Fig. 2. Radius vs. distance

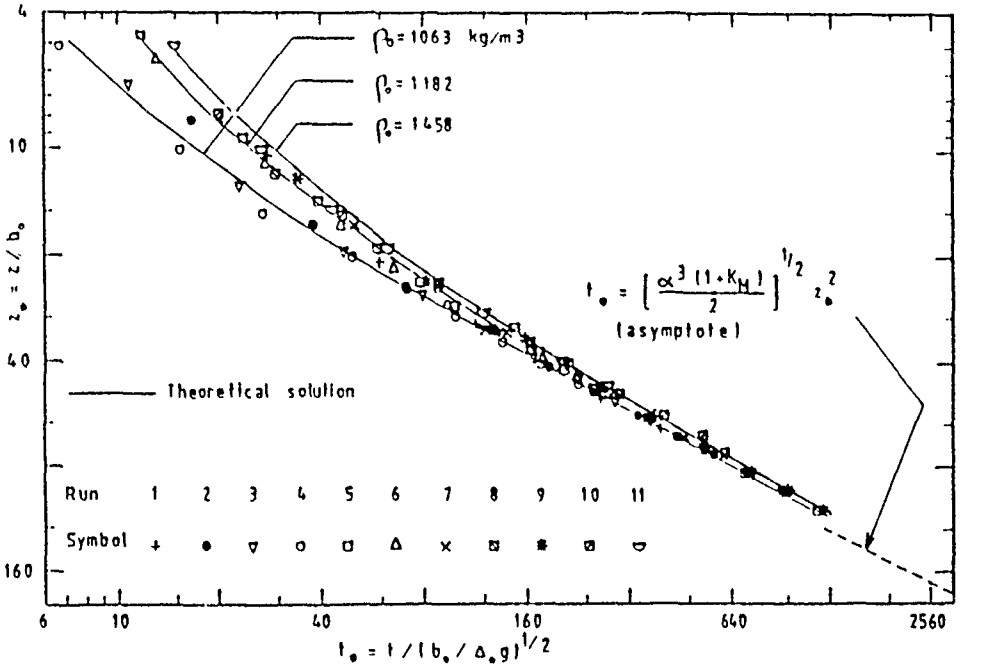

Fig. 3. Distance vs. time

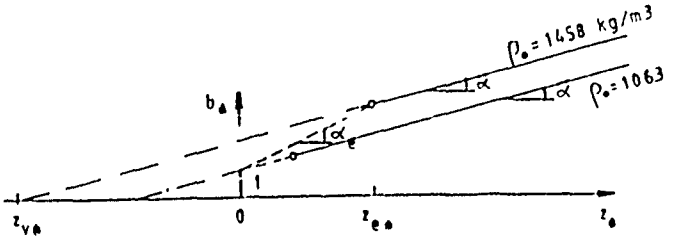

Fig. 4. Virtual origin

EIGHTH SYMPOSIUM ON
TURBULENT SHEAR FLOWS
Technical University of Munich
September 9-11, 1991

A MODEL FOR BURSTING OF NEAR WALL VORTICAL STRUCTURES IN BOUNDARY LAYERS

Paolo Orlandi* and Javier Jiménez+

*Dipartimento di Meccanica e Aeronautica, Università di Roma
+Departamento de Termofluidodinámica, Universidad Politécnica de Madrid

SUMMARY

In the last decade, much effort has been devoted to the understanding of near wall turbulence, both through experimental and numerical observations. Different scenarios have been proposed, but a broad consensus on a basic model for the near wall events has still not been achieved. We present here a simple numerical model for some of the events occurring during the bursting phenomenon. In particular we study the behaviour of longitudinal vortices as they are brought near a wall by an x–dependent external shear, which is the near wall equivalent of a plane strain. We also study the effect of the interaction on the local wall stress, and we calculate the distributions of turbulent stresses to analyse the zones of maximum production in the transversal y-z plane.

INTRODUCTION

The direct simulation of the channel flow by Kim *et al.* (1987), using visualisation techniques similar to those in the experiments of Kim *et al.* (1971), showed the existence of streamwise vortical structures near the wall, very similar to those observed in experiments, and with similar spacings and lengths. Their computational box was 2300×1500 wall units in the streamwise and spanwise directions, and contained many structures, making it difficult to isolate the details of individual events. This is even harder in experimental studies. To achieve a better understanding of individual events near the wall, Jiménez and Moin (1991) introduced the use of numerical simulations in "minimal" channels. In that case only a few structures are present in the computational domain and it is easier to follow them in time and to study how they interact among themselves and with the wall. Because of the intrinsic three-dimensional character of the flow, it is difficult to obtain simple models for the near wall region, but both the full channel and the minimal channel simulations show that the structures are very elongated in the streamwise direction, and that the key event occurs when they come near the wall. Their interaction with the wall induces a layer of secondary wall vorticity of opposite sign, which then diffuses and interacts with the primary structure. During this interaction a very rapid growth of the wall shear stress is observed.

A similar mechanism was observed by Robinson (1991) analysing Spalart's (1988) turbulent boundary layer direct simulation. He came to the conclusion that, in the inner zone, single unpaired near-wall quasi-streamwise vortices generate persistent low-speed streaks, and that counter-rotating vortex pairs are rare. The fact that the whole structure is elongated suggests that a quasi two-dimensional model may be built, in the y-z transverse plane, in which the longitudinal variation is represented only through a variable forcing term in the equations. This permits the use of grids which are unaffordable in a three-dimensional simulations, and the observation of small details which would be unavailable otherwise. On the other hand, the longitudinal variations of the flow are only represented in an approximate manner. As a consequence we expect to find correspondence with experiments in the development of the small spatial scales, and for short time intervals, but not necessarily for large scales or for long times.

Ersoy and Walker (1986) were probably the first ones to investigate numerically two dimensional vortex motion near a wall in connection with the bursting phenomenon, although the basic model was proposed much earlier (Blackwelder and Eckelmann, 1979). They considered the viscous boundary layer induced by a pair of counter-rotating point vortices impinging on the wall at an arbitrary angle, and concluded that the wall layer always separates and generates a violent eruption as a consequence of the pressure field induced by the pair. They concluded moreover that, in asymmetric cases, the effect of vortex nearest to the wall dominates the motion. Their study was done in the context of non-interacting boundary layer theory and, as a consequence, the wall layer became singular in a finite time.

The present study tries to do a more realistic simulation by using the full two dimensional Navier Stokes equations and non singular vortices, and by using parameters derived from direct numerical simulations of the boundary layer. The aim is to study the formation of compact longitudinal cores from initially flat vorticity distributions, to follow the subsequent behaviour of those cores, and to quantify the average (streamwise) wall stress produced by them.

PHYSICAL MODEL

We consider an infinite streamwise vortex subject to a variable shear that increases linearly with the streamwise coordinate, x. From continuity there is a downwash towards the wall which is independent of x. This mean flow is intended as a first approximation to a sweep event, in which a streamwise vortex is pushed towards the wall, and presumably initiates a new bursting cycle. The assumption is that the spatial and temporal scales of the pressure gradient that produces the sweep are large with respect to those of the evolution of the vortex. Under those conditions the mean flow can be assumed to be steady, and a good model is Hiemenz flow (Schlichting, 1987, p. 87), which has the advantage of being itself a steady solution of the Navier-Stokes equations. It can be expressed in terms of a dimensionless function $\phi(y)$ as $U_H(x,y) = ax\phi'(y)$, $V_H(y) = -a\phi(y)$. The function $\phi(y)$ behaves quadratically in y near the wall, so

that the horizontal velocity drops linearly to zero in that region while the normal velocity vanishes quadratically, as in real profiles. Assuming the same x dependance for the perturbations as for the mean flow, we write the streamwise velocity perturbation as $u(x,y,z) = a\,x\,q(y,z)$

The equations for the transverse and longitudinal motion are weakly coupled through the vortex stretching term. The transverse velocity (v,w), is incompressible, and can be characterised by the streamwise vorticity component $\omega = \partial w/\partial y - \partial v/\partial z$, and by a stream function $\psi(y,z)$. From now on we will use dimensionless quantities normalised with Γ, the circulation of the streamwise vortex, and with r_0, the radius of the vortex, and a, related to the variable shear. The dimensionless equation for the longitudinal vorticity is

$$\frac{\partial \omega}{\partial t} + J(\omega,\psi) = Ru\left[(\phi'(y)+q)\,\omega + \phi(y)\,\frac{\partial \omega}{\partial y}\right] + Re\,\nabla^2\omega, \tag{1}$$

with $Re = \Gamma/\nu$, $Ru = a r_0^2/\Gamma$ and $J(\omega,\psi)$ collects the usual convective terms. The first term on the right hand side represents the effect of vortex stretching by the variable shear, while the second one represents advection of vorticity by the resulting normal velocity.

With the assumptions for the perturbation velocities, together with a corresponding one for the perturbation pressure, we can also write a transport equation for the perturbation streamwise velocity, q,

$$\frac{\partial q}{\partial t} + J(q,\psi) = -Ru\left[(q^2 + 2\,\phi'\,q) + \phi(y)\,\frac{\partial q}{\partial y}\right] + \\ + \phi(y)''\,\frac{\partial \psi}{\partial z} + Re\,\nabla^2 q. \tag{2}$$

This quantity behaves approximately as a passive scalar evolving under the effect of viscous diffusion and of advection by the (q,v,w) field. Note that, due to the assumption of two dimensionality, these two equations are exact, except for a "quasi linear" approximation in (2) that $\partial p/\partial y = 0$. We integrate them to evaluate how the vortex evolves under its own induction, coupled to the stretching of the variable shear, and how the streamwise structures affect the longitudinal velocity distribution, including the mean wall stress averaged over the spanwise direction.

Note that the limit $Ru \to 0$, which is reached by letting $a \to 0$ and $x \to \infty$, is that of constant shear and no strain, but satisfies formally the equations. We will present later some simulations in this limit to separate the effects of self induction from those of stretching.

In our calculations, the equations are solved in a rectangular domain with periodic conditions in the spanwise direction. Free-slip conditions are imposed at the upper wall and a very efficient discretisation of the wall vorticity, described in (Orlandi, 1989), is used at the lower, non-slip wall. The main features of the numerical method are described in that paper. It is a scheme with second order time and space accuracy, and with global conservation of energy, enstrophy, and vorticity in the inviscid limit. The dimensionless units used in the numerical calculations can be related to the boundary layer "wall" units by fixing the vortex radius and the kinematic viscosity. The latter is defined as $\nu^+ = 1$, while the former, for reasons given below, will be taken as $r_0^+ = 10$. In the following all results will be expressed in those wall units.

All the calculations are performed within a domain of size equal $z^+ = 100$ in the spanwise direction and $y^+ = 60$ normal to the wall. This corresponds to the average full spacing between consecutive sublayer "streaks" in the spanwise direction but excludes the logarithmic region in the vertical one. All the simulations are performed in a 256×256 grid.

INITIAL CONDITIONS

Robinson (1991), analysing Spalart's (1988) turbulent boundary layer data base from direct simulations, computed distributions of diameters, strengths and wall distances for the quasi-streamwise vortices. He found that the radii have a distribution with a maximum around $r^+ = 5-20$, the wall distance, around $y^+ = 10-50$, and the Reynolds number, $Re = \Gamma/\nu = 60-250$. The value $r_0^+ = 10$ chosen in our computations is intended to represent an average of these vortices.

Some preliminary computations using those values showed that the vorticity was rapidly dissipated. Since the goal of the study was to investigate the vortex dynamics, we decided to increase the Reynolds number to allow for longer lifetimes, and all the simulations presented here are done using $\Gamma^+ = Re = 500$. The discrepancy is most probably due to the three dimensional effects that are neglected in our model. In a strictly two dimensional approximation, like ours, the vorticity rotation terms $\omega_y \partial U/\partial y$ and $\omega_z \partial U/\partial z$ cancel identically, and there is no way to regenerate the streamwise vortices from the transverse vorticity in the mean shear. As a consequence any streamwise vortex is eventually dissipated. On the contrary, it was shown in (Jiménez and Moin, 1991) that those reorientation terms play a significant role in the evolution of the streamwise vorticity in the real boundary layer.

The initial streamwise velocity profile, U_H, has two effects. First, through the scale factor a, it generates the external strain and the normal velocity field that brings the streamwise vortices closer to the wall. Second it is itself convected by the transverse velocity field and generates the shear layers and the wall stress that, although essentially passive in our approximation, are such important features of real flows. Both effects can be studied approximately by using an initially linear profile near the wall, although the consistency of the equations forces us to use a more realistic model such as the Hiemenz flow. Still, all that is required is that $\partial U_H/\partial y \to 0$ as $y \to \infty$, and the detailed profile is quite irrelevant. In particular, the vertical scale of the Hiemenz profile is arbitrarily, and was adjusted in our simulation so that $\phi' = 0.9$ at $y = 4.5$ ($y^+ = 45$), giving an essentially linear profile over most of the region of interest, but levelling to $\phi' = 1$ at the upper edge of the computational domain.

The strain parameter, a, was estimated from direct simulation data. In those, the wall shear has a spotty distribution, in the range $\partial U^+/\partial y^+ = 0-3$, with a streamwise length scale of the order of $x^+ = 50-100$ (Jiménez and Moin, 1991). The corresponding values for the strain are, $a^+ = (\partial^2 U^+/\partial y^+ \partial x^+)/(d\phi'/dy^+)_w \approx 0.5-2.0$. From these data the dimensionless strain in Eqs.(4) and (5) can be approximately evaluated as $Ru = 0.1-0.5$. Because we are interested in investigating the effect of the strain, we considered two cases: the first one with constant shear, $Ru = 0$, and the second one with a strong strain, $Ru = 0.243$.

The choice of the initial vorticity distribution and location for the longitudinal vortices influences in a large measure the evolution of the flow. Rather than introducing circular vortices *ab initio* we decided to study whether they might form naturally by self induction, and we used vortices whose initial shapes were very elongated in the spanwise direction,

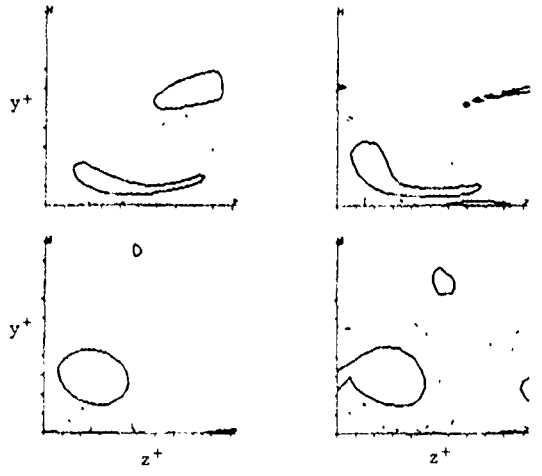

Fig. 1 – Time sequence of ω_x maps in the transverse section of a minimal channel, moving with the approximate convection velocity of the vorticity structures at the wall. Flow is minimal channel from Ref.[3]. Time from left to right and top to bottom.

described by the expression

$$\omega = \omega_M \exp\left(-\frac{y-y_0}{\sigma_y}\right)^2 \sin\left(\pi \frac{x-x_0}{\sigma_x}\right), \quad x \in (0,\sigma_x) \quad (3)$$

where ω_M was adjusted so that $\Gamma = 1$, and with $\sigma_y^+ = 0.75$, $\sigma_x^+ = 10 - 40$, and $y_0^+ = 7.5$. A typical initial condition is shown in Fig. 3.a. These vortex sheets are found often in the near wall region of real boundary layers (see Fig. 1), and it is not immediately obvious whether they result from the deformation of initially circular vortices, or whether they are precursors to them. Our goal in choosing them as initial conditions was to see whether they would evolve spontaneously into circular cores, and how fast. In the case of the simulations presented here, a vortex sheet with $\Gamma^+ = Re = 500$ and $\sigma_x^+ = 20$ rolls up into a compact core in $t^+ \approx 1$, which is shorter than other relevant time scales in the flow.

RESULTS AND DISCUSSION

We were also interested in investigating whether our quasi-two-dimensional model would predict the type of events depicted in Fig. 1, whose most characteristic feature is the presence of intense compact vortices of one sign and weaker, more diffuse, vortices of the opposite sign which seem strained by them into thin sheets. Approximately symmetric vortex pairs are conspicuously absent. We performed several calculations with different initial configurations to study their evolution.

With counterrotating vortices of similar initial circulations and shapes, either with or without external strain, both vortices roll up in approximately half an eddy turnover time. The final configuration is that of Fig. 2, with a vortex pair receding away from the wall. Configurations similar to those of Fig. 1 cannot be achieved. The layers of vorticity of opposite sign which are formed at the wall play an important role in the roll-up process. They are initially very intense, but they later diffuse away from the wall and, subjected to the shear of the main vortex, are dissipated quickly. When an external strain is applied, the vortices are pushed against the wall and become more compact under the effect of the stretching, but the wall interaction mechanism does not change appreciably.

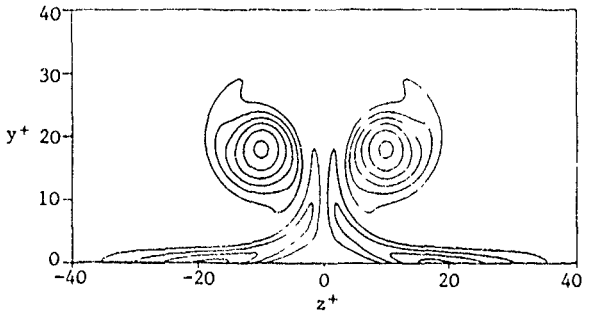

Fig. 2 – Contour plots of vorticity at $t^+ = 4.8$ for a symmetric initial condition. ($\omega_{max} = .52$, $\Delta\omega$ increment $= .10$, $Re = 500$, $Ru = 0$).

When the two counterrotating vortex sheets have the same initial circulation magnitude, but their shapes and distances from the wall are different, the evolution is asymmetric for a while. An example is given in Fig. 3a-c, in which one of the vortices is relatively compact and close to the wall, while the other one is more elongated and located

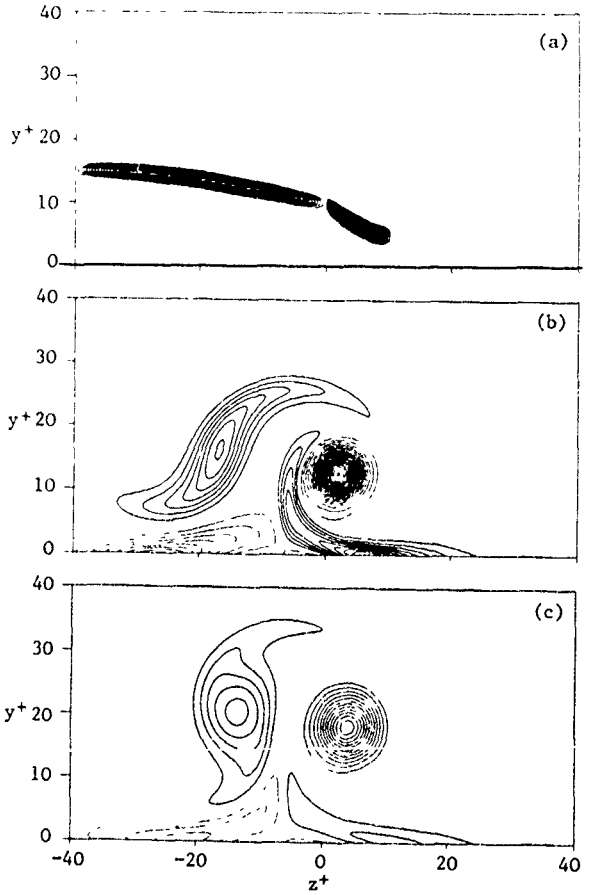

Fig. 3 – Contour plots of vorticity with asymmetric initial conditions. ($\Delta\omega$ increment $= .1$, $Re = 500$, $Ru = 0$). a) $t^+ = 0$; b) $t^+ = 2.4$, $\omega_{max} = .90$; c) $t^+ = 4.8$, $\omega_{max} = .55$.

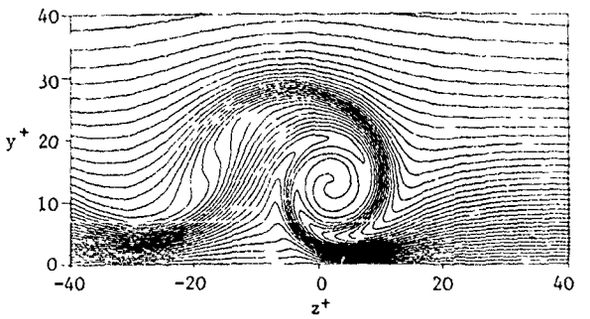

Fig 4 – Contour plots of streamwise velocity corresponding to Fig. 3.b. (Δq increment = .025)

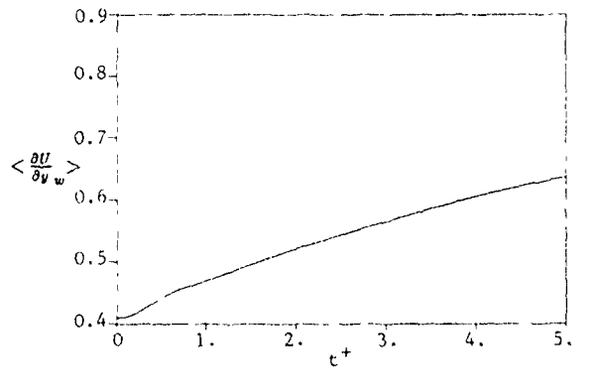

Fig. 5 – $< \partial U/\partial y_w >$ time history for flow in Figures 3-4.

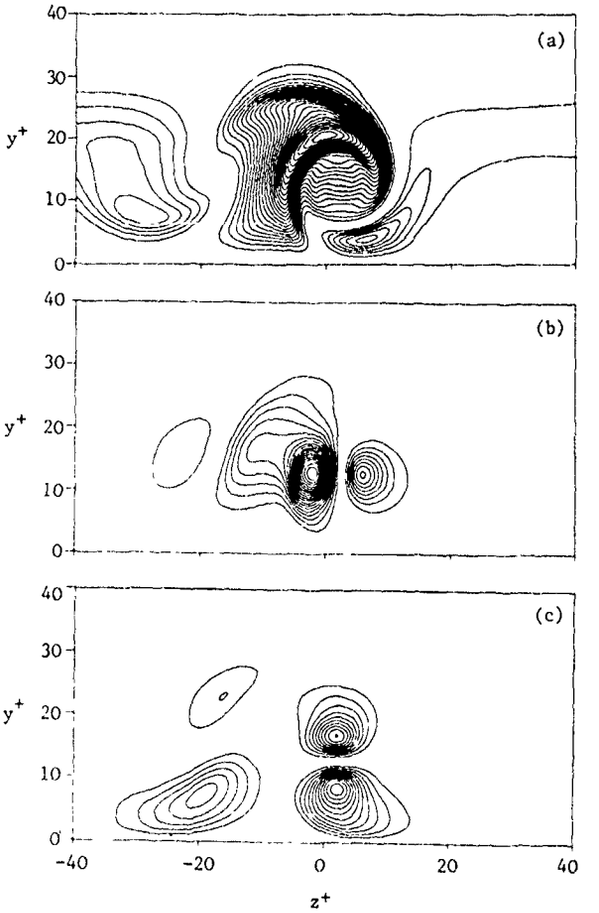

Fig. 6 – Normal stresses distributions for Fig. 3.b. a) q'^2, b) v'^2, c) w'^2. (Δ increment = .00125)

at a greater distance. The small core on the right, having a higher vorticity, assumes a circular shape in a very short time and prevents for a while the roll-up of the more diffuse sheet. The results at $t^+ = 2.4$ (Fig. 3.b) is quite similar to some of the structures in Fig. 1. The main difference is the behaviour of the secondary vortex sheet at the wall, which looks weaker in the three dimensional case. This sheet tends to protrude in between the two members of the vortex pair, shielding the diffuse vortex and allowing it to roll up even in the presence of the strong core. In fact, in the two dimensional case, in which that secondary vorticity is strong, the two cores have essentially rolled up at $t^+ = 4.8$ (Fig. 3.c) and the final result is quite symmetric, similar to that in figure 2. Therefore, a first conclusion of our simulation is that the single structures observed Robinson (1991) have to be caused by very non-symmetric events, e.g. legs of hairpin vortices lying at different distance from the wall, and that the vortex closest to the wall is always dominant.

It is generally accepted that these longitudinal structures are responsible for the formation of the low velocity streaks in the wall region. Fig. 4 shows that this process is caused by the convection of the streamwise velocity field, $U = U_H + u$, by the longitudinal vorticity. In the region of updraft, the initial shear is convected away from the wall, generating a low velocity streak and a detached layer of intense spanwise shear. These are regions of negative u' and positive v' (II quadrant) which generate negative $u'v'$ and production of turbulent energy.

In real three dimensional flows these shear layers probably become unstable and lead to the formation of new longitudinal vortices and of new turbulent cycles, but these effects are absent in our simplified two dimensional model. To the sides of these low velocity regions the downwash pushes the background shear towards the wall and generates a high velocity streak. It is not *a priori* clear whether the two effects would cancel at the wall and whether the global effect would be a increase or a decrease in the wall stress averaged over the span. Figure 5 shows that the former is the case and that the averaged wall stress increases by 50% in $t^+ = 5$, which is a time scale comparable to that estimated for the growth of a burst in (Jiménez and Moin, 1991). Since the eddy turnover time can be estimated as $t_e^+ = (2\pi r_0^+)^2/\Gamma^+ \approx 8$, the increase in wall stress is very rapid, and occur in time which are short compared to an eddy rotation, although longer that those associated to the formation of the compact cores.

Fig. 6 shows the spatial distribution, in the y-z plane, of the velocity perturbations at the particular moment in time which corresponds to Fig. 3.b. These perturbations would contribute to the turbulent intensities u', v' w' in the three dimensional boundary layer, but can only be related directly to them after a randomising and averaging step that was not attempted here. Still, the location of the different contributions is interesting. The fact that the u' perturbation that defines the low velocity streak is wider in the spanwise direction, and stronger, away from the wall than close to it, is well known from experiments. The association, in the cen-

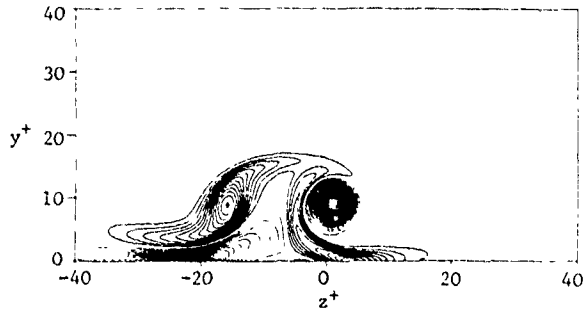

Fig. 7 – Contour plots of vorticity with strain at $t^+ = 2.4$, ($\omega_{max} = 1.30$, $\Delta\omega$ increment $= .1$, $Re = 500$, $Ru = 0.243$).

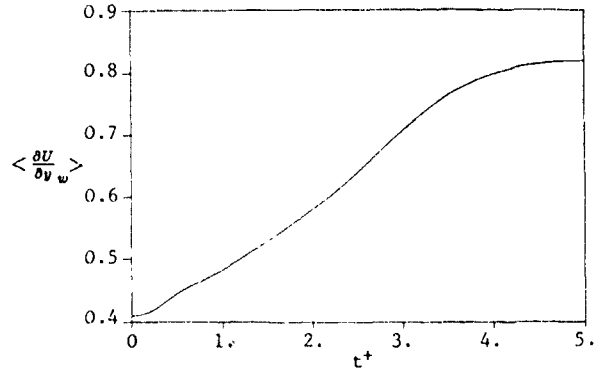

Fig. 9 – $< \partial U/\partial y_w >$ time history for flow in Figures 7-8.

tre of the streak, of $v' > 0$ and $u' < 0$, defines an "ejection" event, and suggests once again that ejections are not transient events in the boundary layer but long lasting states that pass by the stationary probes used in experimental observations (Moin, 1987, Jiménez and Moin, 1991)

From this first simulation, without external strain, we see that our simplified model reproduces some of the features of the bursting event: it is very rapid, it is governed by the presence of longitudinal vortices located near the wall, and during the bursting event there is a large growth of the wall stress.

To analyse how the external strain modifies the flow structure, a simulation was run with $Ru = 0.243$ and with the same initial conditions as those in the previous calculation. In Fig. 7 we show the vorticity distribution at a time comparable to that of Fig. 3.b. The main difference is that now the whole structure is closer to the wall, being convected by the normal velocity created by the strain. This is true both for the original vortex cores and for the secondary vorticity layers at the wall Also, the general intensity of the vorticities has increased, due to the stretching term. As a consequence, all the interactions are stronger and, in particular, the effect of the wall vortex sheet becomes more important than before. The resulting shielding effect prevents the straining of the left vortex by the right one, and the pair becomes more symmetric, even for the severely unsymmetrical initial conditions used here. The end result is that a symmetric pair is always formed, which flies away from the wall even in the presence of downwash created by the strain. The resulting longitudinal velocity distribution is shown in Fig. 8, and also shows the formation of a low velocity streak surrounded by high velocity regions.

Fig. 9 shows the growth of the mean wall shear, which is initially faster than in the unstrained case, but levels off

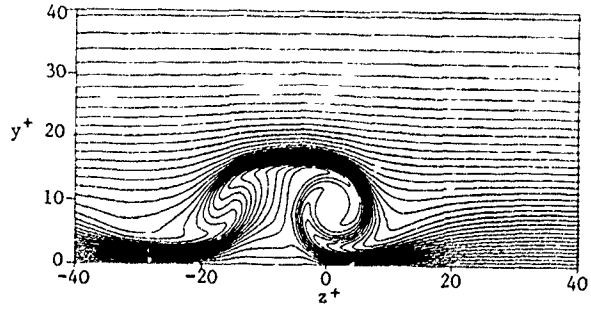

Fig. 8 – Contour plots of streamwise velocity corresponding to Fig. 7. (Δq increment $= .025$)

in a shorter time. This levelling corresponds to the drifting of the symmetric pair away from the wall under its own induction. These characteristics are common to most of the simulations that were carried out including a strain. Asymmetric evolutions could only be achieved in those cases under the most extreme initial conditions. Because the whole boundary layer is contracted vertically towards the wall by the strain, the general level of the longitudinal vorticity gradients is higher, but the structure of the streak is the same as in the unstrained case.

Robinson (1991) found both single vortices and counter-rotating pairs in the wall region, but he notes that the probability of the former is larger than that of the latter. The same was observed in the minimal channel by (Jiménez and Moin, 1991). The present simulations suggest that events with a single vortex are associated to weak streamwise strains while events with vortex pairs correspond to intense strains. At longer times our quasi-two-dimensional simulations always tend to produce symmetric configurations, but it was pointed in the introduction that the model can not be trusted in that range. More interesting is the possible relation of our strained model to the boundary layer in a positive pressure gradient. The results suggest that symmetric pairs should be more common in that case, but we could not find any independent experimental evidence for or against this prediction.

CONCLUSIONS

We have seen that the present simplified quasi-two-dimensional model for the near wall region of the turbulent boundary layer reproduces several of the aspects of the bursting phenomenon, as well as of the structure of the low velocity streaks. In particular it has been shown that flat sheets of streamwise vorticity near the wall roll into compact cores, and that this process, which is a prerequisite for the appearance of strong longitudinal vortices, is fast and relatively independent of the presence of a longitudinal strain. Moreover, the roll-up mechanism is essentially two dimensional (in the y-z plane) and unrelated to the formation of hairpins by longitudinal tilting of the spanwise vorticity. While the latter process has been shown repeatedly to be important in transition of wall flows into turbulence, this new mechanism provides an alternative way for the regeneration of turbulent structures once fully developed turbulent flow has been established. This new mechanism also makes less surprising the relative rarity of symmetrical vortex pairs that has been reported in several recent investigations of the wall region.

On the other hand, our simulations show that even very

asymmetric vortex pairs would eventually roll-up into a more or less symmetric configuration, which then lifts away from the wall under its own induction, and that this tendency is greater in the presence of a positive strain. This suggests that symmetric hairpins should be more common in the outer region of the boundary layer than near the wall, and that the same should be true in layers subject to a favourable pressure gradient. While there is some experimental support for the first trend, we know of no experimental or numerical evidence relating to the second.

The effect of the longitudinal vortices on the average streamwise shear also reproduces well the general structure of the longitudinal streaks found in the wall region. While it has been clear for some time that low speed streaks are associated with the advection of slow fluid away from the wall by the vertical velocities induced by the longitudinal vortices, we believe that this is the first time that it has been shown quantitatively that the net effect of this transport is to increase the *averaged* wall stress. In other words, that the transport of high speed fluid towards the wall is more important than that of low speed fluid away from it. The generation of a high average wall shear is, of course, one of the most characteristic properties of the turbulent boundary layer, and one of its most technologically interesting ones.

On the other hand, most of the three dimensional effects are absent from our model, and the main consequence is that our turbulence will not self sustain. The Reynolds number that we had to use for our vortices to survive for a reasonable time were at least twice larger than those observed in direct numerical simulations. We believe that, even if the present model does give interesting indications of the behaviour of bursting structure for short times, their long time behaviour, and their genesis, depends on the correct understanding of the three dimensional effects.

ACKNOWLEDGEMENTS

This work was started while the authors were visiting the Centre for Turbulence Research, whose support is gratefully acknowledged. We are especially indebted to the fruitful discussions with O. Sendstad, who also produced figure 1. Subsequent research of P. Orlandi was supported with funds by the Ministero Pubblica Istruzione. That of J. Jiménez, by a grant from United Technologies Corporation.

REFERENCES

Blackwelder, R.F. and Eckelmann, H. 1979 Streamwise vortices associated with the bursting phenomenon. *J. Fluid Mech.* **94**, 577–594.

Ersoy, S. and Walker, J.D.A., 1986 Flow induced at a wall by a vortex pair, AIAA Journal, Vol. 24, No. 10, 1597.

Jiménez, J. and Moin, P. 1991 The minimal flow unit in near wall turbulence. *J. Fluid Mech.* **225**, 213–240.

Kim, J., Moin, P. and Moser, R. 1987 Turbulence statistics in fully developed channel flow at low Reynolds number. *J. Fluid Mech.* **177**, 133–166.

Kim, H.T., Kline, S.J. and Reynolds, W.C. 1971 The production of turbulence near a smooth wall in a turbulent boundary layers. *J. Fluid Mech.* **50**, 133.

Moin, P. 1987 Analysis of turbulent data generated by numerical simulations, *AIAA Paper* **87–0194**.

Orlandi, P. 1989 Numerical simulation of vortices motion in presence of solid boundaries. *Proceedings of 8th GAMM Conference on Numerical Methods in Fluid Mechanics* edited by P. Weeseling (Vieweg, Braunschweig), 436–441.

Robinson, S.K. 1991 Coherent motions in the turbulent boundary layer. *Annual Review of Fluid Mechanics*, 601–639.

Schlichting, H., 1968 *Boundary layer theory*, 6th Edition, McGraw-Hill, pg. 87.

Spalart, P.R. 1988 Direct numerical simulation of a turbulent boundary layer up to $R_\theta = 1410$. *J. Fluid Mech.* **187**, 61–98.

EIGHTH SYMPOSIUM ON
TURBULENT SHEAR FLOWS
Technical University of Munich
September 9-11, 1991

COHERENT STRUCTURES IN THE TURBULENT WAKE OF A POROUS BODY

M. Matsumura*, Z. Huang**, J.G. Kawall** and J.F. Keffer**

* Applied Mechanical Engineering, Kitami Institute of Technology, Kitami, Japan

** Mechanical Engineering, University of Toronto, Toronto, Ontario, Canada M5S 1A4

ABSTRACT

The coherent structures within the near region of the plane turbulent wake generated by a porous body are investigated by means of hot-wire anemometry and digital data analysis. The results serve to establish that the coherent structures in question are generally similar to those within the near region of the plane turbulent wake generated by a solid body, such as a vertical flat plate, being essentially two-dimensional vortices, with dominant spanwise vorticity, that occur in a quasi-periodic fashion. There are, however, fundamental differences between the coherent structures within the two types of wakes. To be specific, the relative contributions of these structures to the total Reynolds stresses are definitely not the same. Moreover, the porous-body wake structures are more diffuse than are the solid-body wake structures and, unlike the latter, do not appear to be inter-connected via 'ribs'.

NOMENCLATURE

- f – frequency, Hz.
- L – length of the wake generator in the z direction, m.
- S_u – autospectrum of the fluctuating streamwise velocity component, m^2s^{-1}.
- S_v – autospectrum of the fluctuating lateral velocity component, m^2s^{-1}.
- S_{uv} – co-spectrum of the fluctuating streamwise and lateral velocity components, m^2s^{-1}.
- T – time period, s.
- t – time, s.
- U,V – streamwise and lateral velocities in the x and y directions respectively, ms^{-1} .
- u,v - fluctuating streamwise and lateral velocity components ms^{-1} .
- x,y,z – streamwise, lateral and spanwise coordinate directions, mm.
- ϕ – phase angle, deg.
- ω_z – spanwise vorticity, s^{-1} .

INTRODUCTION

Recent studies (e.g., Zucherman, 1988; Louchez, Kawall and Keffer, 1987; Wygnanski, Champagne and Marasli, 1986) have indicated that the detailed behaviour of a two-dimensional turbulent wake flow, based on its measured statistical properties, is strongly dependent, both in the early stages of its evolution and in its eventual self-preserving state, upon the type of body generating the wake. Moreover, it is now generally accepted that coherent structures play a central role in the dynamics of a turbulent flow. To be specific, these organized motions contribute, along with the random turbulent field in which they are embedded, to the statistical properties of the flow (e.g., Kiya and Matsumura, 1988; Hussain, 1986). This suggests that different types of wake generators give rise to coherent structures that differ significantly in their detailed characteristics, such as, shape, size, orientation, circulation strength, etc., although their general effects on flow-behaviour are similar. If such differences exist, then they should manifest themselves in terms of the relative contributions of the organized motion and the random motion to the statistical properties of wakes produced by different types of bodies. As well, the detailed spectral composition of the turbulent field is likely to depend upon the type of wake generator involved.

The present work concerns an experimental investigation of the near region of the plane turbulent wake generated by a porous body, viz., a vertical mesh-strip. The main objective of the work is to try to establish whether or not the "near-wake" coherent structures in a porous-body wake differ significantly from those in a similar solid-body wake. To this end, certain structural features of the present flow are compared to those of the (solid-body) wake generated by a vertical flat plate, reported by Kiya and Matsumura (1988). The signal-analysis technique of the latter, which is based on the triple-decomposition method (Reynolds and Hussain,1972) is employed here to separate the contributions to the statistical properties of the flow due to the coherent structures and those due to the random turbulent field.

EXPERIMENTAL DETAILS

The experiments for this investigation were performed in the variable-speed low-turbulence recirculating wind tunnel situated in the UTME (University of Toronto, Mechanical Engineering) Turbulence Research Laboratory. This tunnel has a test section 4 m in length and 0.91 m by 1.2 m in cross-section and a speed range of about 1 m/s to about 15 m/s. The wake was generated by means of a mesh-strip with a solidity of about 60%, mounted horizontally at the beginning of the test section. The width (W) of the wake generator was 18 mm and its length (L) was about 0.91 m, so that the aspect ratio (L/W) was about 50. A

free-stream velocity (U_o) of 9.8 m/s was used, so that the Reynolds numbe· based on W was about 11,000.

A Cartesian coordinate system was employed, with x in the streamwise direction, y in the lateral or vertical direction and z in the spanwise direction (parallel to the axis of the wake-generator). The origin of the coordinate system was taken to be in the centre of the wake-generator.

Two streamwise (U) velocity signals and two lateral (V) velocity signals were measured simultaneously at various positions in the flow by means of two DANTEC 45° X-wire probes, in conjunction with four DANTEC 55M constant-temperature-anemometer systems. These signals were low-pass filtered at 5 kHz and digitized by means of a 12-bit A/D converter attached to a PDP-11 computer. The digitization rate was chosen to be 12,500 points per second (to prevent aliasing), and the digital signals were processed on a DEC MICRO-VAX workstation. The length of each signal processed was approximately 28 seconds.

The four velocity signals were measured in the vertical centre-plane of the flow (z = 0) at a streamwise location corresponding to x/W = 24. One X-wire probe was kept fixed near the centre of the wake (y = 0) while the other probe was moved laterally across the wake in increments of approximately 0.1 W between y/W = -2.4 and y/W = +2.1. (Both of these y/W locations were in the free-stream.)

Streamwise velocity (u) autospectra, measured by means of a normal hot-wire probe, established that for x/W locations between about 10 and about 40, a dominant quasi-periodic motion occurred in the flow, signifying that large-scale coherent (i.e., vortical) structures were present in the near region of the wake (~ 10 < x/W < ~ 40). Moreover, these spectra showed that the quasi-periodic motion was most pronounced at x/W = 24. Accordingly, the simultaneous measurements of the two U signals and two V signals were taken at the later x/W location. A typical lateral velocity (v) autospectrum obtained at x/W = 24 and y/W = 0.1 is presented in Fig. 1, where a distinct peak is clearly evident at a frequency (f_o) of about 100 Hz. This frequency is analogous to the Karman vortex shedding frequency in the case of a solid-body wake.

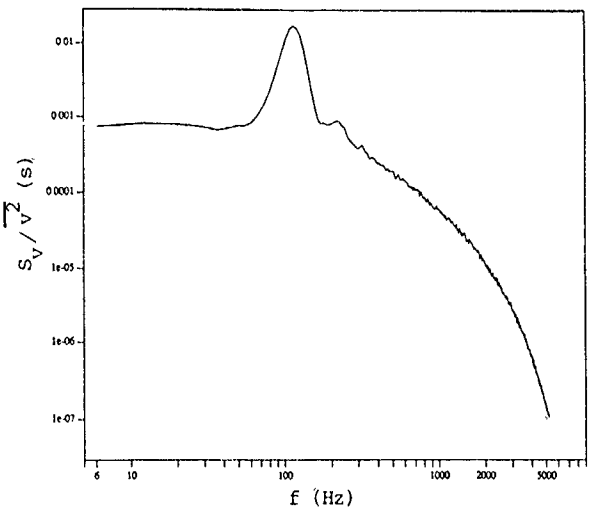

Fig. 1. Lateral velocity autospectrum at x/W=24 and y/W=0.1.

Each V signal measured by the fixed X-wire probe was (digitally) band-pass filtered, with the centre-frequency of the filter set at of f_o. The filtered V signal (v_o) was used to condition each pair of U and V signals measured by the movable probe so that these signals could be decomposed into overall time-averaged components, $\overline{U}$ and $\overline{V}$, coherent components, $\tilde{u}$ and $\tilde{v}$, associated with the organized (vortical) motion and random or incoherent components, u′ and v′, associated with the random turbulent motion.

A typical v_o signal is presented in Fig. 2. As can be seen, this signal has a distinct periodicity (with a period T_o = $1/f_o$), but it is also significantly randomly-modulated. We note that the conditioning signal (v_o) obtained by Kiya and Matsumura (1988), in the case of a solid-body wake, was not randomly-modulated to any significant extent. The implication here is that the large-scale vortical structures within the present porous-body wake exhibit much greater dispersion (with respect to size, shape, orientation, circulation strength, etc.) than do those within the solid-body wake examined by Kiya and Matsumura.

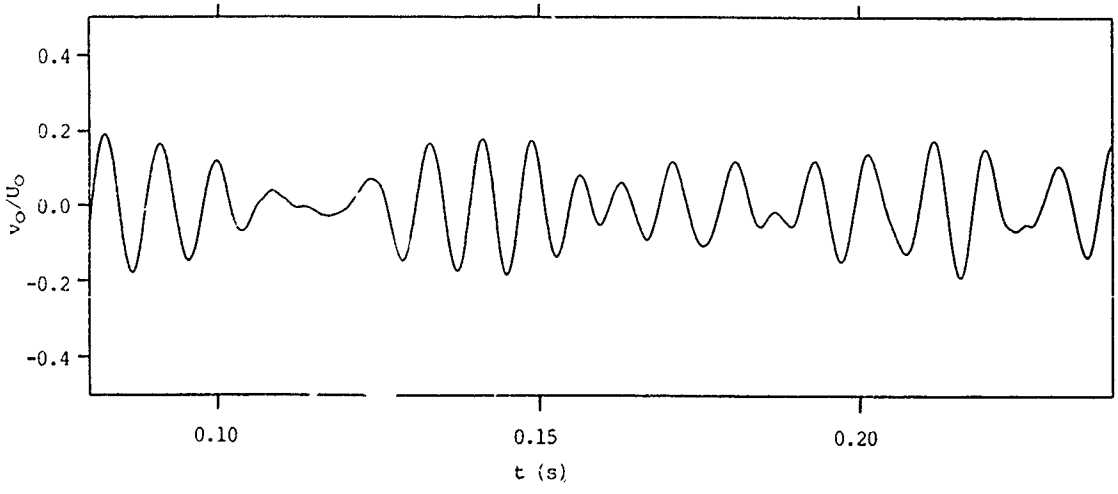

Fig. 2. Band-pass-filtered lateral velocity signal.

With the U and V signals decomposed, appropriate averages, based on the overall fluctuating components u = $\tilde{u}+u'$, v = $\tilde{v}+v'$ and uv, the coherent components, $\tilde{u}$, $\tilde{v}$ and $\tilde{u}\tilde{v}$, and the incoherent components, u', v' and $u'v'$, were determined. These statistics enable the contributions to the statistical properties of the flow due to the organized motion and those due to the random turbulent motion to be obtained.

Isocontours or phase-averaged patterns of various quantities were also determined and plotted in terms of y/W versus the phase angle ϕ, which is given by $\phi = 360\ t/T_o$, where t is time and $T_o = 1/f_o$.

The phase-averaging was accomplished as follows (Kiya and Matsumura, 1988): consecutive instants t_1 and $t_2 = t_1 \pm T_o$ were determined such that the conditioning signal, v_o, satisfied the conditions $v_o = 0$ and $dv_o/dt > 0$ at t_1, the $t_2 - t_1$ intervals were aligned and then averaging was performed. The number of realizations used in the phase-averaging process was approximately 2,800, a value sufficiently large to enable stable phase-averaged patterns to be obtained.

In addition, spectral analysis of the u and v signals was performed, which yielded u & v auto-spectra, uv co-spectra, uv quadrature spectra and uv coherence functions.

RESULTS AND DISCUSSION

An isocontour plot of the phase-averaged spanwise vorticity ($\tilde{\omega}_z = \partial\tilde{v}/\partial x - \partial\tilde{u}/\partial y$), obtained with the aid of Taylor's hypothesis, is presented in Fig. 3. It is evident from this figure that there are large-scale coherent structures present within the porous-body wake at x/W = 24. These structures are vortices possessing a dominant spanwise vorticity (ω_z); also, they occur in a quasi-periodic fashion, with a period $T_o = 1/f_o$, and alternately on either side of the horizontal centre-plane of the flow, with their vorticity concentrated near this plane at approximately y/W = ± 0.5. Isocontour plots of the phase-averaged streamwise and lateral velocities ($\tilde{u}$ and $\tilde{v}$) are presented in Fig. 4 and 5 respectively. As expected, these figures show that (a) the centres of the $\tilde{u}$ isocontours are located on either side of centre-plane of the flow in the vicinity of y/W = ± 1.0, while the centres of the $\tilde{v}$ isocontours are located in the vicinity of y/W = 0.0, and (b) the spacing between the centres is essentially constant, corresponding to $T_0/2$. At this streamwise location (x/W = 24), the present porous-body wake is thus qualitatively similar to a plane solid-body wake in the early stages of its evolution (e.g., Kiya and Matsumura, 1988). It should be emphasized, however, that there is no evidence of large-scale coherent structures in the present flow prior to x/W ≈ 10. In contrast, in the case of a solid-body wake, "Karman" vortices (with dominant spanwise vorticity) occur almost immediately downstream of the wake-generator, i.e., by x/W = 2 (Zucherman, 1988). This difference between a solid-body wake and the present porous-body wake stems from the fact that the coherent structures in the latter flow are the product of the formation and evolution of two shear layers at the upper and lower edges of the wake-generator (i.e., the mesh-strip) which do not roll-up until x/W ≈ 10. Another difference between the two "wake types" is that, in the near region of the porous-body wake (x/W < ~ 10), before the large-scale vortices are completely formed, the central core of the flow is similar to a homogeneous turbulent flow, containing turbulent fluid with a relatively wide range of scales of motion; whereas, the central core of the near region of a solid-body wake contains essentially unstable laminar (vortical) fluid.

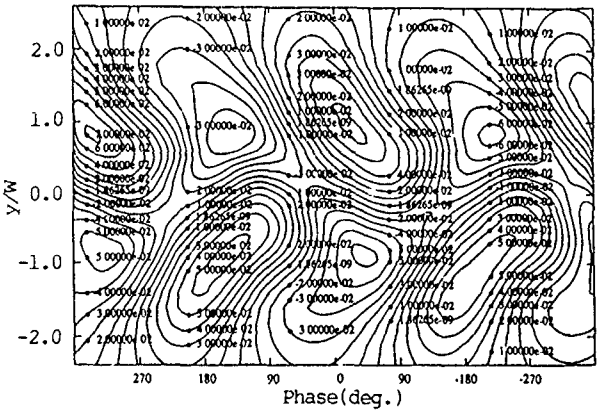

Fig. 4. Phase-averaged streamwise velocity iso-contours.

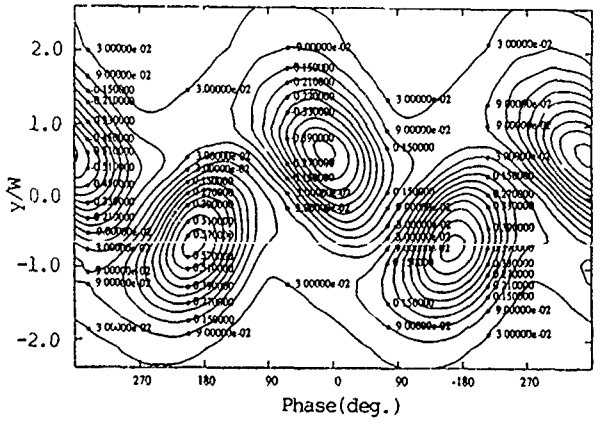

Fig. 3. Phase-averaged vorticity iso-contours.

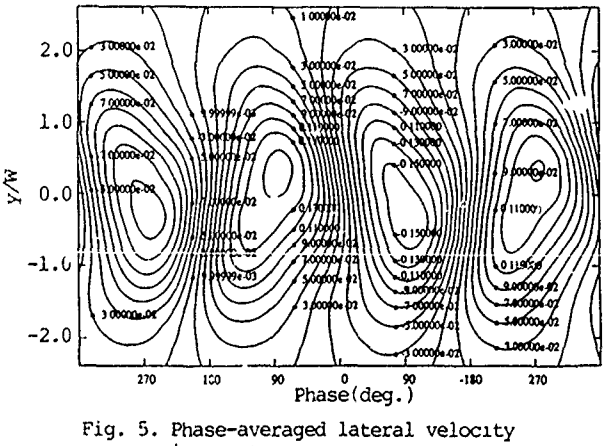

Fig. 5. Phase-averaged lateral velocity iso-contours.

Moreover, the fluid constituting the coherent structures in the porous-body wake is a mixture of laminar fluid and fine-scale turbulent fluid, since, as the two aforementioned laminar shear layers develop, they entrain both turbulent fluid from the core of the wake and potential fluid from the free-stream. On the other hand, the fluid constituting the coherent structures in a solid-body wake is, by comparison, essentially laminar fluid only. The detailed characteristics of the (near-region) coherent structures within a porous-body wake can therefore be expected to be considerably different from those of the (near-region) coherent structures within a solid-body wake. The results presented below serve to establish this difference.

Lateral (y) distributions of the streamwise and the lateral mean-square velocities and the Reynolds shear stresses due to the coherent motions and the random turbulent motions (Fig. 6(a) and (b), Fig. 7(a) and (b), Fig. 8(a) and (b)) indicate that the relative contributions to the overall statistical properties of the flow from the two types of motions are substantially different with respect to the present porous-body wake and the solid-body wake examined by Kiya and Matsumura (1988). To be specific, for the present porous-body wake, the ratio of the maximum value of $\tilde{u}^2$ (coherent) to the value of $\overline{u'^2}$ (random) at the corresponding y/W location is about 0.4, whereas, for the solid-body wake examined by Kiya and Matsumura (1988), this ratio is about 0.2. Also, for the present wake, the ratio of the maximum value of $\tilde{v}^2$ to the value of $\overline{v'^2}$ at the corresponding y/W location is about 3.3, whereas, for the solid-body wake, this ratio is about 1.4. And, for the present wake, the ratio of the maximum value of $\tilde{u}\tilde{v}$ to the value of $\overline{u'v'}$ at the corresponding y/W location is about 2.0, whereas, for the solid-body wake, this ratio is about 0.2.

Further evidence of the difference between the near-region coherent structures within the present porous-body wake and those within a solid-body wake is provided by Figs. 9,10,11 and 12, which show the uv co-spectrum, the u' autospectrum, the v' autospectrum and the $u'v'$ co-spectrum respectively pertaining to y/W = 0.6, where the magnitude of the overall Reynolds shear stress ($\overline{uv}$) is close to its maximum value. (The u' and v' signals on which the spectra in Figs. 10-12 are based were obtained via digital band-pass filtering of the corresponding u and v signals, with the band-pass filter centred at approximately f_0.) As can be seen from Fig. 9, the Fourier components that contribute to

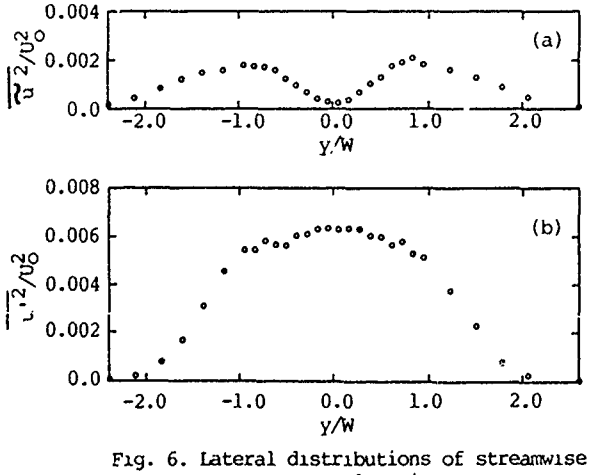

Fig. 6. Lateral distributions of streamwise mean-square velocities:
(a) due to coherent motion,
(b) due to random motion.

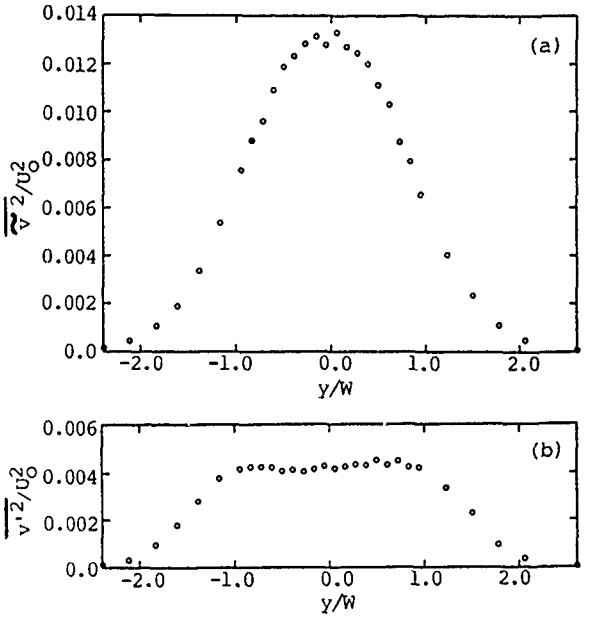

Fig. 7. Lateral distributions of lateral mean-square velocities:
(a) due to coherent motion,
(b) due to random motion.

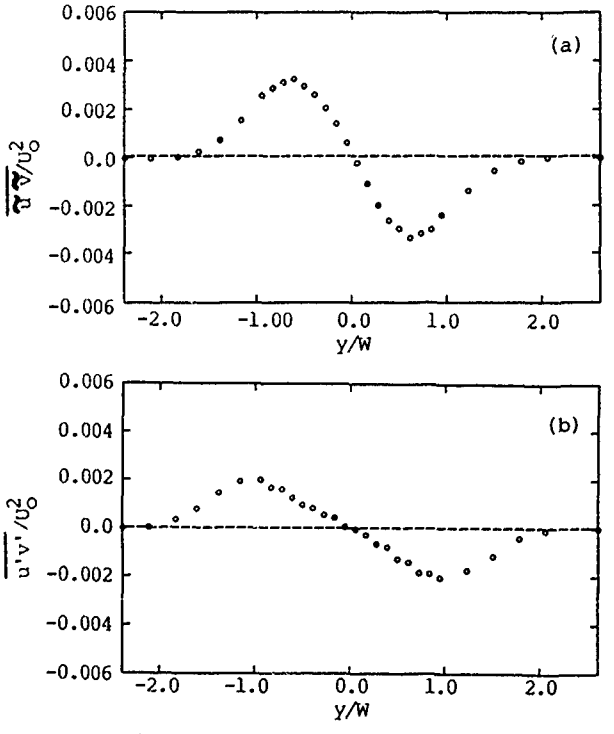

Fig. 8. Lateral distributions of Reynolds shear stresses:
(a) due to coherent motion,
(b) due to random motion.

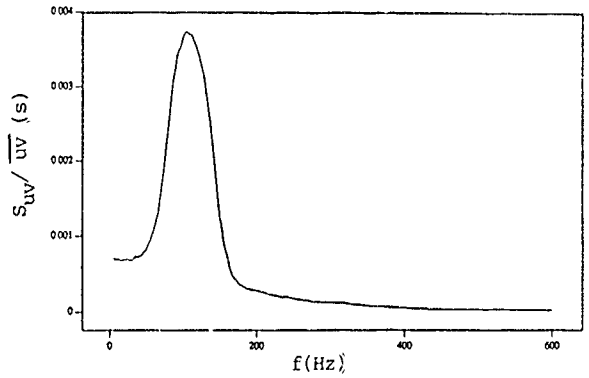

Fig. 9. Streamwise and lateral velocity co-spectrum at x/W=24 and y/W=0.6.

the coherent motion are confined to a relatively narrow band of frequencies centred at f_0 = 100 Hz. On the other hand, it is evident from Figs. 10-12 that the Fourier components contributing to the random motion are spread over a wide band of frequencies extending from 0 Hz to the cut-off frequency of 5000 Hz used in the present work and that there is no frequency centred activity below f_0. In contrast, in the case of the solid body wake examined by Kiya and Matsumura (1988), the $u'v'$ co-spectrum displays a distinct frequency-centred activity in the vicinity of $f_0/2$. As well, these authors established that the Fourier components associated with the latter frequency make the major contribution to $\overline{u'v'}$ (the random Reynolds shear stress) and that there is little contribution from Fourier components associated with frequencies greater than f_0. From this, they inferred that the coherent structures within the near region of their solid-body wake are physically inter-connected via 'ribs' which are themselves organized structures arranged in the spanwise direction, with dominant vorticity perpendicular to the dominant spanwise vorticity of the main structures. The present results serve to show that there are no dominant Fourier components contributing to $\overline{u'v'}$ in the case of the porous-body wake. Thus, it can be concluded that the near-region coherent structures of this flow are not inter-connected via 'ribs'.

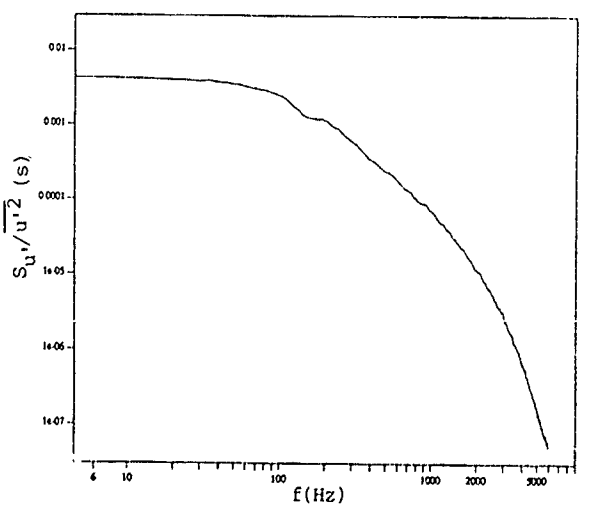

Fig. 10. Random streamwise velocity autospectrum at x/W=24 and y/W=0.6.

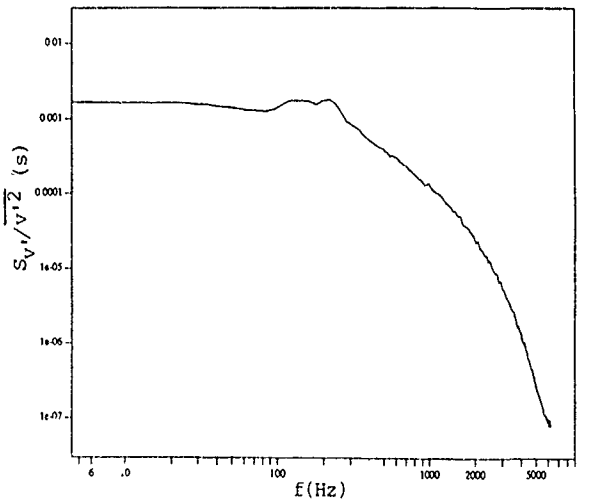

Fig. 11. Random lateral velocity autospectrum at x/W=24 and y/W=0.6.

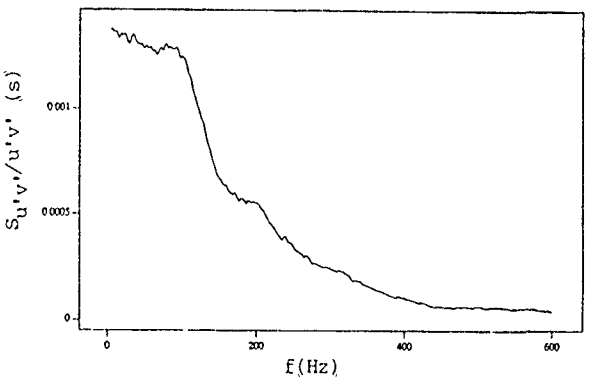

Fig. 12. Random streamwise and lateral velocity co-spectrum at x/W=24 and y/W=0.6.

ACKNOWLEDGEMENT

This research was supported by the Natural Sciences and Engineering Research Council of Canada through Grant A-2746.

REFERENCES

HUSSAIN, A.K.M.F. 1986 Coherent structure and turbulence. *J. Fluid Mech.* 173, 303 - 365.

KIYA, M. and MATSUMURA, M. 1988 Incoherent turbulent structure in the near wake of a normal plate. *J. Fluid Mech.* 190, 343 - 356.

LOUCHEZ, P.R. KAWALL, J.G. and KEFFER, J.F. 1987 Detailed spread characteristics of plane turbulent wakes. *Proc. 5th Symp. on Turbulent Shear Flows, Lectures Notes in Physics*. Springer Verlag, 98 - 109.

REYNOLDS, W.C. and HUSSAIN, A.K.M.F. 1972 The mechanism of an organized wave in turbulent shear flow. Part 3. Theoretical models and comparisons with experiments. *J. Fluid Mech.* 54, 263 - 288.

WYGNANSKI, I., CHAMPAGNE, F. and MARASLI, B. 1986 On the large-scale structures in two-dimensional, small-deficit wakes. *J. Fluid Mech.* 168, 31 - 71.

ZUCHERMAN, L. 1988 An investigation of coherent structures within plane wakes using a pattern-recognition technique. *Ph.D. Thesis,* University of Toronto.

EIGHTH SYMPOSIUM ON
TURBULENT SHEAR FLOWS
Technical University of Munich
September 9-11, 1991

On the Quasi-Coherent Turbulence Structures in the Two-Dimensional Channel Flow

Koichi NISHINO*) and Nobuhide KASAGI)**

*) Department of Mechanical Engineering and Materials Science,
Yokohama National University,
Tokiwadai 156, Hodogaya-ku, Yokohama 240, Japan

**) Department of Mechanical Engineering,
The University of Tokyo,
Hongo 7-3-1, Bunkyo-ku, Tokyo 113, Japan

ABSTRACT

The quasi-coherent turbulence structures have been studied using an experimental data base of a fully-developed two-dimensional turbulent channel flow. The data base was obtained by Nishino & Kasagi (1989) using the three-dimensional particle tracking velocimeter (3-D PTV). The stochastic estimation proposed by Adrian (1975) is used to approximate the flow patterns that most contribute to the Reynolds stress generation. The two flow patterns being estimated reveal the streamwise vortical structures, which are respectively associated with the ejection and the sweep. They are inclined to the wall at 10° with spanwise and streamwise extent of about $50\nu/u_\tau$ and $300\nu/u_\tau$, respectively. Analysis of vorticity fields reveals that typical hairpin-like vortex lines are seldom created near the wall. Based on these results, a conceptual model of the vortical structures is proposed.

NOMENCLATURE

H	: channel width
L_{ij}	: estimation coefficients
l_x, l_z	: length scales in the x- and z- directions
$P(\phi, \theta)$	: joint probability density function of ϕ and θ
Re_c	: Reynolds number $= u_c H/\nu$
Re_τ	: Reynolds number $= u_\tau H/2\nu$
R_{uu}, R_{vv}, R_{ww}	: Two-point correlation functions
u', v', w'	: velocity fluctuations in the x-, y- and z-directions
u_c	: center-line velocity
u_τ	: friction velocity
x, y, z	: streamwise, wall-normal and spanwise directions
ν	: kinematic viscosity
Ω_z	: mean vorticity in the z-direction
ω_x', ω_y', ω_z'	: vorticity fluctuations in the x-, y- and z-directions
ϕ, θ	: angles of velocity vector
$(\ )_{rms}$	: root-mean-square value
$(\hat{\ })$	: conditionally averaged value
$< >$	: ensemble-averaged value

INTRODUCTION

The quasi-coherent structures in turbulent wall shear flows have been studied by many researchers over the past three decades, and various types of the structures have been reported (see, e.g., Kline and Robinson, 1990). Using the direct numerical simulation (DNS) data base, Robinson et al. (1990) extensively studied interrelation among various instantaneous turbulence structures perceived in a simulated turbulent boundary layer. Since those structures show very large variation in their size and strength between realizations, ensemble averaging is necessary to capture their common and universal characteristics that are essential to the better understanding of their role on the turbulence mechanism.

The stochastic estimation devised by Adrian (1975, 1978) is advantageous for obtaining averaged features of the turbulence structures. Unlike the conditional sampling techniques such as the four-quadrant and VITA analyses, this technique is based on unconditional statistics, i.e., correlation functions of fluctuating quantities of interest. This property makes the technique very attractive in providing well-converged results from relatively small number of data. In addition, direct linkage between the estimated flow patterns and the correlation functions allows objective interpretation of the role of the turbulence structures. Despite these advantages, however, it has rarely been applied to the experimental data of turbulent shear flows; a few exceptions are studies by Adrian et al. (1987a), Guezennec and Choi (1988) and Guezennec (1989). This is because it requires full information on the two-point correlation functions which are hard to measure with the conventional velocimeters. Hence, the stochastic estimation has mostly been applied to the analysis of the DNS data base, e.g., Adrian et al. (1987b), Moin et al. (1987) and Adrian & Moin (1988). These studies have revealed in detail important characteristics of the turbulence structures, most of which, however, have not been confirmed experimentally. One of the objectives of the present study is to provide an experimental evidence that can be compared with those DNS results.

The authors have developed a three-dimensional particle tracking velocimeter (3-D PTV) that can measure an instantaneous distribution of all the three velocity components in a measuring volume. Details on this technique can be found in Nishino et al. (1989), Sata et al. (1989) and Kasagi & Nishino (1990). Using this velocimeter, Nishino & Kasagi (1989) measured a fully-developed two-dimensional turbulent channel flow; the flow conditions are compiled in Table 1. The measuring volume was 40×40×40 mm^3 ($200\times200\times200$ ν^3/u_τ^3), which covers the region from the wall to the channel center. An average of 140 instantaneous vectors were simultaneously measured at random positions in the measuring volume, and a total of 32,000 3-D vector distributions were obtained. The data base was qualified in Nishino & Kasagi (1989) through detailed comparison with the previous experimental and DNS data. In the present study, this data base was further analyzed to investigate the quasi-coherent turbulence structures.

Table 1. Basic Flow Conditions

H = 80 mm, $\nu = 0.831\times10^{-6}$ m^2/s, u_c = 78.0 mm/s,
u_τ = 4.27 mm/s, Re_c = 7510, Re_τ = 205.

LINEAR STOCHASTIC ESTIMATION

The linear stochastic estimation is briefly described below; readers should refer to Adrian (1975, 1978) for full information. This technique approximates a conditionally averaged velocity field, $\hat{u}'_i(\mathbf{x}+\mathbf{r})$, as a linear combination of given conditions, $u'_j(\mathbf{x})$, as follows:

$$\hat{u}'_i(\mathbf{x}+\mathbf{r}) = L_{ij}(\mathbf{x},\mathbf{r})u'_j(\mathbf{x}), \qquad i = 1, 2, 3, \tag{1}$$

where repeated subscripts are summed. As the velocity conditions, the present analysis uses three fluctuating velocity components at a prescribed position in the flow field, i.e., (u', v', w') at y^+=14.5. $L_{ij}(\mathbf{x},\mathbf{r})$ are determined so that the mean square error between the estimated velocity field and the instantaneous realization is minimized,

$$< \{\hat{u}'_i(\mathbf{x}+\mathbf{r}) - L_{ij}(\mathbf{x},\mathbf{r})u'_j(\mathbf{x})\}^2 > = \text{minimum}. \tag{2}$$

This equation is formally solved for $L_{ij}(\mathbf{x},\mathbf{r})$ as follows:

$$L_{ij}(\mathbf{x},\mathbf{r}) = <u'_j(\mathbf{x})u'_k(\mathbf{x})>^{-1}<u'_i(\mathbf{x}+\mathbf{r})u'_k(\mathbf{x})>, \tag{3}$$

where $<u'_j(\mathbf{x})u'_k(\mathbf{x})>$ are the one-point, second-order correlations and $<u'_i(\mathbf{x}+\mathbf{r})u'_k(\mathbf{x})>$ are the two-point, second-order spatial correlation functions. It is obvious that $\hat{u}'_i(\mathbf{x}+\mathbf{r})$ represents the most probable velocity field in a sense of the least square error under the given conditions. This feature of the estimation is exploited in order to approximate flow patterns that most contribute to the Reynolds stress generation.

Full components of the two-point, second-order spatial correlation functions are calculated from the data base in the region of $-150 \le x^+ \le 150$, $0 \le y^+ \le 150$ and $-150 \le z^+ \le 150$. Examples of the streamwise and spanwise correlation coefficients are shown in Fig. 1. These results are in reasonable agreement with the DNS data reported by Kuroda (1990, Re_τ=150); some scatter is due to an insufficient sample size. These correlation functions and the one-point correlations previously reported in Nishino & Kasagi (1989) are used to solve Eq. (3) for $L_{ij}(\mathbf{x},\mathbf{r})$.

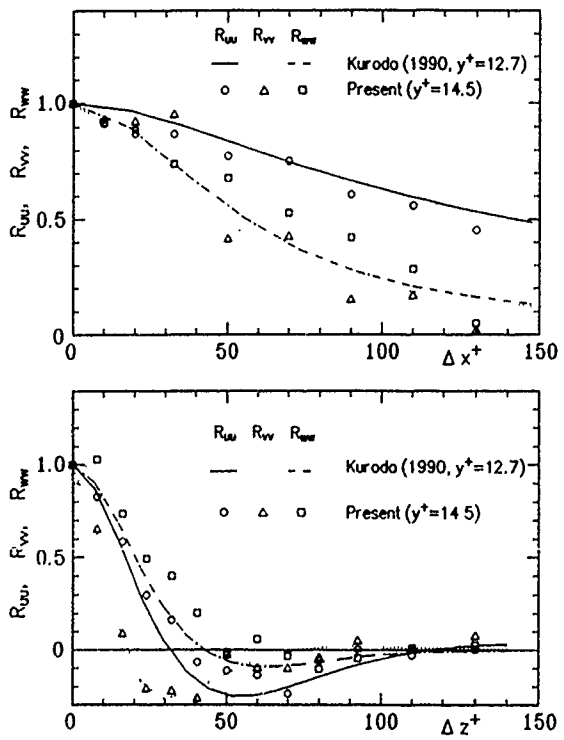

Figure 1. Streamwise and spanwise correlation coefficients calculated from the 3-D PTV data base.

The velocity conditions (u'(x), v'(x), w'(x)) are determined by taking advantage of linearity of the linear stochastic estimation. As described by Moin et al. (1987), the estimated velocity field *does not* alter its pattern with the proportional changes in the intensity of the velocity conditions. For example, the conditions of (u'(x), v'(x), w'(x)) and (ku'(x), kv'(x), kw'(x)) produce exactly the same flow patterns with difference only in their strength by a factor of k. The proportional change preserves the direction of the velocity vector, thus a joint probability density function (PDF) of three-dimensional velocity angles is investigated as below.

The two velocity angles, ϕ and θ, are defined as shown in Fig. 2. With this definition, each quadrant of the ϕ-θ plane, shown in Fig. 3, corresponds to that of the u'-v' plane used in the four-quadrant analysis. In both cases, the first to fourth quadrants respectively represent the outward interaction, the

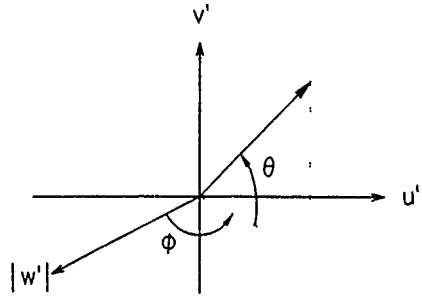

Figure 2. Definition of two vector angles, ϕ and θ.

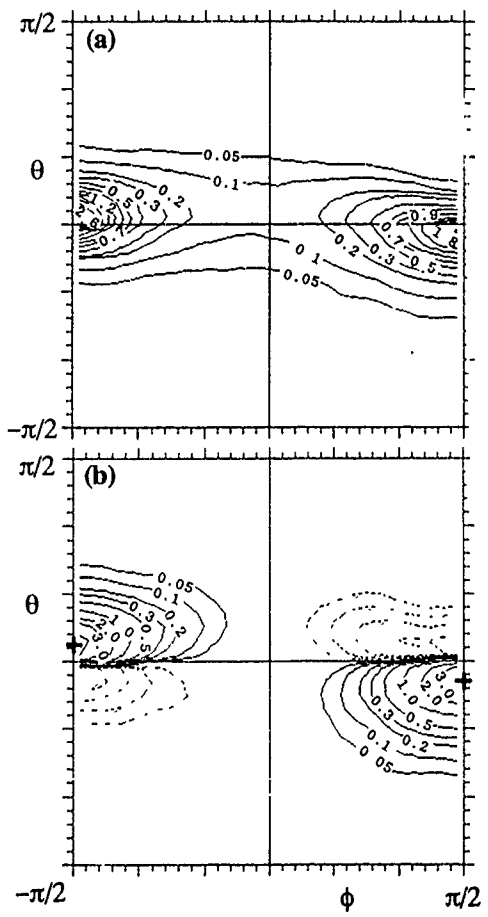

Figure 3. Contour maps at y^+=14.5: (a) PDF of three-dimensional vector angles, P(ϕ, θ), (b) probability weighted Reynolds shear stress, -u'v'P(ϕ, θ).

ejection, inward interaction and the sweep. The joint PDF of ϕ and θ, $P(\phi, \theta)$, is defined as follows;

$$\Pr\{\phi<\Phi\le\phi+d\phi,\ \theta<\Theta\le\theta+d\theta\}=P(\phi,\theta)\sin\theta d\phi d\theta. \quad (4)$$

The contour map of $P(\phi, \theta)$ at $y^+=14.5$ is shown in Fig. 4(a). With this PDF, the probability-weighted Reynolds stress, $-u'v'P(\phi, \theta)$, is calculated: its contour map is given in Fig. 3(b). It exhibits two sharp peaks in the second (ejection) and the fourth (sweep) quadrants; the dominant Reynolds stress generation occurs in these particular vector directions The peak locations are $(\phi, \theta)=(-90°, 7°)$ for the ejection and (90°, -9°) for the sweep with uncertainty of ±2°. Both peaks locate at $|\phi|=90°$, indicating that the spawise velocity component has a negligible influence on the Reynolds stress generation. Moin et al. (1987) used the velocity conditions determined from the probability-weighted joint PDF of u' and v', i.e., $-u'v'P(u', v')$, by assuming w'=0. The present result supports their assumption and is consistent with their values: for the ejection and the sweep, θ=4.8° and -4.5° at y^+=12.06, and 8.4° and -7.3° at y^+=19.22 in their analysis. The velocity conditions corresponding to these peaks are given in the present stochastic estimation. As for the intensity of the conditions, the rms value of u' at y^+=14.5, i.e., $2.7u_\tau$, is used as a representative velocity scale. Thus, the velocity conditions are given as follows;

ejection conditions: $u'^+=-2.7$, $v'^+= 0.33$, $w'^+= 0$,
sweep conditions: $u'^+= 2.7$, $v'^+=-0.43$, $w'^+= 0$.

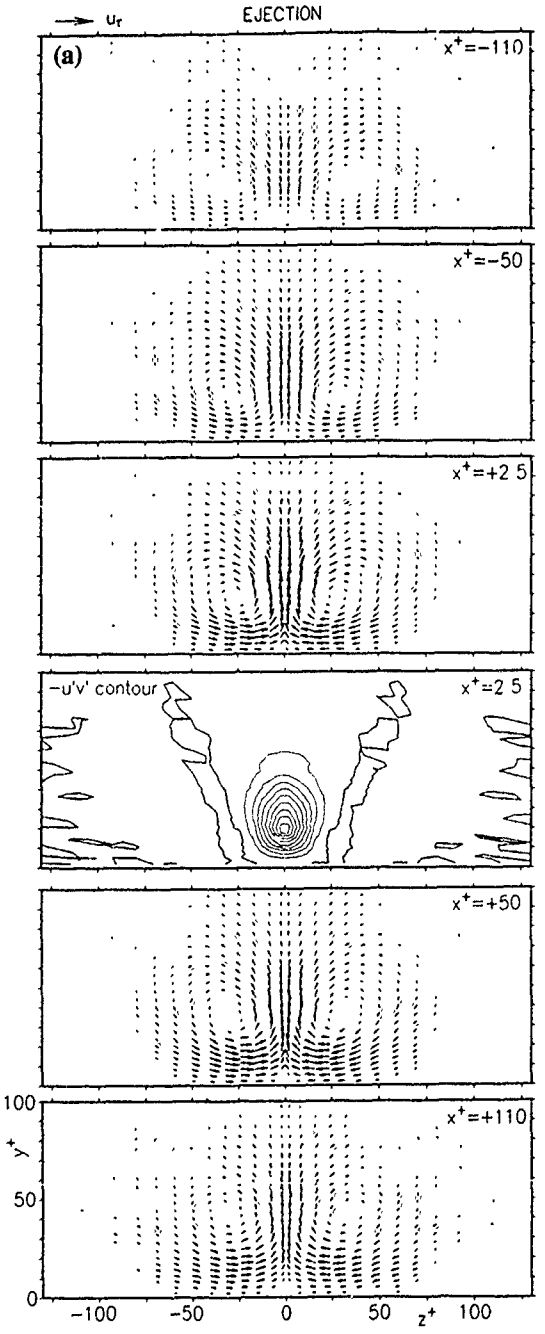

Figure 4. Velocity field estimated for the ejection conditions: (a) cross-flow plane at several streamwise locations (looking downstream), (b) x-y plane at z^+=2, (c) x-z plane at y^+=14.5.

RESULTS AND DISCUSSION

Figure 4 shows the velocity field estimated under the ejection conditions given at $(x^+, y^+, z^+)= (0, 14.5, 0)$. A pair of counter-rotating streamwise vortical structures, between which intense ejection of low-speed fluid is observed, are clearly recognized in Fig. 4(a). This flow pattern is highly similar to that of Moin et al. (1987). Since the given conditions are those having the highest value of $-u'v'P(\phi, \theta)$, the vortical structures shown here most contribute to the generation of the Reynolds shear stress. It is noted that their spanwise symmetry has unavoidably arisen from statistical averaging; some caution is therefore needed when they are compared to an instantaneous flow pattern. The vortical structures are inclined to the wall at a shallow angle of about 10°, and their centers are located at y^+~30 in the plane of x^+=2.5. The spanwise separation of the centers is roughly $50\nu/u_\tau$, which is consistent with the sublayer streak spacing (λ^+=100). To the contrary, their streamwise length seems to be much smaller than that of the streaks; the vortical motions considerably attenuate even at $x^+=\pm110$ while the streaks frequently extend over $1000\nu/u_\tau$ as reported by Iritani et. al. (1985). As shown in Fig. 4(a), the diameter of the vortical structures slightly increases as going downstream. Figures. 4(b) and 4(c) show that the low speed region spreads

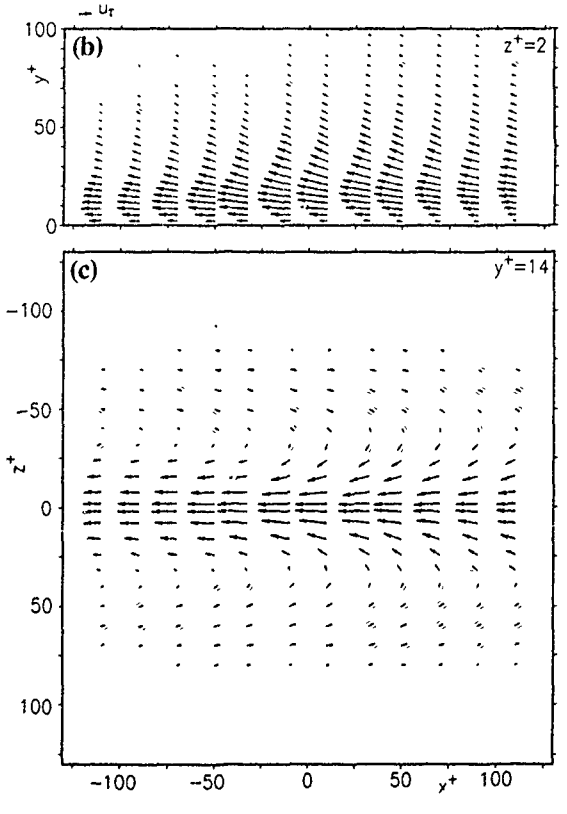

from the wall to the outer layer (y^+~100) and is elongated in the streamwise direction.

The velocity field estimated under the sweep conditions is shown in Fig. 5. A pair of streamwise vortical structures are reconstructed again as the second representative flow pattern responsible for the Reynolds stress generation. Between them, wallward impingement of high-speed fluid is observed. Except for the direction of rotation, their structural features are similar to those estimated for the ejection condition.

It is worth emphasizing that Figs. 4(b) and 5(b) do not show the internal shear layer (ISL) that is detected by the VITA and VISA techniques (see, e.g., Johansson et. al., 1987, 1988). Using the stochastic estimation, Adrian et al. (1987b) approximated the ISL by specifying two sets of the conditions given at two separate positions. The reconstructed flow pattern demonstrate the existence of two pairs of vortical structures aligning in the streamwise direction and interacting with each other. This result is consistent with the previous study of Kim (1985), who revealed that a pair of ejection-associated vortices are followed from upstream by a pair of sweep-associated ones. Judging from these and present evidence, it is concluded that the ISL is a result of the interaction of the two (pairs of) vortical structures such as those shown in Figs. 4 and 5.

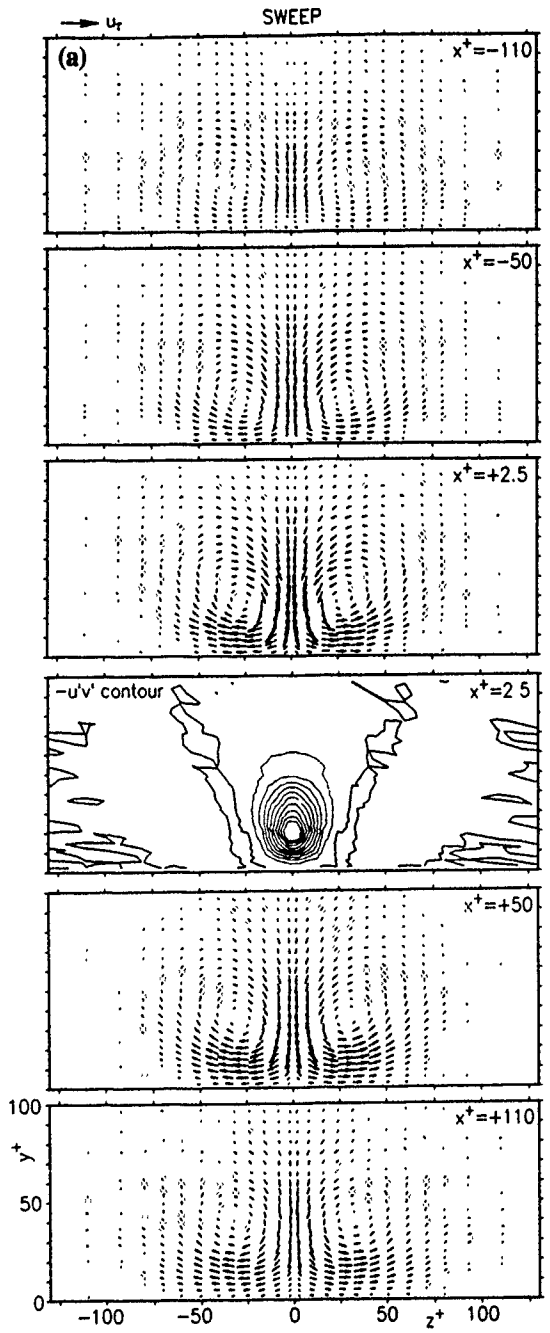

Figure 5. Velocity field estimated for the sweep conditions: (a) cross-flow plane at several streamwise positions (looking downstream), (b) x-y plane at z^+=2, (c) x-z plane at y^+=14.5.

Relationship between the vortical structures and the vorticity fields is investigated. To do this, the estimated velocity fields were smoothly interpolated using 5th-order B-spline functions, then spatial derivatives of velocity fluctuations, $\partial u_i'/\partial x_j$, are calculated. It is verified that the spline functions capture the velocity field reasonably well and they can resolve primary vorticity fields associated with the large vortical motions. Figures 6 and 7 respectively show vortex lines of the total vorticity, $\omega_i'+\Omega_z$, for the ejection and sweep conditions, where Ω_z is calculated from the slope of the mean velocity distribution and each vortex line starts at (y^+, z^+)=(20, 100). The vortex lines are elongated almost straight in the spanwise direction with negligible deformation; it reflects the fact that Ω_z is much larger than ω_x' and ω_y' calculated here.

Since the deformation is affected by the ratio of ω_i' and Ω_z, the intensity of ω_i' for the ejection vortices is tentatively raised by a factor of four. Note that this increase is equivalent to giving the four times stronger conditions to the estimation of the velocity field, thus approximating very strong vortical motions. In Fig. 8, hairpin-like vortex lines can be recognized while the deformation is still insufficient so as to create the typical hairpin shape. The distortion is caused by the outward or inward fluid movement associated with the vortical motions. This result clearly demonstrates that the typical hairpin-like deformation reported in the literature seldom occurs to the vortex lines originating in the near wall region. The hairpin-like deformation of the vortex lines do not necessarily mean the hairpin vortices, rather it can be created by the streamwise vortical structures shown in Figs 4 and 5. For comparison, the vortex lines starting at (y^+, z^+)=(50, 100) are represented in Fig.

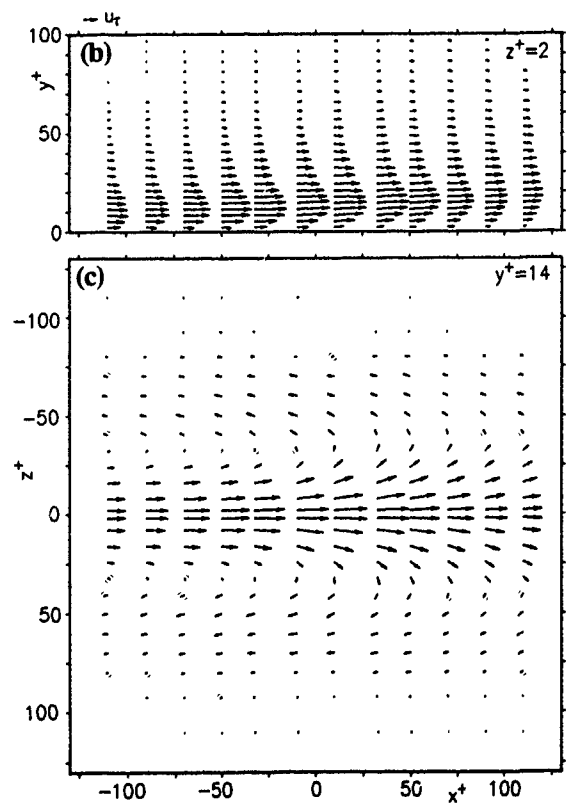

9; the typical hairpin-like vortex lines are formed.

The above discussion leads to a question on the hypothesis that the streamwise vortical structures originate from the roll-up of the spanwise vorticity at the wall For reference, the rms values of ω_i' for the ejection vortices are calculated by taking an average over $-100 \le x^+ \le 100$ and $-100 \le z^+ \le 100$ at each distance from the wall. They are shown in Fig. 10 along with the DNS data of Kuroda (1990). The present values are considerably lower than the DNS data as expected from the common feature of turbulence that major vorticity fluctuations is accompanied with the small scale motions; however general similarities in the profiles suggest that analogous streamwise vortical structures with smaller scale are the major contributor to the vorticity fluctuations. It is noted that multiplication of ω_i' by a factor of four would increase the present values to those comparable to the DNS data. These results demonstrate that the streamwise vortical structures cannot be captured solely by an analysis based on the vortex lines.

Finally, a conceptual model of the streamwise vortical structures are presented in Fig. 11 along with the topological relation with the vortex lines. A separate study of Nishino (1989) shows that these vortical structures move straight downstream with a convention velocity of $10\sim13u_\tau$. General features of the present model are similar to those presented by Nagib & Guezennec (1986) whereas there is a notable difference; i.e., their model has much larger streamwise and spanwise extent ($l_x^+\sim1300\nu/u_\tau$, $l_z^+\sim500\nu/u_\tau$) than the present one ($l_x^+\sim300\nu/u_\tau$, $l_z^+\sim50\nu/u_\tau$).

In a simulated turbulent boundary layer, Robinson et al. (1990) reported the existence of hook-shaped vortical structures which consist of 'head', 'neck' and 'leg' identified as low pressure regions. They also reported that the instantaneous flow fields frequently exhibit simultaneous occurrence of both

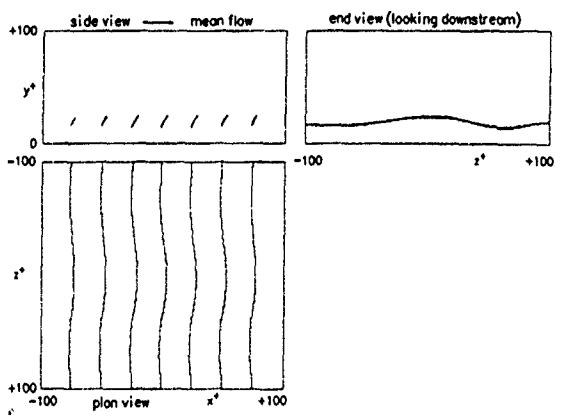

Figure 6. Vortex lines for the ejection conditions: lines start at $(y^+, z^+)=(20, 100)$.

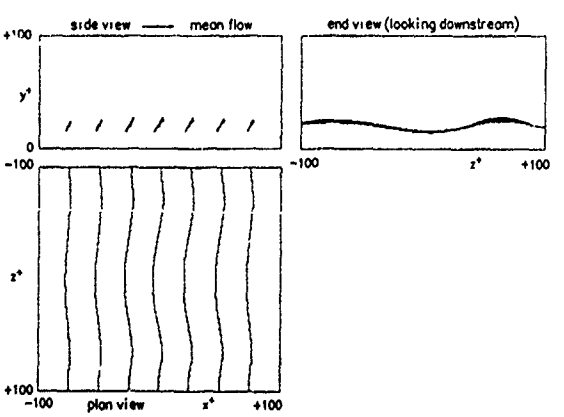

Figure 7. Vortex lines for the sweep conditions: lines start at $(y^+, z^+)=(20, 100)$.

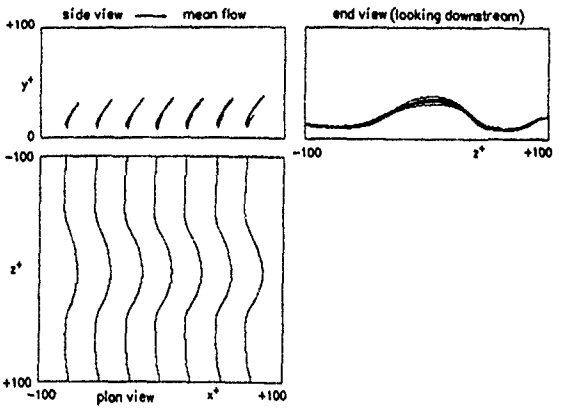

Figure 8. Vortex lines for the ejection conditions: vorticity fluctuations are multiplied by a factor of 4 and lines start at $(y^+, z^+)=(20, 100)$.

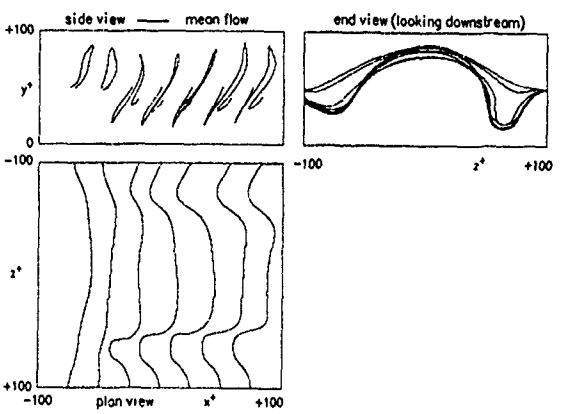

Figure 9. Vortex lines for the ejection conditions: vorticity fluctuations are multiplied by a factor of 4 and lines start at $(y^+, z^+)=(50, 100)$.

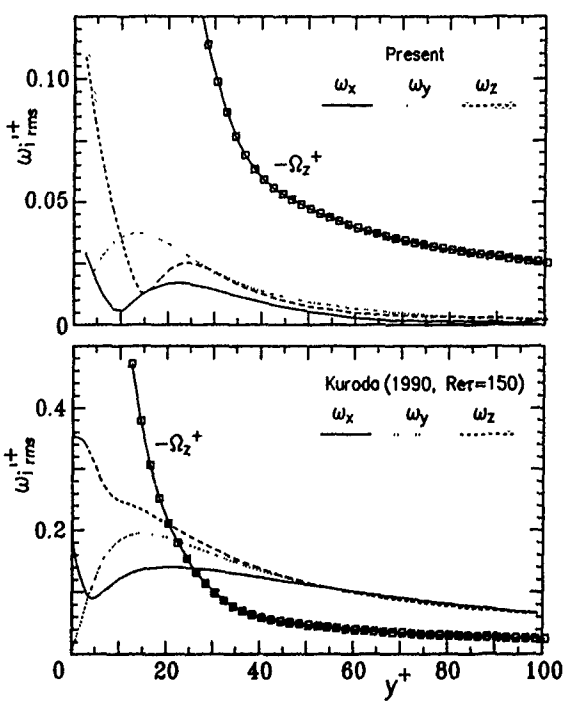

Figure 10. The rms values of vorticity fluctuations.

ejection and sweep, suggesting that a single vortical structure, probably 'leg', is responsible for both of them. These results are not confirmed by the present study which shows that (1) neither 'head' nor 'neck' is found, and (2) the ejection and the sweep are respectively generated by the two vortical motions as shown in Figs. 4 and 5. It is noted that separate estimation of Nishino (1989) under the conditions given further away from the wall, y^+=61 and 102, provide results very consistent with the present ones, thus the disagreement cannot be accounted for by the influence of the distance from the wall. Contrary to the findings of Robinson et al., the recent analysis of a DNS data base of a turbulent channel flow revealed rather infrequent occurrence of the hook-shaped vortical structures in the instantaneous flow fields (Tomita et al., 1991). As manifested by this conflict, objective and statistical analysis on the instantaneous turbulence structures concerning frequency of their occurrence, size and strength, and contribution to the turbulence mechanism is quite important to clarify the above discrepancies. Although some details might be smoothed out by the averaging procedure, the present model, being based on the unconditional statistics, should reflect essential features of the Reynolds stress generating structures in the turbulent channel flow.

CONCLUSIONS

The quasi-coherent turbulence structures have been investigated using an experimental velocity data base of a fully-developed two-dimensional turbulent channel flow. The flow pattern that most contribute to the generation of the Reynolds shear stress are approximated by the linear stochastic estimation. Two pairs of the streamwise vortical structures are shown to exist, each of which is respectively associated with the ejection and the sweep. Their structural features as well as their relationship with the streaks and the internal shear layer are examined. Detailed analysis of the vorticity fields has revealed that the typical hairpin-like deformation of the vortex lines seldom occurs in the near wall region, and that the hairpin-like vortex lines do not necessarily mean the hairpin vortex, rather they are created by the streamwise vortical structure. Based on these findings, a conceptual model of the streamwise vortical structures is proposed and its characteristics are discussed in conjunction with the previous findings.

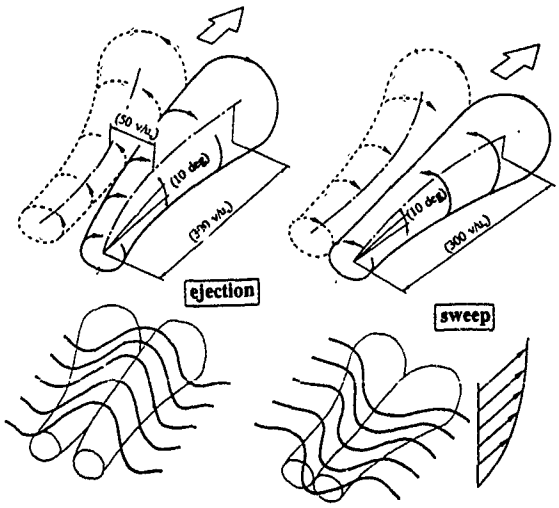

Figure 11. A conceptual model of the streamwise vortical structures.

ACKNOWLEDGEMENT

The authors are grateful to Professor M. Hirata for his cooperation during the course of this work. The first author (KN) acknowledges Professor K. Torii for his valuable cooperation to this work. The financial supports through the Grant-in Aids for General Scientific Research (No. 61460103) and for Encouragement of Young Scientists (No. 62790196) by the Ministry of Education, Science and Culture are acknowledged.

REFERENCES

Adrian, R. J., 1975, On the Role of Conditional Averages in Turbulence Theory, *Turbulence in Liquids*, ed. J. L. Akin and G. K. Paterson, Science Press, Princeton, pp. 323-332.

Adrian, R. J., 1978, Structural Information Obtained from Analysis Using Conditional Vector Events: A Potential Tool for the Study of Coherent Structures, *Coherent Structure of Turbulent Boundary Layers*, ed. C. R. Smith and D. E. Abbott, AFOSR/Lehigh, pp. 416-421.

Adrian, R. J., Chung, M. K., Hassan, Y., Jones, B. G., Nithianandan, C. K. and Tung, A. T. C., 1987a, Experimental Study of Stochastic Estimation of Turbulent Conditional Averages, *Proc. 6th Symp. Turbulent Shear Flow*, Toulouse, p. 6.1.1.

Adrian, R. J., Moin, P. and Moser, R. D., 1987b, Stochastic Estimation of Conditional Eddies in Turbulent Channel Flow, *Proc. Summer Program 1987*, Center for Turbulence Research, NASA/Stanford, pp. 7-19.

Adrian, R. J. and Moin, P., 1988, Stochastic Estimation of Organized Turbulent Structure: Homogeneous Shear Flow, *J. Fluid Mech.*, Vol. 190, pp. 531-559.

Guezennec, Y. G. and Choi, W. C., 1990, Stochastic Estimation of Coherent Structures in Turbulent Boundary Layers, *Near-Wall Turbulence, Proc. 1988 Z. Zarić Mem. Conf.*, ed. S. J. Kline and N. H. Afgan, pp. 453-468.

Guezennec, Y. G., 1989, Stochastic Estimation of Coherent Structures in Turbulent Boundary Layers, *Phys. Fluids A*, Vol. 1, No. 6, pp. 1054-1060.

Iritani, Y., Kasagi, N., and Hirata, M., 1985, Heat Transfer Mechanism and Associated Turbulence Structure in the Near-Wall Region of a Turbulent Boundary Layer, *Turbulent Shear Flow 4*, ed. L. J. S. Bradbury et al., Springer-Verlag, Berlin, pp. 223-234.

Johansson, A. V., Alfredsson, P. H. and Eckelmann, H., 1987, On the Evolution of Shear-Layer Structures in Near-Wall Turbulence, *Advances in Turbulence*, ed. G. Comte-Bellot and J. Mathieu, Springer-Verlag, Berlin, pp. 383-390.

Johansson, A. V., Alfredsson, P. H. and Kim, J., 1990, Velocity and Pressure Fields Associated with Near-Wall Turbulence Structures, *Near-Wall Turbulence, Proc. 1988 Z. Zarić Mem. Conf.*, ed. S. J. Kline and N. H. Afgan, pp. 453-468.

Kasagi, N. and Nishino, K., 1990, Probing Turbulence with Three-Dimensional Particle Tracking Velocimetry, *Proc. Int. Symp. Engineering Turbulence Modelling and Measurements*, Dubrovnik, pp. 299-314, also to appear in Exp. Therm. & Fluid Sci., 1991.

Kim, J., 1985, Turbulence Structures Associated with the Bursting Event, *Phys. Fluids*, Vol. 28, No. 1, pp. 52-58.

Kline, S. J. and Robinson, S. K., 1990, Quasi-Coherent Structures in the Turbulent Boundary Layer: Part I, Status Report on a Community-Wide Summary of the Data, *Near-Wall Turbulence, Proc. 1988 Z. Zarić Mem. Conf.*, ed. S. J. Kline and N. H. Afgan, pp. 200-217.

Kuroda, A., 1990, Direct Numerical Simulation of Couette-Poiseuille Turbulent Flows, (in Japanese), Dr. Eng. Thesis, Department of Mechanical Engineering, The University of Tokyo.

Moin, P., Adrian, R. J. and Kim, J., 1987, Stochastic Estimation of Organized Structures in Turbulent Channel Flow, *Proc. 6th Symp. Turbulent Shear Flows*, Toulouse, p. 16.9.1.

Nagib, H. M. and Guezennec, Y. G., 1986, On the Structure of Turbulent Boundary Layers, *Proc. 10th Symp. on Turbulence*, p. 1.1.

Nishino, K., Kasag , N. and Hirata, M., 1989, Three-Dimensional Particle Tracking Velocimetry Based on Automated Digital Image Processing, *Trans. ASME, J. Fluids Eng.*, Vol. 111, No. 4, pp. 384-391.

Nishino, K. and Kasagi, N., 1989, Turbulence Statistics Measurement in a Two-Dimensional Channel Flow Using a Three-Dimensional Particle Tracking Velocimeter, *Proc. 7th Symp. Turbulent Shear Flows*, Stanford, p. 22.1.1.

Nishino, K., 1989, Study on the Quasi-Coherent Structures of Wall Turbulence Using a Three-Dimensional Particle Tracking Velocimeter, (in Japanese), Dr. Eng. Thesis, Dept. Mechanical Eng., The University of Tokyo.

Robinson, S. K., Kline, S. J. and Spalart, P. R., 1990, Quasi-Coherent Structures in the Turbulent Boundary Layer: Part II, Verification and New Information from a Numerically Simulated Flat-Plate Layer, *Near-Wall Turbulence, Proc. 1988 Z. Zarić Mem. Conf.*, ed. S. J. Kline and N. H. Afgan, pp. 218-247.

Sata, Y., Nishino, K. and Kasagi, N., 1989, Whole Field Measurement of Turbulent Flows Using a Three-Dimensional Particle Tracking Velocimeter, *Flow Visualization V (Proc. 5th Int. Symp. on Flow Visualization)*, Prague, pp. 248-253.

Tomita, Y., Kasagi, N. and Kuroda, A., 1991, Heat Transfer Mechanism Associated with the Quasi-Coherent Structures in Wall Turbulence, *Proc. 28th National Heat Transfer Symp. of Japan*, Fukuoka, pp. 4-6.

EIGHTH SYMPOSIUM ON
TURBULENT SHEAR FLOWS
Technical University of Munich
September 9-11, 1991

AUTOMATIC RECONSTRUCTION OF DYNAMICAL SYSTEM EQUATIONS FROM NUMERICAL SCALAR TIME SERIES

G. Gouesbet

Laboratoire d'Energétique des Systèmes et Procédés,
I.N.S.A. de Rouen, U.R.A. C.N.R.S. 230
BP 08, 76131 MONT SAINT AIGNAN Cédex
FRANCE

ABSTRACT

Vector fields of continuous dynamical systems, or at least of equivalent systems, can be reconstructed from numerical scalar time series. Methods have been previously exemplified for the Rössler equations. This paper is devoted to the case of the Lorenz system.

I - INTRODUCTION

Applied scientists are increasingly interested by dissipative nonlinear dynamical systems. One of the good news is that some complex phenomena produced by partial derivative equations (like Navier-Stokes equations) may be in some cases understood in low-dimensional phase spaces as the consequence of deterministic chaos. Furthermore, metric and dynamical invariants characterizing the (possibly strange) attractors underlying the process may be recovered by analyzing time records of a single experimental scalar variable (an example is provided in Ref 1 in which more than 60 pioneering references are quoted). However, in agreement with Casdagli[2], we may feel disappointed and must remark that the calculated invariants are of limited practical interest. For instance, after having obtained a generalized (fractal) dimension spectrum, the question becomes : what is to be done now ? Actually, the applied scientist might be most interested if, beside the evaluation of invariants, the available numerical scalar time series would automatically allow for the construction of phenomenological models, i.e. for the reconstruction of vector fields. Refs 3-4 addressed this issue in the exemplifying simple case of Rössler equations. Our final motivation is the study of noisy experimental systems. Next item on our agenda was to carry out a similar study for another paradigm, the Lorenz system, to which this paper is devoted.

II - FORMULATION AND CLASSIFICATION OF EQUIVALENT VECTOR FIELDS

II.1 - THE ORIGINAL SYSTEM (OS)

The OS is the Lorenz system reading :

$$\dot{x} = \sigma(y-x) \qquad (1)$$

$$\dot{y} = Rx-y-xz \qquad (2)$$

$$\dot{z} = -bz+xy \qquad (3)$$

with σ=10, R=28, b=8/3 for which the asymptotic motion settles down on to a chaotic attractor[5].

II.2 - STANDARD SYSTEMS AND TRANSFORMATIONS

OS with coordinates (x,y,z) may be given a standard form with coordinates (X,Y,Z) :

$$\dot{X} = Y \qquad (4)$$

$$\dot{Y} = Z \qquad (5)$$

$$\dot{Z} = F(X,Y,Z) \qquad (6)$$

From (1)-(3), the standard function F may be written :

$$Z = AX+CY+DZ+FX^3+GX^2Y+\frac{Y}{X}[BY+EZ] \qquad (7)$$

When constants A,...,G are given their exact values (Table I), we obtain the so-called Standard Exact System (SES). We then define the Direct Standard Transformation (DST) :

constant	exact value	reconstructed values
A	$b\sigma(R-1) = 720$	719. 999 131 704
B	$\sigma + 1 = 11$	10. 999 984 392
C	$-b(\sigma+1) = 29.(3)$	- 29. 333 174 525
D	$-(b+\sigma+1) = -13.(6)$	- 13. 666 652 039
E	1	0. 999 997 892
F	$-\sigma = -10$	- 9. 999 985 331
G	-1	- 1. 000 002 238

Table I Exact and Reconstructed values of Reconstruction Constants.

$$X = x, \quad Y = \sigma(y-x) \qquad (8)$$

$$Z = \sigma[(R+\sigma)x-(\sigma+1)y-xz] \qquad (9)$$

and the Inverse Standard Transformation (IST) :

$$x = X, \quad y = x + Y/\sigma \qquad (10)$$

$$z = (R-1) - [(\sigma+1)Y+Z]/(\sigma x) \qquad (11)$$

We note that there exists a set $\{x=x_c=0\}$ of Lebesgue measure 0 for which the IST is not invertible (Rel 11) and for which the $\dot{Z}$-component of the vector field (Rel 7) is seemingly singular. We may actually show that there exists a limit of $\dot{Z}$ when $x \to x_c$ (we state that (7) is only pseudo-singular) but that, due to the lack of invertibility, $\dot{Z}(x,Y,Z)$ cannot be expressed for $x = x_c$.

The vector field reconstruction will later become a fitting problem leading to the numerical evaluations of constants A,...,G. Standard systems with reconstruction constants A,...,G being given their reconstructed values are called Standard Reconstructed Systems (SRS).

II.3 - INVERSE STANDARD RECONSTRUCTED SYSTEMS (ISRS)

ISRS's can be studied only when the OS is known. They are defined and obtained by starting from SRS's, using the DST to recover original coordinates (x,y,z) and reporting all numerical errors associated with reconstructions on the first component of the vector field, i.e. Rels (2), (3) are satisfied by ISRS's. The ISRS associated with the SRS of Rel (7) is found to be given by :

$$\dot{x} = \frac{1}{x\sigma(R+\sigma-z)}\Big\{\sigma^2(B-E\sigma)(x-y)^2 - E\sigma^2(y-x)(y+xz)$$

$$+ \sigma(C-D\sigma+ER\sigma)x(y-x) + Ax^2 + \sigma(1+\sigma+D)(Rx^2-xy-x^2z)$$

$$- b\sigma x^2z + (F-G\sigma)x^4 + \sigma(G+1)x^3y\Big\} \qquad (12)$$

Rel (12) exhibits a set of singularity of Lebesgue measure 0. However, when the reconstruction constants A,...,G are given their exact values.

ISRS's become an Inverse Standard Exact System (ISES) which simply identifies with the OS owning no singularity. Therefore, for a high quality reconstruction, the amount of parasitic singularity is very small.

II.4 - INVERSE NON STANDARD SYSTEMS (INSS)

The interest of using ISRS's when the OS is known is to provide direct convincing validations of the reconstruction techniques because comparisons can be carried out against the OS itself. When the OS is unknown, ISRS's cannot be used. However, starting from standard systems with coordinates (x,Y,Z), we may introduce Inverse Non Standard Systems (INSS) with coordinates $(x',y',z') \neq (x,y,z)$. When the OS is known, SES's become Inverse Non Standard Exact Systems (INSES). When it is unknown, SRS's become Inverse Non Standard Reconstructed Systems (INSRS). The number of INSS's being infinite, choices must be motivated. Here, the motivation comes from the fact that there is some disadvantage with standard systems because singularities will in practice require a special so-called intervention procedure to integrate the differential equations (Section III-2). We then decide to examine INSS's in which such terms would disappear or at least would become small enough to avoid the need of any special integration procedure. A formal algorithm has been designed in Ref 4 to achieve this aim. Main steps are recalled below and are applied to the SRS of Rel (7).

In Rel (7), the bracket term [BY+EZ] of the pseudo-singular term must be linear, which is here indeed the case. Our INSS's will use coordinates (x,ψ,ϕ). Variable ϕ is defined from the pseudo-singular term as :

$$\phi = \frac{BY+EZ}{Kx} + K' \qquad (13)$$

introducing two free constants K and K'. Also, for the sake of simplicity, we may decide that $\dot{x} = Y$ is given by a linear equation :

$$\dot{x} = Y = K_x x + K_\psi \psi + K_\phi \phi \qquad (14)$$

After some algebraic manipulations, preferably with the aid of symbolic computations, we may then establish a class of INSS's taking the form :

$$\dot{x} = F_1 (x,\psi,\phi,K_x,K_\psi,K_\phi) \qquad (15)$$

$$\dot{\psi} = F_2 (x,\psi,\phi,K,K',K_x,K_\psi,K_\phi,\{R\}) \qquad (16)$$

$$\dot{\phi} = F_3 (x,\psi,\phi,K,K',K_x,K_\psi,K_\phi,\{R\}) \qquad (17)$$

in which (15) identifies with (14), and (16), (17) are not given for the sake of conciseness. In these relations, {R} designates the set of reconstruction constants. Relations (16), (17) still contain a set of singularities of Lebesgue measure 0. However, when the reconstruction constants {R} are given their exact values, INSS's become INSES's in which all singularities disappear. Therefore, for high quality reconstructions, we obtain a class of INSRS's in which the parasitic amount of singularity is small enough to avoid any special procedure during the integration process. Therefore, our aim is fulfilled.

Among the INSES's, the OS is recovered with :

$$K = -\sigma,\ K' = R-1,\ K_x = -\sigma,\ K_\psi = \sigma,\ K_\phi = 0 \qquad (18)$$

As an example, a particular attention will be paid to the INSRS defined by the following free constant values :

$$\left.\begin{array}{l} K_x = K' = 0 \\ K = K_\psi = K_\phi = 1 \end{array}\right\} \qquad (19)$$

This INSRS is then found to be :

$$\dot{x} = \psi + \phi \qquad (20)$$

$$\dot{\psi} = -EA - EFx^2 - \left(\frac{B}{E} + EGx\right)(\psi+\phi) - \frac{\phi}{E}(ED+B) + \frac{\phi}{E}x - \frac{\psi+\phi}{x}\left\{EC - \frac{B}{E}(ED+B) + (F-1)\phi\right\} \qquad (21)$$

$$\dot{\phi} = EA + EFx^2 + EGx(\psi+\phi) + \frac{\phi}{E}(ED+B) + \frac{\psi+\phi}{x}\left\{EC - \frac{B}{E}(ED+B) + (E-1)\phi\right\} \qquad (22)$$

With exact values of the reconstruction constants, this INSRS becomes the following INSES :

$$\dot{x} = \psi + \phi \qquad (23)$$

$$\dot{\psi} = -b\sigma(R-1)+x(\phi+\sigma x)+(\psi+\phi)(x-\sigma-1)+b\phi \qquad (24)$$

$$\dot{\phi} = b\sigma(R-1)-x(\phi+\psi+\sigma x)-b\phi \qquad (25)$$

II.5 - SQUEEZED SYSTEMS

After integration, we find that standard systems lead to attractors exhibiting a great disparity of coordinate scales ($\Delta x \simeq 40$, $\Delta Y \simeq 300$, $\Delta Z \simeq 6000$). Although the disparity is less significant for INSS's, it still exists ($\Delta x \simeq 40$, $\Delta\psi \simeq \Delta\phi \simeq 500$). These disparities lead to underestimation difficulties when evaluating generalized dimensions spectra (Section IV). These difficulties are solved or at least considerably reduced by coordinate rescaling. We then introduce squeezed SFS's (SSES) and squeezed SRS's (SSRS) with coordinates (x,Λ,Δ) by squeezing SES's and SRS's respectively, according to :

$$\Lambda = Y/6.5,\ \Delta = Z/150 \qquad (26)$$

Similarly, we introduce squeezed INSES (SINSES) and squeezed INSRS (SINSRS) with coordinates (x,π,Γ) by squeezing the INSES and the INSRS respectively, according to :

$$\pi = \psi/18,\ \Gamma = \phi/13 \qquad (27)$$

III - RECONSTRUCTION AND QUALITATIVE VALIDATIONS

III.1 - RECONSTRUCTION TECHNIQUE AND CONSTANTS

All dynamical systems in this paper are integrated by using a fourth-order Runge-Kutta algorithm with a time step δt (except standard systems which will require two different time steps δt and $\delta t'$). In particular, integrating the OS, we obtain a time series $\{x_i\}$ which is assumed to be all our knowledge concerning the system and which is treated as an experimental numerical scalar time series. By using an accurate enough finite difference scheme[3], we may determine vectorial time series $\{x_i, Y_i, Z_i, \dot{Z}_i\}$ from scalar time series $\{x_i\}$. We are then left with a function fitting problem to determine the standard function F of Rel (6). We used the same procedure than in Ref 3, starting with a ratio of polynomial expansions, identifying on objective grounds the constants which are equal to 0 in these expansions and, dismissing these constants, we obtain F under the form of Rel (7). This relation may be rewritten as :

$$Ax^2+BY^2+CxY+DxZ+EYZ+Fx^4+Gx^3Y = x\dot{Z} \qquad (28)$$

containing 7 constants. When 7 quadruplets $\{x_i, Y_i, Z_i, \dot{Z}_i\}$ are sampled, we obtain a linear set of equations to be solved to evaluate the reconstruction constants. For the sake of accuracy, it is actually better to solve N_s sets and to carry out averages. The procedure is again the same as in Ref 3, including the use of a discrimination scheme. The research of the best results (in the sense

defined in Ref 3) is carried out by optimizing over the number of quadruplets sampled by pseudo-period $T_0 \simeq 0.73$, the Runge-Kutta time step δt and the number of sets N_s. The final reconstructed values of the reconstruction constants are given in Table I.

III.2 - QUALITATIVE VALIDATIONS

They rely on visual comparisons between graphical displays of exact and reconstructed attractors. All graphical displays presented in this section correspond to an integration of the systems during 100 pseudo-periods T_0 with about 10^2 points sampled per T_0, and a single integration time step $\delta t = 10^{-3}$ (except when stated otherwise for standard systems), with initial conditions taken on the attractors after transient killing.

Fig 1 shows the OS in which we recognize the celebrated Lorenz butterfly. The ISRS (becoming an ISES identifying with the OS for perfect reconstruction) with the $\dot{x}$ of Rel (12) and reconstruction constant values taken from Table I, is shown in Fig 2. The comparison between Figs 1 and 2 is very good indeed.

The SES may be obtained by integrating the OS and applying the DST to each sampled point. This procedure is trivial because no singularity appears in the OS nor in the DST, confirming the pseudo-singular character of the SES-vector field. We then obtain the bow-tie attractor displayed in Fig 3. We note the announced disparity of scales Δx, ΔY, ΔZ.

SES, and more generally, SES's and SRS's, squeezed or not, may be obtained by integrating the corresponding vector fields. A special so-called intervention procedure is there required due to the existence of a critical set $\{x=x_c=0\}$. Although this critical set is of Lebesgue measure 0, i.e the probability of landing on this set during a discrete integration procedure is 0, there is a numerical unsafe domain surrounding x_c in which numerical errors cumulate leading possibly to the ejection of the computed trajectory outside of the attractors. The intervention procedure is described in Ref 4. It uses two time steps δt and $\delta t'$, the second one being activated in a domain surrounding x_c, detects inaccuracies and corrects them. A SES with $\delta t' = 3.10^{-7}$ and the corresponding SRS are displayed in Figs 4 and 5 respectively. Corresponding squeezed systems look rather identical but for the rescaling of coordinates. Figs 3-5 compare very favourably (note that identities between figures should not be expected due to sensitivity to initial conditions).

The INSES of Rels (23)-(25) and the corresponding INSRS of Rels (20)-(22) are displayed in Figs 6 and 7, comparing again very favourably. Corresponding squeezed systems again look rather identical but for the rescaling of scales.

IV - QUANTITATIVE VALIDATIONS

They rely on comparisons between generalized (fractal) dimensions D_q of exact and corresponding reconstructed systems. Computations are carried out by using a fixed-radius approach. Details concerning definitions, notations, algorithms, and extensive literature quotations are available from Refs 1 and 3. Complementary discussions are available from Ref 4. In all cases, we use a resolution $(N,m) = (10^6, 2000)$ in which N is the number of sampled vectors and m the number of central vectors used to average local correlation moments. About 70 vectors are sampled per T_0. Vectors are defined in the phase space of the considered system (R^3), i.e. without any attractor reconstruction in R^n. Local slopes $D_q(r_i)$ are evaluated at 45 r_i-locations separated by equal logarithmic intervals in a range (r_1, r_2). D_q's

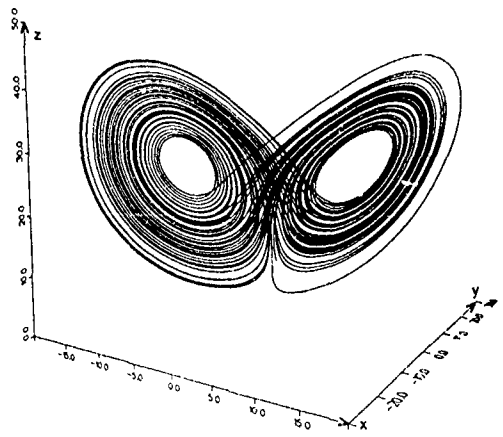

Fig. 1. Original System (OS).

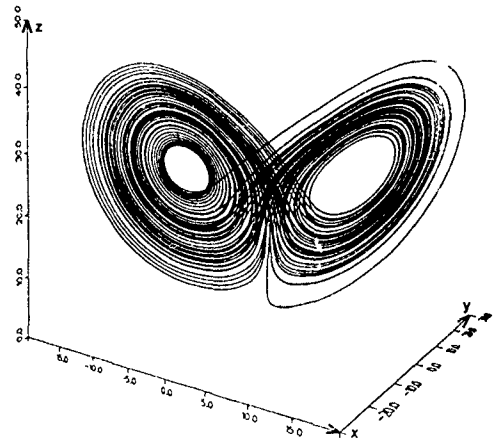

Fig. 2. Inverse Standard Reconstructed System (ISRS).

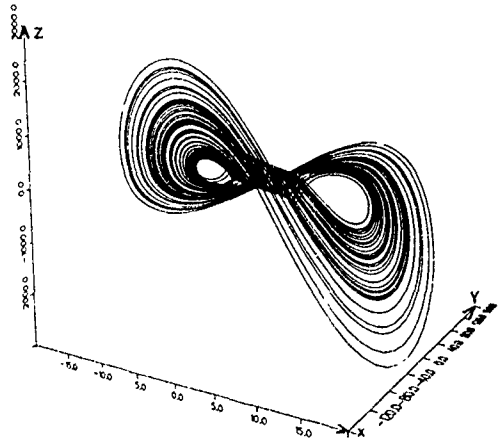

Fig. 3. Standard Exact System (SES) by applying the DST to the OS.

are afterward obtained by averaging local slopes in a r-scaling domain (r_{min}, r_{max}), for which $D_q(r)$ exhibits a plateau within a certain accuracy. The standard mean deviation σ_D of the local slope values in the r-scaling domain provides a criterion reflecting the quality of the plateau. It is well-known that the choice of the r-scaling domain lacks of objectivity and that this feature is actually one of the shortcomings of the algorithm.

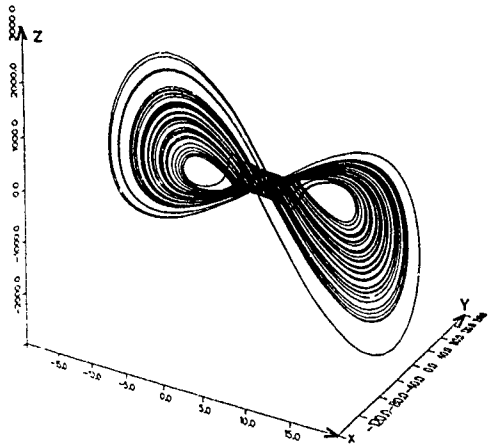

Fig. 4. SES by integrating the vector field with an intervention procedure.

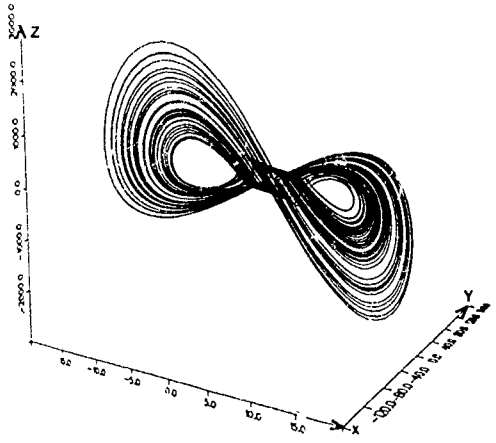

Fig. 5. Standard Reconstructed System (SRS) by integrating the vector field with an intervention procedure.

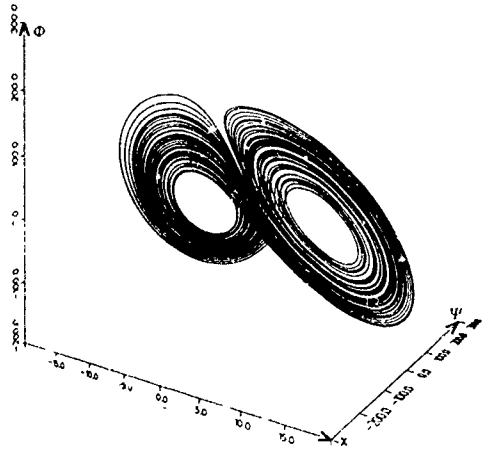

Fig. 6. Inverse Non Standard Exact System (INSES).

Furthermore, the range (r_{min}, r_{max}) generally depends on q. Therefore, we should ideally present specific data expressing $r_{min}(q)$, $r_{max}(q)$, not given to avoid data proliferation. We however mention that our results are rather insensitive to reasonable modifications of the r-scaling domains. Furthermore, instead of being interested with exact values of D_q's, we are more concerned with comparisons between

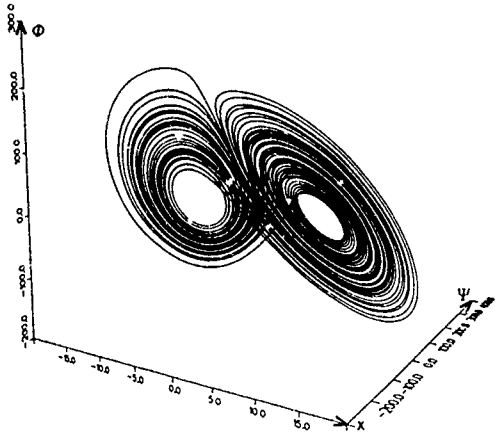

Fig. 7. Inverse Non Standard Reconstructed System (INSRS).

D_q's. Good comparisons provide reconstruction validations, even if the D_q-values themselves are biased. Therefore, exact and reconstructed systems of the same kind are studied with the same ranges (r_{min}, r_{max}). More generally, computations and interpretation of run data are carried out under the same specifications. Table II provides D_q-values and Table III values of σ_D/D_q in % for $q \in [1,50]$. Data concerning $q < 1$ have been evaluated but are omitted to simplify the discussion (they would not modify our conclusions). The reason for dismissing these data in this paper is that D_q's, $q < 1$, probe parts of the attractor where the measure is the most rarefied, leading to poor statistics and inaccurate evaluations. Tables contain 6 columns corresponding to the following systems (for convenience, we shall refer to the ith column by the label Ci) :

C1. OS, Rels (1)-(3), coordinates (x,y,z), Fig 1.

C2. ISRS, Rels (12),(2),(3), coordinates (x,y,z), Fig 2.

C3. SSES, coordinates (x,Λ,Δ), obtained by squeezing with Rel (26) the SES of Fig 4.

C4. SSRS, coordinates (x,Λ,Δ), obtained by squeezing with Rel (26) the SRS of Fig 5.

q	C1	C2	C3	C4	C5	C6
1	2.050	2.049	2.056	2.034	2.131	2.081
2	2.071	2.070	2.032	2.027	2.053	2.059
5	2.130	2.130	1.743	1.773	2.088	2.097
10	2.170	2.173	1.583	1.622	2.118	2.122
30	2.189	2.190	1.481	1.514	2.132	2.123
50	2.181	2.186	1.461	1.489	2.129	2.112

Table II Generalized dimensions D_q.

q	C1	C2	C3	C4	C5	C6
1	0.3	0.2	0.4	0.7	2	4
2	0.4	0.2	0.6	0.5	0.4	0.5
5	0.9	0.6	1	0.7	0.9	0.9
10	0.7	0.7	2	2	1	2
30	1	1	3	3	2	3
50	0.9	2	3	3	2	3

Table III Criterion σ_D/D_q (%) of plateau quality.

C5. SINSES, coordinates (x,π,Γ), obtained by squeezing with Rel (27) the INSES of Fig 6.

C6. SINSRS, coordinates (x,π,Γ), obtained by squeezing with Rel (27) the INSRS of Fig 7.

Among the D_q's, only the information dimension D_1 is invariant under reasonable changes of coordinates according to Ott et al[6]. Relying on the fact that all our systems share the same variable x, we heuristically comment in Ref 4 that the invariance property is expected here to hold whatever q. We shall now comment relative differences ϵ_r% between exact and reconstructed systems in Table II. We shall claim that our results are satisfactory if these ϵ_r's are smaller than the σ_D/D_q's of Table III. We comment in Ref 4 that such a criterion might lead to optimistic statements and we also provide a more sophisticated and more severe way to address the issue. This more sophisticated method cannot be used here for lack of room. However, it would lead to the same conclusions than the ones given below.

The comparison between the OS (C1) and the ISRS (C2) is nearly perfect, agreeing always up to the fourth digit. The worst relative difference ϵ_r % is 0.2 % for q = 50 which does not exceed the best (σ_D/D_q) in C1 and C2 of Table III. Comparisons between C3 (SSES) and C4 (SSRS) are not so good. However, the ϵ_r's are 1, 0.25, 1.7, 2.5, 2.2, 1.9 % for q from 1 to 50 respectively which are smaller than the (σ_D/D_q)'s in C3 and C4 (for q = 2, 30, 50) or not significantly much bigger for the other q's. The comparison C3/C4 is therefore found to be satisfactory. Comparing with the OS and ISRS, we however remark that D_q's are significantly underestimated for $q \geq 5$. For nonsqueezed systems, the underestimations appeared for all q's. Squeezing therefore improves the situation but does not fully solve the problem. This problem may be solved by more general transformations than simple squeezing, a trivial example being provided by the transformations transforming SSES's and SSRS's to OS and ISRS respectively. Underestimations are indeed a classical problem of the algorithm, depending on the structure of the attractor. It might be reduced by increasing the resolution (N,m) but this could lead to unaffordable runs. We however remark that the existence of underestimations does not prevent us to compare D_q-values in so far as these underestimations simultaneously appear for the SSES of C3 and the SSRS of C4. Finally, for the comparison C5/C6 between SINSES and SINSRS, relative differences ϵ_r are always much smaller than (σ_D/D_q)'s in C5, C6 of Table III except for q = 1 when ϵ_r = 2.3 % which however does not poorly compare with the 2 % in C5 and the 4 % in C6, Table III. We therefore conclude that our quantitative validations are very satisfactory. A final comment is that underestimations did appear for INSES and INSRS and that, as evidenced by the results, they are washed out by squeezing.

V - CONCLUSION

Techniques previously used for vector field reconstructions in the case of Rossler equations have been successfully applied to the case of the Lorenz system. Our final aim is the application of vector field reconstructions to the case of noisy experimental systems. In this conclusion, we stress out that two main steps are still required to reach this aim. The first one concerns the standard function fitting problem. Much more general expansions as the ones we used are necessary. A systematic study will be devoted to this step, taking the example of an attractor produced by a simple model of thermal lens oscillations[1]. Due to the existence of a sharp cut-off term in the vector field, this example will provide an acid test. The second step concerns the issue of noise removal and/or smoothing. We have little doubt that these two problems will eventually find adequate solutions, then providing the applied scientist with a new tool of interest for experimental data modelling.

REFERENCES

1. GOUESBET, G 1990 Simple model for bifurcations ranging up to chaos in thermal lens oscillations and associated phenomena, Physical Review A, 42/10, 5928-5945.
2. CASDAGLI, M. 1989 Nonlinear prediction of chaotic time series, Physica D35, 335-356.
3. GOUESBET, G. Schedule : April 1991 Reconstruction of the vector fields of continuous dynamical systems from numerical scalar time series, Physical Review A.
4. GOUESBET, G. Reconstruction of standard and inverse vector fields equivalent to a Rössler system, Submitted to Physical Review A.
5. LORENZ, E.N. 1963 Deterministic nonperiodic flow, J. of Atmospheric Sciences, Vol 20, 130-141.
6. OTT, E., WITHERS, W.D. and YORKE, J.A. 1984 Is the dimension of chaotic attractors invariant under coordinate changes ? J. of Statistical Physics, Vol 36, n° 5/6, 687-697.

EIGHTH SYMPOSIUM ON
TURBULENT SHEAR FLOWS
Technical University of Munich
September 9-11, 1991

Coherent Structure Dynamics: Interaction Between Large and Fine Scales

M.V. Melander+ and F. Hussain*

+Department of Mathematics, Southern Methodist University, Dallas, Texas
*Department of Mechanical Engineering, University of Houston, Houston, Texas

Abstract

Our goal here is to provide a better understanding of the role of large-scale *coherent structures* (CS) and their interactions with incoherent turbulence. We first study the core dynamics of an axisymmetric but variable-diameter laminar vortex and the coupling of the axial flow with meridional flow; we then study the interaction of the vortex with superimposed fine-scale 3D turbulence. Using *complex helical wave decomposition* we gain some insight into the organization of the fine-scale turbulence as well as raise some questions regarding the concept of local isotropy.

1. Introduction

Vortex/vorticity dynamics is an attractive mathematical tool for interpreting the role of CS in turbulent shear flows; e.g. Bridges et al (1990). Studies of idealized vortical structures are therefore unavoidable for first obtaining fundamental understanding before more complex practical situations can be addressed.

The principal issue here is the dynamics of an axisymmetric vortical structure with and without superimposed small-scale 3D turbulence in an incompressible, viscous, constant property fluid. We have two main objectives. *First* is to understand the core dynamics of an axisymmetric viscous vortex with significant self-induced axial flow. A poor understanding of the core dynamics in a 3D vortex is one of the principal obstacles in laminar vortex dynamics. The reason is that the motion of the axis of a curved vortex is very sensitive to changes in the vortex core, hence the importance of the core dynamics. Due to such difficulties the problem is often evaded. For example, many theoretical studies of organized structures in turbulent flows (such as hairpins in boundary layers and homogeneous shear flows) have modeled such structures as being of uniform core diameter and have presumed that a nonuniform core has negligible effect on the flow evolution. *Second* is to understand the effect that background turbulence has on the dynamics of a vortex, as well as how the turbulence itself is changed as a result of interaction with the vortex. Thus this study can be viewed as that of coupling between CS and fine scales–one of the most interesting but least understood facets of turbulence, Hussain (1983). If there were a wide scale separation between CS and fine scales in turbulence, then conventional wisdom would suggest that the coupling between the largely disparate scales is weak; in fact, this is the cornerstone of Kolmogorov's theory and of the *local isotropy* hypothesis. But we have long insisted that the large and fine scales are intimately coupled and thus *local isotropy* is unlikely, Hussain (1984). Here, we directly focus on this coupling by studying the interaction between a well defined, simple, yet dynamically evolving, large-scale vortical structure with fine-scale 3D turbulence. The geometry chosen (an axysymmetric vortex) seems to be the simplest, free from effects of self-induction and of other nearby structures, to address the phenomenon and can indeed be viewed as a segment of typical large-scale CS in practical turbulent shear flows such as mixing layers, jets, wakes, etc.

The laminar cases exhibit helical vortex lines, thus sparking a renewed interest in helicity concepts, Moffat (1969). We discuss a number of tools for analyzing the flow's helical structures. Included are the helicity integral, the helicity densities and the so-called *complex helical wave decomposition*, Lesieur (1990), based on the expansion of the velocity field into eigenfunctions of the curl operator, Moses (1971). The turbulent cases consist of the above laminar vortex superimposed with uniform isotropic homogeneous random velocity fluctuations.

2. The governing equations for an axisymmetric vortex

Let (u,v,w) be the velocities along the cylindrical coordinates (r,θ,z). Let the z-axis be the axis of the axisymmetric vortex, and let θ increase in the direction of the swirl; see Fig. 1. The equations are made dimensionless by introducing characteristic time and length scales, which are derived from the circulation Γ and angular impulse M'^* per unit length. The cylindrical symmetry implies that the pressure gradient in in the momentum equation vanishes and that v does not appear in the continuity equation. For the meridional flow (i.e.in the (r, z)-planes, see Fig. 1),

$$(1)\quad u = \frac{1}{r}\frac{\partial \psi}{\partial z}, \quad v = -\frac{1}{r}\frac{\partial \psi}{\partial r}$$

so that the azimuthal vorticity component becomes,

$$(2)\quad \omega_\theta = \frac{1}{r}\frac{\partial^2 \psi}{\partial r^2} - \frac{1}{r^2}\frac{\partial \psi}{\partial r} + \frac{1}{r}\frac{\partial^2 \psi}{\partial r^2}$$

It is well known, e.g. Batchelor (1967), p.544) that $\xi = rv$ is convected with an inviscid axisymmetric flow; we therefore express equation (2.2) in terms of ξ,

$$(3)\quad \frac{D\xi}{Dt} = \frac{1}{Re}\left[\frac{\partial^2 \xi}{\partial r^2} - \frac{1}{r}\frac{\partial \xi}{\partial r} + \frac{\partial^2 \xi}{\partial z^2}\right]$$

where $D/Dt = \partial/\partial t + u\partial/\partial r + w\partial/\partial z$ in the time derivative following a particle in the meridional flow.

Also, for an inviscid axisymmetric flow without swirl $\eta \equiv \omega_\theta/r$ is convected with the flow. Thus,

$$(4)\quad \frac{D\eta}{Dt} = \frac{1}{r^4}\frac{\partial \xi^2}{\partial z} + \frac{1}{Re}\left[\frac{\partial^2 \eta}{\partial r^2} + \frac{3}{r}\frac{\partial \eta}{\partial r} + \frac{\partial^2 \eta}{\partial z^2}\right].$$

Note that the coupling between swirl and meridional flow is expressed through a single term. In the absence of viscosity, ξ is transported with the meridional flow. However, ξ significantly influences the transport of $\eta = \omega_\theta/r$, and thereby also the meridional flow. The coupling term $(r^{-4}\,\partial\xi^2/\partial z)$ in (4) is most significant in the vortex core center where ξ^2 is usually proportional to r^4. Outside the vortex core where $\xi^2 \approx \Gamma^2/4\pi^2$, the effect is small $O(r^{-4})$, and the term vanishes identically in the potential flow outside an inviscid vortex.

3. Numerical Method and Initial Conditions

We use a 3D spectral method with periodic boundary conditions to simulate the flows. Although this method is not efficient for axisymmetric flows, it has the advantage that the flow may be given non-axisymmetric 3D perturbations, such as fine-grain turbulence, without changing the numerical method. Furthermore, the complex helical wave decomposition, which is a central part of our analysis, is most easily performed using Cartesian coordinates and Fourier transforms.

In all our cases–laminar as well as turbulent–the initial vortex is the same. We concentrate this paper on a single Reynolds number, Re=665.2. The vortex initially has a sinusoidal axial variation of the core size, and the axial vorticity

profile is the same everywhere along the axis, when scaled with the core size. The radial vorticity component is determined such that the vorticity field is divergence free. No axial flow is present initially as the azimuthal vorticity component is set to zero. The initial turbulent background is isotropic homogeneous and consists only of scales represented by wavenumbers in a certain interval, i.e. $\underline{k} \in [k_l, k_h]$. Within this interval, the phases are random with a uniform probability distribution, while the amplitudes are random with a C^∞ probability distribution P times a normalization factor, which serves to give the turbulent velocity field a specified rms-value u'_{rms}. Thus the turbulent background is herewith specified by k_l, k_h and u'_{rms}.

4.Analysis of the Axisymmetric cases

An overall impression of the vortex's evolution is provided by Fig.2, which shows a few characteristic vortex lines at selected times. Due to the axisymmetry it is sufficient to consider vortex lines starting from a single radial rake. In all panels of Fig.2, the vortex lines are drawn starting from a radial rake at the same axial position (z=0) We reemphasize that vortex lines are *almost* never material lines in a viscous fluid, and therefore no explicit time history is implied between the panels in Fig.2. The vortex line geometry at each instant merely indicates the instantaneous dynamics.

At t=0, all vortex lines lie in meridional planes (θ=constant) and therefore momentarily have no torsion (Fig.2a). However, the vortex lines gain torsion immediately, because of axial variations in the swirling motion around the axis; $\dot{\theta} \equiv d\theta/dt = v/r$ is large where the core size is small, and vice versa as indicated in Fig 1 Near $z = \ell \equiv \lambda/2$ the vortex lines rotate slower around the z-axis than near z=0 and 2ℓ Consequently, the vortex lines start twisting between z=0 and z=ℓ (Fig. 2b). Vortex lines close to the axis tend to twist more than lines at larger radii, because $\dot{\theta}$ is in general largest at the axis. Note that the oblique view, because of the symmetry, gives two different views of the same coiled structure. The helical twists propagate towards z=ℓ Meanwhile the vortex core expands near z=0 (2ℓ) and contracts near z=ℓ The onset of uncoiling is clear in Fig. 2e, which shows a reversal in the helical twist of the innermost vortex near z=0 and z=2ℓ At this instant the reversed coiling has not yet affected the outermost vortex line, but later (Fig. 2g) the helical twist of all vortexlines has reversed.

The coiling and uncoiling of the vortex lines continue, but dampen with time and thus the axial flow and the core dynamics die out. Figure 2f shows essentially a rectilinear vortex, except that close to the axis some axial dynamics, though weak, still persists. While Fig.2 gives a qualitative perception of the overall evolution of the vortical field and graphically demonstrates the presence of the helical structures and their axial propagation, it fails, however, to properly reflect other essential aspects, such as the evolution of the vortex core size, the enstrophy, the stretching and compression of vortex lines, as well as the coupling between azimuthal and meridional flows Nor does it provide quantitative measures of the various dynamical properties during the evolution of the process

The vigor of the core dynamics is clearly reflected in Fig. 3, which shows the evolution of the vorticity magnitude. The vorticity transport seen in Fig. 3 appears to take place in the form of "wave packets", because mass and vorticity transports are in opposite directions. This is possible because of the enstrophy production P_ω, which allows variations in vorticity magnitude to propagate along vortex lines.

We now focus on the kinematic relation between the enstrophy production and the inviscid meridional flow. For this purpose we consider the instantaneous meridional stream function ψ, defined in (1), as given. Equation (3) shows that, the circulation along any circular material circuit of the form (r,z) = $(r_m(t), z_m(t))$ is constant in the absence of viscosity. The axisymmetry guarantees that such a material circuit remains circular, as it is displaced by the meridional flow. This is of crucial importance for understanding the nature of both vorticity transport and enstrophy production. Most of the vorticity is in the axial component ω_z whose inviscid evolution is uniquely determined by the motion of circular material circuits. Moreover,the axial vorticity component also gives by far the largest contribution to the enstrophy production P_ω. This is because P_ω is only appreciable near the axis of the vortex, and there ω_z is the only non-vanishing vorticity component. Therefore the enstrophy production is largely determined by the motion of circular material circuits. Their motion is determined by the meridional flow; hence the importance of meridional stream function ψ.

5. Helical wave decomposition

For a detailed study of helical structures we decompose the flow field into "complex helical waves". Following Lesieur (1990) it is possible to construct two vectors $\underline{a}(\underline{k})$ and $\underline{b}(\underline{k})$ which together with $\underline{k}$ form an orthonormal basis such that the "complex helical waves" defined as

(5a) $\underline{V}^+(\underline{k},\underline{x}) \equiv (\underline{b}(\underline{k}) - i\underline{a}(\underline{k}))\exp(i\underline{k}\cdot\underline{x})$,

(5b) $\underline{V}^-(\underline{k},\underline{x}) \equiv (\underline{b}(\underline{k}) + i\underline{a}(\underline{k}))\exp(i\underline{k}\cdot\underline{x})$,

are eigenfunctions of the curl operator corresponding to the eigenvalues $\pm|\underline{k}| \neq 0$. These eigenfunctions are orthogonal with respect to an inner product.

Moreover, the linearly independent eigenfunctions of curl operator may be selected so as to form a complete set and the eigenvalues are real, Moses (1971). The complex helical waves span a subspace of vector functions. Note that a potential vector field is an eigenfunction of the curl operator corresponding to the eigenvalue 0. Thus the velocity field, which is divergence free,can be expressed in terms of complex helical waves and the gradient of a harmonic potential :

(6) $\underline{u}(\underline{x},t) = \underline{u}_R + \underline{u}_L + \nabla\phi$

Here $\underline{u}_R$ is the projection of $\underline{u}$ onto the vectorspace spanned by all eigenfunctions corresponding to positive eigenvalues $(+|\underline{k}|)$ of the curl operator. We call this the right-handed component of $\underline{u}$ $\underline{u}_L$ is the projection of $\underline{u}$ onto the vectorspace spanned by all eigenfunctions corresponding to negative eigenvalues $(-|\underline{k}|)$ of the curl operator. We call this the left- handed component of $\underline{u}$. $\nabla\phi$ is the projection of $\underline{u}$ onto the null space of the curl operator. Since $\underline{u}$ is divergence free we have $\nabla\phi = 0$. Assuming that the potential part of the flow is constant at infinity we have that $\nabla\phi$ is a constant vector field (due to the maximum principle for harmonic functions) and can be removed by choosing an appropriate inertial frame. For the vorticity field we have a similar decomposition where it is assumed that the fluid is not rotating at infinity Since the Fourier transforms of real vector fields have conjugate symmetry, the right and left-handed projections are real in physical space.

The cascade is inhibited when $(\underline{\omega}_R+\underline{\omega}_L) \times (\underline{u}_R+\underline{u}_L)$ together with its first spatial derivatives are small in some region. We shall now analyze this condition when the flow at a given instant is composed of just two eigenmodes of the curl operator (i.e. superposition of two Beltrami flows),

(7) $\underline{\omega}_1 = \nabla \times \underline{u}_1 = \lambda_1 \underline{u}_1$

(8) $\underline{\omega}_2 = \nabla \times \underline{u}_2 = \lambda_2 \underline{u}_2$.

The Lamb vector then takes the form

(9) $(\underline{u}_1 + \underline{u}_2) \times (\underline{\omega}_1 + \underline{\omega}_2) = (\lambda_2 - \lambda_1)\,\underline{u}_2 \times \underline{u}_1$.

Recall that the eigenvalues are real - positive for right-handed and negative for left-handed flow fields. Thus if $\underline{u}_1$ and $\underline{u}_2$ have equal parity (both right handed or both left handed) then $|\lambda_2 - \lambda_1| = ||\lambda_2| - |\lambda_1||$, whereas if $\underline{u}_1$ and $\underline{u}_2$ have opposite parity, then $|\lambda_2 - \lambda_1| = ||\lambda_2| + |\lambda_1||$. This difference is particularly interesting when $|\lambda_2| \approx |\lambda_2|$, an important case as the dominant contribution to the cascade is known to originate from roughly equal scales. In that case the contribution to the cascade from

interaction of eigenmodes with equal parity is small, while the contribution from the interaction of eigenmodes with opposite parity may be large. While the diffusion operator Δ conserves parity , vorticity of one parity can, through nonlinear self-interaction generate opposite parity. If a fully polarized structure ($\underline{\omega} = \underline{\omega}_L$ or $\underline{\omega} = \underline{\omega}_R$) in an inviscid flow generates vorticity of the opposite parity, then the numerical values of $\int \underline{\omega}_R \cdot \underline{u}_R \, dV$ and $\int \underline{\omega}_L \cdot \underline{u}_L \, dV$ both increase. This analysis suggests that vortical structures of strong left or right-handed polarization are persistent or "coherent" features of the flow.

5.2 Helical decomposition applied to the laminar vortex

The spatial distributions of the polarized components are not stationary but move in opposite directions. As the polarized components separate spatially $\underline{\omega}_R$ becomes dominant in some regions, $\underline{\omega}_L$ in others.The helical twists on the vortex lines (Fig. 2) are the results of one polarized component being locally dominant. Where $\underline{\omega}_R$ dominates the local twist is right-handed, and visa versa. As seen in Fig. 4 the motion of the polarized distributions is quite simple, namely the right-handed distribution moves to the left, while the left-handed moves to the right. Thus the helical decomposition gives the unique separation of wave-packets moving in opposite directions on the vortex–a striking result in light of the nonlinearity of the governing equations. In fact, this separation can not be obtained in the general case by any other technique.

6. CS and small-scale organization

Fig. 5 shows contours of $|\underline{\omega}|$ for the same flow with superimposed fine-scale turbulence. The first thing we notice about the vorticity magnitude is that it decreases dramatically in the early part of the simulation. In fact, the incoherent vorticity contributes so much to the initial vorticity amplitude $|\underline{\omega}|$ that the coherent structure is indiscernible in a contour plot (Fig. 5a). We emphasize that the large initial incoherent excitation level is somewhat of an unavoidable constraint, forced by computational limitations Namely, our insistence on a direct simulation rather than a large eddy simulation requires that the smallest scales are strongly damped by viscous effects. Hence the vorticity amplitude of the small scales must be initially high for them to survive long enough to produce appreciable vorticity amplitudes during the organization

At significantly higher Re (say 10 -100 times higher) a much lower initial incoherent excitation level (10 - 100 times lower) can be expected to ultimately produce similar incoherent vorticity scales and amplitudes. While the scales of the incoherent vorticity grow uniformly with time everywhere in the computational domain, it is only near the coherent structure that the incoherent vorticity magnitude remain appreciable,(Figs. 5b-e). The incoherent vorticity magnitude has saturated at about 10% of the coherent vorticity at the end of the simulation. However, for other simulations the saturation level is different and depends on the initial excitation level.

The 3D-isovorticity plots (not shown) reveal that the incoherent vortical structures swirl azimuthally around the coherent structure. In fact, we recognize obvious similarities with the growth of the boundary layer on an impulsively rotated rod. A cross section (Fig. 6) normal to the axis of the coherent structure thus gives an entirely different picture than does Fig. 5, namely that of 2D-like spiral filaments. From Fig.6 alone one could mistake the incoherent vorticity near the vortex for sheet-like structures

It is clear that the small-scale organization process consists of three phases. The *first* phase is an *alignment* of the incoherent vorticity in the azimuthal direction by the shearing of swirling motion of the vortex. This phase is characterized by very strong dissipation (not shown) at the Re we consider. The shear generated by the vortex results in an alignment of the small scale vorticity and thus breaks the initial local isotropy of the incoherent vorticity; compare the cross sections shown in Figs. 5 and 6. The alignment also imposes 2D-like constraints on the incoherent vorticity by giving it a preferred orientation, namely, in the azimuthal direction. The shear provides a continuous stretching in the azimuthal direction, thus attempting to sustain the aligned structures, which can therefore disappear only through local annihilation of antiparallel vorticity. The *second* phase consists of *amalgamations* by transport along the vortex or by pairing. The *third* phase involves the excitation of bending waves of the vortices. This phase can only occur when the smaller scales have become large enough; we call this the *feedback* phase. We emphasize that the distinction between the three phases, alignment,amalgamation and feedback is fuzzy. We can not exactly tell when one phase ends and another begins; in fact one phase may begin before the previous one ends.

7. Conjecture about local anisotropy and conclusions

In the traditional turbulence theory the assumption of local isotropy is generally invoked for scales in the inertial subrange; that is, there is no preferred direction of the vorticity associated with scales which are both much larger than the Komolgorov scale and much smaller than the energy containing integral scale. Consequently, in the limit of $Re \to \infty$ anisotropy is only associated with the large scales of the flow. Note that the assumption of local isotropy does not imply that there are no structures in the inertial subrange, nor does it imply anything about the shape of such structures. What it does imply, however, is that the orientation of small scale structures is statistically random. Local isotropy is indeed a strong assumption, which, however, is very convenient for calculating the transfer of energy between different scales. In essence local isotropy implies a decoupling of large and fine scales. As mentioned in Hussain (1984), the evolutions of large and fine scales are intimately coupled, thus suggesting that local isotropy is suspect in turbulent shear flows.

The presence of the coherent vortex clearly makes the large scales anisotropic.We will now examine how the anisotropy of the largest scales cascades down to the smallest scales. The first step in this cascade is discussed above. Namely, that the coherent vortex gives rise to the formation of secondary vortical structures in the boundary layer around the coherent vortex through alignment and subsequent amalgamation of small scale structures. These secondary structures may then, provided that they are sufficiently strong, dominate the strain rates in their immediate vicinity If the Reynolds number is sufficiently large,so as to allow the existence of even smaller scales, we can then imagine that these smaller scales align and organize azimuthally around the secondary structures. In the $Re \to \infty$ limit this line of reasoning leads to a hierarchy of increasingly smaller scale structures which are organized as schematically suggested in Figs. 7a-c.By construction this figure represents a fractal vortical structure. The present scenario merely adds a concrete physical space picture. An interesting aspect of the fractal vortex shown in Fig. 7 is that the spatial support of the dissipation might also be fractal. Note that the present simulations have Reynolds number which are too low to reveal more than the secondary structures,and thus the existence of a hierarchy of small scale structures is purely a speculation. However, if this speculative scenario has merit then the result is that a coherent structure induces a departure from local isotropy(at all scales).

This research has been supported by ONR grant N00014-89-J-1361 and DOE grant DE-FG05-88ER13839.

References

Bridges, J., Husain, H.S. & Hussain, F. 1990 *Turbulence at the Crossroads* ., 132-151

Hussain, A.K.M.F. 1983 *Phys. of Fluids* 26, 2816

Hussain, A.K.M.F. 1984 *Turbulence and Chaotic Phenomena in Fluids*., 245

Lesieur, M. 1990 *Turbulence in Fluids*, Kluwer

Moffat, H.K. 1969 *J. Fluid Mech.* 35, 117-129

Moses, H.E. 1971 *SIAM J. Appl. Math.* 21, 114-144

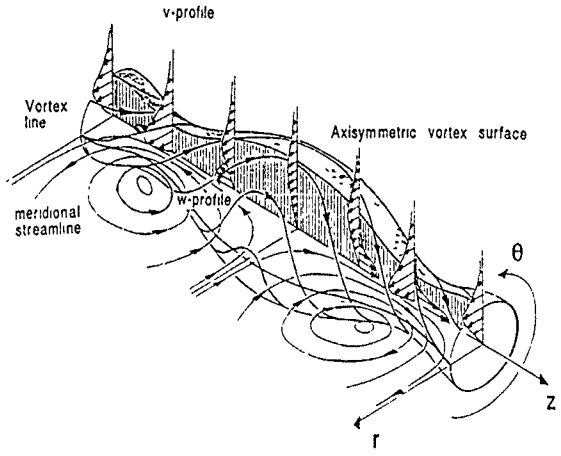

Fig 1 Definition sketch and cartoon of the dynamics

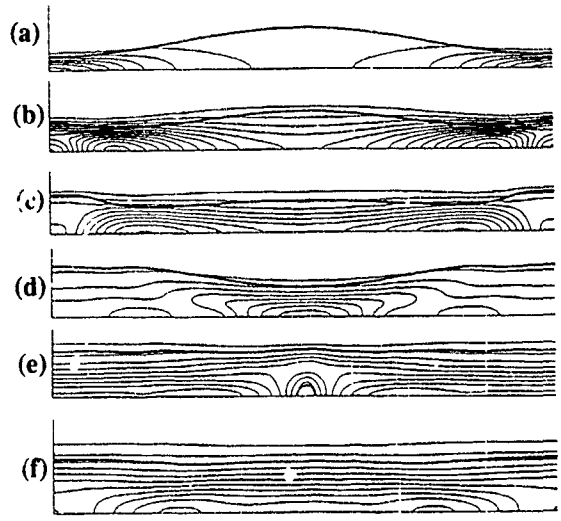

Fig. 3 Contours of the instantaneous vorticity magnitude (a) t=0; (b) t=5.32; (c) t=21 29; (d) t=31.93; (e) t=42 58, (f) t=85 15 In addition, the boundary of the vortex as given by the contour $\mathfrak{B}_k \equiv (\omega^2/2S_{ij}S_{ij})^{1/2}=1$ is overlaid in each frame.

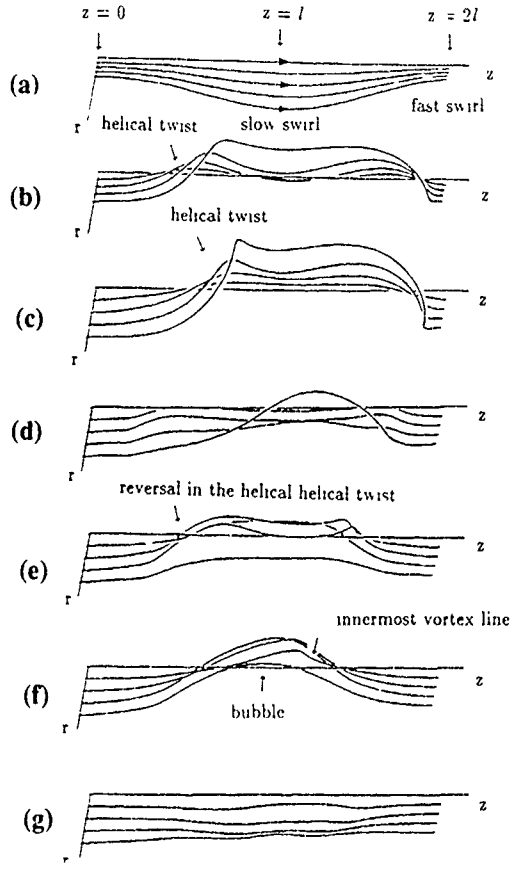

Fig. 2 The evolution illustrated by four typical vortex lines at selected instants (a) t=0, (b) t=5 32, (c) t=10 64, (d) t=21 29; (e) t=31 93, (f) t=42 58; (g) t=85 15

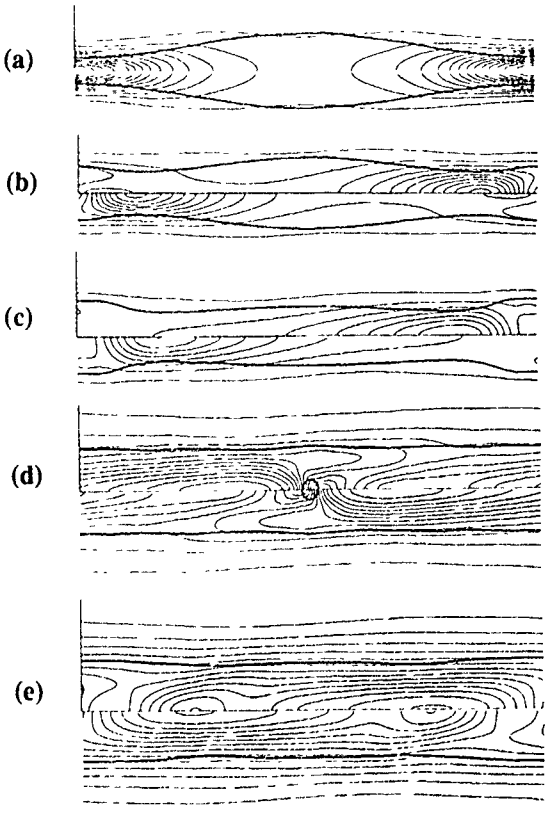

Fig. 4 Contours of $|\omega_R|$ (above the axis) and $|\omega_I|$ (below the axis) (a) t=0; (b) t=5 32; (c) t=10 64; (d) t=42 58; (e) t=85 15 In addition, the contour $\mathfrak{B}_k=1$ is overlaid in each frame.

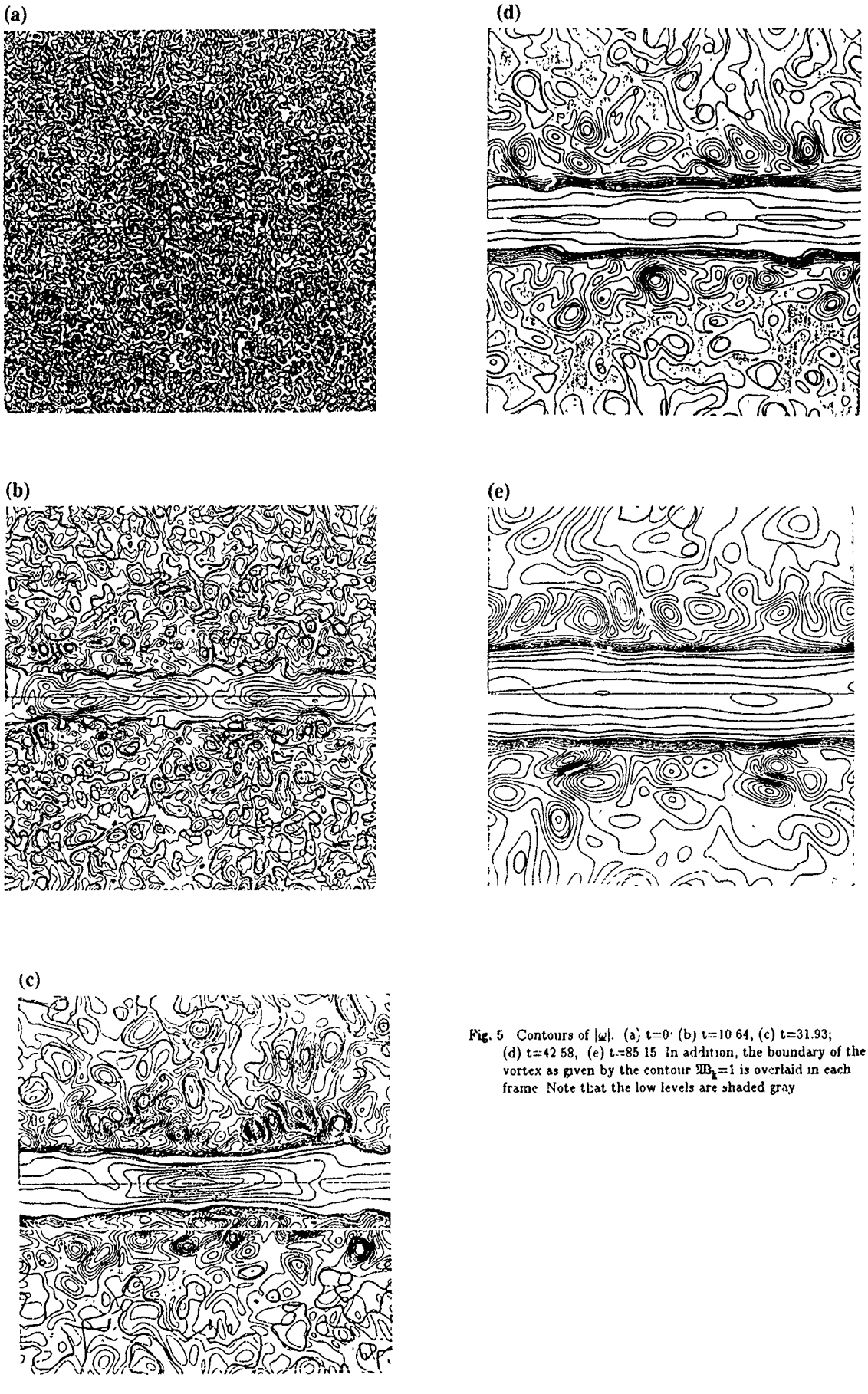

Fig. 5 Contours of $|\omega|$. (a) t=0· (b) t=10 64, (c) t=31.93; (d) t=42 58, (e) t=85 15 In addition, the boundary of the vortex as given by the contour $\mathfrak{B}_k=1$ is overlaid in each frame Note that the low levels are shaded gray

Fig. 6 Cross section of the vortex at t=31.93, $|\omega|$ is shown.

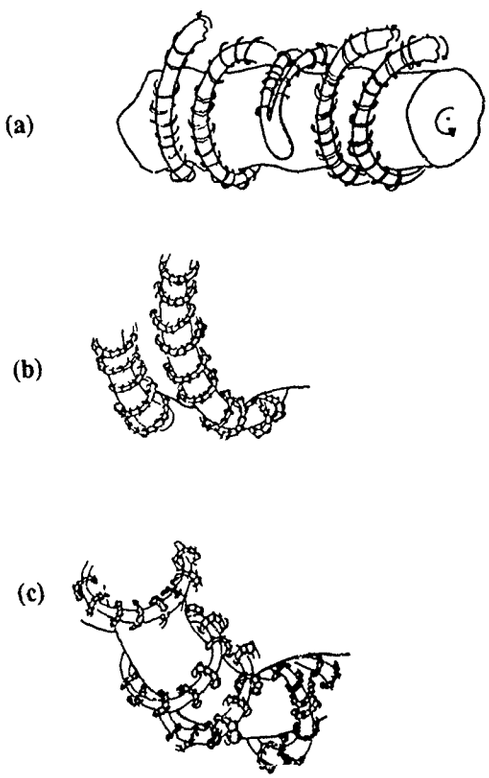

Fig. 7 Conjecture about the fractal nature of the vortex at high Reynolds number (a-c) show successive magnifications

EIGHTH SYMPOSIUM ON
TURBULENT SHEAR FLOWS
Technical University of Munich
September 9-11, 1991

Progress and Paradoxes in Modelling Near-Wall Turbulence

B.E. Launder and D.P. Tselepidakis

Dept. of Mech. Eng., UMIST, P.O. Box 88
Manchester M60 1QD
UK

Abstract

The paper considers the modelling, within the framework of second-moment closure, of the turbulent stress field in the wall-adjacent sublayer. Particular attention is given to handling wall-proximity effects on the pressure-strain (ϕ_{ij}) and stress-dissipation (ε_{ij}) processes. Comparisons of the resultant model with the direct numerical simulations of plane channel flow show close agreement of the Reynolds stress profiles at two Reynolds numbers.

1 Introduction

As research on wall turbulence shifts away from flows where the near-wall region is a strictly constant-stress layer, the limited validity of the 'universal' logarithmic laws is becoming increasingly recognized. This recognition gives impetus to efforts at devising a generally applicable model for the turbulent stresses within this viscosity-affected region. To achieve the desired width of applicability, it is widely acknowledged that full second-moment closure needs to be adopted. While models of this type have been in use for more than 20 years, only recently have computer resources become sufficiently abundant for one to contemplate applying models of this type to a wide range of engineering flows.

The subject of the present paper is the adaptation of the closure for free shear flows, presented at TSF 7 in Stanford [1,2], so as to be applicable in the vicinity of the wall. The particular focus is the problem of accounting for the wall's effect on the pressure-strain (ϕ_{ij}) and dissipation (ε_{ij}) processes.

Traditionally the turbulent Reynolds number, R_t, has been the principal (and often the only) parameter adopted for modifying these processes. There are other, arguably superior, routes for achieving the desired changes in ϕ_{ij} and ε_{ij} as the wall is approached. While the use of R_t has not been entirely eliminated, it has been adopted here as a last rather than a first resort. Moreover, its influence is confined to regions where turbulent transport is no more than one and a half orders of magnitude greater than molecular transport, a limit that appears desirable on physical grounds.

The present contribution documents further progress in the research programme reported in Refs 3 and 4. The latter paper is very recent and naturally, in the few intervening months since its appearance, the ingredients of the model have not undergone major change. Nevertheless, the present demonstration that an explicit wall correction to ϕ_{ij} can be eliminated and the further reconsideration of the limiting behaviour of ε_{ij} may be of interest. Moreover, computational comparisons now include both the "high" and "low" Reynolds number direct simulations of turbulent channel flow [5,6]. In view of the limitations on space, arguments and philosophy developed in Ref 4 will not be repeated here.

2 Closure Proposals

2.1 Preliminary Considerations

The exact transport equations for the kinematic Reynolds stress, $\overline{u_iu_j}$, for a uniform density fluid medium unaffected by force fields may be obtained by taking a velocity-weighted moment of the Navier Stokes equations. The result may be expressed:

$$\frac{D\overline{u_iu_j}}{Dt} = \underbrace{-\left(\overline{u_iu_k}\frac{\partial U_j}{\partial x_k} + \overline{u_ju_k}\frac{\partial U_i}{\partial x_k}\right)}_{P_{ij}} \underbrace{+\overline{\frac{p}{\rho}\left(\frac{\partial u_i}{\partial x_j} + \frac{\partial u_j}{\partial x_i}\right)}}_{\phi_{ij}} \underbrace{-2\nu\overline{\frac{\partial u_i}{\partial x_k}\frac{\partial u_j}{\partial x_k}}}_{\varepsilon_{ij}} \underbrace{+\frac{\partial}{\partial x_k}\left(\nu\frac{\partial \overline{u_iu_j}}{\partial x_k}\right)}_{d^\nu_{ij}} \underbrace{-\frac{\partial}{\partial x_k}\left(\overline{u_iu_ju_k} + \frac{\overline{pu_i}}{\rho}\delta_{jk} + \frac{\overline{pu_j}}{\rho}\delta_{ik}\right)}_{d_{ij}} \quad (1)$$

where upper and lower case U's denote the mean and turbulent parts of the velocity vector and the remaining notation is standard. The closure problem consists of devising models for ϕ_{ij}, ε_{ij} and d_{ij} (since P_{ij} and d^ν_{ij} require no approximation). Of these the first two are generally regarded as the most crucial and it is on these that the present paper focuses.

The aim of adopting second-moment closure is logically to achieve greater width of applicability and a closer proximity to the real processes than is possible with eddy viscosity models. This means that non-local parameters such as the wall friction velocity, the distance from the wall or, worse, the boundary-layer thickness or pipe diameter ought not to appear as elements of these closures. In the past this principle has been widely disregarded - an indication that the problem of devising a set of transport equations for the Reynolds stresses that correctly mimics their diverse variation across the sublayer is sufficiently vexing to drive one to desperate solutions!

A local parameter that is admissible is the turbulent Reynolds number, $R_t \equiv k^2/\nu\varepsilon$. However, this parameter, the valium of the turbulence modelling industry, has been freely (and sometimes irresponsibly) prescribed to fix all modelling problems from the decay of grid turbulence to the spreading rate of the round jet. Side effects are rarely considered. While, in a parallel flow, it may be used to hasten the fall off of the turbulent shear stress as the wall is approached in accord with observations, the variation of the normal stress components remains indifferently captured. Yet R_t is just one parameter, from several, that may be used in the treatment of near-wall turbulence; a satisfactory 'cure' – if one is to be found – demands the use of a more extensive arsenal.

While it may be desirable in the future to consider invariants of the stress *dissipation tensor* [7], for the moment, in addition to R_t we include only the two invariants of the stress tensor itself: $A_2 \equiv a_{ij}a_{ij}$ and $A_3 \equiv a_{ij}a_{jk}a_{ki}$, where $a_{ij} \equiv (\overline{u_iu_j} - \frac{1}{3}\delta_{ij}\overline{u_ku_k})/k$. In fact, in place of A_3, it is convenient to adopt Lumley's [8] "flatness" parameter A:

$$A \equiv 1 - \frac{9}{8}(A_2 - A_3)$$

which ranges in value from unity to zero as the turbulent fluctuations are "flattened" from being isotropic to lying entirely in a plane (as they do on the limit as the wall is approached). The variation of these invariants and R_t across the near-wall region of plane channel flow appears in Fig 1.

2.2 Modelling the Pressure-Strain Process

2.2.1 Adjustments to the Free Flow Form

The starting point for a model of ϕ_{ij} for near-wall flows is logically one for free flows. The version adopted here is basically that developed and used at UMIST for the calculation of a wide range of homogeneous and inhomogeneous free shear flows e.g. [1,2]:

$$\left.\begin{aligned}\phi_{ij} = &- \tilde{c}_1 \left[a_{ij} + c_1' \left(a_{ik}a_{kj} - \tfrac{1}{3}\delta_{ij}A_2\right)\right]\varepsilon \\ &- 0.6\left(P_{ij} - \tfrac{1}{3}\delta_{ij}P_{kk}\right) + 0.3\varepsilon a_{ij}\left(P_{kk}/\varepsilon\right) \\ &- 0.2\left[\frac{\overline{u_k u_j}\;\overline{u_i u_\cdot}}{k}\left(\frac{\partial U_k}{\partial x_i} + \frac{\partial U_i}{\partial x_k}\right)\right. \\ &\left. - \frac{\overline{u_i u_k}}{k}\left(\overline{u_i u_k}\frac{\partial U_j}{\partial x_i} + \overline{u_j u_k}\frac{\partial U_i}{\partial x_i}\right)\right] \\ &- r\left[A_2\left(P_{ij} - D_{ij}\right) + 3a_{li}a_{kj}\left(P_{lk} - D_{lk}\right)\right]\end{aligned}\right\}\begin{aligned}&\phi_{ij1}\\ &\left.\begin{aligned}&\\ &\\ &\\ &\\ &\end{aligned}\right\}\phi_{ij2}\end{aligned} \qquad (2)$$

Equation (2) follows broadly the direction proposed by Lumley [8] and Shih and Lumley [9] though, regarding mean-strain influences, ϕ_{ij2}, there are also some important philosophical and practical differences from that proposed in [13] (see [1]).

The earlier studies noted above included A as a factor in the numerator of $\tilde{c}_1$, a choice which would appear, from Fig 1, to guarantee that the process ϕ_{ij1} vanished at the wall, as desired. However *consistency* of the model with the two-component limit does not unfortunately enforce compliance with it As shown in Ref 3, unless $\tilde{c}_1$ is independently forced to vanish at the wall, $\overline{u_2^2}/k$ remains finite there (x_2 being the direction normal to the surface) and thus neither A nor $\tilde{c}_1$ become zero. Only R_t seems capable of enforcing the desired limit, the form adopted being:

$$\tilde{c}_1 = 6.3\,A\,F(1-f)$$
$$c_1' = 0.7\;;\quad f = \max(1 - R_t/140\,,0)\;;\quad F = \min(0.6\,, A_2^{1/2})$$

The model of the process ϕ_{ij2} has also been constructed so that it vanishes in the two-component limit. Nevertheless, like that for ϕ_{ij1}, it requires minor adaptation as the wall is approached. The problem stems from the cubic term in the shear stress equation $\overline{u_1 u_2}$ for it leads to a sink of shear stress equal to:

$$r\left[(a_{11} - a_{22})\left(\tfrac{1}{2}A_2 - 3\,a_{33}^2\right)\right]k\frac{\partial U_1}{\partial x_2}$$

Both $(a_{11} - a_{22})$ and A_2 soar rapidly as the wall is approached leading to the annihilation of $\overline{u_1 u_2}$. To limit the impact of the term, the free coefficient r is taken as:

$$r = \min(0.6, A)$$

The above proposals differ from the recommendations in [1] for large anisotropies ($A_2 > 0.6$; $A < 0.6$) but in practice such extreme levels of these invariants are only rarely encountered other than in the near-wall region.

2.2.2 Inhomogeneity Correction

The exact pressure-strain process may helpfully be expressed in a form from which the pressure has been eliminated, [10]:

$$\phi_{ij} = \frac{1}{4\pi}\int_{vol}\overline{\left(\frac{\partial^2 u_l u_m}{\partial x_l \partial x_m}\right)'\left(\frac{\partial u_i}{\partial x_j} + \frac{\partial u_j}{\partial x_i}\right)}\frac{dVol}{|r|}$$
$$+\frac{1}{2\pi}\int_{vol}\left(\frac{\partial U_l}{\partial x_m}\right)'\overline{\left(\frac{\partial u_m}{\partial x_l}\right)'\left(\frac{\partial u_i}{\partial x_j} + \frac{\partial u_j}{\partial x_i}\right)}\frac{dVol}{|r|} + S_{ij} \qquad (3)$$

where the primes denote quantities evaluated at distance $|r|$ from where ϕ_{ij} is evaluated and the integration is over all the flow region. S_{ij} refers to surface integrals arising from the fact that in wall flows pressure fluctuations do not vanish at the rigid boundary.

Equation (2) for ϕ_{ij1} and ϕ_{ij2} may, in free flows, be regarded as a model of the terms in (3) involving the volume integrals. In modelling near-wall turbulence, corrections are usually introduced to ϕ_{ij1} and ϕ_{ij2} notionally to account for the effects of the surface integrals (viz §2.2.3). There is, however, a further assumption implicit in eq (2) that becomes highly questionable near the wall, namely the idea that the flow is *homogeneous*. For example, in arriving at the above model for ϕ_{ij2}, the assumption is made that $(\partial U_l/\partial x_m)'$ can be replaced by $(\partial U_l/\partial x_m)$ and thus taken through the integral in eq (3). The process ϕ_{ij2} is then represented as:

$$\phi_{ij2} = \frac{\partial U_l}{\partial x_m}\left(a_{lj}^{mi} + a_{li}^{mj}\right) \qquad (4)$$

where the fourth-rank tensor a_{lj}^{mi} is expressed as a series in ascending powers of a_{ij}, viz. [1,9].

Bradshaw et al [11] have used the data base provided by the direct simulations of channel flow [5] to explore how serious was the error in treating $(\partial U_l/\partial x_m)'$ as $(\partial U_l/\partial x_m)$. They concluded that the error was negligib ., *except for* x_2^+ *less than 30* where it became very large. Evidently, therefore, any closure attempting to span this near-wall sublayer ought to include some inhomogeneity correction. The practice adopted here is to replace $\partial U_l/\partial x_m$ in eq (4) by an *effective* velocity gradient $(\partial U_l/\partial x_m)_{eff}$ where:

$$\left.\frac{\partial U_l}{\partial x_m}\right]_{eff} = \frac{\partial U_l}{\partial x_m} + c_I\, l_n \frac{\partial l_n}{\partial x_k}\frac{\partial^2 U_l}{\partial x_k \partial x_m} \qquad (5)$$

where l_n is a representative length scale normal to the wall, $(k/\varepsilon)(\overline{u_p u_q}\,n_p n_q)^{1/2}$, n_p denoting the unit vector normal to the wall. A discussion of the physical basis for this term and the reason for choosing l_n rather than the more widely adopted length scale $l \equiv k^{3/2}/\varepsilon$ is given in [4]. Results for two values of c_I are reported in §3.

If, as the direct simulations indicate, one needs to recognize inhomogeneities in the mean velocity gradient, one should probably also acknowledge those in the turbulent stress field (in the range $7 < x_2^+ < 20$, for example, the shear stress $\overline{u_1 u_2}$ varies at a rate comparable with $\partial U_1/\partial x_2$. For the present, however, no attempt has been made to do so.

2.3 Wall Reflection Effects

The contribution of the surface integrals S_{ij} in eq (3) is usually handled by way of wall corrections for both ϕ_{ij1} and ϕ_{ij2}. However, the processing of the direct-simulation data of homogeneous shear flow by Brasseur and Lee [12] showed that the volume integral arising from ϕ_{ij1} was associated with much finer-scale interactions than ϕ_{ij2}; thus, in wall turbulence we may expect that the latter process would "feel" the effects of the wall more than ϕ_{ij1}. In view of the fact that ϕ_{ij1} is already damped by the turbulent Reynolds number, we thus apply an explicit wall correction only to the process ϕ_{ij2}. For present purposes we adopt broadly the version of Gibson & Launder [13]:

$$\phi_{ij2}^w = c_2^w\left(\phi_{km2}\,n_k n_m\,\delta_{ij} - \tfrac{3}{2}\phi_{ik2}\,n_k n_j - \tfrac{3}{2}\phi_{jk2}\,n_k n_i\right)\frac{l_n}{x_n} \qquad (6)$$

where x_n is the normal distance from the wall. As discussed in §2.1 the use of wall distance is undesirable since near surfaces of very complex topography it is impossible to identify a physically meaningful distance. In mitigation, the importance of this process in the overall stress budget is here much less than in older closures such as [13]. Indeed, for the case of channel flow, at least, we show in §3 that it can be dropped entirely by suitably increasing the inhomogeneous correction discussed in §2.2.2. (It seems rather doubtful, however, whether the process can be completely eliminated in the case of impinging wall flows such as that considered by Craft and Launder [14] elsewhere in these proceedings).

2.4 The Dissipation Tensor

The most popular route to modelling ε_{ij} is to assume local isotropy and imagine, following Lumley [8], that any anisotropies actually present are absorbed in the model for the process ϕ_{ij1}. In near-wall turbulence there are good reasons for *not* doing this, however: for one thing the limiting values of the relative component dissipation rates are different from and governed by different processes than ϕ_{ij}. Moreover, Kim et al [5] have processed their direct simulation data to provide values of ε_{ij} up to the wall thus providing values for direct comparison with computation.

The usual way of obtaining the limiting ratios of $\varepsilon_{ij}/\varepsilon$ at the wall is to expand the fluctuating velocities in a Taylor series and evaluate the gradient at $x_2 = 0$. This leads to the results [15]:

$$\frac{\varepsilon_{11}}{\varepsilon} = \frac{\overline{u_1 u_1}}{k} \; ; \; \frac{\varepsilon_{33}}{\varepsilon} = \frac{\overline{u_3 u_3}}{k} \; ; \; \frac{\varepsilon_{22}}{\varepsilon} = 4\,\frac{\overline{u_2 u_2}}{k} \; ; \; \frac{\varepsilon_{12}}{\varepsilon} = 2\,\frac{\overline{u_1 u_2}}{k} \quad (7)$$

The coefficients of ε_{12} and ε_{22} differ from unity because the leading term of the series for u_2 is taken proportional to x_2^2 to give $\partial u_2/\partial x_2 = 0$ at $x_2 = 0$. In fact, the use of a series containing only integer exponents of x_2 is not strictly valid if one seeks information about velocity derivatives at $x_2 = 0$. To recognize this one may note simply that $\partial u_2/\partial x_2 = 0$ at $x_2 = 0$ for any leading term $a_n x^{n+1}$ provided that n is greater than zero. Such a generalized form leads to:

$$\frac{\varepsilon_{22}}{\varepsilon}\frac{k}{\overline{u_2 u_2}} = (1+n)^2 \quad ; \quad \frac{\varepsilon_{12}}{\varepsilon}\frac{k}{\overline{u_1 u_2}} = (1+n) \quad (8)$$

While there seems no obvious reason why the Navier Stokes equations should not support a value of n intermediate between zero and unity, as will be seen later the direct simulation data do strongly suggest $n = 1$. The appropriate limiting values may be achieved with the following model:

$$\varepsilon^*_{ij} = \frac{\varepsilon}{k}\left(\overline{u_i u_j} + \overline{u_i u_k}\,n_j n_k + \overline{u_j u_k}\,n_i n_k + \overline{u_k u_l}\,n_k n_l n_i n_j\right)/\left(1 + {}^3\!/_2\,\overline{u_p u_q}\,n_p n_q/k\right) \quad (9)$$

We suppose that this highly non-isotropic limiting form gives way to a more isotropic behaviour away from the wall as the Reynolds number increases and the anisotropy of the stress field diminishes:

$$\varepsilon_{ij} = f_\varepsilon\,\varepsilon^*_{ij} + (1 - f_\varepsilon)\,\varepsilon'_{ij} \quad (10)$$

In principle the quantity ε'_{ij} may be expected to be a Reynolds-number-dependent parameter ranging from the locally isotropic limit $\varepsilon'_{ij} = {}^2\!/_3\delta_{ij}\varepsilon$ at very high Reynolds numbers to $\overline{u_i u_j}\,\varepsilon/k$ as R_t goes to zero. However, for the present we simply adopt the former irrespective of R_t. The weighting function f_ε that produces the changeover between ε^*_{ij} and ε'_{ij} may plausibly be modelled in terms of the stress anisotropy; indeed the parameter A offers a convenient way of doing this; we take:

$$f_\varepsilon = \exp\left(-20A^2\right)$$

The question of a further amendment to the model of ε_{ij} is discussed in §3.

2.5 Stress Diffusion

Aside from viscous effects, our work has retained the model of Daly and Harlow [16] adopted for free shear flows. It is, however, interpreted as the *net* diffusion due to both velocity and pressure fluctuations rather than to velocity fluctuations alone:

$$d_{ij} = -c_s\,\frac{\partial}{\partial x_k}\left(\frac{k}{\varepsilon}\,\overline{u_k u_l}\,\frac{\partial \overline{u_i u_j}}{\partial x_l}\right) \quad (11)$$

where c_s retains the value of 0.22 used in free shear flows.

As the wall is approached however, the turbulent triple products of velocity vanish faster than the pressure-velocity products (since, unlike the fluctuating velocities, pressure fluctuations do not vanish at the wall). It may be demonstrated that inclusion of a viscous-like pressure-diffusion process is essential if the equations for the stress components $\overline{u_1 u_2}$ and $\overline{u_2^2}$ are to balance [4].

Lumley [17] has shown that in the limit of weakly anisotropic turbulence, pressure transport opposes and makes more isotropic transport by triple velocity products. One may suppose an analogous process at work in the sublayer i.e. that due to turbulent pressure fluctuations, the effective viscous diffusion will be reduced and rendered more isotropic. Following this line of argument, the following model of the pressure transport due to viscous effects – denoted d^p_{ij} – is arrived at:

$$d^p_{ij} = -{}^1\!/_3\left(d^\nu_{ik}\,n_k n_j + d^\nu_{jk}\,n_k n_i\right) + {}^1\!/_3\,\delta_{ij}\,d^\nu_{kl}\,n_k n_l \quad (12)$$

and this is added to d_{ij}. It is readily verified that the above form correctly balances the $\overline{u_1 u_2}$ and $\overline{u_2^2}$ equations in the immediate wall vicinity while making a negligible contribution to the $\overline{u_1^2}$ and $\overline{u_3^2}$ budgets.

2.6 The Dissipation Rate Equation

The proposed equation for determining ε is similar to that adopted for free shear flows [1,2]:

$$\frac{D\varepsilon}{Dt} = \frac{\partial}{\partial x_k}\left[\left(c_\varepsilon\frac{\overline{u_k u_l}\,k}{\varepsilon} + \nu\,\delta_{kl}\right)\frac{\partial \varepsilon}{\partial x_l}\right] + \frac{1}{2}c_{\varepsilon 1}\frac{\varepsilon}{k}P_{kk} - c_{\varepsilon 2}\frac{\varepsilon^2}{k} \quad (13)$$

where $c_\varepsilon = 0.18$, $c_{\varepsilon 1} = 1.0$ and $c_{\varepsilon 2} = 1.92/[1 + 0.63(AA_2)^{1/2}]$. Three modifications are introduced, however, to render it suitable for use in the viscous sublayer. Following [18], the sink term in eq (13) is modified to:

$$c_{\varepsilon 2}\,\frac{\varepsilon\tilde{\varepsilon}}{k} \quad ; \quad \tilde{\varepsilon} \equiv \varepsilon - 2\nu\left(\partial k^{1/2}/\partial x_k\right)^2$$

and a term involving the second derivative of the mean velocity is included on the right of (13):

$$2\,c_{\varepsilon 3}\,\nu\,\frac{k}{\varepsilon}\,\overline{u_k u_l}\,\frac{\partial^2 U_i}{\partial x_k \partial x_j}\,\frac{\partial^2 U_i}{\partial x_l \partial x_j}$$

The third modification, proposed originally in [3] is the inclusion of a further term of the right side of eq (13), that is diffusive in character and which notionally represents the effects of pressure diffusion in the viscous sublayer:

$$d^p_\varepsilon = \frac{\partial}{\partial x_k}\left(c_{\varepsilon 4}\,\nu\,\frac{\tilde{\varepsilon}}{k}\,\frac{\partial k}{\partial x_k}\right)$$

where $c_{\varepsilon 4}$ takes the value 0.92. Note that since k varies as x_2^2 near the surface, the term tends to raise the level of ε there. Its effect, like those of the other amendments noted above, is insignificant outside of the sublayer region.

3 Application of the Model to Plane Channel Flows

The $\overline{u_i u_j}$, ε and momentum equations have been solved numerically for the case of fully developed plane channel flow. One hundred nodes covered the region between the wall and the symmetry plane with about half of these concentrated in the region $x_2^+ < 40$. Figure 2 shows the distribution of the normal stresses normalized by k across the near-wall region for a Reynolds number of 5600; here $c_2^w = 0.2$ and $c_l = 0.3$. The DNS distributions are generally well captured by the model computations with $\overline{u_2^2}/k$ falling to zero as the wall is approached. However, for $x_2^+ < 10$, the simulation data show an interesting drop in $\overline{u_1^2}/k$ and a corresponding rise in $\overline{u_3^2}/k$ that is entirely missed by the computations.

The nature of the disagreement seems to suggest a pressure-induced transfer between x_1 and x_3. Such a transfer can be reproduced by the inclusion of the following term in the $\overline{u_i u_j}$ equation:

$$-\,c_1^*\left[2\,a_{ij} + \left(a_{pq}\,n_p n_q\,\delta_{ij} - {}^3\!/_2 a_{pi}\,n_p n_j - {}^3\!/_2 a_{pj}\,n_p n_i\right)\right](\varepsilon - \tilde{\varepsilon}) \quad (14)$$

Note that $\tilde{\varepsilon}$ vanishes at the wall but is negligibly different from ε for $x_2^+ > 10$ so the influence of the term is automatically confined to the viscous sublayer, as desired. With $c_1^* = 0.05$ a much improved distribution of $\overline{u_1^2}$ and $\overline{u_3^2}$ results. While the term is redistributive, it is unlikely that the phenomenon arises from ϕ_{ij} since, in the exact process, both ϕ_{11} and ϕ_{33} vanish at the wall. It seems more likely that the term is really providing a small correction to the model of ε_{ij}. Apart from the effect shown the term seems to be passive and it has thus been retained in all subsequent computations. Figure 3 and 4 show the computed rms velocity profiles and turbulent shear stress for this case; very close accord with the data is achieved. The corresponding profiles at the higher Reynolds number of 13750 appear in Fig 5 and 6: agreement is again acceptably close though, by comparison with the previous case it is clear that the computations exhibit rather less sensitivity to Reynolds number than do the simulations. This is a little surprising since the present model seems to reproduce correctly the shift in the additive constant in the logarithmic law for the mean velocity [4].

In fact the best choice of c_1 and c_2^w is hard to determine because both act in the same sense. Thus a reduction in one can be nearly offset by an increase in the other, at least in a simple shear flow. To illustrate this point, Fig 7 shows the computed rms fluctuating velocity profiles that result from taking $c_1 = 0.4$ and $c_2^w = 0$, i.e. *with the wall reflection term eliminated entirely*. The agreement with the DNS profiles is still very close though not quite as good as in Fig 3. Nevertheless, the prospect that one *may* be able to devise a widely applicable 2nd moment closure that makes no reference to wall distance is certainly interesting from a practical point of view.

Finally Fig 8 considers the normalized dissipation profiles $\varepsilon_{\alpha\beta}\, k/\overline{u_\alpha u_\beta}\,\varepsilon$ (no summation). One notices that the DNS data, Fig 8a, clearly *does* asymptote to the theoretical values given by eq (7) at $x_2^+ = 0$. The comparison serves to make two further points. Firstly, while the Reynolds stress field itself is very accurately predicted by the closure, the same cannot be said of the dissipation components (or, for that matter, the other processes) in the stress budget. Secondly, the variation of the ε_{12} component is so complicated and so at variance with current concepts of the dissipative processes that, if the DNS data are reliable, the modelling of the dissipation tensor will require a great deal of attention in future.

4 Summarizing Remarks

A second moment closure for the near-wall region has been developed that mimics very closely the distribution of the Reynolds stress components obtained by the direct numerical simulations of flow through a plane channel

New features of the model include

- a reduced emphasis on the turbulent Reynolds number as a parameter for modifying the closure
- the inclusion of an *inhomogeneous* correction to ϕ_{ij} which exerts an important influence for levels of x_2^+ below about 50
- a much reduced importance of the model for wall-reflection effects on the fluctuating pressure field (indeed satisfactory behaviour can be obtained with the term eliminated entirely if the importance of the above noted inhomogeneity correction is increased)
- a process, tentatively attributed to ε_{ij}, that increases the relative importance of $\overline{u_3^2}$ relative to $\overline{u_1^2}$ for values of x_2^+ below 10 in accord with the DNS data
- pressure-diffusion model for $\overline{u_i u_j}$ in the viscous sublayer that is necessary to achieve the correct near-wall budget for $\overline{u_1 u_2}$ and $\overline{u_2^2}$.

Nevertheless, consideration of the profiles of ε_{ij} – and in particular the distribution of ε_{12} – suggests that considerably more effort is needed to arrive at a satisfactory modelling of the component processes.

Acknowledgements

We gratefully acknowledge support of this research by the UK SERC under grant GR/D/8285.2. Our thanks also go to Mrs J. Buckley for her help in preparing the camera-ready manuscript.

Authors are listed alphabetically.

References

1. Craft, T J. and Launder, B.E., Paper 17-1, Proc. 7th Symp. Turb. Shear Flows, Stanford University, 1989.
2. Cresswell, R.W., Haroutunian, V., Ince, N.Z., Launder, B.E. and Szczepura, R.T., Paper 12-4, Proc. 7th Symp. Turb Shear Flows, Stanford University, 1989.
3. Launder, B.E. and Tselepidakis, D.P., "Contribution to the second-moment modelling of sublayer turbulent transport", Invited paper, Zoran Zarić Memorial, International Seminar on Near-Wall Turbulence, Dubrovnik, Yugoslavia, 1988.
4. Launder, B.E. and Tselepidakis, D.P., AIAA Paper 91-0219, 1991.
5. Kim, J., Moin, P. and Moser, R., *J. Fluid Mechanics*, **177**, 133, 1987.
6. Kim, J., Personal communication, 1991.
7. Lee, M J. and Reynolds, W.C , Proc. 5th Symp Turb. Shear Flows, p. 17.7, Cornell University, 1985.
8. Lumley, J L., *Adv. in Applied Mech* , **18**, 123. 1978.
9. Shih, T-H. and Lumley, J.L., "Modeling of Pressure Correlation Terms in Reynolds Stress and Scalar Flux Equations", Report FDA-85-3, Sibley School of Mech. and Aerospace Eng., Cornell University, 1985.
10. Chou, P.Y., *Quart. Applied Mathematics*, **3**, 38, 1945.
11. Bradshaw, P., Mansour, N.M. and Piomelli, U., Proc. Summer Program, Center for Turbulence Research, Stanford University, 1987.
12. Brasseur, J. and Lee, M.J., Proc. Summer Program, Center for Turbulence Research, Stanford University, 1987.
13. Gibson, M.M. and Launder, B.E., *J. Fluid Mechanics*, **86**, Part 3, 491, 1978.
14. Craft, T.J. and Launder, B.E., Paper 8-5, Proc. 8th Symp. Turb. Shear Flows, Munich, 1991.
15. Launder, B.E. and Reynolds, W.C., *Phys. Fluids*, **26**, 1157, 1983.
16. Daly, B.J. and Harlow, F.H , *Phys. Fluids*, **13**, 2634. 1970.
17. Lumley, J L , VKI Course "An Introduction to Turbulence Modelling", 1975.
18. Hanjalić, K. and Launder, B.E., *J Fluid Mechanics*, **74**, Part 4, 593, 1976.

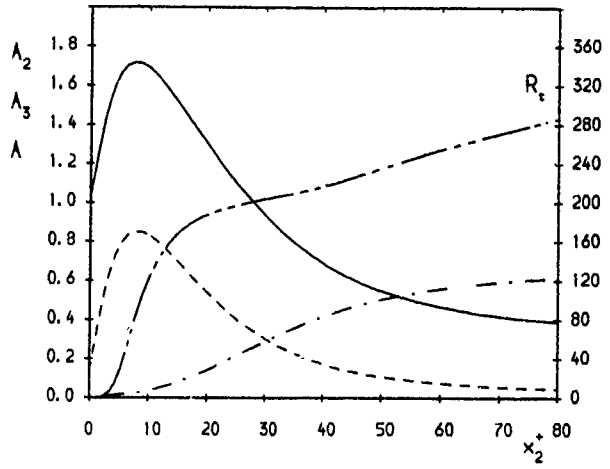

Fig 1: Distribution of invariant parameters across the sublayer region, $Re = 13750$
A_2: ——— ; A_3: - - - - -
A: — · — · — ; R_t: — - — -
(from DNS data, Ref 6)

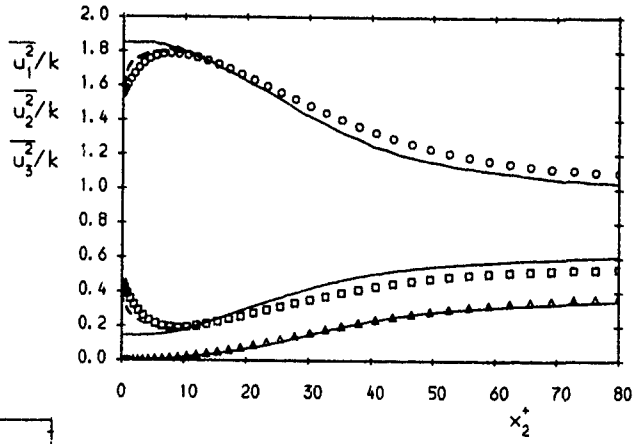

Fig 2: Normalized profiles of normal stresses across sublayer, $Re = 5600$
Symbols: DNS data ;
——— : present computations ;
- - - - - : present computations with inclusion of eq (14)

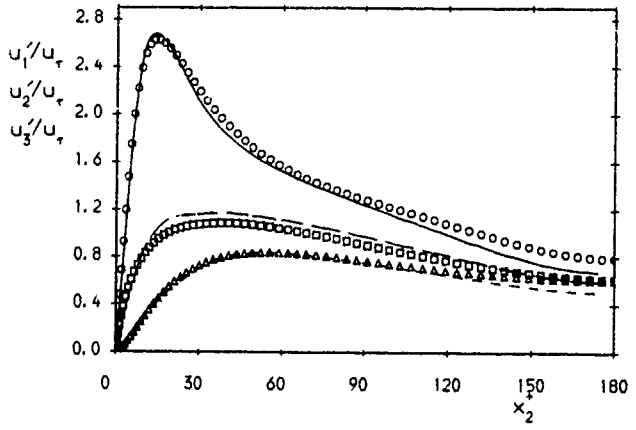

Fig 3: Turbulence intensity profiles in plane channel, $Re = 5600$
Symbols: DNS data ; Lines: present computations

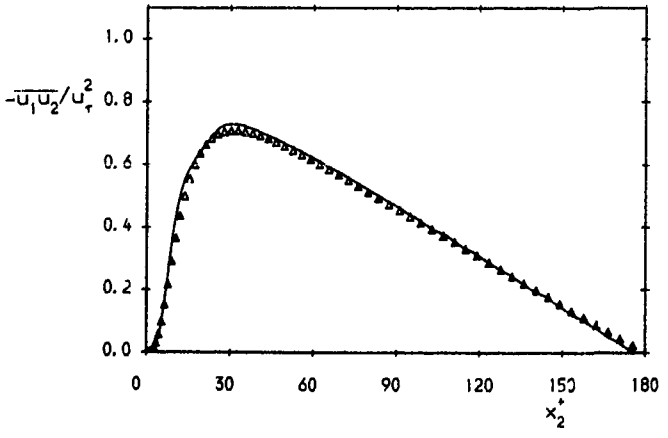

Fig 4: Turbulent shear stress profile in plane channel, $Re = 5600$
Δ : DNS data ; Line: present computations

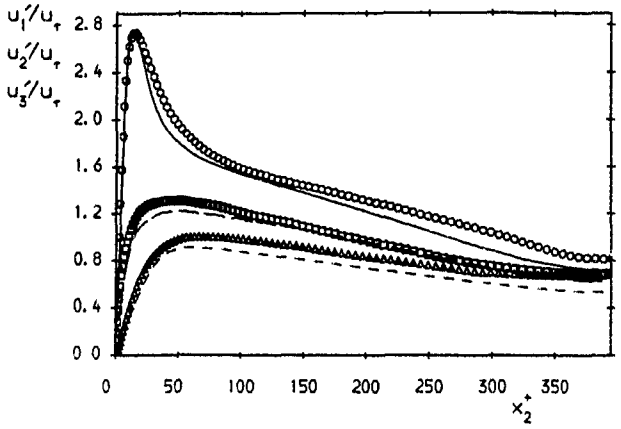

Fig 5: Turbulence intensity profiles in plane channel, Re = 13750
Symbols: DNS data ; Lines: present computations

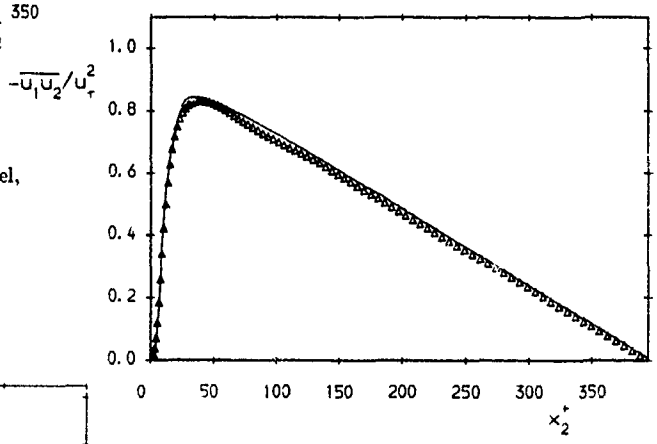

Fig 6: Turbulent shear stress profile in plane channel, Re = 13750
△ : DNS data ; Line: present computations

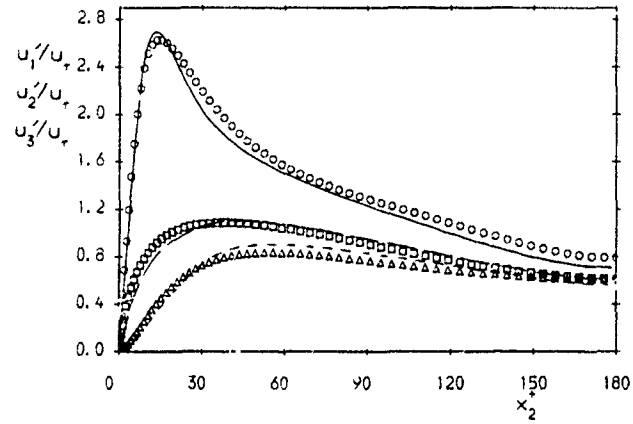

Fig 7: Turbulence intensity profiles in plane channel, Re = 5600
Symbols: DNS data ; Lines: present computations without wall reflection effects (c_1 = 0.4, c_2^w = 0)

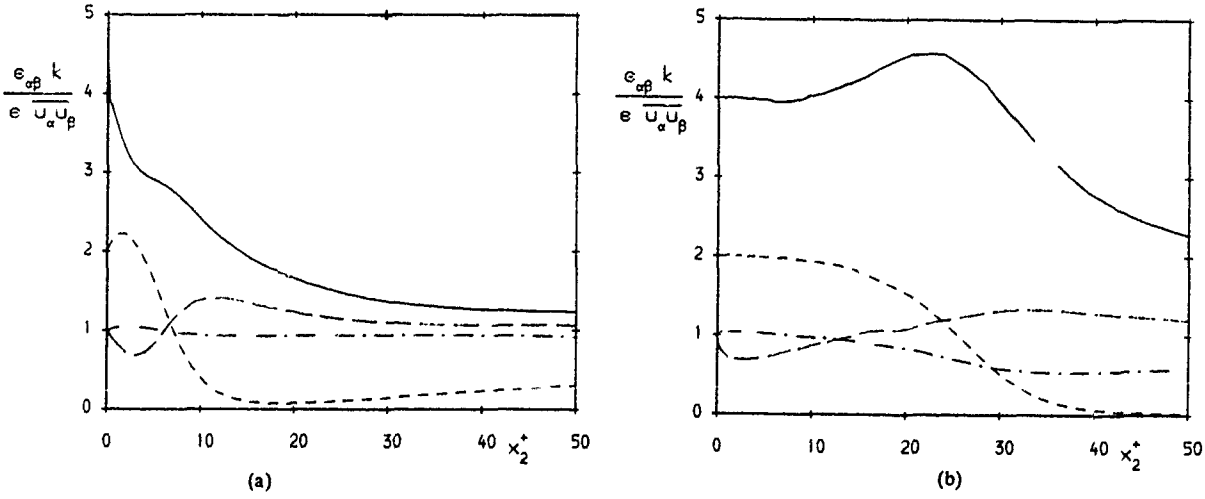

Fig 8: Dissipation/stress profiles across low Reynolds number channel flow (Re = 5600)
. — . — : α=1, β=1 ; ——— : α=2, β=2 ;
— — — : α=3, β=3 ; - - - - : α=1, β=2 .
a) Compiled from DNS data ; b) Present computations

EIGHTH SYMPOSIUM ON
TURBULENT SHEAR FLOWS
Technical University of Munich
September 9-11, 1991

COMPUTATION OF MIXING LAYERS BY A SPECTRAL TRANSPORT MODEL

R. A. Gore, F. H. Harlow, and C. Zemach
Theoretical Division, Group T-3
Los Alamos National Laboratory
Los Alamos, NM 87545

ABSTRACT

A turbulence model based on the transport of the turbulent energy spectrum is applied to the various experimental investigations of a mixing layer. This model allows for the relaxation of the constraint of spectral equilibrium common to one-point closures, such as K-ε. Good agreement is obtained for the spectrally integrated turbulence quantities, such as $\sqrt{\overline{u'^2}}/\Delta U$. The model suggests that the variations (between investigations) found in the self-similar regions of the mixing layer is due to the initial low wavenumber portion of the energy spectrum.

NOMENCLATURE

E_{ij}	spectral turbulent energy component
E	$E_{11} + E_{22} + E_{33}$
Emax	maximum E (function of time and location)
k	wavenumber
K	turbulent kinetic energy
t	time
u_i	flow field velocity
x_i	spatial dimension
θ	momentum thickness
ν	molecular viscosity

INTRODUCTION

The present paper compares data on free shear flows with the predictions of a new turbulence model first described in Besnard, Harlow, Rauenzahn, and Zemach (1990), henceforth, referred to as BHRZ. The model can be described as a two-point spectral transport model. The model aims to describe fluid flows more general than those appropriate to one-point closure schemes, e.g., K-ε and Reynolds stress models. An important limitation in these simpler models (as discussed in BHRZ and elsewhere, e.g., Taulbee (1988)) is that the turbulent energy spectrum must be in equilibrium, that is, the spectrum in wavenumber distribution maintains a constant relative shape. There are many instances in which the spectrum goes through modifications before establishing or re-establishing equilibrium, for example, the initial mixing of two infinite streams (the mixing layer) and the sudden contraction or expansion of grid generated turbulence.

Another important benefit of this model is that the turbulence energy at all scales is calculated. This feature can be of use in many instances, e.g., for chemically reacting flows where it is necessary to judge the turbulent energy at the fine scales where the mixing of species occurs.

As a first step in applying the present two-point spectral scheme to these cases, one may consider how the model can be used to numerically determine the mean velocity field of a flow in spectral equilibrium. This is the purpose of the present paper. Here we will discuss the flow of a two-dimensional planar mixing layer after the spectrum has come to equilibrium.

MODEL DESCRIPTION

The model proposed in BHRZ provides coupled evolution equations for the mean velocity, $u_i = u_i(\underline{x},t)$, and the spectral components, $E_{ij} = E_{ij}(\underline{x},k,t)$, where $2\int_0^\infty E_{ij}dk = \overline{u'_i u'_j}$. The generalized evolution equation for E_{ij} used in this work is:

$$\frac{\partial E_{ij}}{\partial t} = -u_n \frac{\partial E_{ij}}{\partial x_n} - 2\nu k^2 E_{ij} + \frac{1}{2}\nu \frac{\partial^2 E_{ij}}{\partial x_n^2}$$

$$-(1-C_B)(u_{i,n}E_{jn} + u_{j,n}E_{in}) - C_B\frac{2}{3}\delta_{ij}u_{k,n}E_{kn}$$

$$+ C_{B1}\left(u_{n,i}E_{jn} + u_{n,j}E_{in} - \frac{2}{3}\delta_{ij}u_{k,n}E_{kn}\right)$$

$$+ C_{B2}(u_{i,j} + u_{j,i})E$$

$$+ C_D\frac{\partial}{\partial x_n}\left(\int_0^\infty \sqrt{k'E}/k'^2\, dk' \frac{\partial E_{ij}}{\partial x_n}\right)$$

$$- C_1\frac{\partial}{\partial k}\left(k^2\sqrt{kE}\,E_{ij}\right)$$

$$+ C_2\frac{\partial}{\partial k}\left(k^3\sqrt{kE}\frac{\partial E_{ij}}{\partial k}\right)$$

$$- C_m k\sqrt{kE}\left(E_{ij} - E\frac{\delta_{ij}}{3}\right)$$

where $E = E_{nn}$. The physical importance of each term, in order, is: advection, viscous dissipation, viscous diffusion, mean flow

coupling (C_B, C_{B1}, and C_{B2} terms), turbulent diffusion, wave-like k-cascade, diffusion-like k-cascade, and return to isotropy. Note that the C_{B1} and C_{B2} terms were neglected in BHRZ but are included here to judge their importance.

The generalized equations are simplified for the present comparison with experiment by the following assumptions. First, the mean pressure is constant and the flow variables (u_i, E_{xy}, etc.) have spatial variation in the cross-stream (y) direction only. The latter assumption gives rise to a flow field infinite in extent in the stream-wise direction. The time evolution of such a layer is depicted in Fig. 1. It is also assumed that $E_{yy} = E_{zz}$, as indicated by the reported 1-D spectra of Wygnanski and Fiedler (1969).

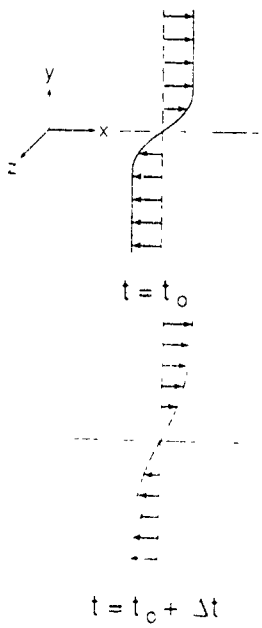

Figure 1. Geometric configuration of the computational flow field.

These assumptions reduce the equations to

$$\frac{\partial u}{\partial t} = \nu \frac{\partial^2 u}{\partial y^2} - \frac{\partial \overline{u'_x u'_y}}{\partial y} ,$$

$$\frac{\partial E_{xx}}{\partial t} = \left(4/3\, C_P - 1\right) \frac{\partial u}{\partial y} E_{xy} + V(E_{xx}) + T(E_{xx})$$

$$+ C_m k\sqrt{kE} \left(1/3\, E - E_{xx}\right) ,$$

$$\frac{\partial E_{xy}}{\partial t} = C_{B2} \frac{\partial u}{\partial y} E + V(E_{xy}) + T(E_{xy})$$

$$- C_m k\sqrt{kE}\, E_{xy} ,$$

and

$$\frac{\partial E_{yy}}{\partial t} = -2/3\, C_B \frac{\partial u}{\partial y} E_{xy} + V(E_{yy}) + T(E_{yy})$$

$$+ C_m k\sqrt{kE} \left(1/3\, E - E_{yy}\right) ,$$

where the V and T operators are, respectively:

$$V = \nu \left(-2k^2 + 1/2 \frac{\partial^2}{\partial y^2} \right)$$

$$T = C_D \frac{\partial}{\partial y} \nu_T \frac{\partial}{\partial y} - C_1 \frac{\partial}{\partial k} k^2 \sqrt{kE} + C_2 \frac{\partial}{\partial k} k^3 \sqrt{kE} \frac{\partial}{\partial k} .$$

This set of equations contain six undetermined constants: C_1, C_2, C_D, C_m, C_B, and C_{B2}.

The evolution equations for $E_{ij}(y,k,t)$ and $u_i(y,t)$ were integrated in a cell-centered, explicit, first order-in-time, finite-difference scheme, using a rectangular mesh with constant cell size for the variables y (cross-stream direction) and z(log k). The advection term in the cascade is approximated by upstream differencing, with $\sqrt{Ek}$ as the effective advection velocity. The use of log k rather than k permitted more efficient allocation of computer time to the dominant-eddy region of the spectrum. The time step dt was estimated by setting an upper limit on the allowed magnitude of $\Delta t = \Delta E/E$ for each term contributing to $\partial E/\partial t$, and adjusting this limit by trial to insure three-digit accuracy in the time integration. The ranges $0 \le y \le y_{max}$ (the y dependencies are symmetric under $y \to -y$) and $z_{min} \le z \le z_{max}$ of the mesh were set so that the E_{ij} were effectively zero at ymax and zmax. The boundary condition at $z = z_{max}$ must allow for loss of energy from the mesh in accordance with the Kolmogorov laws $E \sim k^{-5/3}$, flux-of-E~ constant for large k and small viscosity; this is accomplished by computing k-derivatives at $z = z_{max}$ under the assumption that the E_{ij} follow power-laws in k at this end of the mesh. This is consistent with the vanishing of the E_{ij}, when viscosity dominates at z_{max}.

As mentioned, the present model contains 6 as yet undetermined constants, C_1, C_2, C_d, C_m, C_B, and C_{B2}. A constraint on C_1 and C_2 as presented in BHRZ is $C_1 + 5/3\, C_2 \equiv 54$. This is to assure a match with the Kolmogorov constant for the decay of homogeneous isotropic turbulence. Also constrained are the relative values of C_B, C_{B1}, and C_{B2}. As implied from symmetry and incompressibility conditions (see BHRZ) $C_{B1} = 8C_B - 6$ and $C_{B2} = -3C_B + 11/5$. With $C_{B1} = 0$, which was required to have $E_{yy} = E_{zz}$, C_B and C_{B2} can then be determined. Also needed as input to the code is the initial wave number dependence of the energy spectra. In the limit $k \to 0$, $E(k) \sim k^n$ in the nomenclature of the present model. The final value of n (final meaning the flow has reached self-similarity) depends, not only on the constants in the model equations, but on the initial input. This input, in turn, should depend on the experimental conditions that initially generated the turbulence, of which there is very little information.

We use an 80 by 80 mesh in z and y space which is shown to be sufficient to insure mesh size independence.

RESULTS

The experimental data used for comparison is taken from the investigations of Wygnanski and Fiedler (1969), Zohar (1990), Patel (1973), Liepmann and Laufer (1947), Jimenez et al. (1979), and Huang and Ho (1990). All the experimenters used air as the medium at various velocities. Zohar, Huang and Ho, and Liepmann and Laufer used the mixing of two streams at different velocities while Wygnanski and Fiedler, Jimenez et al., and Patel use the flow far downstream of a step.

The comparison with the mean flow and spectrally integrated turbulence quantities are shown in Figs. 2 through 5. The data points are from the various experimental investigations listed in Table 1. The lines represent the simulation of the mixing layer by the present model. As can be seen in the figures, agreement between experiments and the model are quite good. The two sets of lines correspond to the two different combinations of constants shown in Table 2. Note that n_i is the initial power law behavior at the low wavenumber end of the spectrum. The solid line represents the value of C_D calculated with the constraint of the constant C_μ from the standard K-ε model. The major limitation of the K-ε model is that the turbulent energy spectrum must be in equilibrium, that is, the spectrum scales with only E_{max} and k_{max}. Once this occurs, the self-similar spectrum can be placed into our model and a form of K-ε will be obtained. This gives some basis for predicting what the constants in the present model should be. Unfortunately, the only unambiguous correspondence is between C_D of the present model and C_μ of the standard K-ε. For a discussion of this ambiguity and the method to obtain the correspondence see BHRZ. With this constraint the other constants were set through optimization and with the constraints previously mentioned. The dashed line corresponds to constants set without the constraint of C_D obtained from K-ε. This was done since the K-ε model obtained through our model was not quite the same as the standard K-ε model. There is no evidence that the constants for this modified version of K-ε are the same and relaxing this constraint resulted in a better fit to the experimental data. It should be noted that the values obtained for the constants in the present comparison are the same as those obtained by Clark (1991) in applying the present model to the computation of anisotropic strain. One final note to be made in the discussion of which set of constants is most appropriate is the fact that in direct numerical simulations of the present geometry (1-D mixing layer) some of the spectrally integrated turbulence quantities also show a tendency to be narrower (e.g., Riley, et al. (1986)). Thus it may be that the first set of constants is most appropriate with the second set covering up the different physics in comparing a 2-D mixing (which the experiments are) and the present 1-D approximation.

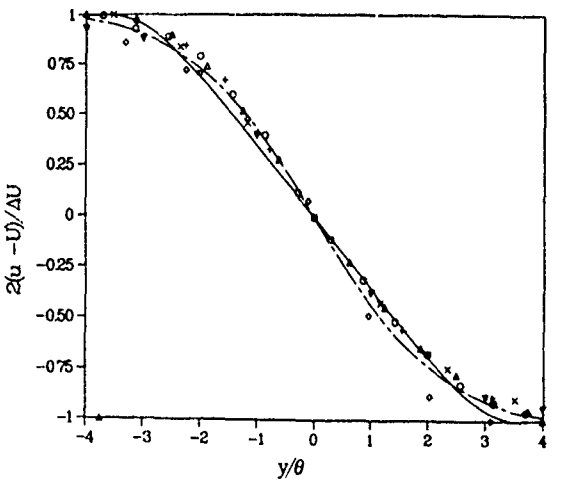

Figure 2. Nondimensional velocity versus cross-stream direction

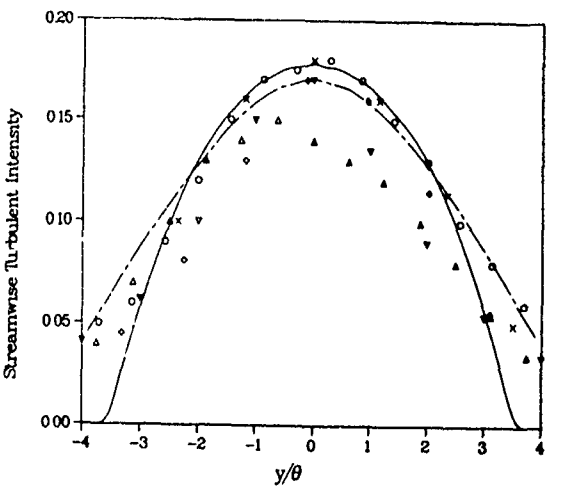

Figure 3. Streamwise turbulent intensity versus cross-stream direction

TABLE 1. REFERENCES USED IN FIGURES 2 THROUGH 5

Symbol	Reference
o	Patel (1973)
△	Liepmann and Laufer (1947)
+	Zohar (1990)
×	Wygnanski and Fridler (1970)
◊	Jimenez et al. (1979)
▽	Huang and Ho (1990)

TABLE 2. CONSTANTS USED IN COMPUTATION

Symbol	n_i	C_m	C_d	C_B	C_{B2}	C_1	C_2
———	3	.43	.116	.75	−.05	.30	.15
— - —	3	.43	.30	.75	−.05	.30	.15

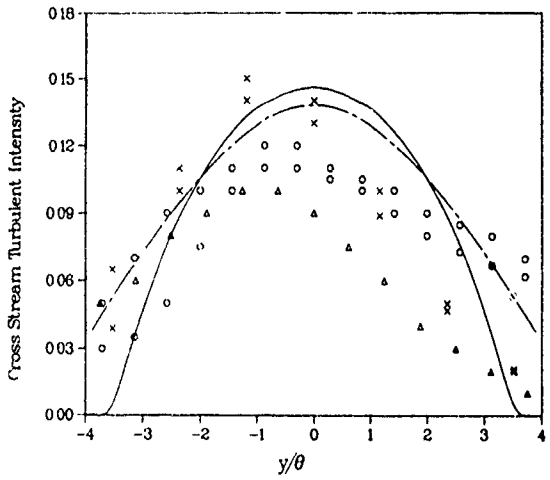

Figure 4. Cross-stream turbulent intensity versus cross-stream direction

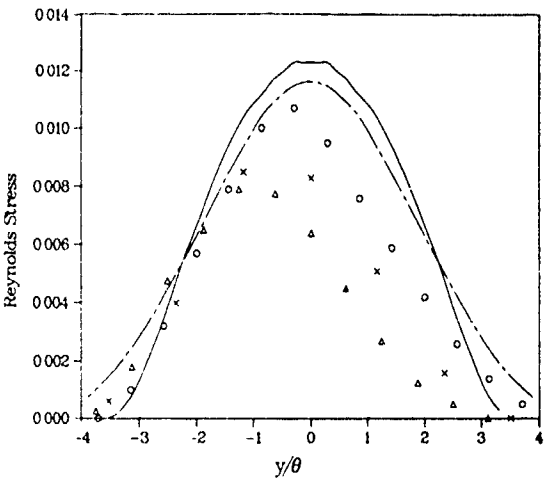

Figure 5. Reynolds stress versus cross-stream direction

One last comparison between experimental data and the model is shown in Fig. 6. Here is plotted the power law decay at high wavenumbers (n, where $E \sim k^n$ as $k \rightarrow \infty$) for the transition to turbulence in a mixing layer. The data points are from the investigation of Huang and Ho (1990) for R = 0.69. The initialization of the model was accomplished by fitting the first data point. At some downstream distance the power, n, has reached the steady-state value of -5/3. As shown, the computation of the rate at which this steady-state value is reached is in good agreement with the experiment.

Figures 7, 8, and 9 show the development of the spectra for a given set of constants but with different initial low wavenumber dependence. The model predictions of the final power law at low wavenumber depends on the ratio C_1/C_2, where C_1 and C_2 are the constants in the k-cascade terms. If $n_i \leq \{3(C_1/C_2) + 3\}/2$ then $E \sim k^{n_i}$ for $k \rightarrow 0$ as $t \rightarrow \infty$; but if $n_i > \{3(C_1/C_2) + 3\}/2$ then $E \rightarrow 0$ for $k \rightarrow 0$ as $t \rightarrow \infty$, where n_i is the initial low wavenumber dependence of the energy spectrum. For the present application $C_1/C_2 = 2$, therefore, $\{3(C_1/C_2) + 3\}/2 = 4.5$. Figures 7, 8, and 9 show the differences in the spectral development for n_i less than 4.5. The figures show that the energy spectrum quickly approaches its asymptotic shape at the high wavenumber end regardless of initial condition. The low wavenumber end, though, takes much longer, and as mentioned the final slope depends on the initial condition. Note that in these figures time is nondimensionalized by $1/(du/dy)_{y=0}$.

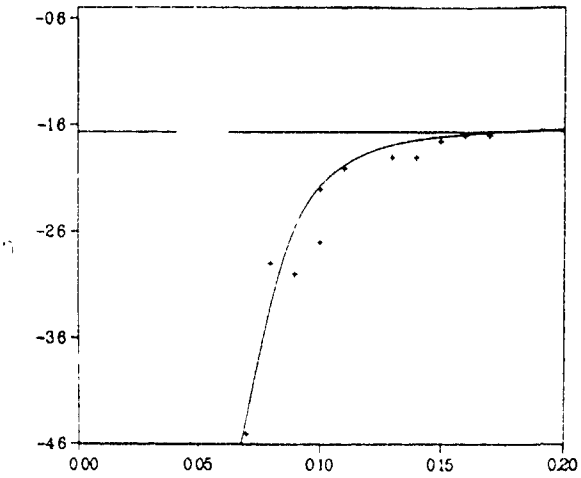

Figure 6. High wavenumber power law versus downstream distance

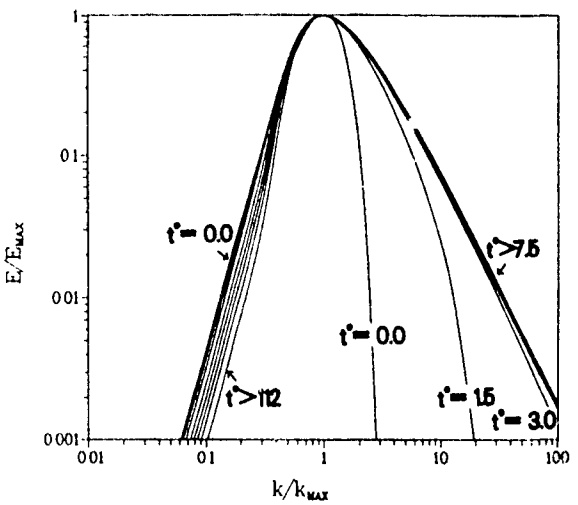

Figure 7. Turbulent energy spectrum as a function of time with $n_i = 3.0$

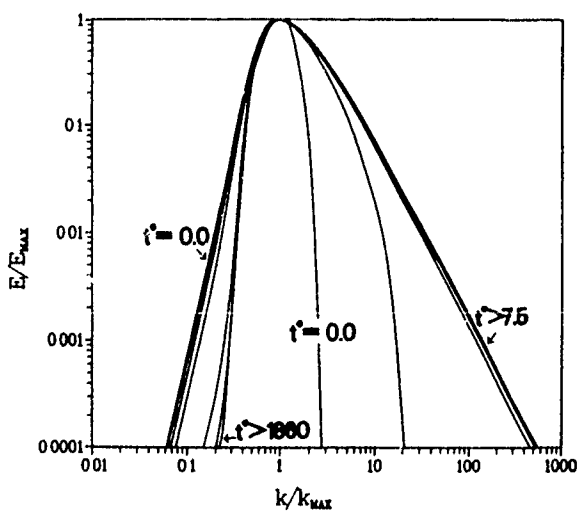

Figure 8. Turbulent energy spectrum as a function of time with $n_i = 4.0$

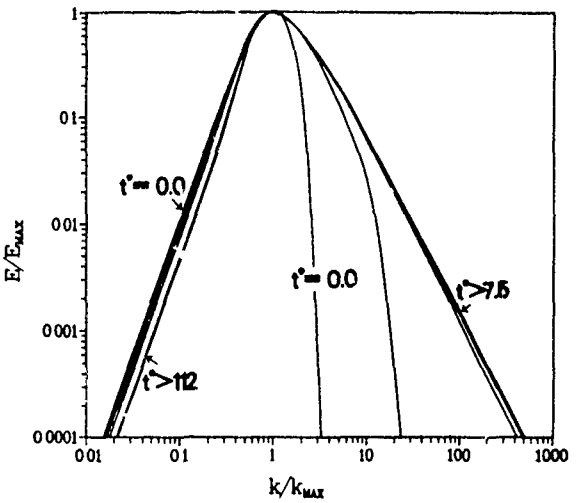

Figure 9. Turbulent energy spectrum as a function of time with ni = 2.0

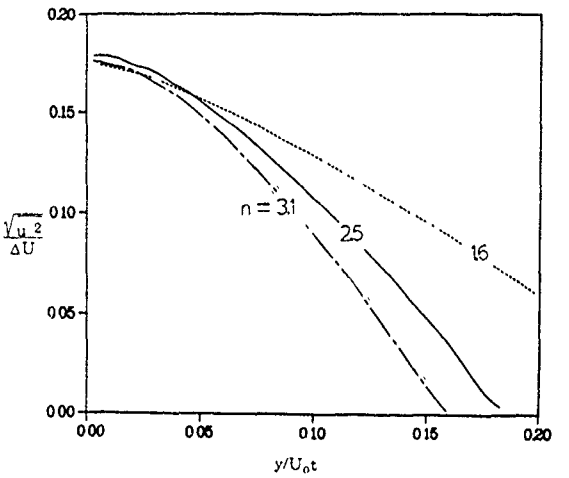

Figure 11. Streamwise turbulent intensity versus cross-stream direction for various initial low wavenumber dependence of the energy spectrum

Not only does the initial low wavenumber dependence affect the final shape of the turbulent energy spectrum but also the final self-similar forms of the mean velocity and spectrally integrated turbulence quantities. This is shown in Figs. 10 and 11. Here are plotted the mean velocity and streamwise turbulent intensity with a given set of constants except the initial low wavenumber dependence is varied. It is shown that this dependence can greatly affect the final self-similar shapes of the profiles. This is a possible explanation of why there is such a large variation in the self-similar profiles as given by the different experimental investigations (see Figs. 2 through 5); that is, the initial low wavenumber dependence will affect the final self-similar form.

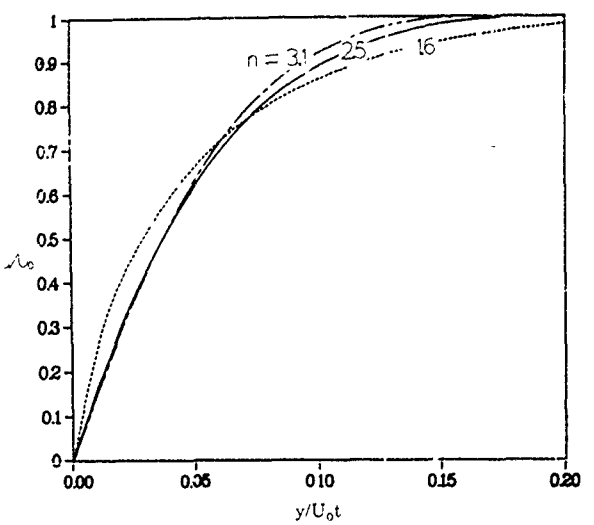

Figure 10. Nondimensional velocity versus cross-stream direction for various initial low wavenumber dependence of the energy spectrum

CONCLUSIONS

The present spectral transport model sufficiently predicts the self-similar behavior of the mixing layer within the variations found in the experiments. Also predicted is the power law dependence of the energy spectrum in the transition to turbulence. Some universality of constants is believed since the present ones fit the data of mixing layers as presented here and anisotropic strain presented in Clark (1991), although questions do arise on the appropriate value of C_D.

Many predictions of the nature of the turbulent energy spectrum can be made with this model, but the most interesting would be the initial low wavenumber dependence of the final self-similar forms of the spectra and mean flow quantities. Experimental verification is hampered by the fact that in general 1-D spectra is commonly measured not the 3-D spectra which the model predicts. The low wavenumber portion of the 1-D spectra does not correspond to that of the 3-D spectra due to aliasing. Further experimental evidence of the nature of the spectrum at low wavenumbers would be very useful in further validation of the model.

REFERENCES

Besnard, D. C., Harlow, F. H., Rauenzahn, R. M., and Zemach, C., 1990, "Spectral Transport Model for Turbulence," Los Alamos National Laboratory report LA-11821-MS.

Clark, T., 1991, Ph.D. Dissertation, University of New Mexico, in progress.

Huang, L. S. and Ho, C. M., 1990, "Small Scale Transition in a Plane Mixing Layer," *J. Fluid Mech.* Vol. **210**, pp. 475–500.

Jimenez, J., Martinez-Val, R., and Rebollo, M., 1979, "On the Origin and Evolution of Three Dimensional Effects in the Mixing Layer," Internal Report DA-ERO-78-G-079, Univ. Politec., Madrid.

Liepmann, H. W. and Laufer, J., 1947, "Investigation of Free Turbulent Mixing," NACA Tech. Note No. 1257.

Patel, R. P., 1973, "An Experimental Study of a Plane Mixing Layer," *AIAA J.*, vol. 11, pp. 67–71.

Riley, J. J., Metcalfe, R. W., and Orszag, S. A., 1986, "Direct Numerical Simulations of Chemically Reacting Turbulent Mixing Layers," *Phys. Fluids*, Vol. 29, pp. 406–422.

Taulbee, D. B., 1990, "Engineering Turbulence Models," in *Advances in Turbulence*, W. K. George and R. Arndt, Eds.

Wygnanski, I. and Fiedler, H. E., 1970, "The Two-dimensional Mixing Region," *J. Fluid. Mech.* Vol. **41**, pp. 327–361.

Zohar, Y., 1990, "Fine Scale Mixing in a Free Shear Layer," Ph.D. Dissertation, University of Southern California.

EIGHTH SYMPOSIUM ON
TURBULENT SHEAR FLOWS
Technical University of Munich
September 9-11, 1991

TURBULENCE MODEL FOR THE DISSIPATION COMPONENTS OF REYNOLDS STRESSES

M Tagawa, Y. Nagano and T. Tsuji

Department of Mechanical Engineering,
Nagoya Institute of Technology
Gokiso-cho, Showa-ku, Nagoya 466, Japan

ABSTRACT

This paper develops a new model for the nonisotropic dissipation rate tensor ε_{ij} to close the Reynolds-stress transport equations. The previous models of ε_{ij} are all algebraic, based on a hypothesis of either the isotropic relationship of the dissipation tensor or the one-to-one relationship of the dissipation anisotropy tensor with that for the Reynolds stresses. However, the recent direct simulation data of the turbulent boundary layer and channel flows have revealed the strongly non-isotropic nature of the dissipation process, which differs considerably from that of the Reynolds-stress components. The present model provides nonisotropic dissipation-rate components through the solutions of approximated transport equations for ε_{ij}, and hence, the conventional prescription of an ad hoc value of ε_{ij} is not needed The proposed model is tested by direct comparisons with the reported full simulation data to validate the performance of the model predictions

NOMENCLATURE

$C_1, C_2, C_1', C_2', \gamma'$ = model constants for Φ_{ij}
$C_{\varepsilon p1}, C_{\varepsilon p2}$ = model constants for ${}^{\varepsilon}\Phi_{ij}$
C_S, C_ε = model constants for the diffusion terms in $\overline{u_iu_j}$ and ε_{ij} equations
$C_{\varepsilon 1}, C_{\varepsilon 2}, C_{\varepsilon 3}$ = model constants for the production and dissipation terms in ε_{ij} equation
${}^{t}D_{ij}, {}^{p}D_{ij}, {}^{\nu}D_{ij}$ = diffusion terms in $\overline{u_iu_j}$ equation [Eq.(8)]
${}^{t\varepsilon}D_{ij}, {}^{p\varepsilon}D_{ij}, {}^{\nu\varepsilon}D_{ij}$ = diffusion terms in ε_{ij} equation [Eq.(10)]
${}^{\varepsilon}E_{ij}$ = dissipation term in ε_{ij} equation [Eq.(10)]
$f_w, f_\varepsilon, f_\mu$ = turbulence model functions
k = turbulent kinetic energy, $= \overline{u_iu_i}/2$
$\overline{P}$, p = mean and fluctuating pressures
$P_{ij}, {}^{1\varepsilon}P_{ij}, {}^{2\varepsilon}P_{ij}, {}^{3\varepsilon}P_{ij}, {}^{4\varepsilon}P_{ij}$ = production terms in $\overline{u_iu_j}$ and ε_{ij} equations [Eqs (8) and (10)]
P_k = production term in k-equation, $= P_{ii}/2$
R_t = turbulence Reynolds number, $= k^2/\nu\varepsilon$
T, T_t = time scales [Eqs. (16) and (11)]
$\overline{U}_i$, u_i = mean and fluctuating velocity components in x_i direction
u_τ = friction velocity, $= \sqrt{\tau_w/\rho}$
x_i = coordinates in tensor notation
x, y = coordinates
y^+ = dimensionless distance from wall, $= u_\tau y/\nu$
δ_{ij} = Kronecker delta
ε, ε_{ij} = dissipation rates of k and $\overline{u_iu_j}/2$
ν, ${}^{t}\nu_{ij}$ = kinematic viscosity and turbulent diffusivity
ρ = density
τ, τ_w = time and wall shear stress
$\Phi_{ij}, {}^{\varepsilon}\Phi_{ij}$ = redistributive terms in $\overline{u_iu_j}$- and ε_{ij}-equations [Eqs. (8) and (10)]
$\overline{(\ )}$ = time mean value
$(\ )_{,i}$ = differentiation by x_i $(= \partial/\partial x_i)$
$(\ )_{(i)}$ = tensor notation without summation convention

INTRODUCTION

The current transport models for the Reynolds-stress equations have the following three challenging problems: modeling of the redistribution term (the pressure-strain correlation) $\phi_{ij} = \overline{(p/\rho)u_{i,j}}$; modeling of triple velocity correlations $\overline{u_iu_ju_k}$; and modeling of the dissipation-rate tensor of Reynolds stress components $\varepsilon_{ij} = \nu\overline{u_{i,k}u_{j,k}}$. All of these exert an important influence on the universality of the Reynolds-stress equation model. There have been many proposals for modeling ϕ_{ij}. At present, the model proposed by Launder, Reece & Rodi (1975) (hereinafter referred to as LRR) is most often used for turbulence predictions, although several more sophisticated models have been proposed (e.g., Launder & Tselepidakis 1990). As for the triple products $\overline{u_iu_ju_k}$, Nagano & Tagawa (1990a; 1991) have developed a new structural model based not on the conventional assumption of gradient-type diffusion but on the statistical and structural characteristics of turbulence (Nagano & Tagawa 1988).

On the other hand, the turbulence model for the dissipative correlation ε_{ij}, which is an important sink term in the Reynolds-stress transport equation, is still rather primitive. The previous models of ε_{ij} are all algebraic, based on a hypothesis of either the isotropic relationship of the dissipation tensor, so that

$$\varepsilon_{ij} = (\delta_{ij}/3)\,\varepsilon \tag{1}$$

or the one-to-one relationship of the dissipation anisotropy tensor with that for the Reynolds stresses at lower Reynolds numbers, i.e.,

$$\varepsilon_{ij} = [(\overline{u_iu_j}/2)/k]\,\varepsilon \tag{2}$$

It is assumed that there is a gradual changeover from this limit, Eq.(2), to local isotropy, Eq.(1), as the turbulence Reynolds number $R_t = k^2/\nu\varepsilon$ becomes large. Thus, Hanjalić & Launder (1976) modeled ε_{ij} as

$$\varepsilon_{ij} = (1 - f_S)(\delta_{ij}/3)\,\varepsilon + f_S[(\overline{u_iu_j}/2)/k]\,\varepsilon \tag{3}$$

with

$$f_S = 1/(1 + R_t/10) \tag{4}$$

Here, the scalar trace of the dissipation-rate tensor, ε $(= \varepsilon_{ii} = \nu\overline{u_{i,k}u_{i,k}})$, is the dissipation rate of the turbulent kinetic energy k $(= \overline{u_iu_i}/2)$.

However, the recent direct simulation data of the turbulent boundary layer and channel flows have revealed the strongly non-isotropic nature of the dissipation process, which differs considerably from the anisotropy of the Reynolds-stress

components (Mansour, Kim & Moin 1988). In view of all these, this paper develops a new model for the non-isotropic dissipation-rate tensor ε_{ij} to close the Reynolds-stress transport equations. The present model provides non-isotropic dissipation-rate components through the solutions of approximated transport equations for ε_{ij}. The proposed model is tested by direct comparisons with both reported full simulation data and measurements of boundary layer flows.

GOVERNING EQUATIONS

The equations governing the flow in an incompressible fluid are

$$\overline{U}_{i,i} = 0 \tag{5}$$

$$D\overline{U}_i/D\tau = -\overline{P}_{,i}/\rho + \nu\overline{U}_{i,jj} - (\overline{u_iu_j})_{,j} \tag{6}$$

where the Einstein summation convention is used and a comma followed by an index indicates differentiation with respect to the indexed spatial coordinate.

In the Reynolds-stress model, the unknown Reynolds stress $\overline{u_iu_j}$ in Eq (6) is determined from the solutions of the following transport equation:

$$D\overline{u_iu_j}/D\tau = P_{ij} - 2\varepsilon_{ij} + \Phi_{ij} + {}^tD_{ij} + {}^pD_{ij} + {}^vD_{ij} \tag{7}$$

where

$$\left.\begin{aligned} P_{ij} &= -(\overline{u_iu_k}\,\overline{U}_{j,k} + \overline{u_ju_k}\,\overline{U}_{i,k}) \\ \varepsilon_{ij} &= \nu\,\overline{u_{i,k}u_{j,k}} \\ \Phi_{ij} &= \overline{(p/\rho)(u_{i,j} + u_{j,i})} \\ {}^tD_{ij} &= -(\overline{u_iu_ju_k})_{,k} \\ {}^pD_{ij} &= -[\overline{(p/\rho)(u_i\delta_{jk} + u_j\delta_{ik})}]_{,k} \\ {}^vD_{ij} &= \nu(\overline{u_iu_j})_{,kk} \end{aligned}\right\} \tag{8}$$

In the above equations, P_{ij} represents the production term, $2\varepsilon_{ij}$ denotes the dissipation rate, Φ_{ij} is the redistribution term (i.e., the pressure-strain term), and ${}^tD_{ij}$, ${}^pD_{ij}$ and ${}^vD_{ij}$ represent the terms of the turbulent, pressure and viscous diffusions, respectively. We need to model all the terms except for $D\overline{u_iu_j}/D\tau$, P_{ij}, ε_{ij} and ${}^vD_{ij}$. The existing Reynolds-stress equation models need the modeling of ε_{ij}, as given by Eqs. (1)-(3) In the present study, however, we determine ε_{ij} from the solutions of the following ε_{ij} transport equation, without modeling ε_{ij} algebraically:

$$D\varepsilon_{ij}/D\tau = {}^{1\varepsilon}P_{ij} + {}^{2\varepsilon}P_{ij} + {}^{3\varepsilon}P_{ij} + {}^{4\varepsilon}P_{ij} - {}^{\varepsilon}E_{ij} + {}^{\varepsilon}\Phi_{ij} + {}^{t\varepsilon}D_{ij} + {}^{p\varepsilon}D_{ij} + {}^{v\varepsilon}D_{ij} \tag{9}$$

where

$$\left.\begin{aligned} {}^{1\varepsilon}P_{ij} &= -\nu\,(\overline{u_{i,m}u_{k,m}}\,\overline{U}_{j,k} + \overline{u_{j,m}u_{k,m}}\,\overline{U}_{i,k}) \\ {}^{2\varepsilon}P_{ij} &= -\nu\,(\overline{u_{i,m}u_{j,k}} + \overline{u_{j,m}u_{i,k}})\overline{U}_{k,m} \\ {}^{3\varepsilon}P_{ij} &= -\nu\,(\overline{u_ku_{i,m}}\,\overline{U}_{j,mk} + \overline{u_ku_{j,m}}\,\overline{U}_{i,mk}) \\ {}^{4\varepsilon}P_{ij} &= -\nu\,(\overline{u_{i,k}u_{j,m}u_{k,m}} + \overline{u_{j,k}u_{i,m}u_{k,m}}) \\ {}^{\varepsilon}E_{ij} &= 2\nu^2\,\overline{u_{i,km}u_{j,km}} \\ {}^{\varepsilon}\Phi_{ij} &= \nu\,\overline{(p_{,m}/\rho)(u_{i,jm} + u_{j,im})} \\ {}^{t\varepsilon}D_{ij} &= -\nu\,(\overline{u_ku_{i,m}u_{j,m}})_{,k} \\ {}^{p\varepsilon}D_{ij} &= -\nu\,[\overline{(p_{,m}/\rho)(u_{i,m}\delta_{jk} + u_{j,m}\delta_{ik})}]_{,k} \\ {}^{v\varepsilon}D_{ij} &= \nu^2\,(\overline{u_{i,m}u_{j,m}})_{,kk} \end{aligned}\right\} \tag{10}$$

Here, the terms ${}^{1\varepsilon}P_{ij} \sim {}^{4\varepsilon}P_{ij}$ denote the production rates, ${}^{\varepsilon}E_{ij}$ represents the dissipation (or destruction), ${}^{\varepsilon}\Phi_{ij}$ is the redistributive term, and ${}^{t\varepsilon}D_{ij}$, ${}^{p\varepsilon}D_{ij}$ and ${}^{v\varepsilon}D_{ij}$ respectively represent the diffusion terms due to turbulent, pressure and viscous effects. Again, all the terms except for $D\varepsilon_{ij}/D\tau$, ${}^{1\varepsilon}P_{ij}$ and ${}^{v\varepsilon}D_{ij}$ should be modeled in Eqs. (9) and (10). In what follows, we take the x_1, x_2 and x_3 axes in the streamwise (x), wall-normal (y) and spanwise (z) directions, respectively

CLOSING THE $\overline{u_iu_j}$ EQUATION

Turbulent Time Scale

We reflect the non-isotropic nature of both turbulent transport and dissipation processes in the present model Thus, we define the "directional" time scale T_i as follows:

$$T_i = \left(\overline{u_{(i)}^2}/2\right)/\varepsilon_{(ii)} \tag{11}$$

where the indices in parentheses do not obey the summation convention rule. Obviously, Eq.(11) gives a time scale equivalent to the relative lifetime of the energy-containing eddies in the x_i direction.

Redistribution (Pressure-Strain Interactions)

In principle, we use the LRR model for the pressure-strain term Φ_{ij} in Eqs. (7) and (8). Thus, we write

$$\Phi_{ij} = {}^1\Phi_{ij} + {}^2\Phi_{ij} + {}^w\Phi_{ij} \tag{12}$$

with

$${}^1\Phi_{ij} = -C_1[\overline{u_iu_j} - (2/3)\delta_{ij}k]/T \tag{13}$$

$$\begin{aligned} {}^2\Phi_{ij} = &-[(C_2+8)/11]\,[P_{ij} - (2/3)\delta_{ij}P_k] \\ &-[(30C_2-2)/55]\,k\,(\overline{U}_{i,j} + \overline{U}_{j,i}) \\ &-[(8C_2-2)/11]\,[Q_{ij} - (2/3)\delta_{ij}P_k] \end{aligned} \tag{14}$$

$$\begin{aligned} {}^w\Phi_{ij} = &[C_1'\{\overline{u_iu_j} - (2/3)\delta_{ij}k\}/T \\ &+C_2'(P_{ij} - Q_{ij}) + \gamma'k\,(\overline{U}_{i,j} + \overline{U}_{j,i})]f_w \end{aligned} \tag{15}$$

where $Q_{ij} = -(\overline{u_iu_k}\,\overline{U}_{k,j} + \overline{u_ju_k}\,\overline{U}_{k,i})$, and $P_k = P_{ii}/2$ is the production rate of turbulent kinetic energy k.

The nondirectional (scalar) time scale T in the above equation can be defined from Eq (11) as:

$$T = \frac{\overline{u_i^2}/2}{\varepsilon_{jj}} = \frac{k}{\varepsilon} \tag{16}$$

As will be described later, some substantial modifications have to be made for the constants in the wall term ${}^w\Phi_{ij}$ of the LRR model so as to satisfy the physical requirements of the wall limiting behavior of turbulence.

Turbulent Diffusion

It was found to be unfavorable to apply a gradient-type diffusion model to the triple correlation $\overline{u_iu_ju_k}$ (Nagano & Tagawa 1988, 1991). However, we adopt the LRR's closures for the $\overline{u_iu_j}$ equation in the interest of brevity. Hence, we use a gradient-type approximation that is implicitly taken to account for both pressure contributions and velocity-driven transport The main difference is that we reflect the non-isotropic nature of turbulent transport process on the turbulent diffusivity ${}^t\nu_{ij}$ and write

$$ {}^{t}D_{ij} + {}^{p}D_{ij} = [C_S f_\mu \, {}^{t}\nu_{km}(\overline{u_i u_j})_{,m}]_{,k} \qquad (17) $$

with

$$ {}^{t}\nu_{ij} = \overline{u_i u_{(i)}}\, T_{(j)} \qquad (18) $$

The turbulent diffusion is strongly damped by fluid viscosity near a wall as the scales become progressively smaller, and thus the damping function f_μ is introduced in Eq.(17) (Prud'homme & Elghobashi 1983).

CLOSING THE ε_{ij} EQUATION

Anisotropy of Dissipation Process Near a Wall

Since, by continuity $u_{i,i} = 0$ and, at the wall ($x_2 = y = 0$), $u_{1,1}$ and $u_{3,3}$ both vanish, it follows that $u_{2,2} = 0$ at the wall. Consequently, from a Taylor-series expansion, turbulence quantities near the wall are represented as follows:

$$
\begin{aligned}
u_1 &= \alpha_1 y + \beta_1 y^2 + \gamma_1 y^3 + \cdots \\
u_2 &= \alpha_2 y^2 + \beta_2 y^3 + \cdots \\
u_3 &= \alpha_3 y + \beta_3 y^2 + \gamma_3 y^3 + \cdots \\
\overline{u_1^2} &= \overline{\alpha_1^2} y^2 + 2\overline{\alpha_1\beta_1} y^3 + (\overline{\beta_1^2} + 2\overline{\alpha_1\gamma_1}) y^4 + \cdots \\
\overline{u_2^2} &= \overline{\alpha_2^2} y^4 + 2\overline{\alpha_2\beta_2} y^5 + \cdots \\
\overline{u_3^2} &= \overline{\alpha_3^2} y^2 + 2\overline{\alpha_3\beta_3} y^3 + (\overline{\beta_3^2} + 2\overline{\alpha_3\gamma_3}) y^4 + \\
\overline{u_1 u_2} &= \overline{\alpha_1\alpha_2} y^3 + (\overline{\alpha_1\beta_2} + \overline{\alpha_2\beta_1}) y^4 + \cdots \\
k &= [(\overline{\alpha_1^2} + \overline{\alpha_3^2})/2] y^2 + (\overline{\alpha_1\beta_1} + \overline{\alpha_3\beta_3}) y^3 + \cdots \\
\varepsilon_{11}/\nu &= \overline{\alpha_1^2} + 4\overline{\alpha_1\beta_1} y + (4\overline{\beta_1^2} + 6\overline{\alpha_1\gamma_1}) y^2 + \cdots \\
\varepsilon_{22}/\nu &= 4\overline{\alpha_2^2} y^2 + 12\overline{\alpha_2\beta_2} y^3 + \cdots \\
\varepsilon_{33}/\nu &= \overline{\alpha_3^2} + 4\overline{\alpha_3\beta_3} y + (4\overline{\beta_3^2} + 6\overline{\alpha_3\gamma_3}) y^2 + \cdots \\
\varepsilon_{12}/\nu &= 2\overline{\alpha_1\alpha_2} y + (3\overline{\alpha_1\beta_2} + 4\overline{\alpha_2\beta_1}) y^2 + \cdots \\
\varepsilon/\nu &= \varepsilon_{ii}/\nu = (\overline{\alpha_1^2} + \overline{\alpha_3^2}) + 4(\overline{\alpha_1\beta_1} + \overline{\alpha_3\beta_3}) y +
\end{aligned}
$$

From the above equations, we obtain the following relationship of the dissipation tensor ε_{ij} in the limit as a wall is approached (Launder & Reynolds 1983):

$$ \frac{\varepsilon_{11}}{\overline{u_1^2}/2} = \frac{1}{4}\frac{\varepsilon_{22}}{\overline{u_2^2}/2} = \frac{\varepsilon_{33}}{\overline{u_3^2}/2} = \frac{1}{2}\frac{\varepsilon_{12}}{\overline{u_1 u_2}/2} = \frac{\varepsilon}{k} \qquad (19) $$

The above equation demonstrates the strongly anisotropic nature of the dissipation process in the near-wall region, and thus the models for ε_{ij} given by Eqs (1)-(3) are all inappropriate. Recently, to overcome this drawback, some attempts have been made by Launder & Tselepidakis (1990), Lai & So (1990) and Hallbäck, Groth & Johansson (1990) However, all of these models are still algebraic.

Production and Destruction of ε_{ij}

Order-of-magnitude analysis indicates that, in the high turbulence Reynolds number regime, the turbulent production rate ${}^{4\varepsilon}P_{ij}$ and the dissipation rate ${}^{\varepsilon}E_{ij}$ dominate the balance equation. These two terms collectively represent the net effect of the production of ε_{ij} due to vortex stretching of turbulent filaments and its destruction by viscous action. Thus, we model collectively these terms as

$$ {}^{4\varepsilon}P_{ij} - {}^{\varepsilon}E_{ij} = [C_{\varepsilon 1}(P_{ij}/2) - C_{\varepsilon 2} f_\varepsilon \varepsilon_{ij}]/T \qquad (20) $$

As to other lower-order terms representing the production rate of ε_{ij}, we apply the following approximation First, ${}^{1\varepsilon}P_{ij}$ does not require modeling, since we may rewrite ${}^{1\varepsilon}P_{ij}$ as

$$ {}^{1\varepsilon}P_{ij} = -(\varepsilon_{ik}\overline{U}_{j,k} + \varepsilon_{jk}\overline{U}_{i,k}) \qquad (21) $$

However, with $\varepsilon_{ik} \sim \overline{u_i u_k}/T$ and $\varepsilon_{jk} \sim \overline{u_j u_k}/T$ (see Eq.(2)), this term can be considered to be involved in the modeled production term on the right side of Eq.(20) The term ${}^{2\varepsilon}P_{ij}$, on the other hand, is negligible compared with the other terms, since mean velocity can be significant only in the direction parallel to the wall (Kebede, Launder & Younis 1985). The gradient production term ${}^{3\varepsilon}P_{ij}$ can be modeled by using the gradient-type diffusion representation:

$$ {}^{3\varepsilon}P_{ij} = C_{\varepsilon 3}\nu \, {}^{t}\nu_{km}(\overline{U}_{i,lm}\overline{U}_{j,lk} + \overline{U}_{j,lm}\overline{U}_{i,lk}) \qquad (22) $$

Note that a function f_ε in Eq.(20) is the model function introduced to fulfill the conditions for the near-wall limiting behavior of turbulence mentioned previously.

Redistribution of ε_{ij}

Since the trace of ${}^{\varepsilon}\Phi_{ij}$ is zero (i e , ${}^{\varepsilon}\Phi_{ii} = 0$), this term does not appear in the transport equation of ε. Thus, ${}^{\varepsilon}\Phi_{ij}$ represents the redistributive process among the anisotropic dissipation components ε_{ij} . The production and dissipation rate of the turbulent kinetic energy are very nearly in balance in near-equilibrium shear flows. Accordingly, it will be legitimate to conjecture that the redistributive process of ε_{ij} occurs, accompanied by the corresponding redistribution phenomena of the turbulence energy components, so that:

$$ {}^{\varepsilon}\Phi_{ij} = C_{\varepsilon p}(\Phi_{ij}/2)/T \qquad (23) $$

However, we have to take into account the difference in the non-isotropic nature between $\overline{u_i u_j}$ and ε_{ij} near the wall (Mansour, Kim & Moin 1988) Thus, in place of Eq.(23), the rational modeling of ${}^{\varepsilon}\Phi_{ij}$ may be written as

$$ {}^{\varepsilon}\Phi_{ij} = {}^{1\varepsilon}\Phi_{ij} + {}^{2\varepsilon}\Phi_{ij} + {}^{w\varepsilon}\Phi_{ij} \qquad (24) $$

$$ {}^{1\varepsilon}\Phi_{ij} = -C_{\varepsilon p1} C_1 f_\varepsilon [\varepsilon_{ij} - (1/3)\delta_{ij}\varepsilon]/T \qquad (25) $$

$$ {}^{2\varepsilon}\Phi_{ij} = C_{\varepsilon p2}({}^{2}\Phi_{ij}/2)/T \qquad (26) $$

$$
\begin{aligned}
{}^{w\varepsilon}\Phi_{ij} = [&C_{\varepsilon p1} C_1' f_\varepsilon \{\varepsilon_{ij} - (1/3)\delta_{ij}\varepsilon\}/T \\
&+ C_{\varepsilon p2}\{C_2'(P_{ij} - Q_{ij}) \\
&+ \gamma' k\,(\overline{U}_{i,j} + \overline{U}_{j,i})\}/2T] f_w
\end{aligned} \qquad (27)
$$

Diffusion of ε_{ij}

Corresponding to Eq.(17), the diffusion of ε_{ij} may be approximated by the following equation:

$$ {}^{t\varepsilon}D_{ij} + {}^{p\varepsilon}D_{ij} = (C_\varepsilon f_\mu \, {}^{t}\nu_{km}\varepsilon_{ij,m})_{,k} \qquad (28) $$

From these considerations, we finally obtain the governing equation for the transport of dissipation components ε_{ij} as follows:

$$
\begin{aligned}
D\varepsilon_{ij}/D\tau = &[C_{\varepsilon 1}(P_{ij}/2) - C_{\varepsilon 2} f_\varepsilon \varepsilon_{ij}]/T \\
&+ C_{\varepsilon 3}\nu \, {}^{t}\nu_{km}(\overline{U}_{i,lm}\overline{U}_{j,lk} + \overline{U}_{j,lm}\overline{U}_{i,lk}) \\
&+ {}^{\varepsilon}\Phi_{ij} + [(C_\varepsilon f_\mu \, {}^{t}\nu_{km} + \delta_{km}\nu)\varepsilon_{ij,m}]_{,k}
\end{aligned} \qquad (29)
$$

MODEL CONSTANTS AND FUNCTIONS

In accordance with the reassessment made by Morris (1984), the model constants C_1 and C_2 in Φ_{ij} are set to $C_1 = 1.7$ and $C_2 = 0.5$. On the other hand, the wall limiting behavior yields:

$$\Phi_{ij} + {}^{p}D_{ij} = -\overline{(1/\rho)(u_i p_{,j} + u_j p_{,i})} \rightarrow 0 \ (y \rightarrow 0) \tag{30}$$

The above relation requires that $\Phi_{ij} \rightarrow 0$ for $y \rightarrow 0$, since Eq.(17) gives that the turbulence diffusion and pressure-driven diffusion both vanish at the wall. In order to meet the requirement that $\Phi_{ij} \rightarrow 0$ for $y \rightarrow 0$, the following relation should be satisfied because of the vanishment of P_{ij}, Q_{ij} and k in the limit as the wall is approached

$$\Phi_{ij} = {}^{1}\Phi_{ij} + {}^{w}\Phi_{ij} = [1 - (C_1'/C_1)f_w]\,{}^{1}\Phi_{ij} \rightarrow 0 \tag{31}$$

From Eq (31), we have $(C_1'/C_1)f_w = 1$. Thus, we finally obtain $C_1' = C_1 = 1.7$, since the modeled function f_w is chosen to become unity at the wall and zero far away from the wall.

The above matter is extremely important. The LRR model has not taken into account this requirement, and hence the physically inappropriate behavior is brought about in the results of near-wall region (Mansour, Kim & Moin 1988).

We adopt the simplest form for the model function f_w, which meets the above-mentioned condition, as

$$f_w = \exp(-0.0065y^+) \tag{32}$$

In this case, the values of $C_2' = 0.055$ and $\gamma' = 0$ are determined as being optimal.

The constant in the diffusion term, Eq (17), is assigned to a standard value of $C_S = 0.21$, and the following simplest form is adopted as the model function f_μ:

$$f_\mu = 1 - \exp(-y^+/5) \tag{33}$$

On the other hand, the contraction of Eq (29) is reduced to the standard ε equation (e.g., see Launder & Tselepidakis 1990) when the local isotropy is assumed for the small scale dissipative motions. Therefore, most of model constants in the ε_{ij} equation (29) are put to agree with those in the conventional ε equation: $C_{\varepsilon 1} = 1.44$, $C_{\varepsilon 2} = 1.9$ and $C_\varepsilon = 0.17$. For the sake of simplicity, however, we put $C_{\varepsilon 3} = 0$. The model constants for ${}^{s}\Phi_{ij}$ are set as $C_{\varepsilon p1} = 3.3$ and $C_{\varepsilon p2} = 1.44$. In addition, in view of the near-wall limiting behavior of turbulence (Nagano & Tagawa 1990b), we set a function f_ε in Eq.(20) as

$$f_\varepsilon = 1 - \exp[-(R_t/18)^{1/2}] \tag{34}$$

MODEL TESTING AND CONCLUDING REMARKS

Calculations with the proposed model are performed for flat-plate turbulent boundary layers since the dissipation-rate components of the Reynolds stresses are quantitatively available from the recent direct numerical simulation (DNS) database of Spalart (1988). To investigate the Reynolds number dependency of the present model predictions, we have varied the momentum thickness Reynolds number, R_θ, as $R_\theta = 1410, 2750$ and 7500.

The numerical technique used is a finite-volume method (Patankar 1980). As described in the previous studies (Nagano & Hishida 1987, Nagano & Kim 1988), the coordinate for regions of very large gradients should be expanded near the wall. Thus, the following nonuniform grid (Bradshaw, Cebeci & Whitelaw 1981) across the layer is employed:

$$y_j = \Delta y_1 (K^j - 1)/(K - 1) \tag{35}$$

where Δy_1, the length of the first step, and K, the ratio of two successive steps, are chosen as 10^{-5} and 1.03, respectively. To obtain grid-independent solutions, 201 cross-stream grid points were used. The first grid point was normally located well into the viscous sublayer. The maximum streamwise step-size was restricted to a sublayer thickness, i.e., $\Delta x < \nu/u_\tau$.

The initial profiles of the Reynolds-stress and dissipation-rate components, $\overline{u_i u_j}$ and ε_{ij}, were provided using the algebraic stress model (ASM) together with the low-Reynolds-number $k - \varepsilon$ model (Nagano & Tagawa 1990b).

The boundary conditions are $\overline{U}_i = \overline{u_i u_j} = 0$, $\varepsilon_{11} = \nu(\partial\sqrt{\overline{u_1^2}}/\partial y)^2$, $\varepsilon_{33} = \nu(\partial\sqrt{\overline{u_3^2}}/\partial y)^2$ and $\varepsilon_{22} = \varepsilon_{12} = 0$ at $y = 0$ (wall); $\overline{U}_1 = \overline{U}_\infty$ and $\overline{u_i u_j} = \varepsilon_{ij} = 0$ at the free stream. Note that the above boundary conditions for ε_{11} and ε_{33} satisfy exactly the wall limiting behavior up to the first order of y.

The predictions of the velocity profiles of a flat-plate boundary layer are shown in Fig. 1. The results are compared with the DNS data (Spalart 1988, $R_\theta = 1410$) and experiment (Gibson, Verriopoulos & Nagano 1982, $R_\theta = 2750$). Although slight dependence on the Reynolds number is seen in the predicted wall-region velocity profiles, particularly at a low Reynolds number case, agreement with the standard log-law profile, $\overline{U}^+ = 2.44 \ln y^+ + 5.0$, is generally good.

To check the performance of the present model in more detail, we have compared the predictions of the Reynolds shear stress, $-\overline{u_1 u_2}/u_\tau^2$, and turbulent kinetic energy, k/u_τ^2, with the DNS data (Spalart 1988) and the experiments (Verriopoulos 1983, $R_\theta = 2750$, Klebanoff 1955, $R_\theta \simeq 7500$) in Figs. 2 and 3. As shown in the figures, a response of these quantities to the change of the Reynolds number is predicted correctly.

To perform the critical evaluation of the present model, we have compared the predicted profiles of the normal stress components with the DNS database of Spalart (1988) at the same momentum thickness Reynolds number of $R_\theta = 1410$. Figures 4 and 5 show the overall and near-wall profiles of $\sqrt{\overline{u_1^2}}/u_\tau$, $\sqrt{\overline{u_2^2}}/u_\tau$ and $\sqrt{\overline{u_3^2}}/u_\tau$, respectively. As seen in Fig. 4, general behavior of the DNS data is well predicted by the present model over the entire region of the boundary layer. As the wall is approached ($y^+ < 40$), the strong anisotropic behavior of the normal stress components is reproduced by

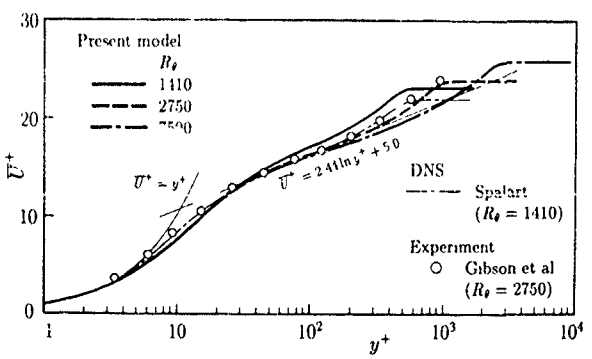

Fig. 1 Mean velocity profiles

the present model (Fig. 5). However, the difference in the $\sqrt{\overline{u_2^2}}$ profile between the DNS data and the present predictions becomes large in the near-wall region ($y^+ < 20$). This shortcoming is also seen, for example, in the results of the recent second-order closure model of Launder & Tselepidakis (1990). Lai & So (1990) have pointed out that to reproduce the correct near-wall anisotropic behavior of the normal stresses, the velocity pressure-gradient term in the $\overline{u_iu_j}$-equation should be modeled without splitting it into Φ_{ij} and ${}^pD_{ij}$ as done in the LRR model. Using the DNS database of a channel flow (Kim, Moin & Moser 1987), Mansour, Kim & Moin (1988) have also shown that, from the standpoint of modellers, the conventional split of the velocity pressure-gradient term is not a good way near the wall and that a judicious choice may be necessary. At the present stage, the model of $\overline{u_iu_j}$-equation is based on the LRR model because of its simplicity and general acceptance. It would be, however, preferable to revise the model of the velocity pressure-gradient term to reduce the predicted level of $\overline{u_2^2}$ profile near the wall (Lai & So 1990).

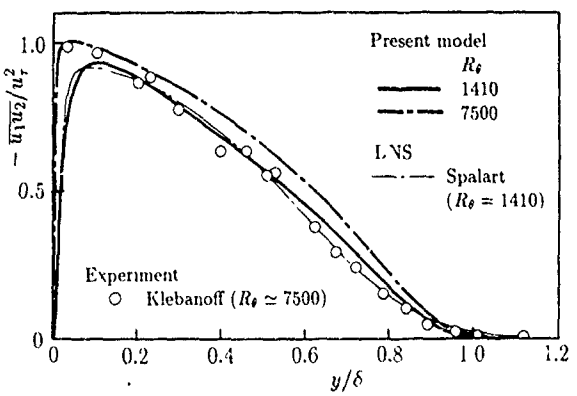

Fig 2 Reynolds shear stress profiles

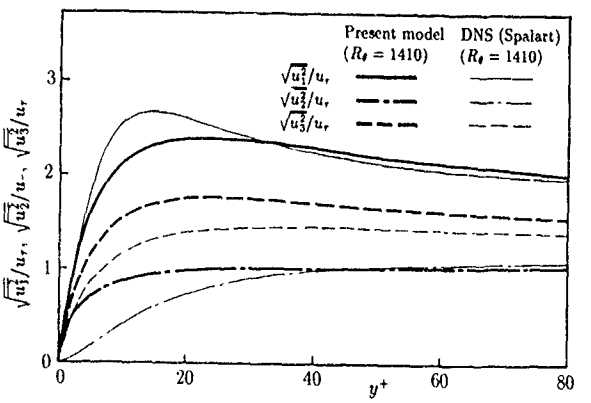

Fig. 5 Turbulence intensities near the wall

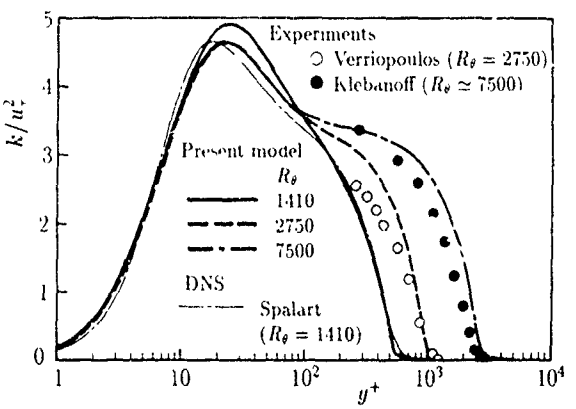

Fig. 3 Turbulent kinetic energy profiles

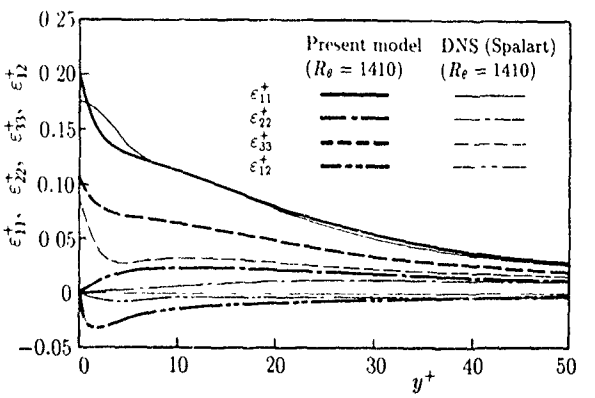

Fig. 6 Dissipation-rate tensor components near the wall

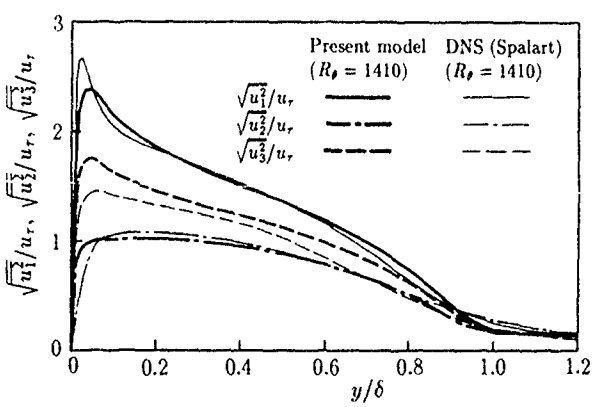

Fig. 4 Turbulence intensities

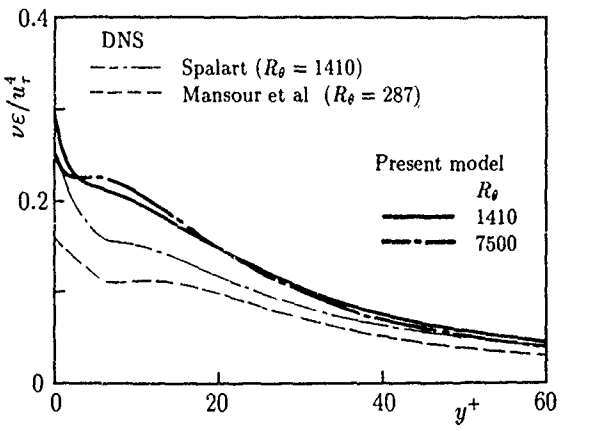

Fig. 7 Dissipation rate of k near the wall

The predictions of the dissipation components ε_{ij}^{+} $(= \nu\varepsilon_{ij}/u_{\tau}^{4})$ are shown in Fig. 6. These are the solutions obtained for the first time from the transport equation of ε_{ij}. It can be seen that the present solutions reproduce the strongly non-isotropic nature of the dissipation process near the wall. Overall agreement of ε_{11}^{+} with the DNS result (Spalart 1988) is very good. Significant improvements may be made in the predictions of ε_{22}^{+} and ε_{33}^{+} through a revision of the model for Φ_{ij} to reduce the level of $\overline{u_2^2}$ and $\overline{u_3^2}$ as discussed above. General behavior of ε_{12}^{+} near the wall accords with the DNS result, though the reduction of the peak level in the vicinity of the wall may be required. The most important and interesting feature of the present results is the realization of the peak values of ε_{11}^{+} and ε_{33}^{+} at the wall. As for this point, an attempt to improve the existing models has just started (e.g., Mansour, Kim & Moin 1989; Launder & Tselepidakis 1990, Shih & Mansour 1990, Lai & So 1990) to create a maximum of ε at the wall as evidenced in the DNS database (Kim, Moin & Moser 1987, Spalart 1988)

The present model results of ε^{+} $(= \varepsilon_{11}^{+}+\varepsilon_{22}^{+}+\varepsilon_{33}^{+})$ are shown in Fig. 7 compared with the existing DNS data of Kim, Moin & Moser (1987) ($R_\theta = 287$) and of Spalart (1988) ($R_\theta = 1410$). It is obvious that the profiles of ε depend greatly upon the flow Reynolds number as pointed out by Mansour, Kim & Moin (1988) The present predictions of ε for $R_\theta = 1410$ well trace the behavior of Spalart's result. Thus, the present approach to the modeling of the dissipation-rate tensor of Reynolds stress components has, we believe, good prospects in developing a full second-order closure.

ACKNOWLEDGMENT

This research was partially supported by a Grant-in-Aid for Scientific Research on Priority Areas from the Ministry of Education, Science and Culture of Japan (No 01613002)

REFERENCES

BRADSHAW, P., CEBECI, T. & WHITELAW, J. H 1981 *Engineering Calculation Methods for Turbulent Flow*, Academic

GIBSON, M. M., VERRIOPOULOS, C. A & NAGANO, Y 1982 Measurements in the heated turbulent boundary layer on a mildly curved convex surface. In *Turbulent Shear Flows* 3 (ed. L J S Bradbury *et al*), pp. 80-89 Springer.

HALLBÄCK, M , GROTH, J & JOHANSSON, A. V. 1990 An algebraic model for nonisotropic turbulent dissipation rate in Reynolds stress closures. *Phys. Fluids* **A2**, 1859-1866

HANJALIĆ, K & LAUNDER, B. E. 1976 Contribution towards a Reynolds-stress closure for low-Reynolds-number turbulence *J. Fluid Mech* 74, 593-610.

KEBEDE, W , LAUNDER, B E & YOUNIS, B A 1985 Large-amplitude periodic pipe flow A second moment closure study. In *Proc 5th Symp on Turbulent Shear Flows*, pp 16.23-16.29 Cornell University

KIM, J., MOIN, P. & MOSER, R 1987 Turbulence statistics in fully developed channel flow at low Reynolds number *J Fluid Mech.* **177**, 133-166.

KLEBANOFF, P. S. 1955 Characteristics of turbulence in a boundary layer with zero pressure gradient. *NACA Report* 1247

LAI, Y G & SO, R M. C. 1990 On near-wall turbulent flow modelling *J. Fluid Mech.* **221**, 641-673.

LAUNDER, B. E., REECE, G. J. & RODI, W. 1975 Progress in the development of a Reynolds-stress turbulence closure. *J. Fluid Mech.* **68**, 537-566.

LAUNDER, B. E. & REYNOLDS, W C 1983 Asymptotic near-wall stress dissipation rates in a turbulent flow. *Phys. Fluids* **26**, 1157-1158

LAUNDER, B. E. & TSELEPIDAKIS, D. P. 1990 Contribution to the second-moment modeling of sublayer turbulent transport. In *Near-Wall Turbulence* (ed. S. J. Kline & N. H. Afgan), pp. 818-833 Hemisphere

MANSOUR, N N., KIM, J. & MOIN, P. 1988 Reynolds-stress and dissipation-rate budgets in a turbulent channel flow. *J. Fluid Mech.* **194**, 15-44.

MANSOUR, N. N., KIM, J & MOIN, P 1989 Near-wall $k-\varepsilon$ turbulence modeling. *AIAA J.* **27**, 1068-1073

MORRIS, P. J. 1984 Modeling the pressure redistribution terms. *Phys. Fluids* **27**, 1620-1623.

NAGANO, Y & HISHIDA, M 1987 Improved form of the $k-\varepsilon$ model for wall turbulent shear flows *Trans ASME J. Fluids Engng* **109**, 156-160.

NAGANO, Y. & KIM, C 1988 A two-equation model for heat transport in wall turbulent shear flows. *Trans. ASME J Heat Transfer* **110**, 583-589.

NAGANO, Y. & TAGAWA, M 1988 Statistical characteristics of wall turbulence with a passive scalar *J Fluid Mech* **196**, 157-185

NAGANO, Y. & TAGAWA, M. 1990a A structural turbulence model for triple products of velocity and scalar. *J Fluid Mech.* **215**, 639-657.

NAGANO, Y. & TAGAWA, M. 1990b An improved $k-\varepsilon$ model for boundary layer flows. *Trans. ASME: J. Fluids Engng* **112**, 33-39.

NAGANO, Y. & TAGAWA, M 1991 Turbulence model for triple velocity and scalar correlations. In *Turbulent Shear Flows* 7 (ed. F. Durst *et al.*), pp. 47-62 Springer.

PATANKAR, S V. 1980 *Numerical Heat Transfer and Fluid Flow*, McGraw-Hill

PRUD'HOMME, M. & ELGHOBASHI, S. 1983 Prediction of wall-bounded turbulent flows with an improved version of a Reynolds-stress model In *Proc. 4th Symp. on Turbulent Shear Flows*, pp. 1.7-1.12. Karlsruhe.

SHIH, T. H. & MANSOUR, N. N. 1990 Modeling of near-wall turbulence. In *Engineering Turbulence Modelling and Experiments* (ed W. Rodi & E. N. Ganić), pp. 13-22. Elsevier.

SPALART, P. R 1988 Direct simulation of a turbulent boundary layer up to $R_\theta = 1410$ *J Fluid Mech.* **187**, 61-98.

VERRIOPOULOS, C. A. 1983 Effects of convex surface curvature on heat transfer in turbulent flow. *Ph.D. Thesis*, Imperial College.

TURBULENT SHEAR FLOWS
Technical University of Munich
September 9-11, 1991

STRUCTURE AND MODELLING IN STRONGLY SHEARED TURBULENT COMPRESSIBLE FLOW

Y. LEBRET*, D. VANDROMME*, H. HAMINH†

* LMFN, URA CNRS 230, INSA de Rouen, BP 8, 76131 M^t S^t Aignan, France.
† IMFT, URA CNRS 005, Av du Prof. C. Soula, 31400 Toulouse, France.

ABSTRACT

Recent works have shown the existence of large scale organised motions in compressible flows. Coherent structures were found in compressible shear layers (PAPAMOSCHOU and ROSHKO [1986]). These structures are unsteady, but play a significant role in the mixing layer spreading rate. Introducing semi-deterministic turbulence modelling, a standard $k-\epsilon$ model was used to calculate unsteady flows The main result is that unsteady features can be resolved with this type of turbulence model A rather good description of the unsteadiness does not give a good estimate of the compressible mixing layer spreading rate. This emphasizes the need for a better statistical treatment with a specific modelling of compressible effects

List of symbols

ρ density

U, V velocity components

a Speed of sound

k turbulent kinetic energy

ϵ turbulent kinetic energy dissipation rate

P_k production of turbulent kinetic energy

M Mach number

$\sigma_k, \sigma_\epsilon$ Turbulent Prandtl/Schmidt numbers for k and ϵ

C_1, C_2, C_μ Turbulence model constants

μ Laminar viscosity

μ_T turbulent viscosity

$\mu_k = \mu + \frac{\mu_T}{\sigma_k}$ $\mu_\epsilon = \mu + \frac{\mu_T}{\sigma_\epsilon}$

INTRODUCTION

Thank to efficient numerical tools, it is now possible to simulate unsteady turbulent compressible flows which present a great interest for basic understanding and practical applications as well These numerical predictions can be obtained either by direct numerical simulations, or by using adequate turbulence modelling. However, the numerous recent simulations do not highlight basic physical aspects of the phenomena, since the analysis of numerical data is strongly dependent of the interpretation. The compressible mixing layer is probably one of the most interesting cases, with well identified unsteady coherent structures resulting from Kelvin-Helmholtz instabilities.

Indeed, coherent structures are recognized as the major agent of large-scale mixing in turbulent shear flows. In incompressible flows, the vorticity field is a suitable indicator to visualize these structures, while compressible flows require different criteria. Interest for the mixing mechanisms is growing with the to-day needs of designing new propulsion devices for high speed transport aircrafts, since the efficiency of combustion systems is depending mostly on mixing phenomena.

In this perspective, the present contribution is devoted to.

- Characterization of the coherent structures in compressible turbulent shear flows.
- Analysis of the filtering features due to the numerical integration
- Evolution of the mixing layer growth with respect to a characteristic Mach number.

TURBULENCE MODELLING

To represent properly the large-scale mixing, HUSSAIN [1983], and more recently HAMINH and VANDROMME [1989], have proposed in the framework of turbulence modelling, a different form of variable decomposition, similar to the splitting used in Large Eddy Simulations Let $f(\vec{x},t)$ the instantaneous value of any dependent variable

$$f(\vec{x},t) = \overline{f(\vec{x})} + f_c(\vec{x},t) + f_r(\vec{x},t) \qquad (1)$$

The first term in the RHS is the *steady state* component. The second term is the *coherent* or *organized* contribution which depends on space and time in a determinstic manner, and the last part is the *random* fluctuation.

Thus the difference with the classical L.E.S approach comes from the relative importance of the three components If the coherent part is small, then the decomposition leads to classical Reynolds averaging If the random part is small, we have the basis for the conventional L.E.S. with subgrid scale modelling. The original contribution in the present work is to consider that random fluctuations are not constrained in scale and frequency. Therefore it is not possible to account completely for them with a space filter (such as the mesh resolution) like subgrid scale modelling does. To represent all random motions (whatever their characteristic scales are), we choosed to use a statistical model i.e. $k-\epsilon$ model. Following the original terminology of HAMINH *et al.*[1989], this approach is called the Semi-Deterministic Modelling. The variable decomposition can be written as:

$$f(\vec{x},t) = < f(\vec{x},t) > + f_r(\vec{x},t) \qquad (2)$$

in which $< f(\vec{x},t) >$ represents the ensemble average of f. Under some circumstances, this quantity could be replaced by the phase average Since this splitting preserves a similar form to the classical turbulence modelling, formally identical models can be derived to represent the random motion effects. The key difference is that the resulting solution would be strongly dependent on the flow haracteristics and the numerical method as well

To illustrate the difference between this new approach and the classical turbulence modelling, it suffices to compare the solutions which would be given by a parabolic space marching code (steady state boundary layer approximation) and a time marching Navier-Stokes solver, when calculating a flow as simple as a plane mixing layer. . Both solutions will be true, but they will show differents views of the reality. Vortex shedding or no vortex shedding, the thruth is in both approaches, only the representation is different.

Thus, in this semi-deterministic approach context, a two equation turbulence model for high Reynolds number flows would be written as

$$\frac{\partial}{\partial t}(< \rho >< k >) + \frac{\partial}{\partial x_i}(< \rho >< k >< U >_i - \mu_k \frac{\partial < k >}{\partial x_i}) = P_k - < \rho >< \epsilon > \quad (3)$$

$$\frac{\partial}{\partial t}(< \rho >< \epsilon >) + \frac{\partial}{\partial x_i}(< \rho >< \epsilon > U_i - \mu_\epsilon \frac{\partial < \epsilon >}{\partial x_i}) = \frac{< \epsilon >}{< k >} < \rho > (C_{\epsilon 1} P_k - C_{\epsilon 2} < \epsilon >) \quad (4)$$

$$P_k = - < \rho >< u_i" u_j" > \frac{\partial < U_i >}{\partial x_j} \quad (5)$$

Equations are averaged according to the Favre decomposition With this formulation all the unknows but ρ, and p are mass-weighted by ρ So the system is now

$$\frac{\partial \overline{\rho} k}{\partial t} + \frac{\partial \overline{\rho} k \tilde{U}_i}{\partial x_i} = P_k + \frac{\partial}{\partial x_i}\left(\mu_k \frac{\partial k}{\partial x_i}\right) - \overline{\rho}\epsilon \quad (6)$$

$$\frac{\partial \overline{\rho} \epsilon}{\partial t} + \frac{\partial \overline{\rho} \epsilon \tilde{U}_i}{\partial x_i} = C_1 P_k \frac{\epsilon}{k} - C_2 \overline{\rho} \frac{\epsilon^2}{k} + \frac{\partial}{\partial x_i}\left(\mu_\epsilon \frac{\partial \epsilon}{\partial x_i}\right) \quad (7)$$

$$P_k = -\overline{\rho} \widetilde{u_i" u_j"} \frac{\partial \tilde{U}_i}{\partial x_j} \quad (8)$$

So far no compressibility terms are added to the equations

NUMERICAL ASPECTS

The numerical method used in this study is the implicit-explicit finite volume scheme of MAC CORMACK [1981] . The scheme is second order accurate in time and in space.

The computational domain is 1.5 m long and 1 0 m high Two different meshes are used, one is made of 90 grid cells in x direction, the other is 120 grid cells in x direction, in the y direction both meshes have 100 cells with a significant clustering in the shear layer zone.

RESULTS

Unsteady features

The first flow which is examined is made of two air streams The two freestream velocities are $U_1 = 432\ m/s$, $U_2 = 137\ m/s$, total temperature T_T and total pressure P_T are identical in the two streams ($T_T = 300°K$, $P_T = 3.67\ 10^6\ Pa$). The Mach numbers of the two streams are respectively $M_1 = 1\ 5$ and $M_2 = 0.4$

VORTICITY FIELD

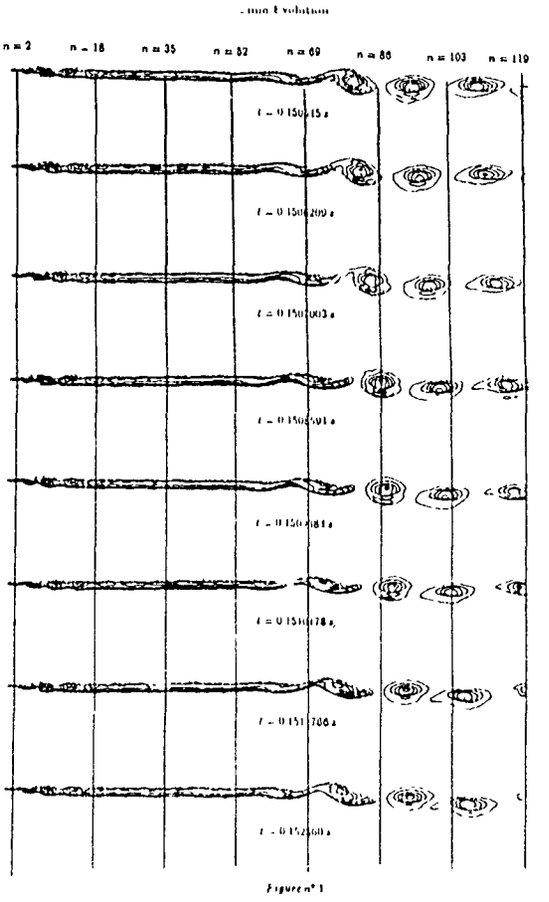

Figure 1 shows the time evolution of the vorticity There is a strong concentration of vorticity in the first part of the domain but no coherent structure are visible. Such structures exist in the second part of the domain. To find the coherent structures, the definition given by HUSSAIN [1983] was used. they are large structures with a high level of vorticity strongly correlated in phase but they appear at random phases. A linear stability study of the Euler equations gives a necessary condition of existence of Kelvin-Helmotz instabilities in the shear layers: the velocity profile must have an inflexion point. The input velocity profile is built with an heavyside fonction without any artificial perturbation to trigger the instability. The criterion used to identify coherent structures consists in finding the peaks of vorticity and pressure. The time evolution of theses peaks allows to determine the convective velocity of the structures. On that flow it has been estimated to be $300 \pm 30\ m/s$. PAPAMOSCHOU and ROSHKO [1986] give a theorical formulation of that velocity. They argue that in the frame which is moving with the convective velocity, a saddle point exists between the structures. This point implies the equality of total pressure

point in the convective motion frame. So that the convective velocity can be defined as.

$$U_c = \frac{a_2 U_1 + a_1 U_2}{a_1 + a_2}$$

With this formulation the convective velocity obtained is: 297 m/s so the agreement is fairly good. Also this phenomenom appears to be quasi periodic

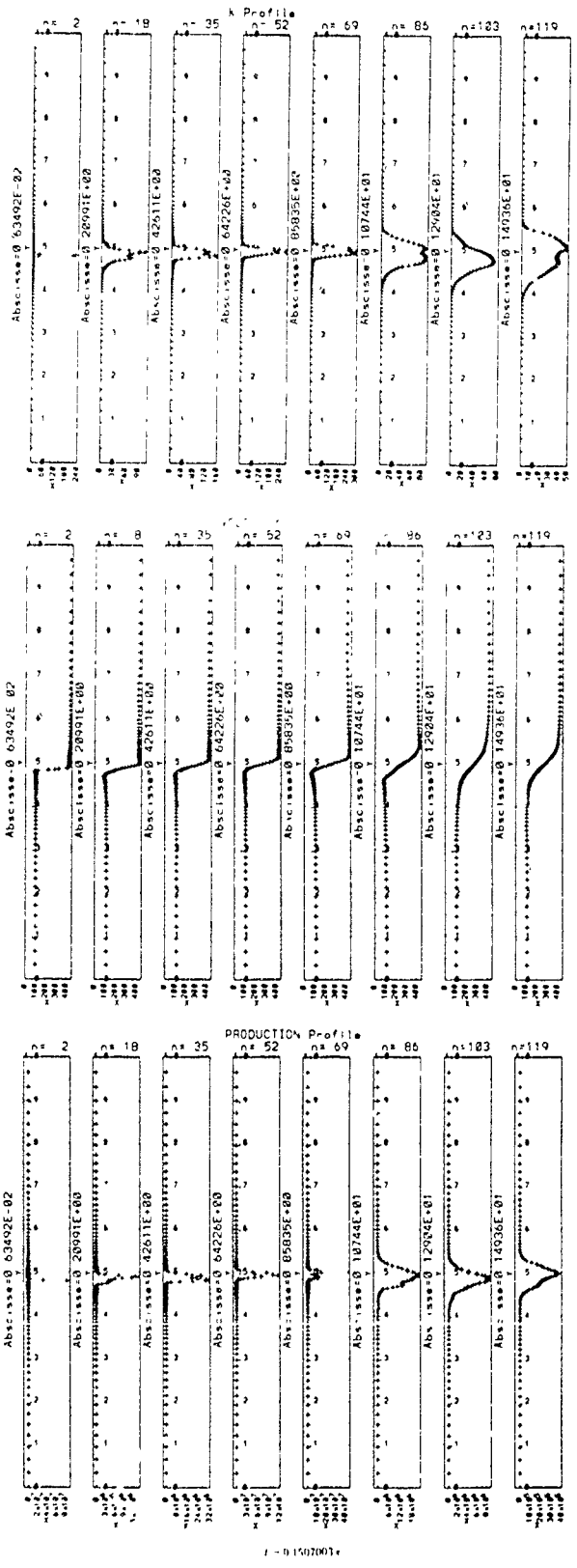

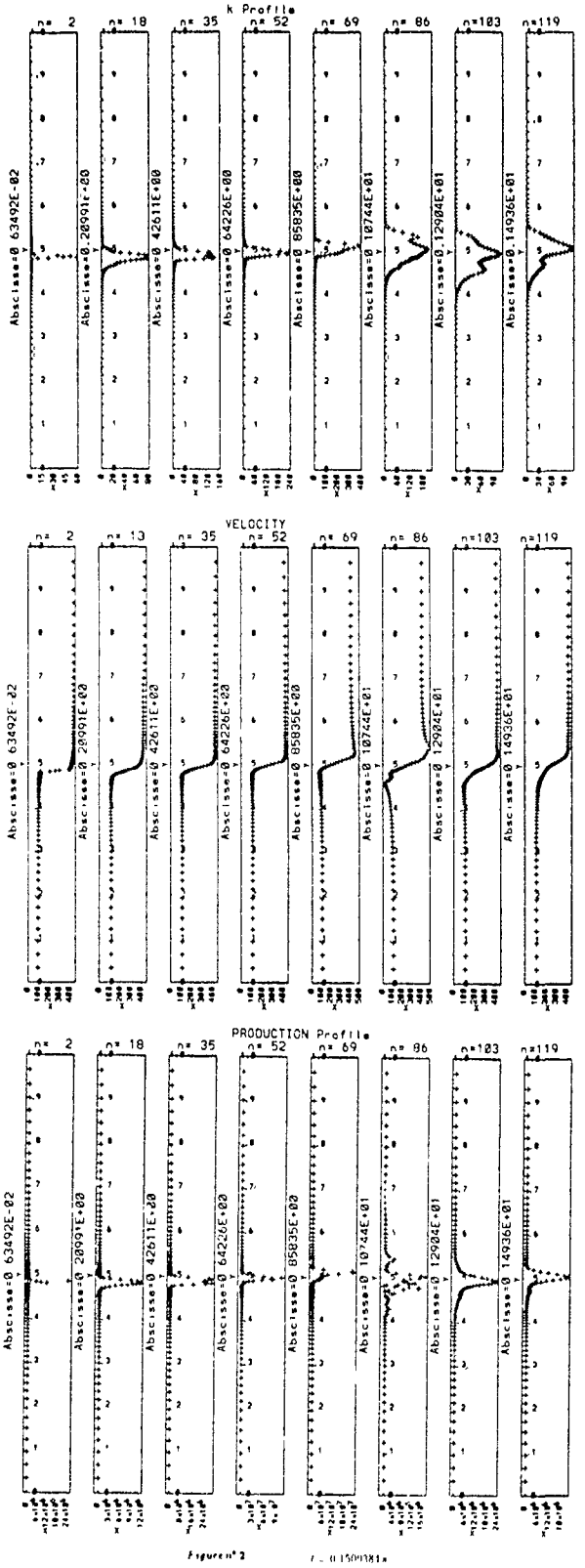

Figure 2 shows profiles at different locations and times. They represent the instantaneous velocity, the turbulent kinetic energy k, and its production rate. The strongest concentration of production of k is located in the shear layer. These profiles change according to the relative position of the structures. This result is better shown on figure 3, the peak of k is concentrated in the core of the coherent structures and is transported with it.

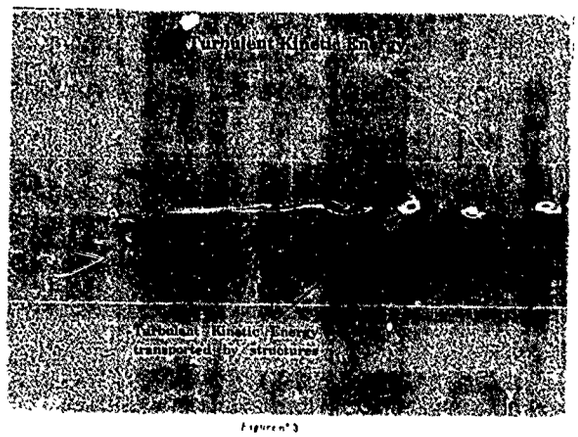

Figure n°3

As figure 4 shows, coherent structures present different aspects according to the variable which is observed. The pressure field shows a succession of nodes, which are alternatively low and high pressure nodes. The peak of low pressure matches with the maximum of vorticity. The passive scalar shows the mixing role of the coherent structures. Also the core of coherent structures is made of fluid coming from the lower stream.

To conclude with these time-dependent features, the results obtained to describe unsteady turbulent flows are quite encouraging, and it seems reasonable to pursue the construction of specific unsteady turbulent models can be developped.

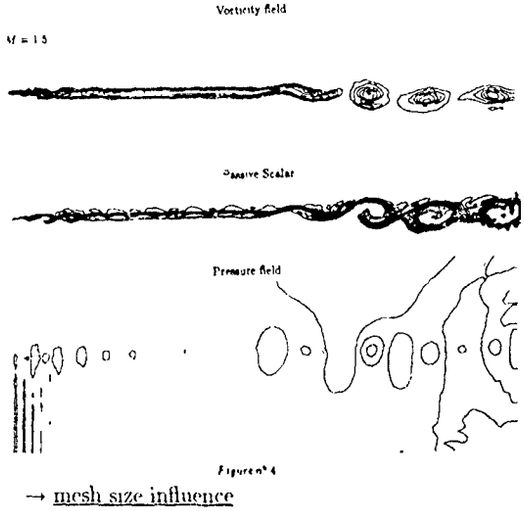

Figure n°4

→ mesh size influence

The mesh size is a very important parameter as far as filtering properties are concerned. A numerical simulation was done on the same flow with a smaller mesh (90 grid cells in y direction), the cells in the y direction and the integration time step was the same as for previous flow calculation.

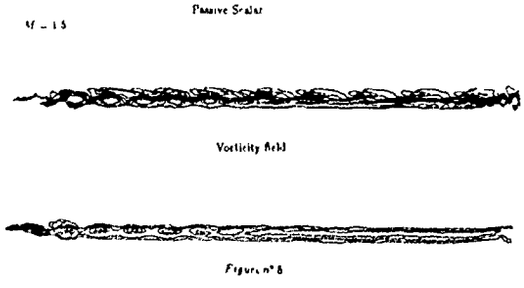

Figure n°5

Figure 5 shows the vorticity field, no structures are appearing. The first conclusion is that the behavior of the flow is strongly dependent of the mesh wich is used. Further investigations are needed to better understand the role of the mesh resolution. It is clear that the mesh can be responsible for filtering mechanims. The time step is also is also responsible for that. Unlike in the L.E.S., mesh cell size and time step are not linked, because of the implicit integration scheme. Further computations are being done to check an asymptotic behaviour of results for finer mesh sizes and time step.

→spreading rate

Three flows were calculated to estimate the influence of Mach number on the mixing layer spreading rate. In this calculation the Mach number are 1.5, 2.5 and 3 for the upper stream, for the lower stream the Mach number are 0.4, 1, and 1.37. The convective Mach numbers are almost the same in the three cases and ranges from 0.4 to 0.48.

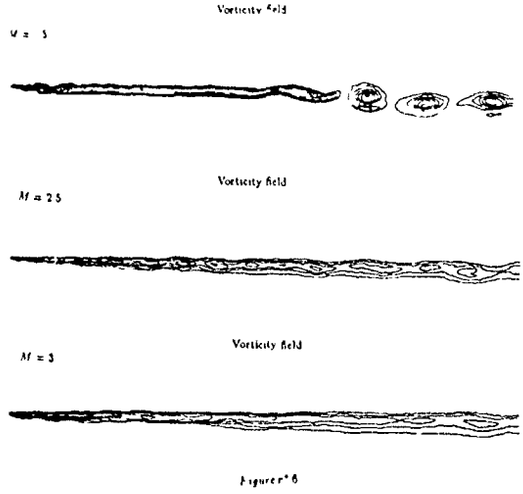

Figure n°6

On figure 6, we can see that as the Mach number increases, the mixing layer growth is reduced.

The velocity used to evaluate the spreading rate is the time averaged profile. The mixing layer thickness is taken as the distance between transverse locations where the time averaged velocity equal to $U_1 - 0.1\Delta U$ and $U_2 + 0.1\Delta U$. To determine the mixing layer growth we consider only the domain where the velocity profile was self similar. Figure 6 shows the evolution of the downstream velocity profile.

With that formulation the growth rate are around 0.06 with a Mach=1.5, and 0.04 if the Mach number is 2.5 and 0.03 in the last case. The value of the convective Mach number is going from 0.4 to 0.48. The growth is found to be nearly the same when the Mach number is 2.5 or 3. To obtain the visual thickness as PAPAMOUSCHOU and ROSHKO defined it, these results are undimensionalised with the incompressible growth formulation. With that formulation the visual thickness obtained is around 0.73 if the Mach number is 1.5 and a convective mach number of 0.4, 0.86 with a Mach number of 2.5 and a convective Mach number of 0.48,

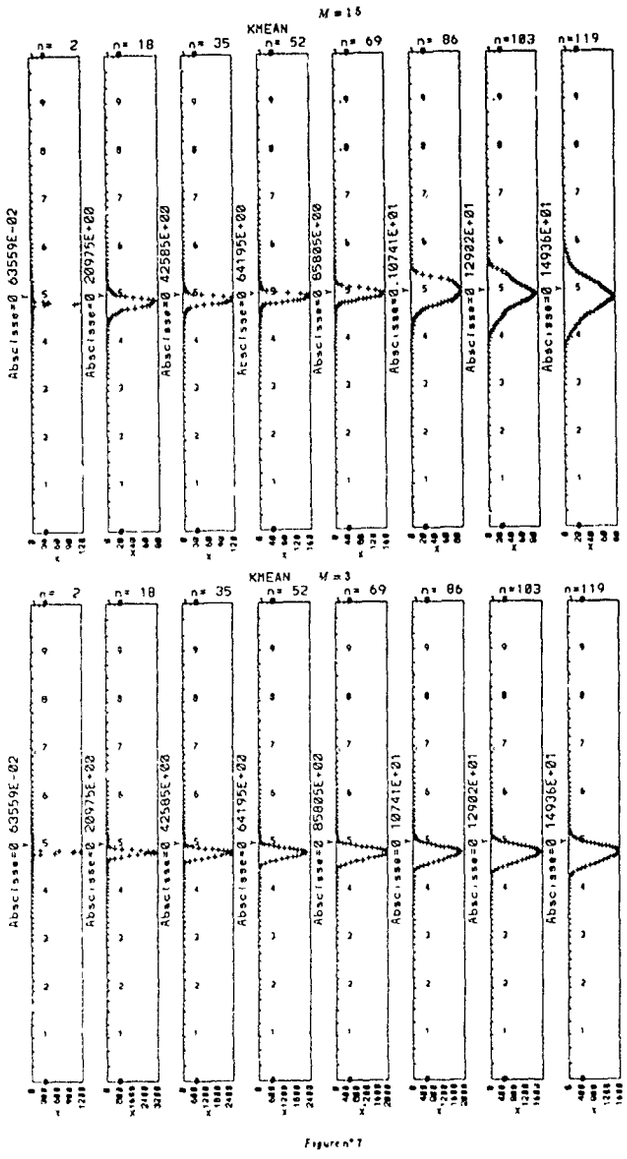

Figure n° 7

and 0.9 with a Mach number of 3 and a convective Mach number of 0 43. The comparison with the results obtained by PAPAMOSCHOU and ROSHKO would be around 0 8 for a convective Mach number of 0.4 and 0 7 for a convective Mach number of 0 5 The badest result is obtained for the higher Mach number calculation An explanation is that no compressibility terms are included in the model, and as the Mach number is increased these effects are more important and the model do not account for compressibility effects So a good time description of the flow do not allow a good description of the compressibility. Some compressibility terms must be added to the turbulence model.

CONCLUDING REMARK

In these study a standard $k - \epsilon$ model was used to calculate unsteady flow. The results obtained are encouraging and it seems reasonable to developp specific unsteady turbulence models. But a good time description of compressible flow does not allow to predict an accurate growth of the shear layer. This can show the need of take into account of the Mach number effects.

ACKNOWLEDGMENT

This work was supported by DRET (Direction des Recherches et des Etudes Techniques) and by the SNECMA (Société Nationale d'Etudes et de Construction Mécaniques Aéronautiques)

The compution time has been provided by CIPHAN (Centre d'Informatique Parallèle de HAute Normandie), CCVR (Centre de Calcul Vectoriel pour la Recherche), and CERFACS (Centre Européen de Recherche et de Formation Avancée en Calcul Scientifique).

REFERENCES

GOEBEL and DUTTON, "Experimental study of compressible turbulent mixing layers", AIAA journal, Vol 29 n^o 4, April 91

HAMINH and VANDROMME, "The compressible mixing layer", Grenoble 1989

HUSSAIN, "Coherent Structure reality and myth", Phys of Fluid n^o 26, 1983, pp 2816-2850

MAC-CORMACK, "A numerical Method for solving the equations of compressible viscous flow", Ames Research Center, NASA, AIAA paper 1981

PAPAMOSCHOU and ROSHKO, "Observation of supersonic Free Shear Layers", AIAA paper n^o 86-0162,January 86

PAPAMOSCHOU, "Experimental Investigation of heterogeneous compressible shear layers", Ph. D. Thesis, Pasadena California 1986

EIGHTH SYMPOSIUM ON
TURBULENT SHEAR FLOWS
Technical University of Munich
September 9-11, 1991

TURBULENCE IN THE VICINITY OF A ROTATING CYLINDER IN A QUIESCENT FLUID: EXPERIMENTS AND MODELLING

H.I. ANDERSSON[*]), B. JOHANSSON[**]), L. LÖFDAHL[**]), and P.J. NILSEN[*])[1]

[*]) Division of Applied Mechanics
The Norwegian Institute of Technology
N-7034 Trondheim, Norway

[**]) Department of Thermo- and Fluid Dynamics
Chalmers University of Technology
S-41296 Gothenburg, Sweden

ABSTRACT

An experimental and numerical investigation of the turbulence field in the vicinity of a rotating cylinder in a quiescent fluid has been carried out. Radial distributions of mean velocity and non-vanishing Reynolds stress components have been measured using hot-wire technique, and corresponding components have been calculated with a low-Reynolds number second-moment closure model. From the measurements it can be concluded that the turbulence field is established in the present set up at a Reynolds number which is roughly twenty times larger than earlier measurements have shown. Comparisons between calculations and measurements yield some deviations. However, a qualitatively good agreement is obtained. In the paper, different methods for the determination of the friction velocity are also described and discussed

INTRODUCTION

Turbulent flows in curved channels and over convex or concave surfaces are of obvious engineering interest Many flows in industrial equipment exhibit strong centrifugal-force fields, and it is well known that the centrifugal forces exerted on a turbulent flow field have important implications not only on the mean flow pattern but also on the turbulence structure, e.g Bradshaw (1973).

To further investigate curvature effects on turbulent shear flows, a centrifugal-force field is created in a very simple and fundamental geometry The one-dimensional boundary layer flow around an infinitely long and constantly rotating cylinder in an otherwise quiescent fluid is studied. In this particular flow case the mean velocity vector is in the azimuthal direction, and the mean velocity and the turbulent stresses vary only in the radial direction, i.e. with the distance from the curved wall.

While Theodorsen & Regier (1944) measured the frictional drag on a rotating cylinder, the radial distributions of the mean velocity and the turbulent stresses have been reported by Kasagi & Hirata (1975) and Nakamura et al. (1983, 1986), respectively. The latter data were obtained for Reynolds number Re = 41000 and above, where Re = $U_w R/\nu$, R is the radius, ν is the kinematic viscosity of the fluid, and $U_w = \omega R$ is the wall velocity. Kasagi & Hirata (1975), on the other hand, studied the flow at lower Reynolds numbers and claimed that their flow visualizations indicated fully developed turbulence for Re > 500.

An objective of the present study is to provide further measurements of the individual turbulent stress components at as low Reynolds numbers as possible. Such data are essential for the verification of low-Reynolds number extensions of second-moment closure models, and, in particular, to demonstrate their ability to mimic curvature-induced changes in the turbulence structure. Another objective of this investigation is therefore to compare numerical predictions based on a low-Reynolds-number second-moment model with the measured radial distribution of the individual stress components.

EXPERIMENTAL SET UP

A PVC tube, 1000mm long and 500mm in diameter, was used as a cylinder. Fixed end plates were fitted in order to minimize the influence of the end effects. An electrical motor, which could be continuously adjusted in the range 200 through 3000 rpm, was used for the accomplishing of the rotation of the cylinder. The lowest number of revolutions corresponds approximately to a wall velocity of 0.6 m/s. A dial test indicator and a vernier scale were used in the near wall region and further out, respectively, for the determination of the distance between the hot-wire and the cylinder surface.

Velocity measurements were performed using a constant temperature anemometer system, Dantech 5600, with standard single- and cross-wire probes, 55P01 and 55P61, respectively. A computerized version of Siddal & Davies' (1972) calibration law was employed for conversion of the anemometer voltage into velocities, and a sampling frequency of 3 kHz was used throughout the measurements. Conventional methods were used for the evaluation of the mean velocities and Reynolds stress components. All these acquisition methods have been tested, and compared to measurements of others, in a two-dimensional turbulent flat plate boundary layer at a Reynolds number of $4.2 \cdot 10^6$, see Löfdahl (1986) and Löfdahl et al. (1989).

[1] Present address VERITEC A/S
P O Box 300, N-1322 Høvik, Norway

An important question in this kind of measurements is whether a disturbance caused by the wake of the hot-wire probe will be transported by the flow along the cylinder circumference and interfere with the measurements. Therefore, a dummy probe was inserted at the same axial position as the measuring probe, but located at different angular positions No influence on the measurements were recorded when the dummy probe was positioned more than 45° upstream the "active" measuring probe. It might thus be concluded that the wake of the measuring probe does not affect the measurements

MODELLING APPROACH

Kasagi & Hirata (1975) and Williamson & Koukousakis (1987) used an algebraic eddy-viscosity model to represent the turbulence field in the vicinity of the rotating cylinder However, the resulting mean velocity distribution deviated significantly from the measured velocities

When the turbulence structure is directly modified by a body-force, like the centrifugal force, a model for the individual Reynolds stress components is needed. In the present approach the recently proposed low-Reynolds-number second-moment transport model of Launder & Shima (1989) is adopted This model is essentially a low-Reynolds-number extension of the Reynolds-stress closure due to Gibson & Launder (1978) The essence of the Launder & Shima model is that some of the model constants are made functions of four dimensionless parameters, namely a turbulent Reynolds number, the ratio of production to dissipation of turbulent kinetic energy, and two Reynolds stress invariants Kristoffersen et al (1990) demonstrated that the Launder & Shima model, with rotational stress generating terms included, accurately captured the most striking Coriolis-force effects induced by system rotation In the present study the model has been adapted to cylindrical polar coordinates, while the empirical values of the model coefficients are retained For the one-dimensional flow under consideration in the present study, the transport equations for mean momentum, Reynolds stresses and dissipation rate reduce to a strongly coupled set of 6 ordinary differential equations, which is solved numerically with a significantly higher degree of accuracy than generally achieved for solutions of systems of PDE's

EXPERIMENTAL RESULTS

Measured mean (azimuthal) velocity profiles are shown in Fig. 1 for different Reynolds numbers Compared to the exact analytic laminar flow solution $U = U_w/(1+(y/R))$, the profiles clearly exhibit turbulent character. A significant Reynolds number dependence can be observed only in the innermost part of the boundary layer, i.e. for $y/R < 0.02$, where $y = r-R$ denotes the radial distance from the wall.

Fig 2 shows the mean velocity profiles in inner variables for three different Reynolds numbers. Here, the inner variables are defined as $u'=U_d/u_*$ and $y'=yu_*/\nu$, where $U_d=U_w-U$ is the velocity defect and $u_*=\sqrt{\tau_w/\rho}$ is the wall friction velocity To obtain this scaling velocity a correlation formula of Theodorsen & Regier (1944) has been used:

$$\frac{1}{\sqrt{c_d}} = -0.6+4.07\log_{10}(Re\sqrt{c_d}) \qquad (1)$$

where the dimensionless drag coefficient c_d is defined as

$$c_D \equiv \frac{\tau_w}{\frac{1}{2}\rho\omega^2R^2} = 2\frac{u_*^2}{U_w^2} \qquad (2)$$

The linear and logarithmic curves $u' = y'$ and $u' = 1/0.41\ \ln(y') + 5.0$ have been shown as a reference. As can be seen, the expected deviation from the log-law due to streamline curvature is present at all Reynolds numbers studied.

The experimental resolution in the linear region is good for Reynolds numbers 20000 and 33000. For the highest Reynolds number Re=100000 the boundary layer becomes thinner and the number of measuring points in the near-wall region is therefore limited by the size of the hot-wire probe. Nevertheless, the friction velocity has been estimated from the slope of the innermost mean velocity data points and compared with u_* computed iteratively from Eqs (1) and (2), see Table 1.

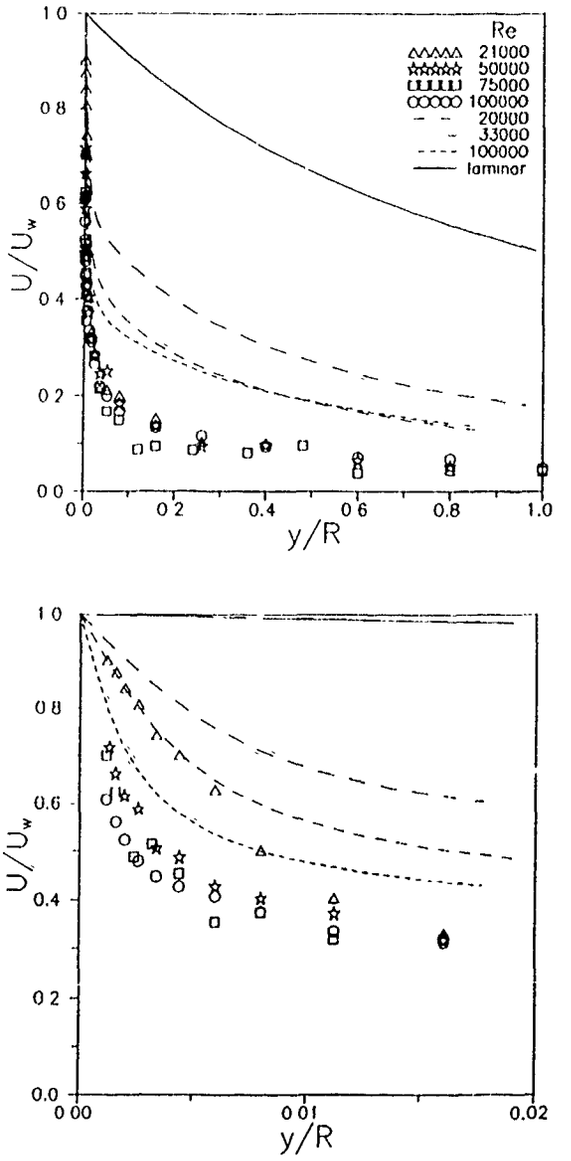

Figure 1 Mean velocity profiles for some different Reynolds numbers.

The measured turbulent intensities u' (azimuthal), v' (radial) and w' (axial) are shown in Fig. 3. Considering the magnitude of the different components, the turbulence intensity in the main flow direction, u', clearly dominates in the innermost part of the boundary layer. Further out, y/R=0.06, the profiles for the axial and radial components merge into each other at an intensity level below u'. The higher level of u' can, however, be explained by the "extra" stress generating terms which appear in the Reynolds stress budget due to the streamline curvature.

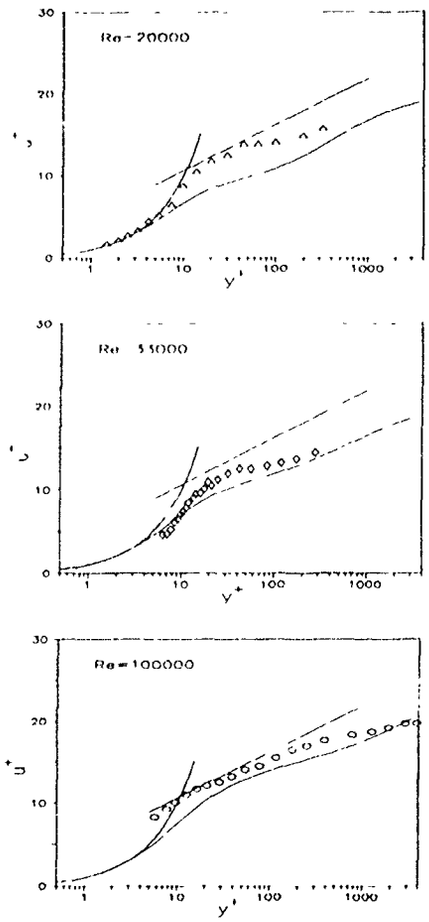

Figure 2 Mean velocity profiles in inner variables for three different Reynolds numbers

Table 1 Estimated friction velocities u_τ/U_w

Method \ Re	20000	33000	100000
Iterative solution of Eq. (1)	0.057	0.053	0.047
Modified constants in Eq. (1)	0.040	0.038	0.034
Extrapolated from measured mean velocity	0.066	0.046	0.060
Extrapolated from measured turbulent shear stress	-----	0.034	0.027
Numerical prediction	0.049	0.045	0.042

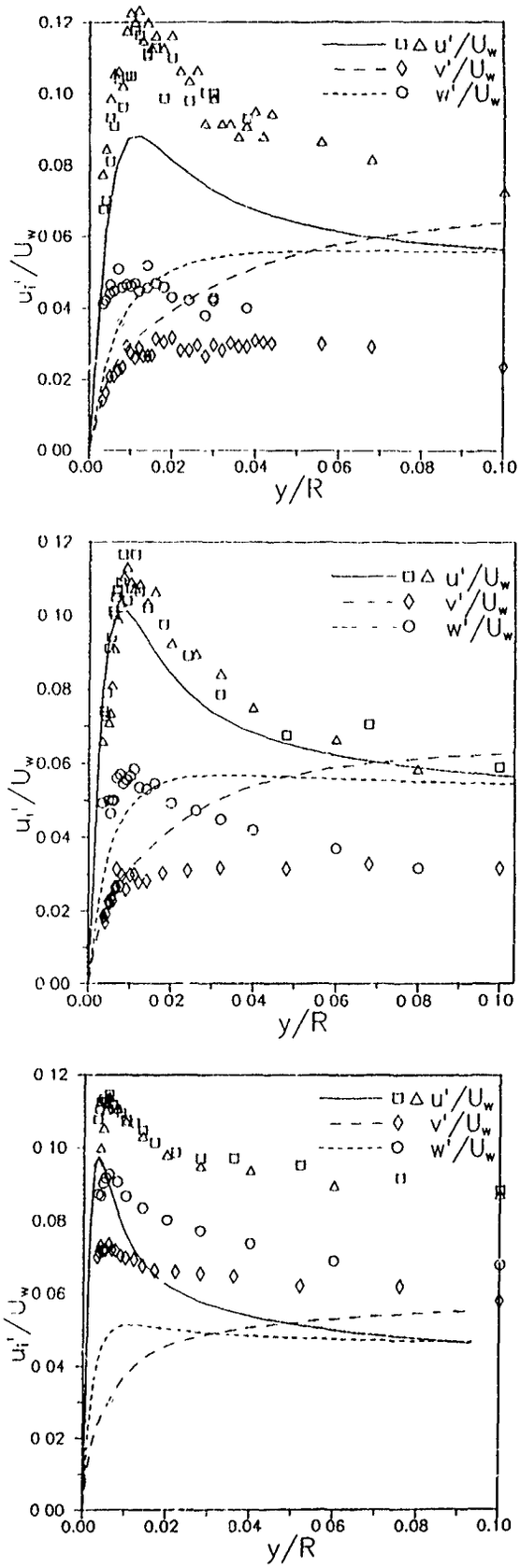

Figure 3 Radial distribution of the turbulence intensities for Reynolds numbers 20000 (upper), 33000 (middle) and 100000 (lower).

In Fig 4, the radial variation of the kinematic turbulent shear stress $\overline{uv}$ is shown, from which it can be observed that the experimental data are consistent with the azimuthal momentum balance (i.e. $r^2\tau$ = constant) away from the wall A fairly constant level of $\overline{uv}r^2$ can thus be used as an alternative way to estimate the wall shear stress τ_w and the friction velocity u_*. The intermittent nature of the flow at the lower Reynolds number complicates the situation and the wall friction can not be accurately obtained from the measured data The two different techniques for obtaining u_* are compared with the correlation (1) due to Theodorsen & Regier in Table 1. Nakamura et al (1983) replaced the dimensionless constants (-0 6,4 07) in Eq (1) by (3.09,4 79) to fit their experimental data Friction velocities based on this alternative set of constants are also included in the table. It is readily observed that the scatter in the data increases with increasing Reynolds number However, a general tendency of decreasing u_* for increasing Reynolds number can be noted, fully in agreement of what can be expected

The dimensionless ratio between the shear stress and (twice) the kinetic energy is shown in Fig 5 The observed level of the structural parameter uv/q^2 away from the cylinder surface is consistent with the experimental findings of Nakamura et al (1986) The present measurements of the individual stress components in Figs. 3 5 cover, however, the innermost part of the turbulent boundary layer more completely than any of the previously published data.

In Fig 6, the intermittency factor γ is plotted Here, γ has been calculated from the flatness factor F(u) for the streamwise velocity component as $\gamma=3/F(u)$, according to Klebanoff (1955) It can be seen from these data that the intermittency factor decreases below one for a certain distance from the cylinder surface for both the studied Reynolds numbers Especially for Re=22000 this means that a highly intermittent flow is prevailing, and this can considerably influence the measured turbulence intensities. If the laminar part of the signal is excluded in the measurements, this will increase the turbulent intensity This effect is clearly pronounced in the outer part of the boundary layer, where the largest deviations between measurements and calculations occur according to Fig. 3 Of course the influence of the intermittency is strongest at the lower Reynolds number and weaker at higher The results for Reynolds number 100000 are in agreement with the data of Nakamura et al (1983), while the results for Reynolds number 22000 are significantly different Only the innermost part of the boundary layer ($y'<20$) is fully turbulent

An important question in the studies of the flow field in the vicinity of a rotating cylinder in a quiescent fluid is at which Reynolds number the transition to turbulence occurs. To gain information of this phenomenon, the intermittency factor was determined at different Reynolds numbers The results from these measurements have been collected in Fig. 7, where the intermittency factors for the fluctuation in the main flow direction are shown as a function of the Reynolds number. The wall distance is kept constant to $y'=50$. At Reynolds numbers roughly above 25000 the intermittency exceeds one, thus indicating a fully turbulent flow.

To further investigate the point of transition, the Reynolds stresses were determined as a function of the Reynolds number (also at a constant $y'=50$). According to Fig. 8 the turbulence intensity in the main flow direction reaches an almost constant value above Re = 25000, thereby indicating a fully developed turbulent regime in agreement with Fig. 7. The two other normal components increase more gradually with increasing Reynolds number. It can be noted, however, that these components tend to zero at a Reynolds number of about 10000, which is much higher than the transition Reynolds number Re = 500 reported by Kasagi & Hirata (1975).

Autocorrelation coefficients for the streamwise fluctuating component are shown in Fig. 9. Here the time delay h is normalised by the period T corresponding to one revolution of the cylinder. The fairly large values of the autocorrelation in the outer part of the boundary layer indicate the existence of large-eddy structures visualized recently by Nakamura et al. (1986).

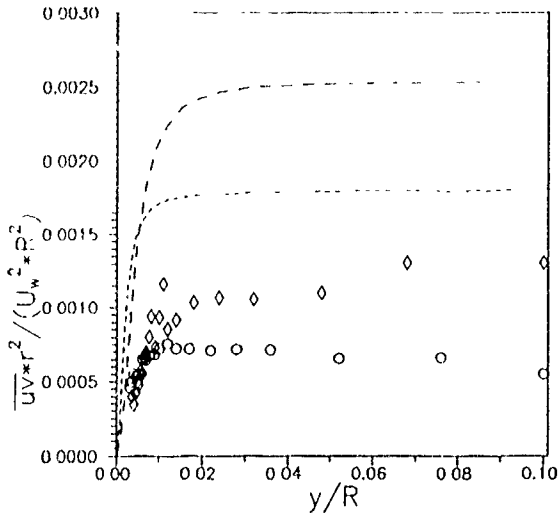

Figure 4 Radial distribution of the turbulent shear stress. For caption see Fig. 5

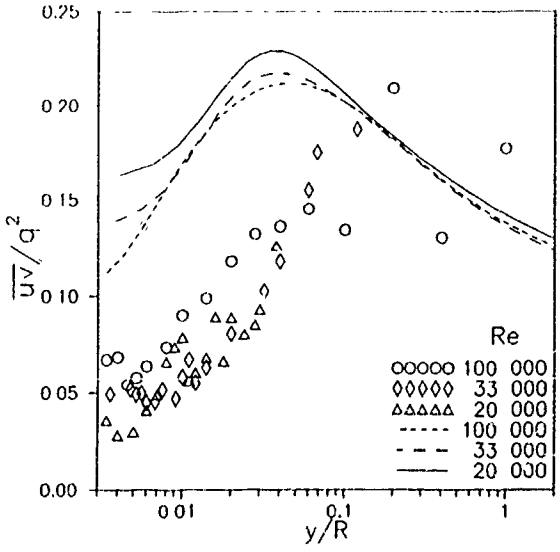

Figure 5 Radial distribution of $\overline{uv}/q^2$ for some different Reynolds numbers.

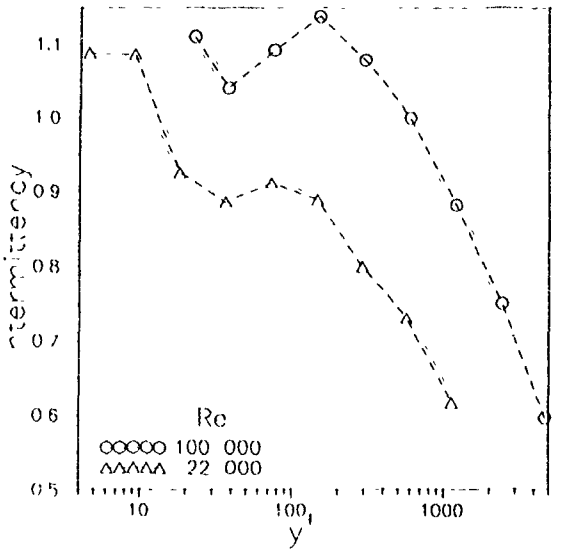

Figure 6 Radial distribution of the intermittency factor at two different Reynolds numbers.

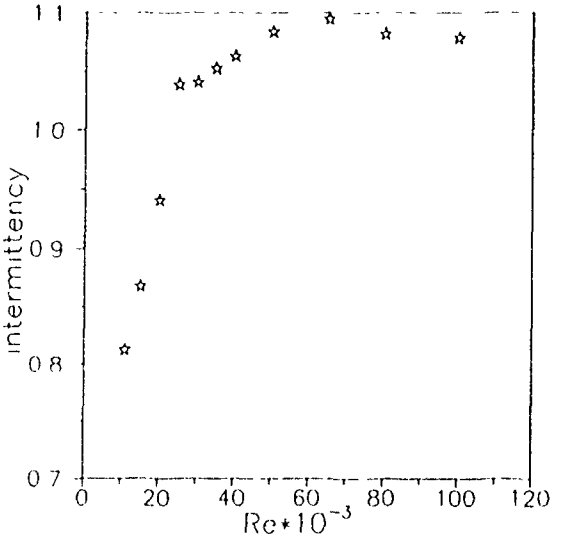

Figure 7 Measured intermittency factor at y'=50 for different Reynolds numbers.

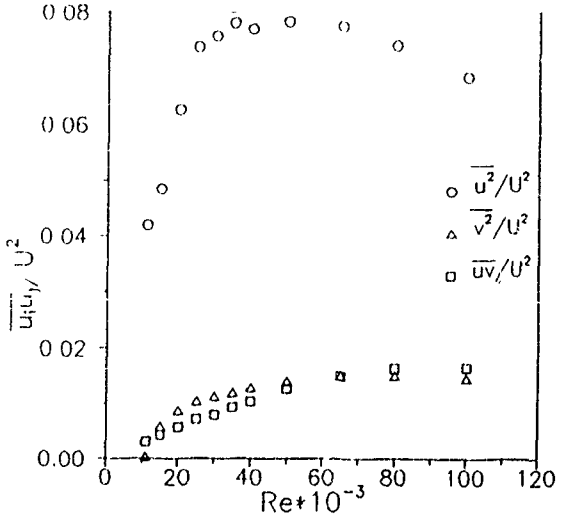

Figure 8 Measured Reynolds stresses at y'=50 for different Reynolds numbers.

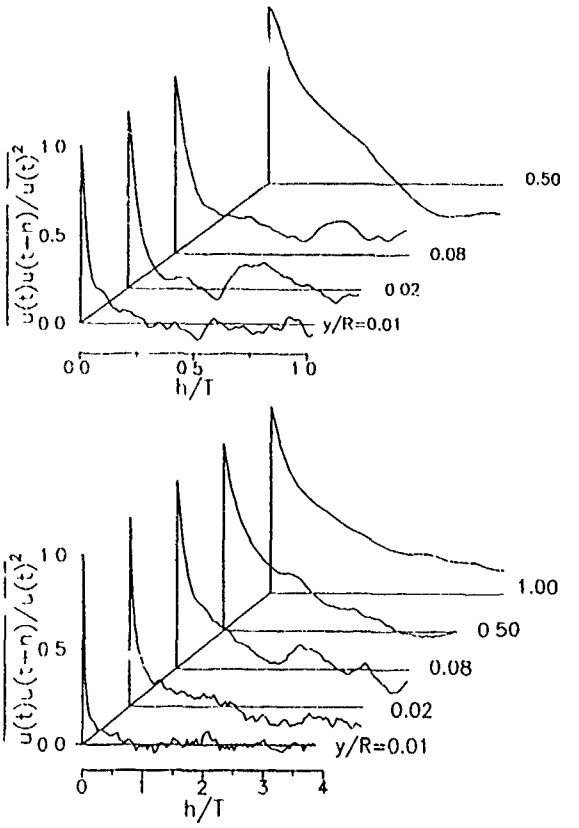

Figure 9 Autocorrelation coefficient for the streamwise fluctuating component at various radial positions for Reynolds number 25000 (upper) and 100000 (lower).

MODEL PREDICTIONS

The low-Reynolds number second-moment closure of Launder & Shima (1989), adapted to cylindrical polar coordinates, has been used to numerically predict the flow field around the rotating cylinder. The results of the calculations are included as lines in Figs. 1-5.

The predicted mean velocity profiles in Fig. 1 deviate significantly from the measurements. This discrepancy is most likely associated with the overpredicted turbulent shear stress (see Figs. 4 and 5). Moreover, unlike the experimental data the predictions in Fig. 1 show a more significant Re-number dependence. Nevertheless, it is encouraging to observe that the predicted velocity profiles in inner variables in Fig. 2 exhibit the typical destabilized appearance due to streamline curvature.

The predicted radial distributions of the turbulence intensities in Fig. 3 compare reasonably with the measurements for the three different Reynolds numbers considered. The radial position of the peak of the u'-distribution is accurately captured by the model, while the peak value itself is slightly underpredicted. The calculated anisotropy in the innermost part of the boundary layer changes only slightly with increasing Reynolds number. This is in contrast to the experimental findings, and can partly be explained by the model formulation of the important pressure-strain term.

CONCLUSIONS

Measurements and calculations of the turbulence field near a rotating cylinder in a quiescent fluid have been carried out from the transition point and up to Re = 100000. From these experiments the following conclusions can be drawn.

The centrifugal force field associated with the streamline curvature clearly indicates a destabilizing effect on the flow field. The mean velocity measurements reveal a clear turbulent flow at the studied Reynolds numbers. For this quantity qualitative agreement between the calculations and experiments is obtained.

Five different methods have been used for the determination of the friction velocity, but none of the methods can be considered to give reliable results throughout the Reynolds number range considered

It can be seen that the agreement between the experiments and the calculations of the turbulence quantities is acceptable in the innermost region of the boundary layer, but large deviations occur further out. This might, however, be explained by the high intermittency of the flow in this region

New data on the structural parameter in the innermost part of the boundary layer is presented Autocorrelation measurements indicate the presence of large-eddy structures in the flow field

Measurements of the turbulent normal stresses and the only non-vanishing off-diagonal component of the Reynolds stress tensor indicate that fully developed turbulence is established in the present set up at a Reynolds number some twenty times higher than reported earlier by Kasagi & Hirata (1975)

From these conclusions two main questions occur, which both require further investigations First, the uncertainty in the determination of the friction velocity, and second, the large deviation as compared to others in the determination of the transition

ACKNOWLEDGEMENT

One of the authors (PJN) acknowledges the support of the "Nordic Fund for Technology and Industrial Development" through a travel grant. The authors' names appear alphabetically

REFERENCES

BRADSHAW, P 1973 Effects of streamline curvature on turbulent flow AGARDograph No. 169

GIBSON, M.M. & LAUNDER, B.E. 1978 Ground effects on pressure fluctuations in the atmospheric boundary layer. J Fluid Mech. 86, 491-511.

KASAGI, N. & HIRATA, M. 1975 Transport phenomena in near-wall region of turbulent boundary layer around a rotating cylinder. ASME-Paper No. 75-WA/HT-58.

KLEBANOFF, P.S. 1955 Characteristics of turbulence in a boundary layer with zero pressure gradient. NACA Report No. 1247.

KRISTOFFERSEN, R., NILSEN, P J. & ANDERSSON, H.I. 1990 Validation of Reynolds stress closures for rotating channel flows by means of direct numerical simulations. Engineering Turbulence Modelling and Experiments, Elsevier Science Publishing, 55-64.

LAUNDER, B.E. & SHIMA, N. 1989 Second-Moment Closure for the Near-Wall Sublayer: Development and Application. AIAA J. 27, 1319-1325.

LÖFDAHL, L. 1986 Hot-wire techniques for the determination of the Reynolds stress tensor in three-dimensional flows. Dantech Information. No. 3, pp. 2-7.

LÖFDAHL, L., STEMME, G. & JOHANSSON, B. 1989 A sensor based on silicon technology for turbulence measurements. J Phys. E: Sci. Instruments 22, 391-393.

NAKAMURA, I., UEKI, Y. & YAMASHITA, S. 1983 A universal velocity distribution and turbulence properties in the shear flow on a rotating cylinder in a quiescent fluid. 4th Turbulent Shear Flows Symposium, pp. 2.21-2.26.

NAKAMURA, I., UEKI, Y. & YAMASHITA, S. 1986 The turbulent shear flow on a rotating cylinder in a quiescent fluid. Bull. JSME 29, 1704-1709.

SIDDAL, R G , & DAVIES, T W. 1972 An improved response equation for hot-wire anemometry Int. J. Heat Mass Transfer 15, 367-368.

THEODORSEN, T. & REGIER, A. 1944 Experiments on drag of revolving disks, cylinders and streamline rods at high speed. NACA Report No. 793.

WILLIAMSON, J W. & KOUKOUSAKIS, C 1987 Turbulent flow around a rotating cylinder. ASME Forum on Turbulent Flows, FED-Vol. 51, 79-83.

EIGHTH SYMPOSIUM ON
TURBULENT SHEAR FLOWS
Technical University of Munich
September 9-11, 1991

STABILIZING AND DESTABILIZING EFFECTS OF SOLID BODY ROTATION ON SHEAR FLOWS

S. Yanase[α,β], C. Flores[α], O. Métais[α] and M. Lesieur[α]

[α]Institut de Mécanique de Grenoble
B.P. 53X - 38041 Grenoble-Cedex, FRANCE

[β] Faculty of Engineering, Okayama University
Okayama 700, JAPAN

ABSTRACT

We examine the effect of a solid-body rotation, characterized by an angular velocity $\vec{\Omega}$, on a mixing layer and on a plane wake (in a plane perpendicular to $\vec{\Omega}$) on which is superposed a small three-dimensional random perturbation. Using Kelvin's theorem in a frame rotating with $\vec{\Omega}$, and with the aid of arguments based on the straining of absolute vortex filaments by the ambiant shear, it is shown that the rotation is always stabilizing (with respect to the non-rotating case) in the cyclonic case. In the anticyclonic case, a slight rotation is destabilizing At a local Rossby number of 1, the absolute vortex lines are disrupted. We perform three-dimensional numerical simulations which confirm these theoretical predictions We find a critical Rossby number at which maximum three-dimensional anticyclonic destabilization is achieved In that case, a detailed examination of the flow structures shows that the flow is highly anisotropic with very elongated streamwise hairpin vortices of small spanwise extent.

INTRODUCTION

Laboratory experiments on shear flows show stabilizing or destabilizing effects of a constant rotation, according to the cyclonic (of vorticity of same sign as the solid-body vorticity) or anticyclonic nature of the eddies considered. Witt and Joubert (1985) found that the wake of a cylinder of axis parallel to the solid-body vorticity becomes asymmetric under the effect of rotation. Chabert d'Hières *et al* (1988) have shown that the wake of a two-dimensional obstacle is two-dimensionalized at low Rossby numbers, whereas cyclonic eddies are reinforced and anticyclonic destroyed for higher Rossby numbers Rotating mixing-layer experiments (Rothe and Johnston, 1979, Tritton, 1990) exhibit the same results according to the cyclonic or anticyclonic nature of the shear layer.

A solid-body rotation of angular velocity $\vec{\Omega} = \Omega\vec{z}$ does not have any influence on a two-dimensional flow in the plane (x, y) (see Lesieur, 1990). Therefore, the phenomena observed in the laboratory experiments can only be explained by considering the influence of rotation on the growth of three-dimensional perturbations.

THE THEORETICAL MODEL

We first try to predict the rotation effects through a theoretical model using Kelvin's theorem in the frame rotating with $\vec{\Omega}$ and based on the straining of absolute vortex filaments by the basic velocity. We consider a two-dimensional mixing layer of relative (spanwise) vorticity ω_{2D}, with primary rollers formed. In the case of the wake, the theory also applies to both sides symmetric to the central plane which have opposite sign spanwise vorticity. The local Rossby number is defined as:

$$R_o = |\omega_{2D}|/2|\Omega| \quad .$$

The rotation is cyclonic if ω_{2D} and Ω have same sign and anticyclonic if not We superpose to this basic two-dimensional flow a turbulent three-dimensional perturbation of low kinetic energy and of vorticity $\vec{\omega}^{(1)}$ ($|\vec{\omega}^{(1)}| << |\omega_{2D}|$). When rotation is present, Kelvin's theorem applies to the *absolute* vorticity

$$\vec{\omega}_a = (\omega_{2D} + 2\Omega)\vec{z} + \vec{\omega}^{(1)} \quad .$$

It is only by a longitudinal straining of the initial *absolute* vortex filament that longitudinal vorticity (corresponding to three-dimensionalization) may be produced. Several cases have to be envisaged (see Figure 1; ω_{2D} is chosen negative) a) cyclonic rotation ($\Omega < 0$): the absolute vortex filament is closer to the z axis than the corresponding relative vortex filament: cyclonic rotation will have a stabilizing effect with respect to the non-rotating case.

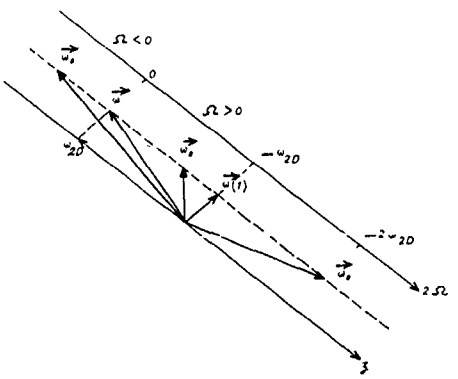

Figure 1: initial absolute vortcity for $\Omega = 0$, $\Omega < 0$ (cyclonic rotation), $\Omega > 0$ (anticyclonic rotation).

b) anticyclonic rotation ($\Omega > 0$).

• $0 < 2\Omega < -2\omega_{2D}$: the initial vortex filament is more perturbed (three-dimensionally) than its relative counterpart. rotation is destabilizing For $\omega_{2D} + 2\Omega \approx 0$ ($R_o \approx 1$), the three-dimensionalization will be maximum since the absolute vorticity now corresponds to the three-dimensional perturbation $\omega^{(1)}$.

• $-2\omega_{2D} < 2\Omega$: the anticyclonic rotation becomes stabilizing again

DIRECT NUMERICAL SIMULATIONS

In order to check the relevance of our theoretical predictions, we have carried out three-dimensional direct-numerical simulations of rotating shear flows Two prototypes of flows are considered: the mixing layer and the plane wake. We assume periodicity in the streamwise, x (temporal hypothesis), and in the spanwise, z, directions The initial conditions result from the superposition of a small-amplitude perturbation onto a one-directional basic profile: a hyperbolic-tangent velocity profile for the mixing layer

$$\overline{u}(y) = U \tanh \frac{2y}{\delta_i}$$

and a gaussian profile for the wake

$$\overline{u}(y) = U_m \exp(-Ln2 \frac{y^2}{r_m^2}) \quad .$$

The initial fluctuations consist in the superposition of two-random perturbations. the first one is three-dimensional of kinetic energy $\epsilon_{3D}\ U^2$ (or U_m^2), the second one is two-dimensional (z independent) of energy $\epsilon_{2D}\ U^2$. In both cases, $\epsilon_{3D} = \epsilon_{2D} = 10^{-5}$. The Rossby number is defined with the initial relative vorticity:

$$R_o^{(i)} = \frac{2U}{|2\Omega|\delta_i}$$

for the mixing layer. For the wake, the maximum vorticity associated with the gaussian profile is $\approx 0\ 7U_m/r_m$. Thus, the initial Rossby number is.

$$R_o^{(i)} = 0\ 7\ \frac{U_m}{|2\Omega|r_m}$$

The numerical method used is of pseudo-spectral type For the mixing layer, a mapping is used in the y direction in order to reject the boundaries at infinity. The results shown here are obtained with $48 \times 48 \times 24$ modes. The calculation involves 2 fundamental Kelvin-Helmoltz billows. The initial Reynolds number $U\delta_i/\nu$ is 150. For the wake, $48 \times 48 \times 48$ modes are used The Karman street is composed of two pairs of opposite sign vortices, $Re = U_m r_m/\nu = 180$.

STATISTICS

Mixing layer

We first consider the mixing layer. The results of these simulations are described in details in Lesieur *et al.*, 1991.

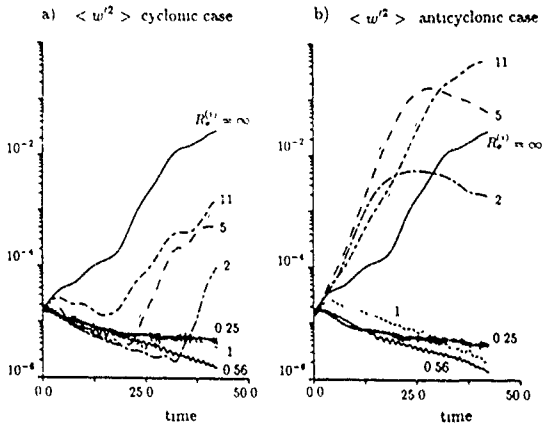

Figure 2· mixing layer; time evolution of the spanwise component of the velocity fluctuation ($< w'^2 >$), $R_o^{(i)} = \infty$, 11, 5, 2, 1, 0 56, 0 25, a) Cyclonic case; b) Anticyclonic case.

Numerical simulations are performed at $R_o^{(i)} = \infty$, 11, 5, 2, 1, 0.56, 0.25 for both cyclonic and anticyclonic cases. In Figure 2, we show the time development of $< w'^2 >$, variance of the spanwise velocity component (z-component), which indicates the degree of three-dimensionality. The brackets denotes the average on the whole computational domain. Figure 2 a) is for cyclonic cases and 2 b) for anticyclonic cases. Figure 2 a) shows that a cyclonic rotation is more and more stabilizing as the initial Rossby number decreases from infinity, up to 0.5. Afterwards the energy exhibits oscillations which are the signature of inertial waves The presence of the waves leads to a reduction of the dissipation rate. Figure 2 b) shows extremely different behaviour in the anticyclonic case. The initial growth rate of $< w'^2 >$ is higher than in the non-rotating case for $R_o^{(i)} = 11, 5, 2$. At $R_o^{(i)} = 5$, the destabilization reaches its maximum. The Rossby number based upon the instantaneous mean-velocity profile decreases with time Thus, the rotation could have a destabilizing effect at the beginning of the evolution and a stabilizing one when the instantaneous Rossby number is lower than a critical value; this could explain the decay of $< w'^2 >$ for $R_o^{(i)} = 11, 5, 2$ at later time. When the Rossby number goes from 2 to 1, a sharp transition takes place, since, from the beginning of the evolution, the rotation is stabilizing as far as the growth of $< w'^2 >$ is concerned. At a lower Rossby number, the evolution is very similar to the cyclonic case, with evidences of inertial wave propagation.

Plane wake

Cyclonic and anticyclonic eddies are now simultaneously present in the computational domain. Figure 3 is the analogue of Figure 2 in the case of the wake. $< w'^2 >$ designates a spatial average of the spanwise velocity variance on the points at which the vorticity is cyclonic for Figure 3 a) and anticyclonic for Figure 3 b). The Rossby number considered here are $R_o^{(i)} = \infty, 7, 2., 2.5\ 0.7$. On the anticyclonic side, similar effects to those described for the anticyclonic mixing layers are observed. However, maximum anticyclonic three-dimensionalization occurs at $R_o^{(i)} = 2.5$. On the cyclonic side, the rotation, in an initial phase, is stabilizing for all considered values of the Rossby number. Afterwards, for

$R_o^{(i)} = 7, 2., 2.5$, the strong three-dimensionalization leads to the generation of cyclonic vorticity on the side of the wake, which was originally anticyclonic. Furthermore, the cyclonic eddies can become more tridimensional because of their interaction with the highly three-dimensional anticyclonic ones. As opposed to the mixing layer's case, this implies a growth of $< w'^2 >$ in cyclonic regions stronger than without rotation.

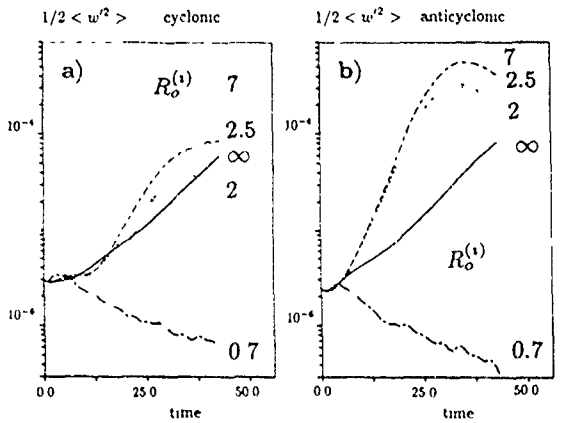

Figure 3: same as figure 2 for the plane wake ($R_o^{(i)} = \infty, 7, 2., 2.5, 0.7$). $< w'^2 >$ designates a spatial average of the spanwise velocity variance on the points at which the vorticity is cyclonic for Figure 3 a) and anticyclonic for Figure 3 b).

In figure 4, we present the time evolution of the total kinetic energy ($1/2 < u'^2 + v'^2 + w'^2 >$) for wavenumber $k_z = 0, 4, 8, 12$ and 16 integrated over all wavenumbers k_x and k_y. Figure 4 a) corresponds to the non-rotating case and figure 4 b) to the most destabilized case ($R_o^{(i)} = 2.5$). The growth of the two-dimensional energy is slightly reduced by the rotation. On the other hand, in the rotating case, the energy growth is more and more pronounced as k_z gets larger. This indicates a strong three-dimensionalization of the wake (on the anticyclonic side) with generation of small scales in the spanwise direction

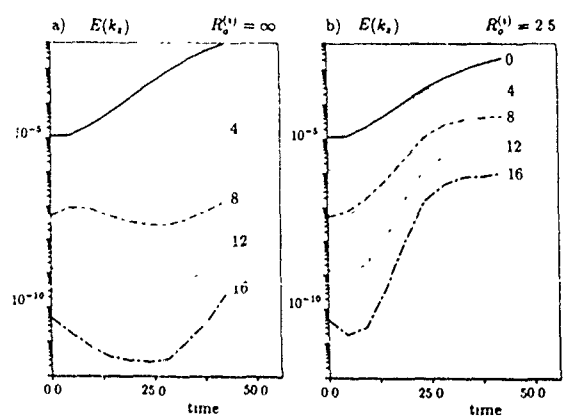

Figure 4: time evolution of the total kinetic energy ($1/2 < u'^2 + v'^2 + w'^2 >$) at wavenumber $k_z = 0, 4, 8, 12$ and 16 integrated over all wavenumbers k_x and k_y. Figure 4 a) non-rotating case; figure 4 b) rotating case ($R_o^{(i)} = 2.5$).

Figure 5 is the analogue of figure 4, but the total kinetic energy is now integrated over k_y and k_z wavenumbers and we consider its time evolution for wavenumbers $k_x = 0, 2, 6$ and 8. The wavenumber $k_x = 2$ is the fundamental mode corresponding to the 2 pairs of alternate-sign primary vortices of the Karman street. The energy corresponding to this mode strongly grows in the non-rotating case. Its growth is slightly reduced in the presence of rotation. In the rotating case, the most striking feature is the rapid growth of the energy at $k_x = 0$. The destabilization of the anticyclonic eddies will give rise to structures of small spanwise extent but very elongated in the streamwise direction. This is confirmed by linear stability analysis performed by Yanase *et al.* (1990).

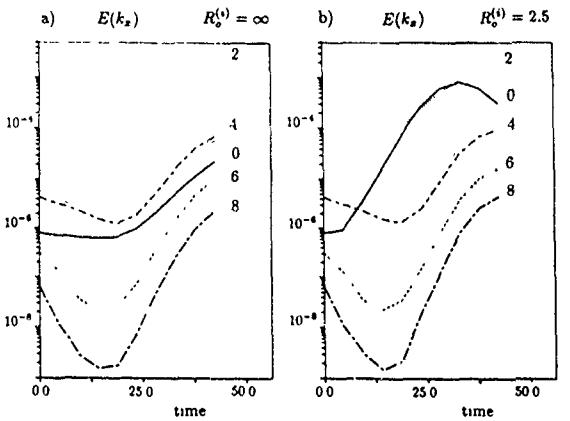

Figure 5: time evolution of the total kinetic energy at wavenumber $k_x = 0, 2, 6$ and 8 integrated over all wavenumbers k_y and k_z. Figure 4 a) non-rotating case; figure 4 b) rotating case ($R_o^{(i)} = 2.5$).

FLOW STRUCTURES

Mixing layer

We have investigated the three-dimensional structure of the eddies at $t = 25\,4$. We use low pressure iso-surfaces to identify the Kelvin-Helmoltz vortices:

a) $R_o^{(i)} = \infty$: one observes two quasi-two-dimensional billows, slightly distorted in the spanwise direction Thin longitudinal vortices are also present shown by longitudinal vorticity isosurfaces (not plotted here).

b) $R_o^{(i)} = 11$ (anticyclonic): figure 6a) shows the pressure field of the anticyclonic case. The eddies are greatly distorted by a strong three-dimensional instability due to the solid-body rotation.

c) $R_o^{(i)} = 5$ (anticyclonic): there is no large cylindrical eddy structure anymore, but the layer is highly three-dimensional, as shown on figure 6b). The pressure contours show now very anisotropic structures of small spanwise extent and very elongated in the streamwise direction. One can check that they correspond to concentration of vortex lines of near zero absolute vorticity which are stretched by the ambiant shear.

At low Rossby number, in both cyclonic and anticyclonic cases, a very strong two-dimensionalization is observed.

Figure 6: a) mixing layer; constant pressure surfaces for (anticyclonic case) for $R_o^{(i)} = 11$ at $t = 25\ 4$

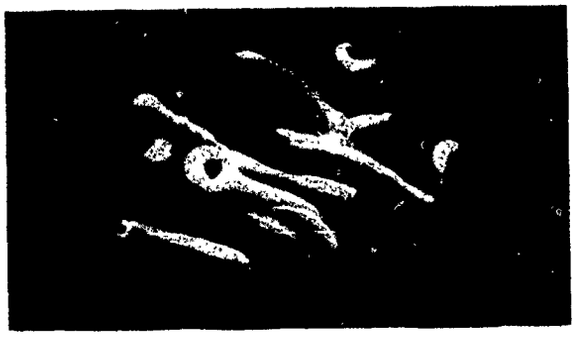

Figure 6: b) mixing layer; constant pressure surfaces (anticyclonic case) for $R_o^{(i)} = 2.5$ at $t = 25.4$

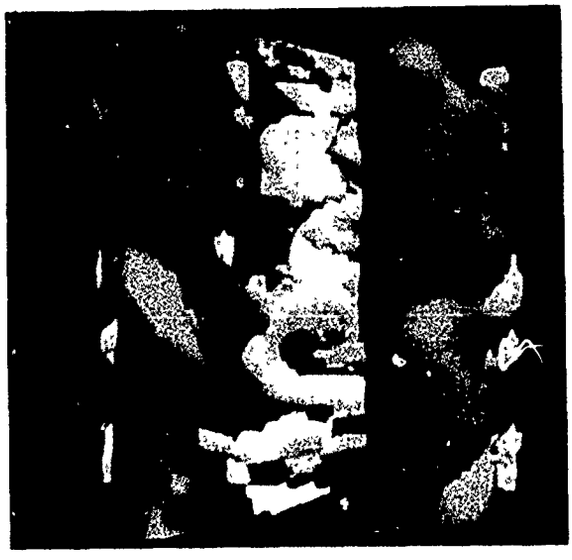

Figure 7. a) plane wake: vorticity contours for the cyclonic spanwise vorticity (light gray) and for the anticyclonic spanwise vorticity (white) for $R_o^{(i)} = 2.5$ at $t = 60$

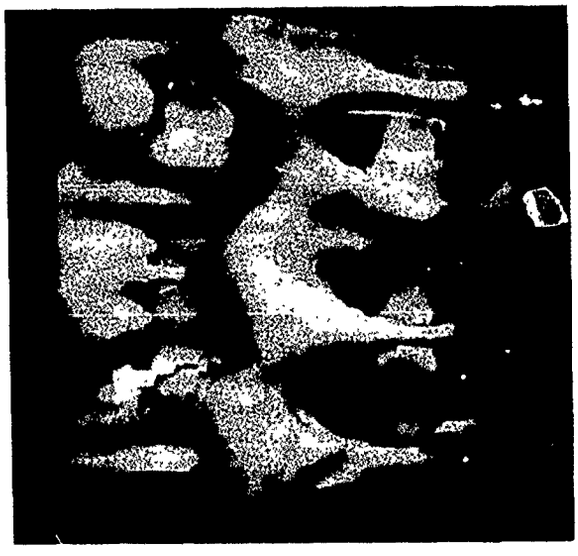

Figure 7: b) plane wake: constant pressure surfaces for $R_o^{(i)} = 2.5$ at $t = 30$

Plane wake

Figure 7a) shows vorticity contours for the cyclonic spanwise vorticity (light gray) and for the anticyclonic spanwise vorticity (white), for the critical Rossby number ($R_o^{(i)} = 2.5$, $t = 60$). Both cyclonic eddies exhibit spanwise oscillations due to the strong interaction with the three-dimensional anticyclonic eddies. Figure 7b) is low-pressure isosurfaces at $t = 30$. The anticyclonic eddies are in the foreground and the cyclonic ones in the background. As for the mixing layer, very elongated streamwise structures are visible on the anticyclonic side. At low Rossby number, both sides are two-dimensionalized.

DISCUSSION

The numerical simulations qualitatively confirm the predictions of our theoretical model: the cyclonic eddies are stabilized, while the anticyclonic eddies are three-dimensionally destabilized upon a critical Rossby number. Since we considered here inflexional unidirectional mean velocity profiles, the vorticity associated to these profiles varies with y (with extrema at the inflexion point(s)). Consequently, strongly three-dimensional absolute vortex lines (at a local Rossby number $R_o \approx 1$) will be surroundered by less-destabilized and also by stabilized lines: the proportion of lines with maximum destabilization will change with varying Rossby number. This explains why there is only an approximate correspondence between the local Rossby number R_o of the

theory and the initial Rossby number $R_o^{(i)}$ based on the mean profile: in the anticyclonic case, $R_o = 1$ corresponds approximately to $R_o^{(i)} \approx 5$ for the mixing layer, and to $R_o^{(i)} \approx 2.5$ for the wake. and the crossover value for the restabilization ($R_o = 0.5$)to $R_c^{(i)} \approx 1$ The striking feature is that the explosive anticyclonic three-dimensionalization leads to very anisotropic absolute vorticity structures. the vorticity originally oriented in the span rotates by an angle of 45° and is ultimately directed in the streamwise direction. The results obtained here present some similarities with what is observed in boundary layer over a curved plate. When the plate is concave, the angular rotation induced by the plate curvature and the vorticity associated with the boundary-layer velocity profile are of opposite direction: there is formation of Görtler streamwise vortices (which can be explained in terms of centrifugal instability) Furthermore, for convex plate, the boundary layer is stabilized Recent calculations (Bartello, private comunication) of rotating homogeneous isotropic turbulence show that the rotation acts upon eddies whose vorticity is parallel to the rotation axis and leads to the formation of quasi-two-dimensional cyclonic eddies. from the original three-dimensional chaotic flow emerge very well-organized cyclonic coherent structures.

CONCLUSION

We have shown , using Kelvin's theorem in a rotating frame, that the straining of absolute vorticity is reduced for a cyclonic rotation leading to an inhibition of shear-flows three-dimensionalization. In the anticyclonic case, rotation is three-dimensionally destabilizing for a local Rossby number larger than 0.5, and stabilizing at smaller Rossby numbers At a Rossby numnber of the order of one (anticyclonic case) , the spanwise component of the absolute vorticity is cancelled by the solid-body vorticity, and the corresponding absolute vortex lines are highly three-dimensional. Mixing layer and plane wake three-dimensional numerical simulations suport the theory, and agree qualitatively with experimental results For the rotation rate corresponding to an explosive anticyclonic three-dimensionalization. low-pressure and high-vorticity structures as well as the statistics show that the absolute vortex lines of near-zero vorticity are rapidly strained by the basic flow This leads to the formation of strong hairpin vortices of small spanwise extent and elongated in the streamwise direction.

The authors are grateful to J.J. Riley for many enlightening discussions.

References

Bidokhti A.A. and D.J. Tritton, 1990 The structure of a turbulent free shear layer in a rotating ' , *submitted to the J. Fluid Mech.*.

Chabert d'Hières G. , P.A. Davies and H. Didelle, 1988: Laboratory studies of pseudo-periodic forcing due to vortex shedding from an isolated solid obstacle in an homogeneous rotating fluid. *20th Int Liège Colloquium on Ocean Hydrodynamics*, 2-6 May, Elsevier Publisher.

Lesieur, M., 1990, *Turbulence in Fluids*, Kluwer Publishers, Dordrecht, 1987, revised edition 1990)

Lesieur, M., S. Yanase and O. Métais, 1991: Stabilizing and destabilizing effects of a solid-body rotation upon quais-two-dimensional shear layers, *Phys. Fluids A*, **3**, pp 403-407.

Rothe, P.H. and J.P. Johnston, 1979: Free shear layer behavior in rotating systems. *J. Fluids Eng.*, **101**, pp. 171-120.

Witt, H.T. and Joubert, P.N., 1985: Effect of rotation on a turbulent wake. *Proc. 5th Symposium on Turbulent Shear Flows*, Cornell, pp 21.25-21.30.

Yanase, S., J.J. Riley, M. Lesieur and O. Métais, 1990: The effects of rotation on transition in a two-dimensional shear layer, *Bulletin of the american physical society*, **35**, No 10, p. 2277

EIGHTH SYMPOSIUM ON
TURBULENT SHEAR FLOWS
Technical University of Munich
September 9-11, 1991

EFFECTS OF CURVATURE ON THE SPECTRA OF SHEARED TURBULENCE

A.G.L. Holloway* and S. Tavoularis**

*Department of Mechanical Engineering, University of New Brunswick
Fredericton, New Brunswick, CANADA, E3B 5A3

**Department of Mechanical Engineering, University of Ottawa
Ottawa, Ontario, CANADA, K1N 6N5

ABSTRACT

One-dimensional spectra from seven uniformly-sheared nearly-homogeneous flows with various degrees of mean flow curvature are presented and analyzed. The data suggest that the flow curvature affects the large-scale motions most strongly, altering the partition of the kinetic energy among its three components and the coherence of the streamwise and transverse fluctuations. For relatively mild curvature, the coherence of large-scale motions diminished in cases where the mean velocity increased away from the center of curvature and increased in cases where the mean velocity decreased away from the center of curvature. For "strong" curvature, the sign of the coherence, was reversed and momentum was transported up the gradient of mean velocity and away from the center of curvature.

NOMENCLATURE

$C_{uv}(k_1)$	the coherence function
dU/dn	gradient of the mean velocity
$F_{uu}(k_1)$, $F_{vv}(k_1)$, $F_{ww}(k_1)$, $F_{uv}(k_1)$	streamwise components of the one-dimensional spectral densities of the velocity fluctuations
k_1	streamwise component of the wavenumber vector
L_{uu}	the integral length scale of the streamwise fluctuations
n	transverse coordinate
R_c	radius of curvature of the tunnel centerline
s	streamwise coordinate
$S = (U_c/R_c)/(dU/dn)$	curvature parameter
u	streamwise velocity fluctuation
$\hat{u}$	Fourier transform of u
U_c	streamwise component of the mean velocity on the tunnel centerline
v	transverse velocity fluctuation
w	spanwise velocity fluctuation
z	spanwise coordinate
ϵ	the rate of viscous dissipation
u	Kolmogorov velocity
ν	kinematic viscosity
η	Kolmogorov microscale

1. INTRODUCTION

It has been well documented that curvature has a strong effect on the structure of sheared turbulence (for a recent review of the literature see Holloway and Tavoularis, 1991). It has also been documented that curvature has a different impact upon turbulent eddies of different sizes. For example, the boundary layer measurements of Ramaprian and Shivaprasad (1978) show that both convex and concave surface curvature affect the integral length scales more than the Taylor microscales. The interaction between shear and curvature in boundary layers is complicated by the presence of wall effects, the entrainment of irrotational flow and inhomogeneity. For the present investigation an effort was made to design a flow to evince the effects of flow curvature on the different scales of a sheared turbulence in relative isolation from wall and entrainment effects. An ideal flow for studying this interaction would be one where turbulence, curvature and shear are homogeneous. Such a flow can be conceived by extending the notion of rectilinear, homogeneous, shear flow to a flow with mean streamlines which are not parallel but form concentric rings. The shear should be assumed uniform in the radial direction but a fluid particle would on the average move along a curved path. It is easy to see that inhomogeneity of the turbulence would inevitably develop under such conditions, as a result of the transverse nonuniformity of curvature and strain. Nevertheless, it seems worthwhile to explore the plausibility of an approximately homogeneous curved shear flow by introducing additional constraints.

Consider a flow field bounded on average by two coaxial circular cylinders with a difference in radius that is large in comparison with the scales of the turbulence but small compared to the mean radius. The mean streamline curvature can be considered as nearly constant within the volume and the turbulence structure in the core of volume can be assumed as independent of wall effects, at least over a sufficiently small time interval. If the turbulence within this volume were homogeneous initially, it would likely remain homogeneous for some time.

An approximation to that flow was materialized by extending previous studies on nearly homogeneous shear flows (Tavoularis and Karnik, 1989). Uniformly sheared turbulent flows were allowed to reach a quasi-self-preserving structure in a straight rectangular duct and then were passed tangentially into a curved duct, also of rectangular cross-section. The near homogeneity of the turbulence and the near uniformity of the shear were preserved, while the structure of the turbulence was modified by the flow curvature.

Details of the experimental apparatus

and measurements of the development of the turbulent stresses and length scales for the present flow have been reported by Holloway and Tavoularis (1991). A primary conclusion of that work was that the effects of curvature appeared to scale with the parameter $S=(U_c/R_c)/(dU/dn)$*, where U_c was the centerline velocity, n was in the direction normal to the mean streamlines and R_c was the radius of curvature at the centerline of the duct. Flows with different values of S were generated by adjusting both the mean shear and R_c. Flows with different values of shear, each having a self-preserving structure, were produced using a shear generator and various combinations of screens and grids. Shears of opposite direction were produced by inverting the shear generator. In addition, two curved ducts were built, corresponding to R_c = 2 m and 5 m, respectively. The combination of curved sections and shears produced 16 distinct flows with S ranging from -.27 to .65.

Measurements of the turbulent stresses indicate that the growth of the turbulent kinetic energy was enhanced for negative values of S and suppressed for positive values of S. Whether the kinetic energy of turbulence grew or decayed, it seemed to do so exponentially and to approach a self-preserving structure, with the components of the Reynolds stress tensor approaching constant ratios.

Seven quasi-self-preserving flows of the type described above, where S=-.27,-.1, -.07,0,.07,.1 and .65 have been chosen as representative cases. Some of their main characteristics are shown in Table 1. These flows have been ranked by their value of S, under the assumption that this is the determining factor, but the wide range of shears, R_λ and R_λ for these flows should not be overlooked. For example, the flow with S=-.1 was being sheared at nearly twice the rate of the flow with S=-.07 and had nearly three times the Reynolds number.

The energy and length scales of the first four flows grew, while those of the last two decayed. The flow with S=.65 was of particular interest, because it exhibited a turbulent momentum flux, in the same direction as the mean shear, opposite to the implications of gradient transport. However, conclusions derived from this flow must be treated with some caution, because its structure near the end of the tunnel might not have reached an asymmptotic state.

2. MATHEMATICAL DESCRIPTION OF THE FLOW

The present flow can best be described in a curvilinear orthogonal system of coordinates, similar to those commonly used in studies of curved boundary layers. These will be denoted by s, n and z, as shown in Figure 1. The s coordinate is the length of a circular arc, with radius R_c, coincident with the flow volume centerline. The n coordinate is normal to s, has its origin on the volume centerline and is positive when directed away from the centre of curvature. The radial extent of the flow volume is assumed to be small compared to R_c. The z coordinate is normal to both s and n and has a direction following the right-hand rule.

The local, instantaneous, velocity vector can be decomposed into means, U,V,W and fluctuations u,v,w, parallel, respectively, to the s,n,z, directions. In flows with uniform mean shear in the n direction alone, the mean velocity can be represented as

$$(U,V,W) = (U_c+(dU/dn)n,0,0) \quad (2.1)$$

The one-dimensional spectral densities, $F_{uu}(k_1)$, $F_{vv}(k_1)$, $F_{ww}(k_1)$ and $F_{uv}(k_1)$ of the fluctuating kinetic energy components and the shear stress are defined as usual (Papoulis, 1984), for example (asterisks indicate complex conjugates)

$$F_{uu}(k_1) = E(\hat{u}\hat{u}^*) \quad (2.2)$$

where k_1 is the component of the wave vector in the streamwise direction, E( ) denotes the mean value and $\hat{u}(k_1)$ is the Fourier transform of the streamwise velocity fluctuation.

$F_{uu}(k_1)$, $F_{vv}(k_1)$ and $F_{ww}(k_1)$ are real and even functions of k_1, while $F_{uv}(k_1)$ is complex with an even real component and an odd imaginary component. Because the imaginary part of $F_{uv}(k_1)$ is odd, only the real part of $F_{uv}(k_1)$ contributes to the shear stress.

The streamwise integral length scale, L_{uu}, is defined from the limiting values of the corresponding spectra at zero wavenumber, as,

$$L_{uu} = \frac{\pi}{\overline{u^2}} \lim_{k_1 \to 0} F_{uu}(k_1) \quad (2.3)$$

3. INSTRUMENTATION AND DATA ACQUISITION

The velocity was measured using a custom-made, cross-wire array (TSI 1248bJT15) and conventional hot wire anemometry procedures. The sensing elements were made of tungsten and had a diameter of 5 μm and a length of 1.2 mm. They were separated by 0.5 mm and had nominal inclinations of ± 45° with respect to the axis of the probe body.

In the present flows the Kolmogorov microscale ranged from .14 to .3 mm, which was at most a quarter of the length of the hot wire. The analysis of Wyngaard (1968) suggests that measurements of fluid motions with sizes less than the wire length would require corrections for the size of the hot wire array.

The anemometer signals were low-pass filtered to 10 kHz, converted to velocities using a modified form of King's law, digitized at two different rates, 2 kHz and 25kHz, and divided into statistically independent records, each of 1024 points. The Fourier transforms of the fluctuating velocity components were estimated using the discrete time series and Taylor's frozen

*This parameter arises naturally from the Reynold stress equations and has been identified by several authors.

flow approximation.

The corresponding spectra computed from the two sets of time series collapsed in the overlapping ranges. However, only the high frequency part of the spectra computed from the 25 kHz sample and the low frequency part of the spectra computed from the 2 kHz sample were retained. The Nyquist criterion was not strictly observed for the 2 kHz sample but the portion of the spectrum which was significantly distorted was removed. The energy estimates for the longest wavelengths were subject to higher uncertainty, due to the finite record length and deviations from flow stationarity. Calculation of L_{uu} from equation (2.3), was done approximately by extrapolation of the spectra at the lowest measured wavelengths to zero.

4. RESULTS

Typical measurements of the spectral density $F_{uu}(k_1)$, normalized with the Kolmogorov scales, have been plotted in Figure 2. The corresponding flows had a range of turbulent Reynolds number, $R_\lambda = u'\lambda/\nu$, from 115 to 370. The theoretical spectral form of Pao (see Hinze, 1975) has been plotted for comparison. For wavenumbers where $k_1\eta > 0.005$, $F_{uu}(k_1)$ appeared to be unaffected by the flow curvature or shear as the data from each flow essentially collapsed into a universal shape, close to Pao's estimate.

At the lower wavenumbers, $F_{uu}(k_1)$ varied widely from flow to flow, due to the different velocity and length scales. These differences may not be entirely attributed to flow curvature, but also too differences in the history of each flow. For example, the flows with $S = \pm.1$ initially had similar scales but, after sustained flow curvature of opposite sense, the kinetic energies of these two flows deviated exponentially and differed by a factor of two at the streamwise position where these spectra were measured. The length scales were affected in a similar way.

To assist in the evaluation of the effects of mean curvature and shear on the spectra, the present results will be compared to the spectra of isotropic turbulence. Among the several approximate forms which have been proposed for the three- dimensional spectrum of isotropic turbulence (see for example Hinze, 1975), one leading to a simple expression for $F_{uu}(k_1)$ and having a good agreement with data from grid- generated turbulence is Karman's interpolation formula

$$\frac{2F_{uu}(k_1)}{\overline{u^2}L_{uu}} = .63\left[1+(1.33\,k_1L_{uu})^2\right]^{-5/6} \qquad (4.1)$$

The spectral densities $F_{uu}(k_1)$, $F_{vv}(k_1)$ and $F_{ww}(k_1)$ have been plotted in Figures 3, 4 and 5. They have been normalized with the streamwise component of the kinetic energy, u^2, and the streamwise integral scale, L_{uu}. The Karman interpolation formula has also been plotted for comparison. The fine-scale structures of each flow were different, so the spectra differed significantly for $k_1L_{uu} > 10$. For $k_1L_{uu} < 10$, the curves for different flows were close to each other and only modestly more energetic than predicted by the Karman formula. One should note, however, that these spectra were forced to agree at the lowest wavenumbers and to cover the same area by the way in which they were scaled.

In each flow $F_{vv}(k_1)$ and $F_{ww}(k_1)$ were different for $k_1L_{uu} < 5$ and generally less energetic than in isotropic turbulence of equal energy. These spectra approached one another at $k_1L_{uu} \sim 10$ and then they diverged again in the viscous range. $F_{vv}(k_1)$ for the flow where S=-.27 appeared to have the greatest proportion of the energy and the flow with S=.65 the least, while $F_{ww}(k_1)$ showed no similar trend. It would appear that shear and curvature make the distribution of energy among its three components at the lower wavenumbers more anisotropic.

$F_{vv}(k_1)$ and $F_{ww}(k_1)$ showed little evidence of inertial subranges (certainly much less than $F_{uu}(k_1)$ did), but this could be partly due to the lower energy levels of these components.

The one-dimensional cross spectral density, $F_{uv}(k_1)$, has been normalized with $F_{uu}(k_1)$ and $F_{vv}(k_1)$ to form the coherence function,

$$C_{uv}(k_1) = F_{uv}(k_1) / \sqrt{\left(F_{uu}(k_1)\,F_{vv}(k_1)\right)} \qquad (4.2)$$

In isotropic turbulence, $C_{uv}(k_1)$ is zero at all wavenumbers while in shear flow, $-1. < C_{uv}(k_1) < 1.$ $C_{uv}(k_1)$ should have a sign opposite to that of the shear, because momentum is on average transferred down the gradient of mean velocity. For the present experiments, flows with positive and negative values of S were generated by reversing the direction of the shear. This would have the result of reversing the sign of $C_{uv}(k_1)$, a result which does not reflect a true change in flow structure but is an artifact of the experimental method. To accurately portray the relationship between $C_{uv}(k_1)$ and the shear we have plotted $C_{uv}(k_1)$ sgn (S) where sgn (S) is -1 if $S \geq 0$ and +1 if $S < 0$. The real part of the coherence is shown in Figure 6 as a function of the normalized wavenumber, k_1L_{uu}. It was relatively weak for motions with $k_1L_{uu} > 10$, which is consistant with the observed local isotropy of $F_{uu}(k_1)$, $F_{vv}(k_1)$ and $F_{ww}(k_1)$. The coherence of the motions with low wavenumbers was a strong function of S, ranging from .9 to -.4. The flow with the strongest, negative S (S=-.27) had the greatest coherence. For the straight flow, where S=0, the coherence exceeded 0.7 at its maximum, which is considerably greater than the values of the correlation coefficient $\overline{uv}/u'v' = 0.45$ in this flow. $C_{uv}(k_1)$ became less positive with increasing S and the strongest affects appeared to be at a wavelength equal to ten times the integral length scale. In the flow with the strongest positive S (S=.65) the coherence reversed its sign so that it was in the same direction as the shear. It would appear then that stabilizing curvature, for which S is positive, does not necessarily reduce the coherence of the streamwise and transverse motions but rather makes them more likely to transport momentum away from the center of curvature.

The imaginary part of the coherence, shown in Figure 7, was relatively weak and highly scattered. This part does not directly influence the turbulent shear stress but does make a contribution to the spatial covariance, in particular it contributes to its asymmetry. This part was largest in the flows with positive S in the wavenumber range where the real part of the coherence changed sign.

5. DISCUSSION

The experimental data seem to indicate that, although the shear and the curvature act uniformly on all turbulent motions, it is the larger motions which are the most strongly affected. In the higher wavenumber range ($k_1 L_{uu} \geq 10$) the distribution of energy differed little from that in isotropic turbulence and the coherence was small. At the low wave numbers, the spanwise and transverse components of the energy spectrum were, in most cases, an order of magnitude lower than the streamwise component and the coherence of the streamwise and transverse motions varied widely from values as high as .9 to as low as -.4.

In an attempt to understand the observed effects of curvature we will first separate the spectra into a low wavenumber range ($k_1 L_{uu} < 1$) and a high wavenumber range ($k_1 L_{uu} > 1$). Hinze (1975) suggested that the mean vorticity, dU/dn, of the flow could only be expected to have a significant effect on the distribution of energy in wave number space if it is of comparable magnitude to the root mean squared fluctuations of the vorticity, $\sqrt{(\epsilon/\nu)}$. Weak mean shear would only serve as a supply of energy and one might expect a nearly isotropic spectrum, similar to the Karman interpolation formula and including a -5/3 slope in the inertial range, if the Reynolds number were large enough. This prediction would presumably be most relevant for relatively small-scale motions. However, at the lower wavenumbers, the spectral density of the dissipation is relatively small and the turbulence distortion could be weak compared to that due to the mean shear. In this wavenumber range the distortion would be strongly influenced by the mean shear and the turbulence could perhaps be considered as passive. Similarly, the importance of mean flow curvature would depend on the instantaneous curvature of the turbulent motions which presumably would increase with increasing wavenumber. The present experiments were designed such that $L_{uu} << R_c$ and in no case was $L_{uu} > .05\ R_c$. However, rough estimates of the spectra for the present flows are presented in Figures 3 to 7 for wavelengths up to $.5\ R_c$.

Attempts have been made to explain the observed development of turbulence in terms of mean flow distortion. In rapid distortion theory, the development of the turbulence is assumed to be completely determined by the mean distortion but, in other approaches, some model of the effects of turbulence on its own evolution is used.

If we neglect the direct effects of the mean flow curvature on the distortion of the turbulence and concentrate on the low wavenumber motions, then the mean distortion can be considered as the sum of a mean strain rate, D_{sn}, and a mean rotation rate, Ω_z, which take the forms

$$D_{sn} = \frac{1}{2}\left(\frac{dU}{dn}\right)(1 - S) \qquad (5.1)$$

$$\Omega_z = \frac{1}{2}\left(\frac{dU}{dn}\right)(1 + S) \qquad (5.2)$$

Equations (5.1) and (5.2) show that flow curvature explicitly affects the rates of mean flow rotation and strain. An irrotational flow would have S = -1 while an unstrained rigid body rotation would have S = 1. Equal rates of strain and rotation, as in a rectilinear shear flow, result in S = 0. Rapid distortion analyses have been performed by other investigators for these three flows and some of the results may be relevant to the present flows.

Townsend (1976) has calculated the redistribution of isotropic energy amongst the three components of kinetic energy due to an irrotational strain whch would appear to correspond, in the present context, to a flow with S = -1. The overall trend is a decrease in the streamwise component of the kinetic energy and an increase in the transverse and spanwise components, especially the transverse one. The predicted shear correlation coefficient, $\overline{uv}/u'v'$, between the streamwise and transverse velocity fluctuations reaches a maximum of .45 after a small amount of strain.

None of the present experimental flows were irrotational on the mean, but the flow with the least rotation had S = -.27. Figure 4 shows that the strength of $F_{vv}(k_1)$ increased relative to $F_{uu}(k_1)$, while $F_{ww}(k_1)$ showed little change from the rectilinear shear flow (Figure 5). The coherence for this flow (Figure 6), was as high as 0.9 at its maximum and the self-preserving nature of this flow seems to suggest that this coherence would not decline with further strain.

When S = 0 the rates of flow rotation and strain are equal and the vorticity is turned away from the principal axis of strain in such a way that the material lines of the flow become parallel with the streamwise direction. Analyses of this flow by several authors (Hinze, 1975) predicted a rather complex development for the turbulence, but, also an increasing concentration of the kinetic energy in the streamwise component and a corresponding reduction of the transverse and spanwise components. The overall shear stress correlation coefficient, $\overline{uv}/u'v'$, was found to reach a maximum of .6.

Each of the present flows at the start of curvature was a rectilinear shear flow (S = 0) with a self preserving structure. For these flows, $F_{uu}(k_1)$ was nearly an order of magnitude greater than $F_{vv}(k_1)$ and $F_{ww}(k_1)$ and the coherence had a maximum of .7 without any indication of decline with further strain.

When S = 1 there is no straining and energy cannot be extracted from the mean flow by the turbulence. A partial analysis of this flow is reported by Townsend (1980)

who suggests that the kinetic energy of the flow is constant but that components of the velocity fluctuations oscillate about their initial values at a rate which depends on the orientation of the waves and the mean rotation rate.

The present flow which is the closest to rigid body rotation on the mean is that with S = .65. The overall kinetic energy of this flow was decaying because the viscous dissipation exceeded the turbulence production, however, Figures 4 and 5 show that $F_{vv}(k_1)$ and $F_{ww}(k_1)$ were declining faster than $F_{uu}(k_1)$ and the coherence shown in Figure 5 had the opposite sign compared to that in rectilinear shear flow. Measurements of this flow were not made for sufficiently large total strains, so that it is uncertain whether this structure was self-preserving or it was a result of oscillations of the type suggested by Townsend (1980).

The distortion of the other four flows could be considered intermediate between the extreme cases discussed above, each having a different proportion of flow rotation and strain. The structure of the low wavenumber motions showed a trend of increasingly negative coherence of the streamwise and transverse motions with increased rates of flow rotation but the effects were not proportional to S; the structure was more strongly affected for S > 0 than for S < 0.

6. CONCLUSIONS

Neither shear nor curvature appear to have a direct influence on the fine structure of turbulence, while they both tended to increase the anisotropy of the large-scale structure. Negative values of S tended to enhance the relative strength of the large-scale transverse motions. Flow curvature modifies the coherence of the streamwise and transverse fluctuations so that momentum is more likely to be transported away from the center of curvature. For flows with negative S this enhances the coherence while for small positive S it diminishes the coherence. For flows with large positive S the curvature effects overcome the tendency for momentum to be transported down the gradient of mean velocity and there is a net transport away from the center of curvature.

REFERENCES

Hinze, J.O. (1975) "Turbulence", 2nd Ed., McGraw-Hill, New York.

Holloway, A.G.L. and Tavoularis, S. (1991) "The effects of curvature on sheared turbulence", J. Fluid Mech. To be published.

Papoulis (1984) "Probability, random variables, and stochastic processes", 2nd Ed., McGraw Hill, New York.

Tavoularis, S. and Karnik, U. (1989) "Further experiments on the evolution of turbulent stresses and scales in uniformly sheared turbulence", J. Fluid Mech. 204, 457-478.

Townsend, A.A. (1980) "The response of sheared turbulence to additional distortion", J. Fluid Mech., 81, 171-191.

Townsend, A.A. (1976) "The structure of turbulent shear flow", 2nd Ed., Cambridge University Press, Cambridge.

Wyngaard, J.C. (1968) "Measurement of small scale turbulence structure with hotwires", J. Sci. Instr., 1, 1105-1108.

S	$\lvert\frac{dU}{dn}\rvert$	R_c(m)	$R_\lambda = \frac{u'L_{uu}}{\nu}$	R_a	$\frac{\overline{uv}}{u'v'}$ sgn S	Symbol
- 27	20	2	4500	370	63	□
- 1	52	2	2900	340	49	○
- 07	30	5	770	160	51	△
0	64	0	2100	280	45	+
+ 07	27	5	470	115	32	X
+ 1	53	2	880	170	30	◇
+ 65	8	2	660	270	0	■

Table 1: Characteristics of the flows, ($U_c \approx 10$ m/s).

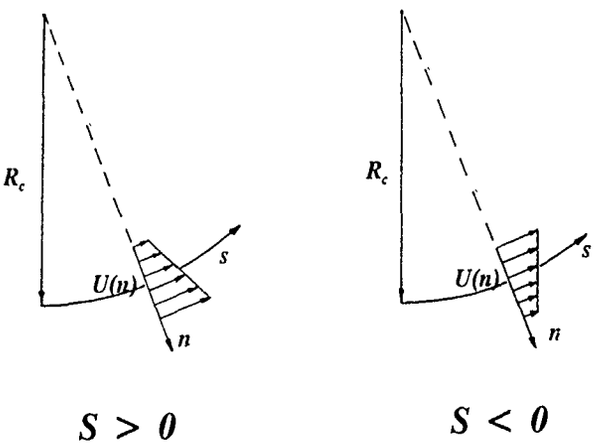

Figure 1: The flow configuration.

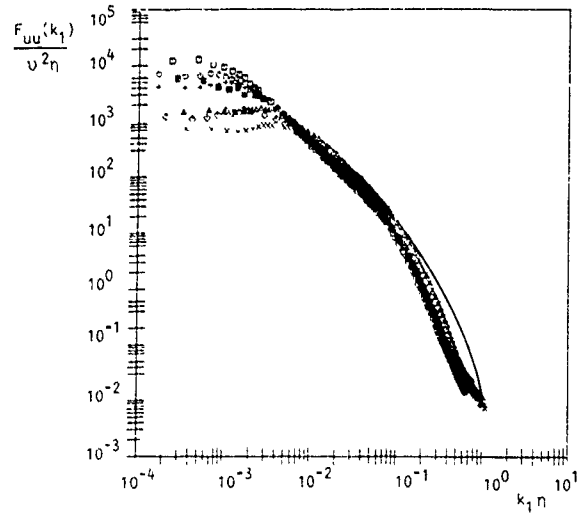

Figure 2: $F_{uu}(k_1)$ normalized with the Kolmogorov scales: symbols in Table 1.

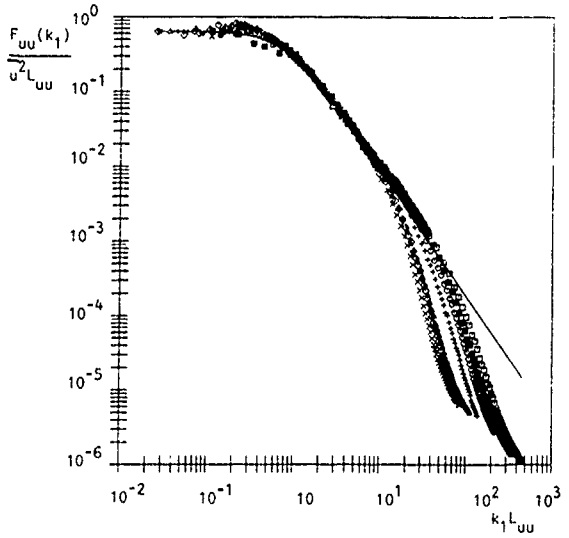

Figure 3: $F_{uu}(k_1)$ normalized with the energy scales.

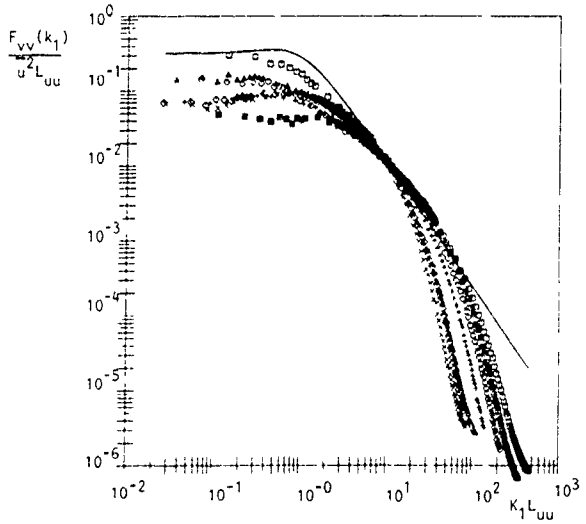

Figure 4: $F_{vv}(k_1)$ normalized with the energy scales.

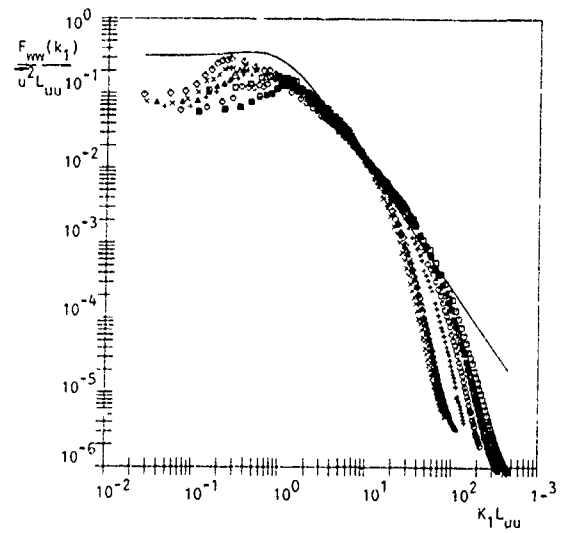

Figure 5: $F_{ww}(k_1)$ normalized with the energy scales.

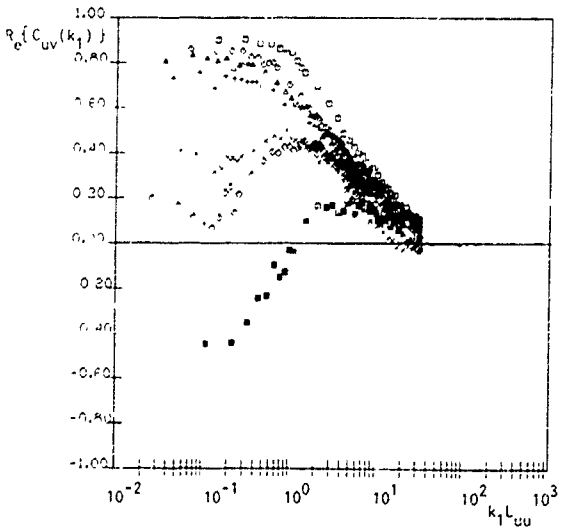

Figure 6: The real part of the coherence function $C_{uv}(k_1)$.

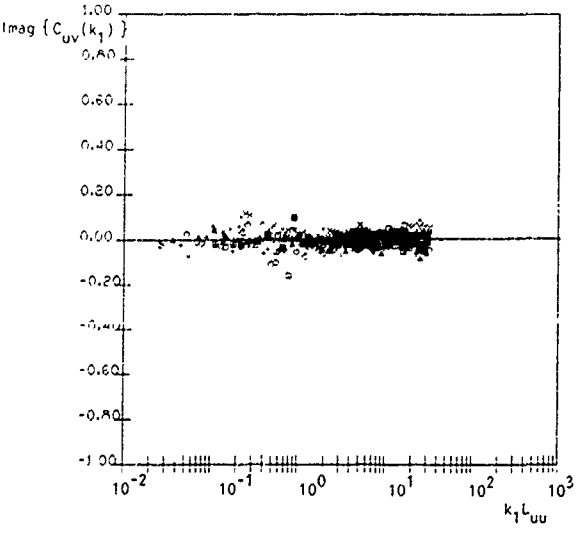

Figure 7: The imaginary component of the coherence function $C_{uv}(k_1)$.

EIGHTH SYMPOSIUM ON
TURBULENT SHEAR FLOWS
Technical University of Munich
September 9-11, 1991

Experimental Investigation of the Three-Dimensional Boundary Layer on a Rotating Disk

Howard S. Littell and John K. Eaton
Dept. of Mechanical Engineering, Stanford University, Stanford CA 94305

ABSTRACT

The velocity field above a large spinning disk has been studied using pressure probes and hotwire anemometers. The flowfield consists of a three-dimensional boundary layer due to a crossflow caused by centrifugal forces. The mean flow in both the laminar and turbulent regimes compares well with previous studies of 'infinite' smooth rotating disks, and all six Reynolds stresses and the ten triple products have been measured using established crosswire anemometry techniques. Selected results are compared to previous three-dimensional boundary layer measurements and several important differences are noted.

INTRODUCTION

Three-dimensional turbulent boundary layers (3DTBL's) are becoming the focus of increased research interest as modellers recognize their practical importance and the key differences between them and their more familiar cousins, the two-dimensional boundary layers. The term three-dimensional boundary layer generally means a wall-attached shear layer in which the flow direction varies with distance from the wall. Thus, regardless of the choice of coordinate system, both velocity components parallel to the wall vary with distance from the wall and both wall-parallel vorticity components are significant.

The turbulence in three-dimensional boundary layers has been studied in a variety of geometries including flow approaching a swept forward-facing step, (Johnston, 1970), flow in ducts simulating infinite swept wings (Elsenaar and Boelsma, 1974, van den Berg et al. ,1975, Bradshaw and Pontikos, 1985), flow approaching obstacles (Dechow and Felsch, 1977, Anderson and Eaton, 1989) and axial flow along a rotating cylinder (Driver and Johnston, 1990). In addition, there have been several recent attempts to explore three-dimensional effects on turbulence using direct numerical simulation (Spalart, 1989, Coleman et al. 1990). In cases where an initially two-dimensional boundary layer is turned, thus becoming three-dimensional, it is generally found that the vector formed by the shear stress components parallel to the wall lags behind the strain rate vector. Also, it is frequently found that the turbulent shear stress levels are reduced relative to the turbulent kinetic energy. It is not clear if this latter effect is caused by sudden turning of the flow or if it is a general feature of all boundary layers containing mean flow three dimensionality.

It is difficult to extract general conclusions from the sum of the previous experiments because they are often complicated by extraneous effects such as streamwise pressure gradient and spanwise inhomogeneity. In many 3DTBL experiments all three space coordinates are significant and any analysis of the Reynolds stress transport equations, for instance, requires an extensive data set. The appropriate reference frame for analysis of the data is not apparent because the flow direction varies in all three directions.

We chose to investigate the flow on a rotating disk to simplify the analysis of the resulting data. There is no externally imposed pressure gradient and the flow is axisymmetric so at most only two space coordinates are needed to describe the experiment. In addition, variations in the radial direction are very slow and can be neglected except near transition. The disk flow does develop a substantial skewing across the boundary layer. At its peak the radial velocity component reaches a level of 11% of the local disk speed. An added advantage of using a disk to investigate 3DTBL's is that the Reynolds number can be changed easily by varying the disk speed. There are key differences, though, between a disk boundary layer experiment and previous 3DTBL experiments. First, the skewing is always present rather than developing as a pressure-induced perturbation. Second, turbulence may eventually reach a state of equilibrium with the imposed three-dimensional strain field. Finally, flow rotation adds the complexity of the Coriolis effects to the basic equation set.

The objectives of the present research program are to supply detailed mean velocity data and turbulence measurements up to third-order quantities. We wish to assess if this 3DTBL, which presumably has reached an equilibrium state, is fundamentally different in its turbulence properties than well understood 2DTBLs.

EXPERIMENTAL APPARATUS

The experimental apparatus consists of a 1 meter diameter aluminum disk mounted on a vertical spindle. The 15 mm thick disk was precision machined and lapped to allow only ± 20 μm vertical deviations when the disk rotates. The disk spins at speeds up to 1100 RPM which corresponds to a tip Reynolds number of 1.8 million. It is driven by a 2 hp DC motor through a belt drive to avoid vibrations. The motor is equipped with solid state speed control allowing smooth variation of the disk speed under manual or computer control. The rotating assembly was carefully balanced by virtue of its precise manufacture, and there is no measurable vibration at any operating speed.

A fixed annular apron approximately 0.3 m wide surrounds the disk to eliminate any interaction between the boundary layers on the top and bottom surfaces. The bottom surface runs in a closed cavity to avoid creating any disturbance in the test cell. A set of 14 spiral-shaped vanes are mounted on the upper surface of the apron to remove the angular momentum of the flow leaving the disk. We observed no significant swirl in the 2.4 m by 2.7 m by 3.4 m isolation cell with the vanes in place.

All experiments are conducted under the remote control of a data acquisition system consisting of an IBM PC-AT with a Metrabyte DAS-20 multifunction card and an SSH-4 simultaneous sample and hold. The computer controls the disk speed and all the measurement systems. Probes are postitioned by a stepper motor traverse mounted on a 1" X 3" beam located 1 meter above the disk surface. The traverse can rotate the probe around its stem axis with a resolution of 0.9° and translate it normal to the disk with a resolution of 1.6 μm.

Mean flow data are acquired using a three-hole probe in a non-nulling mode as described by Anderson and Eaton (1987). The dynamic and differential pressures are measured using a Setra model 239 (± 1.0 "H_2O range) or a model 264 (0–10 "H_2O range) for high speed dynamic pressure. The transducers are thermally insulated to minimize drift and are calibrated against a micromanometer before each run.

Three different hotwire probes are used. Each probe is mounted in a gooseneck stem allowing yaw of the probe without moving the measurement volume. The single-wire probe uses a Dantec 55P05 boundary layer tip strung with Dantec gold plated 5 μm platinum coated tungsten wire with an active length to diameter ratio of l/d = 250. The cross wire probe was custom built. It uses 2.5 μm platinum coated tungsten wire which has been copper plated and subsequently etched for an active length to diameter ratio of l/d = 200 The wire spacing is 0.35 mm. The crosswire can be rotated about its axis in 45° increments allowing determination of all six Reynolds stresses. The third probe is a custom dual wire probe which has two wires at ±45° to the stem axis in the same plane, parallel to the disk surface. This probe is used to provide redundant measurements of the flow direction, and was strung with 5 μm platinum coated tungsten wire, copper plated and etched for an active length to diameter ratio of l/d = 200.

All hotwires are operated in constant temperature mode by a TSI IFA-100 unit modified to eliminate the built-in linearizers. The signals are DC shifted and amplified to utilize the full ±5 Volt range on the Metrabyte A/D. Noise is filtered with a Frequency Devices model 901F1 low-pass filter The test cell temperature is not controlled so it is necessary to calibrate the hotwires for both velocity and temperature variation. This is accomplished by a portable jet apparatus which is placed on the disk and allows precise control of the flow temperature and velocity. A temperature dependent calibration is obtained by varying both the temperature and velocity and fitting King's law in a modification of the temperature correction suggested by Cimbala and Park (1990). In this implementation, the original form of King's law, $Nu = a + b \cdot Re^n$ is used, with fluid properties evaluated using the film temperature $T_f = \frac{1}{2}(T_a + T_w)$. The calibration is then of the following form,

$$U = \nu(P_{atm}, T_f) \left[\frac{B \cdot e^2}{k(T_f) \cdot (T_w - T_a)} - E_o^2 \right]^{1/n}$$

This calibration is implemented using an empirically obtained wire temperature specific to the type of wire, then B and E_o^2 are found with a least squares fit. The typical RMS deviation of the fit from 20 calibration points varying from 1 to 40 m/s was 0.2% at a single temperature, and < 1.5% for a temperature which varied 10°C.

The mean flow velocity and direction are measured using three different techniques, the three-hole probe corrected for shear and wall proximity, the custom dual wire probe, and finally by yawing the single-wire probe in an automated version of the Cham and Head (1969) technique. For mean flow measurements, 4000 samples are acquired at 100 Hz. The crosswire probe is aligned with the previously measured mean flow direction at each measurement point then 10,000 samples of each wire are acquired in each of the four probe orientations. The measured Reynolds stress and triple product tensors are then rotated into appropriate coordinates. The uncertainty involved in the Reynolds stress data are similar to those reported by Anderson and Eaton (1989) near the disk surface, but farther out in the boundary layer the local turbulence intensities became quite large. Therefore the measurements in the outer part of the boundary layer are subject to question. The analysis of Tutu and Chevray (1975) suggests that the crosswire is subject to very large errors for turbulence intensity greater than 35%. However, their analysis predicts a strong disagreement between single-wire and crosswire measurements for large turbulence intensity. Figure 1 shows a comparison of

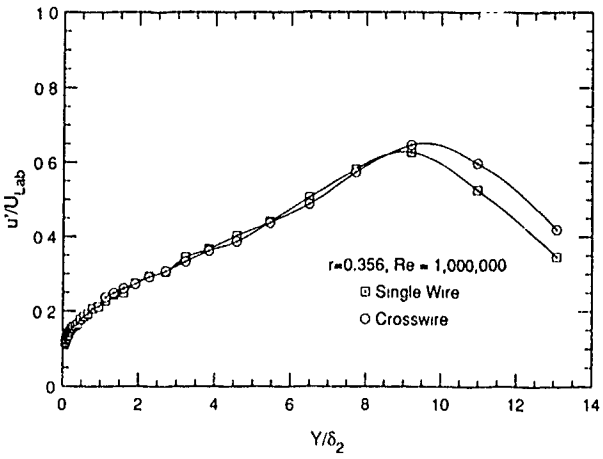

Figure 1: Comparison of measured turbulence intensity between single boundary layer probe and crosswire.

the longitudinal turbulence intensity as measured by the two probes. The agreement is excellent out to a turbulence intensity of at least 60%, and even beyond this point the differences are of the opposite sign than predicted by the analysis Laser Doppler measurements now in progress should shed light on this problem but for now, the Reynolds stress measurements should be treated with caution in the outer part of the boundary layer.

RESULTS AND DISCUSSION

The mean velocity and turbulence measurements are presented in a reference frame rotating with the disk so the velocity profiles appear similar to those in a typical wind tunnel experiment. This also gives direct mathematical formulation of the Coriolis effects, and allows the centrifugal forces to be included into the pressure term. The frame of reference is defined with its origin at the radius of interest and is right-handed with +Y directed upwards from the disk surface, +Z pointing at the axis of rotation, and +X directed in the circumferential direction.

One unwanted consequence of the transformation is that small uncertainties in measured flow angle close to the disk lead to very high uncertainties in the flow angle viewed in the rotating reference frame. This is due to the fact that once the local disk speed is subtracted from the measured velocity, the measurement uncertainty is retained as a percentage of the (large) measured value. For this reason the experimentally measured mean values tend to show much more scatter close to the disk than the scatter in the turbulence statistics, which are not subject to this effect.

Both laminar and turbulent cases were examined. The laminar cases are not shown here because they were used primarily for instrumentation qualification. Agreement with an

Table 1: Disk Flow Turbulent Cases

Symbol	Radius / Re	U_∞ [m/s]	δ_{99} [mm]	δ_2[mm]	H	Re_{δ_2}	U_τ [m/s]	ν/U_τ [μm]
	R = 0.235 m							
×	Re = 400,000	26.13	11.60	0.978	1.342	1657	1.206	12.8
	R = 0.356 m							
⊡	Re = 650,000	28.22	19.22	1.457	1.290	2662	1.255	12.3
⊙	Re = 940,000	41.01	20.05	1.456	1.269	3839	1.750	8.9
	R = 0.421 m							
○	Re = 650,000	23.72	21.04	1.712	1.298	2645	1.051	14.6
□	Re = 1,000,000	36.72	20.61	1.641	1.282	3903	1.556	9.9
△	Re = 1,300,000	48.14	20.39	1.594	1.270	4969	1.997	7.7

analytic solution was excellent for all three probes especially at the inner radii where the disk appeared to the flow as if it were indeed infinite. The turbulent cases to be presented here are listed in Table 1, along with integral properties of the flow in the X direction. The integral properties were calculated by direct numerical integration of the measured velocity profiles and the skin friction was calculated using the two-dimensional law of the wall with $\kappa = 0.41$. It is apparent from this information that relatively high Reynolds numbers are produced with a small experiment, due to the high speeds involved.

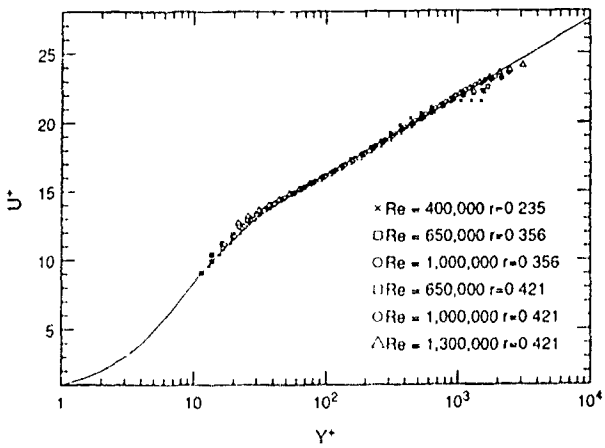

Figure 2: Mean circumferential velocity in wall units

Figure 2 shows the mean flow profiles in the +X direction plotted using wall scaling. One immediately notices the lack of a wake component, which is likewise absent in the data of Cham and Head (1969). This is not the result of a favorable pressure gradient, since the X direction will not support a mean pressure gradient, but instead may be taken as an indication of structural differences between this 3DTBL and the typical zero pressure gradient 2DTBL.

The primary Reynolds stress $\overline{u'v'}$ is shown in Figure 3, normalized with the circumferential shear velocity. It appears much the same as a zero pressure gradient 2DTBL, and totally unlike the 3DTBL flows in Table 2 which all exhibit a peak away from the wall. The effect seen in other 3DTBL's can not be ascribed only to an adverse pressure gradient, but is also the result of some type of structural change in the turbulence which will be discussed more fully below.

The secondary Reynolds stress $\overline{v'w'}$ is shown in Figure 4, normalized with the circumferential shear velocity. This quantity is a measure of the effect on the turbulence of the spanwise strain, so it is identically zero in a 2DTBL. It is interesting to note that $\overline{v'w'}$ has a nearly constant value in the locations the crosswire could acquire data, but must change sign closer to the wall in order to approach the wall shear stress value as expected. The sign change is necessary because the spanwise mean velocity profile has a maximum, and therefore the outer layer sees the opposite shear than the inner layer. The sign of the stress is positive in the region plotted because the crossflow is in the -Z direction. These measurements resemble previous 3DTBL experiments plotted in freestream coordinates.

It is always difficult to gain a physical understanding of the pattern of the turbulent fluctuations from single point statistics, and even more so to compare results between experiments. In the process of Reynolds averaging the Navier Stokes equations, quantities (Reynolds stresses) result which are the consequence of average momentum transport by the fluctuations. In attempts to form 'closure' models for these terms, several quantitative relationships between the various turbulent quantities have been found to have a predictable value or behavior in a certain type of flow. These 'structural parameters' allow similarities and differences in fluctuating fields and thus the physics of flowfields to be compared. Selected structural indicators from the present flow will be compared to previous experiments listed in Table 2. It is important to note

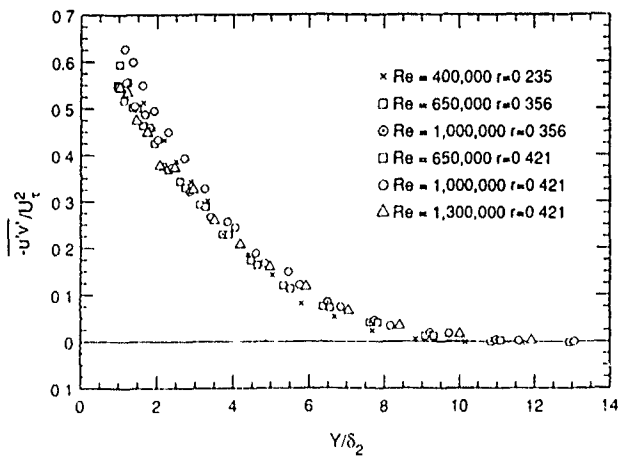

Figure 3: Primary Reynolds stress $\overline{u'v'}$, normalized by the shear velocity.

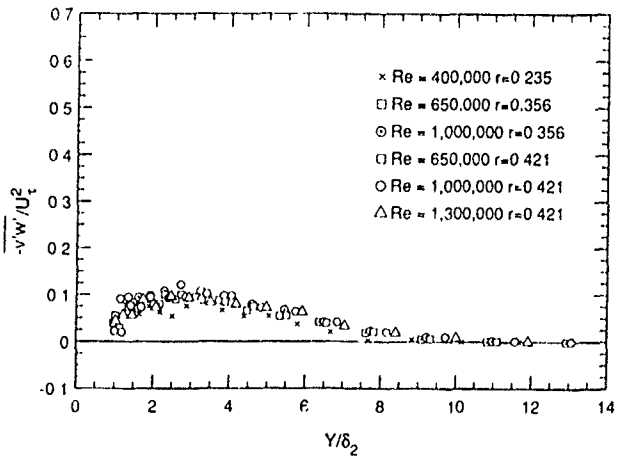

Figure 4: Secondary Reynolds stress $\overline{v'w'}$, normalized by the shear velocity.

that three major categories of 3DTBLs are represented. infinite swept wing, obstacle, and shear driven. These combined with Klebanoff's classic 2DTBL should represent the current state of knowledge of the effect of three-dimensionality on an initially 2DTBL from wind tunnel experiments.

Table 2: Reference Experiments

Symb.	Experiment	Flow Type/Designation
A	Anderson/Eaton (1989)	Obstacle, Case I St 4
P	Bradshaw/Pontikos (1985)	Infinite Wing, X=1092
R	Driver/Johnston (1990)	Shear Driven, St 9
E	Elsenaar/Boelsma (1974)	Infinite Wing, X=1095
K	Klebanoff (1955)	2DTBL Re_{δ_2}= 8000

The ratio of streamwise normal stress to vertical normal stress appears as Figure 5, along with comparisons to the experiments listed in Table 2. This ratio is a measure of the boundary layer's preference for streamwise fluctuations compared to fluctuations normal to the wall. A high value implies that streamwise fluctuations are dominant over wall-normal events, pointing to a decrease in eddy coherence. The behavior seen in each of the 3DTBL experiments, along with the

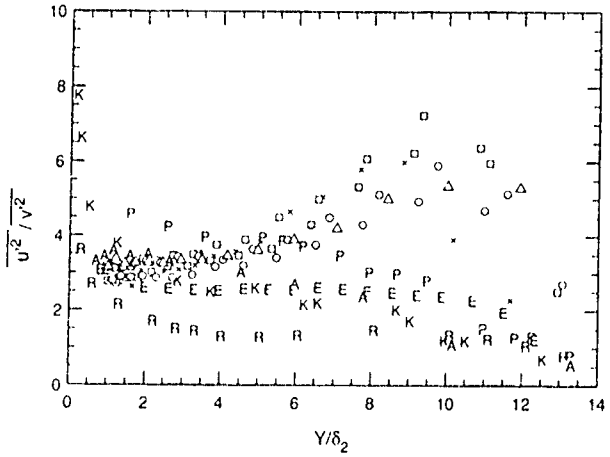

Figure 5: Ratio of streamwise normal stress to vertical normal stress. (Symbols as in Tables 1 and 2)

2DTBL experiment of Klebanoff, show a nearly constant or monotonic decrease in this ratio moving away from the wall. Every case from the present experiment shows a clear peak in the outer region of the boundary layer. The height of this peak is seen to decrease and perhaps move outward with increasing Reynolds number at a given radius. This implies the structure of the boundary layer is substantially different from the other experiments, but has not reached an asymptotic state.

Another commonly investigated structural parameter is the ratio of the vector magnitude of the shear stress to twice the turbulent kinetic energy:

$$A_1 = \frac{\sqrt{\overline{u'v'}^2 + \overline{v'w'}^2}}{q^2}$$

This parameter is approximately constant at 0.15 in a 2DTBL even when the layer is strongly distorted by pressure gradient. The wind tunnel experiments plotted in Figure 6 show the typically observed trend that three-dimensionality depresses A_1 near the wall, and this depression diffuses outward. As noted above, A_1 is not strongly affected by pressure gradient alone, and the general agreement among 3DTBL experiments implies that three-dimensionality affects the flow structure in this qualitatively predictable fashion. The disk flow is vastly different, showing A_1 to decrease almost linearly with distance from the wall for the inner radii, and at least monotonically for the outer radius. The consideration of this effect combined with that in Figure 5 leads one to the conclusion that irrotational (inviscid) motion plays an even bigger role in the outer region of the disk boundary layer than in a wind tunnel layer.

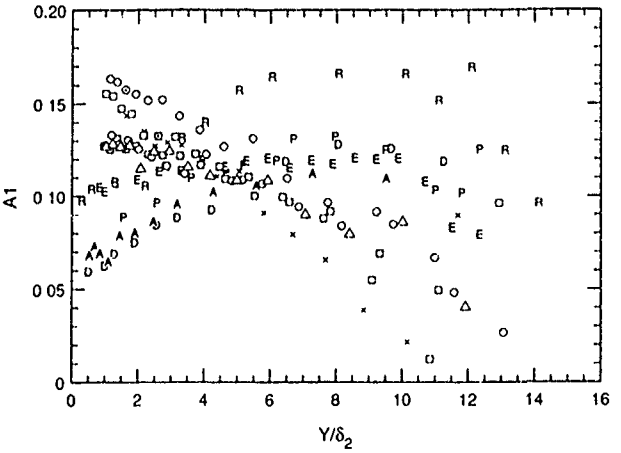

Figure 6: Ratio of shear stress magnitude to twice the turbulent kinetic energy. (Symbols as in Tables 1 and 2)

One of the most common approaches to closure is the assumption that the Reynolds shear stress responds linearly to the imposed strain rate. The constant of proportionality is known as the eddy viscosity, because it is analogous to the molecular viscosity when inserted into the mean momentum equation. The ratio of the relative effectiveness of the turbulence in transporting streamwise and the spanwise momentum is defined as:

$$N_e = \frac{\tan(\gamma_\tau - \gamma_{fs})}{\tan(\gamma_g - \gamma_{fs})}$$

The angle γ_{fs} is that of the local mean velocity, γ_g is the angle of the velocity gradient vector, and γ_τ is the shear stress vector angle. This may also be thought of as the ratio of local spanwise to local streamwise eddy viscosity. The values obtained for N_e are shown in Figure 7. These data exhibit more scatter than most of the other plots because they contain derivatives of experimental data. As concluded by Anderson and Eaton (1989), low values in N_e (as low as 0.2) are observed in sharply turned experiments such as shear driven or obstacle flows, and a value closer to one in slowly turned flows like the infinite wing. This implies that the disk flow more closely resembles a slowly turned flow or equivalently one which has more time to relax to a new state after the imposition of crossflow. The values near unity indicate that an isotropic eddy viscosity should perform well, and this was indeed the case for a simple cross-

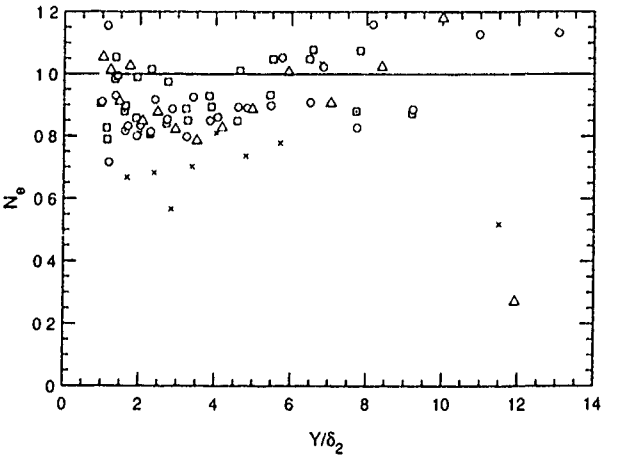

Figure 7: Ratio of eddy eiscosity in coordinates aligned with the local mean velocity. (Symbols as in Table 1)

flow calculation for the disk flow reported by Cham and Head (1969).

One might suspect that the outer region of the boundary layer is dominated by Coriolis effects. The Reynolds stress transport equations for a rotating coordinate system show that Coriolis effects act to redistribute the Reynolds stress among the various components of the tensor. This could lead to the increasing values of $\overline{u'^2}/\overline{v'^2}$ observed in the outer layer. If the outer region were dominated by Coriolis effects, then w' and u' fluctuations must be negatively correlated. However, the correlation coefficient for $\overline{u'w'}$ was calculated and is strongly positive in the outer layer, indicating that Coriolis effects are not a major factor. This then supports the conclusion that the outer region is dominated by irrotational (inviscid) motions, a conclusion also supported by Cham and Head's (1969) measurement of reduced entrainment.

It remains to address the cause of the reduced level of shear stress in the disk boundary layer. Bradshaw and Pontikos hypothesized that turbulent eddies formed in a 2D boundary layer are tilted out of their preferred orientation by the imposition of three-dimensional skewing. Implicit in their discussion was the assumption that normal boundary layer turbulence would eventually develop if the 3D strain field remained constant for a long enough distance. Anderson and Eaton (1989) theorized that the turbulence is stabilized in the region of peak turbulence production by the presence of crossflow. Eaton (1991) took this further, stating that production is reduced because a fraction of the low speed streaks in the boundary layer are eliminated by the crossflow and because longitudinal vortices are attenuated by the crossflow. Implicit in this argument is the assumption that boundary layer turbulence developed in a three dimensional strain field is inherently less efficient at extracting energy from the flow field. The present results support the latter hypothesis. The value of A_1 is suppressed below normal 2D levels even though the entire boundary layer development occurs in a nearly constant three dimensional strain field.

CONCLUSIONS

The disk boundary layer, while subject to Coriolis effects, appears to be a good configuration for studying the fundamental physics of 3DTBL's. Many of the effects observed in wind tunnel 3DTBL's are also observed here. The A_1 structural parameter is less than in comparable 2D boundary layers and a small lag in the shear stress direction behind the mean velocity gradient angle was noted, behaving not unlike a slowly-turned three-dimensional boundary layer.

Some of the results must be treated with caution since the hotwire measurements may be subject to considerable uncertainty. Laser Doppler measurements now underway should resolve such questions. Additional length scale measurements should cast further light on the structural features of the boundary layer.

ACKNOWLEDGEMENTS

This work is supported by the Department of Energy Office of Basic Energy Sciences Grant DE-FG03-86ER13608. The numerous discussions with Prof. James P. Johnston and Prof. Peter Bradshaw are especially appreciated.

REFERENCES

Anderson, S.D. and J.K. Eaton, (1989) "An Experimental Investigation of Pressure Driven Three- Dimensional Boundary Layers," JFM, Vol. 202, pp. 263-294.

Bradshaw, P. and N.S. Pontikos (1985) "Measurements in the Turbulent Boundary Layer on an 'Infinite' Swept Wing," JFM, Vol. 159, pp. 105-130.

Coleman, G.N., J.H. Ferziger, and P R Spalart (1990) "A Numerical Study of the Turbulent Ekman Layer," JFM Vol. 213, pp. 313-348.

Cham, T-S. and M. R. Head, (1969) "Turbulent Boundary-Layer Flow on a Rotating Disk," JFM, vol 37, part 1, pp. 129-147.

Cimbala, J M., W.J. Park (1990) "A Direct Hot-Wire Calibration Technique to Account for Ambient Temperature Drift in Incompressible Flow," Experiments in Fluids, Vol. 8, pp. 299-300.

Dechow, R. and K.O. Felsch (1977) "Measurements of the Mean Velocity and of the Reynolds Stress Tensor in a Three-Dimensional Turbulent Boundary Layer Induced by a Cylinder Standing on a Flat Wall," Proceedings of Symposium on Turbulent Shear Flows, April 18-20, 1977, University Park, Pennsylvania, Vol 1

Driver, D.M. and J.P. Johnston (1990) "Experimental Study of a Three-Dimensional Shear-Driven Turbulent Boundary Layer with Streamwise Adverse Pressure Gradient," NASA TM 102211, and Thermosciences Division Report MD-57

Eaton, J.K. (1991), "Turbulence Structure and Heat Transfer in Three-Dimensional Boundary Layers," 9th Symposium on Energy Engineering Sciences, Argonne National Laboratories

Elsenaar, A. and S.H. Boelsma (1974), "Measurements of the Reynolds Stress Tensor in a Three-Dimensional Turbulent Boundary Layer Under Infinite Swept Wing Conditions," NLR TR 74095 U.

Johnston, J.P. (1970) "Measurements in a Three-Dimensional Turbulent Boundary Layer Induced by a Swept, Forward-Facing Step," JFM Vol. 42 pp 823-844.

Johnston, J.P. (1973) "The Suppression of Shear Layer Turbulence in Rotating Systems," J. Fluids Eng., June, pp. 229-236

Klebanoff, P S. (1955) "Characteristics of Turbulence in a Boundary Layer With Zero Pressure Gradient," NACA Report 1247.

Spalart, P.R. (1989), "Theoretical and Numerical Study of a Three-Dimensional Turbulent Boundary Layer," JFM, Vol. 205, pp. 319-340.

Tutu, N.K. and R. Chevray (1975) "Cross-Wire Anemometry in High Intensity Turbulence," JFM Vol. 71, pp. 785-800.

EIGHTH SYMPOSIUM ON
TURBULENT SHEAR FLOWS
Technical University of Munich
September 9-11, 1991

Effects of Solid Body Rotation on the Transport of Turbulence

Shao L., Michard M. and Bertoglio J.P.

Laboratoire de Mécanique des Fluides et
d'Acoustique,URA CNRS 263,
Ecole Centrale de Lyon, 36 av. Guy de Collongue,
69130 Ecully, France

ABSTRACT.

The mechanism of turbulence transport is studied using a Large Eddy Simulation of a shearless turbulence mixing layer, subjected to solid body rotation. The behaviour of both transport by triple velocity correlations and transport by pressure-velocity correlations is found to be completely different from what is found without rotation. A modified one-point model, that accounts for the effects of rotation, is proposed for the triple correlation transport terms.

1. INTRODUCTION

In a previous study, the mechanisms responsible for transport of turbulent kinetic energy and transport of the components of the Reynolds stress tensor were investigated in a simple case of inhomogeneous turbulence : the case of a shearless turbulence mixing layer, in which two nearly homogeneous fields, having different energy and length scales, were put side by side and were interacting (see the sketches in figures 1 and 2). The study was made using a Large Eddy Simulation (Shao, Bertoglio and Michard, 1990). Results were found to be in qualitative agreement with the experimental data of Veeravalli and Warhaft (1989). Comparisons with results of the classical one-point closure models, like k-ε and Reynolds stress models, were presented in another paper (Shao, Le Penven and Bertoglio, 1990). The main conclusion of the study was that triple velocity correlations were found to be responsible for the energy transport and that pressure-velocity correlations were found to tend to counterbalance the triple correlation transport, their effects remaining small.

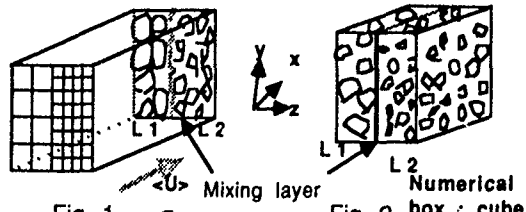

Fig. 1

Fig. 2

Concerning triple velocity correlations : when the Launder, Reece and Rodi (1975) second order model was used, the value $C_S=0.11$ usually retained in the expression for the triple correlation .

$$\langle u_iu_ju_k\rangle = -C_s\frac{k}{\varepsilon}\left(\langle u_ku_m\rangle\frac{\partial\langle u_iu_j\rangle}{\partial x_m}+\langle u_ju_m\rangle\frac{\partial\langle u_iu_k\rangle}{\partial x_m}+\langle u_iu_m\rangle\frac{\partial\langle u_ju_k\rangle}{\partial x_m}\right) \quad (1)$$

in which $k=1/2\langle q^2\rangle=1/2\langle u_iu_i\rangle$ is the turbulent kinetic energy and ε its dissipation rate, was found to be qualitatively suitable but lead to underestimated values of $\langle u_iu_iu_k\rangle$, in particular on the small scale side of the mixing layer when strong effects of intermittency are present. A correction to account for intermittency effects was proposed (Shao and Bertoglio, 1991).

Similarly, in the case of the k-ε model, the expression

$$\frac{1}{2}\langle u_iu_iu_k\rangle = -\frac{C_\mu k^2}{\sigma_k}\frac{\partial k}{\varepsilon\,\partial x_k} \quad (2)$$

was also found to underestimate triple correlations on the small scale side when the classical value $\sigma_k = 1$ was adopted.

Both the C_S constant in the case of the Reynolds stress model and the σ_k constant in the case of the k-ε model, were found to underestimate transport effects. A possible explanation is the following. The shearless mixing layer can be suspected to be the case in which transport mechanisms, acting alone without interacting with other effects, are the most efficient. One can imagine that when other effects, like shear, strain or rotation, are present the build up of triple correlations can be strongly inhibited. The present study is aimed at investigating how transport mechanisms are affected when rotation is present. The effect of solid body rotation is considered. The reason for the choice of rotation as the first external effect to be studied is not only that it is the simplest effect that can be introduced in a Direct Simulation, but also that it has important applications for inhomogeneous flows of practical interest, like swirling flows, and flows in turbomachinery.

2. EFFECTS OF ROTATION ON TURBULENCE

The influence of rotation on turbulence is a complex mechanism, and different consequences of the presence of rotation can be identified, whose importances vary depending on the different situations that are considered. Before describing the problem addressed here, one can briefly discuss the various effects of rotation, and summarize the various modifications that are usually introduced in simple models to account for these effects.

The effect of solid body rotation on homogeneous grid-generated turbulence is now well identified. If turbulence is initially isotropic, the action of rotation typically takes place at the level of the third-order velocity correlations in wave-space. Due to the fact that Fourier modes are rotating about the directions of the wave-vectors, a scrambling effect occurs in the triadic interaction between modes, resulting in an inhibition of the build up of triple correlations. Energy transfer from the large scales to the dissipative eddies is reduced. In the framework of one-point models, heuristic modifications of the ε equation were proposed to account for this cascade inhibition mechanism (Bardina et al. 1983, Aupoix et al.1983). It has to be pointed out that, in this case, another consequence of the presence of rotation can be detected : rotation is also creating anisotropy. The obtained anisotropy is essentially a length scale anisotropy, and therefore the phenomenon is difficult to take into account in existing one-point models. Only models introducing information on the anisotropy of length scales or on energy distribution in Fourier space could permit a description of this effect. Efforts are presently being made along these lines (Cambon, Jacquin and Lubrano,1991).

In the case of initially anisotropic turbulence subjected to solid body rotation, the anisotropy of the Reynolds stress tensor is directly affected by the presence of rotation. The principal axes of the Reynolds stress tensor are rotating under the effect of the Coriolis term. Furthermore there is a more subtle effect due to the rapid part of the pressure strain correlation. This last effect is related to mechanisms that are easy to describe in wave-space, but difficult to model at the level of one-point models. Attempts to take these effects into account are currently being made (Lubrano and Cambon, 1991).

In the case of the simultaneous action of rotation and mean velocity gradients, the most important effect is a coupled effect between production by mean gradients and re-orientation of the Reynolds stress tensor by rotation. This occurs, for example, when turbulence is subjected to a mean shear in a rotating frame. This case is particularly important because of applications to the behaviour of flows inside the blade to blade channels of centrifugal impellers. Either stabilizing or destabilizing effects can occur when rotation is in the plane of the shear, depending on the sign of rotation compared to the shear. These effects are taken into account in Reynolds stress models at the level of the production and the Coriolis terms. The major problem is then whether models for the pressure strain correlation properly account for rotation. Even if existing models are not suitable for every value of the rotation rate compared with the shear rate, they lead to satisfactory predictions, at least qualitatively (see Bertoglio 1982 and Speziale et al. 1990). When other types of mean gradients are considered, more complex effects can be detected (plane strain : "elliptic flows", or axial compression, see Cambon et al. 1985 or Malkus 1990). It is beyond the scope of the present paper to discuss these effects that are difficult to include in simple models.

The effects of rotation summarized in the previous paragraphs are effects that can be described in the framework of homogeneous turbulence. Even if simple models are not yet describing these effects completely, it is clear that the mechanisms are, at least, well identified. Efforts are currently being made to devise improved models. The purpose of the present study in to investigate a different consequence of the action of rotation on turbulence, one which has not yet been studied. We address the problem of an effect typically taking place in inhomogeneous turbulence : the influence of rotation on the transport terms of turbulent kinetic energy and of Reynolds stress components. The physical mechanism is, in this case, essentially the inhibition of the build up of triple velocity correlations at one-point. It is a mechanism taking place in physical space, and not in Fourier space as is the case when the influence of rotation on homogeneous turbulence is considered.

3. STUDY OF THE INFLUENCE OF ROTATION ON TURBULENCE TRANSPORT TERMS

The study is aimed at understanding the influence of rotation on the inhomogeneous transport terms at the level of the equation for the double velocity correlation. The transport terms are the triple correlation : $\partial/\partial x_k \langle u_i u_j u_k \rangle$, and the pressure term : $\partial/\partial x_k \langle p/\rho(\delta_{jk} u_i + \delta_{ik} u_j) \rangle$. In order to investigate the consequences of rotation in the case of a very simple inhomogeneous field, a Large Eddy Simulation of a shearless turbulence mixing layer is performed in a rotating frame. The numerical technique is similar to the one described in Shao, Bertoglio and Michard (1990). Simulations are run on a cubic box with periodic boundary conditions. The initial field consists of two different homogeneous velocity fields put side by side. Z denotes the inhomogeneity direction,

and Y is the axis of rotation (Ω parallel to OY). Subgrid scales are parameterized by using the model proposed by Chollet and Lesieur (1981). Due to the fact that periodicity of the boundary conditions is assumed, two mixing layers are simulated instead of one : one in the middle of the numerical box, the other one at the edges. No mean flow is present in the computation (see the sketch in figure 3). Computations are run on regular grids with 64^3 nodes, using a pseudo-spectral numerical scheme.

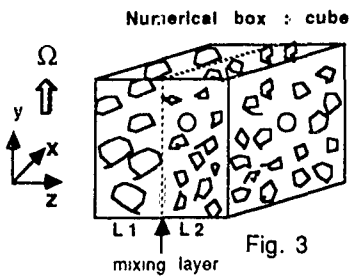

Fig. 3

At the beginning of the computations, on the left side of the box, a turbulent field with strong intensity and large length scales is introduced. On the right side, a turbulent field with lower intensity and smaller length scales is prescribed. The ratio of turbulent kinetic energies between the two sides is nearly equal to two, and the ratio of length scales is approximatively two. This case corresponds to test case 64-02 in the steady frame study proposed in Shao, Bertoglio and Michard (1990). Results are averaged in planes of homogeneity, that is to say in (X,Y) planes. They are also averaged over different realizations in order to improve statistical sampling.

The equations for the double velocity correlations at one point, or Reynolds stress tensor, can be easily written in a rotating frame. The important terms clearly appear in the equations for the diagonal components. Taking into account the symmetries of the problem and homogeneity in the X and Y directions, we obtain :

$$\frac{D\langle u^2\rangle}{Dt} = -\frac{\partial\langle wu^2\rangle}{\partial z} - 0 + \frac{2}{\rho}\left\langle p\frac{\partial u}{\partial x}\right\rangle + \text{vicous term} + \text{Coriolis term}$$

$$\frac{D\langle v^2\rangle}{Dt} = -\frac{\partial\langle wv^2\rangle}{\partial z} - 0 + \frac{2}{\rho}\left\langle p\frac{\partial v}{\partial y}\right\rangle + \text{viscous term} \qquad (3)$$

$$\frac{D\langle w^2\rangle}{Dt} = -\frac{\partial\langle w^3\rangle}{\partial z} - \frac{2\partial\langle pw\rangle}{\rho\,\partial z} + \frac{2}{\rho}\left\langle p\frac{\partial w}{\partial z}\right\rangle + \text{viscous term} + \text{Coriolis term}$$

The first two terms on the right hand sides are respectively, transport terms by triple velocity correlations and by pressure-velocity correlations. The third terms are for pressure redistribution, whose effect is the interchange of energy between components of the Reynolds stress tensor, and which do not affect energy transport. The viscous terms essentially account for molecular dissipation. Viscous effects also contribute to turbulence transport, but their contribution is not discussed here since it vanishes for high Reynolds number flows. The last terms are Coriolis terms, whose trace is zero, since Coriolis forces are not producing energy.

The equation for twice the turbulent kinetic energy is :

$$\frac{D\langle q^2\rangle}{Dt} = -\frac{\partial\langle wq^2\rangle}{\partial Z} - \frac{2}{\rho}\frac{\partial\langle pw\rangle}{\partial Z} + \text{Viscous term} \qquad (4)$$

in which $\langle wq^2\rangle = \langle w^3\rangle + \langle wv^2\rangle + \langle wu^2\rangle$.

The important terms for the transport of turbulence are therefore $\langle w^3\rangle$, $\langle wu^2\rangle$, $\langle wv^2\rangle$ and $\langle pw\rangle$.

The results of the L.E.S. clearly show that rotation does reduce the triple correlation term $\langle u_i u_j u_k\rangle$, as shown in figure 4b where the component responsible for the transport of $\langle w^2\rangle$ in the Z direction, $\langle w^3\rangle$, is plotted as a function of Z. In the present computations, turbulence first evolves without being subjected to rotation between t=0 and t=0.04 s. Then rotation is suddenly switched on at t=0.04 s. The value of Ω is 50 rd/s, corresponding to an initial value of the Rossby number approximatively equal to 0.7 on the high turbulence side of the mixing layer. In figure 4b the normalized quantity, $\langle w^3\rangle/\langle w^2\rangle^{3/2}$, is found to first increase up to a value of about 0.4, reached at the end of the non-rotating phase (t=0.04 s). For larger values of time, this quantity decreases drastically : at time t=0.08 s, it is nearly equal to the statistical noise (in this case, results are averaged on 3 realizations only). In the same case without rotation, larger values of $\langle w^3\rangle/\langle w^2\rangle^{3/2}$ were obtained (case 64-02 in Shao, Bertoglio and Michard, 1990) as shown in figure 4a where this quantity continue to increase between t=0.04 s and t=0.08 s.

In figure 5, the evolution with time of the turbulent kinetic energy profiles is plotted. The cases with (figure 5b), and without (figure 5a) rotation are compared. It immediately appears that higher levels of turbulent kinetic energy are obtained at the end of the simulation on both sides of the box when rotation is present. This is due to the inhibition of the energy transfer between eddies of various sizes, an effect which appears to be consistent with what is found in homogeneous turbulence. A more interesting remark can be made concerning energy distribution along Z : despite the fact that triple correlations are reduced by rotation, the diffusion of turbulent kinetic energy towards the low turbulence side of the box is still comparable to what was found without rotation. The only possible explanation is therefore that,

in the rotating case, a large part of the turbulence transport must be due to the pressure term. When pressure velocity contributions are evaluated, this conjecture is corroborated by the fact that they are much larger than in the case without rotation. In the steady frame case, pressure-velocity correlations tend to counterbalance transport by triple correlations, while they are found to contribute positively to the diffusion mechanism in the rotating case (see figures 6a and 6b). In the non-rotating case, turbulence transport is due to triple velocity correlations, the effect of pressure being to slightly reduce transport. In the rotating case, transport is mainly due to pressure velocity correlations.

In a recent study, Riley (1990) has found very similar results in the case of turbulence subjected to stable stratification : when a slab of stratified turbulence is immersed in a non-turbulent field, diffusion of turbulence appears to be comparable to the diffusion obtained in the non-stratified case, even though triple correlations are strongly reduced. In Riley's work, this effect is attributed to the presence of waves in stratified turbulence. An interesting analogy is possible, since it is known that in the case of rotating flows, waves also exist : inertial waves. If results not averaged over different realizations are plotted as functions of time, irregular profiles are obtained when rotation is present, while, in the non rotating case, smoother behaviours are found. This is, in particular, clear in figures 7a and 7b where profiles of $\langle w^2 \rangle$ are compared. This behaviour can not be considered as evidence for the existence of waves, but it is sufficiently important to be noticed.

4. ONE-POINT MODELS

The aim of the present section is to include in one-point models the reduction of the triple correlation induced by rotation. A model is devised by taking into account the linear term due to Coriolis forces in the equation for the triple velocity correlation. In a second step, a simplified model is proposed.

In the one-point model approach the equation for the triple correlations is written (see Hanjalic and Launder 1972), and the fourth order moments are expressed by introducing Quasi-Normal assumptions. The approach is here extended to the case of rotating turbulence, in which we do not neglect the effects introduced by the presence of rotation. Thus :

$$\frac{\partial \langle u_i u_j u_k \rangle}{\partial t} = -\left(\frac{\varepsilon}{C_s k}\langle u_i u_j u_k \rangle + \langle u_k u_m \rangle \frac{\partial \langle u_i u_j \rangle}{\partial x_m} + \langle u_j u_m \rangle \frac{\partial \langle u_i u_k \rangle}{\partial x_m} + \langle u_i u_m \rangle \frac{\partial \langle u_j u_k \rangle}{\partial x_m} + 2\varepsilon_{ilm}\Omega_l \langle u_j u_k u_n \rangle + 2\varepsilon_{klm}\Omega_l \langle u_i u_j u_n \rangle + 2\varepsilon_{jlm}\Omega_l \langle u_k u_i u_n \rangle\right) \quad (5)$$

In equation (5), ε_{ijk} is the permutation tensor. The quantity $\frac{\varepsilon}{C_s k}\langle u_i u_j u_k \rangle$ is a damping term introduced in order to model the effect of pressure. It can also be regarded as taking into account the effects of the fourth-order cumulants.

When the asymptotic values for $\langle u_i u_j u_k \rangle$ deduced from equation (5) are used in Reynolds stress computations, results show that triple correlation levels are reduced by the presence of rotation - as expected. Consequently, the inhomogeneous transport of turbulence appears to be reduced when compared to the non-rotating case (see figure 8).

A simpler model is also proposed, in which triple correlations are expressed using the classical formulation corresponding to the Hanjalic and Launder model (equation (1)), with C_s replaced by $C_s' = C_s/(1+R_o^{-1})$. R_o is here the Rossby number defined as $R_o = \varepsilon/k\Omega$. Comparisons between results obtained with the simple model and with the complete form are very satisfactory, as appears in figure 8. However, it has to be pointed out that more work is needed to model the pressure-velocity correlation in this case, since one of the conclusions of the Large Eddy Simulation study is that pressure appears to play a very significant role when rotation is present. In order to determine whether the pressure effect was due to the rapid part of pressure or to non-linear effects, a Rapid Distortion study was made, by simply discarding the non-linear terms in the numerical code. The conclusion is that the effect is present in R.D.T. and is consequently a linear effect, which is consistent with the fact that transport is due to inertial waves. At the present time, it seems difficult to model this effect at the level of one-point closure. The problem involves quantities like group velocities that are difficult to take into account in classical models. The case of the axis of rotation parallel to the inhomogeneity direction OZ could also be investigated. In this situation, effects more similar to the mechanisms observed in the experimental study of Hopfinger et al. (1982) are likely to be found.

REFERENCES

- AUPOIX B., COUSTEIX J. and LIANDRAT J., 1983; Effects of Rotation on Isotropic Turbulence, Fourth Int. Symp. Turb. Shear Flows, Karlsruhe, Sept. 83.
- BARDINA J., FERZIGER J.H. and REYNOLDS W.C., 1983; Improved Turbulence Models based on L. E. S. of Homogeneous, Incompressible Turbulent Flows, Report T.F. 19, Stanford Univ., May 83.
- BERTOGLIO J.P., 1982; Homogeneous Turbulent Field within a Rotating Frame, A.I.A.A. Journ., Vol. 20, no 9..
- CAMBON C., TEISSEDRE C. and JEANDEL D., 1985; Etude d'effets couplés de Déformation et de Rotation sur une Turbulence Homogène, Journ. Méc. Théor. Appl., 4.
- CAMBON C., JACQUIN L. and LUBRANO J.L., 1991; Towards a New Reynolds Stress Model for Rotating Turbulent Flows , submitted to Physics of Fluids.
- CHOLLET J.P. and LESIEUR M., 1981; Parameterization of Small Scales of Three-Dimensional Isotropic Turbulence

utilizing Spectral Closures, Journ. of Atm. Sci., Vol. 38.
- HANJALIC and LAUNDER B.E., 1972 A Reynolds stress model of turbulence and its application to thin shear flows , J.F.M. 52 pp 609-638
- HOPFINGER E.J., BROWAND F.K. and GAGNE Y, 1982; Turbulence and Waves in a Rotating Tank. J. F. M.125.
- JACQUIN L., LEUCHTER O., CAMBON C. & MATHIEU J., Homogeneous Turbulence in the Presence of Rotation, J.F.M. 220, pp 1-52, 1990
- LAUNDER, REECE and RODI , 1975 Progress in the developpement of Reynolds stress closure J.F.M. 68.
- LUBRANO J.L. and CAMBON, C. 1991, Personal communication.
- LUMLEY J., 1978; Computational Modeling of Turbulent Flow, Adv. Appl. Mech., 18, pp. 123-176.
- MALKUS, 1990 ; Europ. Turb. Conf., Stockholm, July 90.
- RILEY, 1990, Seminar on Stratified Turbulence, Ecole Centrale de Lyon, Sept. 90.
- SHAO L , BERTOGLIO J.P. and MICHARD M., 1990; Large Eddy Simulation of the Interaction between Two Distinct Turbulent Velocity Scales, Europ. Turb. Conf., Stockholm, July 90, to appear in Springer-Verlag
- SHAO L., LE PENVEN L. and BERTOGLIO J.P., 1990, Study of the Modelling of the Transport Terms in One-point Closures using L. E. S. of Turbulence, Int. Symp. on Eng. Turb. Model. and Measur., Dubrovnik, Sept. 90.
- SHAO L. et BERTOGLIO J.P., Effet de l'Intermittence sur les Termes de Transport Turbulent 10^{e} Cong. Méca. Fr. Sept.1991
- SPEZIALE C.G., GATSKI T.B. and MHUIRIS N.M G., 1990; A Critical Comparison of Turbulence Models for Homogeneous Shear Flows in a Rotating Frame, Phys. Fluids, A2, 9, Sept. 90, pp. 1678-1684.
- VEERAVALLI and WARHAFT , 1989 The shearless turbulence mixing layer J.F.M. 207, 191-229

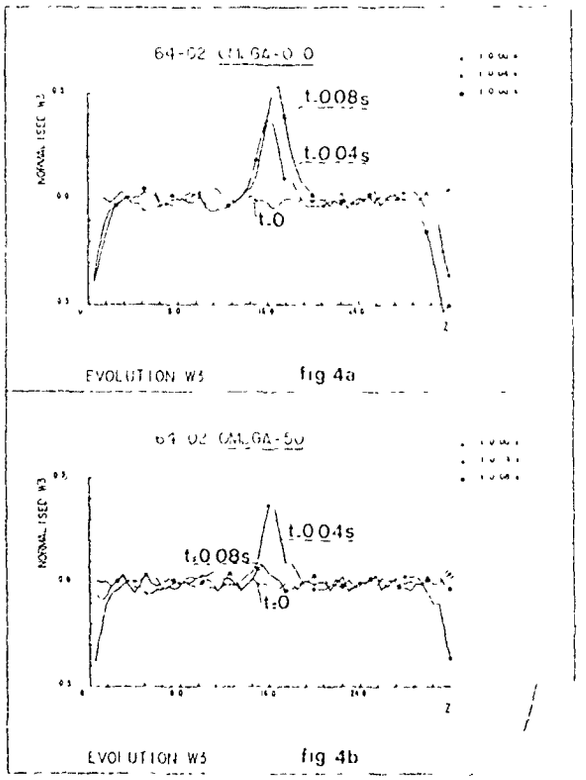

fig 4a

fig 4b

Fig. 4 : Profiles of the normalized triple correlation $\langle w^3\rangle/\langle w^2\rangle^{3/2}$ as functions of the inhomogeneity direction Z for different times. Results averaged over 2 realizations.

Fig 4a : without rotation.
Fig 4b : with rotation Ω = 50 rd/s (rotation switched on at time t=0.04 s).

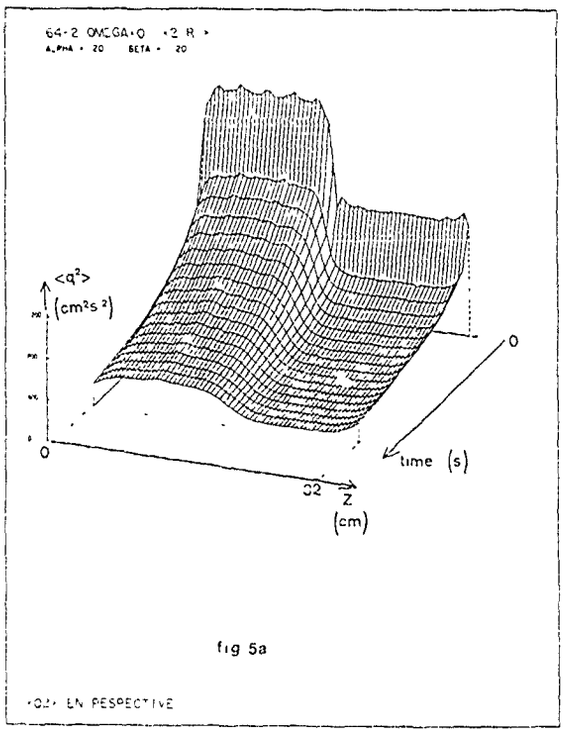

fig 5a

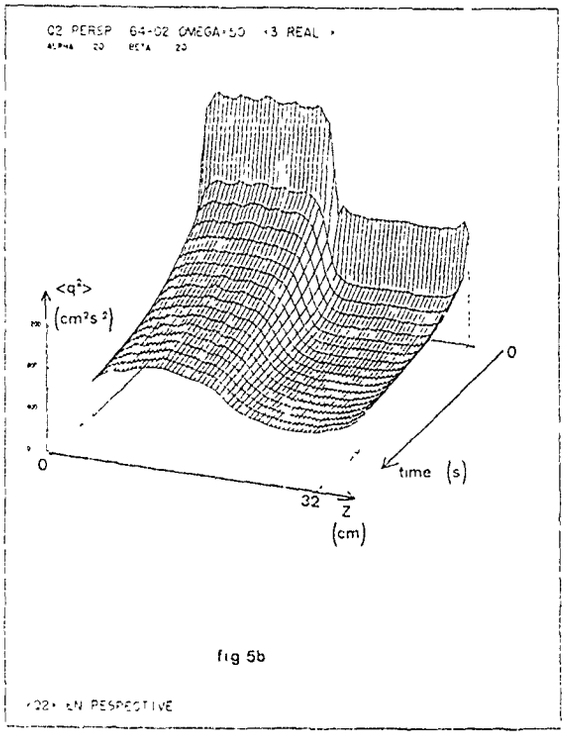

fig 5b

Fig. 5 : Evolution with time of the turbulent kinetic energy profiles. Results averaged over 3 realizations.

Fig. 5a : without rotation.
Fig. 5b : with rotation Ω = 50 rd/s (rotation switched on at time t=0.04 s).

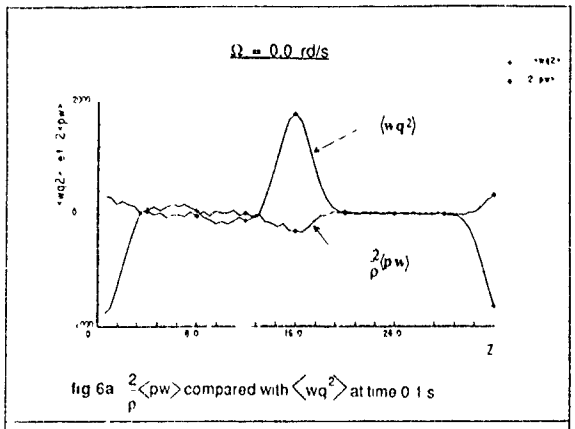

fig 6a $\frac{2}{\rho}\langle pw \rangle$ compared with $\langle wq^2 \rangle$ at time 0 1 s

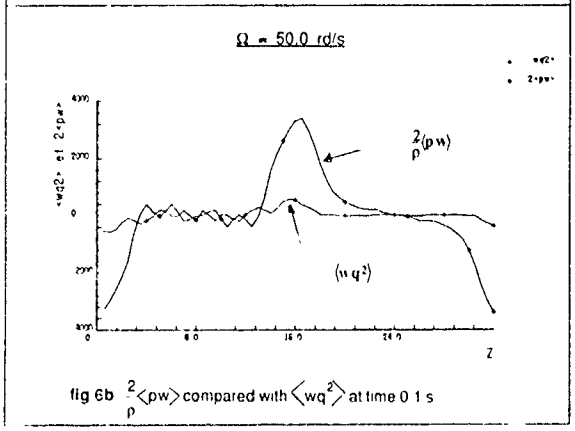

fig 6b $\frac{2}{\rho}\langle pw \rangle$ compared with $\langle wq^2 \rangle$ at time 0 1 s

Fig. 6 : Comparison of the different transport terms in the equation for twice the turbulent kinetic energy : triple correlation term : $\langle q^2 w \rangle$ and pressure term : $2/\rho \langle pw \rangle$. Results averaged over 3 realizations; time=0.1 s.

Fig. 6a : without rotation.
Fig. 6b : with rotation Ω = 50 rd/s (rotation switched on at time t=0.04 s).

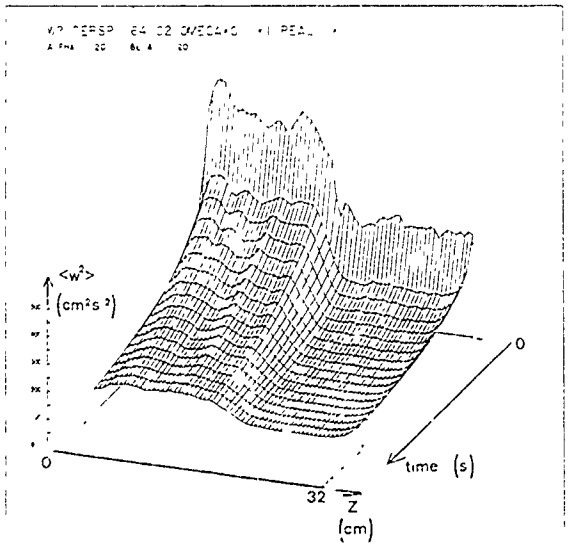

fig 7a

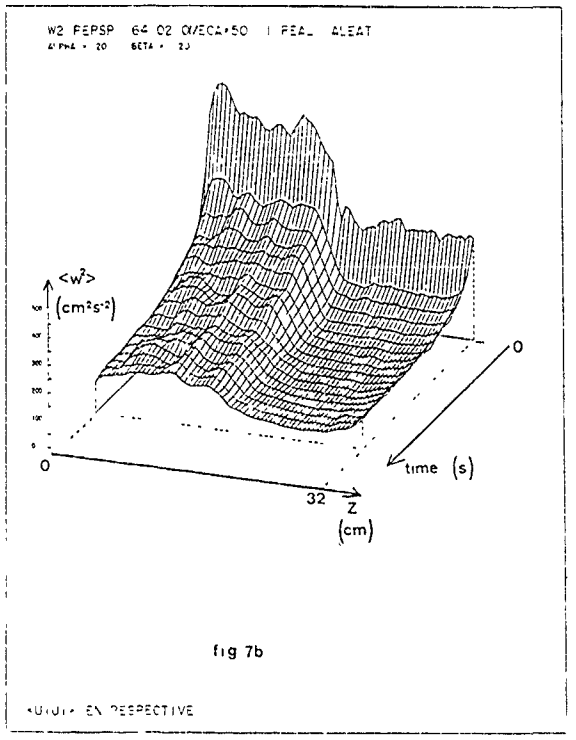

fig 7b

Fig. 7 : Evolution with time of $\langle w^2 \rangle$ profiles. Results corresponding to one realization only.

Fig. 7a : without rotation.
Fig. 7b : with rotation Ω = 50 rd/s (rotation switched on at time t=0.04 s).

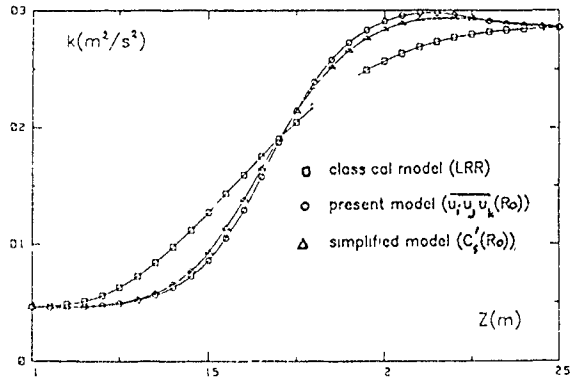

Fig. 8 : Results obtained using the improved one-point models : comparison between results obtained with the complete and simplified models, Ω=20π rd/s, initial profiles corresponding the V.W. experiment (perforated grid).

EIGHTH SYMPOSIUM ON
TURBULENT SHEAR FLOWS
Technical University of Munich
September 9-11, 1991

INTERMITTENCY AND CONCENTRATION PROBABILITY DISTRIBUTION IN TURBULENT SHEAR FLOWS

V.A.Sabelnikov
Central Aerohydrodynamic Institute
Zhukovsky-3, Moskow region, 140160 USSR

ABSTRACT

A self-similar solution of the equation for the concentration probability density function in free turbulent shear flows is investigated. This equation is obtained using the Kolmogorov-Obukhov hypothesis of a statistical independence of fine and large-scale motions in fully developed turbulent flows. The equation for the self-similar probability density function belongs to a new type of singular parabolic equations with an alternating coefficient for the derivative with respect to the time-like variable.

The regions of the sign constancy of the above coefficient are unlimited in the direction of the time-like variable and, hence, both directions of this variable are valid in one and the same extent. A correctly posed boundary-value problem is stated.

It is shown that from the resolvability condition of the boundary-value problem a number of relations between unknown functions entering into the closure hypotheses appear. A numerical solution of the formulated boundary-value problem is obtained.

INTRODUCTION

Many models of turbulent mixing in nonreacting and reacting flows are based upon conserved scalar probability density function [1]. The methods of derivation and closure for concentration probability density function equation are systematized in [1]. The goal of the present paper is to investigate the mathematical properties of the equation for concentration probability density function in free turbulent shear flows derived in [1], formulate the boundary value problem and to obtain a numerical solution.

MAIN EQUATION

The equation for concentration probability density function (PDF) in free turbulent shear flows is derived in [1]. This equation and boundary conditions have a form

$$\langle u\rangle\frac{\partial \gamma F}{\partial x} + \langle v\rangle\frac{\partial \gamma F}{\partial y} + \frac{1}{y^{\iota}}\frac{\partial y^{\iota}\langle v'\rangle_{\eta}\gamma F}{\partial y} = -\gamma\langle N\rangle_{\eta}\frac{\partial^2 F}{\partial \eta^2},$$

$$F(0;x,y) = 0, \quad F(1;x,y) = 0.$$

Here: x is the longitudinal coordinate, y - the transverse coordinate for plane flows and radial coordinate for axially symmetric flows; $\langle u\rangle$ and $\langle v\rangle$ are mean velocities; η - concentration of a passive contaminent ($0\le\eta\le1$); $F(\eta;x,y)$ - concentration PDF in the turbulent fluid, γ - intermittency factor, $\langle N\rangle_{\eta}$ - conditionally averaged scalar dissipation of concentration in the turbulent fluid, $\langle v'\rangle_{\eta}$ - conditionally averaged fluctuation velocity on the conditioned concentration; parameter ι is equal to 0 for the plane flows and to 1 for axisymmetric flows.

Here we will restrict ourselves in looking for the self-similar solutions of this equation for self-preserving turbulent jets or wakes. The equation for the self-similar concentration PDF $f(\zeta,\xi)$ can be written as

$$A\frac{\partial \gamma f}{\partial \xi} + B\gamma\frac{\partial f}{\partial \zeta} = \gamma\frac{\partial^2 f}{\partial \zeta^2} + C\gamma f, \qquad (1)$$

$$F(\eta;x,y) = \langle z\rangle_{\eta}^{-1} f(\zeta,\xi)$$

where $\xi=y/l(x)$, $\zeta=z/\langle z\rangle_{\eta}$; x is the longitudinal coordinate in the direction of flow, y is transverse for plane flows and radial coordinate for axially symmetric flows; $l(x)$ is a cross-stream scale of length, $l=x$ for a jet, $l=\sqrt{xd}$ for a wake; z is a concentration ($z>0$), $\langle z\rangle$ and $\langle z\rangle_{\eta}$ are unconditionally and conditionally averaged concentration in the turbulent fluid respectively, $\langle z\rangle=\gamma\langle z\rangle_{\eta}$, γ is intermittency factor.

The coefficients in (1) are described by the following expressions

$$A=\beta\xi^{-1}\Psi\, Z_{\eta}^{2}\, n_{\eta}^{-1}[1-h\mu^{-1}V], \qquad Z_{\eta}=\frac{Z}{\gamma} \qquad (2)$$

$$B=\beta\xi^{-1}\left(-\frac{\partial\Psi}{\partial\xi}Z_{\eta} - \Psi\frac{\partial Z}{\partial\xi}t\right)[1-h\mu^{-1}V]\, Z_{\eta}n_{\eta}^{-1}\zeta$$

$$C=-B\zeta^{-1}+ Z_{\eta}^{2}n_{\eta}^{-1}\left(\xi^{-1}\frac{\partial\xi^{\iota}W}{\partial\xi} - \zeta\frac{\partial Z}{\partial\xi}t\, Z_{\eta}^{-1}\frac{\partial W}{\partial\zeta}\right)$$

Here

$$W = \beta\xi^{-1}\Psi h\mu^{-1}V, \quad h = \frac{Z}{\Sigma} = \sqrt{\frac{\gamma}{1-\gamma}},$$

$$I_k = \int_0^\infty \zeta^k f d\zeta .$$

$$V = V_o + s\,(1 + \omega^2 s^2)^{-1/2},$$

$$s = h\,(\zeta - \gamma)\,\gamma^{-1} \qquad (3)$$

$$V_o = (1-\gamma)\,h\,(1+\omega^2 h^2)^{-1/2} - \gamma \int_0^\infty s\,(1+\omega^2 s^2)^{-1/2} f d\zeta$$

$$\mu = (1-\gamma)\,h^2(1+\omega^2 h^2)^{-1/2} + \gamma \int_0^\infty s^2(1+\omega^2 s^2)^{-1/2} f d\zeta$$

$\Psi(\xi)$ is the cross-stream profile of the self-similar stream function for a jets, $\Psi(\xi)=\xi$ - for a wake; $n_c(\xi)$ is the cross-stream profile of the self-similar scalar dissipation of concentration in the turbulent fluid, $Z(\xi)$ and $Z_c(\xi)$ are the cross-stream profiles of the self-similar unconditionally and conditionally averaged concentration respectively, $\Sigma(\xi)$ is the cross-stream profile of the self-similar root-mean-square concentration fluctuation; parameter i is equal to 0 for the plane jet/wake and 1 for axisymmetric jet, $\beta=\frac{1+i}{2}$. Note that the functions Ψ, n_c and Z are assumed to be specified (e.g., from experimental data).

The self-similar PDF f must satisfy to the condition of normalization

$$I_o = \int_0^\infty f d\zeta = 1 \qquad (4)$$

and the following boundary condition with respect to ζ:

$$f(0,\xi) = 0; \quad \lim_{\zeta\to\infty} \zeta^k f = 0 \qquad (5)$$

where k is an arbitrary positive number. The first boundary condition in (5) is a consequence of using the Kolmogorov-Obukhov hypothesis of a statistical independence of fine and large-scale motions in fully developed turbulent flows [1].

GENERAL PROPERTIES OF THE EQUATION FOR THE SELF-SIMULAR PROBLEM

If we disregard the fact that the unknown function f enters into coefficients A,B.C (i.e. the problem is nonlinear), then (1) is a parabolic equation. Variable ξ in this case plays the role of time-like variable. It is known from the theory of standard parabolic equations that Cauchy problem is applicable to them, i.e., the initial conditions are given for one value of the time-like variable.

The problem under consideration is essentially different from the classical case as a consequence of the special properties of the coefficient of the derivative with respect to the time-like variable. Part of these properties is caused by the symmetry of the problem. First of all we have A=0 and $\frac{\partial f}{\partial \xi}=0$ when $\xi=0$. Thereby, equation (1) on this line degenerates into an ordinary differential equation. Further it can be shown that $A \sim \xi$ when ξ is small. Therefore, equation (1) is satisfied by solutions of type $\xi^k g(\zeta)$, where k is the arbitrary number, g is some function. With the exception of case k=0, such solutions are physically meaningless. Thus, line $\xi=0$ is singular. Since integral $\int_0^\xi A^{-1} d\xi$ is divergent, this singularity cannot be eliminated by transforming the variable ξ. Thus, PDF on line $\xi=0$ cannot be specified arbitrarily.

An analogous situation also arises on line $\xi=\infty$. Based on the experimental data (see a review of this data in [1]), it is natural to assume that when $\xi\to\infty$ all dimensionless combinations of the conditionally averaged moments in the turbulent fluid tend to finite values. It is possible only when function f has a finite limit when $\xi\to\infty$, i.e.

$$\lim_{\xi\to\infty} f(\zeta,\xi) = f_\infty(\zeta). \qquad (6)$$

The coefficients in (1) must have such a form so that it would degenerate into an ordinary differential equation when $\xi=\infty$. Function f_∞ is determined from this equation. Hence, just as on line $\xi=0$, PDF on line $\xi=\infty$ cannot be specified arbitrarily. Thus, line $\xi=\infty$ is also singular and this singularity is nonremovable. This conclusion formally results from the integral $\int_\xi^\infty A^{-1} d\xi$ being diver-

gent.

In addition to the above mentioned properties, coefficient A in (1) possesses one more very nontrivial feature. It is connected with the geometry of the regions of sign constancy. It follows from the above expressions (2) and (3) for A that these regions are described by the inequalities [1]:

$$A > 0 \text{ at } 0 < \zeta < \zeta_o(\xi),\ 0 < \xi < \infty$$
$$A < 0 \text{ at } \zeta_o < \zeta < \infty,\ 0 < \xi < \infty \qquad (7)$$
$$A = 0 \text{ at } \xi = 0,\ \xi = \infty,\ \zeta = \zeta_o(\xi).$$

The function $\zeta_o(\xi)$ is limited as $\xi \to \infty$, i.e. $\lim_{\xi\to\infty} \zeta_o(\xi) = \text{const}$.

Note that line $\zeta_o(\xi)$ on which coefficient of the derivative with respect to ξ vanishes is not known a priori. Thus, the region of constant sign of A is unlimited in the direction of ξ.

It can be concluded that both directions of the time-like variable ξ for the parabolic equation (1) are valid in one and the same extent. Thus, apparently, for this equation the boundary-value problem must be set not only with respect to variable ζ, but also with respect to variable ξ, i.e. two "initial" conditions must be specified, one for $\xi=0$ and another for $\xi=\infty$.

The exposed property of coefficient A and the presence of the singular lines $\xi=0$ and $\xi=\infty$ indicate that equation (1) possesses essentially nonlocal properties. Let us consider this aspect in more details. Consider for the sake of definiteness a small neighborhood of the singular line $\xi=0$.

In the vicinity of line $\xi=0$ a Taylor series can be constructed with respect to ξ for the required solution $f(\zeta,\xi)$. The coefficients of this series are dependent on variable ζ and satisfy the ordinary differential equations. However, such a solution will not generally satisfy condition (6) and will be singular in the vicinity of line $\xi=\infty$. Hence, it follows that condition (6) is satisfied only for a specific connection between the coefficients in equation (1). Such a connection can be obtained from the solution of the boundary-value problem with respect to ξ and, hence, is of nonlocal character.

Besides this connection, another one exists between coefficients in (1). It follows from the condition of normalization (4) of function $f(\zeta,\xi)$ and has the form of integral equation $I_o=1$ and is, hence, also of nonlocal character.

The conditions of symmetry and the analysis of the results conducted above lead to the following statement of the boundary-value problem. In the region $0 \le \xi < \infty$, $0 < \zeta < \infty$ a nonnegative function $f(\zeta,\xi)$ is sought which satisfies equation (1) and the conditions

$$f(0,\xi)=0, \qquad \lim_{\zeta\to\infty} \zeta^k f = 0$$
$$\frac{\partial^{2i+1} f(\zeta,0)}{\partial \zeta^{2i+1}} = 0, \quad i = 0,1,2, \ldots \qquad (8)$$
$$\lim_{\xi\to\infty} f(\zeta,\xi) = f_\infty(\zeta), \qquad I_o = \int_o^\infty f d\zeta = 1$$

The coefficients of equation (1) include unknown functions of one variable ξ - intermittency factor $\gamma(\xi)$ and function $\omega(\xi)$ which characterizes the process of turbulent diffusion [1]. This two functions are found from two connections mentioned above.

We should particularly note the essential role played by the requirement of nonnegativity of f in the condition of resolvability of the boundary problem. In order to understand the qualitative structure of the solution let us analyze the solution on the singular lines $\xi=0$ and $\xi=\infty$.

SOLUTION ON THE SINGULAR LINE $\xi=0$.

Since A=0 when $\xi=0$, we obtain from (1)

$$f'' + a_1 \zeta f' + a_1 (1+h\mu^{-1}V) f = 0, \qquad (9)$$

where $a_1 = \frac{h^2}{\gamma m}$, $m = \frac{\gamma n_\xi}{\beta u \Sigma^2}$, $u = \xi^{-1} \frac{\partial \Psi}{\partial \xi}$ for a jet,

$$m = \frac{2\gamma n_\xi}{\Sigma^2} \text{ for a wake,}$$

the prime in (9) denotes differentiation with respect to ζ.

Let us elucidate the physical meaning of parameters m and h. Parameter m, as can be established from the equation for the variance of concentration fluctuations, is equal to the ratio of twice the scalar dissipation to the absolute value of advection. Experimental data indicate that $1<m<2.6$ in flows under consideration (see a review in [1]). Parameter h is inversely proportional to the intensity of concentration fluctuation. According to the experimental data it acquires considerable large values h=4-5.

Let us first point out the general pro-

perties of the solution of (9). Among these properties, the most significant is that the nontrivial solution of equation (9) exists upon fulfilling of strict inequality $\gamma<1$. This conclusion follows from the relation which is obtained if (9) is multiplied by ζ, integrating for ζ from 0 to ∞, and use is made of the normalization condition (4)

$$f'(0) = a_1 h\mu^{-1}[\int_0^\infty s(1+\omega^2 s^2)^{-1/2} f d\zeta + h(1+\omega^2 h^2)^{-1/2}] (1-\gamma) . \quad (10)$$

Hence, it is obvious that $f'(0)=0$ when $\gamma=1$. Since $f(0)=0$, the trivial solution exists only when $\gamma=1$. Let us find the number of parameters which this solution is dependent on. We use the following reasoning for this purpose. We assume that the values of quantities ω, h, γ, μ and V_0 appearing in the coefficients of (9) are totally arbitrary and, hence, (9) is a linear differential equation. It is easy to establish that one of the linearly independent solutions of this equation diminishes exponentially when $\zeta\to\infty$, and another diminishes in an algebraic manner. Consequently, the second boundary condition in (5) is nontrivial, and the boundary-value problem is resolvable for specific values of ω. The condition of non-negativity of function f will be fulfilled only for one of these values. The value of ω thus found and $f(\zeta,0)$ contains the unknown h, γ, μ and V_0 as parameters. Since for specified h, γ, μ and V_0 (9) is linear and boundary conditions (5) are homogeneous, $f(\zeta,0)$ is determined with an arbitrary multiplier. We now take into consideration that f must be normalized, and the integrals of f enter into the expressions for quantities μ, V_0, h. Thus, there is the system of four nonlinear equations for five variables μ, V_0, h, γ and the above mentioned arbitrary multiplier. Thus, the solution of equation (9) is found with one arbitrary parameter.

Let us find the asymptotic solution of (9) outside the small neighborhood of $\zeta=0$ and $\zeta=\infty$ when $h\to\infty$. It can be shown that the difference $(1-\gamma)$ is exponentially small when $h\to\infty$ (see relation (13)). Hence, when determining the asymptotic behavior of the coefficients of equation (9), it can be assumed that $\gamma=1$. We will look for the solution in the form of asymptotic series

$$g(s) = g^{(0)} + h^{-1}g^{(1)} + h^{-2}g^{(2)} + \ldots$$
$$\omega = h^{-1}\Omega_1 + h^{-3}\Omega_3 + \ldots \quad (11)$$

where $g(s)=h^{-1}f(\zeta)$, $s=h(\zeta-1)$.

Substituting (11) into (9) and equating the coefficients for the successive exponents of h to zero yield a reccurent system of equations for function $g^{(k)}$. Solving this system we obtain that the function $g^{(0)}$ is described by a Gaussian curve. Thus the concentration PDF on the axis or in the plane of symmetry is close to normal distribution. This result agrees well with the experimental data, a comprehensive review of which is given in [1]. The deviations from the normal distribution are described by functions $g^{(1)}, g^{(2)}, \ldots$ in (11). The skewness A and kurtosis E of the PDF have the form

$$A=\int s^3 g ds = h^{-1}\int s^3 g^{(1)} ds = 2(1-m)h^{-1}$$
$$F=\int s^4 g ds - 3 = h^{-2}\int s^4 g^{(2)} ds \quad (12)$$
$$= [6(1-m)+\frac{15}{9}\Omega_1^2]h^{-2}$$

The values of Ω_1 and Ω_3 are the functions of m, which are found from consideration of the uniform asymptotic solution of (9) on the entire semi-axis $\zeta>0$ [1]. Note that from this asymptotic solution the relationship between intermittency factor γ and parameter h can be obtained as follows

$$1-\gamma = \frac{m^{1/4}(1+\Omega^2)^{3/8}}{h\,\pi^{1/2}} \exp[-h^2(S_1 - \frac{1}{4m}) - S_2] \quad (13)$$

where S_1 and S_2 are some functions of m; expressions for S_1 and S_2 are given in [1].

It is follows from (13) that the difference $(1-\gamma)$ is exponentially small when $h\to\infty$. Thereby, the assumption made when obtaining the asymptotic expansion (11) has been proved.

Let us compare the theoretical and experimental values of the skewness and kurtosis. Measurements of A and E in a wake were conducted in [2]. Obtained in these tests were the values $A=-0.4$, $E=0.1$, $h=4.75$. The parameter $m=2.6$ in a wake [3]. From (12) and (13) we obtain $A=-0.5$, $E=0.13$, $(1-\gamma)\approx 10^{-3}$. It can be concluded that the calculated values of A and E agree well with measurements [2]. Direct comparison of the calculated and measured values of intermittency factor is not possible, since this quantity has not yet been measured with the required

accuracy.

SOLUTION ON THE SINGULAR LINE $\xi=\infty$.

Assumption (6) lies at the basis of the investigation. It may be shown [1] that the equation for the function $f_\infty(\zeta)$ has the form

$$f''_\infty + [a-b\zeta(1+\omega_\infty^2\zeta^2)^{-1/2}]f_\infty = 0, \quad b=\frac{d}{1-\mu} \qquad (14)$$

where a is a positive constant, ω_∞ is constant in the asymptotic behavior of function ω when $\xi\to\infty$.

Simple analysis shows that one of the linearly independent solutions of equation (14) increases exponentially when $\zeta\to\infty$ and, hence, does not satisfy the boundary condition (5)when $\zeta=\infty$. Therefore, if the value of parameter ω_∞ is specified, then the solution of the boundary-value problem (14), (5) exists only for specific values of constant a. The condition of non-negativity of f_∞ can by satisfied at one of these values.

The solution of (14) is obtained numerically. It is shown that the function f_∞ differs noticeably from a normal distribution. The calculated values of skewness and kurtosis in the turbulent fluid are equal to $A_+=0,802$ and $F_+=0,694$ respectively for $\omega_\infty=0$.

NUMERICAL SOLUTION

The main property of the parabolic equation (1), as shown above, is that both directions along the time-like variable ξ are valid in one and the same extent. Therefore, the main requirement of the numerical method which is intended for the solution of the formulated boundary value problem is for the finite difference algorithm to be correctly reflecting this circumstance. Let us briefly explain the idea of the method. The derivative with respect to the time-like variable ξ is replaced by the following difference operator: when A>0 the backward differences are used, and when A<0 the forward differences are used. The first and the second derivatives with respect to ζ are replaced by conventional central-difference operators. The integrals of function f appearing in formulae for Σ, V_o and μ (2), are obtained by the trapezoid rule. The algorithm is first order accurate in the ξ-direction and the second order accurate in the ζ-direction.

In the calculation, instead of the infinite region $0\le\xi<\infty$, $0\le\zeta<\infty$ the rectangle $0\le\xi<\xi_{max}$, $0\le\zeta<\zeta_{max}$ is considered, i.e. boundary conditions at $\xi=\infty$ and $\zeta=\infty$ in (8) are transferred to lines $\xi=\xi_{max}$ and $\zeta=\zeta_{max}$ respectively.

The nonlinear system of finite-difference equations are solved by the standard relaxation method commonly applied to the solution of elliptical equations.The convergence criterion is applied to the ratio defined by $\varepsilon_{i,j}=|f_{i,j}^{(k+1)}-f_{i,j}^{(k)}| \,/\, f_{i,j}^{(k)}$

Iterations are stopping when $\sup(\varepsilon_{i,j})$ is less than a preset small value (equal to 10^{-m}).

It follows from the calculation that the concentration PDF differs a little from the normal distribution in the entire region where the intermittency factor is closed to 1. This conclusion agrees well with the data of measurements of the skewness and kurtosis. It is also supported by direct measurements of the PDF.

The calculated results also enable to conclude that the transformation of PDF into the asymptotic function $f_\infty(\zeta)$ occurs in a fairly narrow region.

CONCLUSIONS

A theory for the PDF of concentration of the dynamically passive contaminant in free turbulent shear flows is developed. A hypothesis of a statistical independence of macro- and microcharacteristics in turbulent flows underlies this this theory. This hypothesis is a central one in the theory of small-scale turbulence, proposed by Kolmogorov and Obukhov.

It is found that the solution of the equation for the concentration PDF which is closed using the above hypothesis is in good agreement with experimental data.

It follows from the hypothesis of a statistical independence of the macro- and microcharacteristics that at all turbulent flows the intermittency coefficient is rigorously less than a unity. It is found that the intermittency determines the structure of solution of the equation for the PDF in all flow regions, also including those where it was considered traditionally to be as unessential.

Mathematical properties of the equation for the concentration PDF are investigated, and it is shown that a number of relations between a priori unknown functions that ap-

pear when the closure hypotheses are formulated follows from the resolvability condition of the boundary-value problem. Using numerical calculations it is found that in free turbulent flows, in full compliance with experimental data, the concentration PDF is of a sufficiently general character: in those regions where the intermittency is small it is close to a normal one, while on the edge of the flow where the intermittency is significant it differs noticeably from a normal distribution but it is also universal and is governed by a single parameter, viz. a conditionally averaged concentration in the fully turbulent fluid. The region's width where occurs a PDF reconstruction from one universal kind to another is rather small.

REFERENCES

1. Kuznetsov V.R. & Sabelnikov V.A. Turbulence and Combustion. Hemisphere. New York, Washington et al..

2. La Rue J.C. & Libby P.A. 1974. Temperature fluctuations in the plane turbulent wake. Phys. Fluids, vol. 17, N 11, pp 1956-1967.

3. Freymuth P. & Uberoi M.S. 1971. Structure of temperature fluctuations in the turbulent wake behind heated cylinder. Phys. Fluids, vol. 14, N 12, pp 2574-2580.

EIGHTH SYMPOSIUM ON
TURBULENT SHEAR FLOWS
Technical University of Munich
September 9-11, 1991

APPLICATION OF PDF METHODS TO PILOTED DIFFUSION FLAMES: SENSITIVITY TO MODEL PARAMETERS

A.T.Norris and S.B.Pope

Sibley School of Mechanical and Aerospace Engineering
Cornell University, Ithaca, New York 14853.

ABSTRACT

The sensitivity of the velocity-dissipation-scalar joint pdf (probability density function) model to variations of model constants and initial conditions is investigated. Using the model problem of a piloted non-premixed turbulent methane flame, a reference solution is obtained, and shown to be numerically accurate. The initial conditions and model constants are then varied, and the solutions of these altered models are compared to the reference solution. It is found that the velocity-dissipation-scalar jpdf model is relatively insensitive to initial conditions, but somewhat more sensitive to variations in the model constants. A comparison of model results to experimental data shows reasonable agreement, however there is some uncertainty about the most appropriate form of the modeled source of dissipation.

INTRODUCTION

Pdf (probability density function) methods have proved particularly suitable in addressing turbulent combustion problems, as the important processes of convection and reaction are treated exactly. One area of current work with these models is the problem of non-premixed turbulent diffusion flames exhibiting local extinction. Comprehensive experimental data have been obtained by Masri and Bilger (1986) and Masri, Bilger and Dibble (1988a,b,c) for such a flow, allowing the effectiveness of different computational schemes to be evaluated.

Chen, Kollmann and Dibble (1989) used a hybrid pdf-moment closure scheme with finite rate chemistry to investigate this problem. In their model, only the scalar pdf is solved for, velocity being computed by a moment closure scheme. Masri and Pope (1990) studied the same problem, but solved the transport equation for the jpdf of velocity and composition, using equilibrium thermochemistry. However a deficiency of this method is that the model contains no time or length scale information that can be used in the modeling of processes such as molecular diffusion and dissipation. To remedy this defect, Pope and Chen (1990) developed a model based on the joint pdf of velocity, dissipation and scalars. By including dissipation in the model, there is now a length scale, $k^{3/2}/\langle\epsilon\rangle$ and a time scale $k/\langle\epsilon\rangle$, where k is the turbulent kinetic energy and $\langle\epsilon\rangle$ is the mean dissipation rate. This model has been extended to inhomogeneous flows by Pope (1991a).

The purpose of this paper is to apply the velocity-dissipation-scalar pdf model to the problem of the piloted methane flame and to investigate the sensitivity of the model to changes in initial conditions and model constants. This provides a useful guide to future model refinement and indicates that this scheme is suitable for application to the piloted jet flame problem.

To achieve the objective we first establish a reference solution using simple modeling assumptions and model constants taken from Pope (1991a) Then model constants and initial conditions are systematically varied and the solution of the adjusted model is compared to the reference solution. During this process, no attempt is made to fit the solution to the experimental data. Due to many simplifying assumptions adopted for this particular problem, we do not expect close agreement with experimental data.

VELOCITY-DISSIPATION-SCALAR MODEL

In this section we present an outline of the velocity-dissipation-scalar model. For a more comprehensive description, we refer the reader to Pope (1985), Pope and Chen (1990) and Pope (1991a,b).

Due to the variable density in the flame, it is convenient to consider density-weighted mean quantities. Such quantities are denoted by a tilde or a subscript ρ. For example the density-weighted mean axial velocity is calculated as $\tilde{U} = \langle U \rangle_\rho = \langle U\rho \rangle / \langle \rho \rangle$, where ρ is the density and $\langle\ \rangle$ is used to denote a mean quantity.

The derivation of the jpdf transport equation is obtained from stochastic models of velocity and dissipation, viewed in a Lagrangian reference frame. These Lagrangian quantities are denoted by an asterisk, so the Lagrangian velocity and dissipation are denoted by U_i^* and ϵ^* respectively.

We define the relaxation rate ω as

$$\omega = \epsilon/\hat{k}, \tag{1}$$

where ϵ is the dissipation and k is the turbulent kinetic energy. The hat is used to denote a ρ and ω weighted mean, for example $\hat{k} = \frac{1}{2}\langle u_i u_i \omega\rho\rangle/\langle\omega\rho\rangle$, where $u_i = U_i - \tilde{U}_i$. This quantity can also be denoted by a subscript $\rho\omega$: i.e. $\langle k\rangle_{\rho\omega}$. The use of $\hat{k}$ rather than $\tilde{k}$ is to improve the model performance in regions of intermittent turbulence and is discussed by Pope (1991a).

On dimensional grounds, it is more convenient to solve for ω rather than ϵ (Pope 1991a) and thus the evolution of the Lagrangian quantity ω^* is modeled as

$$\begin{aligned} d\omega^* &= -\omega^*\tilde{\omega}dt(S_\omega + C_\chi\Omega) + \tilde{\omega}^2 h dt \\ &\quad + \omega^*(2C_\chi\tilde{\omega}\sigma^2)^{1/2}dW, \end{aligned} \tag{2}$$

where

$$\Omega = \ln(\frac{\omega^*}{\tilde{\omega}}) - \langle\frac{\omega}{\tilde{\omega}}\ln(\frac{\omega}{\tilde{\omega}})\rangle_\rho. \tag{3}$$

In the first term of Eq.(2), Pope (1991a) gives $C_\chi = 1.6$ and $S_\omega = C_{\omega 1}S_{ij}S_{ij}/\tilde{\omega}^2 - C_{\omega 2}$, where S_{ij} is the mean rate of strain, $C_{\omega 1} = 0.04$ and $C_{\omega 2} = 0.9$. In the second term, h is defined as

$$\begin{aligned} h &= C_{\omega 3}(1 - \mu_{1/2}/\mu_{1/2G})^2, \quad \mu_{1/2} \le \mu_{1/2G} \\ h &= 0, \qquad\qquad\quad \mu_{1/2} > \mu_{1/2G}, \end{aligned} \tag{4}$$

where $\mu_{1/2} = \langle\omega^{1/2}\rangle_\rho/\langle\omega\rangle_\rho^{1/2}$, $\mu_{1/2G} = \exp(-\sigma^2/8)$, $\sigma^2 = 1.0$ and $C_{\omega 3} = 1.0$. In the third term, dW is a Wiener process, with the properties $\langle dW\rangle = 0$ and $\langle dW dW\rangle = dt$.

The stochastic model for the velocity following a fluid particle is

$$du_i^* = -\frac{1}{\rho}\frac{\partial\langle p\rangle}{\partial x_i}dt + D_i dt + (C_0\hat{k}\tilde{\omega}^*)^{1/2}dW_i, \tag{5}$$

where

$$\begin{aligned} D_i &= -(\frac{1}{2} + \frac{3}{4}C_0)\tilde{\omega}(\frac{\hat{k}}{\tilde{k}})u_i^* + G_{ij}^a u_i^* \\ &\quad -\frac{3}{4}C_0\{(\frac{\hat{k}}{\tilde{k}})\hat{A}_{ij}^{-1}(\omega^* u_j^* - \langle\omega u_j\rangle_\rho) - \tilde{A}_{ij}^{-1}\tilde{\omega}u_j^*\}; \end{aligned} \tag{6}$$

$u_i^* = U_i^* - \tilde{U}_i$; A_{ij} is the normalized Reynolds stress tensor,

$$A_{ij} = 3\langle u_i u_j\rangle/\langle u_l u_l\rangle; \tag{7}$$

and $\tilde{A}_{ij}$ and $\hat{A}_{ij}$ are the ρ and $\rho\omega$ weighted conterparts of A_{ij}. The constant C_0 is given as 3.5, and we set $G_{ij}^a = 0$ as in Pope(1991a). The dW_i term is an isotropic Wiener process, independent of that in Eq.(2).

A stochastic model for a passive scalar is also needed. We adopt the simple relaxation model of Dopazo (1975) which gives the evolution of a scalar ξ as

$$\frac{d\xi^*}{dt} = -\frac{1}{2}C_\xi\tilde{\omega}(\xi^* - \tilde{\xi}), \tag{8}$$

where $C_\xi = 2.0$.

We now write the evolution equation for the density-weighted, one point Eulerian jpdf of U_i, ω and ξ , $\tilde{f}$, corresponding to the stochastic models of ω Eq.(2), U_i Eq.(5) and ξ Eq.(8). With V_i, θ and ψ being the sample space variables corresponding to U_i, ω and ξ respectively, standard techniques (Pope 1985) give

$$\begin{aligned} \frac{\partial\tilde{f}}{\partial t} &= -V_i\frac{\partial\tilde{f}}{\partial x_i} + \frac{1}{\rho}\frac{\partial\langle p\rangle}{\partial x_i}\frac{\partial\tilde{f}}{\partial V_i} - \frac{\partial}{\partial V_i}(\tilde{f}D_i(v_i)) \\ &\quad + \frac{1}{2}C_0\hat{k}\theta\frac{\partial^2\tilde{f}}{\partial V_i\partial V_i} + \tilde{\omega}\frac{\partial}{\partial\theta}\{\tilde{f}\theta(S_\omega + C_\chi\Omega(\theta))\} \\ &\quad - \tilde{\omega}^2 h\frac{\partial\tilde{f}}{\partial\theta} + C_\chi\tilde{\omega}\sigma^2\frac{\partial^2}{\partial\theta^2}(\tilde{f}\theta) \\ &\quad + \frac{1}{2}C_\xi\tilde{\omega}\frac{\partial}{\partial\psi}[\tilde{f}(\psi - \tilde{\xi})], \end{aligned} \tag{9}$$

where $D_i(v_i)$ is Eq.(6) with u_i^* replaced by $v_i^* = V_i - \tilde{U}_i$ and $\Omega(\theta)$ is Eq.(3) with ω^* replaced by θ.

MODEL PROBLEM

The model problem used in this paper is the piloted methane flame of Masri and Bilger (1986). It consists of a central jet of methane, radius R = 3.6mm, surrounded by an annular pilot flame, width 5.4mm, of stoichiometric composition. This flame is situated in a uniform coflow of air. The flow velocities chosen are 27.0 m/s bulk flow for the methane jet, 24.0 m/s for the pilot and 15.0 m/s for the coflow. These correspond to the K flame in Masri and Bilger (1986). This set of flow conditions is chosen as it shows the least local extinction, and so an equilibrium assumption for the thermochemistry can be justified. With such an assumption, all thermochemical quantities can be represented by functions of ξ. Density, ρ, is given as a piecewise function of ξ,

$$\frac{1}{\rho} = \frac{\xi}{\xi_s}\left(\frac{1}{\rho_s} - \frac{1}{\rho_j}\right) + \frac{1}{\rho_j}, \quad \xi \le \xi_s \tag{10}$$

$$\frac{1}{\rho} = \frac{1-\xi}{1-\xi_s}\left(\frac{1}{\rho_s} - \frac{1}{\rho_c}\right) + \frac{1}{\rho_c}, \quad \xi > \xi_s \tag{11}$$

where $\rho_j = 0.65$, $\rho_s = 0.14$ and $\rho_c = 1.20$, referring to the jet, stoichiometric and coflow initial densities respectively. ξ_s is the stoichiometric mixture fraction and is given the value of 0.055, corresponding to that of methane.

SOLUTION PROCEDURE

We assume that the flow is statistically axisymmetric and stationary, allowing us to solve Eq.(9) by a parabolic Monte Carlo scheme, which marches in the axial (x) direction. At each axial station, $\tilde{f}$ is represented by a large number of fluid particles, with each particle having a radial position, (r), a velocity vector, dissipation and scalar value. The number of fluid particles, N is taken to be 80,000 to yield small statistical error, while still providing reasonable CPU times. The width of the solution domain expands to encompass the evolving radial profiles, and the length is restricted to 100 jet radii

from the jet exit. Profiles of mean quantities are obtained by the method of cross-validated least squares cubic splines (Pope and Gadh 1988). Forty eight equidistant basis functions are used to represent these splines. A variable step size, based on the profile spreading rate is used, and the scheme takes approximately 150 steps to reach x/R = 100. Computations were performed on an IBM 3090S, with each run taking approximately 20 minutes CPU time.

INITIAL AND BOUNDARY CONDITIONS

At the jet exit plane, mean profiles of velocity and mixture fraction are specified, in the same manner as those for the K flame in Masri and Pope (1990). The rms velocity profiles however, differ slightly from those of Masri and Pope (1990), being exponential fits to data from Hinze (1975) for turbulent pipe flow and boundary layers. The covariance $\langle uv \rangle$ is given by $\langle uv \rangle = C_{uv}(\langle u^2 \rangle \langle v^2 \rangle)^{1/2}$, with the constant $C_{uv} = 0.4$, as suggested by Tennekes and Lumley(1972). Mixture fraction ξ is given as 1.0 in the methane jet, $\xi_s = 0.055$ in the pilot and 0.0 in the coflow.

We assume here, as in Masri and Pope(1990), that the mean turbulent frequency $\tilde{\omega}$ is initialy uniform across the center of the flow and we adopt the value of $\tilde{\omega} = 8.0$ for the jet and pilot flow, consistent with the value used by Masri and Pope(1990). However we expect that at a large radial distance from the axis of the jet, the value of $\tilde{\omega}$ will be zero, corresponding to non-turbulent flow. Calculating $\tilde{\omega}$ from the dissipation and kinetic energy profiles of the boundary layer, given in Hinze(1975), results in a profile that decays as the distance from the surface increases. This profile is used for the $\tilde{\omega}$ profile in the coflow.

The distribution of $\omega/\tilde{\omega}$ is lognormal, with the variance of $ln(\omega/\tilde{\omega})$ being unity (consistent with $\sigma^2 = 1.0$).

Figures 1 and 2 show the initial profiles used in the calculations. Boundary conditions are implied by the the coflow profiles. For $r/R > 7$, the turbulent flow quantities are approximately zero, with other quantities approximately constant.

STANDARD RESULT

In this section, we present a standard solution that is compared to other solutions in which the model constants or initial conditions have been varied. We also estimate the accuracy of the solution.

Taking the model constants as given by Pope (1990a) and initial conditions as described above, we performed M = 10 runs, identical except for the random number sequence. From these runs we evaluate a set of mean profiles, $\langle p(r) \rangle$, given by

$$\langle p(r) \rangle = \frac{1}{M} \sum_{i=1}^{M} p_i(r), \qquad (12)$$

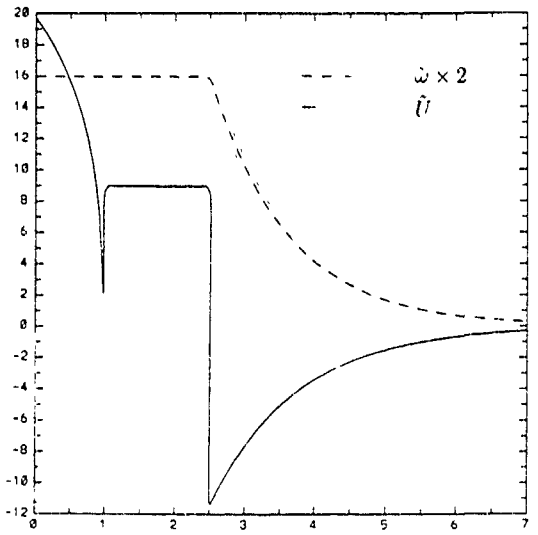

Figure 1. Initial profiles of $\tilde{U}$, and $\tilde{\omega}$

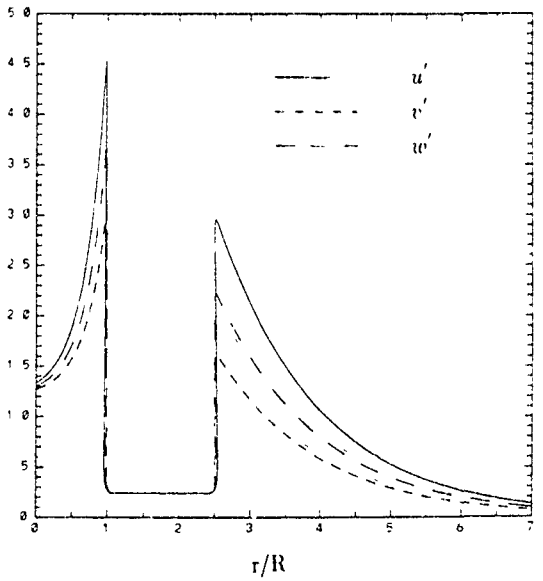

Figure 2 Initial profiles of u', v' and w'

where $p_i(r)$ is the i-th sample profile at radial position r. The 99 percent confidence interval for these profiles can be approximated by

$$\varepsilon = 3[\frac{1}{M-1} \sum_{i=1}^{M} (p_i(r) - \langle p(r) \rangle)^2]^{1/2}. \qquad (13)$$

Figure 3 shows the crossflow profiles at x/R = 100 of: the mean axial velocity, $\tilde{U}$; the mean relaxation rate $\tilde{\omega}$ and the rms of the fluctuating axial velocity, denoted as $u' = \langle u^2 \rangle_\rho^{1/2}$. Figure 4. shows the mean scalar profile $\tilde{\xi}$ and the rms of the scalar component, denoted as ξ' at the same streamwise location.

The size of the error bars in both Figs 3 and 4 shows that an accurate solution is being obtained, even for the higher order moments. The experimental data of Masri and Bilger (1986) is also included as a comparison. A discussion of the

comparison between experimental and calculated profiles is deferred to the end of this paper

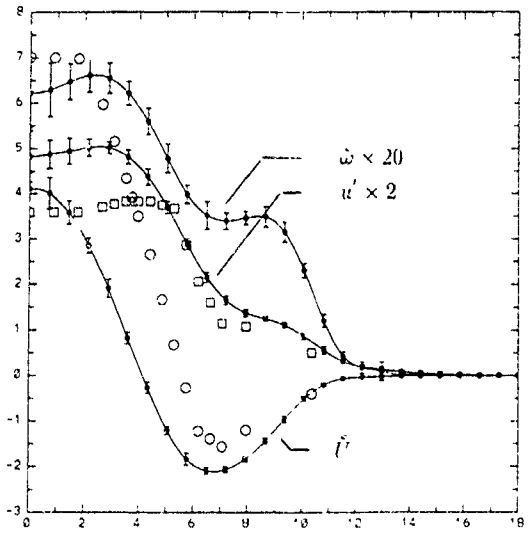

Figure 3. Standard profiles of $\tilde{U}$, u' and $\tilde{\omega}$. Open symbols are experimental data of Masri and Bilger (1986).

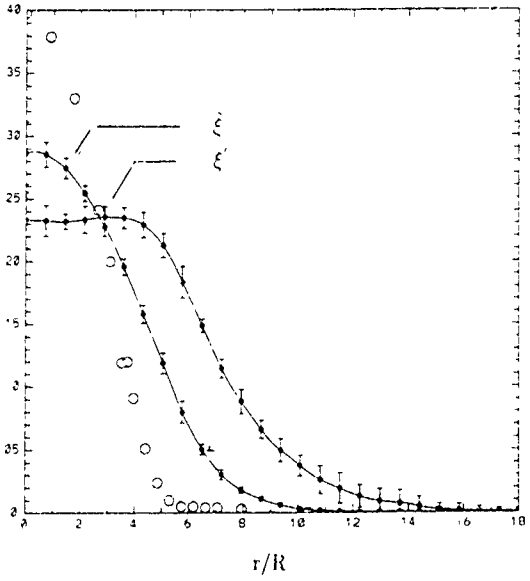

Figure 4. Standard profiles of $\tilde{\xi}$ and ξ' Open symbols are experimental data of Masri and Bilger (1986)

VARIATION OF MODEL CONSTANTS

The first constant varied is the mixing model parameter C_ξ. Figure 5 shows the ξ and ξ' profiles at x/R = 100 for C_ξ = 1 and 4. It is seen that an increase in C_ξ results in an increase in the $\tilde{\xi}$ profile, while the corresponding ξ' profile decreases. The effect on the $\tilde{U}$, u' and $\tilde{\omega}$ profiles is negligible.

Next we vary C_0 and C_χ. Pope and Chen (1990) showed that these two constants are approximately linearly dependent for a fixed value of σ^2 and integral time scale ratio of velocity and ln ω. We use two values for these constants, C_0 = 2.0 and 5.0, corresponding to C_χ = 1.0 and 2.2 respectively. In Fig. 6 we show the mean $\tilde{U}$ and $\tilde{\xi}$ profiles at x/R = 100, as well as the standard case data. The trend to a reduction in profile width with increased values of the constant agrees with the trend observed in Chen and Pope (1990). The profiles of u', ξ' and $\tilde{\omega}$ show negligible change to variations of these constants. The value of C_χ is also varied while holding C_0 constant, and the results display negligible variation from the standard results, indicating that the important constant in this group is C_0.

Pope (1991a) obtained the value of $C_{\omega 1}$ = 0.04 by considering the case of a turbulent boundary layer and adjusting $C_{\omega 1}$ so the model yielded the von Kármán constant. However a different value of $C_{\omega 1}$ = 0.09 is required if the model is to be consistent with the k-ϵ model. Figure 7 shows the $\tilde{U}$ and $\tilde{\xi}$ profiles at x/R = 100 for $C_{\omega 1}$ = 0.090 and 0.064. We observe that the magnitude of the $\tilde{U}$ and $\tilde{\xi}$ profiles increases with larger values of $C_{\omega 1}$ The profile of $\tilde{\omega}$ shows the same sort of response, while the profiles of u' and ξ' remain relatively unchanged

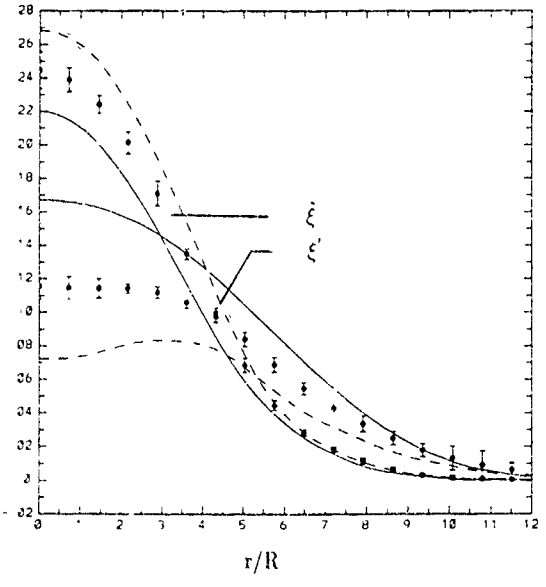

Figure 5 Profiles of $\tilde{\xi}$ and ξ' resulting from variation of C_ξ.

The final constant varied is σ^2. Pope and Chen (1990) showed that experimental data indicate that σ^2 had a weak Reynolds number dependence, and used the value σ^2 = 1.0, corresponding to a Reynolds number based on the Taylor length scale of 110. Figure 8 shows profiles of $\tilde{U}$ and $\tilde{\xi}$ for σ^2 equal to 0.5 and 1.5. It is seen that an increase in σ^2 results in a taller, narrower profile for both $\tilde{U}$ and $\tilde{\xi}$. The same response occurs for $\tilde{\omega}$, while u' and ξ' show little variation.

The remaining constants, $C_{\omega 2}$ and $C_{\omega 3}$ were not varied. $C_{\omega 2}$ is obtained from grid turbulence results and can be considered fixed and the value of $C_{\omega 3}$ has been shown by Pope (1991a) to have a negligible effect on the solution.

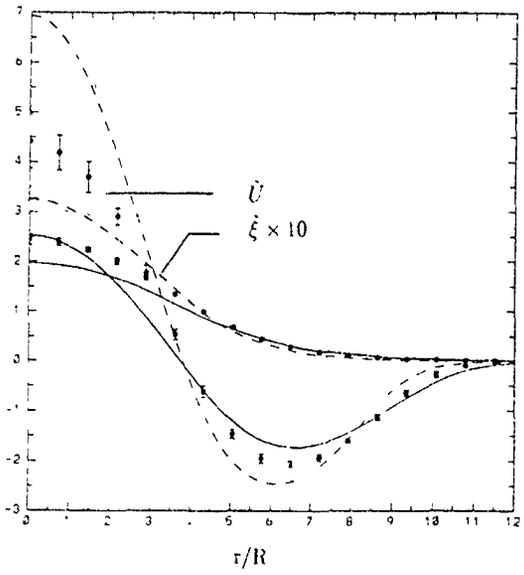

Figure 6 Profiles of $\tilde{U}$ and $\tilde{\xi}$ resulting from variation of C_0 and C_s

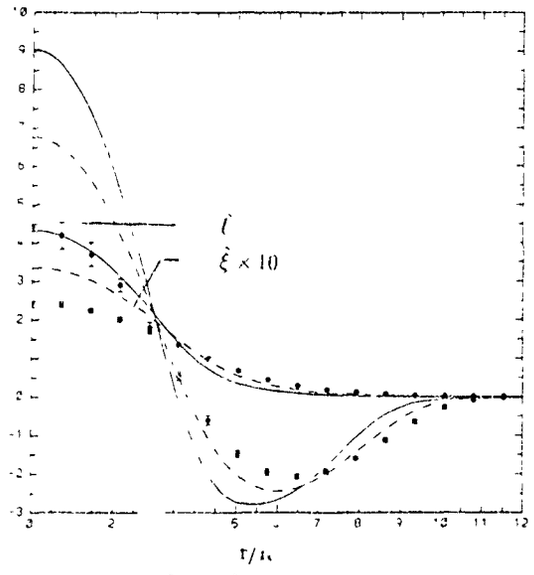

Figure 7 Profiles of $\tilde{U}$ and $\tilde{\xi}$ resulting from variation of $C_{\omega 1}$

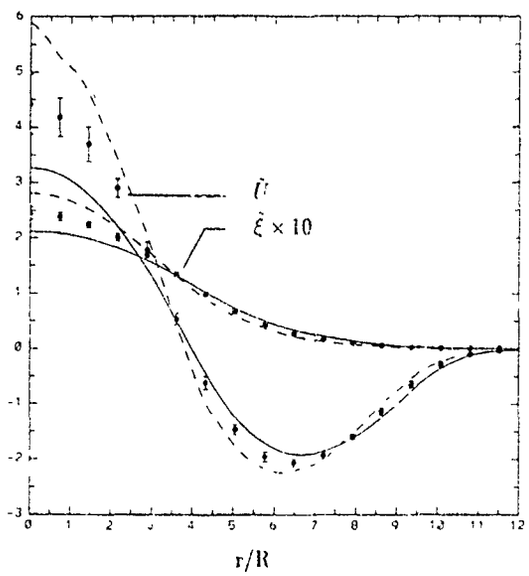

Figure 8. Profiles of $\tilde{U}$ and $\tilde{\xi}$ resulting from variation of σ^2

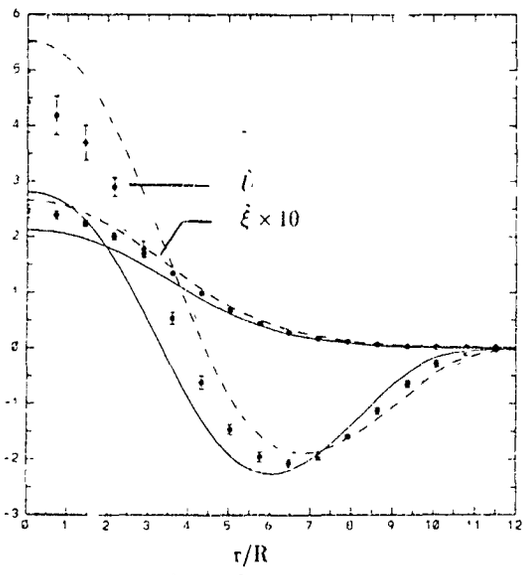

Figure 9. Profiles of $\tilde{U}$ and $\tilde{\xi}$ resulting from variation of ξ_s and axial pilot velocity.

VARIATION OF INITIAL CONDITIONS

Three main classes of initial condition are varied: the density/velocity profiles, the turbulence quantities, and the dissipation profiles.

Figure 9 shows the $\tilde{U}$ and $\tilde{\xi}$ profiles at x/R = 100 that result from the variation of the stoichiometric density and a corresponding change in the pilot jet velocity to maintain the same momentum flow rate. Both the width and the magnitude of the profiles is seen to increase with a lower value of ξ_s, and to a lesser extent this trend extends to the profiles of u', ξ' and $\tilde{\omega}$.

The initial velocity rms profiles of u', v' and w' are varied in the following way: u', which is an experimentally determined quantity is not changed. The two other components are given the value of $\frac{1}{2}u'$ for one run, and equal to u' for the other. The latter specification corresponds to the profiles used by Masri and Pope (1990). What is found is that, at x/R = 100, there is negligible difference between the profiles, suggesting the initial profile of turbulent quantities is not critical.

Finaly we vary the initial profile of $\langle\omega\rangle$. The two cases considered are $\tilde{\omega}$ equal to half the standard case profile, and $\tilde{\omega}$ equal to twice the standard case profile. Despite the magnitude of the change in the initial $\tilde{\omega}$ profile, the results at x/R = 100 show little variation between the profiles. Figure 10 shows the axial value of $\tilde{\omega}$ against axial location for the standard case and the two variants. It can be seen that the values quickly relax to an almost identical time history.

The initial profiles of $\tilde{U}$ and $\tilde{\xi}$ are not varied as these were measured experimentally.

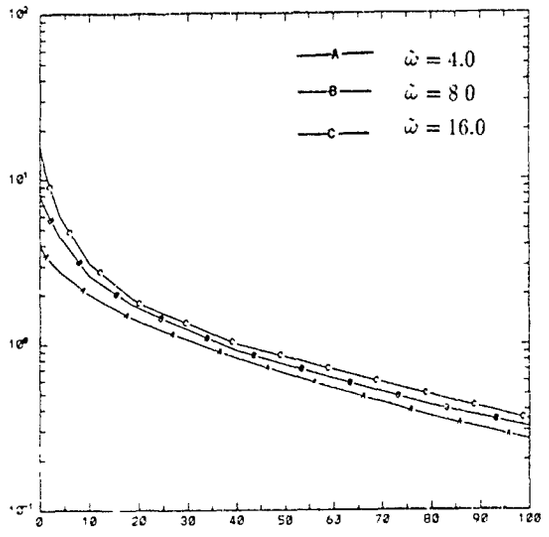

Figure 10. Evolution of centerline $\tilde{\omega}$ for variation in initial $\tilde{\omega}$

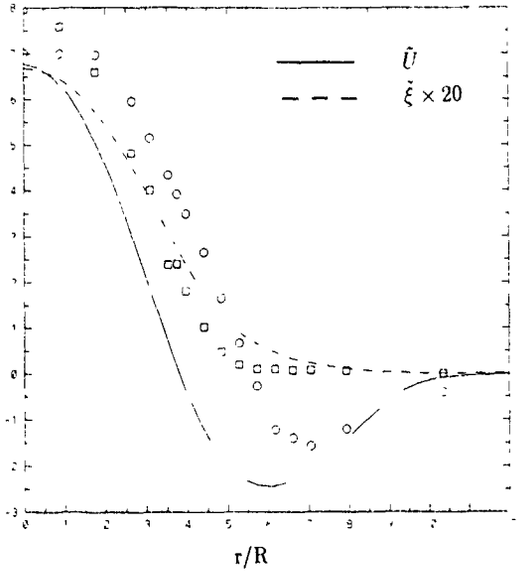

Figure 11. Profiles of $\tilde{U}$ and $\tilde{\xi}$ for $C_\omega = 0.065$. Open symbols are experimental data of Masri and Bilger (1986).

The results of this section show that the sensitivity of the solution to changes in initial conditions is small. The lack of sensitivity to initial profiles of u', v', w' and $\tilde{\omega}$ is reassuring as often these quantities are difficult to specify accurately. The variation of $\tilde{U}$ profiles with density variation is just a reflection of the effect of reaction on the flow, and as density is relatively easy to determine is of no cause for concern

COMPARISON WITH EXPERIMENTAL DATA

While the agreement between the experimental data and computed profiles in Figs 3 and 4 is disappointing, there are several mitigating factors to be considered

The axial location of x/R = 100 was chosen to emphasize the difference between profiles obtained with different model constants and initial conditions. The area of interest in this flow is at x/R = 10, where chemical/turbulence interactions are causing local extinction (Masri and Pope 1990) At this location the agreement between our calculated profiles and the experimental data is good We should also emphasize that the ability of the model to duplicate experimental results is no worse than that of other schemes. The agreement of calculated profiles to experimental data of Masri and Pope (1990) at x/R = 100 shows similar magnitudes of error as our results. The results of Chen, Kollmann and Dibble (1989) show relatively good agreement at x/r = 100, but exhibit a poor match closer to the jet, despite the benefit of finite-rate thermochemistry employed in their scheme.

There are also several differences between the model conditions and the experimental conditions that could cause such a lack of agreement in results. In the experiment the pilot is composed of acetylene, hydrogen and air, made up so the atom balance is the same as for a stoichiometric methane-air flame. This results in a large enthalpy excess at the pilot, which cannot be modeled by a single scalar equilibrium thermochemical model. In addition the experimental data do exhibit some local extinction for this flame, which is not treated by our chemical model

The uncertainty in the value of $C_{\omega 1}$ suggests that the model for dissipation production, S_ω, may be at fault. Figure 11 shows experimental data plotted against profiles of $\tilde{U}$ and $\tilde{\xi}$ generated by the model with $C_{\omega 1} = 0.065$ The agreement with experiment is seen to be superior to that shown in Figs. 3 and 4. Pope (1991a) indicated that the expression for S_ω was tentative, and the present results support this argument

CONCLUSION

We have demonstrated that the velocity-dissipation-scalar pdf model can produce accurate solutions for the piloted non-premixed turbulent methane flame problem. By varying the model constants we have shown that the scheme is sensitive to the choice of a few constants However this sensitivity is restricted to changes in the mean axial velocity and mean scalar profiles: rms quantities being relatively unaffected. The effect on the model due to choice of initial conditions has been shown to be small, justifying the use of approximate initial profiles for certain quantities A comparison of experimental data to solution profiles, suggests that the model for dissipation production needs to be adjusted, to improve the performance of the model. Future work will focus on improving the dissipation production term, and the inclusion of finite rate thermochemistry.

ACKNOWLEDGEMENTS

This work was supported in part by the National Science Foundation Grant CBT-8811655. Computations conducted during the research were performed on the Cornell National Supercomputer Facility, which is supported in part by the National Science Foundation, New York State. The IBM Corporation and members of the Corporate Research Institute.

REFERENCES

CHEN, J. Y., KOLLMANN, W. and DIBBLE, R. W. 1989 *Technical Report SAND89-8403* Combustion Research Facility, Sandia National Laboratories, Livermore, CA 94551

DOPAZO, C. 1975 *Phys. Fluids* **18**(2):389-394.

HINZE, J. O. 1975 *Turbulence* McGraw Hill, Second edition

MASRI, A. R. and BILGER, R. W. 1986 *Twenty-First Symposium (International) on Combustion*, 1511-1520

MASRI, A. R., DIBBLE, R. W. and BILGER, R. W. 1988a *Combustion and Flame*, **71**:245-266, 1988

MASRI, A. R., DIBBLE, R. W. and BILGER, R. W. 1988b *Combustion and Flame*, **73**:261-285

MASRI, A. R., DIBBLE, R. W. and BILGER, R. W. 1988c *Combustion and Flame*, **74**:267-284.

MASRI, A. R. and POPE, S. B. 1990 *Combustion and Flame*, **81**:13-29

POPE, S. B. 1985 *Prog. Energy Combust. Sci.* **11**:119-192

POPE, S. B. 1991a *Phys. Fluids*, in press

POPE, S. B. 1991b *Twenty-Third Symposium (International) on Combustion*, in press

POPE, S. B. and CHEN, Y. L. 1990 *Phys. Fluids A*, **2**(8):1437-1449

POPE, S. B. and GADIL, R. 1988 *Commun. Statist. Simula.*, **17**(2):349-376

TENNEKES, H. and LUMLEY, J. L. 1972 *A First Course in Turbulence*, MIT Press.

EIGHTH SYMPOSIUM ON
TURBULENT SHEAR FLOWS
Technical University of Munich
September 9-11, 1991

An Experimental Study of Laminar, Transitional, and Turbulent Jet Flames of Air-Diluted Methane

R. S. Barlow*, S. H. Stårner** and R. W. Bilger**

*Combustion Research Facility
Sandia National Laboratories
Livermore, California 94551

**Department of Mechanical Engineering
The University of Sydney
NSW 2006, Australia

ABSTRACT

In previous studies the mass fractions of OH and H_2 measured in turbulent methane jet flames near extinction were significantly higher than those measured in laminar flames and predicted by steady strained laminar flame calculations. The present work investigates flames over a range of Reynolds numbers (laminar, transitional, and turbulent) to determine when the measured chemical states begin to deviate from the laminar flame conditions. Simultaneous point measurements of temperature, major species concentration, and the hydroxyl radical concentration are obtained in nonpremixed jet flames of air-diluted methane. Results suggest a gradual increase in OH mass fractions through transition from laminar to turbulent conditions. Conditional pdfs show no further increase in OH mass fractions as the turbulent flame is pushed closer to extinction, so that the elevated OH mass fractions cannot be attributed to extinguishing and reigniting samples. Possible mechanisms for the observed effect of turbulence on chemical states in these flames are discussed.

INTRODUCTION

In recent years, it has become increasingly recognized that finite rate chemical kinetics can have significant effects on the structure of turbulent nonpremixed flames. Modelers of turbulent flames, making use of expanding computational capabilities, have incorporated chemical submodels with increasing detail and complexity in attempts to accurately account for the effects of finite rate chemistry. Pope (1990) has reviewed recent progress in the computation of turbulent reacting flows. Some modelers, such as Haworth et al. (1989) and Rogg et al. (1989) have made use of libraries of strained laminar flame calculations based on detailed reaction mechanisms. An alternative approach taken by Peters & Kee (1987), Chen & Dibble (1991a), Chen (1991), Bilger et al. (1991), and others has been to develop reduced mechanisms, which include only three to five composite reactions that preserve the important chemical kinetic features of detailed reaction mechanisms. These reduced mechanisms are then incorporated into Monte Carlo or pdf simulations of turbulent flames, such as those by Chen (1991) and Chen et al. (1991).

There has been some debate as to the applicability of the flamelet model to turbulent nonpremixed combustion. Peters (1988) argues that the flamelet approach is valid for many turbulent flames of practical importance. Bilger (1989), on the other hand, argues that the width of reaction zones in turbulent flames is often broader than the smallest scales of turbulent mixing, such that reaction occurs in distributed zones that may be affected by internal turbulence structure. Previous experiments at Sandia (Stårner et al., 1990a,b and Barlow et al.,1990a, 1991) have shown that the measured concentrations of OH and H_2 in turbulent flames of air-diluted methane, nitrogen-diluted methane, and undiluted methane are significantly higher than predicted by *steady* strained laminar flame calculations. These previous experiments were conducted using the piloted burner developed at Sydney University by Stårner & Bilger (1985), and all of the cases considered were highly strained turbulent flames that were approaching the blowoff condition and exhibited local extinction. Subsequently, OH concentration profiles were measured by Barlow & Collignon (1991) in laminar opposed-flow (Tsuji-type) diffusion flames and in laminar jet flames using the same OH fluorescence excitation/detection strategy as in the turbulent flame experiments. Results showed good agreement between measurements and laminar flame calculations of the maximum OH concentration.

The present experiment was conducted to determine where, within the regime between laminar low-strain-rate flames and turbulent flames near extinction, the measured mass fractions of OH begin to exceed the range of mass fractions predicted by steady strained laminar flame calculations. Four jet flames of air-diluted methane are investigated. The Reynolds number based on fuel nozzle exit conditions is varied from Re=1,770 (laminar flame, low strain rate) to Re=20,700 (highly strained turbulent flame exhibiting local extinction). Simultaneous point measurements of major species concentrations, temperature, and the hydroxyl radical concentration are obtained using a combination of spontaneous Raman scattering, Rayleigh scattering, and laser-induced fluorescence (LIF).

Results suggest that OH mass fractions increase gradually through transition. High OH mass fractions are attained at a Reynolds number well below that which causes local extinction, indicating that the 'super-flamelet' OH is not associated with the local extinction/reignition process and is due to changes in the structure of the reaction zone caused by turbulence. Possible mechanisms for the observed influence of turbulence on the distribution of chemical states in these methane flames are discussed below.

EXPERIMENTAL METHODS

Facility and Laser Diagnostics

The flow facility, piloted burner, and diagnostic techniques used here have been described in detail by Barlow et al. (1989, 1990b) and Stårner et al. (1990a,b). The axisymmetric burner is mounted just above the contraction section of a vertical wind tunnel that supplies coflowing air at low turbulence intensity. The wind tunnel assembly, including the burner, is mounted on a stepper-motor-controlled three-dimensional traversing mechanism, which allows the flame to be positioned relative to the fixed optical diagnostic system.

The piloted burner consists of a central fuel tube of diameter D=7.2 mm surrounded by a premixed pilot that extends to an 18 mm diameter. The pilot flame serves to anchor the main jet flame in the transitional and turbulent cases, preventing liftoff from the nozzle. Measurements are obtained above the pilot flame at a distance of 20 nozzle diameters from the burner.

Spontaneous Raman scattering is used to measure the concentrations of N_2, O_2, CH_4, CO, CO_2, H_2, and H_2O.

Temperature is determined from the Rayleigh scattering signal and a species-weighted Rayleigh scattering cross section based on the Raman measurements. Both the Raman and Rayleigh measurements are performed using the beam from the Combustion Research Facility's flashlamp-pumped dye laser (532 nm, 2.5 μs, 1 J/pulse). A spherical return mirror doubles the laser energy in the probe volume. The laser probe volume is approximately 0.7 mm in diameter by 1.0 mm in length along the laser beam.

OH concentration measurements are obtained using linear laser-induced fluorescence. The doubled output of a Nd:YAG-pumped dye laser is tuned to the $S_{21}(8)$ (0,0) transition of OH, and this ultraviolet laser beam is combined onto the axis of the Raman laser beam using a dichroic mirror. The LIF probe volume coincides with the Raman/Rayleigh probe volume and has dimensions of 0.5x0.7x1.0 mm. (The laser beam has an elliptical cross section.) The smallest dimension is in the radial direction relative to the axis of the jet flames. The time delay of 3.5 μs between the LIF and Raman laser pulses is small compared to the fluid-dynamic and chemical time scales in the flames of interest. Thus, the measurements may be treated as simultaneous. OH measurements are referenced to the conditions over a calibration burner, where the OH concentration has been measured by absorption.

The Raman/Rayleigh data for temperature and major species concentrations can be used, as described by Barlow et al. (1991), to correct the linear OH fluorescence signals for shot-to-shot variations in the collisional quenching rate and the ground state population fraction. The effect of these quenching and population corrections on the measured OH mass fractions in methane-air flames at atmospheric pressure has been analyzed by Barlow & Colligron (1991), based on collisional quenching cross sections provided by Garland and Crosley (1988). In laminar flames at low and intermediate strain rates the corrections for quenching and Boltzmann fraction tend to offset one another, such that the net change in OH mass fraction is only a few percent. As the strain rate approaches the extinction limit, the calculated quenching rate increases, and the net effect of the corrections on the OH mass fraction approaches 20 percent. However, recent measurements by Jeffries et al. (1988) and modeling of collisional quenching cross sections by Paul et al. (1991) suggest that the Garland & Crosley model overpredicts the temperature dependence of the cross sections at flame temperatures. Thus, the net corrections for quenching and Boltzmann fraction are expected to be small even in highly strained methane flames. Because there is uncertainty due to shot noise in the experimental measurements of temperature and major species concentrations, the application of corrections to the OH fluorescence data in these methane flames increases the standard deviation in the OH mass fractions, even when the average mass fraction is unchanged. For these reasons, the OH mass fractions presented in this paper are uncorrected values Inclusion of the quenching and population corrections would increase the OH mass fractions in the turbulent flames by a few percent, pushing them further from the laminar flame results. Therefore, application of the corrections would not alter the conclusions of this paper.

Flow Conditions and Flame Descriptions

Four flames are investigated, with flow conditions summarized in Table 1. In all cases the central jet fluid is a mixture of 25 percent CH_4 and 75 percent air, by volume. Air-diluted methane has two useful characteristics from an experimental perspective. First, it has a higher extinction limit than undiluted methane or nitrogen-diluted methane. Consequently, laminar flames are easier to stabilize, and the piloted flames can be pushed to relatively high Reynolds numbers before local extinction and blowoff occur. This means that changes in the measured chemical states due to the influence of turbulence on reaction zone structure can be separated from changes resulting from the extinction-reignition process. The second advantage of air-diluted methane is that flames of this mixture are essentially nonsooting. Therefore, energy loss due to particle incandescence is minimized, and fluorescence interference from soot precursors, as described by Masri et al. (1987) is reduced.

Table 1 Flow Conditions for the Air-Diluted Methane Flames

Flame	U_j (m/s)	U_p (m/s)	U_{cf} (m/s)	$Re=U_jD/\nu$
A	4.9	0.0	0.8	1,770
B	12.3	0.75	1.9	4,420
C	24.5	1.5	3.7	8,830
D	57.3	3.0	8.4	20,700

U_j, U_p, and U_{cf} are unburnt jet, pilot, and coflow velocities.

The four flames listed in Table 1 are designated A, B, C and D in order of increasing Reynolds number. Flame A is laminar (Re=1,770) with unsteadiness due to buoyancy-induced instability apparent only near the flame tip. Flame B (Re=4,420) is transitional. It is visibly unsteady, and the reaction zone moves radially (wavers or flaps). However, this flame is not fully turbulent. The reaction zone in flame B is not strongly distorted or curved, and there is no indication of local extinction in the data. Flame C is turbulent, with a modest Reynolds number of 8,830. Local extinction, which is indicated in the measurements by low temperatures and near zero OH mass fractions within the reactive range of mixture fraction, occurs for a small fraction of the samples in flame C. Local extinction occurs when local rates of turbulent mixing or scalar dissipation exceed the rates of the chemical reactions that produce radicals and thermal energy. Flame D (Re=20,700) displays a significant probability of local extinction, is audibly unstable, and has an overall appearance similar to the turbulent flames near extinction reported by Stårner et al. (1990a,b) and Barlow et al. (1991).

As shown in Table 1, the velocities of the coflowing air and the pilot gases (when used) are scaled with the velocity of the central jet. This is done to maintain flow similarity and to keep the contribution of the pilot flame to the total energy release up to the measurement location approximately constant. (Note that he pilot burns a mixture of C_2H_2, H_2, CO_2, N_2 and air that produces the same calculated equilibrium composition and adiabatic flame temperature as a stoichiometric mixture of methane and air.) In the turbulent flames C and D the pilot is estimated to contribute 12 to 15 percent of the integrated energy release up to the measurement location. Therefore, while the pilot has the important effect of stabilizing the transitional and turbulent flames, we do not expect the pilot to contribute to the elevated OH mass fractions discussed in the following section.

Flame A was operated without a pilot because the premixed gas flow rate could not be scaled back sufficiently without causing flashback. OH fluorescence profiles were measured in two piloted laminar flames to determine whether the OH concentration at the measurement location was affected by the pilot. One of these laminar flames had the same pilot flow rate as flame B, and the other had a small hydrogen diffusion flame as a pilot. No significant differences in the peak OH fluorescence signals were observed for these three laminar flames, and the complete Raman/Rayleigh/LIF measurements are reported only for the laminar flame with no pilot.

RESULTS AND DISCUSSION

Measurements were obtained at a fixed axial location 14.4 cm or 20 nozzle diameters above the burner (x/D=20) at the radial location in each flame corresponding to the maximum average OH fluorescence signal. Results for measured temperatures and species mass fractions are plotted vs. the mixture fraction f in Figs. 1, 2, 3, and 4 for flames A, B, C, and D, respectively. Each scatter plot for flame A includes 800 points, while 2000 points are plotted for flames B, C, and D.

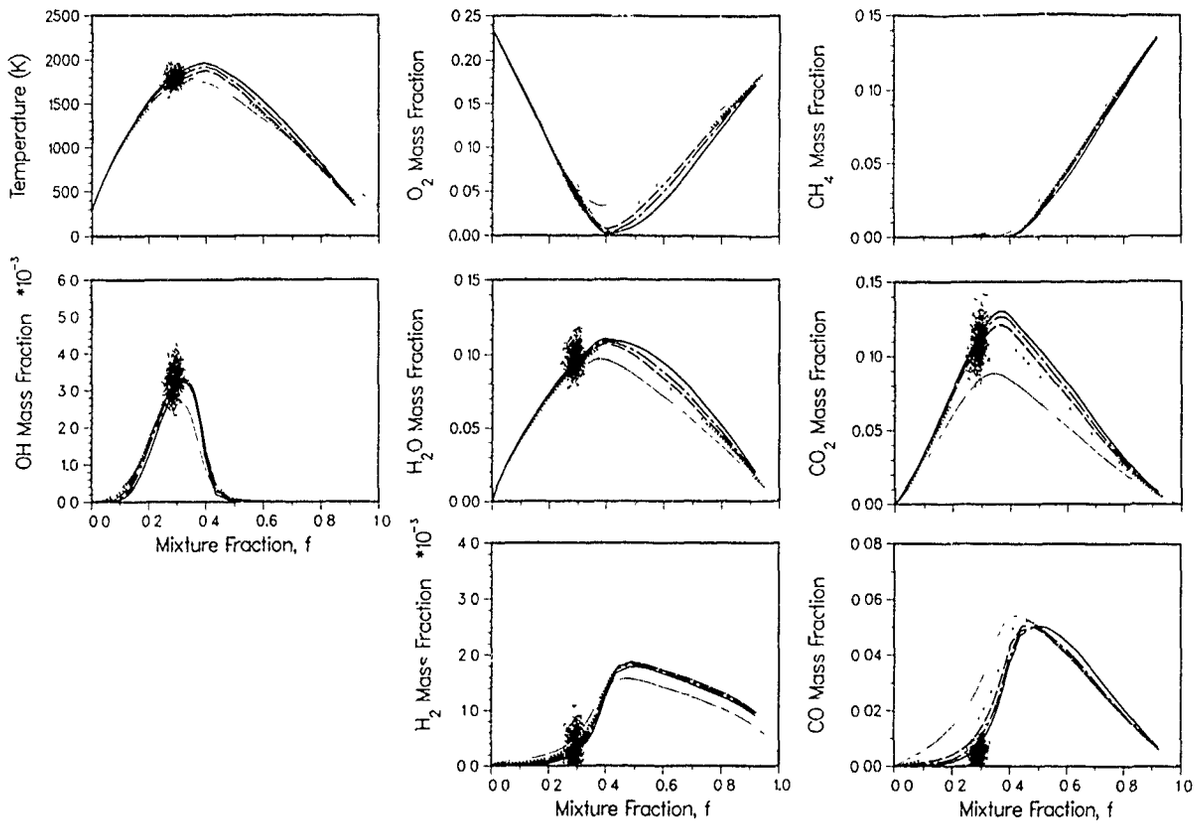

Fig. 1. Scatter plots of temperature and species mass fractions vs. the mixture fraction f in the laminar flame A (Re=1,770). Curves show results of steady laminar flame calculations for values of the strain parameter of: a = 50 s^{-1} (_____), 100 s^{-1} (___ _ ___), 200 s^{-1} (___.___), 400 s^{-1} (_ _ _ _ _), and 800 s^{-1} (.....).

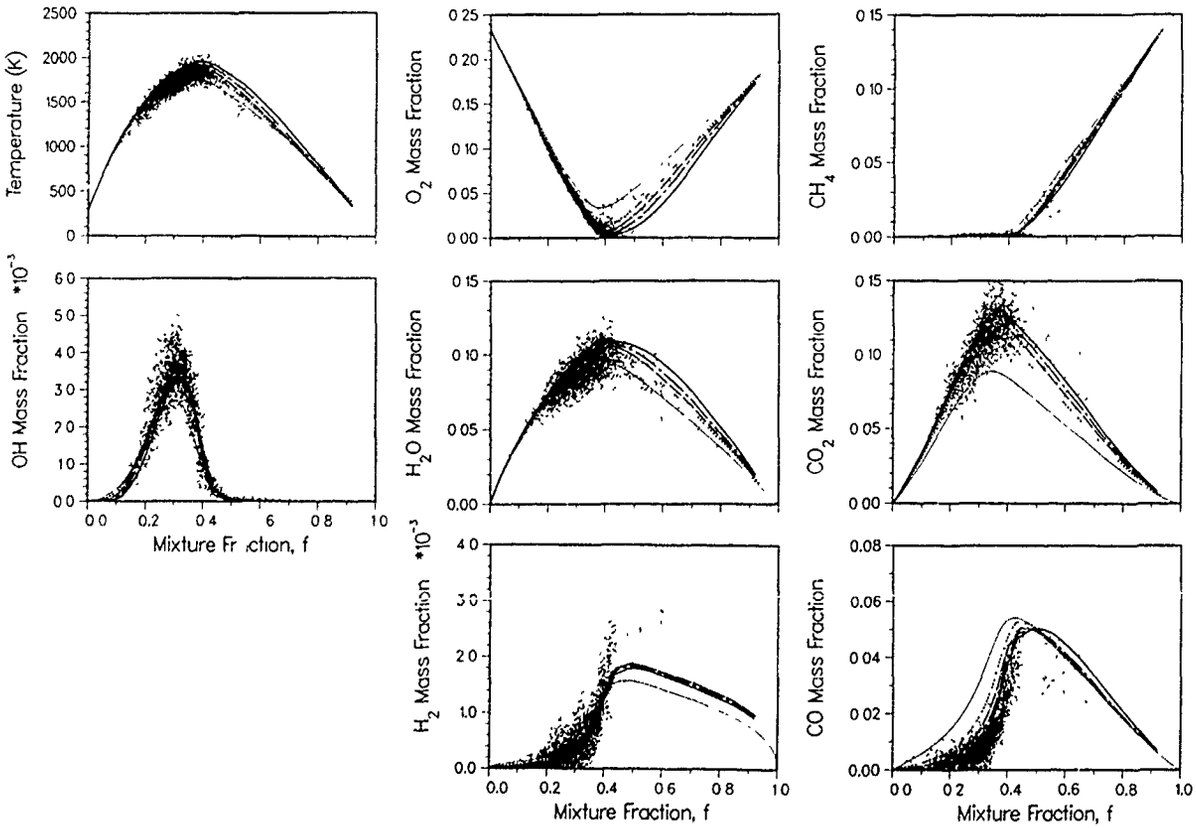

Fig. 2. Scatter plots of temperature and species mass fractions vs. the mixture fraction f in the transitional flame B (Re=4,420). Curves show results of steady laminar flame calculations for values of the strain parameter as in Fig. 1.

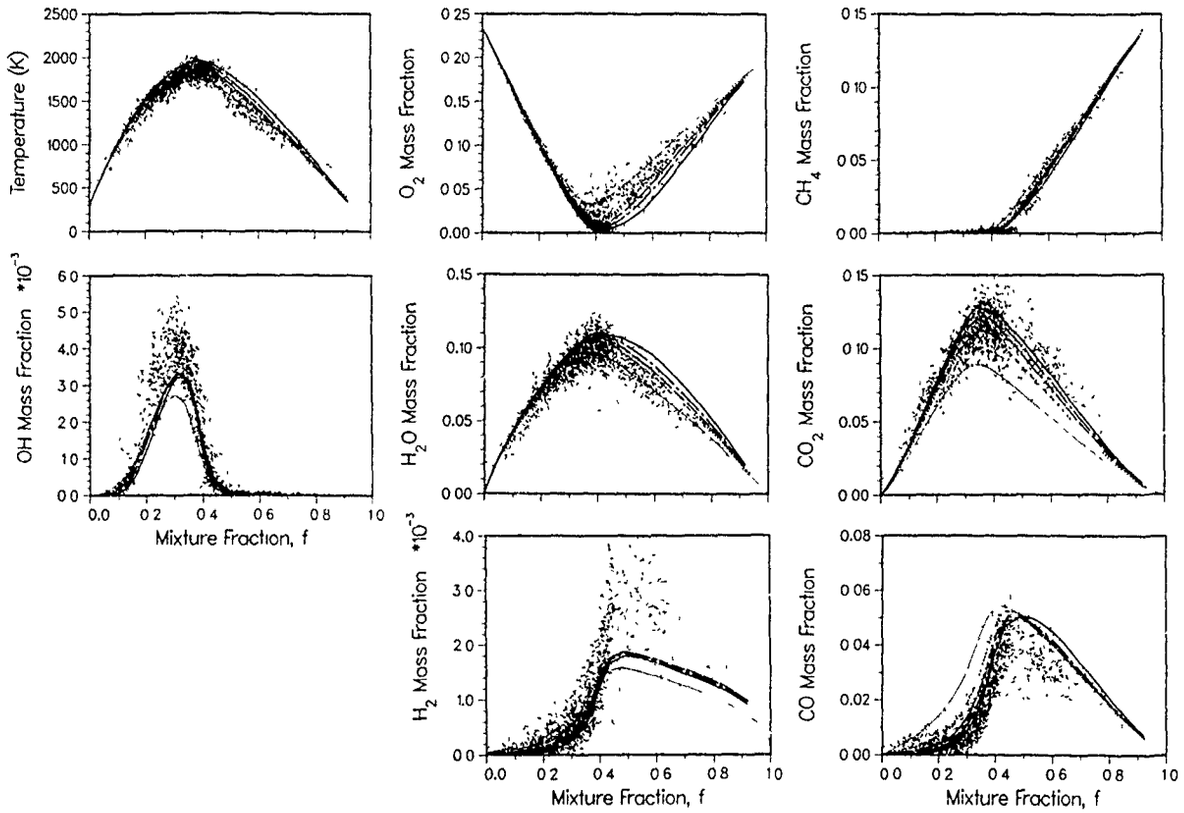

Fig. 3. Scatter plots of temperature and species mass fractions vs. the mixture fraction f in the turbulent flame C (Re=8,830). Curves show results of steady laminar flame calculations for values of the strain parameter as in Fig. 1.

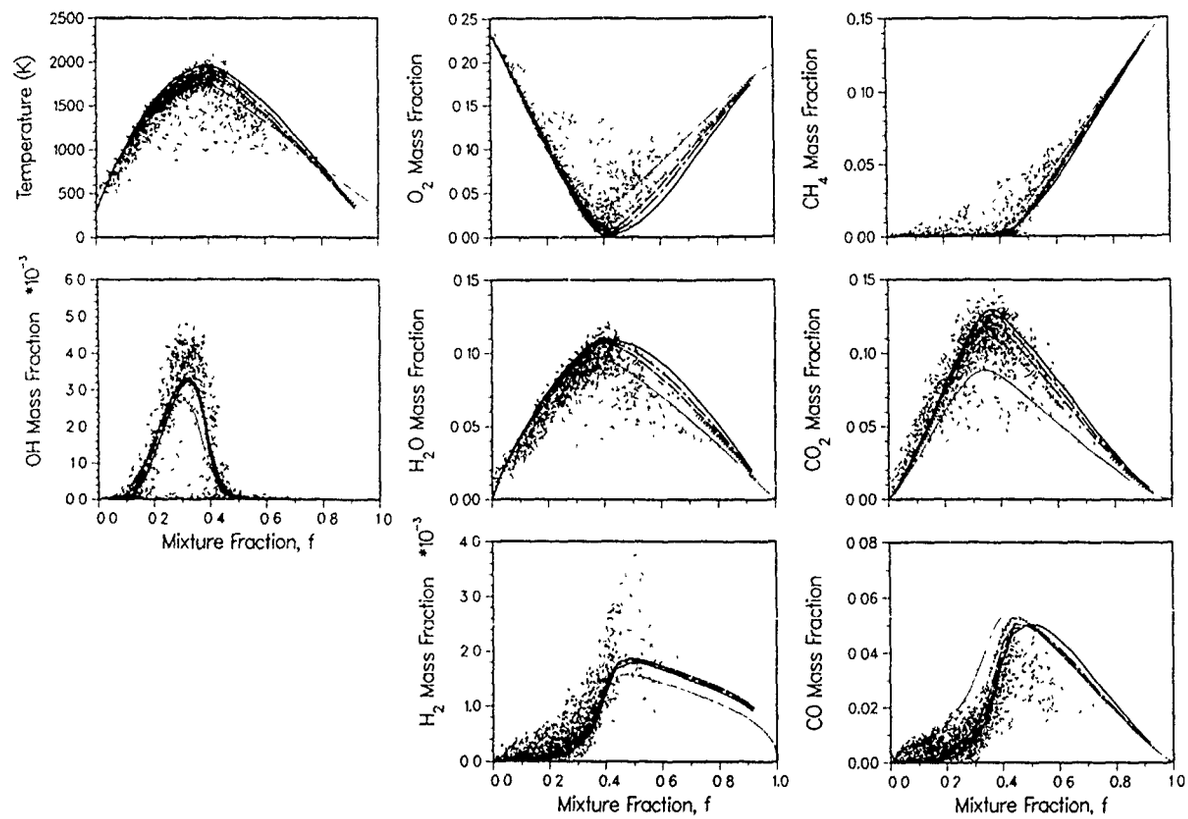

Fig. 4. Scatter plots of temperature and species mass fractions vs. the mixture fraction f in the turbulent flame D (Re=20,700). Curves show results of steady laminar flame calculations for values of the strain parameter as in Fig. 1.

Also plotted in each figure are results from steady strained laminar flame calculations performed using the code and kinetic mechanism described by Smooke et al. (1988). Values of the strain parameter for the laminar calculations are a = 50, 100, 200, 400, and 800 s^{-1}. (The strain parameter for a Tsuji-type laminar stagnation flame is defined as $a = 2U/r$, where U is the velocity of the air flowing toward the cylindrical burner, and r is the burner radius.) Extinction occurs near $a = 860\ s^{-1}$ with the 3:1 air-diluted methane mixture on the 'fuel' side.

The mixture fraction f is a conserved scalar describing the state of mixing between nozzle fluid and air within a fluid sample. The mixture fraction is calculated from the measured species mass fractions according to the expression,

$$f = \frac{\frac{2(Y_C - Y_{C,1})}{W_C} + \frac{(Y_H - Y_{H,1})}{2W_H} + \frac{(Y_{O,1} - Y_O)}{W_O}}{\frac{2(Y_{C,2} - Y_{C,1})}{W_C} + \frac{(Y_{H,2} - Y_{H,1})}{2W_H} + \frac{(Y_{O,1} - Y_{O,2})}{W_O}}$$

Here, W_i is the atomic mass of element i, Y_i is the mass fraction of element i, and the subscripts 1 and 2 refer to the air and nozzle fluid, respectively. The mixture fraction is zero in air, unity in pure nozzle fluid, and has a stoichiometric value of $f_s = 0.353$ for the air-diluted methane.

Temperatures and Major Species Mass Fractions

Scatter plots, such as those in Figs. 1-4, provide an overview of the distribution of chemical states in a flame. This is particularly true in the turbulent flames, where data from a single spatial location includes samples covering a broad range in mixture fraction. In contrast to the scatter plots in Figs. 3 and 4 for the turbulent flames, the data shown in Fig. 1 for flame A are confined to a relatively narrow mixture fraction interval Flame A was observed to be quite steady, and the average values of temperature and species mass fractions measured in this flame are consistent with calculations for laminar flames at low strain rates. Therefore, the spread in the experimental data in Fig. 1 gives a good indication of the single shot uncertainty in the measurements. This is true of the mixture fraction, as well as temperature and species mass fractions This experimental uncertainty must be taken into account when interpreting results for the transitional and turbulent flames.

Differences among the four experimental flames are readily apparent in the results for temperature and the mass fractions of major reactants and products, CH_4, O_2, H_2O, and CO_2. Considering flame B (Fig. 2), we find that the data in this transitional flame are spread over a range in mixture fraction from 0.1 to 0.8. Within the experimental uncertainty, however, the measurements remain consistent with the laminar flame calculations for low and intermediate strain rates. This transitional flame has the visual appearance of a wavy laminar flame, in which the reaction zone moves radially relative to the fixed laser probe volume.

When the Reynolds number is increased to 8,830 (flame C, Fig. 3) the flame becomes turbulent. The data span an even wider range in mixture fraction, and we begin to see evidence of local extinction. A few points within the reactive range of mixture fraction ($0.15 < f < 0.4$) show low temperatures, low product mass fractions, and high reactant mass fractions, indicating that the local strain rate or scalar dissipation rate has exceeded the extinction limit. With the exception of the few extinguished samples, the data for temperature and the mass fractions Y_{CH4}, Y_{O2}, Y_{H2O}, and Y_{CO2} are again consistent with the laminar flame solutions, within the experimental uncertainty. The five laminar flame solutions show that the effect of increased strain is to decrease temperature and product mass fractions. Y_{CO2} drops more rapidly than Y_{H2O} in the calculations due to the slower kinetic rates of the reactions producing CO_2. The turbulent flame data in Fig. 3 reflect this effect of increased strain rates on the CO_2 mass fraction.

The probability of local extinction is highest in flame D (Fig. 4), which has a Reynolds number of 20,700. The scatter plots of temperature and the mass fractions of CH_4, O_2, H_2O, and CO_2 show a significant number of points that are well outside the results of the strained laminar flame calculations. These points represent fluid samples that are extinguished or are in a partially reacted state. Extinction and subsequent reignition of fluid samples presents a significant challenge for turbulent combustion models based upon the laminar flamelet approach.

OH Mass Fractions

The OH mass fractions measured in the turbulent flames show differences from the steady laminar flame calculations beyond those associated with local extinction. The peak value of the OH mass fraction in the laminar flame calculations is relatively insensitive to strain rate and is approximately 3.2×10^{-3} for all but the highest strain rate of 800 s^{-1}. The average OH mass fraction measured in flame A is also 3.2×10^{-3}. Scatter plots in Figs. 1-4 show that the OH mass fractions tends to increase as the Reynolds number increases and the flames become turbulent. This result is shown more clearly in Fig. 5, which includes conditional pdfs of OH mass fraction. Here, only data within the mixture fraction interval $0.265 < f < 0.335$ are included. In terms of the relative mixture fraction, the interval is $0.75 < f/f_s < 0.95$, where f_s = 0.353 is the stoichiometric value of the mixture fraction. The peak OH mass fractions, both measured and predicted, occur within this mixture fraction interval. The conditional pdfs for the two turbulent flames C and D are significantly broader that the pdf for the laminar flame A, and the most probable value of the OH mass fraction in flames C and D is 4.4×10^{-3}. This value is significantly higher than the peak OH mass fractions from the laminar flame calculations.

The conditional pdfs for the two turbulent flames differ at low OH mass fractions due to the higher probability of local extinction in flame D. The pdf for flame D has a spike at zero mass fraction that is not present in the other flames. However, it is important to note that the increase in Reynolds number from 8,830 to 20,700 and the onset of local extinction have no significant effect on the shape of the conditional pdf at the higher OH mass fractions. These results suggest that the elevated OH mass fractions observed in turbulent nonpremixed methane flames cannot be attributed to extinguishing and reigniting fluid samples and that turbulence alters the structure of the reaction zone from that which exists in steady laminar diffusion flames.

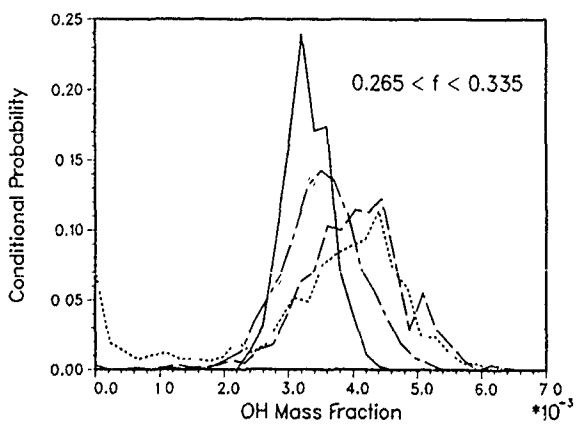

Fig. 5. Conditional probability density functions (pdfs) of measured OH mass fractions within the interval in mixture fraction of $0.265 < f < 0.335$ for each of the four cases: flame A (_____), flame B (_ _ _ _), flame C (_._._), and flame D (_ _ _ _ _).

The conditional pdf for flame B, the transitional case, has characteristics that are intermediate between the laminar and turbulent cases. This transitional pdf is broader than that from the laminar flame but is not as broad as the pdf from the turbulent flames. The most probable value of the OH mass fraction in flame B is 3.5×10^{-3}, which is only slightly higher than in the laminar flame. This result suggests that there may be a gradual change in the structure of the reaction zone as the flame goes through transition from laminar to turbulent. However, additional experiments at several intermediate Reynolds numbers will be required to fully characterize the evolution of the OH pdfs.

Mechanisms for the Effects of Turbulence on Chemical States

There are several possible mechanisms for the observed effect of turbulence on the chemical states in methane flames. These include: i) the response of the kinetic system to unsteady strain, ii) changes in the profile of scalar dissipation through the reaction zone, iii) flame curvature, and iv) changes in the degree of differential diffusion. At this time, the relative importance of these mechanisms is unclear, and this is an area of ongoing research. Recent calculations have shown that flame unsteadiness can cause significant increases in the concentrations of some species. Maub et al. (1990) reported high CO concentrations in unsteady calculations of laminar methane flames. Chen & Dibble (1991b) have observed similar effects in unsteady perfectly stirred reactor calculations. In both studies, flames were pushed very close to extinction (high strain rate or short residence time) and then allowed to relax or reignite. The present experimental results show that elevated OH mass fractions occur in flames that are well away from the extinction condition. Therefore, the high OH mass fractions are not solely the result of an extinction-reignition process, as suggested by Maub et al. Chen has also begun to investigate the temporal response of laminar methane-air flames to sinusoidal variations of the scalar dissipation that do not take the flame close to extinction. Initial results indicate that unsteadiness of this type is unlikely to produce the significant increase in OH mass fractions measured in the turbulent flames. The same computer code can be used to investigate the importance of differential diffusion and of changes in the scalar dissipation profile in determining the peak OH mass fractions. These computational experiments are in progress.

CONCLUSIONS

Simultaneous point measurements of major species concentrations, temperature, and hydroxyl radical concentration have been made in a series of laminar, transitional and turbulent jet flames of air-diluted methane. Reynolds numbers based on the nozzle exit conditions were 1770, 4420, 8830, and 20700. Measured OH mass fractions and major species concentrations in the laminar flame are consistent with steady laminar flame predictions. However, measured OH mass fractions in the turbulent flames are significantly higher than predicted by the steady laminar flame calculations. These high OH concentrations appear in flames where strain rates are well below the level that causes local extinction and, therefore, cannot be explained solely on the basis of a transient extinction-reignition process. This result demonstrates that turbulence alters the structure of the methane-air reaction zone from that which exists in the steady laminar flame calculations. Conditional pdfs of OH mass fraction in the four experimental flames suggest a gradual transition between the laminar and turbulent flame structures. There is no significant evolution in the shape of the conditional pdfs between the two turbulent flames, which differ in Reynolds number by more than a factor of two.

REFERENCES

Barlow, R. S., Dibble, R. W., Stårner, S. H. & Bilger, R. W., "Piloted Diffusion Flames of Nitrogen Diluted Methane Near Extinction: OH Measurements," *Twenty-Third Symposium (International) on Combustion*, The Combustion Institute, Pittsburgh, Pa., in press (1991).

Barlow, R. S. , Dibble, R. W., Stårner, S. H. & Bilger, R. W., AIAA paper 90-0732 (1990a).

Barlow, R. S. & Collignon, A., AIAA paper 91-0179 (1991).

Barlow, R. S., Dibble, R. W. & Lucht, R. P., *Optics Letters* 14: 263-265 (1989).

Barlow, R. S., Dibble, R. W , Chen, J.-Y. & Lucht, R. P., *Combust. Flame*, 82:235-251 (1990b).

Bilger, R. W. , *Twenty-Second Symposium (International) on Combustion*, pp. 475-488, The Combustion Institute, Pittsburgh, Pa. (1989)

Bilger, R. W., Stårner, S. H. & Kee, R. J., "On Reduced Mechanisms for Methane-Air Combustion in Nonpremixed Flames," *Combust. Flame* 80:135-149 (1990).

Chen, J.-Y. , "Reduced Reaction Mechanisms for Methanol-Air Diffusion Flames," *Comb. Sci Tech.*, in press (1991).

Chen, J.-Y., Dibble, R. W. & Bilger, R. W., "Pdf Modeling of Turbulent Nonpremixed $CO/H_2/N_2$ Jet Flames with Reduced Mechanisms," *Twenty-Third Symposium (International) on Combustion*, The Combustion Institute, Pittsburgh, Pa., in press (1991).

Chen, J.-Y. & Dibble, R. W., in Reduced Kinetic Mechanisms and Asymptotic Approximations for Methane-Air Flames, M. D. Smooke, ed., in press (1991a).

Chen, J.-Y. & Dibble, R. W., "A Perfectly-Stirred-Reactor Description of Turbulent Methane-Air Nonpremixed Flames," (IUTAM) Symposium on Aerothermodynamics in Combustors (1991b).

Garland, N. L. & Crosley, D. R., *Twenty-First Symposium (International) on Combustion*, pp. 1693-1702, The Combustion Institute, Pittsburgh, Pa. (1988).

Haworth, D. C. Drake, M. C., Pope, S. B. & Blint, R. J., *Twenty-Second Symposium (International) on Combustion*, p. 1533, The Combustion Institute, Pittsburgh, Pa. (1989).

Jeffries, J. B , Kohse-Höinghaus, K., Smith, G. P., Copeland, R. A. & Crosley, D. R., *Chem. Phys. Let.*, 152:160-166 (1988).

Masri, A. R., Bilger, R. W. & Dibbie, R. W., *Combust. Flame* 68:109-119 (1987).

Maub, F., Keller, D. & Peters, N., "A Lagrangian Simulation of Flamelet Extinction and Re-ignition in Turbulent Jet Diffusion Flames," *Twenty-Third Symposium (International) on Combustion*, The Combustion Institute, Pittsburgh, Pa., in press (1991).

Paul, P. H., Meier, U. E. & Hanson, R. K., AIAA paper 91-0459 (1991).

Peters, N. & Kee, R. J., *Combust Flame* 68:17-30 (1987).

Peters, N., *Twenty-First Symposium (International) on Combustion*, p. 1231, The Combustion Institute, Pittsburgh, Pa. (1988)

Pope, S. B., "Computations of Turbulent Combustion: Progress and Challenges," *Twenty-Third Symposium (International) on Combust.on*, The Combustion Institute, Pittsburgh, Pa., in press (1991).

Rogg, B., Behrendt, F. & Warnatz, J., *Twenty-Second Symposium (International) on Combustion*, p. 589, The Combustion Institute, Pittsburgh, Pa. (1989).

Smooke, M., Puri, I. K. & Seshadri, K., *Twenty-First Symposium (International) on Combustion*, pp. 1783-1792, The Combustion Institute, Pittsburgh, Pa. (1988).

Stårner, S. H. & Bilger, R. W., *Combust. Flame*, 61:29-38 (1985)

Stårner, S. H., Bilger, R. W., Dibble, R. W. & Barlow, R. S., *Comb. Sci. Tech.* 70:111-133 (1990a).

Stårner, S. H. , Bilger, R. W., Dibble, R. W. & Barlow, R. S., *Comb. Sci. Tech.* 72:225 (1990b).

EIGHTH SYMPOSIUM ON
TURBULENT SHEAR FLOWS
Technical University of Munich
September 9-11, 1991

THREE-DIMENSIONAL VORTICAL STRUCTURE OF A TURBULENT FLAME

E Gutmark, . P. Parr, D. M Hanson-Parr, and K C. Schadow

Research Department, Code 3892
Naval Weapons Center, China Lake, CA 93555-6001

ABSTRACT

Two dimensional (i.e , planar) species and temperature imaging experiments, on simple axisymmetric transitional or low turbulence level reacting flows, have indicated that three dimensional effects are of prime importance even at very low Reynolds number. In fact, the 3-D interaction between large scale spanwise vortices and streamwise vortices, in a simple axisymmetric nozzle combustion system, is apparently a majoi mechanism in the breakdown of 2-D (axisymmetric) large scale turbulent structure into fine scale 3-D turbulence required for molecular mixing and good combustion efficiency

To study these complex 3-D flows requires a spatially and temporally resolved non-intrusive diagnostic capability. Advanced laser combustion/flow diagnostics are required to freeze the complex flow structure and display it in resolved three dimensions. In the present work, three dimensional images of a reacting jet were constructed from multiple two-dimensional images acquired at a constant phase angle. The images revealed the strong coupling between the streamwise and spanwise vortices in the flow. The measurements have strong resemblance to results of numerical simulations of a reacting planar shear layer.

INTRODUCTION

Reacting turbulent jets are governed by the interaction of the fluid dynamics, chemical reaction and heat release (Broadwell & Dimotakis, 1986). The fluid dynamics involved in these types of flows are related to a mixing layer flow which is governed by large-scale vortices. The roll-up and growth of these vortices are determined by instability forces and mutual interactions (Brown & Roshko, 1974). The large-scale structures entrain flow from the two sides of the shear layer and mix the flow at both large and small scales, leading to the molecular mixing necessary for reaction. The development of large-scale vortices in the shear layer is influenced by the reaction through heat release and density gradients. In turn, the vorticity controls the reaction by the turbulent mixing process (Mungal & Dimotakis, 1984).

The ability of a circular jet to develop modes of instability which are higher than the axisymmetric mode was demonstrated by linear stability analysis (Fuchs, 1972; Plaschko, 1979; Strange & Crighton, 1983; Mattingly & Chang, 1974, and Michalke & Hermann, 1982). In a relatively large diameter jet with a thin shear layer surrounding its core, many azimuthal modes are equally unstable (Cohen & Wygnanski, 1987). The phase velocity of the higher modes is nondispersive in a wide range of frequencies thus allowing resonant interactions to occur, which amplify these modes. The evolution of azimuthal structures on coherent initially axisymmetric vortices was observed both in cold flow (Browand & Laufer, 1975) and reacting flows in flames (Chen & Roquemore, 1986; Settles, 1985; and Gutmark et al., 1989a).

Preliminary results on the evolution of vortical structures in an annular diffusion flame using OH concentration and planar temperature mapping were described in Gutmark et al (1989b). The effect of forcing on the azimuthal structure of the flame was discussed Gutmark et al. (1989a). Gutmark et al (1988) described the three-dimensional character of the flame coherent structures during their formation and interaction. The flame structure was shown in planes with different orientations. These papers emphasized the complexity of the flame structure which is difficult to describe with conventional flow visualization techniques.

The present paper describes two and three-dimensional structure of a reacting jet using Planar Laser Induced Fluorescence (PLIF)

EXPERIMENTAL ARRANGEMENT

A system for PLIF imaging (Kychakoff et al, 1982) of OH radicals in flames using a XeCl excimer laser at 308 nm was used (Fig. 1) (Gutmark et al., 1989b) The laser beam was expanded into a planar sheet, passed through the flow in a chosen direction: parallel to the jet axis for studying the streamwise evolution of the structures or perpendicular to the axis for azimuthal structures measurements. The resonance fluorescence from OH was imaged with a gated intensified photodiode array camera. The sheet was approximately 0.5 mm wide

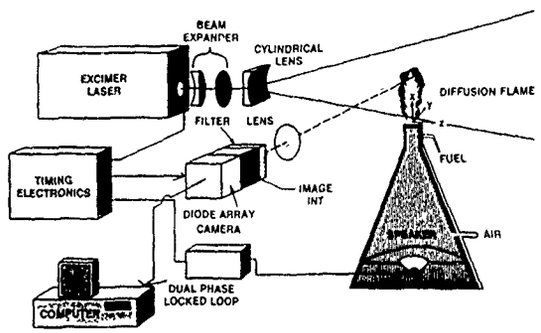

Fig. 1. Experimental Set-Up For PLIF Imaging in 2-D.

The air issued at a velocity of 5 m/s from a 22 mm diameter circular nozzle yielding a Reynolds number of 7000, based on the exit diameter, exit velocity, and the kinematic viscosity of the air at room temperature The propane fuel was injected circumferentially around the air jet nozzle into the initial shear layer, via 24 1.6 mm diameter holes, on a 23.5 mm diameter circle, which are slightly angled into the shear layer. The fuel exit velocity was 0 2 m/sec.

The flow was excited by a set of four speakers mounted in an acoustic resonating chamber (a 45 cm diameter base by 66 cm tall cone) which was used as a settling chamber as well. The speakers were driven at controlled frequencies and amplitudes using a dual phase locked loop and audio power

amplifier. To construct the turbulent structure at a specific phase, the laser system was phase locked to acoustic excitation of the flame jet. The phase angles between the forcing signal and the laser could be varied in a full cycle range. The forcing frequencies, amplitudes, and relative phase angles were monitored (in cold flow) by using a calibrated hot-wire anemometer. The speakers force, and phase lock, only the longitudinal mode of the jet

The azimuthal structure was stabilized by vortex generators in the jet boundary layer upstream of the exit Previous experiments (Gutmark et al., 1989a and 1988) showed that the preferred azimuthal structure has a five-fold symmetry. Therefore, a set of five pairs of split delta-wings were installed at the exit Two configurations of wings were tested. One was generating "mushroom" like vortices and the other a "delta wing" type vortex pair. The triangles forming the semi-delta wing had a base of 4 mm and an apex angle of 30°.

The data was taken in two different modes. Short time exposures were taken yielding instantaneous OH LIF signal level images (18 nsec). Alternately, multiple frames (about 100), taken at a constant phase angle, were averaged together for each image to reduce the chaotic nature of the flow and bring out the coherent portion.

RESULTS AND DISCUSSION

Vortex Dynamics in Reacting Jets

Figure 2a shows a phase-averaged OH concentration taken in a flow that was acoustically excited at the preferred mode of the jet (St = 0 44). The image has a scale attached to it with values (voltages) corresponding to the upper and lower limits indicated. These voltages are proportional to the fluorescence intensity from the OH radicals in the flame. The OH fluorescence intensity seems to be nearly uniform inside the vortex. The structures are highly coherent in shape and location, but the internal details are smeared by the averaging process. An example of a single shot of 18 nsec duration is shown in Fig. 2b for OH fluorescence. It is shown here that following the initial roll-up, the combustion is most intense in the vortex circumference. Time sequences of "instantaneous" images show that as the vortex is convected downstream, the combustion proceeds into the vortex core while the reaction at the circumference is completed.

An efficient combustion reaction occurs in regions where molecular mixing between the fuel and the oxygen is obtained In a diffusion flame the fuel and air are mixed together initially by the large-scale structures. The reaction requires additional small-scale mixing. The small-scale turbulence production was shown to be concentrated at the circumference of the large-scale structures following the roll-up process This previous observation, obtained in cold nonreacting flows can explain the present results concerning the reaction zones in the flame vortices.

Givi et al (1986) investigated the conditions leading to local flame extinction due to the high dissipation rates at the braids formed during the vortices' roll-up. Their findings agree well with the present measurements Both the average and the instantaneous OH fluorescence maps (Fig 2), show the quenching of the flame in the braid region.

Streamwise Vortices and Azimuthal Structures

The circumferential structure of the flame was studied by slicing the flame with the laser sheet perpendicular to the flame axis, at different axial distances from the nozzle. Figure 3 shows the instantaneous measurements of the flame, forced at the harmonic of the preferred mode frequency. Frame 3.1 shows the locations of the perpendicular cuts along the vortex.

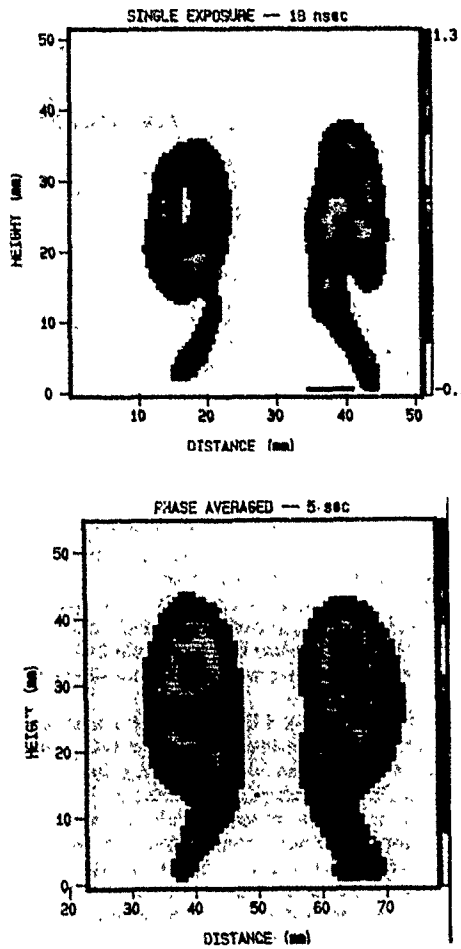

Fig. 2. Phase-Averaged and Short Time Exposure (18 nsec) OH Concentration in a Circular Jet Vortex Forced at the Preferred Mode.

The small vortices, obtained by this forcing, make it possible to follow the circumferential structure along more than one cycle in the vortical structure development. The figure shows the cross-sections of the vortices during three spatial cycles of evolution. The initial structure which is even and symmetric at X/D = 0.23 (frame 3.2) develops wrinkled structure at X/D = 0.7 (frame 3.3) The instantaneous picture shows that the flame sheet is not continuous and there are some regions where local flame extinction occurs These regions move randomly around the braid region. The braid becomes more corrugated closer to the roll-up location and the reaction is concentrated in bulges around the braid. These bulges may be related to the streamwise vortices (or "ribs") which were observed in nonreacting shear flows (Bernal, 1981). It was shown that the ribs increase locally the small-scale turbulence energy and deform the vortices by being wrapped around them. The three dimensionality which is introduced through this process, is amplified and subsequently results in transition to random turbulence of the initially coherent flow. The three dimensional structure in the fully developed vortex (frame 3.4) has more secondary lobes relative to larger vortex generated by preferred mode forcing (Gutmark et al, 1988). This change of the number of secondary structures with the primary vortex core size was also described in Widnall e. al (1974). The number of lobes is reduced at the upper edge of the vortices, as the reaction moves more into the vortex core. At the final stages of the vortex burning, at the upper edges of the flame, the reaction is now concentrated in pockets, which are moving randomly around the flame In the rest of the vortex the OH disappears due to the flame temperature drop caused by mixing with the ambient cooler air.

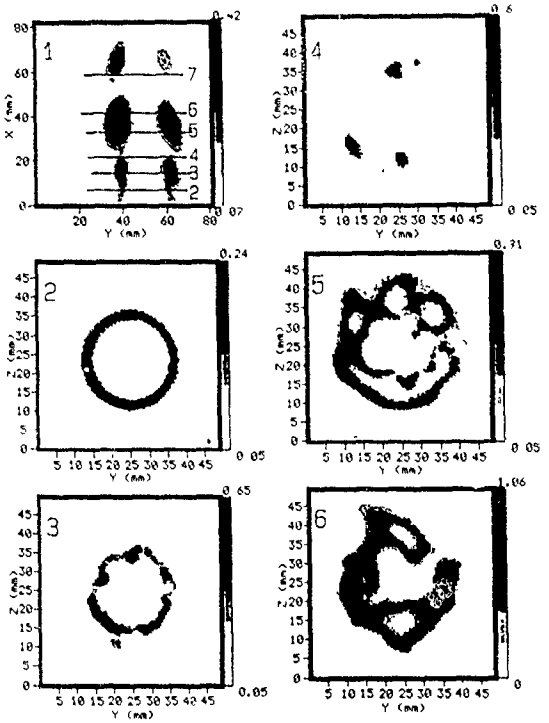

Fig. 3. Instantaneous Planar ages in Cross-Sections Perpendicular to the Jet Axis at Different Axial Locations. The flow is forced at the harmonic of the preferred mode frequency (1) On-axis plane cross-section, (2) x/D = 0.23, (3) x/D = 0.7, (4) x/D = 0.92, (5) x/D = 1.5, (6) x/D = 1.85, (7) x/D 2.66.

Although the spanwise vortex structure is phase locked in these experiments via the acoustic forcing, the azimuthal structure shown in Fig. 3 is not spatially phase locked. Even though this flow system generally led to five azimuthal lobes (M = 5), their position around the center of symmetry was random from one realization to the next. By spatially phase locking the streamwise vortices using five miniature vortex trippers, the azimuthal structure can be locked spatially It was determined that streamwise vortices which were generated in the braid region at the nozzle exit, leads to pinched off portions of the fully developed vortex ring further downstream. The streamwise vortices apparently wrap around the vortex ring and pinch it off, generating the five-fold symmetry in the structure.

Three Dimensional Imaging

By acquiring multiple images with the laser sheet at increasing x/D locations, and a constant phase angle in the vortex roll up process, the 3-D structure of the flame can be built up. Initially the braid region is circular and symmetric, but azimuthal instabilities begin to be evident relatively close to the nozzle and amplify in intensity further downstream. These instabilities are associated with streamwise vortices. Their amplitude are enough to entirely pinch off the fully developed vortex ring and convolute its shape. This leads to azimuthal break up of the vortex and the generation of small scale turbulent structure.

In order to obtain three-dimensional images of the complex structures without an instantaneous 3-D technique, the azimuthal high modes of instabilities were spatially stabilized using a passive forcing system of semi-delta wings. The three-dimensional image of the phase-locked structures was reconstructed from 20 planar slices measured at different axial locations Using this technique it was possible to follow the generation of streamwise vortices in the braid region, their growth and subsequent interaction with the large-scale spanwise vortices.

Two-Dimensional Slices Used For 3-D Reconstruction

The streamwise vortices which were generated by the semi-delta wings had a strong effect on the flame structure. Figure 4 shows the two-dimensional images of radial cross-sections of the flame obtained at increasing axial distances from the flameholder. The initial "braid" region acquires a pentagonal shape due to the flow induced by the streamwise vortices. The shape of these vortices become more evident as the axial distance grows and the axial vortices develop (x/D = 0.62). A close-up figure of the streamwise vortices is shown in Fig. 5 for a phase-averaged and instantaneous image. The "mushroom" shape of the streamwise vortex is evident in both images. The vortex generators produce a highly coherent vortex with low jitter level, thus, resulting in a clear image of the streamwise vortex cross-section. Moving further downstream into the spanwise vortex region, x/D = 0.94 (Fig. 4), it becomes pinched off with a five-fold symmetry, which is related to the longitudinal structures. The interaction between the streamwise vortices and the spanwise coherent structures results in a deformation of the latter and then breakdown to smaller scales. Studying the variation of the stack of radial slices along the axis shows the three-dimensional character of this flame. This feature requires a three-dimensional presentation of the flow to gain understanding of the interaction between the various instability modes in the flame.

3-D images of the flame were constructed from 20 two-dimensional planar images using StansSurf rendering software (Wu & Hesselink, 1988) (or you can have data rendered by Donna using marching cubes algorithm). The perspective views of the flames forced by the "mushroom" type vortices and by the "delta" type vortices are shown in Figs. 6 and 7, respectively. The rendering was done using the phase-averaged set of data, resulting in a relatively smooth interpolated surface. The transition from the streamwise structures to the spanwise pinched vortices is clear in these images. There are some differences between the two flames structures due to the two types of vortex generators. Figure 8 shows the structure of the flame with "delta-wing" axial vortices reconstructed from instantaneous data, at the same phase angle. The roughness of the surface increases considerably due to the small-scale structures of the instantaneous images. However, the coherence of both the spanwise and streamwise structures obtained by using the combined active and passive forcing is sufficient to obtain a consistent structure even from instantaneous data

Further details of the interior and exterior data is obtained using a vertical slice through the flame center (Fig. 9) showing the flame evolution in the jet core The vertical cut also emphasizes the odd-symmetry, such that the right cut is passing through the vortex bulge and the left side between the bulges. Horizontal cut (Fig. 10) through the center of the spanwise structures shows the pinched structure with reaction zones only at the outer parts of the vortex, where the high turbulence level concentrates. Similar three dimensional structures were obtained by using numerical simulation of a reacting planar mixing layer (Grinstein, 1990). Figure 11 shows the product concentration together with the vorticity magnitude. The pinching of the spanwise structures by the streamwise vortices is evident in this case, similar to the axisymmetric experiments data The concentration of product is affected such that there is a reduced product formation where the streamwise vortices wrap around the spanwise vortices. Some reaction is calculated and measured also along the streamwise vortices, but most of it is quenched by high strain rates. Figure 12 depicts a closeup view of the streamwise delta vortex in the braid region of the flame.

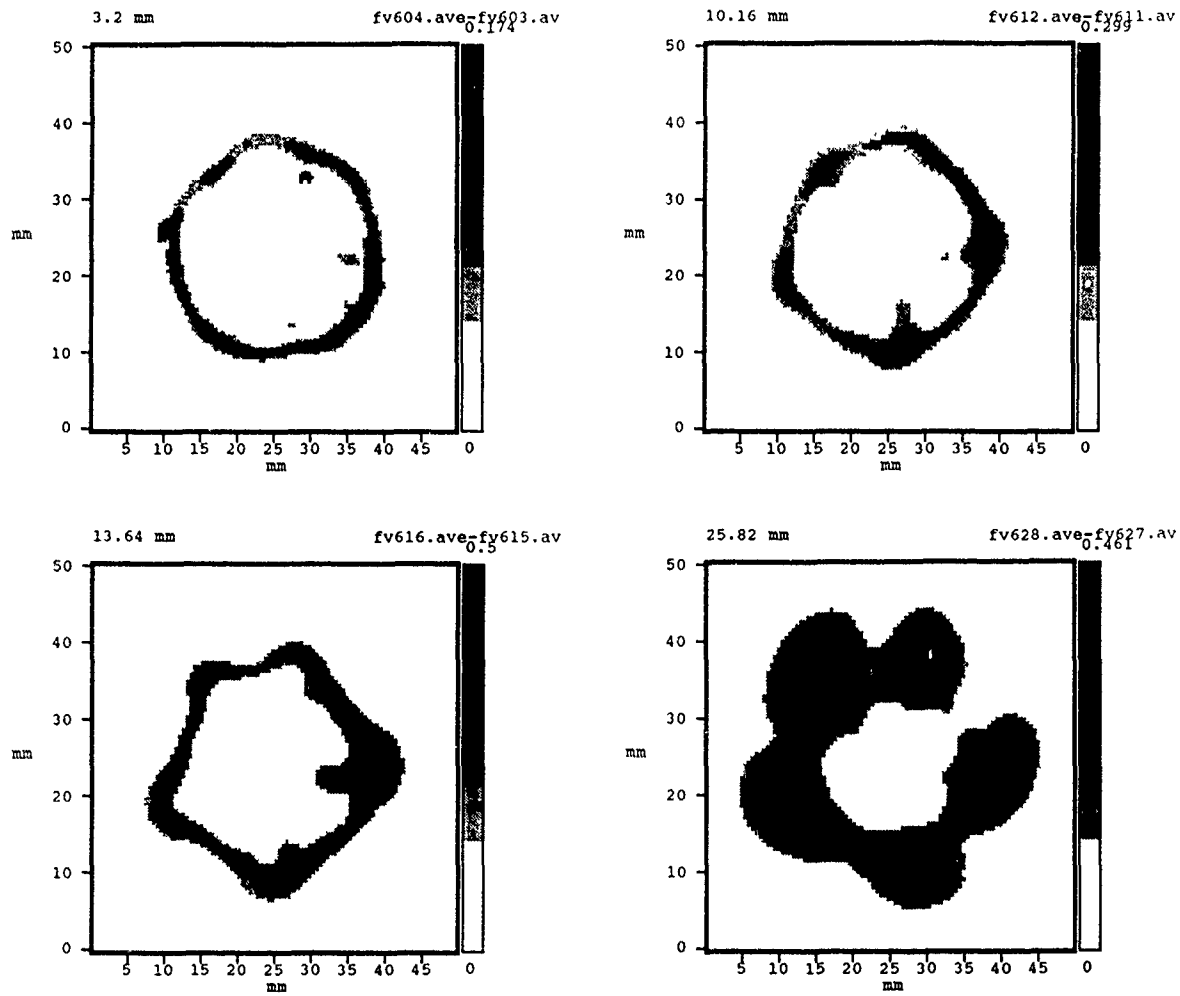

Fig. 4. Multiple Axial Planar Cross-Section Used to Reconstruct a 3-D Image. Azimuthal structure stabilized by semi-delta wing ("mushroom" type vortex) Spanwise structure forced at St = 0.49. (a) x/D = 0.15; (b) x/D = 0.45; (c) x/D = 0 62; (d) x/D = 0.94.

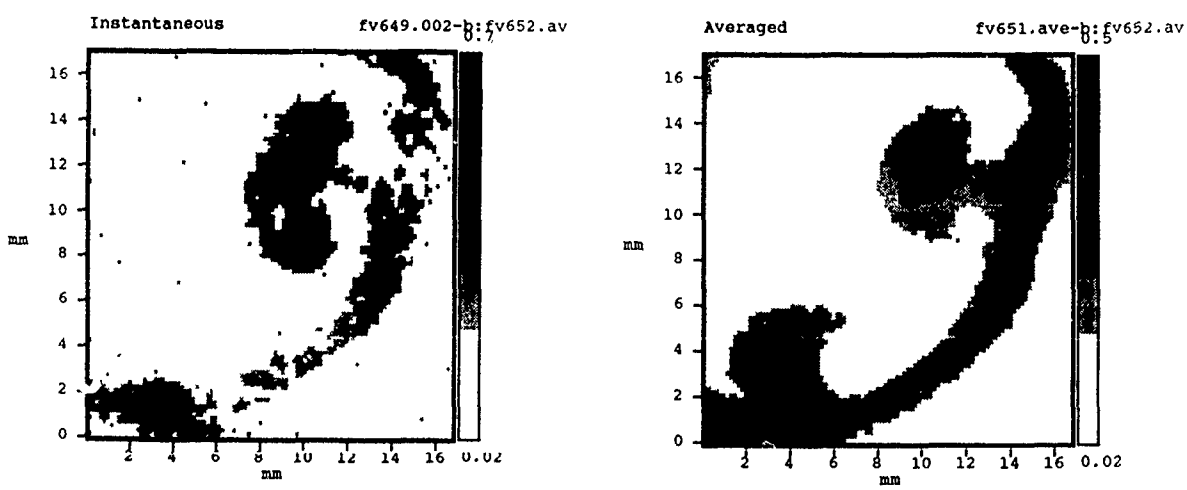

Fig. 5. Close Up Cross Sectional Cut in Streamwise "Mushroom" Type Vortices in "Braid" Region.

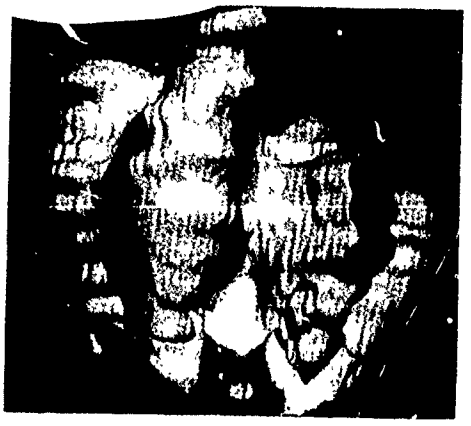

Fig. 6. Phase Averaged 3-D Image of the Azimuthal Structures in the Flow, With Streamwise "Mushroom" type vortices.

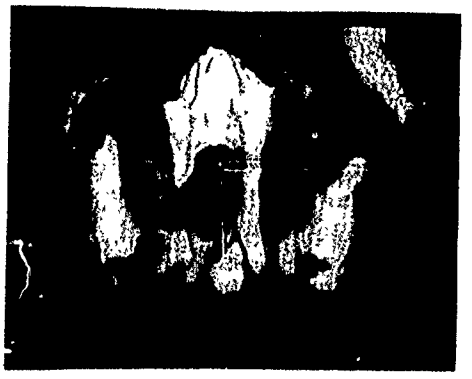

Fig. 9. Vertical Cut Through the Phase Averaged 3-D Image of the Azimuthal Structures in the Flow, With Streamwise "Mushroom" type vortices

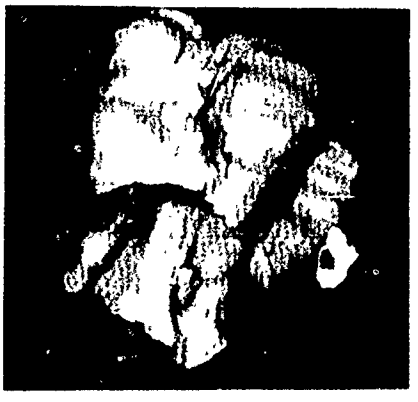

Fig. 7. Phase Averaged 3-D Image of the Azimuthal Structures in the Flow, With Streamwise "Delta type" vortices

Fig. 10. Horizontal Cut Through the Phase Averaged 3-D Image of the Azimuthal Structures in the Flow, With Streamwise "Mushroom" type vortices.

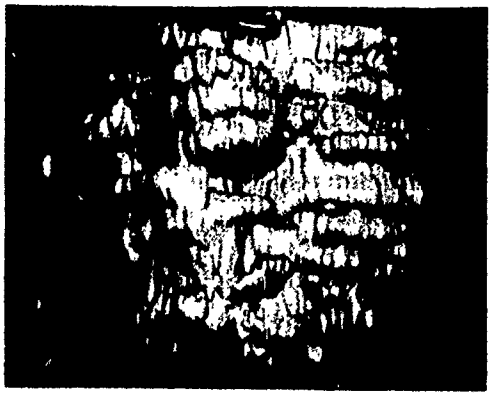

Fig 8. Instantaneous 3-D Image of the Azimuthal Structures in the Flow, With Streamwise "Delta-Wing" type vortices

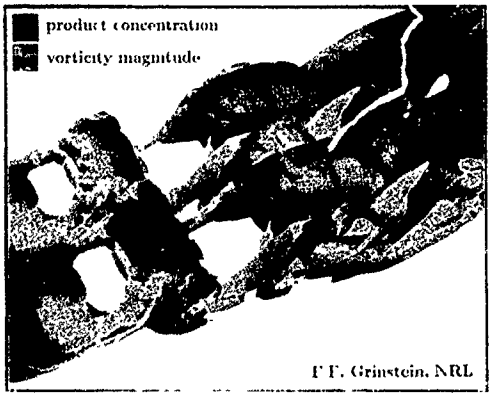

Fig. 11 Numerical Simulation of Product Concentration and Vorticity Magnitude in a Planar Reacting Mixing Layer (Grinstein, 1990)

Fig. 12. Details of Streamwise "Delta type" Vortex in "Braid Region".

CONCLUSIONS

The growth of the jet shear layer in a circular reacting jet determines the large and small scale mixing of the fuel and air. This growth is governed by the roll-ups and merging of the large scale structures in the shear layer. The description of these structures in the literature is usually related to their phase averaged properties. Actually their coherence exists only in the average. The capability of the PLIF technique to give both phase-averaged and instantaneous information opens up the possibility to study their actual highly unsteady and three-dimensional structure. From the different cross-cuts in the flame, it is possible to reconstruct the three-dimensional structure of the flame. The reaction takes place in regions which are randomly distributed in space and time but bounded by the phase-averaged outline of the vortices The extent of the deviation between the instantaneous pictures and the averaged ones is determined by the random turbulence component of the flow. When this component is enhanced the flame becomes more turbulent in nature and it is more difficult to identify its coherent component

The formation of shear streamwise structures in the braid regions which appear as bulges of flamelets in these regions are responsible for the emergence of three-dimensionality in the coherent structures. When these secondary disturbances are amplified they break the large-scale coherence, leading to the transition to small-scale turbulence This process is important to understand the relationship between the evolution of large-scale structures and the transition to small-scale turbulence in reacting shear flows.

The results presented in this paper describe the use of PLIF for 3-D reacting flow visualizations. PLIF is the only currently available experimental technique which is capable of supplying multi-dimensional data of both flow field and reaction process (including temperature and different species) instantaneously and simultaneously. The technique is now extended to have the capability of nearly instantaneous time-resolved 3-D imaging of highly turbulent reacting flows.

REFERENCES

BERNAL, L P. 1981 The Coherent Structure of Turbulent Mixing Layer, Ph D Thesis, California Institute of Technology, 1981.

BROADWELL, J E. & DIMOTAKIS, P. E 1986 AIAA J 24, 875

BROWAND, F K & LAUFER, J 1975 Turbulence in Liquids (J.L Zakin & G K. Patterson, eds., Princeton, N J), p 333

BROWN, G L & ROSHKO, A 1974 J Fluid Mech 64, 775

CHEN, L. D. & ROQUEMORE, W. R 1986 Combust. and Flame 66, 81.

COHEN, J. & WYGNANSKI, I., 1987 J Fluid Mech. 176, 191.

FUCHS, H. V. 1972 J Sound Vib. 22, 77.

GIVI, P., JOU, W. H. & METCALFE, R. W. 1986 21st International Symposium on Combustion, The Combustion Institute.

GRINSTEIN, F. F. 1990 Private Communication.

GUTMARK, E , PARR, . P., HANSON-PARR, D. M. & SCHADOW, K. C. 1988 22nd International Symposium on Combustion, The Combustion Institute, 523.

GUTMARK, E., PARR, . P., HANSON-PARR, D. M. & SCHADOW, K. C. 1989a Combust. and Flame 75, 229.

GUTMARK, E., PARR, . P., HANSON-PARR, D. M. & SCHADOW, K C. 1989b J. of Heat Transfer 3, 148.

KYCHAKOFF, G., HOWE, R D., HANSON, R. K & McDANIEL, J. C. 1982 Appl. Optics 21, 3225.

MATTINGLY, G. E. & CHANG, C. C 1974 J. Fluid Mech. 65, 541.

MICHALKE, A. & HERMANN, G 1982 J. Fluid Mech 114, 343

MUNGAL, M. G. & DIMOTAKIS, P E. 1984 J. Fluid Mech 148, 349.

PLASCHKO, P. 1979 J. Fluid Mech. 92, 209.

SETTLES, G. S 1985 Int. J Heat & Fluid Flow 6, 3.

STRANGE, P J R. & CRIGHTON, D. G. 1983 J Fluid Mech. 136, 231.

WIDNALL, S E., BLISS, P B & TSAI, C. Y. 1974 J. Fluid Mech. 66, 35.

WU, K & HESSELINK, L 1988 Appl Optics 27, 395

EIGHTH SYMPOSIUM ON
TURBULENT SHEAR FLOWS
Technical University of Munich
September 9-11, 1991

TURBULENT TRANSPORT PROCESSES IN SWIRLING RECIRCULATING NON-PREMIXED FLAMES

D. F. G. Durão, M. V. Heitor and A. L. N. Moreira

Instituto Superior Técnico
Technical University of Lisbon
Department of Mechanical Engineering
Av. Rovisco Pais
1096 Lisboa, Codex
PORTUGAL

ABSTRACT

Turbulent transport processes typical of swirling recirculating flows, including those with chemical reaction, are analysed and discussed based upon laser-Doppler measurements of mean and turbulent velocity characteristics. For the combusting flows, the results encompass the study of a non-premixed flame with a heat load of 350kW and include mean temperature measurements. The results show that although combustion does nor alter the mean flow pattern, it increases mean shear and curvature, resulting in increased turbulence levels and anisotropy thoughout the flow. This is associated with large scale motions with a predominant frequency, although their contribution to the time-average turbulent kinetic energy is shown to be small Inspection of the terms in the conservation equations for the turbulent stresses have allowed to quantify the extent up to which the interaction of normal stresses and normal strains influence the flow and suggest the likely magnitude of turbulent diffusion and dissipation.

1. INTRODUCTION

The combustion process in swirling recirculating non-premixed flames is partly dependent on the mixing of the fuel and air streams, which in turn is determined by the state of the flow turbulence. Knowledge of the turbulent structure of swirling recirculating flows is, therefore, essential for the analysis of practical combustion systems and is usually inferred from cold flow conditions as in current modelling practice, largely a carry-over from well-tested approaches in non-reacting flows (e. g., Jones and Whitelaw, 1985). A better understanding of the mechanisms of turbulence generation or supression by combustion is, however, necessary in investigating the extent up to which these practices can be used without modification for variable density flows (e. g. Heitor et al., 1987; Starner and Bilger, 1989) and depends on the availability of detailed experimental data (e. g , Bilger, 1991).

Velocity measurements in swirling recirculating flames have been extensively reported (e. g , Tangirala et al , 1987; Hardalupas et al., 1990), but measurements have been mostly concerned with turbulence intensities and only a few examples of other turbulence properties are available In particular, third-order correlations of velocity fluctuations can provide information on the effects of curvature and proximity of a stagnation zone on the turbulence structure and are necessary to obtain a full second-order closure of the differential equations for turbulent transport of momentum and energy (e. g., Launder, 1989). However, most of the published works reporting higher-order velocity measurements are concerned with the effects of curvature in cold mixing layers (e. g., Smiths et al., 1979; Gibson and Younis; 1983; Gibson et al., 1984) and only a few papers report similar measurements in curved reacting flows (e. g., Stärner; 1986, Heitor et al., 1987). In addition, experiments in which the measurements are used to obtain magnitude estimates of other quantities of direct relevance to turbulence modelling, such as budgets and correlation coefficients of Reynolds stresses, are necessary, but are very demanding in the experimental technique (e. g., Durão and Heitor, 1991). Only recently LDA measurements have been used to derive such information (e. g., Starner and Bilger, 1987; Heitor et al., 1987) but in somewhat simple flows, such as non-reacting mixing layers, axisymmetric jet flames with moderate swirl or bluff-body recirculating flames. Strongly swirled recirculating flows include additional features due to the effects of centrifugal forces and curvature in zones of mean shear (e. g., Takagi et al., 1985; Stärner and Bilger, 1989) but have not been fully adressed.

This paper reports an experimental study of the reacting flow field in the vicinity of a swirl-induced recirculation zone and is an extension of previous work for non-reacting conditions (Durão et al., 1990). The experiments include laser-Doppler measurements of mean velocity and double and triple velocity correlations in the three spatial directions, which are complemented by mean temperature measurements in the reacting flow. The results are used to obtain Favre averaged estimates of the convection and production terms of the transport equations for shear stress and turbulent kinetic energy and provide a basis to improve our understanding of relevant transport processes in industrial burners and to guide turbulence modelling.

2. FLOW CONFIGURATION AND EXPERIMENTAL METHOD

Details on the experimental techniques assessments of accuracy have been reported in a previous work (Moreira, 1991) and only a summary is presented here.

The flow configuration is based on those used under "dual" burning of liquid and gaseous fuels in practical furnaces. It comprises a commercial fuel atomizer with an external diameter of 23mm, assembled in a low velocity co-flow of propane gas (54mm O. D.), which is externally surrounded by a high velocity co-flow of air (84mm O. D.). A diverging quarl typical of those found in the burners of industrial furnaces, was located at the burner exit and could be removed to permit the measurement of boundary conditions. Swirl can be imparted to both streams by means of fixed blades at 45° with resulting swirl numbers, estimated from the geometry of the blades, equal to S_O=0.77 and S_I=0.85 for the outer and inner streams, respectively. The air flow rate was measured by a calibrated standard orifice meter and integrated pitot-tube measurements have shown that the measured flow rates are accurate within 2%. The propane mass flow rate was measured by a rotameter with an absolute error smaller than 0.1g/s, which corresponds to an accuracy of 1.75% for the flow conditions studied here.

The measurements presented here were obtained for reacting and non-reacting conditions in the absence of liquid fuel. The reacting flow corresponds to bulk velocities, defined as the ratio between the flow rate and the cross sectional area, equal to U_O=30m/s (Re_O=49500) in the air stream and U_{gas}=1.8ms (Re_I=3000) in the gas stream, corresponding to a flame with an air to fuel volumetric ratio (AFR) equal to 27.6 and a heat load of about 350kW. The non-reacting flow analysed throughout this work was obtained by replacing the propane gas by air with the same momentum flux, which results in a Reynolds number equal to 4000 in the inner flow.

The origin of the axial axis, x, is taken at the center of the exit plane of the model burner and the tangential velocity is taken positive in the anticlockwise direction, as facing the burner. The burner is located vertically directed upwards and the symmetry of the flow was verified by measuring several complete radial profiles in the horizontal plane.

Velocity measurements have been obtained with a dual-beam laser-Doppler anemometer similar to that described by Durão et al. (1990), based on an argon-ion laser light source at 514.5nm (1W nominal) with sensivity to the flow direction provided by light-frequency shifting from acoustico-optic modulation (double Bragg cells) with a resulting shift of the Doppler signal in the range 0-10MHz. The half-angle between the beams was 4.92° and the calculated dimensions of the measuring volume at the e^{-2} intensity were 1.528 and 0.132mm. The transfer function in the

absence of frequency shift was 0.33MHzm^{-1}s. Forward-scattered ligth was collected and focused into the pinhole aperture (0 300 mm) of a photomultiplier tube with a magnification of 0.74. The band-passed filtered Doppler signals were processed by a commercial frequency co (TSI 1980B) interfaced with a 16-bit microcomputer.

The complete LDV system was fixed and the burner was mounted on a three-dimensional traversing unit, allowing the positioning of the control volume within ±0.25mm. The distributions of the Reynolds shear stresses $\overline{u'v'}$ and $\overline{u'w'}$ and corresponding triple correlations were obtained by traversing the control volume along two normal diameters with the laser beams in the horizontal and vertical planes and at ±45°, as described by Durst et al. (1981)

The accuracy of the velocity measurements obtained in the present flow have been discussed in previous works and only a summary is presented here. Transit broadening (e. g., Zhang and Wu, 1987) and non-turbulent Doppler broadening errors (e. g., Kreid, 1974) affect mainly the variance of the velocity fluctuations and are estimated to be smaller than $5x10^{-5}U_o^2$ and $1x10^{-3}\ U_o^2$, respectively. The number of individual velocity values used to form the averages was always above 15000, which results in statistical (random) errors smaller than 1% and 4%, respectively for the mean and variance values for a 95% confidence interval (e. g., Yanta & Smith, 1978).

Systematic errors due to sampling bias were minimized by using data acquisition rates in the range 5 to 10khz and, therefore, higher than the fundamental velocity fluctuation rate (e. g., Dimotakis, 1978). Following the analysis of Glass and Bilger (1978) for coflowing streams, these errors are less than +9% and -10% for the mean and variance values, respectively. In order to minimize bias errors due to unequal particle densities in the inner and outer air flows, e g., Durão et al (1991), the two streams, as well as the ambient air in the vicinity of the burner head were seeded separately with powdered aluminium oxide (0.6 to 1μm nominal diameter before agglomeration) dispersed in purpose-built cyclone generators (e. g., Glass and Kennedy, 1977). In addition all the measurements were weighted with the time between events in order to minimize bias errors in regions of low particle densities. "Fringe (angle)" bias is minimized by using large values of the frequency shifting (e. g., Durst & Zaré, 1975) and for the present case the acceptance angle (see Lau et al., 1981) was 360° for a fringe to particle velocity ratio larger than 1, which could be achieved with a frequency shift up to 10Mhz

Based on the analysis of Heitor et al. (1987) the velocity averages should be density weighted.

3. RESULTS

Figure 1 shows the measured streamline distributions and indicate the most salient features of the mean flow in the vicinity of the burner head for reacting and non-reacting conditions. The two flows have similar patterns with qualitatively similar distributions of mean velocity (not shown here due to lack of space), which are typical of those observed in highly rotating flows and include a central swirl driven recirculation zone surrounded by an annular forward flow region where the maximum tangential velocities occur with absolute values about 80% of the annular bulk velocity. For reacting conditions the reverse flow zone is characterized by uniform and high mean temperatures, as in other recirculating flames (e g., Heitor et al., 1987; Tangirala et al., 1987). Despite the qualitative similarities between the two flows, combustion induces significant quantitative differences: the mean axial and tangential velocities increase because the density is lowered and the axial and angular momentum must be conserved; the recirculated mass flow rate decreases from 67% in the non-reacting flow to 14% in the reacting flow as a result of the reduction in density; the length of the recirculation zone decreases by 32.5% and its maximum width increases by about 12%. These effects of combustion are similar to those reported in the literature for flames with high swirl numbers (e. g., Claypole and Syred, 1981; Hillmanns et al., 1986; Tangirala et al., 1987) but must be contrasted with measurements reported for flames with low swirl numbers, even though with swirl-induced recirculation zone (e. g , Chigier and Dvorak, 1975, Tangirala et al., 1987).

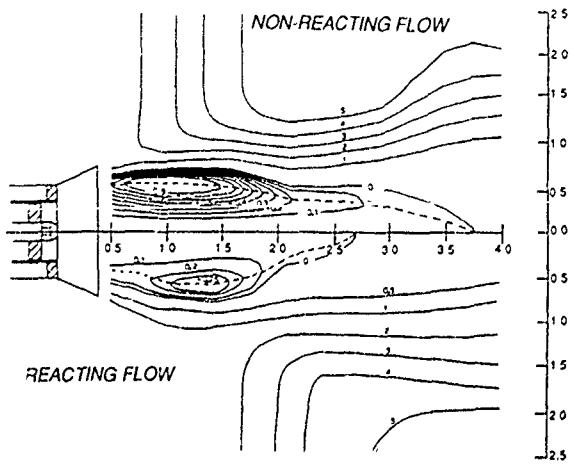

Figure 1 - Measured streamline distributions for non-reacting and reacting (AFR=27) flows, Re=49500.

Inspection of figure 2 reveals that combustion does not affect significantly the turbulent flow upstream of x/D_o=1.0, where the general levels of velocity fluctuations are small inside the recirculation zone and large in the highly strained annular shear layer. In this region turbulence is strongly anisotropic with $\overline{u''^2}_{max}=2.2\overline{v''^2}_{max}=2.2\overline{w''^2}_{max}$ in the non-reacting flow and $\overline{u''^2}_{max}=1.33\overline{v''^2}_{max}=2.0\overline{w''^2}_{max}$ in the reacting flow. Downstream of x/D_o=1.5 both flows show distinct features: in the non-reacting flow, the three normal stresses decrease as the distance to the burner increases, with $\overline{v''^2}$ and $\overline{w''^2}$ sligtly larger than $\overline{u''^2}$ in the vicinity of the rear stagnation point; on the other hand $\overline{v''^2}$ and $\overline{w''^2}$ increase considerably towards the stagnation point in the reacting flow, in a way similar to that observed by Heitor et al (1987) and Castro and Haque (1987) in highly recirculating flows downstream of baffles. The iso-contours of turbulent kinetic energy show that maximum values occur along the edge of the backflow region in the non-reacting flow, while in the reacting flow the largest values occur in the vicinity of the rear stagnation point. As a result, the reacting flow is strongly anisotropic with probability-density distributions suggesting the presence of flow peridiodicity. The evidence of periodic oscillations in the frequency spectra of the velocity fluctuations, could only be observed in the vicinity of the rear stagnation point of the reacting flow (namely around r/D_o=0.0, x/D_o=2.7) where the spectrum of radial velocity fluctuations have shown a peak around 30Hz Analysis (Moreira, 1991) has shown that when this frequency is scaled with the flow parameters in the shear layer adjacent to reverse flow zone, the local Strouhal number is of the order of those characterizing the "bursting" phenomena in turbulent shear layers (e. g., Strickland and Simpson, 1975, Simpson et al , 1981). Although the energy contained in the frequency peak is only about 4% of the total spectral energy, the observation suggests the likely importance of intermittency in the mixing process between the hot fluid inside the recirculation zone and the heterogeneous density field, in a way similar to that observed in other comparatively simple flows with density gradients, e. g., Rajagopalan and Antonia (1981).

The distributions of the shear stress, $\overline{u''v''}$, have maximum values coincident with those of $\overline{u''^2}$, with increased values for the reacting flows. The sign of the shear stress is related to the sign of the shear strain $\partial\tilde{U}/\partial r$ in accordance with a turbulent viscosity hypothesis (e. g., Jones and Whitelaw, 1985) except for a narrow zone in the upstream part of the shear layer adjacent to the reverse flow zone in the reacting flow, where the shear strain is close to zero as in other recirculating flows (see, for example, Heitor et al., 1987).

Structural parameters have been calculated from the results to quantify the extent up to which the nature of turbulence has changed owing to combustion. The correlation coefficient for the shear stress, $R_{uv}=\overline{u''v''}/(\overline{u''^2}+\overline{v''^2})$, in the inner shear layer (where $\partial\tilde{U}/\partial r>0$) is found to follow similar trends in the non-reacting and reacting flows. R_{uv} increases from -0.3 at the exit

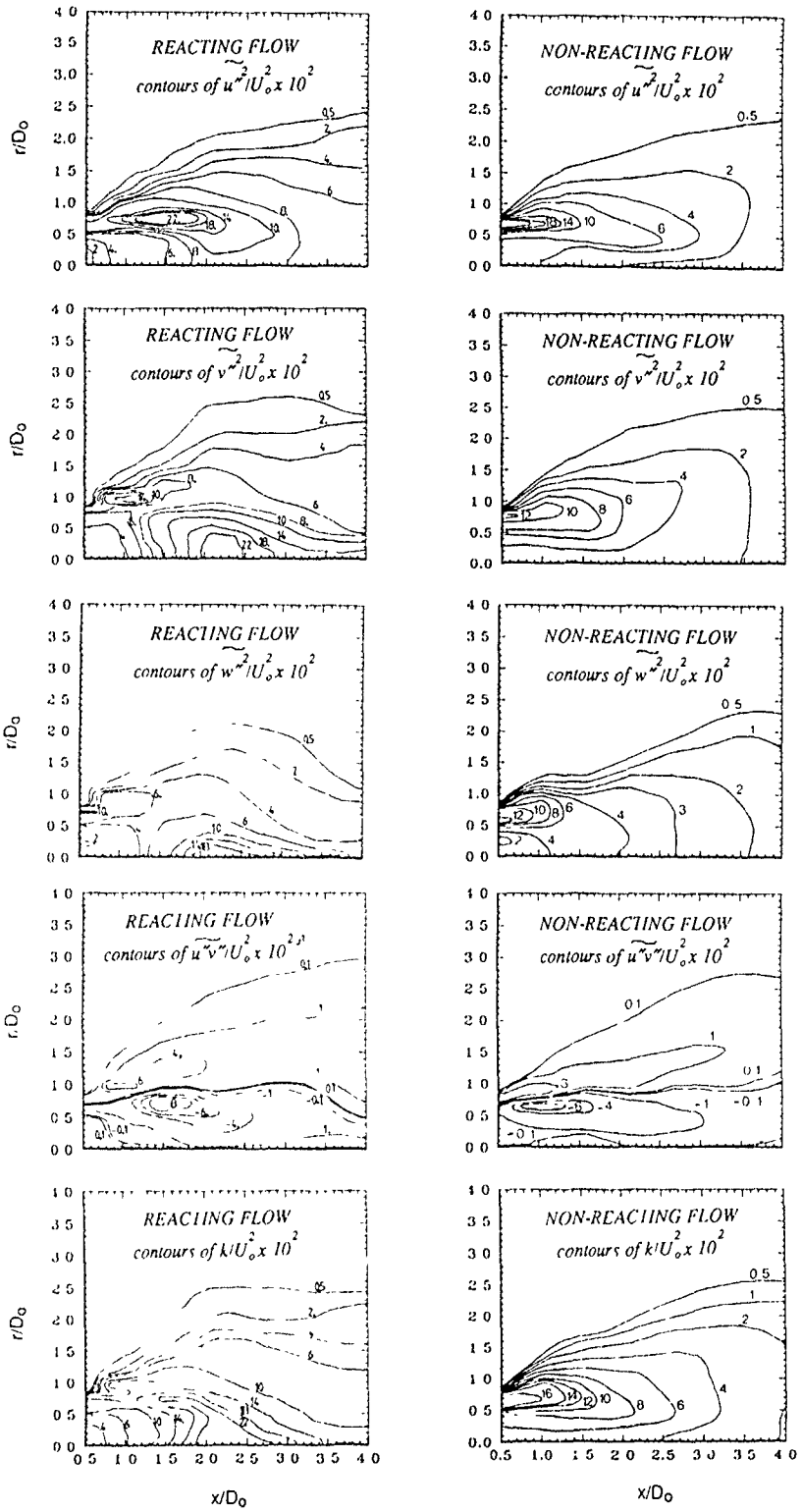

Figure 2 - Iso-contours of Reynolds stresses for non-reacting and reacting (AFR=27) flows, Re=49500; a) Axial normal stress, $\widetilde{u''^2}/U_o^2 x10^2$; b) Radial normal stress, $\widetilde{v''^2}/U_o^2 x10^2$; c) Tangential normal stress, $\widetilde{w''^2}/U_o^2 x10^2$, d) Reynolds shear stress, $\widetilde{u''v''}/U_o^2 x10^2$; e) Turbulent kinetic energy, $k/U_o^2 x10^2$

plane of the quarl (x/D_o= 0.6) up to about -0.7 at x/D_o=1.0 and decreases to a constant value equal to -0.4 far downstream. Similar trends have been observed in other recirculating flows (e. g., Chandrsuda and Bradshaw, 1981; Heitor et al., 1987) and were attributed by Smiths et al. (1979) to the presence of extra-strain rate as a result of streamline curvature. In the outer shear layer (where $\partial\widetilde{U}/\partial r<0$) combustion increases the peak values of R_{uv} from 0.4 in the cold flow to about 0.7, suggesting the presence of competitive effects due to dilatation, as referred by Ballal (1975). In addition, the distributions of the ratio between the shear stress and turbulent kinetic energy, $\widetilde{u''v''}/k$ have shown

values smaller than 0.3 (e. g., Harsha and Lee, 1970) in the inner shear layer of the reacting flow in agreement with the observations of Smiths et al. (1979), Gibson and Younis (1983) and Gibson et al. (1984) and values larger than 0.3 in the outer shear layer. The criteria suggest that the shear stress in our reacting flow is primarily induced by streamline curvature and dilatation effects, respectively in the inner and outer shear layer and that large scale motions are likely to have minor importance in the balance of turbulent kinetic energy.

4 DISCUSSION

The results analysed in the previous paragraphs quantify the effect of combustion on the velocity characteristics of the recirculating flow analysed throughout this work. As in other combustion systems, the heat release accompanying combustion results in acceleration of the flow and in higher levels of the turbulent fluctuations in the high mean velocity regions of the flow. However, the extent up to which this is due to "flame-generated turbulence" (e. g., Bilger, 1986) remains to be quantified. This is because in uniform density flows turbulent kinetic energy is generated by the action of the turbulent shear stresses on the mean velocity gradients and the presence of combustion greatly increases the mean shear by the heat release. Reynolds stresses are also increased in line with the increased turbulence levels and so production of turbulent kinetic energy by mean shear is greatly increased. Therefore, the so called "flame-generated turbulence" could merely be shear-generated turbulence.

The measurements of the mean and turbulent velocity characteristics reported in the previous section allow to estimate the convection and production terms in the transport equations for turbulent kinetic energy and for Reynolds shear stresses and help to quantify the mechanisms involved in the generation of turbulence. The estimates are approximate because of the error in evaluating the spatial gradients, but the values are sufficiently accurate for the purpose of establishing the relative importance of the separate terms in the conservation equations.

Figure 3a) shows radial profiles of the production and convection terms in the equations for turbulent kinetic energy normalized by rU_O^3/D_O for the reacting and non-reacting flows, with convection plotted so that a negative value represents a gain The results show distributions in the outer shear layer (where $\partial\widetilde{U}/\partial r<0$) similar to those observed in mixing layers free of curvature (e. g., Gutmark and Wygnanski, 1976, e. g., Chandrsuda and Bradshaw, 1982): production is mainly due to the interaction between shear stress and shear strain and is balanced by turbulent diffusion and dissipation. In the core of the annular jet turbulence production by normal and shear stresses is negligible and convection is the largest term and represents a gain, which is balanced by turbulent diffusion and dissipation. For smaller radius, in the region of the separation streamline and upstream of stagnation (i. e., $x/D_O<2.0$), the distribution of the various terms for reacting and non-reacting flows resembles that of the mixing layer of Wood and Bradshaw (1981) and upstream of the reattachment zone in the backstep flows of Chandrsuda and Bradshaw (1981) and Pronchick and Kline (1983): convection is small, production is mainly by shear stress and turbulent diffusion and dissipation are important and represent a loss. Around $x/D_O=2.1$, the deflection of the separation streamline (figure 1) occurs in a zone where turbulence production by the interaction of normal stresses with normal strain is large, with maximum values in the vicinity of the centre line for the reacting flow and for larger radius for the isothermal flow. This observation is in accordance with the high values of $\widetilde{v''^2}/\widetilde{u''^2}$ measured in the vicinity of the stagnation point for the reacting flow and agrees with the results of Heitor et al. (1987) in a baffle-stabilized flame.

The terms in the transport equation of shear stress $\widetilde{u''v''}$, not shown here due to lack of space, show that production is dominated over the whole length of the measurements by the

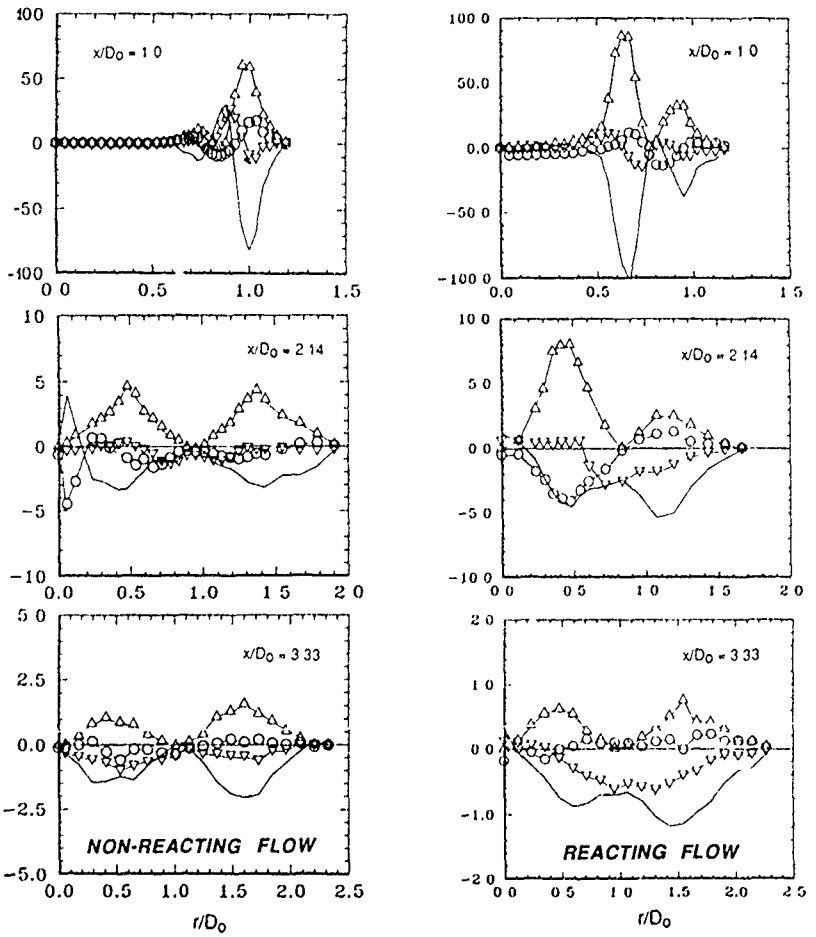

O - Production by normal stresses, Δ - Production by shear stresses, ∇ - Convection, —— Imbalance

Figure 3 - Radial profiles of the production and convection terms in the conservation equation for turbulent kinetic energy in the non-reacting and reacting (AFR=27) flows, Re=49500

interaction of normal stress with shear strain, i. e., $\overline{v''^2}\,(\partial\overline{U}/\partial r)$, as in the swirling jet of Ribeiro and Whitelaw (1980) and in recirculating flame of Heitor et al. (1987). Around the core of the annular jet, where $\overline{u''v''}=0$, this term reverses its sign, but either in the inner or outer parts of the flow is likely to be balanced by pressure-redistribution terms.

It should be noted that distributions of figure 3 for the reacting flow do not include the source terms involving the mean pressure gradient, i. e. $-\overline{u''_i}\,\partial\overline{P}/\partial x_i$, which are associated with the presence of "flame-generated" turbulence (see, for example, Bilger, 1986, Takagi et al., 1985). It is clear that the importance of these terms depends on the co-existence of large values of $\partial\overline{P}/\partial x_i$ with $\overline{u''_i}$, which depends on the particular flame under analysis. For example, they were found to be small in the jet diffusion flame of Starner and Bilger (1989), but of the same order of the shear generation terms and act as to supress the turbulence and mixing in the confined swirling flame of Takagi et al. (1985). Also, Heitor et al. (1987) have shown that although these terms may be small in the conservation of turbulent stresses, the corresponding term in the conservation of turbulent heat fluxe is an important source term in baffle-stabilized flames and gives rise to non-gradient diffusion processes. Estimates of the present mean pressure gradients from the conservation of momentum, not shown here due to lack of space, have shown that and $\partial\overline{P}/\partial r$ are of the same order of magnitude in the vicinity of the stagnation zone, but have opposite signs and act, respectively, as a sink of $\overline{u''^2}$ and a source of $\overline{v''^3}$. It remains rather speculative to conclude that the terms cancel each other and result in a negligible contribution in the conservation of turbulent kinetic energy, as in the recirculating flame of Heitor et al. (1987), but it is clear that they contribute for the increased anisotropy observed in the present reacting flow. The direct implication of these results to the modelling of turbulent flames in swirling burners is that closure should be achieved at the level of transport equations for the individual stresses and that those processes arising from variable density should be represented directly.

Difussion of turbulent energy and shear stress may be associated with the gradients of third-order correlations of velocity fluctuations, which are strongly affected by both longitudinal curvature and proximity of a stagnation zone and has been attributed to large-scale motions (e. g., Castro and Bradshaw, 1976; Ribeiro and Whitelaw, 1980). Figure 4 shows radial profiles across the recirculation bubble of the triple products $\overline{u''^2v''}$, $\overline{v''^3}$, and $\overline{u''v''^2}$, which represent the turbulent radial fluxes of $\overline{u''^2}$, $\overline{v''^2}$ and $\overline{u''v''}$ respectively. The results show that the triple velocity correlations are one order of magnitude smaller than the corresponding Reynolds stresses and have distributions qualitatively similar to those in the shear layer upstream the reattachment zone and within the recirculation region in the backstep flows of Chandrsuda and Bradshaw (1981), Driver and Seegmiller (1983) and Pronchick and Kline (1983) or within the recirculation zone of the baffle-stabilized premixed flame studied of Heitor et al. (1987). The distributions of figure 4 also show that turbulent transport of both normal and shear stresses is mainly in the gradient sense. In addition, $\overline{u''^2v''}$ and $\overline{v''^3}$ are negative along the edge of the recirculation zone and are associated with the transport of turbulent kinetic energy from

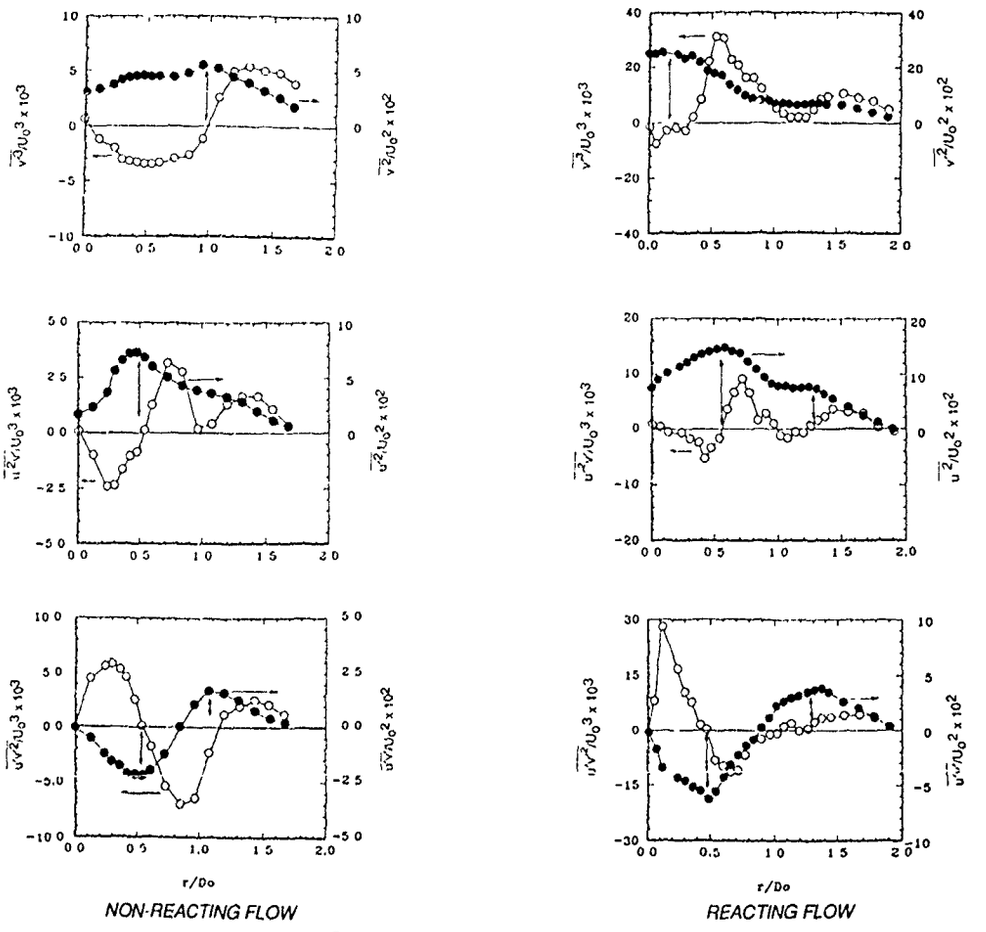

Figure 4 - Radial profiles of third-order velocity correlations at x/D_O= 2.1 for non-reacting and reacting (AFR=27) flows, Re=49500

the highly turbulent shear layer to the backflow region of weak turbulent fluctuations, as in other recirculating flows (e. g., Simpson et al., 1981; Gould et al., 1990). However, minimum values of $\overline{v''^3}$ diffuse towards the centerline faster than those of $\overline{u''^2 v''}$, suggesting that the radial transport of $\overline{v''^2}$ towards the stagnation point is faster than that of $\overline{u''^2}$. This observation is similar to the effect of streamline curvature observed by Gibson et al. (1984) and is consistent with the strong anisotropy induced by combustion in the vicinity of the centerline. In the outer shear layer, where $\partial\overline{U}/\partial r<0$, the distributions of the triple velocity correlations are in agreement with those observed in axisymmetric flames (e. g., Stärner, 1986) and plane mixing layers (e. g., Wood and Bradshaw, 1981).

5 CONCLUSIONS

Laser-Doppler measurements of the flow downstream of a model burner have provided information about the effect of combustion on turbulent transport processes typical of swirling recirculating flames. The results have been obtained for a flow dominated by the presence of a large recirculation zone, which is curved along its length and imposes mean velocity effects on the turbulent field. The velocity characteristics of the combusting flow are qualitatively similar to those of the equivalent isothermal flow, although combustion decreases the recirculated mass flow rate and the length of the recirculation zone and increases its width. The turbulent flows are anisotropic with increased deviations from isotropy around the rear stagnation zone in the reacting flow. Analysis has shown evidence of large scale motions with a predominant frequency around 30Hz, although their contribution to the time average turbulent kinetic energy is shown to be small.

Inspection of the terms in the conservation equations for the turbulent stresses show that the interaction between normal stresses and normal strains influences the turbulent flow in the vicinity of the rear stagnation point and suggest that extra source terms, such as those due to the effects of mean pressure field are unimportant in the present unconfined flame. The results also indicate that turbulent diffusion and dissipation are likely to be important in the balance of turbulent kinetic energy, particularly near the stagnation and along the annular swirling jet.

ACKNOWLEGMENTS

The experiments were performed at the Centro de Termodinâmica Aplicada e Mecânica dos Fluidos da Universidade Técnica de Lisboa, CTAMFUTL-INIC Financial support has been provided by the Comission of the European Communities under the contract SCIENCE SC1-0459

REFERENCES

Bilger, R W (1986). "The use of advanced laser diagnostics for the study of turbulent reacting flows", Proc. 9th Australasian Fluid Mech. Conf, Auckland, 8-12 December, pp. 545-548.

Bilger, R W (1991). "Basic Considerations", In Experimental Methods in Combusting Flows, ed by A M K P Taylor, *Academic Press*, p 1

Castro, I P and Bradshaw, P (1976) "The turbulence structure of a highly curved mixing layer", J. Fluid Mech., 73, pp 265-304.

Castro, I. P. and Hague, A. (1987). "The structure of a turbulent shear layer bounding a separation region", J. Fluid Mech , 179, pp. 439-468

Chandrsuda, C and Bradshaw, P (1981) "Turbulence structure of a reattaching mixing layer", J Fluid Mech., 110, pp 171-194.

Chen, R-H. and Driscoll, J. F (1988) "The role of the recirculation vortex in improving fuel-air mixing within swirling flames", 22nd Symp. (Intl.) on Combustion, *The Combustion Institute*, Pittsburg, pp. 531-540.

Chigier, N A and Dvorak, K (1975) "Laser anemometer measurements in flames with swirl", 15th Symp. (Intl.) on Combustion, *The Combustion Institute*, Pittsburg, pp 573-585.

Claypole, T. C and Syred, N (1982). "The stabilization of flames in swirl combustors", J. Inst. of Fuel, pp 14-19.

De, D S. (1981). "Measurements of flame temperature with multiple element thermocouple", J. Inst. Fuel, pp 113-116.

Dimotakis, P. E. (1978). "Single scattering particle laser-Doppler measurements of turbulence", AGARD Symp on Non-Intrusive Instrumentation in Fluid Mechanics, Saint-louis, France

Driver, D M and Seegmiller, H. C. (1983). Features of a reattaching turbulent shear layer subject to an adverse pressure gradient", paper AIAA 82-1029.

Durão, D. F. G. and Heitor, M V. (1991). "Modern diagnostic techniques for combusting flows. and overview", In. Combusting Flow Diagnostics, ed. by D F. G Durão et al , *Kluwer Academic Publ* , p. 1. in press.

Durão, D. F. G., Heitor, M. V. and Moreira, A. L N. (1991). "Flow Measurements in a Model Burner - Part 1", J. Fluids Eng., to appear.

Durão, D. F. G., Heitor, M V. and Moreira, A. L N (1990). "The Turbulent Characteristics of the Swirling flow in Typical Burners", In: Engineering Turbulence Modelling and Experiments, Edited by W. Rodi and E. N. Ganic, *Elsevier*, pp. 705-716.

Durst, F., Melling, A. and Whitelaw, J. H. (1981). "Principles and Practice of Laser-Doppler Anemometry, *Academic Press*, 2nd edition.

Durst, F. and Zaré, M. (1975). "Laser Doppler measurements in two-phase flows". In: The accuracy of flow measurements by laser Doppler methods, Proceedings of the LDA Symposium, Copenhagen, pp 403-429.

Gibson, M. M. and Younis, B. A (1983). "Turbulence measurements in a developing mixing layer with mild destabilising curvature", Exp. in Fluids, 1, pp. 23-30.

Gibson, M M., Verriopoulos, C. A. and Vlachos, N. S. (1984). "Turbulent boundary layer on a mild curved convex surface", Exp. in Fluids, 2, pp. 17-24.

Glass, M. and Bilger, R. W. (1978). "The turbulent jet diffusion flame in a co-flowing stream - some velocity measurements", Comb Sci. and Tech., 18, pp. 165-177

Glass, M. and Kennedy, I. M (1977). "An improved seeding method for high temperature laser Doppler velocimetry", Comb. and Flame, 29, pp. 333-335.

Gould, R D , Stevenson, W. H. and Thompson, D. (1990). "Investigation of turbulent transport in an axisymmetric sudden expansion", AIAA J., 28 (2), pp. 276-283.

Gutmark, E. and Wygnanski, I. (1976). "The planar turbulent jet", J. of Fluid Mech., 73, part 3, pp 465-495.

Hardalupas, Y,. Taylor, A. M. K. P. and Whitelaw, J. H. (1990) "Velocity and size characteristics of liquid-fuelled flames stabilized by a swirl burner", Proc. R. Soc. London A, 426, pp. 129-155.

Harsha, P. T. and Lee, S. C. (1970). "Correlation between turbulent kinetic stress and turbulent kinetic energy", AIAA J., 8, pp. 1508-1510.

Heitor, M. V., Taylor, A. M. K. P and Whitelaw, J. H. (1987). "The interaction of turbulence and pressure gradients in baffle-stabilized premixed flame", J. Fluid Mech , 181, pp. 387-413.

Heitor, M. V., Taylor, A M. K. P. and Whitelaw, J. H. (1988). "Velocity and scalar characteristics of turbulent premixed flames stabilized on confined axisymmetric baffles", Comb. Sci. and Tech., 62, pp 97-126.

Hillmanns, R., Lenze, B. and Leuckel, W. (1986) "Flame stabilization and turbulent exchange in strongly swirling natural gas flames", 21st Symp. (Intl.) on Combustion, *The Combustion Institute*, Pittsburg, pp. 1445-1453.

Inze, N. Z. and Launder, B. E (1989). "On the computation of buoyancy-driven turbulent flows in rectangular enclosures", Int. J. Heat Fluid Flow, 10, pp. 282-299.

Jones, W. P and Whitelaw, J. H (1985). "Modelling and measurements in turbulent combustion", 20th Symp (Intl.) on Combustion, *The Combustion Institute*, Pittsburg, pp. 233-249.

Kreid. D.K. (1974) "Laser-Doppler velocimetr measurements in non-uniform flow· error estimates". *Appl. Optics*, 13, N° 8, pp. 1872-1881.

Lau, J. C., Whiffen, M C , Fisher, M. J. and Smith, D. M. (1981). "A note on turbulence measurements with a laser velocimeter", J. Fluid Mech., vol. 102, pp. 353-366.

Moreira, A. L. N. (1991).Experimental analysis of combusting systems, (In Portuguese). Ph D. Thesis, Instituto Superior Técnico, Lisboa

Paranthoen , P., Lecordier, J. C., Petit, C. and Gajan, P. (1982). "Survey and recent developments of frequency response studies of cold wires and fine wire thermocouple in turbulent heated flows", 8th Australasian Fluid Mech. Conf., Univ of Newcastle, pp. 6B1-6B4.

Pronchick, S W and Kline, S. J. (1983) "An experimental investigation of the structure of a turbulent reattaching flow behind a backward-facing step", Report MD-47, Thermosci Division, Dept. Mech Eng., Stanford Univ

Rajagopalan, S. R. and and Antonia, R A. (1981) "Properties of the large structure in a slightly heated turbulent mixing layer of a planar jet", J Fluid Mech., 105, pp. 261-281.

Rhine, J M. and Tucker, R J. (1991). Modelling of Gas-Fired Furnaces and Boilers, *British Gas- McGraw-Hill*, London

Ribeiro, M. M. and Whitelaw, J. H (1980) "Coaxial jets with and without swirl", J. Fluid mech., 96, part 4, pp. 769-795.

Strickland, J. H. and and Simpson, R. L. (1975) "Bursting frequencies obtained from wall shear stress fluctuations in a turbulent boundary layer", The Physics of Fluids, 18 (3), pp. 306-308

Simpson, R. L , Chew, Y T. and Shivaprasad, B. G. (1981). "The structure of a separating turbulent boundary-layer. Part 1 Higher order turbulence results", J. Fluid Mech., 113, pp. 53-73.

Smiths, A. J., Young, S. T. B. and Bradshaw, P. (1979). "The effect of short regions of high surface curvature on turbulent boundary layers", J. Fluid mech., 94, part 2, pp. 209-242.

Stärner, S. H (1986). "Some Triple Correlation Measurements of Velocity and Scalars in a Turbulent Diffusion Flame", Comb. Sci. and Tech., 48, pp. 99-105.

Stärner, S. H. and Bilger, R. W. (1987). "Some budgets of turbulent stresses in round jets and diffusion flames", Comb Sci. and Tech , 53, pp. 377-398.

Stärner, S. H. and Bilger, R. W. (1989). "Further velocity measurements in a turbulent diffusion flame with moderate swirl", Comb Sci and Tech., 63, pp. 257-274.

EIGHTH SYMPOSIUM ON
TURBULENT SHEAR FLOWS
Technical University of Munich
September 9-11, 1991

Turbulence Measurements in a Two-Dimensional Wall-Jet

by

H. Abrahamsson, B. Johansson and L. Löfdahl

Department of Thermo- and Fluid Dynamics
Chalmers University of Technology
412 96 Goteborg
Sweden

Introduction.

The high capacity of todays computers has enabled the extension of turbulence models to strongly anisotropic flow fields, i.e. the interest has been focused on the use of models based on the transport equations for the Reynolds stresses. (RST models.) To improve these turbulence models well-defined, simple and fundamental experiments are needed, in which gradients of the different turbulence parameters are determined. Together with direct simulation of the Navier-Stokes equations these experiments yield a good base for the improvement of the modelling of different terms in the Reynolds equations. An excellent presentation of the closure problem and the terms of interest for the development of turbulence modelling has recently been published by Groth (1991).
A fundamental, well-defined and simple flow case is the wall-jet, where an interaction between a wall boundary layer and a free shear layer forms the anisotropy as well as the inhomogeneous character of the flow field.
A comprehensive literature survey of wall-jets was carried out already in the beginning of the eighties by Launder and Rodi (1980), who studied a large number of different more or less well-defined turbulent wall-jet experiments.
The main conclusion of this survey was a lack of well-defined experiments in simple and fundamental geometries. If the study is limited to the two-dimensional case, a further conclusion from the work of Launder and Rodi was that many of the studied flow cases did not fulfil the condition of two-dimensionality. Although more than ten years have passed since the work of Launder and Rodi was presented, very few investigations have been reported in which fundamental wall-jets have been studied. Especially well-defined turbulence measurements are needed, since the anisotropy of the two-dimensional wall-jet yields a case well suited for the evaluation of, e.g. new dissipation models, see Hallbäck, et.al. (1990).
The purpose of the present work was to determine the turbulence field of a two-dimensional wall-jet in a simple and also well-defined geometry without influence of an outer disturbing flow field. To accomplish these measurements a wall-jet rig was used. All turbulence measurements were carried out using hot-wire techniques, single- and cross-wires. The measurements presented here were performed at a Reynolds number of 10^4, based on the slot height, and the extension of the measurements in the flow direction was in the range of x/h = 25 through x/h = 156. (x-coordinate in the main flow direction and h-slot height.)

Experimental set up.

The wall-jet rig consists of two parts, a settling chamber and a two dimensional "wall-jet part". An ordinary fan blows air into a settling chamber, inside which a baffle is placed to decrease the air motions. The outlet of the chamber is designed as a contraction, according to a method suggested by Morel (1975), with a ratio of 10:1. Before the contraction, a honeycomb and two screens with fine mesh, chosen according to Johansson and Alfredsson (1987), are positioned for the accomplishment of a low turbulence intensity in the outlet. From the outlet of the settling chamber, the wall-jet flows over a flat horisontal plate, which in the two-dimensional case is surrounded by vertical side walls. An aspect ratio of 50:1 was employed in the present rig. The horisontal plate has a thin plastic laminate for obtaining a smooth surface.

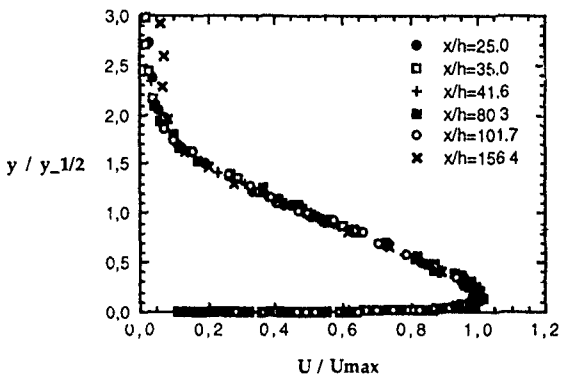

Figure 1. Mean velocity profiles.

The measurements of mean velocities, turbulence intensities and triple correlations were carried out using hot-wire technique. Standard Dantec equipment, i.e. an anemometer system, miniature single- and cross-wires, were employed throughout the whole experiment. In the calibration the voltages were transferred into velocities using a standard function suggested by Siddal and Davies (1972). Standard methods, which could be found for example in Perry (1982), were also used for the evaluation of the turbulence components from the cross-wire measurements. All data aquisitions have been tested in a two-dimensional flat plate boundary layer, as has been described by Löfdahl (1986) and in Lofdahl et.al. (1991).
The friction velocity u^*, was determined using Preston tubes, calibrated according to Patel (1965).

Results and discussion.

To validate the wall-jet rig, hot-wire measurements in the normal as well as spanwise direction were carried out for the determination of the velocity distribution at the outlet of the slot. These measurements showed that the flow was very uniform, the mean velocity variations were less than 1%, and had, as mentioned, an extremely low turbulence intensity in the main flow direction, of order 0.3%.
To check the two dimensionalities of the rig, the momentum loss was computed according to a method suggested by Launder and Rodi (1981). The estimated momentum losses were found to be less than 8% up to x/h = 100, which was accepted as a criterion for a two-dimensional flow by Launder and Rodi. Accordingly, the present wall-jet rig can be considered as a two-dimensional flow case for the investigated region.
Mean velocity profiles were determined from the outlet to a downstream distance of the order 150 x/h. In Figure 1. these results are shown at positions x/h = 25.0, 35.0, 41.6, 80.3, 101.7 and 156.7. It can be noted from these measurements that the agreement between the profiles at different downstream positions is very good, and that the growth of the half width is approximately 7%, which is in full agreement with the values mentioned in the literature, see for example Launder and Rodi (1981).

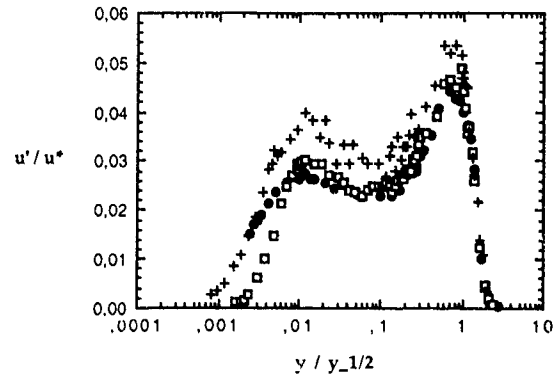

Figure 2. Turbulence intensity in the main flow direction at x/h = 25.0, 41.6 and 101.7 (Legende see Figure 3.)

The turbulence quantities were determined at the same locations as the mean velocities. These measurements are shown in Figures 2 through 6. In Figures 2, 3 and 4 the turbulence intensities at positions x/h = 25.0, 41.6 and 101.7 are shown as a function of the wall distance. Here the typical two maximums of the normal stress in the main flow direction can be observed. One lower maximum in the inner most region, connected to the wall layer, and one further out in the free shear layer. A tendency of these two maxima can be noted in the lateral component, Figure 3, while only the outer maximum is found in the normal component, Figure 4. The reason of the vanishing inner maximum is due to the large measuring volume and the fairly thin boundary layer thickness at the studied positions.

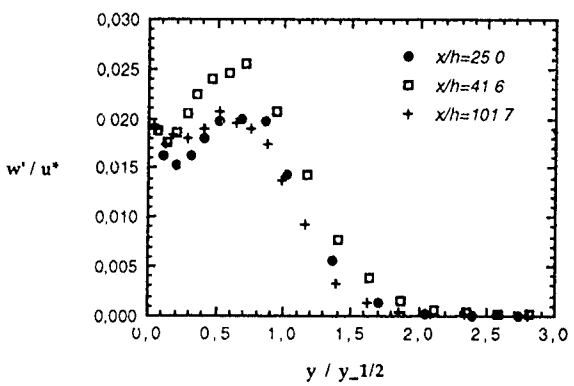

Figure 3. Turbulence intensity in the lateral direction at x/h = 25.0, 41.6 and 101.7

Figure 5 shows the shear stress. Here it can be noted that the change of sign of the shear stress deviates from the position of the maximum of the mean velocity, in accordance with earlier observations, for exemple by Townsend (1976). Further it can be observed from Figures 2 through 6 that the shape and the level of the normal stresses as well as the shear stress agree quite well with the corresponding quantities reported by Dakos et.al. (1984), who studied a slightly similar, but more complex flow field. In Figure 6 the triple correlations at x/h = 41.6 are shown. As can be expected, a comparison with the Reynolds stresses yields a lower level of these correlations. It can also be noted that the studied triple correlations all change sign approximately at $y_{1/2}$ well above the maximum of the mean velocity.

These correlations can also be found in Dakos et.al. (1984), and a comparison yields quite good agreement.

Conclusions.

Turbulence measurements in a well-defined, fundamental and simple two-dimensional wall-jet without outer disturbing flow fields have been carried out. From these measurements the following main conclusions can be drawn:

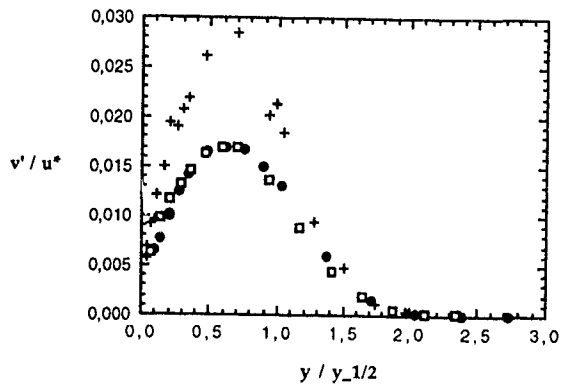

Figure 4. Turbulence intensity in normal direction at x/h = 25.0, 41.6 and 101.7 (Legende see Figure 3.)

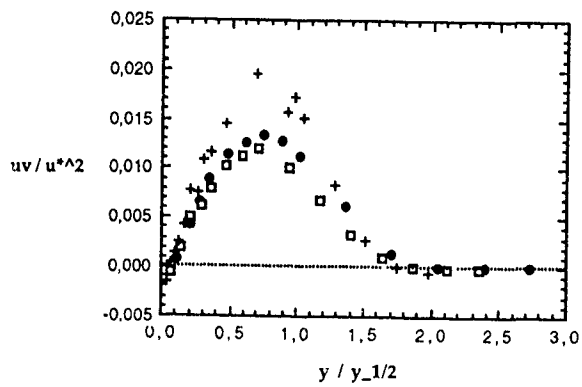

Figure 5. Turbulent shear stress at x/h = 25.0, 41.6 and 101.7 (Legende see Figure 3.)

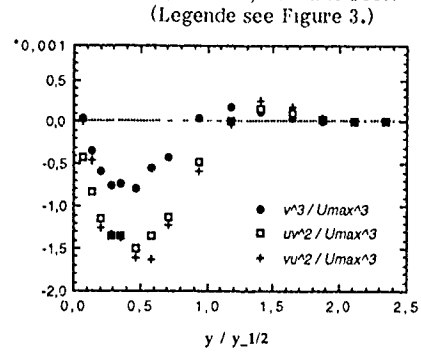

Figure 6. Triple correlations for x/h = 41.6

* The wall-jet rig fulfils the requirements of two dimensionality for the studied region.
* The growth of the wall-jet in the main flow direction has been determined to approximately 7%.
* The turbulence measurements reveal that two clear maximums can be found in the normal stress in the main flow direction. A similar tendency can be found in the other two turbulence intensities.
* The shear stress reveals a change of sign at a certain distance from the wall. This change in the shear stress direction, however, does not concur with the maximum of the mean velocity.
* Three triple correlations have been determined, and all reveal a maximum in the vicinity of the maximum mean velocity. Approximately at $y_{1/2}$ the triple correlation changes sign.

Support from the Swedish National Energy Administration is greatfully acknowledged.

Note: *This paper has been abbreviated by the Editor because it exceeds the given limit of two pages.*

EIGHTH SYMPOSIUM ON
TURBULENT SHEAR FLOWS
Technical University of Munich
September 9-11, 1991

NUMERICAL SIMULATION AND MODELLING OF THE TRANSITION PAST A RECTANGULAR AFTERBODY

M. BRAZA and P. NOGUES

Institut de Mecaniques des Fluides,Laboratoire associe au C.N.R.S
Av. du Professeur Camille Soula, 31400 Toulouse Cedex, France

ABSTRACT

An improved zero-equation turbulence model is implemented in the phase-averaged Navier-Stokes equations. This allows the simulation of the unsteady flow with coherent structures, past a rectangular afterbody in the transition towards turbulence.

INTRODUCTION

The numerical simulation of the onset of transition in an unsteady wake past an obstacle at uniform stream has been the object of numerous experimental and numerical works. Especially in the case of cylindrical configurations, vortex shedding and Strouhal number mesurements have been done (Roshko(1),Tritton(2), Gerrard(3), Williamson (4)) The loss of symmetry in the flow pattern in the case where Reynolds number increases beyond a critical value, and the appearance of vortex shedding, constitute a first step of the flow transition towards turbulence. Recent works by Williamson show the role of the oblique shedding in finding a universal and continuous relation of the Strouhal number versus Reynolds number in the low Reynolds number regime.

In the domain of numerical simulation of this problem, there are also numerous studies solving the unsteady Navier-Stokes equations and predicting the vortex shedding and the Strouhal number with a relative agreement with the physical experiment (Lin & al.(5), Martinez(6), Braza & al.(7), Lecointe & al. (8)). In the case of rectangular bodies, the numerical simulation of Davies and Moore (9) predicts also the vortex shedding for a uniform flow upstream.

However, there are less experimental and numerical works analysing the fundamental mechanism in the case of an externally imposed velocity shear. Experiments made by Brown and Roshko (10) studied in details the onset and the evolution of vortices in mixing layers, whereas Winant and Broward (11) analysed pairing phenomenon between vortices of a free mixing layer. Concerning the mixing layer dynamics past a rectangular body, the experimental study of Bourgeois (12) indicates clearly a change in the flow transition whenever the velocity gradient imposed upstream becomes higher than a critical value. Then the double array of Karman vortices becomes a single array of vortices.

In this paper, an attempt to analyse this mechanism is carried out related to a velocity shear imposed as an inlet boundary condition for the flow past a rectangular afterbody, for Reynolds numbers 500 and 574. Furthermore the transition to turbulence at a higher value at Reynolds number (Re=3000) is studied by proposing a model based on the phase-averaged time dependent Navier-Stokes equations and on the eddy viscosity assumption. This model is adapted to respect the simultaneous development of organised periodic structures and of the random motion, during transition towards turbulence

NUMERICAL PROCEDURE

Theoretical equations

First, every unknown function field is splitted up in two separate parts:

- A first part represented by the phase-averaged operator < >, which regroups all organised characteristics, predictable by Navier - Stokes equations.
- A second part regrouping chaotic characteristics, due to random turbulence, which develops simultaneously with the organised motion

Thus, we adopt the following decomposition of the flow field :

$$U_i = \langle U_i \rangle + u_i . \qquad (1)$$

This decomposition has been applied by Ha Minh and al.(13) as well as by Franke and al.(14), for flows with a periodic component. Owing to this decomposition, and because of the non linear convective term of the Navier - Stokes equations, second order correlations $\langle u_i u_j \rangle$ appear in the phase-averaged equations. These correlations are similar to the Reynolds stresses, and they are modelled according to a turbulent viscosity concept, as follows .

$$- \langle u_i u_j \rangle = \nu_t \left(\frac{\partial \langle U_i \rangle}{\partial x_j} + \frac{\partial \langle U_j \rangle}{\partial x_i} \right) - \frac{2}{3} k \delta_{i,j} . \qquad (2)$$

The introduction of equation (2) in the averaged transport equations yields the following set of equations :

* **Continuity equation** : $\mathrm{div} \langle U_i \rangle = 0 .$ (3)

* **Momentum phase-averaged equation** :

$$\frac{\partial \langle U_i \rangle}{\partial t} + U_j \frac{\partial \langle U_i \rangle}{\partial x_j} = - \frac{\partial}{\partial x_i} \left(\langle P \rangle + \frac{2}{3} \langle k \rangle \right) + \frac{\partial}{\partial x_j} \left[(\nu + \nu_t) \frac{\partial \langle U_i \rangle}{\partial x_j} \right] + \frac{\partial}{\partial x_j} \left(\nu_t \frac{\partial \langle U_j \rangle}{\partial x_i} \right) \qquad (4)$$

where $\langle k \rangle = \langle u^2 + v^2 + w^2 \rangle$ is the turbulent kinetic energy, and ν_t is the turbulent viscosity. In the present work, a zero equation model is adopted: we use the Baldwin-Lomax model in its standard version (15) and in a modified one, adapted to the present flow with organised, coherent structures. This model separates two regions, near and far from the wake, according to two different laws for ν_t. In this model there is no need to fix a boundary between these two regions. This boundary is computed by the continuity of ν_t values. The classical law for the external region gives unacceptable high values for the eddy viscosity, for the present Reynolds number range. For this reason a scaling according to the unsteady vorticity field is introduced in the model (Eq.6). This leads to physically valid results and especially takes into account important transition features carried trough the unsteady vorticity.

Modified Baldwin-Lomax turbulence model

near region : $\nu_t = l^2 |\omega| . \qquad r \le r_c \qquad (5)$

far region : $\nu_t = 0.0269 K_g |\omega| . \qquad r \ge r_c \qquad (6)$

* l = mixing length, for the near wall region, yielded by Prandtl - Van Driest relation: $l = 0.4 (r-a) \left\{ 1 - \exp \left[- 0.0385 (r-a) \sqrt{\frac{\omega_0}{\nu}} \right] \right\}$

ω_0 = wall vorticity.

* K = Klebanoff variable. $K = \max \left\{ 2.5 (r-a)_m h_m ; 0.1 (r-a)_m |u|_m^2 h_m \right\}$

r-a = distance perpendicular to the wall.
$|u|_m$ = maxi. velocity along a section perpendicular to the wall.
h_m = max (h) , with $h = l|\omega|$ along the same section.
$(r-a)_m$ = r - a value , for $h = h_m$.

*g function yielded by the following relation: $g=\left\{1+0.004\left[\frac{r\,a}{(r\,a)_m}\right]^6\right\}^{1}$

v_t is then evaluated by continuity in the variation between the inner and outer law.

The numerical algorithm D.I.A.N.E. has been developed by Braza (16). It is based on a finite-volume, pressure-velocity formulation of the governing equations and on a predictor-corrector pressure scheme by Chorin (17), Amsden & Harlow (18). The finite-volume approximations are second-order accurate in space and time. An Alternating Direction Implicit method (Peaceman & Raschford (19)) is used for the time discretization. The momentum equations are solved for a guess-pressure field $P^* = P^n$. The corresponding approximate velocity field V^* is corrected in order to satisfy the continuity equation by the means of the pressure-correction potential function ϕ and following relation $\vec{V}^{n+1} - \vec{V}^* = -\,\mathrm{grad}\phi$.

This leads to a Poisson equation: $\nabla^2\Phi = \mathrm{div}\,\vec{V}^*$ (7)

Finally, the pressure at (n+1) time step can be evaluated by :

$$\mathrm{grad}P^{n+1} = \mathrm{grad}\left(P^n + \frac{\phi}{\Delta t}\right) + \mathrm{div}\left(V^n\,\mathrm{grad}\phi\right) - \nu\,\nabla^2(\mathrm{grad}\phi). \quad (8)$$

The initial conditions are those of potential flow. The boundary conditions are Dirichlet type for the inlet section and make the assumption that the upper and lower boundaries are stream-lines for the shear layer and the wake flow cases: $\partial u/\partial y=0$ and $v=0$

At the outlet boundary, a carreful study of non-confining and non-reflecting type boundary conditions has been carried out (Braza & al (20)) This leads to the equation :

$$\frac{\partial V}{\partial t} + u\frac{\partial V}{\partial x} - \nu\frac{\partial^2 V}{\partial y^2} = 0\,,\ \text{where V is the velocity vector.} \quad (9)$$

The above sets of boundary conditions allow the vortices to leave out the outlet section, without dangerous feedback effects. Owing to these conditions, the physics of the coherent structures in the computational domain is respected.

Domain scheme

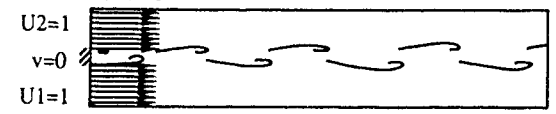

The mesh used is a cartesian one (210 x 300) $(\Delta x)_{min}=\Delta y=0.07$
The time step is $\Delta t=0.01$.

Computation is carried out on the IBM 3090-600-VF computer of the Centre National Universitaire Sud de Calcul (CNUSC).

RESULTS

Some two-dimensional transition features of the flow are simulated at low Reynolds numbers.

a) In the case of uniform upstream flow field (U1=1 and U2=1) the onset of instability leading to alternating vortices is generated naturally in the flow field , without any externally imposed perturbation (fig.1). The dimensionless frequency of the oscillations (Strouhal number) is in very good agreement with the experimental study of Bourgeois for a value of the Reynolds number equal to 500 ($St_{num}=0.192$ and $St_{exp}=0.190$).

b) In the case of an externally imposed shear (U1=0.625 and U2=1.375) the computation at Re=574 and over a long physical time shows that the flow pattern changes completely in fact the double array of vortices is transformed in a single one(fig.2). This can be explained by the action of a global amount of vorticity near the inlet section, which enhances the development of the vortices turning in an opposite sens, relatively to the sens of the inlet shear. However, the periodic character of the present flow pattern (mixing layer) is clearly pointed out.

c) Finally, the performances of the turbulence model for the present flow is studied, for the case of Re=3000, where the onset of turbulence motion is physically clearly pronounced, whereas the organised structures persist. Computation is carried out up to t=100 without any turbulence model. The onset of instability is then clearly obtained. Using the final results as initial conditions, the modified Baldwin-Lomax model is applied. This leads to a flow pattern respecting the physics of the periodic alternating vortices (Fig.3 and 4).

CONCLUSION

Hence, the present study shows the ability of the phase-averaged Navier-Stokes equations with an improved eddy viscosity model to preserve the organised unsteady, periodic motion, developed simultaneously with the onset of turbulence, in the wake past a rectangular afterbody. It is shown that the instability leading to the formation of organized vortices in the wake is clearly obtained without and with application of the present adapted unsteady turbulence model, inserted in the phase-averaged Navier-Stokes equations and taking into account physical characteristics of the transition towards turbulence.

REFERENCES

1/ROSHKO, A. 1954 Report 1191
2/TRITTON, D J. 1971. J. Fluid Mech 45, part 1,203.
3/GERRARD, J H. 1966. J. Fluid Mech 25,1_143.
4/WILLIAMSON, C H.K. 1989 J Fluid Mech , 206.
5/LIN, C., PEPPER, D., LEE, S 1976. AIAA J.14, n°7, 900_907.
6/MARTINEZ, G. 1978. Rapport interne. I.M.F.Toulouse.
7/BRAZA, M ,CHASSAING, P., HA MINH, H 1990. J. Phys. Fluids A , Vol 2 No 8, pp. 1461-1471
8/LECOINTE, Y & PIQUET, J. 1988 *VKY lectures _7*
9/DAVIS, R.W. & MOORE, E F 1982. J Fluid Mech 116,475_506
10/BROWN, G.L.,ROSHKO, A 1974 J. Fluid Mech. 64,775_816
11/WINANT, C D. & BROWARD, F K 1974. J. Fluid Mech. 63, 327
12/BOURGEOIS, M. 1986 Thèse Docteur ès Sciences, U.P.S Toulouse
13/HA MINH, H., VIEGAS , J.R , RUBESIN, M W., VANDROMME, D D & SPALART, P 1989
14/FRANKE, R , RODI, W , SCHONUNG, B 1989 Proc Seventh Symposium on TSF Stanford University August 21-23.
15/BALDWIN, B.S & LOMAX, H. 1978 AIAA paper 78_257
16/BRAZA, M. 1986 Thèse Docteur ès Sciences, I N.P.Toulouse
17/CHORIN, A J. 1968. J. Math. Computation, 22, 745
18/AMSDEN, A A. & HARLOW, F H. 1970. Los Alamos Scientific Laboratory Report L.A -4370
19/PEACEMAN, D.W. & RACHFORD, JR. 1955 J Soc. Indust. Appl Math , 3, N°1, 28.
20/BRAZA, M., JIN, G. & KOURTA, A. 1991 7th International Conference on Numerical Methods in Laminar and Turbulent flow Stanford, CA, U S A

Fig. 1. Isopressure field at T=120, for an uniform flow, with a Reynolds Number of 500. Direct simulation.

Fig. 2. Isopressure field at T=100, for a shear flow, with a Reynolds Number of 574. Direct simulation.

Fig. 3. Isopressure field at T=160, for an uniform flow, with a Reynolds Number of 3000 and the modified Baldwin-Lomax turbulence model.

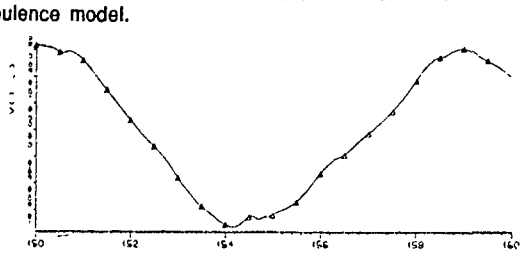

Fig. 4. Time dependent evolution for velocity V component at the point (2,149), with a Reynolds Number of 3000 and the modified Baldwin-Lomax turbulence model.

EIGHTH SYMPOSIUM ON
TURBULENT SHEAR FLOWS
Technical University of Munich
September 9-11, 1991

OSCILLATING AIRFOIL VELOCITY FIELD DURING LARGE AMPLITUDE DYNAMIC STALL

M.S.Chandrasekhara[1] and R.D Van Dyke[2]

[1] Adjunct Research Professor and Assistant Director
[2] Graduate Student

Navy-NASA Joint Institute of Aeronautics
and Fluid Mechanics Laboratory, NASA Ames Research Center
Department of Aeronautics and Astronautics
Naval Postgraduate School, Monterey, CA 93943

1. SUMMARY

The leading edge flow field of an airfoil executing a sinusoidal oscillatory motion and experiencing dynamic stall under compressibility conditions has been studied using a two component LDV system. Phase averaged mean velocity measurements and some flow quantities derived from it are presented and discussed. The results indicate extremely large accelerations of the flow are present around the leading edge with mean velocity values 60% higher than and instantaneous velocities as large as 1.75 times the free stream velocity. The velocity profiles at certain locations over the airfoil resemble that of a *wake*.

2. INTRODUCTION

The problem of dynamic stall of an airfoil is a unique case of forced unsteady separated flows wherein the leading edge flow separates, but the airfoil does not lose lift. It is a complex problem governed by the extremely large flow accelerations that are present around the airfoil leading edge that could result in locally supersonic flow even at very low free stream Mach numbers of 0.2, flow transition to turbulence, movement of the transition point due to the unsteady motion, formation of shock(s) and their interaction with the local boundary layer, the eventual large scale separation at the leading edge with large amounts of vorticity being added to the flow, dependence of all of the above phenomena on the parameters of the unsteady motion such as amplitude, mean angle of attack, degree of unsteadiness and so on. These complexities have defied all attempts to compute the problem with any degree of success at the resolution needed. The understanding of the associated flow physics is crucial before any progress can be made in controlling the dynamic stall flow.

The work to be described pertains to the measurement of flow field in the leading edge region of an airfoil oscillating at a large amplitude when compressibility effects just set in.

3. EXPERIMENT DESCRIPTION

The study is a part of the dynamic stall research project underway at the Navy-NASA Joint Institute of Aeronautics between the Naval Postgraduate School and NASA Ames Research Center(ARC). The experiments were conducted in the Compressible Dynamic Stall Facility (CDSF) in the Fluid Mechanics Laboratory(FML) at ARC. Ref. 1 provides a full description of the facility and its capabilities. It is a unique unsteady flow facility equipped with a drive system located at the top of the test section of an indraft wind tunnel connected to an evacuation compressor. The drive oscillates an airfoil mounted between two optical glass windows sinusoidally. Encoders mounted on the drive provide the airfoil position information continuously. Two component LDV data was obtained for $M = 0.3$ at a reduced frequency of 0.05. Velocities were mappped in a region enveloping $-.167 \leq x/c \leq 0.167$ and $0.083 \leq y/c \leq 0.167$. The complete details of the LDV signal data validation procedures as well as the ensemble averaging method followed could be found in Chandrasekhara and Ahmed.

[1] *Mailing Address: M.S. 260-1, NASA Ames Research Center, Moffett Field, CA 94035*

[2] *Presently: Research Scientist, Naval Weapons Center, China Lake, CA*

4. RESULTS

4.1. Phase Distribution of Velocity

Fig. 1 shows the distribution of the velocity with the phase angle of oscillation,ϕ, at $x/c = 0.067$. It should be noted the drive system causes the airfoil to first to go through a downward motion to an angle of attack, $\alpha = 0$ deg. at $\phi = 90^0$, and then it pitches the airfoil up to an angle of attack of 20 deg. at $\phi = 270^0$ through the static stall angle of 12.4 deg. and back to the mean angle of attack of 10 deg. The velocity drops to its lowest value at $\phi = 90^0$ (at $\alpha = 0^0$) and increases rapidly. For ex. at $y/c = 0.167$, the velocity is approximately equal to the free stream velocity U_∞ at $\phi = 90^0$ and reaches $1.5U_\infty$ at $\phi = 216^0$, where $\alpha = 15.9^0$. This angle corresponds to the dynamic stall angle as determined by the schlieren studies of Chandrasekhara and Carr. From this point, the velocity drops rapidly to $1.25U_\infty$. However, in the fully separated flow, the velocities are still large, $O(U_\infty)$.

One of the most interesting results seen in this graph is the dramatic variation in the behavior seen in the y/c locations closer to the surface of the airfoil. For $y/c = 0.083$ (shown by the symbol ∇),the velocity decreases to $0.9U_\infty$ at $\phi = 90^0$, and begins to increase as expected during the upstroke of the airfoil. However, at $\phi = 155^0$, at $\alpha = 5.5^0$, the velocity drops suddenly to $0.4U_\infty$ over $155^0 \leq \phi \leq 202^0$, corresponding to $5.5^0 \leq \alpha 13.7^0$. Such a drop can be attributed to the presence of a separation bubble that the LDV probe volume encounters as the airfoil pitches up. Once the bubble bursts, the velocity increases quickly as the outer fluid gushes into the void created by the bursting bubble. Eventually at this location, the airfoil blocks off the beams and thus no data can be obtained until a phase angle of $\approx 330^0$, when they are unblocked again. The values seen for the phase angles in between are an artifact of the data processing program. (Also, the copy of the profile seen below is also due to software requiring a pseudo-rectangular grid with equal number of points in each column of the data file.) At the higher locations, the phase angle range over which this dramatic drop occurs decreases as can be expected due to the shape of the bubble. Fig. 1 also shows that the bubble bursts at $\phi = 202^0$, at all y/c locations as could be expected. During this process, the velocity increases. In this figure, excepting at $y/c = 0.167$, all other measurement points are within the separation bubble and the phase variation seen at $y/c = 0.167$ is typical of all points in the flow.

4.2. Velocity Distribution at $x/c = 0.067$

The velocity profiles at various phase angles from 162 degrees to 219 degrees are shown in Fig. 2. At $\phi = 162^0$, the fluid is seen to accelerate closer to the surface. Also, steep changes can be seen in the velocity in the core of the bubble. Eventually as the bubble is cleared (at a phase angle of 202 degrees and beyond), the velocity profile becomes *wake-like*. It appears that the fluid nearer the surface accelerates both above and the below the bubble and the low velocity fluid that was in the bubble has not yet mixed with the fluid surrounding it even though the bubble has burst.

4.3. Velocity Contours at $\phi = 174^0, \alpha = 8.95^0$

The velocity contours at all stations for a phase angle of 174 degrees and an angle of attack of 8.95 degrees are shown in Fig. 3. The range of the velocities encountered here is from $0.9U_\infty$ to $1.45U_\infty$. The interesting feature seen here is that pockets of fluid at the highest velocity could be found 10 - 15% above the

airfoil upper surface, and not close to the surface as theorised by the moving wall effect. This indicates that the effects of the surface acceleration are not just confined to the airfoil boundary layer, which in this case is estimated to be about 0.15 mm. Another interesting result is that at the leading edge, the velocity is $1.35U_\infty$ due to the suction peak. It decreases for a short distance immediately following it, but increases again as the streamlines are accelerated around the bubble, and in the outer flow. It is worth noting here that the largest mean velocities measured were about 1.6 times the free stream value with the instantaneous values reaching about $1.75U_\infty$ at some locations in the flow.

5. CONCLUSIONS

The dramatic changes in the leading edge flow field of an oscillating airfoil undergoing large amplitude dynamic stall has been captured using a non-intrusive measurement technique. Of particular interest are the very large time averaged mean velocities ($\approx 1.6\ U_\infty$) at locations far away from the airfoil surface, the formation and bursting of the separation bubble, and the resulting wake-like velocity distributions. These results indicate the extremely complex nature of the flow being studied and have provided the first ever documentation of the velocity field in these flows.

6. REFERENCES

1 CARR, L.W. and CHANDRASEKHARA, M.S., "Design and Development of a Compressible Dynamic Stall Facility", to appear in *J. Aircraft*.

2. CHANDRASEKHARA, M.S. and CARR, L.W. "Flow Visualization Studies of the Mach Number Effects on the Dynamic Stall of Oscillating Airfoils", *J. Aircraft*, Vol. 27, No. 6, June 1990, pp. 516-522.

3 CHANDRASEKHARA, M.S., and AHMED, S., "Laser Velocimetry Measurements of Oscillating Airfoil Dynamic Stall Field", *AIAA Paper No. 91-1799*, to be presented at the AIAA 22nd Fluid Dynamics, Plasma Dynamics and Lasers Conference.

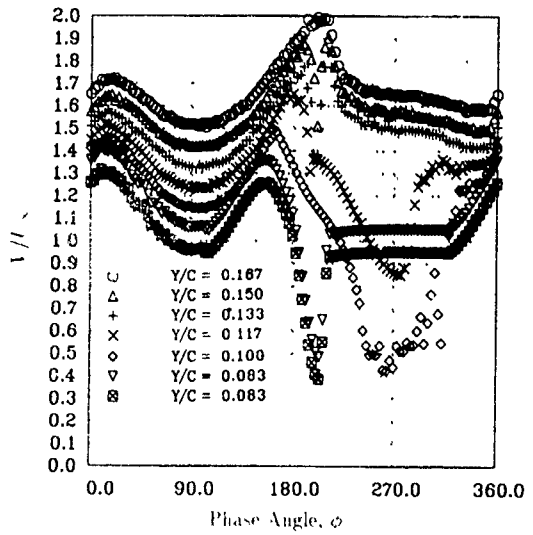

Fig. 1 Distribution of Absolute Velocity with Phase Angle at x/c = 0.067 (Origin Shifted by $0.1U_\infty$ at Each y/c)

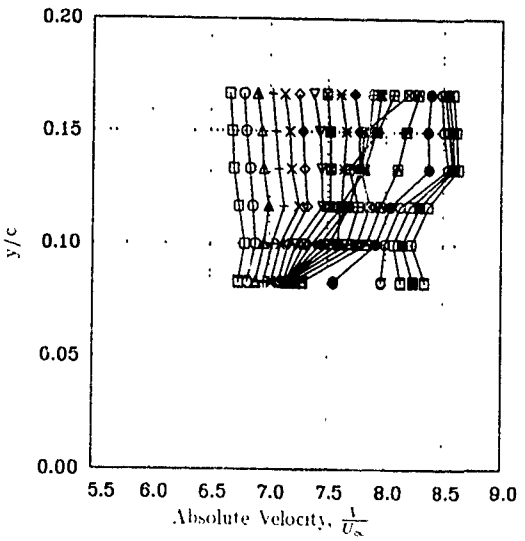

Fig. 2 Velocity Profiles at x/c = 0.067, $\square, \phi = 162^0$, $\Delta\phi = 3^0$ for Successive Profiles

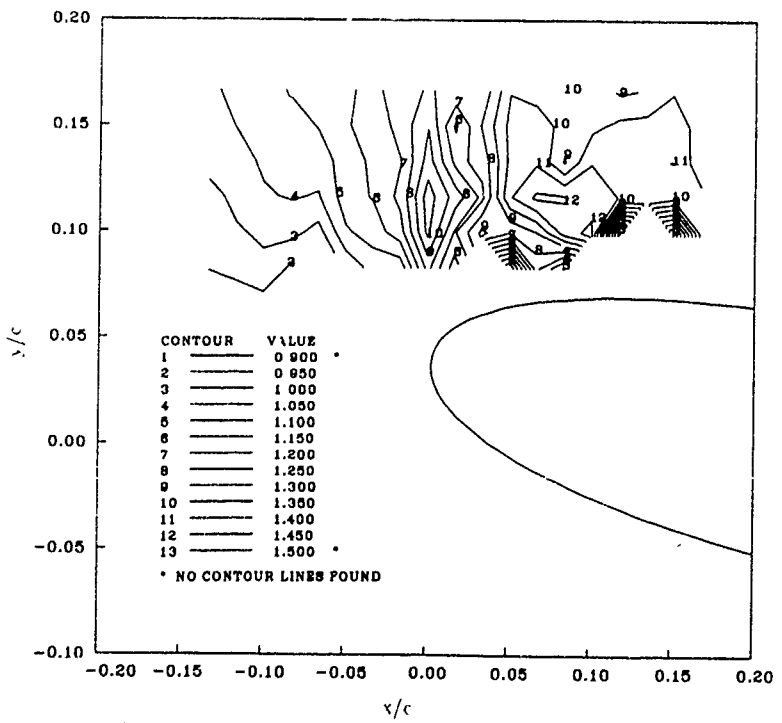

Fig. 3. Velocity Contours at M = 0.3, k = 0.05, $\alpha = 10^0 - 10^0 \sin \omega t$.

EIGHTH SYMPOSIUM ON
TURBULENT SHEAR FLOWS
Technical University of Munich
September 9-11, 1991

VORTEX SHEDDING IN A DRAG REDUCING SURFACTANT SOLUTION

Joachim Dohmann

Lehrstuhl Energieprozeßtechnik
Fachbereich Chemietechnik, Universitat Dortmund
Postfach 500500, W-4600 Dortmund, Germany

ABSTRACT

In turbulent shear flows some cationic surfactant solutions show a number of peculiar effects In this experimental investigation the wakes past circular cylinders were studied by using Laser-Doppler-velocimetry based conditional sampling techniques and flow-visualization
Interesting details of the Kármán- vortex- street and the occurence of vortex shedding were obtained

INTRODUCTION

Some aqueous solutions of cationic surfactant solutions show a peculiar behaviour in turbulent shear flows Most famous is the effect of drag reduction in turbulent pipe flows (Toms effect) which could be observed e g in rough pipes [1] Other investigations [2] indicate a dramatic change in the mechanism of turbulence in the presence of these surfactant additives Mainly the production the developement and the decay of coherent structures a e influenced by the additives The observed effects cannot be understood if only simple rheological propeities are made responsible for them The solutions show a steep increase (factor 4) in viscosity if a critical shear strain is exceeded [3]

Therefore an experimental investigation of a simple system of vortices was performed the study of the Kármán vortex street under the influence of a drag reducing additive (24 mM aqueous solution of tetra-decyltrimethylammonium salicylate with sodium bromide C_{14}TASal+NaBr)

In the Newtonian case the Karman vortex street is a well known system of two rows of alternated counter-rotating vortices in the wake of a circular cylinder It can be described by a set of non- dimensional numbers The rate of vortex shedding is represented by the Strouhal number S (S = f d/U, where f is the shedding frequency, d the cylinder diameter and U the mean flow velocity) The Strouhal number is related to the distance between two vortices Vortex shedding occurs if a critical Reynolds nu.. ber of 30 is exceeded If the Reynolds number is above the value of 300 the Strouhal number becomes a constant (S = 0 21) [4] A collection of these data is shown in Fig 1 as an envelope

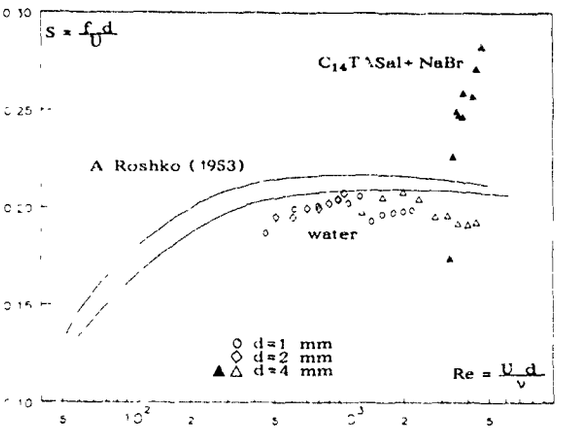

Fig 1 The Strouhal number as a function of the Reynolds number obtained from Fast-Fourier-analysis The critical Re-number is shifted An increased S-number indicates a reduced size of the vortices

Another simple geometry parameter is the lateral spacing h/l as calculated in the theory of v Kármán At last parameters are interesting describing the intensity of the coherent structures which is related to the input into the cascade of the turbulence decay

EXPERIMENTAL SETUP

In the present investigation different cylinders with diameters of 1mm, 2mm and 4mm were installed in a test channel with a mean-flow velocity between 3 m/s and 125 m/s, which led to Reynolds numbers in the range between 300 and 4800 The upstream turbulence level was of about 1% in the Newtonian case and about 4% if the surfactant solution was used
The flow field in the testsection was examined by using two Laser-Doppler-velocimeters (LDV) which are operated simultaneously with two trackers and additional with two burst-spectrum analyzers
Different methods were used to describe the Kármán vortex street at different flow speeds and different distances downstream the cylinder The vortex street was visualized (d= 5mm) by dye injection through a hole at the front stagnation point

EXPERIMENTAL RESULTS

To determine the shedding frequency the **Fast-Fourier-analysis** of the velocity signal was used At well choosen positions the frequency spectra show very clear peaks

In the Newtonian case the obtained Strouhal numbers show good agreement with other published data (see fig 1) A surprising effect shows the surfactant solution The critical Reynolds number of about 50 is shifted up to a value of about 3500 This cannot be explained only with an increased viscosity measured by Ohlendorf et al [3] Strouhal numbers of S= 29 (at Re=4800) could be detected, not having reached a saturation value A simple influence of an increased viscosity would only affect the critical Re-number but not the Strouhal number S

Furthermore two **conditional sampling** techniques were used to obtain the momentary spatial velocity field <U(x)> The velocity signal of a reference LDV was examined for characteristics of the vortices In the first case this was done by using the window- average-gradient algorithm described by Antonia et al [5] The second method used was a hardware application consisting of a signal conditioner and a differentiator circuit It was installed to shorten the detection scheme If a vortex was detected the measurement of the second LDV was triggered By variation of the position of this second LDV the "momentary" conditional velocity field was obtained
This leads to the knowledge of most of the interesting details of the flow The geometrical parameters (size and spacing) of the vortex street were determined from the spatial distribution of the vorticity which could be calculated from the velocity field In the same way the local contributions to the kinetic energy density or the circulation of the vortices could be calculated

The obtained data indicate some important and surprising changes in the mechanism of turbulence production in the presence of surfactant additives The flow field becomes anisotropic with reduced turbulent motions in lateral directions The kinetic energy density of the vortices is reduced even if there are only small changes in the strength of vorticity Fig 2 gives an illustrative impression of the cylinder wake

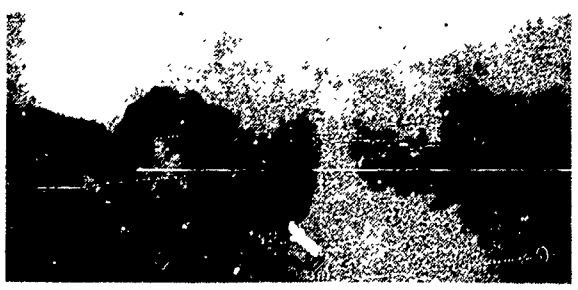

Fig 2 Visualization of the cylinder wake Left The Kármán vortex street in the water flow at high Reynolds number (Re = 5000). Right the wake in the surfactant solution at similiar conditions In both cases the same dye injection rate was choosen to demonstrate not only the changed turbulent diffusion but the molecular diffusion as well

The molecular structure of the aqueous surfactant solution can be made responsible for the observed effect in turbulent shear flows If a critical micelle concentration is exceeded slender rodlike micelles are formed from the monomeres In turbulent shear flows the micelles orientate into flow direction and the fluid becomes anisotropic This behaviour was determined from small angle neutron scattering [6] From own thermodynamical experiments it can be concluded that the micelle-monomere equilibrium depends from the shear strain Under deformation conditions the equilibrium is dropped to lower values of the critical micelle concentration according to an increased length scale of the anisometric micelles or an increased volume fraction of this phase The shear induced state of the material as discussed in literature (eg [3]) could be confirmed by measurements of the refractive index and optical turbitity indicating a shear induced phase transition Under shear strain the material becomes more anisotropic than expected only from orientation effects of the micelles

The peculiarities observed in turbulent shear flows of the aqueous surfactant solutions are related to the occurence of this shear induced phase transitions

REFERENCES

[1] Thiel, H. Widerstandsverminderung bei turbulenten Strömungen in kunstlich rauhen Rohren 1990 Dissertation Universitat Dortmund
[2] Riediger, S. Untersuchung der Turbulenzstruktur in einer ebenen Mischungsschicht und hinter einer Kanalerweiterung bei der Stromung zweier nicht - newtonscher Flussigkeiten 1989 Dissertation Universitat Dortmund
[3] Ohlendorf, D et al. Rheologica Acta, vol 25, 1986, pp 468-486
[4] Roshko, A. NACA technical note 2913 , 1953
[5] Antonia, R A et al. Proc 6th symposium on turbulent shear flows, 1987, Toulouse, France
[6] Bewersdorff, H W et al. Physica B vol 156 & 157, 1989, pp 508-511

ACKNOWLEDGEMENT

The assistance of M F Hibberd during the flow-visualization experiments is greatfully acknowledged

EIGHTH SYMPOSIUM ON
TURBULENT SHEAR FLOWS
Technical University of Munich
September 9-11, 1991

PRESSURE DRAG ON OBSTACLES IN A TURBULENT BOUNDARY LAYER

Stefan Emeis
Sonderforschungsbereich 210
Institut fur Meteorologie und Klimaforschung
Kernforschungszentrum Karlsruhe / Universität Karlsruhe
Postfach 3640, W-7500 Karlsruhe 1
Germany

ABSTRACT

Pressure drag on obstacles in a turbulent boundary layer of a viscous and stratified flow comes due to deformation of the flow over obstacles and generation of turbulence near obstacles, due to the generation of internal waves, and due to blocking of heavier air masses on the upstream side of the obstacle. This leads to a decomposition of pressure drag into form drag, wave drag, and hydrostatic drag, respectively. The decomposition is a prerequisite for parameterizing the drag.

In this paper a scale analysis of the equation of motion will introduce nondimensional numbers which govern the drag. Output from a numerical model will show the dependence of the drag on these numbers. The results for form drag will be compared to flows over rough plates and implications for the parameterization of pressure drag in larger-scale models will be addressed.

SCALE ANALYSIS

Pressure drag per unit length of an obstacle ($2L$) is defined as the integral over the horizontal pressure gradient in a control volume containing the obstacle (2D-flow case)

$$W_D = \frac{1}{2L}\int_{-\infty}^{\infty} p\{x, h(x)\}\frac{dh}{dx}dx = \frac{1}{2L}\iint \frac{\partial p(x,z)}{\partial x}dxdz \quad (1)$$

$h(x)$ is the orography, L is half of the width of the obstacle and $p(x,z)$ is the deviation of the pressure from a basic state without obstacle.

For stationarity, the horizontal equation of motion (integrated over the 2D volume, neglecting horizontal advection, horizontal turbulent fluxes, and pure surface friction terms) reads

$$\iint \frac{\partial p}{\partial x}dxdz = -\int \rho uw\,dx - \int \rho u'w'dx + \iint \rho fv\,dxdz \quad (2)$$

Here u, v, and w are velocity deviations from the basic state due to the presence of the obstacle, resolved by the numerical model used later, u' and w' are subgridscale fluctuations in the numerical model. The integrals over uw, and $u'w'$ are taken at the upper boundary of the control volume.

Scaling the variables with a basic state flow velocity scale U, a turbulent velocity scale $2.466(\nu_t U^2/L)^{1/3}$ (ν_t is turbulent viscosity set to $10\ m^2 s^{-1}$, introduced in analogy to molecular viscosity although it is an internal variable of the boundary layer), a buoyant velocity scale $\sigma^{1/2}L$ ($\sigma = N^2$), and the height and length scales of the obstacle H and L (EMEIS, 1990)

$$\begin{aligned} u &= UH/L \quad u^* & u' &= 2.466(\nu_t U^2/L)^{1/3}H/L \quad u'^* \\ v &= UH/L \quad v^* & w' &= 2.466(\nu_t U^2/L)^{1/3}H/L \quad w'^* \\ w &= \sigma^{1/2}LH/L \quad w^* & p &= \rho U^2 H/L \quad p^* \\ & & x &= L \quad x^* \\ & & y &= L \quad y^* \\ & & z &= H \quad z^* \end{aligned}$$

where the asterisks denote nondimensional values which should be of order unity if the scaling is correct, yields for the pressure drag coefficient $C_W = \frac{W_D}{\frac{1}{2}\rho U^2}$ of a single obstacle

$$C_W = \frac{H^2}{L^2}\left(-\sigma^{*1/2}\int u^*w^*dx^* - \frac{6.082}{Re_t^{2/3}}\int u'^*w'^*dx^* + \frac{1}{Ro_o}\iint v^*dx^*dz^*\right) \quad (3)$$

The term with $\sigma^{*1/2}$ ($= \frac{\sigma^{1/2}L}{U}$) is present only if we have gravity waves (for stable stratification $\sigma^{*1/2}$ is the usual Froude number) which transport momentum vertically ('gravity wave drag'), the term with the turbulent Reynolds number $Re_t = \frac{UL}{\nu_t}$ describes 'viscous form drag' due to deformation of the viscous flow, and the term with the Rossby number $Ro_o = \frac{U}{fL}$ describes a redistribution of momentum from the v- to the u-component ('inertial wave drag'). For neutral stability and no rotation (3) reduces to

$$C_{W,N} = -\frac{H^2}{L^2}\frac{6.082}{Re_t^{2/3}}\int u'^*w'^*dx^* \quad (3a)$$

Including the influence of blocking colder air masses by a Froude number $Fr_H = \frac{NH}{U}$ (although Fr_H is not independent from σ^*, it indicates a different physical process), the influence of a rough surface by a surface Rossby number $Ro_s = \frac{U}{fz_0}$ (numerical results showed that for Ro_s below a certain threshold value, the drag became larger with decreasing Ro_s. This effect cannot be separated from viscous form drag by scale analysis, but only by numerical experiments), and the influence of the density of obstacles by $\lambda = \frac{n|H|}{L_x}$ (n is the number of obstacles in L_x), we have

$$C_W = f_1\left(\frac{H}{L}, \sigma^*, Re_t, Ro_o, Ro_s, Fr_H, \lambda\right) \quad (4a)$$

For form drag this reduces to

$$C_W = f_2\left(\frac{H}{L}, Re_t, Ro_s, \lambda\right) \quad (4b)$$

Keeping U and ν_t fixed, $\frac{H}{L}$, Re_t, and λ describe the deformation of the viscous flow ('viscous form drag'), Ro_s describes the additional production of turbulence at a rough surface of the obstacles ('micro-turbulent form drag'), and $\frac{H}{L}$ additionally controls flow separation ('macro-turbulent form

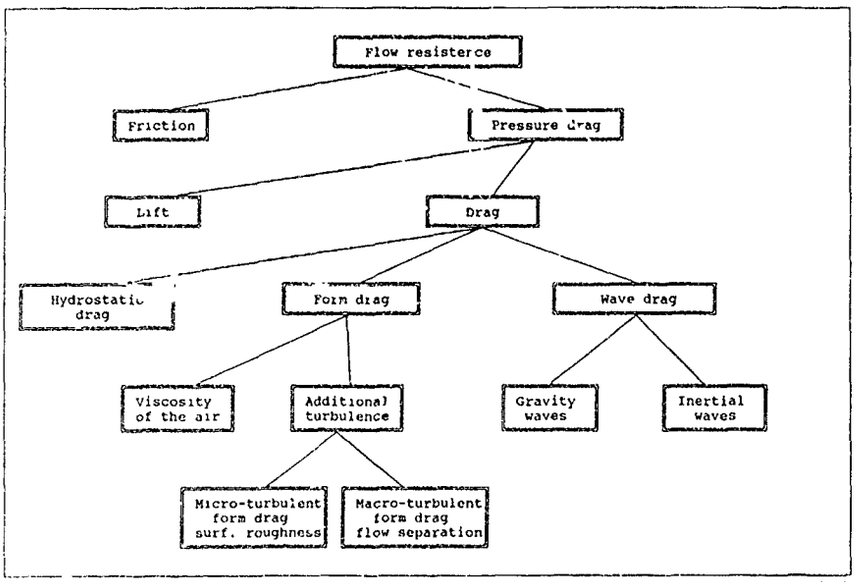

Figure 1

drag') The distinction between micro-turbulent and macro-turbulent form drag is artificial and caused only by the grid resolution of the numerical model used to simulate the drag or by the design of a field experiment Figure 1 shows schematically the different parts of pressure drag

NUMERICAL SIMULATION'

Numerical simulations were carried out with a two-dimensional, mesoscale, prognostic, non-hydrostatic, primitive-equation grid-point model (DORWARTH, 1986), with a turbulence closure using a two-equation model for turbulent viscosity It is iterated until the solution becomes stationary

The numerical results confirm (3a) and (4b) We obtain by empirical evaluation of the numerical data for form drag

$$C_W = (2\,5\cdot(\frac{H}{L})^{2\,17}\;3\,0\;\frac{6\,082}{Re_t^{2/3}} + 0\,15\cdot\frac{Ro_c}{Ro_*})\cdot(1 - 3\,5(\lambda - \lambda_c)) \tag{5}$$

with $Ro_c = 5\;\;10^5$ (for $Ro_c < Ro_*$ this additive term is not present) and $\lambda_c = 0\,02$

$2\,5\;\;(\frac{H}{L})^{2\,17}$ in (5) instead of $(\frac{H}{L})^2$ in (3a) includes the effects of flow separation The difference is the macro-turbulent form drag The term containing Ro_* represents the micro-turbulent form drag. The factor 3 in front of $Re_t^{-2/3}$ shows that the scaling of the viscous form drag in (3) was not completely correct

The effect of obstacle density has been assumed to a first-order approximation to be independent of the three different parts of form drag although flow separation is likely to depend considerably on λ

COMPARISON TO FLOW OVER ROUGH PLATES

Viscous form drag proportional to Re_t can be compared to flow resistence over rough plates proportional to Re (Reynolds number formed with molecular viscosity) For laminar flows dominated by viscous forces the resistence scales with Re^{-1}, for laminar flows dominated by inertial forces with $Re^{-1/2}$, and for turbulent flows with $Re^{-1/3}$ (PRANDTL et al , 1984)

The analogy we found is that a laminar flow over a rough plate corresponds to a turbulent boundary layer flow without flow separation over mesoscale obstacles and a turbulent flow over a rough plate corresponds to a turbulent flow with flow separation over obstacles The dependence of viscous form drag on $Re_t^{-2/3}$ for small $\frac{H}{L}$ (no flow separation) shows that both viscous and inertial forces play a rôle For larger $\frac{H}{L}$ further numerical experiments have shown that viscous form drag more depends on $Re_t^{-1/2}$ showing that we approach flow separation (turbulent flow over a rough plate)

The distinction between friction over rough surfaces and form drag over obstacles is again artificial and is due to the limited resolution of a numerical grid or an experimental network which cannot resolve the single roughness elements of the rough surface For grid sizes which on the other hand cannot resolve mesoscale obstacles, form drag is part of surface friction and can be parameterized via the roughness length-concept

This leads to the introduction of an effective roughness length for parameterizing form drag of mesoscale orographic features in larger-scale models As hydrostatic drag and wave drag are no boundary layer phenomena they cannot be included in an effective roughness length-concept but must be parameterized by effective drag coefficients and respective vertical momentum source distributions

REFERENCES

Dorwarth, G., 1986: Numerische Berechnung des Druckwiderstands typischer Geländeformen *Ber Inst Meteorol Klimaf Karlsruhe, No 6, 152+XII pp. (Available from Institut für Meteorologie und Klimaforschung, Kaiserstr 12, W-7500 Karlsruhe 1, Germany)*

Emeis, S., 1990: Pressure Drag of Obstacles in the Atmospheric Boundary Layer *J Appl Meteorol*, **29**, *461-476*

Prandtl, L. et al, 1984: Fuhrer durch die Stromungslehre *Vieweg, Braunschweig, 622 pp*

ACKNOWLEDGEMENT

The *Sonderforschungsbereich 210* is sponsored by the *Deutsche Forschungsgemeinschaft*

SIMULATION OF TURBULENT VELOCITY PROFILES APPEARING ON ROTATING AND STATIONARY PARTS OF SUBSONIC COMPRESSORS AND TURBINES

J. K. Kaldellis

The Institute for the Development and Management of Natural Resources, University of Piraeus.

Pontou 58, Hellinico
Athens, Greece 16777

ABSTRACT

The successful analysis of the viscous flow field through any type of turbomachine is based on the use of a closed analytical formulation in the primary direction. An extended and improved form of the classical turbulent shear layer theory is developed to take into account the complex flow pattern through rotating and stationary parts of real turbomachines. The resulting model is successfully applied for a large variety of subsonic compressors and turbines.

NOMENCLATURE

F	friction parameter (= u_τ/W_{ref})
Re_δ	Reynolds number (= $W_{ref_w}\delta/\nu$)
$\tilde{W}$	analytical velocity distribution
W_s	longitudinal velocity
δ	shear layer thickness
η	non-dimensional (by δ) normal distance
Π	Cole's wake parameter

INTRODUCTION

The successful analysis of the viscous flow field through any type of turbomachine using the circumferentially averaged Navier-Stokes equations (see for example Kaldellis et al., 1989, Kaldellis et al., 1990, Ktenidis and Kaldellis, 1991, Kaldellis, 1991), is based on two different approaches for the primary and the peripheral flow directions, respectively. In the peripheral direction, the velocity component is computed using the corresponding meridional vorticity distribution (Kaldellis and Ktenidis, 1990), resulting from the solution of the complete form of the meridional vorticity transport equation, written in a partial differential form.

On the other hand, in the primary direction, i.e. the direction of the external (inviscid) flow field, an integral formulation is adopted. For this purpose a non-linear system of integral equations, including the meridional momentum and the total kinetic energy equation, is used in combination with a two-parameter velocity profile family in order to describe the characteristics of the existing turbulent endwall shear layers. More precisely, the solution of the non-linear system of integral equations provides the necessary shear layer parameters to be used by the analytical law in order to reproduce the real flow velocity distributions. Special attention is also payed to estimate the correct external-primary flow direction utilized as the basis for the representation of the velocity profiles. For this reason, the necessary communication between the external and the shear flow field is established via a fast viscous - inviscid interaction scheme (Kaldellis et al. 1990).

THEORETICAL ANALYSIS

Among the numerous analytical velocity laws, the most commonly used is the one based on the law of the wall and the law of the wake, proposed by D. Coles in his early work (Coles D.,1956a & 1956b). The proposed by D. Coles standard equation for the description of the velocity profiles combines the two previously mentioned similarity laws and is based on a detailed analysis of an enormous volume of experimental data for a large variety of two-dimensional turbulent shear flows

In the present work, the appropriate modifications to the classical turbulent shear layer theory in order to take into account the complexity of the flowpattern through the configurations existing in real machines, are briefly described. For this purpose the longitudinal velocity profile (i.e. in the primary direction) can be expressed (see also Kuhn and Nielsen, 1973) as:

$$\tilde{W}/W_{ref_w}=F\{2.439\cdot\ln(1+\eta\cdot Re_\delta\cdot|F|+5.1 - (3.39\eta_1\cdot Re_\delta\cdot|F|+5.1)\cdot\exp(-0.37\eta\cdot Re_\delta\cdot|F|) + 2.439\cdot\Pi\cdot[1-\cos(\pi\eta)]\} \quad (1)$$

or in a more generalized form as:

$$\tilde{W}/W_{ref_w}=f(\eta, Re_\delta, F, \Pi) \quad (2)$$

while the corresponding friction law (see also fig.[1] and Nash J., 1965) can be written as:

$$\Pi=0.205/F-0.5\cdot\ln(1+Re_\delta\cdot|F|)-1.0455 + 0.205\cdot(3.39\cdot Re_\delta\cdot|F|+5.1)\cdot\exp(-0.37\cdot Re_\delta\cdot|F|) \quad (3)$$

A detailed parametrical study is carried out by varying one of the shear layer parameters at a time in order to demonstrate its influence on the shape of the corresponding velocity profile. Only some very characteristic results are given here (see figures [1],[2]) since this study is beyond the scope of the present work. However, it is interesting to mention that the choice of the appropriate primitive parameters, to be used for the representation of the corresponding velocity profile, may be sometimes crucial. These parameters (e.g. the shear layer thickness and the friction velocity at the wall) must fulfil the additional physical constraint to take "normal" values both for strongly decelerated and highly accelerated shear flows. Accordingly, the classical two-dimensional theory must be extended to take into account the extreme pressure gradients (figure [3]), the strong flow deceleration or acceleration through the bladings, and the relative

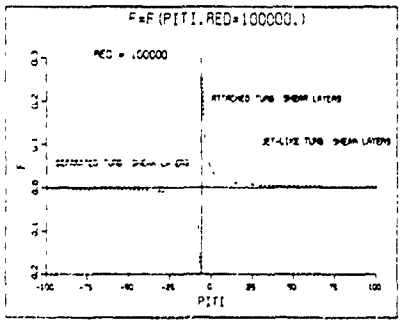

Figure 1: Presentation of the relation F=F(π,Reδ) according the equation (3) for -100. ≤ π ≤ +100.

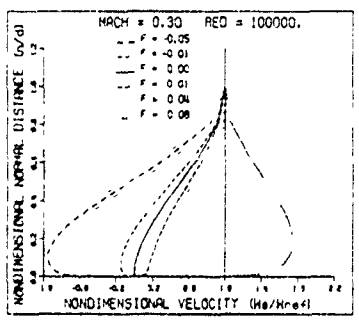

Figure 2: Parametrical presentation of various incompressible velocity profiles W=W(η,F) as a function of F.

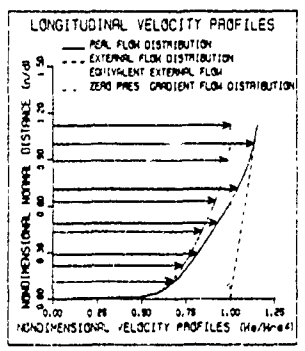

Figure 3: Schematic representation of longitudinal velocity profiles with pressure gradient.

motion of the successive blade rows. For the velocity component W_s, expressed in the relative to the blades of the machine system of coordinates, the expression proposed by Mellor G.(1966) may be used:

$$W_s(\eta) = W_{ref}(\eta) - [W_{ref_v} - \bar{W}(\eta)] \qquad (4)$$

CALCULATION RESULTS - CONCLUSIONS

The results from the analysis of a large variety of industrial configurations are systematically investigated, in order to check the limits and the applicability of the simple similarity theory based on the fundamental physical laws. For this purpose the longitudinal velocity distributions, concerning typical selected stations, from several test cases including a highly loaded compressor cascade with and without tip clearance, two high turning axial turbine cascades, a highly accelerated turbine stator, an industrial radial impeller along with a modern axial fan, are carefully studied.

The majority of the results obtained show that the main physical laws, concerning the turbulent shear flow, are verified for the large variety of the investigated geometries. The slightly decelerated, highly accelerated and jet-like velocity profiles, appearing at the specific inlet-exit planes of a moderately loaded (fig.[4]) and a high turning (fig.[5]) axial turbine cascades, covering a wide range of Reynolds ($50{,}000 \leq Re_6 \leq 230{,}000$.) and Mach ($0.05 \leq Me \leq 0.71$) numbers, are successfully reproduced by the proposed theoretical model. Unusual values of the form shape factor H_{12} at the exit of the stator of an industrial axial turbine (fig.[6]) are closely related to the existence of typical jet-like turbulent shear layers with very small or even negative values of the corresponding displacement thickness, see also Kaldellis and Ktenidis (1990).

The velocity profiles, typical for a strongly decelerated shear layer through a highly loaded compressor cascade are also satisfactorily described for cases excluding clearance (see for example fig. [7]). However, this is not the case when remarkable clearance exists, see Kaldellis et al. (1991).

The effect of the rotation of the blades does not invalidate the proposed model, since the velocity profiles at the inlet and the outlet of a radial impeller (fig.[8]), along with the corresponding velocity profiles at the inlet and the exit of the rotor of a modern axial fan (fig.[9]) are again realistically represented, for the hub region.

The quality of the theoretical results, in comparison to the experimental data, is greatly improved by the choice of the appropriate primitive shear layer parameters. Only under this condition is almost always possible to obtain the corresponding velocity profile, using the results from the solution of the above mentioned non-linear system of integral equations. If this is not taken into account, severe problems may appear.

Summarizing, we can say that according to the analysis of a wide variety of real test cases, the simple laws that dominate the classical turbulent shear flows can be extended to describe with sufficient accuracy the velocity profiles appearing through various industrial configurations, if the proposed modifications and improvements are taken into account. Of course, for some special cases additional investigation is needed, to include tip-clearance effects, endwall shear layer merging and the existence of strong shock waves.

REFERENCES

1. Coles D., 1956a, "The Law of the Wake in the Turbulent Boundary Layer", Jr. Fluid Mech., Vol.1, 191-226.
2. Coles D., 1956b, "The Law of the Wall in Turbulent Shear Flow", 50 Jahre Grenzschicht Forschung, Verlag Fr. Vieweg, Braunschweig.
3. Kaldellis J., Douvikas D., Falchetti F., Papailiou K.D., 1989, "A Secondary Flow Calculation Method for One Stage Axial Transonic Flow Compressors, Including Shock - Secondary Flow Interaction", ASME Paper 89-GT-210, also ASME Jr. of Turbomachinery, Vol. 112, pp. 652-668.
4. Kaldellis J., Ktenidis P., Kodossakis D., 1990, "Energy Exchange and Secondary Losses Prediction in High Speed Axial and Radial Compressors", ASME Paper 90-GT-229.
5 Kaldellis J., Ktenidis P., 1990,"High Turning Limit and Jet Like Profiles in Secondary Flow Field of Axial Turbines", ASME Paper 90-GT-327.
6. Kaldellis J., Katramatos D., Ktenidis P., 1991, "Effects of the Tip Clearance Flow Field on the Secondary Losses", ASME Paper 91-GT-58.
7. Kaldellis J., 1991, "Parametrical Investigation of the Interaction Between Turbulent Shear Layers and Shock Waves, Including Separation", International Conference on the Analysis of Thermal an Energy Systems, ATHENS' 91, Athens, Greece.
8 Ktenidis P., Kaldellis J., 1991, "3-D Axisymmetric Viscous Internal Flows on Rotating and Stationary Surface in Turbomachines", ASME Paper 91-GT-196
9. Kuhn G.D., Nielsen J.N., 1973, "Prediction of Turbulent Separated Boundary Layers", AIAA Paper No 73-663.
10. Mellor G.L., 1966, "The Effects of Pressure Gradients on Turbulent Flow near a Smooth Wall", Jr. of Fluid Mechanics, Vol. 24, pp. 255-274.
11. Nash J.F., 1965, "Turbulent Boundary Layer Behaviour and the Auxiliary Equations", AGARDograph 97, part 1, pp. 245-279.

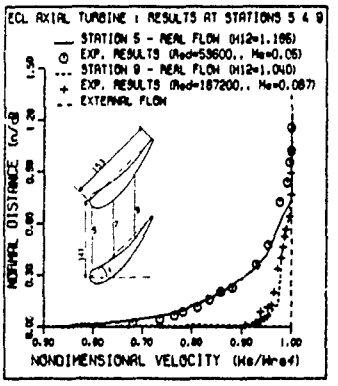

Figure 4. Longitudinal velocity profiles at the inlet and the exit of the ECL axial turbine.

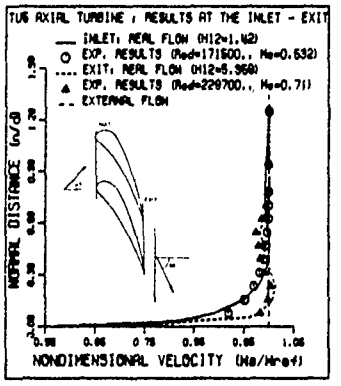

Figure 5: Longitudinal velocity profiles at the inlet-exit of TUG high turning axial turbine.

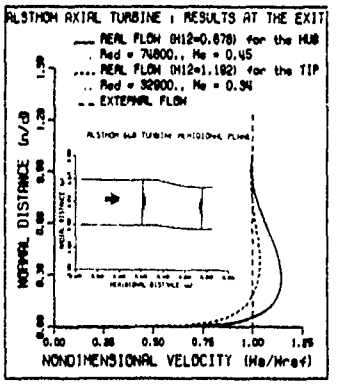

Figure 6: Exit longitudinal velocity profiles for the hub and the tip of the Alsthom axial turbine.

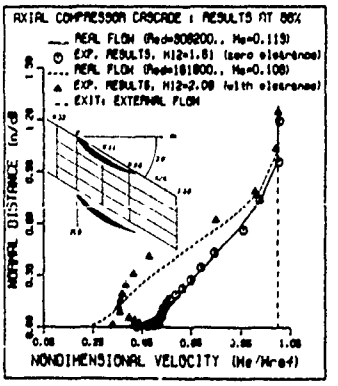

Figure 7: Exit longitudinal velocity profiles, PLOT axial compressor cascade, with and without clearance.

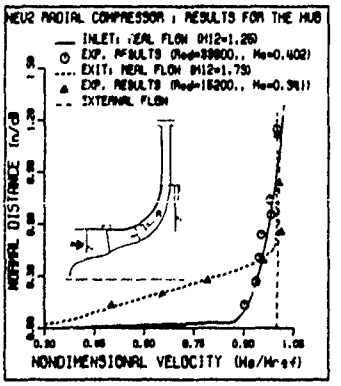

Figure 8: Inlet-exit longitudinal velocity profiles. Relative system of coordinates. NEU2 radial impeller.

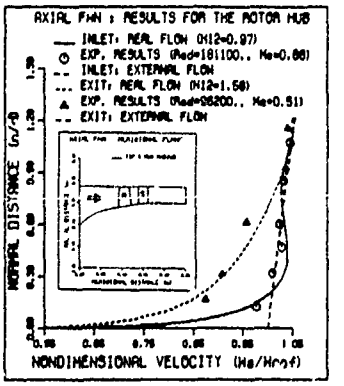

Figure 9: Rotor inlet-exit longitudinal velocity profiles. Relative system of coordinates. CM7 axial fan.

EIGHTH SYMPOSIUM ON
TURBULENT SHEAR FLOWS
Technical University of Munich
September 9-11, 1991

THE CALCULATION OF A COMPRESSIBLE BOUNDARY LAYER PAST A POINTED BODY AND A DELTA WING

E.Krause*), T.V.Poplavskaja and V.N.Vetlutsky**)

*)Aerodynamisches Institut, RWTH Aachen
Wullnerstrasse 5-7, 5100 Aachen, Germany

**)Institute of Theoretical and Applied
Mechanics, USSR Academy of Sciences
Institutskaja 4, 630090 Novosibirsk, USSR

ABSTRACT

The three-dimensional compressible, laminar and turbulent boundary layers past a pointed body and a delta wing by supersonic gas flow at the angle of attack are studied. An implicit absolutely stable difference scheme for a solution of the boundary-layer equations is suggested. Laminar and turbulent boundary layers are calculated for the ogive-cylinder combinations and for the delta wings. The skin-friction coefficients and the Stanton numbers are compared with experimental data.

PROBLEM FORMULATION

The pointed body surface is given in the cylindrical coordinates $r=r(\xi,\zeta)$. The ξ-coordinate coincides with axis of the body, the ζ-coordinate is a meridional angle in a cross section. For the boundary-layer equations the non-orthogonal coordinate system (ξ,η,ζ) is introduced, which is orientated with respect to the body surface. Here the η-coordinate is a normal to the surface (Vetlutsky & Krause 1990).

The three-dimensional compressible boundary-layer equations are considered in the region $\Omega(\ \xi\geq\xi_0,\ 0\leq\eta\leq\eta_e(\xi,\zeta),\ 0\leq\zeta\leq\zeta_K\ )$ for the following set of boundary conditions. At the surface of the body $\eta=0$ the conditions of no-slip and the constant of a wall temperature are set. On the boundary layer $\eta=\eta_e(\xi,\zeta)$ all parameters are taken from inviscid flow around the body previously calculated.

The nose of the body is supposed to be conic. In this case the inviscid flow past the nose is also conic and the boundary-layer equations permit the similarity solution depended only on two variables ζ, $\lambda=\eta/\sqrt{\xi}$. The solution of these similarity equations is used as the initial conditions at $\xi=\xi_0$ for the full boundary-layer equations on the rest of the body surface.

The regimes of the flow-past for a delta wing with sharp leading edges are considered, when a bow wave touches the leading edges. The wing surface is given in the cartesian coordinate system $y=F(x,z)$. For the boundary-layer equations the non-orthogonal coordinate system (ξ,η,ζ) is introduced.

$$\xi=x,\quad \zeta=1-z/f(x)$$

Here $z=f(x)$ is the equation of the leading edge. The same equations and the boundary conditions are used. But in this case it is necessary to have a boundary condition some more on the leading edge. A new variable $\lambda=\eta/\sqrt{\xi\zeta}$ is introduced, which allows to obtain an ordinary differential equations on the leading edge $\zeta=0$ and the similarity equations for the conical nose $\xi\leq\xi_0$.

For the solution of the three-dimensional boundary-layer equations an implicit absolute stable finite-difference scheme of the second order approximation is used (Vetlutsky 1981). In the region, in which large gradients of parameters occur, a coordinate stretching is employed.

Four eddy viscosity models of turbulence suggested by Michel, Cousteix & Quemard (1971), Cebeci & Smith (1974), Pletcher (1969) and Baldwin & Lomax (1978) are taken for calculating of the turbulent boundary layer. The region of the laminar-turbulent transition is determined from a correlation of the Reynolds number based on momentum thickness $Re_\delta{}^{**}$ versus the local Mach number M_e (Thyson, Neuringer, Pallone & Chen 1970).

CALCULATION RESULTS

The calculation of the laminar, transitional and turbulent boundary layer on ogive-cylinder combinations are carried out. The stretching of the normal coordinate λ and the number of steps of the difference grid was chosen in such a way that 3-5 mesh points were in the viscous sublayer. The calculations have shown that all the four models of turbulence yield almost the same values of the flow parameters for the windward and lateral sides. The skin-friction coefficients C_f and the Stanton numbers St calculated were compared with experiments of Kharitonov & Vasenyov (1985), Horstman- Owen (1972), Dolling-Grey (1986) and Sturek & Schiff (1982).

The comparison of the parameter C_f with the data of the last paper ($M_\infty=3$, $\alpha=4.2^\circ$, $Re_D=1.2\cdot10^6$) shows that the calculation with Baldwin-Lomax's model (Fig.1, dotted line) gives the better results with respect to Michel's one (Fig.1, solid line). Fig.2 shows the skin-friction coefficient distribution for the wind side $\zeta=0$ and the lee side $\zeta=3.14$ ($M_\infty=2.95$, $\alpha=2.9^\circ$, $Re_D=3.1\cdot10^6$).

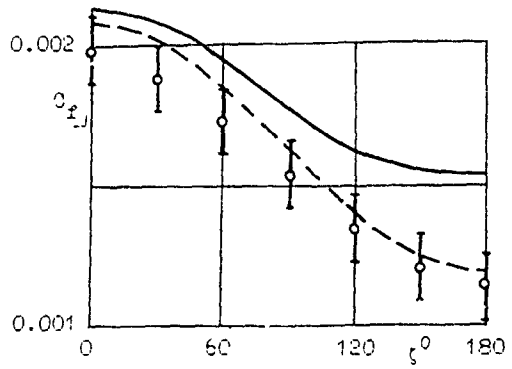

Fig.1. The comparison of the skin-friction coefficient c_f with experiment (Sturek & Schiff 1982).

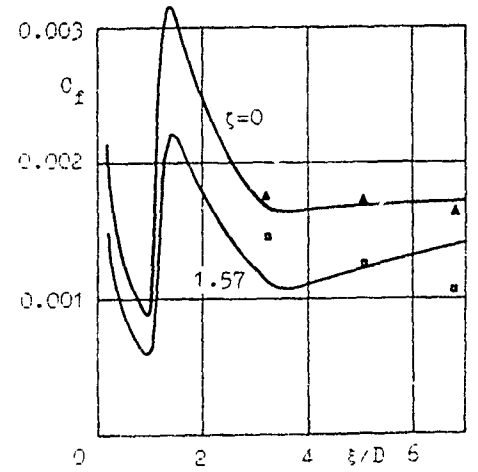

Fig.2. The comparison of the skin-friction coefficient c_f with experiment (Dolling & Gray 1986).

The experimental data of Dolling-Gray are indicated by the triangles and the squares.

The distributions of the skin-friction coefficient $c_f^*=c_f\sqrt{\zeta}$ at the wind side (Fig.3) and the lee side (Fig.4) of the delta wing for $\chi=45^0$, $M_\infty=3$, $\alpha=8^0$, $Re_L=2\cdot10^6$

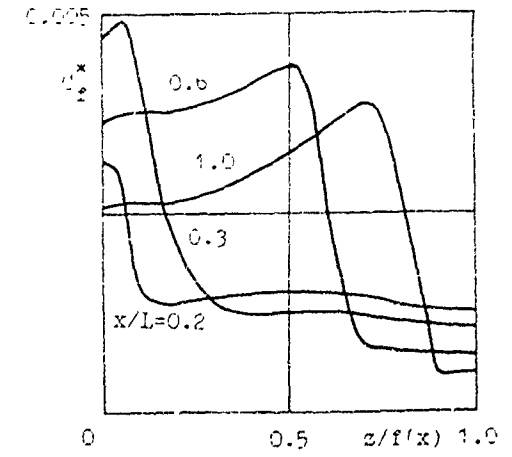

Fig.3. The distribution of the skin-friction coefficient $c_f^*=c_f\sqrt{\zeta}$ at the wind side of the wing.

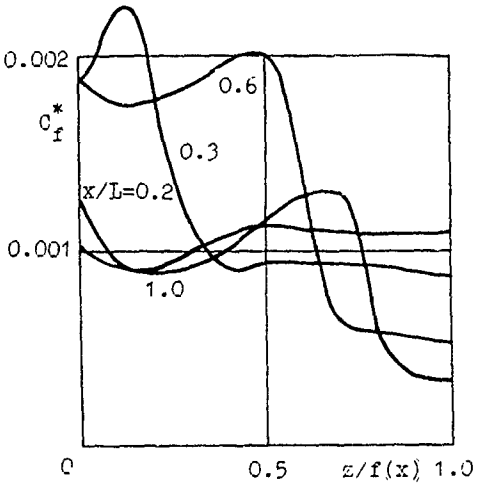

Fig.4. The distribution of the skin-friction coefficient $c_f^*=c_f\sqrt{\zeta}$ at the lee side of the wing.

are represented. One can see that the turbulence arises at first near by the symmetry plane and spreads further to the leading edge. But near by the leading edge the boundary layer is always laminar.

REFERENCES

BALDWIN, B.S. & LOMAX, H. 1978 Thin layer approximation and algebraic model for separated turbulent flows. AIAA Paper 78-257.

CEBECI,T & SMITH,A.M.O. 1974 Analysis of turbulent boundary layers. Academic Press.

DOLLING,D.S. & GRAY,W.K. 1986 Experimental study of supersonic turbulent flow on a blunted axisymmetric body. AIAA J. 24, 793-799.

HORSTMAN,C.C. & OWEN, F.K. 1972 Turbulent properties of a compressible boundary layer. AIAA J. 10, 1418-1424.

KHARITONOV,A.M. & VASENYOV,L.G. 1985 Private communication.

MICHEL,R., COUSTEIX,J. & QUEMARD, C. 1971 Application d'un schema ameliore de longueur de melange a l'etude des counches limites turbulentes tridimensionnelles. AGARD Meeting on Turbulent Shear Flows. London.

PLECHER,R.H. 1969 On a finite difference solution for the constant property turbulent boundary layer. AIAA J.7, 305-311.

STUREK,W.B. & SCHIFF,L.B. 1982 Numerical simulation of steady supersonic flow over spinning bodies of revolution. AIAA J. 20, 1724-1731.

THYSON,N., NEURINGER,J., PALLONE A. & CHEN, K.K. 1970 Nose tip shape change predictions during atmospheric re-entry. AIAA Paper 70-827.

VETLUTSKY,V.N. 1981 Laminar boundary layer on a flat plate with rotating cylinder. Computers and Fluids 9, 427-434.

VETLUTSKY,V.N. & KRAUSE, E. 1990 Berechnung dreidimensionaler Grenzschichten an spitzen Körpern. In Abhandlungen aus dem Aerodynamischen Institut der RWTH Aachen 30, 60-63.

EIGHTH SYMPOSIUM ON
TURBULENT SHEAR FLOWS
Technical University of Munich
September 9-11, 1991

INTERMITTENCY AND FINE-SCALE TURBULENCE STRUCTURE IN SHEAR FLOWS

V.R. Kuznetsov
Central Institute of Aviation Motors
111250, Moscow USSR

A.A. Praskovsky, V.A.Sabelnikov
Central Aerohydrodynamic Institute
Zukovsky-3, Moscow region, 140160, USSR

ABSTRACT

The main ideas and hypotheses formulated in the Kolmogorov inertial-range theories have been verified in a laboratory experiment in flows with a strong external intermittency The measurements are performed at different cross-section points in wakes behind a circular cylinder and an axisymmetric body, in a mixing layer, in the boundary layer, in a large wind tunnel return channel The characteristic dimensions of the most flow investigated are rather great the turbulence integral scale is 5 m At rather high Reynolds numbers Re_λ < 3000 a high spatial resolution is achieved, i e the ratio of the length of the wire to the Kolmogorov scale varies within the range of 0 8-2 5.

RESULTS

The main attention is given to the investigation of the universality of the fine-scale turbulence structure and the intermittency field in all regions including edge of flow boundaries Conditionally averaged characteristics in a turbulent fluid (including two-point ones as well) are determined using the intermittency function It is found that the constants characterizing the inertial subrange of the turbulence spect- rum, i e.the Kolmogorov constant C in the "two thirds law"
$\langle [u_i(x_i + r)-u_i(x_i)]^2 \rangle = C\cdot(\langle\varepsilon\rangle r)^{2/3}$,
$\eta \ll r \ll L$ where x_i - coordinate, u_i - velocity, ε - dissipation, L - turbulence integral scale, $\eta = (\nu^3/\langle\varepsilon\rangle)^{1/4}$ and the constants μ and C_ε in the energy dissipation correlation function
$\langle\varepsilon(x_i)\varepsilon(x_i + r)\rangle = C_\varepsilon\langle\varepsilon\rangle^2 (r/L)^{-\mu}$, change by a factor of more than two, i.e they are not universal The nonuniversality is due to the external intermittency since all data are generalized by introducing a single parameter, namely, the intermittency factor (Fig 1-3, the notations 1-axisymmetric wake, Re_λ=380-1080, 2-three-dimensional wake, Re_λ=340-520, 3 -mixing layer, Re_λ=1040-1660; 4 -plane wake, Re_λ=160-200, 5 -boundary layer, Re_λ=70-150; 6 -return channel, Re_λ = 3000, the curve on Fig 1 corresponds to the dependence $C = const\ \gamma^{1/3}$, the curveon Fig 3 - to the dependence C_ε = const/γ).Similar constants, found from conditionally averaged characteristics in a turbulentfluid, are universal within the measurement accuracy.

The formula μ = 2-q(6), establishing a relation between the constant μ and the exponent q(6) in the structure function of the sixth order, is not confirmed in the experiments (Fig. 4; the horizontal straight line corresponds to formula μ = 2-q(6)). The difference 2-q(6) exceeds the constant μ almost in all cases, this conclusion being valid both for the unconditional and the conditional averaging in the turbulent fluid. The formula for the rate of turbulence energy dissipation ε_r averaged over a sphere of the diameter r $\varepsilon_r \sim v^3/r$ which underlies the deduction of the relation μ = 2-q(6) did not found a convincing confirmation either.

The hypothesis of a statistical independence of small and large-scale motions in the turbulent fluid has been verified. At all points investigated no dependence of conditionally averaged energy dissipation moments $\langle\varepsilon^n\rangle_{t,u_i}$ on the conditioned velocity is detected according to the hypothesis in a rather wide range of the fluctuation amplitude variation (Fig.5,
$e_n = \langle\varepsilon^n\rangle_{t,u_i} / \langle\varepsilon^n\rangle_t$,
$u^o = (u_i-\langle u_i\rangle) \quad \langle(u_i-\langle u_i\rangle)^2\rangle^{-1/2}$.

The intermittency field has a scale similarity in a wide scale range which is indicated by extended exponential subrange in the intermittency spectrum $E_{\gamma\gamma} \sim k^{-\xi}$ (Fig.6). At the most points, the values ξ differ lightly from 0.25. With decreasing γ the value ξ rises.

The boundary between the turbulent and non-turbulent zones is not sharp even at those high Reynolds numbers Re_λ that are obtained in the experiments. The width of the transition zone from the levels of the parameters characteristic of the turbulence fluid to the levels characteristic of the non-turbulent one is equal to a mean turbulent zone length which exceeds the Kolmogorov scale by two or three orders.

REFERENCES

Kuznetsov V.R. & Sabelnikov V A. 1990. Turbulence and combustion. Hemisphere , New York *et al.*

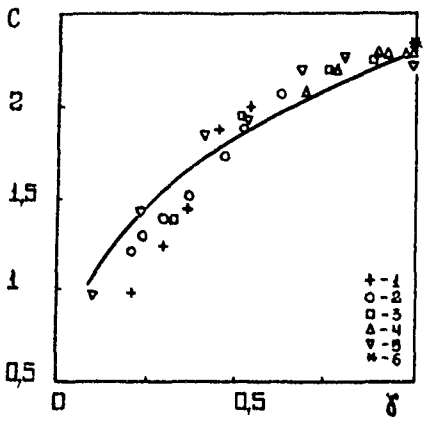

Figure 1

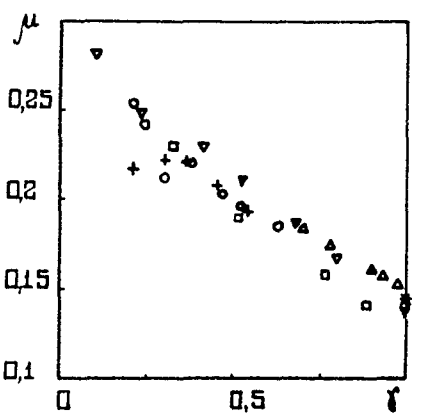

Figure 2

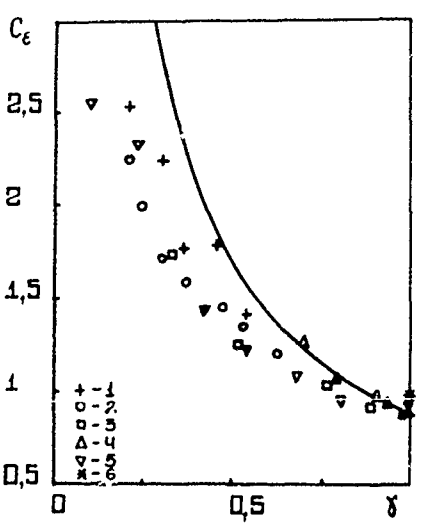

Figure 3

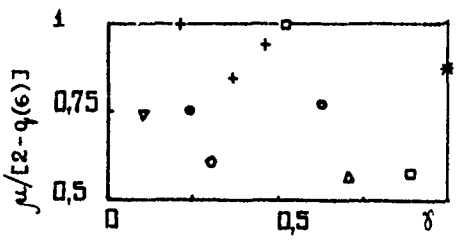

Figure 4

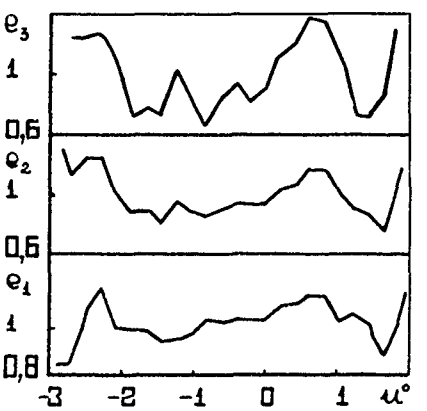

Figure 5

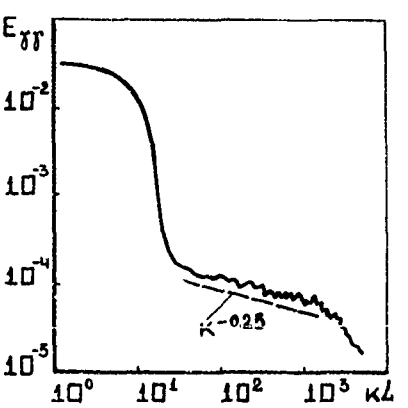

Figure 6

EIGHTH SYMPOSIUM ON
TURBULENT SHEAR FLOWS
Technical University of Munich
September 9-11, 1991

The Formation and Extent of Turbulence-Driven Secondary Flows in a Curved Pipe

Y.G. Lai, R.M.C. So and H.S. Zhang
Mechanical and Aerospace Engineering
Arizona State University
Tempe, AZ 85287

Abstract

If the source of streamwise vorticity generation is analyzed, a turbulence-driven secondary flow is found to be possible in a curved pipe. Recent hot-wire measurements provide some evidence for its existence. To further verify the formation and extent of this turbulence-driven secondary flow, a near-wall Reynolds-stress closure is used to carry out a detailed numerical investigation of a flow in a U-bend with a fully-developed turbulent flow at the bend entrance. Numerical results reveal that there are three vortex pairs in a curved pipe. The primary one is the Dean-type vortex pair. Another pair exists near the pipe core and is a consequence of local pressure imbalance. A third pair is found near the outer bend and is the turbulence-driven secondary flow. It starts to appear around 60° from the bend entrance, grows to a maximum strength at the bend exit, and disappears altogether at about 7 pipe diameters downstream of the bend.

1. Introduction

It is known that Reynolds-stress gradients could generate streamwise vorticity in a turbulent flow. The vortical motion thus generated is classified as turbulence-driven secondary flow by Bradshaw (1987). A typical example of this secondary motion can be found in the flow through a straight square duct (Gessner and Emery 1981, Demuren and Rodi 1984). These investigations reveal that a counter-rotating pair of vortices are present at each corner, and they are superimposed on the primary flow. Other examples of turbulence-driven secondary flows are found in three-dimensional free jets (Sforza et al. 1966) and wall jets (Launder and Rodi 1983).

Up to now, convincing evidence of turbulence-driven secondary flow in a curved pipe has not been found. The reasons for this could be attributed to flow complexity and measurement difficulties. According to Bradshaw (1987), the laser Doppler velocimeter could not be relied on to produce accurate cross-stream flow statistics. On the other hand, if hot-wire technique were used, the stress measurements would be subjected to calibration uncertainties and/or ill-conditioned subtraction of hot-wire signals (Anwer et al. 1989). These difficulties were further compounded by the relatively weak strength of the secondary motion and by its presence near the pipe wall. In spite of these difficulties, hot-wire measurements were attempted by Anwer et al. (1989). The measurements were obtained along the symmetry line AA and the vertical line BB of the pipe cross-section (Fig. 1). Some of their mean radial velocity distributions along AA did suggest the existence of a secondary flow near the outer bend.

The objective of the present study is to investigate the formation and extent of turbulence-driven secondary flows in curved pipes. The source of this generation is first identified. This is followed by a detailed numerical investigation using a suitable near-wall Reynolds-stress closure.

2. Vorticity Generation Near Outer Bend

By considering the torque exerted on a fluid element, Hornung (1988) was able to derive an expression for the vorticity generation source and thereby explain the secondary flow created by anisotropy of the normal stresses due to turbulence or viscoelasticity in pipes of non-circular cross-section. The same approach is used in the present study to examine the existence of turbulence-driven secondary flows in curved pipes. A mean vorticity transport equation obtained by taking the curl of the mean momentum equation is given by:

$$\frac{D\vec{\omega}}{Dt} - \vec{\omega}\cdot\nabla\vec{V} = \frac{1}{\rho}\nabla\times\left(\nabla\cdot\vec{\bar{\sigma}}\right) , \qquad (1)$$

where $\vec{\omega}$ is the mean vorticity, $\vec{V}$ is the mean velocity, $\vec{\bar{\sigma}}$ is the and turbulence viscous stress tensor and ρ is the fluid density. Eq. (1) is written in terms of the usual Reynolds-averaged quantities. It can be seen that the right hand side of Eq. (1) represents the torque exerted on a fluid element and it is this term that is responsible for vorticity generation in an incompressible flow in the absence of body forces.

If the radius ratio, $\epsilon = a/R$, is very small and viscous effects are neglected, dimensional arguments applied to Eq. (1), lead to the neglect of all terms except one turbulent term in the stream component of the vorticity generation source. In toroidal coordinates (Fig. 1), it can be written as:

$$\left(\nabla\times\nabla\cdot\vec{\bar{\sigma}}\right)_\theta = -\frac{1}{r^2}\frac{\partial}{\partial r}\left[r\frac{\partial(\overline{v^2}-\overline{u^2})}{\partial\psi}\right] . \qquad (2)$$

It can be seen that the anisotropy of the cross-stream turbulent normal stresses $(\overline{v^2}-\overline{u^2})$ is primarily responsible for the streamwise vorticity generation near the outer bend of a curved pipe.

Experimentally, it is known that near a wall, the normal stress parallel to the wall is always larger than the normal stress perpendicular to the wall. Therefore, the behavior of the $\overline{v^2}$ and $\overline{u^2}$ near the wall for a particular ψ can be postulated as shown in Fig. 2b. A similar curve for $\psi + d\psi$ can also be constructed. The distribution of $(\overline{v^2}-\overline{u^2})$ at ψ and $\psi + d\psi$ can now be calculated and plotted in Fig. 2c. It should be pointed out that, in the immediate vicinity of the wall, $(\overline{v^2}-\overline{u^2})$ is higher for the $(\psi + d\psi)$ curve because $\overline{v^2}$ has a higher generation due to the Dean-type secondary motion. However, $(\overline{v^2}-\overline{u^2})$ for the $(\psi + d\psi)$ curve would decrease faster away from the wall and at some radial location would fall below the corresponding value for the ψ curve. Therefore, the behavior shown in Fig. 2c represents the consequences of the competing influence between the near-outer-bend secondary flow and the primary streamwise flow. The calculated stress gradient is shown in Fig. 2d. Finally, the vorticity generation term is estimated according to Eq. (2) and shown in Fig. 2e. This rather simple qualitative analysis shows that negative vorticity is generated in the flow near the outer bend on the top half of the pipe.

3. Numerical Verification

The flow through a curved bend with $\alpha = 0.077$ and a Reynolds number of 50,000 has been investigated numerically by Lai et al. (1991). They used a partially parabolized numerical scheme to integrate the governing equations and tested various turbulence closures for their ability to calculate such a flow. Low-and high-Reynolds-number Reynolds-stress closures, with different pressure-strain models are investigated. The calculated mean velocities and turbulence statistics were compared with the measurements of Anwer et al. (1989). Their results show that all closures tested give reasonable predictions of mean velocities. As for turbulence statistics, the best correlation with data is given by the low-Reynolds-number Reynolds-stress closure of Lai and So (1990). The other calculations fail to predict correctly, even in a qualitative sense, the increase in anisotropy of the normal stresses in the entrance region of the pipe. This means that improving the pressure-strain model alone is not sufficient to predict the increase in anisotropy of the normal stresses. Therefore, all closures tested, except that of Lai and So (1990), would not be appropriate for use in the analysis of secondary motions in curved-pipe flows, particularly in the prediction of turbulence-driven secondary cells.

The low-Reynolds-number Reynolds-stress calculations of Lai et al. (1991) are used to verify the arguments given in §2. To do this, the secondary flow pattern and normal stress profiles near the outer bend wall at $\theta° = 112.8$ are shown in Fig. 3. In these plots, the normal stress distributions are shown at $\psi° = 9.31$ while their derivatives are shown at $\psi° = 12.41$. The reason is that $\Delta\psi = 6.21°$ and the ψ - derivatives are evaluated between $\psi° = 9.31$ and $\psi° = 15.52$. Three secondary flow patterns are visible, one is the Dean-type secondary motion, another is the flow reversal near the pipe core, while the third occurs near the outer bend and is the turbulence-driven secondary flow. Plots of the normal stresses and their gradients show that negative vorticity generation in the region $0 < (1-r/a) < 0.1$ is about seven times larger than that at $\theta° = 21.6$ where there is no secondary cell at the outer bend. This means that the vorticity generated is not sufficient to sustain a secondary flow at $\theta° = 21.6$. As expected, negative vorticity generation is obtained in the upper half of the curved pipe. Since there cannot be a net vorticity generation in a curved-pipe flow, a positive vorticity generation of equal strength would also develop near the outer bend in the lower half of the curved pipe.

The close-ups of the cross-stream velocity vector near the outer bend are plotted in Fig. 4, while the normalized mean radial (U/W_o) velocities along AA extending from the outer bend wall to $r/a = 0$ are shown

in Fig. 5. In Fig. 4, the length of the arrow-head line represents the magnitude of the velocity at that point and every plot has the same scale. Therefore, this allows the strength of the secondary cell to be compared directly. These plots clearly show that the turbulence-driven secondary cell starts to appear around $\theta^\circ = 60$ and grows stronger as the flow moves through the bend into the downstream straight pipe. Its strength reaches a maximum at $\theta^\circ = 180$ (Figs. 4 and 5) and then starts to decay exiting into the straight pipe. The reason is the recovery of $(v^2 - u^2)$ to its fully-developed straight-pipe behavior and the approach to axial symmetry. As a result, the gradient of the normal stresses along ψ decreases sharply and so is the vorticity generation source. It takes about 7 pipe diameters to complete this process, even though at this location the Dean-type secondary motion is still quite evident. When the high-Reynolds-number Reynolds-stress calculations are analysed for turbulence-driven secondary flow, the cell is found to form at about $\theta^\circ = 135$ and disappear at adout S/D = 4. Even then, the strength of the cell is substantially weaker than that predicted by the low-Reynolds-number closure.

Finally, it should be pointed out that So et al (1991) have carried out extensive calculations of developing laminar curved-pipe flows to investigate the formation and extent of secondary cells. Their calculations covered an α range of 0.04 to 0.143, a Dean number range of 277.5 to 1360 and a uniform, potential vortex and parabolic inlet flow. The results show that the secondary flow pattern in the cross-stream half plane varies from one cell to three cells dependent on α, Dean number and inlet flow. For parabolic inlet flow, a three-cell pattern exists for all α and Dean Number tested. The three cells consist of the Dean cell, a second cell near the pipe center and a secondary separation cell near the inner bend. There is no secondary cell formed near the outer bend for all conditions examined. Therefore, these results lend credence to the claim that the secondary cell formed near the outer bend in developing curved-pipe flowis turbulence-driven

Research support from the Office of Naval Research under Grant No. N0014-81-K-0428 and from the David Taylor Research Center, Annapolis, MD under Contract No. N00167-86-K0075 is gratefully acknowledged.

Reference

Anwer, M., So, R.M C. and Lai, Y.G. 1989 Perturbation by and recovery from bend curvature of a fully developed turbulent pipe flow. *Phys Fluids A* 1, 1387-1397.

Bradshaw, P. 1987 Turbulent secondary flows *Ann Rev Fluid Mech* 19, 53-74.

Demuren, A.O and Rodi, W. 1984 Calculation of turbulence-driven secondary motions in non-circular ducts *J. Fluid Mech* 140, 189-222.

Gessner, F.B., and Emery, A.F. 1981 The numerical prediction of developing turbulent flow in rectangular ducts *J Fluids Eng* 103, 445-455.

Hornung, H G. 1988 Vorticity generation and secondary slows *AIAA Paper No 88-3751-CP, Proc 1st National Fluid Dynamics Congress* 1, 566-571, July 25-28, Cincinnati, Ohio.

Lai, Y G. and So, R.M.C. 1990 On near-wall turbulent flow modelling. *J Fluid Mech* 221, 641-673.

Lai, Y G , So, R M.C., Anwer, M. and Hwang, B C. 1991 Calculations of a curved-pipe flow using Reynolds-stress closures. *Proc Inst Mech Engrs* , accepted for publication.

Launder, B.E and Rodi, W. 1983 The turbulent wall jet - measurements and modelling. *Ann. Rev Fluid Mech* 15, pp. 429-459.

Sforza, P.M., Steiger, M.H. and Trentacoste, N. 1966 Studies on three-dimensional viscous jets *AIAA Journal* 4, 800-806.

So, R.M.C., Zhang, H.S. and Lai, Y.G. 1991 Secondary cells and separation in developing laminar curved-pipe flows. *Theo. Comp Fluid Dyn* , accepted for publication.

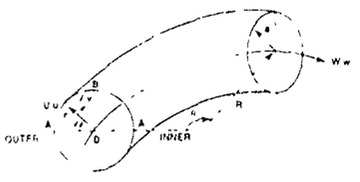

Figure 1. Schematic of a curved pipe and the toroidal coordinate system used.

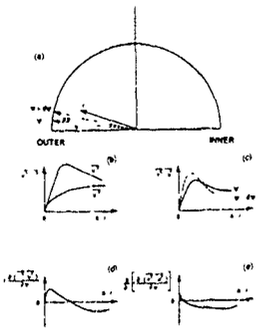

Figure 2. Qualitative behavior of the turbulent normal stresses near the outer bend of a curved pipe.

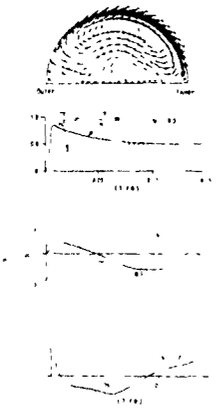

Figure 3. Calculated secondary flow pattern and the behavior of the normal stresses and their gradients near the outer bend at $\theta^\circ = 112.8$.

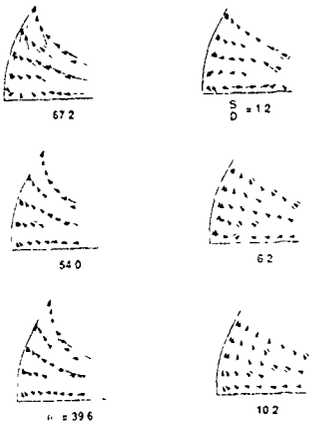

Figure 4. Calculated development of the turbulence-driven secondary flow near the outer bend.

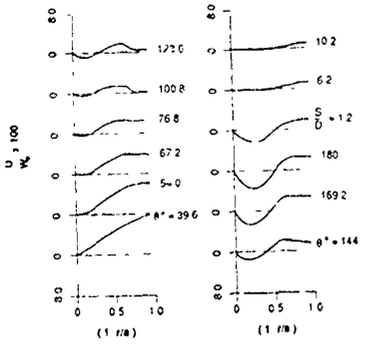

Figure 5. Calculated mean radial velocity distributions along AA at various streamwise locations.

EIGHTH SYMPOSIUM ON
TURBULENT SHEAR FLOWS
Technical University of Munich
September 9-11, 1991

I-10

THE DEVELOPMENT OF FULLY DEVELOPED TURBULENT PIPE FLOW (AN ANALYTICAL AND EXPERIMENTAL STUDY OF THE ENTRANCE REGION)

E.M. Laws and M. Aichouni

Department of Aeronautical and Mechanical Engineering
University of Salford, Salford M5 4WT, Great Britain.

The attainment of fully developed flow conditions starting from the clean, thin boundary layer entry condition has been the subject of considerable interest by a number of research workers .(e.g. Barbin&Jones (1963), Deissler (1955), Priest (1975), Martinuzzi&Pollard (1989)). For a low turbulence intensity flow a clear 'overshoot' of the fully developed flow levels was established following boundary layer merger (after a development length of some 35-40 pipe diameters) after which the flow was assumed to develop asymptotically to its fully developed values. The duct length necessary to establish 'fully developed' flow conditions is not firmly established but work by Reichert&Azad (1976,1979) would suggest that this could be 200-300 pipe diameters, considerably more than the entrance length of approximately 60 pipe diameters considered sufficient by Deissler and Barbin & Jones.

The K-ε turbulence model has been shown to be capable of predicting quite accurately the overshoot phenomenon clearly established experimentally
Beyond a development length of 40 pipe diameters there is however an absence of good test data to allow more detailed comparison of computational and experimental work. Even in the early stages of the development where significant velocity and turbulence changes take place the available data is not sufficient to accurately calculate axial gradients of flow quantities

In addition to establishing that the entrance length was considerably longer than had previously been considered Reichert & Azad concluded that the flow development was clearly non-asymptotic even following the initial overshoot In this they are in agreement with earlier experimental work by Laws,Lim & Livesey (1979,1987) in an investigation into the decay of highly distorted pipe flows. Here the axial development of mean flow and turbulence quantities and their axial gradients were shown to have a pronounced oscillatory nature and it was postulated that this mode of development was a feature of most wall bounded flows.

In the present investigation further experimental work on the decay of a distorted flow has been carried out The preliminary experimental work has focused on the first 12 diameters of the decay/development of a distorted peaked profile with $(u/\bar{u})_{centreline}$ value of ≈1.4 though further work will cover in similar detail a downstream test length within the nominally 'fully developed' range
A very detailed measurement programme involving measurements of time mean velocity, turbulence intensity and shear stress at axial stations of 1/16 pipe diameter pitch has been carried out The aim of the programme was to obtain good high quality test data against which computational models of the decay/development could be properly validated and from which accurate axial gradients could be determined.

The experimental results obtained indicate clearly the two features evident in the earlier studies by the Laws,Lim and Livesey,i.e, the intersection point occurrence (see fig 1) and the oscillatory nature of the development . Because of the closely spaced axial traverse planes it was considered that the data was sufficient to obtain accurate axial

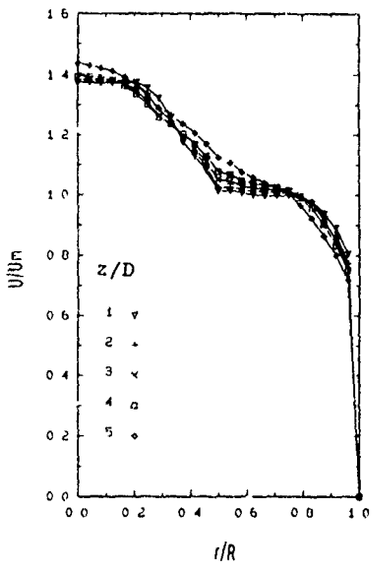

Fig. 1 Velocity Profiles measured every diameter

gradients of mean flow quantities ($\partial u/\partial z$, $\partial^2 u/\partial z^2$ etc) to allow profiles of these quantities and the radial velocity distribution v to be obtained These show (see fig 2) several unusual features associated with the decay process and clearly the radial velocity profiles can be shown to totally change sign at specific z/D locations confirming the oscillatory nature of the flow development. Thus there are a number of axial locations associated with the flow development where the condition $v=0$ is achieved (a condition normally associated with fully developed flow) but these 'quasi' fully developed stations are no more than stationary points in the overall flow development for when $\partial u/\partial z=0$ and hence $v=0$ the development clearly shows that $\partial^2 u/\partial z^2 \neq 0$.

EIGHTH SYMPOSIUM ON
TURBULENT SHEAR FLOWS
Technical University of Munich
September 9-11, 1991

SOME RECENT DEVELOPMENTS IN THE APPLICATION OF RENORMALISATION METHODS TO PROBLEMS IN TURBULENCE

W.D. McComb, M. Filipiak, W. Roberts and A.G. Watt

Physics Department
University of Edinburgh
The King's Buildings
Edinburgh EH9 3JZ

ABSTRACT

Here we report some of the latest results from (a) the LET theory, and (b) the method of iterative averaging.

INTRODUCTION

Fundamental work on turbulence at Edinburgh is divided into the study of renormalised perturbation theory (the Local Energy Transfer theory, or LET) and renormalisation group methods (implemented as the method of iterative averaging). In both cases we study the Fourier components of the velocity field in k space, so we begin by writing down the solenoidal Navier-Stokes equations and all the necessary definitions (see, for instance, McComb(1990)):

$$\left(\frac{\partial}{\partial t}+\nu k^2\right)u_\alpha(\mathbf{k},t) = M_{\alpha\beta\gamma}(\mathbf{k})\int u_\beta(\mathbf{k}-\mathbf{j},t)u_\gamma(\mathbf{j},t)\,d^3j + f_\alpha(\mathbf{k},t) \quad (1)$$

where ν_0 is the kinematic viscosity, f is the stirring force, and

$$M_{\alpha\beta\gamma}(\mathbf{k}) = \frac{1}{2i}\left[k_\beta D_{\alpha\gamma}(\mathbf{k})+k_\gamma D_{\alpha\beta}(\mathbf{k})\right] \quad (2)$$

and the projection operator is given by

$$D_{\alpha\beta}(\mathbf{k}) = \delta_{\alpha\beta}-k_\alpha k_\beta/k^2 \quad (3)$$

LET

LET is a general theory of turbulence and is the only renormalised perturbation theory which yields the Kolmogorov spectrum as its solution in an Eulerian (i.e. laboratory) coordinate frame. It has been investigated numerically for the case of freely decaying isotropic turbulence and has proved to be capable of predicting even the finest statistical details of the turbulence, over a huge range of Reynolds numbers (McComb and Shanmugasundaram(1984,1991), McComb, Shanmugasundaram and Hutchinson(1989)).

The basic hypothesis of LET is that the turbulent response can be represented by an exact propagator:

$$u_\alpha(\mathbf{k},t) = H_{\alpha\beta}(\mathbf{k};t,t')u_\beta(\mathbf{k},t'). \quad (4)$$

H is an averaged quantity. Then, forming a perturbation expansion for the correlation tensor Q, defined for homogeneous turbulence as

$$\langle u_\alpha(\mathbf{k},t)u_\beta(\mathbf{k}',t')\rangle = Q_{\alpha\beta}(\mathbf{k};t,t')\delta^3(\mathbf{k}+\mathbf{k}'), \quad (5)$$

using Eq. (4), and renormalising zero order quantities, we get, for the isotropic case:

$$\left(\frac{\partial}{\partial t}+\nu_0 k^2\right)H(k;t,s)Q(k;s,t') = \int d^3j\, L(\mathbf{k},\mathbf{j}) \times\left\{\int_0^{t'} dt''\, H(k;t',t'')Q(j;t,t'')Q(|\mathbf{k}-\mathbf{j}|;t,t'') - \int_0^{t} dt''\, H(j;t,t'')Q(k;t'',t')Q(|\mathbf{k}-\mathbf{j}|;t,t'')\right\}, \quad (6)$$

where $L(\mathbf{k},\mathbf{j})$ is a geometrical factor.

The same methods can be applied to the transport of a passive scalar, adding the corresponding hypothesis

$$\theta(\mathbf{k},t) = H^{\theta\theta}(\mathbf{k};t,t')\theta(\mathbf{k},t'), \quad (7)$$

resulting in the LET equations for passive scalar transport:

$$\left(\frac{\partial}{\partial t}+\kappa_0 k^2\right)H^{\theta\theta}(k;t,s)\Theta(k;s,t') = \int d^3j\, N(\mathbf{k},\mathbf{j}) \times\left\{\int_0^{t'} dt''\, H^{\theta\theta}(k;t',t'')\Theta(j;t,t'')Q(|\mathbf{k}-\mathbf{j}|;t,t'') - \int_0^{t} dt''\, H^{\theta\theta}(j;t,t'')\Theta(k;t'',t')Q(|\mathbf{k}-\mathbf{j}|;t,t'')\right\}, \quad (8)$$

where

$$\langle\theta(\mathbf{k},t)\theta(\mathbf{k}',t')\rangle = \Theta(\mathbf{k};t,t')\delta^3(\mathbf{k}+\mathbf{k}'), \quad (9)$$

and $N(\mathbf{k},\mathbf{j})$ is a geometrical factor.

Scalar transport computations have been performed at a range of Reynolds numbers and Prandtl numbers. At low R_λ we get self-similar spectra and two-time correlation curves. The velocity-scalar cross derivative skewness values are similar to those shown in Kerr(1985) Fig. 3, but have rather different behaviour with Pr, see Fig. 1

LET is now being extended to treat weakly sheared flows, where the departure from isotropy is small enough to allow simple computations. The application to strongly inhomogeneous flows presents more severe computational difficulties. Such an approach is potentially important in that it could provide synthetic boundary conditions for use with large-eddy simulation.

ITERATIVE AVERAGING

Although the LET Theory offers a rather comprehensive description of turbulence, without recourse to adjustable constants, it is nevertheless *ad hoc* in the sense that it is derived by truncating a renormalised perturbation series at a given order without

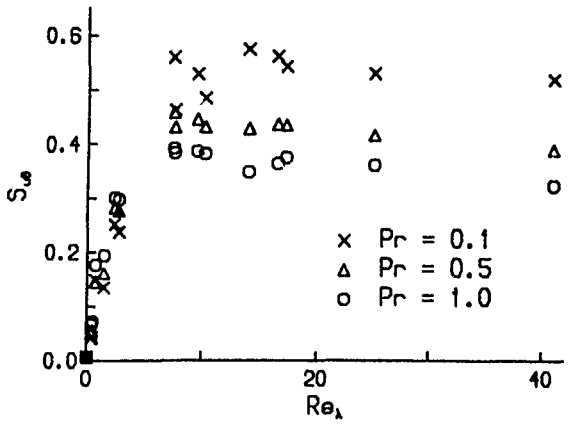

Fig. 1: Velocity-scalar cross derivative skewness against R_λ

any *a priori* justification for so doing. In contrast, while Iterative Averaging offers no more than the prediction of the subgrid stress which represents the effect of eliminated modes, it has been clear from the first that it also offers the hope of basing such a prediction solely on rational approximations.

The thrust of Iterative Averaging, and all RG approaches to the turbulence problem, is to reduce the number of modes that have to be explicitly computed by averaging out the smaller scale modes. We begin by decomposing the velocity field into explicit scales for $k \le k_1$ and implicit scales for $k_1 \le k \le k_0$:

$$\begin{aligned} U_\alpha(\mathbf{k}) &= U_\alpha^- \quad \text{for} \quad 0 \le k \le k_1 \\ &= U_\alpha^+ \quad \text{for} \quad k_1 \le k \le k_0, \end{aligned} \tag{10}$$

where k_1 is defined by

$$k_1 = (1-\lambda)k_0, \tag{11}$$

with the bandwidth parameter λ satisfying the condition $0 \le \lambda \le 1$. Then the RG approach can be carried out as follows:

1. Solve the NSE on $k_1 \le k \le k_0$. Substitute that solution for the high-k modes back into the NSE on $1 \le k \le k_1$. This results in an increment to the viscosity $\nu_0 \to \nu_1 = \nu_0 + \delta\nu_0$.

2. Rescale the basic variables so that the NSE on $0 \le k \le k_1$ look like the original NSE on $0 \le k \le k_0$.

These two stages are then repeated to eliminate the effect of high wavenumbers progressively.

A conditional average is used which smooths out the effect of the high-k modes, while keeping the U^- constant. We represent it by an operator $A[U^+|U^-]$ and denote its effect on the first shell of wavenumbers to be eliminated by $\langle\rangle_0$. It then follows that this operator has the properties:

$$\langle U_\alpha^-(\mathbf{k})\rangle_0 = U_\alpha^-(\mathbf{k}), \tag{12}$$

$$\langle U_\alpha^-(\mathbf{j})U_\beta^-(\mathbf{k}-\mathbf{j})\rangle_0 = U_\alpha^-(\mathbf{j})U_\beta^-(\mathbf{k}-\mathbf{j}) \tag{13}$$

The final result for the fixed-point viscosity is given by

$$\nu(k_n k') = \alpha^{1/2}\epsilon^{1/3}k_n^{-4/3}\tilde{\nu}_n(k'), \tag{14}$$

where the coefficient $\tilde{\nu}_n(k')$ is given by the recursion relationship

$$\tilde{\nu}_{n+1}(k') = h^{4/3}\tilde{\nu}_n(hk') + h^{-4/3}\delta\tilde{\nu}_n(k'), \tag{15}$$

with

$$\delta\tilde{\nu}_n(k') = \frac{1}{4\pi k'^2}\int d^2j' \frac{L(k',j')Q'}{\tilde{\nu}_n(hj')j'^2 + \tilde{\nu}_n(hl')l'^2}, \tag{16}$$

for the wavenumber bands $0 \le k' \le 1, 1 \le j', l' \le h^{-1}$, where $l' = |\mathbf{k}' - \mathbf{j}'|$ and

$$Q' = h^{11/3} - \frac{11}{3}h^{14/3}(l' - h^{-1}) + \ldots \tag{17}$$

The coefficient $L(k',l')$ contains purely geometrical factors.

The Kolmogorov constant α is defined in this method by Eq. (14), and α is plotted against the bandwidth parameter in Fig. 2.

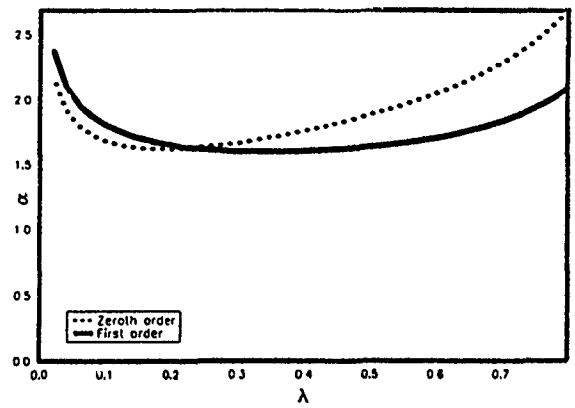

Fig. 2: Dependence of Kolmogorov constant on bandwidth

The Iterative Averaging method has now been applied to scalar transport, with encouraging results, and work is in progress on its application to inhomogeneous turbulence.

REFERENCES

McCOMB, W.D. (1978) J. Phys. A: Math. Gen., 9, 179.

McCOMB, W.D. (1982) Phys. Rev. A, 26, 1078.

McCOMB, W.D. (1990) *The Physics of Fluid Turbulence*, Clarendon Press, Oxford.

McCOMB, W.D. and SHANMUGASUNDARAM, V. (1984) J. Fluid Mech., 143, 95.

McCOMB, W.D. and SHANMUGASUNDARAM, V. (1991) J. Fluid Mech., submitted for publication.

McCOMB, W.D., SHANMUGASUNDARAM, V. and HUTCHINSON, P. (1989) J. Fluid Mech., 208, 91.

McCOMB, W.D., SHANMUGASUNDARAM, V. and WATT, A.G. (1989) Application of RG methods to the large-eddy simulation of fluid turbulence. Joint GAMNI-IMA/SMAI Conf. on Computational Aerodynamics, Antibes, France, May 17-19, 1989.

McCOMB, W.D. and WATT, A.G. (1990) Phys. Rev. Lett., 65, 3281.

EIGHTH SYMPOSIUM ON
TURBULENT SHEAR FLOWS
Technical University of Munich
September 9-11, 1991

VORTEX INTERACTION IN THE WAKE BEHIND AN OSCILLATING AIRFOIL

K Morikawa and H. Grönig

Shock Wave Laboratory, Technical University Aachen
Templergraben 55, 5100 Aachen, Federal Republic of Germany

ABSTRACT

Vortex interaction in the wake behind a NACA 0012 airfoil with pitching oscillation in unsteady flow is investigated. Two sets of experiments have been carried out: while the first one concentrates on the periodic quasi-steady state of the flow, the second one deals with its starting stage. From the flow visualization by the dye injection method, the wake is classified into six types, depending on the reduced frequency and amplitude. Phenomena of transition to turbulence and reorganization of the wake type was interpreted as a result of vortex interaction.

INTRODUCTION

Large-scale coherent structures, especially in the turbulent mixing layer, have been one major topic of turbulence investigation since Brown & Roshkos' experiments[1]. Bloor[2] and Kourta et al. [3] studied the wake-shear layer interaction behind a circular cylinder and showed that a set of non-linear frequency interactions is progressively generated in the wake, finally resulting in transition to turbulence. Such detailed information about a vortex interaction in the wake, however, seems to be available only in the case of a circular cylinder. The main purpose of the present study is to understand phenomena of this kind also in the more complex wake of an oscillating airfoil in unsteady flow. The flow configuration is shown in Fig. 1. The vortices can be classified into two different groups: 1) the large scale vortex (LSV), which is induced each half period of pitching oscillation, and 2) the small scale vortex (SSV), which is generated in the shear layer. Two sets of experiments have been carried out: while the first one concentrates on the periodic quasi-steady state of the flow, the second one deals with its starting stage, where the unsteady effects of the external flow are important. The following experimental parameters are varied in a wide range: frequency and amplitude of oscillation and Reynolds number.

EXPERIMENTAL SETUP

The experimental setup consists of the vertical water-Ludwieg-tunnel (Fig.2), which was proposed by Akamatsu [4] and built at the Aachen Shock Wave Laboratory [5]. The principle of operation is as follows: the high pressure section is separated from the low pressure part by a fast acting valve. When this valve is opened, by gravity and additional pressure difference the flow is accelerated to a steady velocity within the range of tens of milliseconds. The pitching oscillation of the airfoil is driven by a step motor, being controlled by an IBM PC. Center point of the rotation is set 50% of the chord length. Throughout the present study the onset of oscillation is fixed at the instant of flow start. Applied experimental techniques are flow visualization with the dye injection method and velocity measurement by Laser Doppler velocimetry (LDV). The frequency is varied between 0.5 and 20Hz, the amplitude of oscillation between 1° and 5° and the Reynolds number between 4500 and 31000. The Reynolds number is defined by the external steady velocity and the chord length. The type of oscillation is a sinusoidal one around 0°.

RESULTS

From the flow visualization with the dye injection in the first part of the experiments, six wake patterns can be distinguished as shown in Fig. 3. Which type of pattern occurs depends on the reduced frequency K and the amplitude α [°] (with $K=\pi f c/Uo$, f: frequency [Hz], c: chord length [m], Uo: steady external velocity [m/sec]). With increasing reduced frequency K, the wake patterns change from (1) a wavy wake , over (2) a splitted wavy wake, (3) a rolled-up wake, (4) a straight rolled-up wake, (5) a strong rolled-up wake, to (6) a fully turbulent wake. This classification is very similar to the one, which is made by Oshima et al. [6] for the case of heaving motion. Integration of SSVs to LSV is observed near the trailing edge region for the cases of rolled-up wakes (4,5) to fully turbulent wake (6). This process is understood as an onset of the transition to turbulence: the LSVs are interacting on each other. At a certain region the wake loses its two-dimensionality and forms a turbulent region (see Fig.4a). This region progresses upstream but does never reach the trailing edge. Consequently two flow-regimes can be distinguished: a strong rolled-up one and a fully turbulent one. In the case of the high reduced frequency and small amplitude, the following events are observed: LSVs are interacting on each other and form the strong rolled-up wake (5) (see Fig.4b). Within the investigated region this does not develop to the turbulent wake but reorganises to a rolled-up wake (3). The second part of experiments are focused on the development of the starting vortex. After the point of inflection has developed on the wavy-like separated boundary layer, it is rolled up in the wake. This point is supposed to become the center of the vortex.

CONCLUSION

Phenomena induced by vortex interaction in wakes generated behind oscillating NACA 0012 airfoils are investigated. Six groups of wake patterns can be classified: wavy wakes, splitted wavy wakes, rolled-up wakes, straight rolled-up wakes, strong rolled-up wakes and fully turbulent wakes occurring with increasing reduced frequency. The bigger the amplitude of oscillation is, the faster the pattern changes to fully turbulent wakes. Transition to turbulence and reorganization of the wake is understood as a result of vortex interaction. Detailed information of vortex interaction is deduced from LDV measurements and spectral analysis.

REFERENCES

[1] BROWN, G.L., ROSHKO, A. 1974 On density effects and large structure in turbulent mixing layers. J. Fluid Mech. 64, 775-816.

[2] BLOOR, M.S. 1964 The transition to turbulence in the wake of a circular cylinder. J. Fluid Mech. 19, Part2, 290-304.

[3] KOURTA, A., BOISSON, H.C., BRAZA, M., CHASSAING, P. & HA MINH, H. 1985 " Wake-Shear Layer Interaction and the Onset of Turbulence Behind a Circular Cylinder" from "Turbulent Shear Flows 5", 82-97. Springer-Verlag.

[4] AKAMATSU, T 1978 " Application of shock tube and shock wave research to studies of hydrodynamics " from "Shock Tube and Shock Wave Research", 24-35. University of Washington Press.

[5] KERRES, W. 1990 Wirbelsysteme an einem Profil beim Anfahrvorgang, Doctor thesis, Technical University Aacher., VDI rep. 172.

[6] OSHIMA, Y. & OSHIMA, K. 1980 "Vortical Flow Behind an Oscillating Airfoil" from "Theoretical and Applied Mechanics" , 357-368. North-Holland Publishing Company.

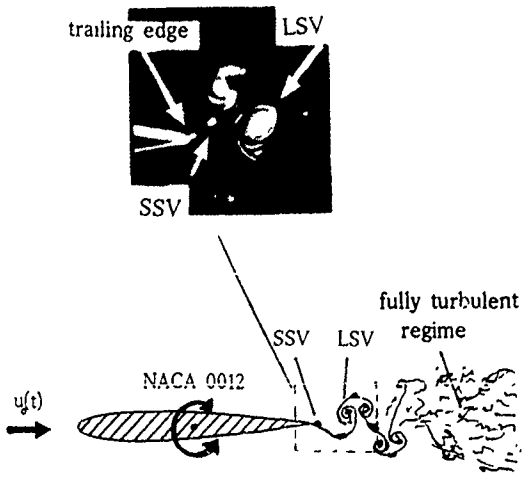

Fig. 1 Flow configuration

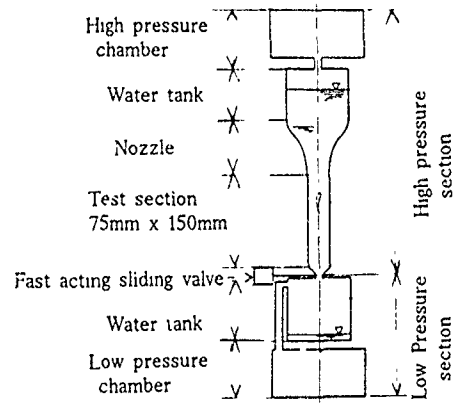

Fig. 2 Schematic diagram of water-Ludwieg-tunnel

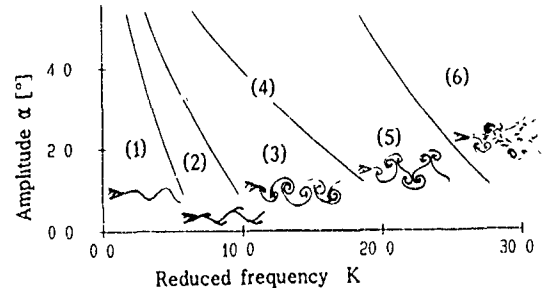

Fig. 3 Classification of wakes, Re=4500

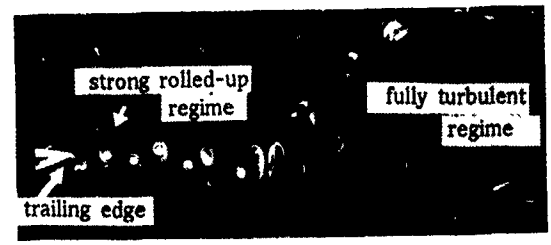

Fig. 4-(a) Phenomena of the transition to turbulence, K=28, Re=4500, α=2°, 1s

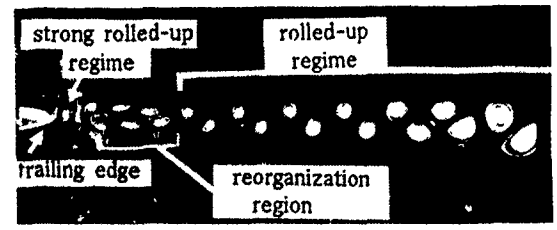

-(b) Phenomena of the reorganization of LSVs, K=21, Re=4500, α=1°, 1s

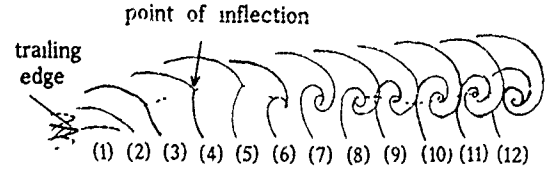

Fig. 5 The development of the starting vortex, K=21, Re=4500, α=2°, Δt=33ms

EIGHTH SYMPOSIUM ON
TURBULENT SHEAR FLOWS
Technical University of Munich
September 9-11, 1991

TURBULENT COUETTE TYPE FLOW WITH AN ALTERNATIVE PRESSURE GRADIENT

K. Nakabayashi, O. Kitoh *) and H. Iwata **)

*)Department of Mechanical Engineering, Nagoya Institute of technology, Gokisocho Showa-ku, Nagoya, 466 Japan

**)Nihon Denso Corp., 1-1 Showacho Kariya, 448 Japan

ABSTRACT

The experimental work has been made for Couette type flow with repeated pressure gradients that are realized in the channel consisted of a wavy fixed wall on one side and a moving wall on the other side (see Fig. 1). This work is an extension of El Telbany and Reynolds (1980) who investigated the Couette type flow with a constant pressure gradient. Measurements of mean velocities and turbulent intensities show that the flow is largely affected by the inertia force and upstream effect of turbulence. This type of flow simulates the flow in the high speed journal bearings operating in turbulent condition.

THEORETICAL BACKGROUND

Theoretical works on Couette type flows with a constant pressure gradient were made by El Telbany & Reynolds (1980) who indicated that the stress gradient across the channel $d\tau/dy$ (τ ;shear stress,y;wall distance) is a dominant parameter to understand the flow. There appears conventional wall law, half power law and defect law regions.

In journal bearing under loaded condition, the clearance changes along moving direction thus the inertia force and the repeated pressure gradient dP/dX, to appear and the equation of motion can be written as

$$\frac{1}{\rho}\frac{d\tilde{P}}{dx} = u\frac{\partial u}{\partial x} + v\frac{\partial u}{\partial y} + \frac{1}{\rho}\frac{dP}{dx} = \frac{1}{\rho}\frac{d\tau}{dy} \qquad (1)$$

Conditions $d\tilde{P}/dx = 0$ and $d\tilde{P}/dx = dP/dx$ correspond to Couette and Couette type flows with a constant pressure gradient respectively and the shear stress can be described by linear relation as $\tau = \tau_w + \frac{dP}{dx} y$. In general, however, there appears an inertia force and the shear stress is no more linear. However If we introduce a locally averaged stress gradients as

$$\alpha_B = \frac{1}{\rho}\left\langle\frac{d\tau}{dy}\right\rangle_B = \frac{1}{\rho y_B}\int_0^{y_B}\frac{d\tau}{dy}dy, \quad \alpha_S = \frac{1}{\rho}\left\langle\frac{d\tau}{dy}\right\rangle_S = \frac{1}{\rho y_S}\int_0^{y_S}\frac{d\tau}{dy}dy$$

, where yB, ys denote wall distance of boundary of buffer and half power regions, the same velocity laws can be developed as ElTelbany & Reynolds.

Close to wall, τ does not change significantly and using Van Driest damping factor A+, the following well known relation holds

$$u^+ = \int_0^{y^+} 1/\left[1 + \left\{1 + 4\kappa^2 y^{+2}\left(1 - \exp(-y^+/A^+)\right)^2\right]^{1/2}\right] dy^+ \qquad (2)$$

where u* is friction velocity and u+=u/u*, y+=yν/u*. AS the wall distance increases, τ can be expressed by the relation,

$$\tau^+ = \tau/\tau_w = 1 + \left\langle\frac{d\tau^+}{dy^+}\right\rangle y^+ = 1 + \frac{\alpha\nu}{u_*^3}y^+ .$$

Applying the mixing length theory to this region, log law and half power laws (Townsend 1961) are

$$u^+ = \frac{1}{\kappa}\log y^+ + B \qquad \left(1 \gg \frac{\alpha_B\nu}{u_*^3}y^+\right) \qquad (3)$$

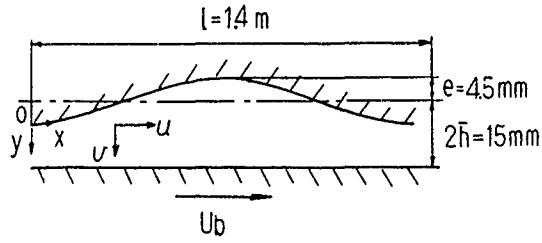

Fig. 1 Test channel having wavy and moving wall.

$$u^+ - \frac{1}{\kappa}\log\left\{\frac{4u_*^3\sqrt{1+y\alpha_s/u_*^2}-1}{\alpha_s\nu\sqrt{1+y\alpha_s/u_*^2}+1}\right\} = (2A+3B)(1+y\alpha_s/u_*^2)^{1/2} + C \quad \left(1 \ll \frac{\alpha_s\nu}{u_*^3}y^+\right) \qquad (4)$$

We assume a constant eddy viscosity in core region and the following relation holds.

$$\frac{u_c - u}{u_*} = D(1 - y/h) + C \qquad (5)$$

The velocity laws developed above were confirmed to hold for constant pressure gradient flows (locally equilibrium turbulent flow) by ElTelbany & Reynolds.

In addition to the inertia effect, there may exist upstream effect of turbulence in present flow which necessitates two-point closure model of turbulence. Comparisons between previous and present measured results in the light of above relations show that whether the present flows are locally equilibrium turbulent flow or not.

Tab. 1 Non-dimensional pressure gradient μ^{-1}

x/l	0	0.125	0.250	0.375	0.500	0.625
μ^{-1}	-0.009	0.017	0.025	0.026	0.018	-0.016
x/l	0 750	0.875				
μ^{-1}	-0.015	-0.023				

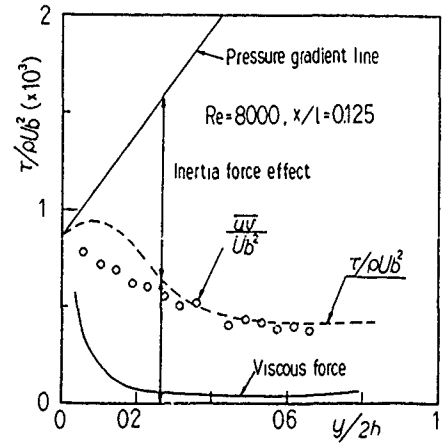

Fig. 2 Shear stress distribution. Balance among various forces, including inertia force.

EXPERIMENTAL RESULTS AND DISCUSSIONS

Figure 1 shows the test channel and coordinate system used. The mean velocity distributions and turbulent intensities are measured at various stream-wise positions of x/l for Reynolds number of Re=5000 and 8000. Non-dimensional pressure gradient parameters $\mu^{-1} = \nu\, dP/dx / \rho u_*^3$ are tabulated in Tab. 1 for Re=8000. Typical shear stress distributions are shown in Fig. 2. A broken line and open circle indicate shear stresses obtained from momentum equation and Reynolds shear stresses measured by hot-wire anemometer respectively. Significant contribution of inertia force on τ can be seen unlike the flow with a constant pressure gradient.

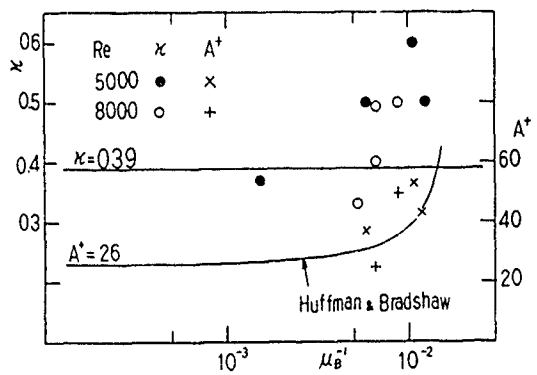

Fig. 3 Variation of Karmann and Van Driest constants with μ_β^{-1} in buffer region.

In buffer and log regions, two parameters κ and A^+ take well known value as functions of shear stress gradient parameter within buffer region $\mu_\beta^{-1} = \nu\omega_\beta / u_*^3$ for equilibrium turbulent flow (Huffman & Bradshaw 1972). Figure 3 compares present results of κ and A^+ with that of Huffman & Bradshaw. A general trend of A^+ is similar with the their results. However, the variation of κ with μ_β^{-1} is quite different. They insisted that κ is sensibly constant while the present results show it increases when $\mu_\beta^{-1} > 5\times10^{-2}$.

In half-power region, the constant (2A+3B) depends on the shear gradient $\lambda_s = \alpha_s k / u_*^2$. Here A equals $1/\kappa$ and B indicates turbulent diffusion coefficient. Figure 4 compares the present results with others for the case of $\alpha_s > 0$. The quantitative agreement can not been obtained although the general trend is the same.

Figure 5 shows the variation of constant D with μ^{-1}. A constant value of D=3.5 was obtained irrespective of μ^{-1} by El Telbany & Reynolds for Couette type flow with a constant pressure gradient. The variation of present values of D along the stream-wise direction follows the loop path instead of taking constant value. This means that the core region receives history effect of upstream.

Figure 6 shows the turbulent intensity profile in wall region. A broken line in the figure indicates the conventional wall similarity curve for u'/u_*. The present results deviate from this curve largely. This implies that the effect of repeated pressure gradient penetrates deep into wall region although it is not quite large. Figure 7 compares turbulent energy production and advection. Unexpectedly large advections are existed which may cause the locally unequilibrium turbulent flow in present case.

REFERENCES

El Telbany, M.M.M. & Reynolds, A.J. 1980 J. Fluid Mech. 100, 1-29.

Huffman, G.D. & Bradshaw, P. 1972 J. Fluid Mech. 53, Pt.1, 45-60.

Townsend, A.A. 1961 J. Fluid Mech. 11, 97-120.

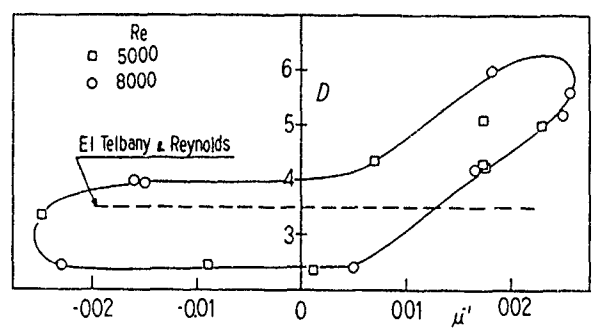

Fig. 5 Hysteresis change of defect law coefficient along stream-wise direction.

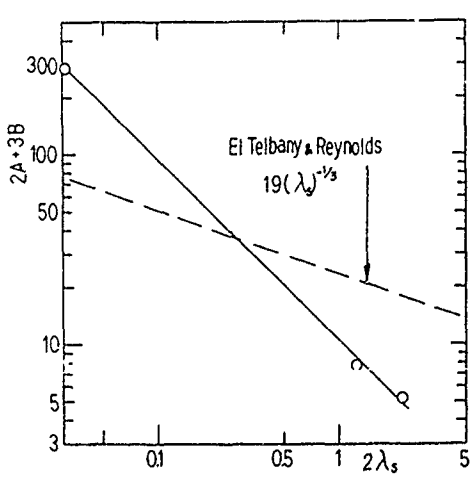

Fig. 4 Coefficient 2A+3B in Townsend type description of half power law.

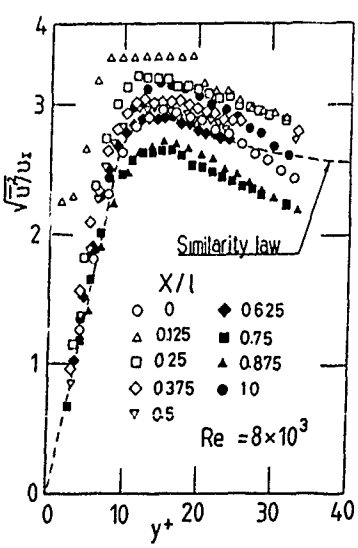

Fig. 6 Distribution of turbulent intensity at various sections.

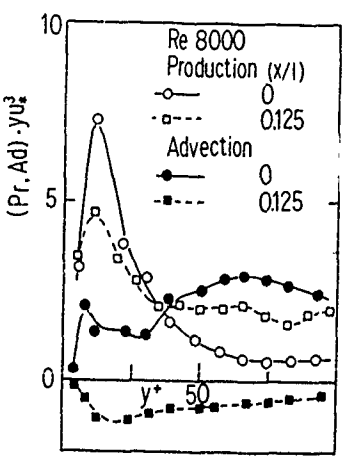

Fig. 7 Production and advection of turbulent kinetic energy.

EIGHTH SYMPOSIUM ON
TURBULENT SHEAR FLOWS
Technic .i University of Munich
September 9-11, 199.

The Coherent Structure in a Corner Turbulent Boundary Layer

by
I. Nakamura*, M. Miyata**, T. Kushida*
and
T. Yamaguchi***

* Department of Mechanical Engineering, Nagoya University
Nagoya, 464-01 Japan
** Department of Mechanical System Engineering, Yamanashi University, Kofu, 400 Japan
*** Matsushita Electric Industrial Co. Ltd.

1. Introduction

As a paradigmatic flow having the secondary flow of Prandtl's second kind, much research has been conducted on the turbulent shear flow along a corner formed by two perpendicular plates. Although a theoretical explanation has not yet been developed on the coherent structure in a flat plate turbulent boundary layer, many experimental and some CFD results have convincedly documented such a structure. Bursting is detected even in a rough wall turbulent boundary layer. It is therefore interesting to investigate how and to what extent the coherent structure will be modified by the secondary current. In what follows we will describe experimental results of the coherent structure in a corner turbulent boundary layer, shown schematically in Fig.1.

2. Measuring Method

Fig.1 also contains the coordinate system used, where y' denotes the corner bisector and z' is perpendicular to both x and y' axes. Uo is a constant free stream velocity which was so adjusted to give a unit Reynolds number of $U_0/\nu=3.5 \times 10^6 m^{-1}$, where ν is the kinematic viscosity of air. The working section of an Eiffel type wind tunnel is 0.5 x 0.3 m^2 and 2 m long. Measurements were performed at a section 1.9 m downstream from the leading edge, using a conventional hot-wire anemometer set.

3. The Effect of a Corner on Bursting

To detect the bursting event the short time variance is defined according to Blackwelder and Kaplan.

Figs.2a and 2b show the variations of the conditional mean velocity distributions during one bursting cycle, measured at a time elapsed from the onset of bursting, as well as the conventional mean velocity profiles denoted by dotted line, both obtained in the two-dimensional region. Well known decelerated and accelerated profiles can be seen clearly just before or after $\tau=0$. The results obtained at z=25mm show similar profiles as Figs.2a and 2b. A typical ejection process was seen to occur at nearly $\tau=-4 \sim -2$ ms and then a sweep process follows. The ensemble averaged velocity profiles differed from those in Figs.2a and 2b. At $\tau=-2$ ms in the section of 25mm, a strong shear layer develops near the region $y^+=30$ and the velocity above it shows a larger value than the conventionally averaged profile, which leads us to infer that a strong clockwise vortex is generated there. The

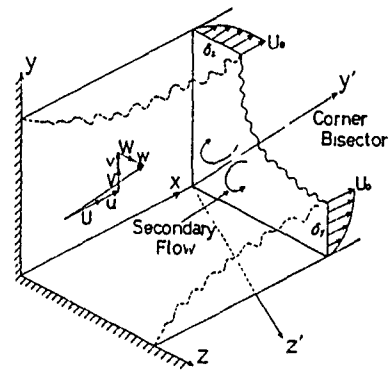

Fig.1. Flow field and coordinate system.

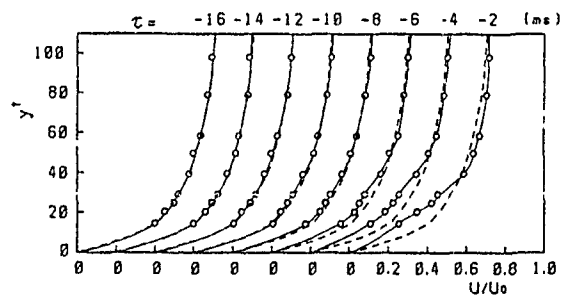

a). ejection period

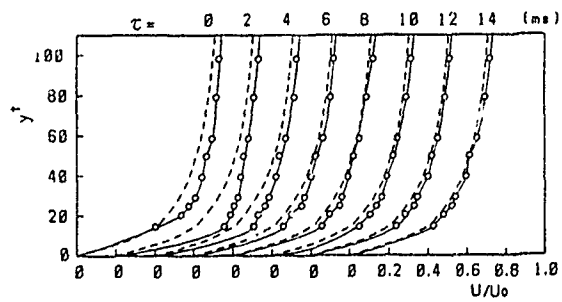

b). sweep period

Fig.2a,b. Variations of conditional mean velocity distributions during one bursting cycle at z=100 mm.

spanwise vortex parallel to the wall is lifted by the effects of both ejection and secondary current and may cause the high shear layer. Figs.3a and 3b show the bursting process at the position nearer to the corner. Ejection and sweep are obvious but the velocity profile shows a

more complex pattern. There are two changes, the one occurring in a small scale found at the region near $y^+=50$ and the other in a larger scale at near $y^+=20 \sim 30$. Specifically, in the sweep stage of $\tau=0 \sim 4$ms, there is a definite dent in the ensemble averaged profiles, which implies inflection point instability.

In order to examine more details of the relation between bursting and the secondary current, space time correlations conditioned by bursting were measured. An averaging time T, i.e. the bursting period, was estimated by $Tu\,\tau^2/\nu = 140$. Typical results of the conditioned space time correlation at z=25 mm are shown in Figs.4a($x_A = x_B$) and 4b($x_B = x_A+\delta$), where the burst detecting probe A is fixed at $y^+=15$ in both figures and the values of y^+ indicate the heights of probe B. In Fig.4a, the pattern of the bursting process changes significantly with the height of probe B, but it is not found in Fig.4b. Also in Fig.4a the peak value of the conditioned correlation shows a rapid decrease near $y^+=58$, indicating a localized character of bursting.

From the results mentioned above, iso-correlation contours conditioned by bursting are produced in Figs.5a, b and c. Comparing with the corresponding results in the two-dimensional region, it is suggested that the eddy conditioned bursting has a smaller scale than that of the conventionally correlated eddy. A similar feature can be found in Figs.5b and 5c and particularly Fig.5c(z=15mm) shows a significantly small spatial extent of the coherent eddy, compared it with 2-D region.

4. Concluding Remarks

From the experimental results described above, we can say that there is clear evidence of bursting in a turbulent boundary layer along a corner and that the bursting process is evidently modified by the interaction with the secondary current near the corner. The effects of the secondary current appear also in the space time correlation curves and the correlation contours conditioned by bursting show a significantly smaller eddy scale than that of a conventional one.

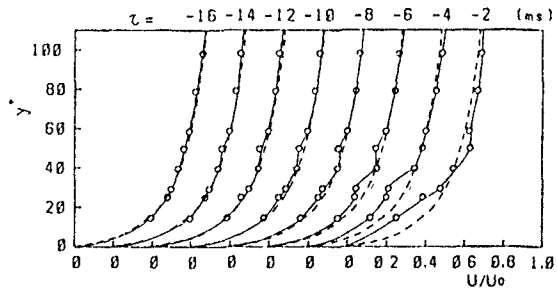

a). ejection period

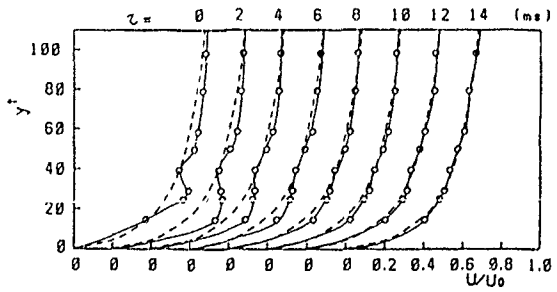

b). sweep period

Fig.3a,b. Variations of conditional mean velocity distributions during one bursting cycle at z=15 mm.

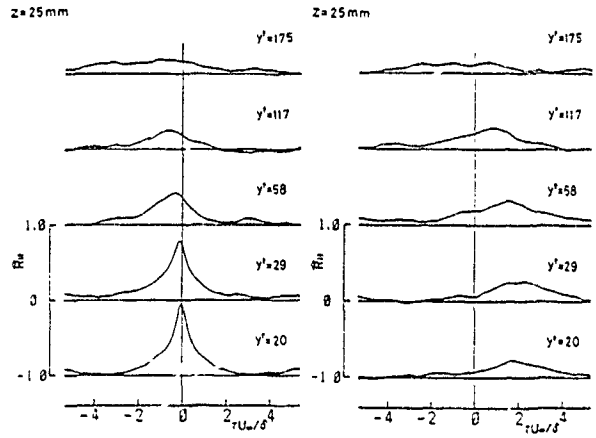

a). $x_A = x_B$ b). $x_B = x_A + \delta$

Fig. 4a,b. Distributions of space time correlation conditioned by bursting.

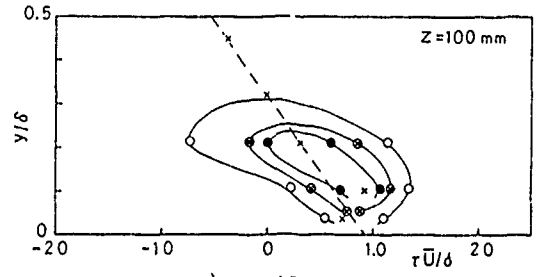

a). z=100 mm

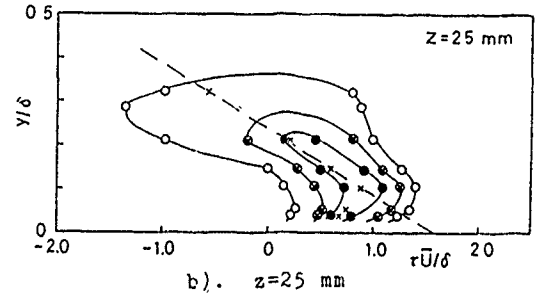

b). z=25 mm

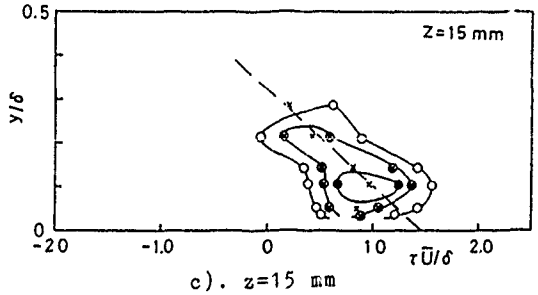

c). z=15 mm

Fig. 5a,b,c. Eddy shapes expressed as iso-correlation curves conditioned by bursting.

EIGHTH SYMPOSIUM ON
TURBULENT SHEAR FLOWS
Technical University of Munich
September 9-11, 1991

THE EFFECTS OF REYNOLDS NUMBER ON TURBULENT WALL LAYERS.

Ronald L. Panton*)
*)Mechanical Engineering Department
University of Texas
Austin TX, 78712, USA

ABSTRACT

This paper displays the theoretical form of composite expansions for mean flow properties and shows how they depend on Reynolds number. It also gives semi-empirical equations that have been fitted to channel flow results . Reynolds number trends of the experiments are well represented by composite expansions.

INTRODUCTION

There has been a interest in the effects of Reynolds number on turbulent wall layers. Much of this comes from the need to interpret flow visualization experiments and direct numerical simulations, Spalart(1988) and Kim et. al. (1987).

It is accepted that turbulent wall layers have a two layer structure; a classical singular perturbation situation. Mathematically the two-layer structure has an analogy with the theory of inviscid flow and boundary layers. One practical difference is that boundary layers and inviscid flow have a thickness ratio of 1/100 (or smaller) while turbulent wall layers the thickness ratio can be as high as 1/4.

Consider a layer of thickness h, centerline velocity U, viscosity ν and friction velocity u_*. The outer layer variable is y/h , the inner $y^+ = y/u_*\nu$ and the ratio is the Reynolds number $Re_* = u_* h/\nu$. An inner function for any variable is

$$f_i(y^+) = f(y+, Re_* = \infty)$$

Similarly the outer function is

$$f_0(\frac{y}{h}) = f(y^+ = \frac{y}{h} Re_*, Re_* = \infty)$$

Matching between f_i and f_0 is aptly called the common part; $f_{cp} = f_0(0) = f_i(\infty)$. Neither f_i nor f_0 are uniformly valid for ail y. What is not discussed in textbooks on turbulence is the idea of a composite expansion. Such an expansion is not only uniformly valid, but it contains the first dependance of the profile upon the Reynolds number. An additive composite expansion is

$$f\,]_{composite} = f_i(y^+) + f_0(\frac{y^+}{Re_*}) - f_{cp}$$

The mean velocity *law of the wall* plus *law of the wake* is a composite expansion, Panton(1990a).

Now, we apply this scheme to the Reynolds stress. For pipe or channel flow theory shows that the Reynolds stress in the outer layer is

$$\frac{-\langle uv\rangle}{u_*^2} = G(\frac{y}{h}) = 1 - \frac{y}{h}$$

From this one can see that the common part is $G_{cp} = G(0) = 1$. The inner layer function $g(y^+)$ is not known. The composite function is

$$\frac{-\langle uv\rangle}{u_*^2}]_{composite} = g(y^+) + G(\frac{y^+}{Re_*}) - G_{cp}(\frac{y^+}{Re_*})$$

$$= g(y^+) + \frac{y^+}{Re_*}$$

In order to explicitly display the trends with Reynolds number a curve fit to experimental data was performed. The equation assumed was

$$g(y^+) = \exp(\frac{-1}{ky^+}) + C_1[\exp(\frac{-C_2}{y^{+2}}) - \exp(\frac{-C_3}{y^{+2}})]$$

A fit of this equation to the $Re^* = 860$ data of Tiederman & Harder(1990). yielded coefficients; $C_1 = 0.517$, $C_2 = 136$, and $C_3 = 2.51$. Figures 1 and 2 show the composite expansions and the experimental data. The constants for all of these curves are the same.

The fluctuation u' was treated similarly. Since at the centerline u' is symmetric, a hyperbola was used for the outer behavior.

$$u'_o = C_1 + \{ C_2^2 + C_3^2[1 - (\frac{y}{h})^2]\}^{1/2}$$

The common part of this is the constant

$$u'_{cp} = C_1 + \{ C_2^2 + C_3^2\}^{1/2} = C_{cp}$$

The inner function was taken as

$$u'_i(y^+) = C_{cp}[1-\exp(-C_4y^+)] + C_5[\exp(-C_6y^+) - \exp(-C_7y^+)]$$

The composite expansion is

$$u(y^+)_{composite} = u'_o + u'_i - u_{cp}$$

This equation was fitted to the data ($Re^*=860$) with values: $C_1=0.527$; $C_2= 0.369$; $C_3= 1.57$; $C_4=0.0697$; $C_5= 90.8$; $C_6= 0.0905$; $C_7 = 0.0948$. The results are compared to data in Fig. 3 and 4.

A model equation for the vertical velocity fluctuation v' was also a hyperbola for the outer behavior. The common part of this is another constant. According to theory the inner function should rise away from the wall $\sim y^2$. A n equation with this property is

$$v'_i(y^+) = C_{cp}\,[1 - \exp(-C_4y^+)] + C_5 \exp(-C_6 y^+)\,[\exp(-C_7y^+) - 1 + C_7 y^+]$$

The composite expansion is

$$v(y^+)_{composite} = v'_o + v'_i - v_{cp}$$

This equation was fitted to the data with values: $C_1=0.447$; $C_2= 0.226$; $C_3= 0.691$; $C_4=0.0509$; $C_5=$

Fig. 1 Reynolds Stress at Various Re*

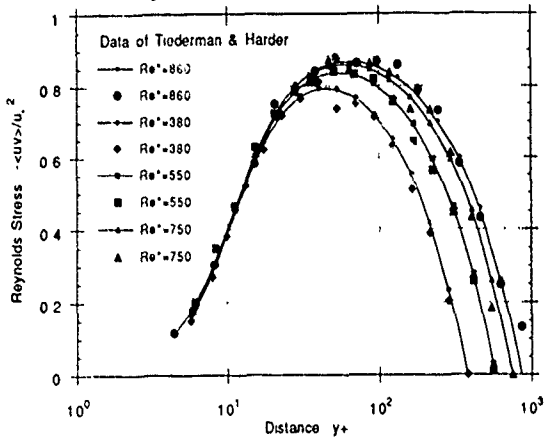

Fig. 2 Reynolds Stress at Various Re*

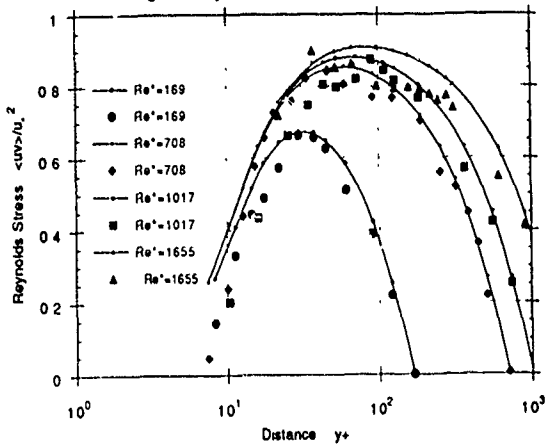

Fig. 3 Re* Effects on u' Fluctions

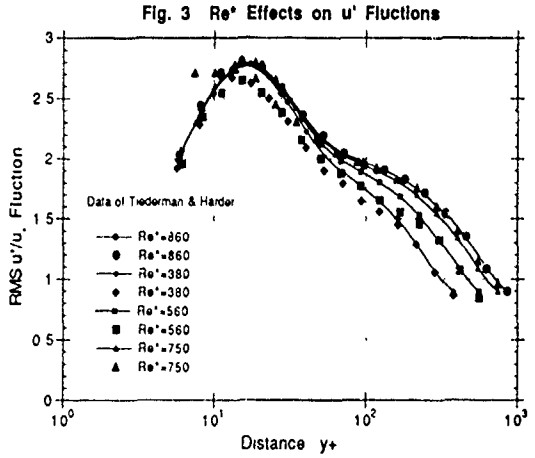

Fig. 4 Re* Effect on u' Fluctions

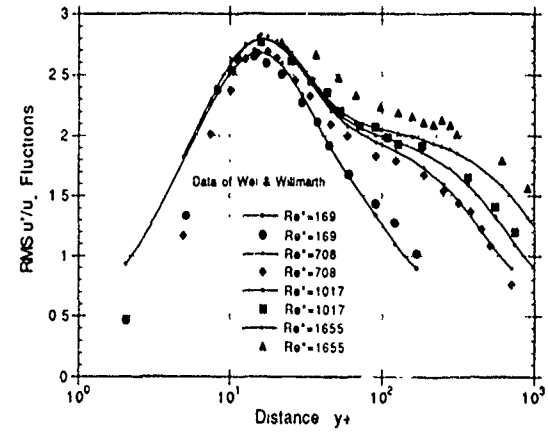

Fig. 5 Effect of Re* on v' Fluctuations

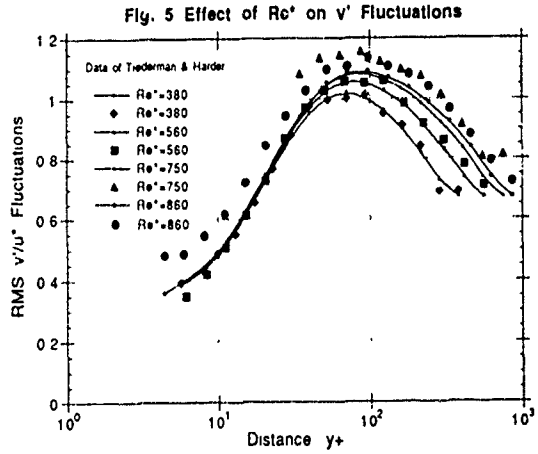

Fig. 6 Effect of Re* on v' Fluctuations

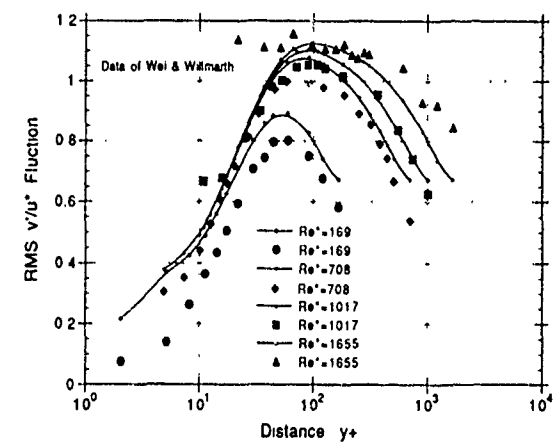

22.0; C_6= 0.539; C_7 = 0.0850. Here the Re*=380 data was used. Figures 5 and 6 show the results.

From the figures it can be seen that the composite expansions exhibit considerable Reynolds number effects, even for y^+ values less than 100. The ability of first order expansions to track these trends to such low Re* indicates that the physics of these layers is much the same as those at higher Reynolds numbers.

This paper was written while the author held a visiting position at the Acoustics Center of Ecole Centrale de Lyon. A fellowship from the REGION of Rhone-Alp is greatly appreciated.

REFERENCES

Spalart, P. R.(1988) J. Fluid Mechanics.**187**, 61.
Kim, J., Moin, P., and Moser, M.(1987) J. Fluid Mechanics.**177**, 133-165.
Tiederman, W. and Harder(1990), private communication.
Wei, T., and Willmarth, W.W., (1990) J. Fluid Mechanics.**187**, 61.
Panton, R. L.,(1990a) Proceedings of 11th Annual Conf of Canadian Appl. Math. Society. Computational Mathematics Publications, Southhampton,UK, 1990.
Panton, R. L.(1990b) J. of Fluids Engr.**112**,425.

EIGHTH SYMPOSIUM ON
TURBULENT SHEAR FLOWS
Technical University of Munich
September 9-11, 1991

A Comparison of Temporal and Spatial Temperature Derivatives in a Strained Turbulent Flow

Hamid R. Rahai
Department of Mechanical Engineering
California State University Long Beach, Ca. 90840.
and
John C. LaRue
Department of Mechanical Engineering
University of California, Irvine
Irvine, Ca. 92717.

Introduction:

Both Taylor's hypothesis and the assumption of local isotropy are routinely applied to flows with a range of mean velocity gradients and velocity intensities. It is well known that the use of Taylor's hypothesis leads to increasing uncertainty with increases in the mean velocity gradient and velocity intensities (cf. Taylor (1938) and Townsend (1976)). The results presented herein quantify this uncertainty and also indicate that the uncertainty depends on the integral length scale of the flow. The recent studies of Sreenivasan et. al. (1977) and Antonia et. al. (1986 a & b) show flows with moderate to small mean velocity gradients are not locally isotropic. The present study complements those of the previous studies and quantifies the effect of mean velocity gradient and integral length scale on departures from local isotropy.

Based on the rapid distortion theory of Batchelor and Proudman (1954) and subject to the same constrains, Cauchy's equation can be used to relate the scalar gradient before and after the application of a mean strain as

$$\frac{\partial q^s}{\partial x_i}\frac{\partial x_i}{\partial a_j} = \frac{\partial q}{\partial a_j} \tag{1}$$

where q corresponds to the spatially resolved scalar, s refers to measurement in the strained field, and x_i and a_j are the components of the position vector, respectively, before and after the application of a strain The strain experienced by the fluid is equal to $\frac{\partial x_i}{\partial a_j}$. If the strain in the downstream or x_1 direction is assumed to be equal to the mean strain, then it is easy to show that

$$\frac{\partial x_1}{\partial a_j} = -\frac{U_1^s}{U_1} \tag{2}$$

where U_1 is the mean velocity in the downstream direction Combining Eqns. 1 and 2, squaring and averaging, leads to the following equation which relates the variance of the spatial gradient of the scalar in the strained flow to that in the unstrained flow·

$$\frac{\overline{\left(\frac{\partial \theta^s}{\partial x_1}\right)^2}}{\overline{\left(\frac{\partial \theta}{\partial x_1}\right)^2}} = \left(\frac{U_1}{U_1^s}\right)^2 \tag{3}$$

Similarly, it can be shown that

$$\frac{\overline{\left(\frac{\partial \theta^s}{\partial x_2}\right)^2}}{\overline{\left(\frac{\partial \theta}{\partial x_2}\right)^2}} = \left(\frac{U_1^s}{U_1}\right)^2 \tag{4}$$

The purpose of the study discussed herein is to determine experimentally the applicability of Taylor's hypothesis and the assumption of local isotropy in a low intensity flow for a range of downstream mean velocity gradients.

Experimental Arrangement and Techniques:

The flow used in this study is the nearly homogeneous and isotropic flow produced downstream of a turbulence grid and heated wire screen. Fig. 1 shows the experimental arrangement. Two different ranges of mean velocity gradients are produced by placing one of two cylinders downstream of the heated wire screen. The integral scale is varied by using two grids of different mesh size. Table 1 provides flow parameters for the experiment.

Two special, two sensor probes are used to measure the time resolved temperature. Probe 1 consists of two platinum wires with a diameter of 0.625 μm which are separated in the downstream direction. The length of the first wire is 1.0 mm and the second is 0.75 mm. The spacing between the wires is 1.0 mm. Probe 2 is similar to Probe 1, except that the wires are separated by 1 mm in either the transverse of spanwise directions. The lengths of both wires are 1.0 mm.

Both wires are operated using two a.c. temperature bridges which have a frequency response of 8 kHz. They are supplied with a constant r.m.s. current of 180μA which makes their velocity sensitivity negligible (cf. LaRue et al. (1975)). The probes are directly calibrated using a calibration jet over the range of 19 to 24°C

The time resolved spatial gradient, $\frac{\partial \theta}{\partial x_1}$, is approximated as

$$\frac{\partial \theta}{\partial x_1} \simeq \frac{\delta \theta}{\delta \beta} \tag{5}$$

where $\delta\theta$ is the time resolved difference in the temperature at the two sensor positions which are separated by a distance $\delta\beta$.

Results:

The present results indicate that in a heated grid-generated turbulent flow approaching two dimensional objects, along the mean stagnation streamline, for $\frac{x_1}{D}$ <1, the variance of the temperature derivative increases in the streamwise direction, decreases in the spanwise, and remains constant in the transverse directions [Fig. 2]. For example, the variance of the streamwise temperature gradient normalized by its undistorted value is near unity when $\frac{x_1}{D} \geq 0.75$ and increase to about 1.40 for $\frac{x_1}{D} = 0.15$. This increase in dissipation is higher for the experiment which has larger $\frac{L_\theta}{D}$ ratio.

For large $\frac{L_\theta}{D}$ ratio, the dissipation obtained based on Cauchy's equation and from the temporal derivative and Taylor's hypothesis agree with the corresponding results obtained from direct measurements when $\frac{x_1}{D}$ is respectively larger than 0.75 and 1.85. Near the stagnation point, results based on Cauchy's equation and from the temporal derivative and Taylor's hypothesis differ from the corresponding result obtained from direct measurements by 60% and 560% respectively [Fig.3].

For small $\frac{L_\theta}{D}$ ratio, the dissipation obtained from all methods agree with each other when $\frac{x_1}{D} \geq 2.0$. However, for $\frac{x_1}{D}$<2.0, near the stagnation point, results based on Cauchy's equation and from the temporal derivative and Taylor's hypothesis differ from the corresponding results obtained from direct measurement by 40%.

Comparing the variance of the temperature derivative in the streamwise direction obtained from direct measurements and the corresponding results obtained from the temporal derivative with Taylor's hypothesis, it can be concluded that in the strained flow, when $\frac{L_\theta}{D} \ll 1$, Taylor's hypothesis can be used over a wide

range of mean velocity gradients to estimate the variance of temperature derivative in the streamwise direction from the temporal derivative However, when $\frac{L_0}{D} \gg 1$., the region where Taylor's hypothesis hold starts at $\frac{\bar{x}_1}{D} > 1.85$, where the mean strain rate is less than 2.85 s^{-1} [Fig 4]

For $\frac{\bar{x}_1}{D} < 2.0$, the isotropy parameters, K_1 and K_2, decrease with decreasing $\frac{\bar{x}_1}{D}$. However, no variation is seen for $\frac{\bar{x}_1}{D} > 2.0$ [Fig. 5.]

References

R A Antonia F Anselmet and A J Chambers, J Fluid Mech 163, 365 (1986)

R A Antonia and L W B Browne, J Fluid Mech 163, 393 (1986)

G K Batchelor and I Proudman, Quart J Mech Appl Math 7 83 (1954)

J C LaRue J Deaton and C H Gibson, Rev Sci Instrum 46, 757 (1975)

H R Rabbu, Ph D thesis, University of California, Irvine (1988)

K R Sreenivasan, R A Antonia and H Q Danh, Phys Fluids, 20, 1238 (1977)

G I Taylor, Proc R Soc Lond A164, 476 (1938)

A A Townsend, The structure of shear flow, Cambridge University Press (1976)

M_1	2.54 cm	5.08 cm
Parameter		
ΔT	0.5 C	0.5 C
U	8.6 $\frac{m}{s}$	5.6 $\frac{m}{s}$
Re_{ω_0}	9297	18594
L_0^1	0.012 m	0.023 m
$Re_{L_0}^1$	79.0	148.0
λ^1	5.2 mm	7.3 mm
Re_λ^1	31	47
L_u^1	45 mm	54 mm

1 At $\frac{L_0}{D}=6$

Table 1

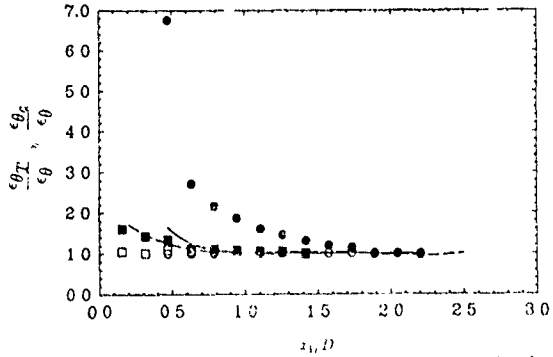

Fig 3 Variation of the dissipation of temperature obtained either from temporal derivative and Taylor's hypothesis or from Cauchy's equation and normalized by the corresponding value obtained from direct measurements -- and - - - are solutions based on Cauchy's equation for $\frac{L_0}{D}$=3.5 and 0.170 respectively The rest of the symbols are the same as on Fig 2

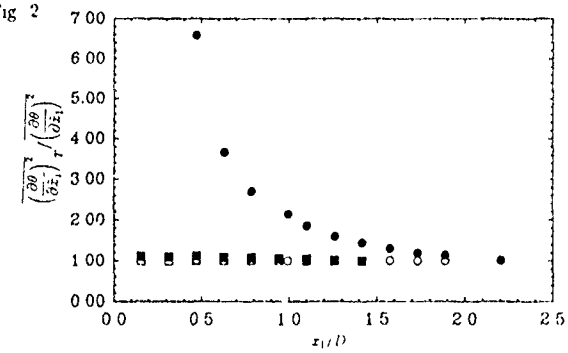

Fig 4 Variation of the variance of the temperature derivative obtained from temporal derivative and Taylor's hypothesis and normalized by its corresponding values obtained from direct measurements Symbs the same as Fig 2

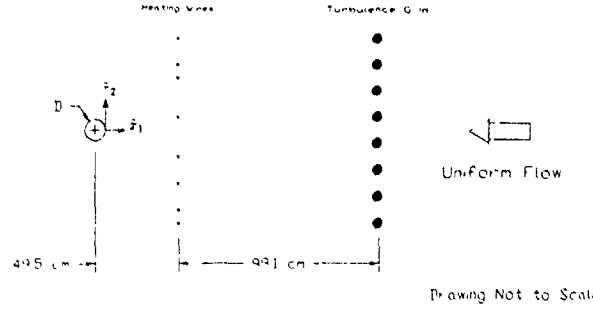

Fig 1 Arrangement of the flow field.

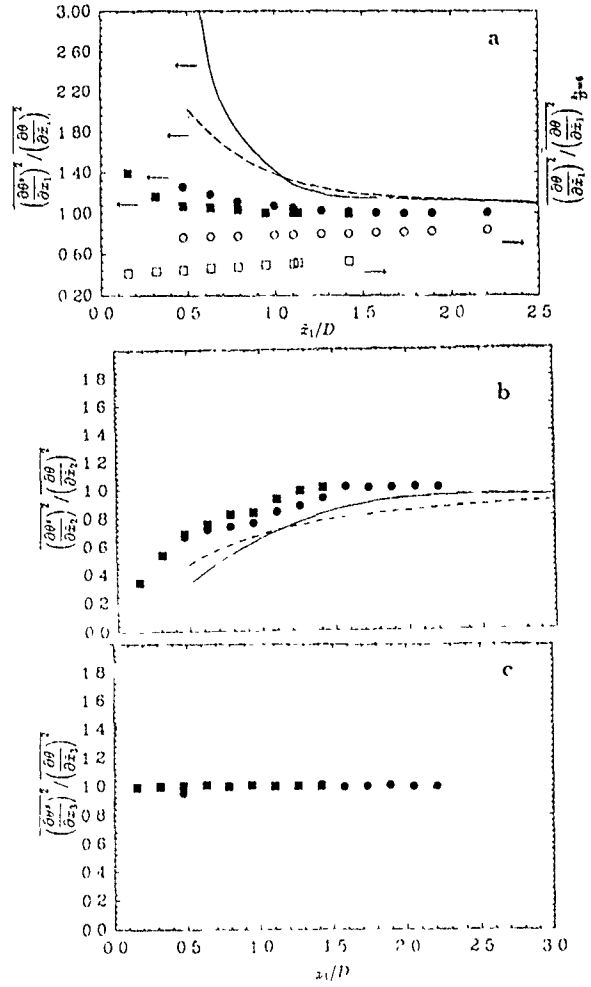

Fig 2 Variation of the variance of the temperature derivative in the (a) streamwise direction, (b) and (c) transverse directions, along the mean stagnation streamline approaching circular cylinders ○ and □ are undistorted values for respectively L_0/D=3.5 and 0.47, ● and ■ are distorted values for respectively L_0/D=3.5 and 0.47

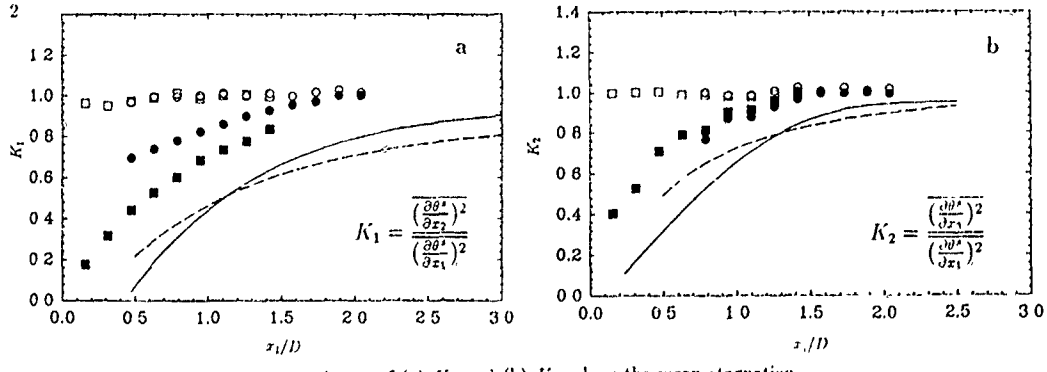

Fig. 5 Variation of (a) K_1 and (b) K_2, along the mean stagnation streamline approaching circular cylinders Symbs The same as Figs 2 and 3.

EIGHTH SYMPOSIUM ON
TURBULENT SHEAR FLOWS
Technical University of Munich
September 9-11, 1991

The preliminary quantitative measurements of the scalar field in the rectangular jet mixing flows

Gong Xin Shen, Jian Jin

Fluid Mechanic Institute
Beijing University of Aeronautics & Astronautics

Abstracts

The preliminary quantitative measurements of the scalar field in the mixing flows of the rectangular jet using Laser Induced Fluorescence (LIF) and Digital Image Capture & Processing techneques are presented.

Introduction

Recent decade, it is well known that the Laser Induced Fluorescence techneque could be and must be a very important and potential approach for attack on deep understanding the complex and turbulent flows . The contribution which has been made by many researchers [1][2][3][4]were involved with itself development of the techeques and its application in various flow field

Also, the non-axisymmetrical jet flows were studied broadly for its background on many industrial application even the flows in practice could be more complicated Certainly, it would be interesting if the experimental observation on the scalar field could be made directly in the rectangular jet mixing flows

Experimental Arrangement

The schematics of the experimental arrangement is shown in Fig.1 The water channel works like as a water tank (water is static here). The jet flows was supplied by a water storage tank in which water was premixed with fluorescence species. The critical diameter of the rectangular nozzle exit is 5^{MM} and its width / height ratios are 1,3,5, repectively A light sheet of laser, which crossed the axies of jet, illuminated a vertical or horizontal section view field of the jet flows The inner view field of flows was captured by a CCD camera (512 × 512 pixel, 8bit darkness level, 25 frames / sec, the spatial resolution 1 22 × 0 92MM^2 / pixel here), then digitized, stored by a image card (DT-2861, 16 frames buffer) and processed by a PC-386 microcomputer

Measurement & Calibration

According to Bear' law, the flourescent intensity (H_f) mainly depended on the incitent intensity of laser beam or sheet (Io) and the concentration of the fluorescent species in the solution (C) Several fluorescent species (Rhodamine 6G, Rhodamine B and Sodium fluorescein) were tested in different conditions (the power of laser (W), as shown in Fig 2, the maximum concentration of the species in the solution (Co), the apature of the CCD camera) It was found that among them, only sodium fluorescein was quite suitable to have fine linear calibration curve at low maximum concentration (Co) and certain power of Lasser. Also the H~ C / Co curves were calibrated respectively in vertical (V) and horizontal (H) section view fields as shown in Fig 3 For a 2-D view field, a fluorescent intensity field $H_f(x,y)$ depends on not only a concentration field c(x,y), but also the local incident intensity field I(x,y)

$$H_f(x,y) = Q[1 - e^{-\varepsilon\int_y^{y+\Delta y}\int_x^{x+\Delta x} C(x,y)dxdy}]I(x,y)$$

when $\varepsilon \cdot c\Delta x\Delta y$ and $\Delta x\Delta y \ll 1$, $H_f(x,y) \sim (Q\varepsilon\Delta x\Delta y)C(x,y)I(x,y)$

So normally the solution of the concentration field has to be a result of alternative procedure because of the concentration field was unknown. Forturnatelly, the decay effect could be neglected in certain degree, as shown in Fig 4 , if the concentration of used species was very low and the intensity resolution of the optical system was enough high The maximum error of concentration value due to decay of incident intensity without alterative correction in our case was estimated roughly about ± 4% (y and z direction) and ± 7.5% (x-direction) for the maximum concentration

Results & Discussion

The preliminary investigation on concentration and scale field for the rectangular jet mixing flows took place in the same condition for the calibration. Renolds numbers is 1000, 2000, 3000, 4000, and 5000 The spatial and temporal resolution could be down to the Taylar scale (for Re = 5000, X / d ≈ 50-100). The typical images of instantaneous concentration field in a rectangular jet mixing flow were shown in Photo 1 and 2 The dankness level or pseullo colour correspanded to the dimensionless concentration C / Co (C / Co = 1 at the exit of the nozzle). Some image processing techneques were used for better displaying the structures and emphasizing main feature of the flow patterns.

It is found that one kind of unsteady and blended large-scale structures (from symmetric pattern to spiral pattern or inverse) exists in the ractangular jet mixing flows as shown in Fig.5(c), except the existing symmetric and spiral-large scale structure which have been found in round jet flows.

The instantaneous profile of the concentration along the axis y and z, as expected, were strongly intermitent , and the instantaneous quantitative distribution of concentration along the X axis is very intermitent too Obviously, all these kinds of the intermitency are connected directly with the scalar interfaces or scalar structures (Certainly, including the large-scale structure). Also the results of present investigation show that the entrainment mechanism in the rectangular jet flows is dominated by large-scale motions. These large scales are engulfing unmixed ambient fluid and transporting it, in significant quantities, deep into regions in the flow interior where it can be subsequently mixed by smaller scalar motion (Kolmogorov and Batchelor scales).

Fig 5 show the typical instantaneous average concentration distributions along the axis x with W / H = 1,3,5 at vertical and horizoutal section respectively By comparison with all the results, it could be found that the average mixing rate and the concentration pattern in rectangular jet flows did not simply monotonously depend on the width / height ratio, also the average mixing rate along the x axis in the vertical section is considerable different with that in the horizontal section. Obviously, the 3-D effect on the concentration field in the rectangular jet flows is considerable strong.

For the further work,the observasion would be down to the smaller scalar field.

Reference

[1] Koochesfahani, M M. [1986] JFM vol.17, 83-112
[2] Hanson, R.K. et al [1987] Experments in Fluids 5, 240-246
[3] Dahm, W.J.A. [1989] 7th Symp. on Turbulent shear Flows 14-1
[4] R.R. Prasad & K.R Sreenivasan [1990] JFM vol.216, 1-34.

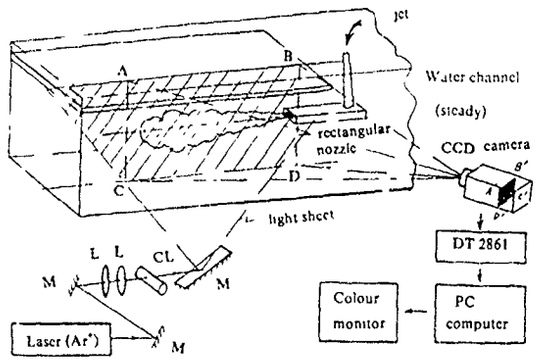

Fig 1 The schematic of the experimental A

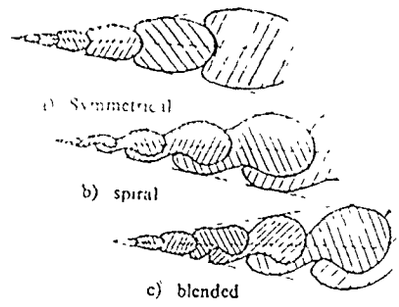

Fig.5 The structure patterns of the rectangular jet flows

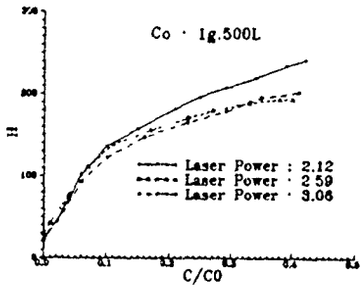

Fig.2 H_f~C curve with laser power (W)

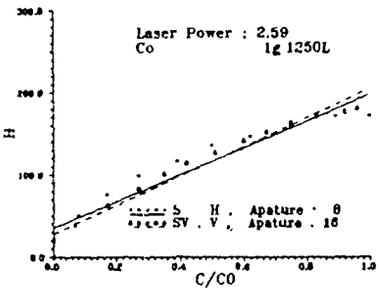

Fig.3 The calibration curve of H~C / Co

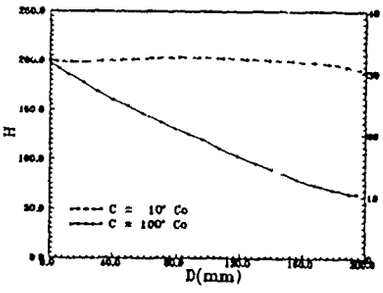

Fig.4 The Dye Obsorpation with distance

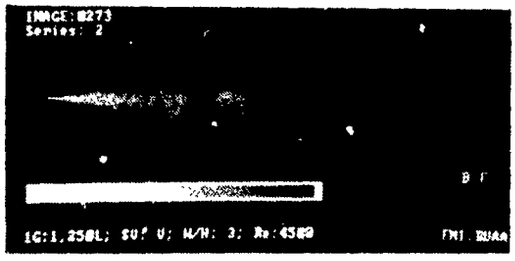

Photo 1 A typical concentration field of jet mixing flow

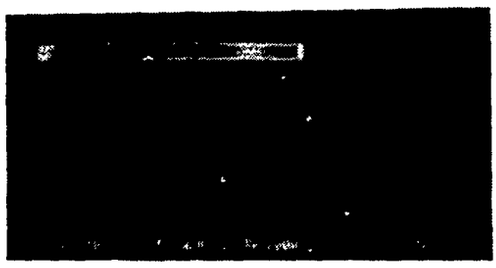

Photo 2 A typical concentration field of Jet Mixing flow with Pseulo Colour

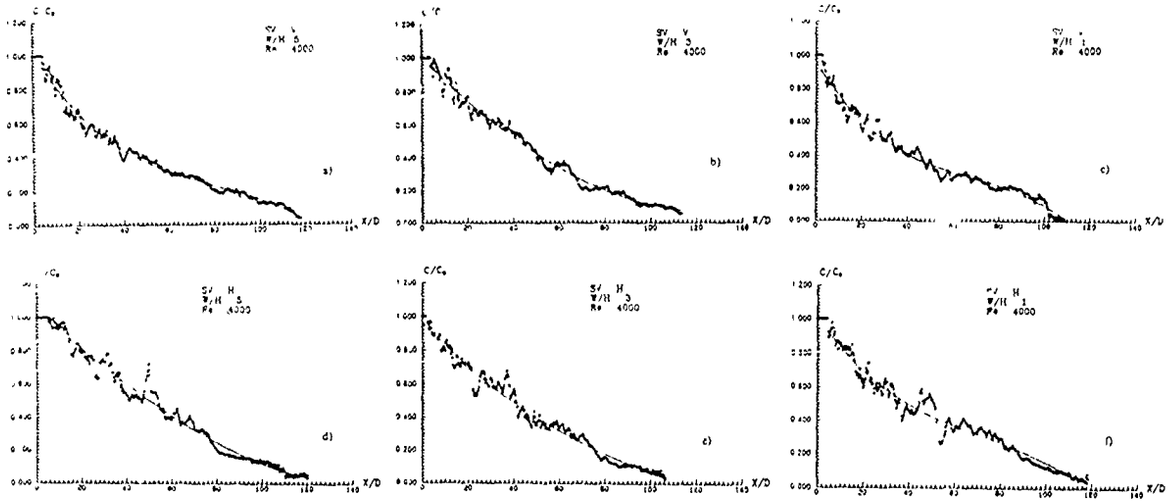

Fig.6 A typical Instantaneous average concentration of jet along the axis X

EIGHTH SYMPOSIUM ON
TURBULENT SHEAR FLOWS
Technical University of Munich
September 9-11, 1991

EFFECTS OF ATTACK ANGLE ON LEG PORTION OF THE HORSESHOE VORTEX AROUND THE IDEALIZED WING

T. Shizawa, S.Homami*) and M.Yamamoto**)

*) SCIENCE UNIVERSITY OF TOKYO, Mech. Engineering. Dept.
1-3 Kagurazaka Shinjuku-ku Tokyo 162, JAPAN

**) ISHIKAWAJIMA-HARIMA HEAVY INDUSTRIES Co.,Ltd.
Tonogaya Mizuho-machi Nishitama-gun Tokyo 190, JAPAN

ABSTRACT

The objectives of the present paper are to make clear the mechanism of horseshoe vortex interaction with two-dimensional turbulent boundary layer, and to clarify the effects of attack angle on leg vortex. Detailed Reynolds-stress measurements at two cross-section planes close to the wing nose will be also helpful to evaluate the three-dimensional flow prediction codes using turbulence models.

INTRODUCTION

This paper presents the mechanism of development of the horseshoe vortex at a surface-mounted obstacle which then interacts with fuselage boundary layer. SHABAKA made clear the diffusion process of the horseshoe vortex, and MOORE reported the natures of the vortex. The coherence between the horseshoe vortex and the curvature at leading edge of the wing was presented by KUBENDRAN. The key to understanding the secondary flows is that the generation of strong vortex is a secondary flow of Prandtl's first kind but that subsequent diffusion of the vortex, and its interaction with the turbulent boundary layer, depend on Reynolds-stresses. The contribution to the rotation of the Reynolds-stress tensor appears in the production terms $-\overline{u'v'}dV/dz$ and $\overline{u'w'}dV/dz$ in the Reynolds-stress $-\overline{u'v'}$ transport equation by means of velocity gradient owing to the secondary flow dW/dz and dV/dz respectively. The term $-\overline{u'^2}dU/dx$ in the turbulent kinetic energy q^2 transport equation represents the effects of attack angle of the wing on the production of q^2 by the streamwise velocity gradient dU/dx.

EXPERIMENTS AND RESULTS

Detailed mean flow and Reynolds-stress measurements were conducted within the leg portion of the horseshoe vortex. An idealized wing having half-circular nose-cone followed by a long parallel section was used (Fig. 1). The half-circular nose can provide constant curvature at the stagnation point even if the wing has an angle of attack. The wing was installed as an obstacle in the two-dimensional turbulent boundary layer over the flat plate. The angle of attack could change zero to ten degrees with respect to the free-stream. Three components of mean flow velocity and six components of Reynolds-stress were measured using a specially designed triple-array hot-wire probe. The center of the three wires are set in a line parallel to the y-axis(along the span of the wing). The probe has prongs with 15 mm long, and the tips are made from copper-plated small prongs with 50 um in diameter and 1 mm in length. The sensing length of 1.4 mm gives a length to diameter ratio of 230.

Fig. 2 shows the surface static pressure. The boundary layer is disturbed at the junction of the flat plate and the wing, and spreads to downstream both in the Pressure- and the Suction-side of the wing. The pressure gradient at mid-span of the wing presents strong favorable pressure gradient at the nose followed by adverse pressure gradient over the parallel section of the wing in the Suction-side The profile looks same but the pressure gradient level is remarkably low in the Pressure-side.

The location of the vortex center determined by zero secondary flow velocity is almost the same at Slot 1, and then sweeps away from the wing as shown in Fig. 3. The distance from the plate to the center is longer in the Pressure-side. The mean flow skews by the z-direction pressure gradient and the vorticity is strong in this side. In the Suction-side, the vortex is swept away from the wing because of the rapid development of the boundary layer over parallel section of the wing by the strong adverse pressure gradient. The scale of the vortex is larger in both cases compared with zero angle of attack.

Turbulent kinetic energy q^2 is shown in Fig. 4. In each case, the data are normalized by the mean velocity at the edge of plate boundary layer. The contours of turbulent kinetic energy show circular shape centered on the vortex center. The peak level is larger in the Suction-side, because the mean flow is accelerated at the nose of the wing. It proves that the high turbulence is caused by the vortex motion of the leg vortex. The peak level of the energy decays rapidly with relatively minor perturbation remaining at Slot 2. The Reynolds normal-stress $\overline{u'^2}$ and $\overline{w'^2}$ take larger level in the Suction-side because of the large vortex motion. The Reynolds normal-stress $\overline{v'^2}$, on the other hand, takes larger level in the Pressure-side by the strong vertical motion at the upwash region of the vortex.

The primary Reynolds-shear stress $-\overline{u'v'}$ takes large negative value as shown in Fig. 5. The region is centered in the vortex center and stretched away from the plate and the wing. The region of negative shear stress is associated with the reversed velocity gradient dU/dy near the center of the vortex. The most important production term in $-\overline{u'v'}$ transport equation is $\overline{v'^2}dU/dy$. The velocity gradient dU/dy at the downwash region takes the same level at both sides of the wing. The Reynolds normal-stress $\overline{v'^2}$ shows larger level in the Suction-side by the strong vorticity, and then the $-\overline{u'v'}$ takes larger value. The wider region of negative stress is observed in the Pressure-side of Slot 2. In this case, strong secondary flow velocity components still remains, and the velocity gradient dU/dy takes negative or small level over the wing.

CONCLUSIONS

An experimental survey was conducted at the leg portion of the horseshoe vortex generated by interacting with the idealized wing, and the wing was mounted on an angle of attack. The diffusing processes depend on the Reynolds-stresses distribution at the region between plate and wing. The vortex motion of the leg vortex is largely influenced by the attack angle. The strong vertical motion in the upwash region affects the Reynolds-stress profiles in the Suction-side. The precise Reynolds-stress measurements data will contribute to model development as test data.

REFERENCES

SHABAKA,I.M.M.A. 1979 Ph.D. Thesis. Imperial College.
MOORE,J. and FORLINI,T.J. 1984 J Engn. Gas Turbines and Power, 106, 668-676.
KUBENDRAN,L.R. et.al. 1986 AIAA J. 24-9, 1447-1452.

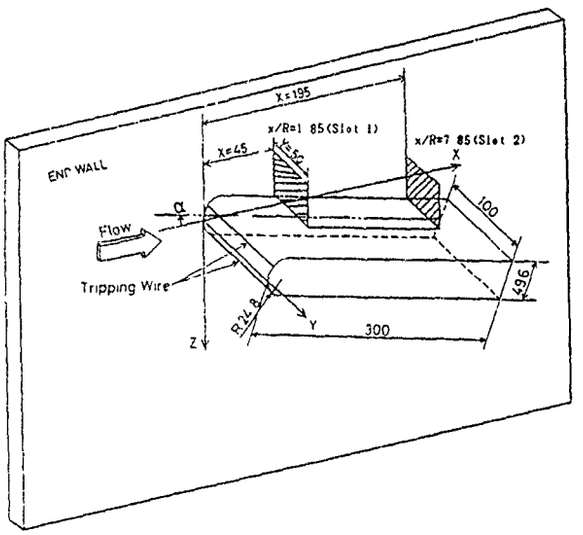

Fig. 1 Idealized Wing With Half-Circular Nose-Cone Followed By Parallel Section (Dimensions in mm)

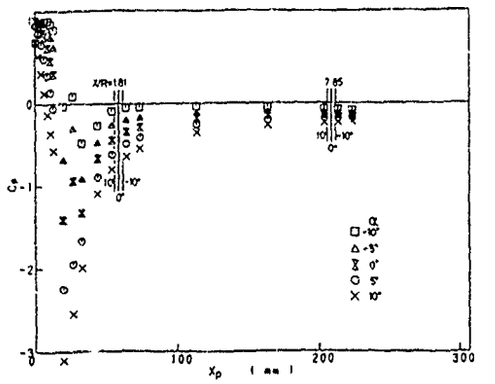

Fig. 2 Surface Static Pressure At The Mid-Span Of The Wing

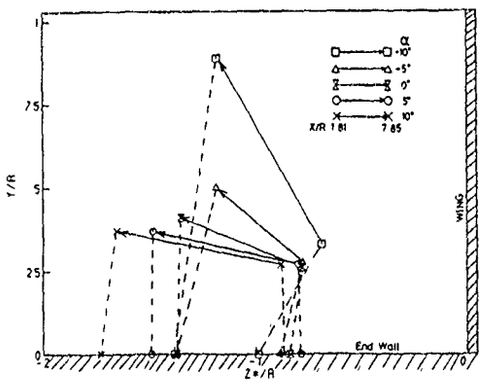

Fig. 3 [illegible] Of Vortex And Boundary Flow [illegible]

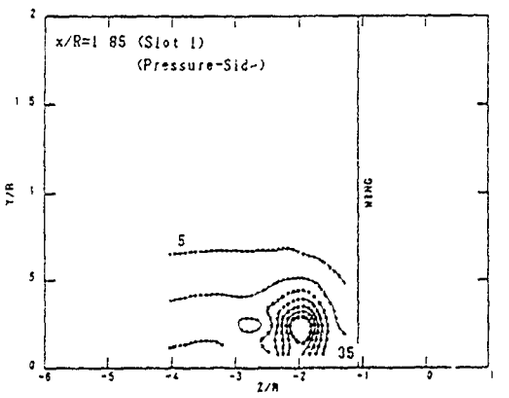

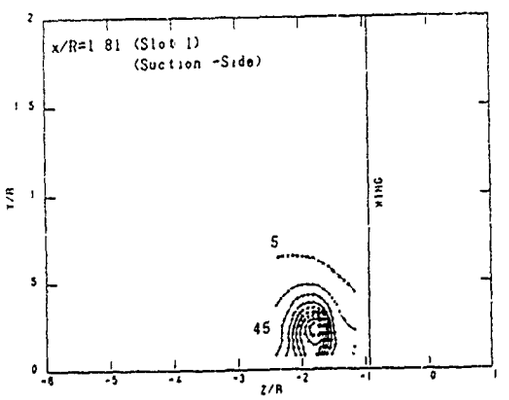

Fig. 4 Turbulent Kinetic Energy
(Contours Level : q^2/U_r^2 = 5, 10, 15, 20, 25, 30, 35, 40, 45)

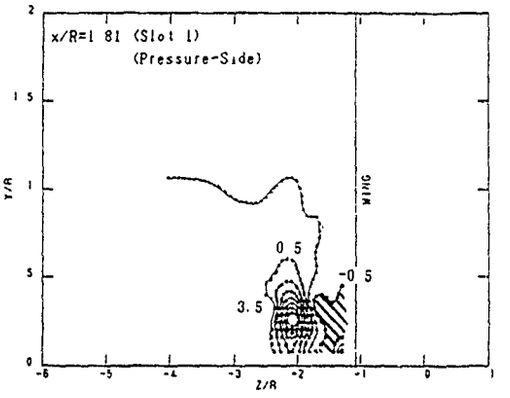

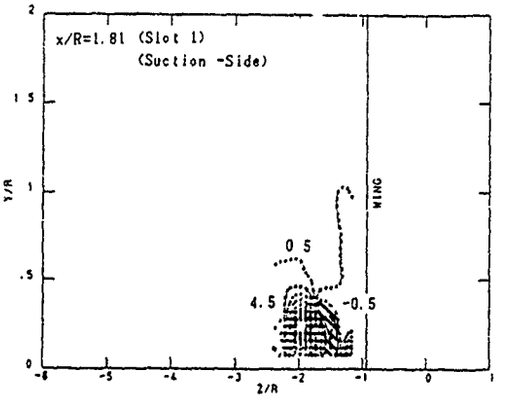

Figure 5 Reynolds Shear Stress $-u'v'$
(Contours Level : $-u'v'/U_r^2$ = 0.00, +0.05, +0.10, +0.15, +0.20, +0.25, +0.30, +0.35, +0.40)

EIGHTH SYMPOSIUM ON
TURBULENT SHEAR FLOWS
Technical University of Munich
September 9-11 1991

EFFECTS OF MULTIPLE EXTRA STRAIN RATES ON THE STRUCTURE OF WALL TURBULENCE

H. Yoshida*), Y. Horiuchi*), R. Echigo*) and K. Suenaga**)

*)Department of Mechanical Engineering, Tokyo Institute of Technology
Meguro-ku, Tokyo 152, Japan

**)Mitsubishi Heavy Industries, Ltd., Chiyoda-ku, Tokyo 100, Japan

ABSTRACT

Effects of multiple extra strain rates on the structure of wall turbulence have been investigated for the flow with lateral divergence and streamline curvature. The turbulence structure changed by the extra strain rates were discussed in relation with the bursting phenomena. The most striking feature of the present turbulent shear flow is the nonlinear interaction between lateral divergence and concave curvature.

INTRODUCTION

The response of shear-layer turbulence to extra strain rates is very important as summarized by Bradshaw (1990). This paper is the second report of our work dealing with turbulent shear flows with lateral divergence. While the previous paper (Yoshida *et al* 1989) described the experiment for the pure effect of lateral divergence, the present one focuses on the interaction between multiple extra strain rates, i.e., lateral divergence and streamline curvature. This is because the authors were stimulated by the study (Smits *et al.* 1979), which discussed the interaction between these two extra strain rates in a turbulent boundary layer over an axisymmetric cylinder-flare body.

In the present paper, an axisymmetric annular flow with lateral divergence is investigated. This flow system has an advantage that since both stabilizing and destabilizing curvatures are included, two kinds of interaction between divergence and curvature can be simultaneously observed. The effects of such extra strain rates on the turbulence structure are examined not only from time-averaged quantities but also from conditionally averaged velocity signals obtained by the Quadrant method (Lu & Willmarth 1973).

APPARATUS AND EXTRA STRAIN RATES

The air channel built for the present investigation is shown in Fig.1. The flow passes first through an annular entrance section (length l_e 3000 mm, outer diameter d_o 196 mm, inner diameter d_i 116mm, hydraulic diameter $d_h = d_o - d_i = 80$mm), and is fully developed before entering the distorting section.

Figure2 shows the flow geometry of the distorting section. The centerline between the inner and outer walls is expressed by a sine curve and a straight line. The sine curve (from 0 to π) was used so that the radius of the curvature changes continuously from the entrance to the distorting section. The reason why a circular curve was avoided in the present work is that such an impulse was too strong to fairly interact with divergence.

The channel height h varies inversely proportional to the distance from the symmetric axis r, namely, $h = h_1 r_1 / r = c / r$ (r_1 and h_1 are the channel dimensions at the start of the distorting section). Hence, the cross-sectional area remains constant, and the stretching ratio $S = r / r_1 = h_1 / h$ increases up to 5 in the streamwise direction. Turbulence measurements by a hot-wire anemometer were made at the stations of S = 1, 1.2, 2, 3.

Figure 3 shows the extra strain rates e calculated from the channel geometry; subscripts d and c denote divergence and curvature, respectively. To estimate substantial contribution by these extra strain rates, the effective extra strain rate e_{eff} is calculated by the lag equation (Smits *et al* 1979), and the results are plotted also in Fig.3.

As demonstrated in the previous paper (Yoshida *et al.* 1989), lateral divergence destabilizes turbulence. On the other hand, streamline curvature exerts destabilizing effects along concave walls, but it exerts stabilizing effects along convex walls. As a result, influences by these extra strain rates on turbulence are summarized as follows:

S = 1: Turbulence has an ordinary structure because there exists no extra strain rate.
S = 1.2: The effects of streamline curvature are dominant, and divergence is negligible. Consequently, turbulence structure becomes highly antisymmetric around the centerline.
S = 2: According to the duct geometry, curvature vanishes, and alternatively divergence becomes large. The effective extra strain rate for curvature, however, is comparable with that of divergence. Hence, these two extra strain rates and the basic strain rate strongly interact among them.
S = 3: The effects of curvature becomes negligible, and the pure effects of divergence appear.

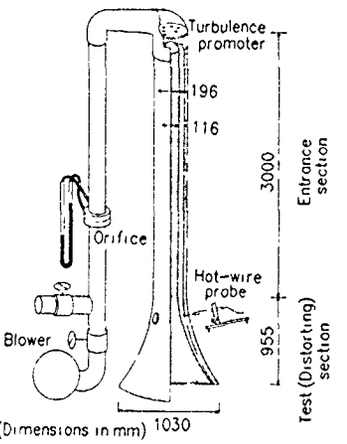

Fig.1. Schematic of experimental facility

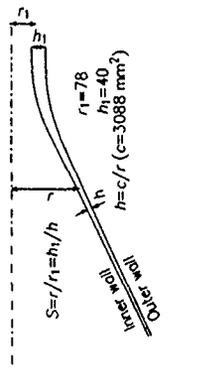

Fig.2. Flow geometry of the distorting section

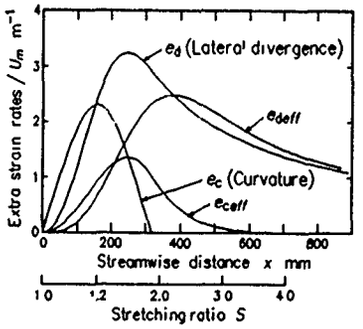

Fig.3. Streamwise variations of extra strain rates

RESULTS

The following data were obtained for Reynolds number Re = $U_m d_h / \nu$ = 50000, where U_m is the bulk-mean velocity. The coordinate origin is taken on the centerline at the start of the distorting section; x is distance measured along the curved centerline, and y is measured along straight lines normal to the centerline and toward the center of curvature. Hence, y / h = - 0.5 is on the inner concave wall, while y / h = 0.5 is on the outer convex wall. U and V are the components of mean velocity in the x and y directions, and u and v the corresponding fluctuating components.

Time-Averaged Quantities Figures 4-7 show the streamwise variations of mean velocity, turbulent intensities, Reynolds stress, turbulent kinetic energy, respectively.

Contributions to Reynolds Stress from Different Events Figure 8 shows the contributions of each quadrant to Reynolds stress. Here, it should be noted that unlike the expression by Brodkey *et al.* (1974) we display the results using absolute values for each quadrant.

Conditionally Averaged Velocity Signals Figures 9 and 10 show the conditionally averaged uv signal obtained by the Quadrant method. Figures 9a and 10a are the results at $y/h = 0.35$ (outer convex side), while figures 9b and 10b are those at $y/h = -0.35$ (inner concave side). Each signal is normalized using the maximum value.

DISCUSSION

$S = 1$ Although in the foregoing chapter we mention that turbulence is ordinary at this station, somewhat antisymmetric nature is observed (especially in Fig.8a). This antisymmetry is considered to be ascribed to the anomaly associated with a turbulent flow in annuli. We now use these data as the base state to assess the effects by extra strain rates.

$S = 1.2$ At the inner concave side turbulence is markedly amplified, while it is attenuated at the outer convex side. These tendencies agree well with those reported on a curved channel (Kobayashi *et al.* 1989). Corresponding to this turbulence behavior, the con-tributions of 2 and 4 quadrants drastically changes as shown in Fig.8b. The conditionally averaged signal for ejection at the concave side (Fig.9b) becomes broad, while that for sweep at the convex side (Fig.10a) becomes narrow.

$S = 2$ Compared with the profile at $S = 1.2$, the streamwise turbulent intensity u_{rms} further increases at the inner concave side, and recovers at the outer convex side. At the inner concave side, however, the normal component v_{rms} slightly decreases, and much more remarkable decrease is seen in the Reynolds stress profile. This fact is very surprising because both divergence and curvature are expected to amplify turbulence; the measured results demonstrate that a simple summation of their separate effects is not valid even qualitatively. (Since the results reported on the similar flow system (Smits *et al.* 1979) do not show such tendencies, we first doubted our experiment. The repeated measurements for two stations which are apart in the circumferential direction, however, showed good reproducibility.) Whereas the mechanism of this nonlinearity is not clear at the present stage, relatively small contribution of the 4 quadrant shown in Fig.8c corresponds to decrease in Reynolds stress; the conditionally averaged signals also show marked reduction both in ejection (Fig.9b) and in sweep (Fig.10b).

$S = 3$ At this station, all the turbulent intensities and Reynolds stress increases owing to lateral divergence, as reported by the previous paper (Yoshida *et al.* 1989). The conditionally averaged signals, however, are not so different from those without extra strain rates (S=1).

REFERENCES

BRADSHAW, P. 1990 Effects of extra rates of strain - Review. In *Near-Wall Turbulence* (eds. S.J.Kline & N.H. Afgan, Hemisphere Publ. Corp.) 106.

BRODKEY, R.S., WALLACE, J.M. & ECKELMANN, H. 1974 Some properties of truncated turbulence signals in bounded shear flows. *J.Fluid Mech* **63**, 209.

KOBAYASHI, M., MAEKAWA, H., TAKANO, T., UCHIYAMA, N., KUBOTA, M. & KOBAYASHI, Y. 1989 Two-dimensional turbulent flow in a curved channel. *JSME Int J*, **32**, 324.

LU, S.S. & WILLMARTH, W.W. 1973 Measurements of the structure of the Reynolds stress in a turbulent boundary layer. *J.Fluid Mech.* **60**, 481.

SMITS, A.J., EATON, J.A. & BRADSHAW, P. 1979 The response of a turbulent boundary layer to lateral divergence. *J.Fluid Mech.* **94**, 243.

YOSHIDA, H., FURUYA, T. & ECHIGO, R. 1989 The effect of lateral divergence on the structure of a turbulent channel flow and its heat transfer. *Turbulent Shear Flows 6* (Springer-Verlag) 269.

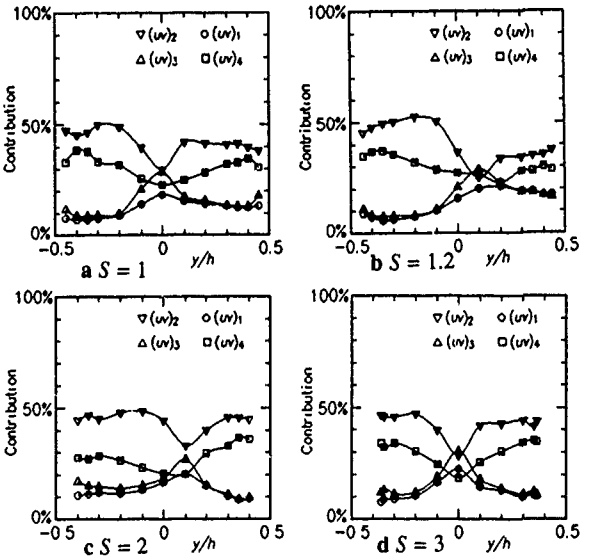

Fig.8 a-d. Contributions of each quadrant to Reynolds Stress

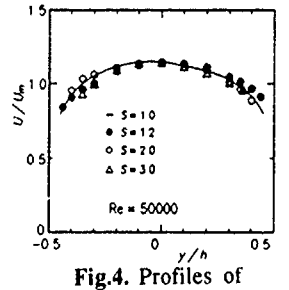

Fig.4. Profiles of mean velocity

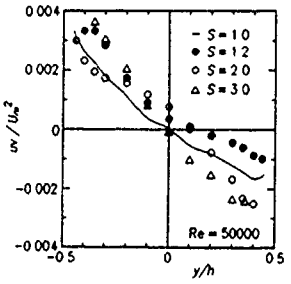

Fig.6. Profiles of Reynolds stress

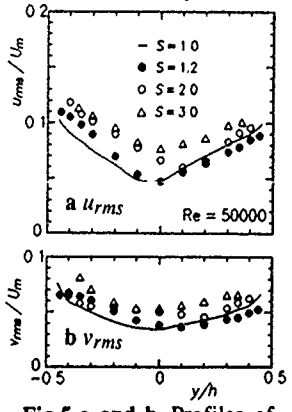

Fig.5 a and b. Profiles of turbulent intensities

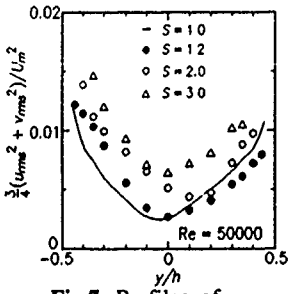

Fig.7. Profiles of turbulent kinetic energy

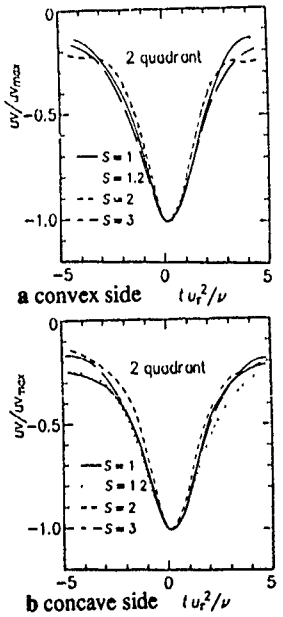

Fig.9. Ensemble-averaged uv using Quadrant (ejection)

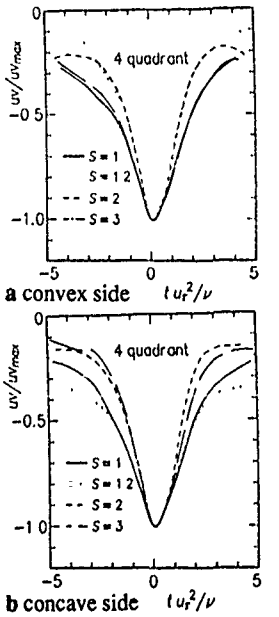

Fig.10. Ensemble-averaged uv using Quadrant (sweep)

EIGHTH SYMPOSIUM ON
TURBULENT SHEAR FLOWS
Technical University of Munich
September 9-11, 1991

EFFECT OF LONGITUDINAL VORTICITY ON THE TURBULENCE STRUCTURE IN THREE-DIMENSIONAL BOUNDARY LAYERS: MODELLING AND PREDICTION

G. Zhang and P. Zhao

Department of Engineering Mechanics
Tsinghua University, Beijing, P. R. China

ABSTRACT

A series of experiments (Ref. 1-4) revealed that the turbulence behaviour in a pressure-driven 3D boundary layer may differ considerably from what one would imagine with the available knowledge about 2D turbulent boundary layers. Departure of the turbulence behaviour in 3D boundary layers form that in 2D boundary layers is attributable to the effects of longitudinal vorticity on the turbulence structure in 3D boundary layers (Ref.5). A survey of experimental data uncovered that, for a boundary layer which is initially 2D and is driven into 3-dimensionality by a lateral pressure gradient, the effects of growth of longitudinal mean vorticity can be summed up as follows. (1) to increase the dissipation rate of turbulence energy; (2) to suppress the turbulent fluctuations normal to the wall, hence to reduce the shear-stress magnitude and the turbulent diffusion of various quantities; (3) to increase the streamwise fluctuations keeping the level of crosswise fluctuation almost unchanged, hence to cause the momentum transport normal to the wall to be anisotropic.

The basic second-moment closure (with IP model for the rapid part of the pressure-strain correlation) is not available for modelling the above mentioned effects in 3D boundary layers. It may predict neither the lag of the shear-stress direction behind the velocity-gradient direction nor the reduction of the shear-stress magnitude.

Refinements of the basic closure are introduced mainly in two aspects:

1. A rationally-developed model originally proposed by Fu et al (Ref.6) is adopted for the rapid part of the pressure-strain correlation. This model contains the quadratic and cubic terms of the Reynolds stress and the latter explicitly represents the effect of 3D vorticity field on the Reynolds-stress transport. The resultant expression is written as

$$\varphi_{ij2} = -0.6\left[P_{ij} - \frac{1}{3}\delta_{ij}P_{kk}\right] + 0.3\varepsilon a_{ij}(P_{kk}/\varepsilon) - 0.2\left\{\frac{\overline{u_k u_j}\ \overline{u_l u_i}}{k}\left[\frac{\partial U_k}{\partial x_l} + \frac{\partial U_l}{\partial x_k}\right] - \frac{\overline{u_i u_k}}{k}\left[\overline{u_l u_k}\frac{\partial U_j}{\partial x_l} - \overline{u_j u_k}\frac{\partial U_l}{\partial x_l}\right]\right\} + r\left[A_2(\overline{u_i u_k}\Omega_{jk} + \overline{u_j u_k}\Omega_{ik}) + 3a_{mi}a_{nj}(\overline{u_m u_l}\Omega_{nl} + \overline{u_n u_l}\Omega_{ml})\right]$$

where Ω_{ik} is the vorticity tensor, A_2 is the second invariant of the stress-anisotropy tensor, and r is a freely assignable parameter. Computational results show that the velocity fluctuation normal to the wall and the magnitude of the shear stress are sensitive to the value of r. In the present case, we assume r to be a linear function of the tangent of streamline-skewing angle, i.e.

$$r = C_{r1} + C_{r2}\tan(\varphi - \varphi_e)$$

where φ is the angle of direction of the velocity in boundary layer, φ_e is that at the outer edge of the boundary layer, and C_{r1}, C_{r2} are constants.

2. A new source term which represents the increase in dissipation rate of turbulence energy due to vortex stretching is added into the dissipation equation. This term is supposed to be simply proportional to $(\vec{\Omega}\cdot\nabla)\vec{V}$, the rate of increase in mean vorticity due to vortex stretching. Thus, the following modified form of dissipation equation is suggested:

$$\frac{D\varepsilon}{Dt} = C_\varepsilon\frac{\partial}{\partial x_l}\left[\overline{u_k u_l}\frac{k}{\varepsilon}\frac{\partial\varepsilon}{\partial x_l}\right] + \frac{1}{2}C_{\varepsilon 1}\frac{\varepsilon}{k}P_{kk} - C_{\varepsilon 2}\frac{\varepsilon^2}{k} + C_{\varepsilon 3}[(\vec{\Omega}\cdot\nabla)\vec{V}]k$$

where $C_{\varepsilon 3}$ is a positive constant to be determined. Obviously, the last term on the right of the equation leads to a greater dissipation rate when the boundary layer is becoming more 3D.

Bradshaw and Pontikos' experiment (Ref.3) with a simulated infinite swept wing was taken as the test case for the refined second-moment closure. The optimized values of newly-introduced constants are

$$C_{r1} = 0.06, \qquad C_{r2} = 2.5, \qquad C_{\varepsilon 3} = 0.18$$

Other constants involved remain as those in the basic

second–moment closure. Predictions of the profiles of mean–velocity components, Reynolds–stress components, turbulence energy and its dissipation rate using the refined second–moment closure and the basic second–moment closure are compared with the measurements as shown in Fig.1 (at the 4th measurement station of Ref.3 for example), where U, W and u, w are components of the mean velocity and the velocity fluctuation normal and parallel to the leading edge of the swept wing respectively, Q_e is the magnitude of mean velocity at the outer edge of the boundary layer, y and v are the coordinate and the velocity fluctuation normal to the wing surface. Other symbols in Fig.1 are the same as those in Ref.3. It is obvious that the prediction of the basic second–moment closure greatly overestimates the magnitude of every component of the Reynolds–stress tensor, whereas the corresponding prediction of the refined second–moment closure is quite agreeable with the measuredment data. The refined second–moment closure may also qualitatively predict the lag of the shear–stress direction behind the velocity–gradient direction.

REFERENCES

1. Johnston, J. P., 1976, Experimental studies in three–dimensional turbulent boundary layers. Rep. MD–34. Thermosciences Div., Stanford University.
2. Van den Berg, B., 1982, Some notes on three–dimensional turbulent boundary layer data and turbulence modelling. Proc. IUTAM Symp. on Three–Dimensional Turbulent Boundary Layers, 1–18.
3. Bradshaw, P. & Pontikos, N.S., 1985, Measurements in the turbulent boundary layer on an 'infinite' swept wing. J. fluid Mech. **159**, 105–130.
4. Anderson, S.D. & Eaton, J.K., 1989, Reynolds stress development in pressure–driven three–dimensional turbulent boundary layers. J. Fluid Mech. **202**, 263–294.
5. Bradshaw, P., 1987, Turbulent Secondary Flows. Ann. Rev. Fluid Mech. **19**, 53–74.
6. Fu, S., Launder, B.E. & Tselepidakis, D.P., 1987, Accommodating the effects of high strain rates in modelling the pressure–strain correlation Rep. TFD / 87 / 5, Dept. Mech. Eng., University of Manchester.

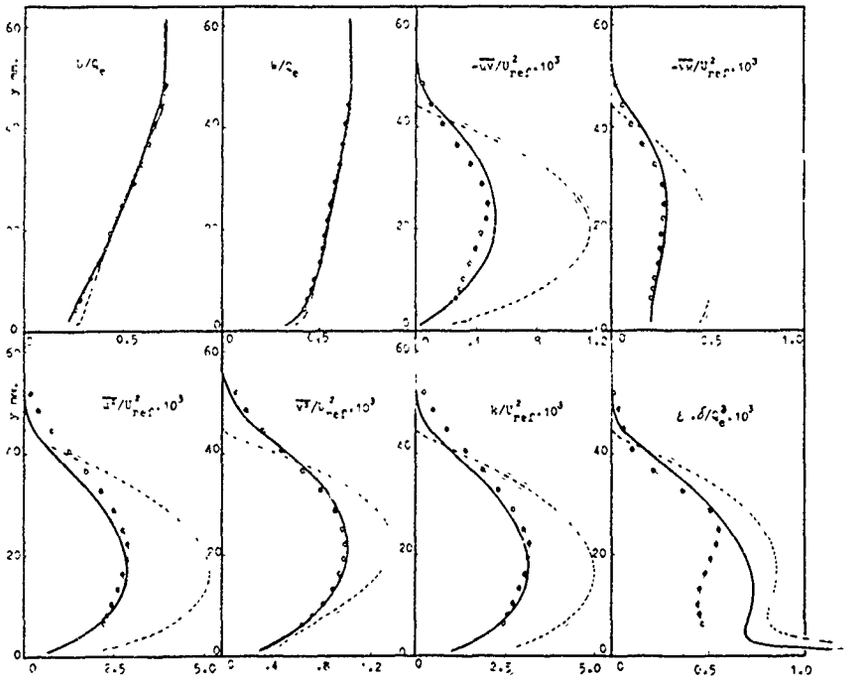

Fig.1 Comparison between predictions of basic and refined second–moment closures and measurements (4th measurement station of Ref.3)

——— refined closure - ---- basic closure

o measurements

EIGHTH SYMPOSIUM ON
TURBULENT SHEAR FLOWS
Technical University of Munich
September 9-11, 1991

LARGE EDDY SIMULATION OF RAYLEIGH-BENARD CONVECTION
A Critical Look at the Wall Function Boundary Condition

D. Angirasa and F.T.M. Nieuwstadt
Laboratory for Aero- and Hydrodynamics, TU Delft
Rotterdamseweg 145, 2628 AL Delft
The Netherlands

ABSTRACT

A numerical study of Rayleigh-Benard convection with large eddy simulation is presented. The gradient transfer hypothesis is adopted for the subgrid closure. Calculations have been performed using a 40^3 grid for a 145 cm x 150 cm x 20 cm computational grid box Some of the results are presented in this summary. A comparison with the experimental data of Adrian et. al. (1986) shows good agreement. Some of the features of the higher moments are discussed. The wall function for temperature boundary condition is examined

INTRODUCTION

The type of turbulent convection that arises by heating a fluid layer from below is called Rayleigh-Benard convection. The warm fluid from the bottom will then raise and is replaced by cooler fluid drawn from the top. This pattern of hot updrafts and cool downdrafts is referred to as coherent structures in atmospheric convection. Much knowledge about the structure of turbulence has been gained by large eddy simulation of such coherent structures in the atmosphere

Large eddy simulation (LES) is an important computational tool in the study of turbulent fluid flow. It has been particularly successful in understanding the structure of the turbulence in the atmospheric convective boundary layer because the atmospheric turbulence comprises of large scale eddies in the form of thermals. Its application to laboratory models and turbulent flow in devices is lagging far behind because wall-bounded turbulent flows pose their own computational problems distinct from the atmospheric convection. In LES, turbulent eddies larger than the grid-size are explicitly resolved by solving the time-dependent three-dimensional Navier-Stokes equations However, eddies of a size smaller than the numerical grid cell have to be modelled These are called the subgrid scales of the motion and we must filter them to solve for the larger eddies. This spatial filtering leaves additional terms in the equations, which are parameterized. Nieuwstadt (1990) presents a review of the LES method and the possibilities of its applications

In the present study, we are concerned with the LES of turbulent buoyant convection in the laboratory situations. The major difficulty in this problem is that we need a wall-function to determine the temperature drop across the first grid cell adjacent to the wall in terms of the heat flux at the wall. Most of the mean temperature variation normal to the horizontal heated wall takes place within the first grid cell, hence the need for a proper wall-function.

LES MODEL

The LES model used in this study was described by Nieuwstadt and Brost (1986), which was meant for the study of the decay of the convective turbulence in the atmosphere. The model is modified for the laboratory situation that is presently under study. In this model the subgrid terms are parameterized by gradient transfer hypothesis. For example, the deviatoric subgrid Reynolds-stress τ_{ij} is given as

$$\tau_{ij} = K \left(\frac{\partial \tilde{u}_i}{\partial x_j} + \frac{\partial \tilde{u}_j}{\partial x_i} \right) \qquad (1)$$

where the tilde denotes the resolvable scale field. The exchange coefficient K is expressed as

$$K = c\, E^{1/2}\, l \qquad (2)$$

where E is the subgrid kinetic energy, for which we solve an additional equation, and l is the mixing length, which is related to the grid-size as

$$l = (\Delta x\, \Delta y\, \Delta z)^{1/3}. \qquad (3)$$

The constant c is interpreted as proportional to the ratio of the filter width to the grid-size. In the present study its value is 0 12.

The calculation domain is a rectangular box. The horizontal dimensions are 145 cm x 150 cm, and the vertical 20 cm. The number of grid points placed in each direction is 40. For all fluctuating variables the horizontal boundary conditions are prescribed to be periodic. At the top vertical velocity and gradients of horizontal velocity components, and temperature are zero. These satisfy adiabatic boundary conditions at the top.

WALL FUNCTION FOR TEMPERATURE BOUNDARY CONDITION AT THE BOTTOM

For prescribing temperature boundary condition on the bottom side, we need a wall-function that gives a functional relation between the wall heat flux and the mean temperature drop across the heated layer in the vertical direction. The horizontally averaged mean temperature drops sharply with height near the wall, and it is not possible to resolve it numerically. In fact, most of this temperature drop takes place within the first numerical grid cell We have faced several difficulties in finding proper wall functions.The thermal structure of the convective layer is quite complex and multiple layer theories have been proposed, with each layer exhibiting its own thermal characteristics. Adrian et al. (1986) discussed the models.

A matching analysis of a two layer model has been performed to obtain a wall-function. In this analysis the inner layer is assumed to be dominated by conduction and the outer layer by convection. The following functional forms of the temperature profile in the overlaying region have been obtained after matching of the two layers

$$\frac{T_o - T}{\Theta_0} = - C \left(\frac{z}{z_0}\right)^{-1/3} + C_N \qquad (4)$$

$$\frac{T - T_\infty}{\Theta_*} = C \left(\frac{z}{z_*}\right)^{-1/3} - C \qquad (5)$$

In the above formulation, the subscripts o and * refer to conduction and convection scales respectively as given in Adrian et. al. (1986). T_o is the mean surface temperature. Extensive comparison is made with the available experimental data to obtain the values of C and C_N. The values suggested are $C \approx 1.0$ and $C_N = 0$ (10.0). C_N appears in the calculation of Nu as follows.

$$Nu = \left[\frac{1}{C_N - C\,(Ra\,Nu\,Pr)^{-1/12}}\right]^{4/3} Ra^{1/3}\, Pr^{1/3} \qquad (6)$$

We have calculated Nu from Eq (6) and found that the calculated values agree well with the measured values. Table 1 presents a comparison. Since Eq (6) is an implicit expression for Nu, iterative procedures have to be employed for calculating Nu In any case, the immediate utility of Eq (6) is in checking the validity of the model constants C and C_N. Nu is not sensitive to the value of C as can be seen from table 1, but its dependence on the value of C_N is rather pronounced. We are carrying out further calculations to fix the value of C_N that matches the experimental data.

In the LES, most of the mean temperature drop above the surface takes place within the first grid-cell. Hence we need the above empirical law to prescribe the drop in the temperature across the grid-cell, as also the temperature on the surface in relation to the heat flux. The equations 4 and 5 together provide this information

Table 1

Pr = 6 0

Ra	Nu Expt.	Nu Present	C	C_N
1.5×10^7	19.43	21.15	0.75	10.0
		21.28	1.0	10.0
		18.7	1.0	11.0
$1\ 18 \times 10^8$	38.64	37.03	1.0	11.0
9.49×10^8	77.42	78 73	1.0	10.5

NUMERICAL RESULTS

Computations have been performed for the following set of conditions:
$Q_0 = 0.0153$ cm/sec, $w_* = 0.45$ cm/sec, $z_* = 20$ cm, $\Theta_* = 0.034\ ^oC$.
Here Q_0 is the kinematic heat flux at the surface, w_* is the convective velocity, z_* is the distance between the two horizontal surfaces and Θ_* is the temperature scale given by Q_0/w_*. From the convective velocity w_*, and the length z_*, we obtain a time scale t_* given by z_*/w_*

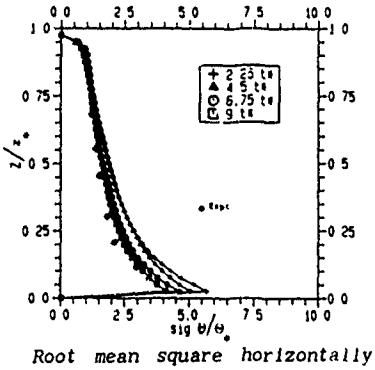

Fig. 1 Root mean square horizontally averaged temperature at various time-levels

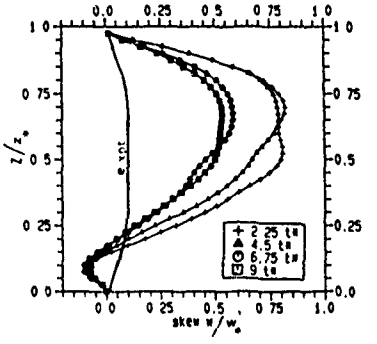

Fig. 2 Time evolution of the vertical velocity skewness

In Fig 1 we present the vertical profiles of RMS temperature at various time levels. A comparison with the experimental data of Adrian et. al. shows good agreement Near the lower boundary the RMS temperature starts at the RMS value of the plate, which is zero in this case, and reaches a maximum, before beginning to decrease. The decrease can be fitted into a power law variation. This behavior is similar to the one observed by Deardorff and Willis (1967). Above $0.5z_*$ the power law variation is no longer valid since the profile becomes linear.

As a final point of interest in this summary, we present the evolution of skewness of vertical velocity in Fig. 2 There is considerable discrepancy between the measurements in the laboratory and the computations of this higher moment. There is also wide disagreement among different measurements and various computations. Moeng and Rotunno (1990) recently discussed these features.

REFERENCES

Adrian, R.J., Ferreira, R.T.D S. & Boberg, T. 1986 Turbulent thermal convection in wide horizontal fluid layers. **Experiments in Fluids 4**, 121-141.

Deardorff, J.W. & Willis, G.E. 1967 Investigation of turbulent thermal convection between horizontal plates. J. **Fluid Mech. 28(4)**, 675-704.

Moeng, C.-H. & Rotunno, R. 1990 Vertical-velocity skewness in the boundary layer. J. **Atmospheric Sci.**

Nieuwstadt, F.T.M. 1990, Direct and large eddy simulation of free convection. **Proc. IX International Heat Transfer Conference - Jerusalem**, Hemisphere, Washington, D.C.

Nieuwstadt, F.T.M. & Brost, R.A. 1986 The decay of convective turbulence. J. **Atmospheric Sci. 43**, 532-546.

EIGHTH SYMPOSIUM ON
TURBULENT SHEAR FLOWS
Technical University of Munich
September 9-11, 1991

LARGE EDDY SIMULATION OF A TURBULENT FLOW WITH SEPARATION

M. Arnal and R. Friedrich

Lehrstuhl für Fluidmechanik
Technische Universität München
Federal Republic of Germany

ABSTRACT

Results of one of a series of numerical simulations of the turbulent flow over a rearward-facing step are presented and discussed. The large eddy simulation technique is used to simulate the statistically-stationary, fully-turbulent, separating and reattaching flow. Statistical quantities are compared with the results of experimental investigations of the same flow at similar Reynolds numbers.

In the present contribution the instantaneous flow field predictions are compared with the mean flow field to illustrate the large fluctuations occurring in the separating shear layer.

NOMENCLATURE

h	characteristic length, step height
L	computational domain length, $L = 24h$
Re_0	global Reynolds No., $Re_0 = U_0 h/\nu$
T_0	characteristic time, $T_0 = L/U_0$
U_0	upstream channel centerline velocity
u, v, w	velocities in the x, y, z directions
X_R	dimensionless reattachment length
x, y, z	streamwise, tangential, and vertical coordinate directions.

INTRODUCTION

The fully-turbulent flow over a backward-facing step has been the subject of many experimental investigations because of its simple geometry and a well-defined separation point. It has also served as a benchmark test-case for the turbulence modelling and simulation communities.

In the present study we apply the large-eddy simulation (LES) technique to predict the developing turbulent flow. In this technique the large, energy-rich structures are directly simulated while the smallest, dissipative scales are modelled. Since the time-dependent, three-dimensional flow field is simulated, instantaneous distributions of the resolvable flow quantities can be obtained. In addition, statistical distributions of the mean velocity field and higher-order correlations may be computed.

MATHEMATICAL MODEL

The governing equations are derived by applying a spatial, lowpass-filter to the Navier-Stokes equations for an incompressible, constant-viscosity fluid. Among the various filter methods in use, we employ Schumann's (1975) "volume balance procedure." In this case filtering is accomplished by integration of the governing equations over a control volume of an equidistant, Cartesian, staggered grid. This leads to a set of ordinary differential equations in time describing the resolvable (grid-scale, GS) flow quantities. In the present study a subgrid-scale (SGS) model of the Schumann-type (1975) is adopted to close the equations. This two-part eddy-viscosity model relates the SGS-stress to the fluctuating and statistically-averaged portions of the filtered deformation tensor. Details of the complete model are given in Friedrich (1988).

NUMERICAL PROCEDURE

The momentum equations are integrated in time using the second-order leapfrog scheme with an initial Euler-step to start the simulations. The pressure field is computed exactly with the use of Chorin's (1968) projection method and a fast elliptic solver. A fast Fourier transformation in the spanwise direction reduces the 3-D problem to a set of decoupled, 2-D Helmholtz problems which are solved in parallel employing the cyclic reduction technique. Further details of the numerical procedure as well as a complete discussion of the boundary conditions is given in Friedrich and Arnal (1990).

RESULTS

Because of space limitations, only a few examples taken from the extensive data set of the rearward-facing step flow is presented. The computational domain consists of an inlet channel upstream of the step and an expansion chamber downstream. The Reynolds number, based on the step-height h and the maximum inlet velocity U_0, is $Re_0 = 1.55 \times 10^5$.

In Figures 1 and 2 a comparison is given of our simulations with experimental studies at similar Reynolds numbers from Tropea (1982) and Durst and Schmitt (1985). Two streamwise locations downstream of the step are shown for the mean streamwise velocity and Reynolds stress profiles. The predicted mean reattachment length of $X_R = 8.6$ compares well with the experimental values of $X_R = 8.6$ (Tropea) and $X_R = 8.5$ (Durst & Schmitt), where the distance is measured from the step location. In general, the mean velocity profiles show good agreement at all streamwise positions in the flow. The Reynolds-stress profiles show regions of larger disagreement however, the uncertainty in the measurements is also remarkable. We note that the location of the predicted maximum stress is further from the reattachment wall than experimentally observed and that the decrease in the stress levels downstream of reattachment occurs more slowly than in the measurements.

In Figure 3 the mean streamwise and cross-stream velocities are compared with instantaneous profiles of the two velocity components. In the figure the mean reattachment length is at $x/h = 12.6$. In this region we note the large fluctuations in the instantaneous profiles, particularly in the cross-stream velocity component. The region of large departures from the mean corresponds roughly with the location of the shear layer.

In Figure 4 the instantaneous, fluctuating velocity vector field downstream of the step is compared with the fluctuating pressure field. A comparison of the figures shows that the instantaneous low-pressure points are the locations of large vortices in the shear layer. As the vortices move downstream of the step they become more inten. (stronger negative values of pressure) and interact with one another and with the reattachment wall. The turbulent production of these large, energy-bearing structures in the shear layer far exceeds the production which occurs in the wall regions. This leads to a maximum in the turbulence energy in the region of the shear layer which decays slowly downstream of the reattachment region.

CONCLUSIONS

The present study has focussed on the simulation of the fully-turbulent flow over a backward-facing step. Comparisons of the mean flow results with experimental studies show good agreement. Improvements are still possible with new SGS models and higher numerical resolution. Of particular value is the availability of the instantaneous veloc-

ity and pressure fields for improved understanding of the physics of separating and reattaching flows.

REFERENCES

CHORIN, A.J. 1968 Numerical solution of the Navier-Stokes equations. Mathematics of Computations 22, 745-762.

DURST, F. & SCHMITT, F. 1985 Experimental study of high Reynolds number backward facing step flow. Proc. 5th Symp. on Turbulent Shear Flows, Aug. 7-9, Cornell University, Ithaca, NY.

FRIEDRICH, R. 1988 Simulation of turbulent flows. Computational Methods in Flow Analysis (H. Niki and M. Kawahara, eds.), 2, 833-843.

FRIEDRICH, R. & ARNAL, M. 1990 Analysing turbulent backward-facing step flow with the lowpass-filtered Navier-Stokes equations. J. Wind Eng. and Ind. Aero., 35, 101-128.

PIOMELLI, U., FERZIGER, J., MOIN, P. & KIM, J. 1989 New approximate boundary conditions for large-eddy simulations of wall-bounded flow. Phys. Fluids A, 1, 1061-1068.

TROPEA, C. 1982 Die turbulente Strömung in Flachkanälen und offenen Gerinnen. Dissertation, University of Karlsruhe, Karlsruhe, Germany.

SCHUMANN, U. 1975 Subgrid scale model for finite difference simulations of turbulent flows in plane channels and annuli. J. Comp. Phys., 18, 376-404.

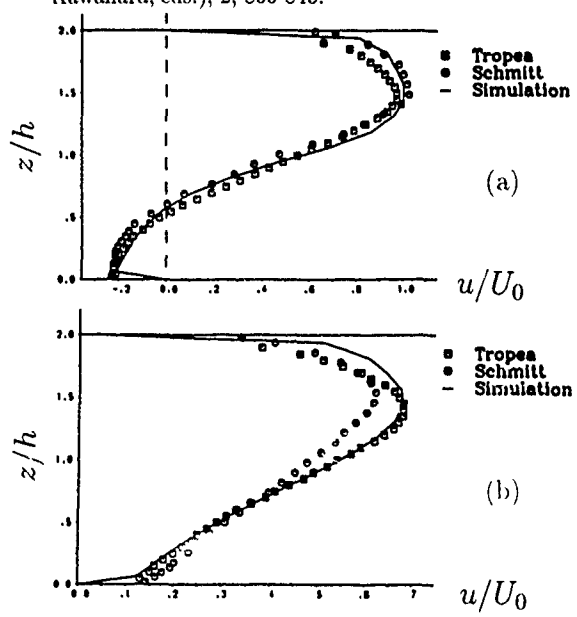

Fig 1 Mean streamwise velocity profile, u/U_0. a) $x/h = 4$. b) $x/h = 10$. Position measured from step location

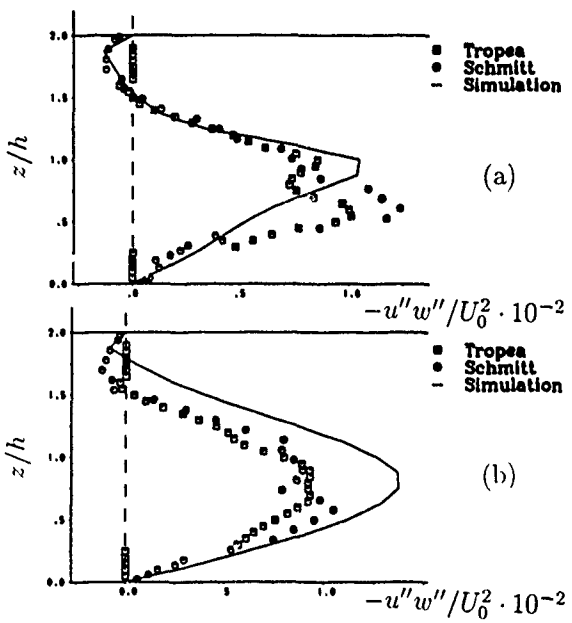

Fig. 2 Reynolds-stress profile, $-u''w''/U_0^2$. a) $x/h = 4$. b) $x/h = 10$. Position measured from step location.

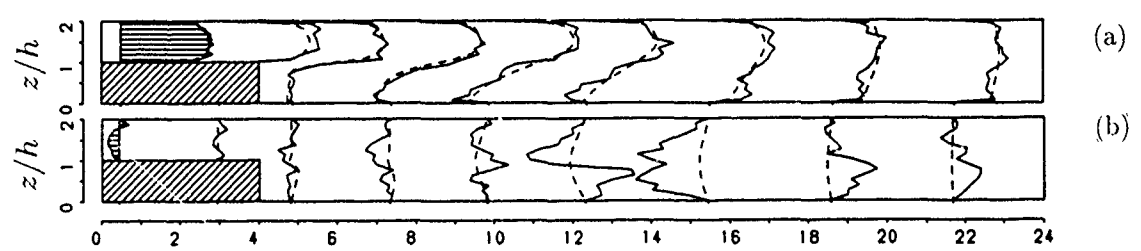

Fig. 3 a) Streamwise velocity, u. b) Cross-stream velocity, w. Comparison of mean and instantaneous profiles.

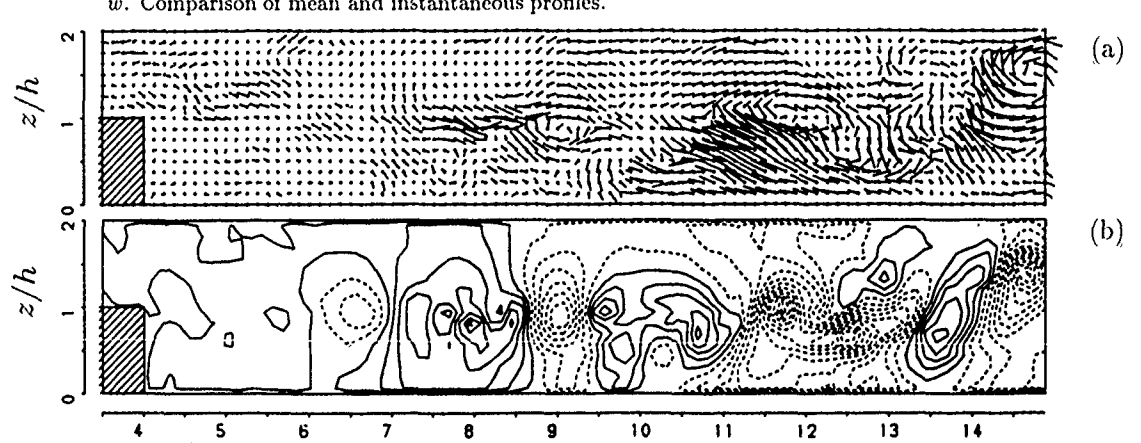

Fig. 4 a) Instantaneous fluctuating velocity vectors in an $x - z$ plane, b) Contours of the instantaneous fluctuating pressure in an $x - z$ plane, $t = 215.4T_0$.

EIGHTH SYMPOSIUM ON
TURBULENT SHEAR FLOWS
Technical University of Munich
September 9-11, 1991

ON THE MODELLING OF TURBULENT SHEAR FLOWS UNDER STRONG BUOYANCY EFFECTS

D.V.Bayandin*), G.Z.Fainburg**), I.I.Vertgeim***)

*) Perm Polytechnical Institute
29 A,Komsomolsky Ave.,614007,Perm,USSR

**) Mining Inst. Urals Branch USSR Acad. Sci.
78A Karl Marx Street,614004,Perm,USSR

***) Institute of Continuous Media Mechanics
Urals Branch USSR Academy of Sciences.
1,Acad.Korolyov Street,614061,Perm,USSR

ABSTRACT

This paper presents some results of wider programme of work to obtain an understanding of turbulent shear flows under strong buoyancy effects and to develop mathematical techniques for their prediction. The purpose of this paper is to compare significance of different approximations of turbulent heat flux and various descriptions of turbulent temperature field.

TURBULENCE MODELS

Turbulent shear flows under strong buoyancy effects are common in both environmental sciences and industrial engineering but a general understanding of their physics and adequate modelling are still far from complete.

The principal turbulence models in use were developed for high Reynolds number forced convective flows. In this case the two-parameter "k-ε" model exhibited a surprising degree of predictive ability. For turbulent buoyancy driven flows however the situation is quite different. The main difficulties are due to the influence of buoyancy forces strongly changing the flow behavior and the heat transfer characreristics. Furthermore, different types of flows with various interactions between turbulent fields exist simultaneously. In particular, in a enclosed rectangular cavity there are the narrow boundary layers near the vertical walls and under (over) the horizontal plates, large stagnant core in the middle of cavity, regions with stable, neutral and unstable stratification. This fact requires universality and high predictive ability of physical and computational models, but also simplicity and suitability for practical computations with the present generation of computers. For the attainment of our purpose we analyzed in detail two problems of closure technique: description of turbulent temperature field and approximation of turbulent heat flux. Three different models were used.

The first model is modified two-parameter low-Reynolds-number "k-ε" model. Turbulent temperature field is characterized by only eddy Prandtl number which must be known a-priori. The description of turbulent heat flux uses gradient approximation.

The second model is four-parameter one of "eddy diffusivity" type. The turbulent energy E, temperature variance θ and their dissipation rates D and Φ are determined by differential equations. This allows to obtain the expressions for turbulent viscosity ν_t and turbulent thermal diffusivity χ_t. Independent description of turbulent temperature field and estimation of eddy Prandtl number became possible.

The third model is four-parameter differential-algebraic one with non-gradient approximations of turbulent heat flux Γ_i and its dissipation rate Q_i:

$$\Gamma_i = c_t \frac{k}{\varepsilon}\left(-1.5R_{ij}\nabla_j T - 0.3\Gamma_j e_{ij} + g\beta\left[2\gamma_i\theta - \right.\right.$$

$$\left.\left. - \pi_0(\pi_1\gamma_i + \pi_2 n_i n_j\gamma_j + \pi_3 e_{ijm}n_j\gamma_m)\sqrt{\theta_M\theta}\right]\right),$$

$$Q_i = c_\Phi \frac{k}{\varepsilon}\left(-3D_{ij}\nabla_j T - c_3 D\Gamma_j e_{ij} + g\beta\left[2\gamma_i\Phi - \right.\right.$$

$$\left.\left. - \pi_0(\pi_1\gamma_i + \pi_2 n_i n_j\gamma_j + \pi_3 e_{ijm}n_j\gamma_m)\sqrt{\Phi_M\Phi}\right]\right),$$

$$D_{ij}/D - \delta_{ij}/3 = b\,(R_{ij}/E - 2\delta_{ij}/3)\,.$$

Here R_{ij} - Reynolds stresses, L_{ij} - dissipation rate of R_{ij}, e_{ij} - mean strain rate, θ_M and Φ_M - values of θ and Φ on the wall, g - gravitational acceleration, $\vec{\gamma}$ - unit vertical vector, $\vec{n}$ - unit normal vector of solid wall, β - volumetric expansion coefficient. The influence of wall is described by function

$$\pi_0 = \exp\left\{-\delta^{-2}\int_{x_M}^{x}\left(\nu_t/\sqrt{E}\right)dx\right\},$$

δ - boundary layer thickness, x - normal coordinate. Source terms in the heat dissipation equation are:

$$I_\Phi = -2Q_k\nabla_k T + c_2\frac{\nu D^2}{E^2}\Gamma_k^2 - \left(c_\Phi\frac{\nu D}{E} + \tilde{c}_\Phi\frac{\chi\Phi}{\theta}\right)\Phi + 2\chi_t(\nabla_k\nabla_m T)^2$$

c_2, c_3, c_Φ, c_Φ, $\tilde{c}_\Phi$, π_1, π_2, π_3 -empirical constants.

All the models are derived by the reduction method from a full second-order model which includes the transport equations for second single-point moments of velocity and temperature fluctuations and their gradients: the Reynolds-stress tensor, turbulent heat flux, temperature variance for fluids and

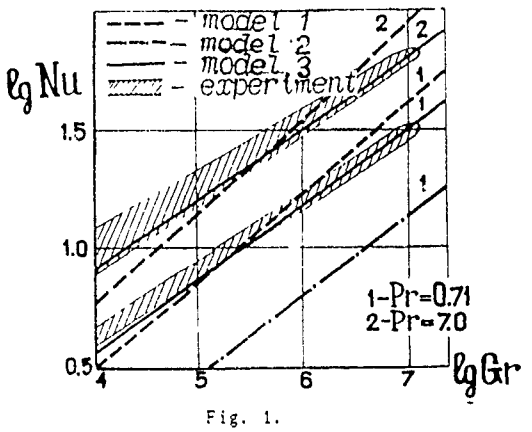

Fig. 1.

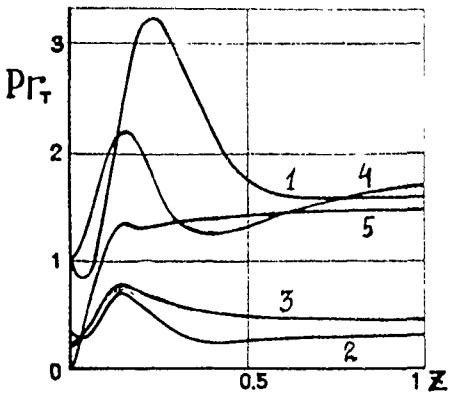

Fig. 2.

surrounding solid and relative dissipation functions In this model [1] the finite thermal conductivity of the surrounding walls and the influence of the latter on pressure fluctuations are taken into account. The tensor approximation method is the basis of closure procedure. Some closure coefficients are determined from the best comparison of computational and experimental data for homogeneous turbulence.

CALCULATION RESULTS

The different turbulent natural convective flows in plane horizontal and vertical layers and enclosures were investigated by numerical methods. Evaluations of stationary and non-stationary flows were made [2]. The numerical experiments enabled us to test different closures.

The results of numerical simulation indicate that all the models predict correctly the qualitative features of the natural convection flows. However the first model overpredicts the values for the heat transfer and for the rate of its growth with the increase of the Grashof number (Fig.1 - horizontal layer heated from below), whereas the other characteristics are in good accord with only if the value of eddy Prandtl number $Pr_t = \nu_t / \chi_t$ is the same as its mean value in real flow. The independent turbulent temperature field description in second model produces the better results. Furthermore the gradient approximation of turbulent heat flux leads to strong increase of mean temperature gradient in the core while in case of stable stratification - to weakening and even to total damping of turbulence.

Considerably better results are yielded by third model with non-gradient approximation of turbulent heat flux and its dissipation rate. Only this model allows to describe the effect "negative" turbulent thermal conductivity existing in horizontal layers under horizontal temperature gradient. This makes possible to predict advective flows in fluid layer between adiabatic horizontal solid boundaries [3]. Regions with heat transfer toward the temperature growing direction are clealy seen near the walls. The turbulence intensity is sufficient everywhere in the layer, despite a stable stratification. In all problems yielded temperature gradients in the flow core regions are small and lie close to experimental data. For the horizontal layer heated from below, the Θ profile in the third model simulation have an expressed maxima, and D profile - minima near the walls. Maxima of E, wich was observed in experiments at the moderate Rayleigh number values, was obtained in a two-dimensional simulation for all the models used.

Evaluations of turbulent Prandtl number for the second and third models show in good accordance with existing experimental data that its value is non-constant, but depends significantly on flow type, boundary conditions, value of similarity criteria, and space coordinates. For example, on Fig.2 the turbulent Prandtl number space distributions, calculated by third model, with typical maxima in near-wall region are presented (1,2 - horizontal layer heated from below, Pr=0.7,7; 3 -vertical slot heated from aside; 4,5 - advective flow between ideally thermoconductive and insulated boundaries).

The most reasonable approach to problem of adequate prediction of turbulent shear flows under strong buoyancy effects at the current time seems to be the use of few-parameter differential-algebraic low-Reynolds / Peclet-number models.

REFERENCES

FAINBURG, G.Z. 1976 Towards natural convection turbulence equations of incompressible fluid // Hydrodynamics (PGPI Scientific Report N 152), Perm. 100-112 (in Russian).

BAYANDIN, D.V., FAINBURG, G.Z. & WERTGEIM, I.I. 1988 Mathematical modelling of turbulent natural convection. Preprint N 83(88), Sverdlovsk. 62 p. (in Russian). Translation submitted for Heat Transfer - Soviet Research (in the press).

BAYANDIN, D.V. 1988 Modelling of turbulent advective flows in fluid horizontal layers // High Temperature Thermophysics, USSR Acad.Sci. 25, 1128-1134.

LARGE EDDY SIMULATION OF CUMULUS CLOUDS

J.W.M. Cuijpers *) and P.G. Duynkerke **)

*) Royal Netherlands Meteorological Institute, P.O Box 201,
3730 AE DE BILT, The Netherlands

**) University of Utrecht, Institute of Meteorology and Oceanography,
P.O. Box 80 000, 3508 TA UTRECHT, The Netherlands

ABSTRACT

A large eddy model used for studying the dry convective boundary layer, has been extended with an equation for the specific humidity and a condensation scheme, to simulate the moist convective boundary layer A simulation has been made based on the observations gathered near Puerto Rico on 15 December 1972. Starting from a clear air situation the model evolves to a situation with small cumulus clouds. Vertical profiles of variances and fluxes show satisfactorily agreement with the experimental data

INTRODUCTION

In buoyant updrafts of the convective atmospheric boundary layer (ABL) the temperature decreases with height Provided that there is enough water vapor this leads to condensation and the formation of clouds The latent heat that is released during this formation enhances the buoyancy of the updrafts and thus the production of turbulence. So, turbulence generation and cloud formation are strongly coupled.

Furthermore, due to the enhanced buoyancy clouds are able to penetrate into the stable layer capping the ABL. This causes mixing over greater depth than would be possible in a situation without clouds.

It is the purpose of this study to investigate the influence of non-precipitating cumulus clouds on the turbulence structure.

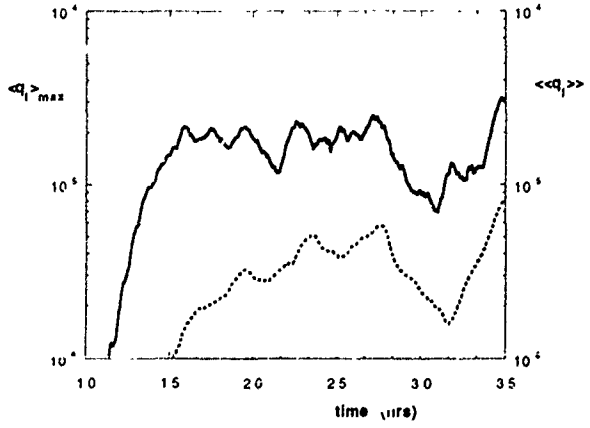

Fig. 1 The temporal evolution of the maximum value of the horizontally averaged cloud water $<q_l>_{max}$ (full line) and the total amount of cloud water averaged over the whole domain $<<q_l>>$ (dashed line).

MODEL DESCRIPTION

The model we use is based on the large eddy model of Nieuwstadt and Brost (1986), who simulated the dry convective boundary layer. In our model the liquid water potential temperature θ_l is used as a conservative variable in the thermodynamical equation. Because of the low cloud cover it does not seem necessary to use a detailed computation of the radiational flux divergence term in the thermodynamical equation. Instead we fixed the radiational cooling to a constant, which was chosen such that the radiational cooling balances the vertical flux of potential temperature. This means that the surface heat flux will remain constant and a stationary situation will be reached

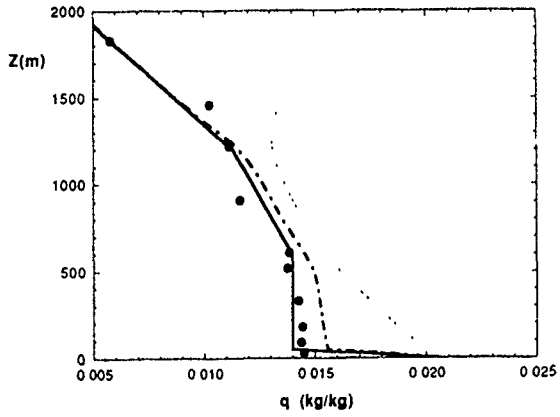

Fig 2 The horizontally averaged profiles of the total water specific humidity at $t=0^h$ (full line) and $t=3^h$ (dash-dotted) compared with the observed values (circles). The dotted line is the horizontally averaged profile of the saturation specific humidity at $t=3^h$.

The model has been extended with an equation for the specific humidity (with the total water $q_t = q_v + q_l$ as conservative variable, where q_v is the specific humidity for vapor and q_l is the liquid water specific humidity).

The condensation scheme we use is the one described by Sommeria and Deardorff (1977), in which it is assumed that a grid volume contains no liquid water until the total water specific humidity exceeds the saturation value q_s. This means that a grid volume is either entirely saturated or entirely unsaturated.

In the model there are 40 grid points in each direction; a grid volume has horizontal dimensions of 125 m by 125 m and a vertical dimension of 50 m.

The initial conditions are chosen such as to reproduce the observed conditions during the NCAR 1972 Puerto Rico experiment. The observations shown here are from the data gathered in the suppressed regions on 15 December [Case II in LeMone and Pennell (1976)].

RESULTS

Initially there are no clouds in the model They appear after about 1 hour of model time and are cumuliform. The temporal evolution of the total amount of cloud water averaged over the whole domain $<<q_l>>$, and the maximum value of the horizontally averaged cloud water $<q_l>_{max}$ is shown in Fig. 1. After an initially increase in cloud water content $<q_l>_{max}$ becomes more or less constant after 1 1/2 hours. The cloud cover is 10 - 15 %. About half an hour later there is a small minimum A second and larger minimum occurs after another half hour period of more or less constant $<q_l>_{max}$ Periods with fewer cloud activity after periods with larger cloud activity might be explained by enhanced buoyancy due to the release of latent heat. This will cause more turbulence and more mixing of cloud air with unsaturated air.

The lowest level where clouds form is at 550 m. Some clouds are able to penetrate into the stable layer which explains the increase in total water specific humidity above 1100 m (Fig. 2) The decrease in potential temperature in this stable layer might be explained by evaporation of these clouds

The virtual potential temperature flux is shown in Fig. 3 for $t = 2^h30^m$ and $t = 3^h00^m$ It decreases linearly with height from surface up to cloud base, where it reaches a negative value of about 10 % of the surface flux. This is close to the 7 % found from the observations The heat flux in the mixed layer does not vary with cloud activity This is in contrast with the vertical flux of total water (Fig 4), which varies in the mixed layer as well as in the cloud layer

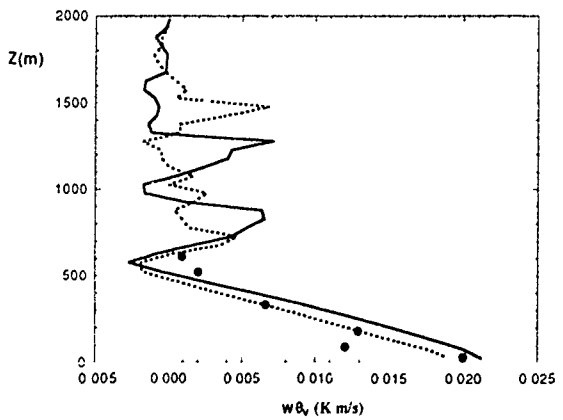

Fig. 3 Profiles of the horizontally averaged virtual potential temperature flux at $t = 2^h30^m$ (full line) and $t = 3^h00^m$ (dotted line) compared with observations (circles).

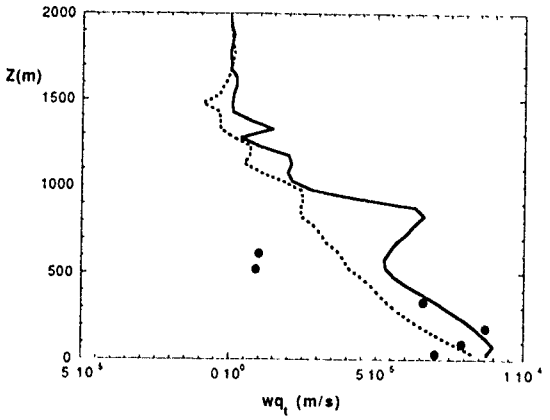

Fig. 4 Profiles of the horizontally averaged total water flux at $t = 2^h30^m$ (full line) and $t = 3^h00^m$ (dotted line) compared with the observed water vapor flux (circles).

CONCLUDING REMARKS

The agreement between the profiles produced by the model and the observations are generally satisfactory. Differences between observations and model output can probably be explained by large scale influences in the observations, that are not taken into account in the model. Clouds produced by the model are rather similar to those observed.

ACKNOWLEDGEMENT

The authors like to thank Dr. M.A LeMone for providing the data of the Puerto Rico experiment We thank F.T.M Nieuwstadt, J. Eggels and M. Pourquie for discussions and structuring the original code of the model. The first author acknowledges financial support by the Netherlands organisation for scientific research (NWO) under contract # 752-365-031.

REFERENCES

LeMone, M.A., and W.T. Pennell, 1976. The relationship of trade wind cumulus distribution to subcloud layer fluxes and structure. *Mon. Wea. Rev.*, **104**, 524-539.

Nieuwstadt, F.T.M., and R A. Brost, 1986: The decay of convective turbulence.*J. Atmos Sci.*, **43**, 532-546.

Sommeria, G , and J.W. Deardorff, 1977: Subgrid-Scale Condensation in Models of Nonprecipitating Clouds. *J. Atmos Sci.*, **34**, 344-355.

EIGHTH SYMPOSIUM ON
TURBULENT SHEAR FLOWS
Technical University of Munich
September 9-11, 1991

TWO-PARAMETER TURBULENCE CLOSURE SCHEMES IN THE SLOPES WIND MODELING

E.E.Fedorovich and A.E.Kirimov

Voeikov Main Geophysical Observatory
Karbyshev str.,7 194018 Leningrad USSR

ABSTRACT

The set of two numerical models of the atmospheric planetary boundary layer flow over the slanting slopes is presented. Models are basing on the alternative two-parameter closure schemes for the turbulent flow thermodynamics equations in the boundary layer approximation. The model results obtained in the framework of (l,b) and (ϵ,b), where l is characteristic scale of turbulent fluctuations, b is turbulent kinetic energy and ϵ is turbulent kinetic energy dissipation rate are discussed. Numerical experiments carried out have shown the essential influence of the slosure scheme on the over slope flow patterns.

INTRODUCTION

The formation of the local atmosperic circulations in the planetary boundary layer (PBL) is rather typical phenomenon under conditions of the thermal and orographical non-uniformity of the underlying surface. Even in the case when the surface is uniform from thermal point of view, but has some inclination, the component of buoyancy force parallel to the slope surface appears, acting upon the airflow and leading to so-called slope effects in the atmospheric PBL. In more general case effects of slope and thermal non-uniformity superpose, forming complex flow pattern in the atmospheric boundary layer over slope.

First works on the mathematical description of slope effects refer to middle of this century, when analytical solutions of corresponding hydrodynamical problems were received (for example: Monin,1949; Dorodnitsyn,1950). In major part of that time works the turbulent exchange in the air flow over slopes was parameterized by constant turbulent exchange coefficient. More complex schemes of turbulent transfer description (two-parameter closure schemes, for example), that appeared later, were just rarely applied to the modeling of the slope effects in the PBL. First of all it refers to the schemes, containing turbulence dissipation rate as one of the parameters. Mainly such schemes were used in the models of PBL over flat, horizontally non-homogeneous terrain and over rather steep orography, where dynamic effects, caused by form drag, prevail over effects of thermal non-uniformity of the flow. In the presented paper the pure problem of the slope effect in the PBL over slightly inclined terrain is solved within the framework of two alternative turbulence closure schemes on the basis of two-parameter approach towards turbulence description. One of scopes of this paper is the comparison of over slope flow patterns, obtained with the aid of different closure schemes.

We consider the atmospheric flow over long, slanting ($|\, tg\alpha \,|$ not more than 0.01-0.02) slope facing up the flow (facing down the flow) and infinite in the direction, normal to the flow. It is assumed, that flow disturbances, stipulated by its interaction with the slope are located within the PBL, depth of which H is the external parameter of the model The distributions of roughness and temperature along the underlying surface are expressed by prescribed functions of horizontal coordinate. Problem is solved in the stationary approximation, the values of meteorological values above PBL are considered to be known. While deriving the model equations system we use the boundary-layer approximation. The horizontal components of turbulent friction are not taken into account due to the small value of slope inclination angle The third equation of motion is written in hydrostatic approximation. The model system has the following initial form:

$$u\frac{\partial u}{\partial x} + w\frac{\partial u}{\partial z} = -\frac{\partial p'}{\partial x} + fv + \frac{\partial}{\partial z}k\frac{\partial u}{\partial z}, \tag{1}$$

$$u\frac{\partial v}{\partial x} + w\frac{\partial v}{\partial z} = -f(u - G) + \frac{\partial}{\partial z}k\frac{\partial v}{\partial z}, \tag{2}$$

$$\frac{\partial u}{\partial x} + \frac{\partial w}{\partial z} = 0, \tag{3}$$

$$\frac{\partial p'}{\partial z} = \beta\theta', \tag{4}$$

$$u\frac{\partial \theta}{\partial x} + w\frac{\partial \theta}{\partial z} = \alpha_\theta\frac{\partial}{\partial z}k\frac{\partial \theta}{\partial z}, \tag{5}$$

where u,v,w - wind velocity components along axes x,y and z respectively, f - Coriolis parameter, k - turbulent exchange coefficient, p' - pressure deviation from hydrostatic value, β - buoyancy parameter, θ - potential temperature, θ' - deviation of θ from background profile, G - geostrophic wind velocity modulus (oX in our case is poarallel to the geostrophic wind vector), α_θ - relation between turbulent exchange coefficients for heat and momentum. To carry out the closure of Eqs.(1)-(5) we have to define the method of k determination. In the framework of two-parameter turbulence closure schemes this coefficient is expressed through two parameters of turbulence. There are two main alternative sets of such characteristics, used in PBL modeling practice: (l,b) set, where l - characteristic scale of turbulent fluctuations, b - turbulent kinetic energy, and (ϵ,b) set, where ϵ - turbulent energy dissipation rate. In the first case k can be expressed through l and b in following form:

$$k = c^{1/4}l\sqrt{b}. \tag{6}$$

In the second case k is evaluated from ϵ and b by the formula:

$$k = \frac{cb^2}{\epsilon}, \tag{7}$$

where c - non dimensional constant, which value is usually assumed be equal to 0.046. For each characteristic l, b or ϵ additional relation has to be constructed. The value of ϵ is determined from the balance equation for this characteristic (Launder et al,1975; Claussen,1988; Beijaars et al,1987):

$$u\frac{\partial \epsilon}{\partial x} + w\frac{\partial \epsilon}{\partial z} = c_1\frac{\epsilon}{b}k[(\frac{\partial u}{\partial z})^2 + (\frac{\partial v}{\partial z})^2] \quad (8)$$
$$- \frac{\epsilon}{b}\alpha_\theta\beta k\frac{\partial \theta}{\partial z} + \alpha_\epsilon\frac{\partial}{\partial z}k\frac{\partial \epsilon}{\partial z} - c_2\frac{\epsilon^2}{b}.$$

The similar equation can be derived for the balance of b (Zilitinkevich,1970):

$$u\frac{\partial b}{\partial x} + w\frac{\partial b}{\partial z} = k[(\frac{\partial u}{\partial z})^2 + (\frac{\partial v}{\partial z})^2] - k\alpha_\theta\beta\frac{\partial \theta}{\partial z} \quad (9)$$
$$+ \alpha_b\frac{\partial}{\partial z}k\frac{\partial b}{\partial z} - c\frac{b^2}{k}$$

In the case of (l,b) closure scheme the mostly widespread formula for l determination can be obtained on the basis of Laikhtman - Zilitinkevich (Zilitinkevich,1970) gradient relation:

$$\frac{\partial l}{\partial z} = \kappa + \frac{l}{2b}\frac{\partial b}{\partial z}, \quad (10)$$

where κ is the von Karman constant. Some improvements of the Eq.(10) were offered in scientific literature, for example those of (Dubov et al,1978):

$$\frac{\partial l}{\partial z} = \frac{\kappa}{1 + a_1 z} + \frac{l}{2b}\frac{\partial b}{\partial z}, \quad (11)$$

where $a_1 = a_1(Ro)$, Ro - Rossby number.

We use the following values for the parameters in the equations for turbulent characteristics: κ =0.4, c_1 =1.44, c_2 =1.92, α_ϵ =0.15 - it can be seen that Launder relation between these parameters is adopted (Launder et al,1975)

$$\frac{c_w c(c_2 - c_1)}{\kappa^2} = \alpha_\epsilon, \quad (12)$$

where $c_w = u_*^2/\sigma_w^2 \approx 1.1$

The transformation of coordinate system is carried out, while solving the system of Eqs.(1)-(5) with Eqs (7)-(9) and alternative system of Eqs.(1)-(5),(6),(9),(11) This transformation let us transfer model area into rectangle and use the uniform step in the vertical direction while realizing the numerical algorithm Boundary conditions are set in the form, traditional to PBL model studies. The profiles of meteorological values in undisturbed flow are evaluated from the model systems in the approximation of horizontally homogeneous flow.

The example of calculations with (ϵ,b) scheme referring to the flow over a slope of 0.01 steepness facing up the flow, at boundary layer depth H equal to 1200m and G=11.8 m/sec, is presented in the Fig.1. The wind components profiles over slope are restored at the distance of 12000m from the foot of the slope.

The results of performed numerical experiments with the both model systems brought us to the following conclusions:

1. The choice of closure scheme essentially tells on the over slope flow patterns.

2. The behavior of the flow in the upper part of the PBL over slope highly depends on the type of the upper boundary conditions for b and ϵ.

3. Divergences in turbulence characteristics profiles, received on the basis of various parameterization schemes can be commensurable with variations caused by the influence of the slope. The velocity profiles are less sensible to the closure scheme choice.

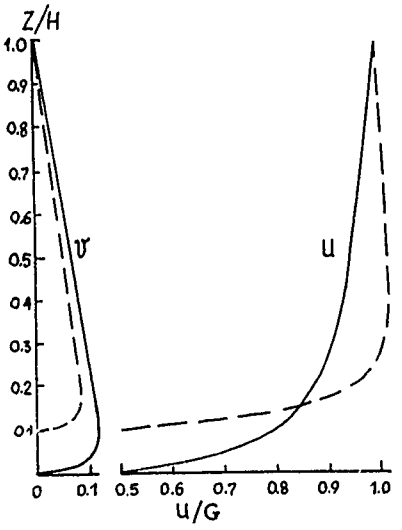

Fig.1 Modification of horizontal velocity components profiles in case the potential temperature of the slope is by 10K higher than the flat surface temperature. The continuous curves present the profiles in the upward undisturbed flow, profiles over slope are marked with dashed lines

REFERENCES

BELJAARS A.C.M., WALMSLEY J.L. & TAYLOR P.A. 1987 A mixed spectral finite-difference model for neutrally stratified boundary layer flow over roughness change and topography. Boundary-Layer Meteorol. 38, 273-283.

CLAUSSEN M. 1988 Models of eddy viscosity for numerical simulation of horizontally inhomogeneous, neutral surface-layer flow. Boundary-Layer Meteorol 42, 545-554.

DORODNNITSYN A.A. 1950 The impact of the earth's surface relief on the air flows. Trudy TIP, 21(48), (in Russ.).

DUBOV A.S., BYKOVA L P. & MARUNICH S.V. 1978 Turbulence in vegetation. Leningrad, Gidrometeoizdat, 184p. (in Russ.)

LAUNDER B.E., REECE C.J. & RODI W. 1975 Progress in the development of a Reynolds-stress turbulence closure J. Fluid Mech. 68, part 3, 537-566.

MONIN A.S. 1949 The slopes wind model Trudy TIP, 8(35) (in Russ.)

ZILITINKEVICH S.S. 1970 The dynamics of the atmospheric boundary layer. Leningrad, Gidrometeoizdat, 292p. (in Russ.)

EIGHTH SYMPOSIUM ON
TURBULENT SHEAR FLOWS
Technical University of Munich
September 9-11, 1991

COHERENT STRUCTURES IN UNSTEADY WALL FLOWS VISUALIZATION RESULTS

M.C. Feng, S. Tardu, G. Binder

Institut de Mécanique de Grenoble
B.P.53 X 38041 Grenoble Cédex-FRANCE

INTRODUCTION

The aim of this work is to investigate the response of near wall coherent structures to imposed oscillations of the flow rate (or of the pressure gradient) in order to gain insight into the mechanisme of turbulent momentum transfer and production in unsteady turbulent wall flows. From the response of structures to forced perturbations one may also expect to learn something about their dynamics in general. The difficulty of the detection of the structures with probes which is a problem in itself already in steady flow(1-2) is compounded in unsteady flow(5-8). Since visualizations provide the least objectionable means of detection (1) it seemed a priori promising to resort to this technique in unsteady flow despite the labor required. Furthermore, an extensive set of data with various probe detections in forced flow has already been gathered in our laboratory and has led to some interesting conclusions. The present work also attemps to bring additional support to these conclusions by means of independent observations.

EXPERIMENTAL SET-UP FLOW CONDITIONS

- Unsteady water channel (5).

Centerline mean velocity: U_c=18 cm/s corresponding to Re_h=9000, u_τ=0,80cm/s.

Oscillating flow: amplitude $a_{\tilde{u}c}$=13%; 20%; frequency f^+x10^4 = 5; 10.6; 24; 31.7; 73.1

- Visualization technique(dimensions in viscous units)

dye slot in wall: 1.5x300; fluorescine, argon laser sheet thickness: z^+=27; CCD-Video camera, 25 frames/s, f_a^+=0.43. The phase reference is provided by a flash of light (duration 0.1s) triggered by the pulsator and simultaneously recored on the video.

DETECTION OF EJECTIONS

The ejection detection is based on the maximum lift-up h_1, h_2 and the corresponding times, which are manually recorded, at two stations: X_1^+=840 and X_2^+=940 (distance from the dye injection slot) where nearly all ejections are marked by the dye. The number of events resulting from a record of length T^+≈20000 was phase averaged in 10 bins covering the cycle with the help of a PC. The detection of ejections is done in two steps: *1)* an event is counted when h_1^+>15 **and** $\Delta h=h_2^+ - h_1^+$ >5; *2)* <Δh> is determined and only events with $\Delta h \geq 0.9<\Delta h>$ are retained. The factor 0.9 has been chosen so that f_e^+ in the quasi-steady case ($f^+=5 \times 10^{-4}$) is the same as in steady flow, i.e. f_e^+ =0.0125. The purpose of this second step is to take some account of the modulation of the turbulent intensity.

RESULTS

1. Time-mean ejection frequency

Fig1. shows that f_e^+ is independent of forcing frequency and close to the steady flow value 0.012 (7).

2. Modulation of the ejection frequency

AMPLITUDE

The fact that $a_{\tilde{f}e}/a_{\tilde{\tau}}$ is about one when $f^+ \rightarrow 0$ and decreases by at least a factor 2 when f^+ reaches the value 0,003 and then stays roughly constant(Figure 2.) shows that the turbulent structures respond less to high frequency forcing as was previously observed with the turbulent intensity(8). The common trend of $a_{\tilde{f}e}/a_{\tilde{\tau}}$ resulting from the two different centerline amplitudes proves that the scaling with $a_{\tilde{\tau}}$ is approciate.

PHASE-SHIFT

Despite the larger scatter, one may distinguish a common trend: first a decrease from zero (expected value in the quasi-steady limit) to about -100° and then a jump to positive values. The first part implies a roughly constant time delay (Δt^+=140) between the ejections and the wall shear stress which should be the finite time required by the ejections to react to the additional stretching imposed by the oscillating shear $\partial\tilde{u}/\partial y$, i.e. $\tilde{\tau}$.

3.Modulation of the lift-up (Figure 4-5)

The relative amplitude of Δh^+ normalized with $a_{\tilde{u}\tilde{\tau}}$ is roughly of order of one and compares fairly well with the modulation of the turbulent wall shear stress fluctuations.

The phase shift of Δh^+ follows the turbulence response quite well. This is an a posteriori justification for the second step in the detection sheme.

4. Modulation of the bursting frequency

Because of the small phase averaged populations (≈20 ejections in each bin on the average), the methods of grouping proposed in (7) do not work with the visualization data. The following iterative method is developed: *step 1*: group ejections satisfying: $\Delta t<0.2\bar{t}_e$ where $\bar{t}_e$ is the mean interarrival time. From this grouping, determine $<t_e>_1$ the interarrival time of ejections belonging to bursts with multiple ejections(BME); *step 2:* recalculate grouping with critera: $\Delta t< 0.7 <t_e>_1$; *step 3:* from the previous grouping determine Δt_{ep} time between last ejection and previous one in BMEs and Δt_{en} time between last ejection of burst and next ejection. Recalculate grouping on critera for last ejection in a burst if: $\Delta t > 0.5(<\Delta t_{ep}>+<\Delta t_{en}>)$. Iterate step 3 till convergence (10 to 20 iterations).

It is seen on Figure 6-7 that the amplitude and phase shift of the BME's vary little with the forcing frequency while for the bursts with single ejection(BSE) the amplitude drops by a factor 3 to 5 and the phase lag with respect to $\tilde{\tau}$ increases to about 250°

when the forcing frequency increases from 0 to 0.002.

The two types of burst do clearly not react in the same way to the forcing in this frequency range. It is also seen that the amplitude and the phase shift of the two families take on similar values when $f^+>0.006$.

CONCLUSION

The visualization data presented in this paper confirm the previous results obtained from hot film signals on the response of ejections and bursts to forced oscillations. When the forcing frequency changes from quasi-steadiness to $\bar{f}_e/4$, the amplitude of the ejection frequency drops by a factor four to five from the quasi-steady value and the amplitude of the BSE's by nearly as much. The response of the BME's on the contrary varies relatively little with the forcing frequency. The difference in the response of the BME's and BSE's suggests that they result from different mechanisms.

ACKNOWLEDGMENTS

Financial support from the European Research Office of the U.S. Army Research Developement and Standardisation Group under contract DAJA 45-87-c-0015 is gratefully acknowledged.

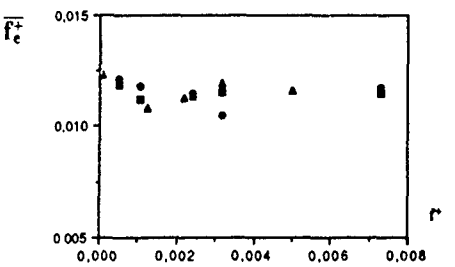

Figure 1. Time-mean ejection frequency vs forcing frequency. ■ $a_{\widetilde{uc}}$=0 20; ● $a_{\widetilde{uc}}$=0.13; ▲ VITA $a_{\widetilde{uc}}$=0 20

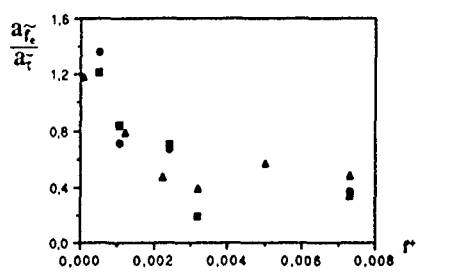

Figure 2. Relative amplitude of ejection frequency modulation vs forcing frequency For legend see Figure 1.

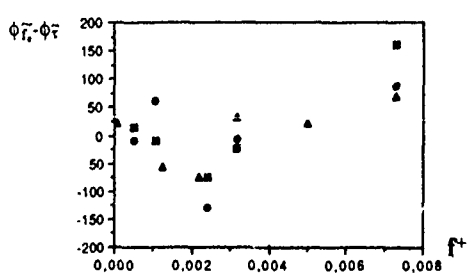

Figure 3. Phase shift of ejection frequency modulation vs forcing frequency.For legend see Figure 1.

REFERENCES

1. Bogard, D. 1982 *PhD.*, Purdue Univ. U.S.A.
2. Bogard, D. & Tiederman, W.G. 1986 *J.Fluid Mech.* 179, 1
3. Cousteix. J, & Houdeville. R, 1985 *5th Symp. Turbulent Shear Flow*, Cornell Univ., USA
4. Kobashi. Y, & Hayakawa. M, 1981 In *Unsteady Turbulent Shear Flow*, Ed. R. Michel, Springer
5. Tardu. S, Binder. G & Blackwelder.R, 1987 *6th Symp.Turbulent Shear Flow*, Toulouse
6. Tardu. S, & Binder. G 1989 *7th Symp. Turbulent Shear Flow*, Stanford U.S.A
7. Tardu. S, & Binder. G, 1990 Submitted to the *J.Fluid Mech.*
8. Tardu.S, 1988 *Doctoral Thesis*

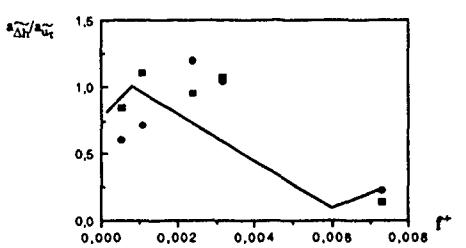

Figure 4. Relative amplitude of ejection lift-up modulation vs forcing frequency. ■ $a_{\widetilde{uc}}$=0.20; ● $a_{\widetilde{uc}}$=0.13; - $a_{\widetilde{\tau}\widetilde{\tau}'}/a_{\widetilde{\tau}\widetilde{\tau}'(qs)}$

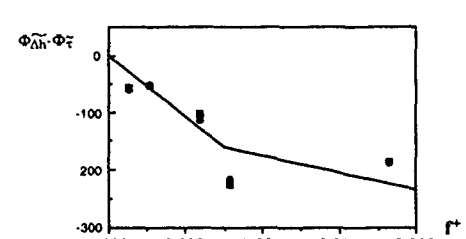

Figure 5. Phase shift of ejection lift-up modulation vs forcing frequency. For legend see Figure

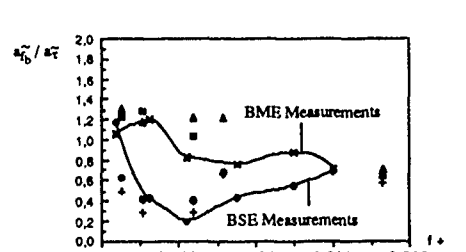

Figure 6. Relative amplitude of burst frequency modulation vs forcing frequency. ▲ BME $a_{\widetilde{uc}}$=0.13; ■ BME $a_{\widetilde{uc}}$=0.20; + BSE $a_{\widetilde{uc}}$=0.13; ● BSE $a_{\widetilde{uc}}$=0.20, x BME Tardu& Binder ; ◆ BSE Tardu&Binder

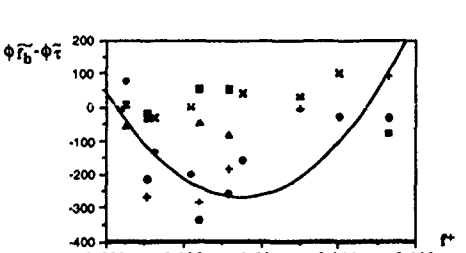

Figure 7. Phase shift of burst frequency modulation vs forcing frequency.For legend see Figure 6.

EIGHTH SYMPOSIUM ON
TURBULENT SHEAR FLOWS
Technical University of Munich
September 9-11, 1991

SIMULATION OF THE CONVECTIVE BOUNDARY LAYER IN COMPARISON TO AIRCRAFT-MEASUREMENTS DURING LOTREX-EXPERIMENT

J. Graf, A.M. Jochum, U. Schumann

DLR, Institut für Physik der Atmosphäre
W-8031 Oberpfaffenhofen, Germany

ABSTRACT

The convective atmospheric boundary layer during a specific case of the field experiment LOTREX is investigated by Large Eddy Simulation (LES). The numerical simulations are initialized using measured profiles of wind and temperature. The lower thermic boundary condition is obtained by extrapolating measured heatflux profiles down to the surface. The calculated vertical profiles of turbulent quantities compare generally well with the corresponding measurements.

INTRODUCTION

During the last years several LES-models have been developed and applied to various problems, but the simulated turbulent quantities are not very often compared with measurements In Deardorff (1974) the simulation results are compared with data from the Wangara-experiment. Moeng and Wyngaard (1989) found good agreement of the calculated velocity variance with corresponding field- and laboratory measurements in the upper boundary layer, whereas in the lower boundary layer differences have been obtained. The model used in this paper is validated for pure convective situations (Schmidt, 1988). The influence of the results on the parameterization scheme is discussed in Schmidt and Schumann (1989). In this paper we simulate the CBL for a specific day. Data for model initialization and intercomparison have been collected during LOTREX. The series of field experiments LOTREX was conducted in North Germany to study land surface processes (Roth et al., 1988). The effect of inhomogeneous heatflux, sheared mean-flow and vertical resolution on the turbulence statistic is investigated in Graf and Schumann (1991).

METHOD AND PARAMETERS

For the present study we use the LES-model as described in Schmidt and Schumann (1989). The model integrates the equations for mass and momentum balances and the first law of thermodynamics in three space dimensions and in time. Here, we are using 100 x 100 x 40 grid cells. The subgrid-scale fluxes are parameterized using a second order closure model. The computational domain extends horizontally over an area of 10 x 10 km^2 and vertically to a height of 2500 m (3 z_i) The horizontal gridspace is 100 m in all simulations. Vertically, the gridspace is either 100 m or 50 m. The results after a total integration-time up to 5 t_*, when the turbulence is quasi stationary are compared with available measurements (Jochum et al., 1990). The experimental area is 15 km by 15 km, almost flat with varying landuse: essentially agricultural with field sizes on the kilometer scale. For the model initialization and comparison data from the quasistationary period around noon on July 13, 1988 are chosen. This day was characterized by light winds and no clouds. The convective boundary layer has a height z_i of 800 m. In addition to 5 surface stations 5 research aircraft were taking measurements . Three powered gliders and a jet all equipped for turbulence measurements were simultaneously flying along the same horizontal flight legs with fixed vertical spacing. Vertical profiles of mean meteorological parameters and of selected concentrations were obtained from a twin-engined aircraft. The data from the different aircraft are combined to yield vertical profiles of mean parameters, fluxes and spectral characteristics. The measurement uncertainty is estimated to be around 30% for fluxes, and 20% for variances. Scales included in the turbulent fluxes and variances range from 17m to 3.5km.

RESULTS

Generally, good agreement is found with respect to vertical profiles of the turbulent heatflux, of temperature and vertical velocity fluctuations.

The simulated profiles of the turbulent quantities correspond with the measured profiles up to the error of the experimental data. In Figure 1 the simulated and measured profiles of the vertical velocity variance are shown. Model and field data agree closely in the lower and upper thirds of the CBL. Around $4z_i$ the model seems to underpredict the data In order to assess the sensitivity of the model two different surface heatfluxes ($80Wm^{-1}$, $100Wm^{-1}$) have been used. Better agreement has been obtained using the larger value, which is closer to observed values.

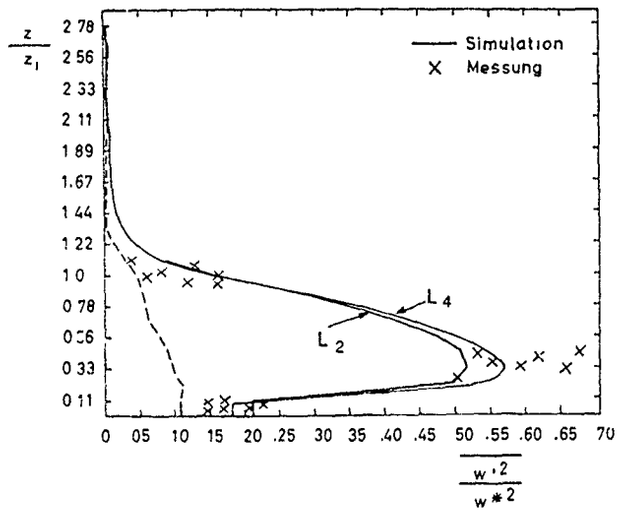

Fig 1. Vertical profiles of the nondimensionalized vertical velocity variance in comparison to measurements for two different surface heatfluxes.

From the power spectra of the vertical velocity fluctuations one can see, that the smaller eddies are predominant in the lower boundary layer and that there is a second minimum at the inversion height (Figure 2) Obviously surface and inversion have a similar effect on the vertical motions. This reproduces well the same features seen in the field data.

With respect to inhomogeneities, the measurements reveal a horizontal variation of the heatflux by 20 %. Corresponding to a unidirectional trend suggested by some of the data, we model the inhomogeneity by assuming a sinusoidally varying heatflux, which varies in only one direction at a wavelength of 10 km Our simulations show a weak decrease of vertical variance over inhomogenous surfaces. The sensitivity studies show very little effect of the mean wind with a maximum of 5 m/s. This was to be expected, because the resultant friction velocity is still very small in comparison to the convective velocity.

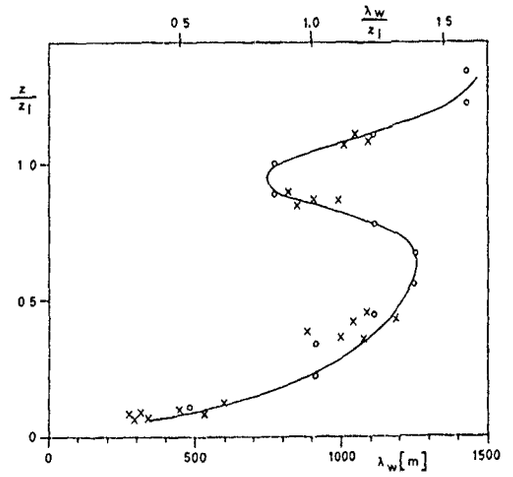

Fig 2.: Maximum wavelength λ_w of the spectra of the vertical velocity fluctuations as a function of z/z_i. The dots denote the calculations (constant heatflux of $80Wm^{-1}$), the crosses the measurements.

CONCLUSIONS

A case study of a comparison between field and LES model data for an undisturbed CBL over moderately inhomogeneous terrain was performed. Generally, the model reproduces well the observed turbulent fluxes and variances and the spectral structure.

REFERENCES

DEARDORFF, J.W., 1074: Three-dimensional numerical study of turbulence in an entraining mixed layer. Bound.Lay.Meteorl.7, 199-226.

GRAF, J., SCHUMANN U., 1991: Simulation der konvektiven Grenzschicht im Vergleich mit Flugzeugmessungen beim LOTREX-Experiment. in press: Met. Rundschau.

JOCHUM, A., ENTSTRASSER, N., FIMPEL, H., MÖRL, P., RÖSLER, F., WILLEKE, H., 1990: Evaporation and energy fluxes in the atmospheric boundary layer during LOTREX. Proc. Symposium on FIFE, Febr. 7-9, 1990 Anaheim, Calif., Amer. Meteorol. Soc., Boston, 177-180.

MOENG, C.H., WYNGAARD, J.C., 1989: Evaluation of turbulent transport and dissipation closures in second-order modeling. J.Atmos.Sci. 46, 2311-2330.

ROTH, R., et al., 1988: LOTREX 10 E / HIBE 88. Experimentplan (in German). Report, Meteor. Inst. Univ. Hannover.

SCHMIDT, H., 1988: Grobstruktur-Simulation konvektiver Grenzschichten. Forschungsbericht DFVLR-FB 88-30, obtainable from DLR.

SCHMIDT, H., SCHUMANN, U., 1989: Coherent structure of the convective boundary layer derived from large-eddy simulations. J. Fluid Mech., 200, 511-562.

TURBULENT SHEAR FLOWS
Technical University of Munich
September 9-11, 1991

LARGE EDDY SIMULATION OF TURBULENT FLOWS AROUND FLAT PLATE ROWS

I. HARADA
Energy Research Laboratory, Hitachi, Ltd.
1168 Moriyamacho, Hitachi,Ibaraki 316, JAPAN

ABSTRACT

A LES(Large Eddy Simulation) program based on a finite difference method is developed to compute the turbulent flow around or in a complex geometry. A turbulent channel flow is computed to verify our LES program A mean velocity profile in the streamwise direction is excellent agreement with the logarithmic velocity profile. Flows around flat plate rows are computed to understand the mechanism of aerodynamic sound generation. Results of both mean velocity and turbulent intensity agree with theory and experiment.

INTRODUCTION

Sound is generated by movement of vorticity predicted by Powell(1964) In this situation, the two-equation turbulence model is not adequate to simulate the flow due to its time averaged model. LES or DS(Direct Simulation) is applicable as higher turbulence models, because these models do not include time averaging in models. DS takes much more CPU time than LES due to a requirement of a fine resolution at high Reynolds number flows, so that LES is chosen as an adequate turbulent model. On the other hands, the jet noise generated by high speed compressible flow has been investigated to clarify the mechanism of aerodynamic sound generation, but sound generation by low speed incompressible flows in such as air conditioners is different from that in compressible flows. Flat plate rows are chosen to simplify the geometry of wings

LES is, therefore, made on a turbulent flow over flat plate rows as a first step to understand the mechanism of sound generation that is closely related to organized structure of turbulence

BASIC EQUATION

Let us take characteristic velocity U , length L , time L/U , nondimensional SGS(subgrid scale) equations given by Deardorff (1970) are

$$\frac{\partial u_i}{\partial x_i} = 0 \tag{1}$$

$$\frac{\partial u_i}{\partial t} + \frac{\partial}{\partial x_j}(u_i u_j) = -\frac{\partial p}{\partial x_j} + \frac{\partial}{\partial x_j}\left[\frac{1}{Re}\frac{\partial u_i}{\partial x_j} + 2\nu_T S_{ij}\right], \tag{2}$$

$$S_{ij} = \frac{1}{2}\left(\frac{\partial u_i}{\partial x_j} + \frac{\partial u_j}{\partial x_i}\right), \tag{3}$$

$$\nu_T = (C\Delta)^2 \sqrt{S_{ij} S_{ij}}, \tag{4}$$

where, u_i is the velocity component of the coordinate x i, p the pressure, t the time, $\Delta (= \sqrt{\Delta_1 \Delta_2 \Delta_3})$ the averaged SGS grid interval, C(=0.1) the universal constant, Re(=UL/ν) the Reynolds number defined by characteristic length(channel width or plate pitch)L , and ν the dynamic viscosity. The turbulent viscosity is given by the Smagorinsky model(1967). Van Driest(1956) wall damping function (A=25) is used as the boundary condition of the wall.

NUMERICAL METHOD

A finite difference method is chosen for solving basic equations, because other method such as FFT used by Horiuti(1987) and Moin & Kim(1982) is not able to applicable to the complex geometry due to its numerical method. Adams-Bashforth and central difference schemes are used for time and space derivatives using the staggered grid arrangement. An algorithm of the present solution procedure is based on the SMAC (Simplified Marker and Cell) method. Pressure is obtained from the Poisson equation solved by ICCG(Incomplete Conjugate Cholesky).

CHANNEL FLOW

A turbulent channel flow is computed to verify our LES program FLOWLENS (FLOW by Large Eddy Numerical Simulation). The computational condition is the same as that in boundary layer splitting model by Harada (1988). A computational domain is Lx(=3.2L), Ly(=0.8L) and Lz(=L) in x,y,z directions, where the channel width is taken as the characteristic length L=62mm The horizontal plane is divided into uniform mesh sizes of 64 grid points in each x ,y direction The mesh sizes increase from the minimum mesh size near the lower or upper wall to keep a ratio of mesh sizes to be constant without using hyperbolic function by Horiuti(1987) and Moin & Kim(1982).

A set of values is chosen such as characteristic velocity U=6.67m/s, friction velocity u_τ=0.309m/s, Re=27800, C=0 10, and a time mesh Δt=0.008. Non-slip and cyclic conditions are imposed on both plates z=0, L and planes x=0, Lx, y=0, Ly as boundary conditions. An initial velocity is given by superimposing the uniform streamwise velocity U to fluctuations produced by random number smaller than 0 05U. The long term time integration is made until t=496 to reach a statistical equilibrium state. The time integration of 62000 cycles required 762 minutes CPU time with 102MB on HITAC S820/60 super computer (1 5 GFLOPS at the maximum speed).

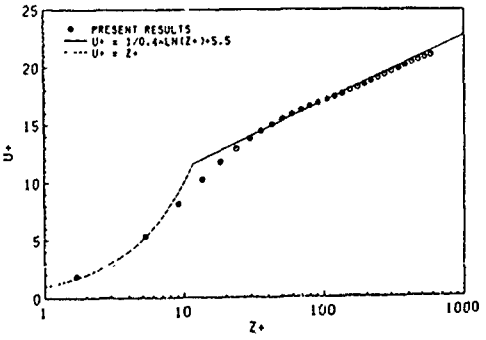

Fig.1 A streamwise mean velocity.

Figure 1 shows the streamwise mean velocity averaged in x-y plane. The profile agrees well with both viscos sublayer and logarithmic layer. The Karman constant κ=0.40 and a constant B=5 5 are good agreement with an experiment B=5.0-5.5. The same result κ=0.40

and B=5.5 is obtained by Moin & Kim(1982) using the residual stress model that is limited to application than the damping model.

FLOWS OVER FLAT PLATE ROWS

Flows over flat plate rows are computed using a similar condition to that of a channel flow. Figure 2 shows a computational domain of flat plate rows The flat plate is placed at the center of computational

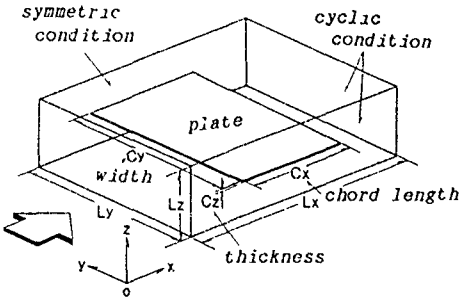

Fig 2 A computational domain of flat plate rows

domain Lx x Ly x Lz. The plate is defined by the length Cx, the thickness Cz and the infinite width in y direction The periodic boundary condition is imposed on x=0,Lx in the streamwise direction and on y=0,Ly in the spanwise direction The symmetry condition is given on upper and lower planes z=0,Lz. Table 1 shows parameters used for present computations The thickness ratio Cz/Cx is varied

Table 1 Parameters used for present computations.

	Lx/L (-)	Ly/l (-)	Lz(=L) (mm)	Cx/L (-)	Cy/L (-)	Cz (mm)	Cz/Cx (%)	X xY xZ direction
CASE-1	3.15	2.36	63	1.58	2.36	1.0	1.6	64x64x68
CASE 2	3.20	2.40	62	1.61	2.40	0	0	64x64x64
CASE 3	4.82	2.36	63	1.58	2.36	1.0	1.6	98x48x64
CASE-4	3.10	2.32	64	1.56	2.32	2.0	3.2	64x48x66

from zero to 3.2% The results are essentially similar to each other so that the CASE-1 is chosen as the typical case The computational domain is divided by 64x64x68 grid points in x,y,z directions. CPU time required 789 minutes for a cycle number 46000 at t=276 to reach statistically equilibrium state on HITAC S820/60 super computer with 107MB using a time mesh $\Delta t=0.006$

From a view of aerodynamic sound generation, velocity fluctuations in the wake play an important role,i.e ,Fukano et al [8] obtained by the experiment that the turbulent intensity in the wake well corresponds to the sound intensity.

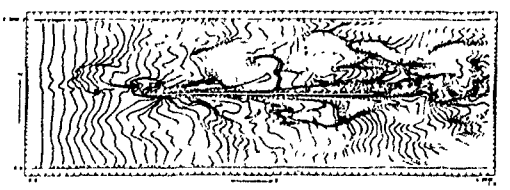

(a) y/Ly=0. 20

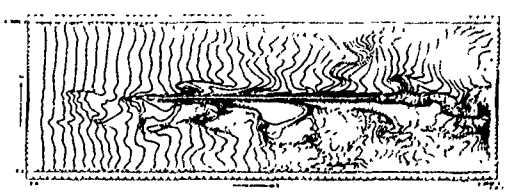

(b) y/Ly=0. 47

Fig.3 Streaks visualized by marker particles in the vertical planes.

Figures 3(a)and (b) show streaks visualized by marker particles generated at upstream in the vertical planes y/Ly=0.20 and 0.47. This corresponds to hydrogen bubbles visualization in experiment Fluctuations are observed behind the rear edge in the wake. The structure is similar to Karman vortex street growing in between flat plates. Figure 4 shows streaks in horizontal plane z/Lz=0.51 near the upper surface of the plate. The streaks show the typical structure of

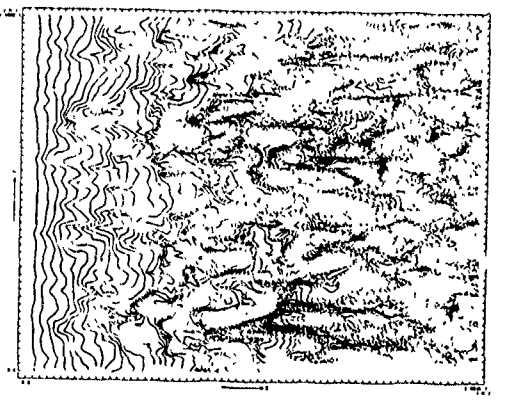

Fig 4 Streaks in horizontal plane z+=28 from the upper surface

peak and valley in turbulent boundary layer Figures 5(a) and (b) show streamwise velocity profiles averaged in horizontal plane of the wake The mean velocity of present results agrees well with theory. The structure is kept until the rear edge where shear force reaches maximum in horizontal plane. This fact explains that the turbulent intensity becomes large near the rear edge in experiment[8]. The maximum turbulent intensity averaged in the wake region is about 4.0 that agrees roughly with 5 2 of experiment

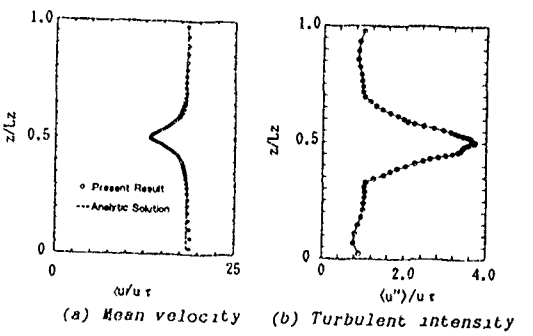

Fig.5 Streamwise mean velocity profiles of the wake

As is shown by present computations, results of LES provide us a clue to the mechanism of sound generation produced by turbulence.

REFERENCES

Deardorff,J W 1970 J.Fluid Mech.41,427-453

Fukano,T.et.al 1985 JSME(B) in Japanese,51,2505-2514.

Harada,I. 1988 Proc.3rd Int.Sym.on Refined Flow Modelling and Turbulence Measurements,69-73.

Horiuti,K.1987 J.Comput.Phys.71,371-390

Moin,P and Kim,J. 1982 J.Fluid Mech.118,341-377

Smagorinsky,S. 1967 Mon Weather Rev.91,99-164

Powell,A 1964 J.Acoust.Soc.Am 33,177-195

Van Driest,E.R 1956 J Aero Soc.23,1000-1007

NUMERICAL SIMULATION OF DENSITY AND VISCOSITY EFFECTS WITHOUT GRAVITY IN FREE TURBULENT JETS

G. Harran and P. Chassaing

Institut de mécanique des fluide : de Toulouse
Laboratoire de Banlève INPT-ENSEEIHT
Avenue du Professeur Camille Soula, 31400 Toulouse (France)

ABSTRACT

A numerical experimentation is used to find out some density and viscosity effects in round turbulent heterogeneous isothermal and non reactive gas jets. The values of the jet/outer-flow density ratio vary from 0.4 to 4.88.

NOMENCLATURE

U_i Instantaneous velocity (i = 1,2,3)
u'_i Instantaneous fluctuating velocity (i = 1,2,3)
ρ' Instantaneous density
C Instantaneous mass fraction
γ' Mass fraction fluctuation
x Longitudinal coordinate
R Radius of the jet
Subscripts:
ax Values along the axis
0 Values at the exit
ext Values outer of the jet

INTRODUCTION

To our knowledge, the effects of global density differences remain poorly characterized. References collected about different nature of gases, give conclusions cross-checking experimental and bibliographical results. Due to the difficulties of controlling the outlet conditions when dealing with experimental studies, a numerical approach is chosen, which allows us to study the influence of one parameter only.

CALCULATION PRESENTATION

Because of the non linearity of the convection terms, new correlations are introduced when averaging the instantaneous equations of a variable density turbulent motion. Thereby, the quantity $\overline{\rho U_i U_j}$ becomes:

$$\overline{M_{ij}} = \overline{\rho U_i U_j} = \overline{\rho}\,\overline{U_i}\,\overline{U_j} + \overline{\rho' u'_i u'_j} + \overline{\rho' u'_i}\,\overline{U_j} + \overline{\rho' u'_j}\,\overline{U_i} + \overline{\rho}\,\overline{u'_i u'_j}$$

Except Lumley/1/, most of the authors use the mass-weighted averages as proposed by Favre in 1958. In 1985, Chassaing/2/ suggested an alternative to the formulation of turbulent motion equation for a variable density fluid, using the conventional averages. This leads to a similar formulation as in the incompressible case. The new proposition regroups $\overline{M_{ij}}$ as:

$$\overline{M_{ij}} = \overline{A_{ij}} + \overline{B_{ij}} + \overline{C_{ij}}$$

$\overline{A_{ij}} = \overline{\rho}\,\overline{U_i}\,\overline{U_j}$ can be considered as characterizing the mean contribution, considering that only mean values of the function appear.

$\overline{B_{ij}} = \overline{\rho u'_i u'_j}$ is a contribution which implies the fluctuating motion through a correlation related with a flux term by classical advective non linearity.

$\overline{C_{ij}} = \overline{\rho u'_i}\,\overline{U_j} + \overline{\rho u'_j}\,\overline{U_i}$ is a contribution that appears as the main component that singularizes the variable density fluid motion. It is henceforth considered as an "external flux" to recall that the equations have no longer a conservative form. Due to the thermodynamical state equation, the $\overline{\rho u'_i}$ and $\overline{\rho \gamma'}$ correlation are exactly linked with the transportable fluxes, when considering the isothermal turbulent mixing.

Second order models were implemented by Chassaing-Hérard-Chibat/3/, considering the Lumley's development technique. The treatment is restricted to the situation $\overline{U}_{i,1} = 0$ which results from the high turbulent Reynolds number assumption. The transport equations are solved numerically using the Patankar and Spalding's procedure. The additional terms, resulting from the choice of the Reynolds decomposition, have been included by new treatments of the "source" terms.

COMPARISON WITH EXPERIMENTAL DATA

The code was first tested by comparison with the experimental results of Chassaing/4/ for a 80% of CO_2/air jet discharging into a quiescent atmosphere. Gravity acts in the same direction as the mean momentum and the exit conditions correspond to a fully developed pipe flow.

$Re_0 = 55100$ $\overline{C}_0 = 80\%$ (concentration of CO_2) $Fr_0 = 35$
$R_0 = 0.018$ m $\rho_0/\rho_{ext} = 1,39$ $\nu_0 = 0.85\ 10^{-5}\ m^2/s$

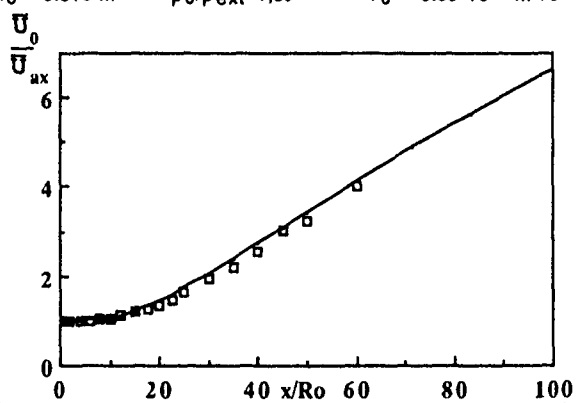

Fig 1 : Velocity along the axis(____ Calculation, □ Experience)

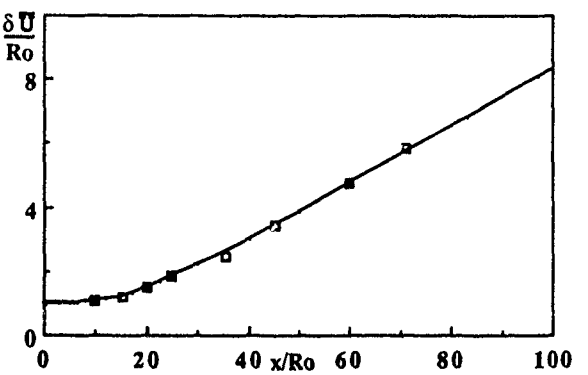

Fig 2 : Half width velocity radius.

According to the imprecisions of the parabolic calculation, the agreement between the calculation and the measurement is fairly correct. Usir. this model and this numerical procedure, we shall now investigate some effects of the physical properties of the jet on the turbulent mixing.

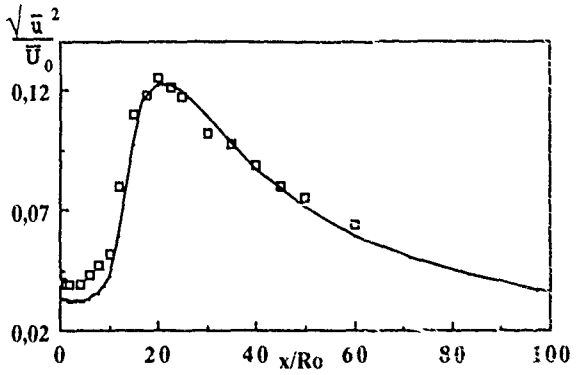

Fig 3 : longitudinal turbulent intensity along the axis

GLOBAL DENSITY VARIATIONS EFFECTS ON THE MIXING

A strict analysis shows that, in a variable density flow, self-similarity is never reached. But, far from the exit, when transversal density gradients are small and if gravity effects are negligible, the self-similarity condition is approached. Introducing an equivalent diameter, Thring and Newby/5/ deduced the following relations for the velocity and the concentration respectively:

$$\frac{\overline{U}}{U_{ax}} = A\,\frac{(x-x_u)}{R_{eq}} \quad \text{and} \quad \frac{\overline{C}}{C_{ax}} = B\,\frac{(x-x_c)}{R_{eq}}$$

with $R_{eq} = R_0\sqrt{\frac{\rho_0}{\rho_{ext}}}$ x_u et x_c : virtual origins

Chen and Rodi/6/ give relations for the halfwidth of the velocity and the concentration profiles respectively:

$$\delta U = A'\,(x-x_u^*) \qquad \delta C = B'\,(x-x_c^*)$$

An other important quantity is the entrainment rate Ricou and Spalding/7/ show that.

$$\frac{Q}{Q_o} = \frac{K}{\sqrt{\pi}}\,\frac{x}{R_{eq}} \quad \text{with } K = 0.28 \text{ for gas jets in air}$$

From the experimental data of Chassaing/4/, we implement numerical experiences where all parameters are fixed, except the density at the exit. We choose to neglect gravity in computations to ensure the similarity laws validity.

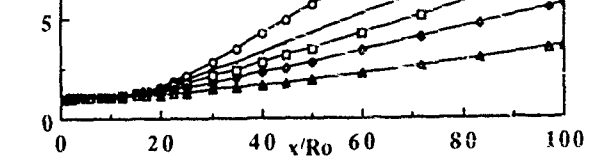

Fig 4 : Density effects on the mean velocity along the axis

The table 1 regroups the constants calculated with our results:

Table 1 : Density effects on the similitude constants

$R_\rho = \frac{\rho_0}{\rho_{ext}}$	A	B	A'	B'	K
0,40	0.0976	0.125	0.090	0 152	0 325
1	0.096		0.086		0.314
1,54	0.0944	0.123	0.085	0.140	0.297
2,44	0.0912	0.116	0.083	0.131	0.292
4,88	0.0780	0.092	0.069	0.102	0.250
Experiences	≡ 0.075	≡ 0.11	≡ 0.080	≡ 0 12	0.282

First, we can see that results are in good agreement with the similarity laws since, from 40 R_0, the evolutions are linear for the concerned quantities(Fig.4). But, as experimentally observed by Pitts/8/ for the constant B(Fig.5), the values decrease as R_ρ increases. This tendency cannot be observed with the literature values because of the flows conditions discrepancies(Fig.5).

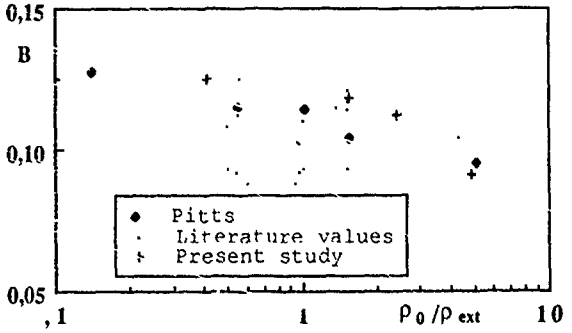

Fig 5 : Density effects on the constant B

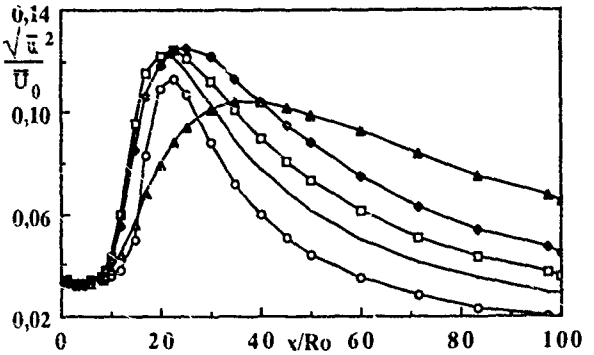

Fig 6 . Density effects on longitudinal turbulent intensity

Fig 6 shows that for high density jets, the turbulent intensity maximum is blunted and retarded .

Moreover, we have investigated the viscosity effects which are often neglected. We observed that increasing the molecular viscosity, tends to increase the similarity constants values and we noted also that the turbulent intensities grow up with the viscosity.

CONCLUSION

Considering a model which results were previously compared with experience, some specific density and viscosity effects were numerically found out without buoyancy

For the density, we have shown that similitude constants are in good agreement with averaged literature values but decrease for high density jets. And more generally, we observed that the mixing is much better when the density ratio R_ρ is less than one.

REFERENCES

1/ SHIH T.H , LUMLEY J.L, JANICKA J. 1987 Second-order modelling of a variable density mixing layer J. Fluid Mech. 180, 93-116.

2/ CHASSAING P. 1985 Une alternative à la formulation des équations du mouvement turbulent d'un fluide à masse volumique variable.J. de Méc. Th. et Ap. 4, 375-389.

3/ CHASSAING P., HERARD J.M 1987 Second order modelling of a variable density turbulent mixing, Sixth symposium of turbulent shear flows 17-8.

4/ CHASSAING P. 1979 Mélange turbulent de gaz inertes dans un jet de tube libre. Thèse INPT Docteur ès-Sciences .

5/ THRING M.W.,NEWBY M.P. 1953 Combustion length of enclosed turbulent jet flames Fourth Symp. of combustion, Pittsburg,The Standing committee of combustion 789-796 .

6/ CHEN C.J,RODI W. 1980 Vertical turbulent buoyant jets-a review of experimental data. Pergamon Press, New York

7/ RICOU F.P, SPALDING D.B 1961 Measurements of entrainment by axisymmetrical jets. J. Fluid Mech. 11, 21-32.

8/ PITTS W.M. 1986 Effect of global density and Reynolds number variations on mixing in turbulent axisymmetric jets. Rapport NBSIR, 86-3340, Dpt of commerce Washington.

EIGHTH SYMPOSIUM ON
TURBULENT SHEAR FLOWS
Technical University of Munich
September 9-11, 1991

AN ASYMPTOTIC ANALYSIS OF TWO-DIMENSIONAL CURVED TURBULENT FLOWS AT HIGH REYNOLDS NUMBERS BY USING REYNOLDS-STRESS EQUATIONS

B. Jeken

Institut für Thermo- und Fluiddynamik
Ruhr-Universität Bochum
W-4630 Bochum 1, Germany

SYMBOLS

U_1	outer flow velocity
L	chord length
ν	mol. viscosity
u_τ	friction velocity
$Re = \frac{U_{10}\, L}{\nu}$	Reynolds number

INTRODUCTION

Turbulent boundary-layers over curved surfaces have been calculated by many authors applying the so called boundary-layer 'approximation' and various turbulence models. Since the governing equations are free of curvature, and because of substantial disagreement with measurements, curvature corrections of different kinds have been implemented. However, no information is available, when and how curvature has to be taken into account for the calculation of turbulent boundary-layers.

The purpose of this paper is therefore, to show by a systematic asymptotic analysis how curvature effects have to be taken into consideration.

ASYMPTOTIC ANALYSIS OF TURBULENT FLOWS

This asymptotic analysis is an extension of the work by *Mellor(1972)*. Consideration of surface curvature and the necessary turbulence model in the analysis are the main further developments of the above mentioned basic work.

The closed system of time-averaged Navier-Stokes equations and modelled Reynolds-stress equations after *Gibson et al.(1981)* are used to describe turbulent flows over curved surfaces. For high Reynolds numbers this system leads to a singular perturbation problem. The perturbation parameter

$$\epsilon = \sqrt{c_{f0}/2}$$

tends to zero when the Reynolds number Re goes to infinity, where c_{f0} is the skin-friction coefficient at a fixed location S_0 on the wall (e.g. start of the fully turbulent regime). The singular perturbation problem is solved by the method of matched asymptotic expansions and leads to a four-layer structure(Fig. 1):

A. Inviscid outer flow region
B. Viscous superlayer
C. Inviscid defect-layer
D. Viscous sublayer.

Each layer has its own scales with respect to thickness, velocities and stresses and hence its own system of equations.

The main analytic results of the analysis are as follows, see also Table 1.

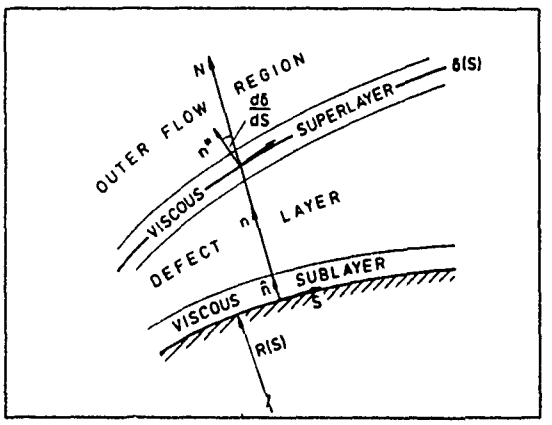

Fig. 1: Four-layer structure of curved turbulent flow

A. INVISCID OUTER FLOW REGION

(scales: L , U_{10} , ρU_{10}^2)

Assuming that the free-stream turbulence level is zero, the first order of the outer flow region describes the potential flow subject to the kinematic flow condition at the wall. Since there is no contribution of the second order, the third order again describes a potential flow but with a nonzero normal velocity $V_3(S,0)$ at the wall, corresponding to the displacement effect of the defect-layer up to second order.

B. VISCOUS SUPERLAYER

(scales : $l^* = \nu/v_{el}^*$, v_{el}^* , ρv_{el}^{*2})

Non-turbulent inviscid fluid of the outer flow region can become turbulent only by viscosity. While the outer

flow region and the defect–layer are not influenced by viscosity at high Reynolds numbers, both layers cannot be matched without the occurrence of singularities The introduction of a viscous layer is therefore necessary to overcome this mismatch. The characteristic length l^* is proportional to the Kolmogorov length scale and the velocity v_{el}^* is the entrainment–velocity, which appears to be constant across this layer. The viscous superlayer is not influenced by curvature and can be solved universally for given entrainment–velocity and Reynolds number. The singularity defines a finite thickness $\delta(S)$ of the defect–layer.

C INVISCID DEFECT–LAYER

(scales: $\delta = L \cdot O(\epsilon)$, U_{10} , ρU_{10}^2 , $\rho u_{\tau 0}^2$)

The first order solution coincides with the first order of the outer flow solution for $N \longrightarrow 0$. The values $u_1(S,n)$ and $p_1(S,n)$ are constant across the layer, whereas $v_1(S,n)$ varies linearly.

In the second order the S–momentum equation is linear and the normal velocity $v_2(S,n)$ occurs only in the continuity equation. Curvature enters at this stage via the turbulence model. An essential requirement to the model is the capability to cope with curvature effects. The dominant parts of the stress–equations are the production terms, which are, in case of a Reynolds–stress model, exact. Curvature alters the nn–component of the stress–tensor, and together with the ss–component both determine the production of the shear–stress and consequently the velocity field Although the momentum equations themselves are free of any normal–stresses the Reynolds–stress equations clearly state that normal–stresses must be taken into account as far as curvature is concerned All turbulence models unable to describe the interactions between all components of the stress–tensor (e.g all eddy–viscosity models) must therefore lead to unsatisfactory results.

D. VISCOUS SUBLAYER

(scales. $\hat{l} = \nu/u_{\tau 0}$, $u_{\tau 0}$, $\rho u_{\tau 0}^2$)

The universal sublayer solution for the streamwise velocity $\hat{u}_2(S,\hat{n})$ is linear for $\hat{n} \longrightarrow 0$ and logarithmic for $\hat{n} \longrightarrow \infty$, as has been shown by many authors The sublayer as well as the superlayer, both very thin at high Reynolds numbers, are not influenced by curvature.

SOLUTION OF THE DEFECT–LAYER EQUATIONS

The main interest is focussed on the solution of the governing set of equations in the defect–layer to second order, while the first order is completely solved without any turbulence modelling. As a result of the foregoing asymptotic analysis curvature effects only appear in the combination $K(S) \cdot U_1(S,0)$, where $U_1(S,0)$ is constant with respect to this layer. Hence curvature has to be included if $K(S) = O(1)$ and can be dropped if $K(S) = O(\epsilon)$.

Now the second order of this asymptotic expansion is comparable to classical boundary–layer theory Without taking curvature into account this theory is incomplete as far as turbulent flows are concerned. In the laminar flow case curvature is a higher–order effect and not included in classical boundary–layer theory. In contrast to the different influence of curvature, the displacement effect is a higher –order effect in both flow regimes.

A characteristic feature of the governing equations in the defect–layer is the linearity of the momentum equation The normal velocity v_2 can be calculated separately after solving the momentum– and stress–equations. The boundary conditions as $n \longrightarrow 0$ are deduced from the matching condition with the sublayer, which leads to the logarithmic law of the wall and the local equilibrium of production P_q and dissipation ϵ_u in the overlapping region.

At the outer edge ($n = \delta$) the defect velocity u_2 and all turbulent quantities go to zero or to their free–stream values respectively, leading to a local discontinuity. Therefore, following *Rotta(1983)*, the solution domain is transformed into a rectangular grid by relating n to the local thickness $\delta(S)$ of the defect–layer. The numerical scheme is based on Keller's box method.

The results show good agreement with measurements and with other Reynolds–stress model calculations

ORDER / LAYER	classical boundary layer theory: FIRST	classical boundary layer theory: SECOND	higher order effects: THIRD
A outer flow region	potential flow		displacement effect
B viscous superlayer		universal solution	normal stresses; pressure field
C defect layer		momentum equations; turbulence model; normal stresses	momentum equations; curvature; normal stresses; turbulence model; normal stresses
D viscous sublayer		universal solution	normal stresses; pressure field

Table 1: Asymptotic–Solution Scheme for Curved Turbulent Flows

REFERENCES

MELLOR,G.L. 1972 The large Reynolds number asymptotic theory of turbulent boundary–layers. Int.J. Engng Sci.10,851–873.

GIBSON,M.M.,JONES,W.P.,YOUNIS,B.A. 1981 Calculation of turbulent boundary–layers on curved surfaces. Phys.Fluids 24,386–395.

ROTTA,J.C. 1983 Einige Gesichtspunkte zu rationeller Berechnung turbulenter Grenzschichten. Z.Flugwiss. Weltraumforsch. 7,417–429.

EIGHTH SYMPOSIUM ON
TURBULENT SHEAR FLOWS
Technical University of Munich
September 9-11, 1991

DIRECT NUMERICAL SIMULATION OF THE LOW PRANDTL NUMBER SCALAR FIELD IN A TWO-DIMENSIONAL TURBULENT CHANNEL FLOW

N. Kasagi Y. Ohtsubo Y. Tomita

Department of Mechanical Engineering
The University of Tokyo

ABSTRACT

A direct numerical simulation (DNS) of the fully developed thermal field in a two-dimensional turbulent channel flow was carried out The simulation was made at a molecular Prandtl number of $Pr = 0.025$ to examine the low Prandtl number effect on the thermal turbulence statistics. The computation was executed on 1,589,248 grid points using a spectral method. The statistics obtained include rms temperature fluctuations, turbulent heat fluxes and so on. They are compared with those obtained at $Pr = 0.71$ Instantaneous thermal fields are also examined to investigate the structure of the scalar field.

NOMENCLATURE

Pr	,	molecular Prandtl number
Pr_t	;	turbulent Prandtl number
Re_m	;	Reynolds number, $2u_m\delta/\nu$
Re_τ	;	Reynolds number, $u_\tau\delta/\nu$
u_m	,	bulk mean velocity
u_τ	;	friction velocity
u, v, w	,	velocity components in the x-, y- and z- directions
x, y, z	;	streamwise, wall-normal and spanwise coordinates
δ	;	channel half width
θ	,	temperature
θ_τ	,	friction temperature
ν	;	kinematic viscosity
$( )'$	;	fluctuating component
$( )^+$	;	normalized by the wall variables, u_τ, ν and θ_τ
$( )_{rms}$	;	root-mean-square value

INTRODUCTION

In recent numerical simulations of turbulent heat transfer in a channel flow of air (Kim & Moin, 1989; Kasagi et al., 1991), it was found that the temperature fluctuation was highly correlated with the streamwise velocity fluctuation. Furthermore, it was shown that the turbulent heat fluxes and the Reynolds stresses were also highly correlated, and controlled by the same transport mechanisms throughout the flow field. As for low Prandtl number fluids, however, the balance in the transport equations seems to be different from that of moderate Prandtl number fluids. Although this is an important question in turbulent heat transfer, the current knowledge is not satisfactory mainly owing to difficulties in performing experiments (especially, of liquid metals).

The aim of this investigation is to offer new information on turbulent heat transfer in very low Prandtl number fluids. For this, we simulate a fully-developed turbulent thermal field in a two-dimensional channel. Mean flow parameters as well as various statistics of the velocity and temperature fields are calculated and compared with previous experimental and numerical results. In particular, extensive comparison is made with the DNS data for $Pr = 0.71$ (Kasagi et al., 1991) in order to examine the Prandtl number dependence of thermal turbulence statistics.

NUMERICAL PROCEDURE

The flow geometry and the coordinate system are shown in Fig. 1. The Reynolds number based on the wall friction velocity u_τ and the channel half width δ is set to be 150. The resultant bulk Reynolds number is 4580. Referring to the numerical procedure used by Kim et al (1987), a fourth-order partial differential equation for v, a second-order partial differential equation for the wall-normal component of vorticity ω_y and the continuity equation are used to solve the flow field. A spectral method, i.e., Fourier series in the x- and z-directions and a Chebyshev polynomial expansion in the y-direction, is used. For the time integration, the second-order Adams-Bashforth and Crank-Nicolson schemes are adopted for the nonlinear and viscous terms, respectively Once the velocity field is calculated at each step, the scalar field is obtained by integrating the energy equation. This is done also by the spectral method. Mercury is chosen as a test fluid, and the Prandtl number is 0.025. Iso-flux boundary conditions are imposed so that the bulk mean temperature linearly increases in the streamwise direction The local temperature is defined as the difference from the wall temperature so that periodic boundary conditions are used in the streamwise and spanwise directions

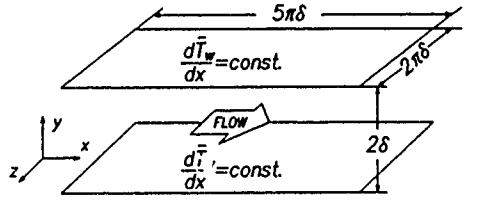

Fig 1 Flow geometry and coordinate system.

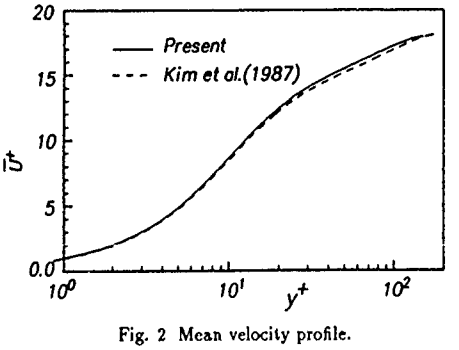

Fig. 2 Mean velocity profile.

RESULTS AND DISCUSSION

The dimensionless mean velocity profile is shown as a function of $y^+(= u_\tau y/\nu)$ in Fig. 2, where good agreement is obtained with the numerical result at $Re_\tau = 180$ (Kim et al., 1987). Figure 3 shows the

distribution of dimensionless mean temperature The previous DNS data of Pr = 0 71 (Kasagi et al , 1991) and the Kader's formula (1981) are also included in the figure. In the case of Pr = 0 71, the logarithmic region is visible, but for Pr = 0 025 it does not exist owing to thickening of the conductive sublayer The calculated Nusselt number agrees well with the value recommended by Kays & Crawford (1980) Figure 4 shows the root-mean-square temperature fluctuation θ'^{+}_{rms}. It is found that the location of the peak value moves away from the wall as the Prandtl number is decreased Figure 5 shows the distribution of streamwise and wall-normal turbulent heat fluxes. In the case of Pr = 0 71, the wall-normal heat flux is by an order of magnitude smaller than the streamwise one However, the difference between them becomes relatively small when the Prandtl number is very low. The turbulent Prandtl number Pr_t is shown in Fig.6 For Pr = 0 71, Pr_t varies moderately across the channel and reaches its maximum of about 1.1 near the wall. For Pr = 0 025, however, it increases rapidly from the wall and gives a maximum value of 3.27 at y^+ = 37. Figure 7 shows contour surfaces of θ'^+ = 0.15 at Pr = 0.025 in an instantaneous computational subvolume, while Fig. 8 shows those of θ'^+ = 4.0 at Pr = 0.71. Although the so-called streaky structures clearly exist in the temperature field for Pr = 0.71, similar structures appear much different in the case of Pr = 0 025. They are thichker in diameter and not so much elongated in the streamwise direction It is also noted that the angle between the high temperature mass and the wall is larger than that for Pr = 0.71.

CONCLUSIONS

A direct numerical simulation of a fully developed two-dimensional channel flow at Re_m = 4580 and Pr = 0.025 has been carried out. Various turbulence statistics are calculated and the following conclusions are derived

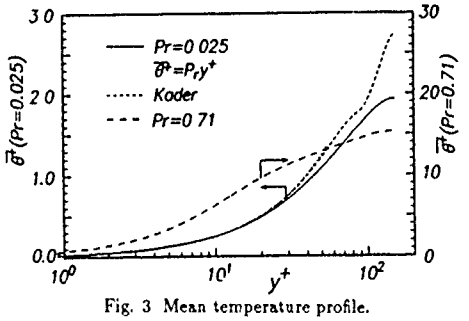

Fig. 3 Mean temperature profile.

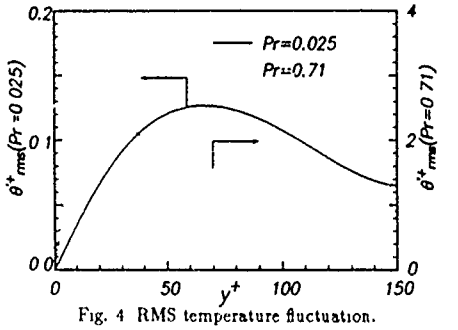

Fig. 4 RMS temperature fluctuation.

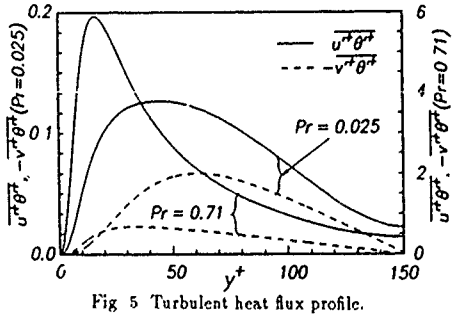

Fig 5 Turbulent heat flux profile.

(1) The effect of molecular conduction on the mean temperature profile is appreciable even in the channel central region and the thermal logarithmic region does not exist.

(2) As the Prandtl number becomes very low, the magnitude of temperature fluctuation is decreased with its peak value moving away from the wall, and the anisotropy of turbulent heat fluxes is also decreased

(3) The turbulent Prandtl number for Pr = 0.025 reaches its maximum of about 3.27 at y^+ = 37. It is much larger than that for moderate Prandtl number fluids.

(4)Much difference is observed between the thermal streaky structures visualized at Pr = 0.71 and Pr = 0.025. Those in the low Pr fluid are thick in size and not so much elongated in the streamwise direction.

The authors acknowledge the financial support through the Grant-in-Aid for Cooperative Research (No 02302043) by the Minitry of Education, Science and Culture.

REFERENCES

KASAGI, N., TOMITA, Y & KURODA, A. 1991 "Direct Numerical Simulation of the Passive Scalar Field in a Two-dimensional Turbulent Channel Flow", ASME/JSME Thermal Engineering Proc. 3, 175–182.

KADER, B A. 1981 "Temperature and Concentration Profiles in Fully Turbulent Boundary Layers", Int J Heat Mass Transfer 24, 1541–1544.

KAYS, W. M. & CRAWFORD, M. E. 1980 Convective Heat and Mass Transfer, 2nd Ed., McGraw-Hill, New York.

KIM, J , MOIN, P. & MOSER, R. 1987 "Turbulence Statistics in Fully Developed Channel Flow at Low Reynolds Number", J. Fluid Mech. 177, 133–166.

KIM, J & MOIN, P 1989 "Transport of Passive Scalars in a Turbulent Channel Flow", in Turbulent Shear Flows VI, Andrè et al eds., Springer-Verlag, Berlin, 85–96

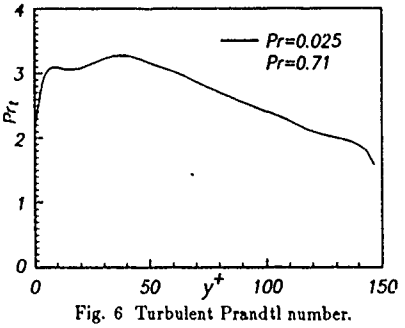

Fig. 6 Turbulent Prandtl number.

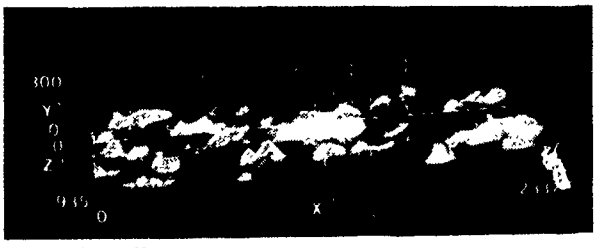

Fig. 7 High temperature regions in the lower half volume of the channel (Pr = 0.025).

Fig. 8 High temperature regions in the lower half volume of the channel (Pr = 0.71).

EIGHTH SYMPOSIUM ON
TURBULENT SHEAR FLOWS
Technical University of Munich
September 9-11, 1991

TURBULENCE IN ROTATING CURVED CHANNEL

K. Kikuyama*), K. Nishibori**), and T. Maeda*)

*)Mechanical Engineering Department, Nagoya University
Chikusa-ku, Nagoya, Japan 464-01

**)Mechanical Engineering Department, Daido Institute of Technology
Daido-cho, Minami-ku, Nagoya, Japan 457

ABSTRACT

Effects of channel rotation and curvature on the turbulent motion are examined experimentally. Flows in the channel are stabilized or destabilized corresponding to the exerting direction of the Coriolis or centrifugal forces.

NOMENCLATURE

l : mixing length
lo : value of l on a flat stationary plate
N : rotation rate(Eq. (1))
r : local curvature radius
Rir: Richardson number for channel rotation
Ric: Richardson number for channel curvature
Ue : velocity outside of boundary layer
Um : longitudinal mean velocity
u,v,w: turbulent velocity components
Ω : angular velocity of channel

INTRODUCTION

In curved rotating channels such as impeller passages of turbomachinery, turbulence exhibits a quite different nature between the pressure and suction sides due to the Coriolis and centrifugal forces exerting on the flow. This paper concerns the stabilizing or destabilizing effect of these forces on the boundary layer inside a rotating curved channel and the relation between the mixing length and Richardson numbers is discussed.

EXPERIMENTAL APPARATUS AND METHOD

Figure 1 shows the configuration of the channel, which has an aspect ratio of 4 and is mounted on a rotating table. Time-mean and turbulent velocity components were measured at the mid-height of the section by traversing hot wire probes. The outputs of the hot wire anemometer were amplified in the rotating system and transmitted to the stationary system through slip rings. In order to make the boundary layer turbulent, tripping wires of 1.5mm diameter were located at the inlet of the curved channel.

Experiments were conducted at the Reynolds number of $Re(= UmD/\nu) = 10^4$ and rotation number of $N(= \Omega D/Um) = 0$, and ± 0.15.

ROTATION RATE AND RICHARDSON NUMBER

The magnitude of the channel rotation was expressed by the following dimensionless parameter as

$$N = \Omega D/Um \qquad (1)$$

where N is defined to be positive or negative according to the clockwise or counter-clockwise rotation of the table, respectively. The effects of the centrifugal and Coriolis forces on the turbulence are expressed in terms of Richardson numbers given by the following equations(Bradshaw, 1969):

for the channel rotation

$$Ric = (2U\partial(Ur)/\partial y/(r\partial U/\partial y)^2 \qquad (2)$$

and for the channel curvature,

$$Rir = -2\Omega(\partial U/\partial y - 2\Omega)/(\partial U/\partial y)^2 \qquad (3)$$

where the positive or negative Richardson number corresponds to the suppression or promotion of the turbulent motion, respectively. Then, the mixing length in the rotating curved channel was assumed to be a linear summation of these two Richardson numbers as(Johnston and Eide, 1976)

$$l/lo = 1 - \beta c\, Ric - \beta r\, Rir \qquad (4)$$

and the validity of the above relation is examined in this paper.

RESULTS OF EXPERIMENTS AND DISCUSSIONS

Time-mean and turbulent velocity components

Figure 2 shows the profiles of time-mean velocity and turbulent components in the convex side of the section of S^{-2} for N = 0 and 0.15. The turbulence intensities are largely suppressed when N = 0 and 0.15, but increases when the channel rotates at N = -0.15. The stabilizing and destabilizing effects of the Coriolis force are more clearly seen in the distribution of Reynolds shear stress component of $(-\overline{uv})$ as shown in Fig. 3. In the concave side the tangential stress $(-\overline{uv})$ for N = 0 and 0.15 exhibits large values by the destabilizing effect of the centrifugal force but is suppressed by the Coriolis force when N = -0.15. On the other hand in the convex side the turbulence motion is largely suppressed by the centrifugal force in the stationary state but destabilized when the channel rotates in the counter-clockwise direction, N = -0.15.

Mixing length

The values of the mixing length l determined from the Reynolds stress and time-mean velocity gradient are plotted in Fig. 4, which shows that the mixing length depends on the wall curvature and rotating direction of the channel. The relations between the mixing length and the Richardson numbers are examined using the relation of Eq. (4). Figures 5(a) and (b) show the changes of $(l/lo)c$ $(= 1/lo + \beta r Rir)$ and $(1/lo)r$ $(= 1/lo + \beta c Ric)$ against Ric and Rir, respectively. The values of βr and βc are determined experimentally to be 2.4 and 3.0. As seen from these figures, the validity of the relation of Eq.(4) is better in the concave side rather than in the convex side.

CONCLUSIONS

(1) The effects of the Coriolis force on the flow become dominant when the channel rotates counter-clockwise so as to destabilize the boundary layer

in the convex side and stabilize in the concave one.

(2) The modified mixing length model is found to be feasible on the concave surface when the flow is subject both to the Coriolis and centrifugal forces.

REFERENCES

Bradshaw, P., J., Fluid Mech., Vol. 36 Pt-1,(1969), 177.

Jphnston, J.P., and Eide, S.A., Trans. ASME, J. Fluids Engng., Vol. 98-1,(1976), 374.

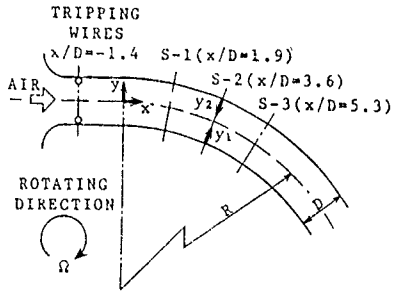

Fig.1 Configuration of rotating channel

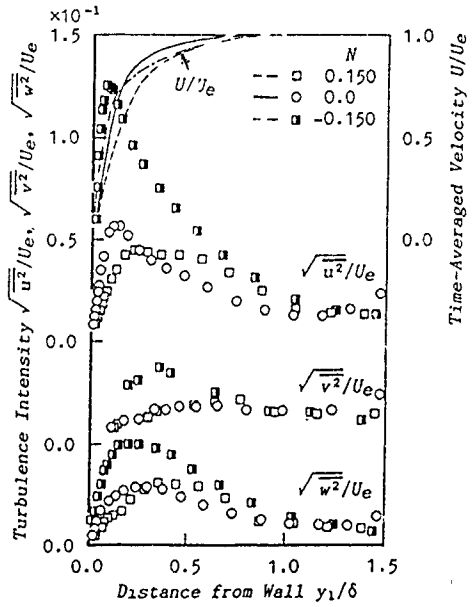

Fig.2 Distributions of time-mean velocity and turbulent components in the convex side

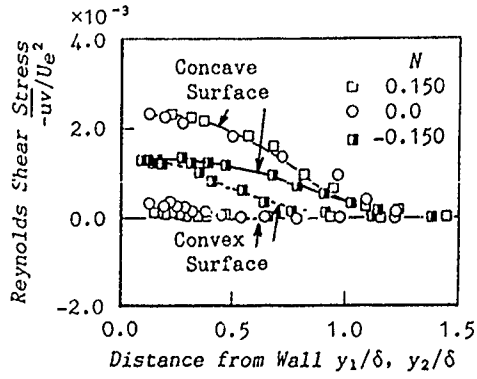

Fig.3 Distributions of Reynolds stress component

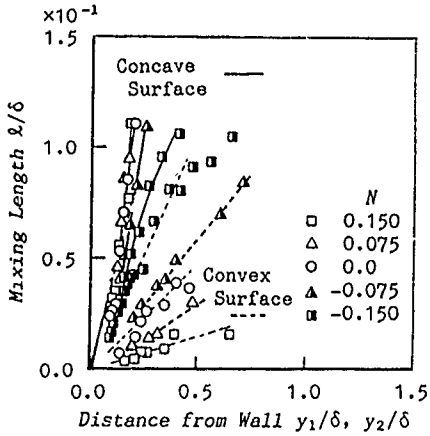

Fig.4 Changes in mixing length

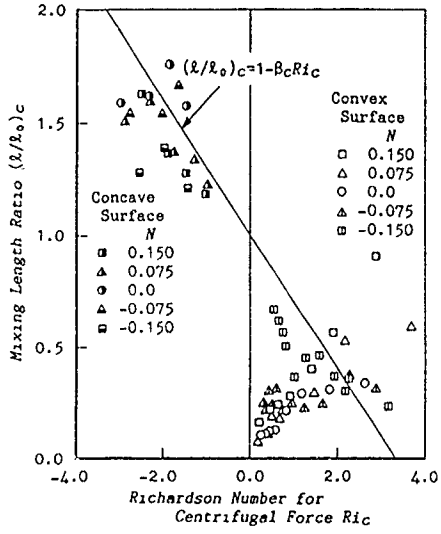

(a) Changes of (1/lo)c

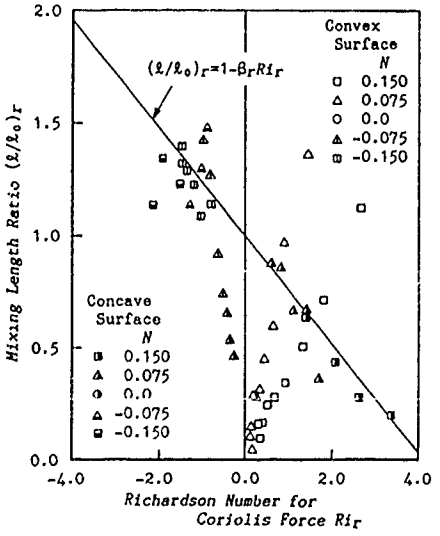

(b) Changes of (1/lo)r

Fig.5 Relation between the mixing length and Richardson number

EIGHTH SYMPOSIUM ON
TURBULENT SHEAR FLOWS
Technical University of Munich
September 9-11, 1991

LARGE SCALE VORTICES OBSERVED IN RIVER FLOW

R. Kinoshita*), T. Utami**) and T. Ueno**)

*) 5-30-11 Asagaya-Kita, Suginami-Ku, Tokyo 166, Japan

**) Ujigawa Hydraulics Laboratory
Disaster Prevention Research Institute, Kyoto University
Yoko-Ohji, Fushimi-Ku, Kyoto 612, Japan

ABSTRACT

Aerial photographs of a flood flow were analyzed using picture processing to obtain two-dimensional distribution of velocity vectors on the water surface. Using the obtained data, the structure of a train of large scale vortices appearing near the edge of a flood plain and its relationship to sediment deposition which results in a spanwise shift of a river channel are examined.

INTRODUCTION

Kinoshita (1984) surveyed the sediment deposition on the flood plain of the Ishikari River just after a major flood in 1981. Some of the results are shown in **Fig.1**. It is noted that there is heavy sediment deposition along the bank of the deep river course (main channel) downstream of the convex bank. A train of large vortices was found in the aerial photographs (**Fig.2**) of the flood flow at that point. In **Fig.2** broken lines mark the bank of the deep river course.

Trains of large vortices are generated by the interaction between the main channel flow and the flow on the flood plain. When the river is meandering, the point where the vortices are generated is fixed and the vortices are sometimes enhanced to reach the scale of the river width. These vortices cause a large amount of sediment deposition along the bank of the main channel, which results in a spanwise shift of the river channel.

In this paper, the aerial photographs of flood flow were analyzed using picture processing to obtain two-dimensional distribution of velocity vectors on the water surface. The structure of a train of large vortices appearing near the edge of a flood plain is elucidated and its relationship to sediment deposition is discussed.

PICTURE PROCESSING

Fig.1 shows the land configuration of the Ishikari River near Uraus, where meandering of the main channel is noticeable. A rectangle outlines the analyzed area.

The density distributions of a pair of photographs of the flood flow taken over a short span of time (about 4 sec) were digitized using a PDS micro-densitometer. Two-dimensional cross-correlations were taken of the density distribution over a small area of the pair of photographs to calculate a two-dimensional distribution of velocity vectors (Utami, Blackwelder & Ueno 1991, Kinoshita, Utami & Ueno 1990). The obtained vectors are shown in **Fig.3** together with the streamlines that were calculated using the data.

CHARACTERISTICS OF THE VORTEX STRUCTURE

In **Fig.3** and the following figures, the outlines of large scale vortices are marked by shadowed lines and the boundary of the main channel by solid lines. Streamline are noticeably wavy around the vortices in phase with the vortices arrangement.

Fig 4 shows the streamlines observed from the frame moving in the mean velocity in the main channel. The regions where the absolute value of divergence exceeds 0.01 (1/s) are also shown in this figure. It is noticeable that the streamline patterns coincide fairy well with the outline patterns of vortices, which suggests the vortices are convected downstream with the mean velocity of the main channel. It is also noticeable in **Fig.4** that divergence has a positive large value inside the vortices, and around the outline of vortices where streamlines converge, divergence is negative. This means strong boils exist inside the vortex and sinks around the outline.

Fig.5 shows the map of vorticity calculated using the obtained velocity. The vorticity is concentrated locally at some points, suggesting the existence of small scale vortices. As the small scale vortices are convected downstream, those which are adjacent each other gather in groups and the peak value of vorticity decays, resulting in a larger scale vortex.

LARGE SCALE VORTICES AND RIVER CHANNEL FORMATION

The conceptual patterns in **Fig.4** and **Fig.5** can be given as **Fig.6**, which suggests a mechanism of growth of the deposition on the slope of the main channel. The highly concentrated flow carrying a suspended load (sediments) near the river bed is lifted up by boils inside the vortices. Near the water surface, they are transported towards the outline of the vortices and then sink down. As flow velocity near the bank slope is low due to large scale vortices, sediments are deposited there. Thus, deposition on the bank slope of the main channel would increase. This process occurs on the bank just downstream of the convex bank. The bed of the opposite bank is scoured as flow velocity is higher. Thus, the river channel shifts spanwise.

Considering that, on the flood plain, the flow velocity is low and the flow is clear, **Fig. 6** also shows why large vortices become visible in the river flow.

REFERENCES

KINOSHITA R. 1984 Proc., JSCE, No.345 II-1, 1-1 (in Japanese).

KINOSHITA, R. 1988 In 'Control of flood flows in fluvial rivers and improvement of safety of river channels during flood (ed. T. Kishi)', 55-68 (in Japanese).

KINOSHITA, R, UTAMI, T & UENO T. 1990 J. Japan Soc. of Photogrammetry and Remote Sensing, Vol.29, No.6, 4-17.

UTAMI, T, BLACKWELDER, R.F & UENO, T. 1991 Experiments in Fluids, 10, 224-229, 1991.

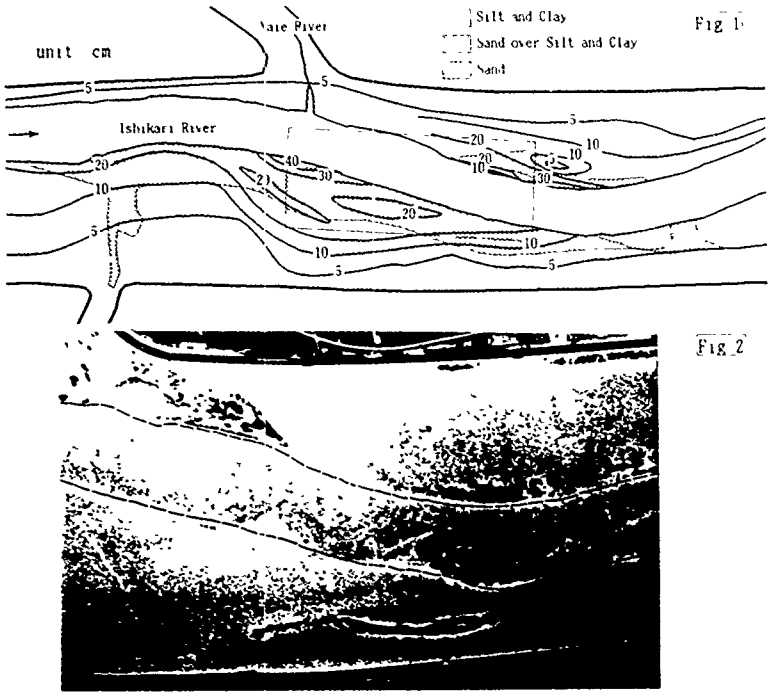

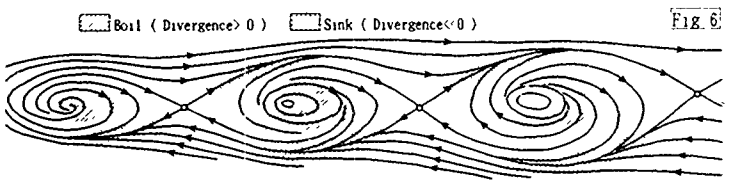

Fig.1 Sediment deposit due to the 1981 flood in the Ishikari River, surveyed by Kinoshta.
Fig.2 An aerial photograph of the 1981 flood flow. Large scale vortices are observec.
Fig.6 A conceptual mocel of vortex structure viewd from a moving frame.

Fig.3 Velocity vectors and streamlines on the surface of flood flow obtained by picture processing of aerial photogrphs.
Fig.4 Streamlines viewed from the frame moving in the mean velocity in the main channel, and a map of divergence.
Fig.5 A map of vorticity.

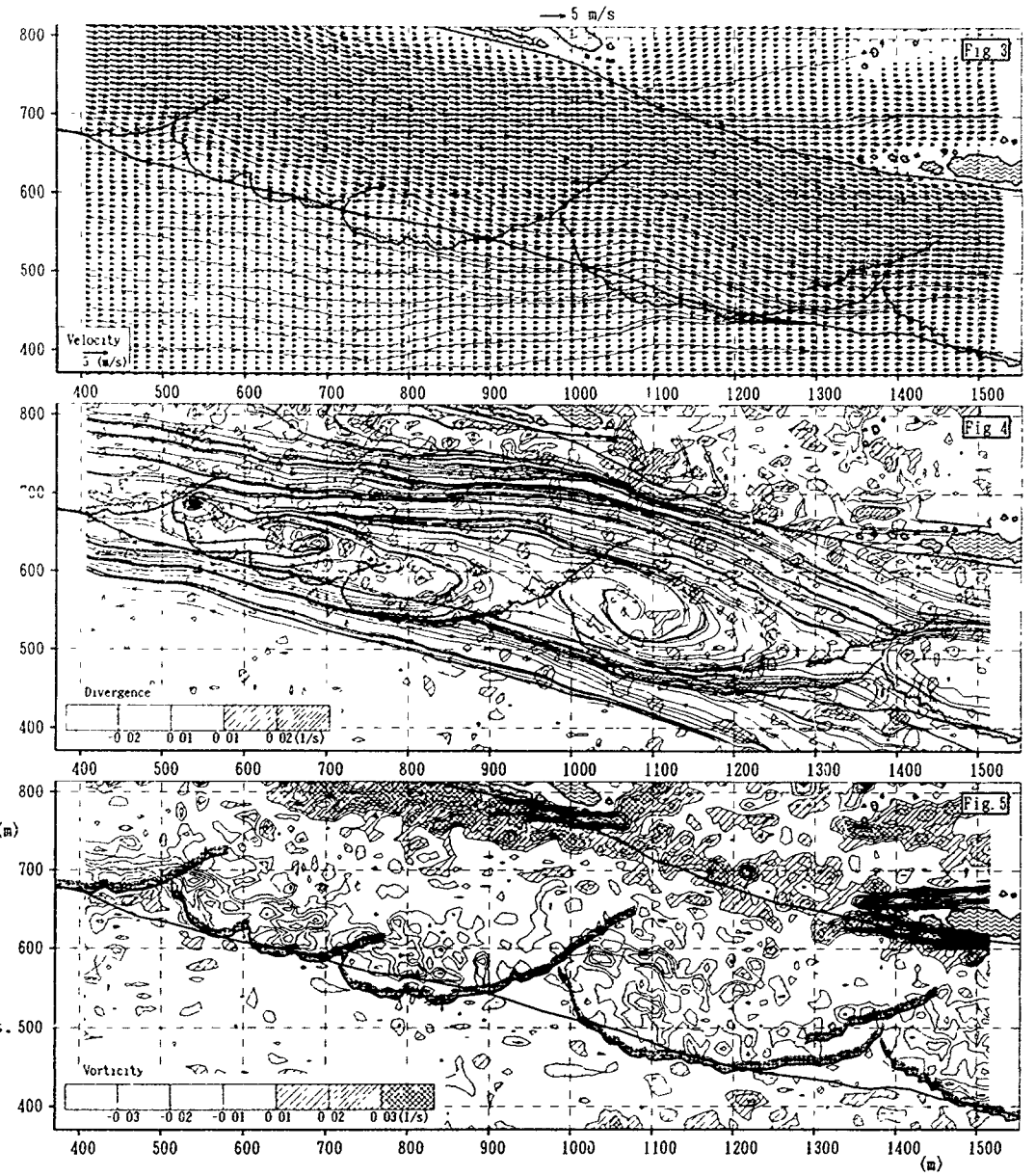

EIGHTH SYMPOSIUM ON
TURBULENT SHEAR FLOWS
Technical University of Munich
September 9-11, 1991

DOPPLER RADAR INVESTIGATIONS OF INTERMITTENT MESOSCALE TURBULENCE IN THE TROPICAL ATMOSPHERE

I.N.Klepikov, S.S.Moiseev, I.V.Prokovskaya
and E.A.Sharkov

Space Research Institute
Profsouznya str., 84/32
117810, Moscow
USSR

Investigations of convective atmosphere turbulence in the scale range above that of the small-scale turbulence are presented.

Experimental measurements of well developed convection in the tropical atmosphere (in Western part of Pacific Ocean) by Doppler radar set based on the ship were made. The computer-oriented experimental instrumentation gives the output informations in the forms of fields of Doppler velocities of cloud drops trapped by atmospheric turbulent flows. Moments, up to order six, of the longitudinal structure function of the streamwise Doppler velocity fluctuations have been measured for two-dimensional Doppler velocity maps made in operating time over 1 min. Investigation of the spatial and temporal variabilities of the structure function due to mesoscale cloud evolution from its appearance to the cloud collapse (1,5-2 hours) are presented.

An important special detail of the structure functions consist in non-regular spatial and temporal variabilities. The slope of the structure function (moments up to the order six) does not agree with Kolmogorov's model (k-4/), log-normal model, b-model and multi-fractal models. Distinguished correlated scales (spatial "thickening") stands out against a background of fluctuating variability, their generations and their evolution both toward large scales (inverse cascade) and to small scales (Kolmogorov's cascade) may be observed. During of the growth of mesoscale cloud and their collapse the structure functions become typical of the like "white noise" random process. Analysis of the altitude dependences of the structure function shows that mesoscale turbulence has a flat-layer character.

The reasons of such strong intermittency of atmosphere turbulence will be discussed. It will be shown that multiplicative noise and its influence on large-scale kinematics are of great importance. It results in faster variabilities of high-order velocity structure functions owing to fluctuations of helicity and viscosity.

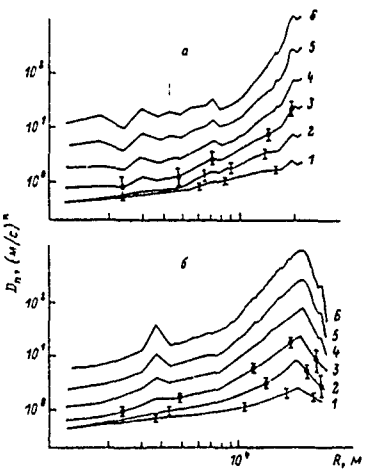

Fig.1. Structure function of n-oder Dn (n=6), multiplied by 5^n, with the turbulent scale R in 4 min. Vertical lines indicate 90% confidence limits.

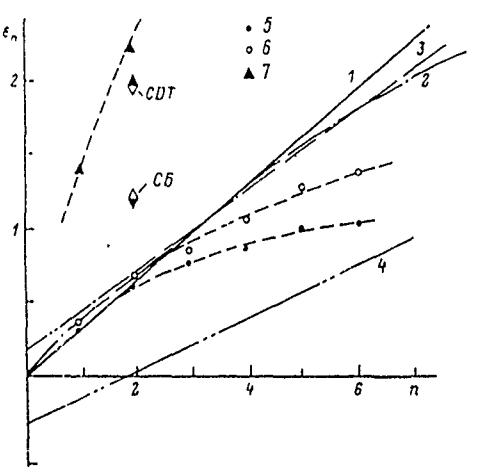

Fig.2. Variation of scale exponent ζ_n as a function of the oder n, 1 - Kolmogorov model, 2 - log normal, 3 - β-model when D=2.83, 4 - multifractal when D=2.83, 5-7 - experimental results for R=5 km and in 4, 31 and 71 min.

EIGHTH SYMPOSIUM ON
TURBULENT SHEAR FLOWS
Technical University of Munich
September 9-11, 1991

THE COMBINED WAKE OF AN ARRAY OF OSCILLATING RIBBONS

D. E. Parekh*) and P. Pulvin**)

*) McDonnell Douglas Research Laboratories
Saint Louis, Missouri 63166 USA

**) Ecole Polytechnique Fédérale
CH-1015 Lausanne, Switzerland

ABSTRACT

This work considers the combined wake of an array of oscillating ribbons oriented parallel to a uniform flow. The characteristics of this wake are documented with flow visualization and hot-wire anemometry for various excitation frequencies and amplitudes.

INTRODUCTION

The wake behind multiple bluff bodies exhibits characteristics and vortex-shedding patterns that can be similar to or quite different from characteristics of the wake from a single body. An understanding of the wake behind multiple bluff bodies is important for analyzing flows about heat exchangers, skyscrapers, marine structures, and ribbon parachutes. Williamson (1985) showed that the symmetry of wake patterns and the synchronization of the vortex shedding behind a pair of cylinders depends critically on the gap size between the bodies. In their studies of flows behind arrays of flat plates oriented normal to the flow, Hayashi, Sakurai, & Ohya (1986) found that the gap flows are biased to one side or the other in a stable manner. Higuchi & Takahashi (1989) demonstrated that arranging flat plates so that the plates form a porous curved surface normal to the flow has a stabilizing and drag-reducing effect on the wake flow relative to an arrangement with no curvature.

In this work we consider the combined wake behind an array of oscillating ribbons oriented parallel to the flow. This work is particularly motivated by the need to understand and control multiple wake interactions and by the need for a well-defined vortical disturbance for boundary layer transition studies. In his analysis of the receptivity of a laminar boundary layer to free-stream turbulence, Kerschen (1990) models the free-stream turbulence as a superposition of periodic vortical disturbances of varying wave number and orientation. Parekh, Pulvin, and Wlezien (1991) found that an array of oscillating ribbons can produce a controllable vortical disturbance useful for receptivity experiments. This work focuses on the far-field characteristics and vortex patterns of the combined wake of an array of oscillating ribbons.

APPROACH

The facility used in this work is a low-disturbance, closed-return, blower-driven wind tunnel. The test section of this tunnel measures 0.91-m wide by 0.66-m high by 5.5-m long, and its inlet contraction has a 9:1 area ratio. The typical streamwise velocity fluctuations from D.C. to 10 kHz are about 0.1% of the freestream velocity, and the transition Reynolds number on a polished flat plate in this tunnel is over 2.6 million.

A schematic of the array of ten ribbons is shown in Fig. 1. The 0.051-mm-thick stainless steel ribbons span the entire width of the tunnel. The vertical spacing, s, between adjacent ribbons is 4.76 mm, and the total height, H, of the array is 43 mm. The local area blockage associated with this array is 1.07%; however, the total blockage is only 0.077% of the tunnel cross-sectional area. The relative streamwise position of the ribbons can be adjusted to produce periodic gusts of various inclinations. When all the ribbons are aligned vertically, as they were in this work, a 0-degree inclination of the vortical disturbance is produced.

A pair of electro-magnetic shakers drove the ribbons in phase. The fundamental resonance frequency of the ribbons, which was set by adjusting ribbon tension, ranged from 90 to 110 Hz. By using excitation frequencies, f, below this fundamental resonance, nearly uniform motion of the ribbons was obtained over their entire span of the tunnel. The tension in the ribbons was sufficient to avoid aerodynamically induced oscillations at flow velocities up to 10 m/s.

Velocity was measured by an x-wire probe mounted on an automated traversing system utilizing micro-stepper motors and a precision linear position indicator. Traverse control and all data acquisition were performed on a VAXlab data-acquisition and processing system. The hot-wire signal was directly digitized and linearized using a fourth-order polynomial and temperature compensation. Accelerometers placed on top of each drive-block assembly provided a detailed measurement of the motion of the ribbon array. Visualization of the wake behind the ribbon array was achieved by strobe illumination of a compact stream of smoke introduced upstream of the inlet contraction.

RESULTS

With no excitation, the flow behind the ribbons appears undisturbed. With excitation, the individual wakes of the ribbons rapidly merge to produce a combined wake. The general shape of the combined wake resembles a sine wave as seen in Fig. 2. Visualizations at different excitation amplitudes and fixed Reynolds number, Re, indicate that the wake possesses a similar shape for ribbon acceleration amplitudes, A, up to 78 m/s^2. Reducing the flow velocity below about 4 m/s, while keeping the frequency and absolute amplitude fixed at f=70 Hz and A=49 m^2/s, respectively, results in vortex shedding patterns similar to a Karman vortex street (Fig. 3).

To characterize the combined wake, a set of velocity profiles spaced 20 mm apart in the streamwise direction was measured. The mean wake profile has a symmetric

velocity deficit which decays with x, resulting in the acceleration of the flow surrounding the wake (Fig. 4). The amplitude of the fundamental component of both the streamwise and normal velocity fluctuations, u' and v', remained nearly constant with x up to the end of the measurement domain, which was 1 m downstream from the ribbons. The variation in y, however, was not identical. The u' component has peaks at the edge of the wake and a 180-degree phase shift across the wake. The v' component is constant in amplitude within the core of the wake and is essentially uniform in phase across the wake at any given streamwise position. Combining the mean flow and the u' and v' profiles, one can compute the streamlines of the velocity field as shown in Fig. 5. The characteristic wavelength, λ, of the wake remains essentially constant in x in the domain considered. The phase speed ($f\lambda/U_0$) of the wake over a range of velocities, U_0, (6 to 10 m/s) and excitation frequencies, f, (50 to 70 Hz) and amplitudes, A, (9.8 to 49.0 m/s^2) is 0.94.

CONCLUDING REMARKS

This work considers the combined wake of an array of oscillating ribbons oriented parallel to the flow. Over a range of Reynolds numbers and excitation amplitudes and frequencies, the wake flow exhibits a stable sinusoidal pattern with an invariant phase speed of 0.94. The visualizations are consistent with the velocity measurements which also indicate a sinusoidally oscillating flow with a characteristic wavelength dependent on excitation frequency. Other wake patterns can be obtained by appropriate adjustment of the flow velocity and relative excitation amplitude.

ACKNOWLEDGEMENTS

This work was conducted under a McDonnell Douglas IRAD program in collaboration with the Ecole Polytechnique Fédérale. The authors thank Edward Kerschen of the University of Arizona and Rich Wlezien of the Illinois Institute of Technology for many useful discussions. The authors also thank Joseph Kroutil and William Faith for their assistance in designing the ribbon array device.

REFERENCES

HAYASHI, M., SAKURAI, A. & OHYA, Y. 1986 Wake interference of a row of normal flat plates arranged side by side in a uniform flow. *J. Fluid Mech.* **164**, 1-25.

HIGUCHI, H. & TAKAHASHI, F. 1989 Flow past two-dimensional ribbon parachute models. *J. Aircraft* **26**, 641-649.

KERSCHEN, E. J. 1990 Boundary layer receptivity theory. *Appl. Mech. Rev.* **43**, S152-S157.

PAREKH, D. E., PULVIN, P., and WLEZIEN, R. W. 1991 Boundary layer receptivity to convected gusts and sound. To be presented at 1st ASME-JSME Fluids Engineering Conference, Portland, OR.

WILLIAMSON, C. H. K. 1985 Evolution of a single wake behind a pair of bluff bodies. *J. Fluid Mech.* **159**, 1-18.

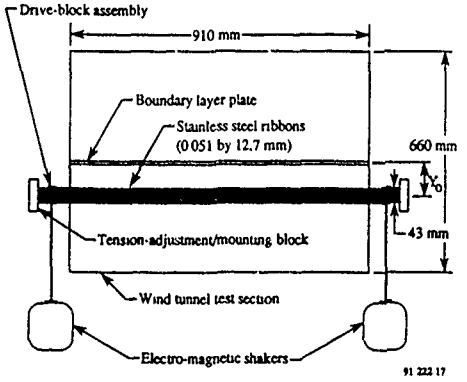

Fig. 1. Front view of gust-generating device and test section.

Fig. 2. Smoke visualization of excited wake for U_0=8 m/s, f=70 Hz, and A=49 m/s^2.

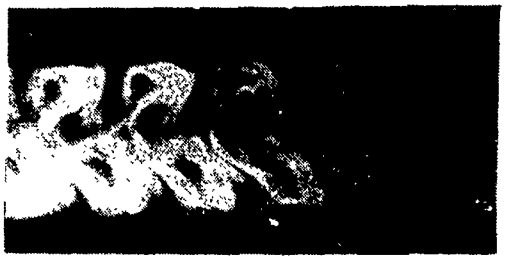

Fig. 3. Smoke visualization of excited wake for U_0=3 m/s, f=70 Hz, and A=49 m/s^2. The magnification is 1.5 times larger than that of Fig. 2.

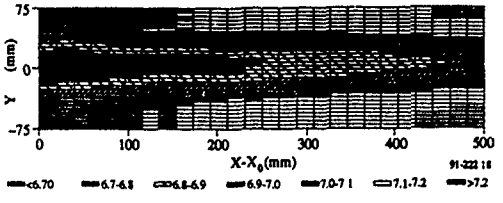

Fig. 4 Mean velocity profile of multiple ribbon wake for U_0=7 m/s, f=70 Hz, A=49 m/s^2, and X_0=400 mm.

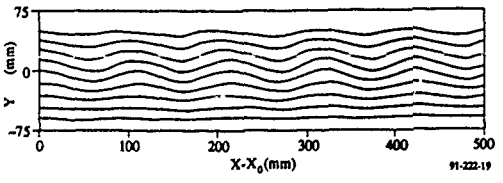

Fig. 5 Streamlines corresponding to the mean velocity plus the fundamental component of the perturbation velocity at a fixed phase of the excitation signal for U_0=7 m/s, f=70 Hz, A=49 m/s^2, and X_0=400 mm. The v' component is amplified by ten for clarity.

EIGHTH SYMPOSIUM ON
TURBULENT SHEAR FLOWS
Technical University of Munich
September 9-11, 1991

LARGE EDDY SIMULATION OF SPATIALLY DEVELOPING PLANE MIXING LAYERS

C Pianese[1] and C Benocci

von Karman Institute for Fluid Dynamics
Chaussée de Waterloo, 72
B - 1640 Rhode Saint Genèse - Belgium

ABSTRACT

Results are presented of a Large Eddy Simulation (LES) of the 2D spatially developing plane mixing layer The numerical approach is based upon a finite differences numerical solution of the Navier-Stokes equations for the large scales in primitive variables formulation Simulations are performed for both *natural* and *forced* mixing layers and the results compared with experiments results and Direct Numerical Simulations (DNS)

INTRODUCTION

The interaction between two co-flowing fluid streams having different velocities gives birth to the *Plane Mixing Layer*, which has been defined in a recent work (Lowery & Reynolds 1986) as "one of the building-block flows upon which the field of fluid mechanics is based" Besides their importance for a number of practical applications plane mixing layers are of paramount interest to the researcher for the insight they offer into the physics of turbulence and, in particular, into the development of large scale vortical structures and their interaction through the *vortex pairing* process

One attractive characteristic of the plane mixing layer is its geometrical simplicity, which makes it amenable to numerical investigations using DNS or LES techniques Lowery & Reynolds and Sandham & Reynolds 1989 have performed DNS of mixing layers subjected to a periodic forcing at the inlet to promote the growth of periodic large structures (*forced* mixing layer), while Comte & al 1989 have studied with LES the case where the vortical structures are allowed to grow naturally from a random initial perturbation (*natural* mixing layer) In the present study both *natural* and *forced* cases are considered in order to attain a more complete understanding of the physical aspects of mixing and assess the performances of LES for this class of flows

LARGE EDDY MODEL

The transport equations for the large scale variables ($\overline{U}_i$, $\overline{P}$) can be written, with obvious meaning of the symbols, as

$$\frac{\partial \overline{U}_i}{\partial x_i} = 0 \tag{1}$$

$$\frac{\partial \overline{U}_i}{\partial t} + \frac{\partial \overline{U}_i \overline{U}_j}{\partial x_j} = -\frac{\partial \overline{P}}{\partial x_i} + \nu \frac{\partial^2 \overline{U}_i}{\partial x_j x_j} - \frac{\partial \overline{u_i u_j}}{\partial x_j} \tag{2}$$

which is consistent with a finite differences discretisation over a staggered mesh (Schumann 1979, Mason 1989)

The contribution $\overline{u_i u_j}$ of the small scales is modeled using the well known Smagorinsky subgrid viscosity approach

$$\overline{u_i u_j} = -2\nu_t S_{ij} \tag{3}$$

$$\nu_t = C_s^2 \Delta^2 (2 S_{ij} S_{ij})^{0.5} \tag{4}$$

where S_{ij} is the strain rate of the large scales , Δ the typical mesh size and C_s the coefficient relating mesh size to filter size (see Mason).

NUMERICAL TECHNIQUES

Eqs (1) to (3) are discretised over a staggered grid with uniform mesh spacing in the longitudinal direction x_1 and non uniform spacing in the transversal direction x_2 using finite differences : a 3th order upwind biased discretisation (Kawamura & al 198?) is used for the advection along x_1 and a centered scheme (4th order accurate on an uniform mesh) for the advection along x_2; all other terms are discretised using 2nd order centered formulae.

Eq (2) is advanced in time with the Adams-Bashforth predictor-corrector scheme and a Direct Poisson Solver is used to solve the pressure equation and find the pressure distribution for which the $\overline{U}_i$ verify Eq. (1)

BOUNDARY CONDITIONS

On the boundary $x_1 = 0$ the mean streamwise velocity $\overline{U}_1$ is assumed to follow a *tanh* profile :

$$\overline{U}_1 = \frac{1}{2}\left[\frac{1}{\lambda} + tanh(2x_2)\right] \tag{5}$$

where λ is the ratio between the *difference* and the *sum* of the two freestream velocities U_{up} and U_{lo}

On the boundary $x_1 = L$ both velocity components are obtained from the wave equation :

$$\frac{\partial \overline{U}_i}{\partial t} + c\frac{\partial \overline{U}_i}{\partial x_1} = 0 \tag{6}$$

where c is the advection velocity of the wave computed from the values of the velocity at the previous timestep

On the two transversal boundaries $\overline{U}_1$ is determined using a stress-free condition, while the transversal velocity $\overline{U}_2$ is found applying Eq (1).

RESULTS

The conditions for the calculation, chosen to allow comparison with Lowery & Reynolds and the experimental results by Oster & Wygnanski 1982, are $r = 0.5$, where r is the lower stream to upper stream velocity ratio, and $Re = 100$, where Re is the Reynolds number based upon the velocity difference between the two streams and the inlet vorticity thickness δ_0 The computational domain was 130 units long and 35 high, discretised with a 340x40 grid The subgrid stress coefficient C_s was taken equal to 0.06

Forced mixing layer

The forced mixing layer is obtained superimposing to the mean inlet velocity a perturbation of the type .

$$u_i = a\sum(sin(\omega_k t) + cos(\omega_k t)) \tag{7}$$

where a is a coefficient and ω_k the fundamental frequency obtained from linear instability theory and its first two armonics

Formation of periodic vortical structures and vortex pairing were observed, as shown in Fig 1, structure wavelength and position of the two pairings agree well with the boundaries of the different regions identified by Oster & Wygnanski in their experimental study of a forced layer. The rms values of the streamwise velocity fluctuation (Fig. 2) show the lack of self-similarity typical of the forced mixing layer, computed values are sensibly higher than corresponding ones from experiments and direct simulation

Natural mixing layer

The natural mixing layer is obtained superimposing a random perturbation with divergence equal to 0 to the initial flowfield

[1] Present address . Facoltà d'Ingegneria, Dipartimento Ingegneria Meccanica per l'Energetica, Università Federico II, I-80125 Napoli, Italy

Formation of large scale vortical structures was observed at random locations in space and time (Figs 3 and 4); vortex wavelengths agree well with the ones found by Oster & Wygnanski The rms values of the streamwise velocity fluctuations are in good agreement with the experimental ones as shown in Fig 5.

CONCLUSIONS

The present LES has shown that it is possible to reproduce numerically the main physical features of both forced and natural plane mixing layer : the process of formation and evolution of vortical structures is in good agreement with the experiments performed by Oster & Wygnanski A significative disagreement however subsists for the forced case, where the numerical solution does not reproduce the typical two-peaks profile of the longitudinal rms fluctuation Causes of this discrepancy are presently under investigation.

REFERENCES

Comte, P , Lesieur, M , Laroche, H., Normand, X., 1989 Numerical Simulation of Turbulent Plane Shear Layer. Turbulent Shear Flows 6, Springer-Verlag, 441-454

Kawamura, T , Takami, H , Kuwahara, K , 1985 New Higher Order Upwind Scheme for Incompressible Navier-Stokes equations Ninth International Conference on Numerical Methods in Fluid Dynamics, Springer-Verlag, 291-295

Lowery, P S & Reynolds, W C , 1986. Numerical Simulation of a Spatially Developing, Forced, Plane Mixing Layer TF-26 Thermoscience Division, Dept. Mech Engineering Stanford University.

Mason, P J , 1989 Large Eddy Simulation of Turbulent Flow. Turbulent Shear Flow, Von Karman Institute Lecture Series 1989-03

Oster, D & Wygnanski, I , 1982 The Forced Mixing Layer between Parallel Streams J Fluid Mech 123, 91-130.

Sandham, N.D & Reynolds, W C., 1989. Some Inlet-Plane Effects on the Numerically Simulated, Spatially-Developing Mixing Layer Turbulent Shear Flows 6, Springer-Verlag, 441-454

Schumann, U , 1975 Subgrid Scale Model for Finite Differences Simulations of Turbulent Flows in Plane Channels and Annuli J Comp Physics 18, 376-404

Fig 1 Isovorticity contours t=269 5. Forced layer

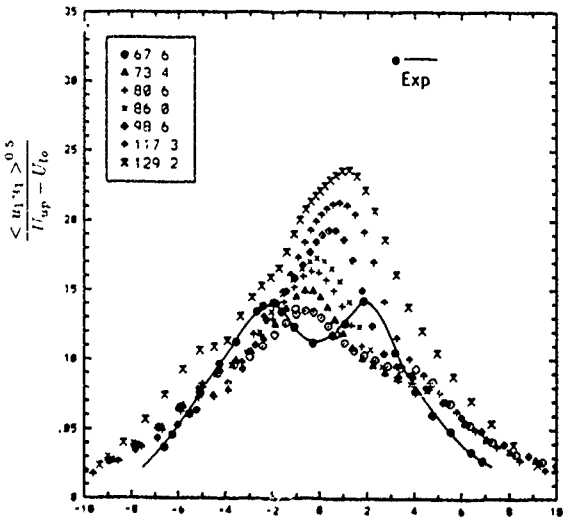

Fig. 2. Resolved longitudinal velocity fluctuations Forced layer.

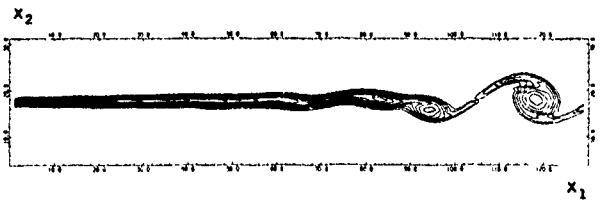

Fig 3. Isovorticity contours t=162 5. Natural layer.

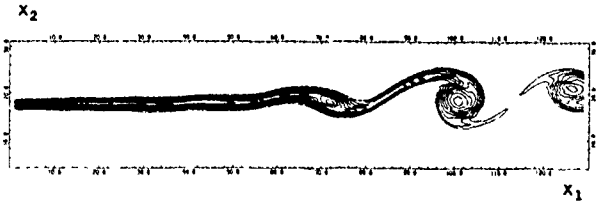

Fig 4 Isovorticity contours t=245 Natural layer.

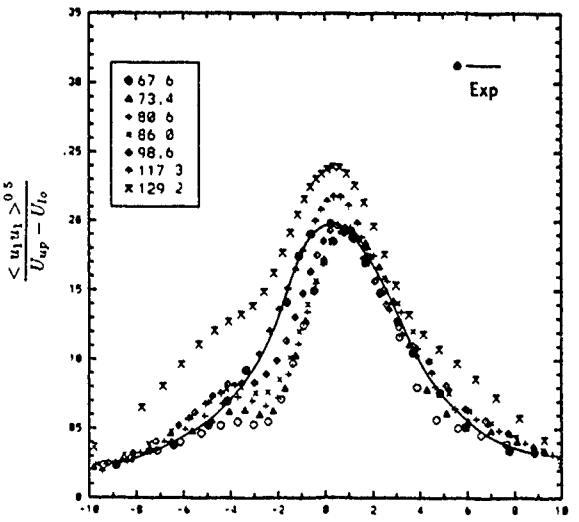

Fig 5 Resolved longitudinal velocity fluctuations Natural layer.

EIGHTH SYMPOSIUM ON
TURBULENT SHEAR FLOWS
Technical University of Munich
September 9-11, 1991

SIGNATURES OF QUANTUM-LIKE MECHANICS AND DETERMINISTIC CHAOS IN ATMOSPHERIC FLOWS

A. Mary Selvam, J.S. Pethkar and S.M. Sholapurkar

Indian Institute of Tropical Meteorology, Pune 411 008, India

ABSTRACT

A cell dynamical system model for atmospheric flows is summarized. The model predicts quantum-like mechanical laws for atmospheric flows manifested as the observed long-range spatiotemporal correlations, now identified as signatures of self-organized criticality or deterministic chaos. The model predictions are in agreement with power spectrum analysis of annual mean COADS surface pressure time series for 100 grid points around the Indian region. The power spectra follow the universal and unique inverse power law form of the statistical normal distribution.

INTRODUCTION

Long-range spatiotemporal correlations manifested as the selfsimilar fractal geometry to the spatial pattern concomitant with inverse power law form for the power spectrum of temporal fluctuations is ubiquitous to real world dynamical systems and is identified as signatures of self-organized criticality (Bak, Tang and Wiesenfeld, 1988) or deterministic chaos. Such non-local connections are manifested in atmospheric flows as the selfsimilar fractal geometry to the global cloud cover pattern concomitant with inverse power law form for the atmospheric eddy energy spectrum documented by Lovejoy and Schertzer (Lovejoy and Schertzer, 1986). Mathematical models of atmospheric flows are by convention based on the nonlinear Navier-Stokes equations which do not have analytical solutions. Finite precision computer realizations of such nonlinear models for atmospheric flows are not totally realistic because of deterministic chaos, i.e., sensitive dependence on initial conditions. Such sensitive dependence on initial conditions, namely, long-range spatiotemporal correlations are also exhibited by real world dynamical systems and is now identified as self-organized criticality as mentioned earlier. The physics of deterministic chaos or self-organized criticality in real world and model dynamical systems is not yet identified. In this paper a non-deterministic cell dynamical system model for atmospheric flows (Mary Selvam 1990a) is summarized.

MODEL PREDICTIONS

(1) The signatures of deterministic chaos in atmospheric flows, namely long-range spatiotemporal correlations are inherent to the quantum-like mechanics governing atmospheric flows. The apparent wave-particle duality is attributed to the bimodal, namely, formation and dissipation respectively of the phenomenological form for energy display in the bidirectional energy flow intrinsic to eddy circulations, e.g., formation of clouds in updrafts and dissipation of clouds in downdrafts giving rise to the discrete cellular geometry to cloud structure. (2) The global atmospheric flow structure consists of a nested continuum of vortex roll circulations with ordered energy feed back between the larger and smaller scales. A complete quantitative description of the atmospheric flow structure, namely, the strange attractor can therefore be given in terms of the component periodicities and their phases. Such a concept of an eddy continuum for the fine structure of the strange attractor has recently been put forth by Cvitanovic (Cvitanovic, 1988). The model predictions are in agreement with the results of continuous periodogram analysis of the annual mean surface pressure data for 28 years (1961-1988) available for about 100 grid points over the Indian region in the Comprehensive Ocean-Atmosphere Data Set (COADS, Release 1, Climate Research Program, ERL, Boulder, Colorado). The percentage contribution to total variance and the cumulative percentage contribution to total variance for normalized standard deviate t values for 20 representative grid points are shown in Figure 1. Since the model predicts logarithmic spiral circulation pattern for atmospheric flows, the t values are obtained as $t = (\log\lambda / \log\lambda_{50}) - 1$ where λ is the period and λ_{50} the period at which the cumulative percentage contribution to total variance is equal to 50 and t=0. The normal and cumulative normal probability density distributions are also plotted in Figure 1. It is seen that the percentage contribution to total variance follows closely the normal distribution. The "goodness of fit" was tested using the standard statistical chi-square test. The arrows at the top and bottom in the figures indicate respectively the values of t up to which the fit is good at 95% level of significance for the normal and cumulative normal probability density distributions.

Incidentially, the power spectrum of the chaotic Lorenz attractor (Lorenz 1963) also exhibits the universal inverse power law form of the statistical normal

dist ibution as shown at Figure 2. The cell dynamical system model concepts described in this paper may therefore be applied to quantify deterministic chaos or self-organized criticality in model dynamical systems also (Mary Selvam 1990b).

CONCLUSION

The signature of self-organized criticality or deterministic chaos, namely, the inverse power law form for the power spectrum of nonlinear fluctuations in real and model atmospheric flows is the same as the universal and unique statistical normal distribution with the normalized standard deviation of the fluctuations expressed as a function of the corresponding wavelengths (eddy). Such a universal quantification for the nonlinear variability of real and model atmospheric flows is a natural consequence of quantum-like mechanics governing the dynamical evolution and implies predictability of the total pattern of fluctuations.

ACKNOWLEDGEMENTS

The author expresses her deep gratitude to Dr. A.S.R. Murty for his keen interest and encouragement during the course of this study. Thanks are due to Shri M.I.R. Tinmaker for typing this manuscript.

REFERENCES

BAK, P., TANG, C. and WIESENFELD, K. 1988 Self-organized criticality. Phys. Rev. A38, 364-374.

BLACKADAR, A. 1990 Computer butterflies : an adventure in chaos. Weatherwise, Aug., 210-215.

CVITANOVIC, P. 1988 Invariant measurement of strange sets in terms of cycles. Phys. Rev. Lett. 61, 2729-2732.

LOVEJOY, S. and SCHERTZER, D. 1986 Scale invariance, symmetries, fractals and stochastic simulations of atmospheric phenomena. Bull. Amer. Meteorol. Soc. 67, 21-32.

MARY SELVAM, A. 1990a Deterministic chaos, fractals and quantum-like mechanics in atmospheric flows. Can. J. Phys. 68, 831-841.

MARY SELVAM, A. 1990b A cell dynamical system model for turbulent shear flows in the planetary atmospheric boundary layer. Proc. Ninth Symp. Turbulence and Diffusion, April 30-May 3, 1990, Roskilde, Denmark, Amer. Meteorol. Soc., 262-265.

Figure 1 : Power spectra of annual mean surface pressure for 28-years (1961-1988) for 4 grid points whose locations in degrees latitude and longitude are indicated at the top.

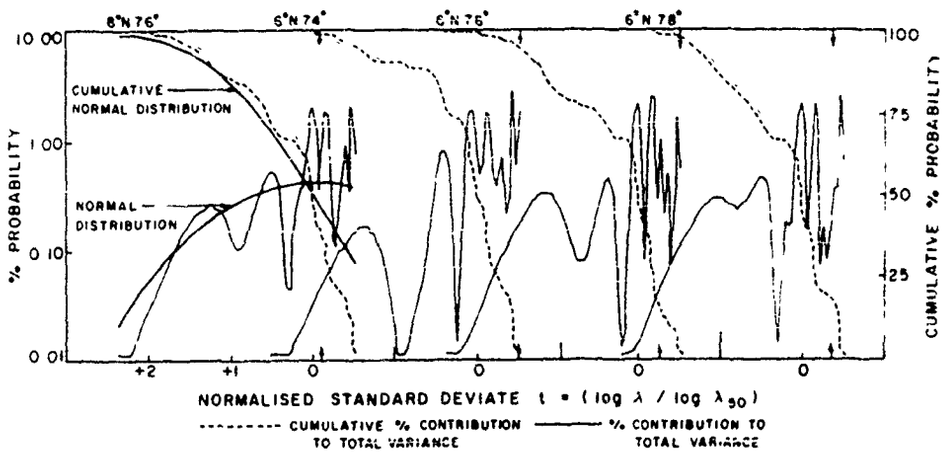

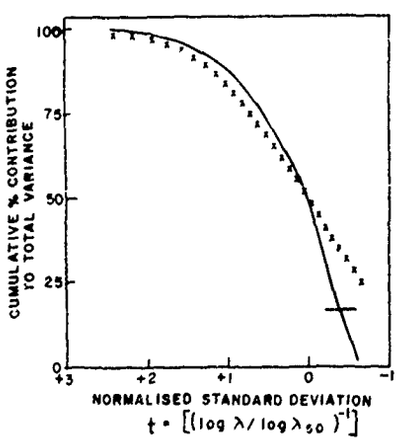

Figure 2 : The power spectrum of the Lorenz attractor follows the universal inverse power law form of the statistical normal distribution. The data series consists of 1000 successive means of 25 y coordinate momenta values starting from the 1001 value. The program written by Blackadar (1990) was used for computing the Lorenz attractor. The crosses refer to the cumulative normal distribution.

EIGHTH SYMPOSIUM ON
TURBULENT SHEAR FLOWS
Technical University of Munich
September 9-11, 1991

DISPERSION IN A TURBULENT BOUNDARY LAYER OVER A LOW HILL

H. Stapountzis

University of Thessaloniki
Department of Mechanical Engineering
Thessaloniki 540 06, Greece

Dispersion in a turbulent boundary layer was measured in a wind tunnel downstream of a long thin heated wire placed normal to the flow. The boundary layer was formed on the floor of the wind tunnel and was tripped at the entrance of the working section. Part of the tunnel floor was occupied by a low symmetric two-dimensional hill of the Jackson and Hunt (1975) type, $y = H/(1+(x/l)^2)$, where H is the height of the hill, see Fig. 1. Thus the boundary layer experiences changes in curvature, from concave to convex, separating in the leeward side of the hill before reaching the convex part. The importance of curvature in a similar type of flow was discussed by Baskaran et al. (1987), who also noticed the formation of an internal, "sub-boundary layer". Our case is different in that the boundary layer height to the height of the hill near the upstream foot of the hill is about 2.0 while in their case was 0.4. However the boundary layer characteristics are qualitatively the same i.e. the skin friction reaches a minimum near the foot of the hill, rises to a maximum before the top and drops to a minimum close to zero near separation. The boundary layer displacement thickness, denoted here by δ^* (and by δ^*_s its value at the source), changes in a reverse manner.

The positions of the line source with respect to the hill are denoted by the letters A, B, C, D in Fig 1. The source was placed at various distances, y_s, from the wall, resulting in dimensionless wall units y^+, between 5 and 90. At position D, where the flow has separated $y_s/H = 0.017$. In all cases $U_0H/\nu \approx 1.2\times10^4$, where U_0 is the free stream speed well upstream of the hill.

The purpose of this experiment was twofold: To simulate corresponding environmental flows and provide data for the validitation of numerical work , based on a Lagrangian Random Flight Model (RFM). We are interested in the effects of inhomogeneity and curvature on turbulent dispersion. The intensity of concentration fluctuations, c_{RMS}/C, far downstream of a line source appears to approach a constant value in grid turbulence, Stapountzis et al. (1986) while continuously decays in a "nearly homogeneous" turbulent shear flow, Stapountzis and Britter (1989). In a plane turbulent boundary layer inhomogeneity, which causes concentration fluctuations to increase, competes against shear and according to Sawford's (1984) calculations the intensity of concentration fluctuations should tend to be constant.

The results of the experimental part of this work are shown in Figures 2 to 6 and compared with other people's work refering to dispersion from line or point sources in flat terrain. The non-dimensionalizing concentration, C_0, is not common to all experiments, therefore there are some differences in the levels of maximum and wall concentrations C_{max} and C_w respectively. In our case $C_0 = P/(\rho U(y_s)c_p y_s)$, where P is the power fed into the wire per unit length, ρ is the air density and c_p the specific heat at constant pressure.

Figure 2 shows the variation of the mean maximum concentration (temperature) downwind of the source at distances x_s, measured along the surface of the hill. For elevated sources such as ours the initial decay rate of C_{max} is close to x_s^{-1}, as found by other workers, it is followed by an increased rate of decay in the leeward side of the adverse pressure gradient of the hill, by a considerably slower rate in the separated region and again a rapid decay after the "end", E, of the hill. For source position D, within the recirculating separated region, concentrations are roughly constant up to the end of the hill. Beyond that point significant drop in the concentrations occur, as also observed by Castro and Snyder (1982) for three dimensional hills. The distance from the surface where the maximum occurs (not shown here) generally decreases as the top of the hill is approached and then increases.

The ground level concentrations, C_w, shown in Figure 3 drop with increasing x_s for all but the mostly elevated, $y_s/\delta_s = 0.9$, source position where a maximum is observed at the top of the hill. The intensity of concentration fluctuations, presented in Figure 4, initially exhibits a dependence on y_s and source size. Our data are in qualitative agreement with the predicted values from the Random Flight Model for a flat boundary layer (Sawford 1984) the main difference being in the location of the maxima. The streamwise position where the intensity is maximum depends on the ratio of the source size to the turbulence length scale at the source elevation, y_s. In the region of the top of the hill the intensity tend to increase and drop again in the leeward side.

The centroid of the mean concentration profiles, $\bar{Y}$, ($\bar{Y} = \int yCdy/\int Cdy$) which is a measure of the mean heated particle displacement from the wall (Chatwin, 1978), is initially of the order of y_s and then increases as x_s^{1}, see Fig. 5. However as the maximum height of the hill is approached it decreases and in the separated region it increases again but faster than x_s^{1}. A slow decrease is observed after the end of the hill. A similar behaviour is noticed for the second centroid centered moment of the concentration profiles ($= \int(y-\bar{Y})^2Cdy/\int Cdy$, a measure of the dispersion of marked particles) which is shown in Figure 6.

References.

BASKARAN V., SMITS A and JOUBERT P.N., 1987, J. Fluid Mech., vol 182, pp 47-83

CASTRO I.P. and SNYDER W.H., 1982, Atm. Env., vol 16, pp 1869-1887.

CHATWIN P.C., 1978, Int. J. Heat Mass Tr., vol 21, pp 367-368

DURBIN P.A. and HUNT J.C.R., 1980, Journ. de Mecanique, vol 19, pp 679-695.

FACKRELL J.E. and ROBINS G., 1982, J Fluid Mech., vol 117, pp 1-26.

JACKSON P.S. and HUNT J.C.R., 1975, Quart. J. Roy. Met. Soc. vol 101, pp 929-955

PARANTHOEN P , FOUARI A , DUPONT A and LECORDIER J.C., 1988, Int. J. Heat Mass Tr., vol 31, pp 159 165.

RAUPACH M.R. and LEGG B.J., 1983, J. Fluid Mech., vol 136, pp 111-137.

SAWFORD B.L., 1984, Workshop on Updating App. Diff. Models, Clearwater, Florida, U.S.A.

SHLIEN D.J. and CORRSIN S., 1976, Int. J. Heat Mass Tr., vol 19, pp 285-295.

STAPOUNTZIS H., SAWFORD B.L., HUNT J.C.R. and BRITTER R.E., 1986, J. Fluid Mech., vol 165, pp 401-424.

STAPOUNTZIS H. and BRITTER R.E., 1989, Turb. Sh. Flows 6, Springer Verlag, pp 97-108.

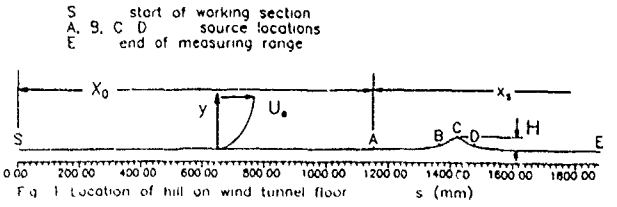

Fig 1 Location of hill on wind tunnel floor

Fig 2 Peak mean concentrations for line and point sources in plane and curved (present work) surfaces B beginning of hill, T Top of hill, E End of hill X_0=48H

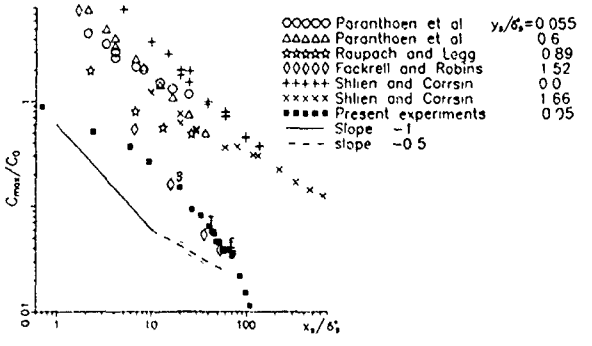

Fig 2 (concluded) Peak mean concentrations, present experiments

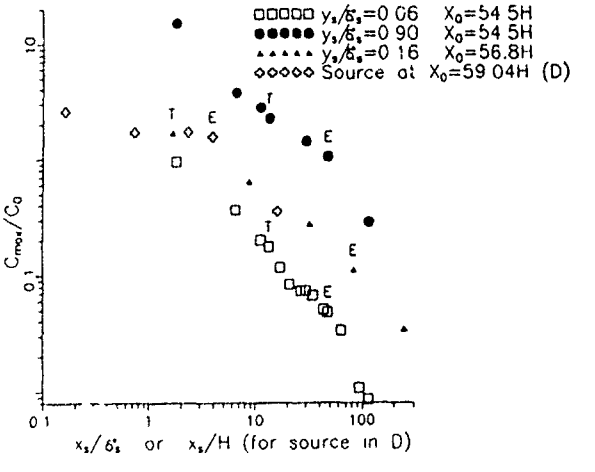

Fig 3 Wall mean concentrations for line and point sources in plane and curved (present work) surfaces B beginning of hill, T Top of hill, E End of hill X_0=48H Other symbols defined in Fig 2

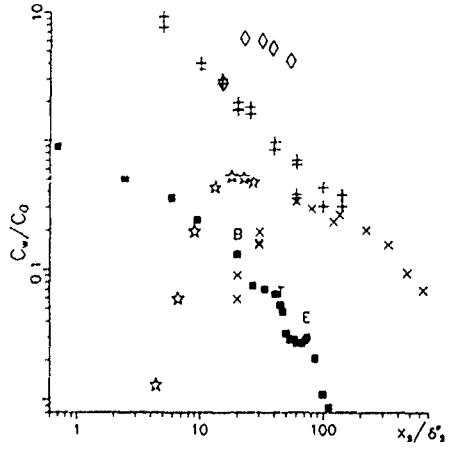

Fig 3 (concluded). Wall mean concentrations, present experiments Symbols as in Figure 2

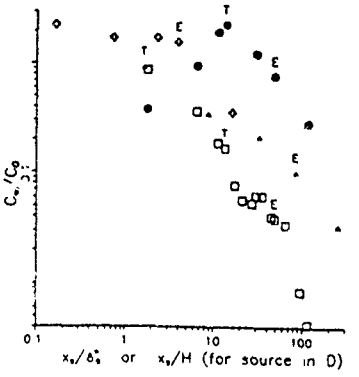

Fig 4 Relative intensity of concentration fluctuations

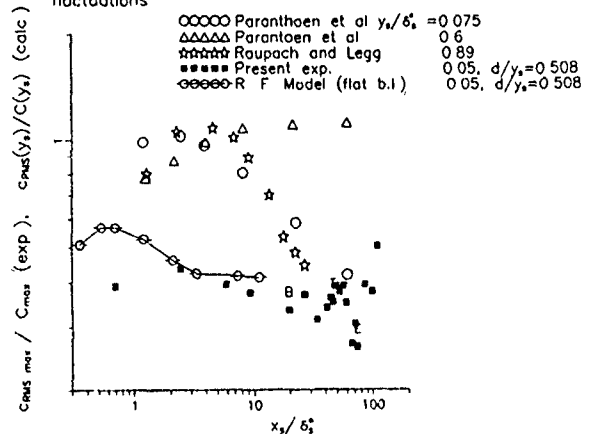

Fig 5. Centroid of mean concentration profiles ($\bar{Y}$ = mean particle displacement)

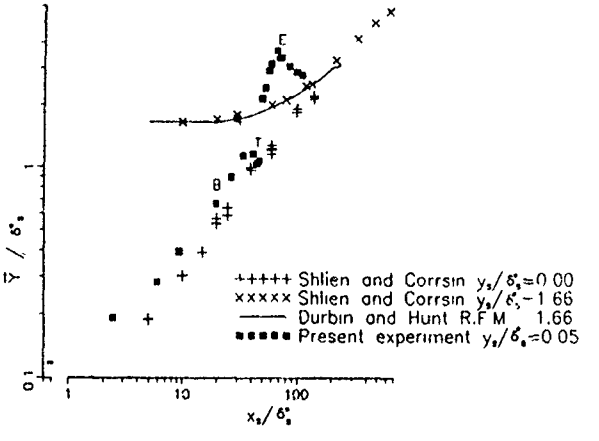

Fig 6. Second centroid centered moment of mean concentration profiles (= particle dispersion) Symbols as in Fig 1

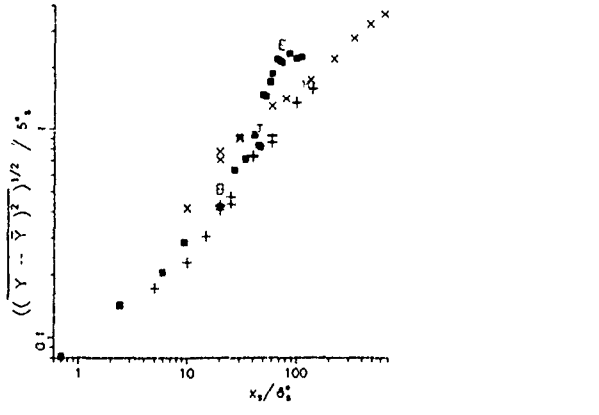

EIGHTH SYMPOSIUM ON
TURBULENT SHEAR FLOWS
Technical University of Munich
September 9-11, 1991

Large Eddy Simulation of Fully-Developed Turbulent Flow in a Straight Duct

M. D. Su and R. Friedrich
Lehrstuhl für Fluidmechanik
Technische Universität München, Germany

Abstract

Large-eddy simulations have been performed in straight ducts with square cross section at a global Reynolds number of 49000 in order to predict the complicated mean and instantaneous flow involving turbulence-driven secondary motion. Isotropic grid systems were used with spatial resolutions of $128 * 32^2$ and more. The secondary flow not only turned out to develop extremely slowly from its initial conditions but also to demand for fairly high resolution. The obtained statistical results are compared with measurements wherever possible.

1. Introduction

The study of fully-developed turbulent flow in straight ducts of square cross-section is of fundamental interest to fluid dynamicists and of practical importance in many engineering applications. In the past a considerable number of experimental and numerical investigations have been carried out Only few of the experimental data refer to really fully-developed flow and can be used for comparison with confidence The reason is that the secondary motion encountered in such noncircular ducts takes very long distances to reach a developed state (certainly more than 150 hydraulic diameters) and that the secondary velocities are very small (of the order of $2-3\%$ of the streamwise bulk velocity) and thus difficult to measure accurately. Most of the numerical investigations are based on the three-dimensional time-averaged Navier-Stokes equations incorporating different turbulence models up to SOC models The state of the art till 1982 is reviewed in Demuren & Rodi (1984) The nonlinear $k-l$ model of Speziale (1987) which has recently been applied by Hur et al. (1990) predicts the flow fairly well, however further work on model development is still desirable.

2. Basic equations and SGS model

We follow Schumann's approach (1975) of integrating the Navier-Stokes equations over the grid volume $\Delta V = \Delta x \Delta y \Delta z$ to obtain the basic filtered equations describing the transport of mass and momentum. In non-dimensional form they are

$$\sum_{j=1}^{3} \Delta A_j \left(\bar{V}_j(x_j + \Delta x_j/2) - \bar{V}_j(x_j - \Delta x_j/2) \right) = 0 \quad (1)$$

$$\Delta V \frac{d\bar{V}_i}{dt} + \sum_{j=1}^{3} [\, \Delta A_j (\bar{V}_j \bar{V}_i + \overline{V_j' V_i'} + \bar{p}\delta_{ij} - \bar{\tau}_{ji})|_{x_j + \Delta x_j/2} - \Delta A_j (\bar{V}_j \bar{V}_i + \overline{V_j' V_i'} + p\delta_{ij} - \bar{\tau}_{ji})|_{x_j - \Delta x_j/2} \,] = 0 \quad (2)$$

The filtered stress tensor is proportional to the filtered deformation tensor $\bar{D}_{ji}$ and reads:

$$\bar{\tau}_{ji} = \frac{1}{Re} \bar{D}_{ji} \qquad Re_b = \frac{H U_b}{\nu} \quad . \quad (3)$$

In (2) and (3) the $\bar{V}_i$ are averages over the cell-surface ΔA_i whereas $\bar{p}$ is defined as a cell-volume average and related to the cell center. (3) is solved in a staggered grid. The subgrid scale (SGS) stress $\overline{V_j' V_i'}$ is computed from a two-part eddy-viscosity model of the Schumann type, see Schmitt (1988). A leapfrog-scheme serves to integrate (3) in time. Chorin's projection method leads to a Poisson equation for the pressure correction which is solved at each time step with direct methods. A FFT of Poisson equation provides a set of decoupled two-dimensional Helmholtz problems which are solved with a cyclic reduction technique dueto Schumann & Sweet (1976). Artifical wall boundary conditions are used following ideas of Schumann (1975) and Piomelli et al. (1989).

3. Results

The flow and computational parameters refering to the presented results are summarized in Table 1.

Reynolds number $Re_b = HU_b/\nu$	49000
Domain size $L_x \cdot L_y \cdot L_z$	$(4 \cdot 1 \cdot 1)H^3$
Numbers of grid points $N_1 * N_2 * N_3$	128*32*32
Mesh volume	$(1/32)^3$
Numbers of time-steps	52000
CPU hours for time averaging, Cray YMP	24hr
Dimensionless time increment $\Delta t = \frac{\Delta T U_b}{H}$	0.025

Table 1. LES parameters

U_b is the bulk velocity. Figure 1 compares the computed mean streamwise velocity profile along the corner bisector (dashed line) with measurements of Brundett & Baines (1964), Gessner & Emery (1980) and with data of Demuren & Rodi's (1984) turbulence model. The LES result agrees well with these data but also with the turbulence model. Mean secondary velocity distributions along the wall bisector are shown in figure 2. The LES (dotted) profile is close to Naot & Rodi's (1982) prediction and Gessner et al's (1980) measurement at least what the maximum is concerned. Contours of the mean primary velocity ($< U/U_{max} >= 0.8, 0.9$) are plotted in figure 3 for comparison with experimental data of Gessner et al. (dashed-dotted line) and predictions discussed in Demuren & Rodi (1984). The LES result ($- \cdot -$) shows undulations in the contour lines which are due to insufficient spatial resolution. Finer grids will remove this effect. Mean secondary flow streamlines are presented in figure 4. The lower half of the diagram corresponds to the LES result, whereas the upper half is taken from Hur et al. (1990) showing predictions with Speziale's nonlinear model (1987) (curve C, $Re = 42000$) and computations of Nakayama et al. (1983) (curve B $Re = 83000$), as well as measurements of Gessner & Jones (1965) (curve A, $Re = 15000$). The Reynolds stress $- < U"W" >$ is compared in figure 5 (upper half) with Speziale's model (1987) (curve C) and measurements of Melling & Whitelaw (1976) (curve D). Undulations in the contour lines obtained from the LES are again a result of the central finite difference scheme used. Instantaneous V- fluctuations in fig. 6 taken from plane $y = H/2$ give an impression of large scale turbulence structures being convected through the duct.

Acknowledgment

The authors acknowledge the financial support of the work through the Deutsche Forschungsgemeinschaft. They are grateful to Dr. L. Schmitt for providing the code FLOWSI.

References

Brundett, E. & Baines W. D. JFM 19, (1964), p375.
Demuren A. O. & Rodi W. JFM 140, (1984), p189
Gessner, F. B. & Emery, A.F.
In *Turbulent Shear Flows 2 (1980)*, Springer Verlag.
Gessner F.B. & Jones J.B. JFM 23. (1965) , p689
Hur N.; Thangam S. & Speziale C.G.
J. Fluids Eng. 112 (1990) , p205
Melling A. & Whitelaw J. H. JFM 78 (1976), p289
Nakayama, A., Chow W.L. & Sharma D.
JFM 128 (1983) , p199
Naot D. & Rodi W. J. Hydr. ASCE 108 (1982) , p948
Piomelli U., Ferziger J. & Moin P.
Phys, Fluids A,1 (1989), p1061
Schmitt L. Dissertation. TU Munchen (1988)
Schumann U. JCP 18 (1975) , p376
Schumann U. & Sweet R.A. JCP 20 (1976) , p171
Speziale C G. JFM 178 (1987), p459

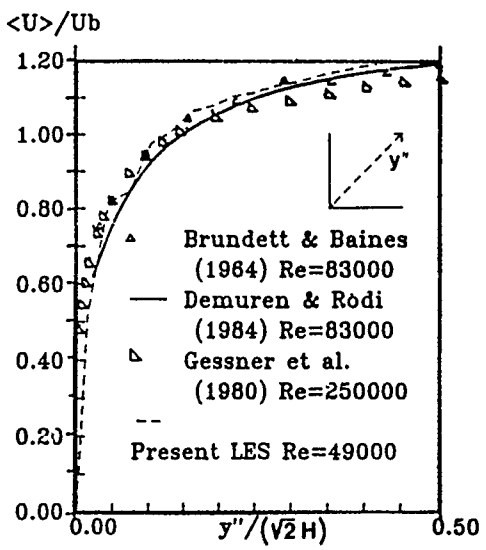

Figure 1: Primary velocity $< U > /U_b$ along corner bisector

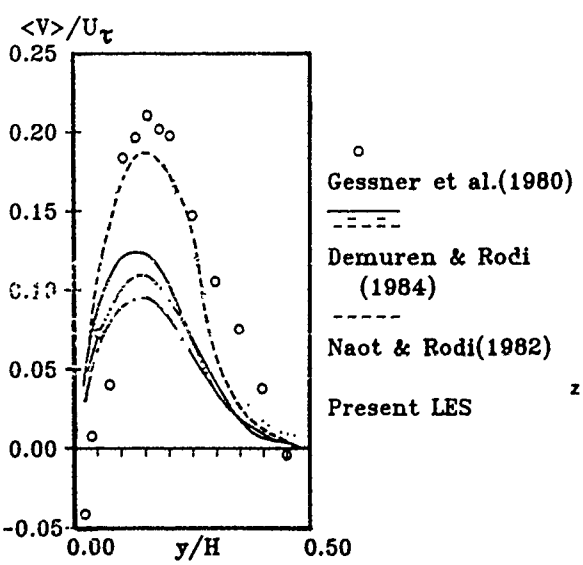

Figure 2: Secondary velocity $< V > /U_\tau$ along wall bisector

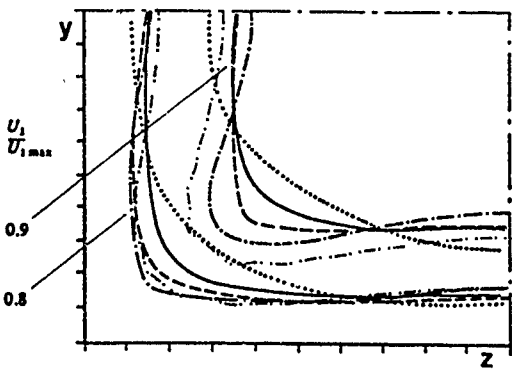

Figure 3: Contours of mean primary velocity: _____ and ····· Demuren & Rodi (1984); – – – – Naot & Rodi (1982), –·–·–· Gessner et al (1980); – ·· – ·· – Present LES

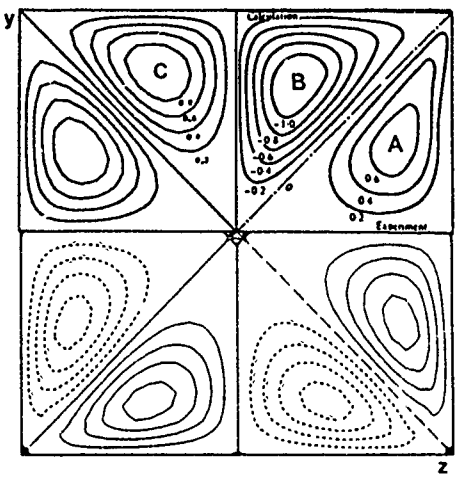

Figure 4: Mean secondary flow in straight square duct: A - Gessner and Jones(Re=15000); B - Nakayama et al. (Re=83000); C - Hur et al. (Re=42000); Other - Present LES (Re=49000)

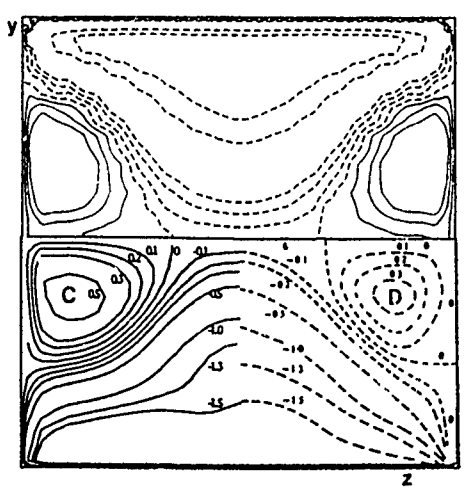

Figure 5: Contours of $< -U''W'' >$: D - Melling & Whitlaw; C - Hur et al.; upper half, present LES.

Figure 6: Contours of V" at $y = H/2$

EIGHTH SYMPOSIUM ON
TURBULENT SHEAR FLOWS
Technical University of Munich
September 9-11, 1991

THEORETICAL MODEL OF THERMOCLINE IN A FRESHWATER BASIN

S.S.Zilitinkevich*) and D.V.Mironov**)

*) RISØ National Laboratory, P.O.Box 49,
DK-4000 Roskilde, Denmark
**) Institute of Limnology, Sevastyanova str 9,
196199 Leningrad, USSR

ABSTRACT

Theoretical model of thermocline is proposed based on heat transfer equation, balance equation for turbulent kinetic energy and hypothesis on governing parameters of intermittent turbulence generated in a thermocline by breaking of internal waves and turbulence/waves interaction. The solution of a propagating-wave type obtained on this basis explains theoretically the approximate self-similarity of temperature profile in a thermocline of Kitaigorodskii & Miropolsky (1970) type The model contains two dimensionless constants whose values are found by means of comparison of the solution with the results of laboratory experiments on penetrative convection (Deardorff et al 1980). The results of numerical simulation of the thermocline in Deardorff & Willis (1982) experiments on shear flow in annulus show reasonable agreement with the laboratory data

1 Two striking empirical facts represent a starting point of the discussion:
(i) vertical temperature profile in a thermocline, a region of supercritical stability adjoining a turbulized layer, proves to be self-similar in a series of laboratory experiments and, though with much less accuracy, in natural water reservoirs (Kitaigorodskii & Miropolsky 1970),
(ii) comparison of the experimental data on kinematic heat flux Q and vertical temperature gradient dT/dz shows that the effective heat conductivity $K = -Q/(dT/dz)$ is much higher than the molecular one, and, rather unexpectedly, is higher the higher is $-dT/dz$, in contrast with the well-known inverse dependence of K on $-dT/dz$ which takes place in a weakly stable shear flows (Gill & Trefethen, unpublished; Turner 1978)

2 The following phenomenological expression for the temperature profile in the oceanic seasonal thermocline was suggested by Kitaigorodskii & Miropolsky (1970):

$$T = \begin{cases} T_s & at \quad 0 \le z \le h \\ T_s - \Delta T \vartheta(\zeta) & at \quad h \le z \le h + \Delta h . \end{cases} \qquad (1)$$

Here z is the depth; h is the mixed layer thickness, Δh is the thickness of the thermocline; ΔT is the temperature difference across it; ϑ is a function of dimensionless variable $\zeta = (z - h)/\Delta h$ satisfying the following boundary conditions: $\vartheta(0) = 0$, $\vartheta(1) = 1$
Laboratory experiments on deepening of the mixed layer in a stably stratified fluid (Linden 1975; Wyatt 1978) confirmed Eq (1) very well. The subsequent processing of the oceanic data, however, revealed so great a scatter of points on the empirical curves $\vartheta(\zeta)$ that the idea of self-similarity of a thermocline became doubtful (Miropolsky et al. 1970; Res' 'ova & Chalikov 1977). Mälkki & Tamsalu (1985) rehabilitated this idea to a certain degree on a phenomenological basis. They noted that the form of the function $\vartheta(\zeta)$ considerably depends on the behaviour of the mixed layer and obtained the following expressions as a result of processing the Baltic Sea data:

$$\vartheta = \begin{cases} 1 - (1 - \zeta)^3 & at \quad dh/dt > 0 \\ 1 - 4(1 - \zeta)^3 + 3(1 - \zeta)^4 & at \quad dh/dt \le 0 . \end{cases} \qquad (2)$$

3. The theoretical explanation of the self-similarity of thermocline in case of the mixed layer growth $dh/dt > 0$ was given by Turner (1978). He noted that the heat transfer equation

$$\frac{\partial T}{\partial t} = \frac{\partial}{\partial z} K \frac{\partial T}{\partial z} , \qquad (3)$$

where K is the effective heat conductivity, has the following self-similar solution of a propagating-wave type in the region $z > h(t)$ at $dh/dt = const > 0$.

$$T(z,t) = T(z') , \qquad where \quad z' = z - h(t) , \qquad (4)$$

which is easily reduced to the form given by Eq (1).
Turner took $K = -[l^2(dh/dt)/\Delta T]dT/dz$, where l is a length scale, and examined the thermocline development in a two-layer fluid, when the boundary conditions are

$$T = T_s \ at \ z = h, \quad T = T_a, \ dT/dz = 0 \ at \ z = h + \Delta h \quad (5)$$

The third one allows to determine the thermocline thickness Δh. At $T_a = const$, $\Delta T = const$ and $l = const$ the solution of the problem belongs to a class given by Eq.(4) and can be written as the second line of Eq.(1), where $\vartheta = 1 - (1 - \zeta)^2$, $\Delta h = 2l$ If T_s varies slowly with time such that $dT_s/dt \gg 2(dh/dt)\Delta T/\Delta h$, the above expression is no longer exact but an approximate solution
In support of his formula for the effective heat conductivity, Turner referred to Gill and Trefethen, who discovered that K in a thermocline increases with the increase of $-dT/dz$ (in contrast with the usual inverse dependence of K on $-dT/dz$ in weakly stable shear flows).

4. The direct dependence of K on $-dT/dz$ in thermocline can be caused by the following mechanism. The disturbances at the lower boundary of the mixed layer generate internal waves which transfer kinetic energy downwards. The occurrence of breaking waves manifests itself in generation of tur-

bulence spots, i.e. the waves expend a part of their energy for maintenance of intermittent turbulence. It is precisely the same mechanism as was implied in Turner (1978). Nevertheless in his formula for K the buoyancy parameter $\beta = g\alpha_T$ (where g is acceleration due to gravity and α_T is thermal expansion coefficient) was somehow overlooked.

Thus, the list of parameters governing the intermittent turbulence in a thermocline must include β, dT/dz and the length scale l, in which capacity Zilitinkevich et al. (1988) assumed the amplitude of disturbances at the mixed-layer/thermocline interface. Then the following formula for K is obtained due to the reasons of dimensionality:

$$K = C'_Q l^2 (-\beta dT/dz)^{1/2}, \qquad (6)$$

where C'_Q is a dimensionless constant.

Using Eq.(6) and solving Eqs (3),(5), we obtain

$$\vartheta = 1 - (1-\zeta)^3, \quad \Delta h = \frac{16}{27} C'^{-2}_Q (\beta \Delta T)^{-1} (dh/dt)^2, \qquad (7)$$

where the half thickness of the thermocline $\frac{1}{2}\Delta h$ serves as the vertical scale l for disturbances at the external boundary of the mixed layer.

The first formula of Eq.(7) coincides with the upper line of the empirical Mälkki and Tamsalu Eq.(2). The second one is confirmed by the data of laboratory experiments on deepening of the mixed layer due to the current shear (Kreiman 1982) and penetrative convection (Deardorff et al. 1980). At $(\beta \Delta T h)^{-1}(dh/dt)^2 > 10^5$ these data are reliably approximated by the expression $\Delta h/h = 7600(\beta \Delta T h)^{-1}(dh/dt)^2$, which gives $C'_Q = 10^{-2}$.

5. To include l into the set of unknown quantities, we make another step by supplementing Eqs (3),(6) with the balance equation of turbulent kinetic energy:

$$\partial e/\partial t = -\partial F/\partial z - \beta Q - \epsilon, \qquad (8)$$

where e is the turbulent kinetic energy per unit of fluid mass; $\beta Q = -\beta K dT/dz$ is the energy loss for overcoming of the buoyancy forces; ϵ and F are viscous dissipation rate and vertical flux of this energy.

We use the hypothesis, according to which β, dT/dz and l are the governing parameters of the turbulence regime under consideration. Then, due to dimensionality reasons, the following expressions for e, βQ, ϵ and F hold true:

$$e = C_E l^2 N^2, \quad \beta Q = C_Q l^2 N^3,$$
$$\epsilon = C_\epsilon l^2 N^3, \quad F = -C_F l^2 N \frac{\partial}{\partial z} l^2 N^2, \qquad (9)$$

where $N = (-\beta dT/dz)^{1/2}$ is the buoyancy frequency; C_E, C_Q, C_ϵ and C_F are dimensionless constants; l is the turbulence length scale. The same expressions for e and Q were obtained earlier by Ozmidov (1983) from consideration of the energy budget in a turbulent spot. The third expression of Eq (9) presents the vertical flux of energy in a traditional form as a product of a turbulent exchange coefficient ($\propto l^4 N$) and the vertical gradient of turbulent energy.

The system of Eqs.(3),(8),(9) is closed. With respect to the vertical coordinate it is of the second order relative to both T and l.

6. The suggested theoretical model is applied to calculation of the vertical structure of thermocline. The analytical solution of the propagating-wave type is obtained and compared with the results of Deardorff et al. (1980) penetrative convection experiments, which allowed to determine the dimensionless constants. Using these constants, numerical simulation of the temperature profile evolution in Deardorff & Willis (1982) shear flow experiments in annulus showed the qualitative agreement between theoretical and laboratory results.

REFERENCES

DEARDORFF, J.W. & WILLIS, G.E. 1982 Dependence of mixed-layer entrainment on shear stress and velocity jump. *J. Fluid Mech.* 115, 123-149.

DEARDORFF, J.W., WILLIS, G.E. & STOCKTON, B.H. 1980 Laboratory studies of the entrainment zone of a convectively mixed layer. *J. Fluid Mech.* 100, 41-64.

KITAIGORODSKII, S.A. & MIROPOLSKY, Yu.Z. 1970 On the theory of the open ocean active layer. *Izv. Akad. Nauk SSSR, Fizika Atmosfery i Okeana.* 6, 176-188.

KREIMAN, K.D. 1982 Laboratory modelling of turbulent entrainment in thermocline. *Trudy LGMI.* N77, 147-149.

LINDEN, P.F. 1975 The deepening of the mixed layer in a stratified fluid. *J. Fluid Mech.* 71, 385-405.

MÄLKKI, P. & TAMSALU, R. 1985 Physical features of the Baltic sea. *Finnish Marine Research.* N252, 110 p.

MIROPOLSKY, Yu.Z., FILYUSHKIN, B.N. & CHERNYSHKOV, P.P. 1970 On the parametric description of temperature profiles in the active ocean layer. *Okeanologiya.* 10, 1101-1107.

OZMIDOV, R.V. 1983 Small-scale turbulence and fine structure of hydrophysical fields in the ocean *Okeanologiya.* 23, 533-537.

RESHETOVA, O.V. & CHALIKOV, D.V. 1977 On the universal structure of the active layer in the ocean. *Okeanologiya.* 17, 774-777.

TURNER, J.S. 1978 The temperature profile below the surface mixed layer. *Ocean Modelling.* N11, 6-8.

WYATT, L R. 1978 Mixed layer development in an annular tank. *Ocean Modelling.* N17, 6-8.

ZILITINKEVICH, S.S., KREIMAN, K.D. & FELZENBAUM, A.I. 1988 Turbulence, heat exchange and self-similarity of the temperature profile in a thermocline. *Dokl. Akad. Nauk SSSR.* 300, 1226-1230.

EIGHTH SYMPOSIUM ON
TURBULENT SHEAR FLOWS
Technical University of Munich
September 9-11, 1991

Two-Scale Double-Layer model in Wall Bounded Turbulent Flow

Eran Arad and Micha Wolfshtein
Technion, Israel Institute of Technology

Abstract

A three equation turbulence model is presented. Two scale equations are used, for the large and for the small eddies. The viscous wall sub-layer is treated by a reduced one-equation model, which produces correct asymptotic behavior near the wall. The predictions of turbulent quantities near walls, are better than those obtained by previous two-equation models.

1. Introduction

1.1 Scale Formulation

Most two equations models use the dissipation rate as a measure of scale. Modeling of this equation is often considered unsatisfactory [1] Thus Bernard [2] reported poor modeling of the pressure diffusion term, while Mansour et al. [3] and Patel et al. [4] reported incompatible Low-Reynolds number damping functions, and wrong asymptotic behavior of turbulent quantities near walls [3]. In particular these drawbacks cause poor prediction of the near-wall peaks of the turbulent kinetic energy and dissipation rate [3]

A possible cause may be that single-point two-equation model requires the assumption of spectral similarity The problem may be overcome by a solution of the energy equation in the wave number space. Hanjalic, Launder and Schiestel [5], suggested a simplification by the use of a small number of domains in the wave number space, and a typical scale for each domain Following [5] we use in the present work two spectral domains, for the large and small eddies

A major difficulty is the rapid change in flow characteristics with the distance from solid walls. Wall-functions or solution up to the wall using Low Reynolds number corrections were severely criticized by several authors [2,3 4,6] On one hand it was shown that the existing Low Reynolds-number models do not provide correct asymptotic behavior near solid walls [3], and on the other hand, in many flows the validity of the Wall Functions assumptions is questionable [6]. An alternative approach, the use of double layer model [6], enables the diffusion of turbulent energy down to the wall, while the known length scale profile near the wall may be easily retained.

1.2 Present contribution

In this work we use two-scale model. a time scale equation for the big, energy carrying eddies and a dissipation equation for the small dissipative eddies. However, as the energy content of the small eddies is negligible, only one turbulent energy equation, for the big scales, is solved. The turbulent diffusion and production of energy are related to the energy and scale of the big eddies, (the time scale τ in this paper [7]), while the decay term in the energy equation is obtained from the high wave number scale (the dissipation rate ϵ). The triple equation model utilizes partial differential equations in the external part of the boundary layer only. In the inner region we follow the practice of Chen and Patel [6], and use a single equation model [8]. The two scales are calculated in the inner layer from algebraic relations and matched with the external solution at the interface. The algebraic scales are so devised as to ensure that they exhibit the correct asymptotic solution on the wall.

2. Presentation of Model

2.1 Outer domain Two-Scale Model

The variables of the triple equation model are the turbulent kinetic energy k, the turbulent time scale τ and the dissipation rate ϵ The energy equation is written in the following form:

$$\rho\frac{Dk}{Dt} = \frac{\partial}{\partial x_j}\left[\left(\mu + \frac{\mu_t}{\sigma_k}\right)\frac{\partial}{\partial x_j}k\right] + P_k - \rho D_k \qquad (1)$$

P_k is the production term and depends on the mean strain. The turbulent viscosity μ_t is calculated by the large-scale-model $k - \tau$, while the decay term is related to the dissipation rate model:

$$\mu_t = C_\mu \rho k \tau \qquad D_k = \epsilon \qquad (2)$$

The time scale equation is written after Zeierman and Wolfshtein [7]:

$$\rho\frac{Dk\tau}{Dt} = \frac{\partial}{\partial x_j}\left[\left(\mu + \frac{\mu_t}{\sigma_\tau}\right)\frac{\partial k\tau}{\partial x_j}\right] + C_{g_\tau}\tau P_k - \rho C_{d_\tau} k \qquad (3)$$

The dissipation rate equation is written in high Reynolds number form.

$$\rho\frac{D\epsilon}{Dt} = \frac{\partial}{\partial x_j}\left[\left(\mu + \frac{\mu_t}{\sigma_\epsilon}\right)\frac{\partial \epsilon}{\partial x_j}\right] + \rho\frac{\epsilon_p \epsilon}{k} - \rho C_{d_\epsilon}\frac{\epsilon^2}{k} \qquad (4)$$

using ϵ_p, the energy transfer rate related to the large scales, defined as follows:

$$\epsilon_p = C_{g_\epsilon}\frac{k}{\tau} \qquad (5)$$

The energy dissipation rate now responds only slowly to the applied mean strain, giving a better representation of a rapidly changing turbulence field. The decay term, on the other hand, depends only on the high wave number region.

2.2 Inner Domain

In the thin wall layer, a single equation for the turbulent energy is solved (eq(1)). Algebraic scales are used for calculation of the turbulent viscosity μ_t and the decay term:

$$\mu_t = \rho(C_\mu f_\mu y)\, k^{\frac{1}{2}} = \rho L_\mu k^{\frac{1}{2}} \qquad \epsilon = \frac{k^{\frac{3}{2}}}{L_\epsilon} \qquad (6)$$

Like in the external two-scale model, different length scales are specified for μ_t and ϵ. It is also consistent with asymptotic analysis of scales near the wall. It can be shown that the scales behave in the following manner for $y \to 0$:

$$\begin{aligned} L_\mu &= A_\mu y^2 - B_\mu y^3 + O(y^4) \\ L_\epsilon &= A_\epsilon y^3 - B_\epsilon y^4 + O(y^5) \end{aligned} \qquad (7)$$

It may be noted that at very small distances from the wall L_μ varies as y^2 while L_ϵ varies as y^3. In the outer part of the inner layer the scales are continuously approaching the values of the outer layer. The scheme is not sensitive to the location of matching interface, as long as it is kept beyond the viscous dominated zone.

3. Numerical Method

The present paper is limited to parabolic boundary layers flow. The solver used belongs to the OCI family and was developed by Israeli and Livne [9]. The scheme is of fourth order accuracy, and can produce rather accurate results with coarse mesh. The method retains the tri-diagonal form of the matrices, and is easy to solve. Implementation of the scheme to boundary layers was described in previous publications [10,11,12].

4. Results and Discussion

The test cases displayed below are a flat plate boundary layer [13], and a 2D diffuser AF0141 [1] (with strong adverse pressure gradient). The flat plat boundary layer is a case which allows reasonable agreement with experimental data. In the diffuser flows, large discrepancies have existed between computation and measurements [10]. Considering first the flat plate case, the solutions obtained by the two-scale double-layer method are compared with solutions obtained by two-equation models. The later are performed with either wall functions (WF) or Low Reynolds number solution up to the wall (SW). The measurements of Klebanoff [13] are also plotted. It is shown in figure 1, that the quality of the prediction of the energy peak near the wall is improved. The improvement is more significant in the presence of adverse pressure gradient: Plots of the kinetic turbulence energy for two x stations (Figures 2-3) show good agreement with experiment of the present model, while the k-l Low-Reynolds model fails to predict the energy peak. Good agreement was also obtained for other turbulent variables, like shear stress or ϵ, but the results are not displayed here because of limitation of space.

5. Conclusions

The two-scale model is highly flexible in treating wall flows. Yet it does not require much more computational resources than two-equation model. Computational results presented show that this model predicts well the turbulence quantities near the wall, where other models performance is poor. The model is now evaluated for other types of wall flows.

6. References

1. Kline S. J., Cantwell B. J. and Lilley G. M. (Ed.), The 1980-81 AFOSR-HTTM Stanford Conf. on Complex Turbulent Flows, Stanford Univ., 1981
2. Bernard P. S., AIAA J., Vol. 24, No. 4, 1986, pp.619-622.
3. Mansour N. N., Kim J. and Moin P., J. Fluid Mech., Vol. 194, 1988, pp.15-44.
4. Patel V. C., Rodi W. and Scheuerer G., AIAA J., Vol. 23, 1985, pp. 1308-1319.
5. Hanjalic E., Launder D. B. and Schiestel R., Proc. Turbulent Shear Flow 2, 1979, pp. 10.31-10.36.
6. Chen H. C. and Patel V. C., AIAA J., Vol. 26, No. 6, 1988, pp.641-648.
7. Zeierman S. and Wolfshtein M., AIAA J., Vol. 24, No. 10, 1986, pp. 1606-1610.
8. Wolfshtein M., int. J. of heat and Mass Trans., Vol. 12, 1969, pp. 301-318
9. Israeli M. and Livne A., Aerodynamic Laboratory Report No. 160-073, Technion, Israel, 1977 (in Hebrew)
10. Arad E. and Wolfshtein M., Proc. Turbulent Shear Flow 7, 1989, pp. 5.4.1-5.4.6.
11. Arad E. and Wolfshtein M., Int. Symp. on Comp. Fluid Dyn., Sydney, Aust., 1987.
12. Arad E. and Wolfshtein M., 16th. Cong. of Int. Council of Aero. Sci., Jerusalem, Israel, 1988.
13. Klebanoff P. S., NACA TN-3133, 1954.

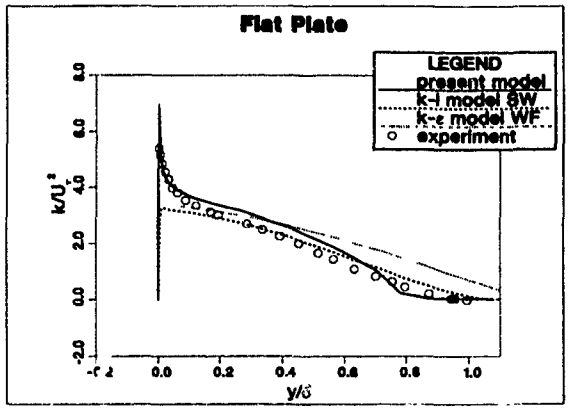

Fig 1: Turbulence kinetic energy profiles for a flat plate flow [13]

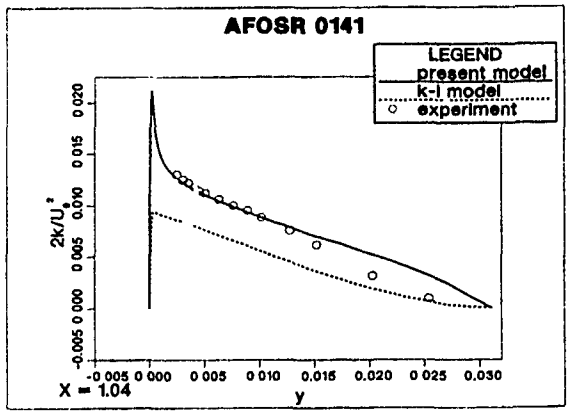

Fig 2: Turbulence kinetic energy profiles for a 2D diffuser flow, X=1.04 (AFOSR0141 [1])

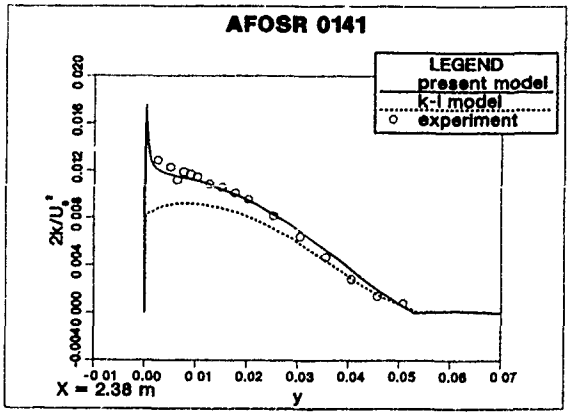

Fig. 3 Turbulence kinetic energy profiles for a 2D diffuser flow; x=2.38 (AFOSR0141 [1])

EIGHTH SYMPOSIUM ON
TURBULENT SHEAR FLOWS
Technical University of Munich
September 9-11, 1991

Analysis of turbulence models for hypersonic boundary layers

B. Aupoix J. Cousteix

ONERA/CERT
Department of Aerothermodynamics
2, Avenue E. Belin
BP 4025
31055 Toulouse Cedex France

ABSTRACT

The predictions of various turbulence models are compared for different compressible boundary layer experiments Algebraic models seem to be superior in the wall region while transport equations are required in the outer part of the boundary layer A two-layer model is thus proposed to improve the prediction

INTRODUCTION

For hypersonic airbreathing aircrafts, a good knowledge of the boundary layer development is important to precisely determine the boundary layer thickness at the engine inlet as well as the friction drag or the wall temperature

Such turbulent hypersonic boundary layers have some specific features the wall region can be thick and fill an important part of the boundary layer, compressibility effects on the turbulent motion are to be expected and should be accounted for in the turbulence model while significant heat transfer occurs in the boundary layer and must be accurately represented

Turbulence models commonly used to compute compressible boundary layers have first been reviewed. The key conclusion is that these models are often crude extensions of incompressible models and that compressible turbulence effects, when accounted for, are generally modelled by using approximations which are not Galilean invariants

COMPARISON WITH EXPERIMENTS

In order to evaluate the capabilities of models and to identify their main advantages and drawbacks, various algebraic, one- and two-equation models have been tested on a set of relevant experiments, using a boundary layer approach to have a fast, cheap and accurate numerical prediction The drawback of a boundary layer approach is that only a few test cases are available which really satisfy boundary layer hypothesis In addition, data on turbulent stresses and heat fluxes are rare The tested turbulence models are .

- A simple mixing length model, using Michel's mixing length formulation, Van Driest damping function, and a constant turbulent Prandtl number is used as a reference,
- The Cebeci-Smith model, with Pletcher's correction for low Reynolds number effects,
- The Baldwin-Lomax model,
- The CLIC model, which uses Cebeci-Smith model in the inner region and Michel's mixing length in the outer region,
- The one-equation model of Rubesin, in the compressible version used by Viegas and Horstman,
- The Jones-Launder $k-\varepsilon$ model,
- The compressible version of this model, as developed by Galmès and Dussauge, with a somewhat different set of coefficients tuned at CERT/DERAT,
- The Wilcox $q-\omega$ model

The prediction of three cases, which exhibit characteristic features encountered in the hypersonic boundary layers discussed above, are mainly detailed, i.e.

- An experiment performed by Owen and Horstman, of an hypersonic boundary layer , at a Mach number about 7.2, without pressure gradient, on a cold wall, to investigate the influence of high Mach numbers and compressiblity effects on turbulence,
- A supersonic boundary layer experiment performed by Carvin, at a Mach number about 2, without pressure gradient, on a hot wall, to investigate the influence of a hot wall and hence a thick wall region,
- A supersonic boundary layer experiment performed by Lewis, Gran and Kubota, with adverse and then favourable pressure gradients and Mach numbers ranging between 2.3 and 4, on an adiabatic wall, to investigate the influence of severe pressure gradients in compressible flows

The main conclusions of this comparison, which are now used as guidelines in the development of hypersonic turbulence models, are the following :

- As in transonic or incompressible flows, algebraic models are well suited to compute the wall skin friction or the wall heat flux, as the turbulence is in equilibrium in the wall region but give poor predictions of the velocity or temperature profiles for boundary layers submitted to severe pressure gradients (Fig. 1). On the contrary, transport equations models give poor predictions of wall values but fair predictions of the velocity or temperature profiles for boundary layers submitted to severe pressure gradients (Fig. 2).
- In the hypersonic case, a large discrepancy is observed between the experimental and computed turbulent stresses and heat fluxes A part may be due to experimental uncertainties The best prediction is achieved with the $k-\varepsilon$ models The scatter between the various predictions evidence the importance of compressibility corrections.
- A model which accounts for the increase of the turbulent Prandtl number in the wall region is needed to better predict the wall region over a hot wall. Viegas model, which predicts a decrease of the turbulent Prandtl number in the wall region, behaves poorly. The turbulent Prandtl number variations affect significantly the shape of the enthalpy/velocity diagram for adiabatic walls but have little influence on cold walls
- In the outer region of the boundary layer, the enthalpy/-velocity diagram is poorly reproduced as the decrease of the turbulent Prandtl number in the outer region and the sharp intermittency profile in hypersonic flows are not well represented by the models (Fig. 3).
- Many models are calibrated to reproduce the slope of the logarithmic law but usually fail to reproduce the intercept value. It is however possible to extend Granville's analysis to compressible flows to improve the intercept value prediction for algebraic models

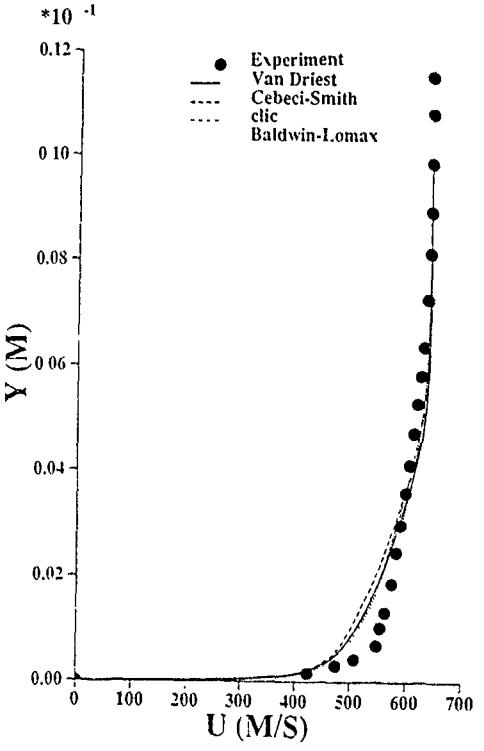

Fig 1 - Lewis et al experiment – Prediction of the velocity profile at the beginning of the favourable pressure gradient region – Algebraic models

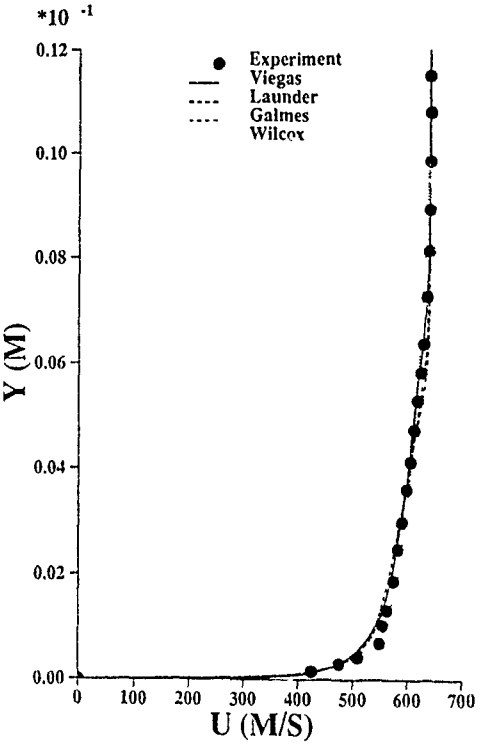

Fig 2 - Lewis et al experiment – Prediction of the velocity profile at the beginning of the favourable pressure gradient region – Transport equations models

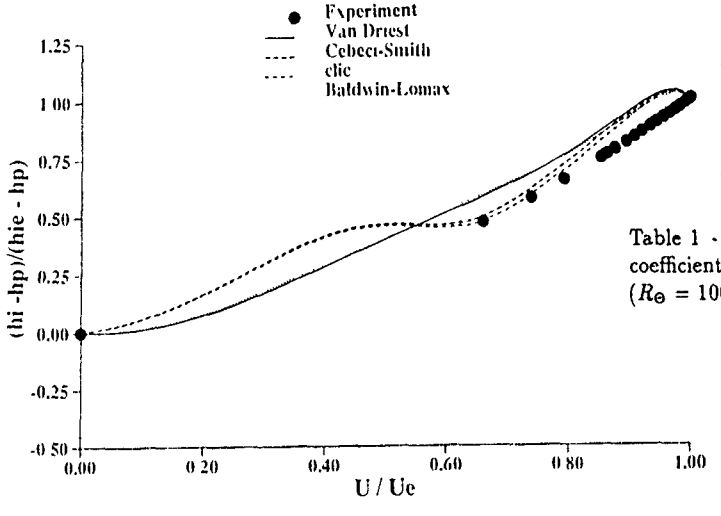

Fig 3 Lewis et al experiment – Prediction of the enthalpy/velocity diagram – Algebraic models

Mach	$10^3 C_f$ (Van Driest)	$10^3 C_f$ (Model)	Ratio
2	1.92	2.018	1 051
3	1 49	1.582	1.062
5	0.912	0.9960	1.092
8	0.504	0.5706	1.132

Table 1 - Two-layer model - Evolution of the skin friction coefficient versus Mach number for an adiabatic flat plate flow (R_Θ = 10000.)

T_w/T_{aw}	$10^3 C_f$ (Model)	$C_f/C_{f_{aw}}$	$2St/C_f$
0.2	1.458	1.464	1.204
0 4	1.311	1.316	1.208
0.6	1.186	1.191	1.211
0 8	1.082	1 087	1.213

Table 2 - Two-layer model - Evolution of the skin friction coefficient versus Mach number for a Mach 5 flat plate flow (R_Θ = 10000)

• The Baldwin-Lomax model, which is often presented as a derivation of Cebeci-Smith model to allow an easier implementation in Navier-Stokes codes, does not include some features of the Cebeci-Smith model such as a variable turbulent Prandtl number or a pressure gradient term in the wall damping function and behaves quite poorly at high Mach numbers. The numerical properties of the model, especially for transport equation models, are important to allow an easy implementation.

TWO-LAYER MODEL

From the above conclusions, a two-layer model is proposed. In the wall region, a simple one-equation model, which is a revised version of the Norris-Reynolds model, is used together with a revised form of the Galmès and Dussauge $k-\varepsilon$ model in the outer region A constant turbulent Prandtl number is presently used but this must be improved. Results of first tests, on the skin friction coefficient and Stanton number variations for a flat plate flow at R_Θ = 10000 , are presented on tables 1 and 2

EIGHTH SYMPOSIUM ON
TURBULENT SHEAR FLOWS
Technical University of Munich
September 9-11, 1991

Characteristics of the Velocity Field in the Central Region of a Spirally Fluted Tube

by

D. S. Babikian and J. C. LaRue
Department of Mechanical and Aerospace Engineering
University of California, Irvine
Irvine, California 92717

H. R. Rahai
Mechanical Engineering Department
California State University, Long Beach
Long Beach, California 90840

Abstract

An experimental study of the effect of swirl on the turbulent flow in a tube is presented herein. The mean rotation is produced by means of small spiral flutes on the tube wall. The flutes are found to lead to a mean fluid rotation rate which, except very near the fluted surface, is much less than that which would correspond to the mean velocity and flute angle The flutes also have an unexpected effect on the mean axial velocity. For example, near the flute valley, the radial gradient of the mean axial velocity is significantly reduced relative to that for a smoothe tube at the same Reynolds number and relative distance from the tube wall while that near the crest is unchanged. As expected, the effect of swirl on the turbulent velocity fluctuations is to reduce the radial component. The azimuthal turbulent velocity component is also reduced while at some radial locations, the axial turbulent velocity component is increased.

Introduction

The goal of the present study is to investigate the effect of swirl on the turbulent velocity field in a tube flow where the swirl or mean azimuthal velocity does not vary with downstream distance. This type of flow is of both fundamental and applied interest. From a fundamental point of view, it is expected (cf. Bradshaw (1973)) that the swirl should lead to a reduction in the root mean square of the turbulent radial velocity component. Tubes with swirling flows have been produced by means of tangential injection, twisted tape inserts, wall slots, rotating tubes, and spiral flutes. However, only tube flows with swirl produced by means of small spiral flutes are found to have pressure drops that are nearly the same as found in corresponding smoothe tube flows (cf Yampolsky (1979)) For this reason, a spirally fluted tube, similar to that used by Yampolsky is used in the present study.

Apparatus and Procedure

A centrifugal air compressor is used to supply filtered laboratory air at a steady flow rate. The air, which is heated to about $30°C$ above ambient by the air compressor, is sent through a set of flow straighteners located in a $5.1cm$ diameter pipe that is just upstream of the $4.0m$ long test section. The downstream $2.4m$ of the test section is centrally placed in a $7.0cm$ diameter tube. Water at a constant flow rate is passed through the annulus formed by the two tubes so as to maintain a constant test section wall temperature of about $38.4°C$. The sensing volume of the probe is placed $0.5mm$ downstream of the exit plane of the test section and is mounted on a vertical traverse which has a radial position resolution of $0.254mm$.

A sketch of the spiral multi-fluted aluminum tube is shown in Fig. 1. The mean radius, R, of the tube, which is measured from the centerline to a position midway between the crest and the valley, is $1.4cm$. The flute height, h, is $0.168cm$ and the flute spacing, S, is $0.235cm$. There are 30 flutes equally spaced around the tube circumference. The angle of the flutes relative to the tube axis, ϕ_f, is 30°. The length to diameter ratio of the test section is about 142. Thus, the flow should be fully developed at the measuring station.

The average or bulk velocity and corresponding Reynolds number are, respectively, $29.8m/s$ and $2.64x10^4$. Comparisons are made to the smoothe tube data of Laufer (1953), Sandborn (1955), and Schildnect et al. (1979) which corespond to bulk Reynolds numbers of 4.49, 4.48, and $1.72x10^4$.

The probe used for the measurements consists of three sensors. Two hot wire sensors, $1.25mm$ in length and $3.8\mu m$ in diam., in an "X" configuration which are separated by $0.5mm$, are used to measure two time-resolved velocity components. In addition, a cold wire sensor, $1.0mm$ in length and $0.625\mu m$ in diam., is mounted normal to the plane of the "X" array, $0.6mm$ upstream of the center of the "X" array. The frequency responses of the hot- and cold-wires are 30 and $8kHz$ respectively. All are calibrated both before and after the collection of data.

The voltages from the two constant temperature anemometers and the A.C. Wheatstone bridge are passed through calibrated buck and gain amplifiers which remove the mean voltage and amplify the fluctuating portion of the signal so for recording on an FM instrumentation tape recorder which has a frequency response of $10kHz$. The recorded signals are played back, low passed filtered at $10kHz$, and digitized at a sample rate of 10240 samples/sec by means of a Tustin 14 bit AD converter which is equipped with simultaneous sample and hold circuits. The data triplets corresponding to $30sec$ of data are analyzed an LSI 11/23 computer.

Two types of data sets are obtained and analyzed. The first set starts at a flute crest, called hereafter crest data, and extends past the center of the tube The second set starts at the flute valley, called hereafter valley data, and extends past the center of the tube

Results and Discussion

The radial profiles of the mean axial velocity normalized by the centerline mean axial velocity plotted as a function of distance from the centerline are shown on Fig. 2. For $(1 - r/R) > 0.15$, the mean axial velocity profiles for the crest and valley data are nearly the same. However, at the same position relative to the centerline, the mean axial velocities for both the crest and valley data are generally lower than the values for the corresponding smooth tube flow. For $(1 - r/R) < 0.15$, the radial gradient of the mean axial velocity for the flute data is less than that for the crest data.

The radial distribution of the mean azimuthal velocity normalized by the centerline velocity for both the crest and valley data are presented in Fig. 3. As expected, the azimuthal velocity is nearly zero at the centerline and rises to a maximum at a circumference corresponding to the crest. The apparent differences in the mean azimuthal velocity for the valley and crest data in the range $0.2 \leq (1 - r/R) \leq 0.6$ are small and probably correspond to the uncertainty in the data. The gradient in the mean azimuthal velocity in the radial direction varies as a function of position. Thus, the fluid is not in solid body rotation.

The intensities of the axial, radial, and azimuthal velocities

normalized by the local mean velocity along with the corresponding smooth tube data are shown in Fig. 4. For both the crest and valley data, the distributions of the root mean square (rms) axial velocity normalized by the centerline velocity are a few percent higher than the corresponding smooth tube data of Schildknecht et al. (1979) and for the mid-radius positions are about 12% higher than the corresponding smooth tube data of Laufer (1953). This slight increase in the axial rms velocity may be due to the swirl which is anticipated to lead to a transfer of turbulent kinetic energy from the fluctuating radial velocity to the fluctuating axial velocity component (cf. Bradshaw (1973)).

Consistent with the hypothesized stabilizing or reducing effect of swirl on the radial velocity fluctuations, the normalized rms radial velocity for $(1 - r/R) \geq 0.1$ for both the crest and valley data is found to be about 14% less than the corresponding smooth tube data.

The normalized rms azimuthal velocity for $(1 - r/R) \geq 0.1$ is about 20% less than the corresponding smooth tube data and about 60% of the rms axial velocity. The reason for the reduction in the rms azimuthal velocity is not clear.

Conclusions

The mean axial velocity profiles in the spiral fluted tube differ from those in a smooth tube. This difference is especially obvious in the valley data where it can be seen that the mean axial velocity can be reduced by as much as 40% compared to the smooth tube values at the same relative distance from the tube surface. Away from the fluted surface, the mean velocity profiles for both the crest and valley data are nearly the same.

The radial gradient of the mean axial velocity for the valley data is about 40% of the corresponding smooth tube value while the radial gradient of the mean axial velocity for the crest data is only slightly less than the corresponding smooth tube value.

The presence of the flutes does induce a mean swirl to the flow but the flow is not in solid body rotation. Near the crest, the rotation rate is only about 35% of that which would correspond to solid body rotation.

The rotation of the flow is seen to lead to a transfer of turbulent kinetic energy from the radial to the axial component.

References

Bradshaw,P., 1973, AGARDograph NO. 169, N.A.T.O

Laufer, J , 1953, "The Structure of Turbulence in Fully Developed Pipe Flow," N.A.C.A., Technical Note 2954.

Sandborn, V.A., 1955, "Experimental Evaluation of Momentum Terms in Turbulent pipe Flow," N.A.C.A Technical Note 3266.

Schildknecht, M., Miller, J.A., and Meier, G E.A., 1979, "The Influence of Suction on the Structure of Turbulence in Fully Developed pipe Flow," J. Fluid Mech., Vol. 90, Part 1, pp. 67-107.

Yampolsky, J.S., 1979, "Spirally Fluted Tubing for Augmented Heat Transfer," General Atomic Report GA-A15442.

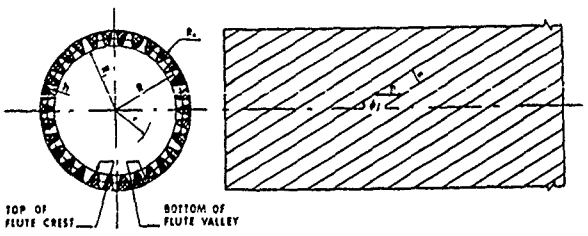

Figure 1: Sketch of spiral fluted tube.

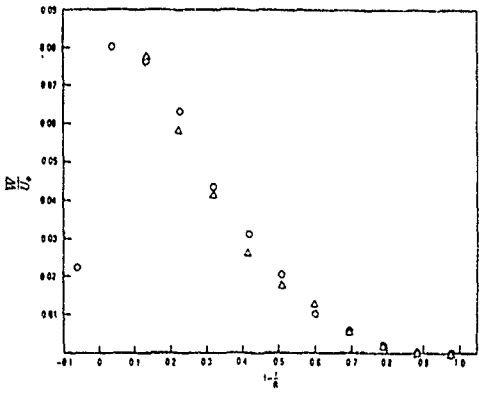

Figure 2: Radial variation of mean axial velocity normalized by the centerline velocity plotted along a radius as a function of radial position measured relative to the centerline: crest to centerline, △; valley to centerline, ○; smooth tube data of Laufer (1953), ◇; smooth tube data of Schildknecht et al. (1979), ▽; and, smooth tube data of Sandborn (1955), □.

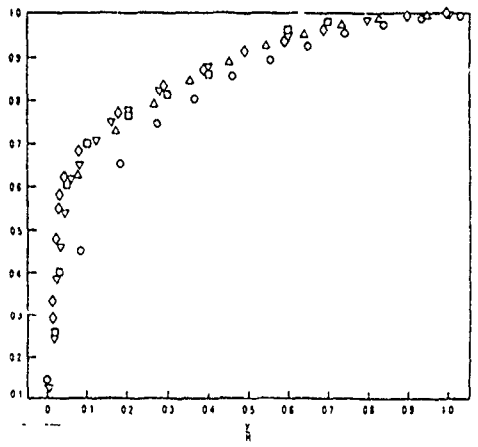

Figure 3: Radial variation of mean azimuthal velocity normalized by the mean axial velocity on the centerline. Symbols have the same meaning as in Fig. 2

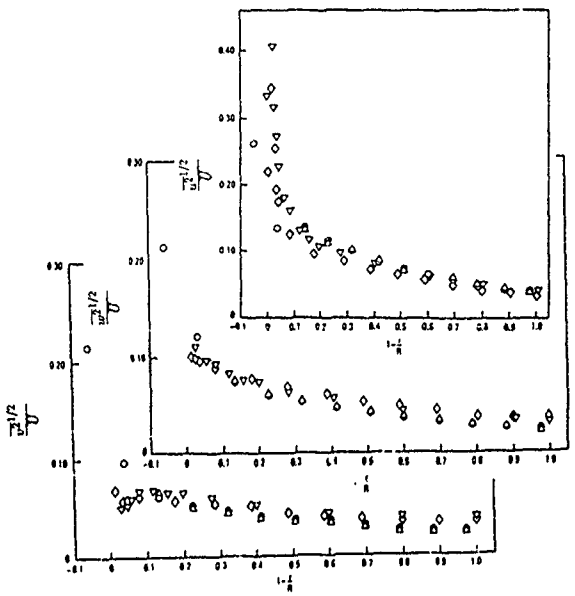

Figure 4: Radial variation of rms axial velocity (top), rms radial velocity (middle), and rms azimuthal velocity (bottom) normalized by the local mean axial velocity. Symbols have the same meaning as in Fig. 2.

EIGHTH SYMPOSIUM ON
TURBULENT SHEAR FLOWS
Technical University of Munich
September 9-11, 1991

A new model for premixed turbulent combustion based on direct simulation results

By Boudier P.[1], Dillies B.[2],
Veynante D., Lacas F. and Poinsot T.

Laboratoire EM2C, Ecole Centrale de Paris
Chatenay Malabry 92295, France
[1] IFP, Rueil Malmaison, FRANCE
[2] PSA, Velizy, FRANCE

1. Introduction

Turbulent combustion models based on the flamelet concept assume that the turbulent reaction zone may be viewed as a collection of laminar flame elements. Under this approach, a central parameter for combustion modelling is the stretch of a flame surface A which is defined by (Candel and Poinsot 1990):

$$K = \frac{1}{A}\frac{dA}{dt}. \quad (1)$$

Small to moderate flame stretch creates active flame surface while high stretch leads to flame quenching. Different expressions may be found in the literature for the mean flame stretch (averaged along the flame front) $\overline{K}$. Considering that small scales control flame stretch, Cant and Bray (1987) propose

$$\overline{K} = \sqrt{\epsilon/\nu}, \quad (2)$$

where ϵ is the dissipation of turbulent kinetic energy and ν is the kinematic viscosity.

Candel et al. (1990) assume that large scales are more relevant to estimate flame stretch and use

$$\overline{K} = \epsilon/k. \quad (3)$$

where k is the turbulent kinetic energy.

These expressions do not take into account any of the flame characteristics and neglect partial quenching of the flame front. A more precised analysis is proposed by Meneveau and Poinsot (1991) who combine a spectral approach with results of direct simulations. The resulting model for the stretch $\overline{K}$ is implemented here in the Coherent Flame Model (CFM) and used to compute a turbulent premixed flame stabilized by a stream of hot gases.

2. The CFM for premixed turbulent combustion

In the Coherent Flame Model (Candel et al 1990), the reaction zone is viewed as a collection of flamelets embedded in the turbulent flow. The mean turbulent reaction rate $\overline{\dot{w}}$ is expressed as the product of the flame area per unit volume Σ by the consumption rate per unit of flame surface w_L.

$$\overline{\dot{w}} = w_L\Sigma. \quad (4)$$

The Coherent Flame description combines three elements:

1) a model of the turbulent flow.

2) a local model providing w_L which is a function of temperature, local stretch rate, local equivalence ratio and may be obtained from numerical computations through a laminar flamelet library (Darabiha et al 1987).

3) a balance equation for the flame area density which, following the initial work of Marble and Broadwell (1977), may be written:

$$\frac{\partial\Sigma}{\partial t} + \frac{\partial\Sigma u_i}{\partial x_i} = \frac{\partial}{\partial x_i}\left(\frac{\mu_t}{\sigma_\Sigma}\frac{\partial\Sigma}{\partial x_i}\right) + \tilde{K}\Sigma - Q_c, \quad (5)$$

where $\tilde{K}$ is the mean stretch rate and Q_c corresponds to flame surface annihilation by mutual interaction of flame fronts.

3. A model for flame stretch based on direct simulation

Meneveau and Poinsot (1991) propose an estimate of the flame mean stretch by combining different approaches:

(1) Use of direct simulations of flame / vortex interactions to predict the effect of a given isolated structure on a laminar flame front (Poinsot et al 1990).

(2) Use detailed experimental data about intermittent turbulence to determine the distribution of stretch along the flame front (Meneveau and Sreenivasan 1987).

(3) Define a net stretch of the flame surface by substracting the rate of destruction by quenching from the rate of increase due to hydrodynamic straining.

This ITNFS model accounts for viscous, curvature and transients effects but neglects non-linearities and flame generated turbulence when deducing the net stretch rate. However, it represents a substantial improvement on classical estimates of the flame stretch. For the present work, it is combined with the CFM to provide (see Meneveau et Poinsot 1991) an expression for the flame stretch

$$\overline{K} = f\left(\frac{u'}{s_L}, \frac{L}{l_F}\right) \quad (6)$$

where u' is the RMS turbulent velocity, L is the integral length scale in the fresh gases, s_L is the laminar flame speed and l_F is the laminar flame thickness. A typical set of ITNFS results is given in Fig. 1. $\overline{K}$ is scaled by the small scales stretch $\sqrt{\epsilon/\nu}$. Regions where $\overline{K}$ is negative indicate global flame quenching.

4 Numerical validation

The model is tested in the case of a two dimensional turbulent premixed flame stabilized in a square duct (100 mm x 100 mm) by a parallel flow of hot gases.

The experimental setup (Fig. 2) was built by P. Moreau at ONERA (France). The combustion of a premixed air-methane flow - 60 m/s fast and 600 K hot - is ignited and stabilized by a flow of stoechiometric burnt products - 120 m/s and 2000 K hot -. The turbulence level of the premixed gases is about 10 percent and the equivalence ratio is 0.8 . The experimental data which were obtained are two transverse profiles for axial velocity (Laser Doppler Velocimetry) and two transverse profiles for temperature (Coherent Anti Stoke Raman Spectroscopy).

The agreement between numerical results and experimental data is fairly good both for temperature profiles (Fig. 3) and axial velocity profiles (Fig. 4). This approach combining the ITNFS analysis of Meneveau and Poinsot and the Coherent Flame Model seems to be promising but needs, of course, further validations.

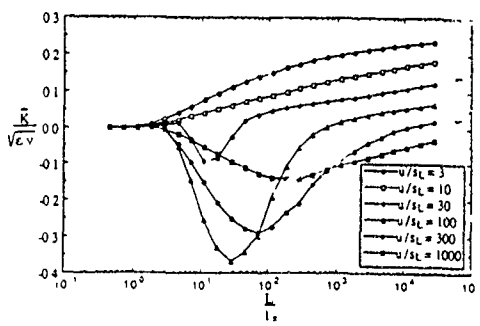

Fig 1 Typical set for the mean ITNFS stretch.

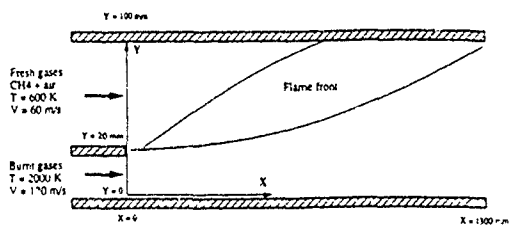

Fig 2 . Experimental setup.

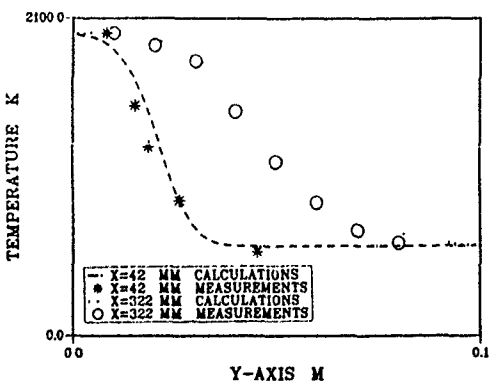

Fig 3 . Comparison of temperature profiles.

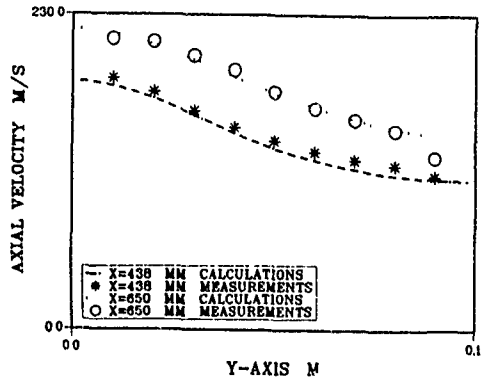

Fig 4 . Comparison of axial velocity profiles.

References

CANDEL S.M. ET POINSOT T. 1990 Flame stretch and the balance equation for the flame area. *Combus. Sci. and Tech.*, **70**, 1-15

CANDEL S., VEYNANTE D., LACAS F., MAISTRET E., DARABIHA N. AND POINSOT T.: *Coherent flame model: applications and recent extensions*, Recent Adv. in Combustion Modelling, B. Larrouturou ed., Series on advances in mathematics for applied sciences, World Scientific, Singapore, 1990 .

CANT R. AND BRAY K.: *Twenty Second Symposium (International) on Combustion*, Strained laminar flamelet calculations of premixed turbulent combustion in a closed vessel, 1988 p. 791, The Combustion Institute.

DARABIHA N., CANDEL S. AND MARBLE F 1986 The effect of strain rate on a premixed laminar flame *Combus. and Flame*, **64**, 203.

MARBLE F.E. AND BROADWELL J.: *Project SQUID*, The coherent flame model for turbulent chemical reactions, 1977 Report TRW-9-PU.

MENEVEAU C. AND POINSOT T. 1991 Stretching and quenching of flamelets in premixed turbulent combustion. *Combus. and Flame*, , to appear.

MENEVEAU C. AND SREENIVASAN K.R. 1987 The multifractal spectrum of the dissipation field in turbulent flows. *Nucl. Phys. B Proc. Suppl.*, **2**, 49.

MOREAU P. AND BOUTIER A.: *Sixteenth Symposium (International) on Combustion*, Laser velocimeter measurements in a turbulent flame, 1976 p. 1747, The Combustion Institute.

MOREAU P : *Fifteenth Aerospace Sciences Meeting*, Turbulent flame development in a high velocity premixed flow, 1977 Los Angeles, AIAA paper 77-49.

MOREAU P.: *Eighteenth Symposium (International) on Combustion*, Experimental determination of probability density functions within a turbulent high velocity premixed flame, 1980 The Combustion Institute, p. 993.

POINSOT T., VEYNANTE D. AND CANDEL S : *J. of Fluid Mech.*, Quenching processes and premixed turbulent combustion diagrams, 1990 228, p. 561.

POINSOT T., VEYNANTE D. AND CANDEL S.: *Twenty Third Symposium (International) on Combustion*, Diagrams of premixed turbulent combustion based on direct simulation, 1990 The Combustion Institute.

EIGHTH SYMPOSIUM ON
TURBULENT SHEAR FLOWS
Technical University of Munich
September 9-11, 1991

INVESTIGATION OF NO_x FORMATION IN TURBULENT NONPREMIXED FLAMES: HYDROGEN-AIR JET FLAMES

J.-Y. Chen*), W. Kollmann**)

*) Combustion Research Facility, Sandia National Laboratories, Livermore, CA 94551-0969, Research supported by the United States Department of Energy, Office of Basic Energy Sciences, Division of Chemical Sciences.
**) MAME Department, University of California at Davis, CA 95616

As a first step toward a better understanding of NO_x formation in turbulent flames, a partial equilibrium chemical model for hydrogen-air combustion is incorporated into a hybrid pdf method, in which the flow field is calculated based on a second moment model. Production of NO_x is assumed to be dominated by the Zeldovich mechanism

$$N_2 + O \rightleftharpoons NO + N \qquad (R1)$$

$$N + O_2 \rightleftharpoons NO + O \qquad (R2)$$

$$N + OH \rightleftharpoons NO + H. \qquad (R3)$$

With the assumption of a steady state for the N atom and $NO/NO_{equil} \ll 1$, the NO formation rate can be approximated by

$$S_{NO} \approx 2k_{f,r1} \cdot N_2 \cdot O$$

Other possible routes for NO formation, such as reactions involving intermediate N_2O, are not considered. To evaluate the possible effects of radiation heat loss on the NO_x formation, a radiation model that approximates the maximum heat loss is included (i.e., with the assumption of optically thin limit).

Numerical calculations have been performed for turbulent jet flames with a fuel mixture of 78%H_2 and 22%Ar. In the past, extensive measurements of these flames have been performed (e.g., Magre and Dibble, 1988) providing us data for comparisons with predictions for flow and scalar fields. Figure 1 presents a comparison of predicted and measured centerline profiles for mean velocity and density showing reasonable agreement. For adiabatic flames, Figure 2 shows the predicted NO_x emission index profiles versus $(U_f - U_{co})/D_f$, which is proportional to the reciprocal of the Damkohler number if the chemical time scale is constant. Two different normalization parameters are used. In Fig. 2a, the NO_x emission index has been normalized by a group of variables which scales with the global flame residence time if the flame volume scales with the cubic of the flame length. However, the normalized NO_x emission index profiles do not collapse to a single curve indicating that in the present unconfined coflowing turbulent jets, the flame volume does not remain similar in shape as the jet diameter is changed. In Fig. 2b, the global flame residence time suggested by Becker and Liang (1978) is used for normalization, and all the results collapse to a single curve. More importantly, the current model predicts the 1/2 slope trend over the large Damkohler regimes as has been observed in the experiment by Chen and Driscoll (1990). However, the model predicts a flat trend when the Damkohler becomes small.

Figure 3 presents the predicted NO_x emission index profiles obtained with and without the radiation heat loss for a fixed jet diameter. Due to the complex nature of radiation transfer, the current radiation model represents the maximum possible heat loss that would occur in the flame. With the radiation heat loss, the NO_x emission index reduces significantly for low velocity jet flames. Moreover, the NO_x emission index trend is totally opposite to that for adiabatic flames in the low jet velocity range. This reverse trend has been observed in turbulent hydrocarbon jet flames (Turns and Lovett, 1989) where substantial radiation heat loss may occur due to the presence of soot. As the jet velocity increases (the flame residence time decreases), the effect of radiation heat loss become less important but it still has influence on the magnitude of the NO_x emission index.

Fig. 4 shows the emission index obtained with the nonequilibrium model and the equilibrium model for round jet flames (upper part of the figure) and for plane jet flames (nonequilibrium model only, lower part of the figure). In contrast to the nonequilibrium jet flames, EI_{NO_x}/τ_R for equilibrium remains almost constant (within the statistical uncertainty) for all jet velocities. As suggested in the scaling parameter section, in the limit of equilibrium chemistry, EI_{NO_x}/τ_R approaches a constant value only if the flame geometry is not a function of flow parameters. This implies that the one-half power dependence is due to the dependence of thermal NO on the flame Damköhler number.

References

Becker, H. A. and Liang, D., "Visible Length of Vertical Free Turbulent Diffusion Flames," *Combustion and Flame*, **32**, 115-137 (1978).

Chen, R.-H. and Driscoll, J. F., "Nitric Oxide Levels of Jet Diffusion Flames: Effects of Coaxial Air and Other Mixing Parameters," *Twenty-Third Symposium (International) on Combustion*, Orleans, (1990).

Magre, P. and Dibble, R. W., "Finite Chemical Kinetics Effects in a Subsonic Turbulent Hydrogen Flame," *Combustion and Flame*, **73**, 195-206 (1988).

Turns, S. R. and Lovett, J. A., "Measurements of Oxides of Nitrogen Emissions from Turbulent Propane Jet Diffusion Flames," *Combust. Sci. and Tech.*, **66**, 233-249 (1989).

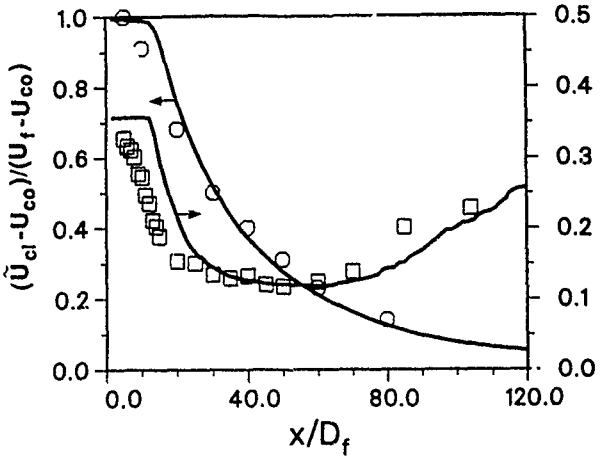

Fig. 1 Centerline velocity and density profiles for a 78%H_2 +22%Ar turbulent jet flame with U_f=225 m/s, U_{co}= 9.2 m/s and D_f=5.2 mm. Symbol: experimental data; lines: predictions

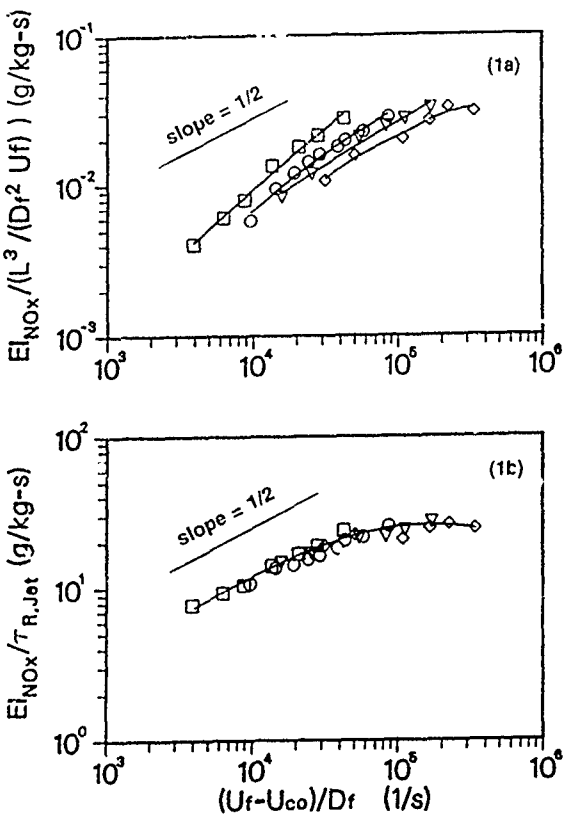

Fig. 2. Predicted NO_x emission index profiles vs. 1/Damköhler number with various fuel jet diameters: ⊔ 10.4 mm; ○ 5.2 mm; ▽ 2.6 mm; ◇ 1.3 mm. (1a) normalized by flame length, jet diameter and jet velocity. (2a) normalized by the residence time for jet flames (Becker and Liang, 1978). Results show an approximate 1/2 slope dependence for large Damköhler numbers consistent with the experimental observation by Chen and Driscoll (1990).

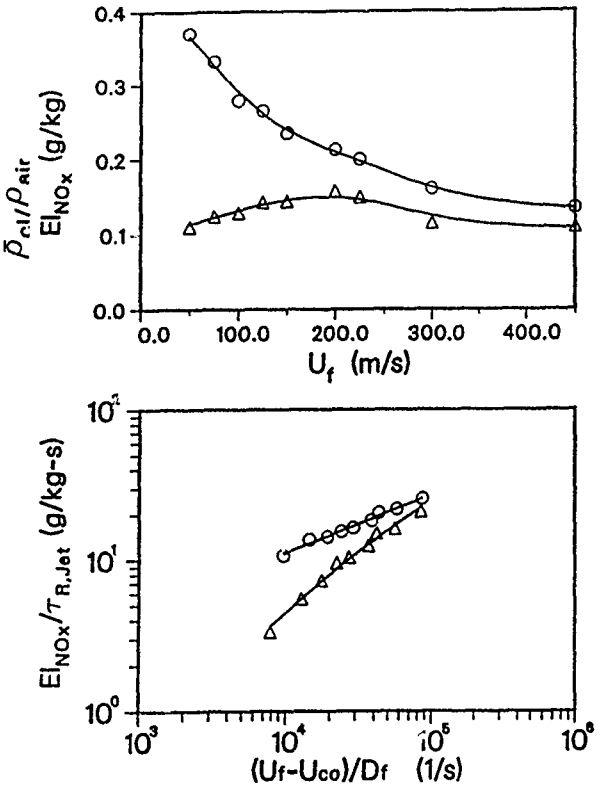

Fig. 3. Predicted NO_x emission index profiles vs fuel jet velocity and 1/Damköhler number for flames with 5.2 mm jet diameter. ○ adiabatic flames; △ with maximum radiation heat loss. Significant reduction in the NO_x formation is observed when the radiation heat loss is included, and, for low jet velocity flames, the NO_x trend becomes opposite to that of adiabtic flames.

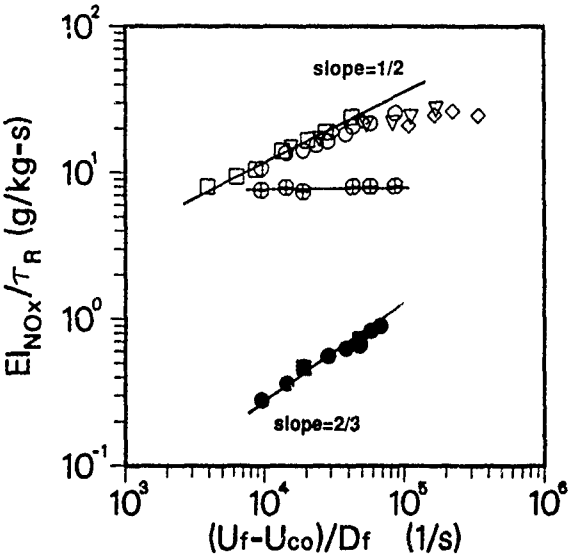

Fig. 4. Comparison of the NO_x emission index scaling trends between axisymmetric jet flames (78%H_2+22%Ar) and planar jet flames (47%H_2+53%Ar) for various jet diameters. ⊔ 10.4 mm, ○ 5.2 mm, ▽ 2.6 mm, ◇ 1.3 mm: round jets with a partial equilibrium chemistry model; ⊕ 5.2 mm: round jet with the equilibrium chemistry; ⊔, 2.6 mm; ○ 5.2 mm: planar jets using the same nonequilibrium chemistry but with a different fuel mixture. Different power dependence of EI_{NO_x}/τ_R on $(U_f - U_{co})/D_f$ is observed consistent with the results from analyses based on self-similar laws for jets.

EIGHTH SYMPOSIUM ON
TURBULENT SHEAR FLOWS
Technical University of Munich
September 9-11, 1991

AN EXAMINATION OF PERIODIC TURBULENT PIPE FLOW USING A LOW-REYNOLDS-NUMBER k~ε TURBULENCE MODEL

M. A. Cotton and J. O. Ismael
Department of Engineering
University of Manchester
Manchester M13 9PL U.K.

ABSTRACT

Turbulent pipe flows in which the mass flow rate varies in time in the form of a sinusoid imposed upon a steady level are computed using the turbulence model of Launder and Sharma (1974). Comparison is made with the experimental data of Tu and Ramaprian (1983) and Burnel et al. (1990).

INTRODUCTION

The present study investigates the performance of the low-Reynolds-number k~ε turbulence model of Launder and Sharma (1974) in the calculation of periodic, spatially fully-developed isothermal pipe flows. The mass flow rate varies as a pure sinusoid of frequency ω imposed on a steady flow (at amplitudes such that the flow remains uni-directional).

The cases we examine from the two sets of data were obtained at approximately the same mean Reynolds number, $Re \simeq 4.7 \times 10^4$. To a limited extent (because of different bulk velocity amplitude modulations, γ) the data allow a study of the effect of a single parameter, the imposed frequency, characterized here in terms of the Stokes number, $\Omega = D\,(\omega/\nu)^{1/2}$ (Table 1). The experimental data (and present calculations) raise interesting questions in relation to the occurrence of 'frozen' turbulence patterns at higher oscillation frequencies: it is seen from Table 1 that Case 2 of Tu and Ramaprian and Case 2 of Burnel et al. are at similar Stokes numbers, however very different Reynolds stress distributions are reported in the two papers.

MODEL FORMULATION

The phase-averaged momentum equation for periodic fully-developed pipe flow may be written as follows:

$$\frac{\partial W}{\partial t} = -\frac{1}{\rho}\frac{dp}{dz} + \frac{1}{r}\frac{\partial}{\partial r}\left[r\left(\nu\frac{\partial W}{\partial r} - \langle vw\rangle\right)\right] \qquad (1)$$

where r and z are radial and axial cylindrical coordinates, W is axial velocity, $\langle vw\rangle$ is phase-averaged Reynolds stress and other symbols have their usual meanings. Reynolds stress is supplied by the turbulence model, the k- and ε- equations being written in appropriate form with all advective terms omitted. An implicit finite volume/finite difference discretization scheme following Leschziner (1982) has been employed. The radial grid consists of 100 nodes and the wall-adjacent node is located at $y^+ \lesssim 0.25$.

RESULTS AND DISCUSSION

In the following presentation of results, phase positions are defined in terms of a cosine variation of bulk velocity (which necessitated a shifting of the time origin in treating the data of Burnel et al.). W_m is the long time mean bulk velocity and $v\tilde{w}$ is the phase-averaged periodic component of Reynolds stress (i.e. the long time mean is subtracted from the simple phase average). y is distance from the wall and R is pipe radius (=D/2).

Experimental measurements are represented as points in the figures below and present computations are shown as lines.

Comparison with the data of Tu and Ramaprian

Reynolds stress profiles at two frequencies examined by Tu and Ramaprian (1983) are shown in Figs. 1 and 2. In the lower frequency case (Fig. 1), the present calculations are in reasonable accord with the experimental measurements of strongly phase-varying Reynolds stress distributions. In contrast, Fig. 2 shows computed profiles which are frozen over the cycle (except close to the wall), whereas the experimental points exhibit considerable variation with phase. It should be noted, however, that the experimental points on Figs. 1 and 2 do not represent direct measurements of Reynolds stress, but are obtained instead from integrations of equation (1) using measurements of wall shear and velocity. Tu and Ramaprian report direct LDA measurements of the streamwise normal Reynolds stress which reveal a frozen structure, similar to that apparent in the present computed results for $v\tilde{w}$.

Table 1 Conditions of the experiments of Tu and Ramaprian (1983) and Burnel et al. (1990)

Authors		fluid	Re	D (m)	ν (m^2/s) [20°C]	f (Hz)	γ (%)	$D(\omega/\nu)^{1/2}$
Tu and Ramaprian	Case 1	water	4.9×10^4	0.0508	1.0×10^{-6}	0.5	64	90
	Case 2					3.6	15	242
Burnel et al.	Case 1	air	4.4×10^4	0.092	1.5×10^{-5}	1.65	26	76
	Case 2					18.0	30	253

Comparison with the data of Burnel, Raelison and Thomas

The experimental data of Burnel et al. (1990) were obtained for different dimensional conditions than those of Tu and Ramaprian. It is seen from Table 1, however, that the Reynolds and Stokes numbers of the low and high frequency tests of Burnel et al. are close to the corresponding Re and Ω values of Tu and Ramaprian's experiments.

Burnel et al. measured Reynolds stress directly using cross hot wire probes. Experimental data and present computational results for phase-averaged periodic Reynolds stress profiles in the two test cases are shown in Figs. 3 and 4. At Ω = 76 (Fig. 3), data and calculations show variation with phase over the entire pipe radius. Results are therefore qualitatively in agreement with Tu and Ramaprian's Case 1 (Ω = 90). In the higher frequency case (Ω = 253, Fig. 4) the measurements of Burnel et al. and present calculations reveal Reynolds stress distributions that are essentially frozen in the core region. This result is in marked contrast to Tu and Ramaprian's Case 2 (Ω = 242, Fig. 2).

CONCLUSIONS

Computational results for periodic pipe flow are compared against the experimental Reynolds stress data of Tu and Ramaprian (1983) and Burnel et al. (1990). Agreement is acceptably close, except in the higher frequency case of Tu and Ramaprian. In the light of the Burnel et al. data and considering the indirect measurement technique used by Tu and Ramaprian, it is thought likely that the source of these discrepancies lies principally with the data.

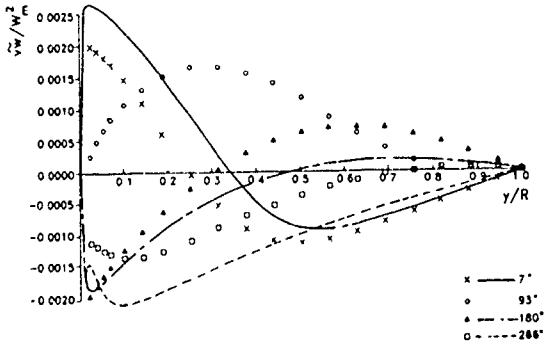

Fig. 1 Phase-averaged periodic Reynolds stress (Tu and Ramaprian Case 1).

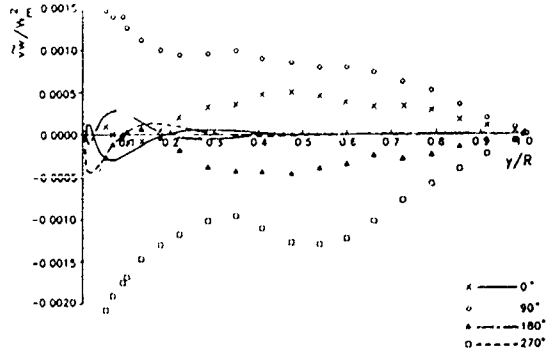

Fig. 2 Phase-averaged periodic Reynolds stress (Tu and Ramaprian Case 2).

ACKNOWLEDGEMENTS

We are grateful to Professors J.D. Jackson, B.E. Launder and B.R. Ramaprian for helpful discussions in the course of this work.

REFERENCES

BURNEL, S., RAELISON, J.C. & THOMAS, J.M. 1990 Radial distribution of the Reynolds stress in a turbulent pulsating flow in a pipe. Engineering Turbulence Modelling and Experiments, eds. Rodi, W. and Ganic, E.N., Elsevier, 419-427.

LAUNDER, B.E. & SHARMA, B.I. 1974 Application of the energy-dissipation model of turbulence to the calculation of flow near a spinning disc. Lett. Heat Mass Transfer, 1, 131-138.

LESCHZINER, M.A. 1982 An introduction and guide to the computer code PASSABLE. Department of Mechanical Engineering, UMIST.

TU, S.W. & RAMAPRIAN, B.R. 1983 Fully developed periodic turbulent pipe flow. Part 1. Main experimental results and comparison with predictions. J. Fluid Mech., 137, 31-58.

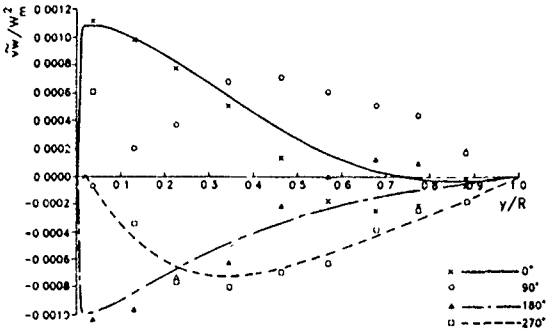

Fig. 3 Phase-averaged periodic Reynolds stress (Burnel et al. Case 1).

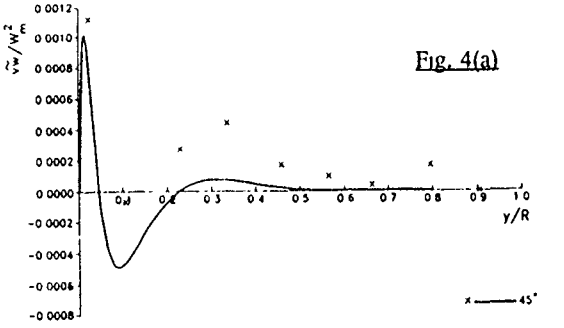

Fig. 4(a)

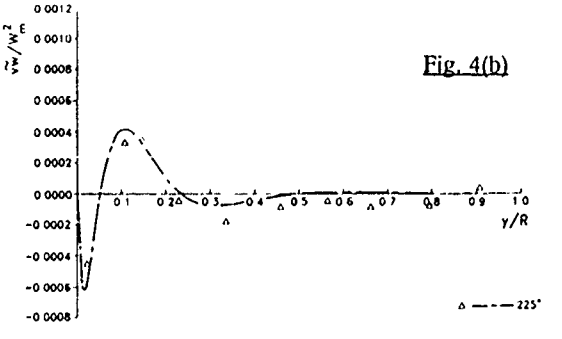

Fig. 4(b)

Fig. 4 Phase-averaged periodic Reynolds stress (Burnel et al. Case 2).

EIGHTH SYMPOSIUM ON
TURBULENT SHEAR FLOWS
Technical University of Munich
September 9-11, 1991

COMPUTER SIMULATION OF SEPARATED FLOW IN A BRANCHED DUCT

H Fu*, M J Tindal*, A P Watkins+ and M. Yianneskis*

*Centre for Heat Transfer and Fluid Flow Measurement
School of Physical Sciences and Engineering
King's College London
Strand, London WC2R 2LS, UK

+Mechanical Engineering Department
UMIST, P O Box 88, Manchester M60 1QD, UK

This paper presents a combined experimental and numerical investigation of the flows in internal combustion engine manifolds. The flow pattern through a single-branch manifold (T-junction) was calculated using a three-dimensional finite-difference numerical code incorporating the k-ε model of turbulence. The flowfield was measured in a steady water flow rig using laser-Doppler anemometry. Detailed measurements of the mean velocity components and corresponding turbulence levels were obtained in order to characterise the flow and provide benchmark data appropriate for the development and assessment of the accompanying calculations. Calculations were also performed for two- and three-branch manifolds.

The flow configuration consisted of a square duct, 50.8 mm x 50.8 mm in cross-section, with four branches, 30 mm x 30 mm in cross-section. For some of the work presented here three of the branches were blocked, so the geometry corresponded to a T-junction with a main duct/side branch area ratio of 2.87. The flow Reynolds number, based on the main duct bulk flow velocity and hydraulic diameter, was 60,000.

The simulation was performed with a computational mesh size of 77 x 18 x 10 in the streamwise and two cross-stream directions respectively in the main duct. In the branch the corresponding grid size was 42 x 12 x 7. The streamline pattern in the symmetry plane of the duct is shown in Figure 1. The results show that the flow is very uniform up to 30 mm upstream of the junction and an elongated recirculation region of 110 mm length and 18 mm width is formed in the side branch.

Figure 2 shows the predicted mean velocity vectors in a cross-stream plane in the side duct. A single vortical motion occupies the duct cross-section. Figure 3 shows a comparison of predicted (solid lines) and measured profiles of kinetic energy of turbulence, k, in the plane of symmetry of the flow. The highest values are found in the vicinity of the recirculation region in the branch, as expected. The comparison of the measured and predicted profiles of k shows excellent agreement between the data and predictions in the main duct and good agreement downstream in the side branch; however in the first profile in the side duct there is some disrepancy with the data in the reverse flow region where the k values are overpredicted.

In the branch, the cross-stream flow comprises two vortical motions, as indicated by the profiles shown in Figure 4. The predicted profiles of velocity are shown as solid lines and are compared with the LDA measurements: notwithstanding the small magnitudes involved, the agreement is very good across most of the duct cross-section.

Figures 5-8 show a characteristic sample of results from the three-branch calculations. The velocity vectors in the plane of symmetry are shown in Figure 5 and a three-dimensional diagram of the flow configuration in Fig. 6. The pressure at the exit of each branch was set to the same value in the calculations, but the predictions showed that about 18% more mass flowed through the middle branch; such findings show the suitability of three-dimensional calculation methods for the prediction of manifold flows.

The predicted velocity vectors in a cross-section of the side and of the main duct are shown in Figs. 7 and 8 respectively. In the upstream plane (Fig. 7) the flow pattern is similar to that in Fig. 4 in that two senses of circulation are evident, whereas in the main duct there is only one vortical motion.

In general the simulations yielded results which showed excellent agreement with the pressure drop data (to within 2 Pa or 0.5 % of the total pressure drop along the duct). The streamwise mean velocity values in the main duct are predicted to within 2 - 3 % of the experimental values. In the side branch the streamwise velocities are in very good qualitative and quantitative agreement with the experimental data, except for the reverse velocities in the recirculation region near the junction which are overpredicted. The comparison of the experimental and numerical results indicates clearly the suitability of the combined approach used for the study of branched flows.

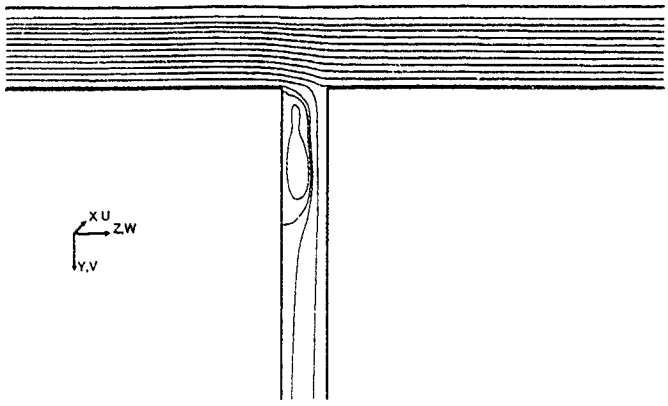

Figure 1 Single-branch configuration: streamline contours in the plane of symmetry .

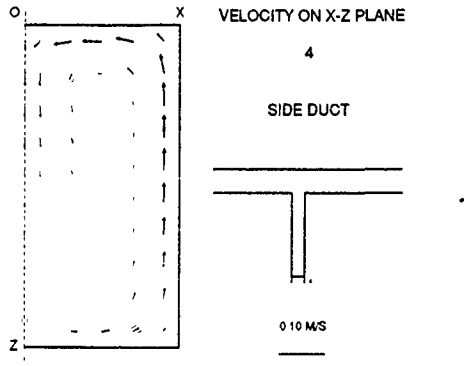

Figure 2 Single-branch configuration: predicted velocity vectors in side duct.

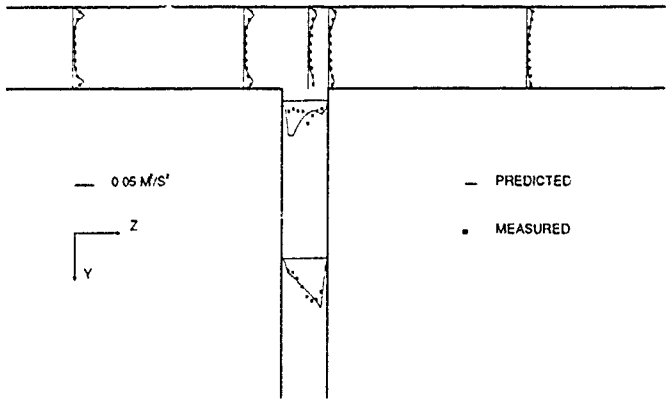

Figure 3 Single-branch configuration: comparison of measured and predicted profiles of kinetic energy of turbulence in the plane of symmetry.

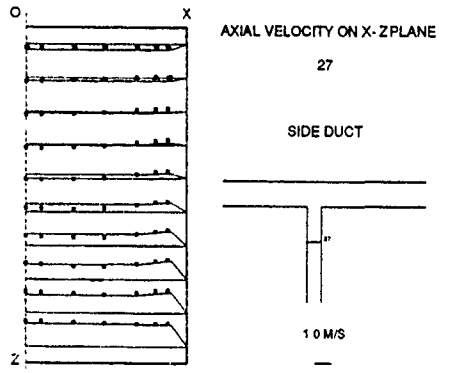

Figure 4 Single-branch configuration: comparison of predicted and measured mean velocities in the side duct. • MEASURED — PREDICTED

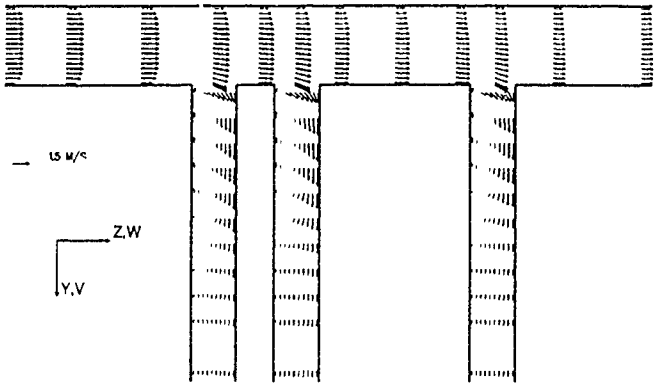

Figure 5 Three-branch configuration: Predicted velocity vectors in the plane of symmetry.

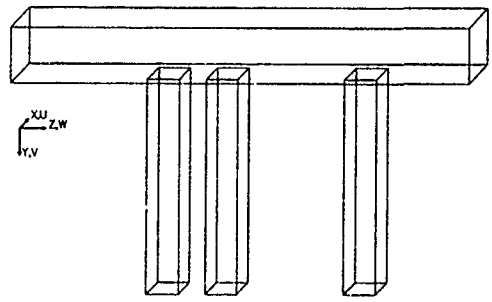

Figure 6 Three-branch configuration: three-dimensional view.

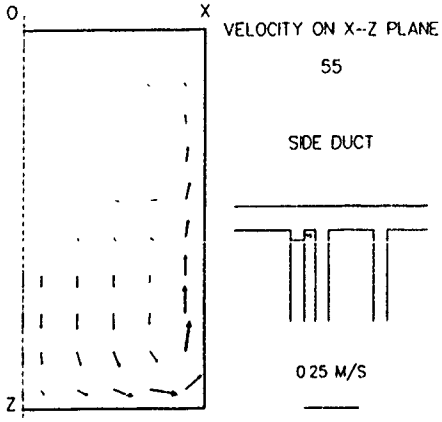

Figure 7 Three-branch configuration: predicted velocity vectors in branch 1.

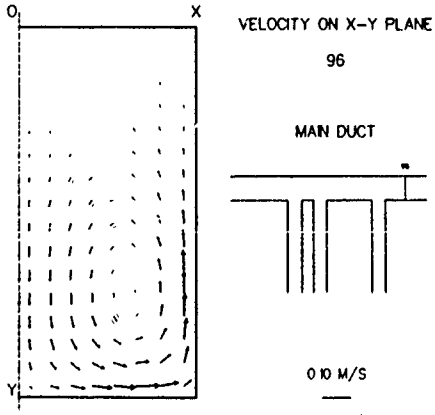

Figure 8 Three-branch configuration: predicted velocity vectors in main duct.

EIGHTH SYMPOSIUM ON
TURBULENT SHEAR FLOWS
Technical University of Munich
September 9-11, 1991

EXPERIMENTAL INVESTIGATION OF THE FLOW STRUCTURE NEAR THE NOZZLE

Motoaki KIMURA, Kiyoaki ONO and Atsushi SAIMA

Department of Mechanical Engineering
College of Science and Technology
Nihon University, Tokyo, Japan

ABSTRACT

The experiments are carried out to investigate the flow structure of jets in the near-nozzle region. Time mean static pressure and pressure fluctuation are measured by the newly developed static pressure probe with a hot-wire anemometer. A schlieren photograph technique is applied to the flow visualization. Axial and radial velocities are measured by LDV. The following results are obtained. The mean static pressure and the pressure fluctuation distributions and the velocity distribution are gotten by the measurement. The mean static pressure distributions in the cross sections have a remarkable transition toward the stream-wise. The static pressure lower than the atmospheric pressure around the jet is one of the important causes of the jet entrainment.

1. INTRODUCTION

Many experimental and analytical studies of turbulent free jets and their diffusion process have been presented (Kataoka, 1986)[1]. There is the complex structure as the entrainment and the coherent eddy both spatially and temporally in the near-nozzle region (Kimura, Ono and Saima, 1990)[2]. The coherent structure has been approached by the flow visualization (Roshko, 1975)[3] and the analysis of measured velocity component (Yule, 1981)[4]. Savas and Gollahalli (1986)[5] investigated the reciprocity of the coherent structure and jet flames. Higaki and Saima (1983)[6] pointed out the importance of the investigation on the flow structure near the nozzle for the stabilization mechanism of lifted diffusion gas flames. It can be considered that the momentum and the mass diffusions relates to the mean static pressure distribution and the pressure fluctuation. It is important to investigate the jet behavior on the near-nozzle region. This experimental study aims at approaching a jet diffusion process in the near-nozzle region, from the potential core to the transitional region which sits up stream the fully developed region. We investigate the relationship of the velocity field and the distribution of the time mean static pressure and the pressure fluctuation. This paper reports the first stage of the investigation.

2. EXPERIMENTAL APPARATUS

Air, carbon dioxide and helium are separately jetted into still air from a vertical round nozzle. These gases are supplied from gas cylinders or a compressor tank. Their flow rate are controlled by pressure reducing valves and measured by the calibrated orifice. The nozzle diameter (d) is 10 [mm]. The exit flow Reynolds number is between 200 and 20000.

For measuring the velocity, the laser doppler velocimeter (LDV) is used as back-scattering mode. Its light source is a He-Ne laser with a power output of 10 [mW]. The condensed oil is seeded with mean diameters of 0.5 to 1 [μm] and a density of 840 [kg/m^3].

A new probe to measure the static pressure was developed by the authors. The static pressure probe is designed to measure the mean static pressure and the pressure fluctuation at the same time. The static pressure measuring system is composed of a Prandtl-type static pressure probe (Fig.1), an air supply system with a constant pressure and a constant temperature hot-wire anemometer. The static pressure probe consists of a static pressure tube and a hot-wire spanning the cross section of the static pressure tube inside as shown in Fig.2. The probe is connected to the constant pressure air supply system. This system supplies the constant pressure (P_1). The constant pressure (P_1) is slightly above the atmospheric pressure (P_o) in order to create a bias flow at the static pressure holes through the hot-wire section. The pressure difference (P_1-P_o=11 [Pa]) can be kept constant with this device. The static pressure probe can be used for any gas, because of the bias flow. The air velocity at the hot-wire is settled by a pressure difference (P_1-P_s) between a static pressure (P_s) and the inside pressure (P_1). Air flow velocity from the static pressure holes is very slow. So the effect of it is negligibly small for the measured flow. When pressure fluctuations are incident on the static pressure holes, induced velocity fluctuation is uniquely determined and a voltage is produced. The relation between the pressure difference and the probe output voltage is linearized from -10 to +10 [Pa] under the atmospheric pressure.

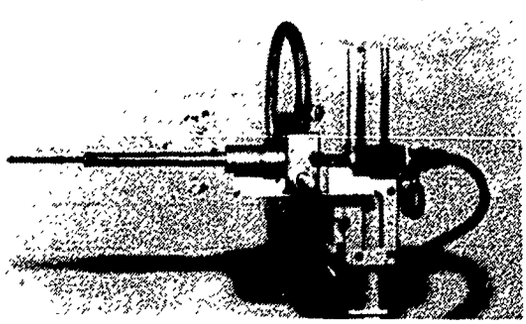

Fig.1 Static pressure probe.

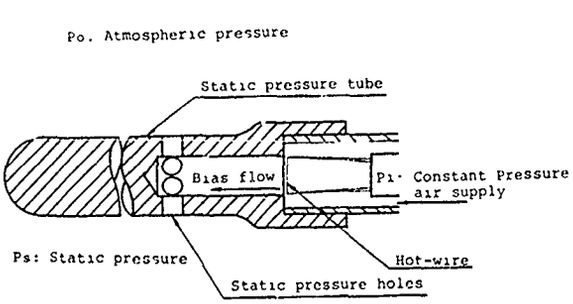

Fig.2 Static pressure tube with hot-wire.

3. RESULTS AND DISCUSSION

Schlieren photograph of carbon dioxide jet into still air is shown in Fig.3. The flow field is quite complex. The jet flow is laminar near the nozzle at small Reynolds number. The break point where the free boundary layer undergoes a remarkable transition from the laminar to the turbulent flow, approaches to the nozzle as Reynolds number increases.

The Stream-wise variation of the time mean radial velocity distribution is shown in Fig.4 in the case of the carbon dioxide jet at Re=5000. X is the axial coordinate. r is the radial coordinate. V is the mean radial velocity. Um is the mean axial velocity on the jet axis. The mean radial velocity is about zero (V/Um=0) under the jet center region in the cross section from X/d=0.06 to 3. This range overlaps the potential core. Thus, the condition, which mean radial velocity profile is flat and almost zero, is one of the potential core characteristics. There is mean radial-flow out side the potential core, and its flow is toward the surrounding. The further outer region is figured by hatching, and there is mean radial-flow from the surroundings toward the jet center. The further outer flow region overlaps the jet entrainment. The spread of this region shows that the entrainment ranges largely.

The Stream-wise variation of time mean static pressure and pressure fluctuation distributions are shown in Fig.5 (a) and (b) in the case of the carbon dioxide jet. p' is the rms pressure fluctuation. Three remarkable characteristics are observed. (1) The mean static pressure distribution at the limit of jet center is the positive static pressure (Ps>Po) in the cross section X/d=3 and 4. Out of this limit region, the mean static pressure distribution is the negative pressure (Ps<Po). (2) This characteristic distribution of the mean static pressure in the jet center exists only in the potential core region. For reference, the potential core length is about 5 times as long as the exit diameter in the case of the carbon dioxide jet. (3) The pressure fluctuation variation in the cross section is intensive in the location where the mean static pressure changes from negative to positive.

We discussed the relation between the mean negative pressure (Ps<Po) and the jet entrainment. For example, in the case of the carbon dioxide jet, the region where the mean radial velocity flows from the surrounding toward the jet center is expanded. The negative pressure (Ps<Po) region expands as large as the spread of the mean radial velocity region. It seems that the negative pressure (Ps<Po) is one of the important causes of the jet entrainment.

4. CONCLUSION

In the near nozzle region, the experiments are carried out to investigate the diffusion structure of gas jets. The following results are obtained. The potential core and the entrainment regions can be described by the time mean radial velocity distributions. The negative pressure (Ps<Po) in the jet diffusion is one of the important causes of the jet entrainment.

REFERENCES

[1] Kataoka,K. 1986 Modeling Turbulent Jets with Variable Density. Encyclopedia of Fluid Mechanics **2**, 511-543, Gulf Publishing Company, Houston.

[2] Kimura,M., Ono,K. and Saima,A. 1990 Velocity and Concentration Fluctuations of Turbulent Buoyant Round Jets. JSME International J. **33**, 562-568.

[3] Roshko,A. 1975 Progress and Problems in Understanding Turbulent Shear Flows. Turbulent Mixing in Nonreactive and Reactive Flows, 295-316, Plenum Press, New York.

[4] Yule,A.J. 1981 Investigations of Eddy Coherence in Jet Flows. Lecture Notes in Physics **136**, 188-207, Springer Verlag, Berlin.

[5] Savas,O. and Gollahalli,S.R. 1986 Flow Structure in Near-Nozzle Region of Gas Jet Flames. AIAA J. **24**, 1137-1139.

[6] Higaki,M. and Saima,A. 1983 Further Experiment on the Stabilization Mechanism of Lifted Diffusion Gas Flames. ASME-JSME Thermal Engineering Joint Conference **4**, 323-330.

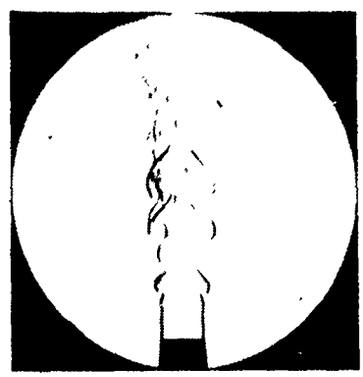

Fig.3 Schlieren photograph; carbon dioxide, Re=5000.

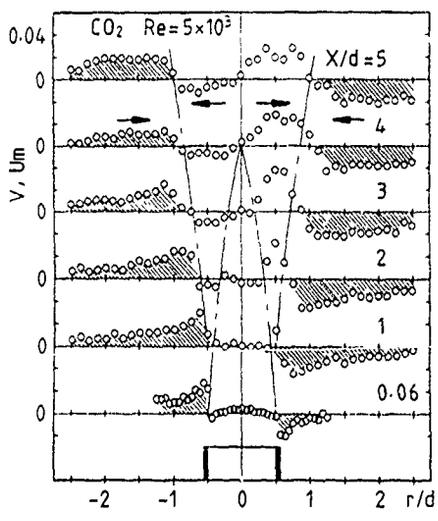

Fig.4 Stream-wise variation of mean radial velocity distribution; carbon dioxide, Re=5000.

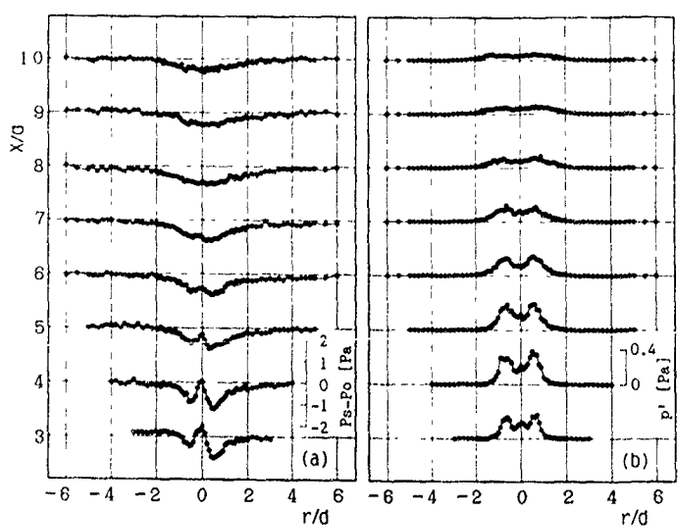

Fig.5 Mean static pressure (a) and pressure fluctuation (b) distributions; carbon dioxide, Re=5000.

EIGHTH SYMPOSIUM ON
TURBULENT SHEAR FLOWS
Technical University of Munich
September 9-11, 1991

A STUDY OF TURBULENT WAKE STRUCTURE BEHIND ELLIPTIC RINGS

S.J. Lee* and P.W. Bearman**

* Dept. of Mechanical Eng., POSTECH, P.O.Box 125, Pohang, Korea

** Dept. of Aeronautics, Imperial College, London, SW7 2BY, England

INTRODUCTION

Although a number of investigations concerning aerodynamics of two dimensional or axisymmetric bluff body have been reported in literature, the corresponding information for an elliptic geometry has received relatively little attention. By systematic variation of eccentricity (ϵ) of the elliptic geometry, one can obtain both circular(ϵ = 1) and flat plate (ϵ = 0) geometries as limiting cases. The elliptical wakes has general flow characteristics which can not be found in the axisymmetric or two-dimensional geometries. As far as wake behind an elliptic bluff body, there have been few investigation. Kuo and Baldwin (1967) studied elliptical wakes behind elliptic disks. They found that the wakes have elliptical cross-sections, and the major axis of the wake is aligned with the minor axis of the body.

Bearman and Takamoto(1988) investigated the wake structure of ring models (ϵ = 1) with various cross-sections. They observed a regular and coherent axisymmetric vortex ring with d/w > 5.0, where d/w is the ratio of mean diameter to ring width.

EXPERIMENTS

The experiments were carried out at in a closed return, low turbulence wind tunnel having a 3 ft square test section. The r.m.s. turbulence intensity in the working section is about 0.03%. A cross-sectional view of a typical elliptic ring model used in this study is shown in Fig. 1.

The models were sharp edged with a 45° angle of inclination on the back face and has a thickness of 4mm. The elliptic ring model was classified by the body eccentricity ϵ (= b_o/a_o), where a_o is the major outer diameter (200mm for all models). Three different elliptic ring models with body eccentricities of 0.5, 0.667 and 0.8 were employed. Ring width w is constant along the elliptic circumference (w = $b_o/7$). The elliptic ring model was mounted normal to the free stream in the center of the wind tunnel. Throughout the experiments, the mean velocity U_o was maintained at 8 m/sec., giving Reynolds numbers based on the ring width between 4×10^4 and 6.4×10^4, depending on the model. Velocity fluctuations were measured by using a TSI hot-wire anemometer. A x-wire probe was traversed along the y and z axis at x = 3.4w and 8.0w downstream from the elliptic ring.

RESULTS

Some of the results of mean velocity profiles at x = 3.4w and 8.0w are shown in Fig. 2-4. The location of maximum velocity defect moves toward the central axis with increasing streamwise distance in the major axis(Z) plane and moves outward in the minor axis(Y) plane. The velocity defects at x=3.4w and x=8.0w have similar magnitude in the minor axis. But the velocity defect in the X-Z plane decreases as the wake width is increased at

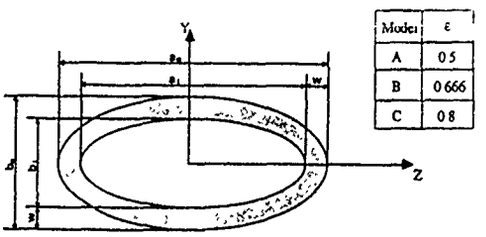

Model	ϵ
A	0.5
B	0.666
C	0.8

Fig. 1 Cross-sectional view of a typical elliptic ring model

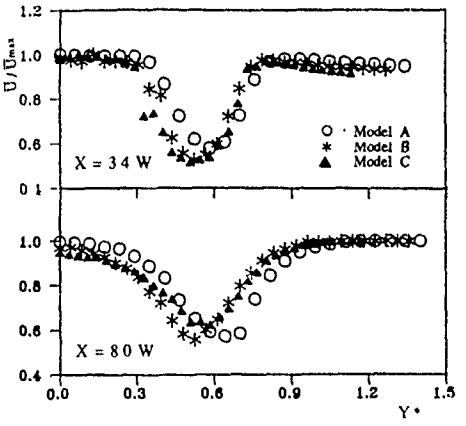

Fig 2 Mean streamwise velocity profiles in the minor axis plane

x=8.0w Mean velocity(V,W) profiles at 3.4w show that the wake is concentrated on the wake center in the minor axis, but expands outward in the major axis.

Streamwise turbulence intensity profiles at x=3 4w are shown in Fig 5. The turbulence intensities are characterized by a double-peak profile, with a larger inside peak With increasing streamwise distance, the profile changes into a parabolic shape and the location of the peak values moves toward the wake center. Turbulent intensity in the minor axis plane is about 20% larger than that of major plane

The Reynolds shear stress $\overline{u'v'}$ and $\overline{u'w'}$ have maximum values of about 0.05, but their profiles are opposite to each other From the velocity measurements, the wake structure was found to have elliptical configurations The wake behind the minor axis of the body increases steadily in the downstream direction and the wake behind the major axis decreases rapidly. These flow characteristics becomes stronger with increasing eccentricity of the ring models.

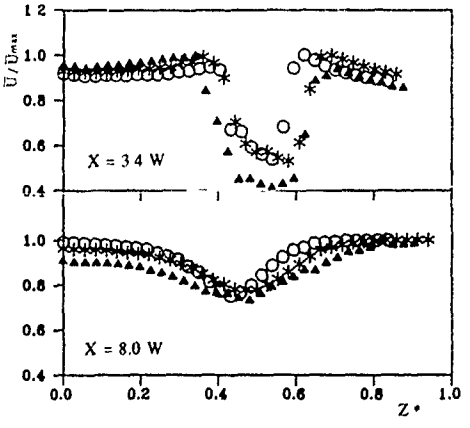

Fig 3 Mean streamwise velocity profiles in the major axis plane

REFERENCES

KUO, Y. & BALDWIN, L.V., 1967, J.Fluid Mech. 27, 353-363

BEARMAN, P.W. & TAKAMOTO, M., 1988, Fluid Dyn. Research 3, 214-218

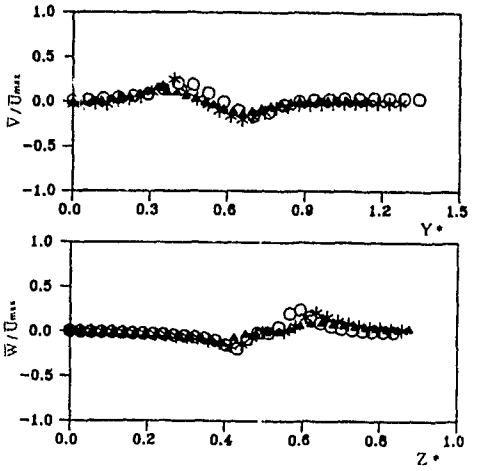

Fig 4 Profiles of mean velocity V and W at X = 3 4W

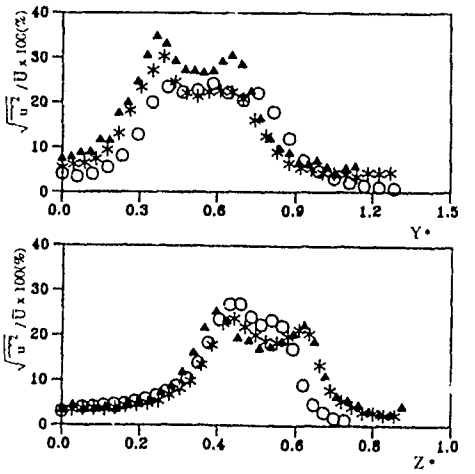

Fig 5 Streamwise turbulence intensity profiles at X = 3 4W

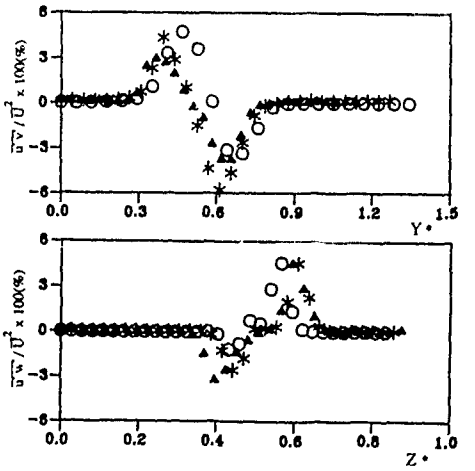

Fig 6 Profiles of Reynolds shear stress $\overline{u'v'}$ and $\overline{u'w'}$ at X = 3 4W

EIGHTH SYMPOSIUM ON
TURBULENT SHEAR FLOWS
Technical University of Munich
September 9-11, 1991

PREDICTION OF TURBULENCE-DRIVEN SECONDARY FLOW IN A SQUARE DUCT WITH AN ANISOTROPIC LOW-REYNOLDS-NUMBER k-ε MODEL

Hyon Kook MYONG *)

*) Air Conditioning and Environmental Control Lab., Korea Institute of Science and Technology
P.O. Box 131 Cheongryang, Seoul 136-650, KOREA

INTRODUCTION

Turbulent flow in a straight non-circular duct is characterized by the occurrence of secondary flow caused by the turbulence. Brundrett and Baines (1964), and Perkins (1970) have shown from their experimental studies that this turbulence-driven secondary flow results from the anisotropy of each Reynolds stress in the cross-sectional plane. Turbulent flows in a straight square duct are thus of special interest to modellers, since this particular flow situation provides a natural vehicle for examining the validity of existing turbulence models. The widely used (isotropic) k-ε model has, however, no built-in mechanism for the development of secondary flow due to its inherent isotropic characteristics. In view of this shortcoming of the k-ε model, this problem has been mostly attempted by using the algebraic stress models, since they certainly have a much greater potential for predicting the anisotropy of Reynolds stresses (e.g. Demuren & Rodi, 1984). But, these models are simplified from the original forms of Reynolds stress models with drastic assumptions; the principles and basic techniques for their modelling has not been established yet, at least, in the near-wall region (Myong & Kobayashi, 1990). Recently, the author has proposed an anisotropic low-Reynolds-number k-ε model (e g, Myong & Kasagi, 1990a). It is just an extended form of its (isotropic) version but broadens the range of applicability whilst maintaining most of popular features of the latter.

In the present study, numerical predictions are presented of fully-developed turbulence-driven secondary flow in a square duct with the author's anisotropic low-Reynolds-number k-ε model. Special attention has been given to both regions close to the wall and the corner, which are known to influence the characteristics of secondary flow a great deal. Hence, instead of the common wall function approach, the no-slip boundary condition at the wall is directly used. Predicted contours of all three mean velocity components and six Reynolds stresses are in detail compared with previous experimental data. It is found that most features of this flow are simulated excellently by the present anisotropic k-ε model. Then, attention is directed to the predicted contours of the turbulence quantities responsible for the secondary flow generation, such as anisotropy of normal Reynolds stresses and the secondary secondary Reynolds shear stress acting in the cross-sectional plane. Finally, the formation of secondary flows is numerically investigated.

Table 1 Anisotropic low-Reynolds-number k-ε model

$$\frac{Dk}{Dt} = \frac{\partial}{\partial x_j}\left[\left(\nu + \frac{\nu_t}{\sigma_k}\right)\frac{\partial k}{\partial x_j}\right] - \overline{u_i u_j}\frac{\partial U_i}{\partial x_j} - \varepsilon$$

$$\frac{D\varepsilon}{Dt} = \frac{\partial}{\partial x_j}\left[\left(\nu + \frac{\nu_t}{\sigma_\varepsilon}\right)\frac{\partial \varepsilon}{\partial x_j}\right] - C_{\varepsilon 1}\frac{\varepsilon}{k}\overline{u_i u_j}\frac{\partial U_i}{\partial x_j} - C_{\varepsilon 2} f_2 \frac{\varepsilon^2}{k}$$

$$\overline{u_i u_j} = \frac{2}{3} k \delta_{ij} - \nu_t\left(\frac{\partial U_i}{\partial x_j} + \frac{\partial U_j}{\partial x_i}\right) + \frac{k}{\varepsilon}\nu_t \sum_{\beta=1}^{3} C_\beta \left(S_{\beta ij} - \frac{1}{3} S_{\beta\alpha\alpha}\delta_{ij}\right)$$

$$+ \frac{2}{3}\nu\frac{k}{\varepsilon}\left(\frac{\partial \sqrt{k}}{\partial x_n}\right)^2 W_{ij}(n, m)$$

$$S_{1ij} = \frac{\partial U_i}{\partial x_\gamma}\frac{\partial U_j}{\partial x_\gamma},\quad S_{2ij} = \frac{1}{2}\left(\frac{\partial U_\gamma}{\partial x_i}\frac{\partial U_j}{\partial x_\gamma} + \frac{\partial U_\gamma}{\partial x_j}\frac{\partial U_i}{\partial x_\gamma}\right),\quad S_{3ij} = \frac{\partial U_\gamma}{\partial x_i}\frac{\partial U_\gamma}{\partial x_j}$$

$$\nu_t = C_\mu \sqrt{k}\, L = C_\mu f_\mu \frac{k^2}{\varepsilon}$$

$$f_\mu = (1 + 3.45/\sqrt{R_t})\{1 - \exp(-y^+/70)\}$$

$$f_2 = \{1 - (2/9)\exp[-(R_t/6)^2]\}\{1 - \exp(-y^+/5)\}^2$$

$$W_{ij}(n, m) = -\delta_{ij} - \delta_{in}\delta_{jn} + 4\delta_{im}\delta_j$$

$$\sigma_k = 1.4,\ \sigma_\varepsilon = 1.3,\ C_{\varepsilon 1} = 1.4,\ C_{\varepsilon 2} = 1.8,\ C_\mu = 0.09$$

$$C_1 = 0.8,\ C_2 = 0.45,\ C_3 = -0.15$$

Note that the indices n and m denote the coordinate normal to the wall and the streamwise coordinate, respectively summation convetion does not apply to n and m.

TURBULENCE MODEL

The author's anisotropic low-Reynolds-number k-ε turbulence model introduced in the present study is shown in Table1. It should be recognized that, contrary to the previous Reynolds (or algebraic) stress models, the present anisotropic model is substantially derived from the standard (isotropic) k-ε model; i.e., the latter one is obtained in the limit as $C_i \rightarrow 0$, and also directly applicable up to the wall. This model has already been proven to perform satisfactorily in several flow situations, including turbulent pipe and channel flows, two-dimensional boundary layer flows with and without pressure gradients (Myong & Kasagi, 1990b). Furthermore, even for developing and fully-developed three-dimensional turbulent flows in a square duct, it is found that the performance of the present model, including the anisotropic normal Reynolds stresses and distributions of U, k and $\overline{uv}$, is by no means inferior to that of the previous higher-order models (Myong & Kobayashi, 1990).

The resulting set of governing equations are simplified only by

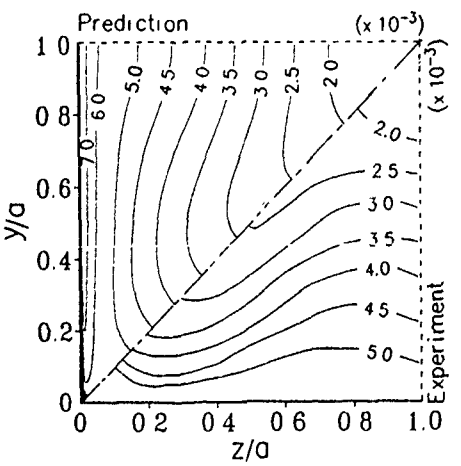

Fig. 1 Turbulent kinetic energy.

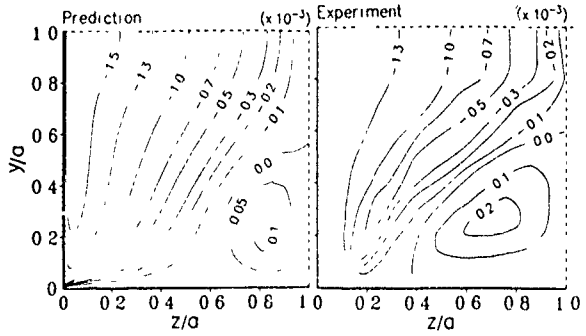

Fig. 2 Primary Reynolds shear stress.

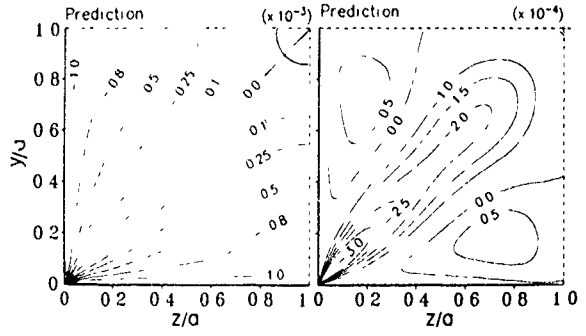

Fig. 3 Predicted contours of the anisotropy of normal Reynolds shear stress components $\overline{w^2} - \overline{v^2}$ and the secondary Reynolds shear stress $\overline{vw}$.

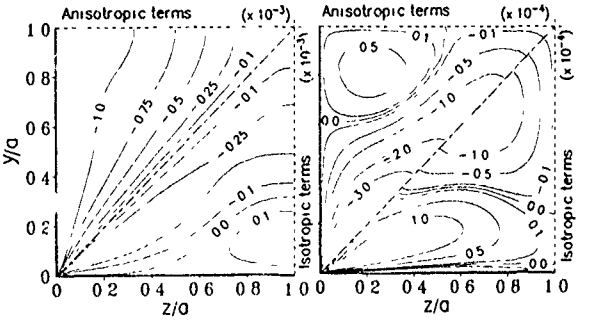

Fig. 4 Relative magnitudes of the secondary to the primary velocity-gradient terms in the algebraic relations for $\overline{w^2} - \overline{v^2}$ and $\overline{vw}$.

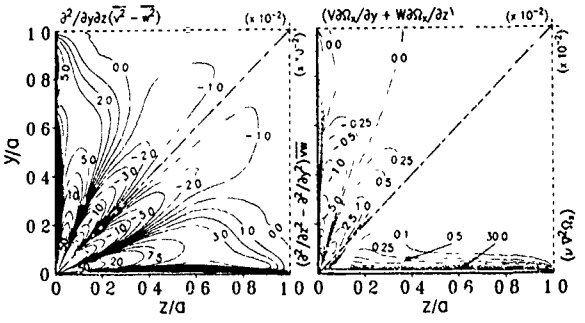

Fig. 5 Streamwise vorticity budget.

the boundary layer assumption and solved with a forward marching numerical procedure for three-dimensional shear layers. The details of the numerical methods are found elsewhere (Myong & Kobayashi, 1990).

RESULTS AND DISCUSSION

Because of the limited paper length, typical results are only presented. The predicted contours of turbulent kinetic energy and primary Reynolds shear stress are shown in Fig. 1 and Fig. 2, respectively, along with the experimental data of Fujita et al. (1986) The predictions confirm the experimental evidence as a whole. The present model also predicts reasonably well their flow patterns in regions close to the corner and the wall, where the experimental measurement is difficult.

The predicted contours of the anisotropy of normal Reynolds stress components $\overline{w^2} - \overline{v^2}$ and the secondary Reynolds shear stress $\overline{vw}$ are shown in Fig. 3. The predictions show clearly the experimental behavior of Brundrett and Bains (1964) and Fujita et al. (1986).

The relative magnitude of the secondary to the primary velocity-gradient terms (or the isotropic to the anisotropic terms) in the algebraic relations for $\overline{w^2} - \overline{v^2}$ and $\overline{vw}$ are compared for the present model in Fig. 4. The present predictions confirm the fact that the secondary velocity gradients contribute significantly to the generation of the secondary shear stress as pointed out by Perkins (1970).

Figure 5 shows the contours of magnitude of each term in the streamwise vorticity equation. The present model has confirmed the fact that, in the streamwise vorticity equation, the production terms by both normal and shear stress terms are dominant ones, being both of the same order of magnitude and of opposite sign with much larger magnitude than the convection terms, while the viscous terms are negligible except for the regions very close to the corner and the wall.

Finally, note that this paper has paid particular attention to the predictions in regions close to the corner and the wall, where little experimental data have been reported due to the difficulty of experimental measurement.

REFERENCES

Brundrett, E. & Baines, W. D. 1964 The Production and diffusion of vorticity in duct flow. *J. Fluid Mech.* **19**, 375-394.

Demuren, A. O. & Rodi, W. 1984 Calculation of turbulence-driven secondary motion in non-circular ducts. *J. Fluid Mech.* **140**, 189-222.

Fujita, h., Yokosawa, H., Iwata, S. & Takahama, H. 1986 Turbulent flow in a square duct with roughened walls on two opposite sides (1st report, measurement of flow velocities and turbulent stresses). *Trans. Japan Soc. Mech. Engrs.* (in Japanese) **52B**, 3491-3497.

Myong, H. K. & Kobayashi, T. 1991 Numerical simulation of three-dimensional developing turbulent flows in a square duct with the anisotropic k-ε model. to appear at *the 1st Joint ASME-JSME Fluids Eng. Conf.*, June 23-27, Portland, U.S.A.

Myong, H. K. 1988 *Fundamental Studies on Two-Equation Turbulence Model for Numerical Predictions of Wall-Bounded Shear Flow and Heat Ttansfer.* Dr. Eng. Thesis, The University of Tokyo, Tokyo.

Myong, H. K. & Kasagi, N. 1990a Prediction of anisotropy of the near-wall turbulence with an anisotropic low-Reynolds-number k-ε turbulence model. *Trans. ASME J. Fluids Eng.* **112**, 521-524.

Myong, H. K. & Kasagi, N. 1990b A new approach to the improvement of k-ε turbulence model for wall-bounded shear flows. *JSME Int. J.*, Ser. II **33**, 63-72.

Myong, H. K. & Kobayashi, T. 1991 Prediction of three-dimensional developing turbulent flow in a square duct with an anisotropic low-Reynolds-number k-ε model. to appear in *Trans. ASME J. Fluids Eng.*

Perkins, H. J. 1970 The formation of streamwise vorticity in turbulent flow. *J. Fluid Mech.* **44**, 721-740.

EIGHTH SYMPOSIUM ON
TURBULENT SHEAR FLOWS
Technical University of Munich
September 9-11, 1991

RESPONSE OF UNIDIRECTIONAL TWO DIMENSIONAL SHEAR FLOW TO DIFFUSIONAL TRANSVERSE MAGNETIC FIELD

D. Naot

Center for Technological Education Holon
P.O. Box 305, Holon 58102, Israel.

The present work is associated with the expansion of the applicability of the Stress transport models[1,2] as well as the related methods such as the algebraic stress models[3] or the subgrid turbulence models, to magnetohydrodynamic flows. Exposing hydrodynamic turbulence to a magnetic field induces two processes: According to the Ampere law the velocity fluctuations induce electric current fluctuations. Simultaneously, according to the Lorentz law, the electric current fluctuations induce force fluctuations. A feedback mechanism is formed changing the structure of the velocity fluctuations in comparison with the same non magnetized hydrodynamic turbulence. The results are twofold: electro-magnetic induced laminarization[4,5] and an enhancement of anisotropy even to the extent of turning turbulence two dimensional[6,7,8].

Generally, the electromagnetic fluctuations are classified according to the value of the magnetic Reynolds number. For high magnetic Reynolds number the fluctuations are termed "Frozen", and for low magnetic Reynolds number the fluctuations are termed "Diffusional". The present work is restricted to the diffusional mode, interpreted as the case in which the electromagnetic fluctuations are driven by the hydrodynamic turbulence enforcing time microscales typical of the velocity fluctuations on the electromagnetic fluctuations[9]. With this assumption, followed by an order of magnitude analysis, the closure of the model equations becomes possible. Apparently, this limits the model. However, interpretation in terms of the hydrodynamic Reynolds number showed[9] for some important liquid metals, such as Hg, Na, NaK and others, a reasonably wide range of applicability.

In developing the present theory[10] use was made of three concepts: local equilibrium, local homogeneity and quasi-isotropy. Consequently, it was suggested[10] to distinguish between the early stage of laminarization of channel flow high level turbulence, and the final stage of laminarization of low level turbulence, and apply the present model to the first only.

Although the theoretical case of shear flow in local equilibrium with no wall proximity effects is an idealization of reality, it is still an important test case as it contains the most important feature of wall turbulence, - a large velocity gradient perpendicular to the flow direction. The case was studied[10] and the influence of the magnetic field was demonstrated by elaborating analytic solutions for three cases with different orientations of the magnetic field. Equilibrium structure was derived for various Hartman numbers, as well as limiting structure for high Hartman number. Two practical and important steps towards the numerical simulation of magnetohydrodynamic channel flow were made[10]: An eddy viscosity suitable for a k-ε presentation of turbulence was derived from the stress transport model for the three cases analyzed, and an algebraic stress model was developed for the case of channel flow with Longitudinal magnetic field.

Recent numerical iterative evaluations[11] for the case of unidirectional two dimensional shear flow subjected to transverse magnetic field, that coincides with one of the coordinates showed somewhat puzzling characteristics:

The description of the main shear stresses $\overline{uv}$ and $\overline{uw}$, associated with the streamwise velocity $\bar{U}$, demand two substantially different eddy viscosities, which are practically independent of the ratio between $\partial\bar{U}/\partial y$ and $\partial\bar{U}/\partial z$. The lateral stress $\overline{vw}/k$, associated with the lateral secondary motion, is practically independent of the magnetic field intensity. Although the magnetic field effects the difference $(\overline{w^2} - \overline{v^2}) / \frac{2}{3} k$, which is the main source for the secondary currents, this effect is practically independent of the ratio between $\partial\bar{U}/\partial y$ and $\partial\bar{U}/\partial z$.

In the present work, a coordinate transformation is used to relate the solutions for the unidirectional two dimensional shear flow with tilted transverse magnetic field to the solutions for one dimensional shear flow with transverse magnetic field also tilting with respect to the coordinate system. With this transformation, it is shown that the abovementioned invariances are due to offects that neutralize each other.

SHEAR FLOW SUBJECTED TO TRANSVERSE TILTED MAGNETIC FIELD

The numerical solutions for the turbulent stresses in the (*) coordinate system where the model reduces to the case of one dimensional shear flow subjected to transverse magnetic field tilted with respect to the coordinates show:

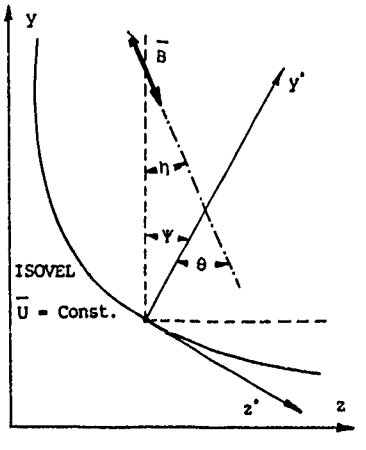

The coordinates systems

(1) Unlike the non magnetized shear flow where the shear stress $\overline{uw}^*$ and $\overline{vw}^*$ do not exist and the relative proportions of the normal stresses are constant, now the shear stresses $\overline{uw}^*$ and $\overline{vw}^*$ are

produced by the electromagnetic interactions which also effect the normal stresses.

(2) The ratio between the shear stresses $\overline{uw}^*$ and $\overline{uv}^*$ which control the streamwise flow is function of the inclination angle θ and the turbulent Hartman number H_t. A limiting line for high H_t shows a maximum value of 0.592.

(3) The sum of the normal stresses $(\overline{w^2}^* + \overline{v^2}^*)/\frac{2}{3}k$ shows moderate monotonic increase with H_t increase which may reach up to 40 percent for high H_t, and weak dependency on θ that does not overpass 7 percent for high H_t. However, the difference between the normal stresses $(\overline{w^2}^* - \overline{v^2}^*)/\frac{2}{3}k$ shows very large alternating sign trend depending on θ that may reach up to 440 percent for high H_t.

(4) Finally, the electromagnetic interactions also produce lateral shear stress $\overline{vw}^*$. The limiting line for high H_t shows a maximum value of 0.57 for the $\overline{vw}^*/\frac{2}{3}k$ ratio.

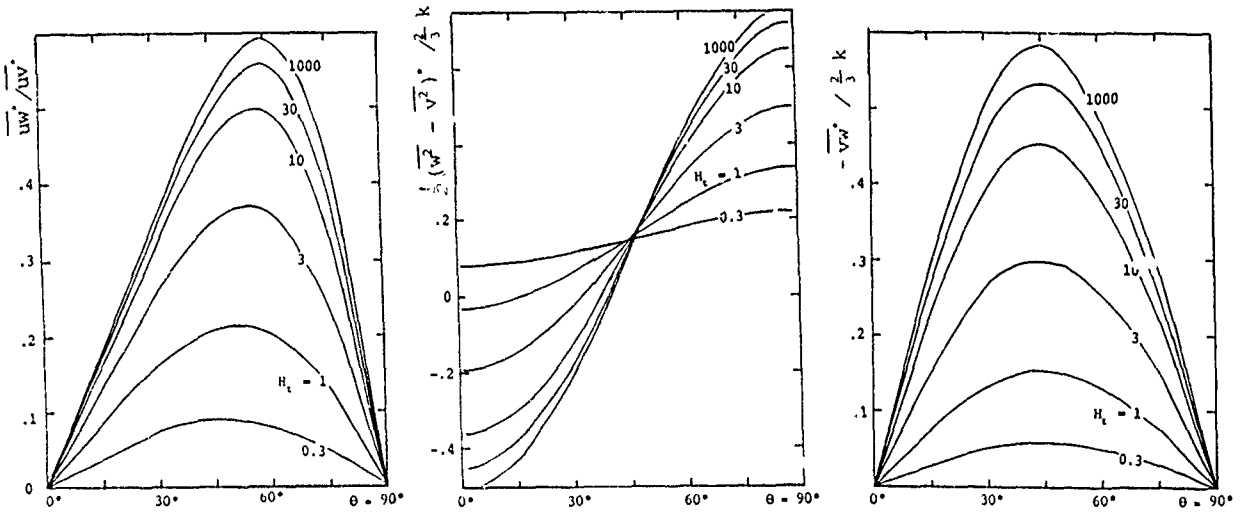

Numerical solutions for the turbulent stresses in the (*) coordinate system

REFERENCES

LAUNDER, B., REECE, G. & RODI, W. 1975 "Progress in the Development of a Reynolds Stress Turbulence Closure", J. Fluid Mech. 68, 537-566.

WOLFSHTEIN, M., NAOT, D. & LIN, A. 1975 "Models of Turbulence" in: Current Topics in Thermal Science, edited by Gutfinger, Hemispher Co. Washington.

NAOT, D. & RODI, W. 1981 "Applicability of Algebraic Models Based on Unidirectional Flow to Duct Flow with Lateral Motion", Int. Jour. for Numerical Methods in Fluids, Vol.1, 225-235.

NARASIMHA, R. 1983 "Relaminarization - Magneto-hydrodynamic and Otherwise" in: Liquid Metal Flow and MHD, AIAA Progress in Astronautics and Aeronautics, Vol.84, edited by Branover, Lykoudis, and Yakhot, AIAA New York.

SUKORIANSKY, S., ZILBERMAN, I. & BRANOVER, H. 1985 "Experiments in Duct Flows with Reversed Turbulence" in: Single and Multi-Phase Flows in an Electromagnetic Field, AIAA Progress in Astronautics and Aeronautics, Vol.100, edited by Branover, Lykoudis and MAA New York.

MOREAU, R. 1983 "Why, How and When MHD Turbulence Becomes Two Dimensional" in: Liquid Metal Flow and MHD, AIAA Progress in Astronautics and Aeronautics, Vol.84, Edited by Branover, Lykoudis and Yakhot, AIAA New York.

SOMMERIA, J. 1985 "Two-Dimensional Behaviour of Electrically Drived Flows at High Hartman Number" in: Single and Multi-Phase Flows in an Electromagnetic Field, AIAA Progress in Astronautics and Aeronautics, Vol.100, edited by Branover, Lykoudis and Mond, AIAA New York.

CAPERAN, P. & ALMANY, A. 1985 "Transition from Three Dimensional to Quasi Two Dimensional MHD Grid Turbulence" in: Single and Multi-Phase Flows in Electromagnetic Field, AIAA Progress in Astronautics and Aeronautics, Vol.100, Edited by Branover, Lykoudis and Mond, AIAA New York.

NAOT, D. & PELED, A. 1988 "MHD Redistribution of Three Dimensional Turbulence", in: Current trends in turbulence research, AIAA Progress in Astronautics and Aeronautics, Vol.112, Edited by H. Branover, Mond, M., and Unger, Y., AIAA New York.

NAOT, D., PELED, A. & TANNY, J. 1990 "Response of Shear Flow Turbulence to Diffusional Electro-magnetic Fluctuations" Appl. Math. Modelling, 14, pp.226-236.

NAOT, D., & TANNY, J. "Towards Quasi Isotropic Turbulence Model for Magnetohydrodynamic Shear Flow" (To be published in an AIAA Progress Series book, 1991).

EIGHTH SYMPOSIUM ON
TURBULENT SHEAR FLOWS
Technical University of Munich
September 9-11, 1991

SOLUTIONS OF THE VON KÁRMÁN-HOWARTH EQUATION BY GRADIENT FLUX APPROXIMATIONS

M OBERLACK
N PETERS
D KIVOTIDES

Institut für Technische Mechanik
RWTH Aachen, Germany

ABSTRACT

A closure model for the von Kármán-Howarth-Equation (K-H-E) is introduced, which describes homogeneous isotropic turbulence in physical coordinates The model holds for a wide range of well accepted turbulence theories for homogeneous isotropic turbulence, as there is Kolmogorovs first and second similarity hypotheses and the invariant theory, which is a generalization of Loitsianskiis and Birkhoffs integrals The invariant theory makes assumptions on the asymptotic decay of the correlation function at infinity Experimental verification of the closure model brings up good agreement in a range of reliable data By neglecting the viscous terms in the K-H-E, the $k-\varepsilon$-equation for isotropic turbulence can be deduced as an integral formulation of the model

NOMENCLATURE

C	Kolmogorov constant
ε	dissipation
f	normalized longitudinal double correlation
k	normalized longitudinal triple correlation
κ_0	model constant
L	integral length scale
ν	kinematic viscosity
$\overline{p'u'}$	pressure-velocity correlation
R_{ij}	two-point double correlation function
$R_{(ik)j}$	two-point triple correlation function
$\overline{u^2}$	mean square velocity fluctuation

TWO-POINT CORRELATION EQUATION

Turbulence shows a wide range of length scales spreading over several decades Common closure models like the $k-\varepsilon$ model, which cannot be derived from basic principles, use a single turbulent length scale the integral length scale To account for length scale variations, a two-point-correlation equation can be derived [1], which can be interpreted as a generalization of a multi scale model Based on this equation, closure models for length-scale equations can be introduced on a more reliable basis Defining the two-point double- and triple-correlation functions

$$R_{ij}(\vec{x},t,\vec{r},\tau)=\overline{u_i'(\vec{x},t)\,u_j'(\vec{x}^{(1)},t^{(1)})}, \tag{1}$$

$$R_{(ik)j}=\overline{u_i'(\vec{x},t)\,u_k'(\vec{x},t)\,u_j'(\vec{x}^{(1)},t^{(1)})}, \tag{2}$$

which are functions of the physical and the correlation space

$$\vec{r}=\vec{x}^{(1)}-\vec{x}, \tag{3}$$

the two-point correlation equation reads as follows

$$\begin{aligned}&\frac{\partial R_{ij}}{\partial t}+\overline{u_k}(\vec{x},t)\frac{\partial R_{ij}}{\partial x_k}+\frac{\partial R_{(ik)j}}{\partial x_k}+\frac{1}{\rho}\frac{\partial\overline{p'u_j'}}{\partial x_i}\\&+R_{kj}\frac{\partial\overline{u_i}(\vec{x},t)}{\partial x_k}+R_{ik}\frac{\partial\overline{u_j}(\vec{x}^{(1)},t^{(1)})}{\partial x_k^{(1)}}-\nu\frac{\partial^2R_{ij}}{\partial x_k\partial x_k}\\&+[\overline{u_k}(\vec{x}^{(1)},t^{(1)})-\overline{u_k}(\vec{x},t)]\frac{\partial R_{ij}}{\partial r_k}-\frac{\partial}{\partial r_k}\left(R_{(ik)j}-R_{i(jk)}\right)\\&-\frac{1}{\rho}\frac{\partial\overline{p'u_j}}{\partial r_i}+\frac{1}{\rho}\frac{\partial\overline{u_ip'}}{\partial r_j}+2\nu\frac{\partial^2R_{ij}}{\partial x_k\partial r_k}-2\nu\frac{\partial^2R_{ij}}{\partial r_k\partial r_k}=0\end{aligned} \tag{4}$$

The first seven terms are similar to those used in one-point closures such as the Reynolds-stress-equations The six additional terms arise from the fact, that the equation generally has to be solved in physical and in correlation space No closure has to be introduced for the pressure velocity correlations, because a Poisson equation for pressure fluctuation can be used that brings up no additional unknown term Owing to the fact, that Eq (4) includes three extra dimensions, the equation implies an infinite number of length scales in contrary to common turbulence models The only remaining term, to be modelled is the gradient of the triple correlation in correlation space.

ISOTROPIC TURBULENCE

Prediction of the decay law of homogeneous isotropic turbulence is one of the basic problems in turbulence theory and a first test for a closure assumption used in the above correlation equation Rewriting the correlation equation under the assumption of isotropic turbulence, Eq (4) can be reduced to the von Kármán-Howarth Equation (K-H-E) [2]

$$\frac{\partial(\overline{u^2}f)}{\partial t}=\frac{1}{r^4}\frac{\partial}{\partial r}\left[r^4\left(2\nu\frac{\partial(\overline{u^2}f)}{\partial r}+\overline{u^2}^{3/2}k\right)\right] \tag{5}$$

A closure model has to be introduced for the dimensionless triple correlation k in terms of known quantities and widely accepted turbulence theories Former closure models where those of Hasselmann [3] and Domaradski and Mellor [4] While the latter showed some intersting results, it did not include all the following behaviour of k at the origin

$$k=\frac{1}{3}k_0'''r^3+ \tag{6}$$

Here we will use Kolmogorov's similarity hypotheses for $r<<L$ and neglect the unstationary term in the following form of Eq (5)

$$\begin{aligned}&-\frac{2}{3}\varepsilon-\underbrace{\frac{\partial}{\partial t}(\overline{u^2}(1-f))}_{\approx 0}\\&\div\frac{1}{r^4}\frac{\partial}{\partial r}\left[r^4\left(\nu\frac{\partial(\overline{u^2}(1-f))}{\partial r}+\overline{u^2}^{3/2}k\right)\right]=0\end{aligned} \tag{7}$$

This parametrises the solution by ε and ν A first integration yields

$$2\nu\frac{\partial(\overline{u^2}(1-f))}{\partial r}+\overline{u^2}^{3/2}k=\frac{2}{15}r\varepsilon \tag{8}$$

Kolmogorov's first and second law are

$$\overline{u^2}(1-f)=\frac{1}{30}\frac{\varepsilon r^2}{\nu} \tag{9}$$

for $r\to 0$ and

$$\begin{aligned}&\overline{u^2}(1-f)=C(\varepsilon r)^{2/3}\\&C\approx 2\,3\end{aligned} \tag{10}$$

for $\eta<<r<<L$, where

$$\eta=(\nu^3/\varepsilon)^{1/4} \tag{11}$$

is the Kolmogorov scale

In contrary to the properties of the correlation funtions for small r, one can introduce a class of invariant integrals which are a generalization of Loitsianskiis [5] and Birkhoffs [6] integrals The latter make assumptions for the behaviour for $r\to\infty$ Continuity requires that f decays faster than r^{-2} at infinity

We propose a closure for the K-H-E by gradient flux approximation, which satisfies Eqs (9) and (10)

$$\overline{u^2}^{3/2}k=\nu_T\frac{\partial(\overline{u^2}f)}{\partial r} \tag{12}$$

$$\nu_T = 2\kappa_0\sqrt{\overline{u^2}(1-f)}$$
$$\kappa_0 = \frac{\sqrt{2}}{5\ C^{3/2}} \approx 0.0811 \tag{13}$$

The resulting equation is of parabolic type

$$\frac{\partial F}{\partial t} = \frac{2}{r^4}\frac{\partial}{\partial r}\left[r^4(\nu + \kappa_0 r\sqrt{F(0,t) - F(r,t)})\frac{\partial F}{\partial r}\right] \tag{14}$$
$$F(r,t) = \overline{u^2}\, f(r,t)$$

Experimental verification for the closure model was done at different levels Fig 1 and 2 shows measured values for k [7] with increasing time compared with the closure hypotheses, while the f function in Eq (12) and (13) have been recorded during the same experiment In a second step, Eq (14) was integrated numerically and compared with experimental data [8] for $\overline{u^2}$ (Fig 4) Initial conditions have been taken from the same experiment Within the measuring range excellent agreement was achieved

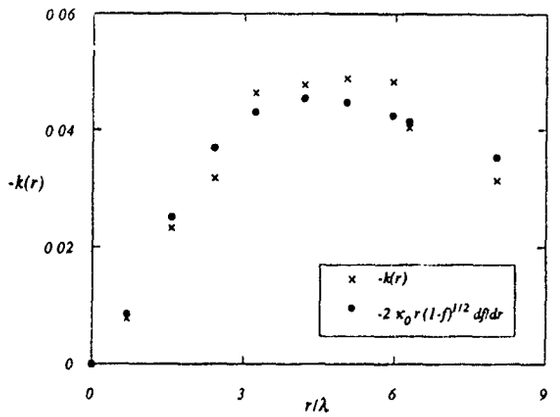

Fig. 1 The triple correlation function

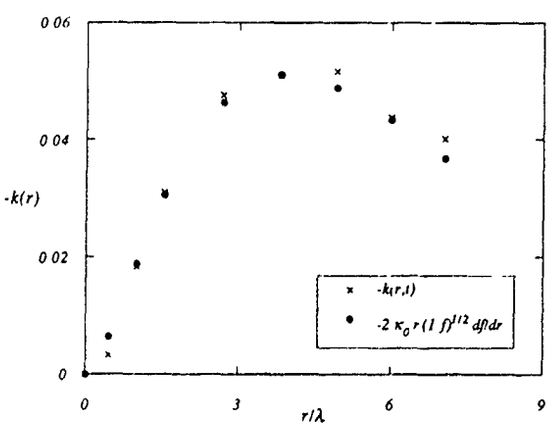

Fig 2 The triple correlation function

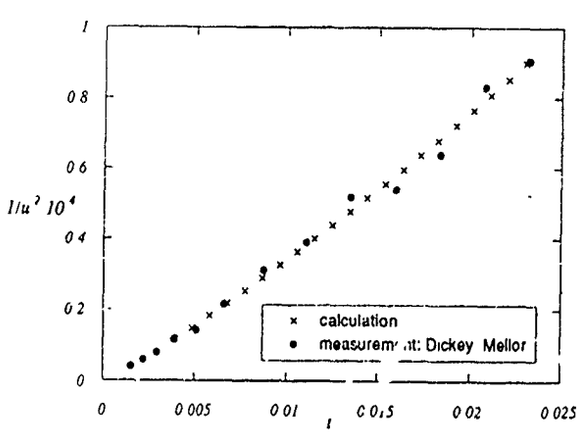

Fig 3 Mean square velocity fluctuation during decay of turbulence

In order to deduce from the K-H-E information about a or one-step closure model an integral formulation is sought Eq (14) yields after one integration the following form

$$\frac{\partial}{\partial t}\int_0^\infty \overline{u^2} f dr = 8\left\{\nu\int_0^\infty \frac{1}{r}\frac{\partial(u^2 f)}{\partial r}dr - \frac{2}{3}\kappa_0\,\overline{u^2}^{3/2}\right\} \tag{15}$$

To evaluate the integrals, an ansatz for $f(r,t)$ similar to the Kármán-Pohlhausen method must be introduced

A first step is to approximate Eq (8) together with the closure Eqs (12) and (13) . This leads to an equation which is only valid for $0 << r << L$

$$\frac{1}{15}r\varepsilon = (\nu + \kappa_0 r\sqrt{b})\frac{db}{dr}, \quad b = \overline{u^2}(1-f) \tag{16}$$

Rescaling and changing the dependent and independent variables, one obtains Abel's differential equation

$$y\frac{dy}{dx} = y\sqrt{x} + 1, \quad b = \frac{\sqrt{\nu\varepsilon}}{\kappa_0\sqrt{15}}x; \quad r = \left(\frac{15\nu^3}{k_0^2\varepsilon}\right)^{1/4} y \tag{17}$$

Because no exact solution of Eq. (17) is known, an approximation satisfying the limits $y \to 0$ and $y \to \infty$ is used

$$y = \sqrt{x} + \frac{2}{3}\sqrt{x^3} \tag{18}$$

The inverse of Eq (18) is given by

$$x = \left\{\left(y - \sqrt{\frac{2^{5/2}}{9} + y^2}\right)^{1/3} + \left(y + \sqrt{\frac{2^{5/2}}{9} + y^2}\right)^{1/3}\right\}^2 \left(\frac{3}{4}\right)^{2/3} \tag{19}$$

Now f will be approximated by

$$f = \exp[-\alpha x], \quad \alpha = \sqrt{\frac{\nu\varepsilon}{15\kappa_0^2\,\overline{u^2}^2}} \tag{20}$$

which satisfies the limit $f = 1 - ax$ for $x \to 0$ and $f \to 0$ for $x \to \infty$ Introducing Eq (20) in Eq (15) and neglecting the viscous term in Eq (15) one obtains after some manipulations the $k-\varepsilon$-model

$$\frac{dk}{dt} = -\varepsilon \tag{21}$$

$$\frac{d\varepsilon}{dt} = -c_{\varepsilon_2}\frac{\varepsilon^2}{k} \tag{22}$$

with

$$c_{\varepsilon_2} = 1\ 89 \tag{23}$$

The standard $k-\varepsilon$-model requires 1 92 for c_{ε_2} which is very close to the value above

CONCLUSIONS

A closure model for the K-H-E is introduced whith a gradient flux approximation for the triple correlation k, satisfying the first and second Kolmogorov law and the invariant theory Comparison with experiments give excellent agreement in the range of reliable data As an example for an integral formulation of this model the $k-\varepsilon$-model for isotropic turbulence is recovered

LITERATURE

[1] Rotta J C *Turbulente Strömungen*, Teubner
[2] de Kármán T , Howarth L *Proc Roy Soc* A 164 (1938), 192-215
[3] Hasselmann K *Dtsch Hydgr Z* 11 (1958), 207-217
[4] Domaradzki J A , Mellor G L *JFM* 140 (1984), 45-61
[5] Loitsianskii L G *Zentr Aero-Hydrodyn Inst* 440 (1939)
[6] Birkhoff G *Comm Pure Appl Math* 7 (1954), 19-44
[7] Stewart R W , Townsend A A *Phil Trans Roy Soc Lon* A 243 (1951), 359-386
[8] Dickey T D , Mellor G L *JFM* 99 (1980), 13-31

EIGHTH SYMPOSIUM ON
TURBULENT SHEAR FLOWS
Technical University of Munich
September 9-11, 1991

QUANTIFICATION OF VORTEX STRENGTH IN BLUFF BODY WAKES USING SPECTRAL MEASUREMENTS

C O Popiel[1], D I Robinson[2] and J T Turner[2]

1 Energy Lab., Faculty of Engineering, Rand Afrikaan University,
PO Box 524, Johannesburg 2000, South Africa
2 Department of Engineering, University of Manchester,
Manchester, M13 9PL, United Kingdom.

Abstract

The unsteady flow properties of the wake produced by a vortex shedding cylinder of unusual cross-sectional shape, developed as a result of a visualisation study, have been quantitatively tested Comparison has been made with the wake produced by a triangular cross-sectioned cylinder using an ensemble averaged frequency spectra method The increased strength and stability of the wake from the new body are demonstrated

Introduction

The complex mechanism of vortex formation in the wake of a bluff body has attracted wide interest [e g Fage and Johansen (1928), Gerrard (1966), Bearman (1967)] Recently methods of quantitatively comparing the strength and stability of coherent wake structures initiated by different cylinder cross-sections have been developed [e g Lucas and Turner (1985), Nichols et al (1986), Pankanin (1985)] The work reported here complements these recent investigations by using the ensemble averaged frequency spectra obtained from a hot wire anemometer signal to compare quantitatively the unsteady flow properties of wakes produced by two very different bodies.

One of the body shapes, consisting of a split circular cylinder with a concave rear surface, was the result of an extensive visualisation study by Popiel and Turner (1988), which aimed to produce the optimum body shape corresponding to the strongest vortex shedding action over an extended Reynolds number range For comparison and to provide a control, a cylinder with equilateral triangular cross-section (one flat face normal to the incident flow) was also examined

Equipment

Figure 1 is a schematic of the wind tunnel used, in which the flow velocity could be varied up to 25 m/s (Re=43,000 based on actual cylinder width of 25.2 mm). Centre-line turbulence intensity was found to be approximately 2 5% over the Reynolds number range considered

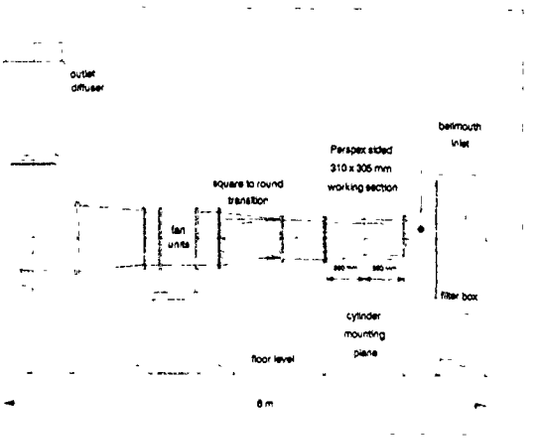

Figure 1 Wind tunnel used for experiments

A constant temperature anemometer (CTA) system was used to obtain the vortex shedding signal The wedge film probe could be traversed both axially and transversly in the flow behind the bluff body Output from the CTA was processed using a digital spectrum analyser and a personal computer to calculate a signal-to-noise ratio (SNR) for the vortex signal The definition of the SNR described in Lucas and Turner (1985), based on the ensemble averaged amplitude of the frequency spectrum, was used

Experimental procedures

Two kinds of experiment were performed.

The Strouhal versus Reynolds number relationship was examined for the new bluff body, noting that this had the same width as the triangular body and the bodies tested by Lucas and Turner (1985) The variations with Reynolds number of the SNR, the vortex shedding frequency, and the peak spectral amplitude at the vortex-shedding frequency, were also determined. During these experiments, the hot film probe was positioned at mid-height, 0 02 diameters (d) behind and slightly to one side of the cylinder, so as to lie in the separated shear layer Measurements were made throughout the available range of Reynolds number (i.e from about 3000 to 43000).

Figure 2 presents some data which show typical variations in Strouhal number, SNR and peak spectral amplitude with Reynolds number, suitably scaled to fit on the same plot

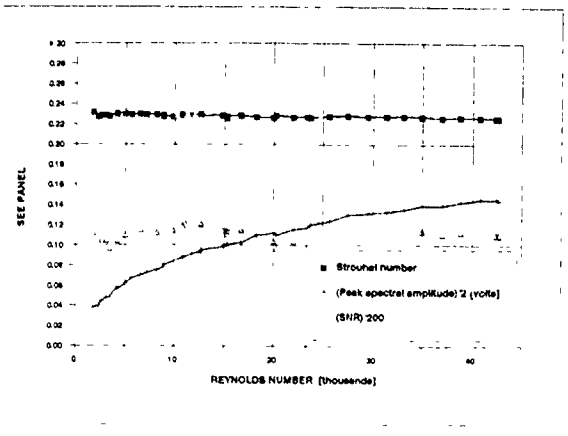

Figure 2 Plots of Strouhal number, SNR and peak spectral amplitude against Reynolds number - new body

In the second series of experiments, changes in SNR and peak spectral amplitude as the position of the hot film probe was varied within the bluff body wake were investigated. These experiments were carried out for both bodies at the same Reynolds number (Re=20,000) as that used by Lucas and Turner (1985) In turn, each cylinder was placed in position in the tunnel and the probe was traversed across the tunnel in the mid-span plane at stations axially 0 04 d, 0 2 d and 0 4 d behind the rear-most point of the body In each probe position, the same parameters as in the first experiment were recorded

Figure 3 shows the variation of SNR for both bodies at each station on the same scale Here the considerably increased strength and stability of the vortex street from the new body is clear

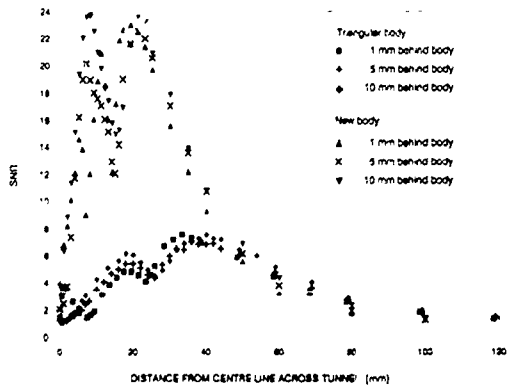

Figure 3 Variation of SNR with position at Re 20 000 - comparison between triangular body and new body

The repeatability of the SNR measurements, using 128 samples on the spectrum analyser for ensemble averaging, was better than 1%, except in the region of maximum free stream velocity where it fell to 4-5%.

Conclusion

The study has yielded detailed data which complement the previous programme of visualisation experiments. Results obtained show, in particular, that the signal-to-noise ratio of the periodic wake behind the new split cylinder is approximately three times that for a triangular cylinder This demonstrates the ability of the spectral measurement approach to quantify in an unambiguous way the strength and stability of the coherent structures in a turbulent wake.

References

FAGE, A AND JOHANSEN, F.C. (1928) "The structure of the vortex street." Phil. Mag. 5, 417-441

GERRARD, J H (1966) "The mechanics of the formation region of vortices behind bluff bodies." J. Fluid Mech. 25, 401-413.

BEARMAN, P.W. (1967) "On vortex street wakes " J. Fluid Mech. 28, 625-641

LUCAS, G.P. AND TURNER J.T. (1985) "Influence of cylinder geometry on the quality of its vortex-shedding signal." Proc Int. Conf. on Flow Measurement, FLOMEKO'85, Melbourne.

NICHOLS, A R., BENTLEY, J.P., BATES, K.L. AND COULTHARD, J (1986) "Experimental investigations of vortex shedding from two rectangular bluff bodies in tandem " Flow Measurement in the mid 80's, NEL, East Kilbride.

PANKANIN, G.L., (1985) "A new approach to the bluff body design in vortex flowmeters " Proc of Int. Symp on Fluid Control and Measurement, FLUCOME'85, Tokyo.

POPIEL, C.O. AND TURNER, J.T (1988) "Vortex shedding from cylinders of various cross-sections at low Reynolds numbers " Confidential report to sponsors

EIGHTH SYMPOSIUM ON
TURBULENT SHEAR FLOWS
Technical University of Munich
September 9-11, 1991

FINITE ELEMENT ANALYSIS OF TURBULENT AND HEAT TRANSFER THROUGH A SUDDEN PIPE EXPANSION

M. S Ravisankar[+], K N. Seetharamu[++] and P. A. Aswath Narayana[x]
Indian Institute of Technology, Madras, India

[+] Graduate Student, Department of Mechanical Engineering
[++] Professor, Department of Mechanical Engineering
[x] Professor, Department of Applied Mechanics

ABSTRACT
The influence of the inlet boundary conditions on the predicted reattachment length is highlighted. Especially, the specification of ε inlet condition is crucial. A new mixing length distribution based on the physical reasoning of the flow field is presented. The $k-l$ model displays excellent numerical stability, on the other hand $k-\varepsilon$ model is highly unstable The predictions using the new mixing length distribution, for l in the $k-l$ model are in good agreement with the existing results.

INTRODUCTION

Flow through a sudden pipe expansion is a good bench mark problem to evaluate any model of turbulence or a numerical technique for its predictive capabilities in axisymmetric geometries The point at which reattachment of the flow takes place forms one of the basis of comparing different models A recent review of internal flows by Nallasamy (1987) compares the reattachment length predicted by different models However the comparison is not justified because the inlet conditions specified are different in each case In the present work it is shown that the problem is sensitive to inlet conditions

The numerical instability of the $k-\varepsilon$ model is well known. The numerical advantages of $k-l$, where the mixing length l is prescribed using an algebraic equation, is highlighted in the present work and also a new mixing length distribution based on physical reasoning of mixing in the flow field is prescribed

NUMERICAL PROCEDURE AND MODELS USED

The problem is simulated using Galerkin finite element technique using Eulerian velocity correction method to solve the momentum equations in unsteady state form Linear triangular elements are used for spatial discretisation Details of the flow geometry are shown in Fig 1.

The low Reynolds number version of $k-\varepsilon$ and $k-l$ models, damped with functions given in Lam and Bremhorst (1981) and Wolfshtein (1970) respectively, are used Three different mixing length prescriptions for 1, the Prandtl's mixing length, modified version of the distribution given in Taylor et al (1981) and a new mixing length model are used.

RESULTS AND DISCUSSIONS

The $k-\varepsilon$ model does not show monotonic convergence towards steady state and it is highly oscillatory. The $k-l$ model exhibits very good numerical stability and it shows monotonic convergence towards steady state. Also the values of k does not become negative The mixing length distribution for all the three models can be given by a general relationship $l = \kappa\, y_{REF}$, where value of κ is 0.4 and y_{REF} is the reference distance.

In Prandtl's mixing length distribution (ML0), $y_{REF} = y_{WALL}$, and y_{WALL} is minimum of the normal distance from either of the walls This distribution over predicts mixing, hence the reattachment length is under predicted

The mixing length distribution specified for flow over backward facing step in Taylor et al (1981) is modified (ML1) to take the present problem

$$y_{REF} = \begin{cases} \min(y_{WALL},\ (x/X_R)H) & \text{if } X \le X_R \\ \min(y_{WALL},\ (2X/X_R - 1)H) & \text{if } X \ge X_R \end{cases} \quad (1)$$

The value of y_{REF} is calculated from equation (1) This distribution under predicts mixing near the axis, close to the expansion. As a consequence results exhibit wiggles Also the physical basis of this distribution is weak.

A new mixing length distribution (ML2) is proposed on the physical reasoning of mixing in the flow field It is highly improbable for an eddy to mix with a region where the direction of the flow field is reversed From the streamline pattern of the flow shown in Fig 1, it is assumed that an eddy in between the line AB and the axis of the pipe can mix freely up to the line AB, where the flow takes place in downstream direction Similar argument is assumed for an eddy in between the walls and line AB, where the flow is in the opposite direction The value of y_{REF} is taken as y_{WALL} beyond the reattachment point and has a value which is minimum of y_{WALL} and the distance from the line AB in the region between the expansion and the reattachment point

The reattachment lengths predicted by the three distributions are shown in table I (S Nos 1,2 & 3). The overall performance of ML2 is good. The quality of predictions made by ML1 distribution is poor. All the three distributions showed monotonic convergence towards the steady state.

The influence of inlet axial velocity profile on the prediction of reattachment length is shown in table I (S. Nos 7&9). The reattachment length predicted is more for uniform axial velocity profile than the profile based on $1/7^{th}$ law. The effect of Reynolds number on reattachment length is marginal as seen in Table I (S. Nos 4 & 5).

The inlet turbulent kinetic energy k, has a marked influence in the prediction of the reattachment length. It is clear from the Table I (S. Nos 5, 6 & 7) that an increase in k decreases the reattachment length The inlet specification of turbulent kinetic energy dissipation ε, is equally important, which is generally not measured The following empirical relationship is used to calculate the value of ε,

$$\varepsilon = 0.09\ k^{3/2} / (0.015D). \qquad (2)$$

The diameter D is conventionally taken as D_{BE} . But this resulted in a severe under prediction of the reattachment length. Instead, if D is taken as D_{AE} as in Pun and Spalding (1977), the predicted value increases by a great margin. This is clearly seen in Table I (S. Nos 7&8).

The effect of different wall boundary conditions on the heat transfer is studied. The computed local Nusselt number variation is in good agreement with experimental results of Zemanick and Dougall (1970). The error in peak Nusselt number is 11.2 % and it is well within the acceptable limits (Launder, 1988). Another peak is seen very close to the expansion as shown in Fig. 3, which is in line with the intuitive argument given by Zemanick and Dougall (1970). The influence of radial wall boundary condition is restricted very close to the expansion as seen in Fig. 3.

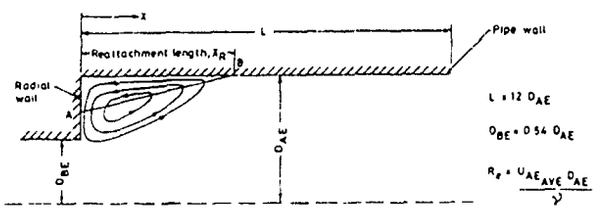

FIG 1 FLOW THROUGH A SUDDEN PIPE EXPANSION

CONCLUSIONS

1. The specification of inlet boundary condition is very critical and its influence on the reattachment length is considerable.
2. The $k - l$ model is potentially a viable model and has good numerical stability.
3. A new approach to mixing length distribution is highlighted and the predictions based on this concept agrees well with the experiment.

TABLE -1 COMPARISON OF REATTACHMENT LENGTHS

S No	Model	Reynolds Number	Inlet k	Inlet ε/ Mixing length	Inlet axial velocity profile	Reattachment length X_R
1	k - l	100 000	0 06	MLO	1/7 law	4 14
2	k - l	100 000	0 06	ML1	1/7 law	7 74
3	k - l	100 000	0 06	ML2	1/7 law	7 10
4	k - l	45 360	0 06	ML2	1/7 law	6 80
5	k - ε	100 000	0 16	0 23	1/7 law	6 10
6	k - ε	100 000	0 11	0 22	1/7 law	8 60
7	k - ε	100 000	0 06	0 0882	1/7 law	10 10
8	k - ε	100 000	0 06	0 1633	1/7 law	5 70
9	k - ε	100 000	0 06	0 0882	Uniform profile	8 90

(All quantities are non-dimensionalized using D_{AE} and average velocity $U_{AE\,AVE}$)

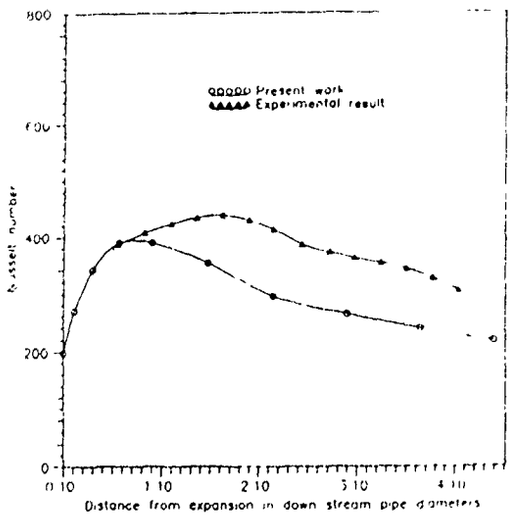

Fig 2 Flow through sudden pipe expansion at Re=48070 Pr 0 71
Model used= k-l length specification based on ML2
Results are compared with experimental results given by Zemanick and Dougall

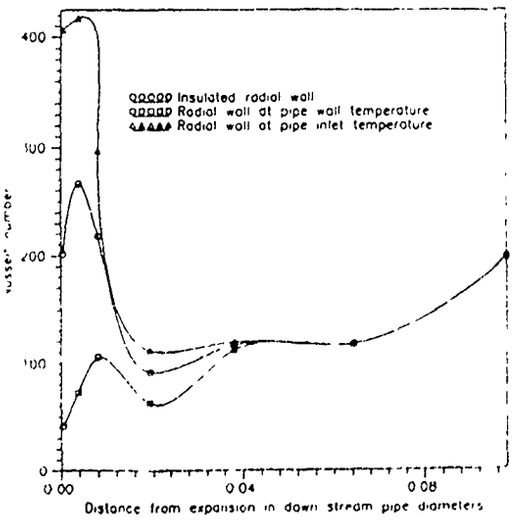

Fig 3 Flow through sudden pipe expansion at Re=48096 and Pr 0 71
Model used= k-l length specification based on ML2
Pipe wall maintained at constant temperature in all the cases

Note: *This paper has been abbreviated by the Editor because it exceeds the given limit of two pages.*

EIGHTH SYMPOSIUM ON
TURBULENT SHEAR FLOWS
Technical University of Munich
September 9-11, 1991

Characterization of the Transport Behaviour of Particles in an Electrohydrodynamic Flowfield with the aid of a Two-Component Laser-Doppler Velocimeter

Claus Riehle and Friedrich Löffler

Inst f. Mech. Verfahrenstechnik u. Mechanik,TU Karlsruhe
Postfach 6980, D-7500 Karlsruhe, Germany

An electrohydrodynamic flowfield is a superposition of a conventional gas flow and a flow of gas ions. Such flowfields occur for example in electrostatic precipitators widely used for the cleaning of flue gases The experimental investigation of the particle velocities within an electrohydrodynamic (EHD) flowfield is therefore necessary to characterize the transport conditions. The interaction between the neutral gas and the gas ions (sometimes called ionic wind) changes the pattern of the streamlines because the gas ions drift along the electric field lines which cross the streamlines of the turbulent main flow. This interrelationship decisivly influences the flowfield structure and hence the transport behaviour of the particles. The EHD flowfield is not only dependent on the Reynolds-number, but also on a second factor. Some authors refer to the N_{EHD}-number, whereby the presented definitions are not always in total compliance [1, 2] *Shaugnesssy et al* have derived this characterstic number from a de-dimensionalized and extended Navier-Stokes equation, and speak of the "Electric Froude number " Fr_{el} [3], for which the following relationship holds:

$$N_{EHD} = \frac{j_{NE}\, 2s}{b\,\rho\, v^2} = \left[\frac{1}{Fr_{el}}\right]^2$$

j_{NE} electric current density (colling area specific)
s channel half-width
v mean gas velocity (flow rate density)
r gas density
b mooility of gasions

The EHD flowfeld was generated in a vertical quadratic test duct and the gas ions were produced with a corona discharge located at five round copper wires (SE) in the middle of the duct (**Fig. 1**). The geometrical parameters were

half duct width (NE-SE)	.	s	=	70.7 mm
wire-to-wire distance (SE-SE)	:	2c	=	70.7 mm
wire radius	:	r_{se}	=	0 35 mm
Length of EHD-zone	:	L	=	350 mm

The realized Laser-Doppler Velocimeter (LDV) allowed a simultaneous measurement of two velocity components of the particles (**Fig. 1**): the migration velocity towards the plate electrodes (NE, y axis) together with the velocity component in the main flow direction (x axis). The resulting parameters are.

$< v_i >$. average velocity of the component i
$\{< v_i'^2 >\}^{0,5}$: r.m s -value of the component i

From these a turbulence intensity Tu_p can be derived:

$$Tu_p = \frac{\sqrt{\frac{1}{2} < v_i'^2 > + \frac{1}{2} < v_j'^2 >}}{\sqrt{< v_i >^2 + < v_j >^2}}$$

The use of the term turbulence intensity for the characterization of particle motion (discriminated by the suffix p) may, at first glance appear unconventional, since this is usually only applied in conjunction with fluid phases. Nevertheless, this has been deliberately used in the following, since the ratio of the average velocity deviations of the disperse phase to the absolute value of the velocity vector is indeed an appropriate parameter for the characterization of the particle motion state. The experiments were conducted using a NaCl aerosol with a number distribution median of $x_{50,0}$ = 1,4 µm and a geometric standard deviation of x_{84}/x_{50} = 1,4 Furthermore it is important to say that in this application of Laser-Doppler velocimetry the light-scattering particles do not play the role of tracers because they are charged, and hence, drift within the electric field relative to the fluid phase. In general it is impossible to measure fluid velocities in an EHD flowfield when using light-scattering techniques.

The aim of the investigations was the characterization of the particle dynamic at different states of the EHD-flowfield. Therefore the experiments have been conducted in dependence of the electrical operational conditions for two average flow velocities. The parameters for each operational setting may be extracted from the following table:

Table: Operational conditions of the EHD flowfield

v	Re_{2s}	U	E	j_{NE}	Fr_{el}	N_{EHD}
m/s		kV	kV/cm	mA/m²		
0,71	6667	0	0	0	∞	0
0,71	6667	20,0	2,8	0,30	1,76	0,32
0,71	6667	35,0	5,0	3,69	0,50	4,00
1,41	13333	0	0	0	∞	0
1,41	13333	20,0	2,8	0,30	3,57	0,08
1.41	13333	35,0	5,0	3,69	1,00	1,00

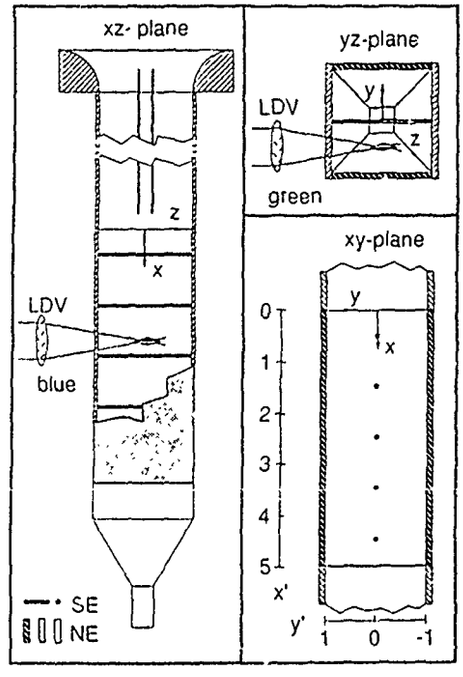

Fig.1 Survey of the measured velocity components together with the plane of measurement

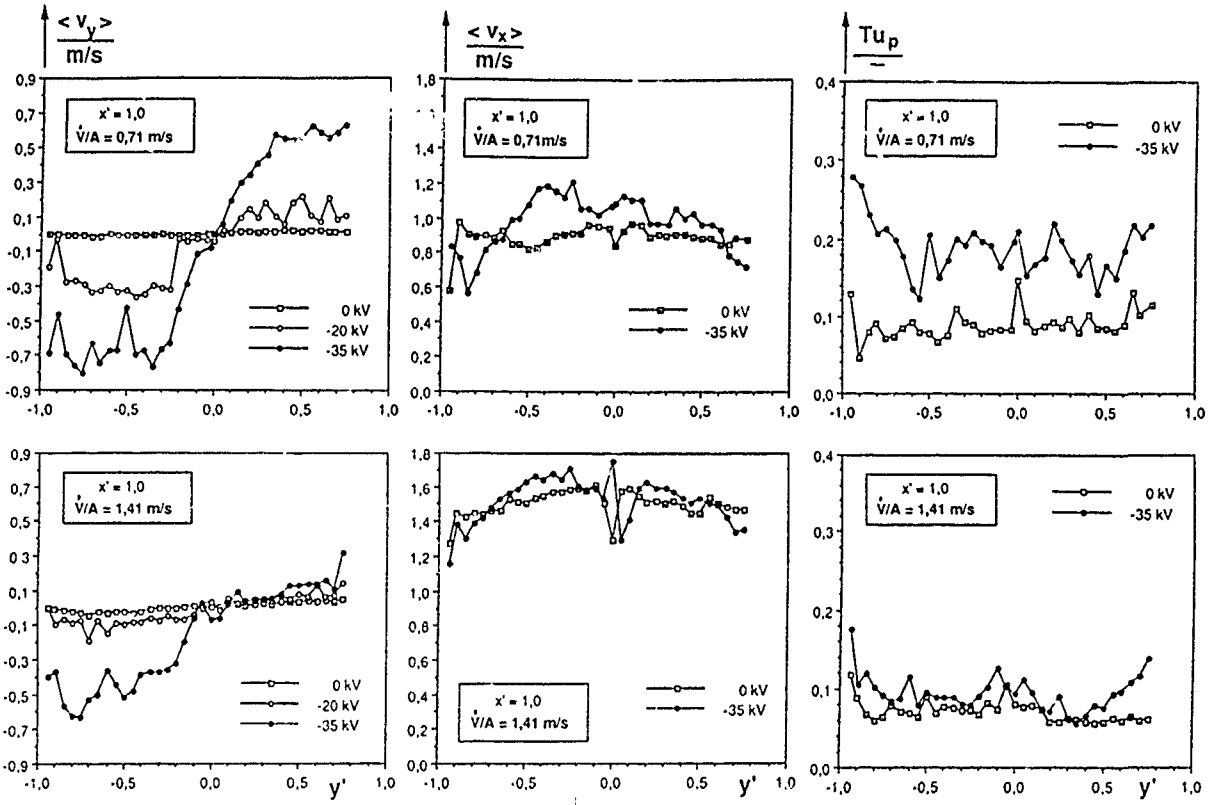

Fig. 2. Averaged particle migration velocity across the main flow between the first and second corona electrode

Fig. 3. Averaged particle velocity profiles in the main flow direction between the first and second corona electrode

Fig. 4: Profiles in the turbulence intensity between the first and second corona electrode

The presentation of the results uses dimensionless coordinates, for which purpose all lengths are de-dimensionalized by the channel half-width s The following figures portray the results of measurements conducted between the first and second corona electrode. This location corresponds to the dimensionless coordinate x' = 1,0 (see Fig. 1). Each graph demonstrates the profiles across the main flow direction between the dimensionless y-coordinate y' = - 1 to y' = + 1, which corresponds to the surfaces of each plate electrode. In the range y' < 0, measurements could be conducted at distances down to 3,5 mm from the plate by turning the precipitator. y' = 0 is the defined location of the corona electrodes Each graph contains the measuring values for two or three applied voltages The upper part of the figure shows results for a mean gas velocity of 0,71 m/s, the lower for 1,41 m/s respectively.

Fig. 2 shows the results of the $\langle v_y \rangle$ measurements which can be related to the residence time and the saturation charge respectively. When compared with calculated values it can be shown that the migration velocity of the particles is approximately three times higher than theoretically expected, provided they receive at least 90 % of their saturation charge.

The results of the $\langle v_x \rangle$ measurements (Fig. 3) distinctly verify that the ionic wind influences the particle motion At a voltage of 35 kV, the velocity profiles change and, as one can observe, this change is more dominant for 0,71 m/s than for 1,41 m/s. In contrast to the 0 kV state, the particle velocity increases at the central channel regions and decreases substantially at the wall zones. This phenomenon can be seen as an indication for the existence of secondary flows as already observed in the case of positive corona fields [4,5]. The ionic wind does induce eddy regions as a result of continuity, which causes the observed particle velocity decrease in the vicinity of the channel walls and the particles can hardly follow such a back-flow of the fluid phase due to the influence of the electrical force.

A comparison between the different EHD states discloses that $N_{EHD} \approx 1$ is a critical value for the mutual interactions between the ionic wind and the neutral gas phase. Whilst for N_{EHD} values > 1, the stochastic particle motion is chiefly determined by the non steady-state character of the negative corona, for N_{EHD} values < 1, however, the particle velocity fluctuations are governed by the turbulence of the neutral fluid. This behaviour is clearly demonstrated by Fig. 4 which shows the measured turbulence intensities Tu_p of the particles.

References:

[1] *Leonard G.L., Mitchner M , Self S.A.:* An experimental study of the electrohydrodynamic flow in electrostatic precipitators; J. Fluid Mech. 127 (1983) 123-140

[2] *Yamomoto T.:*Some aspects of efficiency theory for electrostatic precipitators; Send. Internatinel Conference on Electrostatic Precipitation, Kyoto (1984) 523-521

[3] *Shaugnessy E.J., Davidson J.H., Hay J H.:*The Fluid Dynamics of Electrostatic Precipitators; Aerosol Science and Technology 4 (1985) 471-476

[4] *Yabe A., Mori Y . Nijkate K..*EHD study of the corona wind between wire and plate electrodes, AIAA J. 16 (1978) 340-345

[5] *Yamomoto, T., Velkoff, H.R..*Electrohydrodynamics in an Electrostatic Precipitator; J.Fluid Mech. 108 (1981)1- 18

EIGHTH SYMPOSIUM ON
TURBULENT SHEAR FLOWS
Technical University of Munich
September 9-11, 1991

III-16

SOME FURTHER EXPLORATION OF TURBULENCE MODELS FOR BUOYANCY DRIVEN FLOWS

S. Vasić and K. Hanjalić

Mašinski fakultet, University of Sarajevo
Omladinsko setaliste bb, 71000 Sarajevo, Yugoslavia

ABSTRACT

Based on truncation of general second order closure methods, a simpler form of model is searched which would enable sufficiently faithful reproduction of specific features of buoyancy dominated turbulent flows, but still retain an eddy-viscosity form which could be incorporated easily into the general 3-dimensional Navier-Stokes computer code for complex geometries. Validation of the model was carried out by considering several characteristic buoyancy dominated flow situations

INTRODUCTION

Buoyancy dominated turbulent flows are characterized by several features which can not be modelled successfully by popular k-ε or other eddy-viscosity type models. A strong coupling and a mutual feed-back between the velocity and temperature field, as well as inadequacy of gradient hypothesis by which turbulent flux is usually represented, are some of such specific features. However, most widely used Navier-Stokes codes are not suitable for incorporation of second-order closure scheme which would overcome most of the deficiencies of simple models. Hence, for time being, a compromise is searched which would retain the basic eddy diffusivity formulation, but modified as to account for most important buoyancy effects.

The present paper focuses on the analysis of relatively simple test cases in which "clean" buoyancy effects can be isolated and various modeling ideas explored in details. For that purpose two groups of test cases have been examined, one in which the density stratification vector is collinear with the gravitational vector (bottom heating) and the other with two vectors being perpendicular (side heating and cooling).

We consider first the two test cases which simulate the dynamics of almost one-dimensional, unsteady, mixed layers, driven purely by buoyancy. The first is the well known experiment of Deardorff et al. (1969) [3] of the development of a turbulent mixed layer in the lower region of initially stably stratified quiescent fluid by heating from below, and its upward penetrative convection into the stable layer above it. The second test case is the laboratory model of Markofski and Harleman (1971) [5] of the development of a surface mixed layer due to the surface cooling (simulation of diurnal variation of a termocline) and its downward advancement in the underlying stratified fluid. A common feature of both cases is the creation and growth of highly turbulent mixed layer in which the transport of momentum and heat occurs by turbulent diffusion, while the temperature profiles remain basically uniform, demonstrating clearly the failure of the simple local gradient representation of turbulent flux. Another important feature of these cases is the entrainment of adjacent overlaying or underlaying non- turbulent fluid into the mixed layer and a consequent development of a sharp density jump (termocline) at the interface of turbulent and non- turbulent fluid The penetration of the mixed layer incurs a reversal of sign of the heat flux in the region close to the interface (compensating cooling of the stable fluid in the first case and heating in the second case). All these and other features recorded in the mentioned and other experiments, pose a serious challenge to turbulence modelling.

Second group of considered cases concerns again simplified geometries with side heating and cooling so that the gravitational vector is perpendicular to the mean temperature gradient. The representative cases are the experiments of Cheesewright and coworkers, and of some other authors. A specific feature of these cases is the concentration of steep temperature and velocity gradients as well as high turbulence intensity in the thin boundary layers along the vertical walls and almost quiescent isothermal core region occupying the majority of the channel cross-section.

The enclosed diagrams illustrate the quality of predictions obtained by a simplified version of full stress/flux model as well as by a modified version of k-ε model which produces almost the same accuracy.

RESULTS AND DISCUSSION

Figures 1 to 2 present the comparison of the measured and computed values of two major parameters measured by Deardorff et al. The presented results were computed by a simplified form of the second order model which entails the solution of transport equations for vertical turbulent heat flux and temperature variance in addition to the energy and dissipation equations with the standard Launder-Sharma [4] low-Re-number modifications. The vertical profiles of mean temperatures and total heat flux at different time instants show excellent agreement in full details, including the sign reversal of the heat flux just below the interface. The development of the thickness of the mixed layer (two different definitions, one corresponding to the position of sign reversal, and other to the minimum turbulent heat flux), both show very good agreement, except for the initial period which is uncertain because of unknown initial conditions. The predicted time development of the fluctuating temperature variance (not shown here) at different heights show a qualitatively similar behaviour to those found by experiments, though a large scatter of the experimental data brings in a dose of uncertainty, so that some difference in rates of change can not be explained satisfactory at present.

Figures 3 presents a comparison of measured and computed mean temperature profiles for one of the experiments of Markofski and Harleman [5] for the period of one diurnal cycle with successive heating and cooling of surface layer by radiation and surface convection (here also the simulation was performed of the reservoir inflow and outflow, with changeable water level and variable radiative heat exchange). The computations show a good agreement including the

compensating heating of the entrained fluid below the mixed layer, during the period of surface cooling.

Figures 4 and 5 show the comparison of predicted profiles of vertical mean velocity and mean temperature at the mid height of a 5:1 rectangular channel heated and cooled from sides, compared with measurements of Cheesewright and King [2]. The presented results have been obtained by a kind of low-Re-number algebraic flux model which could be reduced for computational convenience to a form of k-ε model in which a tensorial "Prandtl-Schmidt" number accounts for additional terms originating from truncated full stress model. This procedure generates a more general invariant- instead of simple gradient hypothesis for turbulent heat flux. In addition the length scale correction of Yap [6] was also applied. As shown in diagrams, these modifications brought visible improvements of the predictions. The wall shear stress shown on Fig. 6 agrees reasonably well with the experimental data for both walls (which should have been equal if full symmetry had been attained). Profiles of turbulent shear stress and heat fluxes $\overline{u\theta}$ and $\overline{v\theta}$ at the same cross-section, Figs. 7, 8 and 9 show close magnitudes and qualitatively similar behaviour as measured data but the predictions, tuned to simulate fully symmetric situation, could not follow a visible asymmetry of the experiments.

The paper demonstrates that a form of k-ε model, suitable for incorporation into a general Navier-Stokes code for a complex 3-d flow, but modified on the basis of a truncation of the full stress/flux second order model, can generate a reasonably faithful reproduction of several experiments of distinct features with buoyancy flux being aligned or perpendicular to the imposed external heat flux.

References:

1.Bowles A.& Cheesewright R. 1989 Exp. Heat Transfer 2
2.Cheesewright R.& King K. 1990,9th Int.Heat Trans.Conf.
3.Deardorff J.W et.al. 1969, J.Fluid Mech., vol 35
4.Launder, B.E. & Sharma B.I. 1974, Lett. in H&M Trans.
5.Markofski M.& Harleman D.R.F. 1971, MIT Tech.Rpt.134
6 Yap C. 1987, Ph.D. Thesis, UMIST.

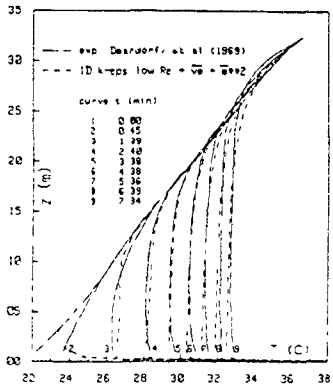

Figure 1 Temperature profiles at different time instants

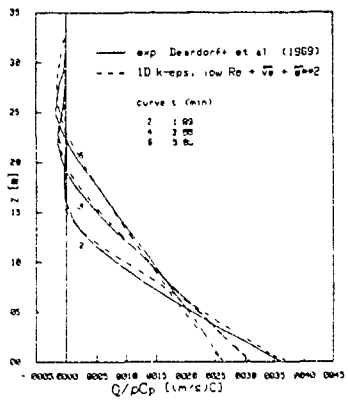

Figure 2 Vertical heat flux at selected times

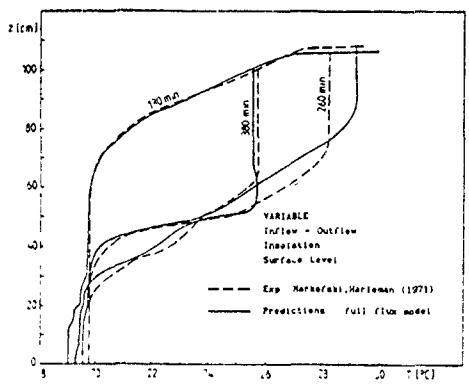

Figure 3 Temperature distribution across the reservoir depth

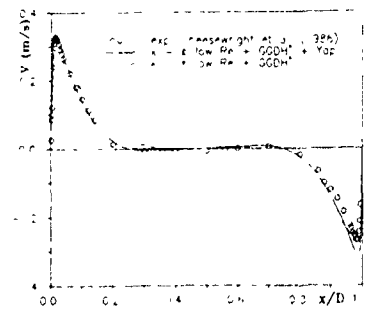

Figure 4 Vertical mean velocity at channel mid-height

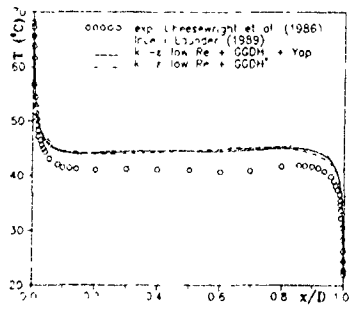

Figure 5 Mean temperature profile at chennel mid-height

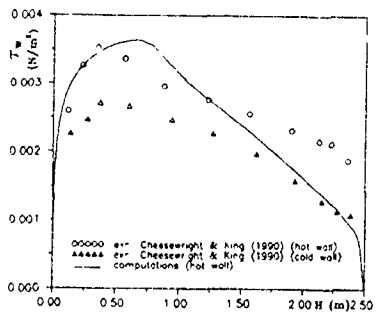

Figure 6. Distribution of wall shear stress allong the walls

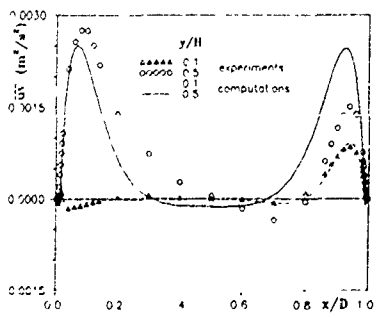

Figure 7 Distribution of $\overline{uv}$ across the channel width

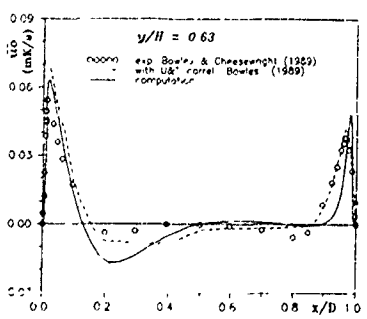

Figure 8. Distribution of $\overline{u\theta}$ across the channel width at H=.63

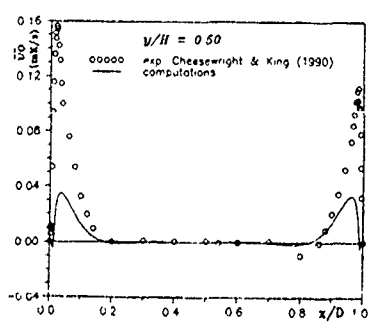

Figure 9 Distribution of $\overline{v\theta}$ across the channel width

EIGHTH SYMPOSIUM ON
TURBULENT SHEAR FLOWS
Technical University of Munich
September 9-11, 1991

STUDY ON THE PRESSURE-STRAIN TERM IN REYNOLDS STRESS MODEL

M. Yamamoto* and C. Arakawa**

* Department of Mechanical Engineering
Science University of Tokyo

** Department of Mechanical Engineering
University of Tokyo

ABSTRACT

In this study we focused on Slow Term model of the pressure-strain correlation. It is well-known that Slow Term represents Return-to-Isotropy (below RTI) phenomenon and RTI process depends on the third invariant III of anisotropy tensor strongly. Four existing models, (i)Rotta (ii)Lumley and Newman (iii)Shima (iv)Sarlar and Speziale, were selected and the numerical results were compared with experimental data. We found that each model can not reproduce the phenomenon correctly in either the case with positive III or the one with negative III. Thus we tried to construct a new non-linear Slow Term model by making constants be functions of invariants. It is shown that our model can predict the RTI phenomenon more reasonably. Further study is needed on the effect of low-Reynolds-number.

1. INTRODUCTION

Reynolds stress transport model (below RSTM) is one of time-averaged turbulence models. RSTM is superior to eddy viscosity models (typically k-ε model) in the universality because it takes accounts of the Reynolds-stress-transport phenomena. A lot of RSTMs have been proposed and investigated, such as Launder-Reece-Rodi and Shima . RSTMs have been constructed on the basis of many assumptions. We think that now it should be done to check again whether each term is modeled reasonably or not. Present study is regarded as the first step of such investigations. We focused on Return-to-Isotropy (below RTI) problem. It is well-known that this process depends on whether the third invariant III is positive or negative. One purpose of this study is to check some models for Slow Term of pressure-strain correlation. Four existing models were selected and the numerical results were compared with experimental data. It is shown that they can not reproduce RTI phenomenon correctly in either the case with positive III or the one with negative III. The other purpose is to construct a new non-linear Slow Term model by making constants be functions of invariants. It is shown that our model is able to predict RTI process more reasonably for both III>0 and III<0.

2. GENERAL EXPRESSION OF RETURN-TO-ISOTROPY

Exact Reynolds stress transport equations include an unknown pressure-strain correlation. Because this is responsible for the energy transfer between each Reynolds stress component, it is very important to model this term correctly in RTMs. Conventionally this correlation is modeled by the following expression.

(Pressure-Strain Correlation)= $\phi_{ij,1}+\phi_{ij,2}+\phi_{ij,w}$ (1)

where $\phi_{ij,1}$, $\phi_{ij,2}$, and $\phi_{ij,w}$ represent the contribution by a turbulence-turbulence interaction, a turbulence-mean flow interaction and a boundary effect, respectively. In the present study we dealt with the first part, so-called Slow Term. This kind of flows is known as Return-to-Isotropy problem and governed by following equations.

$$db_{ij}/dt=-\varepsilon/q\cdot(\Phi_{ij}-2\cdot b_{ij}) \quad (2)$$

$$dq/dt=-2\cdot\varepsilon \quad (3)$$

$$d\varepsilon/dt=-2\cdot C_{\varepsilon 2}\cdot\varepsilon^2/q \quad (4)$$

where $b_{ij}=\overline{u_i u_j}/q-1/3\cdot\delta_{ij}$, $\Phi_{ij}=-\varepsilon\cdot\phi_{ij,1}$, $q=u_i u_j$ and $C_{\varepsilon 2}=1.90$. b_{ij} is called as anisotropy tensor of turbulence. Lumley pointed out that Φ_{ij} can be expressed generally by the next equation.

$$\Phi_{ij}=\alpha_1(II,III)\cdot b_{ij}+\alpha_2(II,III)\cdot(b_{ik}\cdot b_{kj}-II/3\cdot\delta_{ij}) \quad (5)$$

where II and III are defined by $II=b_{ik}\cdot b_{ki}$ and $III=b_{ik}\cdot b_{kj}\cdot b_{ji}$ and are called as the second and the third invariant of anisotropy tensor b_{ij}, respectively.

3. PREDICTABILITY OF EXISTING MODELS

At first we investigated the predictability of existing models. Four models were used for this purpose. According to Eq.(5) they can be summarized as follows.

Model (i) : Rotta
$\alpha_1=3.0$
$\alpha_2=0.0$

Model (ii) : Lumley and Newman
$\alpha_1=2+F/9\cdot\exp(-7.77/Re_t^{1/2})\cdot[72/Re_t+80.1\cdot\ln(1+62.4\cdot(II/2+2.3\cdot III/3))]$
$\alpha_2=0.0$
where $F=1-9/2\cdot II+9\cdot III$ and $Re_t=q^2/(9\cdot\varepsilon\cdot\nu)$

Model (iii) : Shima
$\alpha_1=2+7.297\cdot Fri\cdot F\cdot II$
$\alpha_2=0.0$
where $Fri=1-\exp(-(0.1508\cdot Re_t))$

Model (iv) : Speziale and Sarkar
$\alpha_1=3.4$
$\alpha_2=3.0\cdot(\alpha_1-2.0)$

Model (i) is linear in b_{ij}. Model (ii) and (iii) are quasi-linear. Model (iv) is non-linear. Model (i) is the most popular in conventional RSTMs and succeeds when the turbulence is not strongly anisotropic. Model (iii) was developed in the near-wall calculation.

Calculations have been performed by four step Runge-Kutta method which is second order in the time marching. As the initial εs are not measured, we set them so that the changes of q are matched with the experimental data. Time increments were selected as nearly same magnitude as 1/500·(final time in experiments). In oder to check the appropriateness of this time increments, calculations were performed with 1/1000·(final time). However meaningful discrepancies could not be recognized.

Four experimental data were adopted in this study. (1)Le Penven, Gence and Comte-Bellot (III>0 and III<0), (2)Gence and Mathieu (III>0), (3)Tucker and Reynolds (III<0).

Fig.1 to 4 show the temporal decay of normal Reynolds stresses. Numerical results are compared with the corresponding experimental data. Because of the limited space these figures include the results obtained by our model (Model (v)) which will be described in the next section. From these figures following characteristics are evident. For III>0 Model (i) and (iv) reproduce the correct RTI process, but for III<0 too slow RTI is calculated. On the contrary, Model (ii) and (iv) predict RTI reasonably for III<0, but produce too first RTI process for III>0. In addition, changes in II-III phase space made these aspects more clear (not shown here because of the limited space).

It is easy to conclude that each model can not satisfactorily reproduce both the case with III>0 and the one with III<0. We think that this shortcomings are caused by not having considered the data with either positive or negative III in constructing their models.

4. PROPOSAL OF A NEW MODEL

In order to improve the predictability of Slow Term model, we tried to construct a new model. Especially,

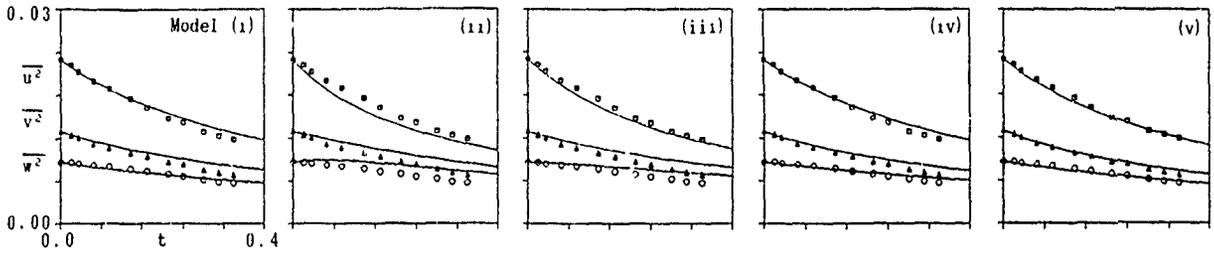

Fig 1 Temporal Decay of Normal Reynolds Stresses (Le Penven et al., III>0. $\overline{u^2}$:○, $\overline{v^2}$:△, $\overline{w^2}$:□, Cal.:—)

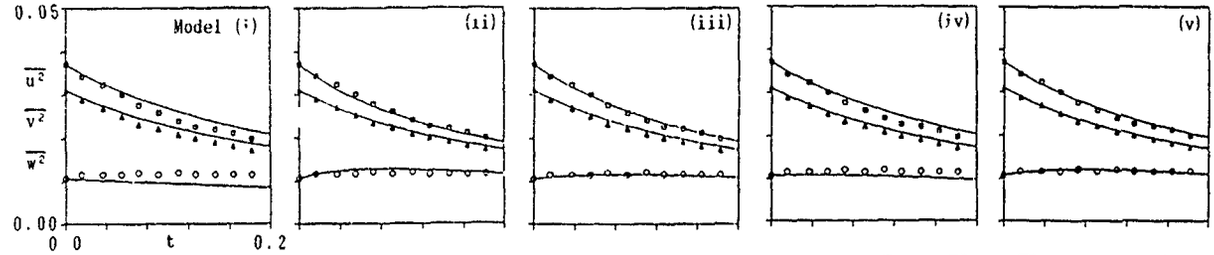

Fig 2 Temporal Decay of Normal Reynolds Stresses (Le Penven et al., III<0. $\overline{u^2}$:○, $\overline{v^2}$:△, $\overline{w^2}$:□, Cal.:—)

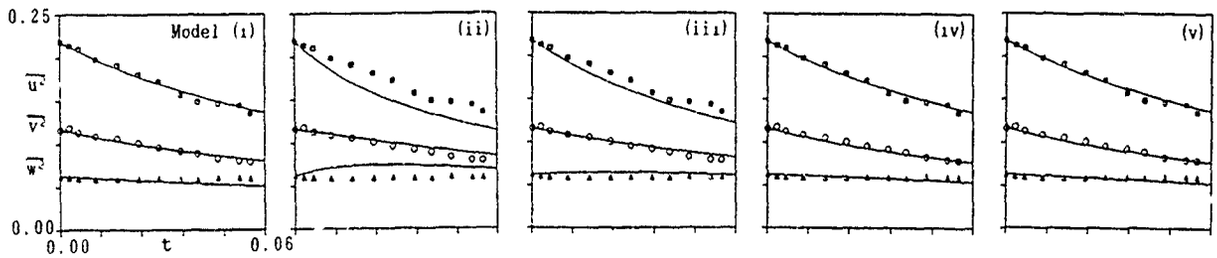

Fig.3 Temporal Decay of Normal Reynolds Stresses (Gence & Mathieu, III>0. $\overline{u^2}$:○, $\overline{v^2}$:△, $\overline{w^2}$ □, Cal.:—)

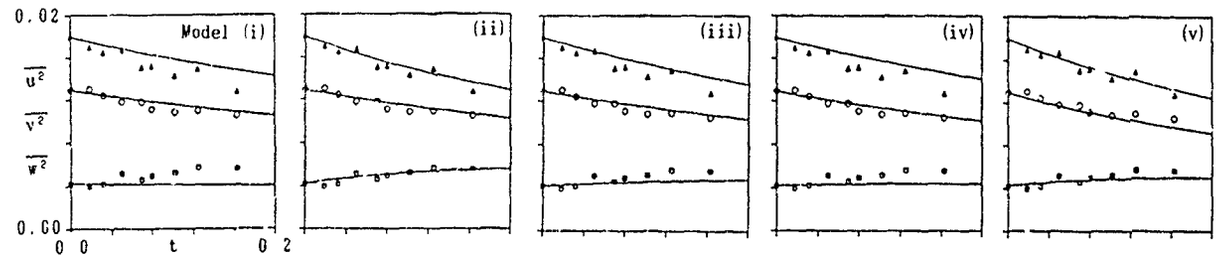

Fig.4 Temporal Decay of Normal Reynolds Stresses (Tucker & Reynolds, III<0, $\overline{u^2}$:○, $\overline{v^2}$:△, $\overline{w^2}$:□, Cal.:—)

different RTI processes for the different sign of III were focused on. As it was found that the model proposed by Sarkar and Speziale is the most promissing in conventional models we made the constants be sensitive functions of III. At first we searched the optimum constants which can lead acceptable results for Le Penven's data because their data are the only ones that include the cases with both III >0 and III<0. After calculating the data with various values for α, we found that α =3.2 for III>0 and α =4.3 for III<0 give good agreement with experimental data. Thus, we had best make the constants be functions so that they realize above values in the initial stage of the experiments and they do not change so much during the experiments. We tried a following expression.

Model (v) . Present Model

$$\alpha = 2 + p * F * (q * |II| + |III| \ \mathrm{sign}(III))$$

$$\alpha = 3 * (\alpha - 2)$$

where p, q, r and s are unknown constants and must be determined by using experimental data or some theoretical techniques. We set p=-12.0, q=-0.65, r=0.4 and s=0.45 from the curve fitting of Le Penven's data and the preriminary calculation.

Same numerical techniques and experimental data used in section 3 have been adopted again. At the right end of Fig.1 to 4 show the results obtained by our non-linear model. From these figures it is easily found that our model can reproduce the RTI phenomenon reasonably for both cases with III>0 and III<0.

In the present study we assumed that Reynolds number of flows was high enough not to consider the low-Reynolds-number effect (eq. Eq (2)-(4)). Thus, we did not introduce such effect in our model. Further investigations will be needed on this point.

5 SUMMARY

We studied RTI problem as the first step of the refinement of Reynolds stress model. Four existing models were selected and the computational results were comared with experimental data. We found that none of them can reproduce the phenomenon satisfactorily. So we tried to construct a new non-linear Slow Term model. It was shown that our model is able to predict RTI phenomenon more reasonably. However, as it does not include a low-Reynolds-number effect, we need further investigations.

Reference

(1) B.E.Launder et al., J.Fluid Mech., (1975), Vol.68, p.537
(2) N.Shima, Trans. JSME (1988), Vol.54, p.2317, (in Japanese)
(3) J.L.Lumley, Adv. Appl. Mech., (1978), Vol.18, p.123
(4) J.C.Rotta, Z.Phys., (1951), Vol.129, p.547
(5) J.L Lumley et al., J Fluid Mech., (1977), Vol.82, p.161
(6) S.Sarkar and C.G.Speziale, NASA CR-181797, (1989)
(7) L.Le Penven et.al., in Frontier in Fluid Mech. edited by S.H.Davis et al, Springer-Verlag, (1985), p.1
(8) J N.Gence et al., J.Fluid Mech., (1980), Vol.101, p.555
(9) H.J Tucker et al., J.Fluid Mech. (1968), Vol 32, p.657

SYMPOSIUM ON
TURBULENT SHEAR FLOWS
Technical University of Munich
September 9-11, 1991

AN EXPERIMENTAL INVESTIGATION OF THE BASE BLEED EFFECT ON THE TWO-DIMENSIONAL TURBULENT WAKE STRUCTURE

V.L. Zhdanov*) and H. Eckelmann**)

*) Institute for Heat and Mass Transfer of the Academy of Sciences of the BSSR, SU - 220072 Minsk, USSR

**) Max-Planck-Institut für Strömungsforschung, D-3400 Göttingen, Germany

ABSTRACT

The flow pattern behind a two-dimensional body with bleeding through a slot at its trailing edge is experimentally investigated. Two bleeding modes are studied: one with maximum pressure at the trailing edge and one with a zero-excess momentum wake. In both cases the slot width, characterized by its width to trailing edge height ratio h/H, varied from 0.095 to 0.019. Distributions of the mean velocity and the longitudinal and transversal fluctuations in the wake are measured and compared to the wake without bleeding.

INTRODUCTION

Base bleed is an effective method to reduce body drag. This method, among a lot of others, is interesting because of its practical application. Bleeding or blowing a certain amount of fluid from the rear part of a body into the flow field leads to a higher pressure at the body base (i.e. a smaller drag) or provides a zero-momentum-excess when the ejected jet compensates the body drag. This phenomena has been given little attention so far: Igaraclú (1978), Dmitrenko, Kovalov, Luchko & Cherepanov (1987), and Cimbala & Park (1990). In particular, the influence of the orifice size through which the bleeding is accomplished on the change of the flow pattern in the wake of a body has not been sufficiently examined yet. As could be shown for a two-dimensional body by Zhdanov & Eckelmann (1990) the magnitude of the base pressure, the velocity defect in the wake, and the shedding frequency are determined by the ratio of the slot width and the height of the body trailing edge. To understand the drag reduction it is of interest to consider at different locations downstream of the body the variation of the mean velocity defect, the level of the turbulent fluctuations and the decay of these quantities.

EXPERIMENTAL SETUP

The investigation is carried out in the open return type wind tunnel of the Max-Planck-Institut fuer Stroemungsforschung described by Kastrinakis & Eckelmann (1983). The test section has a cross section of $280 \times 1400 mm^2$. The coordinate system is chosen such that x is aligned with the mean flow, y is perpendicular to mean flow and span, and z is the spanwise direction. The two-dimensional body, shown in Fig. 1, has a semicircle front followed by a parallel sided part with a blunt trailing edge. The length of the chord (l), the base height (H), and the spanwise width (L) are $l = 200mm$, $H = 40mm$, $L = 280mm$, respectively. All measurements are conducted at 0° incidence, at a free stream velocity of $U_o = 14m/s$ and a free stream turbulence level of 0.1%. The Reynolds number based on U_o and H is 3.7×10^4. The slot on the rear surface of the body is created by two metal blocks fixed by screws at the ends of the upper and lower plates. The slot width can be adjusted by thin metal sheets of $0.5mm$ thickness which are fixed between a block and the upper and lower plates. Four slot widths are examined: Model 1 ($h/H = 0.095$), Model 2 ($h/H = 0.07$), Model 3 ($h/H = 0.045$) and Model 4 ($h/H = 0.019$). Two rows of pressure taps ($d = 1mm$) are drilled into each block to determine the pressure distribution. One row in spanwise direction with nine holes and one in mid-span section with four holes. All taps of a block lead to a central hole of $5mm$ diameter which can be connected to a manometer. The base pressure p_b at a pair of holes, one in the top and one in the bottom block, is obtained by sealing the remaining holes.

The bleed fluid is devided into two lines before it is supplied to the left most chamber of the body from either side. The mass flow rate is quantified by two gas meters installed in each of the lines. To guarantee a uniform velocity distribution in the jet leaving the slot a honeycomb is installed inside of the body.

The mean velocity profiles as well as the profiles of the velocity fluctuations in x and y direction are measured with standard X-wire probes and hot-wire anemometers.

RESULTS AND DISCUSSION

Fig. 2 shows the dependence of the base pressure coefficient $-(C_p)_b = (p_o - p_b)/(\rho U_o^2/2)$ as a function of the bleed coefficient C_q, which is defined as the mass flow rate through the slot area devided by the mass flow rate through the body area in mean flow direction. It can be seen, that increasing the bleed rate from $C_q = 0$ (which corresponds to the pure wake) to higher values leads for all models at the beginning to an increase of p_b (i.e. to a decrease of $-(C_p)_b$ and then after reaching an extremum to a decrease of p_b. The smaller the slot width, the faster occurs the increase and decrease. On the other hand, the larger the slot width the larger is the maximum base pressure. This trend extends the measurements made by Bearman (1968) to a wider range of slot widths. The measurements shown in Fig. 2 were carried out up to bleed rates where the ejected jet just compensates the body drag. For this case, for the maximum base pressure case and for the pure wake ($C_q = 0$) the mean velocity profiles are shown for $x/H = 7$ in Fig. 3.

When the maximumum pressure is reached at the body base the wake structure is very similar to the that of the pure wake. Fig. 4 shows for this case and for the pure wake the normalized decay of the mean velocity in the center of the wake $(U_o - U)/Uo = \Delta U_o/U_o$ and the normalized half width spreading of the wake δ_1/H as a function of the nondimensional distance x/H from the body. From this figure the following laws can be derived $\Delta U_o/Uo \sim (x/H)^{-1/2}$ and $\delta_1/H \sim (x/H)^{1/2}$. In Figs. 5 and 6 are plotted the corresponding dependences of the r.m.s. fluctuations u_1/U_o and u_2/U_o as well as the spreading δ_1/H, δ_2/H of the u_1 and u_2 distributions in the wake as a function of x/H. With bleeding the anisotropy of the fluctuations in the wake decreases, in addition the flow structures become smaller and

the Strouhal number grows (Zhdanov & Eckelmann 1990).

In the case when the bleeding jet compensates the body drag (i.e. the zero momentum excess regime) the flow structure is characterized by a higher dissipation rate. This is manifested in a faster decay of the streamwise r.m.s. fluctuations; here, $u_1, u_2 \sim (x/H)^{-0.81}$. Compared to the maximum pressure case the spreading $\delta_1/H, \delta_2/H$ of the u_1 and u_2 distributions is not changed significantly.

REFERENCES

BEARMAN, P.W. 1966 Investigation into the effect of base bleed on the flow behind a two-dimensional model with a blunt trailing edge. AGARD-CP-4, 485-507.

CIMBALA, J.M. & PARK, W.J. 1990 An experimental investigation of the turbulent structure in a two-dimensional momentumless wake. J. Fluid Mech. **213**, 479-509.

DMITRENKO, Yu.M., KOVALOV, I.I., LUCHKO, N.N. & CHEREPANOV, P.Ya. 1987 Investigation of a plane wake with zero-momentum excess. J. Eng. Phys. **52**, 743-751.

IGARACHI, T. 1978 Characteristics around a circular cylinder with slit. Bul. JSME **21**, 656-664.

KASTRINAKIS, E.G. & ECKELMANN, H. 1983 Measurement of streamwise vorticity fluctuations in a turbulent channel flow. J. Fluid Mech. **137**, 165-186

ZHDANOV, V.L. & ECKELMANN, H. 1990 The effect of jet bleed on base pressure distribution, shedding frequency, and mean velocity profiles in the wake behind a two-dimensional blunt model. MPI für Strömungsforschung Göttingen, Rep. 9/1990

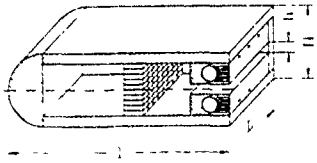

Fig. 1 Section of two-dimensional body

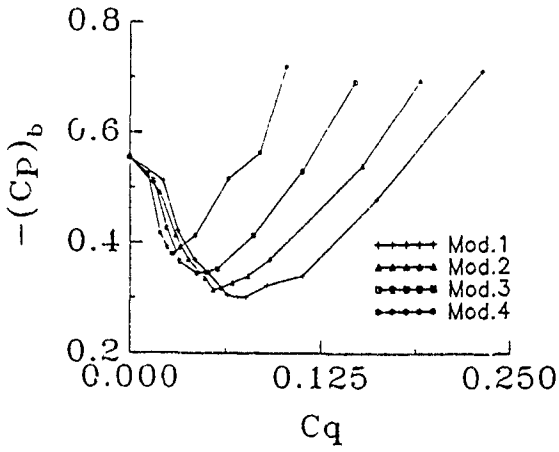

Fig. 2 Base pressure as a function of bleed rate

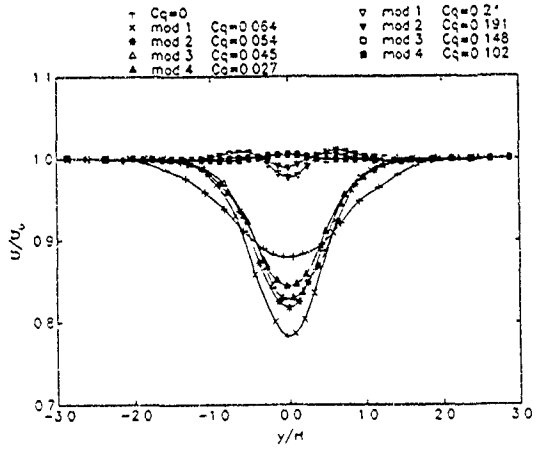

Fig. 3 Mean velocity distribution at x/H = 7

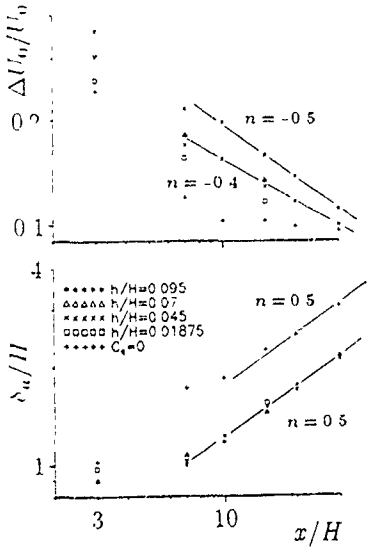

Fig. 4 Decay of the mean velocity in the wake center (top) and spreading of the wake profile

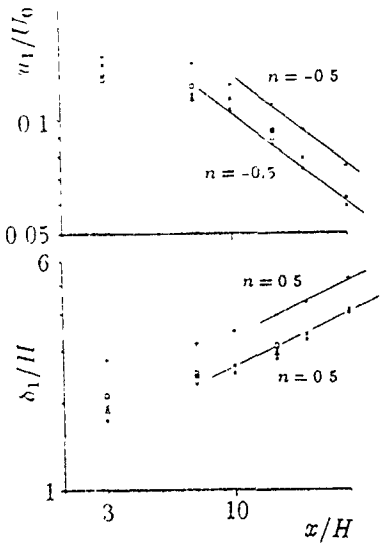

Fig. 5 Decay of the longitudinal velocity fluctuations in the wake center (top) and spreading of the fluctuation profile (maximum base pressure case)

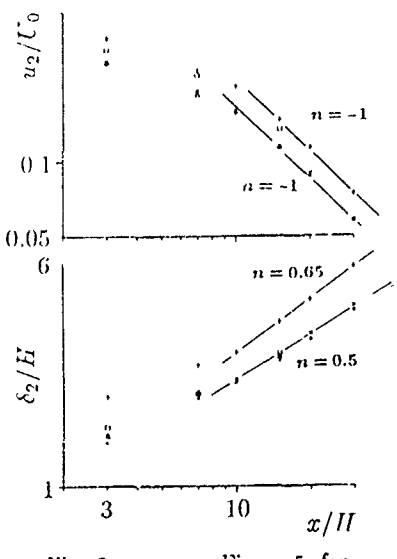

Fig. 6 same as Fig. 5 for the transversal velocity fluctuations

EIGHTH SYMPOSIUM ON
TURBULENT SHEAR FLOWS
Technical University of Munich
September 9-11, 1991

PREMIXED, TURBULENT COMBUSTION OF AXISYMMETRIC SUDDEN EXPANSION FLOWS

A. S. NEJAD AND S. A. AHMED
Advanced Propulsion Division
Aero Propulsion and Power Directorate
Wright-Patterson AFB, Ohio 45433-6563

ABSTRACT

Velocity and low frequency combustor pressure oscillations have been measured in a ramjet dump combustor model. The mean and RMS values of the turbulent velocity field were obtained using a two-component LDV system operating in the backscatter mode. Reacting flow data were obtained for premixed propane and air, while isothermal results were collected after replacing the propane with nitrogen. The velocity data indicated substantial differences between the two cases. Combustor pressure oscillation data were also obtained. The intensity and frequency of the oscillations were found to be dependent on the inlet velocity, combustor length, and equivalence ratio. Results showed that pressure oscillations were controlled by both vortex kinematics in the combustor and acoustic response of the inlet section.

INTRODUCTION

Turbulent sudden expansion flows are of significant theoretical and practical importance. Despite the fact that such flows have been the subject of extensive analytical and experimental studies for decades, many issues are still unresolved. For example, because of the complexity of the flowfield and the associated difficulties with measurements, detailed information on reacting sudden expansion flows are very limited. As a result, development and evaluation of analytical models of the flowfield, especially for confined turbulent recirculating flow configurations, have been hampered by the lack of reliable and detailed experimental data. Therefore, in order to further develop these numerical codes such as the K-ε model to become general (i.e. applicable to more than a limited range of simple configurations), reliable and well documented experimental data are a must. Therefore, the objective of the current study was to obtain a credible and detailed experimental data base and to help in the understanding of the behavior of such flows.

EXPERIMENTAL SET-UP

A major facility to conduct experiments with and without combustion as designed and fabricated. The design incorporated innovative approaches for providing optical access without disturbing the integrity of the axisymmetric flowfield. The combustor section consisted of a water-cooled pipe which terminated in an exhauster used to simulate high altitude conditions.

This modular design allowed optical access for 2-D LDV measurements while preserving the integrity of the combustor flowfield. One of the unique features of this design was the ability of positioning the dump plane relative to the combustor measurement station. Other special features included a 38mm x 38mm (1.5 in x 1.5 in) flat quartz window installed in the inlet pipe for measurements upstream of the dump plane. Inlet flow disturbances were eliminated when measurements in the combustor section were performed, by replacing the quartz window with a plug having the same radius of curvature as the inlet pipe. Similarly, on the combustor section, an air-cooled quartz window used for LDV measurements was assembled on a flexible mount (combination of springs & bolts) to allow for the differential thermal expansion of the quartz and the metal surfaces.

The water cooled stainless steel combustor was conceptually and physically identical to the plexiglas rig used earlier by Favaloro et al., 1989. However, new design methodologies were implemented to allow stable and continuous combustor operation over long periods of time. For the current experiment, four side-injector tubes were utilized for premixed studies. The ports were aligned to point toward the downstream direction. This configuration provided premixed conditions and attenuated flow oscillations, while eliminating flashback over the range of operating conditions reported here. To ignite the fuel/air mixture, two spark plugs, flush mounted 180 degrees apart in the step face, were used.

SUMMARY AND CONCLUSIONS

A detailed experimental investigation was carried out to determine the effects of combustion on the flowfield characteristics of a model ramjet engine. The study also described the low frequency vortex-driven pulsating combustion modes and the nature of the pressure oscillations observed in the flowfield. The results showed the significant effects of combustion on the development of sudden expansion dump combustor flowfield. For example, the mixing layer, inferred by velocity measurements, shifted towards the combustor wall. As a result, corner

recirculation region length decreased by approximately 44%, see Figure 1. This was accompanied by a much faster flow recovery, i.e., flat velocity and turbulence profiles not far from the dump plane.

Systematic manipulation of the combustion instability frequencies showed that the resonant period of the oscillation is determined by the sum of the vortex convection in the combustor and the acoustic feedback time of the inlet, see Figure 2. For shorter combustors, the oscillations were more intense and their frequencies were higher. Similar effects were noticed when the reference inlet velocity was increased.

Further detailed and refined data should become available in the near future. Future studies will include the effects of combustion on the flowfield characteristics of combustors with inlet swirling flows.

ACKNOWLEDGEMENTS

The authors would like to thank Messrs John Hojnacki and Charlie Smith for their continuous support. Special thanks goes to the Air Force Office of Scientific Research and to Dr Julian Tishkoff for providing sponsorship.

REFERENCES

1. Favaloro, S.C , Nejad, A.S., Ahmed, S. A., Miller, T., and Vanka, S. P., "An Experimental and Computational Investigation of Isothermal Swirling Flow in an Axisymmetric Dump Combustor," AIAA Paper No. 89-0620, 1989.

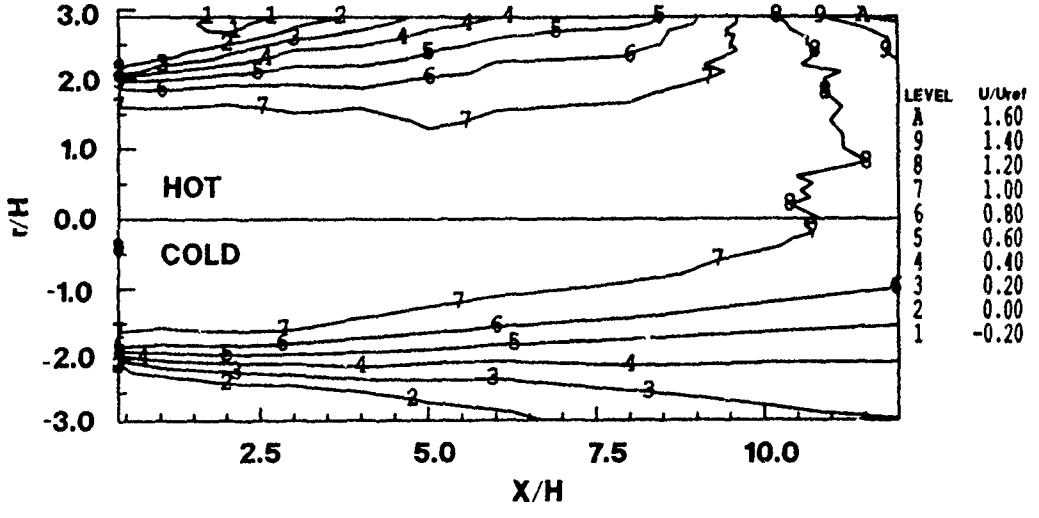

Fig. 1. Contours of Mean Axial Velocity, ϕ = 0.65

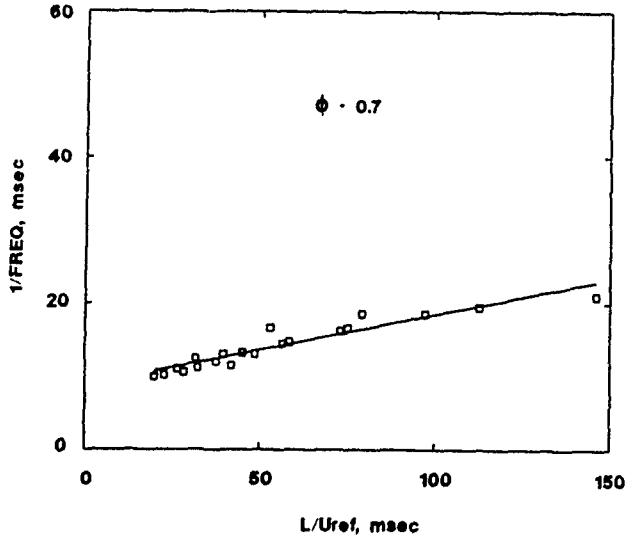

LIST OF AUTHORS